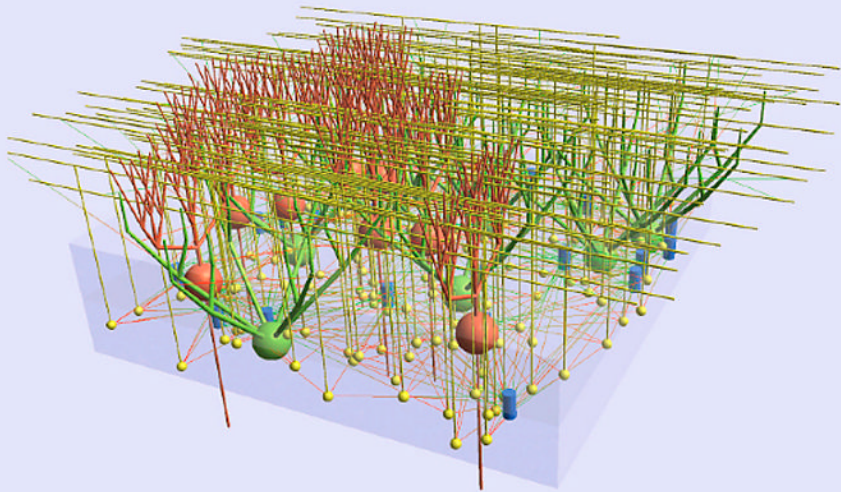


# Computational Neuroscience in **Epilepsy**



*Edited by* Ivan Soltesz • Kevin Staley



# COMPUTATIONAL NEUROSCIENCE IN EPILEPSY

*For Susie, Caiden and Patti*

*This book is also dedicated to the memory of Angel Alonso (1957–2005), who inspired us with his original ideas, fundamental discoveries, generosity, vision and his unyielding pursuit of the secrets of normal and epileptic neuronal excitability.*

# COMPUTATIONAL NEUROSCIENCE IN EPILEPSY

EDITED BY

IVAN SOLTESZ AND KEVIN STALEY



AMSTERDAM • BOSTON • HEIDELBERG • LONDON • NEW YORK • OXFORD  
PARIS • SAN DIEGO • SAN FRANCISCO • SINGAPORE • SYDNEY • TOKYO

Academic Press is an imprint of Elsevier



Academic Press is an imprint of Elsevier  
84 Theobald's Road, London WC1X 8RR, UK  
525 B Street, Suite 1900, San Diego, California 92101-4495, USA  
30 Corporate Drive, Suite 400, Burlington, MA 01803, USA

First edition 2008

Copyright © 2008, Elsevier Inc. All rights reserved.

Cover illustration taken from an image supplied by Padraig Gleeson and R. Angus Silver

No part of this publication may be reproduced or transmitted in any form or by any means, electronic or mechanical, including photocopy, recording, or any information storage and retrieval system, without permission in writing from the publisher.

Permissions may be sought directly from Elsevier's Science & Technology Rights Department in Oxford, UK: phone: (+44) (0) 1865 843830; fax (+44) (0) 1865 853333; email: [permissions@elsevier.com](mailto:permissions@elsevier.com). Alternatively you can submit your request online by visiting the Elsevier web site at <http://elsevier.com/locate/permissions>, and selecting *Obtaining permission to use Elsevier material*

Notice

No responsibility is assumed by the publisher for any injury and/or damage to persons or property as a matter of products liability, negligence or otherwise, or from any use or operation of any methods, products, instructions or ideas contained in the material herein. Because of rapid advances in the medical sciences, in particular, independent verification of diagnoses and drug dosages should be made

**Library of Congress Cataloging-in-Publication Data**

A catalog record for this book is available from the Library of Congress

**British Library Cataloguing in Publication Data**

A catalogue record for this book is available from the British Library

ISBN 978-0-12-373649-9

For information on all Academic Press publications  
visit our web site at [www.books.elsevier.com](http://www.books.elsevier.com)

Printed and bound in the United States of America

08 09 10 11 12 10 9 8 7 6 5 4 3 2 1

Working together to grow  
libraries in developing countries

[www.elsevier.com](http://www.elsevier.com) | [www.bookaid.org](http://www.bookaid.org) | [www.sabre.org](http://www.sabre.org)

ELSEVIER BOOK AID International Sabre Foundation

# CONTENTS

---

CONTRIBUTORS	IX
FOREWORD	XIII
RISE OF THE MACHINES – ON THE THRESHOLD OF A NEW ERA IN EPILEPSY RESEARCH	
DANIEL H. LOWENSTEIN	
INTRODUCTION: APPLICATIONS AND EMERGING CONCEPTS OF COMPUTATIONAL NEUROSCIENCE IN EPILEPSY RESEARCH	XV
IVAN SOLTESZ AND KEVIN STALEY	

## PART I

---

### COMPUTATIONAL MODELING TECHNIQUES AND DATABASES IN EPILEPSY RESEARCH

1 SIMULATION OF LARGE NETWORKS: TECHNIQUE AND PROGRESS	3
WILLIAM W. LYTTON, MARK STEWART AND MICHAEL HINES	
2 THE NEURON SIMULATION ENVIRONMENT IN EPILEPSY RESEARCH	18
N.T. CARNEVALE AND MICHAEL HINES	
3 THE CoCoDAT DATABASE: SYSTEMATICALLY ORGANIZING AND SELECTING QUANTITATIVE DATA ON SINGLE NEURONS AND MICROCIRCUITRY	34
JONAS DYHRFJELD-JOHNSEN AND ROLF KÖTTER	
4 VALIDATING MODELS OF EPILEPSY	43
KEVIN STALEY, WALDEMAR SWIERCZ AND KRZYSZTOF J. CIOS	
5 USING NEUROCONSTRUCT TO DEVELOP AND MODIFY BIOLOGICALLY DETAILED 3D NEURONAL NETWORK MODELS IN HEALTH AND DISEASE	48
PADRAIG GLEESON, VOLKER STEUBER AND R. ANGUS SILVER	
6 COMPUTATIONAL NEUROANATOMY OF THE RAT HIPPOCAMPUS: IMPLICATIONS AND APPLICATIONS TO EPILEPSY	71
DEEPAK ROPIREDDY, SUSAN E. BACHUS, RUGGERO SCORCIONI AND GIORGIO A. ASCOLI	

---

**PART II**

---

**EPILEPSY AND ALTERED NETWORK TOPOLOGY**

- 7 MODELING CIRCUIT ALTERATIONS IN EPILEPSY: A FOCUS ON MOSSY CELL LOSS AND MOSSY FIBER SPROUTING IN THE DENTATE GYRUS 89  
VIJAYALAKSHMI SANTHAKUMAR
- 8 FUNCTIONAL CONSEQUENCES OF TRANSFORMED NETWORK TOPOLOGY IN HIPPOCAMPAL SCLEROSIS 112  
ROBERT J. MORGAN AND IVAN SOLTESZ
- 9 MULTIPLE-SCALE HIERARCHICAL CONNECTIVITY OF CORTICAL NETWORKS LIMITS THE SPREAD OF ACTIVITY 132  
MARCUS KAISER

---

**PART III**

---

**DESTABILIZATION OF NEURONAL NETWORKS**

- 10 COMPUTER SIMULATIONS OF SODIUM CHANNEL MUTATIONS THAT CAUSE GENERALIZED EPILEPSY WITH FEBRILE SEIZURES PLUS 143  
JAY SPAMPAANO AND ALAN L. GOLDIN
- 11 GAIN MODULATION AND STABILITY IN NEURAL NETWORKS 155  
FRANCES S. CHANCE
- 12 NEOCORTICAL EPILEPTIFORM ACTIVITY IN NEURONAL MODELS WITH BIOPHYSICALLY REALISTIC ION CHANNELS 168  
WIM VAN DRONGELEN, AMBER MARTELL AND HYONG C. LEE
- 13 CORTICOthalamic FEEDBACK: A KEY TO EXPLAIN ABSENCE SEIZURES 184  
ALAIN DESTEXHE
- 14 MECHANISMS OF GRADED PERSISTENT ACTIVITY: IMPLICATIONS FOR EPILEPSY 215  
ERIK FRANSÉN
- 15 SMALL NETWORKS, LARGE NETWORKS, EXPERIMENT AND THEORY – CAN WE BRING THEM TOGETHER WITH OSCILLATIONS, HETEROGENEITY AND INHIBITION? 232  
FRANCES K. SKINNER AND ERNEST HO

---

**PART IV**

---

**HOMEOSTASIS AND EPILEPSY**

16	STABILITY AND PLASTICITY IN NEURONAL AND NETWORK DYNAMICS ASTRID A. PRINZ	247
17	HOMEOSTATIC PLASTICITY AND POST-TRAUMATIC EPILEPTOGENESIS MAXIM BAZHENOV, ARTHUR R. HOUWELING, IGOR TIMOFEEV AND TERRENCE J. SEJNOWSKI	259

---

**PART V**

---

**MECHANISMS OF SYNCHRONIZATION**

18	SYNCHRONIZATION IN HYBRID NEURONAL NETWORKS JOHN A. WHITE AND THEODEN I. NETOFF	281
19	COMPLEX SYNAPTIC DYNAMICS OF GABAERGIC NETWORKS OF THE HIPPOCAMPUS GIANMARIA MACCAFERRI	288
20	EXPERIMENTAL AND THEORETICAL ANALYSES OF SYNCHRONY IN FEEDFORWARD NETWORKS ALEX. D. REYES	304
21	MODULATION OF SYNCHRONY BY INTERNEURONS: INSIGHTS FROM ATTENTIONAL MODULATION OF RESPONSES IN THE VISUAL CORTEX PAUL H.E. TIESINGA AND CALIN I BUIA	317

---

**PART VI**

---

**INTERICTAL TO ICTAL TRANSITIONS**

22	CELLULAR AND NETWORK MECHANISMS OF OSCILLATIONS PRECEDING AND PERHAPS INITIATING EPILEPTIC DISCHARGES ROGER D. TRAUB, DIEGO CONTRERAS AND MILES A. WHITTINGTON	335
23	TRANSITION TO ICTAL ACTIVITY IN TEMPORAL LOBE EPILEPSY: INSIGHTS FROM MACROSCOPIC MODELS F. WENDLING AND P. CHAUVEL	356
24	UNIFIED MODELING AND ANALYSIS OF PRIMARY GENERALIZED SEIZURES P.A. ROBINSON, M. BREAKSPEAR AND J.A. ROBERTS	387
25	A NEURONAL NETWORK MODEL OF CORTICOthalamic OSCILLATIONS: THE EMERGENCE OF EPILEPTIFORM ABSENCE SEIZURES PIOTR SUFFCZYNSKI, STILIYAN KALITZIN AND F.H. LOPES DA SILVA	403

26	EXTRACELLULAR POTASSIUM DYNAMICS AND EPILEPTOGENESIS FLAVIO FRÖHLICH, IGOR TIMOFEEV, TERENCE J. SEJNOWSKI AND MAXIM BAZHENOV	419
27	SLOW WAVES ASSOCIATED WITH SEIZURE ACTIVITY ANATOL BRAGIN AND JEROME ENGEL JR	440

## PART VII

### SEIZURE DYNAMICS

28	DYNAMICS OF EPILEPTIC SEIZURES DURING EVOLUTION AND PROPAGATION CHRISTOPHE C. JOUNY AND GREGORY K. BERGEY	457
29	ARE CORRELATION DIMENSION AND LYAPUNOV EXPONENTS USEFUL TOOLS FOR PREDICTION OF EPILEPTIC SEIZURES? YING-CHENG LAI, IVAN OSORIO, MARK G. FREI AND MARY ANN F. HARRISON	471
30	TOWARDS A DYNAMICS OF SEIZURE MECHANICS STEVEN J. SCHIFF, JOHN R. CRESSMAN, ERNEST BARRETO AND JOKŪBAS ŽIBURKUS	496

## PART VIII

### TOWARDS COMPUTER-AIDED THERAPY

31	PRINCIPLES AND PRACTICE OF COMPUTER-AIDED DRUG DESIGN AS APPLIED TO THE DISCOVERY OF ANTIEPILEPTIC AGENTS DONALD F. WEAVER	515
32	COMPUTATION APPLIED TO CLINICAL EPILEPSY AND ANTIEPILEPTIC DEVICES JAVIER ECHAUZ, STEPHEN WONG, OTIS SMART, ANDREW GARDNER, GREGORY WORRELL AND BRIAN LITT	530
33	MICROELECTRODE-BASED EPILEPSY THERAPY: A HYBRID NEURAL PROSTHESIS INCORPORATING SEIZURE PREDICTION AND INTERVENTION WITH BIOMIMETIC MAINTENANCE OF NORMAL HIPPOCAMPAL FUNCTION MICHELLE L. STEPHENS, DENNIS D. SPENCER, IDIL CAVUS, MIN-CHI HSIAO, DONG SONG, SAM A. DEADWYLER, ROBERT E. HAMPSON, DAVID PUTZ, JORGE E. QUINTERO, MERIEM K. BENSALEM-OWEN, KEVIN N. HASUP, ERIN C. RUTHERFORD, B. KEITH DAY, JUSTIN R. NICKELL, FRANCOIS POMERLEAU, PETER HUETTL, JASON J. BURMEISTER, POOJA M. TALAULIKER, VASILIS Z. MARMARELIS, JOHN J. GRANACKI, THEODORE BERGER AND GREG A. GERHARDT	559

# CONTRIBUTORS

---

**Giorgio A. Ascoli** Krasnow Institute for Advanced Study, George Mason University, Fairfax, VA

**Susan E. Bachus** Krasnow Institute for Advanced Study, George Mason University, Fairfax, VA

**Ernest Barreto** Krasnow Institute for Advanced Study, Department of Physics and Astronomy, George Mason University, Fairfax, VA

**Maxim Bazhenov** The Salk Institute for Biological Studies, La Jolla, CA

**Meriem K. Bensalem-Owen** Department of Neurology, University of Kentucky College of Medicine, Lexington, KY

**Theodore Berger** Department of Biomedical Engineering, Program in Neuroscience, Center for Neural Engineering, University of Southern California, Los Angeles, CA

**Gregory K. Bergey** Department of Neurology, The Johns Hopkins Hospital, Baltimore, MD

**Anatol Bragin** Department of Neurology, Brain Research Institute, David Geffen School of Medicine at UCLA, Los Angeles, CA

**M. Breakspear** School of Psychiatry, University of NSW and The Black Dog Institute, Randwick, NSW, Australia

**Calin I Buia** Department of Physics and Astronomy, Computational Neurophysics Laboratory, University of North Carolina at Chapel Hill, Chapel Hill, NC

**Jason J. Burmeister** Center for Microelectrode Technology, Morris K. Udall Parkinson's Disease Research Center of Excellence, University of Kentucky College of Medicine, Lexington, KY

**N.T. Carnevale** Department of Neurobiology, Yale University, New Haven, CT

**Idil Cavus** Departments of Neurosurgery, Psychiatry, Yale University School of Medicine, New Haven, CT

**Frances S. Chance** University of California at Irvine, Irvine, CA

**Krzysztof J. Cios** University of Colorado at Denver, Health Sciences Center, Denver, CO

**Diego Contreras** Department of Neuroscience, University of Pennsylvania School of Medicine, Philadelphia, PA

**John R. Cressman** The Krasnow Institute for Advanced Learning, Department of Physics, Penn State University, University Park, PA

**B. Keith Day** Anatomy and Neurobiology, Center for Microelectrode Technology, Morris K. Udall Parkinson's Disease Research Center of Excellence, University of Kentucky College of Medicine, Lexington, KY

**Sam A. Deadwyler** Department of Physiology and Pharmacology, Center for Neurobiological Investigation of Drug Abuse, Wake Forest University, Winston-Salem, NC

**Alain Destexhe** Integrative and Computational Neuroscience Unit (UNIC), CNRS, Gif-sur-Yvette, France

**Jonas Dyhrfjeld-Johnsen** Department of Anatomy & Neurobiology, Irvine Hall, University of California, Irvine CA

**Javier Echauz** BioQuantix Corp., Atlanta, GA

**Jerome Engel Jr** Department of Neurology, Neurobiology, Psychiatry Biobehavioral Sciences and Brain Research Institute, David Geffen School of Medicine at UCLA, Los Angeles, CA

**Erik Fransén** School of Computer Science and Communication, Royal Institute of Technology, Stockholm, Sweden

**Mark G. Frei** Flint Hills Scientific L.L.C., Lawrence, Kansas

**Flavio Fröhlich** The Salk Institute for Biological Studies, La Jolla, CA

**Andrew Gardner** BioQuantix Corp., Atlanta, GA

- Greg A. Gerhardt** Anatomy and Neurobiology, Center for Microelectrode Technology, Morris K. Udall Parkinson's Disease Research Center of Excellence, University of Kentucky College of Medicine, Lexington, KY
- Padraig Gleeson** Department of Physiology, University College London, London, UK
- Alan L. Goldin** Departments of Microbiology & Molecular Genetics and Anatomy & Neurobiology, University of California at Irvine, Irvine, CA
- John J. Granacki** Information Sciences Institute, University of Southern California, Los Angeles, CA
- Robert E. Hampson** Department of Physiology and Pharmacology, Wake Forest University, Winston-Salem, NC
- Mary Ann F. Harrison** The Institute for Scientific Research, Inc., Fairmount, WV
- Kevin N. Hascup** Anatomy and Neurobiology, Center for Microelectrode Technology, Morris K. Udall Parkinson's Disease Research Center of Excellence, University of Kentucky College of Medicine, Lexington, KY
- Michael Hines** Department of Computer Science, Yale University, New Haven, CT
- Ernest Ho** Department of Physiology, University of Toronto, Toronto Western Research Institute, University Health Network, Ontario, Canada
- Arthur R. Houweling** The Salk Institute for Biological Studies, La Jolla, CA
- Min-Chi Hsiao** Department of Biomedical Engineering, Program in Neuroscience, Center for Neural Engineering, University of Southern California, Los Angeles, CA
- Peter Huettl** Center for Microelectrode Technology, Morris K. Udall Parkinson's Disease Research Center of Excellence, University of Kentucky College of Medicine, Lexington, KY
- Christophe C. Jouny** Department of Neurology, The Johns Hopkins Hospital, Baltimore, MD
- Marcus Kaiser** School of Computing Science, Newcastle University, Newcastle upon Tyne, UK
- Stiliyan Kalitzin** Stichting Epilepsie Instellingen Nederland, Heemstede, The Netherlands
- Rolf Köller** Section Neurophysiology & Neuroinformatics, Department of Cognitive Neuroscience, Nijmegen, The Netherlands
- Ying-Cheng Lai** Department of Electrical Engineering, Department of Physics and Astronomy, Arizona State University, Tempe, Arizona
- Hyong C. Lee** Department of Pediatrics, The University of Chicago, Chicago, IL
- Brian Litt** Department of Neurology and Bioengineering, University of Pennsylvania, Pittsburgh, PA
- F.H. Lopes da Silva** Section Neurobiology, Swammerdam Institute for Life Sciences, University of Amsterdam, Amsterdam, The Netherlands
- William W. Lytton** Department of Physiology, Pharmacology and Neurology, SUNY Downstate Medical Center, Brooklyn, New York
- Gianmaria Maccaferri** Department of Physiology, Northwestern University Feinberg School of Medicine, Chicago, IL
- Vasilis Z. Marmarelis** Department of Biomedical Engineering, Program in Neuroscience, Center for Neural Engineering, University of Southern California, Los Angeles, CA
- Amber Martell** Department of Pediatrics, The University of Chicago, Chicago, IL
- Robert J. Morgan** Department of Anatomy and Neurobiology, University of California, Irvine CA
- Theoden I. Netoff** Department of Biomedical Engineering, University of Minnesota, Minneapolis, MN
- Justin R. Nickell** University of Kentucky College of Pharmacy, Lexington, KY
- Ivan Osorio** Department of Neurology, University of Kansas Medical Center, Kansas City, Kansas
- Francois Pomerleau** Center for Microelectrode Technology, Morris K. Udall Parkinson's Disease Research Center of Excellence, University of Kentucky College of Medicine, Lexington, KY
- Astrid A. Prinz** Department of Biology, Emory University, O. Wayne Rollins Research Center, Atlanta, GA
- David Putz** AD-TECH® Medical Instrument Corporation, Racine, WI
- Jorge E. Quintero** Center for Microelectrode Technology, Morris K. Udall Parkinson's Disease Research Center of Excellence, University of Kentucky College of Medicine, Lexington, KY
- Alex D. Reyes** Center for Neural Science, New York University, New York, NY
- J.A. Roberts** School of Physics and Brain Dynamics Center, Westmead Millenium Institute, University of Sydney, Westmead, NSW, Australia
- P.A. Robinson** School of Physics and Brain Dynamics Center, Westmead Millenium Institute, University of Sydney, Westmead, NSW, Australia
- Deepak Ropireddy** Krasnow Institute for Advanced Study, George Mason University, Fairfax, VA
- Erin C. Rutherford** Anatomy and Neurobiology, Center for Microelectrode Technology, Morris K. Udall Parkinson's Disease Research Center of Excellence, University of Kentucky College of Medicine, Lexington, KY

- Vijayalakshmi Santhakumar** Department of Neurology, UCLA School of Medicine, Los Angeles, CA
- Steven J. Schiff** Center for Neural Engineering, Departments of Neurosurgery, Engineering Science and Mechanics, and Physics, The Pennsylvania State University, University Park, PA
- Ruggero Scorcioni** Krasnow Institute for Advanced Study, George Mason University, Fairfax, VA
- Terrence J. Sejnowski** The Salk Institute for Biological Studies, La Jolla, CA
- R. Angus Silver** Department of Physiology, University College London, London, UK
- Frances K. Skinner** Toronto Western Research Institute, University Health Network, Department of Medicine (Neurology), Physiology and IBBME, University of Toronto, Ontario, Canada
- Otis Smart** Department of Electrical and Computer Engineering, Georgia Institute of Technology, Atlanta, GA
- Ivan Soltesz** Department of Anatomy and Neurobiology, University of California, Irvine CA
- Dong Song** Department of Biomedical Engineering, Program in Neuroscience, Center for Neural Engineering, University of Southern California, Los Angeles, CA
- Jay Spampinato** Department of Neurology, David Geffen School of Medicine, UCLA, Los Angeles, CA
- Dennis D. Spencer** Department of Neurosurgery, Yale University School of Medicine, New Haven, CT
- Kevin Staley** Department of Neurology, Massachusetts General Hospital, Harvard Medical School, Boston, MA
- Michelle L. Stephens** Anatomy and Neurobiology, Center for Microelectrode Technology, Morris K. Udall Parkinson's Disease Research Center of Excellence, University of Kentucky College of Medicine, Lexington, KY
- Volker Steuber** School of Computer Science, Science and Technology Research Institute, University of Hertfordshire, Hatfield, Herts, UK
- Mark Stewart** Department of Physiology, Pharmacology and Neurology, SUNY Downstate Medical Center, Brooklyn, New York
- Piotr Suffczynski** Laboratory of Biomedical Physics, Institute of Experimental Physics, Warsaw University, Warsaw, Poland
- Waldemar Swiercz** Department of Neurology, Boston, MA
- Pooja M. Talauliker** Anatomy and Neurobiology, Center for Microelectrode Technology, Morris K. Udall Parkinson's Disease Research Center of Excellence, University of Kentucky College of Medicine, Lexington, KY
- Paul H.E. Tiesinga** Department of Physics and Astronomy, Computational Neurophysics Laboratory, University of North Carolina at Chapel Hill, Chapel Hill, NC
- Igor Timofeev** Centre de recherche Université Laval Robert-Giffard, Unité de neurobiologie cellulaire, Beauport (Québec), Canada
- Roger D. Traub** Departments of Physiology and Pharmacology, and Neurology, SUNY Downstate Medical Center, Brooklyn, NY
- Wim van Drongelen** Department of Pediatrics, The University of Chicago, Chicago, IL
- Donald F. Weaver** Departments of Medicine (Neurology), Chemistry and Biomedical Engineering, Dalhousie University, Halifax, Nova Scotia, Canada
- F. Wendling** INSERM U642, Laboratoire Traitement du Signal et de L'Image, Université de Rennes, Rennes, France
- John A. White** Departments of Bioengineering and Physiology, Brain Institute, University of Utah, Salt Lake City, UT
- Miles A. Whittington** School of Neurology, Neurobiology and Psychiatry, University of Newcastle, Newcastle, UK
- Stephen Wong** Department of Neurology and Bioengineering, University of Pennsylvania, Pittsburgh, PA
- Gregory Worrell** Department of Neurology, Mayo Clinic, Rochester, MN
- Jokūbas Ziburkus** Department of Biology and Biochemistry, University of Houston, Houston, TX

This page intentionally left blank

# FOREWORD

## RISE OF THE MACHINES – ON THE THRESHOLD OF A NEW ERA IN EPILEPSY RESEARCH

---

DANIEL H. LOWENSTEIN

Recognizing the danger of projecting historical context on the present, I believe the world of epilepsy is at something of a crossroads. The maladies of seizures and epilepsy have been recognized for at least 5000 years and no one can doubt that the past century has brought astonishing advances in our understanding of the nervous system and many of the ways it can be perturbed. And yet, when one considers our current state of the care of the patient with epilepsy and tries to identify advances in epilepsy research that have translated into new and effective therapies, there does not seem to be too much to celebrate of late.

In terms of the treatment of epilepsy, consider this. The first, true ‘drugs’ that were effective and relatively specific as a treatment of epilepsy, phenobarbital and phenytoin, were introduced more than 80 years ago. A dry spell ensued until the discovery of carbamazepine and valproic acid as epilepsy treatments in 1960s and 1970s and this was followed by the introduction of more than 10 new antiepileptic drugs in the last 15 years or so. Most clinicians would agree that the current drug armamentarium offers more choices than ever before, there are some drugs that are easier to use due to less drug–drug interactions and simpler metabolism, and there may be slightly less overall toxicity. Nonetheless, the process of choosing a particular medication for a given patient remains, in many cases, an educated guess, and it is close to impossible to predict whether the drug will be effective in controlling the patient’s seizures and whether the patient will suffer side-effects.

Even with the new drugs, there has thus far been no indication that the overall success of treating epilepsy has changed in a major way. Some 30% of patients with epilepsy do not respond to antiepileptic drugs, used either singly or in combination. And a substantial number of patients, including those with and without seizure control, suffer significant side-effects from their medications, including fatigue, imbalance, mental slowing and simply not feeling like their normal selves. Epilepsy surgery, introduced in the mid part of the twentieth century, has certainly been an extremely useful treatment for selected patients who fail to respond to antiepileptic drugs, and the number of true ‘cures’ has grown as more clinicians recognize the use of surgery as a therapeutic option and patients have more access to this type of high-level care. However, this approach is not always effective, especially when patients are followed for more than the first few years after surgery. Furthermore, we are still trying to understand the extent of morbidity when, for example, we excise the entire anterior temporal lobe for the treatment of refractory temporal lobe epilepsy, knowing that we are removing presumably healthy brain tissue in an effort to ablate the seizure focus.

What about progress on the research front? There have been many successes over the past 80 years or so that have advanced our understanding of the pathophysiology of epilepsy. These include the discovery of the electroencephalogram in the 1920s, the characterization of the ‘paroxysmal depolarization shift’ in the 1950s, creation of new animal models using electrical stimulation, chemoconvulsant drugs and kindling protocols, application of advanced imaging techniques to identify the anatomical and functional substrate of a seizure focus, and recognition of the myriad of changes in ‘plasticity’ of neurons and glia at multiple levels ranging from molecules to synapses to neural networks. And many scientists would agree that progress in the area of epilepsy genetics has been astounding, given that it was only ten years ago that the first true human epilepsy gene was discovered and we now know the causative mutation for a variety of human epilepsy syndromes having Mendelian forms of inheritance.

And yet, for all these advances in epilepsy research, it is difficult to point to many examples where the discoveries have been translated into major advances in the care of patients. True, the identification of the principal neurotransmitters

and receptors involved in the epileptic network has helped focus our attention on the development of appropriately targeted drugs. However, as noted above, there has not yet been a recent, major breakthrough in drug development, despite the attempts at more rational drug design. In fact, of all the research advances that have been made in the last 90 years, I think the two that have seen the greatest translation into clinical practice have been the use of various forms of electroencephalography and high resolution brain imaging to identify the electrophysiologic and anatomical basis of a patient's seizure disorder.

So, why have we not made more headway? Our lack of progress is explained, I believe, by the current technological barriers that are keeping us from understanding the nature of the biological complexity of the mammalian brain. There is no question that everything but the most rudimentary behaviors of our nervous system is a consequence of the activity of large, intricate neural networks. To be sure, we are beginning to get a handle on complex behaviors of individual neurons or small networks. The discovery of long-term potentiation (LTP), for example, and the unraveling of its molecular and structural basis, constitute a major advance that seems likely to aid in our eventual understanding of human memory. The same can be said about the sophisticated and elegant molecular underpinnings of olfaction, or the hierarchical properties of visual perception. However, in the world of epilepsy, although we can measure the electrical activity of individual neurons in a seizure focus, we are at a loss to explain precisely how the hyperexcitability and hypersynchronization of a seizure focus actually develops, or why a seizure spreads. We do not understand how a focal brain insult transforms a previously normal region of brain into one capable of generating seizures. And even more elusive has been any real comprehension of the factors that determine when a seizure occurs in a brain that seems to function entirely normally the vast majority of the time. In my opinion, the ultimate answers to these questions will come only through the discovery and application of new methods for measuring the precise activity of thousands if not tens of thousands of brain cells simultaneously and *in vivo*. This is unlikely to happen anytime soon, at least not in the next few years.

Until then, our best hope for major breakthroughs in understanding the complexity of epilepsy is in the study of high fidelity models of seizures in large neural networks. And here, of course, is where the world of computational biology and informatics is already making its mark. As so elegantly described in the pages that follow, mathematicians, engineers and computer scientists are creating an *in silico* world that is providing new insights into the potential mechanisms of such phenomena as synchronization, seizure spread and transition states. They are modeling the problem at every level, from individual ion channel subunits to large populations of neurons, limited mainly by the development of new approaches in bioinformatics and the computational capacity of machines. Given the consistent acceleration of advances in both of these areas, you are about to be dazzled by a first-look at the initial stages of an exciting, new era in epilepsy research. Enjoy!

# INTRODUCTION

## APPLICATIONS AND EMERGING CONCEPTS OF COMPUTATIONAL NEUROSCIENCE IN EPILEPSY RESEARCH

---

IVAN SOLTESZ AND KEVIN STALEY

Epilepsy, a neurological disorder that affects millions of patients world-wide, arises from the concurrent action of multiple pathophysiological processes. Modern epilepsy research revealed short- and long-term alterations at several levels of neuronal organization in epilepsy, from single amino acid mutations in ion channels and neurotransmitter receptors to large-scale reorganizations of neuronal networks. The power of mathematical analysis and computational modeling can be harvested to facilitate the understanding of the relative importance of such multifaceted, seizure-related changes taking place within highly non-linear and complex neuronal systems, with implications for both basic and clinical epilepsy research. A major goal of this book is to summarize the current ideas and explore future directions of the emerging discipline of computational epilepsy research by presenting chapters addressing relevant basic questions (e.g. neuronal gain control) as well as long-standing, critically important clinical challenges (e.g. seizure prediction). The timeliness of the current volume is indicated by the rapidly increasing number of epilepsy-related papers that employ computational neuroscience techniques, as well as by the similarly high number of lectures, sessions, workshops and symposia devoted to computational epilepsy research at recent meetings organized by the American Epilepsy Society (<http://www.aesnet.org/>), the Gordon Research Conferences (<http://www.grc.org/>; see the recently established, bi-annual Gordon conference on ‘Mechanisms of Epilepsy and Neuronal Synchronization’) and by the Society for Neuroscience (<http://www.sfn.org/>). Similar upward trends can also be observed at regional neuroscience conferences, e.g. at the Southern California Joint Symposium on Neural Computation (<http://www.jsnc.caltech.edu/>) and the Chicago-area conference on complexity (<http://www.northwestern.edu/nico/complexity-conference/>).

The primary target audiences for this book are the graduate students, postdoctoral fellows and faculty-level researchers involved in basic and clinical epilepsy research. In addition to this primary audience, the book should also appeal to a number of other groups, including clinicians working in neurology and epilepsy, computational neuroscientists interested in applications of modeling techniques to clinically relevant problems, and biomedical engineers. The book, demonstrating how this exciting, novel, cross-disciplinary area of modern science can be used to understand the normal and pathological network functions in the brain, should be also appealing and accessible to computer science and biology undergraduates as well.

Although there are several excellent books on computational neuroscience, biophysics of single neurons, ion channels, and epilepsy, there has been no attempt at presenting a volume dedicated to the recent achievements of the emerging discipline of computational epilepsy research. Therefore, the current book is aimed to fill an empty niche in presenting, in a single volume, the various, wide-ranging, cross-disciplinary applications of computational neuroscience in epilepsy, from computational techniques and databases to potential future therapies. The format of the book is multiauthor, where experts from various fields related to computational epilepsy research contributed chapters. Many of the contributors have been working on epilepsy-related topics as their major field of research. However, in order to highlight the true power and potential of computational neuroscience in epilepsy, there are also chapters in the book from computational neuroscientists whose main research focus has not been traditionally epilepsy and seizures. On the other end of the spectrum, we also included a chapter that discusses experimental evidence and not a computational model per se, with the idea that computational approaches can be applied to the problem in the future to understand mechanisms of seizure generation. We believe that such novel, fertile ideas from inter-disciplinary fields can enormously benefit epilepsy research in general, and computational epilepsy research in particular.

As outlined in the Contents, the individual chapters and sections are organized in a (hopefully) logical fashion, with each section building on the previous one. We hope that the interested reader will appreciate the great diversity of topics and the array of novel insights provided by the various chapters. The chapters, in a certain sense, provide real, living testimonials to the lasting impact and penetrating ideas of the early giants of modeling (e.g. David Marr). At the same time, many chapters in the current book also demonstrate the amazingly short time delays between the original publications of novel, fertile ideas from fields that are seemingly unrelated to epilepsy (e.g. the graph theoretical breakthroughs concerning small-world and scale-free networks by Duncan Watts, Steven Strogatz and László Barabási) and their incorporation into specific research projects involving computational neuroscience and epilepsy.

The first section of the book is a pragmatic evaluation of currently available computational techniques and databases. Lytton and colleagues describe the progress in modeling techniques that have improved our understanding of complex atmospheric interactions that create weather and will hopefully provide similar improvements in our understanding of the network dynamics that underlie epilepsy. One of the salient challenges (and opportunity) facing computational neuroscientists is determining where tradeoffs should be made between complexity, realism and speed in a world where computational resources continue rapidly to evolve. One of the chief architects of that evolution for neuroscience has been the team of Carnevale and Hines, responsible for the development of the NEURON modeling environment. They describe the features and capabilities of this unique tool, which is utilized by many of the authors in this book. Of course, before a modeling environment is used, one needs to assemble a myriad of details regarding the function and connectivity of the neurons that are being modeled. Dyhrfjeld-Johnsen and Kötter provide a new advance that addresses this formidable task. They describe an open searchable database that can be used to find and store anatomical and neurophysiological data relevant to the creation of a realistic neural network. This information-sharing effort parallels similar efforts in genetics and represents another critical step in the wider utilization of computational models to study diseases of the brain, including epilepsy. After a model is built and run successfully, it is tempting in epilepsy research to be satisfied with a typically epileptic output. Staley and colleagues sound a note of caution and remind us that the parameters of network models far exceed the complexity of the output, so that validation of epilepsy models is an important goal, albeit one that is not always immediately feasible. Another approach to the problem of producing models that closely correspond to reality is to increase the accuracy of the model, and this requires ever more detailed knowledge of neuronal connectivity.

Gleeson and colleagues provide an important new advance with the introduction of NeuroConstruct, a graphical user interface that enables meaningful network simulations to be created using combinations of NEURON and Genesis modeling environments without prior knowledge of the scripting languages. NeuroConstruct also enables the expansion of network architecture into three dimensions, which improves connectivity maps and makes possible more realistic diffusional analyses. This important new tool is likely to be widely adopted, which may provide the additional advantage of the availability of models that are not so heavily dependent on their creator so that they can be easily adopted by others and compared between investigators. Ropireddy and colleagues provide a preview of an interesting new dataset in which the anatomical relationships of neurons will provide much more accurate data from which to construct connectivity maps in computational models.

The second section of the book moves from creation of accurate models of neural networks to models of epileptic neural networks. Santhakumar provides interesting insights into development of a large-scale model of an epileptic network. While a vast amount of information has been published regarding cell types and connectivity of the neurons in the hippocampal dentate gyrus, there are still many difficult decisions to be made regarding the features of alternative models, computational feasibility and limits of knowledge that must be addressed in the course of building the model. Morgan and Soltesz discuss their large-scale models of the dentate to examine the effects of known anatomical alterations in acquired epilepsy (cell loss and axon sprouting) on network connectivity and input/output function. They find a transition from a both globally and locally connected (small world) network structure to a more regular network structure only with extreme values of cell loss and subsequent sprouting of new network connections. This alteration in network structure occurs at a level of cell loss at which the dentate becomes subject to epileptiform activity. These findings demonstrate insights into how cell loss and sprouting affect network structure and function that are not easily developed from either examination of the neuronal anatomy or the electrophysiology of the dentate. Kaiser expands this analysis to ask how the nature of connections between neural structures, such as adjacent cortical columns, affects the flow of activity between structures. He finds that modular networks stably sustain activity through a wider range of parameters than randomly connected networks. Thus, one of the organizational principles of the brain, the division of cortex into many smaller and more heavily interconnected subregions such as barrels and columns, may represent an anticonvulsant mechanism.

The section addressing the stability of neural networks begins with the work of Spamanato and Goldin describing the wide variety of sodium channel mutations that cause the epileptic syndrome termed ‘Generalized Epilepsy with Febrile

'Seizures Plus'. No unifying proconvulsant mechanism emerged from the study of the biophysical properties of the different channel mutations in various expression systems, but modeling demonstrated that the mutations shared a common trait: they increased the ability of neurons to fire multiple action potentials. This is an excellent example of how modeling can illuminate a mechanism that is not at all evident from the experimental data. A similarly unique insight from modeling is provided by Chance, who describes how synaptic noise can reduce the gain and increase the stability of the input/output relationships of neuronal networks. She suggests that one function of recurrent collateral synapses may be to provide this noise. This provides an interesting perspective on the mechanism of epilepsy in deafferented networks seen in undercut cortex and models employing cytotoxic episodes of status epilepticus – is the reduced network stability related to the reduced deafferentation or to instabilities that arise as neurons attempt to recreate the background noise level via the sprouting of recurrent collateral synapses? One of the least obvious conclusions in the book is provided by Van Drongelen and colleagues, who employ the Argonne Labs supercomputers to run a detailed model of the neocortex. They demonstrate that reductions in excitatory synaptic coupling have effects not predicted from the traditional balance of excitation and inhibition. Rather, they find that reductions in excitatory synaptic strength can be proconvulsant. These surprising findings deserve further scrutiny and are congruent with Spamanato and Goldin's findings on epileptogenic sodium channel mutations.

Destexhe reviews a decade of work that has demonstrated the role of gamma-aminobutyric acid ( $\text{GABA}_B$ ) receptors in the pathogenesis of absence epilepsy. The cooperativity inherent in  $\text{GABA}_B$  receptor activation, in which the receptors only activate when large amounts of GABA are released, allow this receptor to function as an intensity detector. When corticothalamic synaptic volleys reach a threshold intensity level,  $\text{GABA}_B$  receptors are activated, driving neuronal membrane potentials to negative values where rebound firing can occur. The threshold activation of  $\text{GABA}_B$  receptors produces the characteristically abrupt switch from spindling to 3 Hz spike and wave activity. This work was perhaps the first to demonstrate how modeling can elucidate unsuspected mechanisms of epileptogenesis; in this case, how GABA-mediated inhibition can fail by virtue of becoming too intense rather than too weak. There are many other features of neurons that, while important for signal processing, are also capable of destabilizing the network. The chapter by Fransén provides such an example, the neuronal non-specific cation channel. This channel activates very slowly, enabling the integration of inputs over timescales much longer than the neuron's time constant. However, the sustained firing induced by this current has also been demonstrated to be capable of triggering seizure activity when the current is uniformly activated in a network, as for example occurs experimentally when certain pharmacological agonists are applied to the preparation. Understanding the nature of these slow conductances and their regulation may therefore provide important new insights into mechanisms of epileptogenesis. The impact of the  $\text{GABA}_B$  threshold and the non-specific cation conductance on neuronal input/output curves can potentially be understood from simple neuronal models, although large scale models are necessary to determine how such effects are multiplied through the network. Skinner and Ho use such an approach to analyzing the modeling epileptic networks. They begin with 2-cell networks in which the parameter space can be efficiently searched and then use that knowledge to build larger networks. In the third stage, these networks are evaluated in terms of their correspondence to experimental data. The authors point out that there are still many parameter interactions that could arise in the larger networks that are not predicted from the smaller networks, but this approach has the advantage of providing a feasible and efficient means by which to search for the parameters that have the most profound effects.

The concept of neuronal homeostasis is a recent development in synaptic physiology and network dynamics that has important implications for epilepsy research. This section begins with a thought-provoking chapter by Prinz, who considers two conflicting network requirements: plasticity, or the capacity for learning, and stability, reflected in homeostatic mechanisms that restore the neuron's activity to its target level following a variety of perturbations. She speculates that the inherently destabilizing effects of synaptic plasticity could lead to epilepsy if there were genetic or acquired defects in homeostatic mechanisms such as synaptic scaling and modifications of intrinsic conductances. Bazhenov and colleagues address the possibility that, in some circumstances, epilepsy may arise as a consequence of synaptic homeostasis, in which neurons maintain their average activity level by responding to a perturbation in their inputs with an oppositely directed change in overall synaptic weight or voltage-gated conductance. If the original perturbation is a decrease in afferent input as a consequence of cortical injury, homeostatic processes might result in increases in the strength of recurrent excitation or decreases in local inhibition; this might maintain average neuronal firing but at the cost of destabilizing the network when the perturbing alteration in afferent input is too great. The authors suggest that under these conditions, external stimulation might be antiepileptogenic; this is quite a timely idea in light of the gathering empirical interest in brain stimulation as a treatment for epilepsy.

The work of Prinz and Bazhenov and colleagues raise another interesting function of neuronal homeostasis in relation to epilepsy. In response to plasticity that strengthens synapses, homeostatic mechanisms reduce overall excitation and are

clearly anticonvulsant. However, once epilepsy is established, homeostatic mechanisms may underlie the phenomenon of medical intractability, in which every anticonvulsant drug can establish only transient control of the seizure propensity. This might occur if homeostatic mechanisms operated to increase neuronal excitability in the face of the new anticonvulsant.

The section on mechanisms of synchronization begins with a chapter by White and Netoff, who use phase-response analysis to study synchronization of neural networks. This technique measures the impact of weak synaptic inputs on the timing of periodically firing neurons. Maccaferri employs a variety of computational techniques including conductance clamping and simulation to overcome experimental limitations to our understanding of the effects of GABA-mediated synaptic conductances on action potential timing. He uses these techniques to study the role of interneuron inputs in the timing of spikes in principal cells during epileptiform activity, and the impact of electrical coupling of interneurons. These data provide an interesting insight into the determinants of the fine structure of epileptiform activity, which is sometimes overlooked when model outputs look sufficiently epileptiform.

Reyes harnesses advances in models of diffusion to examine the appearance and spread of synchrony in neural networks. The synchronizing effects of common inputs and homogeneous interspike intervals must be offset to stabilize the network. One effective method was the addition of inhibitory interneurons. These results underscore the vulnerability of networks that are disinhibited as a consequence of loss of interneurons and additionally subjected to powerful common inputs as a consequence of interictal EEG spikes. The section concludes with a chapter by Tiesinga and Buia that analyzes attentional processes in the visual cortex to provide new insights into mechanisms of cortical synchronization. They find that inhibitory feedforward interactions between classes of interneurons can effectively induce synchronization by selectively reducing the output of interneurons that provide feedback inhibition of principal cells. Injuries to subclasses of principal cells and interneurons are known to occur in the acquired epilepsies, and these results illustrate an interesting proconvulsant mechanism that may be associated with such selective cell loss.

One of the most disabling aspects of epilepsy is the unpredictable timing of the attacks. Thus, the study of interictal to ictal transitions is important not only for the mechanistic insights that might be provided but also in light of potential clinical applications for seizure detection and warning. Roger Traub, one of the founders of computational modeling of epilepsy, and his colleagues address interictal to ictal transitions and consider whether pre-ictal activity in the form of very fast oscillations may be responsible for state-dependent changes in ion concentrations that subsequently lead to more generalized seizure activity. Gap junctions between axons are evaluated as a potential mechanism for these fast, pre-ictal oscillations. This chapter addresses the potentially very important role of transitional activity in the genesis of ictal activity; this represents an interesting and promising new field of investigation.

The three subsequent chapters utilize mean field models to examine transitions from normal to epileptic states. Wendling and Chauvel describe interictal to ictal transitions in temporal lobe epilepsy. The authors begin with a lucid discussion of the development of the mean-field model, in which the activities of populations of cells are summarized by mean inhibitory and excitatory currents and mean action potential outputs. They find that the structure of hippocampal ictal EEG recordings required the addition of a second, parallel group of interneurons, in order accurately to reproduce the fast rhythmic activity seen at the onset of temporal lobe seizures. This analysis demonstrates that models with very restricted elements can capture salient features of epilepsy. Simplified models serve the important function of focusing attention on those parameters that most heavily influence the structure of the network output during a seizure. Robinson and colleagues utilize the mean-field model to understand state transitions to and from seizures. They demonstrate that this model is well suited to efficient analysis of EEG data. The key strength of this approach is the insight provided into the nature of interictal-ictal transitions. Suffczynski and co-authors also analyze transitions between normal and synchronous thalamocortical activity and demonstrate that such transitions could occur as random state transitions in a bistable network. The transitions from normal to pathological activity are a property of epileptic networks that deserve further study. This work raises two interesting possibilities that deserve further study. First, transitions to ictal activity are not predictable from the prior state of the network and, second, ictal to normal state transitions can be effected by very limited stimuli.

Fröhlich and colleagues address these activity-dependent changes in models of extracellular potassium accumulation during intense synaptic activity that begin to elucidate how activity-dependent changes can lead to the spread of seizure activity as well as to cessation of ictal activity. The modeling suggests that ongoing synchronous activity occurs within a restricted range of excitation and inhibition, and activity-dependent alterations in intra- and extracellular ion concentrations can drive inhibition into or out of the range that supports network synchrony. This work provides new insights into state transitions that may occur uniquely in injured, gliotic cortical areas in which ion homeostasis is likely to be altered. Bragin and Engel present challenging new electrophysiological data regarding slow waves that occur before, during and after seizures. These slow waves may provide novel insights into the pathophysiology of seizure onset spread and termination

and represent a fruitful new area for modelers interested in the roles of the collapse of ion gradients and GABA-mediated inhibition in seizure generation.

The fine structure of seizure activity is analyzed in the section on seizure dynamics. Jouny and Bergey describe the use of computerized methods to track the evolution of a seizure. They discuss both frequency-based measures and clinical measures of seizure evolution and introduce matching pursuit methods that quantify the complexity of the EEG signal. This chapter makes the important point that the evolution of seizure activity is a fundamental aspect of most epilepsies and analysis of this evolution provides a new avenue in which to develop important mechanistic as well as therapeutic insights. Lai and colleagues provide a clear analysis of the applicability of non-linear analyses to seizure description and prediction. Working from basic principles, they analyze EEG datasets and reach the conclusion that non-linear techniques are not more effective than methods based on autocorrelation and do not provide effective tools for seizure detection. They go on to point out potential difficulties such as spurious autocorrelation arising from oversampling in recent publications that have suggested that non-linear analysis is more useful. This thoughtful evaluation is useful to those less familiar with non-linear analysis. It is also a fine example of how careful analysis can avoid pitfalls inherent in the application of powerful new techniques and reminds us of the care that must be employed in ascertaining that intriguing new results are fundamentally sound. The section concludes with a chapter by Schiff and colleagues that analyzes recordings from multiple neurons during epileptiform activity evoked by the convulsant 4 aminopyridine. They point out that the idea of ictal increases in neuronal synchronization may not be absolute. They correct the cross-correlation of activities between neurons for the level of endogenous activity in each neuron and point out that after this correction, in some frequency windows synchronization may decrease during seizures. This thought-provoking chapter indicates that the importance of considering intrinsic excitability versus network effects is relevant not only to developing computational models but also to the analysis of electrophysiological data.

Looking to the future, the final section addresses computer-aided therapies. Weaver describes computer-assisted modeling of anticonvulsant drugs. The selection of targets, the modeling of the structure of small anticonvulsant molecules and predictions of their interaction with targets are reviewed. This is a clear summary of the impact of computational methods on the future of drug design. Of course, drug design must begin with a useful target and computational models of epileptic networks will help identify novel targets for rationale drug design. In the second chapter in this section, Echauz and colleagues provide an insightful, in-depth discussion of the process of seizure detection and prediction. Beginning with EEG acquisition, the chapter presents cutting-edge EEG data processing and computational approaches to seizure detection and pre-emption. The final chapter presents some blue-sky thinking as Stephens and colleagues describe efforts towards closed-loop seizure detection and real-time focal therapy coupled with an artificial hippocampus. The idea not only to abort seizures but also replace the function of the damaged, epileptic hippocampus can only be described as bold, and of course, futuristic. Nevertheless, the authors describe impressive progress on multiple fronts, especially in the development of glutamate-sensing electrodes that couple spike detection and measurements of local glutamate concentration to detect seizures. These chapters illustrate the tremendous potential of computational models and provide some guesses as to where the future may lie.

We hope that this volume will encourage young scientists to think about harnessing the ever-increasing power of computational modeling techniques to solve major challenges facing epilepsy research. As hurricanes can be predicted with increasing precision, perhaps one day epilepsy researchers will also be able to forecast increases in the probability of occurrence of seizures, with enormous benefit to patients. Similarly, futuristic implantable devices may also be able to assist drug therapies to control epileptic neuronal network activity. Nobody can predict the future, but the future can be made a little bit less distant if bright young graduate students and postdoctoral fellows enter this field and dare to dream about all of these ideas. As demonstrated by several chapters in this book, computational modeling techniques are becoming more and more user-friendly, which should encourage even the less mathematically minded experimental researchers to test their ideas using the armamentarium of computational models. Indeed, experimental and computational approaches cross-fertilize in a way that has not been possible before. Experimental techniques offer ever-increasing precision in quantitative measurements on neuronal and network structures and physiological parameters concerning ion channels, synapses and ensemble neuronal activity during both normal and epileptic behaviors. Close integration of hard experimental data into computational models offers the possibility of building highly realistic models of brain areas, as illustrated by several chapters in the current volume (see also the ‘Blue Brain Project’, <http://bluebrain.epfl.ch/>). Such ‘reverse-engineering’ of the brain will provide new insights into complex, frequently intractable dynamical diseases such as epilepsy. As briefly mentioned above, the success of experimental neuroscience has demonstrated beyond any doubt that, in most experimental models of epilepsy, many parameters change simultaneously and highly realistic models have proven to be uniquely helpful in pinpointing the key parameter changes that truly determine the altered network behaviors.

This page intentionally left blank

PART

I

---

COMPUTATIONAL MODELING  
TECHNIQUES AND DATABASES IN  
EPILEPSY RESEARCH

---

This page intentionally left blank

# 1

## SIMULATION OF LARGE NETWORKS: TECHNIQUE AND PROGRESS

WILLIAM W. LYTTON, MARK STEWART AND MICHAEL HINES

### ABSTRACT

Computer models of epilepsy and seizures require simulation of large networks in order to produce emergent phenomenology, but also require inclusion of details of cellular and synaptic physiology to retain connection with pharmacological effectors for therapeutic intervention. The former constraint suggests the use of simplifying approaches: integrate-and-fire models or mean-field approximations. The latter constraint pushes one towards multi-compartment models. Compromise is required. We have developed highly-simplified event-driven complex artificial-cell models that utilize a series of rules to emulate critical underlying phenomena likely important for seizure generation and patterning. These include depolarization blockade, voltage-dependent NMDA activation, afterhyperpolarization and several others. Using these units, we can readily run simulations of 1-2 million units on a single processor. Here, we present results of data-mining 138,240 simulations of a 3,500-unit network. Parameter explorations can then relate single-unit dynamical ‘structure’ to network function. We find that the networks are prone to latch-up, reminiscent of a seizure tonic phase. This can alternate with a slow repetitive clonic-like activity. Parameter dependence of epileptiform features was typically complex. For example, massive initial network response increased with greater unit excitability only in the context of particular AMPA and NMDA strength settings. This consequence of network complexity fits with the multi-site activity of endogenous neuroeffectors and may help explain why ‘dirty’ drugs, those acting at multiple sites, might be particularly effective for seizure control.

### GOALS OF COMPUTER MODELING FOR CLINICAL DISEASE

We use the fruits of computer simulation every day when we consult a weather report. Although weather reporting accuracy remains low for periods of greater than 10 days from the present, the improvement over weather reporting of 50 years ago is striking. The big difference is size: both the size of the data set available for initial conditions and the size of the computers for running the massive simulations that are now used. In the next 50 years we will likely see comparable progress in our ability to:

1. predict seizures
2. understand the genesis of seizures based on alterations in the underlying neurobiological substrate
3. intervene in directed ways to prevent a single seizure or to alter the substrate and prevent seizures from occurring.

Unlike weather simulation, where the underlying factors involved (temperature, wind, humidity) are well characterized and where the interactions are fully understood, the nervous system remains full of under- or uncharacterized neurotransmitters, receptors, second and third messengers and electrical interactions. Also unlike weather, many locations where we would like to measure chemical concentrations or currents are inaccessible. For these reasons, accurate simulation will require growth not only in simulation but also in measuring capabilities.

The hope and expectation is that accurate simulation will lead to rational therapeutics, whether prophylactic or acute, whether pharmacological, electrical or surgical. Acute electrical intervention prior to a seizure is becoming a readily foreseeable scenario with the increasing use of implanted electrodes for other brain diseases. It seems likely that practical efforts in this direction will result from direct analysis of brain signals. Here, modeling will assist by permitting rapid

assessment of many possible stimulation protocols. With regard to prophylaxis, genetic analysis and molecular biology can identify an underlying substrate that predisposes to seizures but cannot trace the dynamical path whereby an abnormality results in a seizure. Characterization of this dynamical pathway, the chain of causality, can identify critical loci where interventions are most practical.

Clinically useful seizure simulations require that connection be made both with clinical observables – the seizure and its electroencephalographic manifestation – and with therapeutic approaches – whether pharmacological or surgical. For this reason, we and others have largely focused on detailed compartmental models which provide explicit modeling of dendritic regions, of voltage-sensitive ion-channel populations and of various synaptic receptor subtypes. These receptors and channels are the targets of pharmacotherapeutic manipulations and can be comparably manipulated in these models. However, simplified alternatives to compartmental models are proving useful for investigation as well.

#### DETAILED VERSUS SIMPLIFYING MODELING

There is a tension between the desire to model as accurately as possible and the desire to simplify, both due to practical limitations of computer size and due to the need to isolate the critical factors and associations that lead to understanding. In the neural modeling literature this tension arises where the study of dynamical systems meets biology.

The most common approach to mathematical modeling of neural systems has involved explicit modeling of individual neurons. However, there is also a long tradition of mean field approaches, utilizing the insights of statistical mechanics. Here, the individual neurons are assumed to be indistinguishable particles whose interactions produce bulk properties, just as the interactions of molecules in a liquid produce the bulk properties familiar from thermodynamics (Wilson and Cowan, 1972). These approaches have lately been applied to epilepsy as well (Wilson et al., 2006).

Moving up toward slightly greater complexity, many followers of the simplifying ethic utilize leaky integrate-and-fire models. These models forego all biological details except for a threshold and a leaky membrane. When the threshold is reached, the cell discharges. The simulated membrane allows inputs to summate while the leakiness permits membrane potential gradually to return to rest after a subthreshold input. At the synapse level, these simulations may utilize instantaneous or brief depolarizing or hyperpolarizing synapses to drive the cell.

N. Brunel and colleagues have been pioneers in studying the dynamics of large networks of leaky integrate-and-fire cells, also using mean field methods to enhance understanding of observed activity patterns (Brunel, 2000; Brunel and Wang, 2003). They identified several different characteristic patterns of firing: asynchronous irregular, asynchronous regular, synchronous irregular and synchronous regular, demonstrating the parameter associations for each of these regimes. In general, firing patterns depended on the strength of network driving and the strength of excitatory connections within the network. They demonstrated that low inhibition states gave fast firing with some coordination and that higher levels of inhibition produced irregular firing that, nonetheless, coordinated in global population oscillations that would produce a high amplitude field potential.

Leaping from these highly simplified models to the other end of the complexity spectrum brings us to the models of Traub and associates (Traub and Wong, 1982; Traub et al., 2005). They pioneered simulations of large networks with detailed compartmental models of the individual neurons. Such compartment models included many details of ion channels, dendritic integration and synaptic dynamics that are omitted from the leaky integrate-and-fire cell models. Compartment models are built by linking up multiple Hodgkin-Huxley parallel-conductance models in trees that reflect the morphology of a real neuron, often one that has been traced microscopically (Figure 1.1). The Hodgkin-Huxley model is comprised of a four state-variable system representing voltage, sodium channel activation, sodium channel inactivation and potassium channel activation. Each additional type of sodium, potassium or calcium channel or synapse in a compartment generally adds from one to three additional state-variables. A somatic compartment (representing the soma or cell body of a neuron) might easily have 10 such channels, while other compartments may have three to four channels. A fully traced neuron may be fairly accurately represented using between 100 and 1000 compartments. Therefore, a full single neuron model with 500 compartments may have 5000–10 000 state-variables corresponding to 5000–10 000 linked ordinary differential equations (ODEs). Although computers have gotten much faster over the past few decades, an accurate simulation of such a model on a desktop computer might still require several minutes to an hour for one second of simulated time, depending on the pattern of activity being observed. Networks corresponding to substantial lumps of brain tissue require the simulation of between one thousand and one million neurons. In many cases, we may also want to do parameter explorations over several hundred to several thousand simulations. Thus, we face the age-old problem: unbounded desire constrained by limited resources.

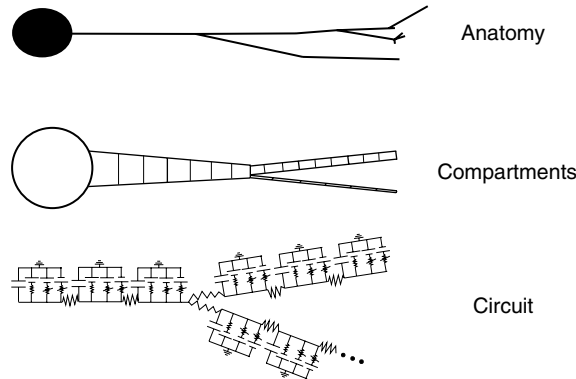


FIGURE 1.1 How to make a compartment neuron.

Compromises must be made. In epilepsy modeling, we need large networks, but we wish to retain connection with membrane physiology. A common approach is to compromise on the number of compartments, sacrificing some of the details of intraneuronal voltage dynamics by reducing representations of each cell from several hundred compartments to between 5 and 20 compartments (Traub and Wong, 1982; Bush and Sejnowski, 1991). A more extreme compromise is to collapse the cell down to only one or two compartments (Pinsky and Rinzel, 1994; Mainen and Sejnowski, 1996).

### NETWORK SIMULATION TECHNIQUE: CONTINUITY AND EVENTS

The heart of realistic neural simulation is the integrator. A major effort in simulator technology has been to optimize integrators to obtain maximal speed without loss of accuracy (Hines, 1989). However, as network simulation has become more important, simulators have been developed that do no integration but instead focus on *events* (Morrison et al., 2005).

Events in the nervous system, as in the rest of nature, occur continuously in time and therefore could be solved using the basic ODE solution methodology typically used for many types of computer simulation applications. However, a short-cut is usually taken: the axon is regarded as a signal delivery system that is not integrated in detail, foregoing the type of axon simulation that was famously done in the original Hodgkin and Huxley work on the squid axon. This classical simulation took many days due to the fact that a ‘computer’ was a woman working a primitive adding machine. (A roomful of these women made up a parallel supercomputer.) Indeed, axon simulation can still take days of supercomputer time if simulated at the level of detail currently available from electron microscopy and single-channel kinetics. Instead of bothering with all of this, the axon is typically reduced to one parameter: a delay. This delay represents the time for action potential transmission from soma to the presynaptic bouton. In some simulations, an additional parameter is used representing the probability of transmission failure (Rhodes, 2006). Synaptic weight is a synaptic property and therefore not an axon parameter.

This short-cut makes neuronal network simulation unusual among the panoply of computer simulation applications. Because nature is continuous in time and space, many computer simulations, like weather, are continuous in time and space. Neuronal network simulations are not spatially continuous since the elemental units of simulation are cells. More importantly, neuronal network simulations are not fully temporally continuous since intermittently occurring spikes trigger events in other neurons. However, the simulation of the individual neuron is a continuous simulation governed by ODE solution.

Hence, neuronal network simulation is a hybrid of multiple continuous simulations interrupted by synaptic events. The approach required for simulating the events, called event-driven simulation, is widely used in industry. Event-driven simulation is used, for example, in internet modeling, where one asks how a packet, following many possible paths through routers, reaches a distant computer. The need to combine event-driven simulation with continuous dynamical (ODE) simulation suggests a variety of approaches, some of which are described below.

### COMPARTMENT CELL TECHNIQUES: VARIABLE STEP METHODS

We have augmented the NEURON simulation system to include a variety of techniques that improve simulation efficiency and allow larger networks to be run in less time. Simulation of the individual neuron, as in other continuous domains, requires the numerical solution of linked ordinary differential equations. These differential equations are of a general form

familiar from kinematics and electricity: e.g. derivative of voltage (change with respect to time) equals some function of voltage, time and other state variables. Groups of linked ODEs typically cannot be solved analytically (i.e. expressed as a function of time). Instead, they are solved approximately on a computer by using small time steps that approximate the infinitely small time step assumed by calculus.

Traditional numerical simulation techniques, some preceding the invention of the computer by centuries, project forward a simulation by a series of fixed time steps. We have been exploiting the CVODES variable time step methods developed by Hindmarsh and collaborators (Cohen and Hindmarsh, 1994; Hindmarsh and Serban, 2002). These allow the time steps to change according to the needs of a simulation. In a neural simulation, this typically means that a time step can increase up to hundreds of milliseconds when a neuron is not firing but drop down into the sub-millisecond range to simulate properly an action potential.

A fixed time-step method suffers two disadvantages: one practical and the other theoretical. The practical issue is speed. The fixed-step method will plod through a simulation at a fixed rate, irrespective of whether the network is spiking furiously or is largely quiet. The variable-step method adapts to the level of activity. Although this can give the variable-step method an advantage during periods of quiet, it may be a significant disadvantage in a network that has a lot of firing. Therefore, the choice of variable-step method or fixed-step method for a particular simulation remains an empirical one.

The theoretical disadvantage of a fixed time-step method is particularly relevant for the case of epilepsy simulation, where issues of synchrony are paramount. A fixed-step imposes an artifactual synchrony on the network by virtue of the fact that all spikes and synaptic activations within the time step must occur at precisely the step boundary. Although this reduction in jitter is slight, it has been shown to alter population activity once it is magnified by network connections (Hansel et al., 1998). This artifactual time locking means that time steps as small as one nanosecond (about one one-millionth the duration of spike and four hundred-thousandth the length of a typical simulation time step) may be required to model accurately spike delivery times when using a fixed-step method (Shelley and Tao, 2001).

Unfortunately, network simulations with variable time-step methods rapidly run into a related problem. Synchrony means that some number of neurons are firing at almost exactly the same time. This produces high event-time densities which results in extremely small time steps. This spike-density crisis occurs with high interconnectivity between synchronous neurons and can lead to time steps being driven down to and below one nanosecond, resulting in performance worse than that of the worst-case fixed-step method noted above. The essential problem is that the integrator is too fastidious, dealing with every spike interval as an individual integration problem, where a fixed-step method would simply aggregate all nearby spikes as occurring in a single moment.

We have considered different approaches to handle this high spike-time density problem. As intimated above, the variable-step method is of the type predictor-corrector, as contrasted with the continuous forward progress of a linear method. Using a predictor-corrector algorithm, the integrator tries out something and then ensures that it is accurate enough before proceeding forward. Although the actual answer and hence the actual error is not known, the error at each step can be approximated by noting gradients of solution convergence with respect to time-step shrinkage. Thus, the voltages and conductances are being assessed at each time step in the continuous neuron integration. However, the issue in an event-driven simulation is not accuracy in voltage but accuracy in time. It would be desirable to produce an error estimate for spike time, but it is not clear how this could be done. Failing this it would, nonetheless, be possible to cut off further accuracy-seeking once the integrator starts making changes that only alter spike times by one microsecond or less, forcing all spikes onto a resolution boundary. We have not yet done investigations in this realm, but have noted that such a minimum interval would permit additional speed-ups through the use of a bin queue for constant-time insertion and removal of events.

The other approach to handling high spike-time density is to break up the problem into multiple integrations. Instead of having one *global* integrator imposing a single global variable time step on the entire problem, we use multiple *local* integrators each of which has its own local variable time step (Lytton and Hines, 2005). This reduces the problem by reducing the density for each integrator, though it does not eliminate it entirely. Additionally, a major advantage to using local variable time step is that each neuron then integrates itself forward at its own rate (Figure 1.2). Active neurons are integrated actively while quiescent neurons do not use any central processing unit (CPU) time. This can produce significant speed-ups in a large network with many interacting subpopulations. On the other hand, busy networks with neurons firing at high rates will likely run faster by stepping through with a consistent fixed time step. Again, the determination of speed-up for any particular simulation is an empirical one.

The major stumbling block in simulation of networks with this method is to ensure that neurons do not run so far ahead that they cannot be influenced by an event. Quiescent neurons can be integrated well forward in time but software must be able to back-track if an event comes in earlier. Fortunately, the CVODES integrator used in NEURON makes it easy

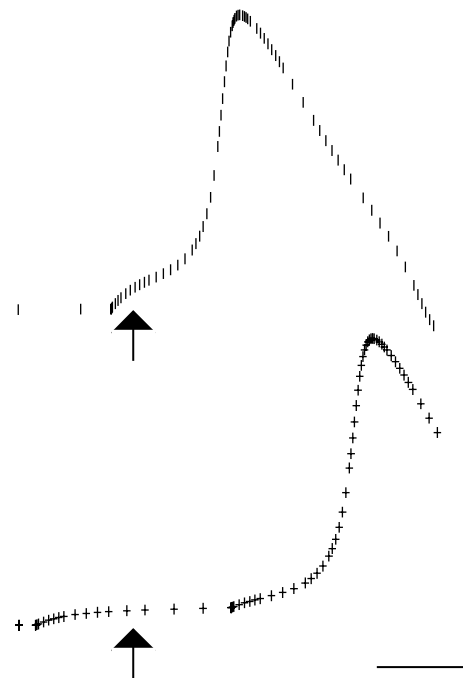


**FIGURE 1.2** Local variable time-step method produces different integration time points for different neurons in a network. As the neuron in upper trace passes through threshold (arrow), time steps are very small (time points close together) near this unstable equilibrium. At the same time the neuron in lower trace is subthreshold and shows large time steps. Note that the peak of the action potential also requires frequent integration. Scale: 1 ms, 20 mV.

to interpolate to any point bounded by the current integration time step. The integration thus lurches forward, integrators back-tracking to pick up spikes as needed.

#### COMPARTMENT CELL TECHNIQUES: SUPERCOMPUTING APPROACHES

Early supercomputers, such as the Cray series, were large CPUs with a lot of memory which could stream in vectors of numbers for simultaneous processing. Modern supercomputers are made up of multiple CPUs, each of which is comparable to a CPU in a laptop which produce speed-ups not by doing more or by spinning faster but by working together. These are therefore considered parallel supercomputers (vector parallelism was used in the earlier supercomputers). We have begun to study expanded versions of a cortical epilepsy model on parallel supercomputers (Figure 1.3; Bush et al., 1999). Thus far, we have used this simulation primarily to improve our supercomputer algorithms, as will now be discussed.

Consideration of the hybrid nature, continuous and event-driven, of neuronal network simulations immediately suggests that they will be amenable to running on modern parallel supercomputers (Hereld et al., 2005; Migliore et al., 2006; Sperelakis and Ramasamy, 2006). Subpopulations of neurons are run on individual processors of the supercomputer and exchange information at intervals. As with the local variable time-step method, care must be taken lest one subpopulation runs too far ahead. This is handled by noting the minimum synaptic delay in the network. This minimum delay represents the maximum interval during which integration can move forward without possibly requiring external information – a spike at the beginning of this interval which must be delivered and consequently integrated at the beginning of the next interval. Within each individual processor, integration of the subpopulation can be performed using either a fixed-or variable-step method.

Speed-up with parallel supercomputers depends on several factors. First, of course, is the number of processors. The size of a ‘supercomputer’ can range from the eight CPUs that can be inexpensively put together in the laboratory to the 2048 CPU and larger behemoths available at national supercomputer centers. Next is the nature of the individual CPUs themselves. There is heterogeneity in CPU speed among machines. Additionally, variation in CPU speed within a single machine can cause unexpected run-time alterations when running across CPUs of different specifications. We found the size of CPU cache to be a critical factor determining run-times. Cache is the onboard memory of the CPU which allows

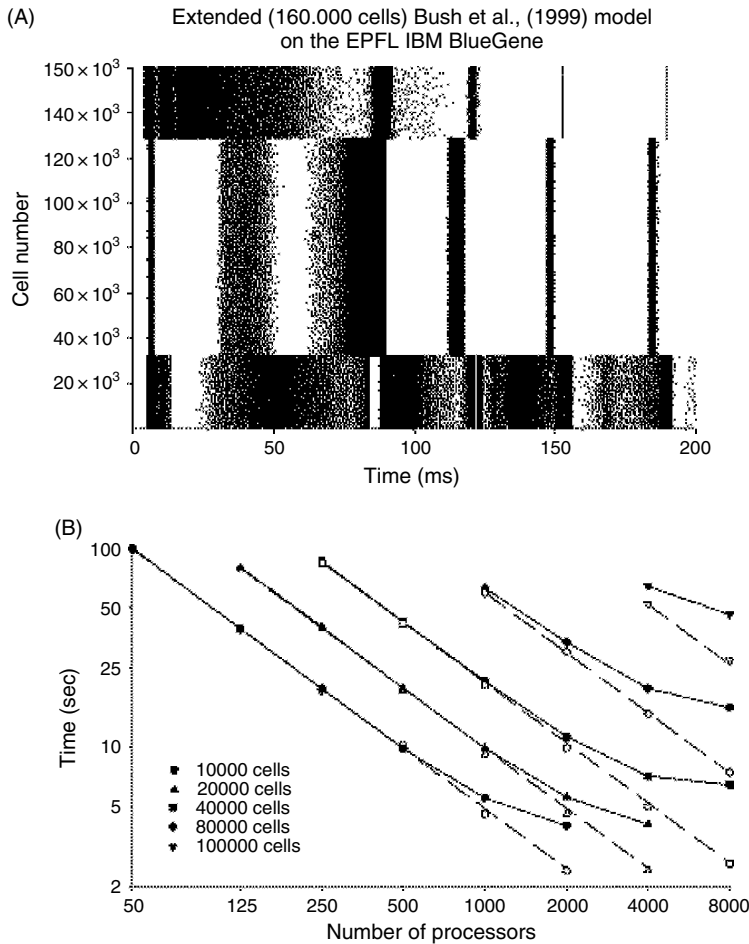


**FIGURE 1.3** Performance of extended Bush et al. simulation (Bush et al., 1999) on parallel supercomputers. (A) Raster plot from a 200 ms 160 000 cell simulation shows development of recurrent synchronous activity most clearly expressed in the regular-spiking excitatory subpopulation (center group). Top group are inhibitory cells and bottom excitatory intrinsically bursting cells. (B) CPU time (open symbols) and total runtime (closed symbols) compared to linear speed-up (dashed lines) for 200 ms simulation. (Reproduced from Bush et al. (1999), Figure 5, with kind permission of Springer Science and Business Media, Copyright Springer Press.)

code and data to be accessed at speeds up to fivefold faster than from main memory (RAM). A simulation that can fit each CPU's apportionment into cache will enjoy a substantial speed-up.

Intrinsic CPU factors are one factor determining simulation speed-up. Another potential factor is organization of the processors – how well can the CPU network run the neuron network? These factors include hardware – how are the CPUs physically connected to one another – and software – how is the network split up into the subpopulations that are assigned to the various CPUs. Although hardware design cannot be readily altered physically, some machines may have software switches that determine the effective connectivity being utilized at a given time. A related design choice occurs when choosing the underlying software protocol used to send information:

1. data can be sent specifically from one CPU to another
2. data can be broadcast from each CPU to all CPUs
3. data can be gathered from all CPUs and then rebroadcast to all CPUs.

In practice, the third option is easiest to implement and appears to be efficient despite the larger amount of data being passed around. However, in any of these cases, there is an advantage to minimizing the size of data-structures carrying the spike-time information among CPUs.

Other factors that involve the layout of subpopulations across CPUs may also play a large role in simulation efficiency. First and most important is load balancing. *A priori*, one does not want to put 10 neurons on one CPU and 1000 neurons on another, but such an apparent imbalance may be desirable in a case where 10 large pyramidal neurons are being run

with 100 active dendritic compartments together in a simulation with 1000 small point neuron interneurons. Similarly, one can envision scenarios where one population of cells fires frequently, require more CPU time and would benefit from being distributed at a lower density. Thus far we have not experimented with these design issues but have simply handed out the neurons to CPUs using a round-robin algorithm, as one uses when dealing cards. Load balance statistics are readily gathered from the supercomputer after a run by looking at wait times for individual CPUs – periods when a CPU had finished its allotted simulation slice and had to wait to ascertain whether there were any inputs (spikes) from neurons in other CPUs. Despite the simple algorithm, load balance has not been a problem until we get down to a few cells per CPU.

Consideration of wait times also leads to another organizational consideration for distributing subpopulations on CPUs. Ideally, cells that wire together should ride together on a CPU so as to minimize off-CPU communications. In addition to the presumably static wiring (assuming here no sprouting during simulation), one would also want to consider here again the dynamics of the simulation. Cells that are firing at high rate will have much more to say and will want to have their follower cells nearby in order to communicate quickly. Of course, any improvements in subpopulation organization will only be valuable if they are supported by the choices made for communication data-structures and inter-CPU data distribution.

### INTEGRATE-AND-FIRE REVISITED: COMPLEX ARTIFICIAL CELLS

This juxtaposition of event-driven and continuous simulation has led several groups to consider circumstances that would allow the time-intensive numerical integration to be jettisoned entirely (Watts, 1994; Mattia and Del Giudice, 2000; Delorme and Thorpe, 2003; Makino, 2003; Rudolph and Destexhe, 2006). The simplest way to do this is to conceive of the neuron as a simple delay mechanism, receiving an event and then reliably producing another event after a certain period of time (Pytte et al., 1991). This retains the influence of the network graph on activity propagation but discards the dynamics of the neuron, including the phenomena of inhibition and of temporal integration. To get these critical phenomena back, we have returned to the integrate-and-fire neuron, revising it to allow it to be processed in an event-driven framework instead of solving it numerically. The resulting model neurons are called artificial cells in NEURON and provide the speed-ups one might expect by going from time steps of 25  $\mu$ s to time steps that largely represent the interval between activity in the network (Carnevale and Hines, 2006).

As noted at the beginning of the chapter, integrate-and-fire models are limited in their usefulness in epileptology or elsewhere in neurobiology since they lack the critical details that permit us to connect the dots from the microworld of genetics and pharmacology (anticonvulsants) to the observables of electrophysiology (EEG) and bulk physiology (fMRI, behavioral alterations and seizures). In order to make these connections, we needed to develop more complex models that are still far simpler and far faster than full compartment models. Approaches to this have included moving from the one-dimensional (one state variable) leaky integrate-and-fire cell model to a two-dimensional model (Izhikevich, 2003, 2004), utilizing a map based model (Rulkov et al., 2004), simplifying within the context of a compartmental model (MacGregor, 1987; Destexhe, 1997), or devising semi-analytic expressions for simulation with integration (Rudolph and Destexhe, 2006).

To bridge simultaneously the performance gap from event-driven to continuous models and the credibility gap between integrate-and-fire neurons and compartmental neurons, we have been developing complex artificial cells that include the details needed to make connection with pharmacology (Lytton and Stewart, 2005, 2006). We do this by progressively adding rules to the three basic rules of a leaky integrate-and-fire neuron:

1. add up the inputs (integrate)
2. slowly relax back to rest in the absence of inputs (leak)
3. trigger an event when threshold is reached (fire).

Typically, standard integrate-and-fire models will also have a fourth rule that will reset the membrane potential to rest after a spike. Each of these rules is controlled by one or more parameters:

1. a synaptic time constant determining the time over which temporal summation will take place (technically a synaptic rather than a cellular parameter but lumped in with the rest of the neuron for convenience)
2. a membrane time constant which also influences temporal integration by determining how long the membrane will stay depolarized or hyperpolarized after an input
3. a threshold voltage above which spiking occurs.

The integrate-and-fire model has a single state variable representing membrane voltage. By contrast, a compartmental model may have 100s of state variables, representing voltage at different locations throughout the dendritic tree, as well as

the conductance states of different ion channels in the soma and dendrites. (It is worth reminding the reader at this point of the difference between parameters and state variables. Parameters are constant values that determine the simulation: e.g. the capacitance or the length of the apical dendrite. States are the dependent variables of ordinary differential equations that vary during the course of the simulation: e.g. voltage.) The far greater complexity of integration for compartmental models is due to the large number of state variables and to the fact that these state variables are linked. The differential equations for most of the state variables include membrane voltage so that any alteration in voltage will change these other state variables which will change voltage which will change more state variables in never-ending loops of positive and negative feedback.

In addition to having more parameters than a leaky integrate-and-fire cell model, the complex artificial cell has more state variables. However, these state variables are not linked to one another, making them far easier to integrate and making it possible to skip numerical integration entirely by updating them as needed using the analytic solution for the single ODE in the context of an event-driven simulation. To create the complex artificial cell model, rules were added to the leaky integrate-and-fire cell model in order to include features thought to be important for neural system dynamics in general and for epilepsy in particular. One of these features is depolarization blockade: a cell will not spike if driven excessively. This feature can be added by including a simple additional rule: a threshold above which spiking does not occur: the cell will fire only within a window between the spike and block thresholds. Clearly, a depolarization blockade threshold is only a very crude approximation to the dynamics of populations of sodium channels leading to depolarization blockade in real neurons. It should here be re-emphasized that the relation of these complex artificial cell models to compartmental models can be taken as that between a sketch and a photograph: reminiscent but without correspondence in detail.

State variables for complex artificial cells can be classified as intrinsic or synaptic. Both types of state variables are handled similarly. In order to avoid linked differential equations, state variables are combined linearly to produce a membrane potential. Membrane potential in this model is therefore a derived value rather than a primary state variable. Four synaptic state variables are maintained in each complex artificial cell: corresponding to excitatory AMPA and NMDA inputs and inhibitory GABA<sub>A</sub> and GABA<sub>B</sub> inputs. (The chemical acronyms AMPA (alpha-amino-3-hydroxy-5-methyl-4-isoxazolepropionic acid), NMDA (N-methyl-D-aspartate), GABA (gamma-aminobutyric acid) are used as a short-hand to refer to receptors with sensitivity to the corresponding compounds.)

The response to an individual synaptic input is a jump in the corresponding state variable. For example, in the case of GABA<sub>A</sub>, weight parameter  $W_{GABA A}$  determines the size of a hyperpolarizing step in state variable  $V_{GABA A}$ . The step is scaled so as to provide a saturation comparable to that which occurs due to the reversal potential with the more realistic conductance change in a compartmental model:  $V_{GABA A}^{step} = W_{GABA A} \cdot \frac{V - E_{GABA A}}{E_{GABA A}}$  ( $E_{GABA A}$  in the denominator is a normalization;  $W_{GABA A}$  is unitless). Following the step,  $V_{GABA A}$  decays with time constant  $\tau_{GABA A}$ . The complex artificial cell utilizes more complex rules for NMDA and GABA<sub>B</sub>. The NMDA mechanism uses standard Mg<sup>++</sup> unblocking equation (Jahr and Stevens, 1990). The GABA<sub>B</sub> mechanism employs a non-linear augmentation with size of presynaptic burst (Destexhe and Sejnowski, 1995).

In addition to the synaptically driven state variables, there is one intrinsic hyperpolarizing state variable (AHP). AHP primarily produces a post-spike afterhyperpolarization ( $I_{AHP}$ , SK channel effect), although it also is used to augment the refractory period ( $I_C$ , BK channel effect). By altering the distance between current voltage and threshold, the AHP state variable produces the same effect as one would get with a varying threshold. Additional intrinsic rules include the aforementioned depolarization blockade and refractory period, post-spike synaptic depression, a bursting mechanism and jitter.

Since the complex artificial cell has no integrator overhead, network simulations depend only on the amount of spiking in the model. At high spiking activity, events may occur with a frequency that is comparable to the time step of a fixed-step integrated model. However, typically only a subset of the neurons, representing only a few equations, need to be updated so that the simulations are still relatively fast.

In a compartment model, physiologically-observable dynamics such as adaptation are dependent on multiple voltage-sensitive ion channels. Each of these voltage-sensitive ion channels has its own parameterization (Borg-Graham, 1991). Changes in channel-level parameters will alter not only the activity aspect of interest but also other neuron-level dynamics. Altering activity in a compartmental model requires manipulations that are two steps removed from the phenomenon of interest. In the complex artificial cell model, a selected neuron dynamic can be altered directly without interfering with other phenomena. For example, the voltage at which depolarization blockade occurs is controlled by a single parameter rather than being a consequence of the density balance for sodium and potassium channels as well as time constants of the state variables determining the dynamics of each.

The complex artificial cell model provides a framework that can incorporate other rules as needed in particular systems where they are thought to be important. For example, some neurons have prolonged bursts with characteristic firing patterns

(Destexhe et al., 1996). These patterns can be incorporated into the rule based either by constructing an analytically calculable dynamical rule or by providing a cut-and-paste spike-form. Similarly, additional rules can be incorporated by providing waveforms copied from electrophysiological records. More flexible rules can be arrived at by emulating the behavior of the more complex compartmental models. In this case, complex artificial cell units can be run together with compartmental simulations in NEURON with use of a fitting algorithm controlling complex artificial cell unit parameters.

A useful additional rule-set would incorporate input/output relations from dendritic inputs. There is considerable debate as to whether dendrites simply provide reach, with all inputs being handled linearly, or provide substantial signal processing. In the latter case, it is possible that the dendrites make the cell into the equivalent of an entire neural network of simplified units (Poirazi et al., 2003). It would be possible to represent dendritic fields as individual complex artificial cell units with separate specialized rule base. A simpler approach would be to take the dendritic transform as a mapping that can be replicated using a multidimensional table look-up.

### EPILEPSY SIMULATION WITH COMPLEX ARTIFICIAL CELLS

We previously referred to the complex artificial cell model as a ‘sketch’ of a neuron. Similarly, network models built with complex artificial cells serve as a network sketch-pad, enabling us rapidly to try many architectures and parameters. Activity sketches that look promising can then be re-evaluated with more complex models, both full compartment models and hybrid networks, comprised of both compartment and complex artificial cell neurons. Hybrid networks use the local time-step method so as to allow the compartment models to be individually integrated while the event-driven complex artificial cells take up no integrator time and jump from event to event as before.

The highly coordinated firing that underlies both normal activity and seizures is a generic property of model networks. Excitatory connections spread firing across a network. The activation can then be coordinated into repetitive activity by the modulating or sculpting effects of inhibition (Lytton and Sejnowski, 1991). Other networks will show incoherent firing with minimal correlations between spikes of individual neurons. We explore parameter changes to see how these effect particular patterns at the network level.

We designed a simple network sketch to illustrate an organizational principle that applies to both slice and *in vivo* epileptogenesis: a subset of cells or a separate brain area provides activation, provoking activity in a set of follower cells that express a seizure (Dudek et al., 1999; Meeren et al., 2002; Van Drongelen et al., 2003; Dominguez et al., 2005). We make the distinction between drivers (provokers) and expressors of epileptic activity to use this organizational principle without specifying whether we are considering local or remote activation. The network was therefore made up of three cell populations:

1. an excitatory population which was made spontaneously active in order to play the role of a driver of activity  
(‘drivers’,  $N_D = 100$  for small network or  $N_D = 1000$  for large network)
2. a larger excitatory population which then expresses epileptiform activity (‘expressors’,  $N_E = 1000$  or  $N_E = 2000$ )
3. an inhibitory population (inhibitors,  $N_I = 250$  or  $N_I = 500$ ).

In addition to ongoing activation from the drivers, the networks are typically activated by a global ‘shock’ which activates about half of the cellular elements simultaneously (Figure 1.4). The expressor cells are the major contributors to the simulated field potential. The drivers (bottom row) have an average firing rate of 2 Hz. Despite random inputs, structure is created in the field due to the tendency of random coincident input to produce brief activation chains that involve a large and changing proportion of the expressors.

Evaluation of simulations showed that excessive excitatory connectivity could easily lead to a *latch-up* (tonic) condition where expressor cells all fire at high rates, at or near the maximum rate allowed by the refractory period. Figure 1.5A shows a network that immediately ramps up to maximal firing in the expressors (E) cells. This activity eventually gives way to a brief period of intermittent (clonic) activity and then returns to tonic activity.

We explored the conditions that would terminate or trigger the latch-up condition. In Figure 1.5B, a slow-building AHP provided a hyperpolarizing influence that terminated the latch-up condition. Figure 1.5C demonstrates that a slow-building depolarization, here caused by NMDA, can lead to latch-up. The apparent dynamic duality of tonic triggering and tonic turn-off hides a distinction with regard to event timing. The gradual build-up in the intrinsic AHP state-variable reliably terminated tonic activity after an interval that depended on the time constant and strength (density) parameters for AHP in the individual cells. By contrast, the timing of the triggering of the tonic state by NMDA activation was far more variable, depending not only on the NMDA parameters (synaptic strength and time constant) but, more importantly, on the coincidence of random inputs that simultaneously pushed a critical number of cells above threshold. This distinction

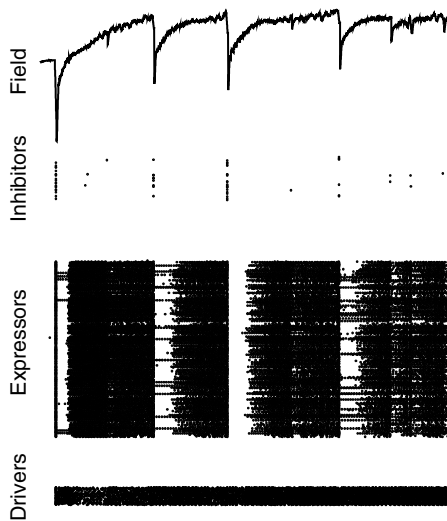


**FIGURE 1.4** Raster plots showing neuron action potentials for three classes of cells during one second of epileptiform activity in a sample network. Simulated field primarily reflects activity in the expressor cells. Note simultaneous activation of multiple cells coincident with first large field potential corresponding to shock stimulation near beginning of trace.

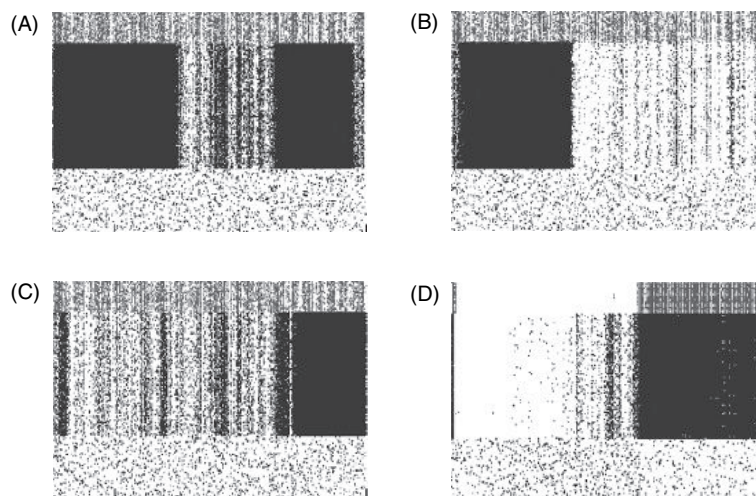


**FIGURE 1.5** Raster plots of 1 s of 3500 cell network simulations. (See text for details.)

between a ramped versus triggered transition did not strictly follow the difference between intrinsic and synaptic parameters, however. Figure 1.5D shows a ramped transition to tonic activity based on the wearing off of synaptic activation associated with a  $\text{GABA}_B$  mechanism. Although  $\text{GABA}_B$  is a powerful inhibitory mechanism that tends to silence the network, in this case the silencing would be the triggered mechanism while the latch-up would be predictable ramped release response.

#### SIMULATION DATA-MINING

Scientific data-mining is a process of seeking patterns among the enormous amounts of data generated by modern scientific techniques. Data-mining infrastructure originally developed in business, where accounting and legal information collected over decades was found to be a valuable resource, a figurative gold-mine of data. In the scientific realm, similar techniques have been developed and adapted over the past decade as massive information veins associated with the genomes of human, fly, mouse and others have come on-line. The complexity of our simulations with the mass production of thousands or millions of simulations for further study has led us to develop a data-mining resource within the simulator environment.

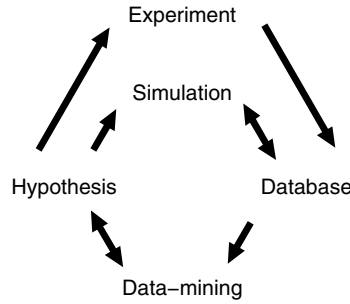


FIGURE 1.6 Simulation and experiment produce massive amounts of data to be stored, managed and analyzed.

We have been using our data-mining system to analyze data from both electrophysiology and simulation, to organize simulation parameters and to relate parameters to simulation results. The large amounts of data involved makes data-mining an explicit endeavor that lies at the juncture of simulation, experiment and hypothesis generation (Lytton, 2006). Figure 1.6 illustrates the use of simulation as a partner to experiment. Data flows out of experiment and simulation into databases from where it is mined to generate hypotheses that can be tested by further experiment or additional simulation. Simulation not only generates data but is also a consumer of data (two-headed arrow at right): a massive parameter complex must be managed and refined by repeated simulation. These parameters are stored in tables that relate to the tables storing simulation output. The need for data-mining implies the luxury of having so much data that it will never be fully explored. In this setting, a new hypothesis will, in some cases, be first assessed by simply looking back at the data already obtained (two-headed arrow at left) in order to determine whether an experiment or simulation already performed provides additional supporting data for that hypothesis.

We have used our data-mining software to evaluate 138 240 parameter sets for the network described above. We evaluated 12 synaptic parameters and two intrinsic parameters (threshold and AHP strength). Various parameter combinations produce a wide variety of responses as indicated by field potential (Figure 1.7). Due to storage limitations, we are only able to save field potentials and not raster plots or single cell spike trains. Several patterns of activity are apparent: spike-and-wave, low-amplitude irregular activity, high-amplitude irregular spiking, and oscillatory responses.

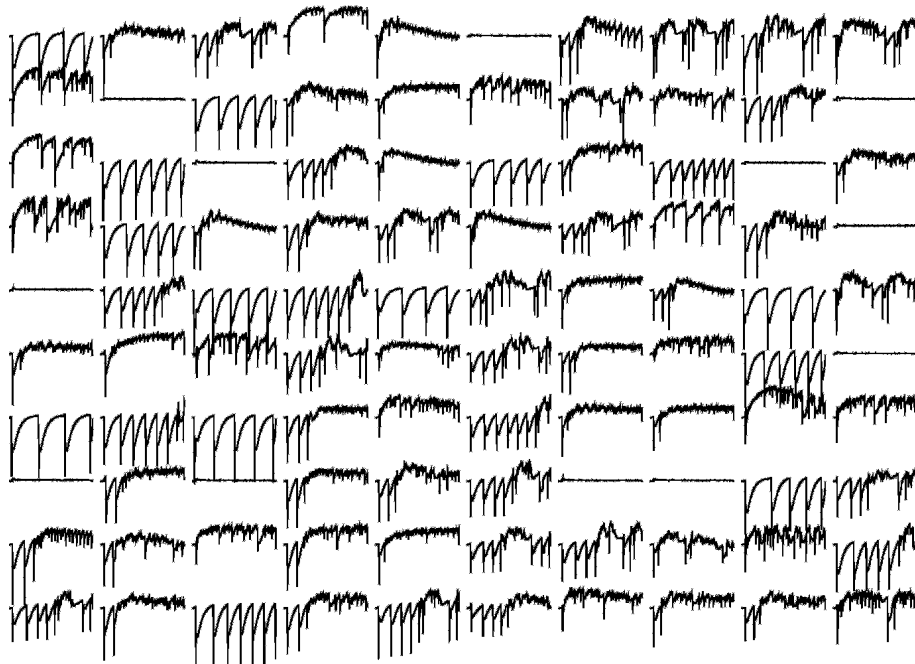


FIGURE 1.7 100 simulated electrographic field traces from 138 240 simulation parameter exploration.

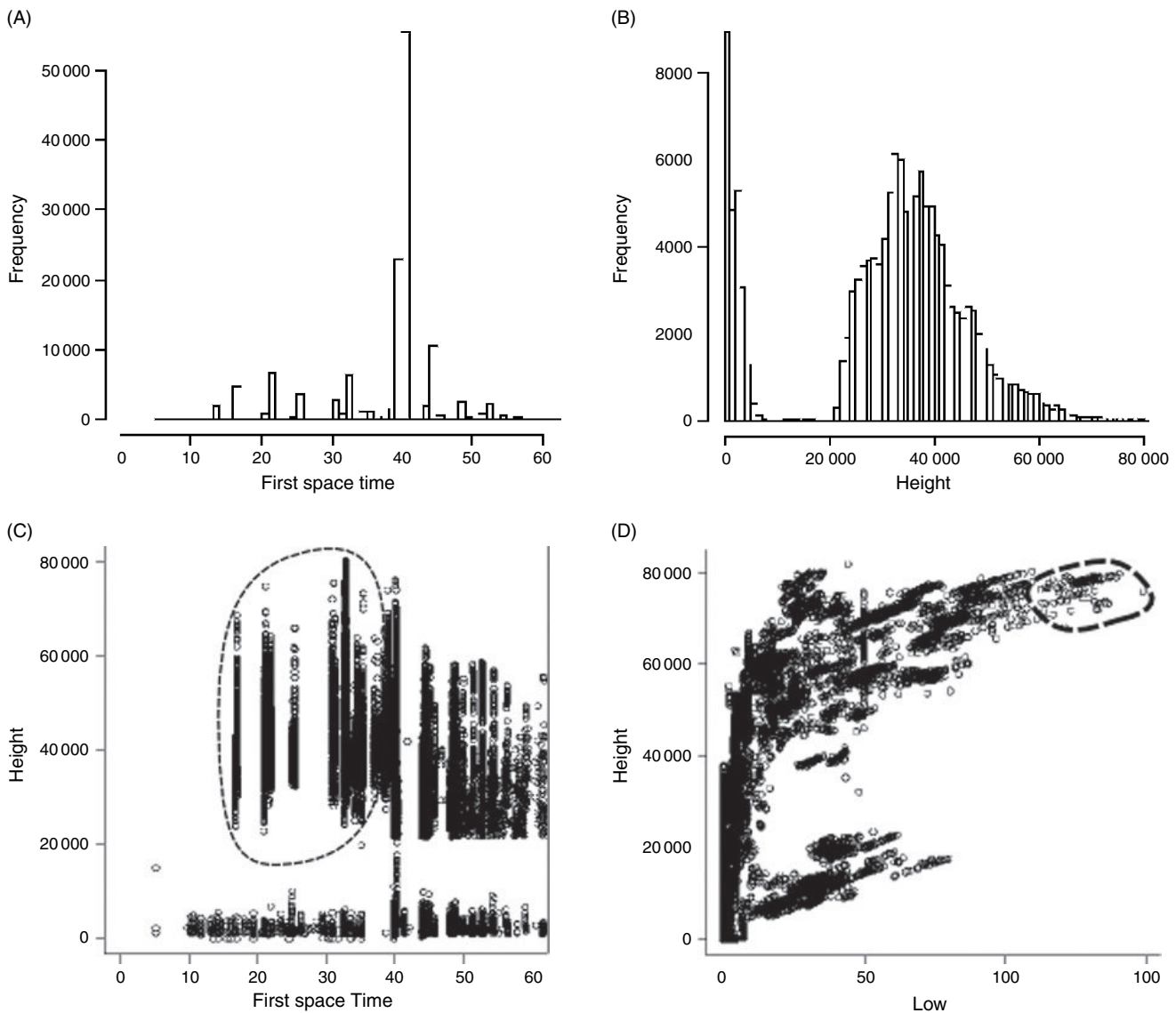


FIGURE 1.8 Statistics of early spikes.

We have begun our exploration of these simulations by looking at simulations that are ‘spontaneously’ active, meaning that they begin spiking due to the introduction of small random excitatory postsynaptic potentials prior to the large ‘shock’ stimulation at 40 ms. We do this by identifying population spike times in the simulated field, measuring such characteristics as size, width and sharpness of the population spike as well as occurrence time for over 8 million individual population spikes. In this simulation set, 23% of traces showed a first spike time prior to the shock-stimulation at 40 ms (Figure 1.8). We identified a bimodal distribution of average spike heights, with 83% of traces showing an average spike height of greater than 20 000 (arbitrary units; Figure 1.8B). Combining these measures demonstrated that 19% of traces had an early spike time and large average spike size (dashed outline in Figure 1.8C). Looking at height and width for individual first spikes for these simulations (rather than per-trace averages) shows several apparent clusters. We looked more closely at the outlying cluster (dashed outline in Figure 1.8D).

The associated set of 110 simulations displayed large repetitive spikes, distinct from the spike-and-wave pattern seen in other traces (Figure 1.9). Some of these persisted through the full second of simulation, while others gave way to low amplitude activity. Parameter analysis of this simulation set demonstrated that these simulations were produced by a combination of low threshold (high neuronal excitability) with high inhibition. Surprisingly, this pattern is associated with relatively low strength of excitatory interconnectivity.

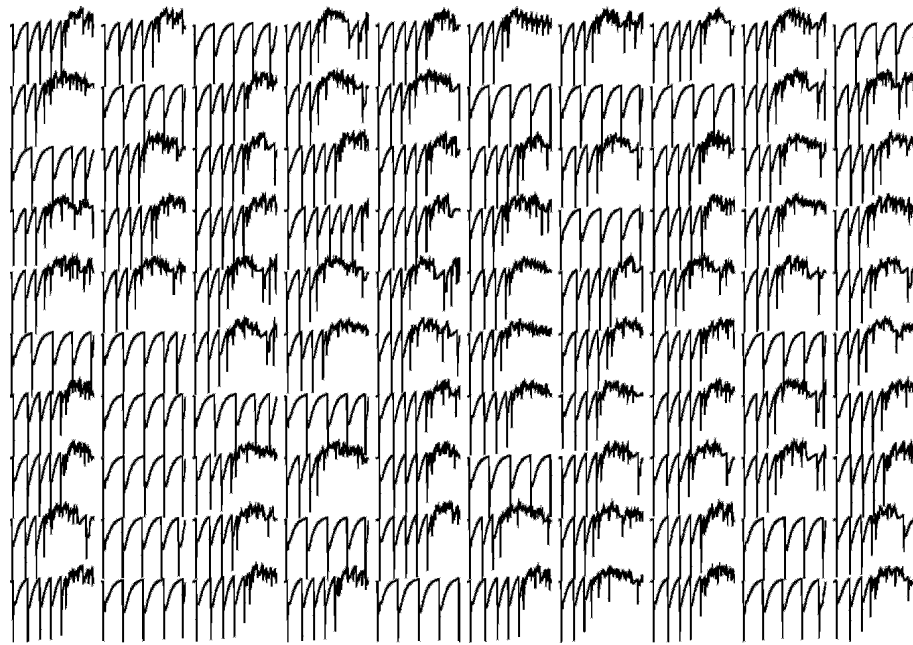


FIGURE 1.9 100 traces with large wide early spikes taken from circled area of Figure 1.8D.

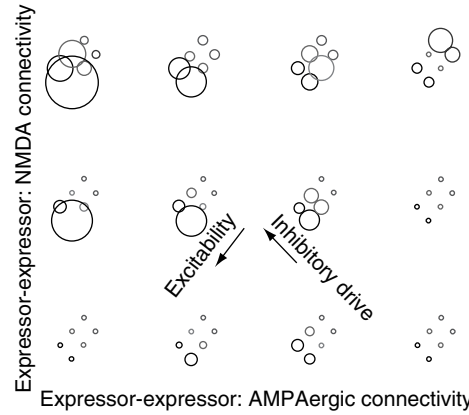


FIGURE 1.10 Parameter dependence of early spikes.

This observation prompted further analysis of the interplay of excitatory interconnectivity and cell excitability producing early large spikes. Figure 1.10 shows the number of early large spikes (size of circle) based on four parameters: excitatory-excitatory AMPAergic connectivity (x-axis), excitatory-excitatory NMDAergic connectivity (y-axis), threshold (first oblique axis; higher threshold produces lower excitability) and inhibitory drive (second oblique axis). Large early spike incidence (large circles) is generally associated with high neuronal excitability but with low AMPAergic connectivity. However, in the setting of high AMPAergic connectivity, increased excitability has the opposite effect, reducing the incidence of large early spikes. Another paradoxical effect is seen with respect to inhibition: large early spikes are associated with high inhibition (not shown) but with low drive onto the inhibitory cells (second oblique axis).

#### RATIONAL PHARMACOTHERAPEUTICS

The foregoing data-mining exercise represents one approach to the goal of rational pharmacotherapeutics: identifying underlying parameters that promote particular network dynamics so as to suggest targets for interventions that would

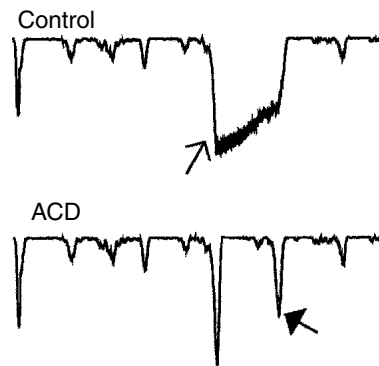


FIGURE 1.11 Effect of burst-suppressing anticonvulsant simulation on tonic activity. ACD: anticonvulsant drug.

convert those dynamics to non-pathological forms. Another approach involves using simulation to map known neuron-level pharmacological effects onto the network level. In general, these neuron-level effects will be expected to reduce identifiable epileptiform characteristics at the network level. On the other hand, our experience with parameter exploration suggests that there will be some parameter domains (subspaces) for which a single parameter alteration will show a paradoxical effect, as demonstrated in Figure 1.10. Thus, it should not be surprising that anticonvulsants can sometimes exacerbate seizures under particular pathological conditions or in some dose ranges.

Several of the variety of current and past anticonvulsants have been found to affect voltage-dependent sodium channels so as to reduce bursting in excitatory cells. This includes older anticonvulsants, such as phenytoin and carbamazepine, as well as newer agents such as lamotrigine (Rogawski and Loscher, 2004a, 2004b). We therefore have looked at the effect of reduction of burst duration on network dynamics.

Above we discussed the prevalence of latch-up tonic activity in simulations with strong excitatory-excitatory connectivity (see Figure 1.5). We looked at the effect of reducing burst size on this latch-up condition. Our preliminary data suggest that this pharmacological effect tends to reduce latch-up with little effect on other aspects of neural dynamics. In Figure 1.11, the latch-up period is eliminated (open arrow) without other alterations of the timing of population spike activity, except for the addition of a spike simultaneous with the termination of latch-up in the control condition (closed arrow). This additional spike in the ACD condition represents coincident synaptic activity. We hypothesize that the same coincident activity that produced a population spike in the ACD condition served conversely to terminate the latch-up condition in the control simulation.

## CONCLUSIONS

Epilepsy, like bad weather, is an ideal pathological condition to explore with simulation technologies. It is primarily a dynamical disease, meaning that it is the expression of enormous numbers of feedback loops, negative and positive, at both short and long intervals. Such dynamics are quite naturally expressed in mathematical form using differential equations. Like the atmosphere, the brain is huge and is subject to innumerable changing influences, external and internal, which are difficult and sometimes impossible to pin down. Nonetheless, more information is coming in all the time from experiments. Simulation technology is advancing. In the next few years we should begin to see the fruits of this convergence with implications for seizure prediction, seizure treatment and epilepsy prophylaxis.

## REFERENCES

- Borg-Graham, L.J. (1991). Modeling the non-linear conductances of excitable membranes. In: *Cellular and molecular neurobiology: a practical approach* (H. Wheal, and J. Chad, ed) pp. 247–275. Oxford, New York.
- Brunel, N. (2000). Dynamics of networks of randomly connected excitatory and inhibitory spiking neurons. *J Physiol (Paris)* 94:445–463.
- Brunel, N. and Wang, X.J. (2003). What determines the frequency of fast network oscillations with irregular neural discharges? I synaptic dynamics and excitation-inhibition balance. *J Neurophysiol* 90:415–430.

- Bush, P.C. and Sejnowski, T.J. (1991). Simulations of a reconstructed cerebellar Purkinje cell based on simplified channel kinetics. *Neural Comput* 3:321–332.
- Bush, P.C., Prince, D.A. and Miller, K.D. (1999). Increased pyramidal excitability and NMDA conductance can explain posttraumatic epileptogenesis without disinhibition: a model. *J Neurophysiol* 82:1748–1758.
- Carnevale, N.T. and Hines, M.L. (2006). The NEURON Book. Oxford, New York.
- Cohen, S.D. and Hindmarsh, A.C. (1994). Cvode user guide. Technical report. Lawrence Livermore National Laboratory, Livermore.
- Delorme, A. and Thorpe, S.J. (2003). Spikenet: an event-driven simulation package for modelling large networks of spiking neurons. *Netw Comput Neural Syst* 14:613–627.
- Destexhe, A. (1997). Conductance-based integrate-and-fire models. *Neural Comput* 9:503–514.
- Destexhe, A., Contreras, D., Steriade, M., Sejnowski, T.J. and Huguenard, J.R. (1996). In vivo, in vitro and computational analysis of dendritic calcium currents in thalamic reticular neurons. *J Neurosci* 16:169–185.
- Destexhe, A. and Sejnowski, T.J. (1995). G-protein activation kinetics and spillover of gamma-aminobutyric acid may account for differences between inhibitory responses in the hippocampus and thalamus. *Proc Nat Acad Sci USA* 92:9515–9519.
- Dominguez, L., Wennberg, R.A., Gaetz, W., Cheyne, D. and Velazquez, J.L. (2005). Enhanced synchrony in epileptiform activity? Local versus distant phase synchronization in generalized seizures. *J Neurosci* 25:8077–8084.
- Dudek, F.E., Patrylo, P.R. and Wuarin, J.P. (1999). Mechanisms of neuronal synchronization during epileptiform activity. *Adv Neurol* 79:699–708.
- Hansel, D., Mato, G., Meunier, C. and Neltner, L. (1998). On numerical simulations of integrate-and-fire neural networks. *Neural Comput* 10:467–483.
- Hereld, M., Stevens, R.L., Teller, J. and van Drongelen, W. (2005). Large neural simulations on large parallel computers. *Int J Bioelectromagn* 7:44–46.
- Hindmarsh, A.C. and Serban, R. (2002). User documentation for cvodes, an ode solver with sensitivity analysis capabilities. Technical report. Lawrence Livermore National Laboratory, Livermore.
- Hines, M.L. (1989). A program for simulation of nerve equations with branching geometries. *Int J Biomed Comput* 24:55–68.
- Izhikevich, E.M. (2003). Simple model of spiking neurons. *IEEE Trans Neural Netwo* 14:1569–1572.
- Izhikevich, E.M. (2004). Which model to use for cortical spiking neurons. *IEEE Trans Neural Netwo* 15:1063–1070.
- Jahr, C.E. and Stevens, C.F. (1990). A quantitative description of NMDA receptor-channel kinetic behavior. *J Neurosci* 10:1830–1837.
- Lytton, W.W. (2006). Neural query system: data-mining from within the neuron simulator. *Neuroinformatics* 4:163–176.
- Lytton, W.W. and Hines, M. (2005). Independent variable timestep integration of individual neurons for network simulations. *Neural Comput* 17:903–921.
- Lytton, W.W. and Sejnowski, T.J. (1991). Inhibitory interneurons may help synchronize oscillations in cortical pyramidal neurons. *J Neurophysiol* 66:1059–1079.
- Lytton, W.W. and Stewart, M. (2005). A rule-based firing model for neural networks. *Int J Bioelectromagn* 7:47–50.
- Lytton, W.W. and Stewart, M. (2006). Rule-based firing for network simulations. *Neurocomputing* 69:1160–1164.
- MacGregor, R.J. (1987). Neural and Brain Modeling. Academic Press, Inc., San Diego.
- Mainen, Z.F. and Sejnowski, T.J. (1996). Influence of dendritic structure on firing pattern in model neocortical neurons. *Nature* 382:363–366.
- Makino, T. (2003). A discrete-event neural network simulator for general neuron models. *Neural Comput Appl* 11:210–223.
- Mattia, M. and Del Giudice, P. (2000). Efficient event-driven simulation of large networks of spiking neurons and dynamical synapses. *Neural Comput* 12:2305–2329.
- Meeren, H.K., Pijn, J.P., Luijtelaar, E.L., Coenen, A.M. and Silva, F.H. (2002). Cortical focus drives widespread corticothalamic networks during spontaneous absence seizures in rats. *J Neurosci* 22:1480–1495.
- Migliore, M., Cannia, C., Lytton, W.W. and Hines, M.L. (2006). Parallel network simulations with neuron. *J Comput Neurosci* 6:119–129.
- Morrison, A., Mehring, C., Geisel, T., Aertsen, A.D. and Diesmann, M. (2005). Advancing the boundaries of high-connectivity network simulation with distributed computing. *Neural Comput* 17:1776–1801.
- Pinsky, P. and Rinzel, J. (1994). Intrinsic and network rhythmogenesis in a reduced Traub model for CA3 neurons. *J Comput Neurosci* 1:39–60.
- Poirazi, P., Brannon, T. and Mel, B.W. (2003). Arithmetic of subthreshold synaptic summation in a model cal pyramidal cell. *Neuron* 37:977–987.
- Pytte, E., Grinstein, G. and Traub, R.D. (1991). Cellular automaton models of the CA3 region of the hippocampus. *Network* 2:149–167.
- Rhodes, P.A. (2006). The role of gap junctions in the context of a simulated thalamocortical column. *Soc Neurosci Abstr* 32.13.
- Rogawski, M.A. and Loscher, W. (2004a). The neurobiology of antiepileptic drugs. *Nat Rev Neurosci* 5:553–564.
- Rogawski, M.A. and Loscher, W. (2004b). The neurobiology of antiepileptic drugs for the treatment of nonepileptic conditions. *Nat Med* 10:685–692.
- Rudolph, M. and Destexhe, A. (2006). Analytical integrate-and-fire neuron models with conductance-based dynamics for event-driven simulation strategies. *Neural Comput* 18:2146–2210.
- Rulkov, N.F., Timofeev, I. and Bazhenov, M. (2004). Oscillations in large-scale cortical networks: map-based model. *J Comput Neurosci* 17:203–223.
- Shelley, M.J. and Tao, L. (2001). Efficient and accurate time-stepping schemes for integrate-and-fire neuronal networks. *J Comput Neurosci* 11:111–119.
- Sperelakis, N. and Ramasamy, L. (2006). Propagation velocity profile in a cross-section of a cardiac muscle bundle from pspice simulation. *Theor Biol Med Model* 3:29.
- Traub, R.D. and Wong, R.K.S. (1982). Cellular mechanism of neuronal synchronization in epilepsy. *Science* 216:745–747.
- Traub, R.D., Contreras, D. and Whittington, M.A. (2005). Combined experimental/simulation studies of cellular and network mechanisms of epileptogenesis in vitro and in vivo. *J Clin Neurophysiol* 22:330–342.
- Van Drongelen, W., Koch, H., Marcuccilli, C., Pena, F. and Ramirez, J.M. (2003). Synchrony levels during evoked seizure-like bursts in mouse neocortical slices. *J Neurophysiol* 90:1571–1580.
- Watts, L. (1994). Event-driven simulation of networks of spiking neurons. In: Advances in neural information processing systems, vol 6 (J.D. Cowan, G. Tesauro, and J. Alspector, eds.) pp. 927–934. Morgan Kaufmann Publishers.
- Wilson, H.R. and Cowan, J.D. (1972). Excitatory and inhibitory interactions in localized populations of model neurons. *Biophys J* 12:1–24.
- Wilson, M.T., Sleigh, J.W., Steyn-Ross, D.A. and Steyn-Ross, M.L. (2006). General anesthetic-induced seizures can be explained by a mean-field model of cortical dynamics. *Anesthesiology* 104:588–593.

# 2

## THE NEURON SIMULATION ENVIRONMENT IN EPILEPSY RESEARCH

N.T. CARNEVALE AND MICHAEL HINES

### ABSTRACT

This article focuses on the NEURON simulation environment from the perspective of how it is useful for epilepsy research. It begins with an overview of the kinds of problems for which NEURON is best suited, then discusses specific features of NEURON's programming language and graphical user interface (GUI) that help users create and manage models of neurons and networks of neurons. These features include strategies and tools for specifying anatomical and biophysical properties of cells, importing morphometric data, spatial discretization ('compartmentalization'), dealing with non-uniform biophysical parameters, adding new biophysical mechanisms, incorporating electronic instrumentation and gap junctions, representing spike-triggered synaptic connections and artificial spiking cells, building network models, running network simulations on parallel computers, and analyzing models.

The first question a busy investigator will probably ask about any potential research tool is 'how might this be useful in my work?' If the answer is favorable, the next question is 'what special features does it have that will help me get the job done?' The aim of this chapter is to provide concise answers to both of these questions with regard to the NEURON simulation environment in the context of epilepsy research. For more detail about the topics discussed here, please see *The NEURON Book* (Carnevale and Hines, 2006) and the on-line documentation at <http://www.neuron.yale.edu/>.

### HOW MIGHT NEURON BE USEFUL IN EPILEPSY RESEARCH?

Like every other simulator, NEURON has its own 'domain of applicability', or range of problems to which it is best suited. The most direct indication of a simulator's domain of applicability may be the kinds of problems that it was designed to solve. Another way to judge a simulator's domain is to find out who has been using it and what they have been using it for.

NEURON has long been recognized for its facility with mechanistic models of single cells that involve complex anatomical and biophysical properties (Hines and Carnevale, 1997). Where models of individual neurons are concerned, NEURON's domain extends 'down' to the level of subcellular mechanisms including: ion accumulation, diffusion and transport; chemical reactions; deterministic and stochastic gating of voltage- and ligand- dependent ion channels. Its domain extends 'up' to the level of the extracellular milieu close to the cell membrane, i.e. local concentrations and electrical field, which is sufficient for modeling phenomena such as extracellular ion accumulation and extracellular stimulation and recording.

Networks represent another dimension of model complexity. NEURON was being used for network modeling even in the early 1990s (Destexhe et al., 1993, 1994a), but over the past decade, there have been two major enhancements to its utility for network modeling. The first was the advent of an event delivery system for computationally efficient simulation of spike triggered synaptic transmission in networks of biophysical and artificial (integrate and fire) spiking cells (Hines and Carnevale, 2003, 2004). The second and more recent enhancement was the ability to execute 'distributed simulations', in which models of single cells and/or networks are distributed over multiple processors in a parallel processing environment (standalone multiprocessor workstation, cluster of workstations, or parallel supercomputer) (Migliore et al., 2006; Brette et al., 2007).

As mentioned above, actual usage is another indicator of a simulator's domain. This has the advantage of being a very practical guide, but it is also a 'lagging indicator' because there may be a significant interval – months to a year or more – between the announcement of a new feature and the appearance of research papers that make use of it.

That said, readers may get a quick idea of who is currently using NEURON, and for what purposes, just by browsing the other chapters of this book. A more complete picture can be gleaned from <http://www.neuron.yale.edu/neuron/bib/usenrnm.html>, NEURON's online bibliography. As of September 2007, we know of more than 660 publications that report work done with it. Many of these were written by well-known neuroscientists engaged in epilepsy research. Some are on mechanisms of action of anticonvulsant drugs (Lytton, 1997; Poolos et al., 2002) or address specific types of epilepsy, such as absence or 'spike and wave' seizures (Lytton et al., 1997; Destexhe 1998, 1999; Destexhe et al., 2001), post-traumatic epilepsy (Bush et al., 1999; Houweling et al., 2005; Santhakumar et al., 2005), or epilepsy associated with channelopathies (Chen et al., 2001; Spampati et al., 2004a, 2004b; Vitko et al., 2005; Barela et al., 2006). Most of the other papers in the bibliography are about cellular mechanisms or network phenomena that are relevant to epilepsy in one way or another. The full scope of these studies is too broad to be covered in this chapter, but some idea of what has been done may be conveyed by the following partial list of topics, which includes a few citations that are provided more for illustration than completeness:

- properties of voltage gated currents in central neurons (Baranauskas and Martina, 2006; Chen et al., 2006)
- synaptic physiology and integration (Carnevale et al., 1997; Kapur et al., 1997a, 1997b; Jaffe and Carnevale, 1999; Magee and Cook, 2000; Gullidge and Stuart, 2003)
- the relationship between neuronal form and function (Mainen and Sejnowski, 1996; Vetter et al., 2001; Migliore et al., 2005a)
- neuronal excitability and bursting (Fleidervish et al., 1996; Colbert and Pan, 2002; Carr et al., 2003; Gillies and Willshaw, 2006)
- dendritic spikes (Migliore et al., 1999; Day et al., 2005; Jarsky et al., 2005; Kampa and Stuart, 2006)
- activity-dependent intra- and extracellular concentration changes and their effects on neuronal function, e.g. intracellular calcium accumulation (Baccus, 1998; Sheasby and Fohlmeister, 1999; Sikora et al., 2005; Gillies and Willshaw, 2006), second messengers (Destexhe et al., 1994b; Destexhe and Sejnowski, 1995) and changes during spreading depression (Kager et al., 2000, 2002; Somjen 2001, 2004)
- networks of inhibitory interneurons (Bartos et al., 2001, 2002; Vida et al., 2006)
- inhibitory interneurons as modulators of neuronal excitability (Pare et al., 1998; Aradi et al., 2002, 2004) and network activity (Aradi and Soltesz, 2002)
- network synchrony (Destexhe et al., 1998; Bartos et al., 2002; Sohal and Huguenard, 2003) and oscillations (Destexhe et al., 1999; Sohal and Huguenard, 2005)
- gap junctions and their effects on neurons (Gibson et al., 2005) and networks (Moortgat et al., 2000; Saraga et al., 2006)
- extracellular fields produced by neuronal activity (Bedard et al., 2004; Moffitt and McIntyre, 2005; Gold et al., 2006)
- brain stimulation with extracellular electrical (McIntyre and Grill, 1999; McIntyre et al., 2004; Miocinovic and Grill, 2004) or magnetic fields (Kamitani et al., 2001).

## HOW NEURON FACILITATES MODELING OF NEURONS AND NETWORKS

Unlike general purpose programming languages and simulation tools which are intended to be used for a wide range of problems, NEURON is specifically designed to be a simulation environment for computational neuroscience research. Its flexibility and convenience are largely attributable to its interpreter and its graphical user interface (GUI).

NEURON's hoc is a much enhanced version of the interpreter first described by Kernighan and Pike (1984). Many of its enhancements are specific to the task of representing the properties of biological neurons, while others include extensions for object-oriented programming, customization of the GUI, optimization and computation in a parallel processing environment. There is also a special language called NMODL for adding compiled functionality to the NEURON executable.

The GUI has powerful tools for setting up and managing the properties of models, running simulations and plotting variables as functions of time and position. For a wide range of problems, the GUI tools eliminate the need to write any code at all. They are particularly helpful in model prototyping, debugging and exploratory simulations and they are often

sufficient to do publication quality work. The most flexible and productive practice is to use the GUI tools in combination with hoc programming in order to exploit the strengths of both.

A full review of NEURON's features that help users deal with common tasks that arise in the course of modeling biological neurons and networks would cover each of these topics:

- model specification and management
- customization of the user interface
- initialization and simulation flow control
- achieving simulation stability, speed and accuracy
- analysis of simulation results.

Space limitations constrain this chapter to model specification and management. Most of the other topics are covered in some detail in NEURON's extensive online documentation and tutorials (see <http://www.neuron.yale.edu/neuron/docs/docs.html>, *The NEURON Book* (Carnevale and Hines, 2006), and, especially with regard to simulation speed and analysis of simulation results, 'Simulation of large networks' by Lytton et al., Chapter 1 in this book).

## MODEL SPECIFICATION AND MANAGEMENT

NEURON's advantages over general purpose programming languages or simulators start to become evident as soon as the conceptual model, which is in the mind of the modeler, is ready to be transformed into a computational implementation. As we point out in chapter 2 of Carnevale and Hines (2006), a computational model can provide insight to a conceptual model only if there is a close match between the two. Establishing and verifying such a match can be difficult with mechanistic models of biological neurons because of anatomical and biophysical complexities. If instrumentation effects must be taken into account, it is also necessary to represent the electrical properties of electrodes and circuit components such as amplifiers and voltage or current sources. Network connections add yet another dimension to the problem.

In any case, models that involve biological neurons are described by families of algebraic equations, ordinary differential equations, kinetic schemes and the cable equation. With a general purpose simulator or programming language, such as Matlab or C++, these equations must be expressed in a form that can be solved by a digital computer. Doing this may require writing hundreds or thousands of lines of code and the end result will not be easy to understand, let alone debug or maintain. This is much simpler with NEURON because its programming syntax and graphical interface tools have many features that are close counterparts to familiar neuroscience concepts. This reduces the effort required to implement a computational model in the first place and the resulting model specifications are far more compact and easier to understand and maintain. In the following sections, we examine NEURON's special features that facilitate creating models of individual cells, expanding its library of biophysical mechanisms, incorporating instrumentation effects and building network models.

## MODELING INDIVIDUAL NEURONS

In NEURON, models of individual nerve cells can be implemented as mechanistic models that include representations of the anatomical and biophysical properties of real cells, or as artificial spiking cells which are mathematical abstractions (e.g. 'integrate and fire cells'). Here, we concentrate on mechanistic models; artificial spiking cells are discussed later in the context of network models.

Creating a mechanistic model of a neuron involves specifying its branched topology, the geometry (physical dimensions) and biophysical properties of its branches, and the spatial discretization (compartmentalization) of the model. In NEURON, this can be done by writing hoc code or by using a GUI tool called the CellBuilder. Writing hoc code is an efficient way to specify the properties of small models or of models that can be constructed algorithmically. The CellBuilder is very convenient for small models, but its greatest strength lies in managing models based on detailed morphometric data and models with biophysical parameters that are spatially inhomogeneous. Both approaches offer features that help users focus on important biological properties rather than being distracted by computational details. To understand these features and why they are helpful, it helps to know something about how mechanistic models of neurons are specified in NEURON.

## BASIC ANATOMICAL AND BIOPHYSICAL PROPERTIES

The building blocks of mechanistic neuron models are *sections*, which are unbranched cables that correspond to individual neurites (see Hines and Carnevale, 2000; chapter 5 in Carnevale and Hines, 2006). Here, we show how sections allow users to create model specifications while thinking about neuronal architecture and biophysical properties, instead of having to recast everything as cable equations. As a concrete example, we will develop a model that consists of a soma with an axon, both of which have the same biophysical properties as the Hodgkin-Huxley squid axon model. This is most easily done with CellBuilder, a graphical tool for specifying the properties of mechanistic model neurons, whether stylized (stick figure) or anatomically detailed. However, for didactic purposes we will set up our model by writing hoc code.

Each section has its own anatomical and biophysical properties, which may vary along its length (e.g. diameter, specific membrane capacitance, channel and pump densities, membrane potential, current densities, ionic concentrations). These are called ‘range variables’ because their dependence on location is described in terms of arc length or ‘range’, which is the fractional distance along the length of a section. That is, range is 0 at one end of a section and 1 at the other, so `axon.v(0.5)` refers to membrane potential at the middle of a section called `axon` (see Hines and Carnevale, 1997; chapter 5 in Carnevale and Hines, 2006).

Sections can be assembled into a tree structure that represents the topology of a cell. For example, this hoc code sets up the topology of a simple model that consists of a soma with an attached axon

```
create soma, axon
connect axon(0), soma(1)
```

by attaching the 0 end of `axon` to the 1 end of `soma`. NEURON automatically takes care of boundary conditions between sections that are connected to each other.

The geometry of a newly created section is a cylinder with diameter 500  $\mu\text{m}$  and length 100  $\mu\text{m}$ , so it is almost always necessary to change these values. To make `axon` 1  $\mu\text{m}$  wide and 1000  $\mu\text{m}$  long, we would use this simple stylized specification of geometry

```
axon.diam = 1
axon.L = 1000
```

Similar statements would set `soma`’s diameter and length to 20  $\mu\text{m}$ . Anatomically detailed models are discussed later in this chapter.

A new section has cytoplasmic resistivity and membrane capacitance, but no membrane conductance. This means that the membrane of `axon` has no ion channels yet, so its electrical properties are described by the equation for a cylindrical cable with capacitive insulation

$$C_m \frac{\partial V}{\partial t} = \frac{D}{4R_a} \frac{\partial^2 V}{\partial x^2} \quad (1)$$

where  $C_m$ ,  $D$  and  $R_a$  are specific membrane capacitance, diameter and cytoplasmic resistivity (default values of  $C_m$  and  $R_a$  are 35.4  $\Omega\text{cm}$  and 1  $\mu\text{f}/\text{cm}^2$ , respectively). In passing, we should mention that the cable properties of any section may be augmented by an ‘extracellular’ mechanism that adds external layers to the cable; this is useful for representing myelination, variations of extracellular resistivity, or for extracellular recording and/or stimulation.

Many sources of electrical or chemical signals, such as voltage-gated ion channels, are distributed over the cell surface or throughout its cytoplasm. In NEURON, these are represented with ‘density mechanisms’ which are quantified with density units such as Siemens per square centimeter. These can be added to a section with the ‘insert’ keyword. For example,

```
axon insert hh
```

puts the Hodgkin-Huxley model’s ion channels into `axon`’s membrane, so that this section is now described by the following cable equation

$$C_m \frac{\partial V}{\partial t} + \bar{g}_{Na} m^3 h (V - E_{Na}) + \bar{g}_K n^4 (V - E_K) + \bar{g}_L (V - E_L) = \frac{D}{4R_a} \frac{\partial^2 V}{\partial x^2} \quad (2)$$

(cf. Eq. 29 in Hodgkin and Huxley, 1952), where the  $\bar{g}_X$  and  $E_X$  are the respective conductance densities and equilibrium potentials, and  $m$ ,  $h$  and  $n$  are the familiar sodium and potassium gating variables.

To summarize what we have seen so far, this hoc code

```
create soma, axon
connect axon(0), soma(1)
soma.diam = 20 // 20 × 20 μm cylinder has same surface area
soma.L = 20 // as a 20 μm diameter sphere
axon.diam = 1
axon.L = 1000
forall insert hh // this inserts hh into all sections
```

specifies the biological properties of a model cell with a 20 μm diameter soma and a 1 μm diameter, 1000 μm long axon. Note that up to this point, we have concentrated entirely on the model's biological properties, while completely ignoring the issue of spatial discretization.

### ANATOMICALLY DETAILED CELL MODELS

Stylized geometry specification is satisfactory for stick figure models, but NEURON also offers a 3-D specification method that gives greater control over section geometry, which is particularly useful for models based on morphometric reconstructions. The 3-D specification accepts a sequence of (x, y, z) coordinates plus local diameters to capture and preserve the complexities of neuronal anatomy (see chapter 5 in Carnevale and Hines, 2006). Creating and managing models based on detailed morphometric data have been greatly simplified by two GUI tools: Import3D and the CellBuilder.

Import3D can read the most common formats (Eutectic, Neurolucida, SWC) and then export a specification of topology and geometry to the CellBuilder for further management (Hines and Carnevale, 2005, online tutorial at <http://www.neuron.yale.edu/neuron/docs/import3d/main.html>). Import3D preserves 3-D information, unlike some older software that destroyed 3-D information and produced stylized geometry specifications. Furthermore, it automatically diagnoses and fixes many common errors that afflict such data and helps users identify and repair problems that require informed judgment.

The CellBuilder is a very convenient tool for specifying the biophysical properties and spatial discretization of anatomically detailed cell models (see online tutorial at <http://www.neuron.yale.edu/neuron/docs/cbtut/main.html>). Its Topology page can even be used to perform ‘cell surgery’ through a sequence of click and drag operations that create, copy, delete, or reposition sections or subtrees. While the CellBuilder can be used in conjunction with the Import3D tool, it can also import topology and geometry directly from an anatomically detailed working model, e.g. one of the published models in ModelDB (<http://senselab.med.yale.edu/senselab/modeldb/>).

Import3D and the CellBuilder have made it much easier to reuse morphologies that are becoming available from a wide range of sources, including ModelDB and databases of anatomical data such as NeuroMorpho.org (<http://neuromorpho.org/>). However, one should always be concerned about data quality (Horcholle-Bossavit et al., 2000; Scorcioni et al., 2004), and of course it is always important to cite the source of any data that one reuses.

### PAINLESS SPATIAL DISCRETIZATION

Regardless of programming language or simulation environment, mechanistic models generally deal with extended neuronal anatomy by discretizing the cable equation (‘breaking the cell into compartments’). The same is true in NEURON, but discretization is handled in such a way that users rarely have to think about compartments.

NEURON discretizes the cable equation according to the central difference approximation, which yields a set of ordinary differential equations (ODEs) that govern membrane potential and current at one or more points (called ‘nodes’) that are spaced evenly along the interior of a section. Each section has its own discretization parameter called nseg, which is a whole number that specifies how many internal nodes it has. The spatial grid in each section therefore has a local resolution given by section length/nseg. It may help to think of a section as being cut into nseg segments of equal length, with a node at the middle of each segment, and all of the membrane properties of a segment lumped together at the segment’s node (Figure 2.1). In terms of normalized distance from one end of the section, the internal nodes are located at  $(j + 0.5) / nseg$  for  $j=0$  to  $nseg-1$ .

The membrane potential  $v_j$  at the internal node of the  $j$ th segment is defined by an ODE of the form

$$c_j \frac{dv_j}{dt} + i_{ion_j}(v_j, t) = \sum_k (v_k - v_j) / r_{jk} \quad (3)$$

where  $c_j$  is the total membrane capacitance of the segment,  $i_{ion_j}$  is the net ionic current through the segment’s membrane,  $v_k$  are the membrane potentials at the nodes of adjacent segments and  $r_{jk}$  are the (cytoplasmic) resistances along the paths

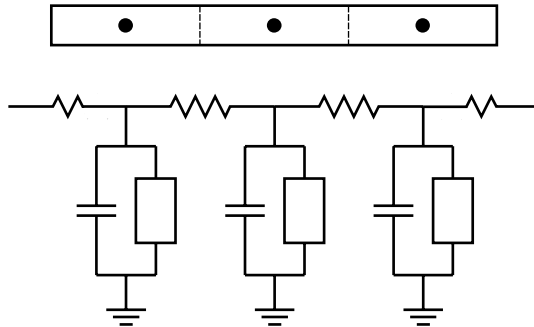


**FIGURE 2.1** Top: Cartoon of a section. Dashed lines indicate boundaries between segments for  $nseg = 3$  and black dots mark the internal nodes (points at which membrane potential and current are computed by numerical integration of the discretized cable equation) which are located at normalized distances of  $1/6$ ,  $1/2$ , and  $5/6$ . Bottom: Equivalent circuit of the same section. The resistors represent the cytoplasmic resistance between adjacent nodes and the capacitors are the total membrane capacitance of each segment. For the sake of clarity, a box is used to represent the parallel combination of each segment's ion channels (or, if you prefer, the total ionic conductances with their associated equilibrium potentials); the current through each box is that segment's net ionic membrane current.

between those nodes and the  $j$ th node. Equation 3 is just the current balance equation for segment  $j$ : the left-hand side is the sum of the membrane capacitive and ionic currents that leave the segment, and the right-hand side is the sum of the axial currents that flow into it from its neighbors.

The default value of  $nseg$  is 1, but larger values may be required for spatial accuracy in sections that are long and narrow, especially if cytoplasmic resistivity and/or specific membrane capacitance is large. A simple assignment statement is all that is necessary to change  $nseg$ , and NEURON will then automatically update the number of ODEs it must solve, calculating the values of  $c_j$ ,  $r_{jk}$ , and the terms necessary to compute  $i_{ionj}$  from surface area, ionic conductance densities or permeabilities, gating variables and equilibrium potentials in each segment of the section. To ensure correct placement of spatially inhomogeneous parameters (e.g. channel densities) and localized signal sources (see Synapses, clamps, and other localized signal sources below), it is a good idea to defer specification of density mechanisms, synapses, voltage and current clamps etc., until after  $nseg$  values have been assigned.

That still leaves the question of how big  $nseg$  should be. We have generally obtained a good balance of spatial accuracy and computational efficiency by using the `d_lambda` rule with a criterion of  $0.1 \lambda_{100Hz}$  (i.e. make  $nseg$  the smallest odd number so that segment length is shorter than one tenth of a space constant at 100 Hz (Hines and Carnevale, 2001; chapter 5 of Carnevale and Hines, 2006). For our model cell, `soma` is electrically compact so we can leave its  $nseg$  unchanged. However, according to the `d_lambda` rule, `axon` needs a value of 21 for good spatial accuracy. Revising our hoc code to include discretization gives us

```

create soma, axon
connect axon(0), soma(1)
soma.diam = 20 // 20×20 μm cylinder has same surface area
soma.L = 20 // as a 20 μm diameter sphere
axon.diam = 1
axon.L = 1000
axon.nseg = 21 // assign nseg before inserting mechanisms
forall insert hh // insert hh into all sections

```

which is a complete specification of the model (note that we followed our advice of assigning the value of  $nseg$  before inserting biophysical mechanisms). Executing these statements with hoc will set up the internal data structures for the family of ODEs that constitute the model's discretized cable equation and which, along with the ODEs for the gating variables, are numerically integrated by NEURON in the course of a simulation. The user never has to write a single cable equation, let alone bother with boundary conditions or discretization. The economy and clarity of this model specification contrasts sharply with the complexity that would be needed with any general purpose programming language or generic mathematical simulation environment.

Before leaving this topic, we should mention that spatial discretization is extremely easy with models managed by the CellBuilder, regardless of model complexity. This is so easy that, even though the `d_lambda` rule can be applied with hoc code (see [http://www.neuron.yale.edu/neuron/docs/d\\_lambda/d\\_lambda.html](http://www.neuron.yale.edu/neuron/docs/d_lambda/d_lambda.html)), we must admit to using the CellBuilder to

discover the appropriate value of `nseg` for the simple example shown above. The Geometry page offers a choice of three different discretization methods which can be applied to any individual section or set of sections:

- manual entry: user specifies value of `nseg`
- `d_X` method: user specifies maximum segment length in microns
- `d_lambda` method: user specifies maximum segment length as a fraction of  $\lambda_{100\text{Hz}}$ .

With the `d_X` and `d_lambda` methods, NEURON automatically chooses the smallest odd value of `nseg` that satisfies the discretization criterion (odd to ensure that there will be a node at the midpoint of the section).

### SPATIALLY INHOMOGENEOUS PROPERTIES

Sometimes it is known that certain kinds of ion channels are present in one region of a cell, but absent from another, or that there is a systematic variation of channel density with position (e.g. Hoffman et al., 1997). Such spatial inhomogeneities can be managed most effectively by grouping sections into subsets, which greatly simplifies the specification of biophysical properties. This can be done with hoc statements, but it is easiest with the CellBuilder, especially for anatomically complex models. This tool's Subsets page has a canvas that provides immediate visual feedback to guide and verify one's selections, plus a menu of selection choices (individual section, subtree) and logical operations (e.g. union, intersection, invert, subtract) that can reduce the effort of creating subsets to just a few mouse clicks.

The simplest application of subsets is to assert uniform properties over a group of sections, e.g. so that only the basilar dendrites have a particular voltage-gated calcium channel, or to reduce the sodium channel density uniformly over the entire apical dendritic tree. In recent versions of NEURON, subsets can be used to specify that biophysical parameters vary with position according to user-specified rules (Hines and Carnevale, 2005, online tutorial at <http://www.neuron.yale.edu/neuron/docs/cbtut/parameterized/outline.html>). This allows the modeler to stipulate that, for all sections in a particular subset, some parameter (e.g. an ion channel density) is governed by  $\text{param} = f(p)$  where  $f$  can be any function, and  $p$  is one of these distance metrics:

- path length from a reference point
- radial distance from a reference point
- distance from a plane ('3-D projection onto a line')

Figure 2.2 shows a CellBuilder in which the density of Hodgkin-Huxley sodium channels in the apical dendritic tree of a model cell decreases linearly with path distance from the soma, from full density ( $0.12 \text{ S/cm}^2$ ) at the proximal end of the apical trunk, to zero at the most distal dendritic termination.

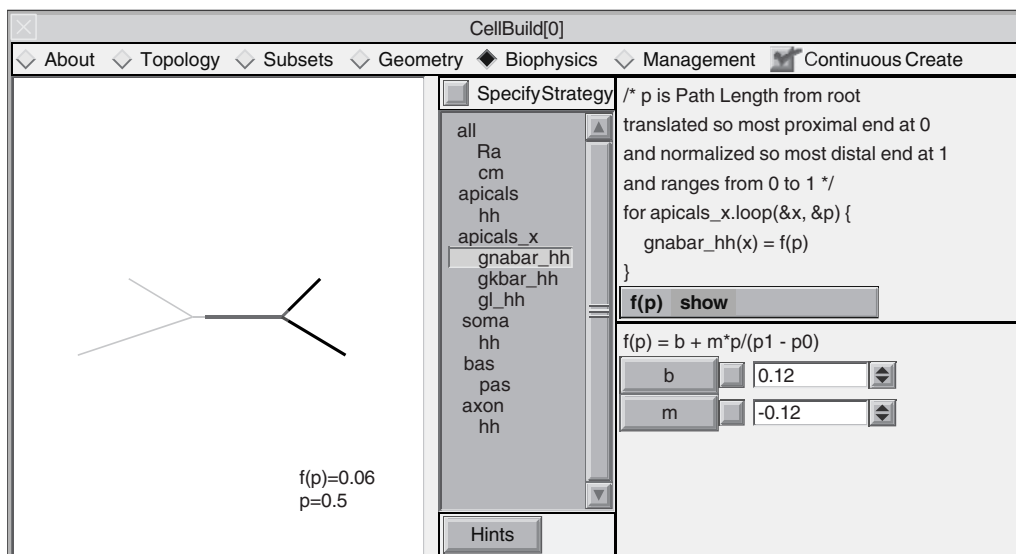


**FIGURE 2.2** Use of the CellBuilder to specify that `gnabar_hh` in the apical dendrites decreases linearly with distance from the origin of the apical tree. In the diagram of the cell, the boundaries between gray and black mark the locations that correspond to the displayed value of  $p$ . In this figure  $p$  is 0.5, which corresponds to locations that are half way from the origin of the apical tree to the most distal dendritic termination.

## SYNAPSES, CLAMPS AND OTHER LOCALIZED SIGNAL SOURCES

Earlier we mentioned that density mechanisms are used to represent biophysical properties that are distributed over the surface of a cell or throughout its cytoplasm. However, models often must include signal sources that are very localized, such as synapses and electrodes, which are best described using localized net current in nanoamperes and conductance in microsiemens. In NEURON, these are represented by ‘point processes’, which are managed with an object syntax. For example, this code creates a new instance of the `IClamp` class and attaches it to the soma of our model cell

```
objref stim
// attach a current clamp to middle of soma
soma stim = new IClamp(0.5)
stim.del = 1    // ms delay
stim.dur = 0.1  // ms duration
stim.amp = 0.5  // nA amplitude
```

## ADDING NEW KINDS OF MECHANISMS

NEURON has a special programming language called NMODL that can be used to enlarge its library of biophysical mechanisms (active currents, buffers, diffusion, exchange/pumps etc.) (Hines and Carnevale 2000; chapter 9 in Carnevale and Hines, 2006) and also to define new types of synapses and artificial spiking cells that can interact with NEURON’s event delivery system (see Modeling networks below). NMODL offers many examples of how NEURON allows modelers to work with familiar concepts and focus on the biology, while shielding them from computational details. Its notation for specifying dynamics is very similar to kinetic schemes or differential equations, as illustrated by these excerpts from the source code for a calcium pump

```
: k1 & k3 are the forward rate constants
~ cai + pump <-> capump (k1, k2)
~ capump <-> pump + cao (k3, k4)
```

and a Hodgkin-Huxley style voltage-gated sodium conductance

```
m' = (minf - m) / mtau
h' = (hinf - h) / htau
```

Complete specifications of biophysical mechanisms tend to be very compact, with each line equivalent to many statements in C, and the NMODL compiler automatically takes care of such details as generating code that works with each of NEURON’s integration methods.

New voltage-and/or ligand-gated channels can also be added with a GUI tool called the Channel Builder (Hines and Carnevale, 2005, online tutorial at <http://www.neuron.yale.edu/neuron/docs/cbtut/main.html>), which borrows much of its design from Robert Cannon’s Catacomb simulator (<http://www.compneuro.org/catacomb/>). Channels may be ohmic or described by the Goldman-Hodgkin-Katz equation, with dynamics defined by kinetic schemes or Hodgkin-Huxley-style differential equations (including the Borg-Graham formulation (Borg-Graham, 1991)). The Channel Builder has several distinct advantages over NMODL, especially where ease of use is concerned. It presents graphs that describe the voltage dependence of gating variables in terms of rate constants (‘alpha and beta’) or steady state values and time constants (‘inf and tau’; Figure 2.3). Clicking on a button switches these graphs back and forth between ‘alpha beta’ and ‘inf tau’ formats. Furthermore, the individual traces have handles (squares on the plots of infC1C2 and tauC1C2 in Figure 2.3) that can be dragged with the mouse in order to explore quickly the effects of shifting or changing the slope of their voltage dependence. Finally, Channel Builder mechanisms actually execute more quickly than equivalent compiled NMODL code, and kinetic scheme state transitions may be deterministic or stochastic.

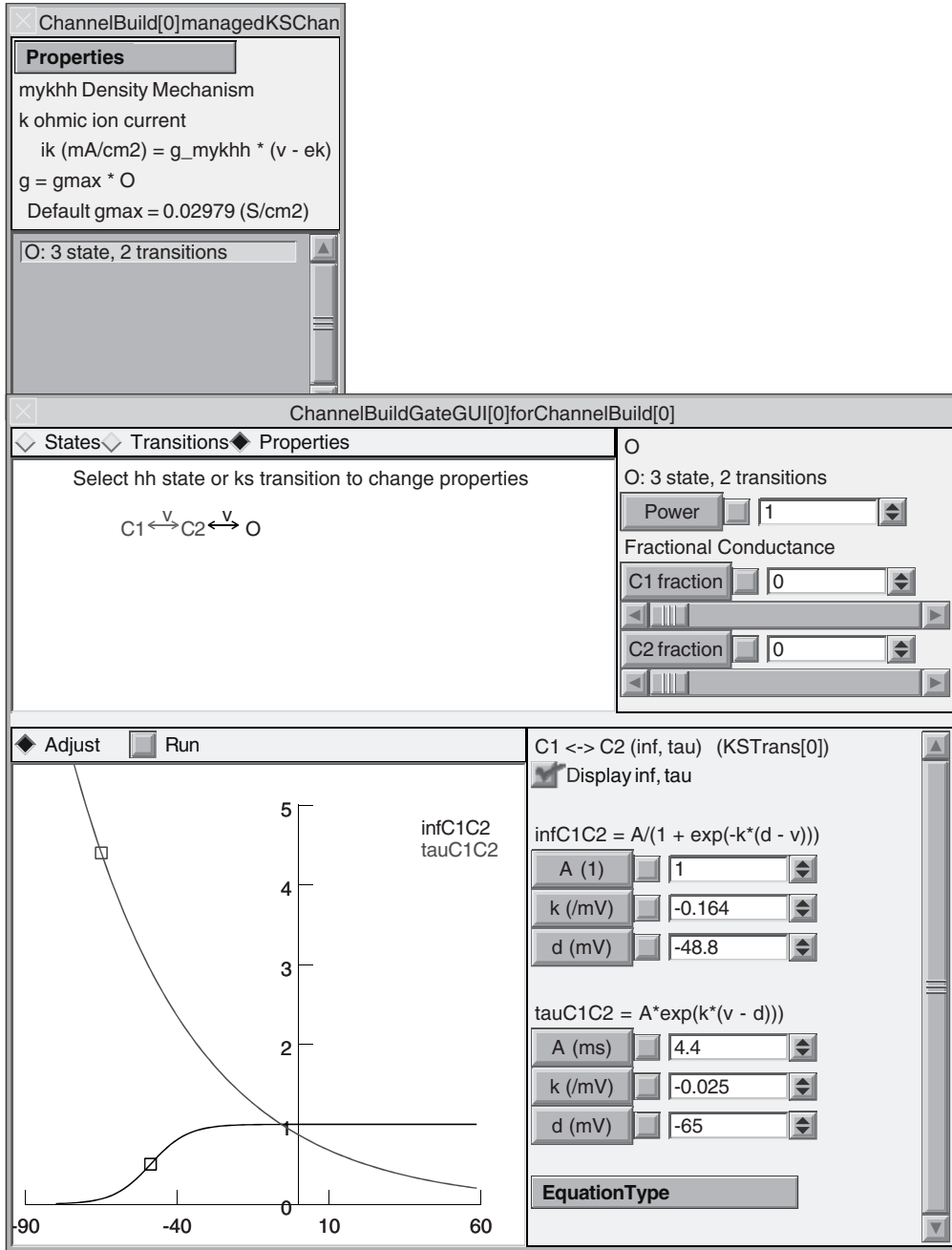


**FIGURE 2.3** A Channel Builder implementation of a three-state kinetic scheme approximation to the Hodgkin-Huxley potassium conductance, with two closed states (C1 and C2) and one open state (O). The small window is actually the Channel Builder's main control panel, where the name of the mechanism and elementary properties such as ion selectivity are specified. The large window is used to specify states, the transitions between them and the equations and parameters that govern these transitions. Here it displays the voltage dependence of the C1–C2 transition in terms of the steady state C2/C1 ratio (infC1C2) and time constant for equilibration (tauC1C2).

#### MODELS THAT INCLUDE ELECTRONIC INSTRUMENTATION

It is often informative to examine the behavior of electronic circuits, study instrumentation artifacts, or simulate experimental methods such as dynamic clamping. Such tasks are simplified by NEURON's Linear Circuit Builder, a GUI tool that makes it easy to build models that have linear circuit elements and may also include neurons. This tool is a graphical front end for the Linear Mechanism class, which adds linear equations to the matrix of current balance equations that NEURON solves

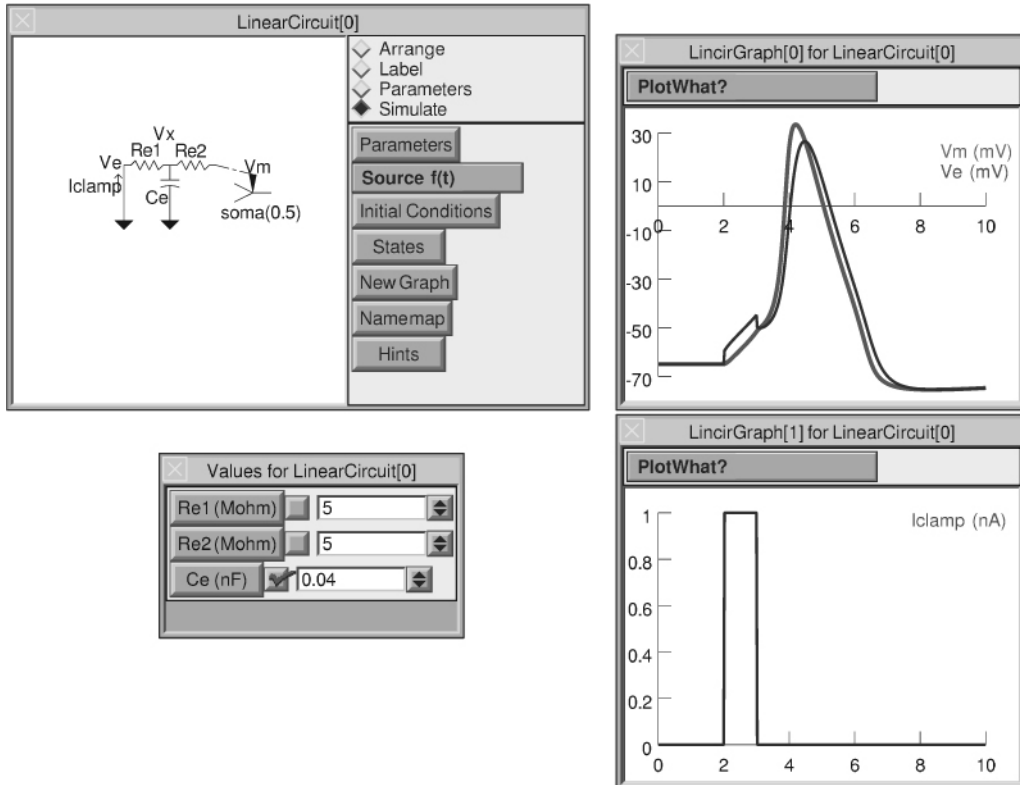


**FIGURE 2.4** Studying the effect of patch electrode capacitance and resistance on stimulation and recording from a current clamped cell. This example uses a very simple model cell that has just one section called soma, with  $\text{diam} = \text{L} = 30\ \mu\text{m}$ ,  $\text{nseg} = 1$ , and Hodgkin-Huxley membrane properties. In the Linear Circuit Builder's diagram, the stick figure cartoon labeled soma (0.5) is a direct connection to the internal node at the 0.5 location of soma. The current clamp is implemented as a current source labeled Iclamp and the electrode's distributed resistance and capacitance are represented by an equivalent T circuit ( $\text{Re1} = \text{Re2} = 5$  megohms,  $\text{Ce} = 0.04$  nF, so total series resistance is 10 megohms and electrode time constant is 0.1 ms).  $V_m$  is the membrane potential at the 0.5 location of soma. The observed potential is  $V_e$ , which shows resistive artifact during the current pulse as well as noticeable delay and attenuation of the observed spike.

during a simulation. The Linear Mechanism class can even be used to implement gap junction coupling between model cells (see Migliore et al., 2005b, source code available from ModelDB via accession number 43039). Figure 2.4 shows a Linear Circuit Builder used to study the effect of electrode capacitance and resistance on stimulation and recording from a patch clamped cell.

## MODELING NETWORKS

A biological neural network consists of neurons and of the connections between them, so what could seem more intuitive than to use computational representations of neurons and their connections as the building blocks of a model network? We already know how to specify the properties of model cells, so what's to stop us from plowing headlong into network modeling?

Nothing, really, except that advance planning might turn up strategies for implementing network models in a way that achieves computational efficiency while preserving conceptual clarity. In the following sections, we review how NEURON helps modelers implement efficient connections and artificial spiking cells, manage large numbers of model cells and connections and prototype small nets in order to generate ‘seed’ code that can be reused in the algorithmic construction of large nets.

## CONNECTIONS BETWEEN CELLS

Communication between cells in biological networks involves some combination of gap junctions, continuous transmitter release from presynaptic terminals and spike-triggered synaptic transmission. In each case, the effect on the postsynaptic

cell is to change some variable in an anatomically localized region, so these three forms of intracellular communication are implemented in NEURON as point processes.

Spike-triggered synaptic transmission is most amenable to efficient modeling chiefly because the axon can be approximated by a threshold detector at the proximal end, followed by a delay that represents conduction latency. Eliminating the mechanistic details of spike propagation along the length of the axon reduces the number of equations that must be solved and results in faster simulations.

In NEURON, presynaptic spike sources are connected to synaptic targets with the NetCon class, which combines the notions of threshold detection, delay and synaptic weight to separate the notion of ‘connections’ from the notion of ‘what is connected’ (see chapter 10 of Carnevale and Hines, 2006). A NetCon object monitors some presynaptic variable (e.g. membrane potential or calcium concentration) for a threshold crossing that indicates the occurrence of a spike. After a spike is detected, an interval is allowed to pass and then an event is delivered that perturbs (‘activates’) the model synapse.

The model synapse could include an elaborate implementation of mechanisms in the presynaptic terminal, but the most common practice is to increase the NetCon’s delay by  $\sim 1$  ms (for synaptic latency) and let the event perturb a variable associated with a synaptic conductance whose dynamics are governed by one or two linear differential equations or a simple kinetic scheme. For example, this code

```
objref syn, nc
dend syn = new Exp2Syn(0.5) // synapse is at middle of dend
// monitor v at middle of soma, deliver events to syn
soma nc = new NetCon(&v(0.5), syn)
nc.delay = 5 // ms
nc.weight = 0.001 // microsiemens
```

allows a spike in soma to activate a biexponential synaptic conductance change at the middle of dend. The conductance change starts after a delay of 5 ms and has a peak magnitude of 1 nS.

Even when mechanistic details of axonal spike conduction and transmitter release are ignored, event-driven model synapses can still reproduce many phenomena attributed to presynaptic mechanisms. Such phenomena include fluctuations of axonal conduction latency or frank conduction failure, use-dependent synaptic plasticity (see ModelDB accession numbers 3264 and 3815 for NEURON implementations of short term potentiation and depression described originally by Varela et al. (1997) and Tsodyks et al. (1998)), and trial-to-trial variation of quantal number or size (see <http://www.neuron.yale.edu/ftp/ted/neuron/chance.zip>).

## ARTIFICIAL SPIKING CELLS

Events are also used to implement artificial spiking cells in NEURON. Artificial spiking cells are highly abstract model neurons, lacking physical extent or membrane properties, that attempt to mimic certain aspects of the function of biological neurons. They have many uses in network modeling, such as prototyping network architectures and generating afferent spike trains that provide a ‘synaptic milieu’ for mechanistic model neurons. For a more detailed introduction to artificial spiking cells, see Hines and Carnevale (2004) or chapter 10 of Carnevale and Hines (2006); recent advances in making their dynamics more ‘biological’ are presented in Chapter 1 (Simulation of large networks: technique and progress) in this book.

The only way an artificial spiking cell can interact with anything is by receiving or sending events, which can be regarded as metaphors for spikes. Arrival of an input event perturbs one or more states of an artificial spiking cell and, when these states satisfy some criterion (e.g. a threshold crossing), an output event is generated. Some kinds of artificial spiking cells have dynamics that allow analytical prediction of the future course of all state variables from the present condition of the cell. Such models are suitable for event-driven simulations, which are very efficient because numerical integration is not necessary to decide if and when a cell will generate an output event. Only algebraic calculations are required, and these are necessary only when a cell receives an input event.

Like synaptic mechanisms and NetCons, NEURON’s artificial spiking cells are managed with an object syntax. This

```
objref pre, post, nc
pre = new NetStim() // generates event trains
post = new IntFire1() // leaky integrate and fire
nc = new NetCon(pre, post)
nc.weight = 0.1
```

creates two different kinds of artificial spiking cells and ensures that events generated by `pre` are delivered to `post`. This is an excitatory connection, because the weight of the NetCon that will deliver these events is positive – each input event will make the membrane state variable (analog to membrane potential) jump up by 0.1; an inhibitory connection would have a negative weight.

In NEURON, events generated by artificial spiking cells and mechanistic model cells look the same to the object that receives them – i.e. anything that can receive events, can receive events from anything that can send them. This means that a network model may involve any combination of mechanistic model cells or artificial spiking cells, connected in any way imaginable.

### AN OUTLINE FOR BUILDING NETWORK MODELS

A network model in NEURON can involve any combination of artificial spiking cells and mechanistic model cells. We already know that biophysical model cells are constructed from sections and density mechanisms. We also know that an event-triggered synapse onto a biophysical model cell is a point process attached to a section, which is capable of responding to an input event by affecting membrane current, concentration of a second messenger, or some other variable at the point of attachment. Finally, we know that NetCons are used to connect event sources, such as artificial spiking cells or a spike trigger zone on a biophysical model cell, to targets such as artificial spiking cells or event-triggered synapses. Now it is time to examine how to put all these pieces together.

In broad outline, building a network model involves these steps:

1. Defining the types of cells that will be used in the net.
2. Creating the cells.
3. Setting up connections between them.

This seems simple enough, but a lot of administrative effort can be required to keep track of all the cells, the synapses attached to them and the connections between pre- and postsynaptic elements. Fortunately, NEURON's GUI and hoc programming language can both make this less onerous in several ways.

### Object-oriented programming in network modeling

The difficulty of managing network models can be reduced by taking advantage of object-oriented programming in hoc. In particular, the code that defines a biophysical model neuron can be used to define a new object class by wrapping it inside a bit of hoc called a template. Such new object classes can be used like cookie cutters to create multiple instances of various kinds of model cells.

As an almost trivial example, suppose we want to make a network that involves 1000 identical model cells, each of which has a single section plus two synapses. This defines a new cell class called `SmallCell`

```
begintemplate SmallCell
public soma, exc, inh
create soma
objref exc, inh
proc init() {
    soma {
        insert hh
        exc = new ExpSyn(0.5) // "ampa"
        inh = new Exp2Syn(0.5) // "gaba-a"
        inh.e = -80
    }
}
endtemplate SmallCell
```

which we can then use to create as many instances of this kind of model cell as we wish

```
objref cells
cells = new List()
for i = 1,1000 cells.append(new SmallCell())
```

Lists can also be handy for dealing with collections of artificial spiking cells and NetCons, in part because they lend themselves to programming styles that can deal with any number of objects without requiring the modeler to keep track of ‘magic numbers’ (numeric counts of how many items there are of each particular kind).

## Generating reusable code with the Network Builder

A template that defines a new cell class can be created by writing hoc code by hand, but generally it is more convenient to create a new cell classes by using the Network Builder and its associated suite of GUI tools first to build a small prototype net. With these tools, the modeler can specify the properties of classes of artificial and mechanistic model cells (the latter can be imported from a CellBuilder), attach synaptic mechanisms to specific locations on mechanistic model cells and set up a simple network architecture of interconnected cells (see tutorial at <http://www.neuron.yale.edu/neuron/docs/netbuild/main.html>). The idea is to use the Network Builder to make a simple prototype net which contains one instance of each kind of cell and synaptic connection that is of interest. This can be saved as a hoc file, which may then be mined for code that is reusable for algorithmically building large-scale nets (see chapter 11 in Carnevale and Hines 2006).

## Network models on parallel computers

NEURON supports parallel simulation of network models in which cells on different processors are coupled by spike events (Migliore et al., 2006). This works for fixed-step and variable-step integration, including the local variable time-step method (Lytton and Hines, 2005). Because of cache effects, speed-up is superlinear if the number of processors is small, and it remains at least proportional to the number of processors as long as each one is integrating more than  $\sim 100$  equations. It is straightforward to write the model specification so that the same code will run on standalone single processor machines or parallel hardware, with setup time scaling properly with the number of processors (e.g. source code for Migliore et al., 2006 and Brette et al., 2007, available from ModelDB via accession numbers 64229 and 83319).

For optimum performance, parallel simulations can be carried out in batch mode, saving only a record of spike activity (time of each spike and identity of the spiking cell). The detailed time course of any variable can then be efficiently recreated from the entire network's spike data. This is done by re-simulating any subset (even 1) of neurons with the aid of the GUI, using the PatternStim class to provide as input just those events that would have been generated by the rest of the network. The results for the subnet are quantitatively identical to the full network simulation.

NEURON's parallel network capabilities have been extended to include interprocessor gap junctions and synapses where postsynaptic state is continuously dependent on presynaptic voltage. Communication overhead is greatly increased for such models since voltages must be exchanged at every time step. At present, gap junctions in combination with discrete events can use only the fixed-step method but this will be soon extended to the global variable-step method.

## The Model View tool: model analysis at runtime

A common problem in debugging and maintaining one's own models, and an almost universal challenge in dealing with anybody else's models, is the difficulty of understanding just what is in any given model. Code has a tendency to grow like Topsy with little overall structure and few comments to guide the reader. Statements that define model properties are often intermingled with user interface, control and initialization code. Differences in programming styles and strategies can make even well-structured code difficult for anyone but the model's author to understand, especially if the model is assembled algorithmically or has a complex initialization.

Model View is a GUI tool that analyzes model properties at runtime and presents the results of its analysis in the form of a compact, browsable outline, with pop-up graphs that display the spatial distribution of inhomogeneous parameters. In the future, Model View will also enable interoperability with other simulators by exporting and importing model specifications in XML.

## SUMMARY

In this chapter, we have presented an overview of features of NEURON that facilitate the specification and management of models of cells and networks. Extensive documentation of these features and other topics related to the construction and use of models is provided in *The NEURON Book* (Carnevale and Hines, 2006) and on-line documentation at <http://www.neuron.yale.edu/>.

## ACKNOWLEDGMENTS

Supported by NINDS NS11613.

## REFERENCES

- Aradi, I. and Soltesz, I. (2002). Modulation of network behaviour by changes in variance in interneuronal properties. *J Physiol* 538:227–251.
- Aradi, I., Santhakumar, V., Chen, K. and Soltesz, I. (2002). Postsynaptic effects of GABAergic synaptic diversity: regulation of neuronal excitability by changes in IPSC variance. *Neuropharmacology* 43:511–522.
- Aradi, I., Santhakumar, V. and Soltesz, I. (2004). Impact of heterogeneous perisomatic IPSC populations on pyramidal cell firing rates. *J Neurophysiol* 91:2849–2858, 2004.
- Baccus, S.A. (1998). Synaptic facilitation by reflected action potentials: enhancement of transmission when nerve impulses reverse direction at axon branch points. *Proc Nat Acad Sci* 95:8345–8350.
- Baranauskas, G. and Martina, M. (2006). Sodium currents activate without a Hodgkin and Huxley-type delay in central mammalian neurons. *J Neurosci* 26:671–684.
- Barela, A.J., Waddy, S.P., Lickfett, J.G. et al. (2006). An epilepsy mutation in the sodium channel SCN1A that decreases channel excitability. *J Neurosci* 26:2714–2723.
- Bartos, M., Vida, I., Frotscher, M., Geiger, J.R.P. and Jonas, P. (2001). Rapid signaling at inhibitory synapses in a dentate gyrus interneuron network. *J Neurosci* 21:2687–2698.
- Bartos, M., Vida, I., Frotscher, M. et al. (2002). Fast synaptic inhibition promotes synchronized gamma oscillations in hippocampal interneuron networks. *Proc Nat Acad Sci* 99:13222–13227.
- Bedard, C., Kroger, H. and Destexhe, A. (2004). Modeling extracellular field potentials and the frequency-filtering properties of extracellular space. *Biophys J* 86:1829–1842.
- Borg-Graham, L.J. (1991). Modeling the nonlinear conductances of excitable membranes. In: *Cellular and Molecular Neurobiology: a Practical Approach*, (H. Wheal and J Chad, eds, pp. 247–275). Oxford University Press, New York.
- Brette, R., Rudolph, M., Carnevale, T. et al. Simulation of networks of spiking neurons: a review of tools and strategies. *J. Comput. Neurosci.* DOI 10.1007/S10827-007-0038-6, 2007.
- Bush, P.C., Prince, D.A. and Miller, K.D. (1999). Increased pyramidal excitability and NMDA conductance can explain posttraumatic epileptogenesis without disinhibition: a model. *J Neurophysiol* 82:1748–1758.
- Carnevale, N.T. and Hines, M.L. (2006). The NEURON Book. Cambridge University Press, Cambridge.
- Carnevale, N.T., Tsai, K.Y., Claiborne, B.J. and Brown, T.H. (1997). Comparative electrotonic analysis of three classes of rat hippocampal neurons. *J Neurophysiol* 78:703–720.
- Carr, D.B., Day, M., Cantrell, A.R. et al. (2003). Transmitter modulation of slow, activity-dependent alterations in sodium channel availability endows neurons with a novel form of cellular plasticity. *Neuron* 39:793–806.
- Chen, K., Aradi, I., Thon, N., Eghbal-Ahmadi, M., Baram, T.Z. and Soltesz, I. (2001). Persistently modified h-channels after complex febrile seizures convert the seizure-induced enhancement of inhibition to hyperexcitability. *Nat Med* 7:331–337.
- Chen, Y.A., Yu, F.H., Surmeier, D.J., Scheuer, T. and Catterall, W.A. (2006). Neuromodulation of Na<sup>+</sup> channel slow inactivation via cAMP-dependent protein kinase and protein kinase C. *Neuron* 49:409–420.
- Colbert, C.M. and Pan, E.H. (2002). Ion channel properties underlying axonal action potential initiation in pyramidal neurons. *Nat Neurosci* 5:533–538.
- Day, M., Carr, D.B., Ulrich, S., Ilijic, E., Tkatch, T. and Surmeier, D.J. (2005). Dendritic excitability of mouse frontal cortex pyramidal neurons is shaped by the interaction among HCN, Kir2, and k(leak) channels. *J Neurosci* 25:8776–8787.
- Destexhe, A. (1998). Spike-and-wave oscillations based on the properties of GABA-B receptors. *J Neurosci* 18:9099–9111.
- Destexhe, A. (1999). Can GABA<sub>A</sub> conductances explain the fast oscillation frequency of absence seizures in rodents? *Eur J Neurosci* 11:2175–2181.
- Destexhe, A. and Sejnowski, T.J. (1995). G-protein activation kinetics and spillover of g-aminobutyric acid may account for differences between inhibitory responses in the hippocampus and thalamus. *Proc Nat Acad Sci* 92:9515–9519.
- Destexhe, A., McCormick, D.A. and Sejnowski, T.J. (1993). A model for 8–10 Hz spindling in interconnected thalamic relay and reticularis neurons. *Biophys J* 65:2474–2478.
- Destexhe, A., Contreras, D., Sejnowski, T.J. and Steriade, M. (1994a). A model of spindle rhythmicity in the isolated thalamic reticular nucleus. *J Neurophysiol* 72:803–818.
- Destexhe, A., Mainen, Z.F. and Sejnowski, T.J. (1994b). Synthesis of models for excitable membranes, synaptic transmission, and neuromodulation using a common kinetic formalism. *J Comput Neurosci* 1:195–231.
- Destexhe, A., Contreras, D. and Steriade, M. (1998). Mechanisms underlying the synchronizing action of corticothalamic feedback through inhibition of thalamic relay cells. *J Neurophysiol* 79:999–1016.
- Destexhe, A., Contreras, D. and Steriade, M. (1999). Cortically-induced coherence of a thalamic-generated oscillation. *Neuroscience* 92:427–443.
- Destexhe, A., Contreras, D. and Steriade, M. (2001). LTS cells in cerebral cortex and their role in generating spike-and-wave oscillations. *Neurocomputing* 38:555–563.
- Fleidervish, I.A., Friedman, A. and Gutnick, M.J. (1996). Slow inactivation of Na<sup>+</sup> current and slow cumulative spike adaptation in mouse and guinea-pig neocortical neurones in slices. *J Physiol* 493:83–97.
- Gibson, J.R., Beierlein, M. and Connors, B.W. (2005). Functional properties of electrical synapses between inhibitory interneurons of neocortical layer 4. *J Neurophysiol* 93:467–480.
- Gillies, A. and Willshaw, D. (2006). Membrane channel interactions underlying rat subthalamic projection neuron rhythmic and bursting activity. *J Neurophysiol* 95:2352–2365.
- Gold, C., Henze, D.A., Koch, C. and Buzsaki, G. (2006). On the origin of the extracellular action potential waveform: a modeling study. *J Neurophysiol* 95:3113–3128.
- Gulledge, A.T. and Stuart, G.J. (2003). Excitatory actions of GABA in the cortex. *Neuron* 37:299–309.
- Hines, M.L. and Carnevale, N.T. (1997). The NEURON simulation environment. *Neural Comput* 9:1179–1209.
- Hines, M.L. and Carnevale, N.T. (2000). Expanding NEURON's repertoire of mechanisms with NMODL. *Neural Comput* 12:995–1007.

- Hines, M.L. and Carnevale, N.T. (2001). NEURON: a tool for neuroscientists. *Neuroscientist* 7:123–135.
- Hines, M.L. and Carnevale, N.T. (2003). NEURON simulation environment. In: *The Handbook of Brain Theory and Neural Networks*, (M.A. Arbib ed.), pp. 769–773. MIT Press, Cambridge.
- Hines, M.L. and Carnevale, N.T. (2004). Discrete event simulation in the NEURON environment. *Neurocomputing* 58–60:1117–1122.
- Hines, M.L. and Carnevale, N.T. (2005). Recent developments in NEURON. *Brains, Minds Media* 1 bmm221 (urn:nbn:de:0009-3-2210).
- Hodgkin, A.L. and Huxley, A.F. (1952). A quantitative description of membrane current and its application to conduction and excitation in nerve. *J Physiol* 117:500–544.
- Hoffman, D.A., Magee, J.C., Colbert, C.M. and Johnston, D. (1997). K<sup>+</sup> channel regulation of signal propagation in dendrites of hippocampal pyramidal neurons. *Nature* 387:869–875.
- Horcholle-Bossavit, G., Gogas, P., Ivanov, Y., Korogod, S. and Tyc-Dumont, S. (2000). The problem of morphological noise in reconstructed dendritic arborizations. *J Neurosci Meth.* 95:83–93.
- Houweling, A.R., Bazhenov, M., Timofeev, I., Steriade, M. and Sejnowski, T.J. (2005). Homeostatic synaptic plasticity can explain post-traumatic epileptogenesis in chronically isolated neocortex. *Cerebr Cort* 15:834–845.
- Jaffe, D.B. and Carnevale, N.T. (1999). Passive normalization of synaptic integration influenced by dendritic architecture. *J Neurophysiol* 82:3268–3285.
- Jarsky, T., Roxin, A., Kath, W.L. and Spruston, N. (2005). Conditional dendritic spike propagation following distal synaptic activation of hippocampal CA1 pyramidal neurons. *Nat Neurosci* 8:1667–1676.
- Kager, H., Wadman, W.J. and Somjen, G.G. (2000). Simulated seizures and spreading depression in a neuron model incorporating interstitial space and ion concentrations. *J Neurophysiol* 84:495–512.
- Kager, H., Wadman, W.J. and Somjen, G.G. (2002). Conditions for the triggering of spreading depression studied with computer simulations. *J Neurophysiol* 88:2700–2712.
- Kamitani, Y., Bhalodia, V.M., Kubota, Y. and Shimojo, S. (2001). A model of magnetic stimulation of neocortical neurons. *Neurocomputing* 38:697–703.
- Kampa, B.M. and Stuart, G.J. (2006). Calcium spikes in basal dendrites of layer 5 pyramidal neurons during action potential bursts. *J Neurosci* 26:7424–7432.
- Kapur, A., Lytton, W.W., Ketchum, K.L. and Haberly, L.B. (1997a). Regulation of the NMDA component of EPSPs by different components of postsynaptic GABAergic inhibition: computer simulation analysis in piriform cortex. *J Neurophysiol* 78:2546–2559.
- Kapur, A., Pearce, R.A., Lytton, W.W. and Haberly, L.B. (1997b). GABA<sub>A</sub>-mediated IPSCs in piriform cortex have fast and slow components with different properties and locations on pyramidal cells. *J Neurophysiol* 78:2531–2545.
- Kernighan, B.W. and Pike, R. (1984). Appendix 2: Hoc manual. In: *The UNIX Programming Environment*, pp. 329–333. Prentice-Hall, Englewood Cliffs.
- Lytton, W.W. (1997). Computer model of clonazepam's effect in thalamic slice. *NeuroReport* 8:3339–3343.
- Lytton, W.W. and Hines, M. (2005). Independent variable timestep integration of individual neurons for network simulations. *Neural Comput* 17:903–921.
- Lytton, W.W., Contreras, D., Destexhe, A. and Steriade, M. (1997). Dynamic interactions determine partial thalamic quiescence in a computer network model of spike-and-wave seizures. *J Neurophysiol* 77:1679–1696.
- Magee, J.C. and Cook, E.P. (2000). Somatic EPSP amplitude is independent of synapse location in hippocampal pyramidal neurons. *Nat Neurosci* 3:895–903.
- Mainen, Z.F. and Sejnowski, T.J. (1996). Influence of dendritic structure on firing pattern in model neocortical neurons. *Nature* 382:363–366.
- McIntyre, C.C. and Grill, W.M. (1999). Excitation of central nervous system neurons by nonuniform electric fields. *Biophys J* 76:878–888.
- McIntyre, C.C., Grill, W.M., Sherman, D.L. and Thakor, N.V. (2004). Cellular effects of deep brain stimulation: model-based analysis of activation and inhibition. *J Neurophysiol* 91:1457–1469.
- Migliore, M., Hoffman, D.A., Magee, J.C. and Johnston, D. (1999). Role of an A-type K<sup>+</sup> conductance in the back-propagation of action potentials in the dendrites of hippocampal pyramidal neurons. *J Comput Neurosci* 7:5–15.
- Migliore, M., Ferrante, M. and Ascoli, G.A. (2005a). Signal propagation in oblique dendrites of CA1 pyramidal cells. *J Neurophysiol* 94:4145–4155.
- Migliore, M., Hines, M.L. and Shepherd, G.M. (2005b). The role of distal dendritic gap junctions in synchronization of mitral cell axonal output. *J Comput Neurosci* 18:151–161.
- Migliore, M., Cannia, C., Lytton, W.W., Markram, H. and Hines, M.L. (2006). Parallel network simulations with NEURON. *J Comput Neurosci* 21:119–129.
- Miocinovic, S. and Grill, W.M. (2004). Sensitivity of temporal excitation properties to the neuronal element activated by extracellular stimulation. *J Neurosci Meth* 132:91–99.
- Moffitt, M.A. and McIntyre, C.C. (2005). Model-based analysis of cortical recording with silicon microelectrodes. *Clin Neurophysiol* 116:2240–2250.
- Moortgat, K.T., Bullock, T.H. and Sejnowski, T.J. (2000). Gap junction effects on precision and frequency of a model pacemaker network. *J Neurophysiol* 83:984–997.
- Pare, D., Lang, E.J. and Destexhe, A. (1998). Inhibitory control of somatodendritic interactions underlying action potentials in neocortical pyramidal neurons *in vivo*: an intracellular and computational study. *Neuroscience* 84:377–402.
- Poolos, N.P., Migliore, M. and Johnston, D. (2002). Pharmacological upregulation of h-channels reduces the excitability of pyramidal neuron dendrites. *Nat Neurosci* 5:767–774.
- Santhakumar, V., Aradi, I. and Soltesz, I. (2005). Role of mossy fiber sprouting and mossy cell loss in hyperexcitability: A network model of the dentate gyrus incorporating cell types and axonal topography. *J Neurophysiol* 93:437–453.
- Saraga, F., Zhang, X.L., Zhang, L., Carlen, P.L. and Skinner, F.K. (2006). Exploring gap junction location and density in electrically coupled hippocampal oriens interneurons. *Neurocomputing* 69:1048–1052, 2006.
- Scorcioni, R., Lazarewicz, M.T. and Ascoli, G.A. Quantitative morphometry of hippocampal pyramidal cells: differences between anatomical classes and reconstructing laboratories. *J Comp Neurol* 473:177–193.
- Sheasby, B.W. and Fohlmeister, J.F. (1999). Impulse encoding across the dendritic morphologies of retinal ganglion cells. *J Neurophysiol* 81:1685–1698.
- Sikora, M.A., Gottesman, J. and Miller, R.F. (2005). A computational model of the ribbon synapse. *J Neurosci Meth* 145:47–61.

- Sohal, V.S. and Huguenard, J.R. (2003). Inhibitory interconnections control burst pattern and emergent network synchrony in reticular thalamus. *J Neurosci* 23:8978–8988.
- Sohal, V.S. and Huguenard, J.R. (2005). Inhibitory coupling specifically generates emergent gamma oscillations in diverse cell types. *Proc Natl Acad Sci USA* 102:18638–18643.
- Somjen, G.C. (2004). Ions in the Brain. Oxford University Press, New York.
- Somjen, G.G. (2001). Mechanisms of spreading depression and hypoxic spreading depression-like depolarization. *Physiol Rev* 81:1065–1096.
- Spampinato, J., Aradi, I., Soltesz, I. and Goldin, A.L. (2004a). Increased neuronal firing in computer simulations of sodium channel mutations that cause generalized epilepsy with febrile seizures plus. *J Neurophysiol* 91:2040–2050.
- Spampinato, J., Kearney, J.A., de Haan, G. et al. (2004b). A novel epilepsy mutation in the sodium channel SCN1A identifies a cytoplasmic domain for beta subunit interaction. *J Neurosci* 24:10022–10034.
- Tsodyks, M., Pawelzik, K. and Markram, H. (1998). Neural networks with dynamic synapses. *Neural Comput* 10:821–835.
- Varela, J.A., Sen, K., Gibson, J., Fost, J., Abbott, L.F. and Nelson, S.B. (1997). A quantitative description of short-term plasticity at excitatory synapses in layer 2/3 of rat primary visual cortex. *J Neurosci* 17:7926–7940.
- Vetter, P., Roth, A. and Häusser, M. (2001). Propagation of action potentials in dendrites depends on dendritic morphology. *J Neurophysiol* 85:926–937.
- Vida, I., Bartos, M. and Jonas, P. (2006). Shunting inhibition improves robustness of gamma oscillations in hippocampal interneuron networks by homogenizing firing rates. *Neuron* 49:107–117.
- Vitko, I., Chen, Y.C., Arias, J.M., Shen, Y., Wu, X.R. and Perez-Reyes, E. (2005). Functional characterization and neuronal modeling of the effects of childhood absence epilepsy variants of CACNA1H, a T-type calcium channel. *J Neurosci* 25:4844–4855.

# 3

## THE CoCoDAT DATABASE: SYSTEMATICALLY ORGANIZING AND SELECTING QUANTITATIVE DATA ON SINGLE NEURONS AND MICROCIRCUITRY

JONAS DYHRFJELD-JOHNSEN AND ROLF KÖTTER

### ABSTRACT

The CoCoDat (Collation of Cortical Data) database system is a powerful tool designed for organizing and selecting quantitative experimental data on single neurons and neuronal microcircuitry. The database has proven useful for reference-keeping, experimental planning and computational modeling by facilitating the time consuming task of collating and organizing quantitative single neuron and microcircuitry data from the literature. CoCoDat provides advanced tools for entering and retrieving published data without *a priori* interpretation or summarizing, taking into account the diversity and method-dependence of single cell and microcircuitry data. The database content is organized consistent with biophysical theory and the concepts of compartmental modeling, enabling flexible combination of data on membrane conductances, ionic and synaptic currents, morphology, connectivity and firing patterns. Data retrieval is expedited by innovative tools with optional relaxation of search criteria along the conceptual mapping dimensions of brain region, cortical layer, cell type and subcellular compartment. CoCoDat has been designed primarily for offline use, but can alternatively be viewed, downloaded and merged from distributed websites in platform-independent XML format using the ODBC interface of the Catalyst software.

### DATA REQUIREMENTS FOR REALISTIC MODELING OF NEURONS AND MICROCIRCUITS IN EPILEPSY

The construction and evaluation of biologically realistic models of neurons, microcircuits and networks require precise descriptions of both intrinsic properties of single cells and their specific connectivity. In epilepsy research, such models have been employed to investigate the role of specific pathologies in epileptogenesis on the single cell and network level, in conjunction with experimental work (see e.g. Lytton et al., 1997; Thomas and Lytton, 1998; Chen et al., 2001; Bazhenov et al., 2004; Heilman and Quattrochi, 2004; Spampati et al., 2004; Traub et al., 2005) or as stand-alone modeling studies (see e.g. Lytton and Sejnowski, 1992; Lytton, 1997; Destexhe, 1999; Yang et al., 2003, 2005; Santhakumar et al., 2005; Park and Durand, 2006).

While individual researchers are intimately familiar with the specific pathological feature investigated, studying the effects of, for example, the altered kinetics of a voltage-gated conductance in a single neuron requires not only a detailed description of the altered conductance itself, but a complete detailed model of the neuron in question. Such single neuron models are generally based on a description of the neuron morphology (determining the passive membrane properties) equipped with subdomain specific distributions of ionic and synaptic conductances that, together with the morphology, determine the behavior of the modeled cell. Even in research groups combining experimental and modeling approaches, such a complete description of the studied neurons is unlikely to have been gathered first hand and reliance on published data from the literature becomes a necessity.

The collation, organization, evaluation and selection of appropriate quantitative experimental data from the literature for the different steps of model construction and validation is very labor intensive and the use of dedicated databasing tools can greatly facilitate the efforts of the modeler. The CoCoDat (*Collation of Cortical Data*) relational database (Dyhrfjeld-Johnsen et al., 2005) is such an advanced tool for organizing uninterpreted quantitative biophysical, anatomical and electrophysiological data from the literature in a manner reflecting the principles of compartmental modeling (Rall, 1964; Koch and Segev, 1989).

### STRUCTURE OF THE DATABASE

CoCoDat is a relational database with individual records in a set of different tables linked hierarchically through unique identifiers to ensure consistency and to avoid fragmentation and disconnection of the database content. The database was originally implemented in Microsoft Access 2000® with a front-end based on Visual Basic for Applications®. It is also available for online browsing in a platform independent XML format (see Section on Accessing the CoCoDat database below).

The types and composition of the tables constituting CoCoDat were derived from an extensive survey of relevant literature on the rat neocortex to reflect the organization of published data. They are organized in four major groups: *Literature*, *experimental methodology*, *mapping of recording site* and *experimental findings* (Table 3.1). Each of these four groups is composed of multiple tables accessible for browsing or data entry through custom designed graphical forms, all opened from the central CoCoDat *SwitchBoard* (Figure 3.1).

The overall flow of data originates in the detailed bibliographical data entered for each publication in question. Subsequently, the datastream diverges to records of methodological data and records mapping the recording site, before re-uniting in the actual quantitative records of experimental data.

The experimental findings are further subdivided into the categories reflecting the principles of compartmental modeling and contain data on *Morphology* describing the basic structure of a neuron, which is subsequently equipped with *Ionic-Conductances*, *IonicCurrents* and *SynapticCurrents* combining to determine *FiringProperties*, and *Connectivity* potentially linking the single cell to others in a network model. All information in CoCoDat is entered exactly as published with extensive references (including specific page, table and figure numbers). This strict 1:1 representation of raw, uninterpreted data ensures transparency and a faithful representation of the original descriptions in the published literature.

**TABLE 3.1** The tables (and their contents) of CoCoDat organized the four major data groups: *Literature*, *Mapping of Recording Site*, *Experimental Methodology* and *Experimental Findings*

Literature	Mapping of recording site
Literature ID, title, year of publication, publication type, abstract, keywords, comments and ID of data collator, URL for additional data accessible on the internet	BrainMaps Entered BrainMaps (General Map and other user-specified parcellation schemes)
Literature_Abbreviations_Journals Predefined list of journal name abbreviations	BrainMaps_BrainSites_BrainSiteTypes Defined BrainSiteTypes
Literature_Authors Authors initials and last names	BrainMaps_BrainSiteAcronyms BrainsiteAcronyms with their full description
Literature_BookChapters Page numbers, editors, book title, publisher, place of publishing	BrainMaps_BrainSites Brainsites given by a combination of Brainmap, BrainSiteAcronym and BrainSiteType
Literature_Books Publisher, place of publishing	BrainMaps_BrainSites_HC Hierarchical relations of BrainSites at each level of organization
Literature_JournalArticles Journal, volume and page numbers, PubMed ID and link to entry	Neurons RecordingSites given by their LiteratureID, BrainRegion, Layer, NeuronType & NeuronCompartment
Literature_LinkTable Links between literature IDs and authors (for search purposes)	
Experimental methodology	Experimental findings
Methods_Electrophysiology Experimental preparation, solution, recording method, stimulation method, species, temperature, text- and figure references, comments	Neurons_Morphology Morphological feature name, value, reconstruction, citations, text- and figure references, comments
Methods_Electrophysiology_Animals Animal strain, age, sex and weight	Neurons_Morphology_RecMethod Morphological reconstruction methods
	Neurons_FiringProperties Firing pattern type, citations, text- and figure references, comments

TABLE 3.1 (Continued)

Experimental methodology	Experimental findings
Methods_Electrophysiology_CompConc <i>Pharmacological components and their concentrations</i>	Neurons_FiringProperties_APduration <i>Action potential duration</i>
Methods_Electrophysiology_Preparations <i>Predefined list of experimental preparations</i>	Neurons_FiringProperties_Rinput <i>Input resistance</i>
Methods_Electrophysiology_RecMethod <i>Predefined list of recording methods</i>	Neurons_FiringProperties_Rintra <i>Intracellular resistance</i>
Methods_Electrophysiology_SliceOrient <i>Slice orientation Predefined list of planes of sectioning</i>	Neurons_FiringProperties_TauM <i>Membrane time-constant</i>
Methods_Electrophysiology_SolutionType <i>Predefined list of solution types</i>	Neurons_FiringProperties_Vrest <i>Membrane resting potential</i>
Methods_Electrophysiology_Species <i>Predefined list of species</i>	Neurons_IonicCurrents <i>Current name, charge-carrier, peak conductance, peak current, reversal potential, voltage threshold, half-activation voltage, peak voltage, citations, text- and figure references, comments</i>
	Neurons_IonicConductances <i>Conductance name, charge-carrier, peak conductance, voltage threshold, half-activation voltage, peak voltage, citations, text- and figure references, comments</i>
	Neurons_SynapticCurrents <i>Synapse type, peak conductance, peak current, peak potential, reversal potential, latency, citations, text- and figure references, comments</i>
	Neurons_Connectivity <i>Target BrainRegion, Layer, NeuronType and Compartment, citations, text and figure references, comments</i>
	Neurons_ChargeCarrier <i>Predefined list of charge carriers (ions)</i>

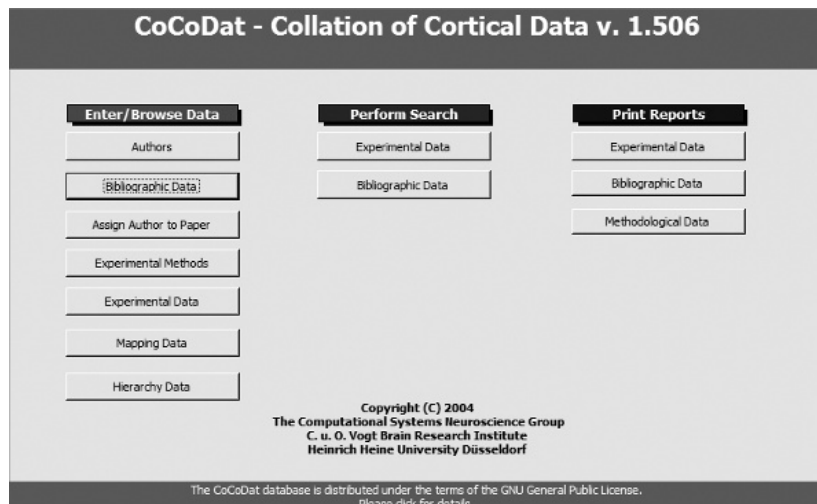


FIGURE 3.1 The central *SwitchBoard* of CoCoDat gives the user access to all graphical forms used for data entry, data queries and generation of printable reports.

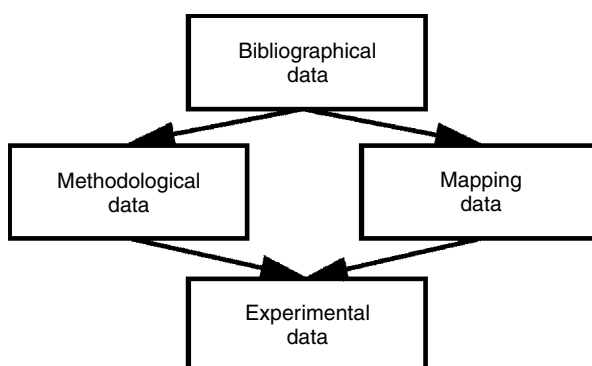
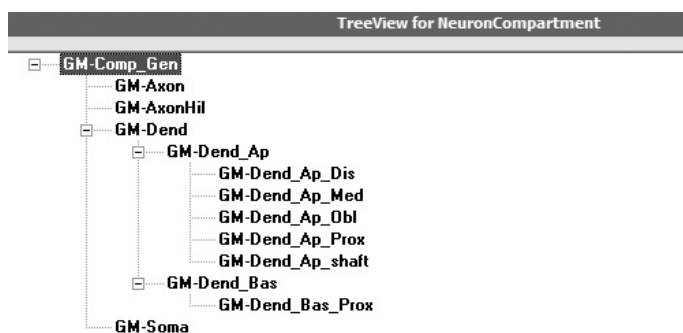


FIGURE 3.2 The hierarchical relationship of the four main data groups in CoCoDat. The flow of data through the database is illustrated using directional arrows.

## MAPPING CONCEPTS

In order to assign experimental data to the correct neuronal source in an accurate but flexible manner, CoCoDat employs *BrainSite* designators, describing the specific *RecordingSite* location using a combined designation of *BrainRegion*, *Layer*, *NeuronType* and *NeuronCompartment* as given in the original specification. These *BrainSite* designators are not cytoarchitectonically delineated structures as, for example, the cortical areas defined in the connectivity database CoCoMac (Stephan et al., 2001; Kötter, 2004), but rather heuristic entities based on the generally accepted nomenclature in the literature. To ensure wide applicability and compatibility with mapping concepts pioneered in the CoCoMac database, these heuristic *BrainSites* are components of an idealized, species-independent and non-delineated *General Map* (GM). The resulting designation of a single *BrainSite* is a combination of a shorthand acronym (e.g. *Ctx\_Vis* for visual cortex) with the GM brainmap designator into an entry of the form *GM-Ctx\_Vis* (visual cortex defined in the framework of the *General Map*).

On each of the four levels of description, the *BrainSites* are arranged in hierarchical relationships, designating conceptual parent/child associations between super- and substructures, as here illustrated for the *NeuronCompartment* level (Figure 3.3).



**FIGURE 3.3** The current hierarchical relationships for *BrainSites* on the *NeuronCompartment* level from the *Hierarchy Data* form accessed through the *SwitchBoard* (*GM-Comp\_gen*, general compartment; *GM-Axon*, axon; *GM-AxonHil*, axon hillock; *GM-Soma*, soma; *GM-Dend*, dendrite; *GM-Dend\_Ap*(*Dis/Med/Obl/Prox/shft*), apical dendrite (distal/medial/oblique/proximal/shaft); *GM-Dend\_Bas*(*Prox*), basal dendrite (proximal)).

In cases where the original publication does not specify the recording location on one or more of the four levels of description, the *general* descriptor residing at the top of each hierarchical level is used (see e.g. *GM-Comp\_gen* for general compartment, Figure 3.3). The hierarchical relationships on each of the four levels of description form the basis of the powerful and flexible search routines described in the section on Extracting and visualizing datasets below.

## ACCESSING THE COCODAT DATABASE

The CoCoDat database can be freely downloaded as a Microsoft Access 2000® database (mdb) file from <http://www.cocomac.org/cocodat> along with a manual detailing the procedures for entering, querying and extracting datasets. CoCoDat is copy-lefted under the GNU General Public License (<http://www.gnu.org/licenses/gpl.html>). By opening the database, the user is automatically taken to the central CoCoDat *SwitchBoard* (see Figure 3.1) that gives access to all forms for entering and retrieving data. Alternatively, the user can choose to browse the current contents of the database as platform independent XML-formatted catalogues derived from the original mdb file using the ODBC (*Open DataBase Connectivity*) interface of the Catalyster software (<http://www.axiope.com>, Goddard et al., 2003). Furthermore, CoCoDat is one of eight databases whose terminology is searchable through the Society for Neuroscience *Neuroscience Database Gateway* interoperability framework currently under development ([http://ndg.sfn.org/interop/ndg\\_lexicon\\_search.aspx](http://ndg.sfn.org/interop/ndg_lexicon_search.aspx)).

The current content of the CoCoDat database reflects modeling efforts concentrating on single cell properties of layer V pyramidal neurons in the rat barrel cortex (Dyhrfjeld-Johnsen et al., 2005; Kötter et al., 2005). However, as all necessary experimental data for a specific model are rarely available from that particular neuronal entity in the literature, CoCoDat contains records from a variety of cortical areas and cell types. The current contents are collated from 38 publications with 89 records on experimental methodology and 71 specific *RecordingSites* with 257 records of experimental data distributed as: Morphology (42 records), FiringProperties (65 records), IonicCurrents (68 records), IonicConductances (51 records), SynapticCurrents (11 records) and Connectivity (20 records).

## EXTRACTING AND VISUALIZING DATASETS

To extract datasets from the MS Access version of CoCoDat, the user opens the *SearchBoard* from the main *SwitchBoard* (see Figure 3.1) by clicking *Experimental Data* under the heading *Perform Search*. To form a query, the user selects the desired combination of *BrainRegion*, *Layer*, *NeuronType*, *NeuronCompartment* and *DataType* (*Morphology*, *FiringProperties*, *IonicConductances*, *IonicCurrents*, *SynapticCurrents* or *Connectivity*) with the optional specification of *Species*. The selected search terms are combined into a final search string using the Boolean AND operator after selecting *Run Search* under the *Perform Action* heading.

Since all experimental data in the CoCoDat database are linked to the specific *RecordingSite* given in the original publication, a query simply combining the four user-selected *BrainSites* would fail to retrieve data linked to neuronal entities located lower in the hierarchy on each of the four levels of description: Specifying, for example, *GM-Dend* (dendrite) as *NeuronCompartment* would fail to retrieve data specifically linked to specific parts of either the apical or basal dendrites; specifying *GM-Ctx\_SeM* (sensorimotor cortex) as *BrainRegion* would fail to retrieve data specifically linked to, for example, somatomotor, somatosensory or barrel cortex. To counter this, the CoCoDat search routine automatically expands the selected *BrainSites* for each query to include all their substructures on each level of description as designated by the hierarchical relationships in the *General Map*. These expanded lists of *BrainSites* are then combined with each other and the selected *DataType* and *Species* in an all-to-all fashion to ensure that all data relevant to the user-specified query are returned. From this expansion of the selected *BrainSites*, it also follows that the user can extract all information contained for a given *DataType* and *Species* by selecting the topmost *BrainSite* in the hierarchy for each of the four levels of description (general cortical region: *GM-Ctx\_gen*; general layer: *GM-L\_gen*; general neuron type: *GM-C\_gen*; general compartment: *GM-Comp\_gen*).

Following a successful query, the distribution of *RecordingSites* which returned relevant data is displayed using branching-tree structures in the four panels under the heading *TreeView Output* (see Figure 3.4). For each level of description, the user specified *BrainSite* for the query is displayed with the number of returned *RecordingSites* it is part of given in parenthesis. By expanding the hierarchies (already done in Figure 3.4 by clicking the '+' next to the *BrainSite*),

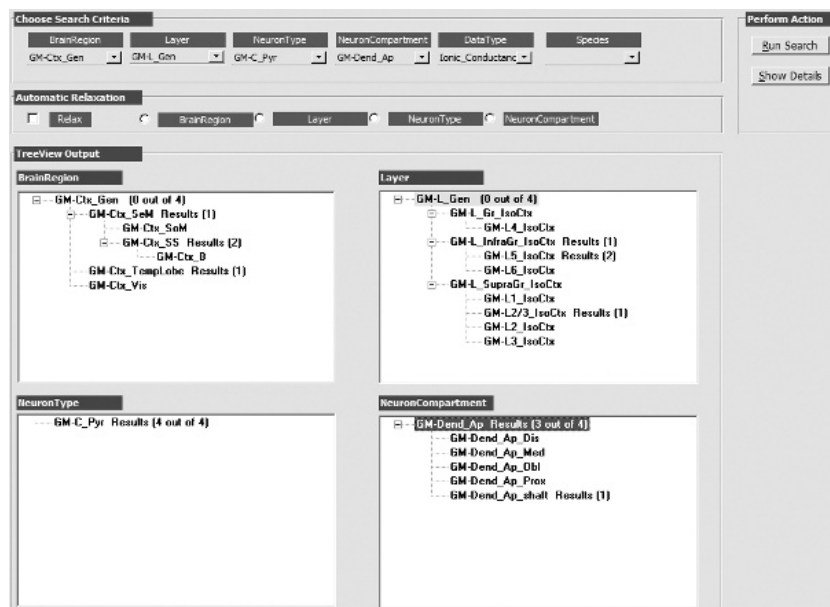


**FIGURE 3.4** Data are queried and extracted from the CoCoDat database using the *SearchBoard* (accessible from the *SwitchBoard* by clicking *Experimental Data* under the *Perform Search* heading; see Figure 3.1). Here, an example illustrates a query for data on *IonicConductances* from *GM-Ctx\_Gen* (general cortex), *GM-L\_Gen* (general layer), *GM-C\_Pyr* (pyramidal cell), *GM-Dend\_Ap* (apical dendrite). In the expanded hierarchies, numbers in parentheses following the *BrainSites* indicate the number of returned *RecordingSites* a given *BrainSite* is part of. In the case of *NeuronType*, only the top level of the hierarchy is part of the four returned *RecordingSites*. No returned *RecordingSite* contains *GM-Ctx\_Gen* (general cortex) at the *BrainRegion* level or *GM-L\_Gen* (general layer), however, three *BrainSites* lower in the hierarchies on both the *BrainRegion* (sensorimotor cortex, somatosensory cortex and temporal lobe) and *Layer* (infragranular layer, layer 2/3 and layer 5) levels of description constitute part of the four returned *RecordingSites*. At the *NeuronCompartment* level of description, the top level *GM-Dend\_Ap* (apical dendrite) is a part of three out of the four returned *RecordingSites* while the final site refers to *GM-Dend\_Ap\_shaft* (the shaft of the apical dendrite).

it is possible to inspect exactly which of the expanded substructures make up the returned *RecordingSites* and appraise the logical distance between the modeled structure and the data available in the CoCoDat database.

In cases where a query does not return any results, the user can employ the *Automatic Relaxation* feature implemented on the *SearchBoard* (see Figure 3.4). By activating the *Relax* tickbox and specifying *BrainRegion*, *Layer*, *NeuronType* or *NeuronCompartment* before resubmitting the query, the search routine systematically steps upwards through hierarchy at the desired level of description until experimental data of the designated *DataType* and *Species* are returned. This allows the modeler to extract data easily from closely matching *RecordingSites* contained in the CoCoDat database.

## INSPECTING AND EXPORTING DATASETS

After a successful query, clicking the *Show Details* button under the *Perform Action* heading will bring up a summary form with a list detailing the returned *RecordingSites* (including their constituent *Literature-IDs* and *BrainSites*) and basic qualitative information on the queried experimental data, i.e. type of ionic conductance, morphological feature (Figure 3.5, top). A detailed list of the authors of the original publication can be opened by double-clicking the content of the *ID\_Literature* field.

By clicking the ‘+’ sign appearing to the left of each *NeuronID* entry, a graphical form displaying the full quantitative details of the experimental record can be expanded (see Figure 3.5, bottom). In addition to, for example, peak conductance and half-activation voltage for an *IonicConductance* record, the form contains a text citation from the original publication along with detailed references to figures and tables as well as the pages the information was extracted from. Furthermore, the *Comments* field can contain any additional information deemed appropriate by the original database collator, including references to further data available. If the database contains experimental records associated with the returned *RecordingSite* in any of the five other data categories than the one currently active, these records can be accessed directly by clicking the five buttons on the right side of the form.

Using the *Display Literature* button at the top right of the expanded form (see Figure 3.5), the user can access the full bibliographic information on the original publication that the experimental data were collated from (Figure 3.6). This form will furthermore display the *Literature-ID* of the publication, the complete abstract as well as a direct link to the PubMed online database when available.

Detailed information on the experimental procedures (Figure 3.7) used in the study can be viewed by clicking *Display Methods* on the top right of the expanded results form (see Figure 3.5). Having detailed records of the methods used to generate the experimental data immediately available enables the modeler to evaluate whether apparent contradictions

The figure shows two windows of the CoCoDat database interface. The top window is a summary form listing three *RecordingSite* entries:

NeuronID	ID_Literature	ID_BrainRegion	ID_Layer	ID_NeuronType	ID_NeuronCompartment	Conductance_n	Charge_carrer	PrintResult
1927746281	B000	GM-Ctx_Sem	GM-L5_IsoCbx	GM-C_Pyr	GM-Dend_Ap	[IA]	K+	<input type="checkbox"/>
1064206191	TB2GMW03	GM-Ctx_Templobe	GM-L2/3_IsoCtx	GM-C_Pyr	GM-Dend_Ap_shft	gKA	K+	<input type="checkbox"/>
2090324329	KHP96a	GM_Ctx_SS	GM_L_InfaGr_IsoC1	GM-C_Pyr	GM_Dend_Ap	EK	K+	<input type="checkbox"/>

The bottom window is an expanded record for the third entry (ID 2090324329). It includes sections for *RecordingSite* details, *IonicConductances* (with fields for ID, Conductance\_name, Charge\_carrer, Peak\_conductance, V\_halfthreshold, V\_halfactivation, V\_peak, Charge\_n, and a note about electrode position), *References* (with fields for Reference\_type, Reference\_id, and Comment), and buttons for *Display Literature*, *Display Methods*, *Histology*, *IonicCurrents*, *HighResponse*, *SynapticInfluences*, and *Connectivity*.

**FIGURE 3.5** The summary form (top of figure) gives a brief overview of returned search results from the example query (see Figure 3.4) shown in tabulated format. By clicking the ‘+’ sign in the leftmost column, individual records can be inspected on a graphical form (bottom of figure) displaying detailed information on the *RecordingSite* and the experimental findings linked to it. Buttons on the form give direct access to records of the bibliographic and methodological data linked to the experimental findings (top of form), while other buttons link to experimental findings in other data categories linked to the displayed *RecordingSite*.

ID	KHP96a
Title	Development of BK channels in neocortical neurons.
Year	1996
Journ./Chapter/Book	J
Abstract	1. Postnatal development of a large conductance $\text{Ca}^{2+}$ -activated $\text{K}^+$ channel [BK channel] was investigated in
IonicCurrents	n
IonicConductances	y
SynapticCurrents	n
Connectivity	n
Morphology	n
FiringProperties	n
 Literature_JournalArticles	
ID_Literature	KHP96a
Journal	J. Neurophysiol.
Volume	76(1)
Pages	188-198
PMID	8836218
PubMed	
Record:	[<] [4] [1] [▶] [▶] [▶*] of 1
 Literature_Books	
ID_Literature	KHP96a
Publisher	
Place	
Record:	[<] [4] [1] [▶] [▶] [▶*] of 1
 Authors	
dbCollator	JDJ
Authors	Last Name Initials First Name
Kang	J
Huguenard	JR
Prince	DA
*	
PhysicalCopy	✓
Comments	-
Record:	[<] [4] [1] [▶] [▶] [▶*] of 3
 Web Data	
URL	
 Literature_BookChapters	
ID_Literature	KHP96a
Pages	
Editors	
Title_Book	
Publisher	
Place	
Record:	[<] [4] [1] [▶] [▶] [▶*] of 1

FIGURE 3.6 Bibliographic data linked to the example query shown in Figure 3.5 (accessed by clicking the *Display Literature* button, see Figure 3.5).

ID	1135746851
ID_Literature	KHP96a
Comments	"These low concentrations of enzymes were used because preliminary experiments showed that concentrations > 0.5 mg/ml markedly affected the voltage dependence"
dbCollator	JDJ
Preparation	Dissociated Neurons
Solution	Ca Block
Recording_Method	Inside-out patch
Stimulation_Method	V-clamp/ramp
Species	Rat
Temperature(°C)	21-22
Reference_Text	p.189-190
Reference_Figures	Fig.1
 Animals	
Animal_Strain	Sprague-Dawley (Simonsen Bre)
Animal_Age	P14
Animal_Sex	mixed
Animal_Weight	-
Record:	[<] [4] [1] [▶] [▶] [▶*] of
 Component_Concentration	
Component	Charybdotoxin (ChTX)
Component_Concent	1 $\mu\text{M}$
Record:	[<] [4] [1] [▶] [▶] [▶*] of
 Slice Orientation	
SliceOrientation	Coronal
Record:	[<] [4] [1] [▶] [▶] [▶*] of

FIGURE 3.7 Methodological data linked to the example query shown in Figure 3.5 (accessed by clicking the *Display Methods* button, see Figure 3.5).

between data obtained in different studies are actual contradictions or merely the result of differing experimental protocols. Additionally, it is imperative to ensure that the data extracted from the database are obtained under circumstances comparable to those simulated in the constructed model, or whether corrections for different ionic environments, temperatures or effects of pharmacological manipulations may be required.

Following detailed inspection of the experimental data associated with the returned *RecordingSites*, the user can select to export desired records to be printed as automatically generated *Reports* by activating the tick-boxes in the right-most

Experimental Data - IonicConductances			
NeuronID	-2090324328	Conductance_name	BK
ID_Literature	KHP96a	Charge_carrier	K+
ID_Methods_Electrophysiology	-135019817	Peak_conductance	0.134+0.008 channels/ $\mu\text{m}^2$
		V_threshold	-
		V_half_activation	-
ID_BrainRegion	GML-Ctx_SS	V_peak	-
ID_Layer	GML-InfaGr_Is		
ID_NeuronType	GML-C_Pyr	Reference_text	p.191
ID_NeuronCompartment	GML-Dend_Ap	Reference_figures	Table 2
Citations	"Patches were excised at a mean distance of 18+2.6 $\mu\text{m}$ from the soma-apical dendritic junction." p191		
Comments	-		

Sunday, October 06, 2006 Page 1 of 1

**FIGURE 3.8** The query result shown in Figure 3.5 displayed as a printable, date-stamped report, selected by activating the *PrintResult* tick-box next to the tabulated entry on the summary form (see Figure 3.5, right-most column). The report is subsequently generated by selecting *Experimental Data* under the *Print Reports* heading on the main *SwitchBoard* (see Figure 3.1).

*Print Results* column on the summary form (see Figure 3.5). Upon returning to the main *SwitchBoard*, reports can be printed for the selected records using the appropriate buttons under the *Print Records* heading (see Figure 3.1, right side). An example report displaying experimental data is show in Figure 3.8.

#### ADDING CONTENT TO THE DATABASE

A detailed guide for data entry and general usage of the CoCoDat database can be downloaded from <http://www.cocomac.org/documents>, however, briefly described, the procedure for data entry follows the general datastream described in the section Structure of the database above: initially, the bibliographic data on the publication in question is using the *Bibliographic Data* form accessible under the *Enter/Browse Data* in the left-most column of the central *SwitchBoard* (see Figure 3.1). Subsequently, the user enters detailed information on the experimental methodology (*Experimental Methods* under *Enter/Browse Data* on the *SwitchBoard*, see Figure 3.1) directly linking it to the *Literature-ID* of the publication. If the necessary *BrainSites* required for the reported *RecordingSites* are already available in the database, the experimental records can be directly entered and linked to a *RecordingSite* and *Methods\_Electrophysiology-ID* using the *Experimental Data* form accessible under the *Enter/Browse Data* heading on the main *SwitchBoard* (see Figure 3.1). If the user is entering data related to a structure presently not described in the CoCoDat *General Map*, the required *BrainSites* can be entered using the *Mapping Data* form and incorporated in the hierarchy on the appropriate level of description using the *Hierarchy Data* form, both accessible from the *SwitchBoard* (see Figure 3.1).

The use of the CoCoDat database is not limited to organization and retrieval of data already published in the literature. Adding, for example, unpublished experimental data from the modelers research group only requires the substitution of the *Literature-ID* on the *Bibliographic Data* form by an alphanumeric ID uniquely identifying the date and recording number used to label the results in the laboratory setting. Subsequently, the procedures for entering methodological, mapping and experimental records are identical to those used for published data from the literature.

#### DISCUSSION

The CoCoDat database provides the user with a powerful and expandable tool for organizing and selecting detailed records of experimental data for biologically realistic modeling of single neurons and microcircuits. With a user constrained, combinatorial algorithm delivering dynamically retrieved search results, CoCoDat allows for customized extraction of

records only limited by the current contents of the database. The selection of optimal data for a given modeling project is facilitated by the grouping of experimental findings according to electrophysiological methodology and the principles of compartmental modeling. Powerful visualization tools allow for instant comparison of data from several *RecordingSites* and give the user the ability visually to appraise the best possibly matching records for the modeling project. Once model construction is finished, additional data from CoCoDat can be used to test emergent model behavior.

Currently, no database resources tabulating single neuron and microcircuitry data from either human epilepsy patients or from animal models of epilepsy are available. Given the multitude of pathological changes occurring both in single neuron properties and network connectivity during epileptogenesis, data collections in a standardized format would greatly facilitate the organization and comparison of experimental data from multiple types and models of epilepsy, as well as providing an invaluable resource for modelers investigating mechanisms of epileptogenesis. Establishing such a data collection within the CoCoDat framework would be straightforward as, for example, the animal model in question would simply be recorded within the existing tables detailing the experimental methodology.

Using the described tools (see Section Adding content to the database) for additional data entry, the local user can gradually expand their personal data collection as additional data are collated for modeling projects. Collaborating research groups can set up a centralized master database with several individual database clients for further data entry, facilitating a rapid accumulation of data for common research projects. To promote general sharing of collated resources and to receive updates on future developments, we encourage all CoCoDat users to subscribe to the CoCoDat mailing list at <http://www.cocomac.org/cocodat>, which distributes communications to other users and developers.

## REFERENCES

- Bazhenov, M., Timofeev, I., Steriade, M. and Sejnowski, T.J. (2004). Potassium model for slow (2–3 Hz) in vivo neocortical paroxysmal oscillations. *J Neurophysiol* 92(2):1116–1132.
- Chen, K., Aradi, I., Thon, N., Eghbal-Ahmadi, M., Baram, T.Z. and Soltesz, I. (2001). Persistently modified h-channels after complex febrile seizures convert the seizure-induced enhancement of inhibition to hyperexcitability. *Nat Med* 7(3):331–337.
- Destexhe, A. (1999). Can GABA<sub>A</sub> conductances explain the fast oscillation frequency of absence seizures in rodents? *Eur J Neurosci* 11(6):2175–2181.
- Dyhrfjeld-Johnsen, J., Maier, J., Schubert, D. et al. (2005). CoCoDat: a database system for organizing and selecting quantitative data on single neurons and neuronal microcircuitry. *J Neurosci Meth* 141(2):291–308.
- Goddard, N.H., Cannon, R.C. and Howell, F.W. (2003). Axiope tools for data management and data sharing. *Neuroinformatics* 1(3):271–284.
- Heilman, A.D. and Quattrochi, J. (2004). Computational models of epileptiform activity in single neurons. *Biosystems* 78(1–3):1–21.
- Koch, C. and Segev, I. (1989). Methods in neuronal modeling: from synapses to networks. MIT Press, Cambridge.
- Kötter, R. (2004). Online retrieval, processing, and visualization of primate connectivity data from the CoCoMac database. *Neuroinformatics* 2(2):127–144.
- Kötter, R., Schubert, D., Dyhrfjeld-Johnsen, J., Luhmann, H.J. and Staiger, J.F. (2005). Optical release of caged glutamate for stimulation of neurons in the in vitro slice preparation. *J Biomed Opt* 10(1):11003.
- Lyttton, W.W. (1997). Computer model of clonazepam's effect in thalamic slice. *Neuroreport* 8(15):3339–3343.
- Lyttton, W.W. and Sejnowski, T.J. (1992). Computer model of ethosuximide's effect on a thalamic neuron. *Ann Neurol* 32(2):131–139.
- Lyttton, W.W., Contreras, D., Destexhe, A. and Steriade, M. (1997). Dynamic interactions determine partial thalamic quiescence in a computer network model of spike-and-wave seizures. *J Neurophysiol* 77(4):1679–1696.
- Park, E.H. and Durand, D.M. (2006). Role of potassium lateral diffusion in non-synaptic epilepsy: a computational study. *J Theor Biol* 238(3):666–682.
- Rall, W. (1964). Theoretical significance of dendritic trees for neuronal input-output relations. In: *Neuronal theory and modeling* (R.F. Reiss, Ed.), pp. 73–97. Stanford University Press, Stanford.
- Santhakumar, V., Aradi, I. and Soltesz, I. (2005). Role of mossy fiber sprouting and mossy cell loss in hyperexcitability: a network model of the dentate gyrus incorporating cell types and axonal topography. *J Neurophysiol* 93(1):437–453.
- Spampinato, J., Aradi, I., Soltesz, I. and Goldin, A.L. (2004). Increased neuronal firing in computer simulations of sodium channel mutations that cause generalized epilepsy with febrile seizures plus. *J Neurophysiol* 91(5):2040–2050.
- Stephan, K.E., Kamper, L., Bozkurt, A., Burns, G.A., Young, M.P. and Kötter, R. (2001). Advanced database methodology for the Collation of Connectivity data on the Macaque brain (CoCoMac). *Philos Trans R Soc Lond B Biol Sci* 356(1412):1159–1186.
- Thomas, E. and Lyttton, W.W. (1998). Computer model of antiepileptic effects mediated by alterations in GABA(A)-mediated inhibition. *Neuroreport* 9(4):691–696.
- Traub, R.D., Contreras, D., Cunningham, M.O. et al. (2005). Single-column thalamocortical network model exhibiting gamma oscillations, sleep spindles, and epileptogenic bursts. *J Neurophysiol* 93(4):2194–2232.
- Yang, K.H., Franaszczuk, P.J. and Bergey, G.K. (2003). The influences of somatic and dendritic inhibition on bursting patterns in a neuronal circuit model. *Biol Cybern* 89(4):242–253.
- Yang, K.H., Franaszczuk, P.J. and Bergey, G.K. (2005). Inhibition modifies the effects of slow calcium-activated potassium channels on epileptiform activity in a neuronal network model. *Biol Cybern* 92(2):71–81.

# 4

## VALIDATING MODELS OF EPILEPSY

KEVIN STALEY, WALDEMAR SWIERCZ AND KRZYSZTOF J. CIOS

### ABSTRACT

Epilepsy has many etiologies that occur in a complex network. In contrast to the diversity of etiologies and the complexity of the network, the output of interest, seizures, is very simple. The simplicity of the output and the small numbers of measured parameters makes model validation difficult. Thus, it is not easy to determine the biological relevance of the manipulations used to generate the seizure output in realistic computer models with many necessary degrees of freedom. There are several ways to address this issue. The realism of the model can be increased by constraining the underlying cortical model to measured parameters. In addition, the output can be required to fit a more complex dataset by including measurements of as many parameters as possible, for example measures of network output that include temporal and physical dimensions. Measuring these parameters under as many experimental conditions as is feasible provides opportunities for additional tests of model accuracy. These constraints are likely to be the most practical approach to model validation in the near future. However, both model realism and model constraints are currently limited by the amount of experimental data available.

Epilepsy can be defined as a propensity for episodes of abnormally synchronous activation of the brain's neural networks. Working from this definition, it is clear that epilepsy is a network problem, i.e. there is no such thing as an 'epileptic neuron'. The recent tremendous interest in neural networks would therefore be expected to lead to a substantial increase in our understanding of epilepsy. This book reflects the initial steps toward such an understanding, but the process of modeling epilepsy entails some unique problems. In this chapter, we discuss the problem of validating models of epileptic neural networks.

One characteristic of epilepsy is the wide variety of pathogenetic mechanisms that lead to the epileptic state (Ottman, 2005; Ferraro et al., 2006). This is also reflected in the overwhelming multitude of laboratory models of genetic (Holmes, 2004; Baraban, 2007) and acquired (Dudek et al., 2002) epilepsy. In fact, the variety of pro-epileptic mechanisms is so extensive that these mechanisms sometimes overlap with anti-epileptic mechanisms. For example, mutations that reduce voltage-dependent sodium channel conductances (Yu et al., 2006) are proconvulsant, whereas global reduction of sodium channel conductances is considered to be the primary action of anticonvulsants such as phenytoin and carbamazepine (Willow et al., 1985). This turns out to be less contradictory than it seems, because the epileptogenic mutations that result in reduced sodium conductances occur in channel proteins whose expression is largely restricted to interneurons. The effects of drugs versus mutations on sodium channel function illustrate two key issues that affect models of epilepsy: first, there is a wide range of biological etiologies of epilepsy, and second, the system in which these etiologies occur is enormously complex. Our hope is that models of epileptic networks can help untangle the effects of diverse proconvulsant mechanisms occurring in a complex system. However, there might be many pathways to alter a complex system to create an epileptic state from a particular biological etiology, but only one of these pathways may be correct. How do we know that we have captured the correct pathway?

In contrast to the variety of defects that lead to the epileptic state, the output of an epileptic neural network during a seizure is very simple. The pathological synchronization of the neurons in the epileptic network implies that most or all neurons in the network are doing the same thing during a seizure. One of the things that neurons do synchronously during a seizure is release neurotransmitters. Because most neurons are glutamatergic, this results in a massive glutamate release that activates excitatory glutamate receptors, causing the paroxysmal depolarization shifts (PDS) in the membrane potential of the neurons in the epileptic network that is a hallmark of seizure activity (Enomoto and Ajmone-Marsan, 1959).

This depolarization is followed by a strong hyperpolarization largely mediated by calcium-activated potassium conductances (Alger and Nicoll, 1980). Thus, during a seizure, neurons go synchronously to an upstate during the PDS and subsequently to a downstate during the afterhyperpolarization, so that the entire network output is essentially binary.

We might define a model as a systematic description of causal relationships between input and output variables. Such a description can take many forms, for example an artificial neural network of spiking neurons, mathematical equations, classifier, etc. Regardless of the structure of the model, the number of independent pieces of information required for estimating or instantiating the model is called the model's degree of freedom. If we develop or read about several different models, how do we determine which is the best? With every model there is always a model error associated with it, which is calculated as the difference between the observed value and the model output value. To choose between several alternative models, we might select the 'best' one (an undertaking referred to as model selection) based on its goodness of fit (fit error) or its goodness of prediction (prediction error, or in machine learning parlance, the generalization error). These errors can be calculated only if training data, meaning known inputs corresponding to known outputs, are available (Cios et al., 2007).

So far, evaluating epileptic models seems feasible. We may have a parameter of interest, say a property of a sodium channel that has been demonstrated to be different in an *in vitro* expression system for a known human epileptogenic mutation. We know that seizures should occur if the model incorporates sodium channels with the property conferred by the mutation and the model should not demonstrate seizures if the property is not expressed.

One problem in evaluating epileptic networks is that the output of interest, a seizure, is very simple (it occurred or not). In contrast, there are a large number of seizure-generating mechanisms such as the aforementioned sodium channel parameters or reductions in synaptic inhibition. However, few of these mechanisms can be directly measured during the seizure and, generally, the model is only required for one or two parameters, such as a field recording of extracellular voltage and perhaps an extracellular ion concentration. In this situation, where the collected data are simple (low dimensional), one should, as a rule of thumb, fit to them a simple model. If instead, we fit to the data a complex model (such as a large network of spiking neurons, where the used neuron model is complex itself) with many degrees of freedom, we might get a very good fit by altering one or few parameters in the model but the biological validity of the model is difficult, if not impossible, to assess; such a model can be simply wrong. It is also difficult to compare various complex models one to another.

After all, any system with sufficient feedback can oscillate between up- and downstates (Mayr, 1970), which is all that we are requiring of the seizing network. In a system as complex as a neural network with abundant recurrent connections, such feedback can be supplied by any one of a very large number of single mechanisms (e.g. Baraban, 2007) or combinations of mechanisms (Ottman, 2005). How can we know if the mechanism we employ in a particular model is relevant to the defect we are modeling? An optimistic approach might be to assume that, in light of the rich variety of etiologies of epilepsy, any model mechanism that results in an epileptic output must be relevant to some biological process.

The optimistic approach might be valid if we were completely confident in the accuracy of the underlying model of the cortex, but computer models are only approximations. The parameters we plug into neural networks are based on noisy recordings that may have been obtained in cells that are different than the particular cells we are modeling; the observations may have been made under temperatures and other conditions that might not occur *in vivo*; the spatial resolution of the observation was probably not at the subcellular level, etc. The challenge is to capture biologically relevant behaviors based on biologically relevant alterations in a model that we know is incomplete and in some regards likely to be just plain wrong. In this context, the ease with which epileptic output can be generated is problematic. The model may behave as we hoped, but for reasons that are not biologically relevant.

One way to address the validation problem is to ascertain that the model is as biologically accurate as possible. Traub and coworkers used this approach in the development of a model for the CA3 area of the hippocampus (Traub and Miles, 1991) and this approach has recently been extended to full-scale models of the neighboring dentate gyrus (Dyhrfjeld-Johnsen, 2007). This approach seems so laudable as to not merit discussion, but of course there are important tradeoffs. Besides the limitation of knowledge discussed above, an important issue with realistic networks is feasibility, as the number of calculations per neuron increases tremendously with the number of interacting channels and receptors. Similar feasibility issues limit the numbers of neurons that can be included in the network. However, feasibility is relative: computational resources continue to become less expensive and code describing individual neurons continues to become more efficient (Carnevale and Hines, 2006). A second potential drawback of very realistic networks is the potential obscuration of relevant mechanisms. If every parameter included were subject to a 10 % error in measurement or instantiation, one could imagine that significant network outputs could occur that were solely due to interactions arising from the errors. Even without errors, it is not always easy to understand how a particular mechanism leads to a network output and this becomes more

difficult as the network becomes more complex. Understanding the input-output relationship is usually the reason the model was built in the first place and is the reason for building parsimonious models, i.e. models with no more than the necessary amount of detail.

Another approach to the validation problem is to recognize that seizures are not the only output of the epileptic cortex. In the human condition, even severely epileptic patients are usually not seizing more than 1% of the time. Depending on the type of epilepsy, the other 99% of the time the output of the epileptic cortex may be normal activity, as is the case for absence epilepsy (Suffczynski et al., 2005), or periodic interictal discharges, as is the case for focal-onset neocortical epilepsies (Staley and Dudek, 2006). So the requirement that the model undergo appropriate interictal-ictal transitions provides a very important constraint. This requirement is not trivial – many models generate only one type of activity. For example, models that generate short bursts of interictal activity usually do not generate longer periods of synchronous activity (Swiercz et al., 2007). The relative ratios of normal, interictal and ictal activity, i.e. the ratio of the time intervals containing only normal EEG background versus interictal spikes versus seizures, are not published to the best of our knowledge, although these data will provide important additional constraints to models of temporal lobe and other neocortical epilepsies. This temporal constraint can be extended to require that models generate ictal patterns that include biologically relevant periods of tonic output (continuous high-frequency output) followed by clonic output (bursts of high-frequency activity output) followed by post-ictal periods of reduced output.

We have utilized temporal constraints in the construction of a very simple and unrealistic model of the CA3 neural network (Staley et al., 2001). The CA3 network of the hippocampus is well known for generating periodic, synchronous network events that resemble interictal EEG spikes (Traub and Miles, 1991). The distribution of time intervals between these spontaneous bursts of population activity can be characterized by a mean and variance, but also by the skew (asymmetry of the distribution about the mean) and the kurtosis (the relative size of the tails of the distribution). We used the details of the shape of the temporal distribution of interspike intervals to test the idea that a single synaptic property was principally responsible for the timing of spontaneous bursts of population activity. The synaptic property of interest was the rate at which synapses recovered from use-dependent depression: during the population burst, it was hypothesized that the synapses connecting pyramidal cells in area CA3 released all readily available glutamate vesicles, so that population bursts were terminated by synaptic failures. The next burst could not occur until synapses had re-accumulated additional releasable glutamate vesicles. We required that a collection of synapses responsible for burst initiation recover in a way that explained all the details of the temporal distribution of spontaneous CA3 bursts. However, this constraint was not sufficient to differentiate our model from other CA3 models in which burst timing was considered to be due to other mechanisms (e.g. Agmon and Wells, 2003).

To extend the temporal constraints, we can further require that the model continue to conform to the details of the temporal distribution of activity under a variety of experimental conditions. For example, the activity-dependent synaptic depression described above can be modified by reducing the synchrony (Jones et al., 2007) or probability of glutamate release using, respectively, strontium or G protein-coupled receptor agonists such as baclofen (Staley et al., 1998, 2001). The effect of synaptically released glutamate, i.e. the probability of triggering an action potential in the postsynaptic neuron, can be modified by the presence of competitive antagonists of glutamate receptors. Network activity can also be modified by increasing the coupling between glutamate release and action potential generation in the postsynaptic neuron, e.g. by depolarizing neurons using increased extracellular potassium. The degree of synaptic inhibition can be increased using allosteric modulators of GABA<sub>A</sub> (gamma-aminobutyric acid) receptors such as benzodiazepines, and decreased using GABA<sub>A</sub> antagonists such as picrotoxin. We have used this series of experimental manipulations together with the constraint of accurately predicting the temporal distribution of network activity in both simple statistical models (Staley et al., 2001) as well as more realistic distributed models of area CA3 (Swiercz et al., 2007) (Figure 4.1). This combination of constraints provides a more rigorous test for comparing model output to electrophysiological measurements. However, we have only begun to address the additional constraint of requiring realistic interictal to ictal transition frequencies, in part because these data are only now becoming available (White et al., 2006).

In addition to increased constraints in the time dimension, models can be constrained in spatial output as well. Although during a seizure all neurons are doing the same thing, the means by which they arrive at that state is not homogeneous across the network. Requiring that a model recapitulate anatomically accurate patterns of seizure initiation and spread provide additional means by which to validate the accuracy of the model architecture and seizure mechanisms. One difficulty with this approach to validation is a lack of data regarding the initiation and spread of seizures. EEG data in general do not have sufficient spatial resolution to provide useful constraints on epilepsy models. Single electrode studies comprise the vast majority of experimental data regarding seizure activity, but clearly these contain no relevant spatial information. Voltage (Ang et al., 2006) and calcium (Trevelyan et al., 2006) imaging are beginning to provide some insights into

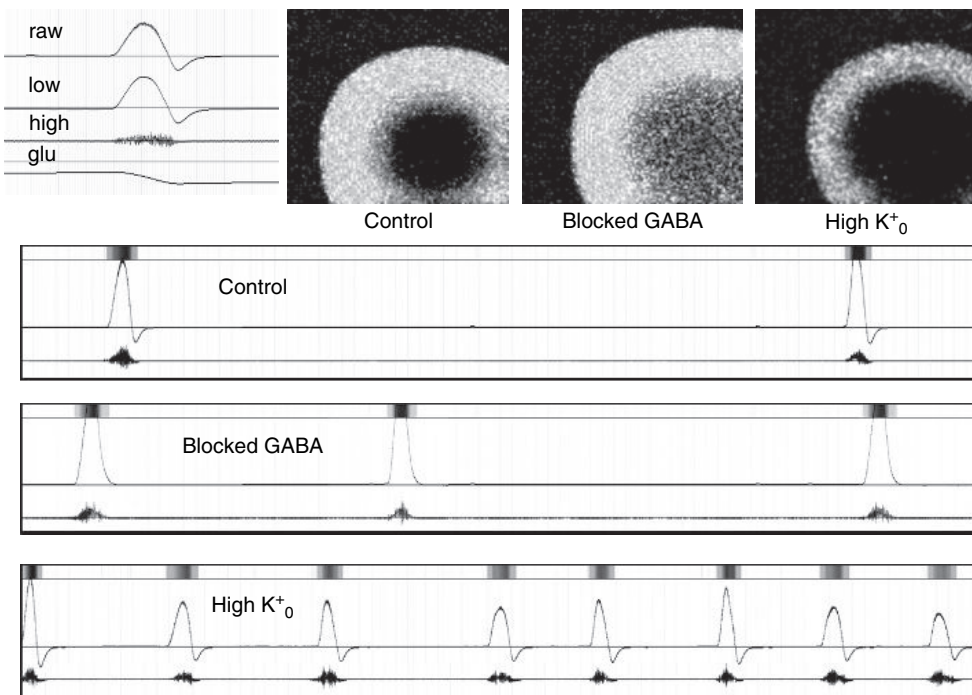


**FIGURE 4.1** Examination of model behavior under a variety of conditions provides additional tests of model accuracy. Upper right: outputs of the  $100 \times 100$  neuron model described in Swiercz et al. (2007). Shown are the calculated extracellular potential, after low-pass filtering (100Hz,  $-6$  dB/octave), high-pass filtering (100Hz,  $-6$  dB/octave) and the relative supply of releasable glutamate at recurrent collateral synapses. Upper left: snapshots of the spread of excitation under three experimental conditions: control, blocked GABA A and B conductances and in 8.5 mM extracellular potassium. Lower panels: calculated extracellular potentials corresponding to the same conditions. These model outputs are compared to the data obtained experimentally under the same conditions in Swiercz et al. (2007).

seizure activity in brain slices. Such network-level studies are clearly a significant advance over single-electrode studies of network phenomena such as epilepsy. However, spatially resolved studies of seizures and epilepsy are in their infancy and there are many questions that remain unanswered. For example, we do not have a clear idea about seizure activity in different cellular subtypes, e.g. interneurons versus pyramidal cells, nor do we know the spatial details regarding transitions between ictal and interictal activity.

## REFERENCES

- Agmon, A. and Wells, J.E. (2003). The role of the hyperpolarization-activated cationic current I(h) in the timing of interictal bursts in the neonatal hippocampus. *J Neurosci* 23(9):3658–3668.
- Alger, B.E. and Nicoll, R.A. (1980). Epileptiform burst afterhyperpolarization: calcium-dependent potassium potential in hippocampal CA1 pyramidal cells. *Science* 210(4474):1122–1124.
- Ang, C.W., Carlson, G.C. and Coulter, D.A. (2006). Massive and specific dysregulation of direct cortical input to the hippocampus in temporal lobe epilepsy. *J Neurosci* 26(46):11850–11856.
- Baraban, S.C. (2007). Emerging epilepsy models: insights from mice, flies, worms and fish. *Curr Opin Neurol* 20(2):164–168.
- Carnevale, N.T. and Hines, M.L. (2006). The NEURON Book. Cambridge University Press, Cambridge.
- Cios, K.J., Pedrycz, W., Swiniarski, R. and Kurgan, L. (2007). Data Mining: A Knowledge Discovery Approach. Springer. [www.springer.com/978-0-387-33333-5](http://www.springer.com/978-0-387-33333-5)
- Dudek, F.E., Staley, K.J. and Sutula, T.P. (2002). The search for animal models of epileptogenesis and pharmacoresistance: are there biologic barriers to simple validation strategies? *Epilepsia* 43(11):1275–1277.
- Dyhrfjeld-Johnsen, J., Santhakumar, V., Morgan, R.J., Huerta, R., Tsimring, L. and Soltesz, I. (2007). Topological determinants of epileptogenesis in large-scale structural and functional models of the dentate gyrus derived from experimental data. *J Neurophysiol* 97(2):1566–1587.
- Enomoto, T.F. and Ajmone-Marsan, C. (1959). Epileptic activation of single cortical neurons and their relationship with electroencephalographic discharges. *Electroencephalogr Clin Neurophysiol Suppl* 11(2):199–218.
- Ferraro, T.N., Drugos, D.J. and Buono, R.J. (2006). Role of genetics in the diagnosis and treatment of epilepsy. *Expert Rev Neurother* 6(12):1789–1800.

- Holmes, G.L. (2004). Models for generalized seizures. *Suppl Clin Neurophysiol* 57:415–424.
- Jones, J., Stubblefield, E.A., Benke, T.A. and Staley, K.J. (2007). Desynchronization of glutamate release prolongs synchronous CA3 network activity. *J Neurophysiol* 97(5):3812–3818.
- Mayr, O. (1970). The origins of feedback control. MIT Press, Cambridge.
- Ottman, R. (2005). Analysis of genetically complex epilepsies. *Epilepsia* 46 Suppl 10:7–14.
- Staley, K.J. and Dudek, F.E. (2006). Interictal spikes and epileptogenesis. *Epilepsy Curr* 6(6):199–202.
- Staley, K.J., Bains, J.S., Yee, A., Hellier, J. and Longacher, J.M. (2001). Statistical model relating CA3 burst probability to recovery from burst-induced depression at recurrent collateral synapses. *J Neurophysiol* 86(6):2736–2747.
- Staley, K.J., Longacher, M., Bains, J.S. and Yee, A. (1998). Presynaptic modulation of CA3 network activity. *Nat Neurosci* 1(3):201–209.
- Suffczynski, P., Lopes da Silva, F., Parra, J., Vélez, D. and Kalitzin, S. (2005). Epileptic transitions: model predictions and experimental validation. *J Clin Neurophysiol* 22(5):288–299.
- Swiercz, W., Cios, K., Hellier, J., Yee, A. and Staley, K. (2007). Effects of synaptic depression and recovery on synchronous network activity. *J Clin Neurophysiol* in press.
- Traub, R.D. and Miles, R. (1991). In: *Neuronal networks of the hippocampus*. Cambridge University Press, Cambridge.
- Trevelyan, A.J., Sussillo, D., Watson, B.O. and Yuste, R. (2006). Modular propagation of epileptiform activity: evidence for an inhibitory veto in neocortex. *J Neurosci* 26(48):12447–12455.
- White, A.M., Williams, P.A., Ferraro, D.J. et al. (2006). Efficient unsupervised algorithms for the detection of seizures in continuous EEG recordings from rats after brain injury. *J Neurosci Meth* 152(1–2):255–266.
- Willow, M., Gono, T. and Catterall, W.A. (1985). Voltage clamp analysis of the inhibitory actions of diphenylhydantoin and carbamazepine on voltage-sensitive sodium channels in neuroblastoma cells. *Mol Pharmacol* 27(5):549–558.
- Yu, F.H., Mantegazza, M., Westenbroek, R.E. et al. (2006). Reduced sodium current in GABAergic interneurons in a mouse model of severe myoclonic epilepsy in infancy. *Nat Neurosci* 9(9):1142–1149.

# 5

## USING NEUROCONSTRUCT TO DEVELOP AND MODIFY BIOLOGICALLY DETAILED 3D NEURONAL NETWORK MODELS IN HEALTH AND DISEASE

PADRAIG GLEESON, VOLKER STEUBER AND R. ANGUS SILVER

### ABSTRACT

In this chapter, we describe *neuroConstruct*, a new software tool for developing, modifying and analyzing neural network models with biologically realistic properties in 3D space (Gleeson et al., 2007). Network models are built and modified through a graphical user interface. The application then automatically writes code for existing simulators (NEURON and GENESIS) which carry out the numerical integration. This makes network modeling accessible to experimental and clinical researchers without programming skills. We focus on how *neuroConstruct* can be used to develop new 3D network models of brain function with anatomical, synaptic and cellular mechanisms with a high degree of biological realism. We illustrate how an existing network model of epilepsy implemented in *neuroConstruct* can be easily modified through the graphical user interface (GUI) and used as a tool for investigating the potential mechanisms underlying this condition. Lastly, we discuss how planned future developments of *neuroConstruct* will extend the types of brain mechanisms that can be simulated, allowing more realistic models of brain function in the future.

### INTRODUCTION

#### NEURAL NETWORKS ARE COMPLEX AND POORLY UNDERSTOOD

We know relatively little about how neuronal networks in the brain achieve the complex computations required for sensory perception, motor coordination and cognition. Neural networks, by definition, are highly interconnected structures and networks in the brain are especially complex due to heterogeneity in the morphology and connectivity of both excitatory and inhibitory cell types. Analysis of the connectivity of cortical networks has revealed common features including the prevalence of local connections (Song et al., 2005; Sporns and Kotter, 2004) and the highly non-random connectivity of local circuits (Lubke et al., 2003; Yoshimura and Callaway, 2005; Yoshimura et al., 2005). Non-random small world connectivity (Watts and Strogatz, 1998) has been found in neural networks of both *Caenorhabditis elegans*, which consist of only a few hundred neurons and in the mammalian dentate gyrus, containing a million neurons (Dyhrfjeld-Johnsen et al., 2007). Such theoretical approaches incorporating graph theory have also been used to examine the relationship between connectivity and how effectively activity spreads through neuronal networks (Masuda and Aihara, 2004). However, the fact that many types of biological and non-biological networks exhibit related connectivity patterns (Watts and Strogatz, 1998) indicates that this theoretical approach alone may be of limited use in understanding the structure–function relationship of a particular region of the brain.

Complexity is not only observed in the intricate 3D anatomical structure of neural networks but also in the spatial distribution and temporal dynamics of the underlying cellular mechanisms. For example, connections between layer 5

pyramidal cells exhibit a lognormal distribution of synaptic weights, which has a bell shape when plotted on a semi-log scale. This suggests that a few strong connections may dominate network activity (Song et al., 2005). Synaptic connections also exhibit time-dependent changes in their strength (plasticity) over many timescales, from a few milliseconds to days (Abbott and Regehr, 2004). Different combinations of the sub-synaptic plasticity mechanisms can result in a wide range of temporal properties at different synaptic connections (Dittman et al., 2000). Lastly, non-synaptic volume signaling mediated by diffusible messengers also contributes to signal processing by affecting the efficacy of particular ion channels or synapses in a particular region. This multiplicity of cellular and intercellular plasticity mechanisms underlies the highly dynamic and history dependent properties of networks in the brain. In healthy systems, network stability is maintained, even during the large changes that occur during development, by related homeostatic mechanisms which keep activity within normal operational bounds (Marder and Goaillard, 2006).

### MULTIPLE NETWORK PARAMETERS CHANGE DURING NEUROLOGICAL DISORDERS

Neurological disorders, including epilepsy, depression and autism, are thought to be caused by multiple genetic and environmental factors and are associated with a wide range of cellular and synaptic changes within particular brain regions. For epilepsy, the causes are often known, including hypoxia, stroke, infection and head trauma, but the mechanisms by which these insults cause epilepsy are poorly understood. Idiopathic epilepsies, which are mainly generalized, are thought to arise primarily from genetic factors, but the genes involved are often unknown. However, in some rare monogenic cases, epilepsy can be linked directly to mutations in specific channels (channelopathies), including sodium, potassium, gamma-aminobutyric acid (GABA) and glutamate channels (Chang and Lowenstein, 2003; Berkovic et al., 2006). While this provides some insight into the underlying mechanisms, even for these simplest cases, where a generalized seizure can be linked to mutations in single genes, such as those encoding voltage-gated  $\text{Na}^+$  channel subunits (Wallace et al., 1998; Escayg et al., 2000), the link between alterations in channel properties and higher level epileptiform activity is still uncertain. This is because so many variables contribute to and are influenced by network activity. For example, some hippocampal neurons appear to be able to compensate for loss of function mutations in  $\text{Na}^+$  channels that causes myoclonic epilepsy in infancy, while interneurons do not (Yu et al., 2006). This raises the possibility that reduced sodium currents in GABAergic inhibitory interneurons underlie this particular case. In general, it is also possible that if homeostatic compensation is incomplete and aberrant activity ensues, this may trigger other plasticity mechanisms. These activity dependent features of networks, which underlie their ability to adapt and store information, make it difficult to disentangle the key determinants of epileptiform activity from their effects. Given this complexity it is clear that a better understanding of network properties in health and disease is required to design successful new interventions for this debilitating condition.

### NETWORK MODELS AS AN AID TO HELP OUR UNDERSTANDING OF BRAIN FUNCTION IN HEALTH AND DISEASE

One approach for developing a better understanding of brain function is to construct neural network models with biologically realistic features. These models consist of interconnected model cells with multiple electrical compartments to mimic the soma and dendrites, Hodgkin-Huxley type voltage gated conductances and semi-realistic synaptic connectivity. Several of these types of models have been implemented using the NEURON (Hines and Carnevale, 1997) or GENESIS (Bower and Beeman, 1997) neural simulation packages, two programs specifically designed for compartmental neuronal modeling. Compartmental models have been used to investigate a wide range of network behaviors. These include synchronous firing in groups of cells (Maex and De Schutter, 1998; Davison et al., 2003), network oscillations in the gamma frequency range (Traub et al., 2005), hippocampal memory (Kunec et al., 2005) and the influence of short-term synaptic plasticity in temporal coding (Buonomano, 2000). They have also provided insights into the potential causes of epileptiform activity. For example, using a large-scale network model of the dentate gyrus (Santhakumar et al., 2005), it has been shown that mossy fiber sprouting, which is characteristic of repeated seizures and head trauma, is capable of generating widespread epileptiform activity in the dentate gyrus, lending support to the idea that this is a contributory mechanism. Moreover, simulations with a detailed thalamocortical model (Traub et al., 2005) suggest that electrical synapses might be involved in generating epileptiform bursts of activity. The advantage of using network models with biologically realistic features is that they are useful tools for understanding how cellular and synaptic mechanisms could potentially influence higher level network function. This approach can be used to identify likely determinants of network dysfunction and allow the effectiveness of potential interventions to be explored.

## LIMITATIONS IN THE BIOLOGICAL REALISM OF CURRENT NEURAL NETWORK MODELS

The power of a model to reproduce and ultimately to predict certain properties of a biological network depends critically on whether the key determinants of network behavior are implemented. Since these are, *a priori*, not known, it seems prudent to reproduce the known properties of the biological mechanisms as closely as possible. Nevertheless, many important biological properties are absent from current network models. For example, 3D anatomical features are absent from most large-scale neural network models due to the severe technical difficulties in reproducing and verifying the highly non-uniform properties of biological neuronal connectivity in 3D. Indeed, with the exception of some preliminary models (Howell et al., 2000; Berends et al., 2004), virtually all models to date utilize highly simplified synaptic connectivity, with abstract neurons connected in either one (Maex and De Schutter, 1998; Santhakumar et al., 2005) or two dimensions (Medina and Mauk, 2000; Schweighofer and Ferriol, 2000).

Network models that include more detailed 3D information would have a number of advantages. A more thorough validation of the model connectivity would be possible through direct comparison with detailed anatomical measurements, which are available for several brain regions including cortex (Somogyi et al., 1998; Thomson et al., 2002; Douglas and Martin, 2004) and cerebellum (Harvey and Napper, 1991; Sultan and Bower, 1998). This is particularly important for brain regions with complex synaptic connectivity patterns such as the cortex. Associating cells and synapses in the model with specific 3D locations could also be used to simulate other important aspects of brain function including the diffusion of signaling molecules and metabolites. The rate at which a diffusant decays (and the peak concentration reached at a particular distance) from an instantaneous point source depends strongly on the number of spatial dimensions, with 3D geometries decaying most rapidly (Crank, 1993). Simulating diffusion processes with the appropriate geometry is important because the number of dimensions will influence the distance over which receptors, of a particular affinity, can be activated by a signaling event. Signaling molecules include both classical neuromodulators (e.g. acetylcholine and serotonin) and substances such as NO (Crepel and Jaijard, 1990; Jacoby et al., 2001; Maffei et al., 2003) and cannabinoids (Alger, 2002; Wilson and Nicoll, 2002; Safo et al., 2006), which can diffuse over tens of micrometers from their site of generation and modulate the weights of both excitatory and inhibitory synapses. Interestingly, the cannabinoid signaling has recently been implicated in homeostatic functions (Marcaggi and Attwell, 2005) and in both epilepsy (Chen et al., 2007) and Parkinson's disease (Kreitzer and Malenka, 2007), highlighting the importance of volume base signaling in network dysfunction. The 3D representation could also be used to implement vasculature in neuronal models and the diffusion of O<sub>2</sub>, CO<sub>2</sub>, glucose and metabolites. This could provide a deeper insight into the relationship between metabolism and neuronal activity, which underlies functional imaging (Attwell and Iadecola, 2002). Extracellular electrical fields could be simulated in 3D, potentially allowing characteristic epileptiform electroencephalogram (EEG) recordings to be modeled at the cellular level. 3D network models would also allow a more direct comparison of the spatiotemporal properties of simulated neural activity with multielectrode recordings (Nicolelis and Ribeiro, 2002; Buzsaki, 2004) or 2-photon imaging of multiunit activity in blocks of tissue (Helmchen and Denk, 2002; Stosiek et al., 2003; Kerr et al., 2005; Ohki et al., 2005; Gobel et al., 2007).

## PRACTICAL DIFFICULTIES OF USING EXISTING NEURAL NETWORK MODELS

While it is clear that network models with greater biological realism are desirable in the future, existing models are still extremely useful research tools for understanding complex network function. Although many single cell and network models are available on public databases (Hines et al., 2004), their use is restricted to those familiar with the specialist simulator specific scripting languages. This makes them inaccessible to a wide range of neuroscientists who have limited programming skills including many experimentalists and clinical researchers. Although graphical user interfaces (GUIs), which allow data to be entered and manipulations to be carried out without programming, have significantly improved the accessibility of single cell models implemented in current simulators such as NEURON (Hines and Carnevale, 1997) and GENESIS (Bower and Beeman, 1997), network models are generally beyond the scope of their GUIs and have typically been developed by writing code through their scripting interfaces. This direct coding approach prevents a wide range of interested scientists from using existing models to test hypotheses about network function in health and disease. It also limits the number of groups that can contribute to the development of new models in the future.

The large number of in-house and publicly available network simulators that have been developed means that accessibility to network models is not only a problem for non-programmers. Models built within these independently developed simulator environments have different internal representations and formats. In practice, this means that a synaptic or neuronal model developed in an application such as NEURON cannot be used as a component part of a GENESIS model unless it is completely rewritten, requiring specialist knowledge of both simulator languages. This multiple format problem has severely limited the interchange and reuse of models within this area of computational neuroscience.

## NEUROCONSTRUCT: A TOOL FOR BUILDING MORE REALISTIC AND ACCESSIBLE MODELS OF BRAIN FUNCTION

In this chapter, we describe a Java-based software application, *neuroConstruct*, that facilitates the creation, visualization and analysis of networks of multicompartmental neurons in 3D space (Gleeson et al., 2007). Network models can be built and modified through a GUI without programming. The internal representations of models within *neuroConstruct* are based on simulator-independent NeuroML standards allowing model reuse and interoperability (Goddard et al., 2001; Crook et al., 2007; Gleeson et al., 2007). This allows the application to generate automatically command scripts for either NEURON or GENESIS, which carry out the numerical integration. We demonstrate how *neuroConstruct* can be used to modify and run an existing model of epileptic behavior (Santhakumar et al., 2005) by simply interacting with the GUI. Furthermore, we show how this program can be used to generate more anatomically realistic network models of other brain regions.

### OVERVIEW OF APPLICATION

#### SCOPE

The software application we have developed is designed to facilitate the creation of 3D networks of multicompartmental, conductance-based neuron models, by building on existing software packages which have been used for many years to create single cell and small network models. The level of ‘biological realism’ of models created with *neuroConstruct* is roughly matched to that supported by the simulation environments: i.e. cell models with 3D morphology at the resolution of electrotonic discretization; membrane conductances based on the Hodgkin-Huxley formalism; phenomenological synaptic models and event based synaptic transmission. *neuroConstruct* provides a framework for specifying the elements of these network models through a graphical interface, managing the complexity inherent in such systems, facilitating access to any cell or network parameter value and use of the 3D positional information for adding extra simulation features (e.g. diffusion mechanisms) or for more detailed analysis of network activity (e.g. identifying spatially dependent correlations).

### APPLICATION PRACTICALITIES

The application is freely available and details can be found at <http://www.neuroConstruct.org>. It is a desktop based application written in Java, and so can be run on a wide range of machine architectures and operating systems. Automatic installers are available for Windows, Mac OS and Linux. The main interface is shown in Figure 5.1A. The network models are organized into projects containing all of the constituent elements (cell types, 3D region information, network connections, etc.). While networks can be built and analyzed through the interface alone, the simulation is run on one of the existing simulators. The script files generated by *neuroConstruct* are in the native language of the chosen simulation platform, making them open to modification and refinement by experienced users.

### FIVE MAIN FUNCTIONALITY AREAS

The functionality of *neuroConstruct* is divided into five main areas (see Figure 5.1B).

#### Importation and validation of morphologies

Many biologically realistic models of neurons use reconstructed morphologies (De Schutter and Bower, 1994; Mainen et al., 1995; Migliore et al., 1995; Rapp et al., 1996; Destexhe and Pare, 1999; Vetter et al., 2001; Poirazi et al., 2003; Schaefer et al., 2003; Hanson et al., 2004; Golding et al., 2005; Jarsky et al., 2005) and public databases have been produced which contain examples of these in a number of different formats (Cannon et al., 1998; Ascoli, 2006). *neuroConstruct* supports importation of morphological data files in various formats including Neurolucida’s \*.asc files (Glaser and Glaser, 1990), GENESIS readcell compatible format (\*.p), most NEURON/ntscable based morphology files (\*.nrn or \*.hoc) and Cvapp (\*.asc) format (Cannon et al., 1998). Morphology files can also be imported and exported in MorphML format (Crook et al., 2007), which is part of the NeuroML standards, as outlined later. The imported files can be validated and checked for errors or artifacts such as zero length or diameter segments of the dendritic tree, which commonly occur during reconstruction. When network models with large numbers of cells are to be generated, representations of cells with reduced numbers of compartments are often used to speed simulations while preserving some aspects of cell region

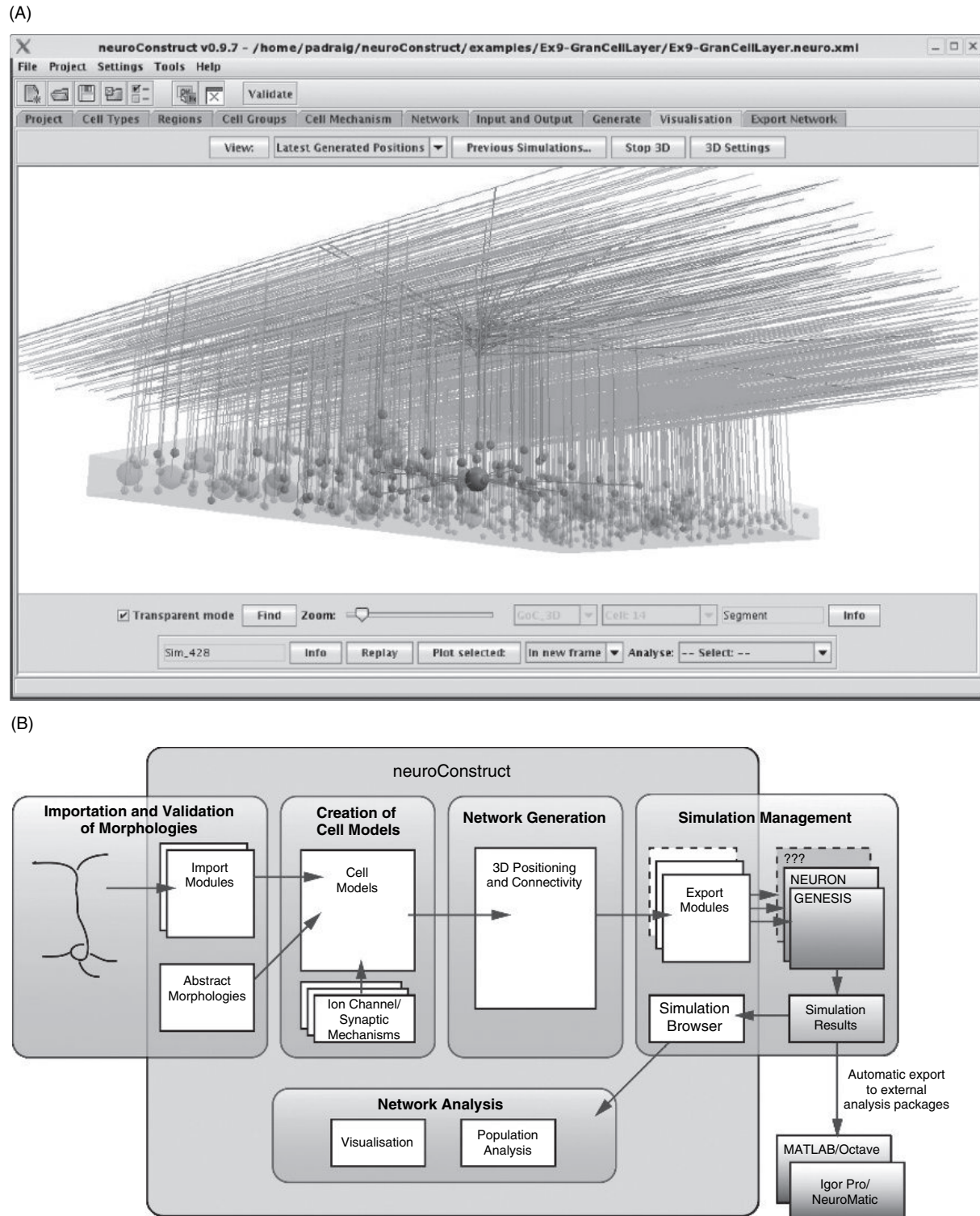


**FIGURE 5.1** Application interface and main functionality. (A) The main interface to *neuroConstruct*, showing a visualization of a network model of the cerebellar granule cell layer in 3D, with a single Golgi cell highlighted to display its pre- and postsynaptic targets. (B) The main functional areas of the application. Modified from Gleeson et al., 2007, with permission. (See Plate 1 in color plate section.)

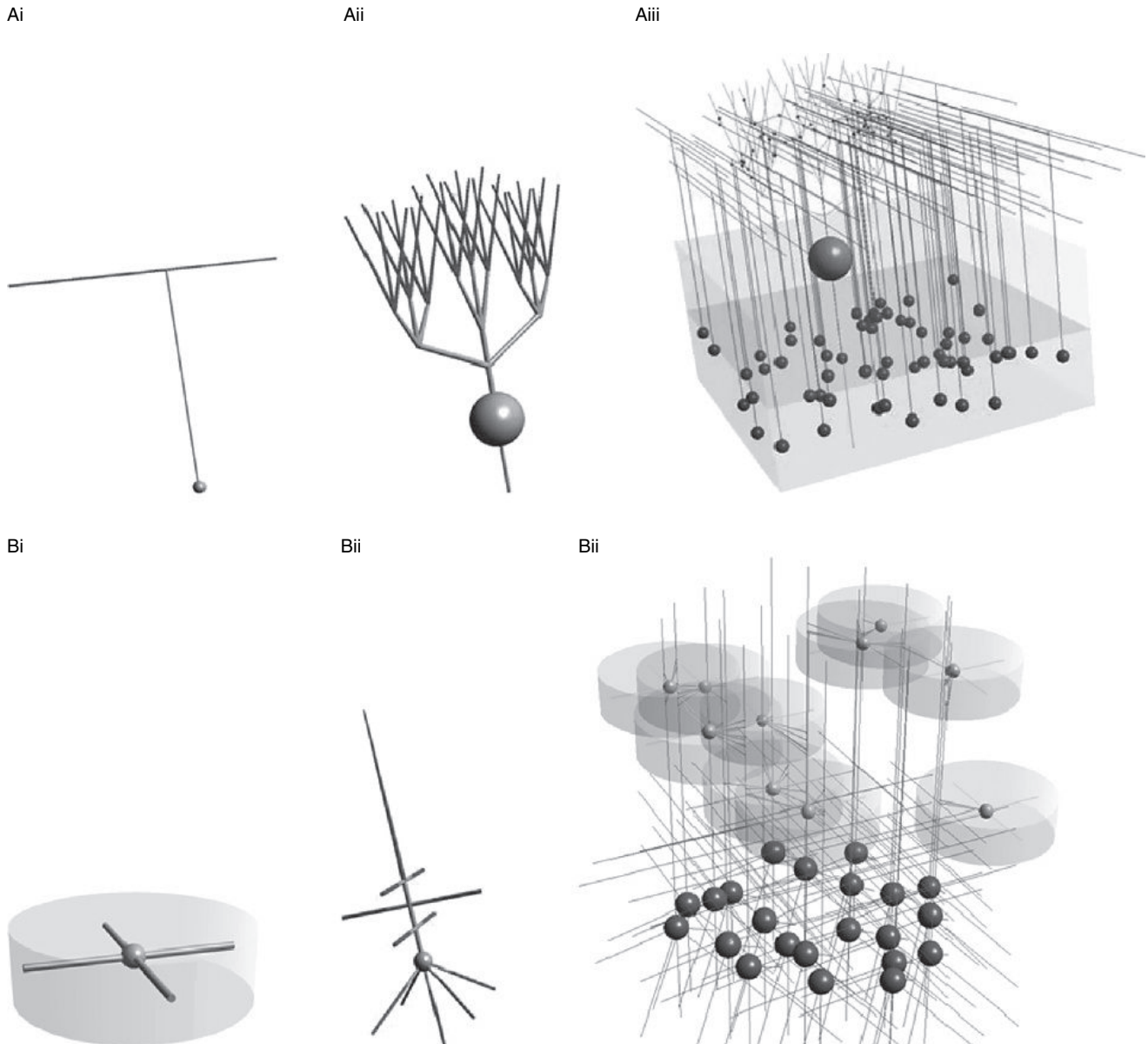


**FIGURE 5.2** Connectivity schemes possible in *neuroConstruct*. (A) Morphology based connection. Connections can be made between specified subregions on the presynaptic granule cell (i) and postsynaptic Purkinje cells (ii). Various other parameters can be set including maximum/minimum length of connections and number of pre-/postsynaptic connections allowed per cell. The connections are shown as green (presynaptic) and red (postsynaptic) spheres connected by lines. (iii) (B) Volume based connection. A region can be specified around presynaptic cells where axonal connections can potentially be made (i). Postsynaptic cells have regions specified associated with this type of connection (ii). Intersections between the 3D axonal regions and permitted dendritic sections can lead to connections, in line with the other rules on numbers of connections per cell (iii). Reproduced from Gleeson et al., 2007, with permission. (See Plate 2 in color plate section.)

specificity of synaptic connections and inhomogeneous channel density (Santhakumar et al., 2005; Traub et al., 2005). These more abstract cells can be created manually in *neuroConstruct* (e.g. see Figure 5.2). For all types of cells, groups of cell sections can be defined, allowing specification of axons, apical and basal dendrites, etc.

### Creation of cell models

To give a cell model realistic electrophysiological behavior, mechanisms representing voltage and ion concentration dependent conductances must be added to the cell membrane. This is a core feature of packages like NEURON and

GENESIS and distinguishes them from more abstract neural network simulators. Models of ion channel conductances, as well as internal ion concentration and synaptic mechanisms, can be created in *neuroConstruct* in one of two ways. Script files in the native language of one of the supported simulators can be reused, allowing simulation only on that platform, or the parameters for the mechanism can be specified in a simulator independent format (ChannelML, see Section on methodologies below), which can be mapped onto the language of the simulators. Electrophysiological cell models in *neuroConstruct* can be created by specifying the conductance densities of channel mechanisms at various locations on the cell membrane. Passive properties of cells can also be set (e.g. axial resistance and specific capacitance) as can the potential location for synaptic connections on different regions of the cell.

### Network generation

Once a number of cells have been added to the project, these can be arranged in 3D space according to a number of packing patterns. These can vary from abstract arrangements to cells packed in a random manner, avoiding somata of other cells and reproducing closely the measured anatomical cell densities (see Section on methodologies below). Connections can be made between cell groups taking into account allowed synaptic locations for each cell and a number of other factors such as maximum and minimum connection length, number of synapses per pre-/postsynaptic cells, etc. Generated networks can be analyzed visually (see Figure 5.1A) and there are a number of inbuilt tools to display connection length distributions, synaptic convergence/divergence ratios, etc. Electrical stimulation of various forms can be applied to subsets of cells of the network.

### Simulation management

The simulator independent representation of the cell and network structures can be mapped onto script files for instantiating the models in NEURON or GENESIS. Additional parameters such as simulation duration, time step and method of numerical integration are specified through the interface, as are lists of variables to record or plot during the simulation (e.g. membrane potentials, synaptic conductances, internal ion concentrations). Simulations are initiated through the interface and run on standard versions of the simulators. There is no interaction between *neuroConstruct* and the individual simulators during the simulation run. Data from the simulation are saved in a simple text format and there is a simulation browsing interface in *neuroConstruct* which lists recorded simulations.

### Network analysis

The simulation results can be loaded back into *neuroConstruct* for analysis. The network behavior can be visualized by replaying the simulation with, for example, cells color coded according to membrane potential or spiking frequency. Plots of individual cell traces can be displayed and there are extra functions present for network wide analysis, e.g. generation of rasterplots of cell groups, spiking histograms, correlation functions between individual cells and other cells in the same group, etc. Importation of simulation data into numerical analysis packages such as MATLAB and IGOR Pro is also possible.

## ACCESSIBILITY AND TRANSPARENCY OF MODELS

Various features of *neuroConstruct* make model construction and analysis more accessible for a wider range of (non-computational) neuroscientists and make the models themselves more portable and their internal structure more transparent.

## VISUALIZATION

As networks and even single cells incorporating a high level of biological realism can get quite complicated, a 3D visualization of the model elements can be essential to verify their representation of the known anatomy. Various views of such elements are possible in *neuroConstruct*, e.g. full 3D depiction of all cell sections, dendritic trees represented by lines, networks with some cells rendered semi-transparent (see Figure 5.1A) or visualization of somata only, etc. The level of detail can be adjusted according to the network size and graphical capabilities of the machine. Accessibility of the underlying information is important too and individual segments (when viewing single cells) or whole cells (in a network view) can be clicked and information displayed on 3D position, connections, etc.

## GUI AS OPPOSED TO SCRIPT

Creating a model on NEURON or GENESIS usually involves writing script files in the language of the simulator to create the cells, channel mechanisms and network connections, set the simulation parameters and record and analyze simulation results. There have been many improvements to the GUI capabilities of the simulators over the years, but most models published by experienced developers are script file based. *neuroConstruct* allows construction of network models from scratch through the graphical interface. A number of templates of cells, channel and synaptic mechanisms are present on which to base new models. All parameters of the simulation are accessible through the interface. Notwithstanding this ‘point and click’ approach, all script generated can be customized by experienced users, as outlined later.

## AUTOMATIC VALIDITY CHECKS

*neuroConstruct* has a number of inbuilt checks to help avoid problems common to compartmental neuronal models and these are designed to catch many potential sources of errors, which will increase as network models become more complex with elements from many different sources. The checks can lead to warnings or errors, depending on the severity of the problem, with explanations of the potential issues. Validity checks are carried out:

1. on cellular morphologies, checking that the description does not contain information which may be problematic on some platforms (e.g. zero diameter segments can be allowed on NEURON but will cause problems on GENESIS)
2. on cellular electrical properties, with checks, for example, on appropriate electronic length and on presence of at least one passive conductance on each section
3. on project wide settings, e.g. for appropriate simulation time step and simulation temperature values.

The user is also alerted when certain actions may lead to problems, for example if a cell model is imported from another project at a different temperature, as the temperature dependence of channel kinetics can cause spurious behavior. Even when a project has errors, networks can still be generated and run, but the accuracy of the simulation results should be viewed in the light of these warnings.

## MODULARITY AND SIMULATOR INDEPENDENT STORAGE OF PARAMETERS

When a neuronal model is published and the source scripts are made available, they are often in a format which mixes cell structure and biophysical properties, cell location and connectivity, simulation settings and data plotting/saving/analysis. Unless the elements are suitably partitioned and commented, reuse in other models on the same platform can be difficult, before even considering the change in language needed to use them on other platforms. *neuroConstruct* is structured so that cells and cell mechanisms can easily be transferred between projects. This modularity also allows easy update of model elements, e.g. if more detailed experimental data become available leading to an updated cell mechanism, this can easily be replaced in the model. The focus is on making the physiologically relevant parameters accessible, without the requirement to encode the information in a format specific for one application. This is the motivation behind the simulator independent standards used by *neuroConstruct*, with files containing only the parameters needed to create, for example, an  $\text{Na}^+$  channel, or a synaptic mechanism with a double exponential conductance waveform (see Figures 5.3 and 5.4). The generation of simulator scripts from these is straightforward once the mappings are available and these technicalities are hidden from the user. This approach leads to greater transparency: the user can check a user friendly, formatted and commented HTML representation of the channel parameters and generate plots of the rate variables (see below). Another advantage is compatibility with future simulators. Models specified in this open format can be made available for use in those new applications by creating suitable mapping files. Testing a model specified in physiological parameters alone on multiple independent platforms checks that the simulation results are not an artifact of an implementation on a single platform.

## SIMULATION MANAGEMENT/BROWSING

An interface is provided to browse, and reload for analysis, saved simulations. This framework makes management of large sets of simulation data easier and increases the chance that simulation data can be reused by others. It also leads to a shorter turnaround time between making a change in a model and seeing the effect on the network behavior, allowing quicker ‘time to insight’.

## SIMULATION CONFIGURATIONS

A detailed neuronal network model will usually be used to study a number of features of interest to researchers. A typical paper describing such a model will contain a discussion of the behavior of each cell, tests made to establish normal network function and detailed examination of the network behavior under different input conditions. However, the scripts which are made available for the model usually only illustrate a limited set or even just the main conclusion of the study. The use of multiple simulation configurations in *neuroConstruct* projects allows different aspects of network behavior to be illustrated. A simulation configuration consists of a subset of cell groups, network connections, inputs and an associated list of parameters to save/plot, which can highlight one aspect of the network functionality. Simulation configurations can be included for each main point in the accompanying paper's argument, or possibly could reproduce each figure. These are also useful at the development stage of the model as changes/updates to a single element of the model might not have obvious changes in one scenario, but all simulation configurations can be rechecked to ensure the behavior in multiple scenarios is not affected by the change.

## TUTORIALS, EXAMPLES AND DOCUMENTATION

The standard distribution of the application includes a number of items designed to help users learn to use the features of the platform effectively. Documentation is available through the interface, explaining some of the core concepts, e.g. platform specific behavior of the application, interaction with the simulators, importation of morphology files and channel mechanisms. An extensive glossary is included outlining the terms used in the applications and providing information on the various methods used by the application. On the interface itself there are a number of pop up tool tips (which can be turned off), which give context specific information for buttons, text boxes, etc. Tutorials are included that guide users through setting up new projects and creating example networks. The examples distributed with the application, some of which are discussed in this chapter, illustrate almost all of the functionality present in the application.

## ADVANCED FEATURES FOR EXPERIENCED USERS

Most experienced NEURON and GENESIS users create models using script files and the command line interfaces of these packages alone. Also, there is a wealth of existing code for cells and cell mechanisms (Hines et al., 2004), not all of which can currently be mapped onto the current version of the simulator independent standards used in *neuroConstruct*. There are two ways *neuroConstruct* allows existing or custom code to be incorporated into network models built through the interface. As mentioned previously, files describing channel, synaptic or ion concentration mechanisms (implemented in NMODL (Hines and Carnevale, 2000) for NEURON, or using the appropriate object in GENESIS) can be reused in *neuroConstruct* with minor modification. Also, blocks of native code can be included in a *neuroConstruct* project which will be inserted at appropriate locations when the code is generated to customize the cells and network, e.g. before cell group creation, just before simulation run, after saving the simulation data. These methods for customization allow the addition of any functionality present in the simulators but not currently supported through the *neuroConstruct* GUI.

Export of data in a simulator independent format also allows investigators to use whatever subset of *neuroConstruct*'s functionality appropriate for their research needs without tying them to the currently supported simulators or inbuilt analysis functions. For example, a cell model can be created and validated, either by hand or from an imported reconstruction, and then exported in MorphML (see below) for use in another application. Networks can be created in *neuroConstruct*, visualized and then exported for further processing by external applications, e.g. to perform graph theoretical analyses on the generated network.

Simulation data saved by *neuroConstruct* generated code can be analyzed with a number of functions built into the application. However, modelers are used to analyzing the data with their own customized scripts. When a simulation is executed, script files in two popular numerical analysis tool formats are generated which allow easy loading of the data into these applications. MATLAB from The MathWorks is a very popular package for data analysis and some basic script files for generation of histograms, rasterplots, etc. are included when the saved simulation data are loaded into this application. GNU Octave (<http://www.octave.org>) is a free, open source package which is compatible with most MATLAB scripts and can also be used for this purpose. Script files are also generated for loading of the simulation data into IGOR Pro from WaveMetrics. NeuroMatic (<http://www.neuromatic.thinkrandom.com>) is an open source set of functions for IGOR Pro, specifically designed for analysis of electrophysiological data and can be used also for analyzing the data generated by the simulators.

## METHODOLOGIES WITHIN NEUROCONSTRUCT

In this section, we discuss some of the technologies and algorithms used by *neuroConstruct* to generate the networks and map them onto the supported simulation environments.

### 3D POSITIONING AND CONNECTIVITY ALGORITHMS

The placement of cell models in 3D and their connection according to parameters based on anatomical measurements is a key feature of *neuroConstruct*.

#### 3D regions and packing

All objects used in networks in *neuroConstruct* are arranged according to a 3D reference space. Regions of interest within this space can also be defined through the *neuroConstruct* interface. Currently supported regions are rectangular boxes, spheres, cylinders or cones. A number of these named, possibly overlapping regions can be added in which to place cells. Cell groups are defined by specifying the type of cell, the 3D region associated with it and the packing pattern for the region. A number of different packing patterns are possible: cubic close packing for maximum density, simple regular packing with soma centers aligned along the x, y, z axes, cells arranged in a 1D line in a specified direction, hexagonally arranged cells in a single layer and cells whose precise location is specified. Moreover, there is also the option to pack a certain number of cells randomly in the specified region. These cells can either occupy any location in the region or can be packed to avoid already placed cells. The density of cells in these regions can be checked against anatomical data.

#### Connectivity mechanisms

The connectivity between cell groups can be specified in two ways, depending on information available about the axonal arborization of the source cell.

##### *Morphology based connections*

Morphology based connections are appropriate when the axon has a well stereotyped shape, as for example for the parallel fiber axons of cerebellar granule cells, for axons such as the cerebellar mossy fiber where the axon terminal is large, or when the axon has been explicitly reconstructed. This scheme uses cells which have explicit representations for both the axons and dendrites, possibly with limited parts of each allowing synaptic connections of a particular kind. Figure 5.2A shows an example of this. An abstract granule cell (GrC) consists of a soma, an ascending segment and a bifurcation leading to the parallel fibers (PFs). This region of the cell is specified as the presynaptic location for the network connection (highlighted in red in Figure 5.2Ai). The Purkinje cell (PC, see Figure 5.2Aii) has a simplified dendritic tree and a subset of this is a potential target for synaptic connections. A number of other settings need to be made for this connection: the number of connections per source or target cell (in this case at most one GrC connection to each PC); the synaptic mechanisms associated with the connection and their weights and delays; the maximum and minimum lengths of connections between axonal/dendritic sections (ensuring PFs only connect to PCs along their path); a speed of propagation of the signal along these connections; the search mechanism to use for finding connections (e.g. connect at random to any postsynaptic point, connect to closest, connect to closest of a pool of connection points selected at random).

##### *Volume based connections*

The volume based connection algorithm is used when the axonal arborization is dense and distributed over a defined region relative to the cell body, possibly with inhomogeneous connectivity probability within that region. Figure 5.2B shows an example of this type of connection between an abstract interneuron and a pyramidal cell in a simple 3D cortex model. The interneuron in Figure 5.2Bi has a cylindrical region around it representing the extent of the axonal arborization in which it can make synaptic contacts. The pyramidal cell in Figure 5.2Bii has some of its dendritic sections specified as accepting synaptic connections of this type. Connections are made from each presynaptic cell in turn, only on suitable dendritic sections which intersect the axonal volume. Similarly to the morphology based connection, the numbers of pre- and postsynaptic connections on cells can be set, as can the speed of propagation of the signal along the connections and the types and weights/delays of the synaptic connections. There is also the possibility to introduce non-uniformity into the connectivity probability within the volume. A function can be defined in terms of x, y, z, relative to the soma (or r, the radial distance) which gives a value between zero and one at each point. When a potential connection point is found, this value is used to decide probabilistically whether to accept the connection or continue with another location. With such a

scheme, connections can be made, e.g. with a Gaussian connectivity probability, which favor local connections but which allow the possibility of some long-range axons.

### Other 3D functionality

A number of other features are included with *neuroConstruct* to make use of the 3D information associated with network model elements.

#### *Action potential propagation substitution*

While explicit representation of the axonal structure may be required to enable correct connectivity (e.g. PF to PC synapse), simulation of all of the compartments of the axon adds extra computational burden. Sections of cells in *neuroConstruct* can be given an action potential propagation speed (APPS), which will be used in place of the axonal sections in simulations. The length along such sections can be calculated and an extra synaptic delay added based on this and the APPS. As well as speeding up the simulations, it is more likely that experimental information will be available on the APPS rather than detailed information on the types and densities of ion channels on the axons that are required for explicit simulation.

#### *Region specific stimulation*

Electrical input of two types can be specified for the cell groups: pulse of a certain duration and amplitude, or random stimulations at a given frequency or range of frequencies. These inputs can be applied to all cells in a cell group, an enumerated subset, a fixed number of cells or a percentage of cells. Another option is to apply the inputs only to cells inside (or outside) a specified 3D region. This allows application of spatially specific input patterns into cell groups, which can be used to analyze the transformation of spatial activity patterns between layers in complex networks.

### 3D diffusion mechanisms

Diffusible signaling substances (e.g. NO, cannabinoids) can have effects tens of microns from their points of release. They diffuse in all directions and can modulate the behavior of numerous types of synaptic and membrane conductance mechanisms. Cell mechanisms in *neuroConstruct* can use information on their 3D positions to calculate location specific effects of changes in other cell mechanism variables. This feature, which currently relies on native simulator mechanism scripts, has been used to create a basic model of release of a diffusible substance which transiently inhibits synapses as a function of distance and time (Gleeson et al., 2007). More support for this type of mechanism, and for simulating the influence of external and internal substances on cell mechanism behavior in general, will be possible with updates to the NeuroML specifications (see discussion).

#### *3D network analysis*

Simulations reloaded into *neuroConstruct* can be analyzed at the single cell and network levels. Also, by defining interesting 3D subregions of the network, subsets of cells can be analyzed separately, to look for local correlations or variations from global behavior (see below).

## NEUROML

### Overview

The Neural Open Markup Language project, NeuroML (Goddard et al., 2001; Crook et al., 2007; Gleeson et al., 2007), is an international, collaborative initiative to create standards for the description and interchange of models of neuronal systems (the latest version of the specifications are available at <http://www.neuroml.org>). The need for standards that allow for greater software interoperability is driving the current NeuroML project, which focuses on the key objects that need to be exchanged among existing applications and tries to anticipate those needed by future neuroscience applications. The standards outline the data required in XML (eXtensible Markup Language) files describing elements of the models. XML is used as this format is portable across many platforms and it is easy for software applications to validate the contents of the files against published schemas, and convert the contents into more usable formats, as outlined later.

### Levels present in NeuroML standards

The current standards are arranged in Levels (Figure 5.3), with each subsequent Level increasing the scope of the specification. Level 1 of the standards provides both a framework for describing specifications of neuroanatomical data (e.g. the branching structure of neurons, histological features) and the metadata associated with a neuronal model (e.g. authorship,

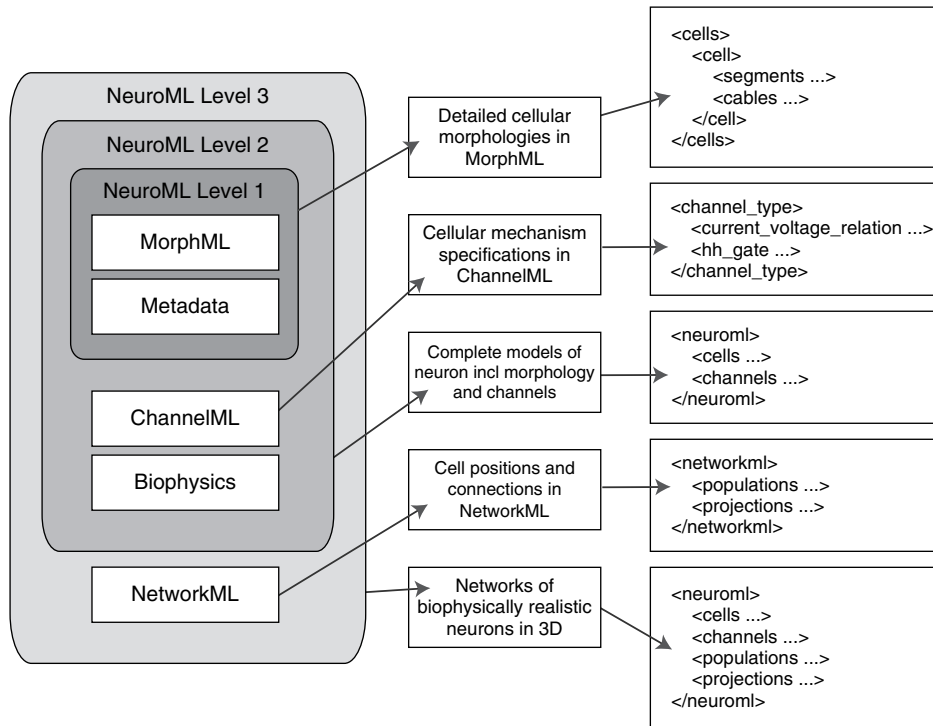


**FIGURE 5.3** Organization of NeuroML specifications. NeuroML standards are arranged in Levels, with each higher Level being a superset of the previous. The first Level specifies MorphML, which can be used to describe neuronal morphologies. This Level also outlines the basic metadata with which to describe compartmental models. Level 2 adds the ability to specify the electrophysiological properties of cells. Models of membrane conductances, synaptic mechanisms and ion concentrations can be modeled with ChannelML. The biophysics specification can be used to describe how these are distributed on the cells, as well as giving the passive cell properties. NetworkML allows populations of cells and their connections to be described, and a NeuroML Level 3 file can contain a mix of all of the aforementioned elements for a full description of a biophysical network model.

relevant citations, etc.). Morphological data from various sources, e.g. Neurolucida reconstructions, can be converted into this format, termed MorphML (Crook et al., 2007) for reuse in compartmental modeling simulators, visualization packages, etc..

Level 2 allows the specification of models of conductance based multicompartmental neurons. Inhomogeneous distributions of membrane conductances, subcellular mechanisms and passive cellular properties can be described for cells whose morphology is based on MorphML. Models of voltage and ligand gated ion channels and synaptic mechanisms can be described with ChannelML. An example of the use of a ChannelML file to create script files for use in simulations is given in the next section.

Level 3 of the specification is aimed at network models. Populations of neurons in 3D can be defined by providing an explicit list of all neuronal locations, or by providing an implicit enumeration (e.g. a grid arrangement or a random arrangement). Similarly, connectivity can be specified using an explicit list of connections or implicitly by giving an algorithm for defining connectivity rules, cell location specificity of synaptic types, etc.

### Use of NeuroML in *neuroConstruct*

The structure of the internal data model for cells in *neuroConstruct* is quite close to that used in MorphML, so that a mapping between the two is straightforward (Gleeson et al., 2007), thus facilitating import and export of files describing the cells. The cells in a *neuroConstruct* project are not currently stored in MorphML, but in another format related to the structure of the Java objects used for cells in *neuroConstruct*. This is because new features are usually added at source code level before becoming part of the MorphML specification. Export of cell structures in MorphML format is also supported in the latest version of NEURON and NeuroML will be used as the main format for storing neuronal data in GENESIS 3/MOOSE (currently under development at <http://sourceforge.net/projects/moose-g3>).

As mentioned previously, specification of channel and synaptic mechanism in ChannelML ensures portability of the mechanism to multiple simulators. Figure 5.4 shows an example of section of a ChannelML file describing a synaptic

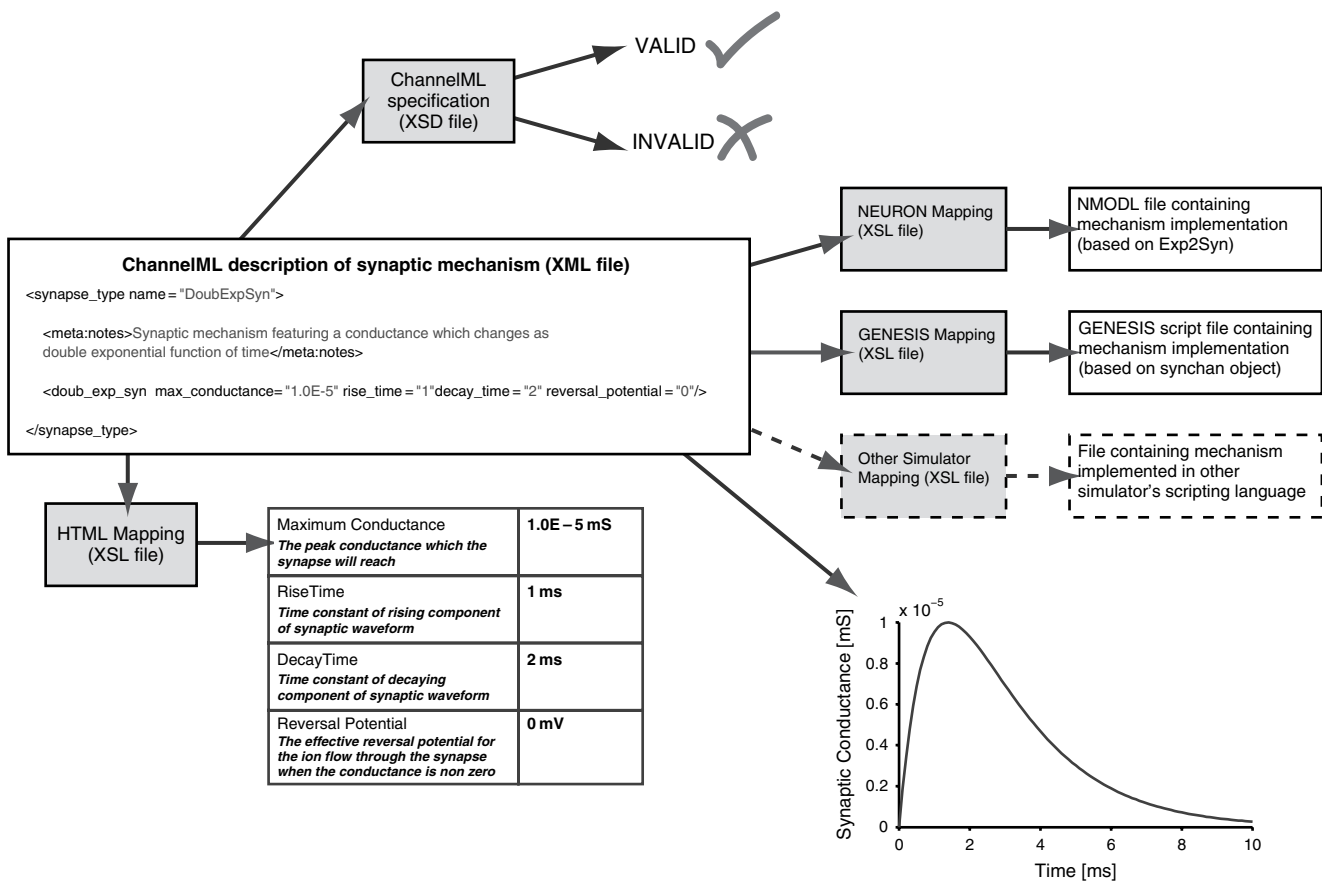


**FIGURE 5.4** Use of a typical ChannelML file. The section of a ChannelML file shown here describes a simple synaptic mechanism whose conductance changes as a double exponential function of time. The validity of a ChannelML file can be checked using an XSD file, which checks that all of the required elements are present and that the values are in the correct format. Mappings of the contents of the XML file can be made to one of the supported simulators to produce script files which can be executed, or to HTML format for easier browsing of contents. Applications supporting NeuroML can easily extract the data for generation of relevant graphs. The gray boxes represent files which can be used on all ChannelML files and are provided as part of the NeuroML framework. Modified from Gleeson et al., 2007, with permission.

mechanism with a double exponential conductance waveform. As this is in XML, it can be checked against a published schema, in this case the XSD (XML Schema Definition) file describing the contents of ChannelML files. This lists the elements and attributes required in the file and conditions on their values (e.g. `rise_time`, `decay_time > 0`). XML files can also be transformed into other formats using XSL (eXtensible Stylesheet Language) mapping files. These have been produced to map the contents into script files for NEURON and GENESIS. The advantage of this approach is that to make channels available for a new simulator, a single XSL file must be produced to create files in its particular format. Structuring the channel information in this way leads to other advantages. As each element and attribute's meaning is known, it is possible to change the values to other unit systems in an automated fashion, unit conversions being a common source of errors in converting neuronal models. Extraction of the information from the ChannelML file makes plotting of the internal data possible. XSL files have also been produced to map the information into HTML format, which can make the contents readable for any neuroscientist. This is particularly helpful when extra information about the model's origin is included in the ChannelML file as metadata.

Networks generated in *neuroConstruct* can be saved and reloaded in NetworkML format, which is frequently much faster than regenerating the network. Automatic zipping of files is also supported, allowing an approximate 90% reduction in size. NetworkML files generated by other applications (e.g. a custom piece of MATLAB or Python code) can be loaded into a *neuroConstruct* project, provided cell group/synapse mechanism names of those elements in the project are used. This allows completely customized networks to be visualized, simulated and analyzed with the application.

The NeuroML specifications are in continuous development. New features planned for the specifications will be utilized by *neuroConstruct* (e.g. greater support for subcellular signaling pathways) as outlined in the discussion.

## EXAMPLE OF NETWORK MODEL OF A NEUROLOGICAL DISORDER

We outline an example of a network implemented in *neuroConstruct* which can be used to illustrate the difference between a network displaying healthy activity and an altered version showing a neurological disorder. The network model of the dentate gyrus we have implemented in *neuroConstruct* was based on a 527 cell model (Santhakumar et al., 2005) constructed to investigate the effects of mossy fiber sprouting and mossy cell loss on the spread of seizure-like activity in the dentate gyrus. This model was used to illustrate that even weak mossy fiber sprouting could lead to the spread of hyperexcitability throughout the network after focal perforant path stimulation. The network consisted of multicompartmental models of 500 granule cells (GrC; whose axons form the mossy fibers), 15 mossy cells, six hilar perforant path associated (HIPP) cells and six basket cells (see Figure 5.5A). The network model has subsequently been extended to incorporate 50 000 GrC (Dyhrfjeld-Johnsen et al., 2007), as has been described previously in this book (Chapter 3). This has been one of the most detailed network models published and represents an ideal model to test the ability of *neuroConstruct* to reproduce the results of an in-depth study of network function.

Our implementation of the model is based on NEURON script files obtained from <http://senselab.med.yale.edu/senselab/modeldb>ShowModel.asp?model=51781>. The four cell types consisted of 9–17 compartment models featuring 11 channel mechanisms distributed inhomogeneously on the cell membranes and cell region specific connectivity (Santhakumar et al., 2005). As not all of the cell mechanisms were supported by ChannelML, the original NMODL files for six of the channels were reused. The network structure recreated in *neuroConstruct* was the topographical strip as opposed to the ring structure used in some of the original simulations. While the ring would reduce edge effects at the boundaries of the network, the strip represented a more realistic network arrangement, albeit in 1D. Figure 5.5A shows the 3D view of the topographical strip, with each cell group arranged in vertically separated 1D lines. The 10 000+ synaptic connections as described in Santhakumar et al. (2005) are not displayed. To investigate the network's behavior in response to a brief current pulse, a perforant path stimulation was applied, mainly to the central 100 GrCs. Figure 5.5B shows the normally connected network's response to the stimulation. Single action potentials (or multiple APs for the basket cell) are evoked in the cells, but the activity does not propagate. The sprouted network differs from the healthy network in that extra connections are made from GrC axons to a pool of local GrC dendrites, an anatomical change which has been found following head injury and is thought to be an important factor in temporal lobe epilepsy (Santhakumar et al., 2001). Figure 5.5C shows the behavior of multiple cells from each cell group in this sprouted network. They clearly show waves of excitation traveling in both directions away from the area of stimulation. The cells in Figure 5.5A have been colored according to membrane potential 110 ms after stimulation. All of the screen shots are taken from *neuroConstruct* and all of these analyses can be performed through the GUI.

The level of sprouting clearly has an effect on the hyperexcitability of the network. Figure 5.6 shows the interface for adjusting the parameters for such a network connection. Some of the values which can be set include: the divergence of the connection (the number of postsynaptic cells per presynaptic cell, which can be a fixed value, random or Gaussian with a defined maximum and minimum value); the maximum and minimum connection length (minimum value can be used to exclude local connections) in radial or one of x, y, z directions; the type of synaptic connection and distributions of mechanism weight and delays. Resetting these parameters and regenerating the network allows rapid and transparent changes in network structure to be made, and the effects quickly examined.

The network model described here is included with the *neuroConstruct* distribution and can be generated, executed and analyzed on standard desktop machines.

## OTHER NETWORK MODELS IN NEUROCONSTRUCT

A number of other published models have been implemented in *neuroConstruct*, which illustrate its ability to handle cell models with complex morphologies and the inbuilt functions for analyzing network functionality in 3D.

### MODEL OF A LAYER 5 PYRAMIDAL CELL

This model of spike initiation in a cortical pyramidal cell (Mainen et al., 1995) builds on an earlier experimental paper (Stuart and Sakmann, 1994) investigating the active properties of dendrites and backpropagation of action potentials. The model, one of the first to include such a detailed dendritic structure, uses a reconstruction of a rat layer 5 pyramidal cell

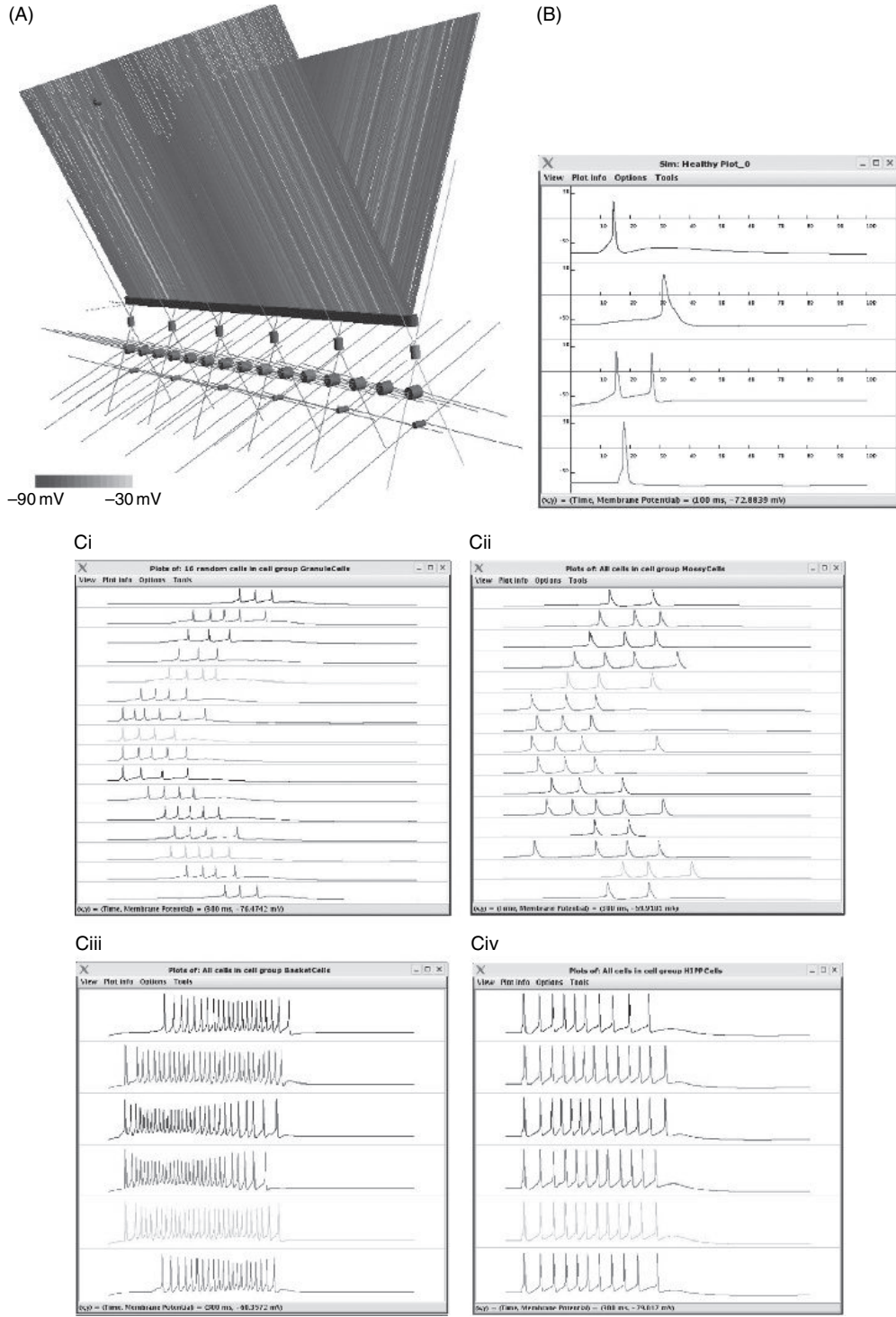


**FIGURE 5.5** Dentate gyrus model in *neuroConstruct*. (A) The cell groups were all aligned in 1D, with a vertical separation added for clarity. The network consisted of (from the top down) 500 granule cells (GrCs), 6 basket cells, 16 mossy cells and 6 hilar perforant path associated (HIPP) cells. Synaptic connections have been removed for clarity (note: conditions on maximum/minimum connection lengths were applied along axis of cell bodies alone (z axis, see Figure 5.3)). The central 100 GrCs receive a pulse of stimulation at 5 ms. The coloring reflects the membrane potential of the cells at 110 ms after the stimulation and in this network, which includes the sprouted connections, the activity can be seen to have traveled to granule cells distant from those receiving the initial input. (B) The behavior of examples of each of the cell types in the normally connected network: a GrC which receives direct stimulation (black trace); a mossy fiber (blue); a basket cell (red) and a HIPP cell (green). All traces are 100 ms long. (C) The behavior of each cell group in the network with 10% mossy fiber sprouting. (i) Membrane potential versus time traces of 16 individual GrCs. These were chosen at random from the 500 GrCs, with cell number increasing from top to bottom of the traces. They illustrate the spread of excitation from the cells at the center which receive the initial input. (ii) Traces for all 15 mossy fibers. (iii) All 6 basket cells. (iv) All 6 HIPP cells. All traces are 300 ms long. Modified from Gleeson et al., 2007, with permission. (See Plate 3 in color plate section.)

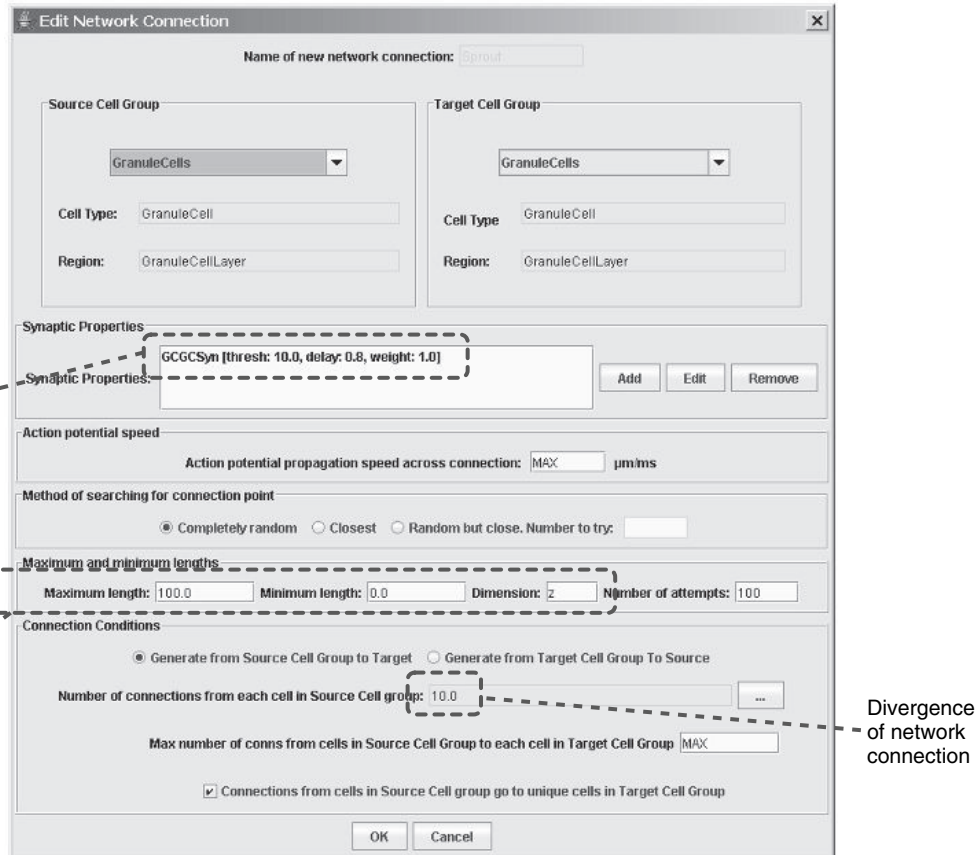


**FIGURE 5.6** Network settings. Screenshot of interface for setting parameters for a network connection, in this case the sprouted connections from the mossy fibers to local granule cell dendrites. The settings for synaptic type and parameters, length of connections and synaptic divergence are highlighted and, by changing these values and regenerating and simulating the network, the influence of these parameters on network behavior can be determined.

(see Figure 5.7). The model was originally created in NEURON and the implementation in *neuroConstruct* was based on script files obtained from <http://senselab.med.yale.edu/senselab/modedb>ShowModel.asp?model=8210>. The morphology was imported and the channels were reimplemented in ChannelML, and the *neuroConstruct* project can reproduce the results of the original paper on both NEURON and GENESIS.

## GRANULE CELL LAYER

We have recently created 3D network model of the granule cell layer of the cerebellum as described in Gleeson et al. (2007) (see Figure 5.8). This was developed from a 1D version (Maex and De Schutter, 1998) which was used to illustrate how synchronous oscillations can result from the feedback loop between granule cells (GrCs) and Golgi cells (GoCs) in the granule cell layer. This model was reimplemented in *neuroConstruct* (based on GENESIS script files obtained from <http://www.tnb.ua.ac.be/models/network.shtml>) using ChannelML descriptions of the channels to allow execution on either NEURON or GENESIS.

The model was extended to 3D by first adding structure to the single compartment cells in the original model. The biophysical properties of the cells were reused and the GrCs were given an ascending segment and parallel fibers (PFs). The GoCs had a single dendrite of similar length to the ascending segment. The cell bodies were packed in a region 500 μm along the PF axis, 1 mm wide and 50 μm deep (see Figure 5.1A). For our simulations, 32 GoCs were first packed into this region followed by 96 single compartments representing the mossy fiber (MF) terminals, and 600 GrCs. Excitatory (AMPAR and NMDAR mediated) connections were made between the MFs and GrCs with each GrC having a number of connections taken from a Gaussian distribution with a peak of 4, a standard deviation of 1, and a max and min of 3 and 7

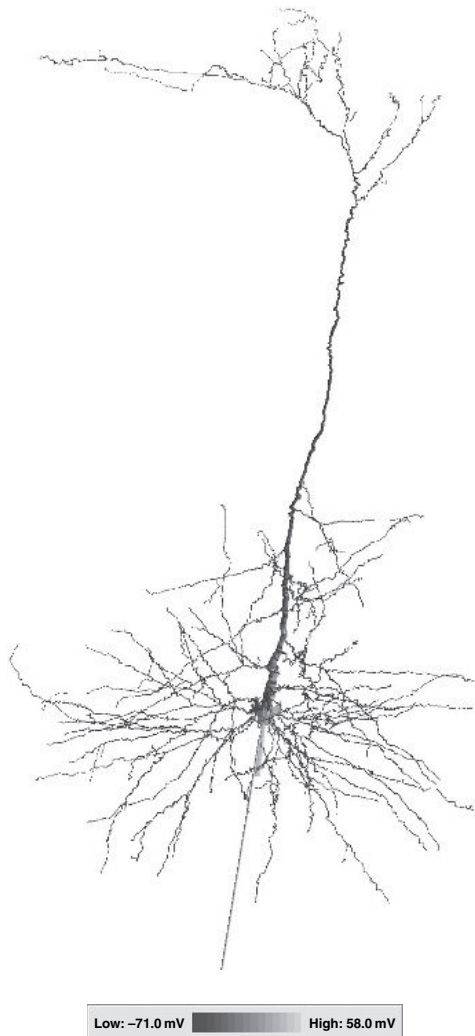


**FIGURE 5.7** Pyramidal cell. Screenshot of a layer 5 pyramidal cell model (Mainen et al., 1995) recreated in *neuroConstruct*, showing coloring based on membrane potential shortly after spike initiation in the initial segment of the axon. (See Plate 4 in color plate section.)

respectively. The AMPAR mediated connections between the PFs and the upper part of the GoC dendrites were also made using the morphology based connections with four connections from each GrC. Inhibitory connections were made between the GoCs and GrCs with each GrC receiving a single GABA-A receptor mediated connection from the nearest GoC. In Figure 5.1A, the network can be seen and a single GoC is highlighted in green along with the pre- and postsynaptic GrCs to which it is connected. The MFs receive 50 Hz random Poisson input.

The synchronous firing of the GoCs arises after approx 100 ms, accompanied by sporadic firing of the GrC entrained by this oscillation. The key difference between this model and the earlier 1D version is that differences in the phase of oscillations can be detected between different PF tracts, as has been observed experimentally (Vos et al., 1999). Figure 5.8A shows the network without axons, dendrites or connections (from Gleeson et al., 2007). Two regions were defined running along the direction of the PFs. A GoC in one of these ‘beams’ was chosen and the synchrony of the cell investigated with respect to the other GoCs in this beam, and in another beam displaced from the first. The GoCs in the second beam connect mainly to different PFs, as can be seen from Figure 5.1A. Figure 5.8B shows the cell’s synchrony with the cells within the same beam. Peaks at approx 40 ms intervals reflect the regular firing of the GoCs at around 25 Hz. There is much less synchrony between this cell and the cells in Beam B (see Figure 5.8C) reflecting the independent input into the GoCs. This example illustrates how a network with 3D anatomical detail can be used to investigate the cellular mechanisms underlying observed experimental behavior.

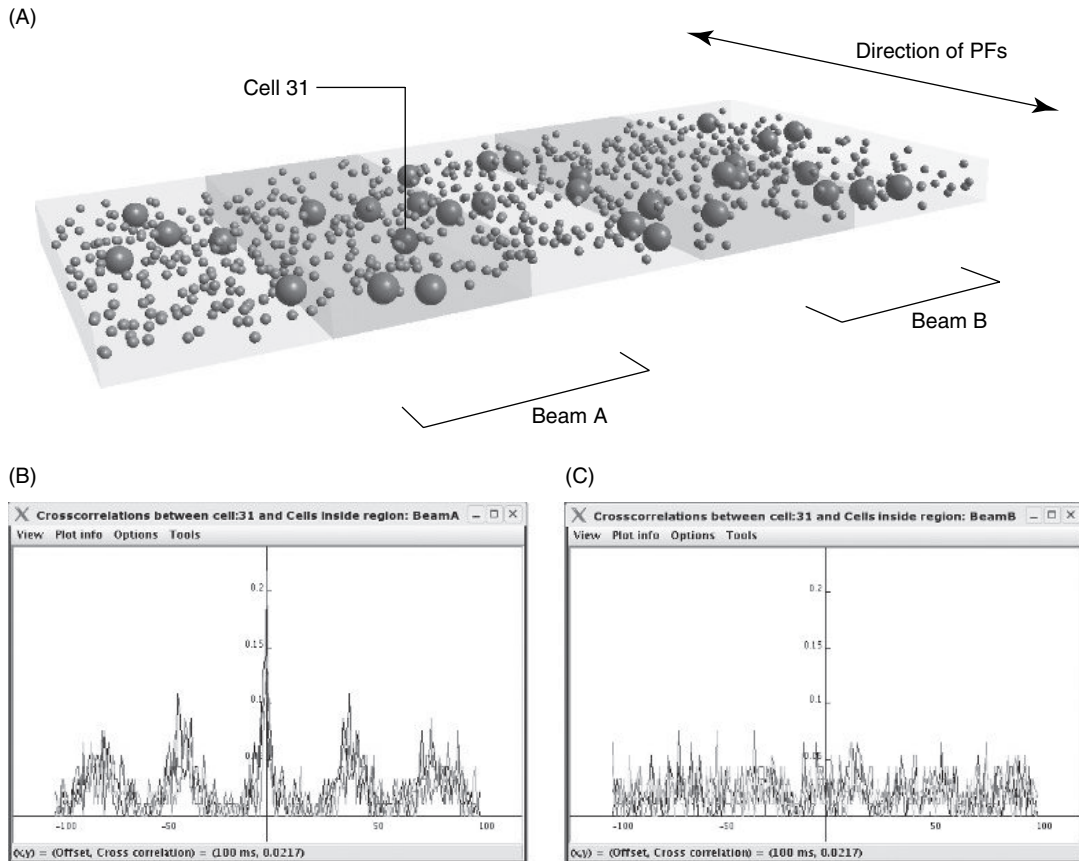


**FIGURE 5.8** Granule cell layer model. (A) Granule cell layer model with 600 granule cells (GrCs, orange), 32 Golgi cells (GoCs, dark green), and 96 mossy fiber terminals. Axons, dendrites and synaptic connections are hidden for clarity (see Plate 1). Two beams are identified within the cell body region, which run the direction of the parallel fibers. (B) Cross-correlation between cell 31 in A and the other 4 GoCs in beam A. Each trace of a different color represents a different cell. The y axis shows the probability of finding a spike in the other cell in a time window of 1 ms with the specified offset. (C) Cross-correlation between cell 31 and the 6 GoCs in beam B. Modified from Gleeson et al., 2007, with permission. (See Plate 5 in color plate section.)

## DISCUSSION AND FUTURE DIRECTIONS

*neuroConstruct* is a new software application that is designed to facilitate the creation, visualization and analysis of networks of multicompartmental neurons in 3D (Gleeson et al., 2007). The aim of this application is to allow greater levels of anatomical detail in network models while managing, in a modular fashion, the large number of parameters used to describe such systems. Cell models are based on the latest NeuroML standards and can therefore be created in a simulator independent fashion, which allows greater transparency of the model parameters. The cell models can be placed and connected in 3D using a number of algorithms to reproduce more closely observed cell density and synaptic connectivity. This increased biological realism can be used to compare the network models to experimentally measured behavior from multicellular recordings at high temporal and spatial resolution.

## CURRENT POSSIBILITIES

Large numbers of cell and network models in the current literature have been developed by implementing them in a variety of specialist simulators. These models illustrate phenomena of general interest, but this approach is often ignored by the wider experimental neuroscience community. There are many reasons for this, one being that to use the models effectively, the scripting language of the simulation environment has to be learned, which can be time consuming. Also, if two or more cell models for a particular brain area have been implemented on different platforms, it can be a major task even for an experienced modeler to convert these to a single simulator, which is necessary before a composite model can be built. We

have recreated a number of published cell models from various brain systems in *neuroConstruct* and intend to add more cell types to this library in the future. The simulator independent representation of models in *neuroConstruct* and their control and potential modification through a GUI, without having to write any specialist simulator code, facilitates the accessibility of these models and therefore permits non-programmers to evaluate the model structure and predictions in detail. This increased accessibility for a wider range of neuroscientists is a key feature of *neuroConstruct* as it allows for continuous feedback and testing of the model predictions in experiments, which is necessary for the ongoing development and improvement of computational models. Moreover, cell models can be designed *de novo* from new experiments and integrated into increasingly larger composite models. It is hoped that the facilitated interchange of models between experimentalists and theoreticians should lead to the development of models that reflect a broad consensus view of the cellular basis of brain function.

The greater availability of models of healthy neuronal systems will also benefit research into the underlying causes of neurological diseases. As models become more biologically realistic, have been open to scrutiny by a wide range of neuroscientists and have been shown in a wider range of scenarios to reproduce aspects of cellular behavior, their usefulness for exploratory research increases. This is the hallmark of a good model: that it can make experimentally testable predictions, which are not directly linked to the underlying assumptions used when building the model. For example, the effects on a normally behaving cell of deletion of a channel can be quickly checked by copying and altering the cell model in *neuroConstruct* and comparing the new cell behavior to experimental data from the cell in the presence of the appropriate blocker. This cell can be switched into the network model and the effect on the overall behavior examined. Also, changes in the network topology, e.g. deletion of a certain cell type or increase/decrease in connectivity, can be implemented, the network generated, visually verified and the simulation run, all in a matter of minutes. This quick turn around time between implementing a pathological change in the cells or network and seeing the effect is aimed at reducing the ‘time to insight’ when using neuronal models for research on neurological disorders. For example, lesions to parts of the modeled network can support research into the causes of symptomatic epilepsies, and changes to the properties of channel models that reflect those occurring following mutations could help shed light on the mechanisms of channelopathy-induced idiopathic epilepsies. Moreover, different forms of pharmacological and non-pharmacological treatment could initially be tested in a model implemented in *neuroConstruct*, including GABA<sub>A</sub> receptor modulators such as benzodiazepines, or even the potentially beneficial effect of removal of a cell class or a part of the network.

The greater accessibility to computational models that is provided by *neuroConstruct* not only facilitates research into the physiology of brain structures, it also provides an advanced tool for teaching. Although *neuroConstruct* in its present form requires some background in neurophysiology and some basic computing skills, the GUI based control of the model parameters and the advanced visualization of the effect of parameter changes are useful for students who want to understand principles underlying the complex interactions in single neurons and networks. As part of a neuroscience course, structured sets of projects in *neuroConstruct* can provide examples of the current understanding of the physiology of different brain structures and highlight how their physiology is affected by different pathologies.

## CURRENT LIMITATIONS AND FUTURE DIRECTIONS

The level of detail possible in network models developed with the current version of *neuroConstruct* is sufficient to reproduce most published conductance-based neuronal network models. However, there are a number of known biological phenomena which would be interesting to model, but which require extensions to the code to be fully supported. Many of these developments will go hand in hand with expansion of the scope of the NeuroML standards. We will outline what can currently be done with *neuroConstruct* and the approaches being taken to increase the functionality of the application.

### Network structure

We have shown that *neuroConstruct* can be used to construct models of various different brain regions, but it is not inconceivable that the specific anatomy of a particular brain region will bring up technical issues that require future software development. *neuroConstruct* currently provides the possibility to create spatial clusters of connections, local subcircuits (Song et al., 2005) and also ‘small world’ networks with a large number of local connections and sparse long-range connections (Watts and Strogatz, 1998). Anything that is currently beyond the capabilities of the GUI can be implemented by adding specialist NEURON or GENESIS code, or by importing networks that are represented by previously generated NetworkML files.

## Scaling up of network models

The scale of network models which can be built and visualized with the current version of *neuroConstruct* is limited by the physical memory of the machine on which it is running and the capabilities of the graphics card, respectively. It is currently possible to visualize and run networks of 50 000 cells in a highly interconnected network on a machine with 256 MB graphics memory and 8 GB RAM. Larger networks can be simulated, but a network of this size is getting close to the maximum feasible on a single machine given the time it takes to execute the simulation.

We are currently investigating the feasibility of automatic generation of code for the parallel version of NEURON (Migliore et al., 2006), which is being used for network simulations in the Blue Brain Project (Markram, 2006). There are also a number of other initiatives to allow parallel execution of neuronal simulations, e.g. PGENESIS (Howell et al., 2000), GENESIS 3/MOOSE, Neurospaces (Cornelis and De Schutter, 2003) and any components added to support parallelization of NEURON (i.e. algorithms for partitioning the cells to computing nodes) could be reused for any supported parallel platform in the future. Support for specification of networks in a distributed environment will also be added to NetworkML, potentially allowing partitioned networks to be generated by other applications and imported into *neuroConstruct*.

## Detailed signaling pathways

*neuroConstruct* can be used to study the effect of pharmacological interventions on network behavior if the effect of a drug on single cell behavior is well characterized phenomenologically, such as the effect of benzodiazepines on GABA<sub>A</sub> receptor physiology. Such effects can be implemented in a network model by using a phenomenological approach, for example by representing the effect of benzodiazepines as slowed decay of GABA<sub>A</sub> receptor-mediated synaptic conductances, possibly with an increase in their peak amplitude. However, the mechanistic effect of drugs on the receptor kinetics is currently beyond the scope of *neuroConstruct*. Moreover, it is not yet possible to model the multitude of complex intracellular processes affecting cytoplasmic calcium dynamics, such as calcium induced calcium release or calcium and buffer diffusion in the presence of obstacles like endoplasmic reticulum (ER) cisternae or mitochondria. In the future, the integration of detailed biochemical models will be facilitated by the development of Level 4 of the NeuroML standards and by collaboration with initiatives in systems biology (Finkelstein et al., 2004; Kitano, 2002) such as SBML (Hucka et al., 2003) and CellML (Lloyd et al., 2004).

## 3D phenomena

Representing neuronal network structure in 3D opens up the possibility to explore phenomena that are directly dependent on 3D spatial information. These phenomena include interactions between neurons that are mediated by diffusible substances, for example neurotransmitter spillover or communication through modulators like endocannabinoids or NO. Although it is already possible to create basic phenomenological models of diffusion of signaling molecules that affect synaptic plasticity in a distance dependent manner, more realistic diffusion models will require further development of *neuroConstruct*. The collaboration with systems biology initiatives should also open up the interaction with more detailed lower-level reaction-diffusion software packages like MCell (<http://www.mcell.cnl.salk.edu>) and VCell (<http://www.nrcam.uchc.edu>), although the difference in levels of description might require the development of separate but interacting models with different amounts of biological details.

The creation of a 3D network also opens up the possibility to generate different types of data that can be used to constrain and test the model. Extracellular electric fields could be simulated in 3D and these data could be compared with extracellular recordings *in vivo* and potentially used to link electroencephalogram (EEG) measurements to neuronal behavior. Vasculature could also be implemented and the modeled diffusion of metabolites and oxygen could be used for comparison with neuronal activity measurements resulting from functional magnetic resonance imaging (fMRI) studies. Moreover, simulating the 3D diffusion of oxygen and metabolites could form the basis of modeling studies into neurodegenerative states that are linked to an altered supply of these substances.

## Inhomogeneous morphologies

When constructing a network comprised of neuronal models with detailed morphologies, *neuroConstruct* currently assumes that all neurons of a given class have the same morphology. In reality, a biological network will contain a variety of morphologies and future developments of *neuroConstruct* will include the possibility to work with heterogeneous neuronal morphologies as have been used in applications like L-Neuron (Ascoli et al., 2001) and NeuGen (Eberhard et al., 2006). This will also allow the possibility to study the effect of variable morphologies on information processing in networks.

## CONCLUSIONS

*neuroConstruct* is a new software tool that facilitates the construction, visualization and analysis of conductance based neuronal network models in 3D space. Simulations are controlled by a user friendly GUI and models are represented in a simulator independent way, which facilitates the construction, testing and interchange of models by experimentalists and theoreticians. The increased accessibility of models, in particular for experimentalists, should provide the possibility for an increased coupling between experiments and computational models and stimulate the design and testing of advanced computational models by the neuroscience community.

## ACKNOWLEDGMENTS

We would like to thank David Attwell, Dmitri Kullmann, Paul Kirkby and Zoltan Nusser for comments on the manuscript. PG was supported by a Medical Research Council Special Research Training Fellowship in Bioinformatics, Neuroinformatics, Health Informatics and Computational Biology, VS was supported by the MRC (0400598; RAS) and RAS is in receipt of a Wellcome Trust Senior Research Fellowship in Basic Biomedical Science.

## REFERENCES

- Abbott, L.F. and Regehr, W.G. (2004). Synaptic computation. *Nature* 431:796–803.
- Alger, B.E. (2002). Retrograde signaling in the regulation of synaptic transmission: focus on endocannabinoids. *Prog Neurobiol* 68:247–286.
- Ascoli, G.A. (2006). Mobilizing the base of neuroscience data: the case of neuronal morphologies. *Nat Rev Neurosci* 7:318–324.
- Ascoli, G.A., Krichmar, J.L., Nasuto, S.J. and Senft, S.L. (2001). Generation, description and storage of dendritic morphology data. *Philos Trans R Soc Lond B Biol Sci* 356:1131–1145.
- Attwell, D. and Iadecola, C. (2002). The neural basis of functional brain imaging signals. *Trends Neurosci* 25:621–625.
- Berends, M., Maex, R. and De Schutter, E. (2004). A detailed three-dimensional model of the cerebellar granule cell layer. *Neurocomputing* 58–60:587–592.
- Berkovic, S.F., Mulley, J.C., Scheffer, I.E. and Petrou, S. (2006). Human epilepsies: interaction of genetic and acquired factors. *Trends Neurosci* 29:391–397.
- Bower, J.M. and Beeman, D. (1997). The book of GENESIS: exploring realistic neural models with the GEneral NEural SImulation System. Springer, New York.
- Buonomano, D.V. (2000). Decoding temporal information: a model based on short-term synaptic plasticity. *J Neurosci* 20:1129–1141.
- Buzsaki, G. (2004). Large-scale recording of neuronal ensembles. *Nat Neurosci* 7: 446–451.
- Cannon, R.C., Turner, D.A., Pyapali, G.K. and Wheal, H.V. (1998). An on-line archive of reconstructed hippocampal neurons. *J Neurosci Methods* 84:49–54.
- Chang, B.S. and Lowenstein, D.H. (2003). Epilepsy. *N Engl J Med* 349:1257–1266.
- Chen, K., Neu, A., Howard, A.L. et al. (2007). Prevention of plasticity of endocannabinoid signaling inhibits persistent limbic hyperexcitability caused by developmental seizures. *J Neurosci* 27:46–58.
- Cornelis, H. and De Schutter, E. (2003). NeuroSpaces: separating modeling and simulation. *Neurocomputing* 52–4:227–231.
- Crank, J. (1993). The mathematics of diffusion, 2nd edn. Clarendon Press, Oxford.
- Crepel, F. and Jaillard, D. (1990). Protein kinases, nitric oxide and long-term depression of synapses in the cerebellum. *Neuroreport* 1:133–136.
- Crook, S., Gleeson, P., Howell, F., Svitak, J. and Silver, R.A. (2007). MorphML: Level 1 of the NeuroML standards for neuronal morphology data and model specification. *Neuroinform* 5:96–104.
- Davison, A.P., Feng, J. and Brown, D. (2003). Dendrodendritic inhibition and simulated odor responses in a detailed olfactory bulb network model. *J Neurophysiol* 90:1921–1935.
- De Schutter, E. and Bower, J.M. (1994). An active membrane model of the cerebellar Purkinje cell. I. Simulation of current clamps in slice. *J Neurophysiol* 71:375–400.
- Destexhe, A. and Pare, D. (1999). Impact of network activity on the integrative properties of neocortical pyramidal neurons in vivo. *J Neurophysiol* 81:1531–1547.
- Dittman, J.S., Kreitzer, A.C. and Regehr, W.G. (2000). Interplay between facilitation, depression, and residual calcium at three presynaptic terminals. *J Neurosci* 20:1374–1385.
- Douglas, R.J. and Martin, K.A. (2004). Neuronal circuits of the neocortex. *Annu Rev Neurosci* 27, 419–451.
- Dyhrfjeld-Johnsen, J., Santhakumar, V., Morgan, R. J., Huerta, R., Tsimring, L. and Soltesz, I. (2007). Topological determinants of epileptogenesis in large-scale structural and functional models of the dentate gyrus derived from experimental data. *J Neurophysiol* 97:1566–1587.
- Eberhard, J.P., Wanner, A. and Wittum, G. (2006). NeuGen: A tool for the generation of realistic morphology of cortical neurons and neural networks in 3D. *Neurocomputing* 70:327–342.
- Escayg, A., MacDonald, B.T., Meisler, M.H. et al. (2000). Mutations of SCN1A, encoding a neuronal sodium channel, in two families with GEFS+. *Nat Genet* 24:343–345.
- Finkelstein, A., Hetherington, J., Li, L. Z. et al. (2004). Computational challenges of systems biology. *Computer* 37, 26–33.
- Glaser, J.R. and Glaser, E.M. (1990). Neuron imaging with Neurolucida – a PC-based system for image combining microscopy. *Comput Med Imaging Graph* 14:307–317.

- Gleeson, P., Steuber, V. and Silver, R.A. (2007). neuroConstruct: a tool for modeling networks of neurons in 3D space. *Neuron* 54:219–235.
- Gobel, W., Kampa, B.M. and Helmchen, F. (2007). Imaging cellular network dynamics in three dimensions using fast 3D laser scanning. *Nat Methods* 4:73–79.
- Goddard, N.H., Hucka, M., Howell, F., Cornelis, H., Shankar, K. and Beeman, D. (2001). Towards NeuroML: model description methods for collaborative modelling in neuroscience. *Philos Trans R Soc Lond B Biol Sci* 356:1209–1228.
- Golding, N.L., Mickus, T.J., Katz, Y., Kath, W.L. and Spruston, N. (2005). Factors mediating powerful voltage attenuation along CA1 pyramidal neuron dendrites. *J Physiol* 568:69–82.
- Hanson, J.E., Smith, Y. and Jaeger, D. (2004). Sodium channels and dendritic spike initiation at excitatory synapses in globus pallidus neurons. *J Neurosci* 24:329–340.
- Harvey, R.J. and Napper, R.M. (1991). Quantitative studies on the mammalian cerebellum. *Prog Neurobiol* 36:437–463.
- Helmchen, F. and Denk, W. (2002). New developments in multiphoton microscopy. *Curr Opin Neurobiol* 12:593–601.
- Hines, M.L. and Carnevale, N.T. (1997). The NEURON simulation environment. *Neural Comput* 9:1179–1209.
- Hines, M.L. and Carnevale, N.T. (2000). Expanding NEURON's repertoire of mechanisms with NMODL. *Neural Comput* 12:995–1007.
- Hines, M.L., Morse, T., Migliore, M., Carnevale, N.T. and Shepherd, G.M. (2004). ModelDB: a database to support computational neuroscience. *J Comput Neurosci* 17:7–11.
- Howell, F.W., Dyhrfjeld-Johnsen, J., Maex, R., Goddard, N. and De Schutter, E. (2000). A large scale model of the cerebellar cortex using PGENESIS. *Neurocomputing* 32–33:1041–1046.
- Hucka, M., Finney, A., Sauro, H.M. et al. (2003). The systems biology markup language (SBML): a medium for representation and exchange of biochemical network models. *Bioinformatics* 19:524–531.
- Jacoby, S., Sims, R.E. and Hartell, N.A. (2001). Nitric oxide is required for the induction and heterosynaptic spread of long-term potentiation in rat cerebellar slices. *J Physiol* 535:825–839.
- Jarsky, T., Roxin, A., Kath, W.L. and Spruston, N. (2005). Conditional dendritic spike propagation following distal synaptic activation of hippocampal CA1 pyramidal neurons. *Nat Neurosci* 8:1667–1676.
- Kerr, J.N., Greenberg, D. and Helmchen, F. (2005). Imaging input and output of neocortical networks in vivo. *Proc Natl Acad Sci USA* 102:14063–14068.
- Kitano, H. (2002). Systems biology: a brief overview. *Science* 295:1662–1664.
- Kreitzer, A.C. and Malenka, R.C. (2007). Endocannabinoid-mediated rescue of striatal LTD and motor deficits in Parkinson's disease models. *Nature* 445:643–647.
- Kunec, S., Hasselmo, M.E. and Kopell, N. (2005). Encoding and retrieval in the CA3 region of the hippocampus: a model of theta-phase separation. *J Neurophysiol* 94:70–82.
- Lloyd, C.M., Halstead, M.D. and Nielsen, P.F. (2004). CellML: its future, present and past. *Prog Biophys Mol Biol* 85:433–450.
- Lubke, J., Roth, A., Feldmeyer, D. and Sakmann, B. (2003). Morphometric analysis of the columnar innervation domain of neurons connecting layer 4 and layer 2/3 of juvenile rat barrel cortex. *Cereb Cortex* 13:1051–1063.
- Maex, R. and De Schutter, E.D. (1998). Synchronization of golgi and granule cell firing in a detailed network model of the cerebellar granule cell layer. *J Neurophysiol* 80:2521–2537.
- Maffei, A., Prestori, F., Shibuki, K., Rossi, P., Taglietti, V. and D'Angelo, E. (2003). NO enhances presynaptic currents during cerebellar mossy fiber-granule cell LTP. *J Neurophysiol* 90:2478–2483.
- Mainen, Z.F., Joerges, J., Huguenard, J.R. and Sejnowski, T.J. (1995). A model of spike initiation in neocortical pyramidal neurons. *Neuron* 15:1427–1439.
- Marcaggi, P. and Attwell, D. (2005). Endocannabinoid signaling depends on the spatial pattern of synapse activation. *Nat Neurosci* 8, 776–781.
- Marder, E. and Goaillard, J.M. (2006). Variability, compensation and homeostasis in neuron and network function. *Nat Rev Neurosci* 7: 563–574.
- Markram, H. (2006). The blue brain project. *Nat Rev Neurosci* 7:153–160.
- Masuda, N. and Aihara, K. (2004). Global and local synchrony of coupled neurons in small-world networks. *Biol Cybern* 90:302–309.
- Medina, J.F. and Mauk, M.D. (2000). Computer simulation of cerebellar information processing. *Nat Neurosci* 3 Suppl:1205–1211.
- Migliore, M., Cook, E.P., Jaffe, D.B., Turner, D.A. and Johnston, D. (1995). Computer simulations of morphologically reconstructed CA3 hippocampal neurons. *J Neurophysiol* 73:1157–1168.
- Migliore, M., Cannia, C., Lytton, W., Markram, H. and Hines, M. (2006). Parallel network simulations with NEURON. *J Comput Neurosci*
- Nicolelis, M.A. and Ribeiro, S. (2002). Multielectrode recordings: the next steps. *Curr Opin Neurobiol* 12:602–606.
- Ohki, K., Chung, S., Ch'ng, Y.H., Kara, P. and Reid, R.C. (2005). Functional imaging with cellular resolution reveals precise micro-architecture in visual cortex. *Nature* 433:597–603.
- Poirazi, P., Brannon, T. and Mel, B.W. (2003). Pyramidal neuron as two-layer neural network. *Neuron* 37:989–999.
- Rapp, M., Yarom, Y. and Segev, I. (1996). Modeling back propagating action potential in weakly excitable dendrites of neocortical pyramidal cells. *Proc Natl Acad Sci USA* 93:11985–11990.
- Safo, P.K., Cravatt, B.F. and Regehr, W.G. (2006). Retrograde endocannabinoid signaling in the cerebellar cortex. *Cerebellum* 5:134–145.
- Santhakumar, V., Ratzliff, A.D., Jeng, J., Toth, Z. and Soltesz, I. (2001). Long-term hyperexcitability in the hippocampus after experimental head trauma. *Ann Neurol* 50:708–717.
- Santhakumar, V., Aradi, I. and Soltesz, I. (2005). Role of mossy fiber sprouting and mossy cell loss in hyperexcitability: a network model of the dentate gyrus incorporating cell types and axonal topography. *J Neurophysiol* 93:437–453.
- Schaefer, A.T., Larkum, M.E., Sakmann, B. and Roth, A. (2003). Coincidence detection in pyramidal neurons is tuned by their dendritic branching pattern. *J Neurophysiol* 89:3143–3154.
- Schweighofer, N. and Ferriol, G. (2000). Diffusion of nitric oxide can facilitate cerebellar learning: a simulation study. *Proc Natl Acad Sci USA* 97:10661–10665.
- Somogyi, P., Tamás, G., Luján, R. and Buhl, E.H. (1998). Salient features of synaptic organisation in the cerebral cortex. *Brain Res Brain Res Rev* 26:113–135.
- Song, S., Sjöström, P.J., Reigl, M., Nelson, S. and Chklovskii, D.B. (2005). Highly nonrandom features of synaptic connectivity in local cortical circuits. *PLoS Biol* 3:e68.

- Sporns, O. and Kotter, R. (2004). Motifs in brain networks. *PLoS Biol* 2:e369.
- Stosiek, C., Garaschuk, O., Holthoff, K. and Konnerth, A. (2003). In vivo two-photon calcium imaging of neuronal networks. *Proc Natl Acad Sci USA* 100:7319–7324.
- Stuart, G.J. and Sakmann, B. (1994). Active propagation of somatic action potentials into neocortical pyramidal cell dendrites. *Nature* 367:69–72.
- Sultan, F. and Bower, J.M. (1998). Quantitative Golgi study of the rat cerebellar molecular layer interneurons using principal component analysis. *J Compar Neurol* 393:353–373.
- Thomson, A.M., West, D.C., Wang, Y. and Bannister, A.P. (2002). Synaptic connections and small circuits involving excitatory and inhibitory neurons in layers 2–5 of adult rat and cat neocortex: triple intracellular recordings and biocytin labelling in vitro. *Cereb Cortex* 12:936–953.
- Traub, R.D., Contreras, D., Cunningham, M.O. et al. (2005). Single-column thalamocortical network model exhibiting gamma oscillations, sleep spindles, and epileptogenic bursts. *J Neurophysiol* 93:2194–2232.
- Vetter, P., Roth, A. and Häusser, M. (2001). Propagation of action potentials in dendrites depends on dendritic morphology. *J Neurophysiol* 85:926–937.
- Vos, B.P., Maex, R., Volny-Luraghi, A. and De Schutter, E. (1999). Parallel fibers synchronize spontaneous activity in cerebellar Golgi cells. *J Neurosci* 19:RC6.
- Wallace, R.H., Wang, D.W., Singh, R. et al. (1998). Febrile seizures and generalized epilepsy associated with a mutation in the Na<sup>+</sup>-channel beta1 subunit gene SCN1B. *Nat Genet* 19:366–370.
- Watts, D.J. and Strogatz, S.H. (1998). Collective dynamics of ‘small-world’ networks. *Nature* 393:440–442.
- Wilson, R.I. and Nicoll, R.A. (2002). Endocannabinoid signaling in the brain. *Science* 296:678–682.
- Yoshimura, Y. and Callaway, E.M. (2005). Fine-scale specificity of cortical networks depends on inhibitory cell type and connectivity. *Nat Neurosci* 8:1552–1559.
- Yoshimura, Y., Dantzker, J.L. and Callaway, E.M. (2005). Excitatory cortical neurons form fine-scale functional networks. *Nature* 433:868–873.
- Yu, F.H., Mantegazza, M., Westenbroek, R.E. et al. (2006). Reduced sodium current in GABAergic interneurons in a mouse model of severe myoclonic epilepsy in infancy. *Nat Neurosci* 9:1142–1149.

# 6

## COMPUTATIONAL NEUROANATOMY OF THE RAT HIPPOCAMPUS: IMPLICATIONS AND APPLICATIONS TO EPILEPSY

DEEPAK ROPIREDDY, SUSAN E. BACHUS, RUGGERO SCORCIONI  
AND GIORGIO A. ASCOLI

### ABSTRACT

The hippocampus subserves important cognitive functions of the mammalian brain, including the consolidation of episodic and declarative memories in humans and spatial navigation in rodents. Much is known about hippocampal anatomy, electrophysiology and behavioral involvement. Yet, the relationship between structure, activity and function in the hippocampus is far from obvious. To aid data integration between the cellular and system levels, we completely reconstructed and segmented the fine cytoarchitectural structure of the rat hippocampus from thin cryostatic slices. A custom developed computational framework transforms the digital trace stack into volumetric representations with arbitrary voxel size. This enables the 3D embedding of morphological reconstructions of individual neurons, oriented according to the transversal and longitudinal hippocampal curvatures. Virtually packing the neuropil volume of all layers and subregions with available cellular arborizations allows the estimation of macroscopic stereological properties such as space occupancy and neuritic overlap. We present a preliminary volumetric analysis of the individual cytoarchitectural layers within the whole hippocampus and illustrate the stereological analysis of spatial occupancy and overlap for a portion of the dentate region. Moreover, we describe the suitability of this approach to compute potential synaptic connectivity patterns for specific cell classes as a function of local spatial position. Finally, we exemplify the use of a single cell computational model to examine the regulation of neuronal spiking by synaptic inhibition, a phenomenon particularly relevant to the pathophysiology of epilepsy. Our novel anatomical construct could lead to a dramatic improvement in the realism, predictive power and experimental relevance of these numerical simulations.

### INTRODUCTION

The cognitive role of the mammalian hippocampus in learning and memory gained recognition after the seminal clinical case of the epileptic patient HM, whose bilateral surgical resection of the medial temporal lobes resulted in a severe impairment in forming new memories (Scoville and Milner, 1957). Countless studies over past decades have corroborated the involvement of the hippocampus in the storage and retrieval of episodic memory in humans (O'Keefe and Nadel, 1978; Squire and Zola-Morgan, 1991; Eichenbaum and Cohen, 2001) and in the representation and encoding of spatial memory in infrahumans (O'Keefe and Nadel, 1978; Morris et al., 1982; Eichenbaum and Cohen, 2001). The neural substrates behind these important cognitive processes have been under rigorous investigation over the last couple of decades. In particular, the rodent hippocampus has become and remains one of the most popular and active research areas in neuroscience.

This endeavor has greatly enhanced our understanding of hippocampal structure and physiology. Anatomical studies generated a wealth of detailed knowledge on the organization of the intrinsic hippocampal circuitry (Witter and Amaral, 2004), revealing greater complexity than imagined with the 'lamellar hypothesis' embraced by earlier physiologists

(Andersen et al., 1971). At the cellular level, modern day experimental and computational techniques (Ascoli et al., 2001; Van Pelt et al., 2001) have highlighted tremendous morphological variation between and within neuronal classes in the hippocampus (Claiborne et al., 1990; Rihn and Claiborne, 1990; Ishizuka et al., 1995; Pyapali et al., 1998; Cannon and Wheal, 1999; Scorcioni et al., 2004). With respect to biophysical properties, hippocampal neurons have been shown to possess a rich array of active conductances (Reyes, 2001; Migliore and Shepherd, 2002), which play a decisive role in shaping electrophysiological behavior. At the network level, population oscillations such as theta, gamma and ripples (Buzsáki, 1989, 2002; Traub et al., 2000; Buzsáki and Draguhn, 2004) are theorized to play a key role in the memory consolidation processes.

Several computational studies attempted to investigate directly the relationship between structure and activity over the past decade, bridging the two fields of anatomy and physiology at the level of single cells (Mainen and Sejnowski, 1996; Migliore et al., 1999, 2004; Krichmar et al., 2002; Migliore, 2003; Poirazi et al., 2003a, 2003b). In particular, the compartmental simulation approach incorporates complete morphologies and appropriate ion channel distributions, providing fundamental insights into the link between neuronal geometry and function and complementing experimental evidence (Vetter et al., 2001; Schaefer et al., 2003). In spite of these advances, the functioning of the hippocampus is far from understood at the system level.

In particular, the difficulty to characterize the details of anatomical structure comprehensively and quantitatively continues to constitute a formidable challenge in systems neuroscience, which is particularly non-amenable to direct experimental investigation. Two specific characteristics of cortical architecture stand out as major impediments in this quest. First, the principal cells have diffuse projections spread over all spatial directions (e.g. in the hippocampus proper, both septo-temporally and in the transverse direction, as observed by e.g. Li et al., 1994). How this intrinsic architecture of the circuitry contributes to cognitive function remains an open question. Secondly, cortical principal cells are heavily modulated by GABAergic (gamma-aminobutyric acid) inhibition across the dendritic trees as well as peri-somatically. At least 16 distinct types of interneurons have been described in the CA1 region alone based on electrophysiological characteristics and specific calcium binding markers (Freund and Buzsáki, 1996; Somogyi and Klausberger, 2005), providing both feedforward and feedback inhibition to the pyramidal cells. These complex interneuronal networks play a prominent but as of yet not fully determined role in the generation of population oscillations.

The local ‘canonical’ circuits within the broader organization of the hippocampus are determined by the position of synapses and further modulated by the biophysical properties underlying synaptic integration, such as calcium spike propagation (Shepherd, 2004). Synaptic circuitry constitutes an important component in capturing network dynamics, which is interdependent with and complementary to the connectivity within and between the various neuronal classes. Activity dependent changes in synaptic efficiency through long-term potentiation (Bliss and Collingridge, 1993) validated Hebb’s original hypothesis (Hebb, 1949). These network changes, possibly accompanied by the continuing evolution of cell assemblies (Harris et al., 2003; Maurer et al., 2006), could underlie a fundamental functional mechanism in the hippocampus. The importance of structural studies in this endeavor cannot be overemphasized.

In order to integrate the current architectural and functional knowledge and to attempt linking the structure and activity, a framework is needed to relate information regarding the characteristic of intrinsic connectivity patterns, like small-world networks (Watts and Strogatz, 1998), all-to-all (Kalisman et al., 2005) or random graphs, to the simulation of anatomically realistic neural networks (Bernard and Wheal, 1994; Patton and McNaughton, 1995; Ascoli and Atkeson, 2005). In this regard, we view a complete, 3D digital model of the hippocampus with a cellular level resolution as a necessary condition. In addition to mapping out potential connectivity patterns, such a construct would enable a layer-by-layer stereological analysis across the entire hippocampus, which is completely impractical with current experimental techniques (Fiala and Harris, 2001; Schmitz and Hof et al., 2005).

In keeping with these goals, we have completed a full digital reconstruction of the adult rat hippocampus from thin cryostatic sections. Moreover, we are developing a robust computational framework to embed reconstructed cells and transform the digital trace stack into arbitrary voxel size. Previous efforts in this direction were initiated by Scorcioni et al. (2002) in the dentate gyrus, but were not extended to a volumetric representation. Preliminary results of this work were presented in conference formats (Ropireddy et al., 2005). In this chapter, we describe the methodology and potential applications of this approach.

We further report a detailed volumetric analysis of individual cyto-architectonic layers and of the total volume of the hippocampus. We continue with an illustration of the potential for stereological analysis when a section of neuropil volume is packed with principal cells. This enables us to estimate the distribution of space occupancy fractions and overlaps of dendritic trees and their variations upon the position within the cyto-architectonic layers and the septo-temporal position. Moreover, we discuss future extensions to estimate the intrinsic potential connectivity patterns in the

hippocampus using available digital reconstructions of axonal morphologies. Finally, we offer a compartmental model-based example of the importance of synaptic position (peri-somatic versus distal) in the inhibition of principal cells. Thus, the construct described in this chapter could be qualitatively and quantitatively utilized towards investigating the biophysics of excitatory and inhibitory dynamics, and their relevance to seizure generation and spread in epilepsy. More generally, this approach could potentially contribute to a better understanding of the structure, function and activity of the hippocampus as well as of their inter-relations, bringing us closer to the formulation of a unified theory of the resulting cognitive processes.

## EXPERIMENTAL DESIGN

### IMAGE AND DATA ACQUISITION

Fresh-frozen brains of three male 45-day-old Long-Evans rats (226–237 g) were cryostatically sectioned at 16  $\mu\text{m}$  in dorso-ventral, ventro-dorsal and lateral-medial orientations, respectively, and mounted on gelatin-subbed slides. The dorso-ventral approach resulted in the least distortion in the hippocampal region and was thus selected for further analysis (presented here). In order to evaluate the shrinkage factor in the two dimensional plane of the section, prior to cutting we acquired whole mount pictures of the block face for 10 slices in the medial portions of the hippocampus, using a Kodak digital camera at 300 dpi resolution. Slides were Nissl stained with thionin by standard protocol (Simmons and Swanson, 1993) and cover-slipped. Images were acquired using an EPSON 3200 dpi scanner and contrast enhanced using the Matlab routine *imcontrast*. By overlaying these whole mount pictures over the corresponding histological scanned images, we computed a shrinkage factor of 7 ( $\pm 0.78\%$ ), assumed isotropic in the XY plane.

After loading the image stack into the *Reconstruct* tool (Fiala, 2005) with appropriate pixel/ $\mu\text{m}$  conversion (see Figure 6.1), a mid-line guided image alignment was manually performed (see Figure 6.1B). For every section, we traced inner and outer boundaries of the cyto-architectonic layers of the hippocampus based on Swanson's and Paxinos' standard rat atlases as validation references. Each resulting digital contour consisted of a set of pixels representing these boundaries as closed polygons (see Figure 6.1A). In particular, the following layers were identified and traced: stratum granulosum (GC), stratum moleculare (ML) and hilus proper (HI) of the dentate gyrus; and stratum lacunosum moleculare (LM), stratum radiatum (RA), stratum pyramidale (PC) and stratum oriens (OR) of Ammon's horn. Missed slices (42 out of 290) were interpolated based on their neighboring sections (see Figure 6.1C).

### TRIANGULATION ALGORITHM AND SURFACE REPRESENTATION

Each individual pixel-based closed polygon representing a cyto-architectonic layer boundary in a given section was ‘triangulated’ to identify or ‘fill’ all pixels inside the contour, representing an inner position of the respective anatomical subregion. The novel algorithm, written in C++ and illustrated in Figure 6.2, uses circular linked lists (Kernighan and Ritchie, 1998) and is applicable to both convex and concave polygons. This procedure is analogous to the Marching Cube approach (Lorensen and Cline, 1987), but extends it beyond iso-surface rendering of volumetric data. Additionally, this process also estimates the centroid of the polygon. The locations of the outer boundary centroids of each individual section were used to refine further the manual registration. In particular, ten zones were visually identified based on the geometrical discontinuity of these boundaries along the rostro-caudal axis. For example, the ventral hippocampus emerges approximately at one-third of the rostro-caudal extent (slice 105) and the dorsal and ventral regions merge together at one half of the same span (slice 146). The segregation into these ten zones accounted for these changes and avoided the drastic shift in the centroid position between adjacent boundaries. A three-point average was then applied on the centroid location until convexity or concavity was reached in each separate zone. Finally, every section was translated based on the new centroid coordinates. This approach yielded a smooth and satisfactory post-alignment registration.

The resulting data can be displayed based on surface or volume. Surface rendering (Figure 6.3A–G) is particularly amenable to visualization in Virtual Reality Modeling Language (VRML, Ames et al., 1997). Voxel-based volume representation (Figure 6.3H,I), on the other hand, enables the direct implementation of stereological analyses. The triangulation/filling algorithm described above can yield an arbitrary pixel size, or resolution of the digital reconstruction. In order to maintain 3D isotropy (cubic voxels), a shrinkage-corrected pixel size of 16  $\mu\text{m}$  was selected, corresponding to the nominal cryostatic section thickness.

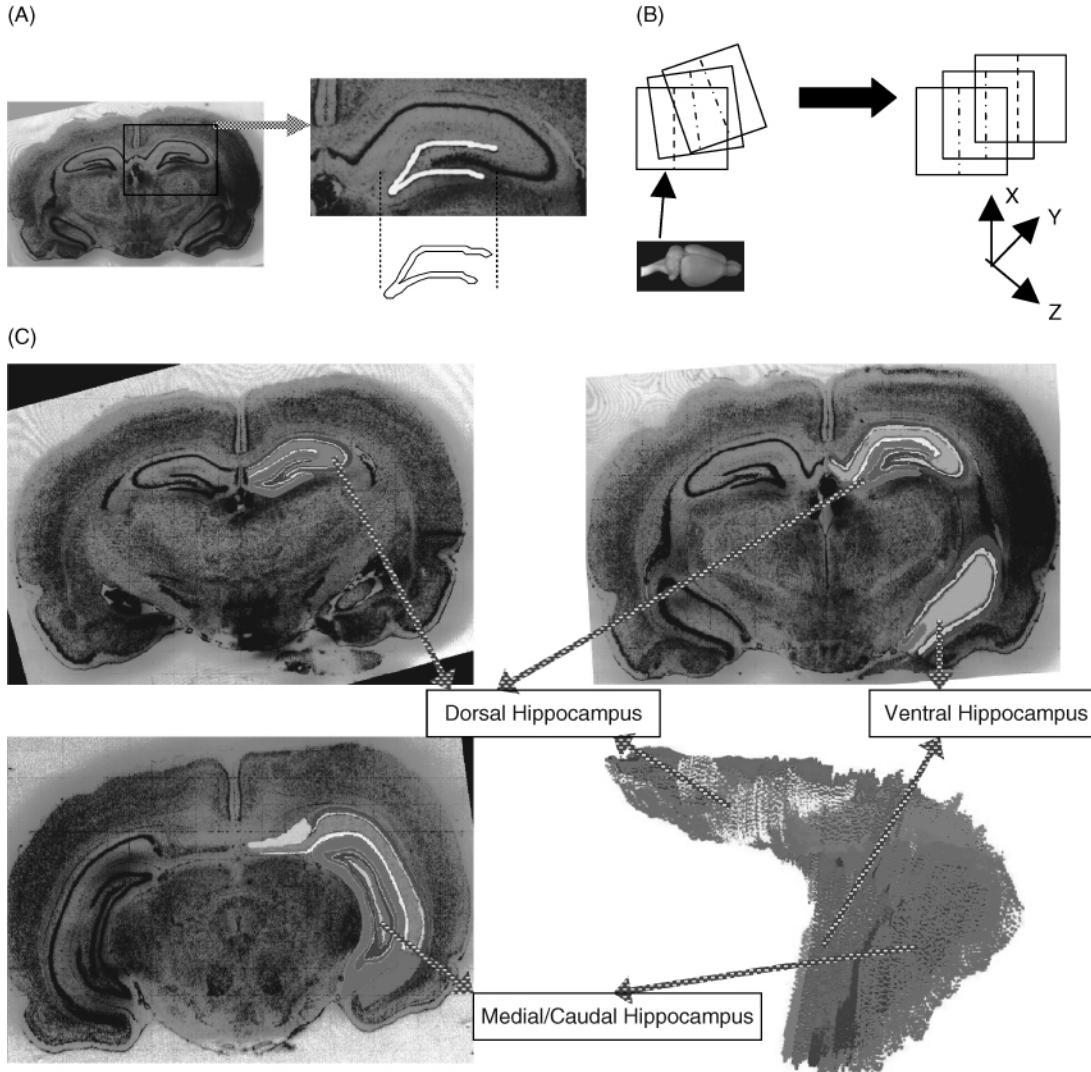


**FIGURE 6.1** Image and data acquisition. (A) Representative Nissl stained section of the rat brain. Inset shows the dorsal hippocampus at a magnified resolution with granule cell layer segmented (shaded in white). The clearly distinguishable cyto-architectonic layers allow a reliable segmentation of the hippocampus. (B) Preliminary mid-line guided registration. (C) Manual segmentation of the internal and external boundaries of the hippocampus. Three different coronal sections depict the dorsal, ventral and medial/caudal hippocampus. A surface view of the hippocampus in the medio-lateral view is also shown. (See Plate 6 in color plate section.)

#### VOLUMETRIC ANALYSIS

The computational framework described above decomposes the 3D volume of the hippocampus into  $4096 \mu\text{m}^3$  ( $16 \mu\text{m} \times 16 \mu\text{m} \times 16 \mu\text{m}$ ) voxels. The centers of the voxels within the granule and pyramidal cell layers are assigned to correspond to a soma location, approximating the tight neuronal packing of principal cells in the real tissue (Claiborne et al., 1990; Ishizuka et al., 1995). The resulting number of soma positions in the granule cell layer covering the whole septo-temporal extent was  $\sim 0.9 \times 10^6$ . For comparison, the stereological estimates are around  $10^6$ , varying with the age and strain of the animal (Gaarskjaer, 1978; Boss et al., 1987; Amaral et al., 1990). Throughout the hippocampal volume, voxels are named according to their cyto-architectonic layers in order to facilitate information retrieval within the computational framework. The volume of each layer is computed by voxel counting or by summing the total areas of individual triangles multiplied by the section thickness ( $16 \mu\text{m}$ ). The total hippocampal volume, given by the sum of the seven individual layers (including both dentate gyrus and Ammon's horn) across the rostro-caudal extent amounted to  $34.89 \text{ mm}^3$ .

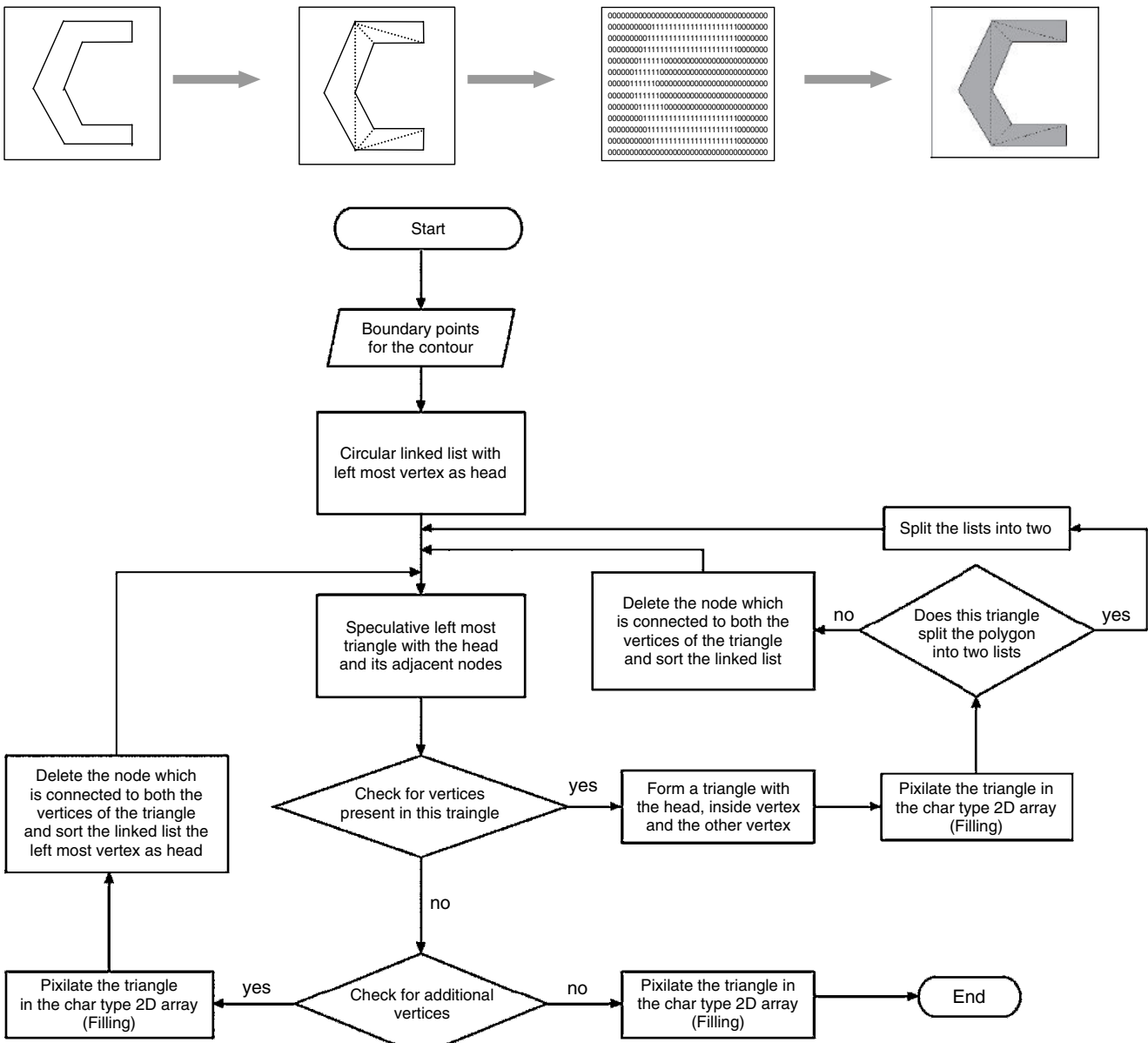


**FIGURE 6.2** Triangulation and filling algorithm. Top: schematic representation of the process. Bottom: flowchart of the steps to triangulate the ‘pixel-based closed polygon’ and pixilate the individual triangles. The program initially reads the contour and structures the vertices of the polygon in a circular linked list with the left most vertex/node (‘least X value’) as its head. The recursive procedure starts with forming a speculative triangle with the head and its adjacent nodes and checks for any vertices/nodes inside this triangle. If none are present, the triangle is pixilated by changing the corresponding 2D array null values into ‘1’s. The first node is then removed, the list re-sorted and the recursive triangle check repeated. If a vertex/node is present inside the triangle, a new triangle is formed with the head node, inside vertex/node and the left most other vertex/node. This triangle is pixilated in the 2D array and, if this operation splits the lists into two, the iteration is applied to both. The recursive triangulation ends when there are no additional vertex/nodes and the final triangle is pixilated.

The reconstructed volume was analyzed based upon hippocampal subregions, layers and coronal slicing order (Figure 6.4). Volume distributions are not uniform within the hippocampus, with the medial region contributing more ( $16.25 \text{ mm}^3$ ) than the dorsal ( $12.31 \text{ mm}^3$ ) and ventral ( $6.33 \text{ mm}^3$ ) regions. Percentage wise, the rostro-dorsal volume accounted for 35 % of the hippocampus proper, with the rostro-ventral region amounting to 18 % and the remaining portion (over 46 %) taken up by the caudal hippocampus. In the highly curved posterior (or caudal) regions (Figure 6.4B), Ammon’s horn (CA) regions were altogether nearly three times larger than dentate gyrus (DG) volumes, but they had similar sizes in the rostral portions (ventral plus dorsal volumes: DG~ $7 \text{ mm}^3$ , CA~ $11 \text{ mm}^3$ ). The CA layers in the posterior region

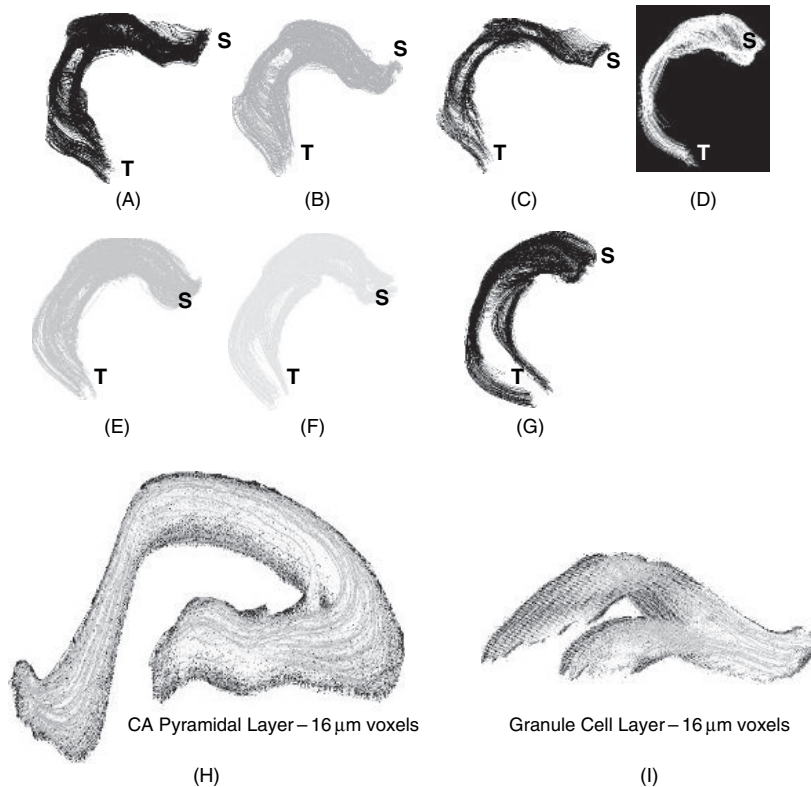


**FIGURE 6.3** Surface (A–G) and volumetric (H,I) views of the outer and inner boundaries. ‘S’ and ‘T’ mark septal and temporal poles respectively. (A) Stratum granulosum, (B) stratum moleculare, (C) hilus proper, (D) stratum lacunosum moleculare, (E) stratum radiatum, (F) stratum pyramidale, (G) stratum oriens, (H) middle portion of stratum pyramidale, (I) middle portion of stratum granulosum.

exceeded those in the dorsal or ventral regions (Figure 6.4A), but this relation was reversed for DG layers, where the dorsal portion is predominant (Figure 6.4C). Interestingly, LM is least in the ventral regions compared to the dorsal and medial regions (Figure 6.4F), while the RA layer is predominantly in the medial region (Figure 6.4A,C,D). The change in volume fraction in the coronal slicing order is more incremental for CA (except for LM) than for DG layers (Figure 6.4E). These volumetric measures are consistent with (but substantially extend) earlier reports (Boss et al., 1987; Tinsley et al., 2001).

#### CELLULAR EMBEDDING AND SPATIAL OCCUPANCY

The volumetric representation of the hippocampal reconstruction lends itself to further stereological analysis. In particular, the inclusion of cellular morphology (e.g. 3D dendritic arborizations) in this construct enables the estimation of spatial occupancy and overlaps, as well as of the potential connectivity across various neuronal classes in the hippocampus. An important prerequisite for this kind of analysis is the ability to embed reconstructed cells within the proper volume based upon their location and alignment in the hippocampus. In our framework, digital morphological reconstructions of pyramidal and granule cells, available at NeuroMorpho.Org (Ascoli, 2006), are algorithmically embedded based upon the following criteria: (a) the first principal axis of the dendritic arborization passes through the soma and is perpendicular to the cellular layer (Scorcioni et al., 2002); (b) the second (orthogonal) axis lies on the septo-temporal plane (Claiborne et al., 1990; Ishizuka et al., 1995); (c) the third axis is orthogonal to the above two. The 3D coordinates of the dendritic and axonal arborizations are read from the digital reconstruction files (Ascoli et al., 2001) and rotated along the above principal axes using standard numerical recipes (Press et al., 1992).

VRML files can be generated on the fly for visualization purposes with the freeware *vrmlview* viewer ([www.sim.no](http://www.sim.no)). Figure 6.5 illustrates renderings of such embedding along with septo-temporal and coronal views. This process accurately reflects the organization of the neuronal arbors observed *in vitro*: the granule cells dendritic tree spread in the septo-temporal and transversal directions in our construct averaged 351.28  $\mu\text{m}$  and 170.59  $\mu\text{m}$ , respectively, compared to the reported experimental values of 347  $\mu\text{m}$  and 182  $\mu\text{m}$ , respectively (Claiborne et al., 1990).

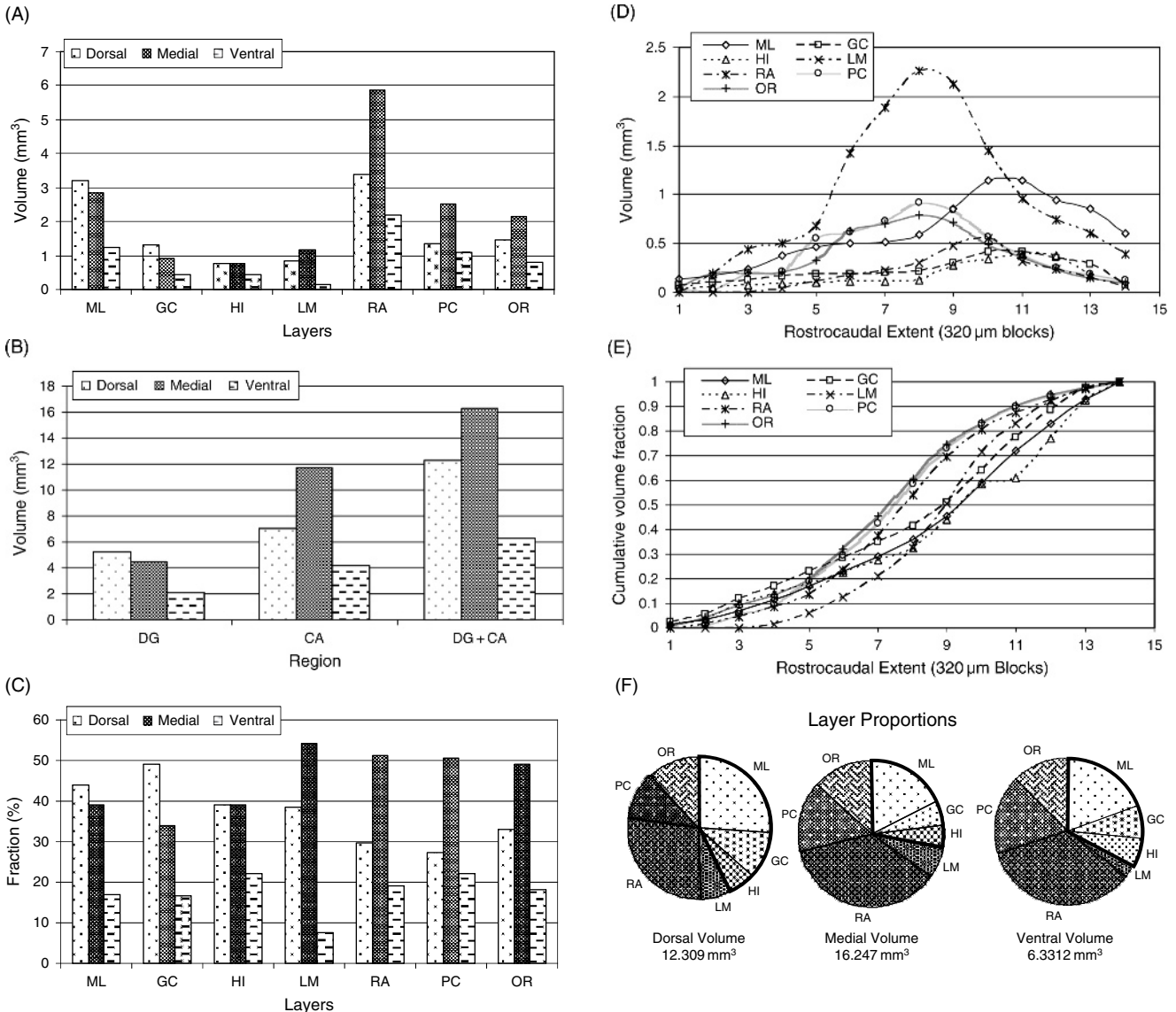


**FIGURE 6.4** Volumetric measures of the reconstructed hippocampus. Absolute (A, B, D) and relative (C, E, F) analyses refer to individual layers (A, C, D, E, F), regions (B), and sections (A, B, C, F). Dorsal, ventral and medial sections, demarcated by landmarks as shown in Plate 6C, encompass slices 1–145, 105–145 and 146–290, respectively.

We used these data and approach to estimate the dendritic occupancy and overlap as a function of the 3D position. Spatial occupancy is the volume fraction occupied by embedded dendrites and averaged across all the voxels of a given subregion and cyto-architectonic layer. Spatial overlap is the number of occurrences in which one and the same 3D location is occupied by distinct dendritic branches. Here, we present the results of the initial analysis carried out on a portion of the dentate gyrus. In particular, we embedded replicas of 39 reconstructed granule cells (Rihm and Claiborne, 1990) in their corresponding supra-pyramidal blade locations within the middle third of the septo-temporal extent.

The septo-temporal length of the whole hippocampus calculated along the centroid positions is 6.50 mm, which leaves 2.17 mm for the middle third portion as the extent available for cell packing. However, voxels at the edges of this extent are not suitable for estimation of space occupancy and overlaps, because they are only invaded by the arborizations of the cells from one direction and not the other. To account for this edge factor, the volume that encompasses half of the maximum arborization span in the corresponding orientation (the tree ‘depth’) at both of the edges is discarded from the computation of spatial occupancy and overlap. In turn, the region of interest corresponds to the septo-temporal range from 2.29 mm to 4.19 mm. An analogous edge factor is also applied in the transversal direction, thus preventing the computation of space

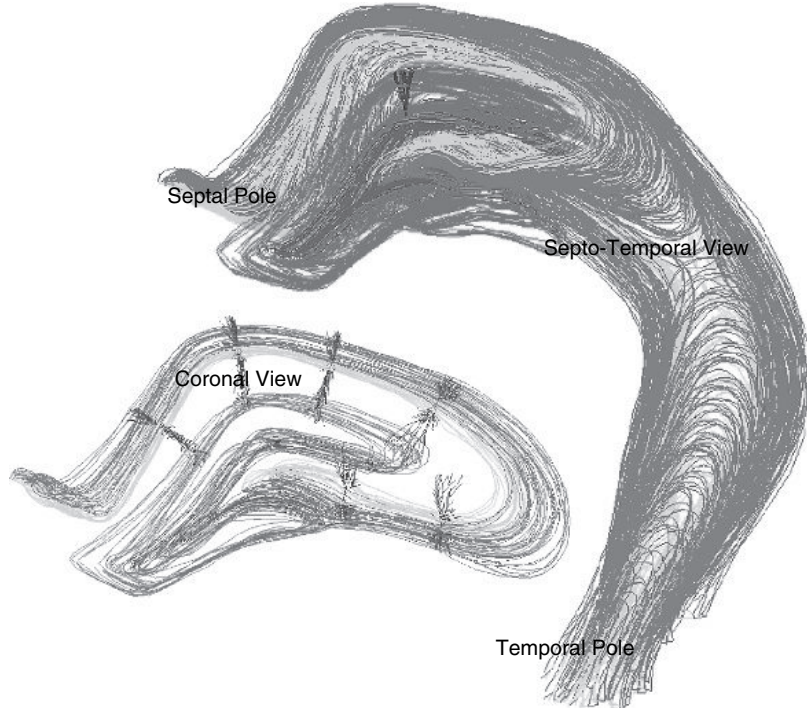


**FIGURE 6.5** Separate views of a granule cell in the appropriate location and orientation of the whole hippocampal reconstruction, and of six pyramidal cells embedded in the (algorithmically identified) CA3c, CA3b, CA2, CA1a, CA1b and CA1c subregions (only a subset of the coronal sections are displayed for clarity). Dendritic trees are in blue, while the boundaries of the oriens, pyramidal, molecular and granule layers are in pink, yellow, green, and red, respectively. (See Plate 7 in color plate section.)

occupancy and overlap in the volume corresponding to half of the maximum tree width at the dentate crest and tip (the edges of the supra-pyramidal blade). Even though these volumes are excluded from the computation of space occupancy, they are still sampled for the embedding process.

In order to emulate the high packing density of principal cells *in vivo*, all granule layer voxels within the range of potential overlap with a given position are embedded with a granule cell soma and the corresponding arborization is oriented accordingly in the surrounding space. The region of interest is sequentially traversed in unit boxes crossing the entire granular and molecular layers and sized as the average transversal and septo-temporal spreads of the 39 available granule cells. The spatial range of potential overlap whose granular layer needs to be packed with embedded cells to estimate occupancy in these unit boxes extends half the maximum width and depth in both directions. The resulting embedding space around each unit box is  $\sim 825 \mu\text{m}$  wide and  $\sim 430 \mu\text{m}$  deep.

From the pool of reconstructed cells, those whose reported position (Rihm and Claiborne, 1990) is consistent with the appropriate transverse location are sampled for each voxel. To approximate the natural alignment variability of the principal dendritic component with the direction normal to the local surface, the primary axis of each cell is stochastically tilted between 0 and 5 degrees around a random (0–360 degree) rotation angle. The resultant direction falls within a 5 degree cone centrally aligned with the original normal axis. The other two orthogonal axes are correspondingly adjusted for both the tilt and rotation factor.

The distance from the granule cell soma (or initial embedding voxel) to the outer molecular layer boundary (hippocampal fissure) is also measured along the unit normal. The vertical span of the dendritic tree (height) along the normal vector is then calculated and used to scale the geometry of the tree appropriately. In particular, the three coordinates and diameters of all branches in each embedded neuron are multiplied by the ratio between the soma-fissure distance and the original dendritic height, ensuring that the farthest tips of the dendrites terminate at the end of the molecular layer.

To evaluate efficiently the spatial occupancy of dendritic trees, we sequentially probe the voxels that fall within the three-dimensional span of each given tree. This process is repeated through all the soma-points. Digital reconstructions of neuronal morphology consist of sets of cylinders. Three conditions are checked to determine whether a cylinder intersects a voxel. The first tests for the presence of the two cylinder end points in (or on the planes of) the voxel. If this condition is satisfied, the entire volume of the cylinder is added into the occupied fraction for the voxel. If only one end point lies inside

the voxel, the intersection between the cylinder and one of the face planes of the voxel is calculated and the corresponding (partial) volume added to the occupied fraction. If neither of the above conditions is met, the cylinder end points lie outside the voxel. In this case, the two intersecting points and resulting volume, if any, are calculated and treated as above.

For both spatial occupancy and overlaps, results are averaged over one embedding unit box (single neuron span) based on the cyto-architectonic position, namely granule cell layer (GC) and proximal, medial and distal thirds of the molecular layer (ML-1/3, ML-2/3, and ML-3/3, respectively). The region of interest of this analysis spanned 20 embedding units in the longitudinal axis (Figure 6.6) and two in the transversal axis (adjacent to the blade crest and tip, respectively).

Spatial occupancy has a moderate dependence on the septo-temporal position (Figure 6.6A,B) and varies according to layer and blade position (crest or tip). The ML-2/3 voxels have the maximum occupancy compared to other regions, with a range of 0.4–0.7. Interestingly, the ordering of the rest of the voxels varies over the septo-temporal position. These results suggest that the dendritic volume changes non-uniformly with the distance along the extent of the molecular layer. Recent studies based on electron microscopy have shown that the wiring fraction (dendritic and axonal volumes) constitutes 55% of the neuropil in the CA1 radiatum area (Chklovskii et al., 2002). These authors observe that this fraction might not hold for the dentate gyrus. Thus, our report has interesting implications with respect to the volume available to axons, spines, boutons and glia within the dentate. The outer two-thirds of the ML layer are highly innervated by the entorhinal perforant path projections emanating from layer II (Witter and Amaral, 2004). The difference in space occupancy between ML-2/3 and ML-3/3 could correspond to a change in the density of spines along the granule cell dendritic tree.

The average number of spatial overlaps (Figure 6.6C,D) also changes with the position in the DG. The ML-2/3 and GC voxels have respectively the maximum and minimum number of overlaps. Noticeably, the number of overlaps in the tip exceeded that in the crest. The high incidence of overlaps could reflect an intrinsic signaling mechanism to form

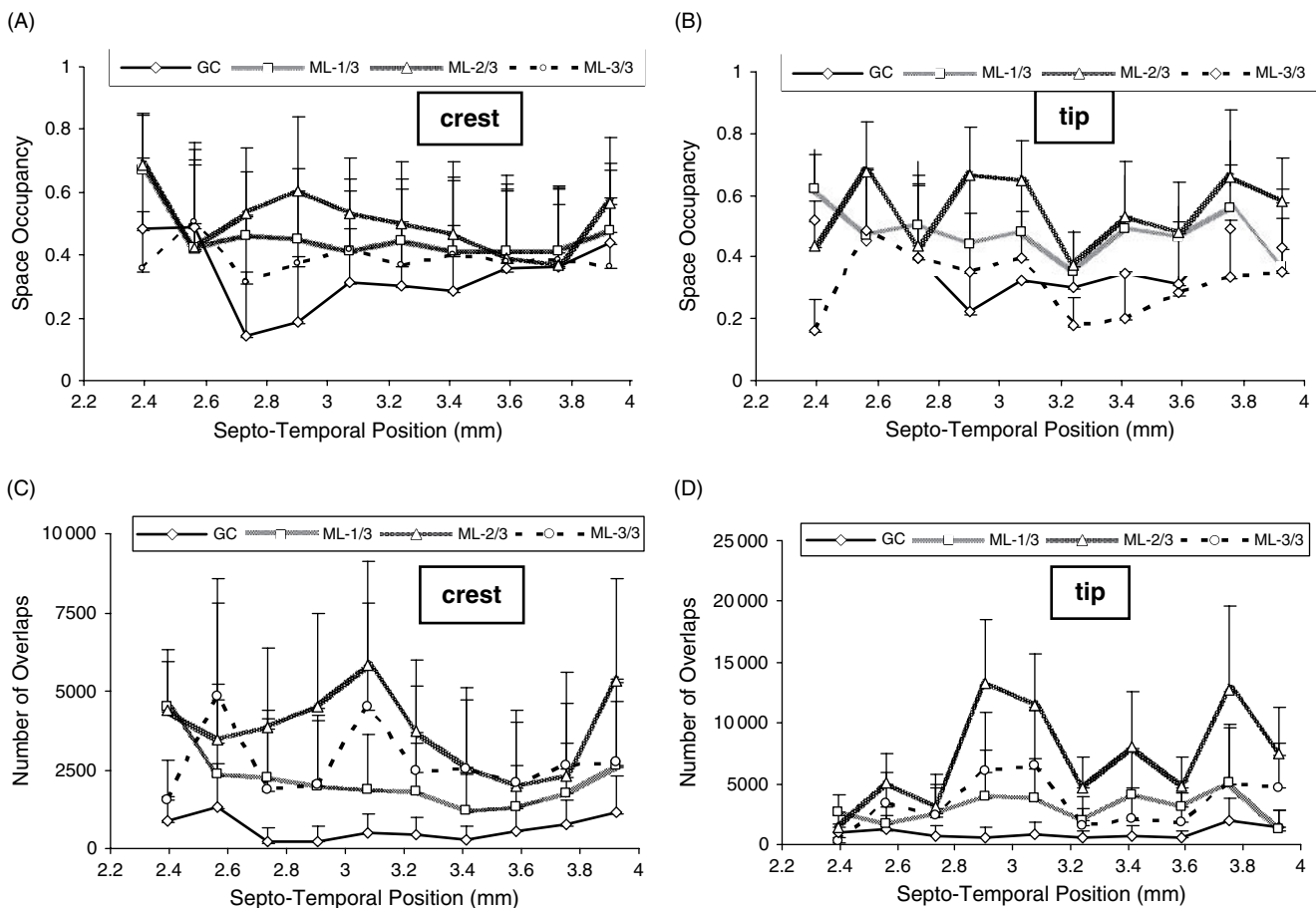


FIGURE 6.6 Spatial occupancy (top) and overlaps (bottom) of granule cell dendrites in the crest (left) and tip (right) halves of the supra-pyramidal blade of the dentate gyrus. Four sub-layers are distinguished and analyzed across their relevant longitudinal extent: granular (GC), inner molecular (ML-1/3), middle molecular (ML-2/3), and outer molecular (ML-3/3).

multineurite sites (Cove et al., 2006) in order to economize the wiring pattern (Chklovskii et al., 2002; Buzsáki et al., 2004). The difference in the number of overlaps in the crest and tip regions could be due to a differential dendritic recognition mechanism to avoid or promote contacts between adjacent cells (Sestan et al., 1999).

### INTRINSIC POTENTIAL CONNECTIVITY PATTERNS

Electron microscopy showed that synaptic specialization may exist without a physical contact between an axon and a dendrite (Palay, 1958; Gray, 1959a, 1959b). Experiments have demonstrated the plastic nature of spines in establishing and remodeling a synaptic contact with the presynaptic machinery (Lendvai et al., 2000; Matsuzaki et al., 2004). In this context, a *potential synapse* can be defined as the condition of an axonal segment passing within a specified distance (depending on the type of synapse) from a dendritic segment. For excitatory synapses, the typical spine length ( $\sim 2 \mu\text{m}$ ) is taken as the distance parameter (Spacek and Hartmann, 1983; Harris and Stevens, 1989; Harris, 1999; Kalisman et al., 2003; Stepanyants and Chklovskii, 2005). For (presumably inhibitory) synapses on shafts and gap junctions, the critical distance can be obtained as the sum of the radii of the dendrite and axonal segments, typically  $0.4\text{--}1.0 \mu\text{m}$  (Stepanyants and Chklovskii, 2005).

Several studies over the past years have estimated potential synaptic connectivity in the neocortex from detailed morphological data (Kalisman et al., 2003; Stepanyants et al., 2004) and simplified arbor shapes (Liley and Wright, 1994) through analytical and computational means. In addition, the functional connectivity between CA3 and CA1 has been investigated experimentally (Brivanlou et al., 2004). However, most approaches based on *in vitro* (slice) conditions are typically limited to a narrow anatomical region and cannot be assumed to extend representatively to surrounding areas. Our framework is in principle suitable to map out probabilistic connectivity patterns across the septo-temporal extent quantitatively. Digital reconstructions of dendritic arborizations are especially abundant in the morphology database (NeuroMorpho.Org) for the rat hippocampus. Complete projection axons were traced algorithmically from available *in vivo* data (Tamamaki et al., 1988; Tamamaki and Nojyo, 1990, 1991; Scorcioni and Ascoli, 2005). For example, Figure 6.7A shows the axodendritic spread of a CA2 pyramidal cell with a CA1 cell co-embedded in the framework.

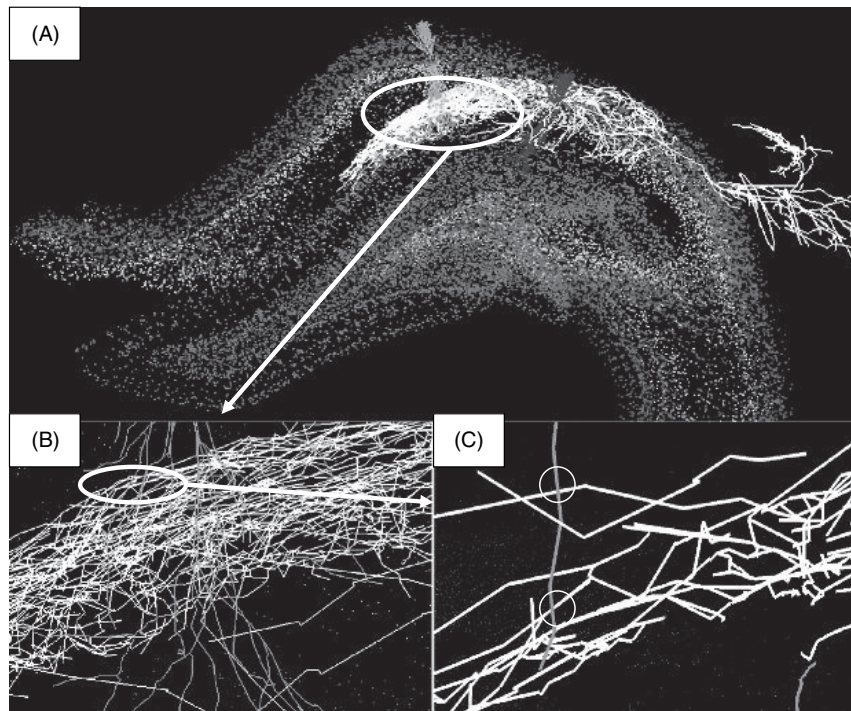


**FIGURE 6.7** Estimating potential connectivity: (A) the axonal arborization (white) of a CA2 pyramidal cell (blue dendritic tree) invades a large portion of the CA radiatum region, and could establish synaptic contacts with a CA1 pyramidal cell (light green dendrites). (B) Spread of the axonal collaterals and possible overlaps with the CA1 dendritic tree. (C) Further magnification highlighting potential synapses (circles). (See Plate 8 in color plate section.)

To account for variability in the arbor shapes due to pooling of data from different rat brains and imprecision in measurements, the arbor skeleton can be convolved with a Gaussian filter (Stepanyants and Chklovskii, 2005). After embedding the neuronal tree in the appropriate hippocampal volume, the voxels appropriate to the axonal density can be probed for the occurrence of potential synapses (see Figure 6.7B,C). This protocol is suitable to map out the intrinsic connectivity patterns among principal cells and between principal cells and interneurons within the whole hippocampus. This strategy will thus establish a quantitative relation between the spatial positions of the pre- and postsynaptic cell and their synaptic connectivity in probabilistic terms. Such a result would constitute a monumental step in the full characterization of the hippocampal circuitry.

#### INFLUENCE OF INHIBITORY SYNAPSE POSITION ON CA1 PYRAMIDAL CELL FIRING

At least 16 distinct types of inhibitory interneurons synapse on CA1 pyramidal cells (Gulyas et al., 1999; Somogyi and Klausberger, 2005). These highly layer specific contacts play a pivotal role in the generation of population oscillations by sculpting the firing pattern of pyramidal cells by both feedforward and feedback inhibition. The laminar organization of this architecture raises the question of the biophysical importance of GABAergic synapse position. A single CA1 pyramidal cell synapse can make an interneuron fire (Gulyas et al., 1993; Marshall et al. 2002). If this interneuron has feedforward inhibitory connection onto another CA1 pyramidal cell, how does the efficacy of this latter synapse depend on its somato-dendritic placement? Can a single peri-somatic or axo-dendritic inhibitory synapse prevent pyramidal cell firing? To explore this problem, we adapted an existing CA1 pyramidal cell model (Migliore et al., 1999; <http://senselab.med.yale.edu>) available for the NEURON simulation environment (Hines and Carnevale, 2001). The model had a total of 200 compartments (soma: 13, apical: 127, basal: 60). We distributed the inhibitory synapses on the dendritic tree following the available experimental characterization (Megias et al., 2001). Accordingly, an inhibitory synapse was associated with one of the compartments in somatic, proximal radiatum, medial radiatum, distal radiatum and lacunosum-moleculare compartments (Figure 6.8).

The simulated firing frequency of the CA1 pyramidal cell is 40 Hz (Figure 6.8A) in response to a 0.15 nA somatic current injection (Migliore et al., 1999; Graham, 2001). Inhibitory synapses were activated at a regular, constant rate of 10 Hz, corresponding to the spontaneous firing of stratum lacunosum-moleculare interneurons (Lacaille and Schwartzkroin, 1988). The rise and decay times for the inhibitory synapses, corresponding to  $\tau_{au1}$  and  $\tau_{au2}$  in the NEURON *Exp2Syn* object, were 0.75 and 37 ms, respectively (Kapur et al., 1997), with a reversal potential of  $-80$  mV and a synaptic current of 0.001 nA. The effect of activating individual inhibitory synapses after 50 ms varies dramatically with synaptic location (see Figure 6.8). A single GABAergic input in the peri-somatic and proximal dendritic region can inhibit the neuron from firing (see Figure 6.8B,C). Inhibition in the intermediate apical tree can slow down, but not fully block, spiking (see Figure 6.8D). In the most distal (outer radiatum and lacunosum-moleculare) layers, four synchronous inhibitory synapses are still insufficient to affect firing (Figure 6.8E,F). These simulations illustrate the importance of synaptic placement on CA1 pyramidal cell firing pattern. A thorough modeling study implemented with realistic synaptic connectivity could help investigate hippocampal dynamics.

#### IMPLICATIONS AND APPLICATIONS TO EPILEPSY

Homeostasis in brain circuits is essential for normal functioning and its disruption can lead to pathological states such as temporal lobe epilepsy (TLE). A critical way to maintain homeostasis is a delicate balance between excitatory and inhibitory circuits. This balance requires a careful assembly of highly complex topological and structural elements. Seemingly small changes in this configuration may lead to a hyper-excitable state, tipping the system into recurrent seizures.

Almost every pathological case of epilepsy seems to be associated with an anatomical abnormality, such as in the lamination of the hippocampus (Forster et al., 2006). Animal models attribute the genesis of seizure activity in the dentate gyrus to mossy fiber sprouting ('synaptogenesis'), or alternatively to hilar mossy cell loss (Sutula, 2002; Avoli et al., 2005). In contrast, the surviving CA1 pyramidal cells in human epileptic tissue receive intact peri-somatic inhibitory input (Wittner et al., 2005). However, mesial TLE patients have sclerosis of tissue and cell loss in the dentate hilus, as well as in the CA region (Mathern et al., 1994). As a result, there are significant volume and morphological changes in the

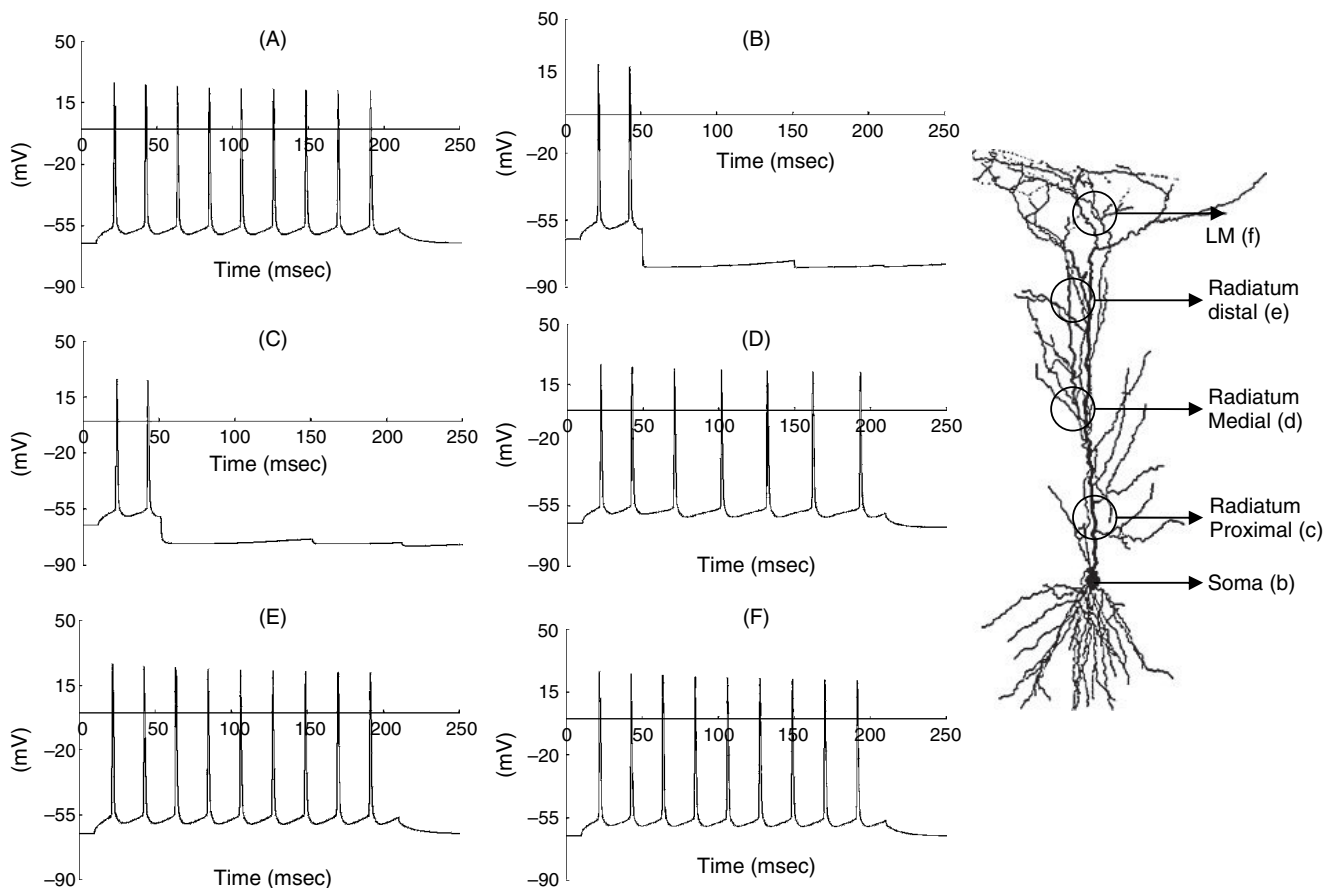


**FIGURE 6.8** Effect of the inhibitory synapse location on the dendritic tree of a CA1 pyramidal cell: (A) 0.15 nA soma current injection leading to 40 Hz spiking. Inhibitory synapses on the soma (B), proximal radiatum (C), medial radiatum (D), distal radiatum (E) and lacunosum-moleculare (F) compartments have varying effects on firing rate when activated at  $t = 50$  ms. Side panel shows a real CA1pc morphology image with synapse positions.

cellular and non-cellular layers in these pathological cases. These changes in turn can affect the intrinsic circuitry and the stereological properties, such as space occupancy and overlaps, which have a direct effect on the biophysical state of the system. These factors could be collectively dubbed as ‘anatomical correlates of epilepsy’.

In order to understand the dynamics of seizure initiation and spread, the anatomical complexity and organization should be taken into consideration in computational models of epilepsy. In recent years, there has been considerable effort to embrace a data-driven and connectivity based approach to simulate and investigate epileptiform activity (Netoff et al., 2004; Santhakumar et al., 2005; Dyhrfjeld-Johnsen et al., 2007). The framework described in this chapter is well positioned to strengthen and expand these kinds of studies by providing *in vivo*-like spatial connectivity patterns within various cell groups depending on their spatial position. A modeling approach as illustrated in the previous section, and implemented using a realistic spatial organization and morphology of principal and inhibitory cells in normal and pathological cases, could yield insights into the mechanism of TLE. These models could also become useful in the detection of pre-seizure states (Wong et al., 2007) and to provide a feedback signal to seizure detection and prevention devices.

#### ACKNOWLEDGMENT

This Human Brain Project/Neuroinformatics research is funded by National Institute of Neurological Disorders and Stroke, the National Science Foundation and the National Institute of Mental Health (R01 NS39600 to GAA).

## REFERENCES

- Amaral, D.G., Ishizuka, N. and Claiborne, B. (1990). Neurons, numbers and the hippocampal network. In: *Progress in brain research: understanding the brain through the hippocampus: the hippocampal region as a model for studying structure and function* (J. Storn-Mathisen, J. Zimmer and O.P. Ottersen, eds) pp. 1–11, Elsevier, Amsterdam.
- Ames, A.L., Nadeau, D.R. and Moreland, J.L. (1997). *The VRML 2.0 Sourcebook*. John Wiley & Sons, Inc., New York.
- Andersen, P., Bliss, T.V.P. and Skrede, K.K. (1971). Lamellar organization of hippocampal excitatory pathways. *Exp Brain Res* 13: 222–238.
- Ascoli, G.A. (2006). Mobilizing the base of neuroscience data: the case of neuronal morphologies. *Nat Rev Neurosci* 7:318–324.
- Ascoli, G.A. and Atkeson, J. (2005). Incorporating anatomically realistic cellular cellular-level connectivity in neural network models of the rat hippocampus. *Biosystems* 79:173–181.
- Ascoli, G.A., Krichmar, J.L., Nasuto, S.J. and Senft, S.L. (2001). Generation, description and storage of dendritic morphology data. *Phil Trans R Soc Biol Sci* 356:1131–1145.
- Avoli, M., Louvel, J., Pumain, R. and Kohling, R. (2005). Cellular and molecular mechanisms of epilepsy in the human brain. *Prog Neurobiol* 77:166–200.
- Bernard, C. and Wheal, H.V. (1994). Model of local connectivity patterns in CA3 and CA1 areas of the hippocampus. *Hippocampus* 4:497–529.
- Bliss, T.V.P. and Collingridge, G.L. (1993). A synaptic model of memory: long-term potentiation in the hippocampus. *Nature* 361:31–39.
- Boss, B.D., Turlejski, K., Stanfield, B.B. and Cowan, W.M. (1987). On the numbers of neurons in fields CA1 and CA3 of the hippocampus of Sprague-Dawley and Wistar rats. *Brain Res* 406:280–287.
- Brivanlou, I.H., Dantzker, J.L.M., Stevens, C.F. and Callaway, E.M. (2004). Topographic specificity of functional connections from hippocampal CA3 to CA1. *Proc Natl Acad Sci* 101:2560–2565.
- Buzsáki, G. (1989). Two-stage model of memory trace formation: a role for ‘noisy’ brain states. *Neuroscience* 31:551–570.
- Buzsáki, G. (2002). Theta oscillations in the hippocampus. *Neuron* 33:325–340.
- Buzsáki, G. and Draguhn, A. (2004). Neuronal oscillations in cortical networks. *Science* 304:1926–1929.
- Buzsáki, G., Geisler, C., Henze, D.A. and Wang, X.-J. (2004). Circuit complexity and axon wiring economy of cortical interneurons. *Trend Neurosci* 27:186–193.
- Cannon, R.C. and Wheal, H.V. (1999). Dendrites of classes of hippocampal neurons differ in structural complexity and branching patterns. *J Comp Neurol* 413:619–633.
- Chklovskii, D.B., Schikorski, T. and Stevens, C.F. (2002). Wiring optimization in cortical circuits. *Neuron* 34:341–347.
- Claiborne, B.J., Amaral, D.G. and Cowan, W.M. (1990). Quantitative, three-dimensional analysis of granule cell dendrites in the rat dentate gyrus. *J Comp Neurol* 302:206–219.
- Cove, J., Blinder, P., Abi-Jaoude, E., Lafreniere-Roula, M., Devroye, L. and Baranes, D. (2006). Growth of neurites toward neurite-neurite contact sites increases synaptic clustering and secretion and is regulated by synaptic activity. *Cerebr Cort* 16:83–92.
- Dyhrfjeld-Johnsen, J., Santhakumar, V., Morgan, R.J., Huerta, R., Tsimring, L. and Soltesz, I. (2007). Topological determinants of epileptogenesis in large-scale structural and functional models of the dentate gyrus derived from experimental data. *J Neurophysiol* 97:1566–1587.
- Eichenbaum, H. and Cohen, N.J. (2001). *From conditioning to conscious recollection*. Oxford University Press, New York.
- Fiala, J.C. and Harris, K.M. (2001). Extending unbiased stereology of brain ultrastructure to three-dimensional volumes. *J Am Med Informat Assoc* 8:1–16.
- Fiala, J.C. (2005). Reconstruct: a free editor for serial section microscopy. *J Microsc* 218:52–61.
- Forster, E., Zhao, S. and Frotscher, M. (2006). Laminating the hippocampus. *Nat Rev Neurosci* 7:259–267.
- Freund, T.F. and Buzsáki, G. (1996). Interneurons of the hippocampus. *Hippocampus* 6:347–470.
- Gaarskjaer, F.B. (1978). Organization of the mossy fiber system of the rat studied in extended hippocampi. I. Terminal area related to number of granule and pyramidal cells. *J Comp Neurol* 178:49–72.
- Graham, B.P. (2001). Pattern recognition in a compartmental model of a CA1 pyramidal neuron. *Network* 12:473–492.
- Gray, E.G. (1959a). Electron microscopy of synaptic contacts on dendritic spines of the cerebral cortex. *Nature* 183:1592–1593.
- Gray, E.G. (1959b). Axo-somatic and axo-dendritic synapses of the cerebral cortex: an electron microscope study. *J Anat (Lond)* 93:420–433.
- Gulyas, A.I., Miles, R., Sik, A., Toth, K., Tamamaki, N. and Freund, T.F. (1993). Hippocampal pyramidal cells excite inhibitory neurons via a single release site. *Nature* 366:683–687.
- Gulyas, A.I., Megias, M., Emri, Z. and Freund, T.F. (1999). Total number and ratio of excitatory and inhibitory synapses converging onto single interneurons of different types in the CA1 area of the rat hippocampus. *J Neurosci* 19:10082–10097.
- Harris, K.M. (1999). Structure, development, and plasticity of dendritic spines. *Curr Opin Neurobiol* 9:343–348.
- Harris, K.M. and Stevens, J.K. (1989). Dendritic spines of CA1 pyramidal cells in the rat hippocampus: serial electron microscopy with reference to their biophysical characteristics. *J Neurosci* 9:2982–2997.
- Harris, K.D., Csicsvari, J., Hirase, H., Dragoi, G. and Buzsáki, G. (2003). Organization of cell assemblies in the hippocampus. *Nature* 424:552–556.
- Hebb, D.O. (1949). *Organization of behavior: a neuropsychological theory*. John Wiley, New York.
- Hines, M.L. and Carnevale, N.T. (2001). NEURON: a tool for neuroscientists. *Neuroscientist* 7:123–135.
- Ishizuka, N., Cowan, W.M. and Amaral, D.G. (1995). A quantitative analysis of the dendritic organization of pyramidal cells in the rat hippocampus. *J Comp Neurol* 362:17–45.
- Kalisman, N., Silberberg, G. and Markram, H. (2003). Deriving physical connectivity from neuronal morphology. *Biol Cybernet* 88:210–218.
- Kalisman, N., Silberberg, G. and Markram, H. (2005). The neocortical microcircuit as a tabula rasa. *Proc Natl Acad Sci* 102:880–885.
- Kapur, A., Lytton, W.W., Ketchum, K.L. and Haberly, L.B. (1997). Regulation of the NMDA component of EPSPs by different components of postsynaptic GABAergic inhibition: computer simulation analysis in piriform cortex. *J Neurophysiol* 78:2546–2559.
- Kernighan, B.W. and Ritchie, D.M. (1998). *The C programming language*, 2nd edn. Prentice Hall, Inc.
- Krichmar, J.L., Nasuto, S.J., Scorcioni, R., Washington, S.D. and Ascoli, G.A. (2002). Effects of dendritic morphology on CA3 pyramidal cell electrophysiology: a simulation study. *Brain Res* 941:11–28.

- Lacaille, J.C. and Schwartzkroin, P.A. (1988). Stratum lacunosum-moleculare interneurons of hippocampal CA1 region. II. Intrasomatic and intradendritic recordings of local circuit synaptic interactions. *J Neurosci* 8:1411–1424.
- Lendvai, B., Stern, E.A., Chen, B. and Svoboda, K. (2000). Experience-dependent plasticity of dendritic spines in the developing rat barrel cortex in vivo. *Nature* 404:876–881.
- Liley, D.T.J. and Wright, J.J. (1994). Intracortical connectivity of pyramidal and stellate cells: estimates of synaptic densities and coupling symmetry. *Network* 5:175–189.
- Li, X.G., Somogyi, P., Ylinen, A. and Buzsáki, G. (1994). The hippocampal CA3 network: an in vivo intracellular labeling study. *J Comp Neurol* 339:181–208.
- Lorensen, W.E. and Cline, H.E. (1987). Marching Cubes: A high resolution 3D surface reconstruction algorithm. *Comput Graph* 21:163–169.
- Mainen, Z.F. and Sejnowski, T.J. (1996). Influence of dendritic structure on firing pattern in model neocortical neurons. *Nature* 382:362–366.
- Marshall, L., Henze, D.A., Hirase, H., Leinekugel, X., Dragoi, G. and Buzsáki, G. (2002) Hippocampal pyramidal cell-interneuron spike transmission is frequency dependent and responsible for place modulation of interneuron discharge. *J Neurosci* 22:RC197:1–5.
- Matheron, G.W., Leite, J.P., Pretorius, J.K., Quinn, B., Peacock, W.J. and Babb, T.L. (1994). Children with severe epilepsy: evidence of hippocampal neuron losses and aberrant mossy fiber sprouting during postnatal granule cell migration and differentiation. *Brain Res Devel Brain Res* 78:70–80.
- Matsuzaki, M., Honkura, N., Ellis-Davies, G.C. and Kasai, H. (2004). Structural basis of long-term potentiation in single dendritic spines. *Nature* 429:761–766.
- Maurer, A.P., Cowen, S.L., Burke, S.N., Barnes, C.A. and McNaughton, B.L. (2006). Organization of hippocampal cell assemblies based on theta phase precession. *Hippocampus* 16:785–794.
- Megias, M., Emri, Z.S., Freund, T.F. and Gulyas, A.I. (2001). Total number and distribution of inhibitory and excitatory synapses on hippocampal CA1 pyramidal cells. *Neuroscience* 102:527–540.
- Migliore, M. (2003). On the integration of subthreshold inputs from perforant path and schaffer collaterals in hippocampal CA1 pyramidal neurons. *J Comput Neurosci* 14:185–192.
- Migliore, M. and Shepherd, G.M. (2002). Emerging rules for the distribution of active dendritic conductances. *Nat Rev Neurosci* 3: 362–370.
- Migliore, M., Hoffman, D.A. and Johnston, D. (1999). Role of an A-type K<sup>+</sup> conductance in the back-propagation of action potentials in the dendrites of hippocampal pyramidal neurons. *J Comput Neurosci* 7:5–15.
- Migliore, M., Messineo, L. and Ferrante, M. (2004). Dendritic Ih selectively blocks temporal summation of unsynchronized distal inputs in CA1 pyramidal neurons. *J Comput Neurosci* 16:5–13.
- Morris, R.G.M., Garrud, P., Rawlins, J.N. and O'Keefe, J. (1982). Place navigation impaired in rats with hippocampal lesions. *Nature* 297:681–683.
- Netoff, T.I., Clewley, R., Arno, S., Keck, T. and White, J.A. (2004). Epilepsy in small world networks. *J Neurosci* 24:8075–8083.
- O'Keefe, J. and Nadel, L. (1978). The hippocampus as a cognitive map. Oxford University Press, Oxford.
- Palay, S.L. (1958). The morphology of synapses in the central nervous system. *Exp Cell Res* 14 (Suppl 5):275–293.
- Patton, P.E. and McNaughton, B. (1995). Connection matrix of the hippocampal formation: I. The dentate gyrus. *Hippocampus* 5:245–286.
- Poirazi, P., Brannon, T. and Mel, B.W. (2003a). Arithmetic of subthreshold synaptic summation in a model CA1 pyramidal cell. *Neuron* 37:977–987.
- Poirazi, P., Brannon, T. and Mel, B.W. (2003b). Pyramidal neuron as two-layer neural network. *Neuron* 37:989–999.
- Press, W.H., Teukolsky, S.A., Vetterling, W.T. and Flannery, B.P. (1992). Numerical recipes in C, the art of scientific computing, 2nd edn. Cambridge University Press, Cambridge.
- Pyapali, G.K., Sik, A., Penttonen, M., Buzsáki, G. and Turner, D.A. (1998). Dendritic properties of hippocampal CA1 pyramidal neurons in the rat: intracellular staining in vivo and in vitro. *J Comp Neurol* 391:335–352.
- Reyes, A. (2001). Influence of dendritic conductances on the input-output properties of neurons. *Ann Rev Neurosci* 24:653–675.
- Rihm, L.L. and Claiborne, B.J. (1990). Dendritic growth and regression in rat dentate granule cells during late postnatal development. *Brain Res. Devel Brain Res* 54:115–24.
- Ropireddy, D., Scorcioni, R., Bachus, S. and Ascoli, G.A. (2005). Three-dimensional reconstruction of the rat hippocampus: stereology and embedding of neuronal arborizations. Society for Neuroscience 2005, Program No. 458.8.
- Santhakumar, V., Aradi, I. and Soltesz, I. (2005). Role of mossy fiber sprouting and mossy cell loss in hyperexcitability: a network model of the dentate gyrus incorporating cell types and axonal topography. *J Neurophysiol* 93:437–453.
- Schaefer, A.T., Larkum, M.E., Sakmann, B. and Roth, A. (2003). Coincidence detection in pyramidal neurons is tuned by their dendritic branching pattern. *J Neurophysiol* 89:3143–3154.
- Schmitz, C. and Hof, P.R. (2005). Design-based stereology in neuroscience. *Neuroscience* 130:813–831.
- Scorcioni, R. and Ascoli, G.A. (2005). Algorithmic reconstruction of complete axonal arborizations in rat hippocampal neurons. *Neurocomputing* 65–66:15–22.
- Scorcioni, R., Boutiller, J.M. and Ascoli, G.A. (2002). A real scale model of the dentate gyrus based on single-cell reconstructions and 3D rendering of a brain atlas. *Neurocomputing* 44–46:629–634.
- Scorcioni, R., Lazarewicz, M.T. and Ascoli, G.A. (2004). Quantitative morphometry of hippocampal pyramidal cells: differences between anatomical classes and reconstructing laboratories. *J Comp Neurol* 473:177–193.
- Scoville, W.B. and Milner, B. J. (1957). Loss of recent memory after bilateral hippocampal lesions. *J Neurol Neurosurg Psychiatr* 20:11–21.
- Sestan, N., Artavanis-Tsakonas, S. and Rakic, Pasko. (1999). Contact-dependent inhibition of cortical neurite growth mediated by notch signaling. *Science* 286:741–746.
- Shepherd, G.M. (2004). Introduction to synaptic circuits. In: *The Synaptic Organization of The Brain*, 5<sup>th</sup> edn (G.M. Shepherd, Ed.). Oxford University Press, Oxford..
- Simmons, D.M. and Swanson, L.W. (1993). The Nissl stain. In: *Neuroscience protocols* (F.G. Wouterlood, Ed.), pp 1–7. Elsevier Press, Amsterdam.
- Somogyi, P. and Klausberger, T. (2005). Defined types of cortical interneurone structure space and spike timing in the hippocampus. *J Physiol* 562(1):9–26.
- Spacek, J. and Hartmann, M. (1983). Three-dimensional analysis of dendritic spines. I. Quantitative observations related to dendritic spine and synaptic morphology in cerebral and cerebellar cortices. *Anat Embryol* 167:289:310.
- Squire, L.R. and Zola-Morgan, S. (1991). The medial temporal lobe memory system. *Science* 253:1380–1386.

- Stepanyants, A. and Chklovskii, D.B. (2005). Neurogeometry and potential synaptic connectivity. *Trend Neurosci* 28:387–394.
- Stepanyants, A., Tamas, G. and Chklovskii, D.B. (2004). Class-specific features of neuronal wiring. *Neuron* 43:251–259.
- Sutula T. (2002). Seizure-induced axonal sprouting: assessing connections between injury, local circuits, and epileptogenesis. *Epilepsy Curr* 2:86–91.
- Tamamaki, N. and Nojyo, Y. (1990). Disposition of the slab-like modules formed by axon branches originating from single CA1 pyramidal neurons in the rat hippocampus. *J Comp Neurol* 291:509–519.
- Tamamaki, N. and Nojyo, Y. (1991). Crossing fiber arrays in the rat hippocampus as demonstrated by three-dimensional reconstruction. *J Comp Neurol* 303:435–442.
- Tamamaki, N., Abe, K. and Nojyo, Y. (1988). Three-dimensional analysis of the whole axonal arbors originating from single CA2 pyramidal neurons in the rat hippocampus with the aid of a computer graphic technique. *Brain Res* 452:255–272.
- Tinsley, C.J., Bennett, G.W., Mayhew, T.M. and Parker, T.L. (2001). Stereological analysis of regional brain volumes and neuron numbers in rats displaying a spontaneous hydrocephalic condition. *Exp Neurol* 168:88–95.
- Traub, R.D., Bibbig, A., Lebeau, F.E.N., Buhl, E.H. and Whittington, M.A. (2000). Cellular mechanisms of neuronal population oscillations in the hippocampus in vitro. *Ann Rev Neurosci* 27:247–278.
- Van Pelt, J., Van Ooyen, A. and Uylings, H.B. (2001). The need for integrating neuronal morphology databases and computational environments in exploring neuronal structure and function. *Anat Embryol* 204:255–265.
- Vetter, P., Roth, A. and Hausser, M. (2001). Propagation of action potentials in dendrites depends on dendritic morphology. *J Neurophysiol* 85:926–937.
- Watts, D.J. and Strogatz, S.H. (1998). Collective dynamics of ‘small-world’ networks. *Nature* 393:440–442.
- Witter, M.P. and Amaral, D.G. (2004) Hippocampal formation. In: *The rat nervous system*, 3rd edn (G. Paxinos, Ed.). Elsevier Academic Press, San Diego.
- Wittner, L., Eross, L., Czirjak, S., Halasz, P., Freund, T.F. and Magloczky, Z. (2005). Surviving CA1 pyramidal cells receive intact perisomatic inhibitory input in the human epileptic hippocampus. *Brain* 128:138–152.
- Wong, S., Gardner, A.B., Krieger, A.M. and Litt, B. (2007). A stochastic framework for evaluating seizure prediction algorithms using hidden markov models. *J Neurophysiol* 97:2525–2532.

This page intentionally left blank

PART

II

---

## EPILEPSY AND ALTERED NETWORK TOPOLOGY

---

This page intentionally left blank

# 7

---

## MODELING CIRCUIT ALTERATIONS IN EPILEPSY: A FOCUS ON MOSSY CELL LOSS AND MOSSY FIBER SPROUTING IN THE DENTATE GYRUS

---

VIJAYALAKSHMI SANTHAKUMAR

### ABSTRACT

Epilepsy is a disease characterized by changes that occur at various levels of the network from alterations in properties of single channels and neurons to structural reorganizations of circuits. While experimental biology has made immense progress in identifying the physiological and structural alterations in epileptic tissue, the specific effects of each pathological change and, more importantly, how these alterations act in concert to produce the emergent epileptic network behavior is still unclear. Although the presence of confounding potentially epileptogenic and compensatory changes that occur in parallel render an experimental approach impractical, a biologically motivated modeling approach is ideally suited to examine how the various alterations observed in epilepsy act both independently and in the context of coincident changes. Using the example of the dentate gyrus model developed to examine the effects of mossy fiber sprouting and hilar cell loss on the excitability and synchrony in dentate circuits, this chapter describes the general approach and considerations for developing large-scale models of neuronal circuits with an emphasis on biological realism. The novel insights into the development and progression of epilepsy revealed by simulation studies offer a compelling case for the use of data-driven simulations in understanding complex network diseases such as epilepsy. It is anticipated that network modeling methods will make it possible to test the circuit effects of specific therapeutic manipulations and allow for uniquely tailoring treatment to the distinct underlying cause of a seizure disorder.

### INTRODUCTION

Understanding a complex network phenomenon like epilepsy requires a conceptual framework that links the biophysical properties of individual neurons and the circuit where the disease manifests. Computational modeling provides a means to bridge these levels and is ideally suited to study dynamical diseases such as epilepsy. Temporal lobe epilepsy, a disease with a multitude of etiological factors, is characterized by abnormal circuit reorganizations in the dentate gyrus. The dentate gyrus is uniquely designed to gate seizure propagation in the limbic system (Heinemann et al., 1992; Lothman et al., 1992). The dentate gyrus possesses a compact distribution of the mossy fibers (Buckmaster and Dudek, 1999) and a strong feedforward and feedback perisomatic inhibition by basket cells. These characteristics provide the dentate network with the ability to regulate signaling between the entorhinal cortex and the hippocampus (Buzsaki and Eidelberg, 1983) and restrict the runaway spread of network activity. While the above features are retained in epileptic tissue, the most typical pathological change in temporal lobe epilepsy in humans and in seizure models is the loss of hilar mossy

cells and interneurons and sprouting of mossy fiber (granule cell axon) collaterals. Although the mossy fiber sprouting-related appearance of new recurrent excitatory feed-back loops is generally considered to be a plausible mechanism of hyperexcitability (Sutula et al., 1992; Coulter, 1999; Nadler, 2003), identifying its specific contribution to dentate excitability has been confounded by the presence of several cellular changes in biological systems. It has also been difficult to identify the role the compact, lamellar distribution of the sprouted recurrent mossy fibers, observed in animal models of spontaneous recurrent seizures (Buckmaster and Dudek, 1999; Buckmaster et al., 2002b), plays in the spread of granule cell excitability. For instance, it may be hypothesized that a less spatially restricted, extra-lamellar sprouting would be more conducive to the spread of seizure-like activity patterns. In addition to these two major questions regarding the hyperexcitability-enhancing roles of mossy fiber sprouting, another controversial issue concerns the relative importance of the loss and survival of mossy cells from the hilus following seizures and trauma (reviewed in Ratzliff et al., 2002). There is increasing physiological evidence for a role for mossy cells in spreading hyperexcitability through their long-range connections (Santhakumar et al., 2000; Scharfman et al., 2001). Implementation of large-scale models of the dentate gyrus allows for examining the net effect of these distinctive network alterations on the function of the dentate ‘gate’ independent of changes intrinsic, extracellular or ephaptic properties.

### HOW DETAILED DOES THE MODEL NEED TO BE?

The answer, of course, lies in the specific questions that the model seeks to answer. To examine the effects of loss of specific subgroups of cell types requires that the model capture the relative changes in cell densities, necessitating the development of large-scale models. The need to examine changes in connectivity due to loss of cells with distinctive somato-dendritic projection zones and unique intrinsic properties provides a compelling case for the use of biophysically realistic multicompartmental single cell models in the network. This chapter will provide an overview of the general approach and considerations for developing a large-scale model to study epileptogenesis with the focus on simulating the effects of mossy fiber sprouting and hilar cell loss in the dentate circuits. Where relevant, results of simulation studies will be presented to highlight the applicability of the technique and insights obtained based on such large-scale modeling approaches.

### SOFTWARE CONSIDERATIONS

Modeling the dentate circuitry entails the use of realistic compartmental representations of different classes of single neurons, cloning several copies of the neurons and making specific connections to form a network. The NEURON simulation package (<http://www.neuron.yale.edu/neuron/>) allows for development of detailed multicompartmental single cell models (Carnevale and Hines, 2006) and has the script language dedicated to the forming and tracking several network connections. An alternative, the GENESIS simulation package (<http://www.genesis-sim.org/GENESIS/>) has extensive functions focused on developing network simulations (Bower and Beeman, 1995). While the above software packages make large-scale modeling accessible to modelers and experimentalists alike, the pioneering work on large-scale modeling by Traub and coworkers utilizes custom FORTRAN code (Traub et al., 1992). A useful general review on methods in single cell and network modeling can be found in the book titled *Computational neuroscience – Realistic modeling for experimentalists* (De Schutter, 2000).

### UNDERSTANDING THE NETWORK TO BE MODELED

With over a million cells and minimally eight cell types in the dentate gyrus, the first step in designing the model is to determine anatomical structure of the dentate network. This can be approached by developing a connection matrix of the dentate gyrus (Patton and Mcnaughton, 1995; Dyhrfjeld-Johnsen et al., 2006), drawing on data from a single species when possible. This process itself entails several distinct steps that I will outline here and describe in detail below. As an initial step, eight types of dentate cells can be identified as anatomically well-described: granule cells, mossy cells, basket cells, axo-axonic cells, molecular layer cells with axonal projections to the perforant path (MOPP cells), hilar cells with axonal projections to the perforant path (HIPP cells), hilar cells with axonal projections to the commissural-associational pathway (HICAP cells) and interneuron-specific (IS) cells (Figure 7.1A) (Santhakumar and Soltesz, 2004). Next, the number of cells for each of these eight neuronal types can be estimated from published data (Table 7.1). The third step in assembling

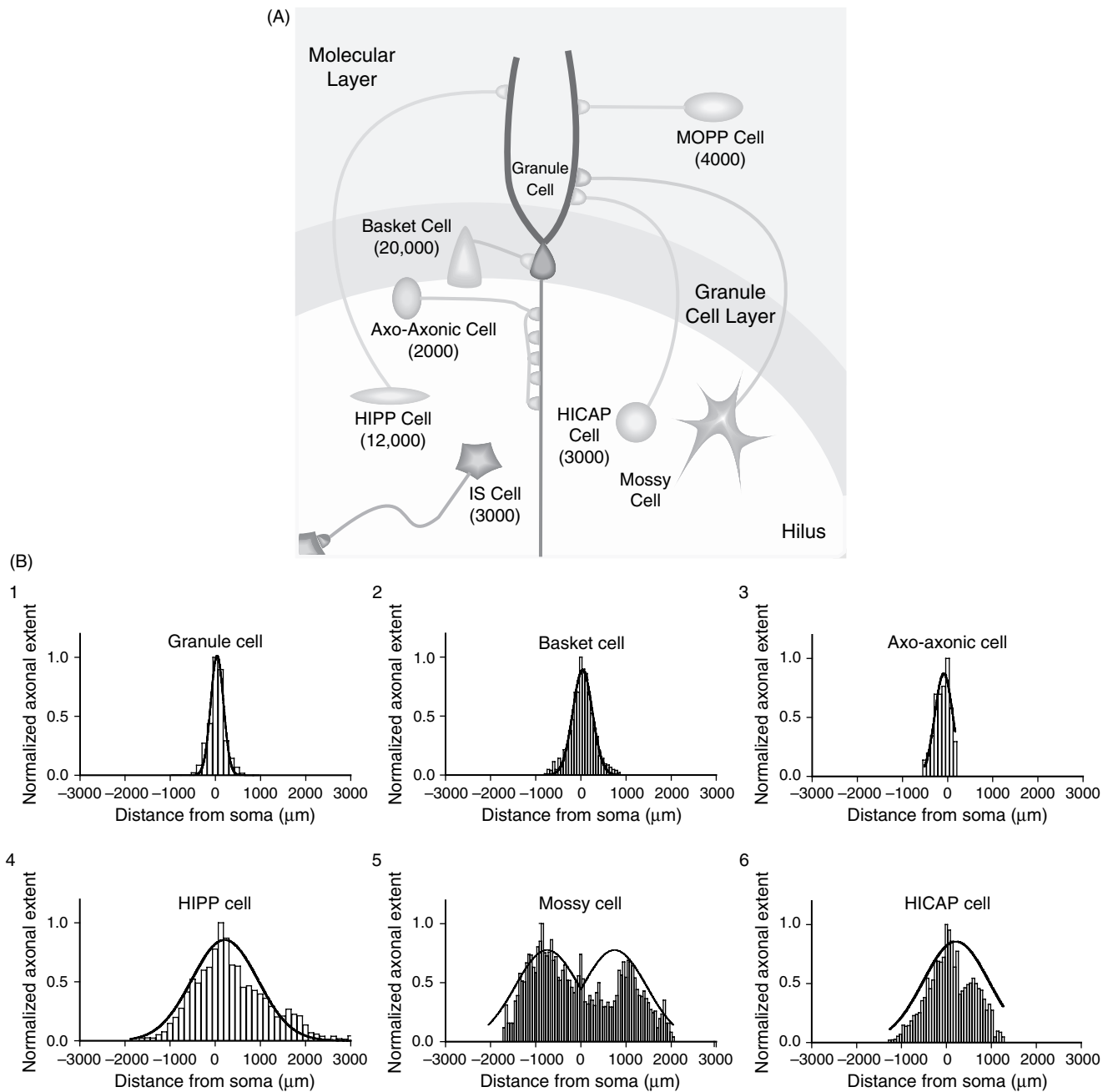


**FIGURE 7.1** Schematic of the basic circuitry and axonal distributions of the cell types in the dentate gyrus. (A) Illustration of the network connections between the eight major cell types of the dentate gyrus. The schematic shows the characteristic location of the various cell types within the three layers of the dentate gyrus. Adapted from Santhakumar and Soltesz (2004) with permission. (B) (1) Plot shows the averaged axonal distribution of 13 granule cells (Buckmaster and Dudek, 1999) and the corresponding Gaussian fit. (2) Fit to the septo-temporal distribution of axonal lengths of a filled and reconstructed basket cell (Sik et al., 1997). (3) Fit to the axonal distribution of a CA1 axo-axonic cell (Li et al., 1992). (4) Gaussian fit to the averaged axonal distributions of 3 HIPP cells from gerbil (Buckmaster et al., 2002a). (5) Fit to averaged axonal distributions of 3 mossy cells illustrates the characteristic bimodal pattern of distribution (Buckmaster et al., 1996). (6) Histogram of the axonal lengths of a HICAP cell along the long axis of the dentate gyrus (Sik et al., 1997) and the Gaussian fit to the distribution. All distributions were based on axonal reconstruction of cells filled *in vivo*. In all plots, the septal end of the dentate gyrus is on the left (indicated by negative coordinates) and the soma is located at zero. Adapted with permission from Dyrhøj-Johnsen et al. (2006).

**TABLE 7.1** Estimation of cell counts in the dentate gyrus. The table illustrates the considerations and procedures adopted to estimate the numbers of the various dentate cell types (NOS: Nitric oxide synthase; SS: Somatostatin; CR: Calretinin; NPY: Neuropeptide Y)

Layer	Cell type	Number	Estimation/reference	
<b>Molecular layer interneurons</b>	MOPP cell	4000	Buckmaster and Jongen-Relo (1999) estimated ~10 000 GAD-positive cells in molecular layer which includes MOPP cells, and projection cells such as OLM cells and aspiny calretinin positive cells (Ceranik et al., 1997). MOPP cells present only in inner molecular layer (Han et al., 1993). If the density of cells in the molecular layer is ~ uniform then ~3333 in each layer therefore estimated 4000 MOPP cells	
	Others: diverse group including OML cells, aspiny CR positive cells	~6000		
<b>Granule cell layer and hilar border</b>	Granule cells	1 000 000	Chauvet and Berger (2002) from Gaarskjaer (1978); Boss et al. (1985); West (1990); Patton and McNaughton (1995); Freund and Buzsaki (1996)	
<b>Hilus</b>	<b>Interneurons</b>	Basket cells	10 000	There are over 10 000 basket cells which constitute about 2% of GCL (Babb et al., 1988; Woodson et al., 1989)
		Axo-axonic cell	2000	In the CA1 region of the rat hippocampus, the ratio of pyramidal cells to axo-axonic cells (AAC) is estimated to be 200–600:1 (Li et al., 1992), whereas the ratio of granule cells to axo-axonic cells in the dentate is estimated to be in the higher end of this range (Patton and McNaughton, 1995). Assuming a GC:AAC ratio of 500:1, we estimated the number of axo-axonic cells to be 2000
	Mossy cells		30 000	Buckmaster and Jongen-Relo (1999) estimated the total number of GAD-mRNA positive neurons in the molecular layer of the dentate gyrus to be ~10 000
	<b>Interneurons (~20 000) GAD positive hilar cells (Buckmaster and Jongen-Relo, 1999)</b>	HIPP cell	12 000	HIPP cells are thought to be identical to the somatostatin positive interneurons in the dentate hilus (Freund and Buzsaki, 1996; Katona et al., 1999). Buckmaster and Jongen-Relo (1999) estimated that 12 000 somatostatin positive neurons in the hilus, we included 12 000 HIPP cells in the dentate network
		HICAP cell	4000	These cells are thought to be NOS positive (Freund and Buzsaki, 1996). There are about 7000 NOS cells in the hilus (estimated from Nomura et al., 1997a, 1997b). They also estimated that 50% of the NOS neurons were labeled singly (i.e. not double labeled for SS/NPY or CR) ~3500 cells. There was some overlap with CR and SS. Giving a conservative estimate of 4000 cells
		IS cell	3000	There are an estimated 6500 CR pos cells in the hilus (Nomura et al., 1997a, 1997b) ~30% of which are SS positive. Assuming about 50% of the hilar CR cells are aspiny IS cells gives an estimate of ~3000

the database is estimation of the connectivity matrix. This matrix quantifies how many postsynaptic cells among each of the eight cell types a single presynaptic neuron of a given type innervates (e.g. from the second row, second column in Table 7.2: a single mossy cell innervates about 32 500 granule cells; mean and ranges are indicated). As a final step, spatial constraints in connectivity need to be considered. For each cell type, the extent of the axons of single cells along the septo-temporal axis of the dentate gyrus can be determined from *in vivo* single cell fills published in the literature (Figure 7.1B).

TABLE 7.2 Connectivity matrix of the dentate gyrus

	Granule cells	Mossy cells	Basket cells	Axo-axonic cells	MOPP cells	HIPP cells	HICAP cells	IS cells
<b>Granule cells</b>	<b>X</b>	<b>9.5</b>	<b>15</b>	<b>3</b>	<b>X</b>	<b>110</b>	<b>40</b>	<b>20</b>
	X	7–12	10–20	1–5	X	100–120	30–50	10–30
<b>Mossy cells</b>	<b>32 500</b>	<b>350</b>	<b>7.5</b>	<b>7.5</b>	<b>5</b>	<b>600</b>	<b>200</b>	<b>X</b>
	30 000–35 000	200–500	5–10	5–10	5	600	200	X
<b>Basket cells</b>	<b>1250</b>	<b>75</b>	<b>35</b>	<b>X</b>	<b>X</b>	<b>0.5</b>	<b>X</b>	<b>X</b>
	1000–1500	50–100	20–50	X	X	0–1	X	X
<b>Axo-axonic cells</b>	<b>3000</b>	<b>150</b>	<b>X</b>	<b>X</b>	<b>X</b>	<b>X</b>	<b>X</b>	<b>X</b>
	2000–4000	100–200	X	X	X	X	X	X
<b>MOPP cells</b>	<b>7500</b>	<b>X</b>	<b>40</b>	<b>1.5</b>	<b>7.5</b>	<b>X</b>	<b>7.5</b>	<b>X</b>
	5000–10 000	X	30–50	1–2	5–10	X	5–10	X
<b>HIPP cells</b>	<b>1550</b>	<b>35</b>	<b>450</b>	<b>30</b>	<b>15</b>	<b>X</b>	<b>15</b>	<b>X</b>
	1500–1600	20–50	400–500	20–40	10–20	X	10–20	X
<b>HICAP cells</b>	<b>700</b>	<b>35</b>	<b>175</b>	<b>X</b>	<b>15</b>	<b>50</b>	<b>50</b>	<b>X</b>
	700	30–40	150–200	X	10–20	50	50	X
<b>IS cells</b>	<b>X</b>	<b>X</b>	<b>7.5</b>	<b>X</b>	<b>X</b>	<b>7.5</b>	<b>7.5</b>	<b>450</b>
	X	X	5–10	X	X	5–10	5–10	100–800

Connectivity values were estimated from published data for granule cells, mossy cells, basket cells, axo-axonic cells, molecular layer interneurons with axons in perforant-path termination zone (MOPP), hilar interneurons with axons in perforant-path termination zone (HIPP), hilar interneurons with axons in the commissural/associational pathway termination zone (HICAP) and interneuron selective cells (IS) as described in the text. Connectivity is given as number of connections to a postsynaptic population (row 1) from a single presynaptic neuron (column 1). The average number of connections is given in **bold**. The estimated range of connectivity is given below in the lower cell. Adapted with permission from Dyhrfjeld-Johnsen et al. (2006).

### DETERMINATION OF CELL TYPES

The cell types in the dentate gyrus can be classified based on a combination of several factors including:

1. the nature of the neurotransmitter released
2. location in the laminar structure of the dentate gyrus
3. morphological features such as shape of the soma and dendritic arbors and axonal distribution patterns
4. presence of specific markers such as calcium binding proteins and neuropeptides (for detailed description of the different cell types see Freund and Buzsaki, 1996).

Based on these criteria, the dentate gyrus contains two excitatory cell types, granule cells and mossy cells releasing the neurotransmitter ‘glutamate’ at their axonal terminals and a minimum of six inhibitory interneurons releasing gamma-aminobutyric acid (GABA) at their axon terminals (see Figure 7.1A).

### ESTIMATING CELL NUMBERS

A practical approach to determining the numbers of cells in each class is illustrated in Table 7.2. This involves identifying the cell layers and the total number of neurons in each region followed by estimating the numbers of various subtypes based on cell counts of neurons with specific markers (Buckmaster et al., 1996, 2002a; Nomura et al., 1997a, 1997b). The dentate gyrus is composed of three cell layers, the molecular layer, granule cell layer and the hilus (see Figure 7.1A). Granule cells (GC) are the primary projection cells of the dentate gyrus. These are densely packed small (diameter  $\sim 10\text{ }\mu\text{m}$ ) cells, typically located in the granule cell layer of the dentate gyrus. The number of granule cells in the dentate gyrus of the rat is estimated to be 1 000 000 (Gaarskjaer, 1978; Boss et al., 1985; West, 1990; Patton and Mcnaughton, 1995; Freund and Buzsaki, 1996). The next major cell type, the mossy cells, are excitatory cells located in the hilus and do not express the GABA synthetic enzyme GAD. Buckmaster and Jongen-Relo (1999) estimated the number of GAD-mRNA negative neurons in the dentate hilus (presumed mossy cells) to be 30 000. The GABAergic interneurons are located in all three layers of the dentate gyrus. The perisomatically projecting basket cells express either the calcium binding protein, parvalbumin

(PV) or the neuropeptide cholecystokinin (CCK). The remaining interneuronal subtypes include PV expressing axo-axonic cells that project axon terminals exclusively to the axon-initial-segment of excitatory cells, somatostatin positive HIPP cells (Freund and Buzsaki, 1996; Katona et al., 1999), HICAP cells that are thought to be NOS-positive (Freund and Buzsaki, 1996) and aspiny, calretinin positive hilar IS cells (Gulyas et al., 1996). As outlined in Table 7.1, one can estimate the number of GABAergic cell types of the granule cell hilar border and the hilus based on published histochemical data (Buckmaster et al., 1996, 2002a; Nomura et al., 1997a, 1997b). As for the molecular layer of the dentate gyrus, Buckmaster and Jongen-Relo (1999) estimated  $\sim 10\,000$  GABAergic interneurons in this region. Assuming an even distribution between inner, medial and outer molecular layers, there are 4000 MOPP cells, with somata located in the inner molecular layer (Han et al., 1993). Note that this estimate excludes the molecular layer interneurons with a majority of their postsynaptic targets outside the dentate gyrus, like the outer molecular layer interneurons projecting to the subiculum (Ceranik et al., 1997).

### ESTIMATION OF CONNECTIVITY

Within the last decade, large amounts of high-quality experimental data have become available on the connectivity of the rat dentate gyrus both in controls and after seizures. Such data are crucial in assembling the cell type-specific connectivity matrix for the dentate gyrus. The connectivity for each cell type, summarized in Table 7.2 and described below, is based on detailed survey of the literature on anatomical data on the convergence and divergence of various cell types. The assumption of uniform bouton density along the axon of the presynaptic cell, in agreement with the *in vivo* data in (Sik et al., 1997), greatly simplifies the estimation of connectivity from anatomical data on axonal length and synapse density per unit length of axon.

#### **Granule cell**

Mossy fibers (granule cell axons) in the healthy rat dentate gyrus are primarily restricted to the hilus (97%), with few collaterals (3%) in the granule cell layer (Buckmaster and Dudek, 1999). In addition to mossy cells (Acsady et al., 1998b), mossy fibers have also been shown to contact basket cells (Buckmaster and Schwartzkroin, 1994; Geiger et al., 1997) and PV-positive interneurons (Blasco-Ibanez et al., 2000). With a total of 400–500 synaptic contacts made by a single mossy fiber (Acsady et al., 1998b), the 3% of each axon located in the granule cell layer (Buckmaster and Dudek, 1999) is estimated to contact 15 basket cells and 3 axo-axonic cells. In the hilus, a single granule cell has been shown to project to 7–12 mossy cells forming large complex mossy fiber boutons (Acsady et al., 1998b), while an estimated 100–150 mossy fiber terminals target hilar interneurons with approximately one synapse per postsynaptic interneuron (Acsady et al., 1998b). Gulyas et al. (1992) estimated that a single spiny CR-positive cell (presumed HIPP cell) is contacted by about 9000 granule cells. With 12 000 HIPP cells and 1 000 000 GCs, each granule cell can be estimated to contact about 110 HIPP cells and 40 HICAP cells. Additionally, in agreement with the presence of mossy fiber terminals on aspiny calretinin positive interneurons (Acsady et al., 1998b), 15 mossy fiber synapses on to IS cells. Since mossy fibers avoid the molecular layer (Buckmaster and Dudek, 1999) in the healthy dentate gyrus, it is assumed that they do not contact MOPP cells. However, during sclerosis, sprouted mossy fibers have been shown to contact up to 500 postsynaptic granule cells (Buckmaster et al., 2002b), thus there may be an average of 50 to 500 connections from a single granule cell to other granule cells at maximal sclerosis.

#### **Mossy cells**

A single filled mossy cell axon has been reported to make 35 000 synapses in the inner molecular layer (Buckmaster et al., 1996; Wenzel et al., 1997). Assuming a single synapse per postsynaptic cell, a single mossy cell is estimated to contact 30 000–35 000 granule cells. Of the 2700 synapses made by a single mossy cell axon in the hilus, about 40% (approximately 1000 synapses) target GABA-negative neurons (Wenzel et al., 1997). As each mossy cell is estimated to make 1–5 synaptic contacts on a postsynaptic mossy cell (Buckmaster et al., 1996), it is estimated that each mossy cell contacts about 350 other mossy cells. The remaining 60% of the hilar mossy cell axons target GABA-positive cells (Buckmaster et al., 1996; Wenzel et al., 1997), with no reports supporting mossy cell targeting of IS cells. Assuming that there is no preferential target selectivity between HIPP and HICAP cells, and that each postsynaptic hilar interneuron receives two synaptic contacts from a single mossy cell axon (Buckmaster et al., 1996), each mossy cell is estimated to contact 600 HIPP and 200 HICAP cells. With very low mossy cell to interneuron connectivity in the inner molecular layer (Wenzel et al., 1997), mossy cells could contact 5–10 basket and axo-axonic cells and approximately 5 MOPP cells with somata in the inner molecular layer (Han et al., 1993).

### Basket cells

In the CA3 region of the rat hippocampus, each principal cell is contacted by about 200 basket cells (Halasy and Somogyi, 1993), whereas it is suggested a granule cell in the dentate is contacted by as few as 30 basket cells. Assuming that each of the 1 000 000 granule cells is contacted by 115 basket cells each making 1–20 synaptic connections (Halasy and Somogyi, 1993; Acsady et al., 2000), it can be estimated that each basket cell contacted about 1250 granule cells. Mossy cells receive 10–15 basket cell synapses (Acsady et al., 2000) leading to an estimate of 75 mossy cells contacted by a single basket cell. Approximately 1% of the 11 000 synapses made by a single basket cell axon in the granule cell layer of the dentate are onto other basket cells (Sik et al., 1997) with 3–7 synapses per postsynaptic cell (Bartos et al., 2001). Consequently, each basket cell in the dentate gyrus may be estimated to contact 35 other basket cells. Since hilar and molecular layer interneurons are not a major target of basket cells (Halasy and Somogyi, 1993), basket cell may contact 0–1 HIPP cells. Similarly, the basket cell synapses onto axo-axonic cells, HICAP and MOPP cells are assumed to be negligible. As PV-positive cells preferentially contact other PV-positive cells in the hilus (Acsady et al., 2000), it is assumed that basket cells do not contact the calretinin-positive IS cells (Gulyas et al., 1992).

### Axo-axonic cells

Most synapses made by axo-axonic cell axons are thought to target granule cell axon initial segments (Halasy and Somogyi, 1993), however, a small fraction of axon collaterals also descend into the superficial and deep hilus (Han et al., 1993; Freund and Buzsaki, 1996). In neocortex, an axo-axonic cell makes 4–10 synapses on the postsynaptic cells axon initial segment (Li et al., 1992). With 22 000 000 estimated axon initial segment synapses in the granule cell layer (Halasy and Somogyi, 1993) and assuming 4 synapses per postsynaptic cell (based on the data from the neocortex from Li et al., 1992), each of the 2000 axo-axonic cells are estimated to target about 3000 granule cells. Mossy cells receive axo-axonic cell inhibition (Ribak et al., 1985) and, with the comparatively small fraction of axons from axo-axonic cells in the hilus (Han et al., 1993; Freund and Buzsaki, 1996), it is estimated that axo-axonic cells targeted a number of mossy cells equal to about 5% of their granule cell targets, corresponding to 150 mossy cells. As axo-axonic cells primarily target the axon initial segment of non-GABAergic cells (Halasy and Somogyi, 1993; Freund and Buzsaki, 1996), it may be assumed that these cells do not project to interneurons.

### HIPP cells

HIPP cells have been estimated to contact about 1600 granule and 450 basket cells with 1–5 synapses per postsynaptic cell (Sik et al., 1997). Mossy cells can have one dendrite in the molecular layer (Buckmaster et al., 1996) which can be targeted by HIPP cell axons, whereas granule cells have two primary dendrites (Claiborne et al., 1990; Lubke et al., 1998). With the mossy cell population corresponding to 1/30 of the granule cell number, the mossy cell dendrites constitute a target for HIPP cells about 1/60 of that of granule cells. Increasing this fraction to about 1/45 to account for the presence of a few HIPP cell contacts on mossy cells in the hilus (Buckmaster et al., 2002a) suggests that each HIPP cell contacts about 35 mossy cells. HIPP cell axonal divergence onto HICAP and MOPP cells in the molecular layer can be assumed to be similar as found for somatostatin-positive cells in CA1 (Katona et al., 1999) and set to 15 connections to each population. The HIPP cell axonal divergence to axo-axonic cells is estimated to be between the divergence to basket and HICAP cells, therefore the HIPP cell axon likely contacts 30 axo-axonic cells.

### MOPP cells

MOPP cells target an estimated 7500 granule cells in the rat dentate gyrus. While MOPP cells have a horizontal axonal extent similar to HIPP cells, they show considerably less branching (Han et al., 1993), leading to estimate that they only contact half as many MOPP and HICAP cells as HIPP cells. As MOPP cell axons are restricted to the molecular layer (Han et al., 1993) and do not target the basal dendrites of basket cells, they were assumed to contact less than 1/10 the number of basket cells targeted by HIPP cells. Likewise, MOPP cells with axons restricted to the outer and middle molecular layers (Han et al., 1993) would not target the hilar dendrites of axo-axonic cells (Soriano et al., 1990) and the axo-axonic cells with somata and proximal dendrites in the hilus (Han et al., 1993), it is estimated that MOPP cells only contact 1–2 axo-axonic cells. As the MOPP cell axonal arbors in the molecular layer (Han et al., 1993) do not overlap with major parts of the dendritic arborizations of mossy cells (Frotscher et al., 1991), HIPP cells (Han et al., 1993; Sik et al., 1997; Katona et al., 1999) and IS cells (Gulyas et al., 1996), the connectivity to these cells can be deemed negligible.

### HICAP cell

Sik et al. (1997) estimated that the septo-temporal extent and bouton density of HICAP cell axons was similar to the HIPP cell axons, whereas the estimated axonal length of HICAP cells was approximately half of the HIPP cell axonal length. Thus, it is estimated that HICAP cells contacted about half the number of granule cells contacted by HIPP cells but, as the HICAP cells have an additional 3% of axon collaterals in the hilus (Sik et al., 1997), their number of postsynaptic mossy cells were assumed to be the same as that of the HIPP cells. HICAP cells were assumed to contact less than half the number of basket cells targeted by HIPP cells ( $\sim 175$ ) and a negligible number of axo-axonic cells. With a total of 26 000 from a single HICAP cell axon (Sik et al., 1997), approximately 700 synapses should be present in the hilus. Assuming 2–5 synapses per postsynaptic cell, each HICAP cell could contact 100–300 hilar cells. It can be assumed that each HICAP cell targets 50 HIPP and HICAP cells which, along with 35 synapses on mossy cells, is in the estimated range. Although the total axonal length of HICAP cells is only about half of that of HIPP cells, the number of MOPP cells targeted was assumed to be the same ( $\sim 10$ –20), as the HICAP cell axons primarily project to the inner molecular layer where both cell bodies and proximal dendrites of MOPP cells are located (Han et al., 1993).

### IS cells

IS cells contact an estimated 100–800 other IS cells and 5–10 (presumably CCK positive) basket cells (Gulyas et al., 1996). Acsady et al. (2000) suggested that CCK cells would include both BC and HICAP morphologies and that IS cells furthermore project to somatostatin-positive presumed HIPP cells. We therefore estimate that IS cells also project to 5–10 HICAP cells and HIPP cells.

## AXONAL DISTRIBUTIONS

Axonal reconstructions from cells filled *in vivo* and reconstructed are available in the literature for a number of cell types and can be used to determine the septo-temporal extent and shape of the distribution (Li et al., 1992; Buckmaster et al., 1996, 2002a; Sik et al., 1997; Buckmaster and Dudek, 1999). As illustrated in Figure 7.1B, it appears that most axonal arbors in the dentate gyrus conform to a Gaussian distribution with the maximum density centered in the same lamella as the location of their soma. The notable exception are the mossy cells that have the largest longitudinal span and a bimodal distribution with a decrease in axonal density close to the location of the soma (Buckmaster et al., 1996).

## DECIDING THE DETAILS OF THE MODEL NETWORK

### SOURCES OF NETWORK MODIFICATION

Since our aim is to generate a model that captures the principal network features of dentate sclerosis, let us now consider the changes to the healthy dentate that the model proposes to simulate. In terms of the structural reorganization of the neuronal networks during limbic epileptogenesis, the loss of hilar cells and the sprouting of mossy fibers are two key factors underlying the process of ‘end-folium’ (meaning the dentate gyrus) sclerosis (Margerison and Corsellis, 1966; Mathern et al., 1996). Although the biological process of sclerosis encompasses more than the loss of cells and sprouting of axons (e.g. it also entails gliosis), from the point of view of neuronal network reorganization in the dentate gyrus, the loss of hilar cells and the sprouting of mossy fibers are the two major factors. Therefore, the important changes in epileptic dentate circuits are, first, the loss of hilar cells entailed the loss of both the excitatory mossy cells and the inhibitory hilar interneurons (Buckmaster and Jongen-Relo, 1999). Second, progressive sprouting of recurrent mossy fiber collaterals innervating predominantly the granule cell proximal dendrites. Third, spatially restricted distribution of the mossy fiber sprouting from a single granule cell (i.e. both the control and the sprouted mossy fibers originating from a single granule cell are confined to a single hippocampal lamella, about 600  $\mu\text{m}$ ) (Buckmaster et al., 2002b).

### CELL TYPES TO INCLUDE

Next, let us consider the major players in the above changes. The granule cells are the primary output cells and are both the source and major target of sprouting and, for sure, form an essential part of the model. Mossy cells, the second most numerous cell type in the dentate also possess the widest axonal span and maximum number of connections (see Tables 7.1, 7.2 and Figure 7.1B). Loss of this excitatory cell type is likely to influence directly the excitability of the

network (Ratzliff et al., 2002). Interestingly, despite the controversy about the extent of mossy cell loss and its ultimate influences on dentate excitability, there is a general agreement that these are key players in the network (Ratzliff et al., 2004). Therefore, inclusion of mossy cells, in addition to being an essential component of the circuit and an important factor that changes in epilepsy, also gives us the opportunity to explore the controversial role of these cells during the progression of sclerosis.

The judgment on which of the six interneuronal subtypes to include in the model hinges on several factors. In the case of the dentate gyrus, the basket and HIPP cells together make up more than half the entire interneuronal population. Not surprisingly, these are the interneurons that have been most extensively characterized (Geiger et al., 1997; Lubke et al., 1998; Buckmaster et al., 2002a). Apart from the numerical dominance and availability of physiological data, a critical consideration is the major functional characteristics of the inhibition in the circuit and how it is altered in epilepsy. Inhibition can operate in two principal modes, feedforward inhibition where the interneuron is activated by the same afferent input as the excitatory neuron that it contacts. The basket cell is a classic example and the primary source of feedforward inhibition in the dentate gyrus (Kneisler and Dingledine, 1995a; Freund and Buzsaki, 1996). The second, feedback inhibition, is where interneurons are activated by the principal cells in the network which they in turn inhibit. The basket cells and HIPP cells are two of the key feedback inhibitory cells in the dentate (Kneisler and Dingledine, 1995a; Freund and Buzsaki, 1996; Buckmaster et al., 2002a). Another aspect of inhibition is the somato-dendritic region of the principal cell contacted by the interneuron. Perisomatic inhibition by basket cells is considered crucial in maintaining the low level of granule cell firing in response to activation of the afferent input (Kraushaar and Jonas, 2000). The HIPP cells, on the other hand, provide direct inhibition in the dendritic region where the afferent input terminates and are likely to influence granule cell activity by modulating integration of dendritic inputs. Indeed, the loss of dendritic inhibition with an essentially intact or increased somatic inhibition has been proposed to be particularly relevant to epileptogenesis (Cossart et al., 2001). Furthermore, basket cells characterize the interneurons that are resistant to cell death and HIPP cells are the prototypical interneuronal subtype that is vulnerable in epileptic tissue (Buckmaster et al., 2002a). These features make the basket and HIPP cells essential constituents of the dentate model.

The remaining four interneurons possess certain other unique features of inhibition. The MOPP cells operate by providing granule cells with feedforward dendritic inhibition (Halasy and Somogyi, 1993). The HICAP cells are feedback inhibitions of proximal dendritic region of granule cells, an important region where mossy cell axons terminate (Freund and Buzsaki, 1996). The axo-axonic cells provide synaptic GABAergic input at the axon initial segments of granule and mossy cells and could play powerful roles in modifying spike initiation (Freund and Buzsaki, 1996; Howard et al., 2005; Szabadics et al., 2006). The IS cells form a well connected network of interneurons that contact exclusively other interneurons and could modulate the overall excitability and synchrony of the network (Gulyas et al., 1996). However, detailed physiological data for the development of realistic models of MOPP, HICAP, axo-axonic and IS cells are not readily available. Therefore, in an approach that avoids errors of commission, one could choose to include only basket and HIPP cells in the network. However, this would make it essential to perform control simulations to examine whether augmenting inhibition, an attempt to compensate for the cell types excluded in the model, influences the overall outcome of the network simulations.

### MODEL NETWORK SIZE

Now we need to consider how many cells of each type must be included in the model. From the data on the cell numbers in the dentate gyrus, we know that GC:MC:BC:HIPP ratio is 1000:30:10:12. In agreement with these ratios, the Lytton et al. (1998) model that focused on the network effects of sprouting included 50 granule cells, 2 mossy cells and 2 interneurons. Using this relatively small network representation of the dentate, the study demonstrated that the effect of sprouting on enhancing network excitability was strongly limited by the intrinsic adaptation properties of granule cells. This model predicted that low levels of mossy fiber sprouting could lead to dentate hyperexcitability. However, a caveat is the highly interconnected nature of a small network and the high perforant path synaptic conductance used in the study that might facilitate abnormally synchronous activity in the network. When we consider modeling the effects of progressive cell loss in addition to sprouting, it becomes essential to include a larger number of hilar cells which proportionately increases the size of the model. Increasing the size of the Lytton (1998) model by 10-fold entails building 1:20 000 scale dentate with 500 granule cells, 15 mossy cells, 6 basket cells and 6 HIPP cells. This 500+ cell model can be readily simulated on a laptop and allows for manipulating hilar cell numbers and connectivity patterns (Santhakumar et al., 2005). With the increasing computational power of state of the art multiprocessor computers, the size of the model can be scaled up further to 1:200 scale model with 50 000 granule cells (Dyhrfjeld-Johnsen et al., 2006; Howard et al., 2006). While it is true that developing a model closer to the scale of the real network will avoid issues of synaptic strength and convergence scaling (discussed below), some degree of scaling down might be necessary to maintain computational feasibility of large-scale simulations.

## MULTICOMPARTMENTAL SINGLE CELL MODELS

Since our aim is to develop a network model that simulates dendritic and somatic inhibition by locating synaptic contacts on specific dendritic compartments it becomes essential to develop multicompartmental, biophysically realistic models of individual cell types. The ModelDB (<http://senselab.med.yale.edu/senselab/modeldb/>) is a searchable resource of published model cells that can be readily adapted. Models of several cell types including dentate granule cell (Aradi and Holmes, 1999a; Santhakumar et al., 2005) are currently available at this site. The structure of the multicompartmental models of the other dentate cell types can be developed based on morphology of the cell types reported in the literature (Buckmaster et al., 1993, 2002b; Freund and Buzsaki, 1996; Geiger et al., 1997; Bartos et al., 2001). The axons may be modeled explicitly as a single sodium rich compartment (Manor et al., 1991) or implicitly, such that when the membrane potential of the presynaptic cell crossed a preset threshold the target synapse is activated after a period equivalent to the synaptic delay (Bartos et al., 2001).

## APPROACHES TO MODEL FITTING AND PARAMETER SEARCH

The intrinsic properties of cell types can be modeled based on data from whole cell physiological experiments obtained in the presence of blockers of synaptic activity (Lubke et al., 1998). Detailed description of how to model passive and active properties of individual cells can be found in specialized sources including *The NEURON Book* (Carnevale and Hines, 2006) and *Computational Neuroscience – Realistic modeling for experimentalists* (De Schutter, 2000). Generally speaking, the key issue is to develop a single cell model that can reproduce the experimentally generated current and voltage changes observed in the neuron. Since the experimental data on the actual densities, distributions and channel parameters are not readily available, the modelers turn to various methods to search for the ‘optimal set of parameters’ that generate the best ‘fit’ to the experimental data. In most cases, this is done by the trial-and-error method where the fitness is assessed by eye. To make the fit-by-eye method more effective, it is useful to identify the parameters that have the maximum impact on model fitness. Recently, it has been proposed that *sensitivity analysis*, a financial risk analysis technique that evaluates the degree to which a small changes in parameter value affects model fitness results, can be used to identify the parameters that are crucial to model behavior (Ambros-Ingerson et al., 2006).

The availability of fast computing techniques has lead to an increasing interest in the use of sophisticated automated parameter search methods for neuronal modeling. Of the several automated parameter-search methods, comparative studies have shown that techniques based on *simulated annealing* methods are most effective for models with relatively few parameters and *genetic algorithms* are equally effective for models with a large number of parameters (Vanier and Bower, 1999). *Simulated annealing*, a process based on the principles of thermodynamics, is a probabilistic algorithm for locating a good approximation to the global optimum of a given function in a large search space. It is based on the idea that heating a metal facilitates atoms to get unstuck from their initial position and, when followed by slow cooling, it gives a better chance of finding a minimal energy optimum. Similarly, simulated annealing algorithms replace the current solution by a random ‘nearby’ solution, chosen with a probability that depends on the difference between the function values and on a global parameter  $T$ , analogous to *temperature* in metallurgy, that is gradually decreased during the process. The alternative is the use of a *genetic algorithm*, a popular type of *evolutionary algorithm* which is an automated search strategy inspired by evolutionary processes such as inheritance, mutation, selection and recombination. As in evolution, the process usually starts with a randomly generated set of parameter vectors and progresses in generations. In each generation, the fitness of each vector in the population is evaluated, multiple vectors are stochastically selected from the current population (based on their fitness), and modified (mutated or recombined) to form a new population. The new population vectors are then used in the next iteration of the algorithm. Although this process requires several model evaluation steps and long computational time, it has been shown to be effective for large models (Vanier and Bower, 1999; Keren et al., 2005). Some automated parameter search tools are available for use with the GENESIS simulation package and offer an alternative to the traditional fit-by-eye methods.

## SPECIFIC CONSIDERATIONS IN MODELING THE DENTATE CELLS

Getting back to the specific issue in modeling of the dentate cell types, granule cells (Desmond and Levy, 1985) and mossy cells (Amaral, 1978) are characteristically rich in dendritic spines and this makes it necessary that the membrane area contribution of dendritic spines be accounted for (Rall et al., 1992). Briefly, correction for the membrane contribution of spines can be performed by decreasing membrane resistivity (increasing leak conductance) and increasing the capacitance

(Aradi and Holmes, 1999b). An additional consideration is the presence of spontaneous activity in some cells such as the mossy cells (Ishizuka et al., 1995; Ratzliff et al., 2004), and their lower input resistance as a consequence of the background synaptic activity (Lubke et al., 1998; Ratzliff et al., 2004) could influence the role of these cells in the network and must be included. The synaptic background activity can be simulated as a fluctuating point conductance with balanced excitation and inhibition, as described by Destexhe et al. (2001). As illustrated in Figure 7.2B, synaptic background activity and a constant current injection can be included to simulate spontaneous firing rate of mossy cells (Santhakumar et al., 2005). As shown in Table 7.3 and illustrated in Figure 7.2A, it is useful to draw direct comparisons between specific

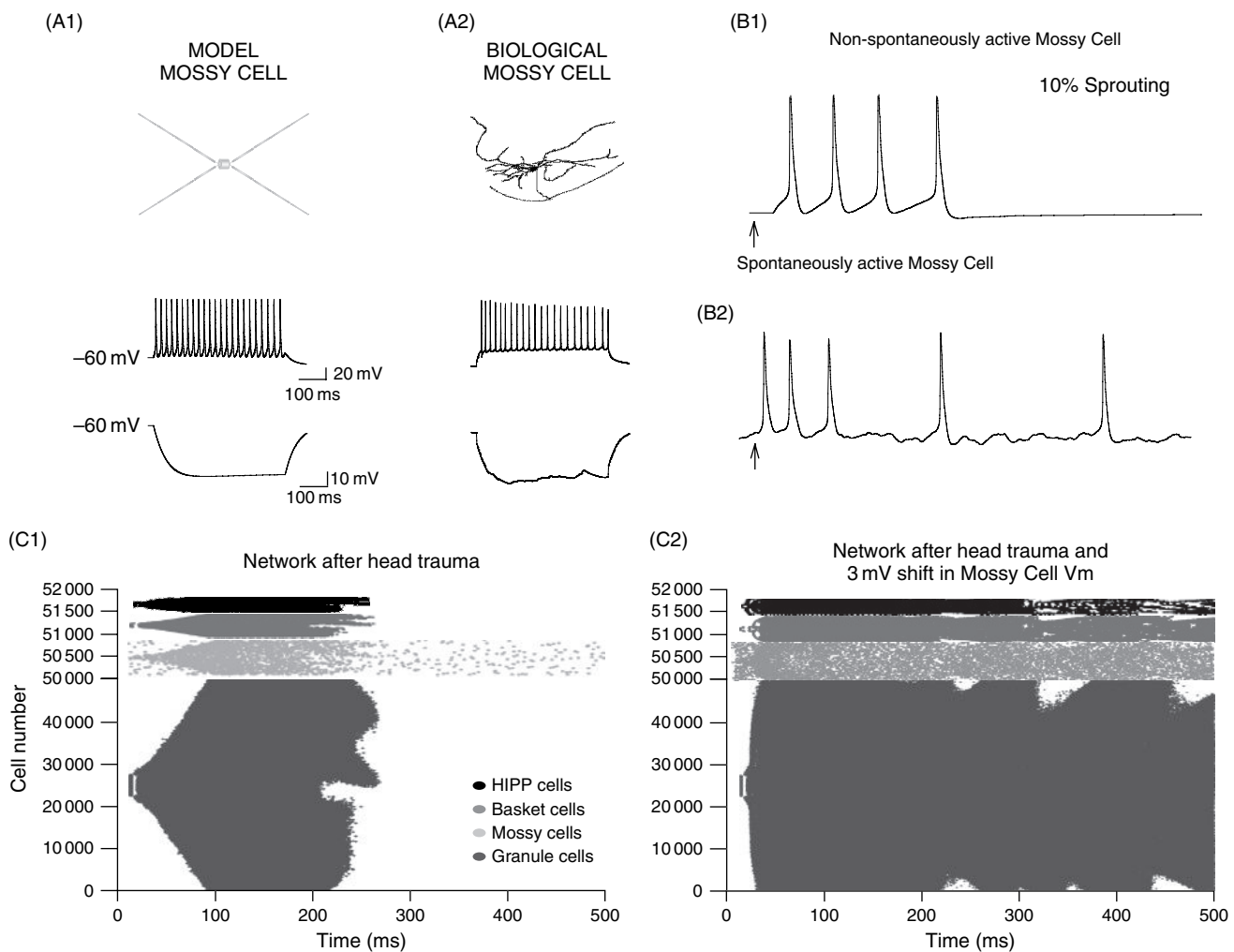


**FIGURE 7.2** Modeling mossy cells and their role in network excitability. (A1) Illustration of the structure of the model mossy cell (top) and membrane voltage responses to  $+360\text{ pA}$  (middle) and  $-200\text{ pA}$  (bottom) current injections. Adapted with permission from (Santhakumar et al., 2005). (A2) Camera lucida drawing of a biocytin filled mossy cell (Santhakumar et al., 2000) and membrane voltage responses to  $+360\text{ pA}$  (middle) and  $-200\text{ pA}$  (bottom) current injections in a biological mossy cell for comparison. (B1, B2) Representative membrane voltage traces from non-spontaneously active (B1) and spontaneously active (B2) model mossy cells in response to perforant path stimulation (arrow) of in networks with 500+ cells and low (10%) levels of mossy fiber sprouting. Note the membrane potential fluctuations and decrease in evoked response in the spontaneously active mossy cell in B2. Adapted with permission from Santhakumar et al. (2005). (C1, C2) Spike raster plots illustrating effect of changes in mossy cell intrinsic properties on the dentate network simulating the moderate sprouting and hilar cell loss after experimental head trauma. Dentate network activity is plotted as time versus cell number in a 50 000+ cell network, in response to a single simulated perforant path stimulation at  $t = 5\text{ ms}$ . Each dot represents an action potential in one cell. Note that the scale for granule cell numbers is smaller than that for other cells. (C1) Activity in the network after head trauma, which was derived from a 'healthy' control network with the addition of biologically realistic levels of mossy fiber sprouting and hilar cell loss. The network incorporated the spontaneously active model of mossy cells illustrated in B2. (C2) Network hyperexcitability increased when mossy cell resting membrane potential was depolarized by  $3\text{ mV}$ . Note the increase in spontaneous activity of mossy cells with the modest  $3\text{ mV}$  membrane depolarization. Adapted with permission from Howard et al. (2006).

TABLE 7.3 Physiological properties of individual cell types

Physiological property	Granule cell		Mossy cell		Basket cell		HIPP cell	
	Model	Biol.	Model	Biol.	Model	Biol.	Model	Biol.
RMP (mV)	-70.4	-75±2	-60	-59.7±4.9	-60	-56–66	-70	-65±6
R <sub>in</sub> (MΩ)	183	107–228	210	199±19	64.7	56±9	350	371±47
τ <sub>memb</sub> (ms)	30	31±2	54	24–52	8	9–11	17.6	16.9±1.8
AP amp. (mV)	80	86.6±0.7	88	89.8±1.1	78	~74	90	~83
AP threshold (mV)	-48.70	-49±0.8	-52	-47.33±1.45	-49	-40.5±2.5 < -52	-50	-50
Fast AHP (mV)	-7.91	-22.5 – -3.4	-12.2	-15.5	-23.39	-24.9 to -14.9	-18.5	-20 – -7
Spike frequency adaptation	0.31	0.3	0.86	0.8	0.97	0.98	0.8	0.82±0.42
Sag ratio	1	0.97±0.01	0.97	0.81±0.02	1	0.9–1	0.83	0.78–0.86
Source of biological cell parameters	Staley, et al., 1992; Lubke et al., 1998; Santhakumar et al., 2000	Lubke et al., 1998; Santhakumar et al. 2000; Ratzliff et al. 2004			Geiger et al., 1997; Mott et al., 1997; Lubke et al., 1998; Bartos et al., 2001; Harney and Jones, 2002		Mott et al., 1997; Lubke et al., 1998	

The table provides a detailed comparison of the passive and active properties of the four dentate cell type models to the corresponding parameters from biological cells obtained during whole cell recordings. Amplitude of the fast afterhyperpolarization (Fast AHP) was measured relative to the action potential threshold and sag ratio quantified by the ratio of the steady state voltage to the peak voltage in response to current injections of -50 to -300 pA (Lubke et al., 1998). Spike frequency adaptation was measured as the ratio between the inter spike intervals of the last 2 and the first two spikes. Adapted with permission from Santhakumar et al. (2005).

characteristic intrinsic properties of the model cells and their biological counterparts. Developing network models with biophysically realistic mossy cells has made it possible to predict how specific changes in intrinsic parameters of a single cell types can modify overall excitability of the circuit. Recently, Howard et al (2006) used this strategy to demonstrate that a modest 3 mV depolarization in the resting membrane potential of mossy cells after experimental head trauma could result in a marked increase in network excitability (Figure 7.2C).

## WIRING UP THE HEALTHY DENTATE NETWORK

### RECEPTORS AND SYNAPSES

The first step in connecting the network is to decide the neurotransmitter-receptor types that must be included in the network. To examine the effects of interneuronal loss and sprouting, the minimal requirement is to incorporate ionotropic glutamatergic AMPA ( $\alpha$ -amino-3-hydroxy-5-methyl-4-isoxazolepropionic acid) synapses and GABA<sub>A</sub> synapses. With increasing availability of data in the normal and epileptic dentate tissue it will become possible to include NMDA (N-methyl-D-aspartate) receptors and metabotropic receptors. Further information regarding the nature of short-term plasticity at individual synapses and how they change during epilepsy would make an interesting addition to the model. However, the basic circuit effects of sprouting and cell loss can be simulated by including AMPA and GABA<sub>A</sub> synapses.

Postsynaptic conductances can be represented as a sum of two exponentials (Bartos et al., 2001). The peak conductance ( $g_{max}$ ), rise and decay time constants and the synaptic delay (distinct from the axonal conduction delay below) for each pre-postsynaptic cell pair can be obtained from experimental data (Kneisler and Dingledine, 1995b; Geiger et al., 1997; Bartos et al., 2001). Since the data for synaptic conductances are typically obtained by paired recording or unitary synaptic data from several different groups, care must be taken to account and correct for the temperature at which the recordings were performed. Synaptic transmission can be implemented as a change in conductance in the postsynaptic cell when there is a spike in the presynaptic cell. The NEURON simulation software has the NetCon class of ‘synapse objects’ which changes the membrane conductance of the postsynaptic cell when a preset threshold is reached in the presynaptic cell. This process allows for the experimentally determined delay, maximal conductance and rise and decay kinetics to be directly used as synapse parameters. The approach on which the NetCon objects of NEURON are built permit essentially unlimited convergence and divergence in the network with a limited increase in computational effort making this an extremely effective tool for building large-scale models (Carnevale and Hines, 2006).

### NON-TOPOGRAPHIC NETWORK CONNECTIONS

The dentate gyrus of the rat is approximately 6 mm in septo-temporal extent (West et al., 1978) and has a distinct lamellar structure. In the biological situation, a hippocampal lamella is defined by the septo-temporal (longitudinal) extent of the mossy fibers (600  $\mu$ m) (Buckmaster and Dudek, 1997). In general, two types of networks must be constructed in order to be able to study the effects of axonal arborization patterns: non-topographic and topographic networks. In the non-topographic network, the postsynaptic targets of each cell are selected at random from the total pool of potential target neurons while maintaining only the cell type specific divergence and convergence. The axonal divergence of each cell type estimated from biological dentate gyrus will thus be scaled down in the 1:20 000 and 1:2000 model networks. The non-topographic networks are not constrained by the axonal arborization pattern of the individual cell types (e.g. the spatial distribution of a single mossy fiber in the biological hippocampus is restricted to a single hippocampal lamella). Their layout might be considered random or amorphous since their structure cannot be defined to be a linear or ring network.

### TOPOGRAPHIC NETWORK CONNECTIONS

The topographic network, on the other hand, incorporates the spatial distribution of the axonal arbors of the different cell types (both excitatory and inhibitory cells), in addition to their estimated divergence and convergence. Therefore, in addition to the mere existence of connections between two particular cell types (codified in Table 7.2), the probability of connections from one particular cell A to a given cell B also depends on the extent of the axonal arbor of cell A, and the relative distance between cells A and B. Hence, synapses from granule cells to mossy cells must conform to the compact lamellar distribution of mossy fibers (Buckmaster and Dudek, 1997; Acsady et al., 1998b). Similarly, synaptic contacts from mossy cells should be distributed in the bimodal pattern observed in experimental data from cells filled *in vivo*

(see Figure 7.1B5) (Buckmaster et al., 1996). The model mossy cells in the topographic network will have a low probability connecting to granule cells located in the lamella as their cell body, and preferentially contacting granule cells in adjacent lamellae on either side.

Ideally and especially in a large-scale (1:2000) model, the topographic dentate structure can be simulated as a linear strip that it is in reality. However, in a smaller 1:20 000 model a linear structure might lead to a significant *edge effect*. The *edge effects* in a small linear circuit result from the practical issue that neurons at either end of the network will send and receive fewer connections when the spatial restrictions of the axonal arbors are imposed. This will essentially decrease the contribution of a sizeable population of cells at either end of the network to the ongoing activity. Therefore, it might be worth considering distributing the neurons in a ring structure in the case of a significantly scaled down network model (Wang et al., 2004; Santhakumar et al., 2005). Each cell type, including the granule cells, mossy cells, basket cells and the HIPP cells, can be evenly distributed along the ring or linear structure. The cells can then be linked according to cell-type specific connection probabilities derived from the average number of projections from the pre- to the postsynaptic neuronal class in the literature (according to a scaled version of the connectivity matrix in Table 7.2). The cell type-specific connection probability needs to be further modified by a factor obtained by the normalized Gaussian fits to the experimentally determined axonal distributions of the presynaptic cells and the relative positions of the pre- and postsynaptic neurons in the graph. Target synapses can then be placed in the compartment corresponding to the location of synaptic contacts in filled and reconstructed axons (Buckmaster et al., 1996; Geiger et al., 1997; Sik et al., 1997; Acsady et al., 1998a).

### AFFERENT INPUT

The afferent, perforant path input to the network is located on the dendrites of all granule cells and the apical dendrites of all basket cells. Since 15% of mossy cells have been shown to receive direct perforant path input (Scharfman, 1991; Buckmaster et al., 1992), a direct perforant path input can be included to some mossy cells. Mass stimulation of the perforant path can be simulated by activating a maximum peak AMPA conductance in response to stimulation (Santhakumar et al., 2000). In the biological network and in physiological studies, it is unlikely that the entire network is activated simultaneously. Instead, one might expect focal activation of the perforant path input which can be simulated by activating the input to granule cells and basket cells located in a model hippocampal ‘lamella’.

An alternative method of simulating biologically realistic activity in the network model is to model the effect of spontaneous activity. While some cells such as the mossy cells have intrinsic firing that can be simulated (as discussed above), the *in vivo* activity in the granule cells can be simulated by uncorrelated activation of each granule cell by assigning individual perforant path inputs with Poisson distributed interspike intervals. This allows for studying the spontaneous emergence of foci of hyperexcitability and spread of network activity with the sprouting and cell loss in simulations of the epileptic dentate gyrus.

### MODEL EVALUATION

The reliability and predictive power of the network model can be evaluated by comparing the activity patterns in the individual cells and the network evoked by probe stimuli to the responses observed in experimental studies under similar simulation paradigms *in vivo* and *in vitro*. In the case of the dentate gyrus, there is a large body of data on the responses of the major cell types to mass stimulation of the perforant path input. In agreement with the recordings from granule cells *in vitro* (Fricke and Prince, 1984; Santhakumar et al., 2000), granule cells in the normal (non-sprouted) model dentate fire a single action potential in response to direct activation of the perforant path input both in the presence and absence of inhibition. The stimulation paradigm also evokes monosynaptic excitatory postsynaptic potentials (EPSPs), resulting in a single action potential in the directly activated mossy cells (Figure 7.3A) and polysynaptic EPSPs with or without firing in mossy cells postsynaptic to the stimulated granule cells. This response is consistent with experimental data demonstrating EPSPs or single action potentials in mossy cells after perforant path stimulation recorded in NMDA receptor antagonists (Scharfman, 1993). Similar to biological interneurons (Buckmaster et al., 2002a), dentate input activation also evokes long latency action potentials in HIPP cells, in contrast to the short latency burst firing in basket cells (Figure 7.3A). These simulations demonstrate convincingly that the model network can reproduce the normal (control) behavior of the various cell types in the dentate gyrus.

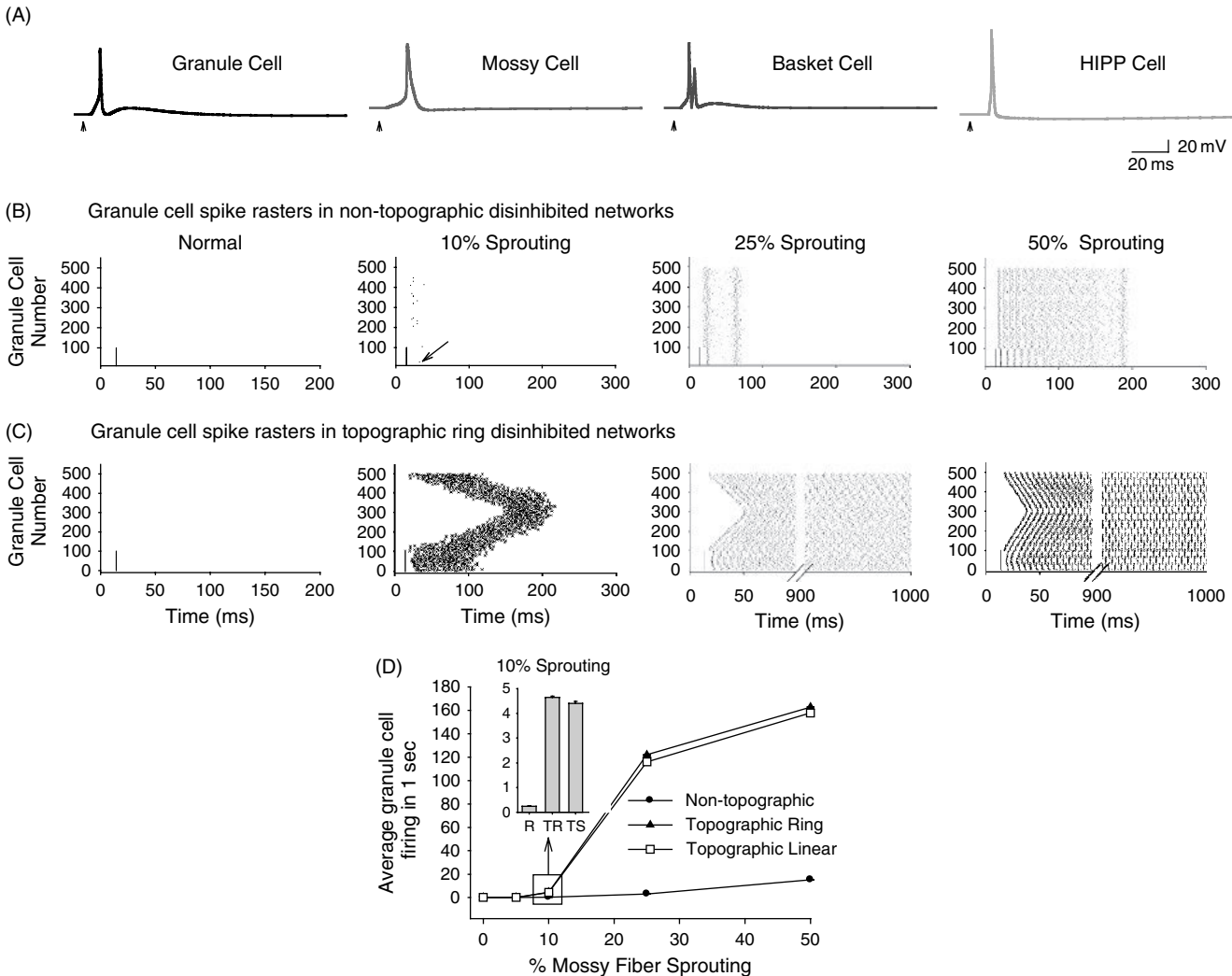


**FIGURE 7.3** Mossy fiber sprouting enhances excitability in the dentate excitatory network. (A) Example traces of the perforant path-evoked responses in the model cells. Arrowheads indicate the time of perforant path stimulation. The directly activated granule, mossy and basket cells have a short latency spike. The HIPP cell receiving polysynaptic excitation is activated at a longer latency. (B) Spike raster plots showing the activity of granule cells in the non-topographic networks in response to stimulation of the perforant path input to the network. The degree of mossy fiber sprouting was increased progressively from left to right. Arrow in the second panel points to a polysynaptic spike of a granule cell that fired more than one action potential in response to stimulation. (C) Granule cell spike rasters from topographic-ring networks illustrate the spread of perforant path-evoked activity with increasing mossy fiber sprouting. The activity from the directly stimulated granule cells (no.1–100) spreads to adjacent cells on either side of the ring resulting in a >-shaped spread of activity. (D) Summary plot showing the effect of sprouting on the average granule cell firing in the non-topographic network, topographic-ring network and topographic-linear network. Inset: histogram of the average granule cell firing in networks with 10% sprouting in the boxed region in (C) in non-topographic network (NT), topographic-ring (TR) network and topographic-strip (TS) network. In simulations in panels B–D, the GABA<sub>A</sub> conductances were set to zero in order to simulate a disinhibited network in the presence of GABA<sub>A</sub> receptor antagonists. Figures adapted with permission from Santhakumar et al. (2005).

#### SIMULATING MOSSY FIBER SPROUTING AND CELL LOSS

There are three important features that needed to be considered during the sprouting and hilar cell loss. First, the loss of hilar cells entails the loss of both the excitatory mossy cells and the inhibitory hilar interneurons. Second, the extent of mossy fiber sprouting from a single granule cell remains spatially restricted (i.e. both the control and the sprouted mossy fibers originating from a single granule cell are confined to a single hippocampal lamella, Buckmaster et al., 2002b). Third, cell loss and sprouting can be modeled as a progressive condition and implemented by considering the maximal hilar cell

loss (100%) as the state when all hilar cells are removed and maximum sprouting (100%) and the addition of the densest, anatomically quantified number of mossy fiber contacts reported in the literature (Buckmaster et al., 2002b). Since these salient changes occur together during sclerosis, we can simulate the progression of sclerosis as parallel increases in hilar cell loss and sprouting.

### MODELING MOSSY FIBER SPROUTING

Mossy fiber sprouting can be modeled by adding synaptic connections from granule cells to the proximal dendrites of granule cells. Experimental data from filled and reconstructed granule cells in the pilocarpine model of seizures, a model system with a particularly high density of mossy fiber sprouting (Nadler, 2003), indicate that 80–90% of the granule cells sprout approximately 500 new synapses in the inner molecular layer of the dentate gyrus (Buckmaster et al., 2002b). The peak conductance of the unitary sprouted synapse is expected to be  $\sim 0.5$  nS, consistent with the values estimated from unitary mossy fiber EPSCs in granule cells in the pilocarpine model of seizures (Molnar and Nadler, 1999). Hence, if we estimate that there are 400 new synapses with 0.5 nS peak conductance, this would result in a maximum sprouted synaptic input of 200 nS ( $g_{\max}$ ) in granule cells. In the case of the 1:20 000 scale model with 500 granule cells, adding several hundred sprouted synapses would result in an unrealistically highly interconnected network. This necessitates that the maximum number of sprouted contacts be decreased and the unitary synaptic conductance be increased by an equivalent factor in order to maintain the net granule cell conductance increase due to sprouting while avoiding a highly interconnected network. For instance, we could decide to decrease the convergence by a factor of fourfold and simultaneously increase the unitary conductance of the sprouted synapse to 2 nS (from 0.5 nS), a situation where the maximal sprouting would result in 100 new mossy fiber to granule synapses. Simulations conducted in a 1:20 000 scale model of the dentate (500+ cells) with systematically increasing the degrees of mossy fiber sprouting from 0% to 50% have shown that even 10% sprouting (simulating an addition of  $\sim 40$  recurrent mossy fiber contacts per granule cell as in our fourfold convergence scaling paradigm explained above) causes hyperexcitability in the dentate network (Santhakumar et al., 2005).

A caveat to the above strategy is that increasing the unitary conductance might simulate an unrealistically synchronous synaptic activity and this must be explicitly tested for. It is useful to compare the network activity between simulations with the experimentally determined unitary conductance of 0.5 nS and the predicted mossy fiber convergence to granule cells to simulations with the fourfold scaling, at low levels of sprouting to check for such effects (when high interconnectivity is not an issue, Santhakumar et al., 2005). In our example with a fourfold decrease in convergence, we could perform control simulations at 5% sprouting, each granule cell receiving 20 new granule cell inputs with 0.5 nS maximal conductance instead of 5 synapses with a maximum conductance of 2 nS. These simulations will help verify whether the increased unitary conductance of the sprouted synapse, assumed in order to avoid an artificially high degree of connectivity, alters the overall network behavior. Alternatively, the use of a large-scale model (e.g. the 1:20 000 scale dentate model with 50 000 granule cells, Dyhrfjeld-Johnsen et al., 2006; Howard et al., 2006) will allow for use of realistic numbers of sprouted connections.

While the preceding paragraphs focus on the quantitative aspect of representing the increase in conductance as a consequence of mossy fiber sprouting, we still need to address the spatially specific compact topography of the sprouted mossy fiber contacts. As introduced above, simulations with and without the lamellar topological constraints on sprouted contacts can be performed to assess the contribution of the tight, intra-lamellar distribution of sprouted mossy fibers *in vivo* (Buckmaster et al., 2002b) to network excitability. Developing non-topographic and topographic network models gives us the opportunity to explore certain interesting questions regarding the structural organization of the dentate gyrus and mossy fiber sprouting that cannot be directly addressed by experimental biology.

### Does the structural organization of the dentate gyrus impact the spread of activity from a focus of increased excitability?

Simulations comparing non-topographic and topographic dentate networks with sprouting (i.e. identical changes in granule cell conductance due to sprouting) show that inclusion of the tight topological constraints for the dentate network and sprouted mossy fibers (observed in biology) augments the excitability and spread of focal network activity in both the ring and linear dentate representations (Figure 7.3B–D). These results demonstrate that the lamellar organization and connectivity patterns of the dentate allows for robust spread of activity in the presence of sprouting.

### So, does the compact distribution of the sprouted mossy fibers promote or restrict the spread of network activity following focal excitation?

Modeling studies have examined the effects of systematically increasing the spread of a fixed number of sprouted contacts and demonstrated that the spatially restricted, intra-lamellar distribution of the sprouted mossy fibers (Buckmaster and Dudek, 1999) may play a central role in the induction and spread of hyperexcitability, especially when the levels of sprouting is mild (Santhakumar et al., 2005).

### How does the distribution of sprouted mossy fibers modify the spread of focally evoked excitability?

Although increasing the spatial spread of mossy fiber sprouting is expected to aid in the propagation of the activity beyond the initial focus, it is also likely to reduce the convergence of active inputs on neighboring granule cells and thus decrease the ability of the network to sustain firing. Simulations show that the interaction of these two opposing factors (i.e. the broader spatial spread of the sprouted mossy fibers aiding propagation of the activity beyond the initial focus but simultaneously decreasing the convergence of the excitatory mossy fiber inputs important for sustaining the activity) aids in the propagation of a small focus of network activity in the presence of a compact distribution of sprouted axons, especially if the degree of mossy fiber sprouting is mild. If the spatial spread of sprouting is too wide, too few cells are likely to be recruited outside the initial focus to sustain the network activity (Santhakumar et al., 2005). However, when the number of stimulated granule cells is increased, a wider mossy fiber sprouting distribution becomes the most conducive to maximal granule cell firing. Moreover, when the density of sprouting increases, even a small initial focus of activity will be sufficient to generate the initial critical level of focal activity and the spatial features of sprouted mossy fibers have little effect on network activity. Indeed, these results suggest that the compact distribution of sprouting augments excitability at the early stages of sprouting and might play a role in evolution of hyperexcitability in the dentate gyrus.

### SIMULATING THE LOSS OF HILAR MOSSY CELLS AND INTERNEURONS

There is general agreement that cells in the dentate hilus are lost in epilepsy and in animal models of seizure disorders. There is evidence that the loss of the various cell populations in the hilus occurs to a similar degree without preferential loss of a specific subpopulation of cells (Toth et al., 1997; Ratzliff et al., 2002). Therefore, the progression of cell loss can be simulated as a parallel loss of all hilar interneuronal classes. In practice, the loss of mossy cells and hilar interneurons can be simulated by removing all synaptic contacts to and from the ‘dead’ cells. In a spatially organized (topographic) model, it is crucial to simulate the network with its full (control) complement of cells and select the cells destined to ‘die’ at random. Alternatively, random assignment of the ‘surviving’ cells to the various lamellae instead of the above randomized deletion process will help avoid erroneous results as a consequence of all the cell loss being simulated at one pole of the lamellar structure.

The role of progressive loss of mossy cells has been examined in simulation studies. Modeling data have demonstrated that mossy cells participate in the spread of evoked network activity and likely aided in the propagation of firing in networks with mossy fiber sprouting. Systematically deleting mossy cells, at low levels (10%) of mossy fiber sprouting, decreases both the average granule cell firing and the number of granule cells involved in the network activity (Figure 7.4). Complete mossy cell loss results in a further decrease in the spread of activity in the network (Figure 7.4). These results are in agreement with experimental data showing that deletion of mossy cells decreases granule cell activity (Santhakumar et al., 2000; Ratzliff et al., 2004). However, when the degree of mossy fiber sprouting is increased, mossy cell loss appeared to cause little change in the average firing and spread of network activity (Figure 7.4). The simulations show that mossy cell loss is less effective at decreasing excitability when the degree of mossy fiber sprouting increases, presumably because once the degree of sprouting reaches a certain level, the seizure-like activity can sustain itself and propagate through the sprouted mossy fibers even in the absence of mossy cells.

Simulations also demonstrate that removal of mossy cells decreases granule cell excitability and impedes the propagation of network hyperexcitability (Santhakumar et al., 2005), indicating that surviving mossy cells amplify dentate excitability even without changes in intrinsic or synaptic properties (Ratzliff et al., 2002). However, these results contradicted the predictions of the ‘dormant basket cell’ hypothesis (Sloviter, 1991; Sloviter et al., 2003), according to which mossy cell loss should lead to a hyperexcitable response as a consequence of basket cell disinhibition due to the loss of excitatory inputs from mossy cells. Here, too, network simulations have been used to examine if removal of mossy cell excitation to basket cells could enhance dentate excitability. Under conditions of maximized mossy cell excitation of basket cells, implemented by increasing the mossy cell to basket cell synaptic conductance up to 20 times the unitary conductance, simulations in which mossy cells were deleted decreased granule cell activity (Figure 7.4D, Santhakumar et al., 2005).

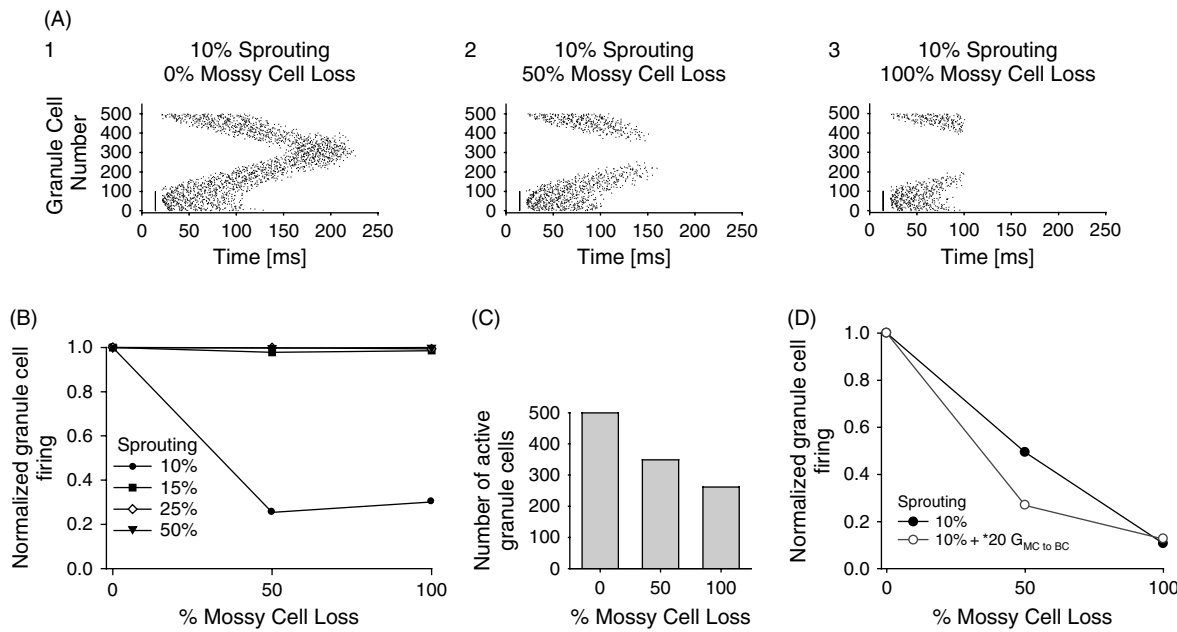


**FIGURE 7.4** Effect of mossy cell loss on dentate excitability. (A1–3) Granule cell spike-time raster evoked by stimulation of 100 granule cells in dentate gyrus under conditions of mild (10%) sprouting without inhibition. Networks were simulated with 0% (A1), 50% (A2) and 100% (A3) mossy cell loss. (B) Summary plots of the granule cell activity with varying degrees of mossy cell loss and sprouting. The plot illustrates the decrease in network excitability with mossy cell loss at low levels of sprouting. Mossy cell loss has minimal impact on network excitability when sprouting increases. Since the network activity increased with the degree of mossy fiber sprouting, the granule cell activity in each plot was normalized to the firing without mossy cell loss. (C) Summary histogram of the effect of mossy cell loss on the number of granule cells activated by stimulation of the perforant path input to one model lamella in networks with 10% mossy fiber sprouting (simulations illustrated in A). In simulations in panels A–C, the GABA<sub>A</sub> conductances were set to zero in order to simulate the isolated excitatory dentate circuit in the presence of GABA<sub>A</sub> receptor antagonists. (D) Effect of mossy cell loss on the perforant path-evoked granule cell activity in networks incorporating basket and HIPP cell inhibition and 10% mossy fiber sprouting. The \*20G<sub>MC to BC</sub> plot represents summary data from network simulations with 20 times the mossy cell to basket cell unitary conductance. Figures adapted with permission from Santhakumar et al. (2005).

This is in contrast to the enhanced activity due to mossy cell loss predicted by the disinhibition hypothesis. Furthermore, network simulations have demonstrated that mossy cell loss is neither necessary nor sufficient to increase excitability, since deletion of mossy cells consistently resulted in decreased excitability in the model networks (Santhakumar et al., 2005), in agreement with recent experimental data (Ratzliff et al., 2004).

#### EVALUATING EXCITABILITY AND OUTCOME IN THE MODEL

The activity of the network in response to focal activation of the perforant path input can be visualized in the form of spike time rasters. Excitability of the model dentate gyrus can be assessed by a number of measures, including:

1. Total duration of the granule cell discharges in the network, a measure of the time from the first spike fired by a granule cell in the network to the last spike fired by a granule cell in the network. The first and the last granule cell spikes may originate from different granule cells
2. Mean number of spikes per granule cell
3. Latency to spread of activity from the perforant path activation to the firing of the most distant granule cells in the network
4. Coherence of granule cell discharges.

The population coherence for a pair of discharging neurons can be calculated by the following method described previously (White et al., 1998; Foldy et al., 2004). Trains of square pulses are generated for each of the cells, with each pulse of height unity being centered at the spike peak, and the width being 20% of the mean firing period (interspike interval) of

the faster cell in the pair. Next, the cross-correlation is calculated at zero time lag of these pulse trains, which is equivalent to calculating the shared area of the unit height pulses. Coherence can be defined as the sum of the shared areas divided by the square root of the product of the total areas of each individual train. Average coherence can be calculated from the coherence values obtained for all cell pair combinations. In large-scale networks, similar coherence measures can be obtained independently for local and distant cell groups to assess focal and global synchrony in the network.

## CONSIDERATION OF LIMITATIONS

### AXONAL CONDUCTION DELAYS

Realistic simulations of individual neurons in spatially and topologically organized networks require dealing explicitly with distance dependant conduction delays. Minimally, in a network with long range projection cells like the mossy cells, it is crucial to perform a set of control simulations to verify that the overall results bear out in the presence of axonal conduction delays. Conduction delays can be implemented by including an axonal conduction velocity of 0.25 m/s (Bartos et al., 2002) and determining distance based on the number of lamella between the somata of the presynaptic cell and the location of the synapse.

### SCALING

Current computing resources dictate that the size of the model network be scaled down from its original biological size. Thus, anyone performing large-scale simulations is faced with the problems associated with scaling down the size of the network. This is an important issue, since many functional and active properties of individual cells depend on the presence of adequate input convergence. If a network is scaled down without increasing either the connection probability or strength of unitary synaptic contacts the individual neurons will not reach threshold. These issues apply not only to the model of the healthy dentate network but also to the formation of sprouted contacts as described above.

### OTHER FEATURES TO CONSIDER WHILE MODELING CELL LOSS AND SPROUTING

The dentate gyrus has several other anatomical features that could potentially influence the overall outcome of the generation and spread of activity that might be interesting to consider:

1. The density of neurons along the septo-temporal axis has been shown to vary in a cell type-specific manner in the dentate gyrus. Specifically, the density of granule cells decreases dramatically at the temporal pole (Fricke and Cowan, 1978), while the densities of mossy cells and hilar interneurons increase at the temporal pole (Buckmaster and Jongen-Realo, 1999).
2. Autoradiographic studies have shown that within a given lamella, the density of associational fibers from hilar cells to their molecular layer targets appears to double from the tip of the ventral blade to the tip of the dorsal blade (Fricke and Cowan, 1978).
3. The cell type-specific axonal distributions (see Figure 7.2) are based on *in vivo* fills obtained from cells situated some distance away from the septal and temporal poles of the dentate gyrus. Since there are no data on the axonal arbors at the septal and temporal poles of the dentate, it is unclear how the connectivity patterns are modified at the poles of the dentate.
4. Another interesting feature of the dentate gyrus is its bilateral structure with expansive commissural projections from both hilar mossy cells and interneurons. Briefly, mossy fibers do not cross the commissure (Blackstad et al., 1970; Zappone and Sloviter, 2001). However, mossy cells have extensive commissural projections (Frotscher et al., 1991) with almost all cells projecting bilaterally (Deller, 1998). It is therefore interesting to consider how unilateral sprouting might impact bilateral spread of network activity and hyperexcitability.

Apart from the features of the healthy dentate gyrus, another aspect to consider is the evolution of sprouting and cell loss. Previous studies have reported a strong correlation between the degree of hilar neuron loss and mossy fiber sprouting in both specimens from patients with temporal lobe epilepsy (Gabriel et al., 2004) and animal models (Nadler and Jiao, 2004). However, it would also be informative to consider situations where sprouting and cell loss fail to occur in parallel.

## FUTURE DIRECTIONS

Development of large-scale models that can simulate brain circuits with greater realism is essential to understand the experimentally determined cellular and molecular underpinnings of network disorders such as epilepsy. Large-scale simulations will also make it possible to test the circuit effects of specific therapeutic manipulations and allow for uniquely tailoring treatment to distinct pathological processes in different types of seizure disorders. Inclusion of a complete complement of interneuronal subtypes, various receptor and modulator systems, realistic channel distributions, dendritic integration processes and synaptic plasticity will further enhance the scope of the questions that the models can address and their predictive power. It is only with increasingly realistic modeling that we can hope to bridge the gap in understanding the evolution of changes in molecules and circuits to behavior and disease.

## REFERENCES

- Acsady, L., Katona, I., Buzsaki, G. and Freund, T.F. (1998a). Selective perisomatic innervation of hilar interneurons and mossy cells by local gabaergic afferents. *Eur J Neurosci* 10:41.
- Acsady, L., Kamondi, A., Sik, A., Freund, T. and Buzsaki, G. (1998b). GABAergic cells are the major postsynaptic targets of mossy fibers in the rat hippocampus. *J Neurosci* 18:3386–3403.
- Acsady, L., Katona, I., Martinez-Guijarro, F.J., Buzsaki, G. and Freund, T.F. (2000). Unusual target selectivity of perisomatic inhibitory cells in the hilar region of the rat hippocampus. *J Neurosci* 20:6907–6919.
- Amaral, D.G. (1978). A Golgi study of cell types in the hilar region of the hippocampus in the rat. *J Comp Neurol* 182:851–914.
- Ambros-Ingerson, J., Grover, L.M. and Holmes, W.R. (2006). Sensitivity parameter analysis by evolutionary search method in hippocampal CA1 pyramidal cell model. In: Society for Neuroscience pp. 101–114. Atlanta, GA.
- Aradi, I. and Holmes, W.R. (1999a). Role of multiple calcium and calcium-dependent conductances in regulation of hippocampal dentate granule cell excitability. *J Comput Neurosci* 6:215–235.
- Aradi, I. and Holmes W.R. (1999b). Active dendrites regulate spatio-temporal synaptic integration in hippocampal dentate granule cells. *Neurocomputing* 26–27:45–51.
- Babb, T.L., Pretorius, J.K., Kupfer, W.R. and Brown, W.J. (1988) Distribution of glutamate-decarboxylase-immunoreactive neurons and synapses in the rat and monkey hippocampus – light and electron-microscopy. *J Comp Neurol* 278:121–138.
- Bartos, M., Vida, I., Frotscher, M., Geiger, J.R.P. and Jonas, P. (2001). Rapid signaling at inhibitory synapses in a dentate gyrus interneuron network. *J Neurosci* 21:2687–2698.
- Bartos, M., Vida, I., Frotscher, M. et al (2002). Fast synaptic inhibition promotes synchronized gamma oscillations in hippocampal interneuron networks. *Proc Natl Acad Sci USA* 99:13222–13227.
- Blackstad, T.W., Brink, K., Hem, J. and Jeune, B. (1970). Distribution of hippocampal mossy fibers in the rat. An experimental study with silver impregnation methods. *J Comp Neurol* 138:433–449.
- Blasco-Ibanez, J.M., Martinez-Guijarro, F.J. and Freund, T.F. (2000). Recurrent mossy fibers preferentially innervate parvalbumin-immunoreactive interneurons in the granule cell layer of the rat dentate gyrus. *Neuroreport* 11:3219–3225.
- Boss, B.D., Peterson, G.M. and Cowan, W.M. (1985). On the number of neurons in the dentate gyrus of the rat. *Brain Res* 338:144–150.
- Bower, J.M. and Beeman, D. (1995). The book of Genesis: exploring realistic neural models with the general neural simulation system, 2nd edn. The Electronic Library of Science.
- Buckmaster, P.S. and Dudek, F.E. (1997). Network properties of the dentate gyrus in epileptic rats with hilar neuron loss and granule cell axon reorganization. *J Neurophysiol* 77:2685–2696.
- Buckmaster, P.S. and Dudek, F.E. (1999). In vivo intracellular analysis of granule cell axon reorganization in epileptic rats. *J Neurophysiol* 81:712–721.
- Buckmaster PS, Jongen-Relo AL (1999). Highly specific neuron loss preserves lateral inhibitory circuits in the dentate gyrus of kainate-induced epileptic rats. *J Neurosci* 19:9519–9529.
- Buckmaster, P.S. and Schwartzkroin, P.A. (1994). Hippocampal mossy cell function: a speculative view. *Hippocampus* 4:393–402.
- Buckmaster, P.S., Stowbridge, B.W., Kunkel, D.D., Schmiege, D.L. and Schwartzkroin, P.A. (1992). Mossy cell axonal projections to the dentate gyrus molecular layer in the rat hippocampal slice. *Hippocampus* 2:349–362.
- Buckmaster, P.S., Stowbridge, B.W. and Schwartzkroin, P.A. (1993). A comparison of rat hippocampal mossy cells and CA3c pyramidal cells. *J Neurophysiol* 70:1281–1299.
- Buckmaster, P.S., Wenzel, H.J., Kunkel, D.D. and Schwartzkroin, P.A. (1996). Axon arbors and synaptic connections of hippocampal mossy cells in the rat *in vivo*. *J Comp Neurol* 366:270–292.
- Buckmaster, P.S., Yamawaki, R. and Zhang, G.F. (2002a). Axon arbors and synaptic connections of a vulnerable population of interneurons in the dentate gyrus *in vivo*. *J Comp Neurol* 445:360–373.
- Buckmaster, P.S., Zhang, G.F. and Yamawaki, R. (2002b). Axon sprouting in a model of temporal lobe epilepsy creates a predominantly excitatory feedback circuit. *J Neurosci* 22:6650–6658.
- Buzsaki, G. and Eidelberg, E. (1983). Phase relations of hippocampal projection cells and interneurons to theta activity in the anesthetized rat. *Brain Res* 266:334–339.
- Carnevale, N.T. and Hines, M.L. (2006). The NEURON Book. Cambridge University Press.

- Ceranik, K., Bender, R., Geiger, J.R.P. et al. (1997). A novel type of GABAergic interneuron connecting the input and the output regions of the hippocampus. *J Neurosci* 17:5380–5394.
- Chauvet, G.A. and Berger, T.W. (2002). Hierarchical model of the population dynamics of hippocampal dentate granule cells. *Hippocampus* 12:698–712.
- Claiborne, B.J., Amaral, D.G. and Cowan, W.M. (1990) Quantitative, three-dimensional analysis of granule cell dendrites in the rat dentate gyrus. *J Comp Neurol* 302:206–219.
- Cossart, R., Dinocourt, C., Hirsch, J.C. et al. (2001). Dendritic but not somatic GABAergic inhibition is decreased in experimental epilepsy. *Nat Neurosci* 4:52–62.
- Coulter, D.A. (1999). Chronic epileptogenic cellular alterations in the limbic system after status epilepticus. *Epilepsia* 40 Suppl 1:S23–33; discussion S40–21.
- De Schutter, E. (2000). Computational neuroscience – Realistic modeling for experimentalists. CRC Press, Boca Raton.
- Deller, T. (1998). The anatomical organization of the rat fascia dentata: new aspects of laminar organization as revealed by anterograde tracing with Phaseolus vulgaris-Luecoagglutinin (PHAL). *Anat Embryol (Berl)* 197:89–103.
- Desmond, N.L. and Levy, W.B. (1985). Granule cell dendritic spine density in the rat hippocampus varies with spine shape and location. *Neurosci Lett* 54:219–224.
- Destexhe, A., Rudolph, M., Fellous, J.M. and Sejnowski, T.J. (2001). Fluctuating synaptic conductances recreate in vivo-like activity in neocortical neurons. *Neuroscience* 107:13–24.
- Dyhrfjeld-Johnsen, J., Santhakumar, V., Morgan, R.J., Tsimring, L. and Soltesz, I. (2006). Topological determinants of epileptogenesis in large-scale structural and functional models of the dentate gyrus derived from experimental data. *J Neurophysiol* (in press).
- Foldy, C., Aradi, I., Howard, A. and Soltesz, I. (2004). Diversity beyond variance: modulation of firing rates and network coherence by GABAergic subpopulations. *Eur J Neurosci* 19:119–130.
- Freund, T.F. and Buzsaki, G. (1996). Interneurons of the hippocampus. *Hippocampus* 6:347–470.
- Fricke, R. and Cowan, W.M. (1978). An autoradiographic study of the commissural and ipsilateral hippocampo-dentate projections in the adult rat. *J Comp Neurol* 181:253–269.
- Fricke, R.A. and Prince, D.A. (1984). Electrophysiology of dentate gyrus granule cells. *J Neurophysiol* 51:195–209.
- Frotscher, M., Seress, L., Schwerdtfeger, W.K. and Buhl, E. (1991) The mossy cells of the fascia dentata: a comparative study of their fine structure and synaptic connections in rodents and primates. *J Comp Neurol* 312:145–163.
- Gaarskjaer, F.B. (1978) Organization of mossy fiber system of rat studied in extended hippocampi .1. Terminal area related to number of granule and pyramidal cells. *J Comp Neurol* 178:49–71.
- Gabriel, S., Njunting, M., Pomper, J.K. et al. (2004). Stimulus and potassium-induced epileptiform activity in the human dentate gyrus from patients with and without hippocampal sclerosis. *J Neurosci* 24:10416–10430.
- Geiger, J.R.P., Lubke, J., Roth, A., Frotscher, M. and Jonas, P. (1997). Submillisecond AMPA receptor-mediated signaling at a principal neuron-interneuron synapse. *Neuron* 18:1009–1023.
- Gulyas, A.I., Miettinen, R., Jacobowitz, D.M. and Freund, T.F. (1992). Calretinin is present in nonpyramidal cells of the rat hippocampus .1. A new type of neuron specifically associated with the mossy fiber system. *Neuroscience* 48:1–27.
- Gulyas, A.I., Hajos, N. and Freund, T.F. (1996). Interneurons containing calretinin are specialized to control other interneurons in the rat hippocampus. *Eur J Neurosci* 16:3397–3411.
- Halasy, K. and Somogyi, P. (1993). Subdivisions in the multiple gabaergic innervation of granule cells in the dentate gyrus of the rat hippocampus. *Eur J Neurosci* 5:411–429.
- Han, Z.S., Buhl, E.H., Lorinczi, Z. and Somogyi, P. (1993). A high-degree of spatial selectivity in the axonal and dendritic domains of physiologically identified local-circuit neurons in the dentate gyrus of the rat hippocampus. *Eur J Neurosci* 5:395–410.
- Harney, S.C. and Jones, M.V. (2002). Pre- and postsynaptic properties of somatic and dendritic inhibition in dentate gyrus. *Neuropharmacology* 43:584–594.
- Heinemann, U., Beck, H., Dreier, J.P., Ficker, E., Stabel, J. and Zhang, C.L. (1992). The dentate gyrus as a regulated gate for the propagation of epileptiform activity. *Epilepsy Res Suppl* 7:273–280.
- Howard, A., Tamas, G. and Soltesz, I. (2005). Lighting the chandelier: new vistas for axo-axonic cells. *Trends Neurosci* 28:310–316.
- Howard, A.L., Neu, A., Morgan, R.J., Echegoyen, J.C. and Soltesz, I. (2006). Opposing modifications in intrinsic currents and synaptic inputs in post-traumatic mossy cells: evidence for single-cell homeostasis in a hyperexcitable network. *J Neurophysiol*
- Ishizuka, N., Cowan, W.M. and Amaral, D.G. (1995). A quantitative analysis of the dendritic organization of pyramidal cells in the rat hippocampus. *J Comp Neurol* 362:17–45.
- Katona, I., Acsady, L. and Freund, T.F. (1999). Postsynaptic targets of somatostatin-immunoreactive interneurons in the rat hippocampus. *Neuroscience* 88:37–55.
- Keren, N., Peled, N. and Korngreen, A. (2005). Constraining compartmental models using multiple voltage recordings and genetic algorithms. *J Neurophysiol* 94:3730–3742.
- Kneisler, T.B. and Dingledine, R. (1995a). Spontaneous and synaptic input from granule cells and the perforant path to dentate basket cells in the rat hippocampus. *Hippocampus* 5:151–164.
- Kneisler, T.B. and Dingledine, R. (1995b) Synaptic input from CA3 pyramidal cells to dentate basket cells in rat hippocampus. *J Physiol* 487 (Pt 1):125–146.
- Kraushaar, U. and Jonas, P. (2000). Efficacy and stability of quantal GABA release at a hippocampal interneuron-principal neuron synapse. *J Neurosci* 20:5594–5607.
- Li, X.G., Somogyi, P., Tepper, J.M. and Buzsaki, G. (1992). Axonal and dendritic arborization of an intracellularly labeled chandelier cell in the CA1 region of rat hippocampus. *Exp Brain Res* 90:519–525.
- Lothman, E.W., Stringer, J.L. and Bertram, E.H. (1992). The dentate gyrus as a control point for seizures in the hippocampus and beyond. *Epilepsy Res Suppl* 7:301–313.

- Lubke, J., Frotscher, M. and Spruston, N. (1998). Specialized electrophysiological properties of anatomically identified neurons in the hilar region of the rat fascia dentata. *J Neurophysiol* 79:1518–1534.
- Lytton, W.W., Hellman, K.M. and Sutula, T.P. (1998). Computer models of hippocampal circuit changes of the kindling model of epilepsy. *Artif Intell Med* 13:81–97.
- Manor, Y., Gonczarowski, J. and Segev, I. (1991). Propagation of action potentials along complex axonal trees. Model and implementation. *Biophys J* 60:1411–1423.
- Margerison, J.H. and Corsellis, J.A. (1966). Epilepsy and the temporal lobes. A clinical, electroencephalographic and neuropathological study of the brain in epilepsy, with particular reference to the temporal lobes. *Brain* 89:499–530.
- Matherne, G.W., Babb, T.L., Leite, J.P., Pretorius, K., Yeoman, K.M. and Kuhlman, P.A. (1996). The pathogenic and progressive features of chronic human hippocampal epilepsy. *Epilepsy Res* 26:151–161.
- Molnar, P. and Nadler, J.V. (1999). Mossy fiber-granule cell synapses in the normal and epileptic rat dentate gyrus studied with minimal laser photostimulation. *J Neurophysiol* 82:1883–1894.
- Mott, D.D., Turner, D.A., Okazaki, M.M. and Lewis, D.V. (1997). Interneurons of the dentate-hilus border of the rat dentate gyrus: morphological and electrophysiological heterogeneity. *J Neurosci* 17:3990–4005.
- Nadler, J.V. (2003). The recurrent mossy fiber pathway of the epileptic brain. *Neurochem Res* 28:1649–1658.
- Nadler, J.V. and Jiao, Y. (2004). Mossy fiber sprouting correlates with loss of GluR2-immunoreactive hilar neurons. In: Society for Neuroscience, Program. No. 566.521. San Diego.
- Nomura, T., Fukuda, T., Aika, Y. et al (1997a). Laminar distribution of non-principal neurons in the rat hippocampus, with special reference to their compositional difference among layers. *Brain Res* 764:197–204.
- Nomura, T., Fukuda, T., Aika, Y. et al (1997b). Distribution of nonprincipal neurons in the rat hippocampus, with special reference to their dorsoventral difference. *Brain Res* 751:64–80.
- Patton, P.E. and McNaughton, B. (1995). Connection matrix of the hippocampal-formation .1. The dentate gyrus. *Hippocampus* 5:245–286.
- Rall, W., Burke, R.E., Holmes, W.R., Jack, J.J., Redman, S.J. and Segev, I. (1992). Matching dendritic neuron models to experimental data. *Physiol Rev* 72:S159–186.
- Ratzliff, A.H., Santhakumar, V., Howard, A. and Soltesz, I. (2002). Mossy cells in epilepsy: rigor mortis or vigor mortis? *Trends Neurosci* 25:140–144.
- Ratzliff, A.H., Howard, A.L., Santhakumar, V., Osapay, I. and Soltesz, I. (2004). Rapid deletion of mossy cells does not result in a hyperexcitable dentate gyrus: implications for epileptogenesis. *J Neurosci* 24:2259–2269.
- Ribak, C.E., Seress, L. and Amaral, D.G. (1985) The development, ultrastructure and synaptic connections of the mossy cells of the dentate gyrus. *J Neurocytol* 14:835–857.
- Santhakumar, V. and Soltesz, I. (2004). Plasticity of interneuronal species diversity and parameter variance in neurological diseases. *Trends Neurosci* 27:504–510.
- Santhakumar, V., Bender, R., Frotscher, M. et al. (2000). Granule cell hyperexcitability in the early post-traumatic rat dentate gyrus: the ‘irritable mossy cell’ hypothesis. *J Physiol* 524 Pt 1:117–134.
- Santhakumar, V., Aradi, I. and Soltesz, I. (2005). Role of mossy fiber sprouting and mossy cell loss in hyperexcitability: a network model of the dentate gyrus incorporating cell types and axonal topography. *J Neurophysiol* 93:437–453.
- Scharfman, H.E. (1991). Dentate hilar cells with dendrites in the molecular layer have lower thresholds for synaptic activation by perforant path than granule cells. *J Neurosci* 11:1660–1673.
- Scharfman, H.E. (1993). Characteristics of spontaneous and evoked EPSPs recorded from dentate spiny hilar cells in rat hippocampal slices. *J Neurophysiol* 70:742–757.
- Scharfman, H.E., Smith, K.L., Goodman, J.H. and Sollas, A.L. (2001). Survival of dentate hilar mossy cells after pilocarpine-induced seizures and their synchronized burst discharges with area CA3 pyramidal cells. *Neuroscience* 104:741–759.
- Sik, A., Penttonen, M. and Buzsaki, G. (1997). Interneurons in the hippocampal dentate gyrus: an in vivo intracellular study. *Eur J Neurosci* 9:573–588.
- Sloviter, R.S. (1991). Permanently altered hippocampal structure, excitability, and inhibition after experimental status epilepticus in the rat: the ‘dormant basket cell’ hypothesis and its possible relevance to temporal lobe epilepsy. *Hippocampus* 1:41–66.
- Sloviter, R.S., Zappone, C.A., Harvey, B.D., Bumanglag, A.V., Bender, R.A. and Frotscher, M. (2003). Dormant basket cell hypothesis revisited: relative vulnerabilities of dentate gyrus mossy cells and inhibitory interneurons after hippocampal status epilepticus in the rat. *J Comp Neurol* 459:44–76.
- Soriano, E., Nitsch, R. and Frotscher, M. (1990). Axo-axonic chandelier cells in the rat fascia dentata: Golgi-electron microscopy and immunocytochemical studies. *J Comp Neurol* 293:1–25.
- Staley, K.J., Otis, T.S. and Mody, I. (1992). Membrane properties of dentate gyrus granule cells: comparison of sharp microelectrode and whole-cell recordings. *J Neurophysiol* 67:1346–1358.
- Sutula, T., Cavazos, J. and Golarai, G. (1992). Alteration of long-lasting structural and functional effects of kainic acid in the hippocampus by brief treatment with phenobarbital. *J Neurosci* 12:4173–4187.
- Szabadics, J., Varga, C., Molnar, G., Olah, S., Barzo, P. and Tamas, G. (2006). Excitatory effect of GABAergic axo-axonic cells in cortical microcircuits. *Science* 311:233–235.
- Toth, Z., Hollrigel, G.S., Gores, T. and Soltesz, I. (1997). Instantaneous perturbation of dentate interneuronal networks by a pressure wave-transient delivered to the neocortex. *J Neurosci* 17:8106–8117.
- Traub, R.D., Miles, R. and Buzsaki, G. (1992). Computer simulation of carbachol-driven rhythmic population oscillations in the CA3 region of the in vitro rat hippocampus. *J Physiol* 451:653–672.
- Vanier, M.C. and Bower, J.M. (1999). A comparative survey of automated parameter-search methods for compartmental neural models. *J Comput Neurosci* 7:149–171.
- Wang, X.J., Tegnér, J., Constantinidis, C. and Goldman-Rakic, P.S. (2004). Division of labor among distinct subtypes of inhibitory neurons in a cortical microcircuit of working memory. *Proc Natl Acad Sci USA* 101:1368–1373.
- Wenzel, H.J., Buckmaster, P.S., Anderson, N.L., Wenzel, M.E. and Schwartzkroin, P.A. (1997). Ultrastructural localization of neurotransmitter immunoreactivity in mossy cell axons and their synaptic targets in the rat dentate gyrus. *Hippocampus* 7:559–570.

- West, M.J. (1990). Stereological studies of the hippocampus – a comparison of the hippocampal subdivisions of diverse species including hedgehogs, laboratory rodents, wild mice and men. *Prog Brain Res* 83:13–36.
- West, M.J., Danscher, G. and Gydesen, H. (1978). A determination of the volumes of the layers of the rat hippocampal region. *Cell Tissue Res* 188:345–359.
- White, J.A., Chow, C.C., Rit, J., Soto-Treviño, C. and Kopell, N. (1998). Synchronization and oscillatory dynamics in heterogeneous, mutually inhibited neurons. *J Comput Neurosci* 5:5–16.
- Woodson, W., Nitecka, L. and Benari, Y. (1989). Organization of the gabaergic system in the rat hippocampal-formation – a quantitative immunocytochemical study. *J Comp Neurol* 280:254–271.
- Zappone, C.A. and Sloviter, R.S. (2001). Commissurally projecting inhibitory interneurons of the rat hippocampal dentate gyrus: a colocalization study of neuronal markers and the retrograde tracer Fluoro-gold. *J Comp Neurol* 441:324–344.

# 8

## FUNCTIONAL CONSEQUENCES OF TRANSFORMED NETWORK TOPOLOGY IN HIPPOCAMPAL SCLEROSIS

ROBERT J. MORGAN AND IVAN SOLTESZ

### ABSTRACT

Cranial insults such as head trauma can lead directly to temporal lobe epilepsy in which a number of distinct alterations occur to previously normal brain circuitry. In the hippocampus, some of the most marked changes occur within the dentate gyrus, where large populations of cells are lost and there is widespread sprouting of granule cell axons that for the first time create synapses onto other granule cells. Additionally, there are numerous intrinsic cellular and synaptic modifications as well as gliosis. Experimentally, it is quite difficult, if not impossible, to separate the structural changes that occur in the pathological dentate from the molecular, cellular and synaptic changes. However, computational modeling provides the optimal environment in which to accomplish this very goal. In this chapter, we discuss how computational modeling of the dentate gyrus using large-scale, biophysically realistic, data-driven models allows us to characterize the structure of the dentate in both healthy and injured scenarios. Furthermore, we explore the relationship between the structural alterations that occur after head injury and the function of the dentate gyrus neural network, concluding that structural changes alone can result in hyperexcitability.

### INTRODUCTION

Following repetitive seizures, head trauma and ischemia, the dentate gyrus undergoes dramatic structural reorganization (Buckmaster and Jongen-Relo, 1999; Ratzliff et al., 2002; Sutula et al., 2003), thereby providing an excellent model to study the effects of structural alterations during epileptogenesis. The two primary structural changes that occur, loss of hilar cells and mossy fiber (granule cell axon) sprouting, are hallmarks of seizure-induced end-folium sclerosis (Margerison and Corsellis, 1966; Mathern et al., 1996) in temporal lobe epilepsy and create a fundamentally transformed dentate gyrus microcircuit. Of course, these structural changes are superimposed on a background of intrinsic cellular and synaptic alterations that are occurring simultaneously, so the question arises of how to study the effects of structural changes in isolation.

Computational modeling is a fantastic tool to help isolate and identify the effects of neuronal network architectural alterations. There have been several modeling studies to date that have provided a basis for studying structural changes in disease states (Buzsaki et al., 2004; Netoff et al., 2004; Percha et al., 2005), but these studies have used idealized networks that lack many necessary features. In order to model processes involved in epileptogenesis and make confident experimental predictions, model networks must be strongly data-driven and include detailed structural and functional properties (Bernard et al., 1997; Ascoli and Atkeson, 2005; Traub et al., 2005a, 2005b). Modelers should also strive to use realistic cell numbers, as scaling can have unpredictable and undesirable effects on such things as efficacy of synaptic inputs and synchronization.

In this chapter, we will discuss results obtained from a computational study in which Dyhrfjeld-Johnsen et al. (2007) constructed two extraordinarily large model networks: a 1:1 scale structural model of the rat dentate gyrus with over 1 million nodes and a 1:20 scale functional model, containing over 50 000 multicompartmental neurons representing

four different cell types and reliably reproducing firing properties recorded from electrophysiological experiments. These networks were characterized using graph theoretical tools, recently utilized to study a number of real world networks such as the electric grid, the Internet (Watts and Strogatz 1998; Albert et al., 1999; Barabasi et al., 2000; Jeong et al., 2000; Eubank et al., 2004), the *Caenorhabditis elegans* worm nervous system (Watts and Strogatz, 1998) and model neuronal circuits (Masuda and Aihara, 2004; Netoff et al., 2004; Roxin et al., 2004; Lin and Chen, 2005). The structural model revealed for the first time the topological characteristics of the dentate gyrus and examined how the topology changes during epileptogenesis. Then, the functional model allowed for the determination of the functional relevance of the topological changes, leading to the fascinating conclusion that hyperexcitability can result solely from structural alterations in neuronal networks.

This chapter is divided into five main sections:

1. Construction of the networks
2. Assessment of the structural and functional properties of the networks
3. Results from structural calculations and functional simulations
4. Model limitations, control simulations and tests for robustness
5. Conclusions, relevance of findings to temporal lobe epilepsy and future directions.

## CONSTRUCTION OF THE MODEL NETWORKS

In the past decade, a vast amount of information about the connectivity of the dentate gyrus has been collected and it is these data upon which the models discussed in this chapter are based. While this section will provide a summary of how the models were constructed and include the necessary details, the interested reader should refer to Dyhrfjeld-Johnsen et al. (2007) for a highly detailed description of model components and justifications. Chapter 7 in this book also provides a very detailed explanation of many components of the models. Additionally, detailed descriptions of the single cell models can be found in Santhakumar et al. (2005). Finally, the models themselves are available on ModelDB, located online at <http://senselab.med.yale.edu/senselab/modedb/>.

## THE STRUCTURAL MODEL

As noted above, the structural model is a complete 1:1 scale representation of the rat dentate gyrus. It contains eight anatomically distinct and well-described cell types: granule cells, mossy cells, basket cells, axo-axonic cells, molecular layer cells with axonal projections to the perforant path (MOPP cells), hilar cells with axonal projections to the commissural-associational pathway (HICAP cells), hilar cells with axonal projections to the perforant path (HIPP cells), and interneuron-specific (IS) cells (a diagram of the eight cell types and their connections to other cell types is shown in Figure 8.1A). The number of cells of each type included in the model and their connectivity is based on published data and indicated in Table 8.1. Table 8.1 is the connectivity matrix for the model network and it displays the numbers of postsynaptic targets of each cell type that a single presynaptic neuron of a given type innervates (e.g. looking at the third row, second column of Table 8.1, a single basket cell innervates approximately 1250 granule cells; mean and ranges are indicated along with references). For further details and justifications regarding the connectivity estimates given in Table 8.1, please refer to Appendix A2 in Dyhrfjeld-Johnsen et al. (2007) and Chapter 7 in this book.

In addition to the number of connections made by any given cell, the distribution of these connections along the septo-temporal axis of the dentate gyrus is very important. Fortunately, *in vivo* single cell fills have been performed which provide a very complete description of the axonal extent of these eight cell types. For the model, averages of these *in vivo* axonal distributions were fit with either a single or double Gaussian for each cell type which then defined the model axonal distribution for each cell of that type (Figure 8.2). Cells were distributed evenly among 100 bins along a simulated 6 millimeter strip and connectivities between cells were determined probabilistically based on the Gaussians described above.

Following the construction of the connectivity matrix, the model was represented as a ‘graph’ in the computer, with ‘nodes’ representing individual cells and ‘links’ representing synapses. Each node was given the identity of a single cell in the network, complete with the connectivity pattern it would be expected to have in the biological dentate gyrus. The end result of this representation was a graph of over 1 million nodes connected by over 1 billion directed synaptic links.

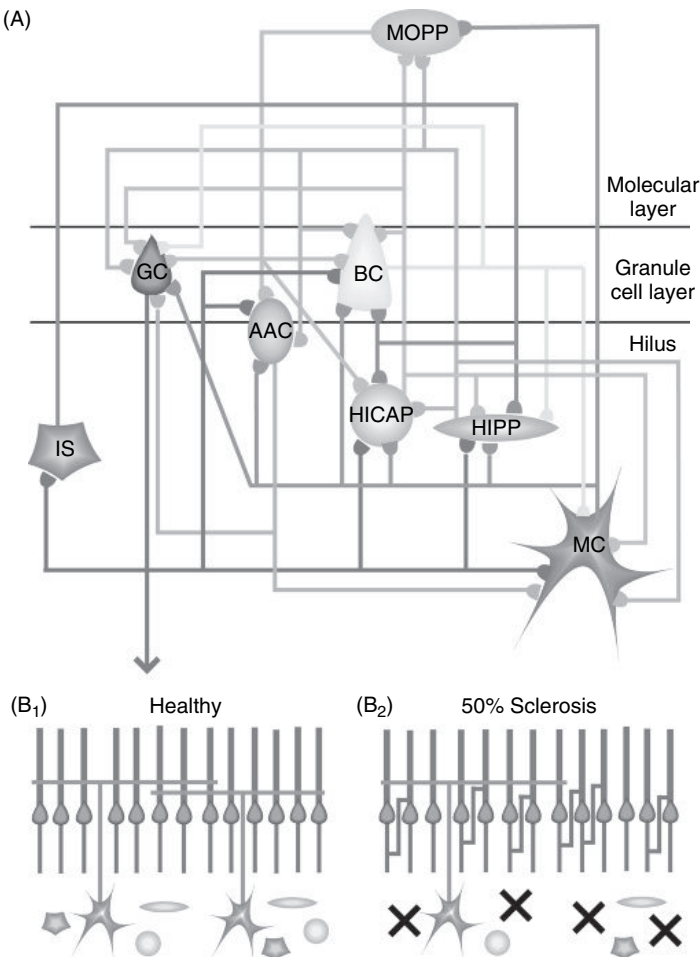


**FIGURE 8.1** Schematic of the basic circuitry of the dentate gyrus and the changes to the network during sclerosis. (A) Relational representation of the healthy dentate gyrus illustrating the network connections between the eight major cell types (GC: granule cell; BC: basket cell; MC: mossy cell; AAC: axo-axonic cells; MOPP: molecular layer interneurons with axons in perforant-path termination zone; HIPP: hilar interneurons with axons in perforant-path termination zone; HICAP: hilar interneurons with axons in the commissural/associational pathway termination zone and IS: interneuron selective cells). The schematic shows the characteristic location of the various cell types within the three layers of the dentate gyrus. Note, however, that this diagram does not indicate the topography of axonal connectivity (present in both the structural and functional dentate models) or the somato-dendritic location of the synapses (incorporated in the functional network models). (B1) Schematic of the excitatory connectivity of the healthy dentate gyrus is illustrated (only cell types in the hilus and granule cells are shown). Note that the granule cell axons (the mossy fibers) do not contact other granule cells in the healthy network. (B2) Schematic of the dentate gyrus at 50% sclerosis shows the loss (indicated by the large Xs) of half the population of all hilar cell types and the 50% sprouting of mossy fibers that results in recurrent connections between granule cells (note that, unlike in this simplified schematic, all granule cells formed sprouted contacts in the structural and functional models of sclerosis; thus, progressive increase in sprouting was implemented by increasing the number of postsynaptic granule cells contacted by single sprouted mossy fibers; see Materials and Methods). Reproduced with permission from Dyhrfjeld-Johnsen et al. (2007).

### THE FUNCTIONAL MODEL

The functional model network was constructed in a very similar manner to the structural model described above. The two networks differ in several important ways, however. First, the functional model contains only 4 cell types: granule cells, mossy cells, basket cells and HIPP cells. These are the only cell types for which the electrophysiological characterizations were sufficient for detailed single cell models to reproduce the cells' firing characteristics. Note that the reason there is so much more information about these four cell types is because they are the two excitatory cell types (granule and mossy cells) and the two major, numerically dominant and functionally important types of interneurons (the parvalbumin- and somatostatin-positive interneurons). The second major difference between the functional and structural models is that the functional model is a 1:20 scale representation of the dentate, rather than 1:1. This change was made because this was

TABLE 8.1 Connectivity matrix for the neuronal network of the control dentate gyrus

	Granule cells	Mossy cells	Basket cells	Axo-axonic cells	MOPP cells	HIPP cells	HICAP cells	IS cells
<b>Granule cells</b> <b>(1 000 000)</b> ref. {1–5}	X X ref. {6}	<b>9.5</b> 7–12 ref. {7}	<b>15</b> 10–20 ref. {6–9}	<b>3</b> 1–5 ref. {6,7,9}	X X ref. {6}	<b>110</b> 100–120 ref. {4,10,11}	<b>40</b> 30–50 ref. {4,7,10,11}	<b>20</b> 10–30 ref. {7}
<b>Mossy cells</b> <b>(30 000)</b> ref. {11}	<b>32 500</b> 30 000–35 000 ref. {4,11–13}	<b>350</b> 200–500 ref. {12,13}	<b>7.5</b> 5–10 ref. {13}	<b>7.5</b> 5–10 ref. {13}	<b>5</b> 5 ref. {14}	<b>600</b> 600 ref. {12,13}	<b>200</b> 200 ref. {12,13}	X X ref. {15}
<b>Basket cells</b> <b>(10 000)</b> ref. {16,17}	<b>1250</b> 1000–1500 ref. {4,16–19}	<b>75</b> 50–100 ref. {11,16,17,19}	<b>35</b> 20–50 ref. {16,17,20,21}	X X ref. {18}	X X ref. {18}	<b>0.5</b> 0–1 ref. {18}	X X ref. {18}	X X ref. {10,20}
<b>Axo-axonic cells</b> <b>(2000)</b> ref. {4,22}	<b>3000</b> 2000–4000 ref. {4,18,22}	<b>150</b> 100–200 ref. {4,5,11,14,23}	X X ref. {5,18}	X X ref. {5,18}	X X ref. {5,18}	X X ref. {5,18}	X X ref. {5,18}	X X ref. {5,18,19}
<b>MOPP cells</b> <b>(4000)</b> ref. {11,14}	<b>7500</b> 5000–10 000 ref. {14}	X X ref. {14,24}	<b>40</b> 30–50 ref. {14,25}	<b>1.5</b> 1–2 ref. {14,26}	<b>7.5</b> 5–10 ref. {14,25}	X X ref. {14,20,25}	<b>7.5</b> 5–10 ref. {14,25}	X X ref. {14,15}
<b>HIPP cells</b> <b>(12 000)</b> ref. {11}	<b>1550</b> 1500–1600 ref. {4,11,20}	<b>35</b> 20–50 ref. {4,11,12,27,28}	<b>450</b> 400–500 ref. {4,11,20}	<b>30</b> 20–40 ref. {20,25}	<b>15</b> 10–20 ref. {25}	X X ref. {14,20,25}	<b>15</b> 10–20 ref. {25}	X X ref. {15,20}
<b>HICAP cells</b> <b>(3000)</b> ref. {5,29,30}	<b>700</b> 700 ref. {4,11,20}	<b>35</b> 30–40 ref. {20}	<b>175</b> 150–200 ref. {4,11,20}	X X ref. {20}	<b>15</b> 10–20 ref. {14,20}	<b>50</b> 50 ref. {20}	<b>50</b> 50 ref. {20}	X X ref. {20}
<b>IS cells</b> <b>(3000)</b> ref. {15,29,30}	X X ref. {15}	X X ref. {15}	<b>7.5</b> 5–10 ref. {15,19}	X X ref. {15}	X X ref. {19}	<b>7.5</b> 5–10 ref. {19}	<b>7.5</b> 5–10 ref. {19}	<b>450</b> 100–800 ref. {15}

Cell numbers and connectivity values were estimated from published data for granule cells, mossy cells, basket cells, axo-axonic cells, molecular layer interneurons with axonal projections to the perforant path (MOPP), hilar interneurons with axonal projections to the perforant path (HIPP), hilar interneurons with axonal projections to the commissural/associational pathway (HICAP) and interneuron specific cells (IS). Connectivity is given as number of connections to a postsynaptic population (row 1) from a single presynaptic neuron (column 1). The average number of connections used in the graph theoretical calculations is given in **bold**. Note, however, that the small world structure was preserved even if only the extreme low or the extreme high estimates were used for the calculation of L and C. References given in table correspond to: <sup>1</sup>Gaarskjaer, 1978; <sup>2</sup>Boss et al., 1985; <sup>3</sup>West, 1990; <sup>4</sup>Patton and McNaughton, 1995; <sup>5</sup>Freund and Buzsaki, 1996; <sup>6</sup>Buckmaster and Dudek, 1999; <sup>7</sup>Acsady et al., 1998; <sup>8</sup>Geiger et al., 1997; <sup>9</sup>Blasco-Ibanez et al., 2000; <sup>10</sup>Gulyas et al., 1992; <sup>11</sup>Buckmaster and Jongen-Relo, 1999; <sup>12</sup>Buckmaster et al., 1996; <sup>13</sup>Wenzel et al., 1997; <sup>14</sup>Han et al., 1993; <sup>15</sup>Gulyas et al., 1996; <sup>16</sup>Babb et al., 1988; <sup>17</sup>Woodson et al., 1989; <sup>18</sup>Halasy and Somogyi, 1993; <sup>19</sup>Acsady et al., 2000; <sup>20</sup>Sik et al., 1997; <sup>21</sup>Bartos et al., 2001; <sup>22</sup>Li et al., 1992; <sup>23</sup>Ribak et al., 1985; <sup>24</sup>Frotscher et al., 1991; <sup>25</sup>Katona et al., 1999; <sup>26</sup>Soriano et al., 1990; <sup>27</sup>Claiborne et al., 1990; <sup>28</sup>Buckmaster et al., 2002; <sup>29</sup>Nomuar et al., 1997a; <sup>30</sup>Nomura et al., 1997b. Reproduced with permission from Dyhrfjeld-Johnsen et al. (2007).

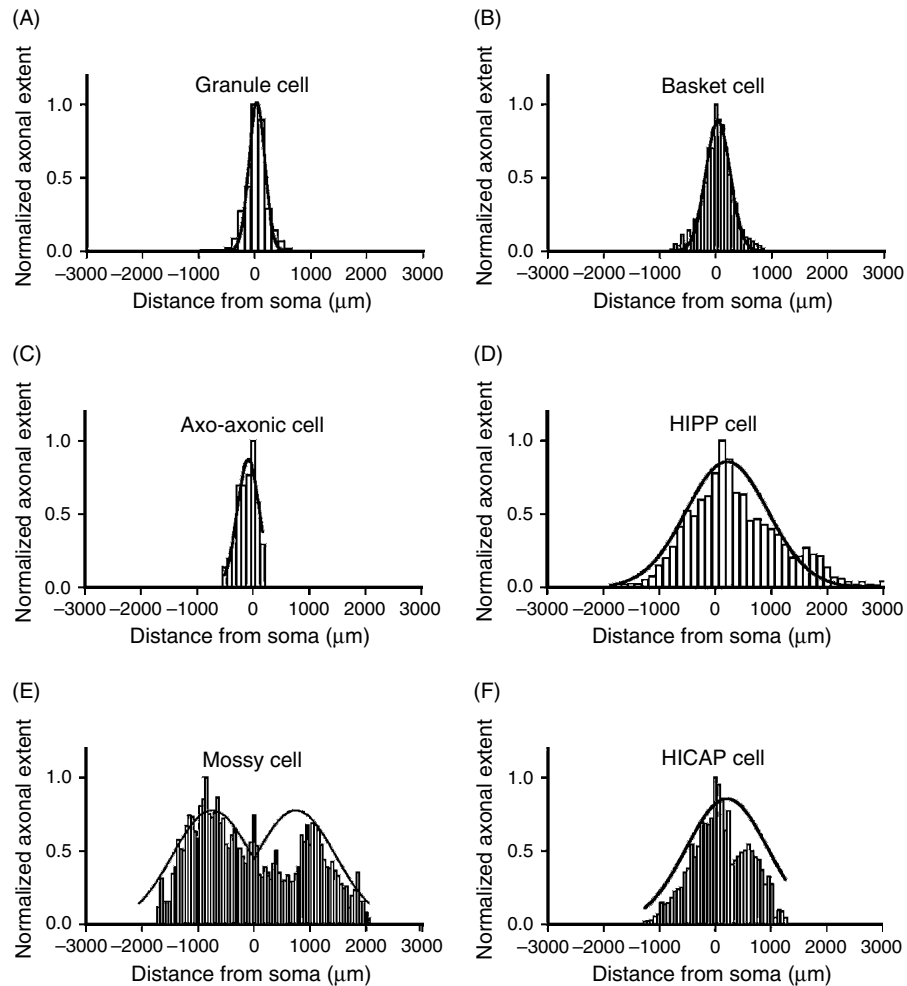


**FIGURE 8.2** Gaussian fits to experimentally determined distributions of axonal branch length used in construction of the models of the dentate gyrus. (A) Plot shows the averaged axonal distribution of 13 granule cells (Buckmaster and Dudek, 1999) and the corresponding Gaussian fit. (B) Fit to the septo-temporal distribution of axonal lengths of a filled and reconstructed basket cell (Sik et al., 1997). (C) Fit to the axonal distribution of a CA1 axo-axonic cell (Li et al., 1992). (D) Gaussian fit to the averaged axonal distributions of 3 HIPP cells from gerbil (Buckmaster et al. 2002). (E) Fit to averaged axonal distributions of 3 mossy cells illustrates the characteristic bimodal pattern of distribution (Buckmaster et al. 1996). (F) Histogram of the axonal lengths of a HICAP cell along the long axis of the dentate gyrus (Sik et al., 1997) and the Gaussian fit to the distribution. All distributions were based on axonal reconstruction of cells filled *in vivo*. In all plots, the septal end of the dentate gyrus is on the left (indicated by negative coordinates) and the soma is located at zero. Reproduced with permission from Dyhrfjeld-Johnsen et al. (2007).

the largest network that was computationally tractable. The number of cells remains extremely large, however, with over 50 000 detailed model cells represented in the network, and the network itself maintains the topological characteristics of the full scale model (these data are discussed later in the chapter). Third and finally, the functional model network includes active, functional model cells. Rather than simply being a collection of nodes and links useful for characterizations of network topology, the functional network is a collection of biophysically realistic model neurons, connected with directed, weighted synapses. Each neuron is capable of firing action potentials and accurately reproduces a number of input-output characteristics determined experimentally. For details of the specific single cell properties and comparisons to electrophysiological data, please refer to Santhakumar et al. (2005) and Chapter 7 of this book.

#### IMPLEMENTATION OF SCLEROSIS AND TOPOLOGICAL ALTERATIONS

'End-folium' sclerosis (referred to subsequently as sclerosis) refers to a number of pathological changes that occur in the dentate gyrus including hilar cell loss, mossy fiber sprouting and gliosis. While gliosis is an important alteration that

can significantly alter the function of the pathological dentate, hilar cell loss and mossy fiber sprouting are the primary determinants of altered network structure, and thus they were the two factors that were incorporated into the model and will be referred to as sclerosis in this chapter.

In order to implement progressive levels of sclerosis, maximal sclerosis was first defined as complete hilar cell loss (i.e. loss of all hilar interneurons and all mossy cells) together with a maximal number of new mossy fiber contacts, as reported in the literature (an average of 275 new contacts per granule cell; note that mossy fiber sprouting was represented in the model as the addition of exclusively new granule cell to granule cell connections). Following from this definition, any intermediate level of sclerosis could be represented by simply taking percentages of this maximum. For example, at 50% sclerosis, 50% of mossy cells and hilar interneurons were lost, and 50% of the maximum number of mossy fiber contacts was added. A schematic of the sclerotic process is shown in Figure 8.1B. Structural and functional analyses were performed at multiples of 10% of maximal sclerosis. This procedure was the same for both the structural and functional models, although the numbers of neurons and connections were scaled down appropriately in the functional model.

## ASSESSMENT OF THE TOPOLOGICAL AND FUNCTIONAL CHARACTERISTICS OF THE NETWORKS

### ASSESSMENT OF THE STRUCTURAL NETWORK

In order to understand the results of the analyses and the conclusions about dentate gyrus structure and function, it is necessary to explain the parameters that define network topology. Two measures that Watts and Strogatz (1998) originally employed to assess the structure of the nervous system of the worm *C. elegans* were used, the average path length, L, and the average clustering coefficient, C. The average path length is defined as the average number of steps required to move from any node to any other node in the network and it is therefore a measure of how well connected the network is globally. The average clustering coefficient, on the other hand, is a measure of local connectivity. It is defined as the fraction of all possible connections between ‘postsynaptic’ nodes of a given node that are actually formed. The average clustering coefficient for an entire network is simply the average of the clustering coefficients for each node in the network.

The topological measures, C and L, can be best thought of in terms of a social network, or a network of friends. C measures the probability that any two friends of a given person also know each other. L measures how many steps in a chain of friends or acquaintances would be necessary to connect two random people. A common theory that utilizes this parameter is that anyone on the planet is separated from anyone else by up to six degrees of separation, or six people. While this theory has never been satisfactorily proven, it has led to interesting experiments and even a party game called the Six Degrees of Kevin Bacon, in which the participants have to connect any actor or actress to Kevin Bacon through their film roles in as few steps as possible.

Based on these two topological measures, networks can be divided into three classes:

1. Regular, with a long path length and large clustering coefficient
2. Random, with a short path length and small clustering coefficient
3. Small world, with a short path length and large clustering coefficient.

Representative graphs of these types of networks are displayed in Figure 8.3.

As shown, the regular network (Figure 8.3A) is characterized by a high local connectivity, but the distance (via connected nodes) between any two random nodes, especially nodes at the ends of the graph, can be quite large. On the other hand, the random network (Figure 8.3B) contains many long distance connections, contributing to a very short average path length. There is little local connectivity, however, as nodes are just as likely to connect to far away nodes as they are to their neighbors. The small world network (Figure 8.3C) acts as a sort of compromise between the random and regular graphs. Indeed, there is a high degree of local connectivity combined with a number of long-range connections, yielding a both locally and globally well-connected network. Small world networks can also be thought of in terms of social networking. Humans often form a cohesive group of friends who are well connected locally due to various constraints such as geography, common activities and so on. Additionally, any given person in the group may know some people who are totally unrelated to the local group, but who each have cohesive local groups of their own, thus creating numerous long distance connections between the locally well-connected networks.

Although it is clear that L and C values are very important for classifying networks, it is difficult to understand the network topology alterations during sclerosis by simply looking at their absolute values, since the size of the network is

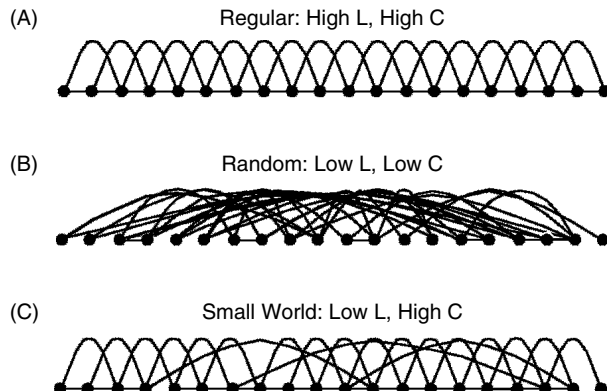


**FIGURE 8.3** Schematics of three basic network topologies. (A) Regular network topology. The nodes in a regular network are connected to their nearest neighbors, resulting in a high degree of local interconnectedness (high clustering coefficient  $C$ ), but also requiring a large number of steps to reach other nodes in the network from a given starting point (high average path length  $L$ ). (B) Random network topology. In a random network, there is no spatial restriction on the connectivity of the individual nodes, resulting in a network with a low average path length  $L$  but also a low clustering coefficient  $C$ . (C) Small world network topology. Reconnection of even a few of the local connections in a regular network to distal nodes in a random manner results in the emergence of a small world network with a high clustering coefficient  $C$  but a low average path length  $L$ . Reproduced with permission from Dyhrfjeld-Johnsen et al. (2007).

not constant as sclerosis progresses. Rather, it is important to compare the network of interest to a random network of equivalent size, with an equivalent number of edges. Taking the ratios of  $C/C_{\text{random}}$  and  $L/L_{\text{random}}$  normalizes each network and allows a direct determination of the randomness (or lack thereof) of its topological features. Both absolute values and these ratios will be displayed in this chapter, but keep in mind that the ratios are most meaningful.

#### ASSESSMENT OF THE FUNCTIONAL NETWORK

Activity in the functional model network was stimulated by a simulated perforant path input to 5000 granule cells, 10 mossy cells and 50 basket cells in the center of the network, 5 ms after the start of the simulation. No further stimulations were provided for the duration of the simulation. Four different measures were used to quantify the activity of the functional networks:

1. Duration of granule cell firing (the time of the last granule cell action potential in the network minus the time of the first granule cell action potential)
2. Average number of action potentials per granule cell
3. Time until activity of the most distant granule cells from the stimulation point (i.e. latency to full network activity)
4. Synchrony of granule cell action potentials.

To assess synchrony, a previously published coherence measure was used (White et al., 1998; Foldy et al., 2004); details of these measurements can be found in the Methods section of Dyhrfjeld-Johnsen et al. (2007).

#### RESULTS DERIVED FROM THE MODELS

##### IT'S A SMALL WORLD AFTER ALL

Analysis of the dentate gyrus neural network began with examinations of the structural model in the healthy case, also referred to as the control model or the model at 0% sclerosis. Interestingly, the average path length was quite low ( $L = 2.68$ , marked  $\circ$  in Figure 8.4A), despite the large size of the network. This means that any two neurons in the dentate gyrus neural network are separated by fewer than 3 synapses on average. To put this finding into perspective, the average path length of the *C. elegans* nervous system is 2.65, although it has only 282 nodes, a full four orders of magnitude smaller than the dentate! Additionally, the *C. elegans* calculations did not take into account the directionality of the synapses, while the dentate network contained only directed synapses, thus making the similarity of the path lengths even more astounding.

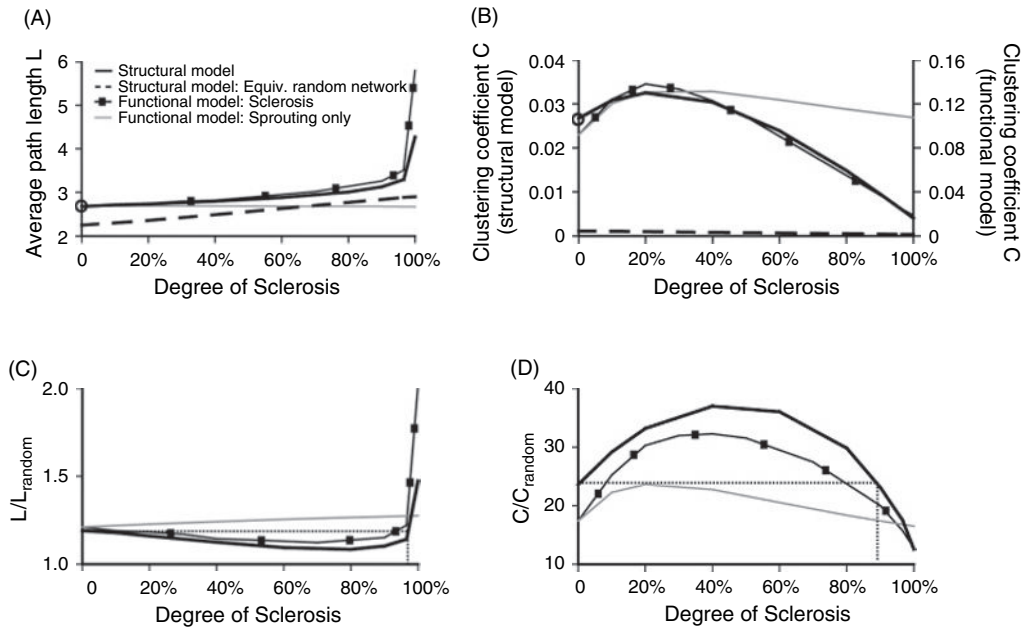


**FIGURE 8.4** Alterations in  $L$  and  $C$  with sclerosis for the various models of the dentate gyrus. (A,C) Changes in average path length  $L$  with sclerosis; (B,D) Changes in clustering coefficient  $C$  with sclerosis. Explanation of symbols in (A) also applies to (B–D). Explanation of symbols in (E) also apply to (F). Black lines in (A–D): Full-scale structural models; black lines in (E–F): isolated excitatory/inhibitory graphs. Black lines with squares: structural model of the functional model with sclerosis; gray lines: structural model of the functional model network with sprouting only. Dashed lines in (A,B): equivalent random graphs of the full-scale structural model. (A,B) Plots of the changes in  $L$  and  $C$  of the various dentate graphs. The  $L$  and  $C$  for the full-scale structural model of the healthy (i.e. at 0% sclerosis) dentate gyrus are marked with '○' on the y-axis. (C,D) Plots for relative  $L$  ( $=L/L_{\text{random}}$ , from panel A) and relative  $C$  ( $=C/C_{\text{random}}$ , from panel B). In (C,D), dotted horizontal lines indicate the relative  $L$  and  $C$  for the full-scale structural model of the healthy dentate graph, while vertical dotted lines indicate the degree of sclerosis where the relative  $L$  exceeds, and the relative  $C$  decreases below the values for the control graph. Note the close similarity of the relative  $L$  and  $C$  changes during sclerosis in the structural model of the functional model network (50 000+ nodes; black lines with squares) and in the full-scale structural model (over 1 million nodes; solid black lines). Note the two y axes in panel (B). Reproduced with permission from Dyhrfjeld-Johnsen et al. (2007).

When the average path length of the control dentate network was compared to a random graph of equivalent size with the same number of connections, an  $L/L_{\text{random}}$  ratio was obtained that was very close to one (1.19; horizontal dotted line in Figure 8.4C). This indicates that the control dentate graph is extremely well-connected globally, so well in fact, that the average path length is only slightly increased from the case of a random network. At first this seems to indicate that perhaps the neural network of the dentate gyrus simply *is* a random graph. However, calculations of the clustering coefficient and comparisons to the clustering of an equivalent random graph demonstrated that this was not the case at all. In fact, the calculation of the  $C/C_{\text{random}}$  ratio resulted in a remarkably high value ( $C/C_{\text{random}} = 0.026751/0.001135 = 24.7$ ; horizontal dotted line in Figure 8.4D; the absolute value for  $C$  in the control network is marked with a ○ in Figure 8.4B), demonstrating a high degree of local connectivity. Taken together, these data ( $L \sim L_{\text{random}}$  and  $C > C_{\text{random}}$ ) indicate that the dentate gyrus is a small world network.

#### SCLEROSIS ENHANCES SMALL WORLD TOPOLOGY, THEN TRANSFORMS IT

Following the analysis of the structural characteristics of the control dentate graph, the same calculations were performed during the progression of sclerosis (hillock cell loss combined with mossy fiber sprouting). At first glance, it appeared likely that the small world structure would be destroyed as sclerosis progressed, as a relatively small (4.5%) number of nodes was lost at 100% sclerosis compared to control (48 000 hillock cells are lost out of 1 064 000 total cells), but there was a massive (74%) decrease in the number of connections (953 198 800 links are removed out of a total of 1 287 363 500). This discrepancy is due to the loss of the richly connected hillock mossy cells and interneurons, while the maximal amount of mossy fiber sprouting forms a comparatively small number of new links.

Despite the massive loss of connections from the network as sclerosis progressed, the results of the structural graph calculations revealed that  $L$  was not significantly increased until beyond 90% sclerosis (solid black line in Figure 8.4A).

Furthermore, the  $L/L_{\text{random}}$  ratio actually decreased below the control value during sub-maximal sclerosis (solid black line in Figure 8.4C; control value indicated by horizontal, dotted line in Figure 8.4C), indicating that the graph became *more* globally well connected. Analysis of the clustering coefficient demonstrated quite similar results. The  $C/C_{\text{random}}$  ratio increased and remained above the control value until approximately 90% sclerosis (solid black line in Figure 8.4D; control marked with dotted horizontal line in Figure 8.4D). These data show that there is an enhancement of small world characteristics at sub-maximal sclerosis, with an increase in *both* global and local connectivity.

Beyond 90% sclerosis, the structure of the dentate graph changed dramatically. The absolute value of  $L$  increased rapidly (solid black line in Figure 8.4A) and the  $L/L_{\text{random}}$  ratio increased above the control value at 96.6% sclerosis (vertical dotted line in Figure 8.4C). Additionally, the  $C/C_{\text{random}}$  ratio decreased below the control value at approximately 90% sclerosis (vertical dotted line in Figure 8.4D). Recall that to be considered small world, a network must have both a short path length and a large clustering coefficient. Since the path length greatly increased and the clustering coefficient decreased but remained high compared to an equivalent random network, the network topology transformed from a small world into a more regular network structure (high  $L$ , high  $C$ ). We will show later in this chapter that this biphasic transformation of network architecture (from enhanced small world to a more regular, lattice-like structure) has significant functional consequences. Next, however, we will discuss the mechanisms underlying the topological alterations occurring during sclerosis.

### WHAT CAUSED THE OBSERVED BIPHASIC STRUCTURAL ALTERATIONS?

The two major findings from the previous section were:

1. The healthy dentate gyrus is a small world network, with a low path length and a high clustering coefficient
2. At sub-maximal levels of sclerosis there is a transient enhancement of small world features followed by a transition to a more regular network structure at maximal sclerosis.

While this biphasic transformation of network topology is interesting, the question remains: which factors were the main contributors to the sclerosis-related changes in topology? In order to answer this question, the excitatory and inhibitory parts of the dentate gyrus graph were studied in isolation. In other words, a graph was constructed that contained only nodes and connections corresponding to the excitatory cell types (granule and mossy cells) and a second graph was constructed that contained only nodes representing the inhibitory cell types.

The results obtained from the isolated excitatory graph (solid black lines in Figure 8.5) closely resembled those discussed above from the complete dentate graph (solid black lines in Figure 8.4). Notice that the average path length was quite low until after 90% sclerosis, at which point it rapidly increased. The clustering coefficient also displayed the same biphasic pattern seen in the full graph, with an initial increase followed by a decrease as sclerosis progressed. This finding indicates that the major players in the alteration of network structure are the mossy cells and granule cells (the two excitatory cell types in the model) and, more specifically, the loss of long range connections resulting from mossy cell loss and the addition of new recurrent granule cell connections through mossy fiber sprouting. Since there were two important factors, it was necessary to dissociate them and this was done by considering graphs that incorporated only mossy fiber sprouting, in the absence of hilar cell loss.

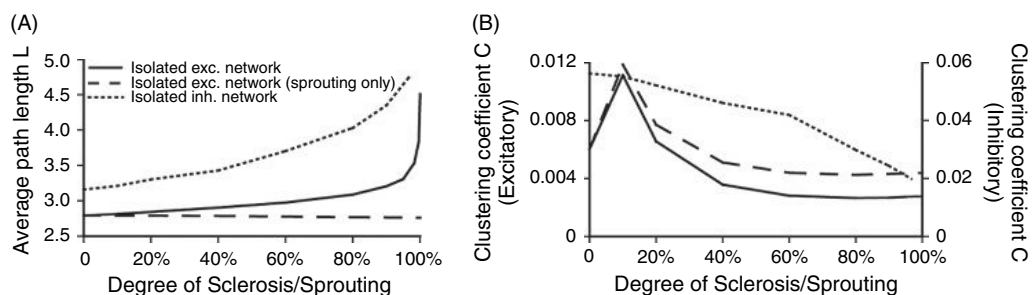


**FIGURE 8.5** Alterations in  $L$  and  $C$  for the isolated excitatory and inhibitory graphs. (A,B) Plots of changes in  $L$  and  $C$  for the isolated excitatory and inhibitory graphs with sclerosis and for the isolated excitatory graphs with sprouting alone (without mossy cell loss). Changes in  $L$  and  $C$  for inhibitory interneurons following hilar interneuron loss: dotted lines; for excitatory cell types (granule cells and mossy cells): solid lines; for mossy fiber sprouting in the absence of concurrent mossy cell loss: dashed lines. Note the two y axes in panel B. Reproduced with permission from Dyhrfjeld-Johnsen et al. (2007).

These ‘sprouting-only’ graphs did not affect the path length in the isolated excitatory graph (dashed line in Figure 8.5A), demonstrating that the surviving long range connections provided by mossy cells are the main determinant of L. On the other hand, the clustering coefficient followed a biphasic pattern in the sprouting-only isolated excitatory graph (dashed line in Figure 8.5B), almost identical to the pattern seen in the graph incorporating both sprouting and hilar cell loss (solid line in Figure 8.3B), indicating that mossy fiber sprouting is the primary determinant of the alterations in C. While these conclusions may at first seem trivial in light of the explanation of small world networks and the diagrams showing how these networks are constructed, we will show later that the unaltered L and the biphasic changes in C in the sprouting-only isolated excitatory network reveal important information about the role of L and C in the functional properties of the dentate gyrus microcircuit.

If the excitatory network contained the primary determinants of the biphasic alterations seen in both L and C, what happened in the isolated inhibitory network? As sclerosis progressed in this network, hilar interneurons were lost, resulting in an increasingly sparse network. This in turn caused a monotonic increase in average path length and a monotonic decrease in the clustering coefficient (dotted lines in Figure 8.5). The most interesting finding in this graph was that at 0% sclerosis the absolute value of the clustering coefficient ( $C = 0.0561$ ) was an order of magnitude higher than in the isolated excitatory graph ( $C = 0.0060$ ). This result demonstrates an effect of the highly interconnected nature of inhibitory interneuronal circuits.

To summarize, the results above show that there are two primary determinants to the biphasic alterations in network topology seen during sclerosis. The most important factor during sub-maximal sclerosis is mossy fiber sprouting, as it maintains a high degree of local connectivity and indirectly connects granule cells to surviving mossy cells. As sclerosis becomes more severe, however, the main factor influencing network topology switches to the loss of the hilar cells and specifically the mossy cells. The increased local connectivity created by mossy fiber sprouting is insufficient to compensate for the massive loss of long distance connections normally provided by mossy cells. Long distance connections disappear, the average path length rises dramatically and the network transforms from a small world into a more regular, lattice-like structure.

### NETWORK EXCITABILITY CHANGES DURING SCLEROSIS

The structural changes we have described thus far are quite intriguing and this is the first time that a mammalian microcircuit has been characterized in a graph where each neuron is represented as a single node. However, understanding the full meaning of the structural alterations is difficult without experiments demonstrating how the structural changes affect the activity of the network. To this end, the activity in all of the network architectures we have described thus far was analyzed using the 1:20 scale functional model of the dentate gyrus described previously. The results of these simulations give keen insight into how structural changes can affect excitability in a network that plays a key role in temporal lobe epilepsy, insight that cannot be gleaned from experimental approaches where structural alterations cannot be dissociated from underlying cellular or synaptic modifications.

### FUNCTIONAL ACTIVITY MIRRORS THE BIPHASIC STRUCTURAL ALTERATIONS

Prior to conducting the functional experiments, it was necessary to verify that the scaled down functional model had the same structural properties as the full-scale dentate graph. A structural graph of the 1:20 scale model was therefore constructed, and the same L and C calculations were performed as described for the full-scale model. The results of the 1:20 scale graph were extremely similar to the full-scale graph and the biphasic properties were retained for both L and C (lines with squares in Figure 8.4; compare with solid black lines in the same panels). Given the success of this verification of structural properties, it was possible to proceed to functional simulations in the 1:20 scale functional dentate model.

The functional model cells were detailed, biophysically realistic single cell models that were able reliably to reproduce the firing properties attributed to them by electrophysiological experiments. Accordingly, a network composed of these cells should reproduce activity patterns recorded from the biological dentate gyrus. Indeed, the healthy non-sclerotic dentate model showed very limited firing in response to a single perforant path input (Figure 8.6A), in accordance with the biological data (Santhakumar et al., 2001). Additionally, as sclerosis progressed, the functional network became increasingly hyperexcitable up to approximately 80% sclerosis (Figure 8.6B–E), again in accordance with *in vitro* measures of epileptiform activity (Rafiq et al., 1995) and in accordance with the structural alterations causing enhanced small world network features. A very interesting phenomenon occurred, however, at levels of sclerosis exceeding 80%. Hyperexcitability

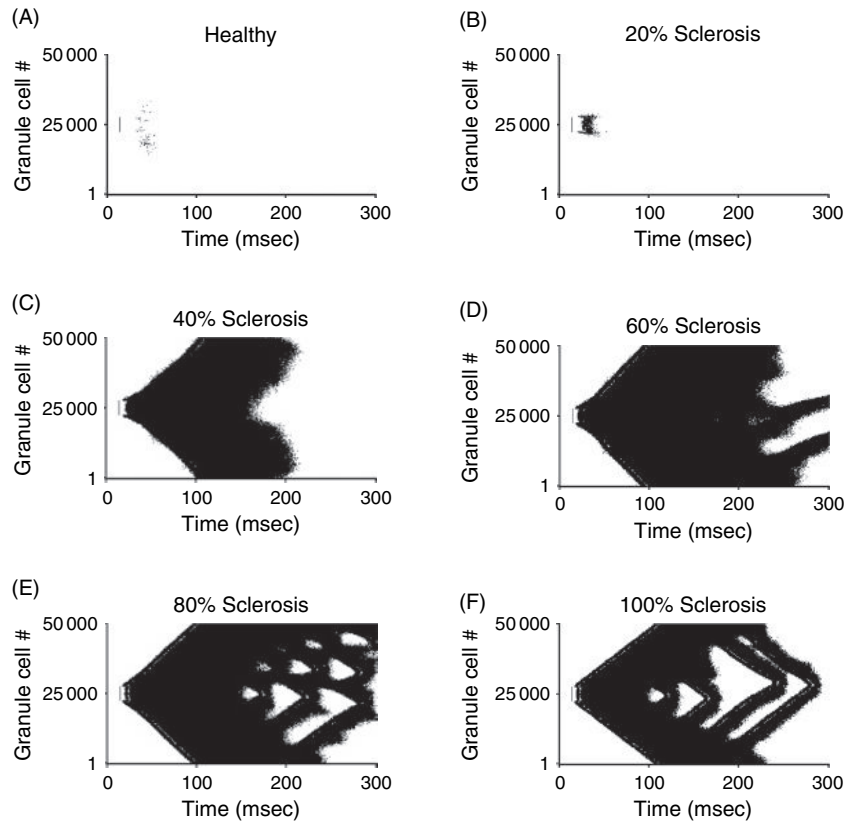


**FIGURE 8.6** Effects of the sclerosis-related topological changes on granule cell activity in functional model networks. (A–F) Raster plots of the first 300 ms of action potential discharges of granule cells in the functional model network (Granule cells no. 1–50 000, plotted on the y-axis) at increasing degrees of sclerosis. Network activity was initiated by a single stimulation of the perforant path input to granule cells no. 22 500 to 27 499 and to 10 mossy cells and 50 basket cells (distributed in the same area as the stimulated granule cells) at  $t = 5$  ms (as in Santhakumar et al., 2005). Note that the most pronounced hyperactivity was observed at sub-maximal (80%) sclerosis (for quantification, see Figure 8.7A–D). Reproduced with permission from Dyhrfjeld-Johnsen et al. (2007).

of the functional model network actually decreased (Figure 8.6F)! The level of sclerosis at which hyperexcitability diminished corresponds perfectly to the point at which the network transformed from a small world structure to a more regular network. Thus, the functional network followed the same biphasic pattern that was seen in the structural network and the functional effects were solely due to the structural network alterations. Interestingly, network dynamics were also affected by structural changes; a relatively uniform pattern of granule cell activity (from 40 to 60% sclerosis; Figure 8.6C,D) transformed into a pattern with distinct waves of activity (from 80% to 100% sclerosis; Figure 8.6E,F) that could collide and mutually annihilate (Netoff et al., 2004; Roxin et al., 2004).

Quantifications of the changes in activity can be seen in Figure 8.7. As described earlier in the chapter, network activity was quantified using four separate measures: maximal activity duration, mean number of action potentials per granule cell, latency to full network activation, and synchrony. The black lines in Figure 8.7A and B show that both the maximal duration of activity and the mean number of action potentials per granule cell increased from 0% to 80% sclerosis and subsequently decreased. Latency to full network activation (solid black line in Figure 8.7C) followed a similar pattern with the fastest full network response at 60% (89.7 msec; latency was not measured for levels of sclerosis below 40%, since the full network did not become active), followed by an increase in latency thereafter (106.2 msec at 100% sclerosis). Synchrony was assessed on both a local (within 0.12 mm along the virtual dentate strip; dashed lines in Figure 8.7D) and a global (up to 2.5 mm separated sampled granule cells; solid lines in Figure 8.7D) scale. Comparisons of the dashed black line representing local synchrony and the solid black line representing global synchrony show that both measures were similar at moderate levels of sclerosis (40–60%). However, global synchrony decreased with more severe ( $>60\%$ ) sclerosis, while local synchrony increased substantially. Again, these data demonstrate that sclerosis leads to a fundamentally transformed

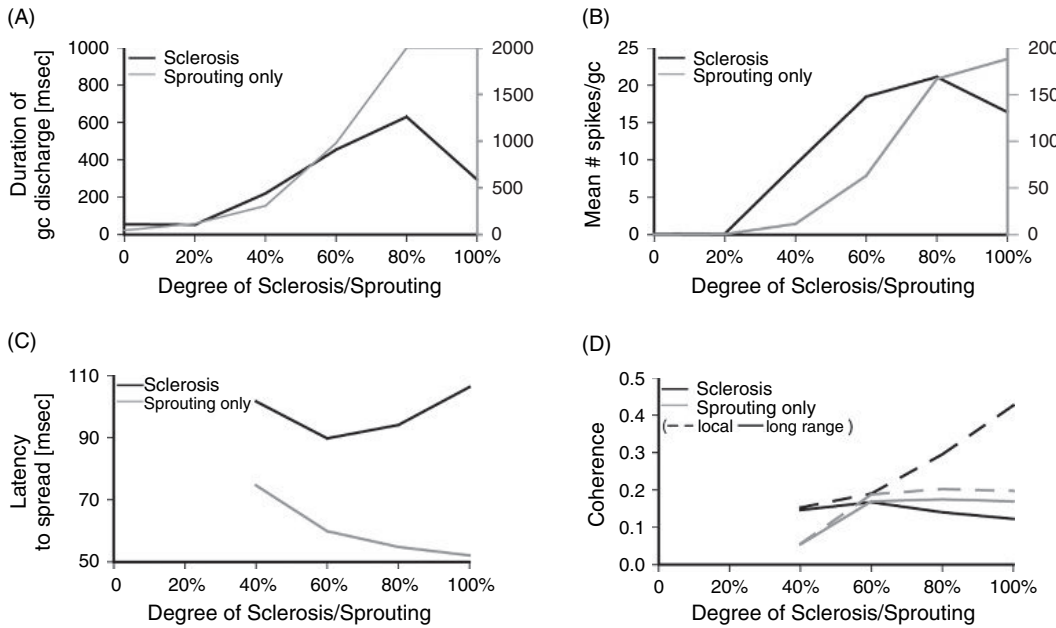


**FIGURE 8.7** Biphasic changes in granule cell firing in the functional model of the dentate gyrus during progressive sclerosis and the lack of biphasic changes when sprouting occurs without hilar neuron loss. Black lines: sclerosis; gray lines: sprouting alone, without concurrent hilar cell loss. (A) Changes in the maximal duration of perforant path stimulation-evoked granule cell firing (for a description of this measure, see Materials and Methods) as a function of sclerosis or sprouting alone (note that granule cell firing persisted beyond 2000 ms at 80% and 100% sprouting in the sprouting only case). (B) Mean number of spikes fired per granule cell with progressive sclerosis or sprouting without cell loss. (C) Latency to firing of granule cells in all 100 bins, in networks with persistent activity in all granule cell bins. (D) Local (dashed line, all-to-all comparison of action potential firing in granule cells no. 25 000–25 999) and long range (solid line, pair-wise comparison of the activity in granule cells no. 25 000–25 999 to granule cells no. 45 000–45 999) coherence of granule cell firing in the time interval of 100 ms to 200 ms for 40–100% sclerosis or sprouting without cell loss. Note that in C and D, results are only shown for 40–100% sclerosis or sprouting, where activity spread to the entire network and persisted beyond 100 ms. Reproduced with permission from Dyhrfjeld-Johnsen et al. (2007).

microcircuit that follows a biphasic pattern of activity caused by biphasic changes in structure seen in the previously described models.

Another possible explanation for the observed changes in activity is that granule cells simply receive different net excitatory and inhibitory conductance at varying levels of sclerosis and the functional network responds to these conductance changes rather than to structural alterations. To test this hypothesis, the net excitatory and inhibitory conductance was measured at each level of sclerosis (Figure 8.8). The black lines in Figure 8.8 indicate that both net excitatory and inhibitory peak conductance declined in a monotonic fashion as sclerosis progressed, a pattern that could not solely reproduce the biphasic changes in activity observed in the model.

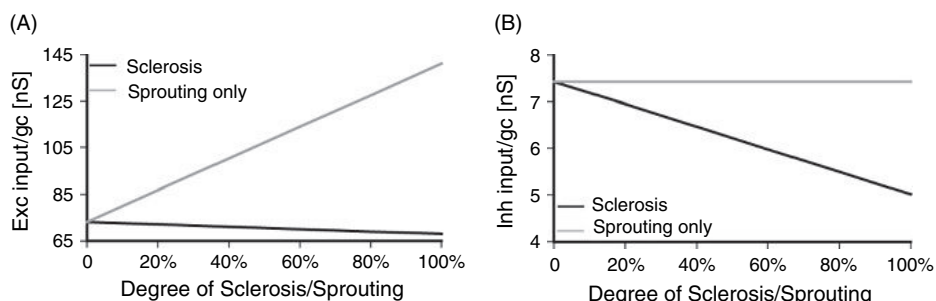


**FIGURE 8.8** Changes to peak conductance onto granule cells in sclerotic or sprouting-only networks. (A,B) Changes in average total peak conductance of excitatory (A) and inhibitory (B) synapses onto the model granule cell during sclerosis or sprouting in the absence of cell loss. Note that the lack of biphasic changes in Figure 8.7A–D, when sprouting took place without hilar cell loss, corresponds to the monotonic increase in excitatory drive seen here in panel A (gray line). Reproduced with permission from Dyhrfjeld-Johnsen et al. (2007).

### NETWORK ACTIVITY IN SPROUTING-ONLY NETWORKS

As was alluded to earlier in the chapter when we discussed the structural alterations that occur in sprouting-only networks, the functional network incorporating sprouting in the absence of cell loss provides interesting insight into the roles of L and C in determining network activity. Recall that in the structural model, sprouting-only networks led to a stable path length, but a clustering coefficient that followed the familiar biphasic pattern as sclerosis progressed. Therefore, sprouting-only experiments were performed using the functional model in order to reveal definitively whether the biphasic change in the clustering coefficient, in the absence of a biphasic change in path length, could have accounted for the biphasic change in network excitability.

Again, prior to this series of experiments, a 1:20 scale structural model of the sprouting-only network was constructed to ensure that the expected changes in both L and C occurred at the smaller scale. Indeed they did, as shown with gray lines in Figure 8.4, where biphasic changes in the clustering coefficient were accompanied by a stable average path length.

The results of the functional sprouting-only networks show obvious differences when compared to those networks incorporating both sprouting and cell loss. Instead of seeing a biphasic pattern of activity with decreased excitability at maximal sclerosis, there was a monotonic increase in excitability as sprouting progressed, even to 100% (Figure 8.9). This result was consistent among all four of the measures used to quantify network activity, as shown in Figure 8.7. Comparing the black and gray lines in Figure 8.7A and B (note the y axis differences), it is clear that the duration of granule cell activity and the mean number of spikes per granule cell increased monotonically in the sprouting-only networks and even exceeded the values calculated for the sprouting and cell loss (sclerotic) networks at equivalent levels of sclerosis. Accordingly,

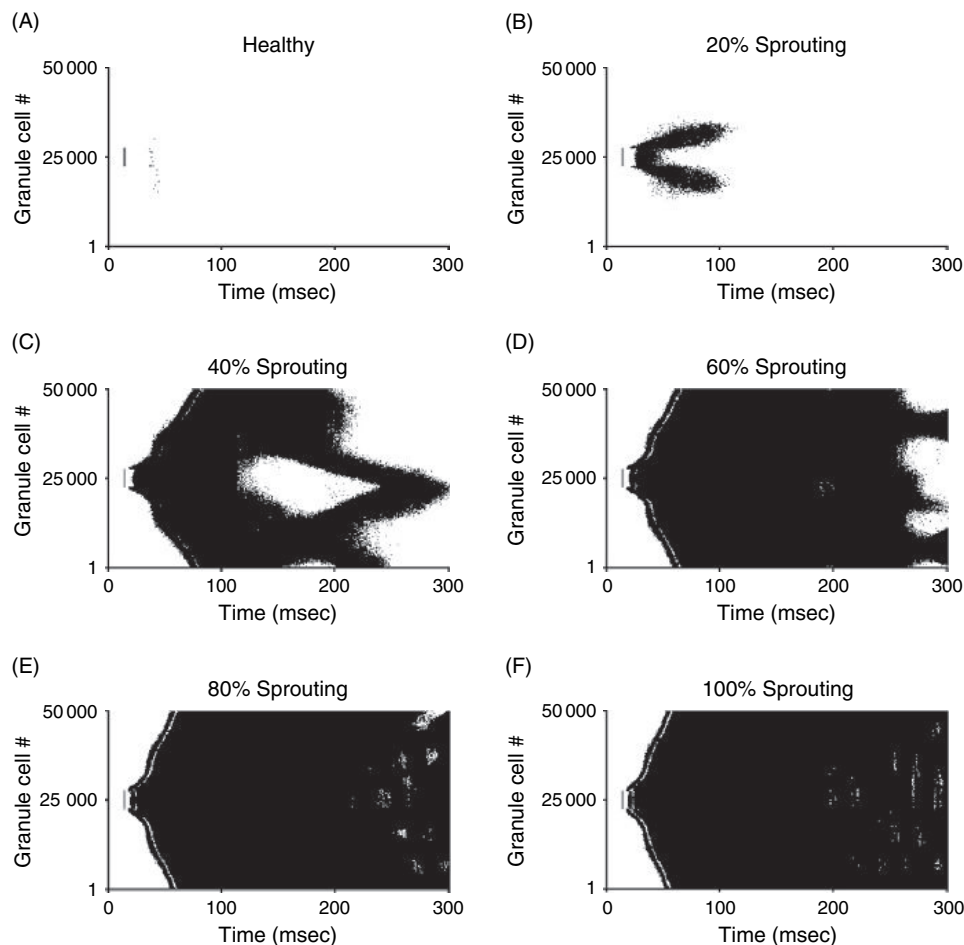


**FIGURE 8.9** Functional effects of sprouting without hilar neuron loss in the functional model network. (A–F) Raster plots of action potential discharges of granule cells in the functional model networks at increasing degrees of mossy fiber sprouting. Network activity was initiated as in Figure 8.6. Note that maximal hyperactivity occurred at maximal sclerosis (for quantification, see Figure 8.7A–D). Reproduced with permission from Dyhrfjeld-Johnsen et al. (2007).

the latency to full network activation decreased as levels of sprouting increased (gray line in Figure 8.7C). The levels of global and local synchrony remained relatively constant throughout the progression of sprouting (Figure 8.7D, gray lines), a finding that contrasts nicely with the notable decrease in global synchrony combined with increased local synchrony in networks with both sprouting and cell loss (Figure 8.7D, black lines). In order better to understand the mechanism underlying the functional activity changes observed in the sprouting-only networks, the net inhibitory and excitatory drive to the granule cells (Figure 8.8, gray lines) was calculated. In this case, the firing properties reflected a monotonic increase in excitatory drive (68 nS increase per granule cell from 0% to 100% sprouting; gray line in Figure 8.8A).

These results demonstrate that biphasic alterations in the clustering coefficient alone cannot cause the biphasic changes in excitability observed in the sclerotic networks. Rather, the combination of sprouting and cell loss is required first to enhance small world network properties and eventually cause the shift to a more regular network structure. These structural network alterations are the key to the biphasic shift in activity seen in the functional model.

#### MODEL LIMITATIONS, CONTROL SIMULATIONS AND TESTS FOR ROBUSTNESS

It is important to consider that no model can ever fully replicate the system that it is modeling. As a result, it is crucial to be certain that results and conclusions derived from models are robust under a number of potentially confounding situations. In the case of the models described in this chapter, a great deal of care was taken to ensure that available biological data were represented and accounted for. However, a number of specific components of the dentate circuit and connectivity were not modeled due to lack of precise data. Additionally, several factors known to change in epilepsy, such as intrinsic cellular and synaptic properties, were purposely omitted from the functional model since the experiments were designed to study structural alterations in isolation. For these reasons, an extensive series of control simulations were performed to test the effects of a wide variety of conditions that were not well constrained by the available experimental data. Controls performed for the structural model were the following:

1. Variations in cell numbers
2. Variations in connectivity estimates
3. Inhomogeneous distribution of neuron densities along the septo-temporal axis
4. Inhomogeneity in connectivity along the transverse axis
5. Altered axonal distributions at the septal and temporal poles (the anatomical boundaries of the dentate gyrus)
6. Offset degrees of sprouting and hilar neuron loss
7. Implementation of a bilateral model of the dentate gyrus including commissural projections.

All of the controls employed for the structural model were also used as controls for the functional model. In addition, the function model had its own set of controls, including:

1. Double inhibitory synaptic strengths
2. Axonal conduction delays
3. Spontaneous instead of stimulation-evoked activity.

In all cases, the results of the control calculations of L and C and the simulations of functional activity strongly supported the main conclusions. Figure 8.10 shows the results of the control simulations for the functional parameters described above. When the functional network was constructed, only two inhibitory cell types were included due to lack of sufficiently detailed data for other inhibitory cell types. This omission effectively reduced the number of inhibitory connections in the network by 50%. In order to be sure that the amount of inhibition did not alter the basic conclusions, the strength of all inhibitory connections were doubled. The results from the network with doubled inhibition (Figure 8.10A<sub>1-3</sub>) demonstrated that the biphasic changes in network activity were still present, indicating that the main conclusions did not rely on the strength of inhibition in the functional network.

Another potential confounding variable in the functional simulations was the absence of an axonal conduction delay in the model cells. Therefore, simulations were performed in which an axonal conduction velocity of 0.25 m/s (Bartos et al., 2002) was incorporated to add distance dependent delays to any connections made outside of the 60 μm bin in which the presynaptic neuron was located. This change resulted in a 0.24 ms delay for each bin separating the pre- and postsynaptic cells, but it had no effect on the results of the simulations. As shown in Figure 8.10B<sub>1-3</sub>, the biphasic changes in network activity persisted in the presence of axonal conduction delays, a finding which further supported the robustness of the main conclusions.

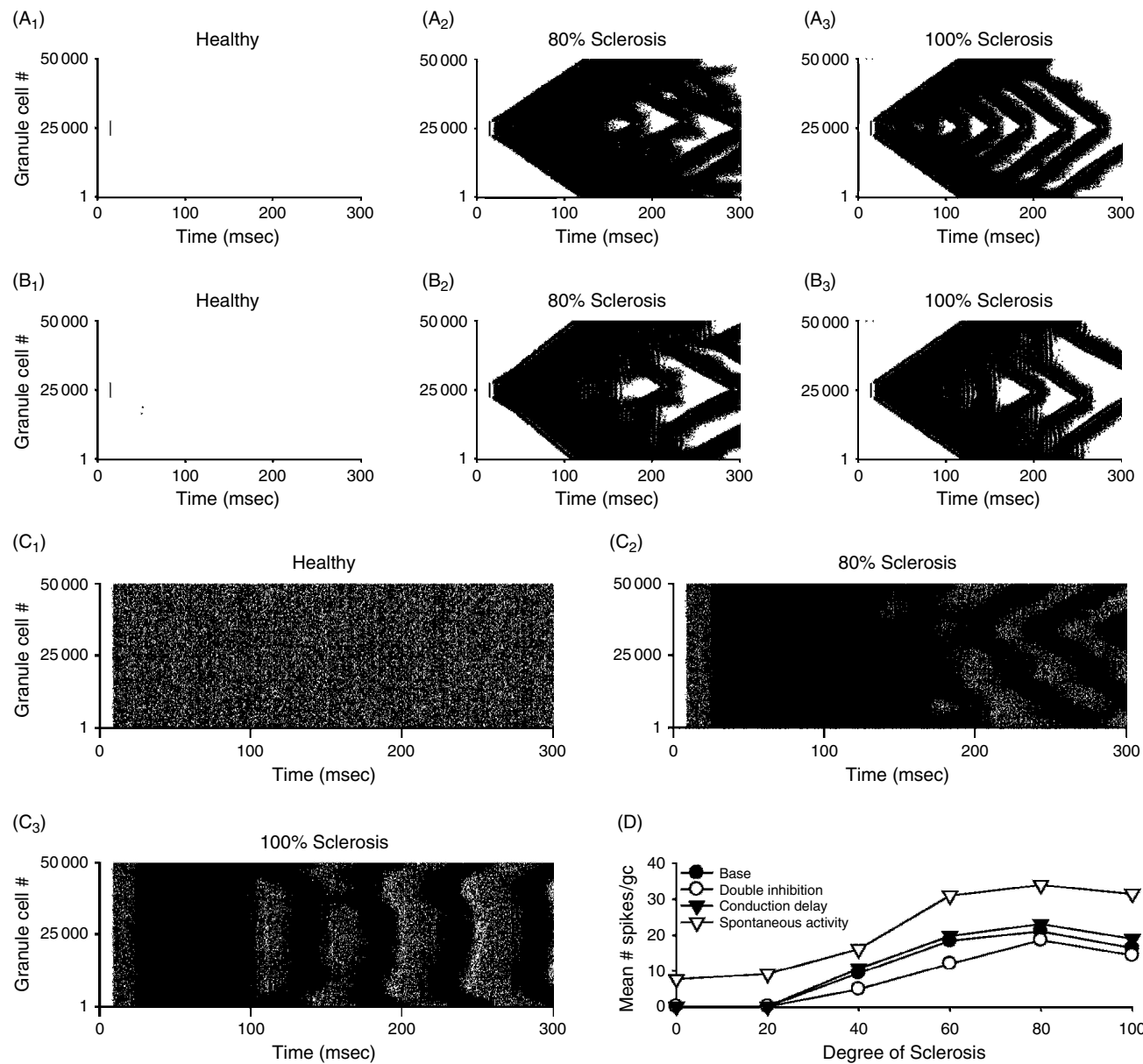


**FIGURE 8.10** Control simulations for functional parameters. (A) Granule cell activity in functional model networks with double inhibition (the maximal conductance of all inhibitory synapses was doubled compared to the base network used in the rest of the simulations). (B) Granule cell activity with axonal conduction delays included in the network (an axonal conduction velocity of 0.25 m/s (Bartos et al., 2002) was implemented in the network). (C) Granule cell activity in functional model networks with spontaneous activity (simulated 10 Hz Poisson-distributed perforant path inputs were applied independently to all granule cells, all basket cells and 100 mossy cells, as a function of increasing degree of sclerosis). A<sub>1</sub>,B<sub>1</sub>,C<sub>1</sub>: 0% sclerosis; A<sub>2</sub>,B<sub>2</sub>,C<sub>2</sub>: 80% sclerosis; A<sub>3</sub>,B<sub>3</sub>,C<sub>3</sub>: 100% sclerosis. (D) Summary plot of granule cell activity for the base model described in the rest of the chapter, and for the three control simulations depicted in this figure. Note that, in spite of large changes in functional parameters, the characteristic biphasic shape of the changes in activity with sclerosis (the drop in activity with the progression of sclerosis from 80 to 100%) was present in all simulations. Reproduced with permission from Dyhrfjeld-Johnsen et al. (2007).

The third control for the functional network tested the dependence of network activity on the perforant path stimulus. Instead of stimulating a selected portion of the cells via a simultaneous perforant path input, spontaneous network activity was simulated by uncorrelated activation of each granule cell, basket cell and 100 evenly distributed mossy cells. This was done by assigning individual perforant path inputs to each cell with Poisson distributed interspike intervals. Again, the biphasic changes in activity were pronounced as sclerosis progressed, indicating that the main conclusions of the study were not dependent on the specific stimulus parameters.

## CONCLUSIONS AND FUTURE DIRECTIONS

The study we have discussed in this chapter contained five major findings:

1. The dentate gyrus is a small world network
2. The small world network characteristics of the dentate gyrus were initially enhanced (i.e. the relative average path length decreases and the relative average clustering coefficient increase) as the dentate endured moderate levels of sclerosis. This enhancement of small world features was followed by a transition to a more regular network structure as L rose rapidly and C declined
3. Experiments in isolated excitatory and inhibitory networks showed that hilar cell loss and mossy fiber sprouting fulfilled different roles in forming the biphasic structural and functional alterations seen in the networks. At sub-maximal levels of sclerosis, mossy fiber sprouting was the main determinant of the enhanced small world features, since it compensated for the loss of long distance connections from mossy cells and connected granule cells to surviving mossy cells. As sclerosis became severe, however, hilar cell loss defined network topology, as mossy fiber sprouting was no longer able to compensate for the loss of extreme numbers of long distance connections. The network took on a more regular network structure due to the rapidly increasing average path length
4. Functional simulations demonstrated that network excitability closely mimicked changes in network topology. Thus, enhanced small world features led to network hyperexcitability, while the transition to a more regular network structure decreased the hyperexcitability of the network at maximal levels of sclerosis
5. Functional analysis of sprouting-only networks revealed that the biphasic change in the clustering coefficient was insufficient to reproduce the biphasic changes in network activity. Therefore, the biphasic change in relative path length, contributed primarily by the loss of hilar neurons, was required for diminished network excitability at maximal sclerosis. This indicates that the survival of a small number of long distance projecting mossy cells was crucial for the maintenance of a hyperexcitable dentate gyrus circuit.

## THE SIGNIFICANCE OF A SMALL WORLD

The dentate gyrus was found to be a small world network, with a high degree of both global and local connectivity. It is so well connected, in fact, that any given neuron is separated from any other neuron by fewer than three total synapses, just as in the *C. elegans* neuronal network (Watts and Strogatz, 1998), despite the many-fold size difference mentioned earlier in this chapter. It is interesting to speculate that perhaps an evolutionary pressure is at work to keep L relatively constant as network size increases. However, many more networks must be examined to test this hypothesis, since the only networks for which L and C values have been determined, with individual neurons considered as distinct nodes, are *C. elegans* (Watts and Strogatz, 1998), culture systems (Shefi et al., 2002) and the dentate gyrus (Dyhrfjeld-Johnsen et al., 2007). Other networks have been studied, but these have used entire brain areas as nodes rather than single cells (Stephan et al., 2000; Sporns and Zwi, 2004; Achard et al., 2006). Studies that describe the small world topology of these inter-area brain connectivity networks (Stephan et al., 2000; Sporns and Zwi, 2004) predict that L is unlikely to increase substantially when further areas of the limbic system are incorporated into the networks, in agreement with the presence of long range connections between limbic areas (Sik et al., 1994; Ceranik et al., 1997; Buzsaki et al., 2004).

The presence of a large number of local and long range connections in a small world network suggests that such a network should be capable of both fast local computations and efficient signal relays to distant parts of the network. Indeed, several studies have found that this is in fact the case; small world networks display fast signal propagation and long range synchronization (Lago-Fernandez et al., 2000; Barahona and Pecora, 2002; Li and Chen, 2003; Masuda and Aihara, 2004). In the networks described in this chapter, a marked enhancement of small world characteristics of the sub-maximally sclerotic dentate gyrus was accompanied by increasing hyperexcitability. The enhancement of small world characteristics was unexpected and counter-intuitive because it took place despite a massive loss of connections from the network, long distance connections in particular. It was made possible, however, by mossy fiber sprouting which compensated for the loss of long range connections and maintained a low path length. This compensation was not entirely innocuous though, as it also caused an increased clustering coefficient, thereby leading to an increased local connectivity and enhanced network hyperexcitability, very serious and potentially disastrous changes contributing to epileptogenesis.

The functional importance of network topological alterations during hippocampal sclerosis and epileptogenesis was perhaps best demonstrated by the surprising decrease of hyperexcitability at maximal sclerosis. This decrease took place when the network transitioned from an enhanced small world topology to a more regular structure due to the loss of the

final hilar cells and their long range connections. This finding not only supports the important role of structural alterations in determining functional network activity, but it is in agreement with experimental observations in both epileptic animals and humans. Indeed, no studies that quantified hilar cell loss in animal models of epilepsy ever reported 100% cell loss (Cavazos and Sutula, 1990; Cavazos et al., 1994; Leite et al., 1996; Buckmaster and Dudek, 1997; Matherne et al., 1997; Buckmaster and Jongen-Relo, 1999; Gorter et al., 2001; van Vliet et al., 2004; Zappone and Sloviter, 2004). Additionally, in surgically removed specimens from pharmacologically intractable human temporal lobe epilepsy patients (Gabriel et al., 2004), cell counts showed that only approximately 80% of hilar cells were lost, even in patients with severe sclerosis (Blumcke et al., 2000). This finding coincides perfectly with the period of maximal hyperexcitability in the functional model networks, observed at 80% sclerosis.

### WHERE DO WE GO FROM HERE?

The experiments described in this chapter provide a clear message that structural alterations in disease states are very important for determining the function of neural networks. Unfortunately, the exact structural changes that occur in many pathological states such as epilepsy are as yet unknown. For example, recent evidence indicates that local connection probability in various brain areas may be modified by intra-class correlations (Yoshimura and Callaway, 2005; Yoshimura et al., 2005) and over-representation of small network motifs (Milo et al., 2002; Reigl et al., 2004; Sporns and Kotter 2004; Song et al., 2005). While no direct evidence is present to implicate such factors in the dentate gyrus, it is likely that unknown structural alterations have a significant impact on network activity. Computational modeling studies provide an excellent tool for determining what the probable result of a wide variety of structural alterations could be. Subsequent animal model experiments could then be carried out to look for the most likely structural alterations predicted by the computation models. In an example of this type of approach, Morgan and Soltesz (2006) have studied probable connectivity patterns within the recurrent granule cell network that results from mossy fiber sprouting. Their results indicate that the presence of a small number (less than 5%) of granule cells with increased connectivity (approximately 5 times the average number of connections) could serve as hubs and strongly promote hyperexcitability within the dentate gyrus network. Interestingly, this finding is supported by the presence, in epileptic rats, of a small percentage of granule cells that have basal dendrites (Spigelman et al., 1998) and which receive a vast number of additional mossy fiber contacts (Buckmaster and Thind, 2005). Computational modeling studies provide the best way of isolating structural changes from intrinsic cellular and synaptic changes that occur simultaneously in virtually all pathological states. Therefore modeling will continue to be very important for understanding the functional role of structural alterations in epilepsy and many other neurological disorders.

### ACKNOWLEDGMENTS

The authors would like to thank Dr Jonas Dyhrfjeld-Johnsen for his helpful comments on the chapter and his contributions to the research discussed here. This work was funded by NIH grant NS35915 to IS and UCI MSTP to RM.

### REFERENCES

- Achard, S., Salvador, R., Whitcher, B., Suckling, J. and Bullmore, E. (2006). A resilient, low-frequency, small-world human brain functional network with highly connected association cortical hubs. *J Neurosci* 26:63–72.
- Acsady, L., Kamondi, A., Sik, A., Freund, T. and Buzsaki, G. (1998). GABAergic cells are the major postsynaptic targets of mossy fibers in the rat hippocampus. *J Neurosci* 18:3386–3403.
- Acsady, L., Katona, I., Martinez-Guijarro, F.J., Buzsaki, G. and Freund, T.F. (2000). Unusual target selectivity of perisomatic inhibitory cells in the hilar region of the rat hippocampus. *J Neurosci* 20:6907–6919.
- Albert, R., Jeong, H. and Barabasi, A.L. (1999). Internet – Diameter of the World-Wide Web. *Nature* 401:130–131.
- Ascoli, G.A. and Atkeson, J.C. (2005). Incorporating anatomically realistic cellular-level connectivity in neural network models of the rat hippocampus. *Biosystems* 79:173–181.
- Babb, T.L., Pretorius, J.K., Kupfer, W.R. and Brown, W.J. (1998). Distribution of glutamate-decarboxylase-immunoreactive neurons and synapses in the rat and monkey hippocampus – light and electron-microscopy. *J Comp Neurol* 278:121–138.
- Barabasi, A.L., Albert, R. and Jeong, H. (2000). Scale-free characteristics of random networks: the topology of the World-Wide Web. *Physica A* 281:69–77.

- Barahona, M. and Pecora, L.M. (2002). Synchronization in small-world systems. *Phys Rev Lett* 89:054101.
- Bartos, M., Vida, I., Frotscher, M., Geiger, J.R.P. and Jonas, P. (2001). Rapid signaling at inhibitory synapses in a dentate gyrus interneuron network. *J Neurosci* 21:2687–2698.
- Bartos, M., Vida, I., Frotscher, M. et al. (2002). Fast synaptic inhibition promotes synchronized gamma oscillations in hippocampal interneuron networks. *Proc Natl Acad Sci* 99:13222–13227.
- Bernard, C., Cannon, R.C., Ben-Ari, Y. and Wheal, H.V. (1997). Model of spatio-temporal propagation of action potentials in the Schaffer collateral pathway of the CA1 area of the rat hippocampus. *Hippocampus* 7:58–72.
- Blasco-Ibanez, J.M., Martinez-Guijarro, F.J. and Freund, T.F. (2000). Recurrent mossy fibers preferentially innervate parvalbumin-immunoreactive interneurons in the granule cell layer of the rat dentate gyrus. *Neuroreport* 11:3219–3225.
- Blumcke, I., Suter, B., Behle, K. et al. (2000). Loss of hilar mossy cells in Ammon's horn sclerosis. *Epilepsia* 41 Suppl 6:S174–180.
- Boss, B.D., Peterson, G.M. and Cowan, W.M. (1985). On the number of neurons in the dentate gyrus of the rat. *Brain Res* 338:144–150.
- Buckmaster, P.S. and Dudek, F.E. (1997). Network properties of the dentate gyrus in epileptic rats with hilar neuron loss and granule cell axon reorganization. *J Neurophysiol* 77:2685–2696.
- Buckmaster, P.S. and Dudek, F.E. (1999). In vivo intracellular analysis of granule cell axon reorganization in epileptic rats. *J Neurophysiol* 81:712–721.
- Buckmaster, P.S. and Jongen-Relo, A.L. (1999). Highly specific neuron loss preserves lateral inhibitory circuits in the dentate gyrus of kainate-induced epileptic rats. *J Neurosci* 19:9519–9529.
- Buckmaster, P.S. and Thind, K. (2005). Abstract in translational research: basic mechanisms doi:10.1111/j.1528-1167.2005.460801\_14.x. *Epilepsia* 46: 91–131.
- Buckmaster, P.S., Wenzel, H.J., Kunkel, D.D. and Schwartzkroin, P.A. (1996). Axon arbors and synaptic connections of hippocampal mossy cells in the rat *in vivo*. *J Comp Neurol* 366:270–292.
- Buckmaster, P.S., Yamawaki, R. and Zhang, G.F. (2002). Axon arbors and synaptic connections of a vulnerable population of interneurons in the dentate gyrus *in vivo*. *J Comp Neurol* 445:360–373.
- Buzsaki, G., Geisler, C., Henze, D.A. and Wang, X.J. (2004). Interneuron diversity series: circuit complexity and axon wiring economy of cortical interneurons. *Trends Neurosci* 27:186–193.
- Cavazos, J.E. and Sutula, T.P. (1990). Progressive neuronal loss induced by kindling: a possible mechanism for mossy fiber synaptic reorganization and hippocampal sclerosis. *Brain Res* 527:1–6.
- Cavazos, J.E., Das, I. and Sutula, T.P. (1994). Neuronal loss induced in limbic pathways by kindling: evidence for induction of hippocampal sclerosis by repeated brief seizures. *J Neurosci* 14:3106–3121.
- Ceranik, K., Bender, R., Geiger, J.R.P. et al. (1997). A novel type of GABAergic interneuron connecting the input and the output regions of the hippocampus. *J Neurosci* 17:5380–5394.
- Claiborne, B.J., Amaral, D.G. and Cowan, W.M. (1990). Quantitative, three-dimensional analysis of granule cell dendrites in the rat dentate gyrus. *J Comp Neurol* 302:206–219.
- Dyhrfjeld-Johnsen, J., Santhakumar, V., Morgan, R.J., Huerta, R., Tsimring, L. and Soltesz, I. (2007). Topological determinants of epileptogenesis in large-scale structural and functional models of the dentate gyrus derived from experimental data. *J Neurophysiol* 97(2):1566–1587.
- Eubank, S., Guclu, H., Kumar, V.S. et al. (2004). Modelling disease outbreaks in realistic urban social networks. *Nature* 429:180–184.
- Foldy, C., Aradi, I., Howard, A. and Soltesz, I. (2004). Diversity beyond variance: modulation of firing rates and network coherence by GABAergic subpopulations. *Eur J Neurosci* 19:119–130.
- Freund, T.F. and Buzsaki, G. (1996). Interneurons of the hippocampus. *Hippocampus* 6:347–470.
- Frotscher, M., Seress, L., Schwerdtfeger, W.K. and Buhl, E. (1991). The mossy cells of the fascia dentata: a comparative study of their fine structure and synaptic connections in rodents and primates. *J Comp Neurol* 312:145–163.
- Gaarskjaer, F.B. (1978). Organization of mossy fiber system of rat studied in extended hippocampi 1. terminal area related to number of granule and pyramidal cells. *J Comp Neurol* 178:49–71.
- Gabriel, S., Njunting, M., Pomper, J.K. et al. (2004). Stimulus and potassium-induced epileptiform activity in the human dentate gyrus from patients with and without hippocampal sclerosis. *J Neurosci* 24:10416–10430.
- Geiger, J.R.P., Lubke, J., Roth, A., Frotscher, M. and Jonas, P. (1997). Submillisecond AMPA receptor-mediated signaling at a principal neuron-interneuron synapse. *Neuron* 18:1009–1023.
- Gorter, J.A., van Vliet, E.A., Aronica, E. and Lopes da Silva, F.H. (2001). Progression of spontaneous seizures after status epilepticus is associated with mossy fibre sprouting and extensive bilateral loss of hilar parvalbumin and somatostatin-immunoreactive neurons. *Eur J Neurosci* 13:657–669.
- Gulyas, A.I., Miettinen, R., Jacobowitz, D.M. and Freund, T.F. (1992). Calretinin is present in nonpyramidal cells of the rat hippocampus. 1. A new type of neuron specifically associated with the mossy fiber system. *Neuroscience* 48:1–27.
- Gulyas, A.I., Hajos, N. and Freund, T.F. (1996). Interneurons containing calretinin are specialized to control other interneurons in the rat hippocampus. *J Neurosci* 16:3397–3411.
- Halasy, K. and Somogyi, P. (1993). Subdivisions in the multiple gabaergic innervation of granule cells in the dentate gyrus of the rat hippocampus. *Eur J Neurosci* 5:411–429.
- Han, Z.S., Buhl, E.H., Lorinczi, Z. and Somogyi, P. (1993). A high-degree of spatial selectivity in the axonal and dendritic domains of physiologically identified local-circuit neurons in the dentate gyrus of the rat hippocampus. *Eur J Neurosci* 5:395–410.
- Jeong, H., Tombor, B., Albert, R., Oltval, Z.N. and Barabasi, A.L. (2000). The large-scale organization of metabolic networks. *Nature* 407:651–654.
- Katona, I., Acsady, L. and Freund, T.F. (1999). Postsynaptic targets of somatostatin-immunoreactive interneurons in the rat hippocampus. *Neuroscience* 88:37–55.
- Lago-Fernandez, L.F., Huerta, R., Corbacho, F. and Siguenza, J.A. (2000). Fast response and temporal coherent oscillations in small-world networks. *Phys Rev Lett* 84:2758–2761.
- Leite, J.P., Babb, T.L., Pretorius, J.K., Kuhlman, P.A., Yeoman, K.M. and Mather, G.W. (1996). Neuron loss, mossy fiber sprouting, and interictal spikes after intrahippocampal kainate in developing rats. *Epilepsy Res* 26:219–231.
- Li, C. and Chen, G. (2003). Stability of a neural network model with small-world connections. *Phys Rev E Stat Nonlin Soft Matter Phys* 68:052901.

- Li, X.G., Somogyi, P., Tepper, J.M. and Buzsaki, G. (1992). Axonal and dendritic arborization of an intracellularly labeled chandelier cell in the CA1 region of rat hippocampus. *Exp Brain Res* 90:519–525.
- Lin, M. and Chen, T. (2005). Self-organized criticality in a simple model of neurons based on small-world networks. *Phys Rev E Stat Nonlin Soft Matter Phys* 71:016133.
- Margerison, J.H. and Corsellis, J.A. (1966). Epilepsy and the temporal lobes. A clinical, electroencephalographic and neuropathological study of the brain in epilepsy, with particular reference to the temporal lobes. *Brain* 89:499–530.
- Masuda, N. and Aihara, K. (2004). Global and local synchrony of coupled neurons in small-world networks. *Biol Cybern* 90:302–309.
- Matheron, G.W., Babb, T.L., Leite, J.P., Pretorius, K., Yeoman, K.M. and Kuhlman, P.A. (1996). The pathogenic and progressive features of chronic human hippocampal epilepsy. *Epilepsy Res* 26:151–161.
- Matheron, G.W., Bertram, E.H. 3rd, Babb, T.L. et al. (1997). In contrast to kindled seizures, the frequency of spontaneous epilepsy in the limbic status model correlates with greater aberrant fascia dentata excitatory and inhibitory axon sprouting, and increased staining for N-methyl-D-aspartate, AMPA and GABA(A) receptors. *Neuroscience* 77:1003–1019.
- Milo, R., Shen-Orr, S., Itzkovitz, S., Kashtan, N., Chklovski, D. and Alon, U. (2002). Network motifs: simple building blocks of complex networks. *Science* 298:824–827.
- Morgan, R.J. and Soltesz, I. (2006). Abstract in Investigator's Workshop: Annual Meeting of the American Epilepsy Society doi: 10.1111/j.1528–1167.2006.00001\_4.x. *Epilepsia* 47 (s4):18–28.
- Netoff, T.I., Clewley, R., Arno, S., Keck, T. and White, J.A. (2004). Epilepsy in small-world networks. *J Neurosci* 24:8075–8083.
- Nomura, T., Fukuda, T., Aika, Y. et al. (1997a). Distribution of nonprincipal neurons in the rat hippocampus, with special reference to their dorsoventral difference. *Brain Res* 751:64–80.
- Nomura, T., Fukuda, T., Aika, Y. et al. (1997b). Laminar distribution of non-principal neurons in the rat hippocampus, with special reference to their compositional difference among layers. *Brain Res* 764: 97–204.
- Patton, P.E. and McNaughton, B. (1995). Connection matrix of the hippocampal-formation 1. The dentate gyrus. *Hippocampus* 5:245–286.
- Percha, B., Dzakpasu, R., Zochowski, M. and Parent, J. (2005). Transition from local to global phase synchrony in small world neural network and its possible implications for epilepsy. *Phys Rev E Stat Nonlin Soft Matter Phys* 72:031909.
- Rafiq, A., Zhang, Y.F., DeLorenzo, R.J. and Coulter, D.A. (1995). Long-duration self-sustained epileptiform activity in the hippocampal-parahippocampal slice: a model of status epilepticus. *J Neurophysiol* 74:2028–2042.
- Ratzliff, A.H., Santhakumar, V., Howard, A. and Soltesz, I. (2002). Mossy cells in epilepsy: rigor mortis or vigor mortis? *Trends Neurosci* 25:140–144.
- Reigl, M., Alon, U. and Chklovskii, D.B. (2004). Search for computational modules in the *C. elegans* brain. *BMC Biol* 2:25.
- Ribak, C.E., Seress, L. and Amaral, D.G. (1985). The development, ultrastructure and synaptic connections of the mossy cells of the dentate gyrus. *J Neurocytol* 14:835–857.
- Roxin, A., Riecke, H. and Solla, S.A. (2004). Self-sustained activity in a small-world network of excitable neurons. *Phys Rev Lett* 92:198101.
- Santhakumar, V., Ratzliff, A.D., Jeng, J., Toth, and Soltesz, I. (2001). Long-term hyperexcitability in the hippocampus after experimental head trauma. *Ann Neurol* 50:708–717.
- Santhakumar, V., Aradi, I. and Soltesz, I. (2005). Role of mossy fiber sprouting and mossy cell loss in hyperexcitability: a network model of the dentate gyrus incorporating cell types and axonal topography. *J Neurophysiol* 93:437–453.
- Shefi, O., Golding, I., Segev, R., Ben-Jacob, E. and Ayali, A. (2002). Morphological characterization of in vitro neuronal networks. *Phys Rev E Stat Nonlin Soft Matter Phys* 66:021905.
- Sik, A., Ylinen, A., Penttonen, M. and Buzsaki, G. (1994). Inhibitory CA1-CA3-hilar region feedback in the hippocampus. *Science* 265:1722–1724.
- Sik, A., Penttonen, M. and Buzsaki, G. (1997). Interneurons in the hippocampal dentate gyrus: an in vivo intracellular study. *Eur J Neurosci* 9:573–588.
- Song, S., Sjostrom, P.J., Reigl, M., Nelson, S. and Chklovskii, D.B. (2005). Highly nonrandom features of synaptic connectivity in local cortical circuits. *PLoS Biol* 3:e68.
- Soriano, E., Nitsch, R. and Frotscher, M. (1990). Axo-axonic chandelier cells in the rat fascia dentata: Golgi-electron microscopy and immunocytochemical studies. *J Comp Neurol* 293:1–25.
- Spigelman, I., Yan, X.X., Obenaus, A., Lee, E.Y., Wasterlain, C.G. and Ribak, C.E. (1998). Dentate granule cells form novel basal dendrites in a rat model of temporal lobe epilepsy. *Neuroscience* 86:109–120.
- Sporns, O. and Kotter, R. (2004). Motifs in brain networks. *PLoS Biol* 2:e369.
- Sporns, O. and Zwi, J.D. (2004). The small world of the cerebral cortex. *Neuroinformatics* 2:145–162.
- Stephan, K.E., Hilgetag, C.C., Burns, G.A., O'Neill, M.A., Young, M.P. and Kotter, R. (2000). Computational analysis of functional connectivity between areas of primate cerebral cortex. *Philos Trans R Soc Lond B Biol Sci* 355:111–126.
- Sutula, T.P., Hagen, J. and Pitkänen, A. (2003). Do epileptic seizures damage the brain? *Curr Opin Neurol* 16:189–195.
- Traub, R.D., Contreras, D., Cunningham, M.O. et al. (2005a). Single-column thalamocortical network model exhibiting gamma oscillations, sleep spindles, and epileptogenic bursts. *J Neurophysiol* 93:2194–2232.
- Traub, R.D., Pais, I., Bibbig, A. et al. (2005b). Transient depression of excitatory synapses on interneurons contributes to epileptiform bursts during gamma oscillations in the mouse hippocampal slice. *J Neurophysiol* 94:1225–1235.
- van Vliet, E.A., Aronica, E., Tolner, E.A., Lopes da Silva, F.H. and Gorter, J.A. (2004). Progression of temporal lobe epilepsy in the rat is associated with immunocytochemical changes in inhibitory interneurons in specific regions of the hippocampal formation. *Exp Neurol* 187:367–379.
- Watts, D.J. and Strogatz, S.H. (1998). Collective dynamics of 'small-world' networks. *Nature* 393:440–442.
- Wenzel, H.J., Buckmaster, P.S., Anderson, N.L., Wenzel, M.E. and Schwartzkroin, P.A. (1997). Ultrastructural localization of neurotransmitter immunoreactivity in mossy cell axons and their synaptic targets in the rat dentate gyrus. *Hippocampus* 7:559–570.
- West, M.J. (1990). Stereological studies of the hippocampus – a comparison of the hippocampal subdivisions of diverse species including hedgehogs, laboratory rodents, wild mice and men. *Progress in Brain Research* 83: 13–36.
- White, J.A., Chow, C.C., Ritt, J., Soto-Treviño, C. and Kopell, N. (1998). Synchronization and oscillatory dynamics in heterogeneous, mutually inhibited neurons. *J Comput Neurosci* 5:5–16.

- Woodson, W., Nitecka, L. and Benari, Y. (1989). Organization of the gabaergic system in the rat hippocampal-formation – a quantitative immunocytochemical study. *J Comp Neurol* 280:254–271.
- Yoshimura, Y. and Callaway, E.M. (2005). Fine-scale specificity of cortical networks depends on inhibitory cell type and connectivity. *Nat Neurosci* 8:1552–1559.
- Yoshimura, Y., Dantzker, J.L. and Callaway, E.M. (2005). Excitatory cortical neurons form fine-scale functional networks. *Nature* 433:868–873.
- Zappone, C.A. and Sloviter, R.S. (2004). Translamellar disinhibition in the rat hippocampal dentate gyrus after seizure-induced degeneration of vulnerable hilar neurons. *J Neurosci* 24:853–864.

# 9

## MULTIPLE-SCALE HIERARCHICAL CONNECTIVITY OF CORTICAL NETWORKS LIMITS THE SPREAD OF ACTIVITY

MARCUS KAISER

### ABSTRACT

An essential requirement for the representation of functional patterns in complex neural networks, such as the mammalian cerebral cortex, is the existence of stable network activations within a limited critical range. In this range, the activity of neural populations in the network persists between the extremes of quickly dying out, or activating the whole network. Whereas standard explanations for balanced activity involve populations of inhibitory neurons for limiting activity, we observe the effect of network topology on limiting activity spreading. A cluster hierarchy at different levels – from cortical clusters such as the visual cortex at the highest level to individual columns at the lowest level – enables sustained activity in neural systems and prevents large-scale activation as observed during epileptic seizures. Such topological inhibition, in addition to neuronal inhibition, might help to maintain healthy levels of neural activity.

### INTRODUCTION

The nerve fiber network of the mammalian cerebral cortex possesses a modular organization extending across several levels of organization. Using a basic spreading model without inhibitory nodes, we investigated how functional activations of nodes propagate through such a hierarchically clustered network. The simulations demonstrated that persistent and scalable activation could be produced in clustered networks, but not in random networks of the same size. Moreover, the parameter range yielding critical activations was substantially larger in hierarchical cluster networks than in small world networks of the same size. These findings indicate that a hierarchical cluster architecture may provide the structural basis for the stable and diverse functional patterns observed in cortical networks in addition to the functional role of inhibitory neurons.

### CURRENT MODELS FOR BALANCED ACTIVITY

Natural systems operate within a critical functional range, sustaining diverse dynamical states (Bak et al., 1987; Newman, 2005) on the basis of their intricate system architecture. For instance, in neural systems, such as the cerebral cortical networks of the mammalian brain, this critical range is indicated by the fact that initial activations result in various neuronal activity patterns that are neither dying out too quickly, nor spreading across the entire network (Beggs and Plenz, 2003). What are the essential structural and functional parameters that allow complex neural networks to maintain such a dynamic balance? In particular, which factors limit the spreading of persistent neural activity to the whole brain, thus preventing a pathological state resembling epilepsy?

Most current models of neural network dynamics focus on maintaining the right balance of network activation and rest through functional interactions among populations of inhibitory and excitatory nodes (Beggs and Plenz, 2003; Haider

et al., 2006). However, the topology of the networks may also make a significant contribution toward critical network dynamics, even in the absence of inhibitory nodes. Earlier studies at a single level of neural organization had shown that a small world organization of a network of excitatory neurons was related to patterns of synchrony (Masuda and Aihara, 2004) and epilepsy spreading (Netoff et al., 2004; Dyhrfjeld-Johnsen et al., 2007). In our model, we observe spreading phenomena across different levels of the neural network architecture.

### HIERARCHICAL CLUSTER ORGANIZATION OF NEURAL SYSTEMS

It is known from the anatomy of the brain that cortical architecture and connections are organized in a hierarchical and modular way, from cellular microcircuits in cortical columns (Binzegger et al., 2004) at the lowest level, via cortical areas at the intermediate level, to clusters of highly connected brain regions at the global systems level (Hilgetag et al., 2000; Hilgetag and Kaiser, 2004; Sporns et al., 2004). At each level clusters arise, with denser connectivity within than between the modules. This means that neurons within a column, area or area cluster are more frequently linked with each other than with neurons in the rest of the network.

Cluster organization at the global level is, for example, visible in the pattern of corticocortical connectivity between brain areas in the cat (Scannell et al., 1995, 1999). Based on the structural connectivity of anatomical fiber tracts it is possible to distinguish four clusters which closely resemble different functional tasks (Figure 9.1). Cluster organization is also visible at the level of cortical regions, for example, about 30–40% of synapses within visual regions come from distant cortical areas or thalamic nuclei (Young, 2000), the majority of connections runs within a region. Within cortical columns of area 17 of the cat, two-thirds of synapses within layers come from external neurons in different layers (Binzegger et al., 2004). Nonetheless, neurons within one layer are more likely to be connected than neurons within that layer and any other layer.

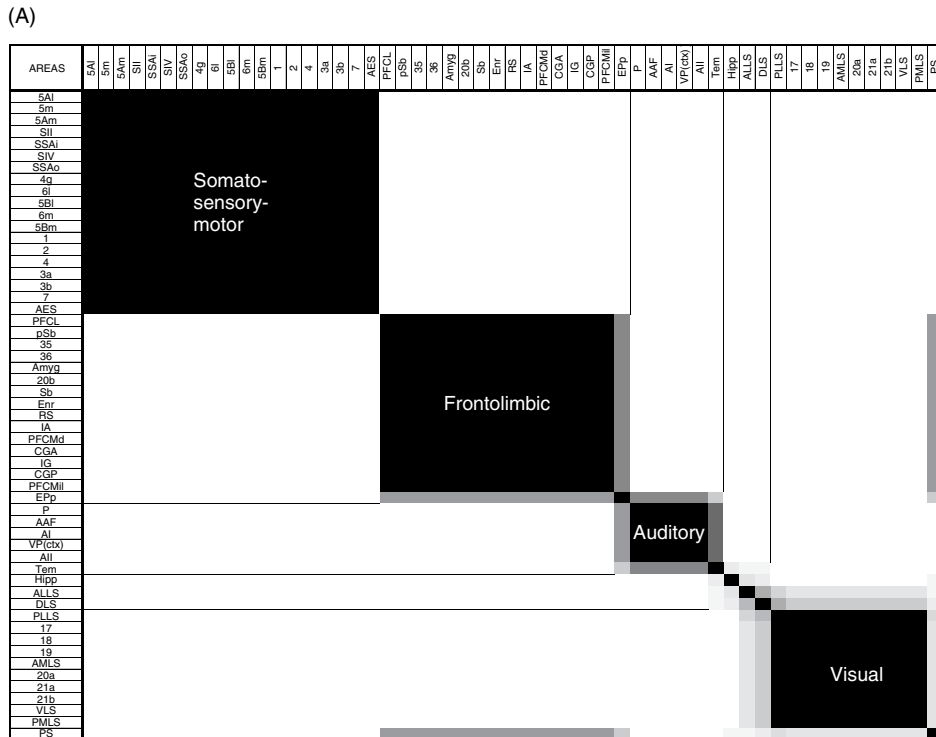


**FIGURE 9.1** Clustered organization of cat cortical connectivity. (A) Cluster count plot, indicating the relative frequency with which any two areas appeared in the same cluster, computed by stochastic optimization of a network clustering cost function (Hilgetag et al., 2000). Functional labels were assigned to the clusters based on the predominant functional specialization of areas within them, as indicated by the physiologic literature. (B) Cat cortical areas are arranged on a circle in such a way that areas with similar incoming and outgoing connections are spatially close. The ordering by structural similarity is related to the functional classification of the nodes, which was assigned as in (A).

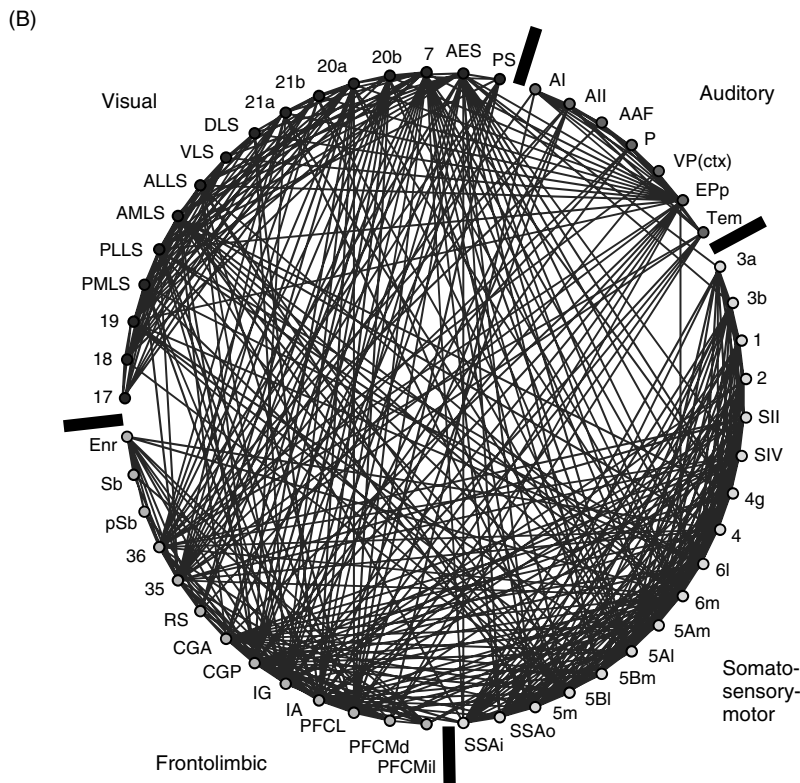


FIGURE 9.1 (Continued)

## SPREADING IN HIERARCHICAL CLUSTER NETWORKS

### MODEL OF HIERARCHICAL CLUSTER NETWORKS

We used a basic spreading model to explore the functional potential of different network topologies, particularly those possessing a clustered organization, for producing persistent yet contained node activations. More recently, spreading analysis has also been applied to cortical networks (Kötter and Sommer, 2000) and to other complex networks with a non-random organization (Pastor-Satorras and Vespignani, 2001; Dezso and Barabási, 2002; Hufnagel et al., 2004).

The present model operates without explicit inhibition, as we were specifically interested in the contributions of different network topologies to maintaining critical activations. This feature also reflects a structural attribute of cortical systems networks (Latham and Nirenberg, 2004) and other complex networks, for instance, social networks (Pastor-Satorras and Vespignani, 2001), that do not possess explicit inhibition, at least at some level of organization.

In our model, individual network vertices represent cortical columns whereas the connectivity follows the different levels of hierarchical organization (Figure 9.2A). Networks were undirected graphs with  $N = 1000$  vertices and  $E = 12\,000$  edges. To create the hierarchical cluster network, 1000 vertices were parcellated into 10 disjoint sets ('clusters'), each consisting of 100 vertices. Each cluster was further divided into 10 'sub-clusters', containing 10 vertices each. The network was wired randomly, such that 4000 edges (one third of the total 12 000 connections) connected vertices within the same sub-clusters, 4000 edges connected vertices within the same clusters and 4000 were randomly distributed over all nodes of the network (Figure 9.2B). The edge density in these networks was 0.025, whereas the clustering coefficient was 0.15. The characteristic path length (2.6), however, was similar to that of random networks (2.5), indicating properties of small world networks (Watts and Strogatz, 1998).

We compared spreading in hierarchical cluster networks with spreading in random and small world benchmark networks with the same number of vertices and edges (see Kaiser et al., 2007, for details). The small world networks with a rewiring probability of  $P = 0.5$  had similar clustering coefficient (0.11) and characteristic path length (2.6) to the hierarchical networks but lacked the characteristic cluster architecture. We also generated Erdős-Rényi random networks (Erdős and Rényi, 1960). More information, including Matlab code for generating hierarchical networks, is available at <http://www biological-networks.org>.

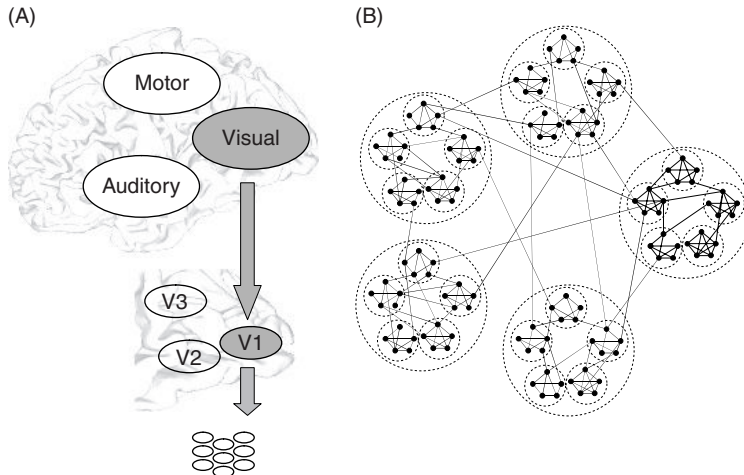


**FIGURE 9.2** (A) The hierarchical network organization ranges from cluster such as the visual cortex to sub-cluster such as V1 to individual nodes being cortical columns. (B) Schematic view of a hierarchical cluster network with five clusters containing five sub-clusters each.

### MODEL OF ACTIVITY SPREADING

We used a simple threshold model for activity spreading where a number  $i$  of randomly selected nodes was activated in the first step. An additional component was the extent of localization of the initial activation  $i_0$ . For initialization,  $i$  ( $i \leq i_0$ ) nodes among the nodes 1 to  $i_0$  were selected randomly and activated in the first time step. The networks nodes were numbered consecutively. Hence, by setting  $i_0$  to, for example, 10, 20 or 100, only nodes in the first sub-cluster, the first two sub-clusters, or the first cluster, respectively, were activated during initialization. Thus,  $i$  determined the number of initially active nodes while  $i_0$  controlled the localization of initial activations, with smaller values resulting in more localized initial activity. At each time step, inactive nodes became activated if at least  $k$  neighbors were activated (neighbors of a node are nodes to which direct connections exist). Activated nodes could become inactive with probability  $\nu$ . As default we used  $k = 6$  and  $\nu = 0.3$ . For determining different spreading patterns, we observed the fraction of activated nodes after 200 time steps.

### SPREADING SIMULATION OUTCOMES

Across different simulation conditions, the hierarchical cluster network showed a larger variety of behaviors than the random or small world networks and it produced persistent yet contained network activity for a wider range of initial activation conditions. Moreover, in contrast to random networks, the activation behavior of the hierarchical cluster network was also influenced by the localization of the initial activity.

Examples exhibiting the behaviors of the different networks are given in Figure 9.3. The figure shows the result of 20 simulations in all three networks when 10% of the nodes were randomly selected for initial activation. In the random

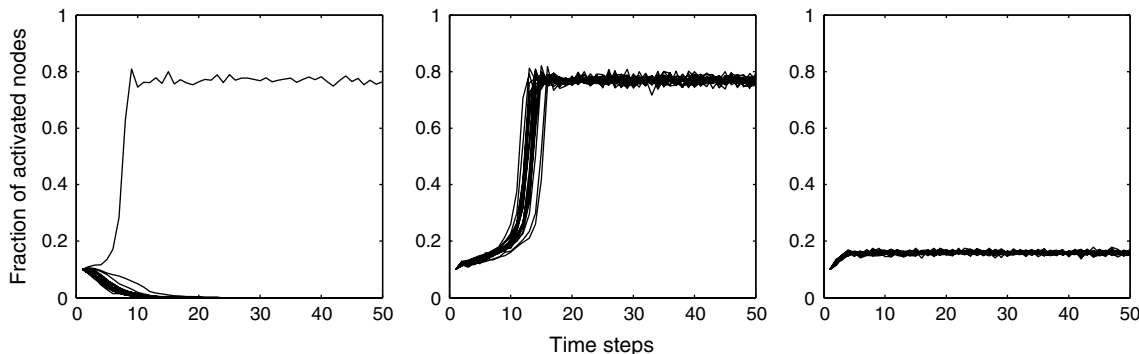


**FIGURE 9.3** Examples for spread of activity in (A) random, (B) small world and (C) hierarchical cluster networks ( $i = 100$ ,  $i_0 = 150$ ), based on 20 simulations for each network.

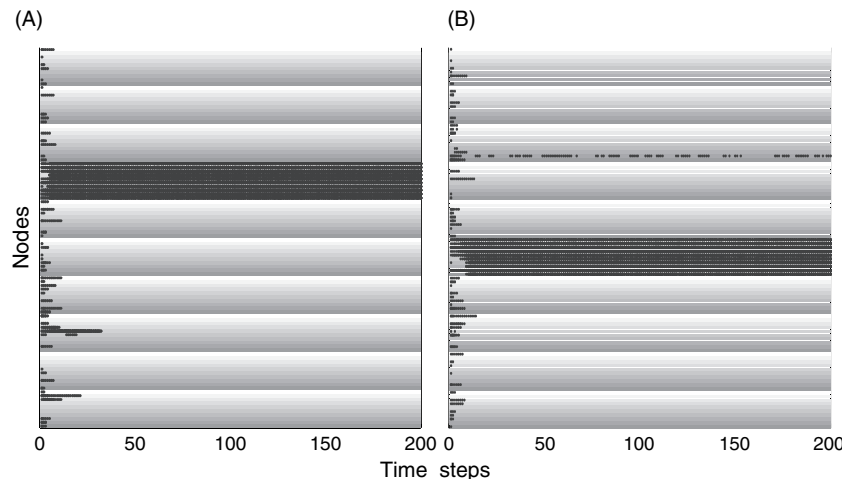


**FIGURE 9.4** Examples for different sustained activity patterns in hierarchical cluster networks ( $i = 90$ ,  $i_0 = 000$ ). Graded gray background shading indicates the 10 sub-clusters within each of the 10 clusters. Black dots represent nodes active at the respective time step. (A) One cluster showing sustained activity; (B) one cluster remaining active with frequent coactivation of one external sub-cluster.

network, activity died out in most cases. In the small world network, spread of activity resulted in almost complete activation. Note, that 100% cannot be reached as active nodes can turn inactive at each step. In contrast to the previous two types of networks, the hierarchical cluster network produced cases in which spreading was limited. Such persistent activation could be sustained with different patterns and varying extent of involved nodes (Figure 9.4).

#### Delay until large-scale activation

In the random network, if activity spread at all, it did so quickly, typically in less than 10 time steps. Even if the initial activity was in the borderline range for all-or-none network activation, not more than 15 time steps were required in any of the cases. This was in contrast to the small world and hierarchically clustered networks, for which a wide range of delay times was observed. For the small world network, delayed spreading depended on whether initial activity was strictly localized ( $i_0 = i$ ). Setting  $i_0 = i = 90$  typically resulted in about 40 time steps for spreading, whereas for  $i_0 = 190$ ,  $i = 90$ , spreading in the small world network appeared similar to that in the random network.

By contrast, for the hierarchically clustered network, spreading to the global level did not arise when the initial activation was too strictly localized. A maximum delay for spreading was achieved by localizing the initial activity within two or three clusters (e.g. delay around 40 steps for  $i_0 = 200$ ,  $i = 90$ ).

#### Robustness of sustained activity cases

We systematically explored the network activation behaviors resulting from different settings of the initial node activation and localization parameters. Both the number of initially activated nodes and their localization had a critical influence on the resulting spreading patterns (Kaiser et al., 2007). Since initial activation is typically small in neural systems, we limited the maximum number of initially active nodes to 250, i.e. one quarter of all network nodes. Persistent contained activity in hierarchical networks was robust for a wide range of initial localization and activation parameters (indicated by gray parameter domain in Figure 9.5). For small world networks, however, parameters needed to be finely tuned in order to yield sustained activity. Thus, hierarchical networks showed sustained activity for a wider range of initial conditions.

The results were also robust in terms of the spreading parameters  $k$  and  $v$ . Using a Monte Carlo approach, for each pair of  $k$  and  $v$ , we generated 20 small world and 20 hierarchical networks. For each network, the dynamics for 1000 randomly chosen parameters  $i$  and  $i_0$  were tested (Figure 9.6). A trial was considered to show sustained activity if less than 50% of the nodes were activated at the end of the simulation. For each pair of spreading parameters  $k$  and  $v$ , the average ratio of cases for which sustained activity occurred, related to the ratio of the gray space in Figure 9.5, was larger for hierarchical cluster networks than for small world networks. The maximal ratio was 67% of the cases for hierarchical cluster networks compared to 30% of the cases for small world networks.

Sustained spreading in hierarchical cluster networks did still occur for different ratios of connectivity within and between clusters and sub-clusters. Reducing the number of connections within clusters or sub-clusters blurred the boundaries of

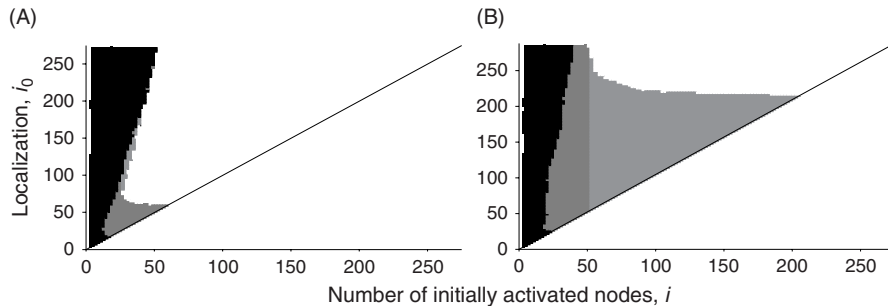


**FIGURE 9.5** Parameter space exploration of the critical range for all combinations of initial activation parameter  $i$  and localization parameter  $i_0$ , based on 1000 test cases. Simulation outcomes are indicated by gray level (black: activity died out; gray: limited spreading; white: complete spreading). (A) Small world network; (B) hierarchical cluster network.

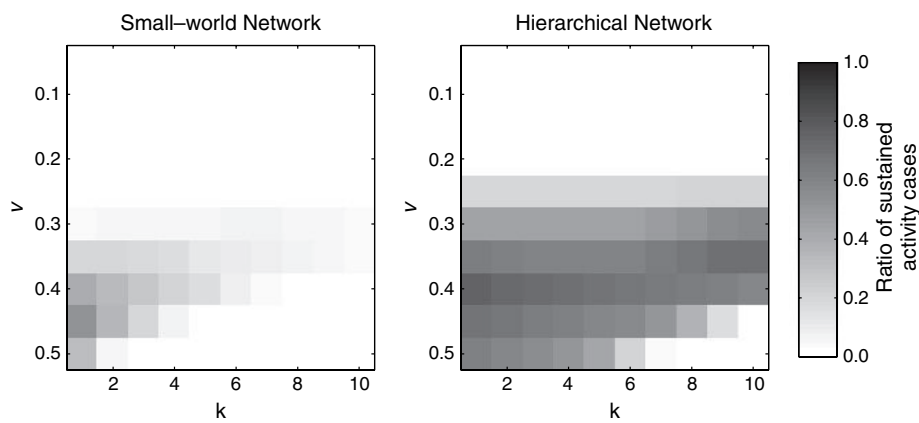


**FIGURE 9.6** Ratio of sustained activity cases depending on the spreading parameters  $k$  (activation threshold) and  $v$  (deactivation probability) for (A) small world and (B) hierarchical cluster networks.

local network modules and reduced the proportion of cases with sustained activity, but the proportion was still larger than that for small world networks. On the other hand, increasing the number of connections within sub-clusters and clusters led to a higher proportion of cases with sustained activity. At the same time, as the total number of edges remained constant, the number of connections between cluster and sub-clusters was reduced. Now, three or more clusters could be persistently activated without a subsequent spread through the whole network (Figure 9.7). In these cases, the limited number of inter-cluster connections formed a bottleneck for activation of the remaining clusters. These results for spreading dynamics are in line with earlier studies on the important role of inter-cluster connections for structural network integrity (Kaiser and Hilgetag, 2004a).

For the above model, activated nodes might stay active for a long time, potentially till the end of the simulation. However, energy resources for sustaining neural network activations are limited in real neural systems. For instance, exhaustion occurs during epileptic seizures, reducing the duration of large-scale cortical activation. Therefore, we also tested the effect of restricting the number of time steps that nodes could be consecutively active from 7 to 1 steps. Sustained network activation could still occur in the hierarchical cluster network, despite different degrees of limiting node exhaustion. Furthermore, sustained activity was largely independent of the exhaustion threshold parameter. The range of parameters for which sustained activity occurred remained similar to that in the previous analyses, with no clear correlation to the number of steps (average ratio of sustained activity cases over all pairs of the spreading parameters was  $0.272 \pm 0.068$ ).

Simulations with similar results could also be performed for networks in which all nodes were represented by integrate-and-fire (IF) neurons (Koch and Laurent, 1999). These simulations also showed easier activation of the hierarchical cluster network compared to the random network, as well as the existence of intermediate states of activation in the hierarchical

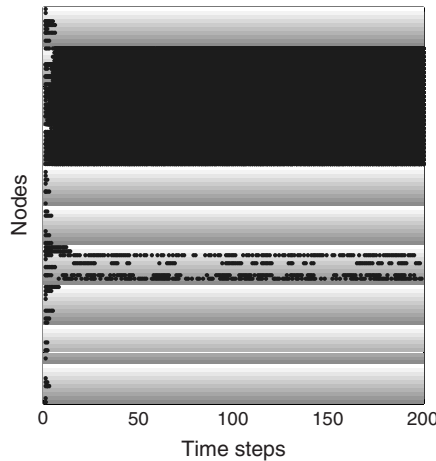


**FIGURE 9.7** Sustained activity in three clusters, without subsequent spreading through the rest of the network, was possible when the number of connections between clusters was reduced. These few inter-cluster connections created a bottleneck for further activity spreading.

cluster, but not the random network (T. Jucikas, private communication). Thus, our results do not appear to depend on the specific neuronal model, but are generally based on the topology of the studied networks.

## DISCUSSION

Our simulations demonstrated a strong impact of network topology on spreading behavior. Clustered networks were more easily activated than random networks of the same size. This was due to the higher density of connections within the clusters, which facilitated local activation. At the same time, the sparser connectivity between clusters prevented the spreading of activity across the whole network. The prevalence of persistent yet contained activity in hierarchical cluster networks was robust over a large range of model parameters and initial conditions.

The present hierarchical cluster model, which reflects the distributed multilevel modularity found in biological neural networks, is different from ‘centralistic’ hierarchical modular networks (with most nodes linked to network hubs) that have been described previously (Ravasz et al., 2002). While developmental algorithms have been suggested for the latter type of network, there are currently no algorithms for producing the hierarchical cluster networks presented here. However, single-level clustered network architectures can be produced by models for developmental spatial growth (Kaiser and Hilgetag, 2004b) or dynamic self-organization of neural networks (Izhikevich et al., 2004) and such models may serve as a starting point for exploring the biological mechanisms for developing multilevel clustered neural architectures.

Present results provide a proof of concept for three points. First, persistent but contained network activation can occur in the absence of inhibitory nodes. This might explain why cortical activity does not normally spread to the whole brain, even though top-level links between cortical areas are exclusively formed by excitatory fibers (Latham and Nirenberg, 2004). While the involvement of inhibitory neurons and other dynamic control mechanisms may further extend the critical range, the present results indicate that the hierarchical cluster architecture of complex neural networks, such as the mammalian cortex, may provide the principal structural basis for their stable and scalable functional patterns. Second, in hierarchical clustered networks, activity can be sustained without the need for random input or noise as an external driving force. Third, multiple clusters in a network influence activity spreading in two ways: bottleneck connections between clusters limit global spreading whereas a higher connection density within clusters sustains recurrent local activity.

## OUTLOOK

It will be important to see how the topological inhibition based on the cluster architecture relates to neuronal inhibition from inhibitory neurons. At this point, we want to outline some predictions from network topology that could be tested experimentally. Here, we use ‘cluster’ to indicate highly-connected parts of the network independent of the level of organization (e.g. column or area level).

### ROLE OF NEURONAL INHIBITION

The most effective way for inhibitory neurons to limit activity spreading from its own cluster to another cluster would be to reduce the activity in excitatory neurons that project to the other cluster.

The most effective way for inhibitory neurons to stop activation of another cluster – independent of the activation of its own excitatory projection neurons to that cluster – would be to establish direct long-range inhibitory projections to that cluster.

### ROLE OF TOPOLOGICAL INHIBITION

An increase in the number of axons between clusters will enhance the likelihood for activity spreading. At the cortical level, this would be visible as changes in white matter volume that could be detected by tract tracing or diffusion tensor imaging.

Another way to increase the probability of activity spreading to other clusters would be a larger connection strength of existing inter-cluster connections.

The model of topological inhibition may have practical implications and may guide future research. For instance, it might be worthwhile to test whether epileptic patients show a higher degree of connectivity between cortical network clusters or other changes in structural connectivity which would facilitate spreading. Such changes might be reflected in certain aspects of functional connectivity (Salvador et al., 2005) or be demonstrated more directly by structural changes in brain connectivity (as, for example, observable by diffusion tensor imaging).

### ACKNOWLEDGMENTS

I thank Claus Hilgetag, Matthias Görner and Bernhard Kramer for helpful comments on this chapter. I also thank Tadas Jucikas for performing control simulations with integrate-and-fire networks. Financial support from the German National Merit Foundation, EPSRC (EP/E002331/1) and Royal Society (RG/2006/R2) is gratefully acknowledged.

### REFERENCES

- Bak, P., Tang, C. And Wiesenfeld, K. (1987). Self-organized criticality: an explanation of the 1/f noise. *Phys Rev Lett* 59:381–384.
- Beggs, J.M. and Plenz, D. (2003). Neuronal avalanches in neocortical circuits. *J Neurosci* 23:11167–11177.
- Binzegger, T., Douglas, R.J. and Martin, K.A.C. (2004). A quantitative map of the circuit of cat primary visual cortex. *J Neurosci* 24:8441–8453.
- Dezso, Z. and Barabási, A.-L. (2002). Halting viruses in scale-free networks. *Phys Rev E* 65:055103.
- Dyhrfjeld-Johnsen, J., Santhakumar, V., Morgan, R.J., Huerta, R., Tsimring, L. and Soltesz, I. (2007). Topological determinants of epileptogenesis in large-scale structural and functional models of the dentate gyrus derived from experimental data. *J Neurophysiol* 97(2):1566–1587.
- Erdős, P. and Rényi, A. (1960). On the evolution of random graphs. *Publ Math Inst Hung Acad Sci* 5:17–61.
- Haider, B., Duque, A., Hasenstaub, A.R. and McCormick, D.A. (2006). Neocortical network activity in vivo is generated through a dynamic balance of excitation and inhibition. *J Neurosci* 26(17):4535–4545.
- Hilgetag, C.C. and Kaiser, M. (2004). Clustered organisation of cortical connectivity. *Neuroinformatics* 2:353–360.
- Hilgetag, C.C., Burns, G.A.P.C., O'Neill, M.A., Scannell, J.W. and Young, M.P. (2000). Anatomical connectivity defines the organization of clusters of cortical areas in the macaque monkey and the cat. *Phil Trans R Soc Lond B* 355:91–110.
- Hufnagel, L., Brockmann, D. and Geisel, T. (2004). Forecast and control of epidemics in a globalized world. *Proc Natl Acad Sci USA* 101:15124–15129.
- Izhikevich, E.M., Gally, J.A. and Edelman, G.M. (2004). Spike-timing dynamics of neuronal groups. *Cereb Cortex* 14:933–944.
- Kaiser, M. and Hilgetag, C.C. (2004a). Edge vulnerability in neural and metabolic networks. *Biol Cybern* 90:311–317.
- Kaiser, M. and Hilgetag, C.C. (2004b). Spatial growth of real-world networks. *Phys Rev E* 69:036103.
- Kaiser, M., Goerner, M. and Hilgetag, C.C. (2007). Criticality of spreading dynamics in hierarchical cluster networks without inhibition. *New J Phys* 9:110.
- Koch, C. and Laurent, G. (1999). Complexity and the nervous system. *Science* 284:96–98.
- Kötter, R. and Sommer, F.T. (2000). Global relationship between anatomical connectivity and activity propagation in the cerebral cortex. *Philos Trans R Soc Lond B* 355:127–134.
- Latham, P.E. and Nirenberg, S. (2004). Computing and stability in cortical networks. *Neural Comput* 16:1385–1412.
- Masuda, N. and Aihara, K. (2004). Global and local synchrony of coupled neurons in small-world networks. *Biol Cybern* 90:302–309.
- Netoff, T.I., Clewley, R., Arno, S., Keck, T. and White, J.A. (2004). Epilepsy in small-world networks. *J Neurosci* 24:8075–8083.
- Newman, M.E.J. (2005). Power laws, pareto distributions and zipf's law. *Contemp Phys* 46:323–351.
- Pastor-Satorras, R. and Vespignani, A. (2001). Epidemic spreading in scale-free networks. *Phys Rev Lett* 86:3200.

- Ravasz, E., Somera, A.L., Mongru, D.A., Oltvai, Z.N. and Barabási, A.-L. (2002). Hierarchical organization of modularity in metabolic networks. *Science* 297:1551–1555.
- Salvador, R., Suckling, J., Coleman, M.R., Pickard, J.D., Menon, D. and Bull-more, E. (2005). Neurophysiological architecture of functional magnetic resonance images of human brain. *Cereb Cortex* 15(9):1332–1342.
- Scannell, J., Blakemore, C. and Young, M. (1995). Analysis of connectivity in the cat cerebral cortex. *J Neurosci* 15(2):1463–1483.
- Scannell, J.W., Burns, G.A., Hilgetag, C.C., O’Neil, M.A. and Young, M.P. (1999). The connectional organization of the cortico-thalamic system of the cat. *Cereb Cortex* 9(3):277–299.
- Sporns, O., Chialvo, D.R., Kaiser, M. and Hilgetag, C.C. (2004). Organization, development and function of complex brain networks. *Trends Cogn Sci* 8:418–425.
- Watts, D.J. and Strogatz, S.H. (1998). Collective dynamics of ‘small-world’ networks. *Nature* 393:440–442.
- Young, M.P. (2000). The architecture of visual cortex and inferential processes in vision. *Spat Vis* 13(2–3):137–146.

PART

III

---

DESTABILIZATION  
OF NEURONAL NETWORKS

---

This page intentionally left blank

# 10

---

## COMPUTER SIMULATIONS OF SODIUM CHANNEL MUTATIONS THAT CAUSE GENERALIZED EPILEPSY WITH FEBRILE SEIZURES PLUS

---

JAY SPAMPANATO AND ALAN L. GOLDIN

### ABSTRACT

Generalized epilepsy with febrile seizures plus (GEFS+) is an autosomal dominant familial syndrome with a complex seizure phenotype. It is caused by mutations in one of three voltage gated sodium channel subunit genes (*SCN1B*, *SCN1A* and *SCN2A*) or the GABA<sub>A</sub> receptor  $\gamma 2$  or  $\delta$  subunit genes (*GBRG2* and *GABRD*). The biophysical characterization of four mutations (T875M, W1204R, R1648H and D1866Y) in *SCN1A*, the gene encoding the CNS voltage-gated sodium channel  $\alpha$  subunit Na<sub>v</sub>1.1, demonstrated a variety of functional channel defects. To determine how these changes in sodium channel function might affect neuronal firing, we used the NEURON simulation software to design a computational spiking neuron model based on the experimentally determined properties of each GEFS+ mutant sodium channel. Despite the different effects on channel function, each mutation altered action potential generation in a manner that was consistent with hyperexcitability. The computational model was utilized to demonstrate further multiple mechanisms by which one mutation (D1866Y) might enhance neuronal excitability through its supralinear dominance over wild-type function in a mixed population.

### INTRODUCTION

Generalized epilepsy with febrile seizures plus (GEFS+) is a familial syndrome encompassing an array of clinical seizure phenotypes. Identification of a GEFS+ family requires diagnosis through multiple generations of febrile seizures that persist beyond 6 years of age and one or more of the following: generalized epilepsies (including absence), myoclonic seizures, atonic seizures and myoclonic-astatic epilepsy (Scheffer and Berkovic, 1997; Singh et al., 1999). GEFS+ is inherited in an autosomal dominant manner with incomplete penetrance (Scheffer and Berkovic, 1997; Singh et al., 1999) and is caused by missense mutations consisting of single amino acid changes in one of three voltage-gated sodium channel genes (*SCN1B*, *SCN1A* and *SCN2A*), or the  $\gamma$ -aminobutyric acid (GABA<sub>A</sub>) receptor  $\gamma 2$  or  $\delta$  subunit genes (*GBRG2* and *GABRD*) (Wallace et al., 1998, 2001; Escayg et al., 2000, 2001; Abou-Khalil et al., 2001; Baulac et al., 2001; Sugawara et al., 2001; Harkin et al., 2002; Annesi et al., 2003; Audenaert et al., 2003; Cossette et al., 2003; Fujiwara et al., 2003; Lossin et al., 2003; Nabbout et al., 2003; Dibbens et al., 2004; Spampanato et al., 2004b; Barela et al., 2006). The majority of known mutations have been found in *SCN1A*, and each individual mutation represents a unique GEFS+ family with the exception of a mutation in *SCN1B* that has been identified in two separate families (Wallace et al., 1998, 2002).

*SCN1A* mutations are not unique to GEFS+. They are also known to result in intractable childhood epilepsy with generalized tonic-clonic seizures (ICEGTC) and severe myoclonic epilepsy of infancy (SMEI), a more severe form of GEFS+ characterized by febrile and afebrile seizures, ataxia and mental retardation (Claes et al., 2001, 2003; Scheffer et al., 2001; Viggiani et al., 2001; Ohmori et al., 2002; Sugawara et al., 2002; Fujiwara et al., 2003; Gennaro et al., 2003; Nabbout et al., 2003; Wallace et al., 2003). However, the majority of SMEI mutations arise *de novo* and are nonsense

mutations that introduce a premature stop-codon causing an early end of protein translation that most likely results in a non-functional sodium channel.

*SCN1A* encodes the central nervous system (CNS) voltage-gated sodium channel  $\alpha$  subunit  $\text{Na}_v1.1$ , which is a 260 kDa transmembrane protein with four homologous domains (DI–DIV), each with six transmembrane segments (S1–S6). The schematic diagram in Figure 10.1A illustrates the homologous arrangement of these domains and segments as well as the relative location of the known GEFS+ mutations.  $\text{Na}_v1.1$  is one of three sodium channel  $\alpha$  subunits (along with  $\text{Na}_v1.2$  and  $\text{Na}_v1.6$ ) responsible for initiation and propagation of action potentials in the adult mammalian CNS. The  $\alpha$  subunit is the primary component of the voltage-gated sodium channel. It contains an ion conducting pore, a selectivity filter that allows primarily sodium ions through the channel, a voltage sensor that responds to changes in membrane potential thereby opening the channel, and an inactivation gate that includes three hydrophobic amino acids (IFM – isoleucine, phenylalanine, methionine) that bind the open channel and inhibit the inward flow of sodium ions. CNS sodium channel  $\alpha$  subunits are typically associated with two of four different  $\beta$  subunits ( $\beta 1$ – $\beta 4$ ) that modulate function and are important for localization.

Voltage-dependent gating is the result of conformational changes initiated by the multiple positively charged residues in the S4 transmembrane segments of each domain, which enable the channel to sense voltage changes across the cell membrane. Sodium channels function by switching between three primary states termed closed, open and inactivated (Catterall, 2000). At rest, the channels are in a closed state from which they can be activated by membrane depolarization, resulting in a rapid transient flow of sodium ions into the cell followed within several milliseconds by inactivation. Inactivation is the result of the binding of the IFM motif located in the DIII–DIV cytoplasmic linker region of the channel to the cytoplasmic region of the ion conducting pore of the channel (Patton et al., 1992; West et al., 1992). Inactivated channels must first return to the closed state before they can be activated again. This process is termed recovery and requires a hyperpolarization of the cell membrane.

A disproportionate number of GEFS+ mutations have been identified in *SCN1A*. These mutations are located throughout the protein, with most of them within or adjacent to transmembrane segments or the pore region of the channel. One hypothesis is that the severity of the seizure disorder that results from a given *SCN1A* mutation correlates with the severity of channel dysfunction caused by that mutation. For example, missense mutations associated with GEFS+ might cause sodium channel dysfunction resulting in mild seizures while nonsense mutations associated with SMEI would cause severe seizures due to complete loss of 50% of the  $\text{Na}_v1.1$  channels (haplo-insufficiency). However, missense mutations have also been observed in patients with SMEI and ICEGTC, and analysis of these patients has not demonstrated a direct correlation between the type of mutation and the severity of the seizure phenotype (Fujiwara et al., 2003; Fujiwara, 2006). To begin to test this hypothesis more directly, we determined the effect of each mutation on sodium channel function using a heterologous expression system. Because the ultimate goal is to determine how these changes affect the function of single neurons and complex neuronal circuits in the brain, we then used computer modeling to predict how the alterations in channel function might affect neuronal activity to produce seizures and epilepsy.

### EFFECTS OF GEFS+ MUTATIONS

To determine how mutations in  $\text{Na}_v1.1$  could produce epilepsy, a disease of synchrony and hyperexcitability, specific missense mutations were individually cloned into an *in vitro* cDNA expression vector containing the full length rat homologue of  $\text{Na}_v1.1$ , which is 98% identical to the human channel at the amino acid level. A complete biophysical characterization of channel function was conducted in the presence of the  $\beta 1$  subunit using the *Xenopus* oocyte expression system (Spamanato et al., 2001, 2003, 2004b). The  $\beta 1$  subunit was included in the analysis of GEFS+ mutations because it is both physiologically relevant (Smith and Goldin, 1998) and mutations in the  $\beta 1$  subunit are known to cause GEFS+ (Wallace et al., 1998, 2002).

Each GEFS+ mutation discussed in this chapter replaces an evolutionarily conserved residue in a different region of the channel (Figure 10.1A). The T875M mutation replaces a threonine at position 875 with a methionine in the S4 segment of DII (Escayg et al., 2000). The W1204R mutation replaces a hydrophobic phenylalanine with a positively charged arginine at position 1204 in the cytoplasmic linker between DII and DIII (Escayg et al., 2001). The R1648H mutation replaces a positively charged arginine with an uncharged histidine at position 1648 in the S4 segment of DIV (Escayg et al., 2000). Finally, the D1866Y mutation replaces a negatively charge aspartate with a tyrosine residue at position 1866 in the cytoplasmic C-terminus of the channel (Spamanato et al., 2004b). Not surprisingly, functional analysis of these different mutations located throughout different structural and functional regions of the channel resulted in unique phenotypes (Figure 10.1).

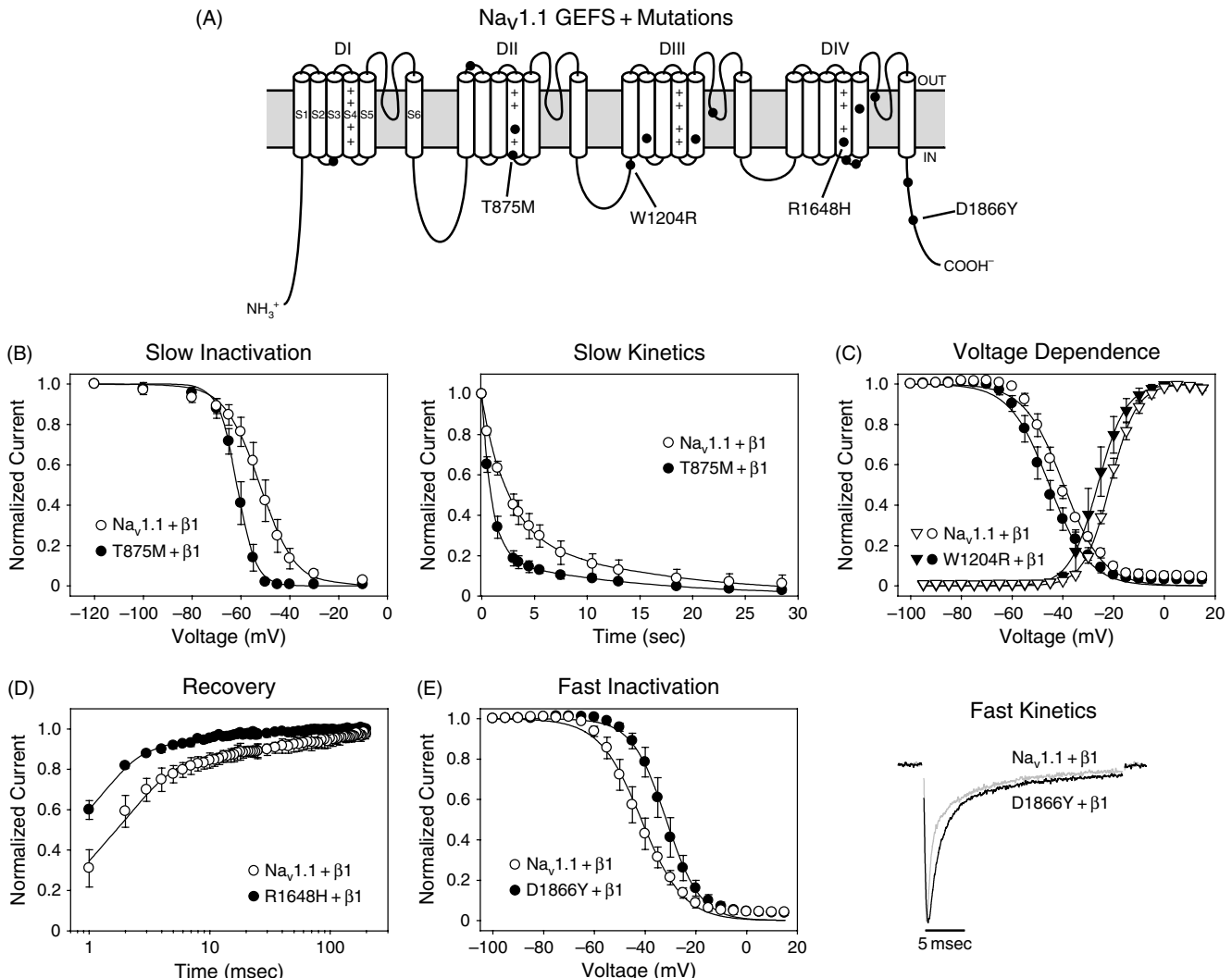


**FIGURE 1O.1** Effects of GEFS+ mutations on sodium channel function. (A) Schematic diagram of the  $\text{Na}_v1.1$  sodium channel  $\alpha$  subunit illustrating the four homologous domains (DI-DIV), each containing six transmembrane segments (S1–S6). The voltage-sensing S4 segment has multiple positively charged amino acids (+). The known GEFS+ mutations (filled circles) are distributed throughout the functional regions of the channel. The four mutations that are discussed in this chapter are labeled in the figure (T875M, W1204R, R1648H and D1866Y). (B) The T875M mutation (filled circles) caused a negative shift in the voltage-dependence of slow inactivation, as illustrated by the shift towards lower values of normalized current at more negative voltages compared to  $\text{Na}_v1.1$  (left panel), and an accelerated rate of entry into the slow inactivated state, illustrated by the faster decrease in normalized current (right panel). (C) The W1204R mutation (filled symbols) caused a negative shift in the voltage-dependence of both activation and inactivation, as illustrated by a left shift in both curves compared to  $\text{Na}_v1.1$ . (D) The R1648H mutation (filled circles) accelerated recovery from inactivation, demonstrated by the faster increase in normalized current compared to  $\text{Na}_v1.1$  during the recovery time after the channels had been fast inactivated. (E) The D1866Y mutation (filled circles) caused a positive shift in the voltage-dependence of inactivation, demonstrated by the right shift in the curve (left panel) and slower inactivation, illustrated by the normalized current recordings (right panel) of D1866Y (black line) and  $\text{Na}_v1.1$  (gray line). In each panel, the symbols represent the means from multiple trials and the error bars represent standard deviations. The lines were calculated as best fits of the data using a two-state Boltzmann equation for voltage-dependence and a double-exponential equation for kinetics. Experimental details are presented in Spampinato et al. (2001, 2003, 2004b).

The T875M mutation was the only mutation exclusively to affect the slow-gated properties of  $\text{Na}_v1.1$  (Spampinato et al., 2001). Most sodium channel activity occurs on a time scale of milliseconds. However, the sodium channel has a second gating mechanism that occurs on the scale of seconds, allowing it to respond to long sustained depolarizations differently than to short depolarizations. The T875M mutation shifted the voltage-dependence of slow inactivation to more negative potentials by a magnitude of approximately 10 mV, which resulted in an increase in the rate of entry into the slow

inactivated state (see Figure 10.1B). These channels slow inactivated up to eightfold faster than wild-type channels and recovered from slow inactivation approximately twofold slower. These effects resulted in an increase in use-dependence, a measure of channel availability during high-frequency depolarizations (Spampanato et al., 2001).

The W1204R, R1648H and D1866Y mutations exclusively altered the fast-gated properties of the sodium channel (Spampanato et al., 2001, 2003, 2004b). The W1204R mutation produced a 5 mV shift towards more negative potentials in the voltage-dependence of both activation and inactivation (see Figure 10.1C). The R1648H mutation produced rapid recovery from fast inactivation, up to threefold faster than the wild-type channel (see Figure 10.1D). Finally, the D1866Y mutation resulted in a 10 mV shift towards more positive potentials of the voltage-dependence of inactivation (see Figure 10.1E). The D1866Y mutation is the only one to have an effect that is amplified in the presence of the  $\beta 1$  subunit, and its effect can be more accurately described as a failure of the  $\beta 1$  subunit to shift inactivation to more negative potentials, a known function of co-expressing the  $\beta 1$  subunit with  $\alpha$  in oocytes (Smith and Goldin, 1998). These three mutations are all predicted to increase channel availability and the R1648H and D1866Y both decrease use-dependence of the channel.

Three of the above mutations (T875M, W1204R and R1648H) have also been separately examined in human  $Na_v 1.1$  expressed heterologously in the human embryonic kidney (HEK) cell line tsA201 (Lossin et al., 2002). In this expression system, each mutation produced an increase in persistent sodium current. Persistent sodium current is defined as a non-inactivating steady state current level that is maintained during a sustained depolarization.  $Na_v 1.1$  typically reaches a fully inactivated state within milliseconds after opening. The T875M, W1204R and R1648H mutations expressed in tsA201 cells maintained between 1% and 5% of the peak transient current levels (Lossin et al., 2002). This effect was not observed in the oocyte expression system, suggesting that there may be differences in channel function based on the expression system. However, neither expression system is a particularly good model for a neuron, so that the ability of either system accurately to replicate the function of  $Na_v 1.1$  in neurons is a matter of debate. No GEFS+ mutation has been expressed in neurons, and neurons typically contain more than one type of sodium channel making it impossible at this time to isolate and record currents through  $Na_v 1.1$  channels alone. However, it is interesting to note that the W1204R mutation produced an identical 5 mV shift in the voltage-dependent gating of the channel in both expression systems. Slow gated properties were not analyzed for T875M in the human channel expressed in tsA201 cells, so a direct comparison for this mutation cannot be made. Likewise, a different recovery protocol was used between the two studies, so it is difficult to compare directly the results for the R1648H mutation.

In addition to the four mutations that are discussed in this chapter, six other GEFS+ mutations (D188V, R859C, V1353L, I1656M, R1657C and A1685V) have been studied in HEK cells or oocytes (Cossette et al., 2003; Lossin et al., 2003; Barela et al., 2006). The effects of these six mutations were also quite varied. None of these mutations increased the non-inactivating persistent current, and their effects included accelerated recovery from slow inactivation (D188V and R1657C), positive shifts in voltage-dependent activation (R859C, I1656M and R1657C), reduction of current density (R859C and R1657C), delayed recovery from slow inactivation (R859C) and complete loss of sodium current in the heterologous system (V1353L and A1685V). The loss of current could have resulted from a non-functional channel or it could have resulted from a failure in protein trafficking to the membrane.

#### APPROACH TO MODELING

It is clear from these results that the GEFS+ mutations have a wide spectrum of effects on sodium channel properties, resulting in a conundrum with respect to neuronal function. Each individual mutation alters the basic biophysical properties of  $Na_v 1.1$ , but the specific effect of one mutation can be diametrically opposed to that of another mutation. For example, different mutations shift the voltage-dependence of activation and inactivation in positive or negative directions, and other sets of mutations accelerate or delay recovery from slow inactivation. Despite these differences, all of the GEFS+ mutations produce similar seizure phenotypes and the same clinical disorder. These differences make predicting the effect of GEFS+ mutations on neuronal function extremely difficult. It is not apparent that each mutation produces a hyperexcitable channel, and even less apparent that each mutation will produce a hyperexcitable neuron or network. To begin to address the question of how these mutations might affect the function of a single neuron, we used a simple computer modeling technique.

Computer modeling was chosen for a number of reasons. As mentioned, sodium channels are responsible for the initiation and propagation of action potentials in neurons. Firing an action potential is a dynamic event during which the individual properties of activation, inactivation, recovery and even slow inactivation combine to produce a certain sodium conductance. The study of the biophysical properties of each mutation identifies their effects on these steady-state

properties individually and exclusive of one another. Construction of a computer model allows us to look at the dynamic interactions of changes in these properties on action potential generation. Furthermore, in cases in which the mutation alters several properties, the computer model allows us to isolate each property individually to understand further the individual and combined effects.

Although the ideal approach would be to study the effects of each mutation in neurons under natural conditions, this technique is not possible at the present time. GEFS+ is rare and often not severe enough to warrant surgery, so there is no available source of human tissue for experimentation. In addition, there are no transgenic animal models of GEFS+, though a number of investigators are actively working to construct such models. Production of a transgenic mouse is complicated, costly and time consuming, so that it is unlikely to be feasible to produce a mouse model for each individual GEFS+ mutation. Furthermore, there is a strong genetic background component to GEFS+. The variety of seizure phenotypes is not always observed in each individual and the disease displays incomplete penetrance. Since it is well known that seizure susceptibility in several established laboratory models of epilepsy differs widely among mouse strains, it will be very difficult to extrapolate from a mouse model to human GEFS+ (Ferraro et al., 1995, 1999, 2002; Schauwecker and Steward, 1997; Royle et al., 1999; Frankel et al., 2001; Yu et al., 2006). Finally, the computer simulations can provide guidance for studying mouse models to determine how the individual mutations produce epilepsy. Another experimental approach would be the heterologous expression of GEFS+ mutant channels in cultured neurons or brain slices through transfection of the cloned gene. This would help to clarify the nature of the biophysical effects of each mutation on channel function by expression in a more native environment. However, this approach is also technically challenging because of the difficulty in successfully transfecting neurons in culture. For all of these reasons, we used the technique of computer modeling to obtain insight into how the GEFS+ mutations cause seizures.

$\text{Na}_v 1.1$  is expressed in principal cells and interneurons throughout the CNS (Brysch et al., 1991; Furuyama et al., 1993; Black et al., 1994; Novakovic et al., 2001; Yu et al., 2006). Within these cells, the channel is localized to the somata and proximal dendritic region (Westenbroek et al., 1989; Kaplan et al., 2001), which places it in an ideal position to affect action potential initiation and propagation. To study the effects of GEFS+ mutations on action potential firing, we constructed Hodgkin-Huxley type conductance-based models of spiking neurons using the NEURON simulation software (Hines and Carnevale, 1997), which is freely available at: <http://www.neuron.yale.edu/neuron/>. A Hodgkin-Huxley type model utilizes the experimentally defined steady-state properties of the channel conductances to predict how they might respond to dynamic conditions such as a membrane depolarization, which occurs repeatedly in real neurons. We constructed single compartment models of neuronal soma that contained  $\text{Na}_v 1.1$  or GEFS+ sodium channels and delayed rectifier potassium channels, the minimum necessary components for firing an action potential. Although the interaction of the wild-type and mutant sodium channels with potassium channels could vary depending on the type of potassium channels that are present, we chose to use a simplified model containing only delayed rectifier potassium channels so that any differences in the firing of action potentials between the mutant and wild-type cells could be attributed exclusively to changes in the sodium channel conductances. Passive parameters similar to the passive properties of hippocampal principal cells (Spruston and Johnston, 1992; Staley and Mody, 1992) were adapted from previous models (Aradi and Soltesz, 2002). The input resistance of the soma was  $100\text{ M}\Omega$  and the resting membrane potential was  $-60\text{ mV}$ . Details concerning the equations and modeling design are presented in Spampinato et al. (2004b).

## COMPUTER SIMULATIONS

After the equations describing the experimental data were defined and assigned to the model neurons, the NEURON software was used to simulate a typical neurophysiology experiment. The model neurons were stimulated by injection of current and the output changes in membrane potential were generated using the computer model. Beginning with a subthreshold stimulus, we gradually increased the amplitude of the current injection until the model neurons fired a single action potential. Using this type of experiment, we found that two of the GEFS+ mutations affected the action potential threshold (Figure 10.2), the minimum current required to stimulate the firing of a single action potential, whereas all four mutations affected the propensity of the model neuron to fire multiple action potentials (Figures 10.3 and 10.4). The results for all four of these mutations were consistent with a hypothesis of hyperexcitability (Spampinato et al., 2004a, 2004b), though similar analysis of a different mutation predicted a reduction in sodium channel availability (Barela et al., 2006).

The only GEFS+ mutation predicted to lower the action potential threshold was the W1204R mutation. This result is not surprising since the biophysical characterization of that mutant channel showed a shift in the voltage-dependence

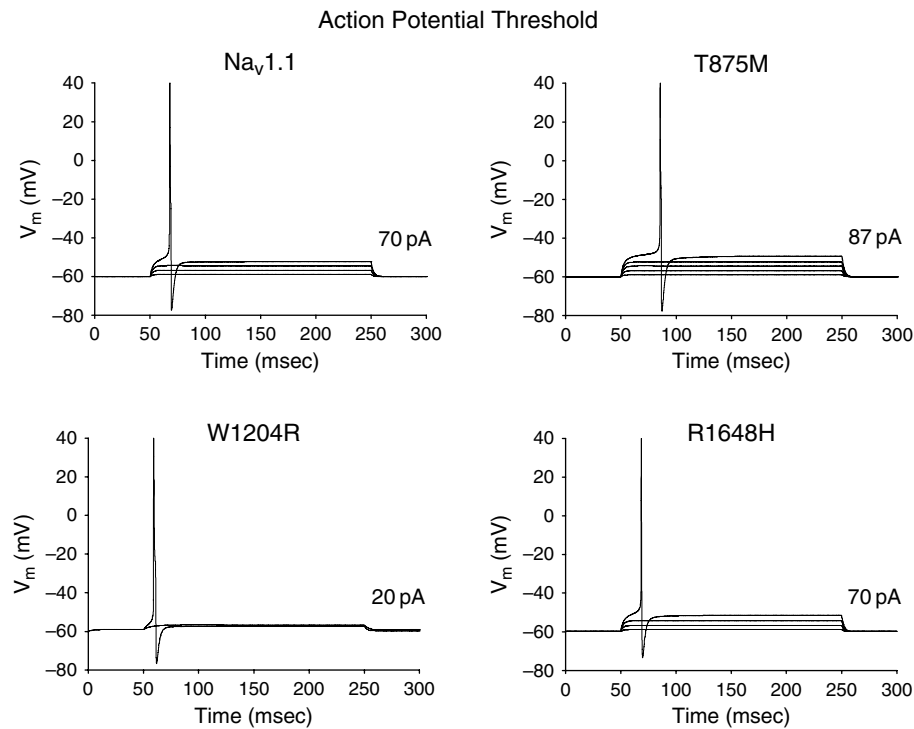


**FIGURE 10.2** Action potential threshold predicted by the model. Action potential threshold was determined using the current clamp function of NEURON. Model neurons expressing either wild-type  $\text{Na}_v1.1$ , T875M, W1204R or R1648H channels were injected with increasing amounts of current starting with a 10 pA stimulation for 200 ms. The intensity of the stimulation was increased by 20 pA until an action potential was recorded. Each step shown is in response to a 20 pA increase in stimulation. The minimum current necessary to elicit an action potential was 70 pA for  $\text{Na}_v1.1$ , 87 pA for T875M, 20 pA for W1204R and 70 pA for R1648H.

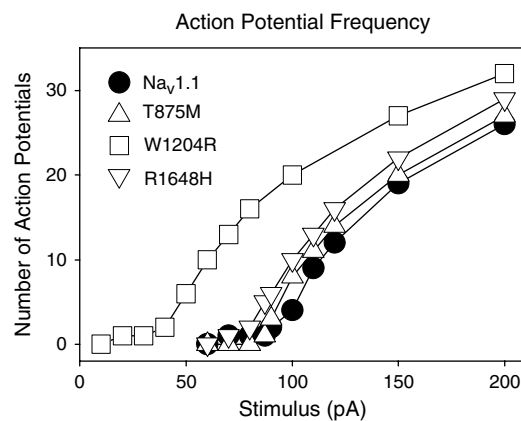


**FIGURE 10.3** Model neurons with the GEFS+ mutant sodium channels fire action potentials at higher frequencies than those with the wild-type channel. Action potential frequency was determined for model neurons expressing either wild-type  $\text{Na}_v1.1$  (circles), T875M (up triangles), W1204R (squares) or R1648H (down triangles) sodium channels. Action potentials were elicited by current injections starting with 10 pA and increasing by 20 pA. The number of action potentials elicited in response to a 200 ms stimulus was counted manually and plotted against the corresponding current injection stimulus.

of activation towards more negative potentials. This shift means that the channel is more sensitive to a depolarizing current injection, similar to those used in the simulations. Although this mutation also caused a similar shift in the voltage-dependence of inactivation, that shift was insufficient to counteract the effect of the shift in activation. In contrast, the T875M mutation increased the action potential threshold of the model neurons. This mutation is unique among the GEFS+ mutations that we analyzed in that it did not alter any of the fast-gated properties of channel function.

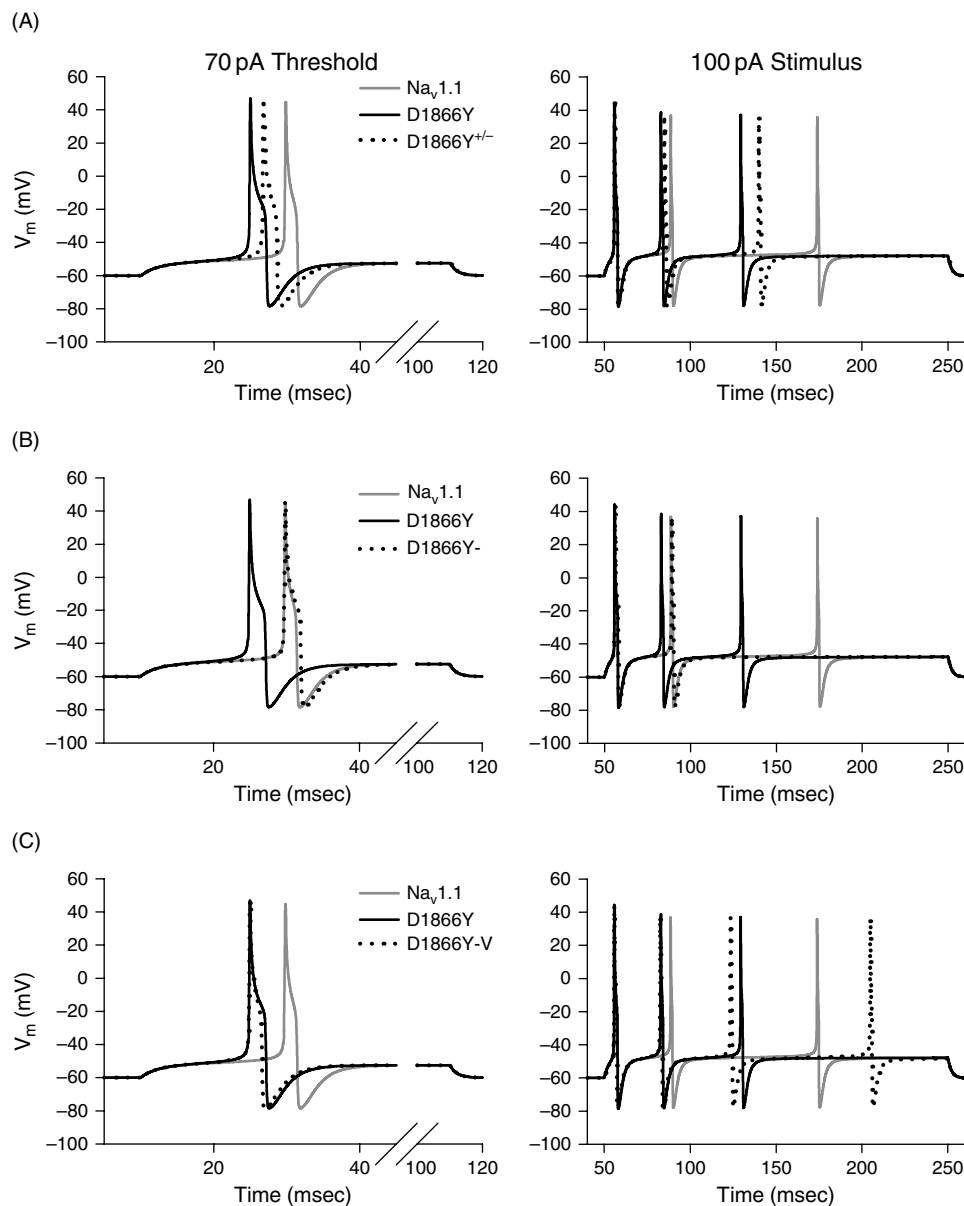


**FIGURE 1O.4** D1866Y mutant channels produce a different type of hyperexcitable model neuron. (A) At a single action potential threshold stimulus (70 pA), the D1866Y mutant model neuron (black line) fired a single action potential with a shorter onset delay than the wild-type  $\text{Na}_v1.1$  model neuron (gray line). When the population of channels was mixed in a 1:1 ratio (D1866Y $^{+/-}$ , black dotted line), the mutant channels displayed a dominant effect, resulting in a shorter onset delay for firing a single action potential. This effect is more pronounced at an increased stimulus intensity of 100 pA, which elicited multiple action potentials. (B) When the delayed kinetics of the D1866Y mutation were modeled independently of the voltage-dependence of inactivation (D1866Y- $\tau$ , black dotted line), the mutant model neuron fired an action potential in response to a 70 pA threshold stimulus with timing that was comparable to that of the wild-type  $\text{Na}_v1.1$  model neuron. When the stimulus intensity was increased to 100 pA, the D1866Y- $\tau$  model neuron still behaved in a manner similar to the wild-type neuron, but it failed to fire a third action potential. (C) When the positive shift in the voltage-dependence of inactivation was modeled independently of the delayed kinetics (D1866Y-V, black dotted line), the mutant model neuron fired a single action potential with a shorter onset delay than the wild-type  $\text{Na}_v1.1$  model neuron (gray line). When the stimulus intensity was increased to 100 pA, the D1866Y-V model neuron produced more rapid action potentials resulting in generation of an additional action potential. These results demonstrate that the positive shift in the voltage-dependence of inactivation was sufficient to decrease the delay for action potential initiation. Reproduced, with permission, from Spampinato et al. (2004b).

Therefore, the increase in action potential threshold must be due to the effects of the mutation on slow gating of the channel. It is likely that the shift in the voltage-dependence of slow inactivation caused some channels to enter into the slow inactivated state before they could participate in the firing of an action potential, effectively reducing the sodium current density of the model neuron prior to injection of current. The model neurons had a resting membrane potential of  $-60\text{ mV}$  and the T875M mutation shifted the voltage-dependence of slow inactivation to potentials more negative than this potential.

The R1648H and D1866Y mutations did not alter action potential threshold, but the D1866Y mutation produced an interesting difference compared to the wild-type channel with respect to the action potential threshold stimulus. Though both the D1866Y mutant and the wild-type model neuron fired a single action potential in response to the same minimum current injection, the D1866Y mutation reduced the delay between stimulus onset and action potential firing. This effect is not immediately obvious from the experimental data. The positive shift in inactivation and delayed rate of fast-inactivation produced by the D1866Y mutation likely resulted in more channels remaining in the closed state immediately following current injection. This would effectively increase the pool of available channels that are ready for activation and firing of an action potential as the neuron is depolarized towards threshold. Therefore, while the threshold itself is not changed, the timing of the action potential is accelerated. This simple modeling experiment helps to demonstrate the fact that firing of an action potential itself is only part of the information that one neuron transmits to the next neuron. The other critical piece of information is the timing between action potentials. A decrease in the delay for firing an action potential could lead to increased synchronization in a network of neurons expressing the D1866Y mutant channels.

All four GEFS+ mutations altered the firing of multiple action potentials when a suprathreshold stimulus was given. The T875M, W1204R and R1648H mutations increased the propensity of the model neurons to fire multiple action potentials (see Figure 10.3), with multiple action potentials in response to a smaller current injection than for the wild-type model neuron. The magnitude of this effect was different for each mutation, with the most severe being W1204R and the least severe being T875M. Although the D1866Y model neuron did not fire more action potentials than the wild-type neuron, this mutation resulted in successive action potentials occurring more quickly following the preceding ones, thus reducing the spike-to-spike interval and effectively increasing the spontaneous firing frequency (see Figure 10.4).

To obtain additional insight into how a GEFS+ mutations might cause seizures, we used the computer model to analyze further the effects of the D1866Y mutation. GEFS+ is an autosomal dominant disorder, which means that affected individuals have a heterozygous mix of mutant and wild-type channels, presumably in a ratio that is approximately 1:1. It is difficult to reproduce this ratio experimentally using a heterologous expression system, but it is very easy to assign any ratio of wild-type and mutant channels to a model neuron. The two significant effects of the D1866Y mutation were to decrease the latency between stimulus onset and action potential generation at threshold, and to decrease the time between action potentials at a higher input stimulus (see Figure 10.4). At the threshold stimulus, the reduced latency to action potential generation was maintained when both mutant and wild-type channels were included in the same model neuron at a ratio of 1:1 ( $\text{D1866Y}^{+/-}$ ). When the stimulus intensity was increased, the D1866Y mutation was dominant and not simply additive, since the  $\text{D1866Y}^{+/-}$  heterozygous neuron behaved more like the mutant model neuron than the wild-type model neuron (see Figure 10.4A).

The D1866Y mutation produced two effects on channel function: a positive shift in inactivation and delayed kinetics of inactivation (see Figure 10.1E). These two effects cannot be separated experimentally, but they can easily be defined separately in the model. To determine which alteration in sodium channel function was responsible for the change in neuronal firing, we constructed model neurons in which the channels had either delayed kinetics of inactivation ( $\text{D1866Y-}\tau$ ) or a positive shift in the voltage-dependence of inactivation ( $\text{D1866Y-V}$ ). When the  $\text{D1866Y-}\tau$  model neuron was activated with a threshold stimulus of  $70\text{ pA}$ , the model neuron fired a single action potential whose timing was identical to that of the wild-type model neuron (see Figure 10.4B). When the stimulus intensity was increased to  $100\text{ pA}$ , the timing of the first and second action potentials was similar for the  $\text{D1866Y-}\tau$  and wild-type model neurons, but the  $\text{D1866Y-}\tau$  model neuron did not fire a third action potential (see Figure 10.4B). In contrast, the model neuron with only the positive shift in the voltage-dependence of inactivation ( $\text{D1866Y-V}$ ) fired an action potential sooner than the wild-type model neuron with a threshold stimulus of  $70\text{ pA}$  (see Figure 10.4C). Therefore, the shift in the voltage-dependence of inactivation was responsible for the major difference between the D1866Y mutant and wild-type model neurons. When the  $\text{D1866Y-V}$  model neuron was stimulated with  $100\text{ pA}$ , it generated action potentials with an even shorter spike-to-spike interval than the D1866Y model neuron, which resulted in the generation of a fourth action potential (see Figure 10.4C). This result indicates that the two changes in sodium channel function, delayed kinetics of inactivation and a positive shift in the voltage-dependence of inactivation, had compensatory effects resulting in the firing of exactly three action potentials at a suprathreshold stimulus.

Because the D1866Y mutation produced a positive shift in the voltage-dependence of inactivation, it was likely that the mutant model neuron would be resilient to inactivation during a subthreshold incoming stimulus that caused sustained resting membrane depolarization. To determine the effects of a positive shift in resting membrane potential, the model neurons were first injected with a subthreshold stimulus, which shifted the resting membrane potential to a more positive voltage, followed by injection of additional current to elicit action potentials. The conditioning stimulus was applied for 0, 20, 40, 60 or 80 ms and the membrane potential was plotted from the start of the stimulus (Figure 10.5). The wild-type  $\text{Na}_v1.1$  model neuron failed to fire an action potential when the subthreshold depolarization was maintained for 60 ms or

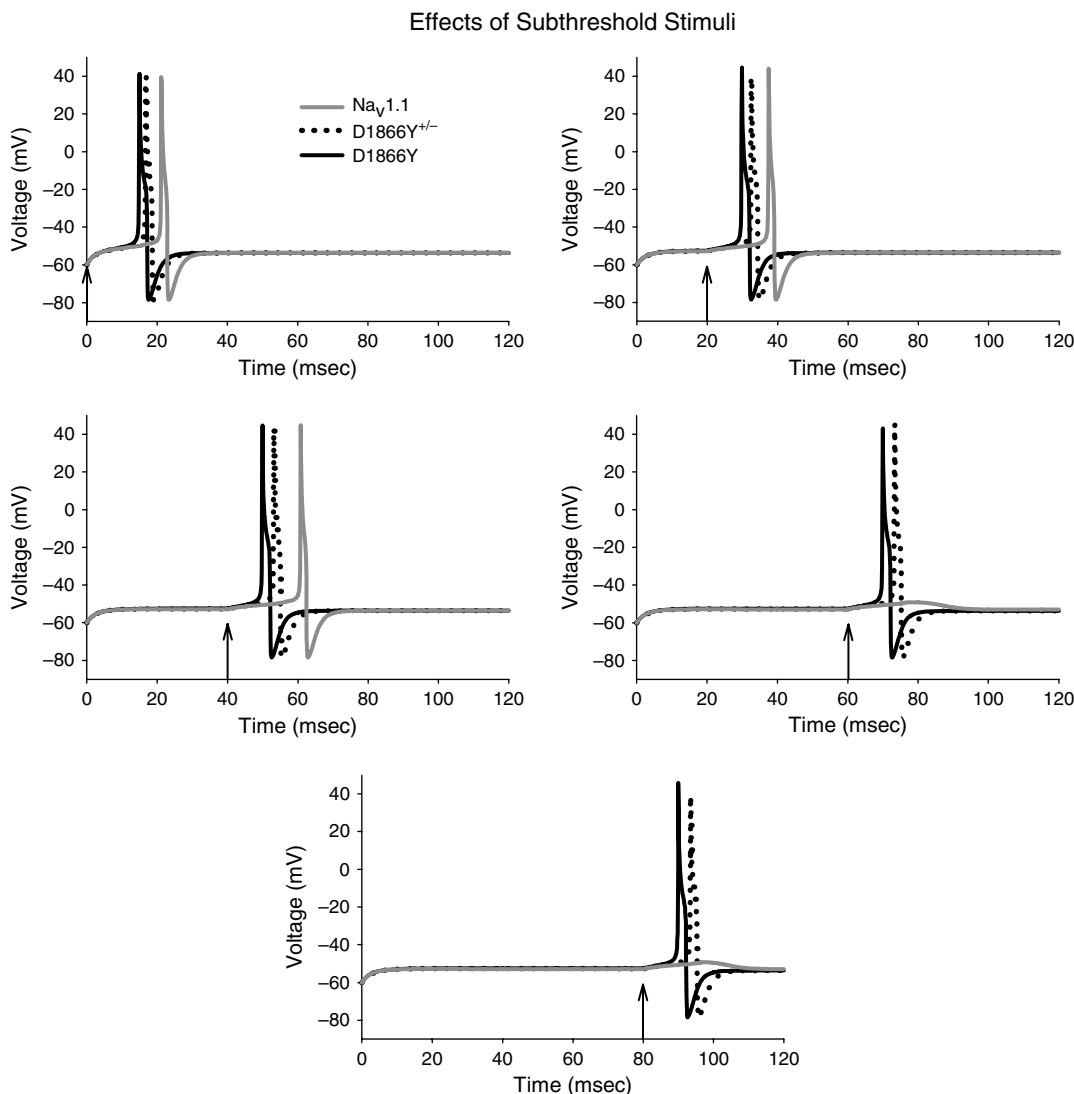


**FIGURE 10.5** D1866Y mutant model neuron action potential firing is resilient to subthreshold stimuli. Subthreshold current injections of 60 pA were applied to model neurons containing wild-type  $\text{Na}_v1.1$  (gray lines), mutant D1866Y (black lines) and a 1:1 heterozygous population of mutant and wild-type channels ( $\text{D}1866\text{Y}^{+/-}$ , dotted traces). The duration of the conditioning depolarization started at 0 ms and was increased in 20 ms increments. The conditioning depolarizations were immediately followed by injection of an additional 10 pA of current to test for action potential generation. Each plot begins with the application of the 60 pA conditioning pulse and the arrows indicate the time at which the additional 10 pA test injection was applied. The top panel shows a 0 ms conditioning pulse as a positive control. The D1866Y and  $\text{D}1866\text{Y}^{+/-}$  model neurons fired single action potentials with shorter onset delays than for  $\text{Na}_v1.1$  following subthreshold stimuli up to 40 ms. The D1866Y and  $\text{D}1866\text{Y}^{+/-}$  model neurons also remained capable of firing action potentials following longer subthreshold stimuli, whereas the  $\text{Na}_v1.1$  model neurons did not fire action potentials after subthreshold stimuli of 60 ms or longer. Reproduced, with permission, from Spampinato et al. (2004b).

longer, while the mutant was capable of firing an action potential regardless of the length of the conditioning depolarization. The D1866Y<sup>+/−</sup> heterozygous model neuron behaved more like the D1866Y model neuron, demonstrating the dominant nature of the D1866Y mutation (Figure 10.5). This trend was consistent for subthreshold stimuli longer than 160 ms (not shown).

### SHORTCOMINGS AND FUTURE DIRECTIONS

As we have shown in this chapter, Hodgkin-Huxley type models of cellular currents and action potential generation can be a useful tool in the analysis of sodium channel mutations that cause GEFS+. These models help to predict how dramatically different alterations in the biophysical properties caused by different mutations might affect the physiological activity of a neuron to produce similar effects. The usefulness of a model such as this can be increased by incorporating more detailed characteristics of the neuron, such as the dendritic structure and the array of different voltage- and ligand-gated channels that are present. However, the Hodgkin-Huxley type model is not without its limitations. The intricate and inter-dependent steady-state transitions that underlie sodium channel gating are more accurately modeled using a Markovian-based approach (Horn and Vandenberg, 1984; Clancy and Kass, 2004). Markovian-based models include state-dependent coupling of gating transitions that are otherwise independent in the Hodgkin-Huxley models. While this approach more accurately models sodium channel gating transitions, it may not provide a significant advantage with respect to predicting the effects on neuronal activity, especially considering the importance of other factors that affect neuronal physiology such as morphology and the presence of other ion channels. A recent study illustrated the importance of these considerations by demonstrating that a single sodium channel mutation can cause both hypo- and hyperexcitability when expressed in two different types of neurons, with the major factor determining neuronal excitability being the presence or absence of a different sodium channel isoform (Rush et al., 2006).

GEFS+ mutant sodium channels have not yet been studied in neurons, so the results obtained using heterologous expression systems may not accurately represent the *in vivo* situation. Aside from the effects of additional types of channels, it remains possible that neurons express some protein processing or modulatory activity that changes the function of a given mutation that has not been replicated in the heterologous expression systems. On the other hand, recent studies of the biophysical properties of pooled or specific native and ectopically expressed sodium channels in neurons demonstrate similarities in sodium conductances between neurons and heterologous systems (Ellermann et al., 2003; Rush et al., 2006; Scalmani et al., 2006; Yu et al., 2006). Furthermore, similarities at the biophysical level between neuronal and non-neuronal expression systems have been reported for sodium channel function associated with inherited or experimentally induced epilepsies (Ellermann et al., 2003; Scalmani et al., 2006).

For the purposes of our modeling experiments, we assumed that the biophysical properties of GEFS+ mutant sodium channels in heterologous expression systems are similar to those in neurons. Even if this is the case, however, it is not simple to extrapolate to neurons. The Na<sub>v</sub>1.1 sodium channel expressing the GEFS+ mutation may be expressed primarily in a subpopulation of cells, such as inhibitory interneurons or excitatory pyramidal cells. Depending on the cell type, the effects of the same biophysical alteration would be dramatically different on network firing. There is some evidence that the relative proportion of current contributed by Na<sub>v</sub>1.1 to the total sodium current of the cell is substantial for interneurons but negligible for pyramidal cells (Yu et al., 2006). This finding suggests that there is a specific defect in interneuron function for Na<sub>v</sub>1.1 associated epilepsies, which is consistent with the role that interneurons play in providing both inhibition and synchronization throughout the CNS (Buzsáki et al., 2004; Maglóczky and Freund, 2005). Na<sub>v</sub>1.1 is predominantly expressed in the soma and dendrites of neurons (Westenbroek et al., 1989; Kaplan et al., 2001), whereas action potential initiation likely occurs outside of the soma (Stuart and Sakmann, 1994; Colbert and Johnston, 1996; Stuart et al., 1997; Colbert and Pan, 2002). The situation is clearly complex, in that there is also evidence that the soma and dendrites may be capable of firing spikes as well as initiating action potentials in normal neurons, so the effects of GEFS+ mutations may distort the balance between soma and axon initiation sites (Colbert and Johnston, 1996; Golding and Spruston, 1998; Häusser et al., 2001; Colbert and Pan, 2002; Khalil and Raman, 2006).

This type of modeling provides a starting point from which experiments can be designed to test the effects of mutations in Na<sub>v</sub>1.1 on neuronal function and network activity in the brain. Ultimately, our goal is to test the predictions of these models using transgenic mice expressing GEFS+ sodium channel mutations. If the model is inaccurate, we will then use the data obtained from the transgenic mice to refine the model. Once we have developed a model that accurately predicts the effects of the mutations on neuronal function, we can then study subsequent mutations without constructing a transgenic mouse for each one.

## REFERENCES

- Abou-Khalil, B., Ge, Q., Desai, R. et al. (2001). Partial and generalized epilepsy with febrile seizures plus and a novel SCN1A mutation. *Neurology* 57:2265–2272.
- Annesi, G., Gambardella, A., Carrideo, S. et al. (2003). Two novel SCN1A missense mutations in generalized epilepsy with febrile seizures plus. *Epilepsia* 44:1257–1258.
- Aradi, I. and Soltesz, I. (2002). Modulation of network behaviour by changes in variance in interneuronal properties. *J Physiol (Lond)* 538:227–251.
- Audenaert, D., Claes, L., Ceulemans, B., Löfgren, A., Van Broeckhoven, C. and De Jonghe, P. (2003). A deletion in SCN1B is associated with febrile seizures and early-onset absence epilepsy. *Neurology* 61:854–856.
- Barela, A.J., Waddy, S.P., Lickfett, J.G. et al. (2006). An epilepsy mutation in the sodium channel SCN1A that decreases channel excitability. *J Neurosci* 26:2714–2723.
- Baulac, S., Huberfeld, G., Gourfinkel-An, I. et al. (2001). First genetic evidence of GABA<sub>A</sub> receptor dysfunction in epilepsy: a mutation in the g2-subunit gene. *Nat Genet* 28:46–48.
- Black, J.A., Yokoyama, S., Higashida, H., Ransom, B.R. and Waxman, S.G. (1994). Sodium channel mRNAs I, II and III in the CNS: cell-specific expression. *Mol Brain Res* 22:275–289.
- Brysch, W., Creutzfeldt, O.D., Luno, K., Schlingensiepen, R. and Schlingensiepen, K.-H. (1991). Regional and temporal expression of sodium channel messenger RNAs in the rat brain during development. *Exp Brain Res* 86:562–567.
- Buzsáki, G., Geisler, C., Henze, D.A. and Wang, X.-J. (2004). Interneuron diversity series: circuit complexity and axon wiring economy of cortical interneurons. *Trends Neurosci* 27:186–193.
- Catterall, W.A. (2000). From ionic currents to molecular mechanisms: the structure and function of voltage-gated sodium channels. *Neuron* 26:13–25.
- Claes, L., Del-Favero, J., Ceulemans, B., Lagae, L., Van Broeckhoven, C. and De Jonghe, P. (2001). De novo mutations in the sodium-channel gene SCN1A cause severe myoclonic epilepsy of infancy. *Am J Hum Genet* 68:1327–1332.
- Claes, L., Ceulemans, B., Audenaert, D. et al. (2003). De novo SCN1A mutations are a major cause of severe myoclonic epilepsy of infancy. *Hum Mutat* 21:615–621.
- Clancy, C.E. and Kass, R.S. (2004). Theoretical investigation of the neuronal Na<sup>+</sup> channel SCN1A: abnormal gating and epilepsy. *Biophys J* 86:2606–2614.
- Colbert, C.M. and Johnston, D. (1996). Axonal action-potential initiation and Na<sup>+</sup> channel densities in the soma and axon initial segment of subiculum pyramidal neurons. *J Neurosci* 16:6676–6686.
- Colbert, C.M. and Pan, E. (2002). Ion channel properties underlying axonal action potential initiation in pyramidal neurons. *Nat Neurosci* 5:533–538.
- Cossette, P., Loukas, A., Lafrenière, R.G. et al. (2003). Functional characterization of the D188V mutation in neuronal voltage-gated sodium channel causing generalized epilepsy with febrile seizures plus (GEFS). *Epilepsy Res* 53:107–117.
- Dibbens, L.M., Feng, H.-J., Richards, M.C. et al. (2004). GABRD encoding a protein for extra- or peri-synaptic GABA<sub>A</sub> receptors is a susceptibility locus for generalized epilepsies. *Hum Molec Genet* 13:1315–1319.
- Ellermann, R.K., Remy, S., Chen, J. et al. (2003). Molecular and functional changes in voltage-dependent Na<sup>+</sup> channels following pilocarpine-induced status epilepticus in rat dentate granule cells. *Neuroscience* 119:323–333.
- Escayg, A., MacDonald, B.T., Meisler, M.H. et al. (2000). Mutations of SCN1A, encoding a neuronal sodium channel, in two families with GEFS+. *Nat Genet* 24:343–345.
- Escayg, A., Heils, A., MacDonald, B.T., Haug, K., Sander, T. and Meisler, M.H. (2001). A novel SCN1A mutation associated with generalized epilepsy with febrile seizures plus and prevalence of variants in patients with epilepsy. *Am J Hum Genet* 68:866–873.
- Ferraro, T.N., Golden, G.T., Smith, G.G. and Berrettini, W.H. (1995). Differential susceptibility to seizures induced by systemic kainic acid treatment in mature DBA/2J and C57BL/6J mice. *Epilepsia* 36:301–307.
- Ferraro, T.N., Golden, G.T., Smith, G.G. et al. (1999). Mapping of loci for pentylenetetrazol-induced seizure susceptibility in mice. *J Neurosci* 19:6733–6739.
- Ferraro, T.N., Golden, G.T., Smith, G.G., DeMuth, D., Buono, R.J. and Berrettini, W.H. (2002). Mouse strain variation in maximal electroshock seizure threshold. *Brain Res* 936:82–86.
- Frankel, W.N., Taylor, L., Beyer, B., Tempel, B.L. and White, H.S. (2001). Electroconvulsive thresholds of inbred mouse strains. *Genomics* 74:306–312.
- Fujiwara, T. (2006). Clinical spectrum of mutations in SCN1A gene: severe myoclonic epilepsy in infancy and related epilepsies. *Epilepsy Res* 70:S223–S230.
- Fujiwara, T., Sugawara, T., Mazaki-Miyazaki, E. et al. (2003). Mutations of sodium channel a subunit type 1 (SCN1A) in intractable childhood epilepsies with frequent generalized tonic-clonic seizures. *Brain* 126:531–546.
- Furuyama, T., Morita, Y., Inagaki, S. and Takagi, H. (1993). Distribution of I, II and III subtypes of voltage-sensitive Na<sup>+</sup> channel mRNA in the rat brain. *Mol Brain Res* 17:169–173.
- Gennaro, E., Veggio, P., Malacarne, M. et al. (2003). Familial severe myoclonic epilepsy of infancy: truncation of Na<sub>v</sub>1.1 and genetic heterogeneity. *Epileptic Disord* 5:21–25.
- Golding, N.L. and Spruston, N. (1998). Dendritic sodium spikes are variable triggers of axonal action potentials in hippocampal CA1 pyramidal neurons. *Neuron* 21:1189–1200.
- Harkin, L.A., Bowser, D.N., Dibbens, L.M. et al. (2002). Truncation of the GABA<sub>A</sub>-receptor g2 subunit in a family with generalized epilepsy with febrile seizures plus. *Am J Hum Genet* 70:530–536.
- Häusser, M., Major, G. and Stuart, G.J. (2001). Differential shunting of EPSPs by action potentials. *Science* 291:138–141.
- Hines, M.L. and Carnevale, N.T. (1997). The NEURON simulation environment. *Neural Comput* 9:1179–1209.
- Horn, R. and Vandenberg, C.A. (1984). Statistical properties of single sodium channels. *J Gen Physiol* 84:505–534.
- Kaplan, M.R., Cho, M.-H., Ullian, E.M., Isom, L.L., Levinson, S.R. and Barres, B.A. (2001). Differential control of clustering of the sodium channels Nav1.2 and Nav1.6 at developing CNS nodes of Ranvier. *Neuron* 30:105–119.
- Khaliq, Z.M. and Raman, I.M. (2006). Relative contributions of axonal and somatic Na channels to action potential initiation in cerebellar Purkinje neurons. *J Neurosci* 26:1935–1944.

- Lossin, C., Wang, D.W., Rhodes, T.H., Vanoye, C.G. and George, A.L. Jr (2002). Molecular basis of an inherited epilepsy. *Neuron* 34:877–884.
- Lossin, C., Rhodes, T.H., Desai, R.R. et al. (2003). Epilepsy-associated dysfunction in the voltage-gated neuronal sodium channel SCN1A. *J Neurosci* 23:11289–11295.
- Maglóczky, Z. and Freund, T.F. (2005). Impaired and repaired inhibitory circuits in the epileptic human hippocampus. *Trends Neurosci.* 28:334–340.
- Nabbout, R., Gennaro, E., Bernardino, B.D. et al. (2003). Spectrum of SCN1A mutations in severe myoclonic epilepsy of infancy. *Neurology* 60:1961–1967.
- Novakovic, S.D., Eglen, R.M. and Hunter, J.C. (2001). Regulation of  $\text{Na}^+$  channel distribution in the nervous system. *Trends Neurosci.* 24:473–478.
- Ohmori, I., Ouchida, M., Ohtsuka, Y., Oka, E. and Shimizu, K. (2002). Significant correlation of the SCN1A mutations and severe myoclonic epilepsy in infancy. *Biochem Biophys Res Commun* 295:17–23.
- Patton, D.E., West, J.W., Catterall, W.A. and Goldin, A.L. (1992). Amino acid residues required for fast sodium channel inactivation. Charge neutralizations and deletions in the III-IV linker. *Proc Natl Acad Sci USA* 89:10905–10909.
- Royle, S.J., Collins, F.C., Rupniak, H.T., Barnes, J.C. and Anderson, R. (1999). Behavioural analysis and susceptibility to CNS injury of four inbred strains of mice. *Brain Res* 816:337–349.
- Rush, A.M., Dib-Hajj, S.D., Liu, S., Cummins, T.R., Black, J.A. and Waxman, S.G. (2006). A single sodium channel mutation produces hyper- or hypoexcitability in different types of neurons. *Proc Natl Acad Sci USA* 103:8245–8250.
- Scalmani, P., Rusconi, R., Armatura, E. et al. (2006). Effects in neocortical neurons of mutations of the  $\text{Na}_v1.2 \text{ Na}^+$  channel causing benign familial neonatal-infantile seizures. *J Neurosci* 26:10100–10109.
- Schauwecker, P.E. and Steward, O. (1997). Genetic determinants of susceptibility to excitotoxic cell death: implications for gene targeting approaches. *Proc Natl Acad Sci USA* 94:4103–4108.
- Scheffer, I.E. and Berkovic, S.F. (1997). Generalized epilepsy with febrile seizures plus. A genetic disorder with heterogeneous clinical phenotypes. *Brain* 120:479–490.
- Scheffer, I.E., Wallace, R., Mulley, J.C. and Berkovic, S.F. (2001). Clinical and molecular genetics of myoclonic-astatic epilepsy and severe myoclonic epilepsy in infancy (Dravet syndrome). *Brain Dev* 23:732–735.
- Singh, R., Scheffer, I.E., Crossland, K. and Berkovic, S.F. (1999). Generalized epilepsy with febrile seizures plus: a common childhood-onset genetic epileptic syndrome. *Ann Neurol* 45:75–81.
- Smith, R.D. and Goldin, A.L. (1998). Functional analysis of the rat I sodium channel in *Xenopus* oocytes. *J Neurosci* 18:811–820.
- Spampinato, J., Escayg, A., Meisler, M.H. and Goldin, A.L. (2001). Functional effects of two voltage-gated sodium channel mutations that cause generalized epilepsy with febrile seizures plus type 2. *J Neurosci* 21:7481–7490.
- Spampinato, J., Escayg, A., Meisler, M.H. and Goldin, A.L. (2003). The generalized epilepsy with febrile seizures plus type 2 mutation W1204R alters voltage-dependent gating of  $\text{Na}_v1.1$  sodium channels. *Neuroscience* 116:37–48.
- Spampinato, J., Aradi, I., Soltesz, I. and Goldin, A.L. (2004a). Increased neuronal firing in computer simulations of sodium channel mutations that cause generalized epilepsy with febrile seizures plus. *J Neurophysiol* 91:2040–2050.
- Spampinato, J., Kearney, J.A., de Haan, G. et al. (2004b). A novel epilepsy mutation in the sodium channel SCN1A identifies a cytoplasmic domain for b subunit interaction. *J Neurosci* 24:10022–10034.
- Spruston, N. and Johnston, D. (1992). Perforated patch-clamp analysis of passive membrane properties of three classes of hippocampal neurons. *J Neurophysiol* 67:508–529.
- Staley, K.J. and Mody, I. (1992). Membrane properties of dentate gyrus granule cells: comparison of sharp microelectrode and whole-cell recordings. *J Neurophysiol* 67:1346–1358.
- Stuart, G., Schilling, J. and Sakmann, B. (1997). Action potential initiation and propagation in rat neocortical pyramidal neurons. *J Physiol (Lond)* 505:617–632.
- Stuart, G.J. and Sakmann, B. (1994). Active propagation of somatic action potentials into neocortical pyramidal cell dendrites. *Nature* 367:69–72.
- Sugawara, T., Tsurubuchi, Y., Agarwala, K.L. et al. (2001). A missense mutation of the  $\text{Na}^+$  channel aII subunit gene Nav1.2 in a patient with febrile and afebrile seizures causes channel dysfunction. *Proc Natl Acad Sci USA* 98:6384–6389.
- Sugawara, T., Mazaki-Miyazaki, E., Fukushima, K. et al. (2002). Frequent mutations of SCN1A in severe myoclonic epilepsy in infancy. *Neurology* 58:1122–1124.
- Veggiotti, P., Cardinali, S., Montalenti, E., Gatti, A. and Lanzi, G. (2001). Generalized epilepsy with febrile seizures plus and severe myoclonic epilepsy in infancy: a case report of two Italian families. *Epileptic Disord* 3:29–32.
- Wallace, R.H., Wang, D.W., Singh, R. et al. (1998). Febrile seizures and generalized epilepsy associated with a mutation in the  $\text{Na}^+$ -channel b1 subunit gene SCN1B. *Nat Genet* 19:366–370.
- Wallace, R.H., Scheffer, I.E., Barnett, S. et al. (2001). Neuronal sodium-channel a1-subunit mutations in generalized epilepsy with febrile seizures plus. *Am J Hum Genet* 68:859–865.
- Wallace, R.H., Scheffer, I.E., Parasivam, G. et al. (2002). Generalized epilepsy with febrile seizures plus: mutation of the sodium channel subunit SCN1B. *Neurology* 58:1426–1429.
- Wallace, R.H., Hodgson, B.L., Grinton, B.E. et al. (2003). Sodium channel a1-subunit mutations in severe myoclonic epilepsy of infancy and infantile spasms. *Neurology* 61:765–769.
- West, J.W., Patton, D.E., Scheuer, T., Wang, Y., Goldin, A.L. and Catterall, W.A. (1992). A cluster of hydrophobic amino acid residues required for fast  $\text{Na}^+$  channel inactivation. *Proc Natl. Acad Sci USA* 89:10910–10914.
- Westenbroek, R.E., Merrick, D.K. and Catterall, W.A. (1989). Differential subcellular localization of the  $R_I$  and  $R_{II}$   $\text{Na}^+$  channel subtypes in central neurons. *Neuron* 3:695–704.
- Yu, F.H., Mantegazza, M., Westenbroek, R.E. et al. (2006). Reduced sodium current in GABAergic interneurons in a mouse model of severe myoclonic epilepsy in infancy. *Nat Neurosci* 9:1142–1149.

# 11

## GAIN MODULATION AND STABILITY IN NEURAL NETWORKS

FRANCES S. CHANCE

### ABSTRACT

The highly recurrent architecture of cortex suggests that cortical circuits operate as high gain amplifiers of incoming signals. While this feature is likely to be essential for cortical function, a drawback is that such circuitry can be prone to instabilities. How can such circuits be stabilized? Although increasing inhibition can prevent uncontrolled activity, this action simply moves the network away from the point of instability rather than removing the unstable regime. As will be discussed, an unstable regime can only be removed through a decrease in the gain of the network. This chapter discusses a mechanism of gain modulation that makes use of the noisy background synaptic activity that is a characteristic feature of much of *in vivo* cortex. For this particular gain modulation mechanism, increases in local activity lead to decreases in neuronal gain. We show that recurrent cortical circuits can be stabilized by increases in background activity. Interestingly, because an increase in local activity is associated with a decrease in gain for this mechanism, increases in excitation may help to stabilize a network.

### INTRODUCTION

A fundamental feature of cortical circuitry is the high degree of local recurrent connectivity. Feedforward thalamocortical afferents comprise only a small percentage of the total number of inputs (McGuire et al., 1984; Kisvárday et al., 1986; LeVay, 1986; White, 1989; Braintenberg and Shüz, 1991; Douglas and Martin, 1991; Peters and Payne, 1993; Peters et al., 1994), the remainder consisting of feedback and local recurrent connections. Many of the recurrent connections are excitatory-to-excitatory (Kisvárday et al., 1986), suggesting that their function may be to amplify incoming signals to cortex (Douglas et al., 1989, 1995). Indeed, many modeling studies have demonstrated the effectiveness of recurrent circuitry at amplifying incoming signals. For example, amplification by recurrent circuitry has been shown to enhance neuronal response selectivities such as orientation-tuning (Ben-Yishai et al., 1995; Somers et al., 1995; Carandini and Ringach, 1997; Sompolinsky and Shapley, 1997), direction-selectivity (Suarez et al., 1995; Maex and Orban, 1996) and complex-cell spatial-phase insensitivity (Chance et al., 1999; Tao et al., 2004) in primary visual cortex.

For strong amplification to occur, the cortical network must operate at high gain. In other words, small changes in input lead to large changes in the output of the network, allowing the recurrent circuitry to amplify signals that might otherwise be undetectable. One disadvantage of this configuration, however, is that a high gain network is susceptible to instability. We illustrate this using a simplified version of the cortical amplifier. In this case, the network is represented by a single neuron and the recurrent excitatory connections are replaced by a single autapse (the neuron sending excitatory feedback to itself through a single synapse, see Seung, 2000). The total input received by the neuron at any point in time is the feedforward input ( $I$ ) to the neuron plus the response of the neuron multiplied by the strength of the autapse ( $W$ ). The firing rate ( $r$ ) in response to such input depends on the neuronal gain ( $G$ ):

$$\tau \frac{dr}{dt} = -r + G [I + Wr]_+$$

In the above equation,  $\{\}_+$  indicates rectification, which keeps the firing rate from becoming negative. The time constant ( $\tau$ ) in the above equation is determined by a number of factors, including the gain of the neuron.

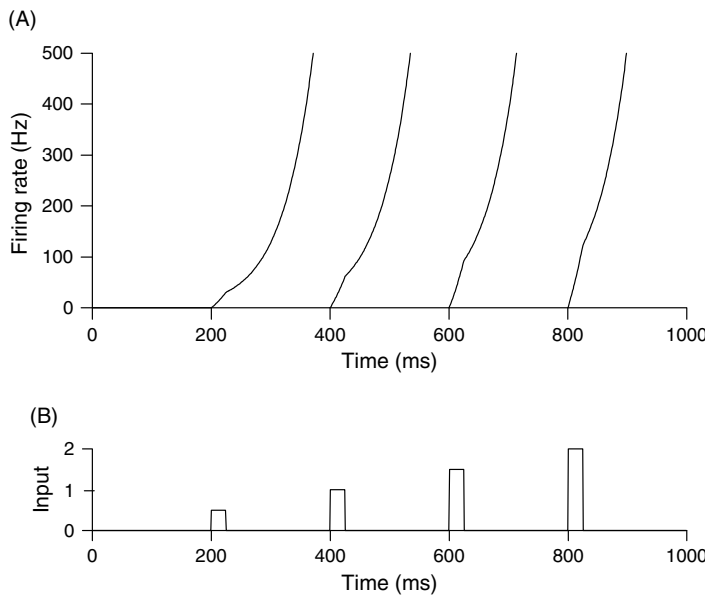


**FIGURE 11.1** Responses of a network with feedback gain greater than one.  $GW$  was 1.01 and  $\tau$  was set to 0.5 ms. Bottom panel: a series of successively larger input pulses was presented to the neuron. Top panel: firing rate responses to the input pulses. Firing rate was set to zero immediately before each input pulse.

In this model,  $G$  defines the gain of the neuron, or the relationship between its output and its input. The network amplification is  $GW$ , the neuronal gain times the strength of the autapse. If the strength of the feedback connection is increased to the point that the network amplification ( $GW$ ) becomes greater than one, the network is unstable. In Figure 11.1, a series of increasing input pulses is presented to the network. These pulses may be thought of as steps of injected current. Because of the high gain of the network, any non-zero input results in the firing rate rapidly growing without bound. Even in the absence of input, these upswings in firing rate, once initiated, will continue indefinitely. For clarity, the firing rate was reset to zero by hand immediately before each input pulse (at 200, 400, 600 and 800 ms) so that the response to the next input pulse could be observed.

Increasing inhibition can move such a network away from the point of instability, but it cannot remove the unstable regime. Figure 11.2C illustrates the effect of subtractive inhibition on the responses of the model neuron in the absence of the autapse. The solid curve in Figure 11.2C is the linear firing rate curve of the neuron. The additional inhibitory component subtracts away a portion of the input to the neuron, shifting the firing-rate curve along the input-axis. The resulting firing-rate curve is the dashed line. This form of inhibition is called subtractive because the new firing-rate curve is parallel to the original one and it has an offset along the input axis.

With subtractive inhibition included, the network response is stable for the first two input pulses (see Figure 11.2A). The response to the first input pulse, however, has been abolished. In addition, the third and fourth input pulses are large enough to push the network into the unstable regime. Adding inhibition has merely delayed rather than removed the instability. Because a significant portion of recurrent connections within cortex are inhibitory, increasing inhibition in cortex may have more complicated and/or more robust effects than those illustrated here. Nevertheless, simply increasing inhibition, without invoking other homeostatic mechanisms, is unlikely to eliminate the instability.

In Figure 11.3, the gain ( $G$ ) of the model neuron is reduced to stabilize the network. The effect of reducing neuronal gain is inhibitory, but of a different form than subtractive inhibition. This is illustrated in Figure 11.3C. Again, as in Figure 11.2C, the solid curve is the firing-rate of the neuron in the absence of any inhibition. To produce the firing-rate curve indicated by the dashed-dotted line, the gain of the neuron was reduced from 1.01 to 0.8. The effect of reducing the gain of the neuron is a divisive scaling of the firing-rate curve, so this form of inhibition is referred to as ‘divisive’ (or ‘multiplicative’) inhibition. In contrast to subtractive inhibition, its effect does not constitute a shift along the input axis, but instead a change in the slope of the firing-rate curve. Because these firing-rate curves are linear, a change in slope is equivalent to dividing the entire firing-rate by a factor. If the firing-rate curve is non-linear, one must compare multiplicatively scaled versions of the firing-rate curves to determine if this is truly a divisive effect (see Figure 11.5).

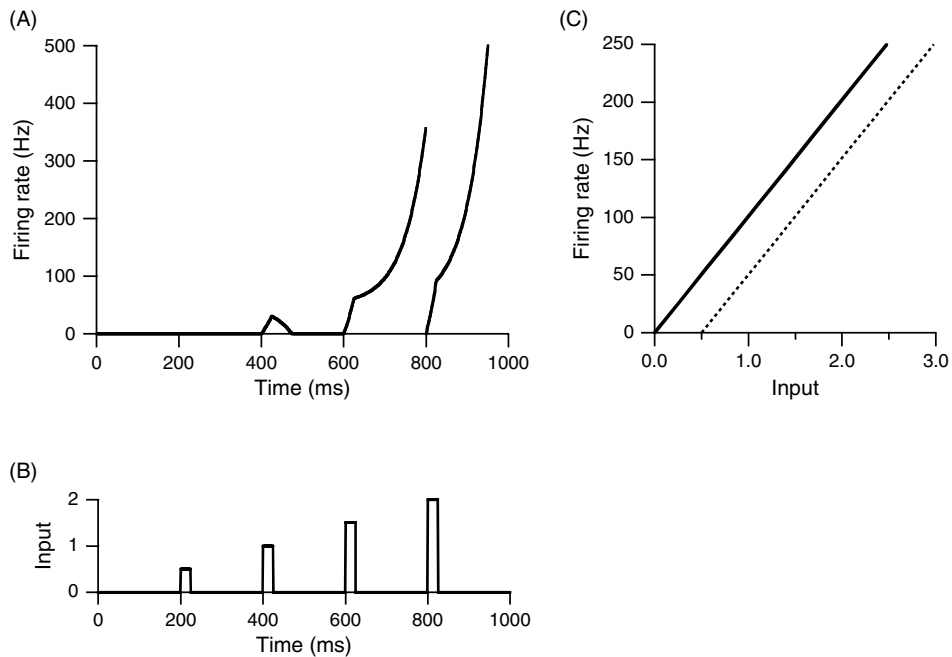


FIGURE 11.2 Responses of an unstable network with subtractive inhibition included. (A) Firing-rate responses to the input pulses. Firing-rate was set to zero at 800 ms, immediately before the fourth input pulse. (B) The input to the neuron was a series of successively larger input pulses. (C) Firing-rate curves of the model neuron without recurrent input. Solid and dotted lines are the firing-rate curve without and with inhibition.

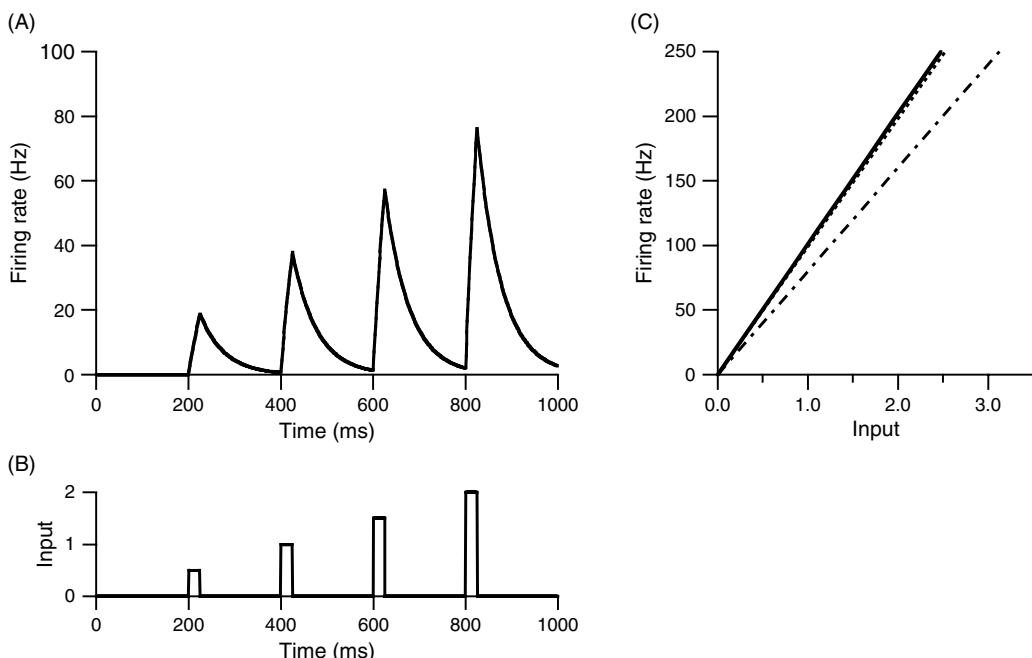


FIGURE 11.3 (A) Firing-rate of a high-gain (network amplification was 0.99) network as a function of time and in response to the input pulses presented in (B). (B) A series of successively larger input pulses was presented to the neuron. (C) Firing-rate of the model neuron as a function of input, but without the recurrent input through the autapse. For the dash-dotted line,  $G = 0.8$  and for the dotted line  $G = 0.99$ .

For the simulation results presented in Figure 11.3A, the neuronal gain was reduced by less than 2%, reducing the network amplification factor from 1.01 to 0.99. The dotted line in Figure 11.3C is the firing-rate curve of the neuron that produced the responses drawn in Figure 11.3A. Although barely visible, the actual firing-rate curve (dotted line) is included to illustrate just how little a gain change is required to stabilize the network. The change in the network amplification factor is likewise small, but the effect on the stability of the network is quite dramatic. By lowering the gain of neurons in the network only slightly, the network is now stable for all inputs.

The term ‘gain’ refers to the relationship between the output of a system and its input. For the purposes of this chapter, we define neuronal gain as the slope of the firing-rate curve. Thus while subtraction and division are both forms of inhibition, only the latter changes the gain of the neuron. In this chapter, we refer to divisive or multiplicative effects on the neuronal firing-rate response curve as ‘gain modulation’.

In the model that we have been discussing, changing the gain of the neuron and changing the strength of the autapse are almost equivalent with regard to stabilizing the network. In the highly recurrent circuitry of the cortex, however, decreasing  $W$  would require scaling down all recurrent synapses by the same factor if neuronal selectivities are to be maintained. Changing the neuronal gain, on the other hand, modifies neuronal sensitivity to all inputs, essentially adjusting the volume of a neuron’s response (Chance et al., 2002). Gain modulation can thus remove an instability while maintaining neuronal selectivities.

We highlight the difference between subtractive and divisive forms of inhibition here because, although both decrease neuronal excitability, the two forms of inhibition have different effects on neuronal gain and this difference has important consequences for the stability of the network. Subtractive (or additive) effects such as the one illustrated in Figure 11.2 arise through simple changes in inhibition or excitation, for example injecting constant current. Changes in membrane conductance also result in additive or subtractive responses (Gabbiani et al., 1994; Holt and Koch, 1997; Chance et al., 2002; Prescott and DeKoninck, 2003; Ulrich, 2003). Mechanisms that produce changes in gain (Doiron et al., 2000; Chance et al., 2002; Smith et al., 2002; Mitchell and Silver, 2003; Prescott and DeKoninck, 2003; Mehaffey et al., 2005) have proven more difficult to find (although see Murphy and Miller, 2003 for a discussion of how a subtractive effect can appear divisive when combined with a non-linear response function). Later in this chapter, we describe a truly divisive gain modulation mechanism in depth.

Understanding the mechanisms underlying gain modulation is important because gain modulation is a prominent feature of neural activity recorded in behaving animals (for a review, see Salinas and Thier, 2000). Within the visual system alone, gain modulation has been proposed as a mechanism for the neural computation of coordinate transformations relevant for tasks ranging from visually guided reaching (Zipser and Andersen, 1988; Salinas and Abbott, 1995; Pouget and Sejnowski, 1997) to invariant object recognition (Salinas and Abbott, 1997). Multiplicative or divisive processes appear to underlie the gaze-direction dependence of visual neurons in posterior parietal cortex (Andersen and Mountcastle, 1983), contrast-dependent normalization of responses in primary visual cortex (Heeger, 1992; Carandini and Heeger, 1994; Carandini et al., 1997) and the effects of attention in a number of areas (McAdams and Maunsell, 1999; Treue and Martínez-Trujillo, 1999; but see Reynolds and Pasternak, 2000; Martínez-Trujillo and Treue, 2002). In addition to having important implications for computational processing, mechanisms of gain modulation may play a critical role in ensuring the stability of cortical networks.

#### A MECHANISM FOR MULTIPLICATIVE GAIN MODULATION

Recent work has proposed that multiplicative gain modulation, as observed *in vivo*, can arise through changing levels of noisy excitatory and inhibitory synaptic inputs. This background of synaptic activity is ‘balanced’ (the majority of excitation is cancelled by inhibition) and thus is not particularly effective at driving the neuron. Nevertheless, we will see that this noisy background activity is an effective gain modulation mechanism that may be used *in vivo*. We will first examine this gain modulation mechanism using a single-compartment computational model of a neuron and then we will discuss how this mechanism of gain modulation may be useful in stabilizing a high-gain network.

We first study a leaky integrate-and-fire neuron, one of the simplest single-compartment neuron models. The equation describing the membrane potential of this model is

$$C \frac{dV}{dt} = g_L(E_L - V) + I$$

In the above equation,  $C$  is the membrane capacitance,  $g_L$  is the resting membrane conductance, and  $I$  is any additional injected current. An action potential is fired if the membrane potential depolarizes above a threshold potential,  $V_{\text{th}}$ .

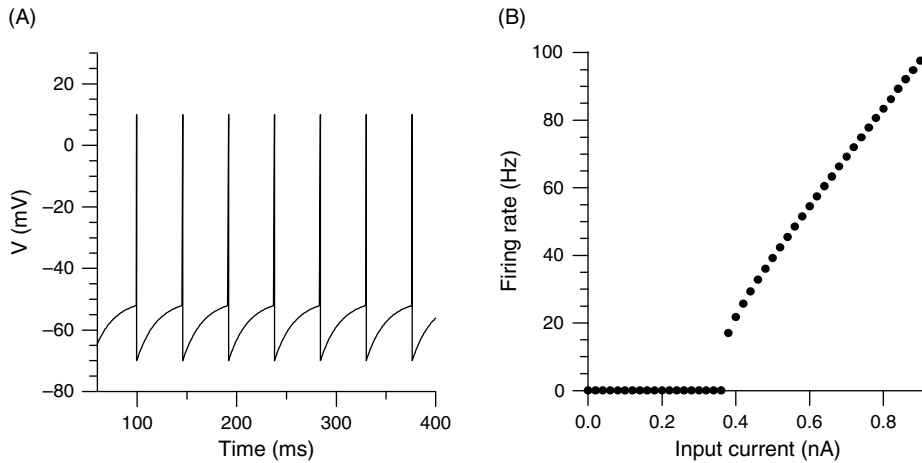


FIGURE 11.4 (A) Membrane potential of a leaky integrate-and-fire neuron being driven at approximately 20 Hz by constant injected current. (B) Firing-rate as a function of injected current for the same model neuron.

Immediately after the action potential, the membrane potential is set to the reset potential,  $V_{\text{reset}}$ . For the simulations presented here,  $V_{\text{th}} = -52 \text{ mV}$ ,  $V_{\text{reset}} = E_L = -70 \text{ mV}$ ,  $g_L = 20 \text{ nS}$ , and  $C = 0.4 \text{ nF}$ .

The firing of the integrate-and-fire neuron in response to constant injected current is shown in Figure 11.4A. The plot in Figure 11.4B is the firing-rate curve of the model neuron. The responses of the model illustrated in Figure 11.4 are much like what one would record in a quiescent slice. The firing pattern of the neuron is quite regular provided that the injected current is constant over time.

Neurons *in vivo* are continuously bombarded by background synaptic input (Holt et al., 1996; Paré et al., 1998; Destexhe and Paré, 1999; Tiesinga et al., 2000; Destexhe et al., 2001, 2003). Although neuronal firing-rates in cortex remain relatively low, this background synaptic input has been shown to affect dramatically the integrative properties of neurons *in vivo*. The membrane conductance of neurons measured *in vivo* is significantly higher than the membrane conductance of the same type of neurons measured *in vitro*, presumably because of the high level of synaptic input (Woody and Gruen, 1978; Borg-Graham et al., 1998; Hirsch et al., 1998; Paré et al., 1998; Destexhe and Paré, 1999; Steriade et al., 2001). The high level of background synaptic activity also causes cortical responses to be extremely variable, as can be observed by examining the high degree of irregularity in spike times as well as the membrane potential deflections in between spikes (Softky and Koch, 1993; Holt et al., 1996; Shadlen and Newsome, 1998; Stevens and Zador, 1998). We now modify the integrate-and-fire model to include this background activity.

The background activity that we have discussed in this chapter is a fundamental feature of the *in vivo* cortical environment (Holt et al., 1996; Paré et al., 1998; Destexhe and Paré, 1999; Tiesinga et al., 2000; Destexhe et al., 2001, 2003). We model the background activity as randomly arriving excitatory and inhibitory synaptic inputs. The arrival times of each synaptic input are generated such that the spikes obey Poisson statistics. With these synaptic conductances included, the equation for the membrane potential of the integrate-and-fire neuron is:

$$C \frac{dV}{dt} = g_L(E_L - V) + g_e(E_e - V) + g_i(E_i - V) + I$$

The excitatory and inhibitory synaptic conductances and their reversal potentials are  $g_e$ ,  $g_i$ ,  $E_e$ , and  $E_i$ , respectively. With each incoming excitatory or inhibitory input spike, the appropriate conductance (excitatory or inhibitory synaptic conductance) is increased by a specified quantity representing the unitary conductance change arising from a single synaptic input. For excitatory inputs, this change in conductance was 0.1 times the leak conductance and for inhibitory inputs it was 0.25 times the leak conductance. Between inputs, both excitatory and inhibitory synaptic conductances decayed exponentially towards zero with a time constant of 5 ms.

The effect of background synaptic activity on the membrane potential of the integrate-and-fire neuron model is illustrated in Figure 11.5A. Here we see three membrane potential traces of the integrate-and-fire model receiving three different levels of background synaptic activity. The underlying arrival rate of excitatory and inhibitory synaptic inputs in the top panel of Figure 11.5A was 3000 Hz. For the middle panel, arrival rates were increased to 6000 Hz and for the bottom panel

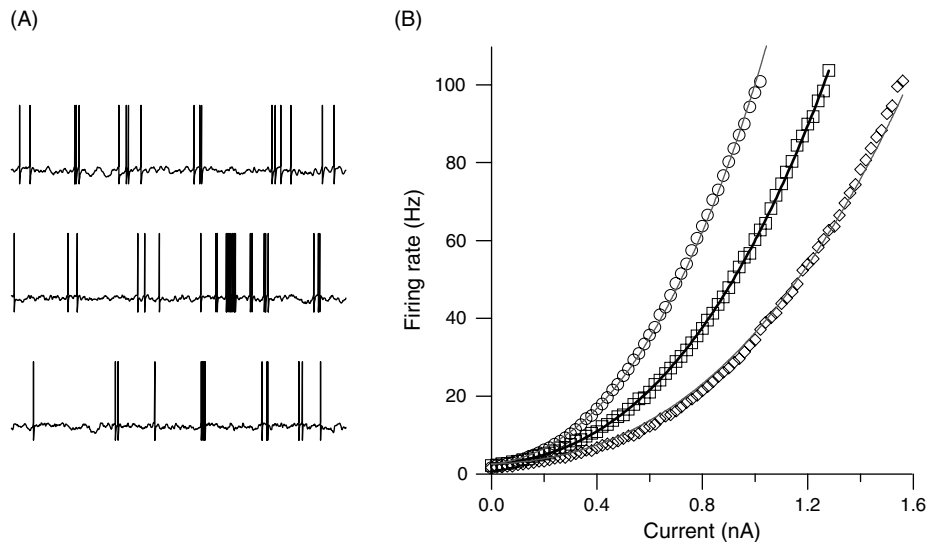


**FIGURE 11.5** (A) Example membrane potential traces of the integrate-and-fire model for total synaptic input rates of 3000 Hz (top), 6000 Hz (middle) and 9000 Hz (bottom). (B) Firing-rate as a function of input current for three levels of background activity. The input rates were 3000 Hz, 6000 Hz and 9000 Hz (same as in A) for the open circles, squares and diamonds, respectively. The thick curve is the best fourth-order polynomial fit to the open squares. This curve was multiplicatively scaled (see text for details) to best fit the open circles and diamonds (thin gray curves).

to 9000 Hz. For each membrane potential trace, the injected current was adjusted so that the neuron fired at approximately 20 Hz. Surprisingly, the change in background activity level does not significantly affect the variability of the interspike intervals, nor does it significantly change the variability of the membrane potential (see Chance et al., 2002 for a full explanation). Briefly, the variance of the membrane potential ( $\sigma_V^2$ ) is:

$$\sigma_V^2 = \sigma_I^2 \tau_s / (g^2 (\tau_m + \tau_s))$$

where  $\sigma_I^2$  is the input noise (variance of the input current),  $\tau_s$  is the synaptic time constant and  $\tau_m$  is the membrane time constant. As background activity increases,  $\sigma_I^2$  and  $g$  increase while  $\tau_m$  decreases. These effects cancel each other and the result is that the membrane potential variability does not change as background activity increases.

Figure 11.5B shows the firing-rate curves of the integrate-and-fire model neuron receiving these three different levels of background synaptic activity as a function of the magnitude of an additional constant injected current. The data recorded when synaptic inputs arrived at an overall rate of 3000 Hz are plotted with open circles. For synaptic input rates of 6000 Hz and 9000 Hz, the firing-rate curves are plotted using open squares and open diamonds, respectively. Comparing the firing-rates measured for any given level of injected current reveals that increasing the rate of background synaptic activity has an inhibitory effect on the responses of the neuron. Somewhat surprisingly, the effect is divisive, a form of inhibition like that seen in Figure 11.3 (changing the gain of the model neuron) rather than subtractive (see Figure 11.2). The solid curves in Figure 11.5B are multiplicatively scaled versions of each other and are included to demonstrate the divisive effect of the background activity. The thickest curve is a fourth-order polynomial fit to the firing-rate curve under the middle-level of background activity (open squares). To generate the thinner gray curves, this fit was multiplied by or divided by 1.7. This fourth-order polynomial fit included a small firing-rate offset (2.55 Hz) that was not scaled when generating the thinner curves. The good fits of the thinner curves to the firing-rate curves recorded with low (open circles) and high (open diamonds) levels of background activity demonstrate that the dominant effect of changing the level of background activity is a multiplicative (or a divisive) scaling of the firing-rate curve.

Increasing background synaptic activity has two important effects: the overall membrane conductance increases and the variance of the synaptic current (input noise) increases. These two components of background activity combine to produce the divisive effect observed in Figure 11.5 (see Chance et al., 2002 for a full explanation). Figure 11.6A demonstrates the effect of simply increasing membrane conductance. The thin firing-rate curve is identical to the open circles in Figure 11.5B (the firing-rate curve measured in the lowest level of background activity). For the dashed and thick firing-rate curves in Figure 11.5B, two levels of additional tonic conductance were introduced into the neuronal membrane. The sizes of the additional conductances were chosen so that the overall conductance of the membrane was equal to the average

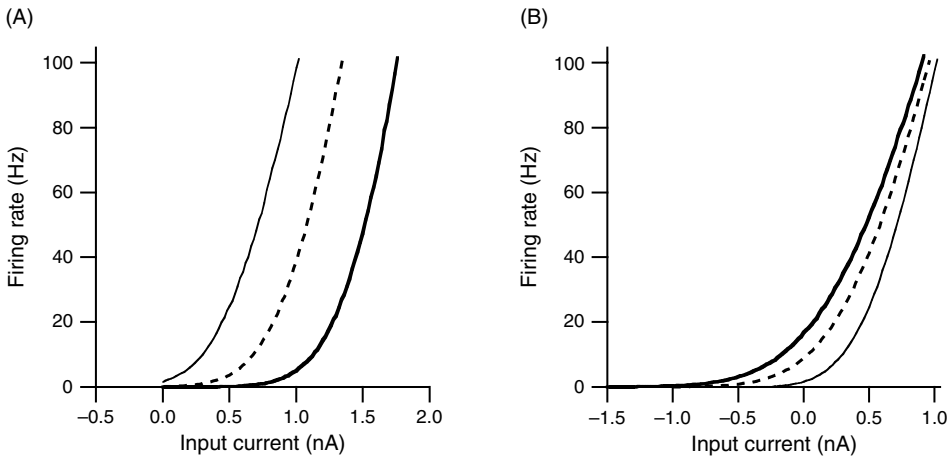


**FIGURE 11.6** In both panels, the thin curve is the replotted firing-rate curve for the lowest level of background activity from Figure 11.5B. (A) Firing-rate plotted against input current when the overall membrane conductance was increased to match the membrane conductance for the middle (dashed line) and high (thick line) levels of background activity in Figure 11.5B (see text). (B) Firing-rate versus input current when the input noise level was increased to match the input noise levels of the middle (dashed line) and highest (thick line) levels of background activity.

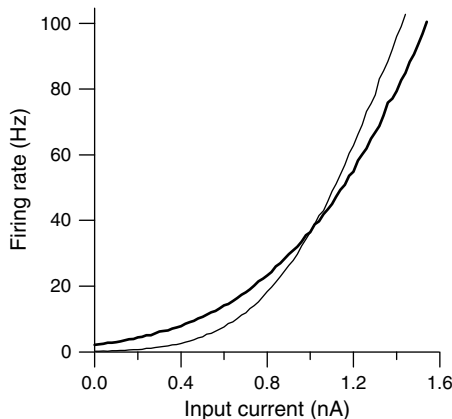
membrane conductance of the neuron in the presence of the middle (for the dashed curve) and highest (for the thick curve) levels of background activity in Figure 11.5B (open squares and open diamonds). The reversal potential of the additional conductance was chosen to be equivalent to the effective reversal potential of the combined synaptic conductances arising from the background activity. Thus, these firing rate curves demonstrate the effects of increasing membrane conductance.

Figure 11.6A demonstrates that increasing membrane conductance has a subtractive effect on the firing-rate curve of a neuron. This effect of increasing membrane conductance has been previously documented in computational (Gabbiani et al., 1994; Holt and Koch, 1997) as well as experimental studies (Chance et al., 2002; Prescott and DeKoninck, 2003; Ulrich, 2003). Intuitively, one might expect that increasing conductance should have a divisive effect on the neuronal response because Ohm's law dictates that increasing membrane conductance will act divisively on any deflections in membrane potential, shunting the effect of an input. However, the increased membrane conductance also decreases the membrane time constant, speeding up the shunted membrane potential deflection. Because of the altered temporal dynamics, the effect of conductance changes on firing-rates is subtractive not divisive (see Chance et al., 2002 for more details).

The effects of increasing input noise are illustrated in Figure 11.6B. To isolate input noise, the sizes of the unitary conductance changes arising from each synaptic input spike were scaled by a factor while, at the same time, synaptic input rates were divided by the same factor. This causes the variance of the input current to increase without changing the overall conductance evoked by the synaptic input. In Figure 11.6B, the thin curve is identical to the thin curve in Figure 11.6A, and also the open circles in Figure 11.5B. For the dashed curve, the sizes of the unitary conductance changes were doubled while the synaptic input rates were halved. This effectively doubles the input noise without changing membrane conductance. For the thick curve, the input noise was tripled in the same manner. These manipulations were chosen to match the increases in input noise evoked by doubling and tripling the levels of background activity in Figure 11.5B (open squares and open diamonds, respectively).

Increasing input noise increases neuronal firing-rate. This effect can be seen by comparing the firing-rate evoked in response to any particular input current for different levels of input noise (see Figure 11.6B). The increase in firing-rate is larger at lower rates (and thus smaller inputs) than at higher firing-rates, however. Because of this differential effect, one result of increasing input noise is a decrease in the slope of the firing-rate curve. To be more accurate, the effects of increased input noise are a decrease in slope combined with an additive shift (to the left) along the input axis.

When the effects of increased conductance and increased input noise are combined, the total effect is a subtractive shift (from the additional membrane conductance) combined with a decrease in slope and an additive shift (arising from the increased input noise). Under certain conditions, the additive shift arising from the increased input noise cancels the subtractive shift resulting from the increase in membrane conductance. This cancellation isolates the slope change and the net effect is a divisive inhibition of neuronal firing-rate. This is how divisive gain modulation arises from increases in background synaptic activity.



**FIGURE 11.7** firing-rate curves in the presence of two levels of background activity. All synaptic parameters are the same as in Figure 11.5, except that for the thinner firing-rate curve the excitatory and inhibitory input rates were 3400 Hz and 4000 Hz, respectively, and for the thicker firing-rate curve the excitatory and inhibitory input rates were 10 200 Hz and 10 000 Hz, respectively.

If the additive and subtractive effects arising from increased noise and increased conductance do not cancel, the effect of the increased background synaptic activity is mixed. In Figure 11.7, the thin firing-rate curve was generated when the excitatory input rate was 3400 Hz and the inhibitory input rate was 4000 Hz. The thicker firing-rate curve describes the neuronal firing-rate as a function of input current when the excitatory synaptic input rate is 10 200 Hz and the inhibitory synaptic input rate is 10 000 Hz. The slope of the firing-rate curve still decreases in the presence of higher background synaptic activity, indicating a decreased gain. However, in this case, the additive and subtractive shifts arising from the increases in input noise and membrane conductance do not completely cancel and we are left with a net additive shift. In this example, the effect of increasing the background activity in this configuration is a combination of a divisive effect and an additive one.

#### GAIN MODULATION OF RESPONSES TO TIME-VARYING INPUTS

Because external stimuli are continuously varying, a neuron's task *in vivo* is often to respond to specific synaptic inputs rather than constant or time-averaged input (the case we have been considering so far). We now turn to how background synaptic activity affects neuronal sensitivity, or gain, to individual synaptic inputs. Understanding the effects of background activity on neuronal sensitivity to EPSCs (excitatory postsynaptic currents) is important not only because EPSCs represent more biologically realistic stimuli, but also because making precise statements about network responsiveness requires a definitive method for describing how neurons affect each others' firing patterns through their synaptic connections. In this chapter, we use a recently-proposed method (Chance, 2007) for describing neuronal sensitivity to individual EPSCs. This analysis is related to receiver-operating-characteristic (ROC) analysis for determining the detection performance of a system (see Green and Swets, 1988). Here, this analysis is used to describe the performance of the integrate-and-fire model neuron at detecting an EPSC (referred to as the 'input EPSC') amongst a background of noisy synaptic input.

In an ROC curve for this particular application, the probability that a neuron fires an action potential within a short (15 ms) time window after the input event (hit rate) is plotted against the probability that the neuron will fire an action potential within the same time window but in the absence of the input EPSC (false-alarm rate). The false-alarm rate is directly related to the average firing-rate of the neuron in the absence of the input EPSC. Because we have chosen a time window of 15 ms and the false-alarm rate cannot be greater than one, we are examining the neuron's detection performance over an average firing-rate ranging between zero and 67 Hz.

We define the neuron as having detected the input EPSC when it fires an action potential within 15 ms after the input EPSC occurs. If the neuron were a perfect detector, the hit rate would always be one, independent of the false-alarm rate. The ROC curve would thus be a straight line (hit rate of one) across the top of the graph. If the neuron's performance is random, the ROC curve will lie on the diagonal, because the hit rate will equal the false-alarm rate. With this analysis, the area under the ROC curve (ranging between one-half and one) is the measure of detection performance.

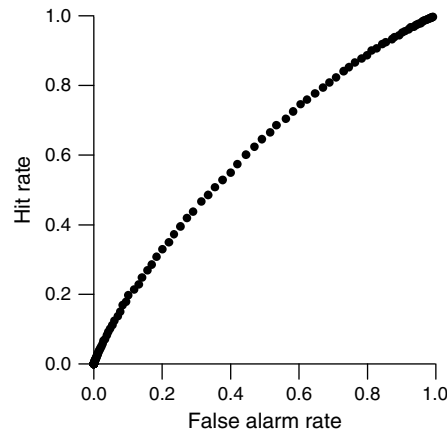


FIGURE 11.8 ROC curve of the integrate-and-fire neuron detecting the input EPSC. Hit rate is defined as the probability an action potential is fired within 15 ms after the input EPSC. False-alarm rate is the probability of an action potential within a 15 ms time period that does not contain the input EPSC. The background activity level is equal to the lowest level described in Figure 11.5.

The input EPSC is modeled as an instantaneous rise in current followed by an exponential decay (with a time constant of 5 ms) to zero. In the absence of any background synaptic input, the peak membrane potential deflection evoked by this EPSC is approximately 1 mV. There is no conductance change associated with the input EPSC. This is analogous to an input arriving at a distal portion of the dendrite so that the effects of the conductance change do not affect somatic integration.

As with the earlier simulations in which we discussed the effects of background synaptic activity on neuronal gain to constant input, here we examine the effects of background synaptic input on neuronal gain to time-varying input. Figure 11.8 shows the ROC curve of the model integrate-and-fire neuron in the presence of background activity. The background activity is identical to the lowest level in Figure 11.5 (3000 Hz synaptic input rates). Constant injected current was used to drive the neuron at different average firing-rates (thus varying false-alarm rate) to produce the data points (filled circles).

We next tripled the synaptic input rates and examined the ROC curve of the neuron's performance again (open diamonds) in Figure 11.9. This level of background activity is equivalent to the highest level in Figure 11.5 (9000 Hz synaptic input rates). The filled circles in Figure 11.9 are identical to those in Figure 11.8. With increased levels of background activity, the ROC curve flattens towards the diagonal (filled circles to open diamonds). This effect corresponds to a decrease in detection performance. In other words, just as an increase in background activity led to a decrease in neuronal gain to constant inputs, here the increase in background activity decreases neuronal gain or sensitivity to time-varying inputs.

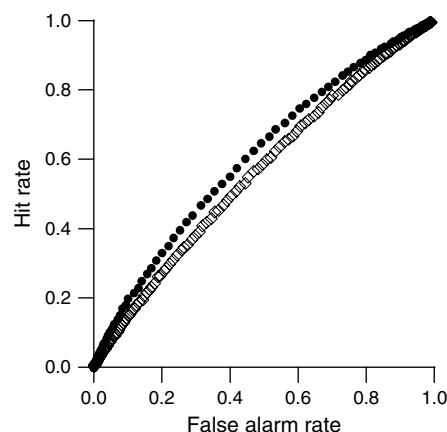
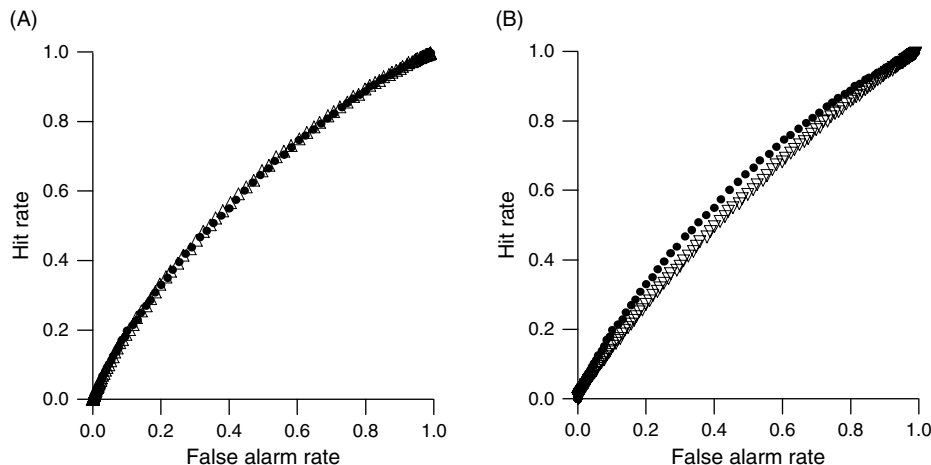


FIGURE 11.9 The filled circles are identical data to those in Figure 11.8. The open diamonds describe the ROC curve with increased background activity, at a level equal to that of the open diamonds in Figure 11.5B.



**FIGURE 11.10** In both panels, the filled circles are identical to those in Figures 11.8 and 11.9. (A) The open triangles are the ROC curve of the neuron with increased membrane conductance. An additional conductance, designed to mimic the conductance change evoked by the higher level of background activity in Figure 11.9, was introduced into the neuronal membrane. (B) The open inverted triangles are the ROC curve with increased input noise. The input noise was increased by decreasing the input rates to one third the original value and tripling the size of the unitary conductance changes for both the excitatory and inhibitory synaptic inputs.

In a similar approach to the one taken earlier in this chapter, we next separately consider the effects of increased membrane conductance and increased input noise arising from the higher level of background activity. The effects of each of these components in turn are compared in Figure 11.10. In both panels of Figure 11.10, the ROC curve represented by filled circles is replotted from Figure 11.8 and demonstrates the detection performance of the neuron with a low level of background synaptic input. In Figure 11.10A, the open triangles were measured after an additional shunt conductance was introduced into the model neuron's membrane. The magnitude and reversal potential of this additional conductance were chosen to match the effects of the conductance change evoked by the highest level of background synaptic activity that produced the open squares in Figure 11.9. This additional conductance is the same as that introduced into the neuron to produce the open diamonds in Figure 11.5B. Surprisingly, the two ROC curves are identical, demonstrating that the additional conductance does not change the neuronal sensitivity (defined by this method) to input EPSCs.

In Figure 11.10B, the ROC curve described by the open inverted triangles was measured under conditions of high input noise. The size of the unitary conductance change evoked by each excitatory and inhibitory synaptic input was tripled, while the input rates were reduced to one-third of the values that produced the filled circles. In the presence of increased input noise, the detection performance decreased (the ROC curve is flatter). As with the studies of neuronal responses to constant input current, a change in input noise is required to change neuronal sensitivity, in this case to EPSCs. Taken together, the results presented here show that increasing input noise is an effective mechanism for decreasing neuronal gain, whether in response to constant or time-varying inputs.

Although increasing input noise and increasing background activity are both manipulations that decrease detection performance (see Figures 11.9 and 11.10B), they have different effects on the average firing-rate of the neuron. The data in Figure 11.6B demonstrate that increasing input noise enhances firing-rate, while Figure 11.5B shows that increasing background synaptic input decreases firing-rate. Thus, it is possible, through changing the parameters defining the background input, to modulate gain independently of overall firing-rate. ROC analysis has been used to measure neuronal sensitivity to individual synaptic inputs because this method provides a firing-rate independent measure with which to describe neuronal gain. Other measurements of synaptic efficacy, for example the commonly used cumulative sum technique (Ellaway, 1977, 1978; Türker and Powers, 2002), are confounded by the average firing-rate of the neuron (Reyes and Fetz, 1993; Türker and Powers, 2002; Shu et al., 2003a; Azouz, 2005; Chance, 2007). While these are effective measurements in other situations, describing neuronal gain independently of overall firing-rate is important when considering the impact of neuronal sensitivity on network activity.

Figure 11.11 shows three firing-rate histograms generated from the integrate-and-fire neuron responding to the input EPSC in the presence of background activity. For Figure 11.11A, the excitatory and inhibitory input rates were 4000 Hz and 3000 Hz, respectively. With this level of background activity, the neuron fired at approximately 30 Hz without any additional current. The hit rate was 0.52 under these conditions. To produce the firing-rate histogram in Figure 11.11B,

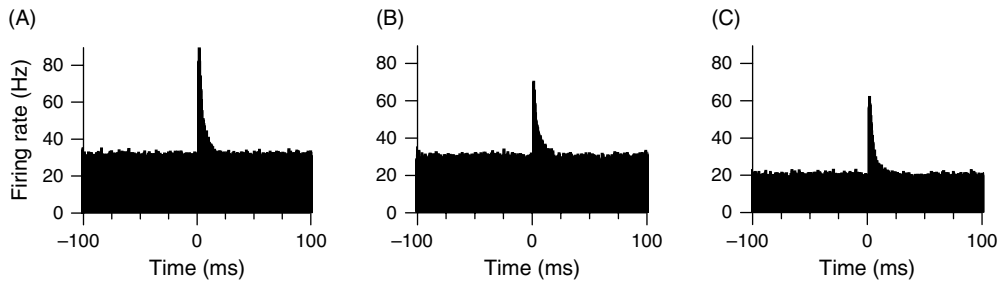


**FIGURE 11.11** Firing-rate histograms of the integrate-and-fire neuron responding to the input EPSC. The input EPSC always occurred at time = 0. Excitatory and inhibitory input rates were (A) 4000 Hz and 3000 Hz, (B) 10700 Hz and 9000 Hz and (C) 4000 Hz and 3200 Hz.

total synaptic input rates were first tripled and then the excitatory synaptic input rate was adjusted to maintain the overall firing-rate of the neuron. The final excitatory and inhibitory input rates were 10700 Hz and 9000 Hz, respectively. With this increased level of background activity, the hit rate was 0.38. Because the overall firing-rate (and thus false-alarm rate) was not significantly changed, the decrease in hit rate corresponds to a flattening of the ROC curve. The decrement in detection performance may also be seen by comparing the peaks of the firing-rate histograms in Figures 11.11A and 11.11B.

The background activity in Figure 11.11C is the same as in Figure 11.11A, except that the inhibition rate was increased slightly to match the hit rate of Figure 11.11B. Although the hit rate was 0.38 in both conditions, the peak of the firing-rate histogram appears slightly lower in Figure 11.11C (compared to Figure 11.11B) because the membrane time constant is much reduced in Figure 11.11B (and thus more spikes appear in the first bin of the response). In this case, hit rate and false-alarm rate are not modulated independently of each other and the overall firing-rate decreases along with the hit rate (compared with Figure 11.11A). The effects in Figure 11.11C result from the addition of inhibition, a mechanism that we have already demonstrated is subtractive. Thus, while hit rate is decreased, the result is not a change in neuronal gain.

The differences between the effects illustrated in Figure 11.11B and in Figure 11.11C (relative to Figure 11.11A) have important implications when considering their impact on network stability. In both cases, the probability of the neuron firing an action potential in response to the input EPSC is decreased by the same amount. However, in Figure 11.11C, adding inhibition to the network decreases overall activity as well. Moreover, we saw in Figure 11.2 that adding inhibition can abolish responses to some inputs and still allow the network to become unstable for others.

In Figure 11.11B, the response to the input EPSC is modulated independently of overall firing-rate. Through a mechanism such as this, it is possible to modulate the responses of a neuron independently of overall activity. This corresponds to the gain modulation effect in Figure 11.3, where decreasing the gain of the neuron stabilized the network effectively without abolishing responses to particular inputs.

This mechanism of gain modulation has been examined in a variety of single-compartmental neuronal models and found to be quite robust (Chance et al., 2002; Prescott and DeKoninck, 2003). Qualitatively similar effects occur in detailed multicompartmental neuronal models in which the synaptic inputs are distributed over the dendritic arbor and active conductances are included in the dendrites (Destexhe et al., 2001). The same effects of increased background activity have been demonstrated in living slices (Chance et al., 2002; McCormick et al., 2003). The similarities between the effects observed in single-compartment neuronal models, detailed multicompartmental models and *in vitro* suggests that the background input is a biologically viable mechanism for *in vivo* gain modulation.

The neural circuitry contained within a cortical slice can spontaneously generate sustained periods of neural activity (Sanchez-Vives and McCormick, 2000; Shu et al., 2003a, 2003b). Studies of these ‘active periods’ in slice have compared this activity to ‘up’ states observed in *in vivo* cortex and also have shown that excitation and inhibition co-vary during these bouts of high synaptic activity (Shu et al., 2003b). Based on these works, a significant portion of the background activity observed *in vivo* appears to be generated by local recurrent circuitry in cortex.

Our results suggest that increasing the level of background activity may be one mechanism for stabilizing neural networks. During periods of high background activity, a neuron may be more active but at the same time have lower gain. Thus, it is possible that increasing the activity of a network can have a stabilizing effect. Given that the recurrent circuitry of cortex appears to be capable of self-generating the required background activity, little external input may be required to decrease neuronal gain. Thus, this stabilization mechanism may be used in cortex.

A common approach to stabilizing a neural network is to add inhibition (as in Figure 11.2). However, for a cortical network that contains many excitatory and inhibitory recurrent connections, it is possible that manipulations that increase the level of recurrent excitation will be effective mechanisms for stabilizing the gain of the network, provided that the

circuitry generates co-varying recurrent inhibition. Evidence from slice experiments suggests that active states can be artificially triggered by brief excitatory inputs (Sanchez-Vives and McCormick, 2000; Shu et al., 2003a, 2003b). Thus, increases in excitatory input may be effective at initiating background activity that will lead to a gain decrease. Likewise, manipulations that increase recurrent excitation may be effective at stabilizing an unstable network if they lead to increased background activity. Future work exploring these effects will provide interesting and important insights into understanding the role of background activity in cortical processing and network stability.

## REFERENCES

- Andersen, R.A. and Mountcastle, V.B. (1983). The influence of the angle of gaze upon the excitability of light-sensitive neurons of the posterior parietal cortex. *J Neurosci* 3:532–548.
- Azouz, R. (2005). Dynamic spatiotemporal synaptic integration in cortical neurons: neuronal gain, revisited. *J Neurophysiol* 94:2785–2796.
- Ben-Yishai, R., Bar-Or, R.L. and Sompolinsky, H. (1995). Theory of orientation tuning in visual cortex. *Proc Natl Acad Sci* 92:3844–3848.
- Borg-Graham, L.J., Monier C. and Frégnac, Y. (1998). Visual input evokes transient and strong shunting inhibition in visual cortical neurons. *Nature* 393:369–373.
- Braitenberg, V. and Shüz, A. (1991). Anatomy of the cortex. Springer, Berlin.
- Carandini, M. and Heeger, D.J. (1994). Summation and division by neurons in primate visual cortex. *Science* 264:1333–1336.
- Carandini, M. and Ringach, D.L. (1997). Predictions of a recurrent model of orientation selectivity. *Vision Res* 37: 3061–3071.
- Carandini, M., Heeger, D.J. and Movshon, J. A. (1997). Linearity and normalization in simple cells of the macaque primary visual cortex. *J Neurosci* 17:8621–8644.
- Chance, F. S. (2007). Receiver operating characteristic (ROC) analysis for characterizing synaptic efficacy. *J Neurophysiol* 97:1799–1808.
- Chance, F.S., Nelson, S.B. and Abbott, L.F. (1999). Complex cells as cortically amplified simple cells. *Nat Neurosci* 2:277–282.
- Chance, F.S., Abbott, L.F. and Reyes, A.D. (2002). Gain modulation from background synaptic input. *Neuron* 35:773–782.
- Destexhe, A. and Paré, D. (1999) Impact of network activity on the integrative properties of neocortical pyramidal neurons in vivo. *J Neurophysiol* 81:1531–1547.
- Destexhe, A., Rudolph, M., Fellous, J-M. and Sejnowski, T.J. (2001). Fluctuating synaptic conductances recreate in vivo-like activity in neocortical neurons. *Neuroscience* 107:13–24.
- Destexhe, A., Rudolph, M. and Paré, D. (2003). The high-conductance state of neocortical neurons in vivo. *Nat Rev Neurosci* 4:739–751.
- Doiron, B., Longtin, A., Berman, N. and Maler, L. (2000). Subtractive and divisive inhibition: effect of voltage-dependent inhibitory conductances and noise. *Neural Comput* 13:227–248.
- Douglas, R.J. and Martin, K.A.C. (1991). A functional microcircuit for cat visual cortex. *J Physiol* 440:735–769.
- Douglas, R.J., Martin, K.A.C. and Whitteridge, D. (1989). A canonical microcircuit for neocortex. *Neural Comput* 1:480–488.
- Douglas, R.J., Koch, C., Mahowald, M., Martin, K.A.C. and Suarez, H. (1995). Recurrent excitation in neocortical circuits. *Science* 269:981–985.
- Ellaway, P.H. (1977). An application of cumulative sum technique (cusums) to neurophysiology. *J Physiol* 265:1P–2P.
- Ellaway, P.H. (1978). Cumulative sum technique and its application to the analysis of peristimulus time histograms. *Electroencephalogr Clin Neurophysiol* 45:302–304.
- Gabbiani, F., Midtgård, J., and Knöpfel, T. (1994). Synaptic integration in a model of cerebellar granule cells. *J Neurophysiol* 72:999–1009.
- Green, D.M. and Swets, J.A. (1988). Signal Detection Theory and Psychophysics. Peninsula Publishing, Los Altos.
- Heeger, D.J. (1992). Normalization of cell responses in cat striate cortex. *Visual Neurosci* 9:181–197.
- Hirsch J.A., Alonso, J-M., Reid, R.C. and Martinez, L.M. (1998). Synaptic integration in striate cortical simple cells. *J Neurosci* 18:9517–9528.
- Holt, G.R. and Koch, C. (1997). Shunting inhibition does not have a divisive effect on firing rates. *Neural Comput* 9:1001–1013.
- Holt, G.R., Softky, W.R., Koch, C. and Douglas, R.J. (1996). Comparison of discharge variability in vitro and in vivo in cat visual cortex neurons. *J Neurophysiol* 75:1806–1814.
- Kisvárdy, S.F., Martin, K.A.C., Freund, T.F., Maglóczky, Zs., Whitteridge, D. and Somogyi, P. (1986). Synaptic targets of HRP-filled layer III pyramidal cells in the cat striate cortex. *Exp Brain Res* 64:541–552.
- LeVay, S. (1986). Synaptic organization of claustral and geniculate afferents to the visual cortex of the cat. *J Neurosci* 6:3564–3575.
- Maex R. and Orban, G.A. (1996). Model circuit of spiking neurons generating directional selectivity in simple cells. *J Neurophysiol* 75:515–545.
- Martínez-Trujillo J.C. and Treue, S. (2002). Attentional modulation strength in cortical area MT depends on stimulus contrast. *Neuron* 35:355–370.
- McAdams, C.J. and Maunsell, J.H.R. (1999). Effects of attention on orientation-tuning functions of single neurons in macaque cortical area V4. *J Neurosci* 19:431–441.
- McCormick, D.A., Shu, Y., Hasenstaub, A., Sanchez-Vives, M., Baldouan, M. and Bal, T. (2003). Persistent cortical activity: mechanisms of generation and effects on neuronal excitability. *Cereb Cortex* 13:1219–1231.
- McGuire, B.A., Hornung, J-P., Gilbert, C.D. and Wiesel, T.N. (1984). Patterns of synaptic input to layer 4 of cat striate cortex. *J Neurosci* 4:3021–3033.
- Mehaffey, W.H., Doiron, B., Maler, L. and Turner, R.W. (2005). Deterministic multiplicative gain control with active dendrites. *J Neurosci* 25:9968–9977.
- Mitchell, S.J. and Silver, R.A. (2003). Shunting inhibition modulates neuronal gain during synaptic excitation. *Neuron* 38:433–445.
- Murphy, B.K. and Miller, K.D. (2003). Multiplicative gain changes are induced by excitation or inhibition alone. *J Neurosci* 23:10040–10051.
- Paré, D., Shink, E., Gadreau, H., Destexhe, A. and Lang, E.J. (1998). Impact of spontaneous synaptic activity on the resting properties of cat neocortical pyramidal neurons in vivo. *J Neurophysiol* 79:1450–1460.
- Peters, A. and Payne, B.R. (1993). Numerical relationships between geniculocortical afferents and pyramidal cell modules in cat primary visual cortex. *Cereb Cortex* 3:69–78.

- Peters, A., Payne, B.R. and Budd, J. (1994). A numerical analysis of the geniculocortical input to striate cortex in the monkey. *Cereb Cortex* 4:215–229.
- Pouget, A. and Sejnowski, T. (1997). Spatial transformations in the parietal cortex using basis functions. *J Cog Neurosci* 9:222–237.
- Prescott, S.A. and DeKoninck, Y.D. (2003). Gain control of firing rate by shunting inhibition: roles of synaptic noise and dendritic saturation. *Proc Natl Acad Sci* 100:2076–2081.
- Reyes, A.D. and Fetz, E.E. (1993). Effects of transient depolarizing potentials on the firing rate of cat neocortical neurons. *J Neurophysiol* 69:1673–1683.
- Reynolds, J.H. and Pasternak, T. (2000). Attention increases sensitivity of V4 neurons. *Neuron* 26:703–714.
- Salinas, E. and Abbott, L.F. (1995). Transfer of coded information from sensory to motor networks. *J Neurosci* 15:6461–6474.
- Salinas, E. and Abbott, L.F. (1997). Invariant visual responses from attentional gain fields. *J Neurophysiol* 77:3267–3272.
- Salinas, E. and Thier, P. (2000). Gain modulation: a major computational principle of the central nervous system. *Neuron* 27:15–21.
- Sanchez-Vives, M.V. and McCormick, D.A. (2000). Cellular and network mechanisms of rhythmic recurrent activity in neocortex. *Nat Neurosci* 3:1027–1034.
- Seung, H.S. (2000). The autapse: a simple illustration of short-term analog memory storage by tuned synaptic feedback. *J Comput Neurosci* 9:171–185.
- Shadlen, M.N. and Newsome, W.T. (1998). The variable discharge of cortical neurons: implications for connectivity, computation, and information coding. *J Neurosci* 18:3870–3896.
- Shu, Y., Hasenstaub, A., Badoual, M., Bal, T. and McCormick, D.A. (2003a). Barrages of synaptic activity control the gain and sensitivity of cortical neurons. *J Neurosci* 23:10388–10401.
- Shu, Y., Hasenstaub, A. and McCormick, D.A. (2003b). Turning on and off of recurrent balanced cortical activity. *Nature* 423:288–293.
- Smith, M.R., Nelson, A.B. and Du Lac, S. (2002). Regulation of firing response gain by calcium-dependent mechanisms in vestibular nucleus neurons. *J Neurophysiol* 87:2031–2042.
- Softky, W.R. and Koch, C. (1993). The highly irregular firing of cortical cells is inconsistent with temporal integration of random EPSPs. *J Neurosci* 13:334–350.
- Somers, D.C., Nelson, S.B. and Sur, M. (1995). An emergent model of orientation selectivity in cat visual cortical simple cells. *J Neurosci* 15:5448–5465.
- Sompolinsky, H. and Shapley, R. (1997). New perspectives on the mechanisms for orientation selectivity. *Curr Opin Neurobiol* 7:514–522.
- Steriade, M., Timofeev, I. and Grenier, F. (2001). Natural waking and sleep states: a view from inside neocortical neurons. *J Neurophysiol* 85:1969–1985.
- Stevens, C.F. and Zador, A.M. (1998). Input synchrony and the irregular firing of cortical neurons. *Nat Neurosci* 1:210–217.
- Suarez, H., Koch, C. and Douglas, R. (1995). Modeling direction selectivity of simple cells in striate visual cortex within the framework of the canonical microcircuit. *J Neurosci* 15:6700–6719.
- Tao, L., Shelley, M., McLaughlin, D. and Shapley, R. (2004). An egalitarian network model for the emergence of simple and complex cells in visual cortex. *Proc Natl Acad Sci* 101:366–371.
- Tiesinga, P.H.E., José, J.V., and Sejnowski, T.J. (2000). Comparison of current-driven and conductance-driven neocortical model neurons with Hodgkin-Huxley voltage-gated channels. *Phys Rev E* 62:8413–8419.
- Treue, S. and Martínez-Trujillo, J.C. (1999). Feature-based attention influences motion processing gain in macaque visual cortex. *Nature* 399:575–579.
- Türker, K.S. and Powers, R.K. (2002). The effects of common input characteristics and discharge rate on synchronization in rat hypoglossal motoneurons. *J Physiol* 245:245–260.
- Ulrich, D. (2003). Differential arithmetic of shunting inhibition for voltage and spike rate in neocortical pyramidal cells. *Eur J Neurosci* 18:2159–2165.
- White, E.L. (1989). *Cortical Circuits: Synaptic Organization of the Cerebral Cortex*. Birkhäuser, Boston.
- Woody, C.D. and Gruen, E. (1978). Characterization of electrophysiological properties of intracellularly recorded neurons in the neocortex of awake cats: a comparison of the response to injected current in spike overshoot and undershoot neurons. *Brain Res* 158:343–357.
- Zipser, D. and Andersen, R.A. (1988). A back-propagation programmed network that simulates response properties of a subset of posterior parietal neurons. *Nature* 331:679–684.

# 12

## NEOCORTICAL EPILEPTIFORM ACTIVITY IN NEURONAL MODELS WITH BIOPHYSICALLY REALISTIC ION CHANNELS

WIM VAN DRONGELEN, AMBER MARTELL AND HYONG C. LEE

### ABSTRACT

Computational models can be used to examine potential neuronal mechanisms underlying epileptiform neuronal network activity. We review the principles of biophysical modeling by describing the relationship between membrane structure and function, the construction of multicompartment cell models, the synaptic channels that link these model neurons together and, finally, how to calculate the overall electrical activity emerging from model networks. Based on these principles, we describe a specific model of neocortex that includes two layers of pyramidal cells and a layer with four types of inhibitory interneurons: local-, median-, and wide arbor basket cells, plus the axo-axonic (chandelier) cell type. We find that this model's behavior exhibits three distinct types of network bursting activity as the level of network coupling is varied from high to low: irregular bursting, fast oscillations and regular bursting. Both the irregular and regular bursting patterns depend on the presence of spontaneously bursting neurons, whereas the oscillations do not depend on this cell type. The oscillatory pattern resembles seizure-onset activity and is characterized by a modest level of synchrony between the individual neurons. These model results are supported by experimental evidence for oscillatory seizure-like activity evoked by a reduction in excitatory coupling, for the role played by spontaneously bursting neurons in driving network burst activity, and for low levels of synchrony during experimental seizures.

### INTRODUCTION

Epilepsy is a neurological disorder characterized by chronic seizures. It affects about 50 million people worldwide (about 1% of the population); a large fraction ( $\sim \frac{1}{4}$ ) of these patients are not fully controlled with medication (Kwan and Brodie, 2000) and live in constant fear of having a seizure at any time. The lack of understanding of the mechanisms underlying epilepsy is perhaps the most important reason for the limited success in therapy. Complicating matters is the fact that epilepsy is not characterized by one specific behavior or a unique electrographic signature, but is instead a disease that encompasses a wide variety of behavioral and electrographic abnormalities. Indeed, many different phenotypes and genotypes have been described and it seems that epileptic seizures are the final common path for a broad range of pathologies. Models in epilepsy therefore commonly focus on a particular aspect of the disease. In this chapter, we focus on partial seizures originating in a focal area in neocortex, a seizure type often encountered in pediatric patients.

Two pathological electrographic features are commonly associated with epilepsy: interictal discharges and seizure activity (the ictal events). Interictal activity is characterized by isolated spikes and/or bursts occurring frequently, but irregularly, throughout the day. A seizure usually displays electrical activity characterized by a repetitive, (almost) periodic pattern, usually of high amplitude; in partial seizures, this activity may propagate from a small focal site to a larger area (Figure 12.1A). These changes in amplitude and rhythmicity during seizure have led clinicians to associate epileptiform activity with an elevation both in the level of activity of individual elements in a neuronal network (hyperactivity) and in their tendency to act in concert (hypersynchrony) (e.g. Delgado-Escueta et al., 1999).

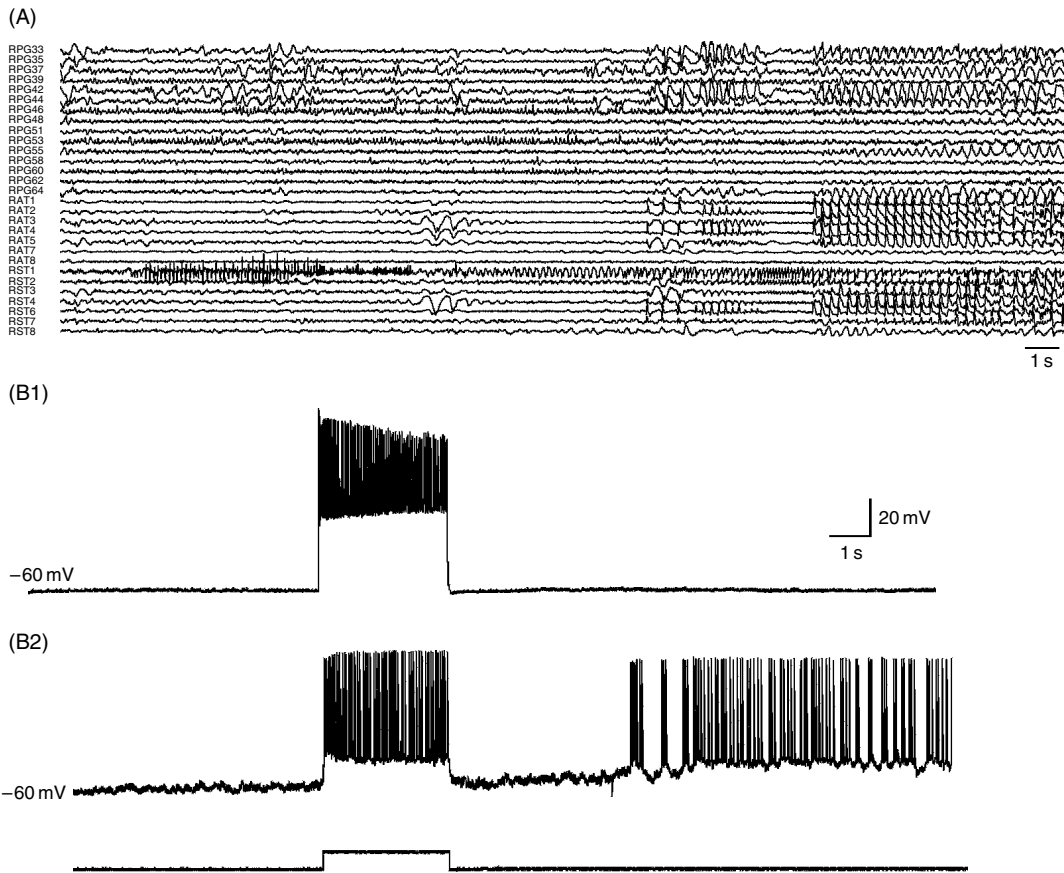


**FIGURE 12.1** Seizure activity and cellular behavior. (A) Electrical activity during seizure onset recorded from intracranial electrodes. Seizure activity starts in the temporal area (RST1) and then propagates to include large portions of the temporal and parietal lobes. (B) Evoked cellular response upon a current injection of 150 pA. Responses from pyramidal neurons originating from a juxtafocal area (B1) and from the focal area (B2). The neuron in the focal area shows intense after discharges following the current injection. The neuron shown in (B2) originates from the area covered by electrode RST1 in (A).

Despite the apparent simplicity of the rhythmic bursting behavior of a seizing network, it is clear that many serious problems remain to be solved. For example, it is unclear why seizures start or stop, how seizure activity is sustained, or how it propagates. More importantly, it is not clear how to stop ongoing seizure propagation or reliably to prevent seizure activity. In addition to the unresolved problems, even the long-held belief in a link between hyperactivity and hypersynchrony on the one hand, and seizure activity on the other, may not be justified in all cases. In several instances, both computational and experimental models have shown that low levels of excitatory coupling may be a prerequisite for some types of seizure onsets (e.g. Pumain et al., 1985; Feng and Durand, 2004; Van Drongelen et al., 2005). In addition, it has been shown that hypersynchrony is not necessary for experimental preparations to produce seizure-like bursting (e.g. Netoff and Schiff, 2002; Van Drongelen et al., 2003a).

Considerable research effort has been expended on trying to understand which neuronal properties are important in initiating and sustaining seizure activity. The most direct approach uses single- and multiunit recording techniques to study the behavior of single cells or small networks that seize spontaneously, or are induced into seizure-like activity; this has been done both in intact animals (*in vivo*) and in brain slices (*in vitro*) (e.g. Gutnick et al., 1982; Connors, 1984; Connors and Amitai, 1993; Avoli and Williamson, 1996; Steriade et al., 1998; Neckelmann et al., 2000; Sanchez-Vives and McCormick, 2000; Netoff and Schiff, 2002; Van Drongelen et al., 2003a, 2006). In addition, the removal of the epileptic focus from some patients as part of their treatment has afforded the opportunity to perform *in vitro* studies of human tissue. Surprisingly, it has been difficult to find clear differences between neurons from human focal tissue and from tissue located just outside the focus (juxtafocal) (e.g. Wuarin et al., 1990; Dudek et al., 1995; Tasker et al., 1996), though evidence has been found that, in some patients, the propensity for bursting activity appeared to be predominantly present in the focal as compared to juxtafocal tissue (see Figure 12.1B) (Van Drongelen et al., 2003b).

Despite often Herculean efforts, current electrophysiological studies remain severely limited in the number of neurons that can be recorded simultaneously, the level of detail of recorded network activity and the experimental control of physiological parameters. All of these limitations can be addressed by modeling the neuronal network computationally. Any property of an *in silico* model can be modified or recorded, so the relationship between the input parameters and the output cellular or network activity patterns can be investigated in ways that would be difficult or impossible to duplicate experimentally (e.g. Lytton and Sejnowski, 1991; Traub and Miles, 1991; Traub et al., 1994; Fleidervish et al., 1996; Golomb and Amitai, 1997; Golomb, 1998; Destexhe and Pare, 1999; Wang, 1999; Kepecs et al., 2002; Van Drongelen et al., 2002, 2004, 2005, 2006; Van Drongelen and Hecox, 2003). For instance, the relative contribution of cellular properties (e.g. individual ion channels) and network parameters (e.g. synaptic coupling) to activity patterns at different scales can be determined cleanly, without the undesired or unknown side effects of the pharmacological approach used on real neuronal networks. Although computational models can be enormously helpful in gaining insight into the mechanisms underlying neuronal function, it must be emphasized that modeling cannot replace experimentation. Computational neuronal network models are (like all models) a simplified version of reality that is designed to capture the fundamental properties of the actual neural structure. The ultimate goal in computational neuroscience is to translate simulated results and insights into testable hypotheses or, conversely, test hypotheses generated by experimental or clinical observations.

In this chapter, we summarize the principles of modeling with biophysically realistic ion channels, describe in detail a model of neocortex and show its utility in exploring network seizure-like activity at the cellular and network levels. We then relate model behavior with experimental findings in neocortical structures. Our model gives new insights into the role that a weakened excitatory drive, intrinsic cellular bursting and decreased synchrony levels may play in epileptic behaviors.

#### PRINCIPLES OF BIOPHYSICAL MODELING

This section summarizes some of the basic principles involved in modeling of neural function. (See Bower and Beeman (1998) or Lytton (2002) for a more complete treatment.)

#### EQUIVALENT CIRCUIT FOR A SIMPLE NEURON

The electrical behavior of neurons can be thought of as arising from electrical circuits (Figure 12.2) that can be modeled by systems of differential equations. We represent the inside and outside of the cell separated by the phospholipid membrane as a capacitor ( $C$ ) while a resistor ( $R$ ) represents the ion channels present in the membrane. The equivalent circuit for such a model neuron is shown in Figure 12.2, where the battery ( $E$ ) represents the electrochemical driving force of the ion species associated with a particular channel type. Using Kirchhoff's first law (all currents in a circuit node must add up

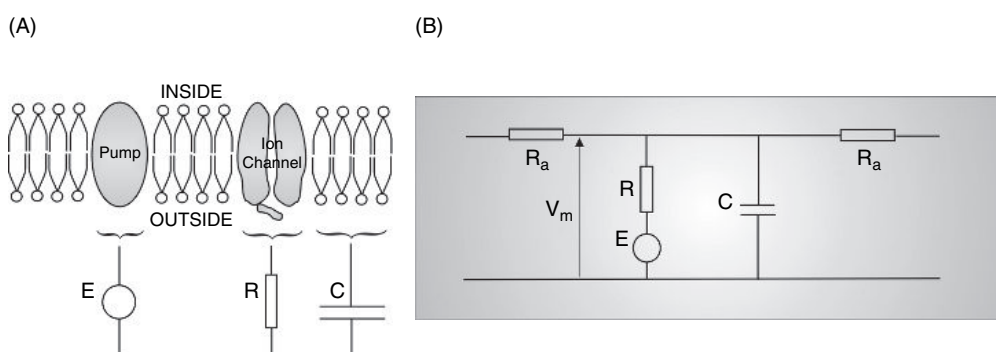


**FIGURE 12.2** The neuronal membrane as an electrical circuit. (A) Membrane structure is dominated by a bilayer of phospholipids that separates the cell's inside from the outside. Embedded are ion transport structures: pumps that consume energy and transport ion species against the gradient and channels that allow leakage of the ions. An electronic equivalent circuit can be used to represent these structures: the pump is a battery  $E$ , the channel a resistor  $R$ , and the isolating phospholipid layer separating the cell's inside and outside can be represented by a capacitor  $C$ . (B) The electronic components form circuitry that can generate electrical membrane function. (From Van Drongelen, 2006).

to zero), we may state that the sum of all ion currents creates the charge ( $Q$ ) of the membrane capacitance ( $C$ ). Thus, the currents in the membrane equivalent circuit are described by the following equation:

$$\frac{dQ}{dt} = C \frac{dV_m}{dt} = \sum_n I_n \quad (1)$$

$V_m$  represents the membrane potential and  $I_n$  represents the different membrane currents.

### RESTING MEMBRANE POTENTIAL

The resting membrane potential ( $V_m$ ) is produced by a difference in potential across the membrane. The ion pumps that are incorporated into the membrane create concentration differences of ion species between the inside and outside of the cell that, in turn, gives rise to a potential difference across the membrane. Potassium accumulates inside the neuron and sodium is pumped out, e.g.  $[K]_{out} = 2.5 \text{ mM}$ ;  $[Na]_{out} = 120 \text{ mM}$ ;  $[K]_{in} = 140 \text{ mM}$ ;  $[Na]_{in} = 9.2 \text{ mM}$ . The resting membrane potential can be determined using the Goldman equation, which accounts for differences in both the permeability and the concentrations of each ion species. If we simplify our model and only consider the compound effect of  $\text{Na}^+$  and  $\text{K}^+$  ions, the potential is determined by the following equation:

$$E_{NaK} = \frac{RT}{F} \ln \left( \frac{p_{Na} [Na_{out}] + p_K [K_{out}]}{p_{Na} [Na_{in}] + p_K [K_{in}]} \right) = 58 \log_{10} \left( \frac{p_{Na} [Na_{out}] + p_K [K_{out}]}{p_{Na} [Na_{in}] + p_K [K_{in}]} \right) = -89 \text{ mV} \quad (2a)$$

The potential difference  $E_{NaK}$  created by a difference of concentrations of ion species  $\text{Na}^+$  and  $\text{K}^+$  was calculated given the concentrations stated previously and a ratio  $p_{Na}/p_K = 0.013$ . The constants  $R$ ,  $T$  and  $F$  are the gas constant, absolute temperature and Avogadro's number respectively.

Ion channels for specific ion species counteract the pump's work by allowing leakage of ions. The Nernst equation computes the equilibrium potential for each ion. The following equations show how to compute this value for both sodium and potassium ions:

$$E_{Na} = 58 \log_{10} \left( \frac{[Na_{out}]}{[Na_{in}]} \right) = 65 \text{ mV}, \quad (2b)$$

and for  $\text{K}^+$ :  $E_K = 58 \log_{10} \left( \frac{[K_{out}]}{[K_{in}]} \right) = -101 \text{ mV}$

The pumps must work to maintain a concentration difference over the membrane against the leakage through the ion channels. We assume that the pump is able to compensate for the leakage so that concentration differences remain constant. However, this assumption may not hold during seizures because extracellular ion concentrations are known to fluctuate in epileptic tissue (Gorji et al., 2006).

### MEMBRANE CHANNELS

We can model each type of ion channel ( $n$ ) as a resistor ( $R$ , see Figure 12.2) through which the ions are driven by a battery (pump). The potential of the battery, or reversal potential ( $E$ ), is determined by the permeability of the ions for that specific channel along with the Nernst potential for each ion ( $E$  in Figure 12.2), and the potential difference across the ion channel ( $R$ ) is the difference between the membrane potential and reversal potential. This creates an ion current ( $I_n$ ) that can be calculated with Ohm's law, which takes the form:

$$I_n = G_n (V_m - E_n), \quad (3a)$$

with  $G_n$  representing the channel conductance,  $V_m$  the membrane potential and  $E_n$  the reversal potential.

#### Leak channels and voltage-gated channels

The conductance ( $G_n$ ) for a leak channel can simply be represented by a constant corresponding to the inverse of the resistance for the leakage of ions through the membrane.

Voltage-gated conductances will be treated in the Hodgkin-Huxley fashion (Hodgkin and Huxley, 1952):

$$G_n = g_{max,n} m^x h^y \quad (3b)$$

The variable  $m$  represents probability of activation, while  $h$  represents the probability of not being inactivated ( $h$  would be unity for those channels that do not inactivate). If different from unity, the powers  $x$  and  $y$  introduce non-linearity into the expression for  $G_n$ . The dynamics of the variables  $m$  and  $h$  are modeled by the equations:

$$\frac{dm}{dt} = (m_\infty(V) - m)/\tau_m(V), \quad \frac{dh}{dt} = (h_\infty(V) - h)/\tau_h(V) \quad (4a)$$

where  $\tau_m$  and  $\tau_h$  are the voltage-dependent time constants while  $m_\infty$  and  $h_\infty$  are the steady state activations at a given potential ( $V$ ).

It is illustrative to consider how Equations (4a) arise from the underlying dynamics; since the underlying dynamical model for all coefficients is the same, we show the reasoning only for the coefficient  $h$ . Consider a process represented by  $h \xrightarrow[\alpha]{\beta} 1 - h$  with  $\alpha$  and  $\beta$  being rate constants dependent only on the membrane potential  $V_m$ , i.e.  $\alpha = \alpha(V_m)$  and  $\beta = \beta(V_m)$ . This process can be described with the first order ordinary differential equation (ODE):

$$\frac{dh}{dt} = \alpha(1 - h) - \beta h \quad (4b)$$

The steady state value of  $h$  is, by definition, that value of  $h$  for which  $dh/dt = 0$ ; Equation (4b) has the steady state solution  $h_\infty = \alpha/[\alpha + \beta]$ . Now, solving Equation (4b) for  $h$ , and expressing the solution in terms of  $h_0 \equiv h(t = 0)$  and  $h_\infty$ , we find

$$h = (h_0 - h_\infty) e^{-(\alpha+\beta)t} + h_\infty \quad (4c)$$

The solution in Equation (4c) takes the form of an exponential decay toward  $h_\infty$  with a voltage-dependent time constant  $\tau_h = 1/(\alpha + \beta)$ . The inverse relationships are:  $\alpha = h_\infty/\tau_h$  and  $\beta = (1 - h_\infty)/\tau_h$  and substitution of these expressions for  $\alpha$  and  $\beta$  in Equation (4b) generates the expression for  $dh/dt$  in Equation (4a).

Most models described in the literature include expressions for  $\alpha$  and  $\beta$  as a function of  $V_m$  for each of the coefficients, but some authors, for example Golomb and Amitai (1997), define  $h_\infty$  and  $\tau_h$  with a Boltzmann function. The Boltzmann type function is valued between zero and one, and is given by:

$$c = 1/(1 + e^{-(V_m - \Theta)/\sigma}) \quad (5)$$

Here,  $V_m$  is the membrane potential, the value of  $\Theta$  is the position on the abscissa where the function is at 50% of its maximum, and  $\sigma$  determines the slope. The sign of the exponent determines if the function decreases (negative exponent) or increases (positive exponent) with  $V$ . The advantage of using the Boltzmann type equation over the use of  $\alpha$  and  $\beta$  is that its parameters  $\Theta$  and  $\sigma$  are easily determined from experimental data.

### Synaptic channels

A synaptic channel on a model neuron can be represented by a synaptic current ( $I_{syn}$ ) evoked by a presynaptic action potential. Because we represent postsynaptic function as current, we can include it as one of the currents  $I_n$  in Equation (1). The sign of the current determines its function: excitatory synaptic currents depolarize the membrane while inhibitory synaptic currents hyperpolarize the membrane. Representing the postsynaptic portion of the synapse as an ion channel (similar to the voltage sensitive ones above), we may calculate the post-synaptic current as:

$$I_{syn} = g_{syn}(V_m - E_{syn}) \quad (6a)$$

with  $E_{syn}$  and  $g_{syn}$  representing the synaptic reversal potential and the synaptic conductance, respectively. In contrast to the voltage sensitive channels discussed in the previous paragraphs, the conductance is usually independent of voltage but increases with the presence of neurotransmitter, released upon arrival of a presynaptic action potential. Upon arrival of a presynaptic action potential, the conductance can be modeled with an alpha function:

$$g_{syn} = \overline{g_{syn}} \frac{t}{\tau} e^{(1-t/\tau)} \quad (6b)$$

$\overline{g_{syn}}$  is the maximum conductivity value for  $g_{syn}$ , which will be reached rapidly at  $t = \tau$ . After reaching the peak, the decay back to zero is slower than the rise to  $\overline{g_{syn}}$ . Alternatively, one might use a double exponential function with two time constants  $\tau_1$  and  $\tau_2$ :

$$g_{syn} = \frac{C\overline{g_{syn}}}{\tau_1 - \tau_2} (e^{-t/\tau_1} - e^{-t/\tau_2}), \quad \text{with } \tau_1 > \tau_2 \quad (6c)$$

The scaling value  $C$  is adjusted so that the maximum value of  $g_{syn}$  reaches  $\overline{g_{syn}}$ . All of these parameters are found by fitting these equations to experimental data.

### COMPARTMENTS AND EXTRACELLULAR CURRENT

Real neurons have complex shapes. In spite of all the detail described in the previous paragraphs, the representation of a nerve cell by a set of non-linear electronic components forming one circuit is a significant oversimplification. For example, the spatial effects of synapses on the dendritic part of a neuron, or the action potential generation in the initial segment of the axon, cannot be modeled with such a system. To solve this problem, the real shape of the nerve cell can be approximated by a set of coupled compartments each in the shape of a cylinder. Each compartment is considered a segment of membrane small enough that its surface may be considered iso-potential, i.e. having the same potential  $V_m$  within the whole compartment. These compartments then couple to adjacent compartments via resistors that model the axial resistance ( $R_a$ , see Figure 12.2). The electrical behavior for each compartment is then given by a small modification of Equation (1) to include inter-compartmental currents  $I_{ic}$ , which is obtained from the potential differences between the neighbor compartments and the axial resistance  $R_a$  that separates them. In the case of compartment  $a$  and  $b$  with membrane potentials  $V_a$  and  $V_b$  we determine inter-compartmental current with Ohm's law:

$$I_{ic} = (V_a - V_b)/R_a \quad (7a)$$

In a single compartment model all currents add up to zero (Equation (1)). Because there is no net current sink or source associated with this model, there is no direct method of modeling extracellular current. By contrast, in multicompartamental models, an extracellular current component can easily be computed because it is implicitly available as the inter-compartmental current. Because charge in electrical circuitry cannot magically appear or disappear, a current that flows between the compartments within the model cell must also flow (in the opposite direction) outside of it. Just as in a real electrophysiological preparation, this external current can be measured by an electrode on the outside of the neuron. The effect of the current decreases with distance; if the neuron is assumed to be in an infinite volume conductor, the extracellular potential  $V_e$  measured as a result of  $N$  current sources with currents  $i_n$  ( $n = 1, 2, \dots, N$ ) is (Nunez, 1981):

$$V_e = \frac{1}{4\pi s} \sum_{n=1}^N \frac{i_n}{D_n} \quad (7b)$$

Here,  $s$  is the conductivity of the extracellular medium (brain tissue) and  $D_n$  the distance between the  $n^{\text{th}}$  cell and the recording site. For a brain cell, typical values of these parameters are as follows:  $s \approx 0.05 \Omega^{-1} \text{ m}^{-1}$  (a resistance of  $2 \text{ k}\Omega\text{cm}$ );  $D_n \approx 10^{-3} \text{ m}$  (1 mm);  $i_n \approx 20 \times 10^{-12} \text{ A}$  (20 pA).

### BUILDING THE NEOCORTICAL MODEL

To study the relationship between neural function at the cell membrane and multiunit extracellular recordings in neocortex, we constructed a realistic computational model incorporating histological data and Hodgkin and Huxley type membrane currents (Hodgkin and Huxley, 1952). In this section, we describe how the principles described in the previous paragraphs were used to create a computational neuronal network model of neocortex.

### CELL TYPES AND NEOCORTICAL STRUCTURE

The gray matter in the neocortex is organized in horizontal layers 1 to 6 and vertical modules, columns, or micro-columns (Szentagothai, 1978; Nieuwenhuys, 1994; Mountcastle, 1997; Somogyi et al., 1998; DeFelipe et al., 2002; Binzegger et al., 2004). The major neural component of the neocortex consists of two types of pyramidal cells: the superficial pyramidal

cells in layers 2 and 3 and the deep pyramidal cells in layers 5 and 6. This distinction between the superficial and deep cells relates to their laminar position but is also related to the target of their axons: intracortical targets for the superficial cells and intracortical plus subcortical targets for the deep ones. This structure was the basis for a canonical circuit for the neocortex, first proposed by Douglas and Martin (1990), which included two excitatory cell modules coupled to an inhibitory unit. The circuit was later extended to include intrinsic bursting cells by Connors and Amitai (1993). In layer 4 of the primary sensory areas of the cortex, a third excitatory cell type, known as the stellate neuron, is present. This cell type receives inputs from the thalamus. Since epileptiform activity can initiate from areas of neocortex with a minimal amount of stellate cells, we chose to model a patch of cortex without this type of neuron.

The inhibitory cells in the neocortex can be divided into several subtypes.

- Basket cells inhibit the pyramidal cell's soma and receive inputs from the pyramidal cells. Basket cells also inhibit other interneurons (Nieuwenhuys, 1994; Wang et al., 2002). Krimer and Goldman-Rakic (2001) examined basket cells in the neocortex of the ferret and identified 3 types of basket cells which were classified on the basis of the range of the axon arbor into local ( $<300\text{ }\mu\text{m}$ ), medium ( $<600\text{ }\mu\text{m}$ ) and wide arbor ( $<900\text{ }\mu\text{m}$ ) cells.
- Chandelier cells inhibit the initial segment of the pyramidal cell. It should be noted that Szabadics et al. (2006) have shown that the GABA ( $\gamma$ -aminobutyric acid) receptors on the intial segement may have a more depolarized reversal potential than their perisomatic counterparts which could lead to an excitatory influence on the cell in some situations. It is speculated that intracortical fibers form the input to these units (Douglas and Martin, 1990). Krimer and Goldman-Rakic (2001) found a connection between a pyramidal neuron and a chandelier cell within  $30\text{ }\mu\text{m}$ .
- Double-bouquet cells and a number of other interneuron cell types can be summarized as miscellaneous inhibitors that often inhibit at the dendritic level (i.e. horizontal cells, Martinotti cells, etc). These cell types are not included in the current model.

Diagrams of the model neurons in the neocortical module are depicted in Figure 12.3A. The superficial pyramidal cell in layers 2 and 3 (S) contains a soma, an initial segment (IS), two apical dendritic compartments (SD1, SD2) and one basal dendritic compartment (SB). Both soma and IS are active with Hodgkin-Huxley type channels for sodium and potassium. Neurons with bursting properties also include persistent sodium channels in the soma (Van Drongelen et al., 2006).

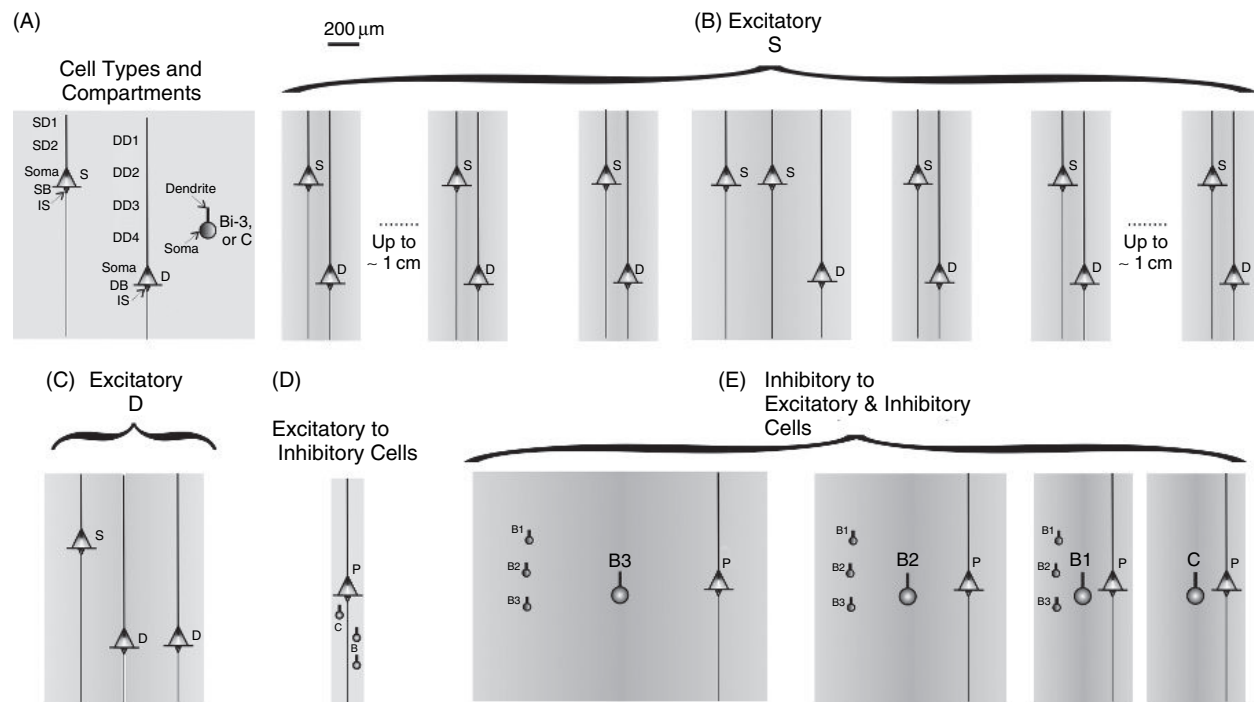


**FIGURE 12.3** The model neurons and their connections. Compartmental cell models (A) and connectivity for each cell type (B–E). The extent to which synapses can occur is indicated by the rectangles around the cell; the centrally located cell type in the diagram is the source and the other cells positioned outside the center represent target cell types.

The deep pyramidal cell (D) in layers 5 and 6 contains a soma, four dendritic compartments (DD1–DD4) and one basal dendritic compartment (DB). The soma and IS are active with Hodgkin-Huxley type channels for sodium and potassium. All inhibitory neurons have two compartments (soma and dendrite) with active Hodgkin-Huxley type channels in the soma. In the current model, there are three types of basket cell (B1, B2 and B3) and a chandelier (C) cell type. We include the dendritic compartment in the inhibitory neurons to generate the membrane current used to estimate EEG and to model the gap junctions between the dendritic compartments.

The pyramidal compartments are based on the reduced models described by Bush and Sejnowski (1993). The reduced model described by these authors is further simplified in our current model. We represented the basal dendrite compartments of Bush and Sejnowski by a single compartment. The two segments in parallel were collapsed to one by taking the average of the lengths and setting the new radius to  $\sqrt{r_1^2 + r_2^2}$ . The obliques of Bush and Sejnowski were combined with the apical dendrite in the same manner. At several places we collapsed two successive segments into one segment; in these cases, the lengths were added and the new radius was calculated as the sum of the previous radii weighted by the lengths of the corresponding segments. For example, a segment of length 50  $\mu\text{m}$  and 4  $\mu\text{m}$  radius connected to a segment of 150  $\mu\text{m}$  and 7.1  $\mu\text{m}$  radius were collapsed to a single segment of  $150 + 50 = 200 \mu\text{m}$  with a radius of  $(150 \times 7.1 + 50 \times 4)/(150 + 50) = 6.3 \mu\text{m}$ . The cells constructed in this way showed intrinsic firing properties similar to the reduced and full neuronal models in Bush and Sejnowski (1993). The compartment sizes, included ion channels and the presence of gap junctions in the model neurons are summarized in Table 12.1.

In order to create a realistic representation of the cell density, the cell spacing of each type of pyramidal neuron is set to 5  $\mu\text{m}$ . Since pyramidal cells make up 70–80% of all neurons (e.g. Douglas and Martin, 1990; Nieuwenhuys, 1994), the spacing of the four types of inhibitory neurons (B1, B2, B3, C) must be considerably sparser; we account for this in the model by spacing the inhibitory cells 3× farther apart than the pyramidal cells. For a neocortical patch of 1 × 1 mm, the number of superficial and deep pyramidal cells is  $2 \times 200 \times 200 = 80\,000$ , whereas the four types of inhibitory cells equal  $4 \times 66.6 \times 66.6 = 17\,778$ . This brings the ratio of pyramidal cells/inhibitors to 4.5/1 and the cell density to  $\sim 10^5/\text{mm}^2$  cortex. This cell density is in agreement with Connors and Amitai (1993), Douglas et al. (1999), and Mountcastle (1997) – estimates of these authors range from 0.5 to  $2 \times 10^5$  neurons/ $\text{mm}^2$ . The depth of the superficial pyramidal cells, the inhibitory neurons and deep pyramidal cells is chosen to be 350  $\mu\text{m}$ , 900  $\mu\text{m}$  and 1450  $\mu\text{m}$ , respectively.

TABLE 12.1 Overview of cell compartments, compartment size (length and radius of the cylinder), associated voltage-sensitive ion channels, synaptic channels and gap junctions

Cell type compartment	Cylinder length ( $\mu\text{m}$ )	Cylinder radius ( $\mu\text{m}$ )	V-channels	Synapse
<b>S_Pyramidal_Soma</b>	22	16.1	Na, K, NaP	i
_sd1	140	2	–	–
_sd2	190	3.3	–	e
_bd	200	2.4	–	–
_is	50	2.2	Na, K	i
<b>D_Pyramidal_Soma</b>	22	16.1	Na, K	i
_dd1	250	2	–	
_dd2	400	2.9	–	
_dd3	400	4.4	–	e
_dd4	400	4.7	–	
_bd	200	6.3	–	
_is	50	2.2	Na, K	i
<b>BASKET1-3_Soma</b>	5.5–22	4–16.1	Na, K	e, l
_d	300–900	2	–	gj
<b>CHANDELIER_Soma</b>	5.5	4	Na, K	e, l
_d	150	2	–	gj

sd1, sd2 and dd1–dd4 are the apical dendritic compartments for the superficial and deep pyramidal neurons; bd is the basal dendritic compartment, its represents the initial segment, and d is the dendrite of the inhibitory cell types. Excitatory and inhibitory synaptic channels are indicated by e and i, and the gap junctions between the inhibitory cells by gj. From van Drongelen et al. (2006a).

## NETWORK CONNECTIVITY

The microcircuitry of the network consists of excitatory and inhibitory connections (Figure 12.3). The pyramidal units (S and D) exhibit reciprocal excitation through glutamatergic synapses (Figure 12.3). We specifically model the fast AMPA ( $\alpha$ -amino-3-hydroxy-5-methyl-4-isoxazolepropionic acid) receptors at these synapses. Both the basket (B) and chandelier cells (C) inhibit the pyramidal units (Figure 12.3) via GABAergic synapses. GABA<sub>A</sub> ( $\text{Cl}^-$  mediated) receptors mediate the inhibitory effect from both basket and chandelier cells. Diagrams of the spatial characteristics of the connectivity for each cell type are depicted schematically in Figure 12.3B–E. Each diagram includes the source cell type of the connection (centrally located cell), the target cells around it and a rectangle whose width shows the relative maximum range of the synaptic connections between source and target cell types. The area of connectivity between superficial pyramidal neurons to both superficial and deep pyramidal neurons is shown in Figure 12.3B. Here, it can be seen that two types of connectivity exist for S: first, there is the area in the immediate vicinity around the superficial pyramidal neuron (source) and, second, there are domains of connectivity at 1 mm intervals up to about 1 cm from the source. The connections going out from deep pyramidal cell (D) are represented in Figure 12.3C; although there are long range intracortical connections going out from D, we only show the ones relevant for the microcircuitry at the millimeter scale. The excitatory connections from both pyramidal cell types (P) to the inhibitory population is shown in Figure 12.3D and the inhibitory connectivity in Figure 12.3E. Because all the panels in Figure 12.3 are at the same scale, it can be appreciated that the potential area of connectivity from excitatory → inhibitory or excitatory populations is smaller than that from the inhibitory → excitatory cells, thus creating circuitry in which local excitation can remain spatially contained by a surrounding area of inhibition.

## IMPLEMENTATION

The above information was used to create a computational model of neocortex whose implementation has been described in detail elsewhere (Van Drongelen et al., 2002, 2004, 2005, 2006, in press). To summarize, we implemented the model with a set of pGENESIS (Bower and Beeman, 1998) scripts that were designed for parallel computation and which run on a parallel cluster located at Argonne National Laboratory. The parallel script allows for efficient parameter searching with sufficient detail in both the neural elements and the network. The scripts must handle many of the details of the parallel implementation explicitly: they distribute cells to the available nodes, provide functions to map a particular cell to the node that hosts it and vice-versa, coordinate creation and connection of cells via explicit barrier calls, define dedicated nodes for saving data and channeling output, etc. The pGENESIS code is a tool to perform *in-silico* experiments from which both cellular activity and extracellular network behavior may be analyzed.

## MODEL BEHAVIOR

This section presents the features of the cellular and network activities exhibited by our model that may be important in the development of seizures.

## CELLULAR BEHAVIOR

Individual cells in the model can be broadly categorized into two types depending on their behavior in isolation: regular spiking (RS) neurons generate a fairly regularly spaced train of action potentials when injected with a current above a certain threshold, while intrinsically bursting (IB) neurons generate bursts of action potentials even in the absence of an injected current. RS neurons, including the small interneurons in our model, possess both fast sodium and delayed rectifier potassium currents. IB neurons (currently only a subset of the superficial pyramidal cells) also include a persistent (slowly inactivating) sodium channel. In the current model, this channel is responsible for the slow conductivity changes that cluster action potentials into bursts (Van Drongelen et al., 2006).

## NETWORK ACTIVITY AND SYNAPTIC COUPLING

Our model generated a variety of extracellular behaviors that depended critically on the strength of the synaptic connections between neurons and the presence of spontaneously bursting neurons. An overview of the extracellular activity patterns showing their dependence on the maximum excitatory and inhibitory synaptic conductances is shown in Figure 12.4A,B.

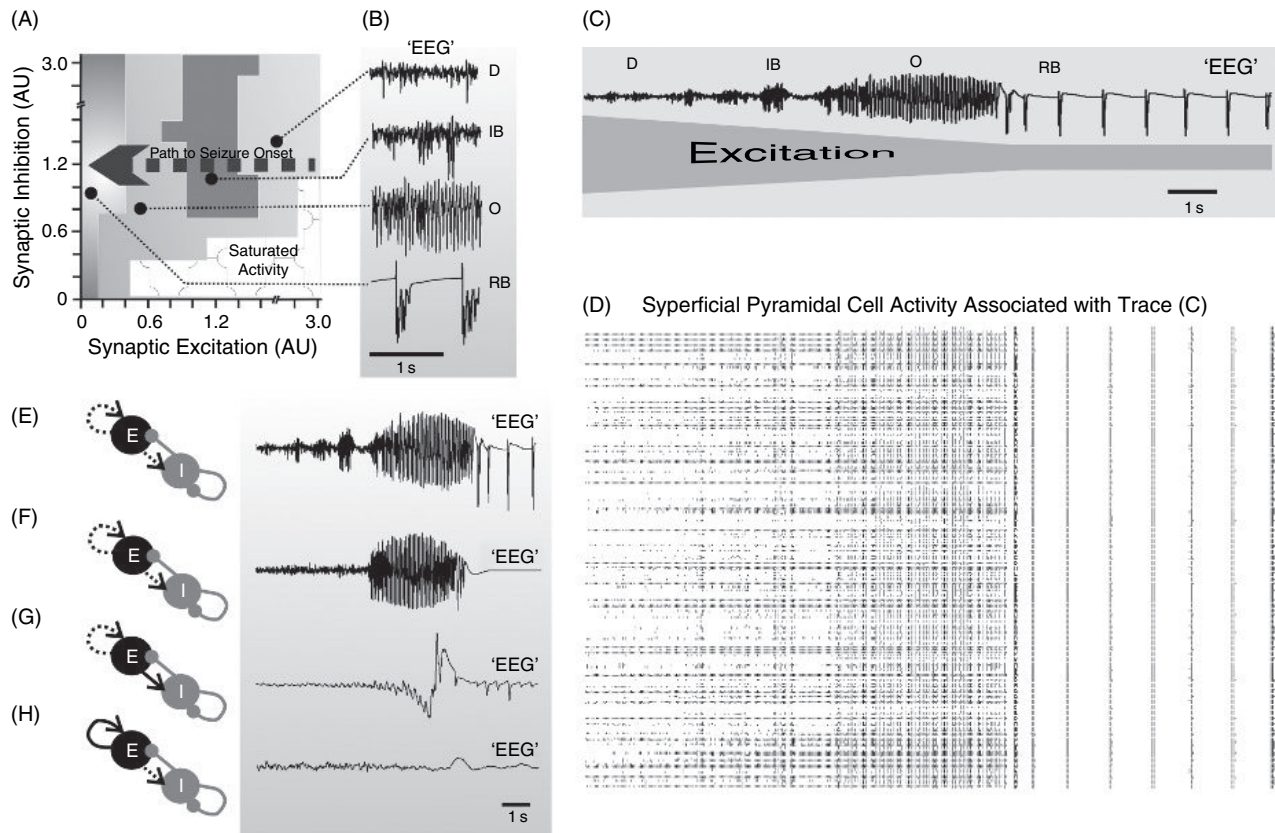


**FIGURE 12.4** Model behavior. (A) The effects of synaptic excitation (abscissa) and inhibition (ordinate) on the network activity of the neocortical model. (B) The different 'EEG' patterns associated with the domains in panel (A): D: desynchronized; IB: irregular bursting; O: oscillation; RB: regular bursting. Levels of excitation and inhibition are indicated in arbitrary units – AU. (C) Electrical activity of the cell populations during a reduction of excitatory synaptic conductance. The raster in (D) shows the activity of the superficial pyramidal cells; each line is a neuron and each dot an action potential. (E–H) Effects of the reduction of excitatory synaptic coupling and bursting neurons on the overall electrical activity. Panel (E) shows reduction of both excitatory to excitatory ( $E \rightarrow E$ ) and excitatory to inhibitory ( $E \rightarrow I$ ) connections. In panels (G) and (H) only one of the connections is reduced in strength,  $E \rightarrow E$  and  $E \rightarrow I$  respectively. Trace (F) is the same as (E) but without bursting cells included in the network. (After Van Drongelen et al., 2005).

Generally speaking, the network behavior could be classified as desynchronized (D), oscillatory (O), irregular bursting (IB), regular bursting (RB) and inactive (Figure 12.4A,B). Regular bursting and oscillatory behavior resembled recorded epileptiform activity and were only observed in weakly connected networks. In contrast, higher levels of excitatory connectivity resulted in desynchronized activity or irregular bursting.

Behavior similar to recordings of seizure onset was obtained when the synaptic excitation strength was dynamically reduced from a high initial value (Figure 12.4C,D). Highly synchronized bursting occurred at strengths  $\leq 0.4$  (Arbitrary Units – AU) in networks that included spontaneously bursting neurons. Raster plots of superficial pyramidal cell activity (Figure 12.4D) showed that the pattern changed from desynchronized activity at synaptic excitation strengths around 3 to modestly synchronized at the onset of the seizure-like discharge.

To exclude the possibility that an indirect reduction in inhibition, via a reduction in the impact of excitatory activity on the inhibitors, was responsible for the observed effects, we investigated the effect of reducing the excitatory synaptic strength to different populations of neurons (Figure 12.4E,G and H). Figure 12.4E shows the same results as discussed previously, i.e. the network behavior corresponding to a reduction in the strength of all excitatory synapses. In contrast, Figure 12.4G and H show the effect of reducing the excitatory drive onto either other pyramidal neurons or the inhibitory interneurons, respectively. When the reduction in synaptic coupling is confined to connections between pyramidal neurons, the resulting network behavior differs drastically from that in Figure 12.4E, with only a small RB phase at low levels of excitation remaining similar between the two. Reducing excitation to the inhibitory population likewise produces a totally different result: the path to seizure onset is no longer visible and, in fact, none of the seizure-like behaviors remains. This analysis suggests

that the seizure behavior cannot be explained only by decreased inhibition: it appears that a reduction in both excitation and inhibition, mediated through a decreased excitatory synaptic drive, is needed to generate the path to seizure onset.

### SEIZURE ACTIVITY AND BURSTING

We have found that spontaneously bursting neurons play an important role in the path to seizure outlined above. In fact, the IB and RB network states only appear when these neurons are present in the network. In network simulations without spontaneously bursting neurons, the IB state is replaced by an active desynchronized activity, while the RB activity is never observed (see Figure 12.4F). Instead, the network becomes inactive at low levels of excitatory transmission and does not reveal the rhythmic seizure-like behavior. Interestingly, the 20–30 Hz oscillation, which may be important in the production of some seizures, appears to be independent of the presence of spontaneously bursting neurons.

### SYNCHRONY

The prevailing opinion amongst neurophysiologists is that high levels of synchrony (hypersynchrony) must exist during epileptiform activity (e.g. Delgado-Escueta et al., 1999). Therefore, the degree of synchronization between neurons was also examined during each type of model network behavior described above. In our case, we define synchrony as the percentage of neurons in our model population that are firing in phase. One way to see easily the extent to which the neurons act in concert is via a raster plot of their action potentials, such as that shown for the superficial pyramidal cells in Figure 12.4D. The plot shows that, as one would expect, low to moderate levels of synchrony exist during the irregular bursting (IB) phase and very high levels during regular bursting (RB). More surprisingly, in light of the assumed high synchrony between neurons during seizure, the fast oscillations (O) that most resemble the quasi-periodic high amplitude EEG recorded during seizure exhibited only moderate levels of synchrony. The synchronization hypothesis may still be valid for this behavior, but it is important to understand that the notion of synchrony does not necessarily imply that all, or even a majority, of the neuronal oscillators are in-phase during an epileptiform event. A relatively small number of synchronized oscillators (the minority) may generate a signal that stands out from the background signal generated by the desynchronized activity of the rest of the neurons (the majority).

### OVERVIEW

To summarize, our computational model shows a variety of network bursting behavior when the level of excitatory drive to all the neurons is gradually reduced; this activity ranges from slow bursting behavior (IB and RB) to fast oscillations (O) between the pyramidal cell layers (Table 12.2). The fast oscillations did not depend on the presence of bursting neurons; this type of activity was sustained by activity propagating between populations. In contrast to the fast oscillations, slow

**TABLE 12.2** Overview of properties underlying network bursting in the model network

Activity Properties	IB	O	RB
Excitation Level:	High	Moderate	Low
Bursting pattern:	Aperiodic	'Periodic'	'Periodic'
Burst Frequency:	–	High	Low
Synchrony Level:	Low	Moderate	High
Driving Force:	Bursters	Network	Bursters
Propagation Type:	'Pacemaker'	Oscillatory wave	'Pacemaker'

IB: irregular bursting; O: oscillation; RB: regular bursting.

bursting behavior (both periodic (RB) and aperiodic (IB)) was critically dependent on the presence of bursting cells (see Figure 12.4F). The prevailing opinion in neurology holds that seizure activity is associated with hypersynchrony and high levels of excitation. However, the level of excitatory coupling is surprisingly low for both of the seizure-like behaviors (fast oscillations (O) and periodic bursting (RB)), while the synchrony between the neurons in the network is lower than expected during the fast oscillations (O). The properties underlying the network behavior are summarized in Table 12.2.

## EXPERIMENTAL SUPPORT

The rationale for studying models of neocortical structure that generate epileptiform activity is to understand better the potential mechanisms underlying epilepsy. Simulations can be used to help form hypotheses for experimental validation or (vice versa) to examine the potential mechanisms behind existing experimental findings. In this section, we describe some experimental results showing that some aspects of the behavior of the model – which constitute predictions – are also reflected in real systems.

### LOW LEVELS OF EXCITATION AND SEIZURE ONSET

Physiologists often translate the hyperactivity associated with epilepsy to hyperexcitatory connectivity and therefore infer that the presumed increase in excitatory coupling is due to an elevation in the number of synaptic contacts, their strength, or both. Clearly, some level of excitatory coupling is required for activity to propagate through a network, but our model of neocortex reveals that a decrease in excitatory drive may be a condition for some types of epileptic behavior. Experimental validation is needed to assess the accuracy of the model and, indeed, there do exist many experimental indications that a weakening of excitation can play a role in seizure-like behavior.

Low levels of 6-cyano-7-nitroquinoxaline-2,3-dione (CNQX), an AMPA receptor blocker, have caused network bursting *in vitro* (Figure 12.5A). We have found, from *in vitro* recordings of mouse, that addition of CNQX to active networks leads to seizure-like activity in many cases (Van Drongelen et al., 2005). In addition, Beggs and colleagues at Indiana

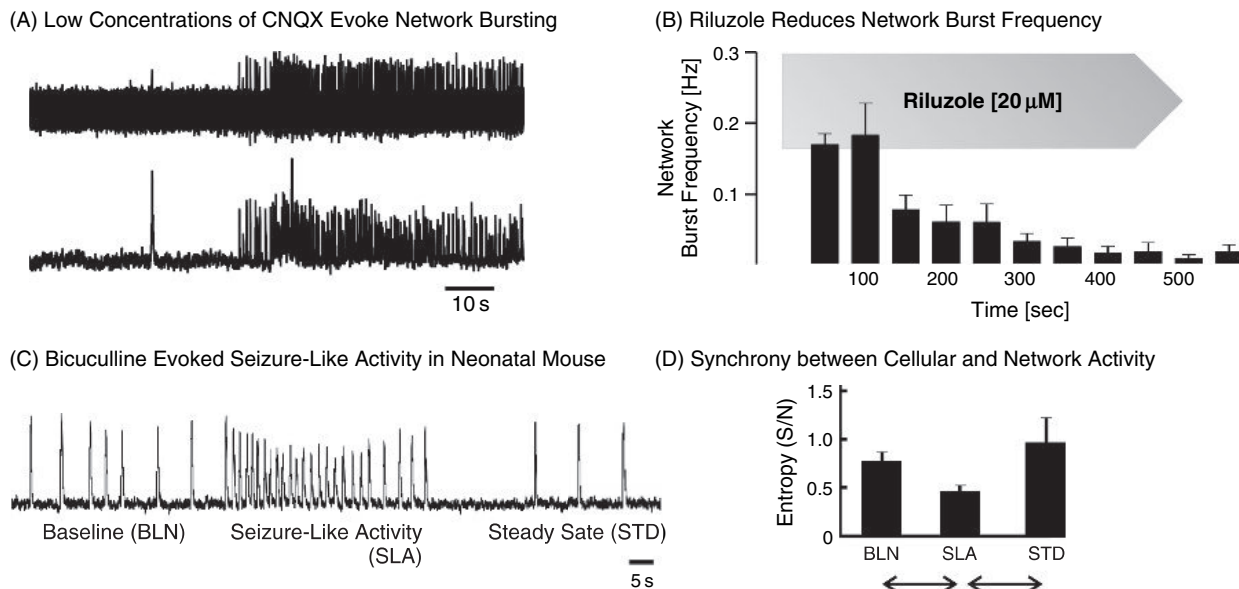


**FIGURE 12.5** Experimental evidence. (A) Increased activity in neocortical slices of mouse after application of a low dose of CNQX ( $<6\text{ }\mu\text{M}$ ). The signal from the extracellular electrode is depicted in the top trace and its rectified-and-integrated version in the bottom trace. The rectified-and-integrated ( $\int$ ) technique generates an index of overall action potential activity in the trace. In some of the experiments full seizure-like episodes were observed, in other cases bursting patterns were seen (from Van Drongelen et al., 2005). (B) Riluzole, a persistent sodium channel blocker associated with cellular bursting reduces network bursting activity (from Van Drongelen et al., 2006). (C) An extracellular recording around a bicuculline evoked experimental seizure shows three distinct phases: baseline activity followed by seizure-like bursting which transitions into a steady state of slow bursting. (D) Synchrony between cellular action potential activity and the network action potential activity (quantified by an entropy measure; see text for details), is significantly lower ( $P < 0.05$ ) during seizure-like activity (SLA) as compared to the baseline and steady state activity patterns (from Van Drongelen et al., 2003a).

University have also found that addition of CNQX to an acute slice preparation after bathing in high K<sup>+</sup> and low Mg<sup>2+</sup> results in synchronized bursting field potential activity for up to two hours or more (J. Beggs, personal communication).

Bicuculline (20 μM) applied to mouse neocortical slices from neonates (P8–P13) also evoked a series of seizure-like, transient bursts at frequencies >1 Hz (Figure 12.5C) (Van Drongelen et al., 2003a). Khazipov et al. (2004) described a similar observation for young rats, in which bicuculline evoked seizure-like bursting in neocortical slices from animals younger than P15. While bicuculline, a GABA<sub>A</sub> antagonist, is normally considered a disinhibitory agent, its effect in mouse and rat is age-dependent: due to developmental differences in the intracellular {Cl<sup>-</sup>}, the GABA<sub>A</sub> receptor actually has a depolarizing (excitatory) effect in juveniles younger than P15 and a hyperpolarizing (inhibitory) effect in older neocortex (Owens et al., 1996; Benitez-Diaz et al., 2003). Therefore, bicuculline reduces excitatory coupling in these juveniles by blocking the GABA<sub>A</sub> receptor, and the observed bicuculline evoked seizure-like bursting in this age group is consistent with the hypothesis that a reduction in excitatory coupling causes seizures to occur.

In addition, diminished levels of extracellular calcium, which could reduce the amount of transmitter released, are known to be associated with propagating neocortical seizures in the baboon (Pumain et al., 1985). Low concentrations (20–60 μM) of Cd<sup>++</sup> (added to block Ca<sup>++</sup>-mediated processes) also cause repetitive network bursting *in vitro*, supporting the notion that weakened excitation can lead to seizures (Van Drongelen et al., 2005).

### SEIZURE ACTIVITY AND BURSTING

As mentioned previously, bursting neurons play an important role in the behavior of our model and are required in order for the irregular bursting and rhythmic bursting network states to appear (see Figure 12.4F). Encouragingly, bursting neurons are also associated with many experimental seizure types that mimic rhythmic bursting behavior. These neurons are found in various models of epilepsy, including the long-term changes that occur with epileptogenesis *in vivo*, the acute animal models of epilepsy, *in vitro* models of seizure-like activity and human pediatric epileptic tissue. In one model of trauma-induced epileptogenesis following chronic cortical deafferentation *in vivo*, an increase in the amplitude of the slow-wave sleep oscillations leading to paroxysmal discharges was correlated with an increase in neuronal firing rate and bursting patterns (Nita et al., 2006). Indeed, Timofeev and Steriade (2004) report that, in a seizure model that produces activity mimicking Lennox-Gastaut-type seizures, intrinsically bursting neurons are rhythmically active during spike wave (SW) discharges, polyspike wave (PSW) complexes and fast runs. Chronic studies of the long-term changes elicited by an episode of status epilepticus or pilocarpine treatment have noted a significant excess of bursting neurons compared to controls (Sanabria et al., 2002; Doczi et al., 2003). Jacobs et al. (1999) find enhanced bursting properties in neurons in genetic models of cortical malformation associated with epilepsy and Topolnik et al. (2003), studying an acute experimental model of trauma-induced epilepsy with partially deafferented cortex *in vivo*, found that an increase in the incidence of intrinsically bursting neurons led to seizure-like activity.

*In vitro* models of seizure-like activity also suggest an association between bursting neurons and the bursting network state associated with seizures. During seizure-like activity elicited in neocortical slices by NMDA (N-methyl-D-aspartate) or bicuculline, bursting activity appeared in neurons that were previously silent (Van Drongelen et al., 2003a). Not surprisingly, this cell type appears once again in neocortical pediatric epileptic tissue (Foehring and Wyler, 1990; Van Drongelen et al., 2003b). Van Drongelen et al. (2006) have recently shown that cellular bursting activity resulting from the persistent sodium current is needed to drive the network to burst. Inhibiting this sodium current reduced the percentage of bursting cells without affecting the regular spiking neurons, in addition to also blocking network bursting activity (Figure 12.5B) (Van Drongelen et al., 2006). Chagnac-Amitai and Connors (1989) even suggest that bursting neurons drive the synchronized excitatory and inhibitory input into other cells. Neuronal bursting is therefore vital in many neocortical network bursting phenomena.

### SYNCHRONY

Moderate to low levels of synchrony, as found for the fast oscillatory component of our model, can also be found in the literature related to epileptic behavior. In many cases, the level of synchrony at seizure onset may be modest compared to a further developed seizure state (Steriade and Contreras, 1995; Netoff and Schiff, 2002; Van Drongelen et al., 2003a). In one experiment, application of bicuculline (10 μM) elicited seizure-like activity with three distinct phases: baseline activity, rhythmic repetitive seizure-like bursting and slow steady state bursting (see Figure 12.5C). Analysis of cellular activity during these extracellular phases reveals different levels of synchrony. In this case, synchrony was defined as the component of cellular activity consistently locked with the network bursting (Van Drongelen et al., 2003a). In this

definition, the time locked signal of the cellular activity is considered as synchronous, the remainder of the activity is considered the asynchronous component or noise. Entropy measures can be applied to estimate these synchronous (signal) and asynchronous (noise) components of the cell's activity (Van Drongelen et al., 2003a). In the steady-state phase, neurons fired only when the network was active, suggesting high levels of synchrony. At baseline and in the initial seizure stage, however, individual firing was only loosely correlated to network activity; this result is suggestive of lower levels of synchrony (see Figure 12.5C,D). Indeed, intraoperative recordings from epilepsy patients indicate that real seizures also exhibit initially modest levels of synchrony (e.g. Wyler et al., 1982). A study by Babb et al. (1987) reported low levels of synchrony between unitary activity and field potentials recorded with depth electrodes during different seizure types in patients with epilepsy.

## CONCLUSIONS

The network model of neocortex described in this work exhibits epileptiform behavior under conditions that include relatively low levels of excitatory drive and the presence of intrinsically bursting neurons. The oscillatory, seizure-like activity is accompanied by relatively low levels of synchrony in the overall population of neurons. These properties of our model seizures are supported by existing evidence in the experimental literature and we have also found support for them in our own recordings. The unexpectedness of some of these properties illustrates the value of a systematic survey of the mechanisms that may underlie epileptiform activity, as opposed to the currently accepted intuition-driven hypotheses. Biophysically realistic computational models, such as the one described here, are good tools in conducting such a survey because they allow the investigator much more control over the system under study, and much more information about phenomena observed from that system, than a comparable experimental preparation. Indeed, we would not have considered performing recordings with reduced excitatory synaptic coupling to look for seizure-like activity if our model had not indicated that such activity would arise. Of course, the insights gained from modeling must ultimately generate verifiable predictions and it is for this reason that we advocate an interdisciplinary approach in which mechanisms of seizure onset are systematically examined in a model and subsequently validated in physiological and clinical settings. This may create a breakthrough for finding mechanisms underlying epileptiform activity and ultimately lead to a rational approach in anticonvulsant therapy.

## ACKNOWLEDGMENTS

Part of this work was supported by the Falk Foundation and the Linn Family. We thank A. Mrejeru and Dr M.H. Kohrman for providing Figure 12.1, Drs M. Hereld and R.L. Stevens for their help with the simulations and Dr J. Beggs for providing information regarding the CNQX evoked network bursting.

## REFERENCES

- Avoli, M. and Williamson, A. (1996). Functional and pharmacological properties of human neocortical neurons maintained in vitro. *Prog Neurobiol* 48:519–554.
- Babb, T.L., Wilson, C.L. and Isokawa-Akesson, M. (1987). Firing patterns of human limbic neurons during stereoencephalography (SEEG) and clinical temporal lobe seizures. *Electroencephalogr Clin Neurophysiol* 66:467–482.
- Benitez-Diaz, P., Miranda-Contreras, L., Mendoza-Brinco, R.V., Pena-Contreras, Z. and Palacios-Pru, E. (2003). Prenatal and postnatal contents of amino acid neurotransmitters in mouse parietal cortex. *Dev Neurosci* 25:366–374.
- Binzegger, T., Douglas, R.J. and Martin, K.A. (2004). A quantitative map of the circuit of cat primary visual cortex. *J Neurosci* 24:8441–8453.
- Bower, J.M. and Beeman, D. (1998). The book of GENESIS. Springer-Verlag, New York.
- Bush, P.C. and Sejnowski, T.J. (1993). Reduced compartmental models of neocortical pyramidal cells. *J Neurosci Meth* 46:159–166.
- Chagnac-Amitai, Y. and Connors, B.W. (1989). Synchronized excitation and inhibition driven by intrinsically bursting neurons in neocortex. *J Neurophysiol* 62:1149–1162.
- Connors, B.W. (1984). Initiation of synchronized neuronal bursting in neocortex. *Nature* 310: 685–687.
- Connors, B.W. and Amitai, Y. (1993). Generation of epileptiform discharge by local circuits of Neocortex In: *Epilepsy* (P.A. Schwartzkroin, ed.) pp. 388–423. Cambridge University Press, New York.
- DeFelipe, J., Alonso-Nanclares, L. and Arellano, J.I. (2002). Microstructure of the neocortex: comparative aspects. *J Neurocytol* 31:299–316.

- Delgado-Escueta, A.V., Wilson, W.A., Olsen, R.W. and Porter, R.J. (1999). New waves of research in the epilepsies: crossing into the third millennium. In: *Advances in Neurology 79: Jasper's basic mechanisms of epilepsies*, 3rd edn, (A.V. Delgado-Escueta et al., eds) pp. 3–58. Lippincot, Williams & Wilkins, Philadelphia.
- Destexhe, A. and Pare, D. (1999). Impact of network activity on the integrative properties of neocortical pyramidal neurons in vivo. *J Neurophysiol* 81:1531–1547.
- Doczi, J., Bernaskova, K., Kubova, H. et al. (2003). Long-term changes of activity of cortical neurons after status epilepticus induced at early developmental stages in rats. *Neurosci Lett* 352:125–128.
- Douglas, R.J. and Martin, K.A.C. (1990). Neocortex. In: *The synaptic organization of the brain* (G.M. Shepherd, ed.) pp. 389–438. Oxford University Press, Oxford.
- Douglas, R., Koch, C., Mahowald, M. and Martin, K. (1999). The role of recurrent excitation in neocortical circuits. In: *Cerebral cortex 13. Models of cortical circuits* P.S. Ulinski, E.G. Jones and A. Peters, eds) pp. 251–282. Kluwer Academic/Plenum, New York.
- Dudek, F.E., Wuarin, J.P., Tasker, J.G., Kim, Y.I. and Peacock WJ (1995). Neurophysiology of neocortical slices resected from children undergoing surgical treatment for epilepsy. *J Neurosci Meth* 59:49–58.
- Feng, Z. and Durand, D.M. (2004). Suppression of excitatory synaptic transmission can facilitate low-calcium epileptiform activity in the hippocampus in vivo. *Brain Res* 1030:57–65.
- Feidervish, I.A., Friedman, A. and Gutnick, M.J. (1996). Slow inactivation of  $\text{Na}^+$  current and slow cumulative spike adaptation in mouse and guinea-pig neocortical neurones in slices. *J Physiol* 493:83–97.
- Foehring, R.C. and Wyler, A.R. (1990). Two patterns of firing in human neocortical neurons. *Neurosci Lett* 110:279–285.
- Golomb, D. (1998). Models of neuronal transient synchrony during propagation of activity through neocortical circuitry. *J Neurophysiol* 79:1–12.
- Golomb, D. and Amitai, Y. (1997). Propagating neuronal discharges in neocortical slices: computational and experimental study. *J Neurophysiol* 78:1199–1211.
- Gorji, A., Stemmer, N., Rambeck, B. et al. (2006). Neocortical microenvironment in patients with intractable epilepsy: potassium and chloride concentrations. *Epilepsia* 47:297–310.
- Gutnick, M.J., Connors, B.W. and Prince, D.A. (1982). Mechanisms of neocortical epileptogenesis in vitro. *J Neurophysiol* 48:1321–1335.
- Hodgkin, A.L. and Huxley, A.F. (1952). A quantitative description of membrane current and its application to conduction and excitation in nerve. *J Physiol* 117:500–544.
- Jacobs, K.M., Kharazia, V.N. and Prince, D.A. (1999). Mechanisms underlying epileptogenesis in cortical malformations. *Epilepsy Res* 36:165–188.
- Kepcs, A., Wang, X.J. and Lisman, J. (2002). Bursting neurons signal input slope. *J Neurosci* 22: 9053–9062.
- Khazipov, R., Khalilov, I., Tyzio, R., Morozova, E., Ben Ari, Y. and Holmes, G.L. (2004). Developmental changes in GABAergic actions and seizure susceptibility in the rat hippocampus. *Eur J Neurosci* 19:590–600.
- Krimer, L.S. and Goldman-Rakic, P.S. (2001). Prefrontal microcircuits: membrane properties and excitatory input of local, medium and wide arbor interneurons. *J Neurosci* 21:3788–3796.
- Kwan, P. and Brodie, M.J. (2000). Early identification of refractory epilepsy. *N Engl J Med* 342:314–319.
- Lyttton, W.W. (2002). From computer to brain: foundations of computational neuroscience. Springer-Verlag, New York.
- Lyttton, W.W. and Sejnowski, T.J. (1991). Simulations of cortical pyramidal neurons synchronized by inhibitory interneurons. *J Neurophysiol* 66:1059–1079.
- Mountcastle, V.B. (1997). The columnar organization of the neocortex. *Brain* 120:701–722.
- Neckelmann, D., Amzica, F. and Steriade, M. (2000). Changes in neuronal conductance during different components of cortically generated spike-wave seizures. *Neuroscience* 96:475–485.
- Netoff, T.I. and Schiff, S.J. (2002). Decreased neural synchronization during experimental seizures. *J Neurosci* 22:7297–7307.
- Nieuwenhuys, R. (1994). The neocortex. An overview of its evolutionary development, structural organization and synaptology. *Anat Embryol* 190:307–337.
- Nita, D.A., Cisse, Y., Timofeev, I. and Steriade, M. (2006). Increased propensity to seizures after chronic cortical deafferentation in vivo. *J Neurophysiol* 95:902–913.
- Nunez, P.L. (1981). Electric fields of the brain: the neurophysics of EEG. Oxford University Press, Oxford.
- Owens, D.F., Boyce, L.H., Davis, M.B.E. and Kriegstein, A.R. (1996). Excitatory GABA responses in embryonic and neonatal cortical slices demonstrated by gramicidin perforated-patch recordings and calcium imaging. *J Neurosci* 16:6414–6423.
- Pumain, R., Menini, C., Heinemann, U., Louvel, J. and Silva-Barrat, C. (1985). Chemical synaptic transmission is not necessary for epileptic seizures to persist in the baboon Papio papio. *Exp Neurol* 89:250–258.
- Sanabria, E.R., da Silva, A.V., Spreafico, R. and Cavalheiro, E.A. (2002). Damage, reorganization, and abnormal neocortical hyperexcitability in the pilocarpine model of temporal lobe epilepsy. *Epilepsia* 43:96–106.
- Sanchez-Vives, M.V. and McCormick, D.A. (2000). Cellular and network mechanisms of rhythmic recurrent activity in neocortex. *Nat Neurosci* 3:1027–1034.
- Somogyi, P., Tamas, G., Lujan, R. and Buhl, E.H. (1998). Salient features of synaptic organization in the cerebral cortex. *Brain Res Rev* 26:113–135.
- Steriade, M. and Contreras, D. (1995). Relations between cortical and thalamic cellular events during transition from sleep patterns to paroxysmal activity. *J Neurosci* 15:623–642.
- Steriade, M., Amzica, F., Neckelmann, D. and Timofeev, I. (1998). Spike-wave complexes and fast components of cortically generated seizures. II. Extra- and intracellular patterns. *J Neurophysiol* 80:1456–1479.
- Szabadics, J., Varga, C., Molnar, G., Olah, S., Barzo, P. and Tamas, G. (2006). Excitatory effect of GABAergic axo-axonic cells in cortical microcircuits. *Science* 311:233–235.
- Szentagothai, J. (1978). The Ferrier Lecture, 1977. The neuron network of the cerebral cortex: a functional interpretation. *Proc R Soc Lond B Biol Sci* 201:219–248.
- Tasker, J.G., Hoffman, N.W., Kim, Y.I., Fisher, R.S., Peacock, W.J. and Dudek, F.E. (1996). Electrical properties of neocortical neurons in slices from children with intractable epilepsy. *J Neurophysiol* 75:931–939.

- Timofeev, I. and Steriade, M. (2004). Neocortical seizures: initiation, development and cessation. *Neuroscience* 123:299–336.
- Topolnik, L., Steriade, M. and Timofeev, I. (2003). Hyperexcitability of intact neurons underlies acute development of trauma-related electrographic seizures in cats *in vivo*. *Eur J Neurosci* 18:486–496.
- Traub, R.D. and Miles, R. (1991). Neural networks of the hippocampus. Cambridge University Press, New York.
- Traub, R.D., Jefferys, J.G., Miles, R., Whittington, M.A. and Toth, K. (1994). A branching dendritic model of a rodent CA3 pyramidal neurone. *J Physiol* 481:79–95.
- Van Drongelen, W. (2006). Signal processing for neuroscientists: introduction to the analysis of physiological systems. Elsevier, Amsterdam.
- Van Drongelen, W. and Hecox, K. (2003). Desynchronization of neural activity in a network model. *Neurocomputing* 52–54: 425–430.
- Van Drongelen, W., Hereld, M., Lee, H.C., Papka, M.E. and Stevens, R.L. (2002). Simulation of neocortical activity. *Epilepsia* 43 Suppl. 7:149.
- Van Drongelen, W., Koch, H., Marcuccilli, C., Peña, F. and Ramirez, J.M. (2003a). Synchrony levels during evoked seizure-like bursts in mouse neocortical slices. *J Neurophysiol* 90:1571–1580.
- Van Drongelen, W., Koch, H., Peña F. et al. (2003b). Differences in bursting properties between least and most abnormal tissue obtained from pediatric patients with intractable epilepsy, Program No. 99.15.2003 Abstract Viewer/Itinerary Planner. Society for Neuroscience, Washington, DC.
- Van Drongelen, W., Lee, H.C., Hereld, M. et al. (2004). Simulation of neocortical epileptiform activity using parallel computing. *Neurocomputing* 58–60:1203–1209.
- Van Drongelen, W., Lee, H.C., Koch, H. et al. (2005). Emergent epileptiform activity in neural networks with weak excitatory synapses. *IEEE Trans Neur Sys Rehab* 13:236–241.
- Van Drongelen, W., Koch, H., Elsen, F. et al. (2006). The role of persistent sodium current in bursting activity of mouse neocortical networks *in vitro*. *J Neurophysiol* 96:2564–2577.
- Van Drongelen, W., Lee, H., Stevens, R. and Hereld, M. Propagation of seizure-like activity in a model of neocortex. *J Clin Neurophysiol* in press.
- Wang, X.J. (1999). Fast burst firing and short-term synaptic plasticity: a model of neocortical chattering neurons. *Neuroscience* 89:347–362.
- Wang, Y., Gupta, A., Toledo-Rodriguez, M., Wu, C.Z. and Markram, H. (2002). Anatomical, physiological, molecular and circuit properties of nest basket cells in the developing somatosensory cortex. *Cereb Cortex* 12:395–410.
- Wuarin, J.P., Kim, Y.I., Cepeda, C. et al. (1990). Synaptic transmission in human neocortex removed for treatment of intractable epilepsy in children. *Ann Neurol* 28:503–511.
- Wyler, A.R., Ojemann, G.A. and Ward, A.A. (1982). Neurons in human epileptic cortex: correlation between unit and EEG activity. *Ann Neurol* 11:301–308.

# 13

## CORTICOthalamic FEEDBACK: A KEY TO EXPLAIN ABSENCE SEIZURES

ALAIN DESTEXHE

### ABSTRACT

Over the last years, decisive experimental data have been obtained concerning the biophysical mechanisms and ion channels properties important for seizure generation. Computational models have succeeded in proposing plausible mechanisms to explain the sudden emergence of hypersynchronized oscillations at  $\sim 3$  Hz (or 5–10 Hz in some species), which are associated with ‘spike-and-wave’ complexes in the electroencephalogram (EEG). The underlying mechanisms of such seizures involve thalamocortical loops, the particular oscillatory properties of thalamic neurons and the particular biophysical properties of some receptor types (such as the GABA<sub>B</sub> receptor). Here, we overview these mechanisms step by step, starting from the genesis of hypersynchronized oscillations by thalamic circuits. We next consider how cortical circuits can generate spike-and-wave EEG patterns. These mechanisms are then merged together in thalamocortical loops, where we emphasize the central role played by the ‘feedback’ projections from cortex to thalamus. If for some reason the corticothalamic feedback becomes too strong, thalamic circuits can switch to a slower and hypersynchronized oscillatory mode, which in turn entrains the whole thalamocortical system into hypersynchronized oscillations with spike-and-wave EEG patterns. We suggest that the key to explain absence seizures is this switching mechanism of thalamic circuits, induced by exceedingly strong corticothalamic feedback. Such a switch was identified in experiments *in vitro*, in which oscillatory properties could be controlled by stimulating corticothalamic fibers. According to this mechanism, absence seizures result from anomalously high cortical excitability with a physiologically intact thalamus.

### INTRODUCTION

Absence epileptic seizures (also called ‘petit-mal’) are characterized in humans by a sudden appearance of  $\sim 3$  Hz large-amplitude oscillations in the electroencephalogram (EEG) (Figure 13.1). These generalized oscillations have a sudden onset and the seizure seems to invade the entire cerebral cortex nearly simultaneously. The typical pattern of the oscillation consists of one or several sharp deflections (‘spikes’) followed by a surface-positive ‘wave’. Spike-and-wave patterns of similar characteristics are also seen in a number of experimental models in cats, rats, mice and monkeys.

Like many other pathologies, absence epilepsy can result from the disturbance of mechanisms of synaptic transmission (reviewed in Gloor and Fariello, 1988; Crunelli and Leresche, 2002). In particular, disturbing inhibitory interactions have been found to be extremely effective for generating seizures, sometimes with contrasting effects (reviewed in Sperk et al., 2004). In thalamus and cortex, inhibitory transmission essentially uses  $\gamma$ -aminobutyric acid (GABA) as transmitter and operates through two main receptor types, called GABA<sub>A</sub> and GABA<sub>B</sub>. These two receptors mediate fast and slow inhibition, respectively. Both types of receptor are of primary importance in seizure mechanisms, as overviewed in detail here.

In this chapter, we review mechanisms that generate seizures and computational models that simulate these mechanisms. We consider successively the different ingredients of absence seizures: thalamic circuits can generate hypersynchronized oscillations at  $\sim 3$  Hz, cortical circuits can generate spike-and-wave patterns and thalamocortical circuits can display generalized spike-and-wave seizures under certain conditions. In particular, we will show that a key ingredient in seizure generation is the feedback connections from cortex to thalamus. In the final section, we review critical experiments that successfully tested this corticothalamic feedback mechanism for absence seizure generation. We terminate by a summary of possible mechanisms for  $\sim 3$  Hz seizures (or 5–10 Hz in rodents).

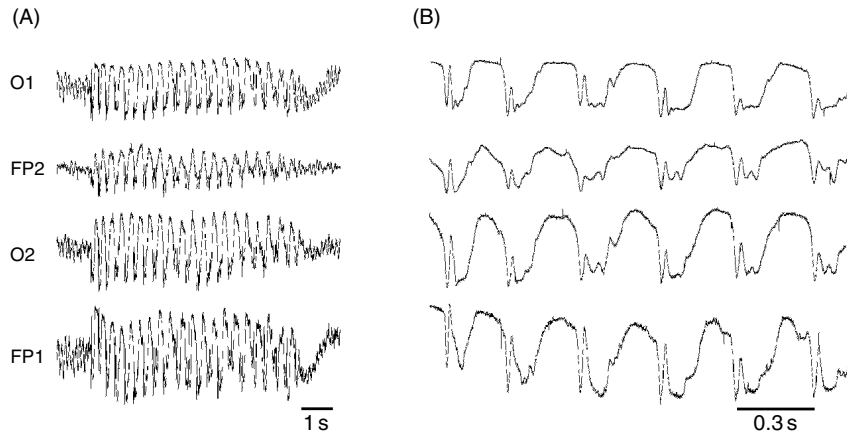


**FIGURE 13.1** Electroencephalogram (EEG) recording during an absence seizure in a human subject. (A) Absence seizure in different EEG leads (FP1 and FP2 measure the potential difference between frontal and parietal regions of the scalp, whereas O1 and O2 correspond to the measures between occipital regions). The seizure lasted approximately five seconds and consisted of an oscillation at around 3 Hz which appeared nearly-simultaneously in all EEG leads. (B) Same seizure at higher temporal resolution, which reveals the ‘spike and wave’ patterns during each cycle of the oscillation. Modified from Destexhe, (1992).

## THALAMIC MECHANISMS FOR HYPERSYNCHRONIZED OSCILLATIONS

### EVIDENCE FOR THALAMIC PARTICIPATION IN SEIZURES

The fact that absence seizures start suddenly and generalize extremely rapidly over the entire EEG suggest that seizures are generated in a central structure projecting widely to cerebral cortex. The thalamus is a possible candidate for such a structure, as suggested more than sixty years ago (Jasper and Kershman, 1941). This ‘centrencephalic’ view is now supported by several findings:

1. Simultaneous thalamic and cortical recordings in humans during absence seizures demonstrated a clear thalamic participation during the seizure (Williams, 1953). The same study also showed that the oscillations usually started before signs of seizure appeared in the EEG.
2. A thalamic participation in human absence seizures was also shown by positron emission tomography (PET) (Prevett et al., 1995).
3. In some experimental models, spike-and-wave seizures disappear following thalamic lesions or by inactivating the thalamus (Pellegrini et al., 1979; Avoli and Gloor, 1981; Vergnes and Marescaux, 1992).
4. Electrophysiological recordings in experimental models of spike-and-wave seizures show that cortical and thalamic cells fire prolonged discharges in phase with the ‘spike’ component, while the ‘wave’ is characterized by a silence in all cell types (Pollen, 1964; Steriade, 1974; Fisher and Prince, 1977b; Avoli et al., 1983; McLachlan et al., 1984; Buzsaki et al., 1988; Inoue et al., 1993; McCormick and Hashemiyoon, 1998; Seidenbecher et al., 1998; Staak and Pape, 2001). Electrophysiological recordings also indicate that spindle oscillations, which are generated by thalamic circuits (Steriade et al., 1990; 1993), can be gradually transformed into spike-and-wave discharges and all manipulations that promote or antagonize spindles have the same effect on spike-and-wave seizures (Kostopoulos et al., 1981a, 1981b; McLachlan et al., 1984).
5. Knock-out mice lacking the gene for the T-type calcium current in thalamic relay cells display a resistance to absence seizures (Kim et al., 2001), which clearly demonstrates that the thalamus and, in particular, the T-type current mediated bursting of thalamic cells, are involved in this type of seizure activity.

Pharmacological manipulations suggest that the critical receptor type involved in thalamic hypersynchronized oscillations are the  $\text{GABA}_B$  receptors. In rats,  $\text{GABA}_B$  agonists exacerbate seizures, while  $\text{GABA}_B$  antagonists suppress them (Hosford et al., 1992; Snead, 1992; Puigcerver et al., 1996; Smith and Fisher, 1996). More specifically, antagonizing thalamic

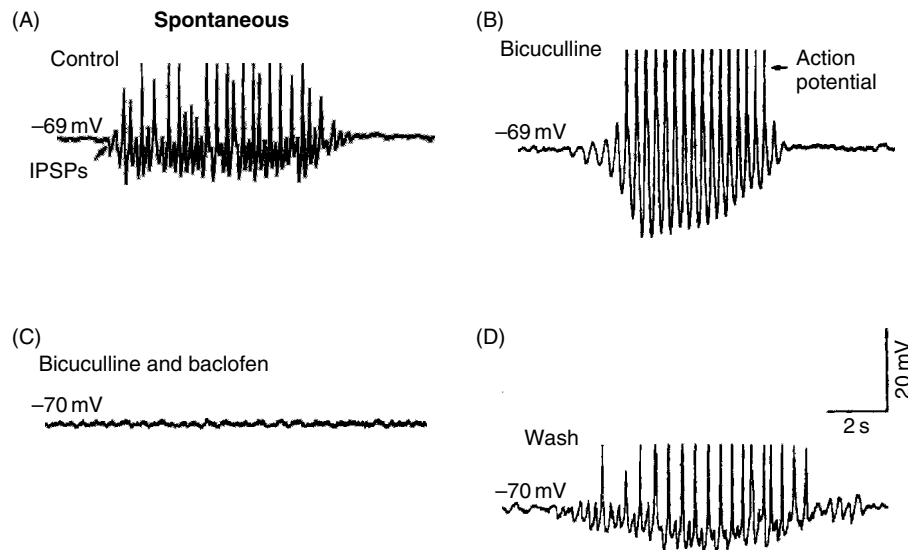


**FIGURE 13.2** Bicuculline-induced 3 Hz oscillation in thalamic slices. (A) Control spindle sequence ( $\sim 10$  Hz) started spontaneously by an IPSP (arrow). (B) Slow oscillation ( $\sim 3$  Hz) following block of  $\text{GABA}_A$  receptors by bicuculline. (C) Suppression of the slow oscillation in the presence of the  $\text{GABA}_B$  antagonist baclofen. (D) Recovery after wash. Modified from von Krosigk et al. (1993).

$\text{GABA}_B$  receptors leads to the suppression of spike-and-wave discharges (Liu et al., 1992), which is another indication for a critical role of the thalamus.

The two main thalamic cell types involved in generating oscillations are the thalamocortical (TC) cells, also called relay cells, and the inhibitory neurons of the thalamic reticular (RE) nucleus. In some area of the thalamus and in some species, RE cells provide the sole source of inhibition to relay cells. The connections from RE to TC cells contain both  $\text{GABA}_A$  and  $\text{GABA}_B$  receptors, and there is evidence that  $\text{GABA}_B$  receptors are critical to generate hypersynchronized oscillations. In particular, clonazepam, a known anti-absence drug ( $\text{GABA}_A$  antagonist), was shown indirectly to diminish  $\text{GABA}_B$ -mediated inhibitory postsynaptic potentials (IPSPs) in TC cells, reducing their tendency to burst in synchrony (Huguenard and Prince, 1994a; Gibbs et al., 1996). The action of clonazepam appears to reinforce  $\text{GABA}_A$  receptors within the RE nucleus (Huguenard and Prince, 1994a; Hosford et al., 1997). Indeed, there is a diminished frequency of seizures following reinforcement of  $\text{GABA}_A$  receptors in the RE nucleus (Liu et al., 1991).

One of the strongest evidences for the involvement of the thalamus was that in ferret thalamic slices, spindle oscillations can be transformed into slower and more synchronized oscillations at  $\sim 3$  Hz following blockade of  $\text{GABA}_A$  receptors (Figure 13.2; von Krosigk et al., 1993). This behavior is similar to the transformation of spindles to spike-and-wave discharges in cats following the systemic administration of penicillin, which acts as a weak  $\text{GABA}_A$  receptor antagonist (Kostopoulos et al., 1981a, 1981b). Moreover, like spike-and-wave seizures in rats, the  $\sim 3$  Hz paroxysmal oscillations in thalamic slices are suppressed by  $\text{GABA}_B$  receptor antagonists (Figure 13.2; von Krosigk et al., 1993).

Taken together, these experiments suggest that thalamic neurons are actively involved in the genesis of spike-and-wave seizures and that both  $\text{GABA}_A$  and  $\text{GABA}_B$  receptors play a critical role. It is important to note, however, that although such results clearly suggest that the thalamus is important in seizure generation, there is also considerable evidence that the cortex plays a primary role. The role of the cortex will be developed in the next section, while we exclusively focus on thalamic mechanisms in the present section.

### COMPUTATIONAL MODELS OF THALAMIC HYPERSYNCHRONIZED OSCILLATIONS

#### Early models

The introduction of an experimental model for thalamic oscillations in ferret thalamic slices demonstrated the spontaneous occurrence of spindle oscillations (von Krosigk et al., 1993). It was also demonstrated that spindles can be transformed into  $\sim 3$  Hz oscillations by blocking  $\text{GABA}_A$  receptors (see Figure 13.2). It was further shown that this oscillation is sensitive to blockade of  $\text{GABA}_B$  receptors by baclofen (see Figure 13.2) and is also suppressed by glutamate  $\alpha$ -amino-3-hydroxy-5-methyl-4-isoxazolepropionic acid (AMPA) receptor antagonists (von Krosigk et al., 1993). These *in vitro* experiments

thus suggested that  $\sim 3$  Hz paroxysmal thalamic oscillations are mediated by a reciprocal interaction between TC and RE cells, with GABA<sub>B</sub> IPSPs (RE  $\rightarrow$  TC) and AMPA EPSPs (TC  $\rightarrow$  RE).

This mechanism was investigated with computational models using a simple TC-RE circuit consisting of a single TC cell reciprocally connected to a single RE cell (scheme in Figure 13.3; Destexhe et al., 1993b). In this model, and all other models reviewed in this chapter, the neurons were described by the generic membrane equation:

$$C_m \frac{dV}{dt} = -g_L(V_i - E_L) - \sum_j I_{int}^{ji} - \sum_k I_{syn}^{ki} \quad (1)$$

where  $V_i$  is the membrane potential,  $C_m = 1 \mu\text{F}/\text{cm}^2$  is the specific capacity of the membrane,  $g_L$  (in  $\text{mS}/\text{cm}^2$ ) is the leakage conductance density and  $E_L$  (in mV) is the leakage reversal potential. Intrinsic and synaptic currents are respectively represented by  $I_{int}^{ji}$  and  $I_{syn}^{ki}$  (in  $\mu\text{A}/\text{cm}^2$ ).

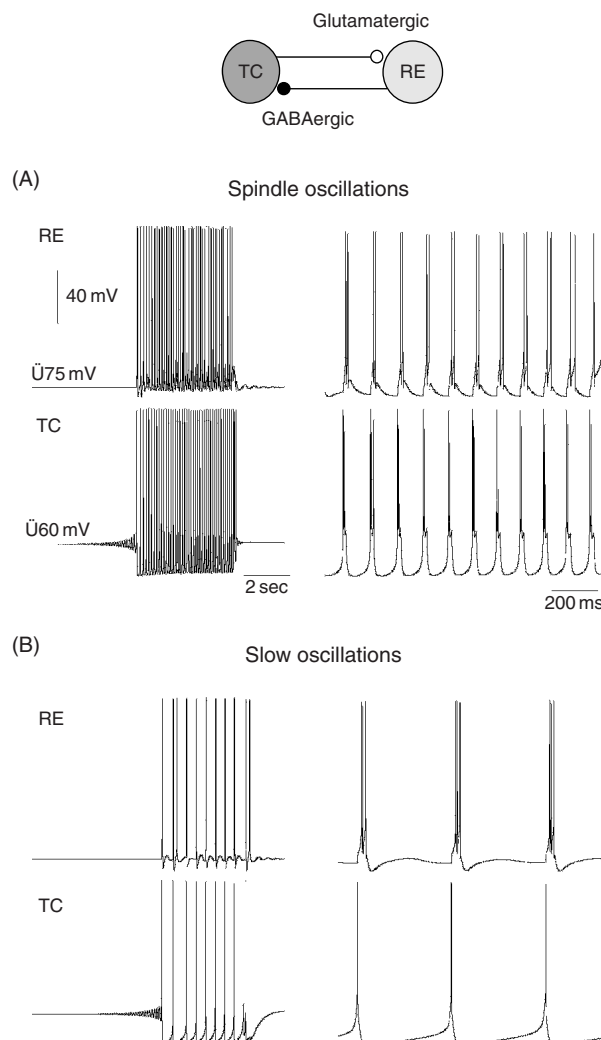


**FIGURE 13.3** Transition from 8–10 Hz spindle oscillations to  $\sim 3$  Hz oscillations by slowing down the kinetics of GABAergic currents. (A) 8–10 Hz spindle oscillations from a simple circuit consisting of one TC cell interconnected with one RE cell. The left panel shows a detail of a few cycles within the oscillation at 10 times higher resolution. Glutamatergic AMPA receptors were used from TC  $\rightarrow$  RE and GABAergic GABA<sub>A</sub> receptors from RE  $\rightarrow$  TC (decay rate constant  $\beta = 0.1 \text{ ms}^{-1}$ ). (B) Slower oscillations for slow GABAergic synapses. The decay rate constant of the GABAergic synapse was  $\beta = 0.003 \text{ ms}^{-1}$ , similar to the decay rate of GABA<sub>B</sub> currents. Modified from Destexhe et al. (1993b).

Intrinsic voltage-dependent or calcium-dependent currents were modeled using kinetic models of the Hodgkin and Huxley (1952) type. These intrinsic membrane currents were described by the following generic equation:

$$I_{int} = \bar{g}_{int} m^N h^M (V - E_{int}) \quad (2)$$

$$\frac{dm}{dt} = \alpha_m (1 - m) - \beta_m m \quad (3)$$

$$\frac{dh}{dt} = \alpha_h (1 - h) - \beta_h h \quad (4)$$

where  $I_{int}$  is the intrinsic membrane current,  $\bar{g}_{int}$  (in mS/cm<sup>2</sup>) is the maximal conductance density and  $E_{int}$  is the reversal potential. The gating properties of the current dependent on  $N$  activation gates and  $M$  inactivation gates, with  $m$  and  $h$  representing the fraction of gates in open form, with respective rate constants  $\alpha_m$ ,  $\beta_m$ ,  $\alpha_h$  and  $\beta_h$ . Rate constants were dependent on either membrane voltage (V) or intracellular calcium concentration.

The intrinsic firing behavior of the model TC cell was determined by  $I_T$  and  $I_h$ ; these currents were modeled using Hodgkin-Huxley type of models based on voltage-clamp data in TC cells. Calcium regulation of  $I_h$  accounted for the waxing-and-waning of oscillations, as described previously (Destexhe et al., 1993a). The intrinsic firing properties of the RE cell were determined by  $I_T$ ,  $I_{K[Ca]}$  and  $I_{CAN}$  using Hodgkin-Huxley type kinetics and calcium-activated schemes as described previously (Destexhe et al., 1994a). The two cell types also included the fast  $I_{Na}$  and  $I_{Kd}$  currents necessary to generate action potentials with kinetics taken from Traub and Miles (1991).

Synaptic interactions were mediated by glutamatergic and GABAergic receptors using kinetic models of postsynaptic receptors (Destexhe et al., 1994b, 1998b).

$$I_{syn} = \bar{g}_{syn} m (V - E_{syn}) \quad (5)$$

$$\frac{dm}{dt} = \alpha [T] (1 - m) - \beta m \quad (6)$$

where  $I_{syn}$  is the postsynaptic current,  $\bar{g}_{syn}$  is the maximal conductance,  $m$  is the fraction of open receptors,  $E_{syn}$  is the reversal potential,  $[T]$  is the transmitter concentration in the cleft,  $\alpha$  and  $\beta$  are forward and backward binding rate constants of  $T$  to open the receptors. This scheme was used to simulate AMPA, NMDA and GABA<sub>A</sub> types of receptors (see Destexhe et al., 1998b for parameters).

The circuit of interconnected TC and RE cells displayed waxing-and-waning spindle oscillations at a frequency of 8–10 Hz (Figure 13.3A; Destexhe et al., 1993b). The circuit also displayed a transformation to ~3 Hz oscillations when the kinetics of the GABAergic current were slowed (Figure 13.3; Destexhe et al., 1993b). The decay of inhibition greatly affected the frequency of the spindle oscillations, with slow decay corresponding to low frequencies. When the decay was adjusted to match experimental recordings of GABA<sub>B</sub>-mediated currents (obtained from Otis et al., 1993), the circuit oscillated at around 3 Hz (Figure 13.3B; Destexhe et al., 1993b).

### Biophysical models of cooperative GABA<sub>B</sub> responses

Although the above model could simulate the essential features of the slow thalamic oscillation, it was not satisfactory because the slowing down of GABA currents from 10 ms to 200 ms decay time constant is not plausible biophysically. So more realistic mechanisms must be considered for the transformation of normal spindles to slow hypersynchronized oscillations, which is critical to explain the emergence of pathologies such as absence seizures.

The essential biophysical ingredient to explain this transformation to hypersynchrony is the cooperativity of GABA<sub>B</sub> responses. A detailed biophysical modeling of synaptic transmission on GABAergic receptors (Destexhe and Sejnowski, 1995) explored the idea that single-synapse postsynaptic mechanisms could explain the non-linear stimulus dependence observed for GABA<sub>B</sub> responses. We hypothesized that this non-linearity arises from the transduction mechanisms underlying GABA<sub>B</sub> responses, in particular at the level of the activation of K<sup>+</sup> channels by G-proteins. The assumption that four G-proteins must bind to K<sup>+</sup> channels to open them provides the non-linearity required to account for GABA<sub>B</sub> responses (Destexhe and Sejnowski, 1995); this is consistent with the tetrameric structure of K<sup>+</sup> channels (Hille, 2001). With these assumptions, the GABA<sub>B</sub> model reproduced the typical non-linearity of GABA<sub>B</sub> responses: intense release conditions (such as high-frequency bursts) are necessary to activate significant GABA<sub>B</sub> currents. This effect arises locally at the synapse and should be detectable using dual recordings, a prediction that was later confirmed experimentally (Kim et al., 1997; Thomson and Destexhe, 1999).

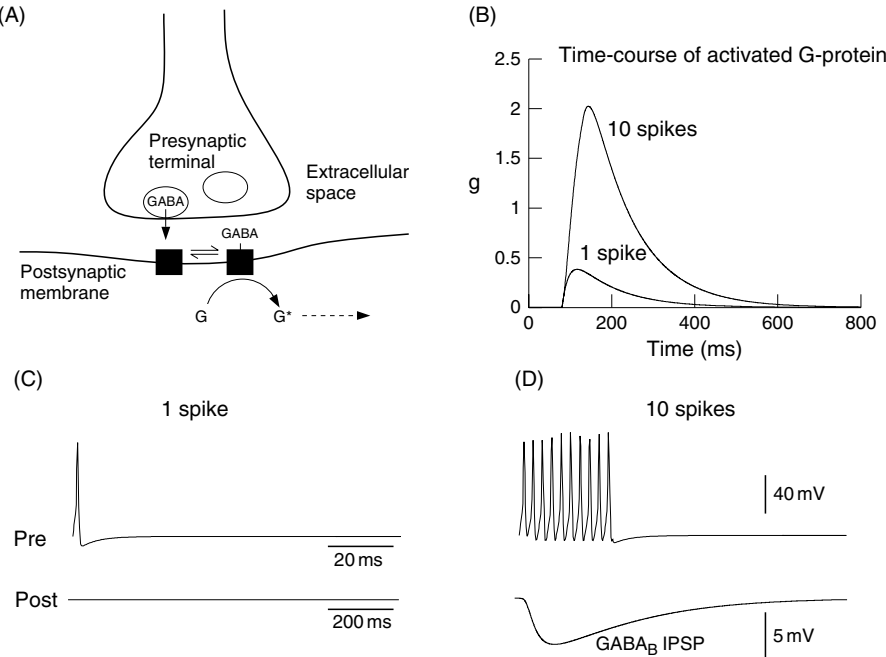


**FIGURE 13.4** Modeling nonlinear GABA<sub>B</sub>-mediated responses. (A) Scheme of the release of GABA, activation of the receptor by binding of GABA, and catalysis of G-proteins into activated form (G\*) by the bound receptor. Subsequently, activated G-proteins may affect the gating of ion channels as well as participating in other biochemical mechanisms, or be degraded into inactive form (dashed arrow). To yield responses in agreement with experiments, the binding of four G-proteins was needed to activate the K<sup>+</sup> channels (Destexhe and Sejnowski, 1995). (B) Typical slow time-course of G-protein concentration following one or 10 presynaptic spikes at 200 Hz. (C) Simulation of GABA<sub>B</sub>-mediated responses with a single presynaptic spike. No detectable GABA<sub>B</sub> IPSP is observed. (D) Same simulation as in (C), but with 10 presynaptic spikes at high frequency. In this case, the stimulus recruited a strong GABA<sub>B</sub>-mediated IPSP. (A-B) modified from Thomson and Destexhe, (1998). (C-D) modified from Destexhe, (1998). Model from Destexhe and Sejnowski, (1995).

The activation properties of GABA<sub>B</sub> receptors were based on the following steps (Figure 13.4A):

1. binding of GABA on the GABA<sub>B</sub> receptor, leading to activated receptor
2. the activated GABA<sub>B</sub> receptor catalyzes the activation of G-proteins in the intracellular side
3. binding of activated G-proteins to open a K<sup>+</sup> channel.

These steps are described by the following equations:

$$I_{GABA_B} = \bar{g}_{GABA_B} \frac{s^n}{s^n + K_d} (V - E_K) \quad (7)$$

$$\frac{dr}{dt} = K_1 [T] (1 - r) - K_2 r \quad (8)$$

$$\frac{ds}{dt} = K_3 r - K_4 s \quad (9)$$

where [T] is the GABA concentration in the synaptic cleft, r is the fraction of GABA<sub>B</sub> receptors in the activated form, s is the normalized G-protein concentration in activated form,  $\bar{g}_{GABA_B}$  is the maximal postsynaptic conductance of K<sup>+</sup> channels,  $K_d$  is the dissociation constant of G-protein binding on K<sup>+</sup> channels, V is the postsynaptic membrane potential and  $E_K$  is the equilibrium potential for K<sup>+</sup>. Fitting of this model to experimental GABA<sub>B</sub> responses led to the following values of parameters (Destexhe et al., 1998b):  $K_d = 100$ ,  $K_1 = 9 \times 10^4 M^{-1} s^{-1}$ ,  $K_2 = 1.2 s^{-1}$ ,  $K_3 = 180 s^{-1}$  and  $K_4 = 34 s^{-1}$  with  $n = 4$  binding sites.

This model reproduced the typical non-linear behavior of GABA<sub>B</sub>-mediated responses. A single presynaptic spike induced a relatively low amplitudes of G-protein (Figure 13.4B), and no GABA<sub>B</sub>-mediated IPSP in the postsynaptic cell (Figure 13.4C). In contrast, a burst of high-frequency spikes evoked a strong GABA<sub>B</sub>-mediated IPSP (Figure 13.4D).

The main hypothesis of this model is that the typical non-linearity observed in  $\text{GABA}_B$  responses is explainable by transduction kinetics at the level of a single GABAergic synapse (for details, see Destexhe and Sejnowski, 1995). We will see in the next section that this property enables one to explain several important experimental observations relevant to absence seizures.

### Cooperative $\text{GABA}_B$ responses can explain the effect of clonazepam in thalamus

As a first step towards explaining the genesis of hypersynchronized oscillations, the cooperative model of  $\text{GABA}_B$  responses was used to investigate possible mechanisms to account for the effect of the anti-absence drug clonazepam. Experiments showed that clonazepam reduces  $\text{GABA}_B$ -mediated IPSPs in TC cells (Huguenard and Prince, 1994a; Gibbs et al., 1996), but that the action of clonazepam was not on TC cells, but was to reinforce  $\text{GABA}_A$  receptors in the RE nucleus (Huguenard and Prince, 1994a). To explain this effect, we constructed a circuit comprising model RE cells including a low-threshold calcium current and lateral  $\text{GABA}_A$ -mediated synaptic interactions within the RE nucleus (Figure 13.5A; Destexhe and Sejnowski, 1995). Under normal conditions, stimulation in the RE nucleus evoked biphasic IPSPs in TC cells, with a rather small  $\text{GABA}_B$  component (Figure 13.5B). We mimicked an increase of intensity by increasing the number of RE cells discharging. The ratio between  $\text{GABA}_A$  and  $\text{GABA}_B$  IPSPs was independent of the intensity of stimulation in the model (Destexhe and Sejnowski, 1995), as observed experimentally (Huguenard and Prince, 1994b). However, this ratio could be changed by blocking  $\text{GABA}_A$  receptors locally in the RE nucleus, leading to enhanced burst discharge in RE cells and a more prominent  $\text{GABA}_B$  component in TC cells (Figure 13.5C). This is consistent with the effect of clonazepam in reinforcing the  $\text{GABA}_A$  IPSPs in the RE nucleus, resulting in diminished  $\text{GABA}_B$  IPSPs in TC cells (Huguenard and Prince, 1994a). The reduction of the  $\text{GABA}_B$  component was a direct consequence of cooperativity of  $\text{GABA}_B$  responses.

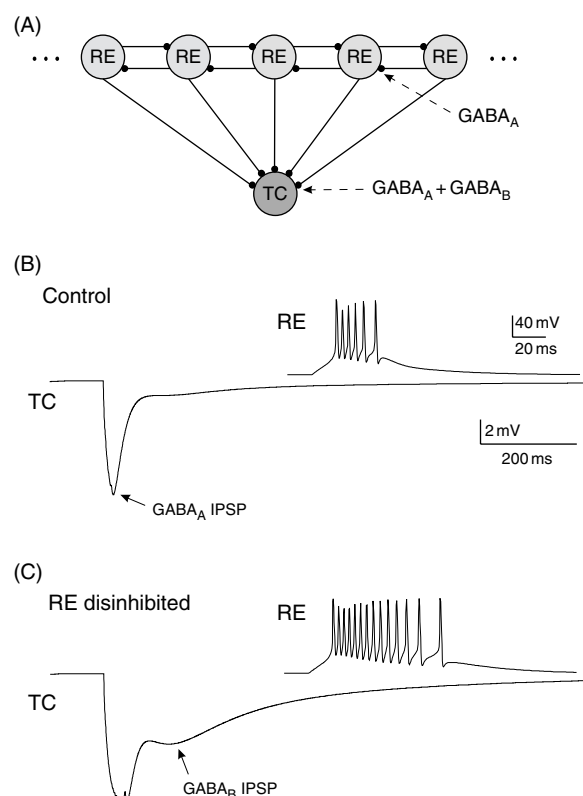


**FIGURE 13.5** Simulation of the effect of clonazepam in the thalamus.  $\text{GABA}_B$  responses were enhanced in TC cells through disinhibition in the thalamic RE nucleus. (A) Connectivity: a simple network of RE cells was simulated with  $\text{GABA}_A$  receptor-mediated synaptic interactions. All RE cells project to a single TC cell with synapses containing both  $\text{GABA}_A$  and  $\text{GABA}_B$  receptors. Models of the RE cells were taken from Destexhe et al. (1994a). (B) In control conditions, the bursts generated in RE cells by stimulation have 2–8 spikes (inset) and evoke in TC cells a  $\text{GABA}_A$ -dominated IPSP with a small  $\text{GABA}_B$  component. (C) When  $\text{GABA}_A$  receptors are suppressed in RE, the bursts become much larger (inset) and evoke in TC cells a stronger  $\text{GABA}_B$  component. Modified from Destexhe and Sejnowski, (1995).

### Cooperative GABA<sub>B</sub> responses can explain the genesis of thalamic hypersynchronized oscillations

This cooperative model of GABA<sub>B</sub> responses was integrated in a circuit comprising TC and RE cells and the different receptor types mediating their interactions (GABA<sub>A</sub> and GABA<sub>B</sub> receptors from RE to TC, AMPA receptors from TC to RE; see scheme in Figure 13.6; Destexhe et al., 1996a). In control conditions (Figure 13.6A), the circuit generated spindle oscillations with characteristics consistent with electrophysiological recordings. Suppression of GABA<sub>A</sub> receptors led to slower oscillations (Figure 13.6B). These oscillations were a consequence of the properties of GABA<sub>B</sub> responses as described in Figure 13.5. Following removal of GABA<sub>A</sub>-mediated inhibition, the RE cells could produce prolonged bursts that evoked strong GABA<sub>B</sub> currents in TC cells. These prolonged IPSPs evoked robust rebound bursts in TC cells, and TC bursts in turn elicited bursting in RE cells through EPSPs. This mutual TC-RE interactions recruited the system into a 3–4 Hz oscillation, with characteristics similar to those of bicuculline-induced paroxysmal oscillations in ferret thalamic slices. The mechanisms responsible for these oscillations were similar to those that give rise to normal spindle oscillations, but the shift in the balance of inhibition leads to oscillations that were slower and more synchronized (Figure 13.6C; see details in Destexhe et al., 1996a).

Other mechanisms have been proposed to account for the effects of blocking of GABA<sub>A</sub> receptors in thalamic circuits (Wallenstein, 1994; Wang et al., 1995; Golomb et al., 1996). The model of Wallenstein (1994) tested the proposition

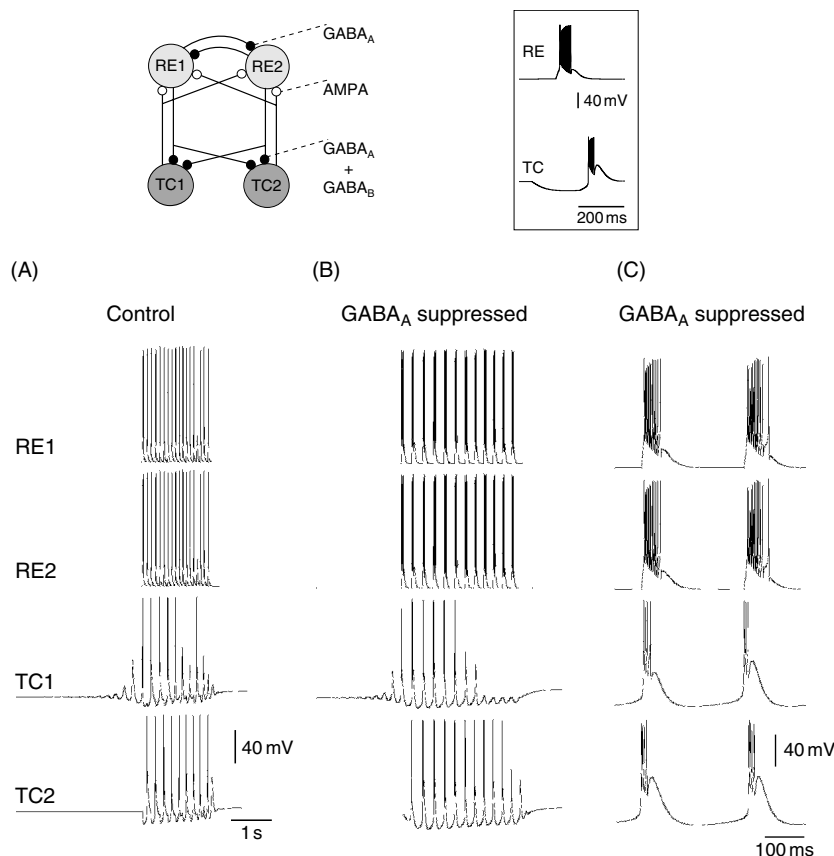


**FIGURE 13.6** Oscillations in a four-neuron circuit of thalamocortical and thalamic reticular cells. Top scheme: circuit diagram consisting of two TC and two RE cells. Synaptic currents were mediated by AMPA/kainate receptors (from TC to RE;  $\bar{g}_{AMPA} = 0.2 \mu S$ ), a mixture of GABA<sub>A</sub> and GABA<sub>B</sub> receptors (from RE to TC;  $\bar{g}_{GABA_A} = 0.02 \mu S$  and  $\bar{g}_{GABA_B} = 0.04 \mu S$ ) and GABA<sub>A</sub>-mediated lateral inhibition between RE cells ( $\bar{g}_{GABA_A} = 0.2 \mu S$ ). Right: inset showing the simulated burst responses of TC and RE cells following current injection (pulse of 0.3 nA during 10 ms for RE and -0.1 nA during 200 ms for TC). (A) Spindle oscillations arose as the first TC cell (TC1) started to oscillate, recruiting the two RE cells, which in turn recruited the second TC cell. The oscillation was maintained for a few cycles and repeated with silent periods of 15–25 s. (B) Slow 3–4 Hz oscillation obtained when GABA<sub>A</sub> receptors were suppressed, mimicking the effect of bicuculline. The first TC cell (TC1) started to oscillate, recruiting the two RE cells, which in turn recruited the second TC cell. The mechanism of recruitment between cells was identical to spindle oscillations, but the oscillations were more synchronized, of slower frequency, and had a 15% longer silent period. The burst discharges were prolonged due to the loss of lateral inhibition in the RE. (C) Magnification of one cycle of the oscillation from (B), showing the high synchrony of the slow oscillation. Modified from Destexhe et al., (1996a).

that disinhibition of interneurons projecting to TC cells with GABA<sub>B</sub> receptors may result in stronger discharges when GABA<sub>A</sub> receptors are antagonized (Soltesz and Crunelli, 1992). A model including TC, RE and interneurons (Wallenstein, 1994) reproduced the stronger discharges in TC cells following application of bicuculline. Although it is possible that this mechanism plays a role in thalamically-generated epileptic discharges, it does not account for experiments showing the decisive influence of the RE nucleus in preparations devoid of interneurons (in this case, the sole source of inhibition is the RE nucleus; see Huguenard and Prince, 1994a, 1994b). Increased synchrony and stronger discharges were also reported in the model of Wang et al. (1995), but the synchronous state coexisted with a desynchronized state of the network, which has never been observed experimentally. The cooperative activation proposed for GABA<sub>B</sub> receptors (Destexhe and Sejnowski, 1995) produced robust synchronized oscillations and traveling waves at the network level (Golomb et al., 1996; Destexhe et al., 1996a), similar to those observed in thalamic slices (Kim et al., 1995). This property also led to the transformation of spindles to ~3 Hz paroxysmal oscillations following block of GABA<sub>A</sub> receptors (Destexhe et al., 1996a). The latter study remains so far the only one consistent with the largest body of experimental data, including the effect of clonazepam, the characteristic non-linearity of GABA<sub>B</sub> responses and network effects such as traveling oscillations.

In conclusion, biophysical models incorporating the known intrinsic properties of thalamic neurons, together with the properties of their receptor types, account for the genesis of hypersynchronized oscillations. Several ingredients are essential to this mechanism. First, the presence of lateral inhibitory (GABA<sub>A</sub>-mediated) connections in the RE nucleus normally prevent RE cells from producing excessive burst discharges. Diminishing the efficacy of these connections enables RE cells to produce prolonged bursts. Second, due to non-linear properties of GABA<sub>B</sub> responses discussed above, significant GABA<sub>B</sub>-mediated IPSPs are seen only when presynaptic cells produce prolonged discharges. Therefore, if for some reason (such as diminishing the efficacy of GABA<sub>A</sub> receptors), RE burst discharges become stronger, they activate significant GABA<sub>B</sub>-mediated responses in TC cells and entrain the entire thalamic circuits into slow synchronized oscillations. The GABA<sub>A</sub>-mediated interactions between RE cells therefore act as a powerful means of avoiding hypersynchrony (Sanchez-Vives and McCormick, 1997; Huntsman et al., 1999).

## CORTICAL MECHANISMS FOR SPIKE-AND-WAVE PATTERNS

### EVIDENCE FOR CORTICAL MECHANISMS IN SPIKE-AND-WAVE GENERATION

Although the results discussed above clearly suggest a decisive thalamic participation to spike-and-wave seizures, there is also strong evidence that the cortex plays a key role. Thalamic injections of high doses of GABA<sub>A</sub> antagonists, such as penicillin (Ralston and Ajmone-Marsan, 1956; Gloor et al., 1977) or bicuculline (Steriade and Contreras, 1998) led to 3–4 Hz oscillations with no sign of spike-and-wave discharge. This suggests that the slow hypersynchronized oscillation induced by these drugs is not sufficient to explain seizures. In contrast, injection of the same drugs to the cortex, with no change in the thalamus, resulted in seizure activity with spike-and-wave patterns (Gloor et al., 1977; Fisher and Prince, 1977a; Steriade and Contreras, 1998). In addition, the threshold for epileptogenesis was much lower in the cortex compared to the thalamus (Steriade and Contreras, 1998). Finally, it was shown that a diffuse application of a dilute solution of penicillin to the cortex resulted in spike-and-wave seizures, although the thalamus was intact (Gloor et al., 1977).

As we have seen above, spike-and-wave seizures disappear following thalamic lesions or by inactivating the thalamus (Pellegrini et al., 1979; Avoli and Gloor, 1981; Vergnes and Marescaux, 1992). In some experiments, however, a purely cortical spike-and-wave activity was observed in the isolated cortex or athalamic preparations in cats (Marcus and Watson, 1966; Pellegrini et al., 1979; Steriade and Contreras, 1998). These experiments revealed a slow type of spike-and-wave (1–2 Hz), with a less prominent ‘spike’ component. In contrast, such intracortical spike-and-wave activity does not occur in rats (Vergnes and Marescaux, 1992) and has never been reported in neocortical slices. Nevertheless, the experiments in cats show that at least some cortical structures are capable of endogenously generating spike-and-wave activity and further confirm the importance of the cortex in generating seizures, although the typical spike-and-wave patterns of generalized seizures require both cortex and thalamus.

Finally, it was shown that absence seizures in rats seem to start in a focus located in somatosensory cortex (Meeren et al., 2002), suggesting that not all of the thalamus participates in seizures and that full-blown bursts may be seen only in some nuclei. The same study (Meeren et al., 2002) also demonstrated that interhemispheric synchrony is larger than intrahemispheric synchrony during the seizure, which would argue for an important role of callosal fibers in the synchrony and generalized aspects of the seizure.

In the present section, we examine the genesis of spike-and-wave patterns by the cortex, by first investigating how to generate the typical ‘spike’ and ‘wave’ field potentials. Next, we investigate how to obtain a purely cortical form of spike-and-wave activity.

#### COOPERATIVE GABA<sub>B</sub> RESPONSES CAN EXPLAIN THE GENESIS OF SPIKE-AND-WAVE PATTERNS IN LOCAL FIELD POTENTIALS

To study the genesis of spike-and-wave patterns, we used a computational model of local field potentials (LFPs). A passive single-compartment model was simulated with postsynaptic currents generated by 100 excitatory synapses (AMPA and NMDA receptors) and 100 inhibitory synapses (GABA<sub>A</sub> and GABA<sub>B</sub> receptors; see scheme in Figure 13.7A). Extracellular field potentials were calculated from postsynaptic currents in single-compartment models, according to a simple model based on Coulomb’s equation (see Nunez, 1981):

$$V_{ext} = \frac{R_e}{4\pi} \sum_j \frac{I_j}{r_j} \quad (10)$$

where  $V_{ext}$  is the electrical potential at a given extracellular site,  $R_e = 230 \Omega\text{cm}$  is the extracellular resistivity,  $I_j$  are the total membrane currents (spikes excluded) and  $r_j$  is the distance between the site of generation of  $I_j$  and the extracellular site.

The field potentials generated by this model for different stimulus conditions are shown in Figure 13.7B,C. With presynaptic trains consisting of single spikes, the voltage showed mixed EPSP/IPSP sequences and the field potential was dominated by negative deflections (Figure 13.7B). In contrast, bursts of high-frequency presynaptic spikes produced mixed EPSP/IPSPs followed by large GABA<sub>B</sub>-mediated IPSPs in the cell (Figure 13.7C). In the latter case, the fast EPSP/IPSPs generated spiky field potentials, followed by a slow positive wave due to GABA<sub>B</sub> currents. This simple model shows that synchronous high-frequency discharges of excitatory and inhibitory cells in the presence of GABA<sub>B</sub> receptors is sufficient to generate field potentials waveforms resembling interleaved ‘spikes’ and ‘waves’.

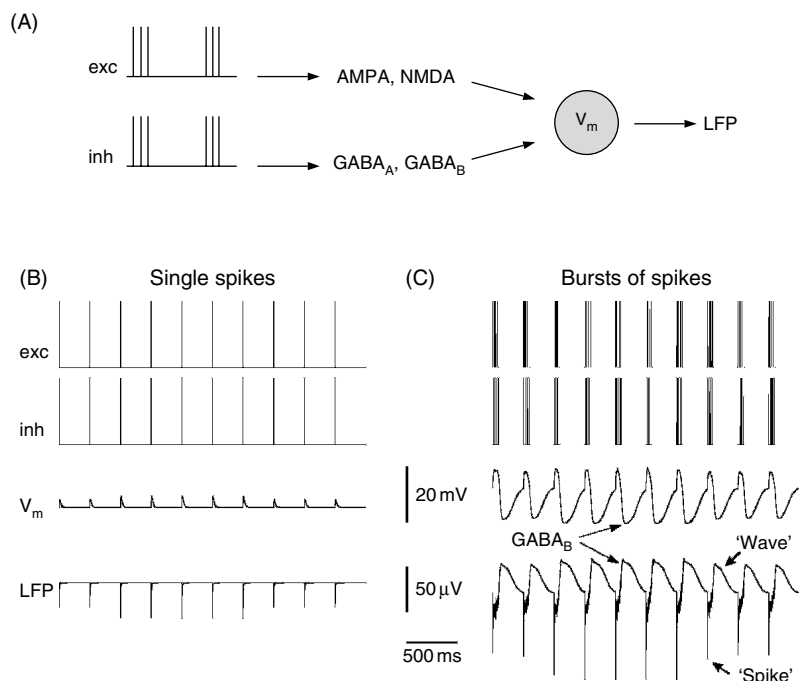


**FIGURE 13.7** Simulation of spike-and-wave field potentials based on the properties of GABA<sub>B</sub> receptors. (A) Scheme for the model of local field potentials. Excitatory and inhibitory presynaptic trains of action potentials stimulated AMPA, NMDA, GABA<sub>A</sub> and GABA<sub>B</sub> postsynaptic receptors at 100 synapses of each type on a single compartment model and used to calculate the extracellular field potential at a distance of 5  $\mu\text{m}$  from the simulated neuron. (B) Field potentials generated by single presynaptic spikes. The mixed EPSP/IPSP sequence in the cell led to negative deflections in the field potentials (bottom trace). (C) Same simulation as in (B), but using bursts of presynaptic spikes. In this case, fast spiky components (‘Spike’) alternate with slow positive deflections (‘Wave’), similar to spike-and-wave patterns. These slow positive waves were due to the activation of GABA<sub>B</sub>-mediated currents (arrows). Conductance values were 4 nS, 1 nS, 1.5 nS and 4 nS for individual AMPA, NMDA, GABA<sub>A</sub> and GABA<sub>B</sub> synapses, respectively. Modified from Destexhe, (1998).

## GENESIS OF CORTICAL SPIKE-AND-WAVE OSCILLATIONS

### Experiments

Intracortically-generated spike-and-wave seizures were described experimentally in cats under barbiturate anesthesia using multisite field potential recordings (Steriade and Contreras, 1998; Destexhe et al., 2001; see scheme in Figure 13.8A). In control conditions, the LFPs displayed 7–14 Hz spindle oscillations, typical of barbiturate anesthesia (Figure 13.8B). After application of the GABA<sub>A</sub> antagonist bicuculline to the cortex, this activity developed into seizures with spike-and-wave complexes, at a frequency of 2–4 Hz (Figure 13.8C). Experiments were also realized in athalamic cats, where a complete thalamectomy was performed (histological controls described in Steriade and Contreras, 1998). Similar to above, application of bicuculline to the cerebral cortex after thalamectomy led to the development of seizures with spike-and-wave patterns (Figure 13.8D). In this case, however, the morphology of the spike-wave complexes was different as the negative ‘spike’ was less pronounced (compare C and D in Figure 13.8) and the oscillation frequency was slower (about 1.8 Hz in Figure 13.8D; range 1.8–2.5 Hz).

### Models of intracortical spike-and-wave seizures

The main hypothesis explored by the model is that the rebound bursting properties observed in a subset of cortical cells, combined with GABA<sub>B</sub> IPSPs, could generate this intracortical form of spike-and-wave seizures (Destexhe et al., 2001). *In vivo* intracellular recordings were performed in the same area of neocortex from which the intracortical seizures were recorded. Low-threshold spike (LTS) activity was observed in a significant fraction (about 10%) of intracellularly-recorded cells (Figure 13.9A). These LTS neurons generate adapting trains of action potentials in response to depolarizing current injection (Figure 13.9A, left panel), similar to the classic ‘regular-spiking’ response of cortical neurons (Connors and Gutnick, 1990). In addition, they can generate a burst of action potentials in response to injection of hyperpolarizing current pulses (Figure 13.9A, right panel). This property was also identified in deep layers of guinea-pig cerebral cortex *in vitro* (de la Peña and Geijo-Barrientos, 1996; Figure 13.9B) and was shown to be due to the presence of the T-type (low-threshold) calcium current  $I_T$ .

Computational models reproduced these intrinsic firing properties based on single-compartment representations of pyramidal neurons. To generate the classic ‘regular-spiking’ behavior (see Figure 13.9C, -70 mV), the model included three voltage-dependent currents represented by Hodgkin-Huxley (1952) type kinetics: a slow voltage-dependent K<sup>+</sup> current termed  $I_M$  (kinetics from McCormick et al., 1993), as well as the  $I_{Na}$  and  $I_K$  currents for action potential generation (kinetics from Traub and Miles, 1991). In addition, to generate rebound bursting behavior, the T-type calcium current was included

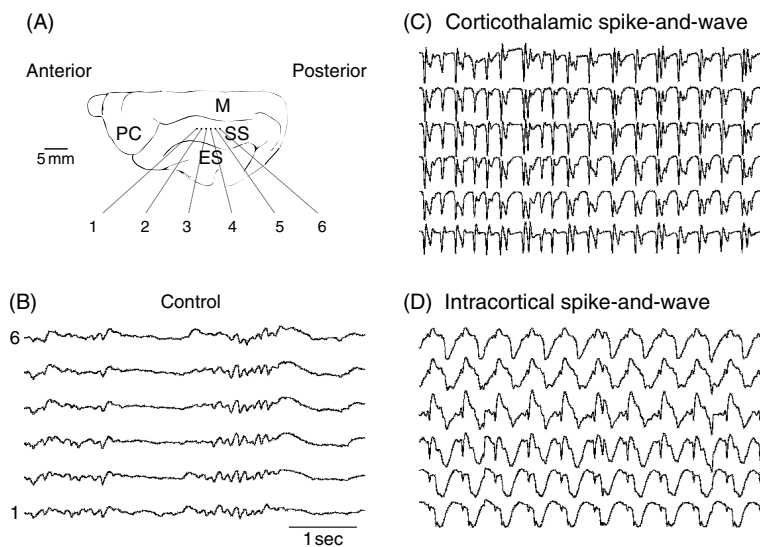


**FIGURE 13.8** Multisite field potential recordings in cat suprasylvian cortex. (A) Scheme illustrating the disposition of recording electrodes (SS suprasylvian gyrus; PC postcruciate gyrus, ES ectosylvian gyrus, M marginal gyrus). (B) ‘Control’ spindle oscillations during barbiturate anesthesia. (C) Spike-and-wave paroxysms in the same animal after injection of bicuculline in cortex (between electrodes 3 and 4). (D) Spike-and-wave oscillation in the same brain area after complete thalamectomy (different animal as in A-B). Modified from Destexhe et al. (2001).

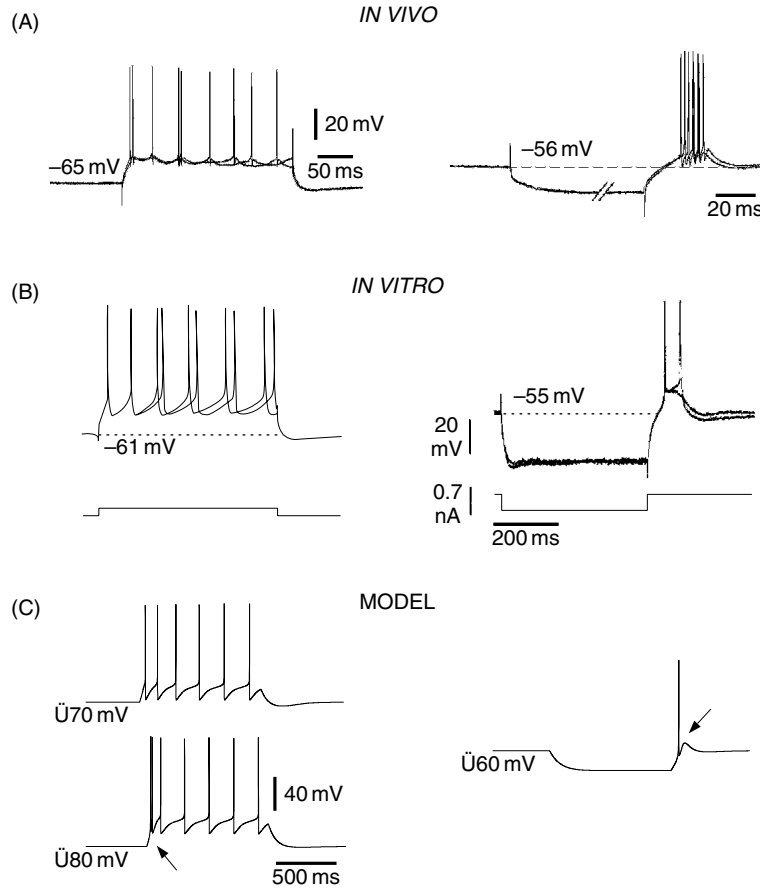


**FIGURE 13.9** Rebound bursting properties of cortical pyramidal cells. (A) Rebound bursting cell from cat cerebral cortex *in vivo*. (B) Rebound bursting cell from guinea-pig frontal cortex *in vitro* (adapted from de la Peña and Geijo-Barrientos, 1996). (C) Model pyramidal cell comprising  $I_{Na}$ ,  $I_K$ ,  $I_M$  and  $I_T$  currents. Left: repetitive firing with adaptation following injection of depolarizing current (0.1 nA). Right: rebound burst response at the offset of a hyperpolarizing current pulse ( $-0.1$  nA; the pulse was 200 ms in (A) and was truncated for clarity). Arrows indicate bursts of action potentials mediated by  $I_T$ . Modified from Destexhe et al. (2001).

(kinetics from Destexhe et al., 1998b) and its peak amplitude was adjusted to match voltage-clamp recordings of this current in pyramidal neurons (de la Peña and Geijo-Barrientos, 1996). A density of T-channels of  $0.8\text{ mS/cm}^2$  was needed to match the relatively small amplitude of this current measured in pyramidal neurons. Note that the peak amplitude of  $I_T$  in pyramidal neurons ( $0.4\text{--}0.8\text{ nA}$  in guinea-pig cerebral cortex; de la Peña and Geijo-Barrientos, 1996) is much smaller than in TC neurons ( $5.8 \pm 1.7\text{ nA}$ ; Destexhe et al., 1998b). Using this relatively moderate T-current density, the model generated weak rebound bursts at the offset of hyperpolarizing current (see Figure 13.9C,  $-60\text{ mV}$ ). From hyperpolarized levels, this model generated an initial burst followed by an adapting train of action potentials (see Figure 13.9C,  $-80\text{ mV}$ ), which is a feature commonly observed in neocortical neurons (Connors and Gutnick, 1990).

Network models were then constructed to investigate the genesis of cortical spike-and-wave seizures. The network consisted of excitatory (pyramidal) neurons and interneurons, whose connectivity was mediated by AMPA,  $GABA_A$  and  $GABA_B$  receptors (Figure 13.10A). In control conditions, no oscillatory behavior could be observed if a significant proportion of pyramidal neurons (up to 20%) had LTS properties similar to Figure 13.9C. This is due to the fact that, in control conditions, all cells in the network generate brief discharge patterns, which lead to the activation of IPSPs that are dominated by the  $GABA_A$  component, with negligible  $GABA_B$  activation. Because of the relatively weak conductance of  $I_T$  in LTS cortical cells,  $GABA_A$ -mediated IPSPs were not sufficient to activate any rebound burst in these neurons.

In contrast, when  $GABA_A$ -mediated inhibition was suppressed, mimicking the effect of bicuculline, the disinhibited network generated self-sustained oscillations (see Figure 13.10B). Due to the removal of fast inhibition, all cells in the network produced prolonged discharge patterns. The prolonged discharge of interneurons was optimal to activate

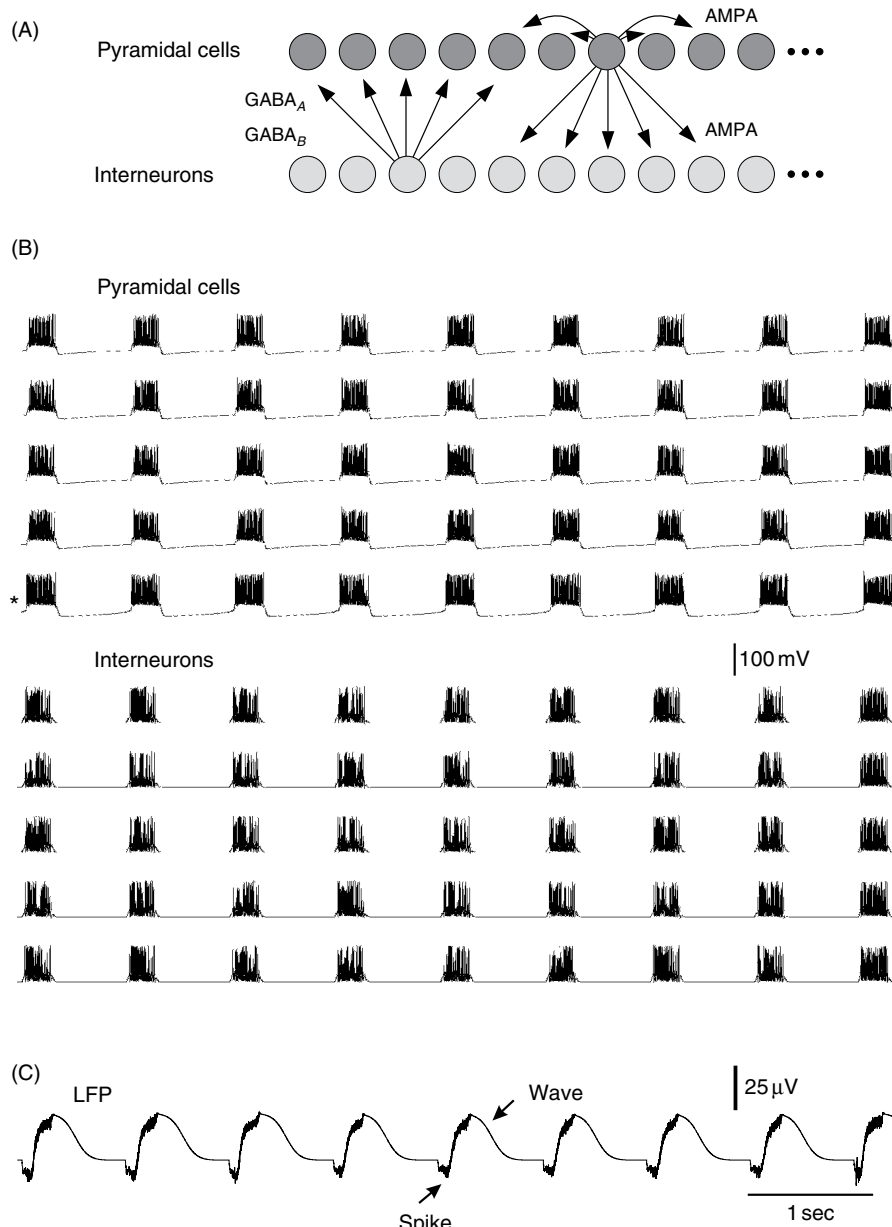


**FIGURE 13.10** Simulation of intracortically-generated spike-and-wave oscillations. (A) Scheme of the network: all pyramidal cells had  $I_{Na}$ ,  $I_K$  and  $I_M$  currents, and 5% of pyramidal neurons were rebound bursting cells containing an additional weak density of T-current (as in Figure 13.9C). (B) Oscillatory activity after removing  $GABA_A$  connections. All cells displayed prolonged discharges in phase, separated by periods of silences dominated by  $K^+$  currents, at a frequency of  $\sim 1.3$  Hz. \* indicates a rebound bursting pyramidal cell. No thalamic cells were included in this simulation. (C) Field potentials calculated from the same simulation showed spike-and-wave complexes. Modified from Destexhe et al. (2001).

$GABA_B$ -mediated inhibition in pyramidal cells, in agreement with the highly non-linear activation properties of these receptors (see above). If the  $GABA_B$  conductance was sufficiently large (0.05–0.1  $\mu$ S),  $GABA_B$ -mediated IPSPs could activate a rebound burst in the pyramidal neurons that contained  $I_T$ , similar to current injection in Figure 13.9. The oscillation therefore consisted in  $GABA_B$  IPSP-rebound sequences, in which the rebound of the entire network was triggered by a minority of pyramidal neurons containing  $I_T$ . A small proportion of LTS pyramidal cells, as small as 5%, depending on the connectivity used, was sufficient to generate slow oscillations in the disinhibited network.

In calculated extracellular field potentials, this slow oscillation generated spike-and-wave patterns. Similar to cooperative  $GABA_B$  responses (see above), the synchronized discharge of all cells in the network generated a negative ‘spike’ component

(see Figure 13.10C). The subsequent activation of  $GABA_B$  IPSPs induced a period of silence in the network, during which pyramidal neurons were hyperpolarized by  $K^+$  currents (a mixture of  $GABA_B$ -mediated IPSPs and voltage-dependent  $K^+$  currents). These outward currents generated a slow positive ‘wave’ in the field potentials (see Figure 13.10C). Therefore, the disinhibited cortical network can generate its own a form of spike-and-wave oscillation.

Similar findings were also reported in a model of cortex consisting of interconnected pyramidal neurons and interneurons (Timofeev et al., 2002). This model included an  $I_h$  current in pyramidal neurons and the elevated extracellular  $K^+$  concentration in the epileptic focus, leading to particularly strong rebound properties of  $I_h$ -containing pyramidal neurons, entraining the network in slow hypersynchronized oscillations.

The intracortical mechanisms leading to spike-and-wave activity in this model are based on the following sequence of events:

1. Due to suppressed  $GABA_A$ -mediated inhibition, the disinhibited cortical network generated prolonged discharges. These events generated a negative ‘spike’ in simulated field potentials.
2. Due to the prolonged firing of interneurons, powerful  $GABA_B$ -mediated IPSPs hyperpolarized pyramidal cells, stopping their discharge. These slow IPSPs, as well as other slow  $K^+$  currents, maximally activated due to the prolonged firing, generated a slow positive ‘wave’ in field potentials.
3. At the offset of  $GABA_B$  IPSPs, a fraction of pyramidal cells generated a rebound burst, entraining the entire network in prolonged discharges and restarting the oscillation cycle.

#### THALAMOCORTICAL MECHANISMS FOR ABSENCE SEIZURES

As reviewed above, thalamic circuits can generate hypersynchronized oscillations at  $\sim 3$  Hz, resembling the typical oscillation frequency during absence seizures. However, there is ample evidence that the thalamus is not sufficient to explain seizure generation.  $GABA_A$ -receptor antagonists induce spike-and-wave seizures when applied to cerebral cortex (Gloor et al., 1977; Fisher and Prince, 1977a; Steriade and Contreras, 1998), while they fail to generate such paroxysms when injected to the thalamus (Ralston and Ajmone-Marsan, 1956; Gloor et al., 1977; Steriade and Contreras, 1998). A majority of thalamic neurons are steadily hyperpolarized and completely silent during cortical seizures (Steriade and Contreras, 1995; Lytton et al., 1997; Pinault et al., 1998). Finally, seizure activity can be observed in cortex following thalamic inactivation or thalamectomy (Marcus and Watson, 1966; Pellegrini et al., 1979; Steriade and Contreras, 1998). Several features of such intracortical seizures can be accounted for by computational models (Destexhe et al., 2001; see above).

Although such data may suggest that seizures could be generated intracortically, the thalamus appears to be necessary, as reviewed above. The main argument is that spike-and-wave seizures disappear following thalamic lesions or by inactivating the thalamus (Pellegrini et al., 1979; Avoli and Gloor, 1981; Vergnes and Marescaux, 1992). Blocking thalamic  $GABA_B$  receptors also leads to the suppression of spike-and-wave seizures (Liu et al., 1992). Finally, it was shown that a diffuse application of a dilute solution of penicillin to the cortex resulted in spike-and-wave seizures, although the thalamus needed to be intact (Gloor et al., 1977).

Taken together, these data show that both cortex and thalamus are necessary for absence seizures (reviewed in Gloor and Fariello, 1988; Danober et al., 1998). In this section, we review computational models that addressed mechanisms for seizure generation based on thalamocortical loops, where the thalamus acts as the generator of the  $\sim 3$  Hz oscillation (or 5–10 Hz in rodents) while the cortex generates the spike-and-wave patterns (Destexhe, 1998, 1999). We will show that a single mechanism can be consistent with all of the experiments reviewed above (for details, see Destexhe and Sejnowski, 2001).

#### MODEL OF $\sim 3$ Hz SPIKE-AND-WAVE OSCILLATIONS IN THE THALAMOCORTICAL SYSTEM

##### **Intact thalamic circuits can be forced into $\sim 3$ Hz oscillations due to $GABA_B$ receptor cooperativity**

The first question we address is how the behavior of thalamic circuits is controlled by the cortex. Thalamic networks have a propensity to generate oscillations on their own, such as the 7–14 Hz spindle oscillations (Steriade et al., 1993; von Krosigk et al., 1993). Although these oscillations are generated in the thalamus, the neocortex can trigger them (Steriade et al., 1972; Roy et al., 1984; Contreras and Steriade, 1996) and corticothalamic feedback exerts a decisive control over thalamic oscillations (Contreras et al., 1996).

In computational models, this cortical control required more powerful corticothalamic EPSPs on RE cells compared to TC cells (Destexhe et al., 1998a). In these conditions, excitation of corticothalamic cells led to mixed EPSPs and IPSPs in TC cells, in which the IPSP was dominant, consistent with experimental observations (Burke and Sefton, 1966; Deschênes

and Hu, 1990; Contreras et al., 1997). If cortical EPSPs and IPSPs from RE cells were of comparable conductance, cortical feedback could not evoke oscillations in the thalamic circuit due to shunting effects between EPSPs and IPSPs (Destexhe et al., 1998a). The most likely reason for ‘inhibitory dominance’ in TC cells is that RE cells are exquisitely sensitive to cortical EPSPs (see Contreras et al., 1993 for experiments, and Destexhe, 2000; Destexhe and Sejnowski, 2002 for models), probably due to powerful T-current in their dendrites (Destexhe et al., 1996b). Moreover, the quantal conductance of cortical EPSPs is about twice as large in RE neurons compared to TC cells ( $266 \pm 48 \text{ pS}$  versus  $103 \pm 25 \text{ pS}$ , respectively; see Golshani et al., 2001). In addition, cortical synapses contact only the distal dendrites of TC cells (Liu et al., 1995a) and are likely to be further attenuated for this reason. Taken together, these data suggest that corticothalamic feedback operates mainly by eliciting bursts in RE cells which, in turn, evoke powerful IPSPs on TC cells that largely overwhelm the direct cortical EPSPs.

The effects of corticothalamic feedback on the thalamic circuit were investigated with the thalamic model (Figure 13.11; Destexhe, 1998). Simulated cortical EPSPs evoked bursts in RE cells (Figure 13.11B, arrow), which recruited TC cells

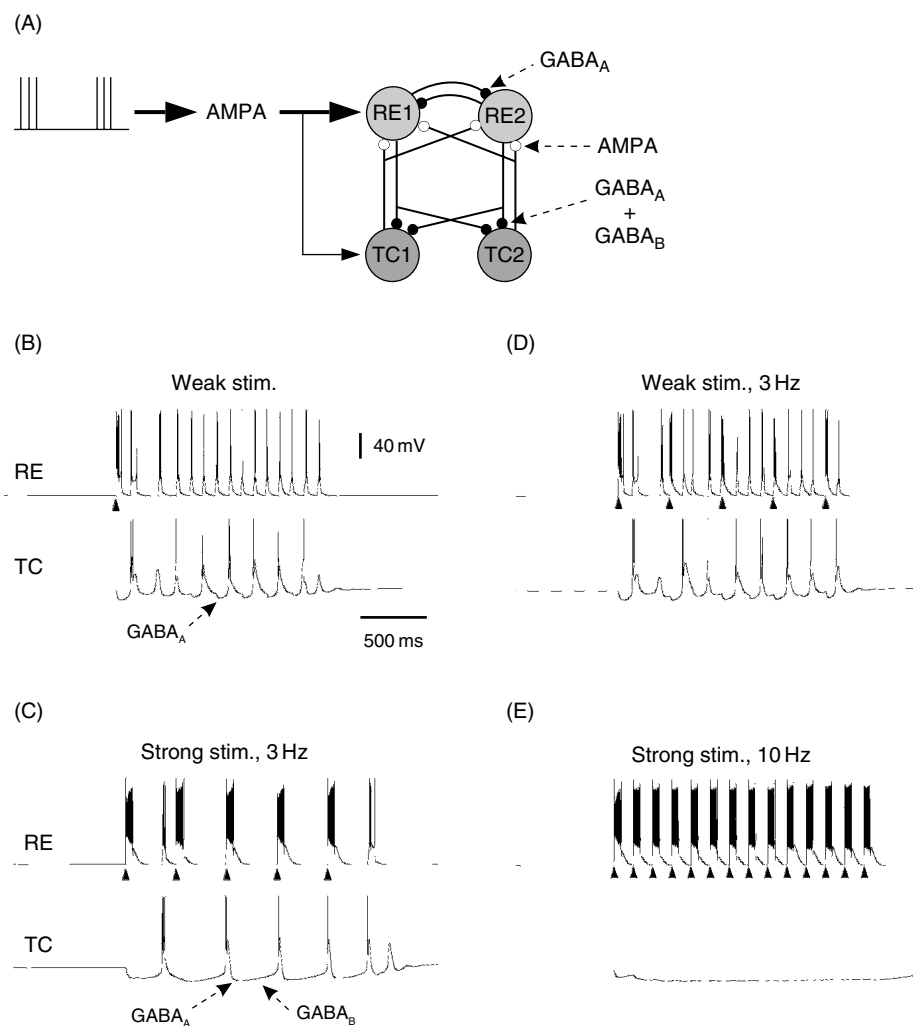


**FIGURE 13.11** Corticothalamic feedback can force thalamic circuits into  $\sim 3\text{Hz}$  oscillations due to the properties of  $\text{GABA}_B$  receptors. (A) Connectivity and receptor types in a circuit of thalamocortical (TC) and thalamic reticular (RE) neurons. Corticothalamic feedback was simulated through AMPA-mediated synaptic inputs (shown on the left of the connectivity diagram; total conductance of  $1.2 \mu\text{S}$  to RE cells and  $0.01 \mu\text{S}$  to TC cells). (B) A single stimulation of corticothalamic feedback (arrow) entrained the circuit into a  $10\text{Hz}$  mode similar to spindle oscillations. (C) With a strong-intensity stimulation at  $3\text{Hz}$  (arrows; 14 spikes/stimulus), RE cells were recruited into large bursts, which evoked IPSPs onto TC cells dominated by  $\text{GABA}_B$ -mediated inhibition. In this case, the circuit could be entrained into a different oscillatory mode, with all cells firing in synchrony. (D) Weak stimulation at  $3\text{Hz}$  (arrows) entrained the circuit into spindle oscillations (identical intensity as in B). (E) Strong stimulation at  $10\text{Hz}$  (arrows) led to quiescent TC cells due to sustained  $\text{GABA}_B$  current (identical intensity as in C). Modified from Destexhe, (1998).

through IPSPs and triggered a  $\sim 10$  Hz oscillation in the circuit. During the oscillation, TC cells rebound once every two cycles following GABA<sub>A</sub>-mediated IPSPs and RE cells only discharged a few spikes, evoking GABA<sub>A</sub>-mediated IPSPs in TC cells with no significant GABA<sub>B</sub> currents (Figure 13.11B). These features are typical of spindle oscillations (Steriade et al., 1993; von Krosigk et al., 1993).

However, a different type of oscillatory behavior could be elicited from the circuit by repetitive stimulation at 3 Hz with high intensity (14 spikes every 333 ms; see Figure 13.11C). All cell types were entrained to discharge in synchrony at  $\sim 3$  Hz. On the other hand, repetitive stimulation at 3 Hz at low intensity produced spindle oscillations (see Figure 13.11D) similar to Figure 13.11A. High-intensity stimulation at 10 Hz led to quiescence in TC cells (see Figure 13.11E), due to sustained GABA<sub>B</sub> currents, similar to a previous analysis (see Figure 12 in Lytton et al., 1997).

These simulations indicate that strong corticothalamic feedback at 3 Hz can force thalamic circuits in a 3 Hz oscillation (Destexhe, 1998). Cortical EPSPs force RE cells to fire large bursts (see Figure 13.11C, arrows), fulfilling the conditions needed to activate GABA<sub>B</sub> responses. The consequence was that TC cells were ‘clamped’ at hyperpolarized levels by GABA<sub>B</sub> IPSPs during  $\sim 300$  ms before they could rebound. The non-linear properties of GABA<sub>B</sub> responses are therefore responsible here for the coexistence between two types of oscillations in the same circuit: moderate corticothalamic feedback recruited the circuit in  $\sim 10$  Hz spindle oscillations, while strong feedback at 3 Hz could force the intact circuit at the same frequency due to the non-linear activation properties of intrathalamic GABA<sub>B</sub> responses.

### **~3 Hz spike-and-wave oscillations in thalamocortical circuits**

A thalamocortical network consisting of different layers of cortical and thalamic cells was simulated to explore the impact of this mechanism at the network level (Destexhe, 1998). The network included thalamic TC and RE cells and a simplified representation of the deep layers of the cortex, in which pyramidal (PY) cells constitute the major source of corticothalamic fibers. As corticothalamic PY cells receive a significant proportion of their excitatory synapses from ascending thalamic axons (Hersch and White, 1981; White and Hersch, 1982), these cells mediate a monosynaptic excitatory feedback loop (thalamus-cortex-thalamus) which was modeled here. The structure of the network, with TC, RE, PY and cortical interneurons (IN), is schematized in Figure 13.12A. Each cell type contained the minimal set of calcium- and voltage-dependent currents necessary to account for their intrinsic properties: TC cells contained I<sub>T</sub>, I<sub>h</sub> and a calcium-dependent upregulation of I<sub>h</sub>, RE cells contained I<sub>Ts</sub>, PY cells had a slow voltage-dependent K<sup>+</sup> current I<sub>M</sub> responsible for spike-frequency adaptation similar to ‘regular-spiking’ pyramidal cells (Connors and Gutnick, 1990). All cell types had the I<sub>Na</sub> and I<sub>Kd</sub> currents necessary to generate action potentials. All currents were modeled using Hodgkin-Huxley (1952) type kinetics based on voltage-clamp data. Synaptic interactions were mediated by glutamate AMPA and NMDA receptors, as well as GABAergic GABA<sub>A</sub> and GABA<sub>B</sub> receptors, and were simulated using kinetic models of postsynaptic receptors (Destexhe et al., 1994b, 1998b). All excitatory connections (TC  $\rightarrow$  RE, TC  $\rightarrow$  IN, TC  $\rightarrow$  PY, PY  $\rightarrow$  PY, PY  $\rightarrow$  IN, PY  $\rightarrow$  RE, PY  $\rightarrow$  TC) were mediated by AMPA receptors, some inhibitory connections (RE  $\rightarrow$  TC, IN  $\rightarrow$  PY) were mediated by a mixture of GABA<sub>A</sub> and GABA<sub>B</sub> receptors, while intra-RE connections were mediated by GABA<sub>A</sub> receptors. Simulations were also performed using NMDA receptors added to all excitatory connections (with maximal conductance set to 25% of the AMPA conductance) and no appreciable difference was observed. They were not included in the present model. Extracellular field potentials were calculated from postsynaptic currents in PY cells according to the model described above, assuming that all cells were arranged equidistantly in a one-dimensional layer (see details in Destexhe, 1998).

In control conditions (see Figure 13.12B), the thalamocortical network generated synchronized spindle oscillations with cellular discharges in phase between all cell types, as observed experimentally (Contreras and Steriade, 1996). TC cells discharged on average once every two cycles following GABA<sub>A</sub>-mediated IPSPs, while all other cell types discharged roughly at every cycle at  $\sim 10$  Hz, consistent with the typical features of spindle oscillations observed intracellularly (Steriade et al., 1990; von Krosigk et al., 1993). The simulated field potentials displayed successive negative deflections at  $\sim 10$  Hz (see Figure 13.12B), in agreement with the pattern of field potentials during spindle oscillations (Steriade et al., 1990). This pattern of field potentials was generated by the limited discharge in PY cells, which fired roughly one spike per oscillation cycle.

Diffuse application of the GABA<sub>A</sub> antagonist penicillin to the cortex, with no change in thalamus, leads to spike-and-wave oscillations in cats (Gloor et al., 1977). In the model, this situation was simulated by decreasing GABA<sub>A</sub> conductances in cortical cells, with thalamus left intact. Alteration of GABA<sub>A</sub> receptors in the cortex had a considerable impact in generating spike-and-wave. Under these conditions, the spindle oscillations transformed into 2–3 Hz oscillations

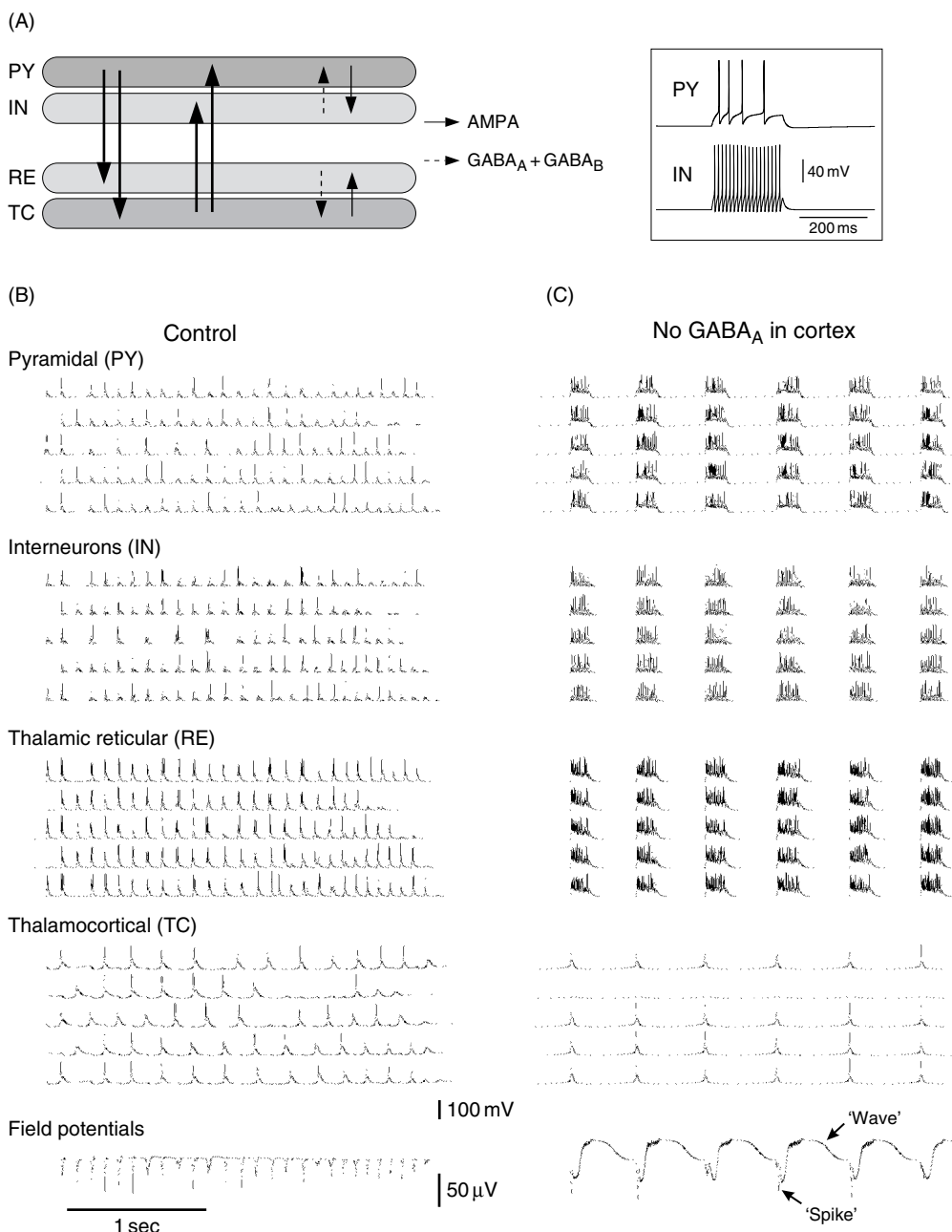


**FIGURE 13.12** Transformation of spindle oscillations into  $\sim 3$  Hz spike-and-wave oscillations by reducing cortical inhibition in a thalamocortical network model. (A) Connectivity between different cell types: 100 cells of each type were simulated, including TC and RE cells, cortical pyramidal cells (PY) and interneurons (IN). The connectivity is shown by continuous arrows, representing AMPA-mediated excitation, and dashed arrows, representing mixed GABA<sub>A</sub> and GABA<sub>B</sub> inhibition. In addition, PY cells were interconnected using AMPA receptors and RE cells were interconnected using GABA<sub>A</sub> receptors. The inset shows the repetitive firing properties of PY and IN cells following depolarizing current injection (0.75 nA during 200 ms;  $-70$  mV rest). (B) Spindle oscillations in the thalamocortical network in control conditions. 5 cells of each type, equally spaced in the network, are shown (0.5 ms time resolution). The field potentials, consisting of successive negative deflections at  $\sim 10$  Hz, is shown at the bottom. (C) Oscillations following the suppression of GABA<sub>A</sub>-mediated inhibition in cortical cells with thalamic inhibition intact. All cells displayed prolonged discharges in phase, separated by long periods of silences, at a frequency of  $\sim 2$  Hz. GABA<sub>B</sub> currents were maximally activated in TC and PY cells during the periods of silence. Field potentials (bottom) displayed spike-and-wave complexes. Thalamic inhibition was intact in (B) and (C). Modified from Destexhe, (1998).

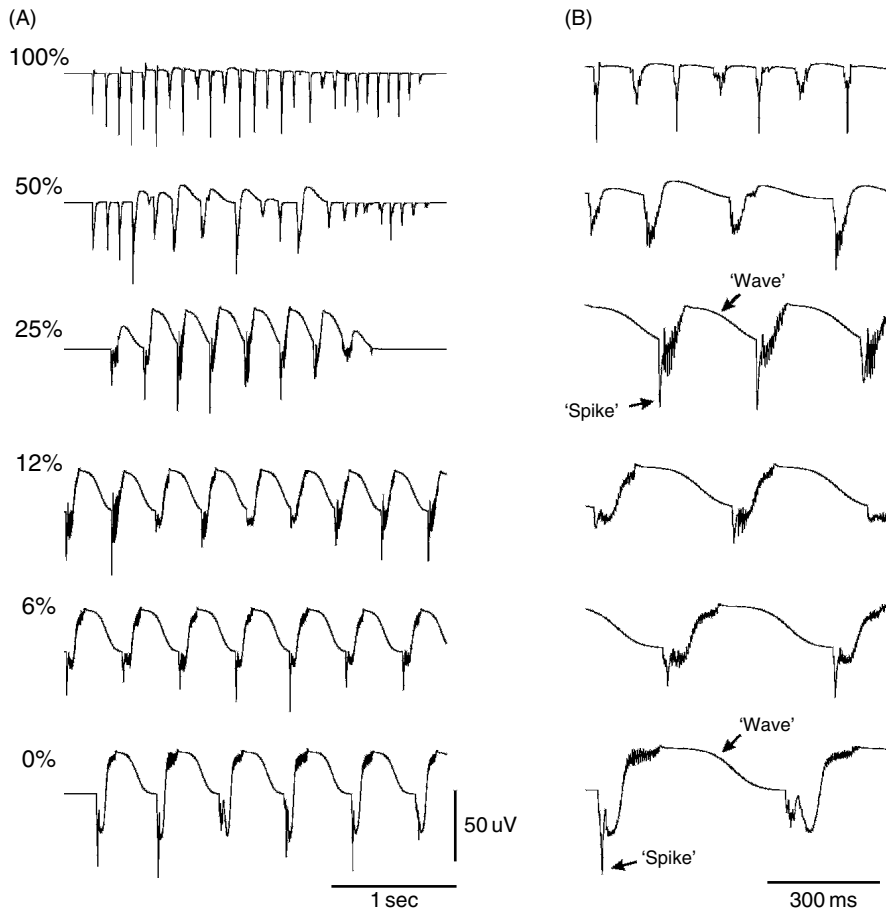


**FIGURE 13.13** Gradual transformation of spindles to spike-and-wave complexes. (A) Field potentials obtained from simulations similar to those of Figure 13.12 for different levels of cortical GABA<sub>A</sub>-mediated inhibition. The conditions were identical except that intracortical GABA<sub>A</sub>-mediated inhibition (IN→PY) was reduced, with total conductance values of 0.15 μS (100%), 0.075 μS (50%), 0.0375 μS (25%), 0.018 μS (12%) and 0.009 μS (6%). At 100% GABA<sub>A</sub> intracortical inhibition there was a spindle sequence (as in Figure 13.12B) and at 0% there were fully-developed spike-and-wave complexes (as in Figure 13.12C); intrathalamic inhibition was intact in all cases. (B) Same simulations at higher temporal resolution. Modified from Destexhe, (1998).

(see Figure 13.12C; Destexhe, 1998). The field potentials generated by these oscillations reflected a pattern of spikes and waves (see Figure 13.12C, bottom).

Spike-and-wave discharges developed progressively from spindle oscillations. Reducing the intracortical fast inhibition from 100% to 50% increased the occurrences of prolonged high-frequency discharges during spindle oscillations (Figure 13.13; Destexhe, 1998). Further decrease in intracortical fast inhibition led to fully-developed spike-and-wave patterns similar to Figure 13.12C (Destexhe, 1998). Field potentials displayed one or several negative/positive sharp deflections, followed by a slowly-developing positive wave (see Figure 13.12C, bottom). During the ‘spike’, all cells fired prolonged high-frequency discharges in synchrony, while the ‘wave’ was coincident with neuronal silence in all cell types. This portrait is typical of experimental recordings of cortical and thalamic cells during spike-and-wave patterns (Pollen, 1964; Steriade 1974; Avoli et al., 1983; McLachlan et al., 1984; Buzsaki et al., 1988; Inoue et al., 1993; Seidenbecher et al., 1998). Some TC cells stayed hyperpolarized during the entire oscillation (second TC cell in Figure 13.12C), as also observed experimentally (Steriade and Contreras, 1995). A similar oscillation arose if GABA<sub>A</sub> receptors were suppressed in the entire network (not shown).

These simulations suggest that spindles can be transformed into an oscillation with field potentials displaying spike-and-wave and that this transformation can occur by alteration of cortical inhibition with no change in the thalamus, in agreement with spike-and-wave discharges obtained experimentally by diffuse application of diluted penicillin onto the cortex (Gloor et al., 1977). The mechanism of the ~3 Hz oscillation of this model depends on a thalamocortical loop where

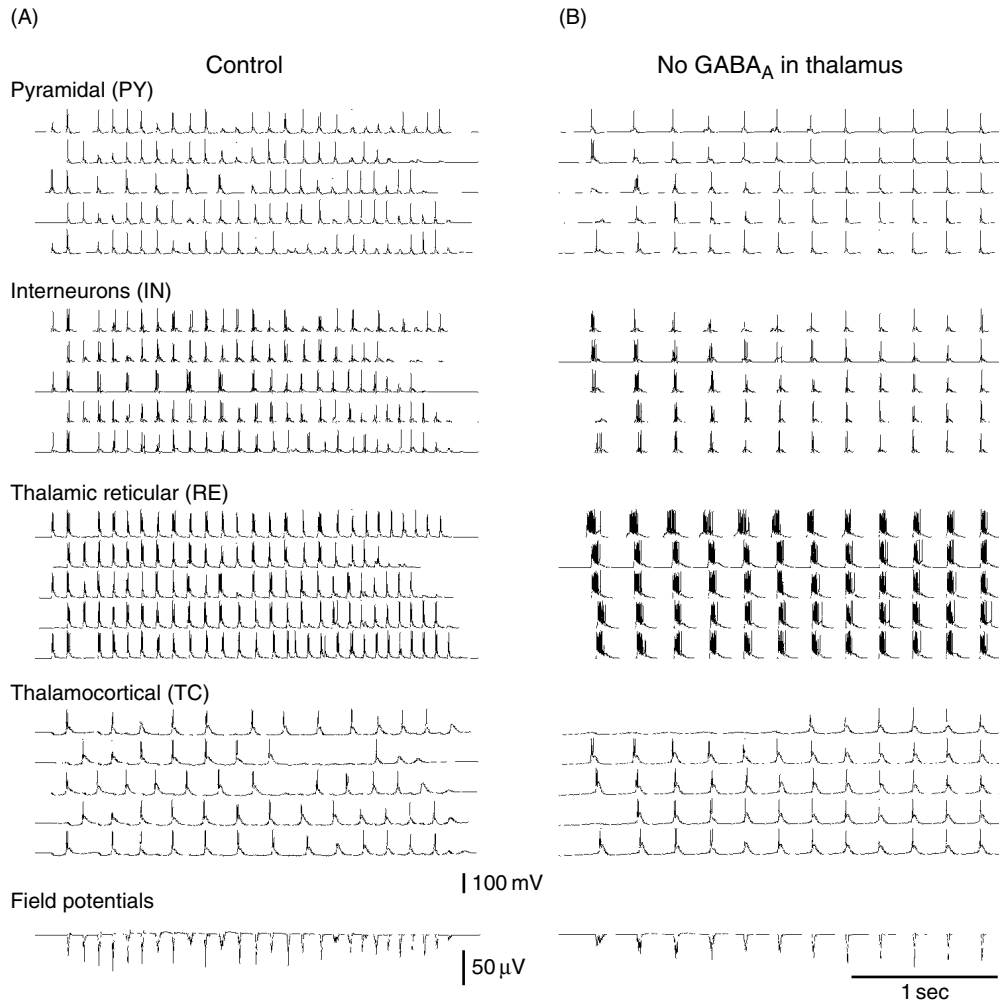


**FIGURE 13.14** Transformation of spindle oscillations into  $\sim 4$  Hz oscillations by blocking thalamic inhibition in thalamocortical networks. (A) Spindle oscillations in the thalamocortical network in control conditions. 5 cells of each type, equally spaced in the network, are shown (0.5 ms time resolution). The field potentials, consisting of successive negative deflections at  $\sim 10$  Hz, is shown at the bottom. (B) Oscillations following the suppression of GABA<sub>A</sub>-mediated inhibition in thalamic cells with cortical inhibition intact (all GABA<sub>A</sub> conductances postsynaptic to RE cells were suppressed). The network generated synchronized oscillations at  $\sim 4$  Hz, with thalamic cells displaying prolonged discharges. The pattern of discharges in PY cells were resembled spindles but at a lower frequency, as reflected in the field potentials (bottom). Modified from Destexhe, (1998).

both cortex and thalamus are necessary, but none of them generates the 3 Hz rhythmicity alone (see details in Destexhe, 1998).

Removing intrathalamic GABA<sub>A</sub>-mediated inhibition also affected the oscillation frequency, but did not generate spike-and-wave, because pyramidal cells were still under the strict control of cortical fast inhibition (Figure 13.14; Destexhe, 1998). This is in agreement with *in vivo* injections of bicuculline into the thalamus, which exhibited slow oscillations with increased thalamic synchrony, but no spike-and-wave patterns in the field potentials (Ralston and Ajmone-Marsan, 1956; Steriade and Contreras, 1998).

In the model, spike-and-wave oscillations may follow a similar waxing-and-waning envelope as spindles and were a network consequence of the properties of a single ion channel ( $I_h$ ) in TC cells (Destexhe, 1998). A calcium-dependent upregulation of  $I_h$  was included in TC cells similar to previous models (Destexhe et al., 1993a, 1996a). The possibility that  $I_h$  upregulation underlies the waxing and waning of spindles at the level of thalamic networks has been demonstrated *in vitro* (Bal and McCormick, 1996; Lüthi and McCormick, 1998, 1999) and predicted by models (Destexhe et al., 1993b; 1996a). This mechanism may also underlie the waxing and waning of spindles at the level of thalamocortical networks (Destexhe

et al., 1998a). The present model suggests that the upregulation of  $I_h$  in TC cells is responsible for temporal modulation of spike-and-wave oscillations and may evoke several cycles of spike-and-wave oscillations, interleaved with long periods of silence ( $\sim 20$  s), as is observed experimentally in sleep spindles and spike-and-wave epilepsy, thus emphasizing further the resemblance between the two types of oscillation.

### MODEL OF ‘FAST’ (5–10 Hz) SPIKE-AND-WAVE OSCILLATIONS IN THE THALAMOCORTICAL SYSTEM

Experimental models of absence seizures in rats display a ‘fast’ form of spike-and-wave activity, around 5–10 Hz (Vergnes and Marescaux, 1992; Coenen and Van Luijtelaar, 2003), which is also associated with pharmacological and behavioral characteristics of absence seizures, but display faster oscillation frequency compared to the typical  $\sim 3$  Hz spike-and-wave discharges during absence seizures in humans and cats. This type of ‘fast’ spike-and-wave seizure was modeled phenomenologically, based on coexisting attractor dynamics (Suffczynski et al., 2004).

To build biophysical models for this type of seizure activity, it is necessary to account for their specific difference with 3 Hz spike-and-wave activity. Intracellular recordings from the thalamus in the ‘generalized absence epilepsy rat from Strasbourg’ (GAERS) reported that, during 5–10 Hz spike-and-wave discharges, TC cells are paced by GABA<sub>A</sub> IPSPs (Pinault et al., 1998). In contrast, in the model of  $\sim 3$  Hz spike-and-wave seizures, TC cells are paced by GABA<sub>B</sub> IPSPs. This raises the question of whether the 3 Hz mechanism also applies to rodents, or if the fast spike-and-wave seizures observed in these species stem from a fundamentally different mechanism.

This question was investigated using computational models, which explored the hypothesis that a different balance of GABAergic conductances in TC cells might explain both the fast (5–10 Hz) and slow (2–3 Hz) type of spike-and-wave oscillations based on similar thalamocortical mechanisms (Destexhe, 1999). The above thalamocortical model of spike-and-wave was used, with three differences:

1. TC cells had a depolarized resting membrane potential of  $-56$  mV, as observed experimentally in GAERS (Pinault et al., 1998)
2. the GABA<sub>B</sub> conductance from RE  $\rightarrow$  TC was smaller than in the previous model ( $0.015 \mu\text{S}$  versus  $0.04 \mu\text{S}$ )
3. the GABA<sub>A</sub> conductance from RE  $\rightarrow$  TC was larger than in the previous model ( $0.03 \mu\text{S}$  versus  $0.02 \mu\text{S}$ ).

In ‘control’ conditions, the network generated 8–12 Hz spindle oscillations, in which all cell types produced moderate rates of discharge approximately in phase, while the field potentials displayed successive negative deflections (Figure 13.15A). These features are in agreement with experimental observations in thalamic and cortical neurons during sleep spindles (Steriade et al., 1990). In the model, these oscillations were not critically dependent on the strengths of GABA<sub>A</sub> and GABA<sub>B</sub> conductances in TC cells, as shown in Figure 13.15A.

The excitability of the cortical network was increased by decreasing the effectiveness of GABA<sub>A</sub>-mediated intracortical inhibition, as in the previous model, but the network generated a different type of oscillation (Figure 13.15B) in which cortical (PY, IN) and thalamic RE cells fired prolonged discharge patterns in synchrony, interleaved with periods of silence that occurred simultaneously in all cell types. This cellular pattern generated spike-and-wave field potentials: the ‘spike’ component was generated by fast EPSPs followed immediately by GABA<sub>A</sub>-mediated IPSPs in PY cells, while the positive ‘wave’ was due to activation of slow K<sup>+</sup> currents (GABA<sub>B</sub>-mediated and voltage-dependent  $I_M$ ) in PY cells.

The oscillatory pattern of discharge depended on the positive feedback in the corticothalamic loop, which was also essential here, as in the 3 Hz spike-and-wave model. The 5–10 Hz oscillation shown in Figure 13.15B differed, however, from the 2–4 Hz frequency in Figure 13.12B. The fast oscillation frequency of the discharge of TC cells was shaped by GABA<sub>A</sub>-mediated IPSPs (arrows in Figure 13.15B2). GABA<sub>B</sub> receptors also contributed to the oscillation but produced a sustained hyperpolarization in TC and PY cells, a feature that has also been observed experimentally (Pinault et al., 1998; Charpier et al., 1999). This sustained hyperpolarization contributed to maintaining the oscillations, since smaller GABA<sub>B</sub> conductances led to a markedly reduced tendency to oscillate and larger GABA<sub>B</sub> conductances led to a slower, 2–3 Hz spike-and-wave oscillation (Destexhe, 1999). Reducing the conductance of the GABA<sub>A</sub> IPSPs markedly reduced oscillatory sequences and increasing them led to prolonged oscillations, thus the spike-and-wave seizures in this model critically depend on a balance between both types of IPSPs (see details in Destexhe, 1999).

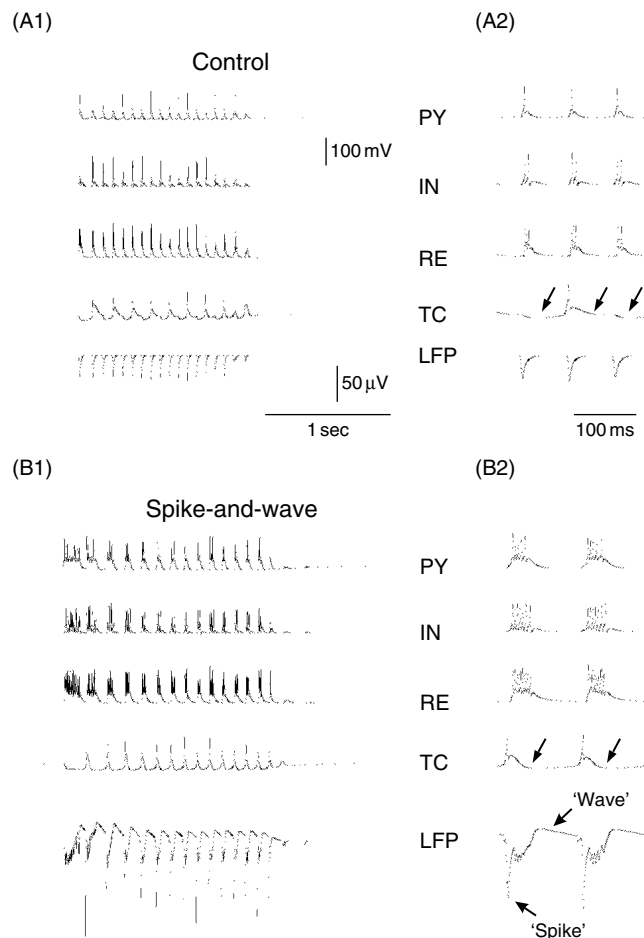


**FIGURE 13.15** Fast spike-and-wave oscillations with stronger GABA<sub>A</sub> conductances in TC cells. (A1) Control spindle oscillations elicited by injection of depolarizing current into PY cells (1 nA during 20 ms). All cell types displayed moderate discharges at 10–12 Hz accompanied by negative deflections in the local field potential (LFP). (B1) Spike-and-wave oscillations following increase of cortical excitability (same simulation as in A with intracortical GABA<sub>A</sub> conductances decreased from 0.15 µS to 0.04 µS). All cell types displayed synchronized discharges at 5–10 Hz and the field potentials consisted of spike-and-wave patterns. The right panels (A2, B2) show two oscillation cycles at higher temporal resolution. Arrows indicate GABA<sub>A</sub> IPSPs in TC cells (modified from Destexhe, 1999).

#### TESTING THE MECHANISMS

The models reviewed above account for the main features of the experimental data about absence seizures in different experimental models. A series of predictions were generated by these models, which we discuss in this section.

#### CORTICOTHALAMIC FEEDBACK

As discussed above, it is necessary to reconcile the data suggesting thalamic participation on one hand, and cortical participation on the other hand. This apparent paradox can be explained by the fact that *physiologically intact* thalamic circuits can be forced to oscillate at a frequency of ~3 Hz by the action of corticothalamic feedback, as depicted in above (see Figure 13.11; Destexhe, 1998). This model makes a very strong prediction: it should be possible to force intact thalamic circuits at a slow hypersynchronized frequency of ~3 Hz, and this forcing should depend on GABA<sub>B</sub> receptors.

Experiments were realized to test these predictions in thalamic slices (Bal et al., 2000; Blumenfeld and McCormick, 2000). In this experiment, the activity of thalamic relay cells was used to trigger the electrical stimulation of corticothalamic fibers (Figure 13.16A). With this feedback, the activity in the slice depended on the stimulus strength. For mild feedback,

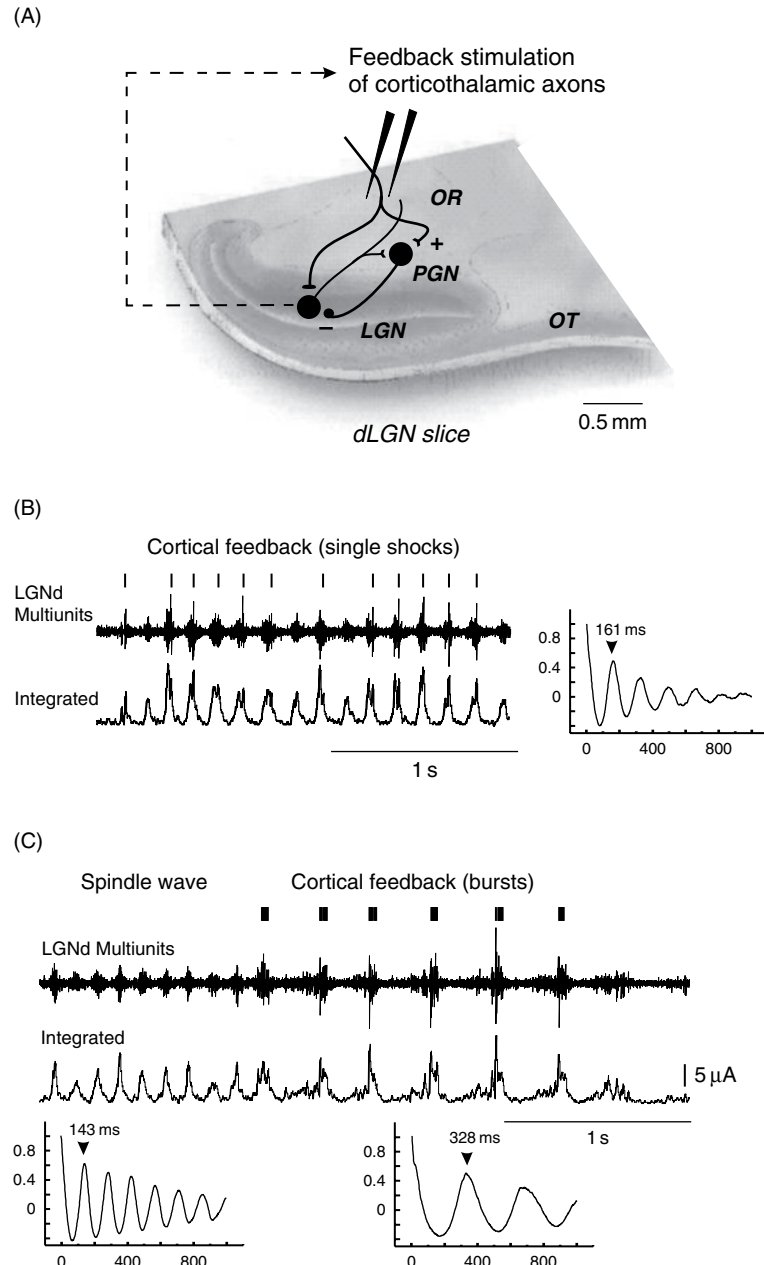


**FIGURE 13.16** Control of thalamic oscillations by corticothalamic feedback in ferret thalamic slices. (A) Schematic thalamic slice. Corticothalamic axons run in the optic radiation (OR) and connect thalamocortical cell in the LGN layers and GABAergic interneurons in the perigeniculate nucleus (PGN). Bipolar stimulating electrodes were placed in the OR (OT: optic tract). (B) Weak (single shock) stimulation at a latency of 20 ms after the detection of multiunit bursts activity (upper trace). Lower trace: smooth integration of the multiunit signal. (C) A 7 Hz control spindle is robustly slowed to 3 Hz oscillation by the feedback stimulation (5 shocks; 100 Hz; 20 ms delay). Modified from Bal et al. (2000).

the slice generated normal spindle oscillations (Figure 13.16B). However, for strong stimulation of corticothalamic fibers, the activity switched to slow synchronized oscillations at  $\sim 3$  Hz (Figure 13.16C). This behavior was dependent on  $GABA_B$  receptors, as shown by its sensitivity to  $GABA_B$  antagonists (Bal et al., 2000; Blumenfeld and McCormick, 2000). These results suggest that strong corticothalamic feedback can force physiologically intact thalamic circuits to oscillate synchronously at 3 Hz.

Further experiments (Bal et al., 2000; Blumenfeld and McCormick, 2000) revealed that this forcing of intact thalamic circuits was accompanied by:

1. a strong synchronization of the discharges of TC cells
2. an enhancement of the burst discharges of RE cells.

The latter is in agreement with the fact that prolonged discharge patterns underlie the emergence of a dominant  $\text{GABA}_B$  IPSP, as also predicted by the model.

Thus, it seems that an exceedingly strong corticothalamic feedback can switch thalamic circuits into a different oscillatory mode, slow and hypersynchronized, and which requires the activation of  $\text{GABA}_B$ -mediated currents in TC cells. This oscillation is similar to the slow oscillation observed in the presence of bicuculline (see above). This oscillation arises because of prolonged discharges in RE cells, which can be caused either by pharmacologically suppressing  $\text{GABA}_A$ -mediated lateral inhibition between RE cells, or by providing a strong excitatory input to RE cells via corticothalamic synapses. Large burst discharges were indeed observed in RE cells during seizures in GAERS (Slaght et al., 2002).

### COOPERATIVE PROPERTIES OF $\text{GABA}_B$ RECEPTORS

As outlined above, one of the essential biophysical ingredients in the mechanisms for absence seizures is the non-linear properties of  $\text{GABA}_B$  responses. Such responses only appear under intense release conditions and it was hypothesized that this property arises from the activation characteristics of  $\text{GABA}_B$ -mediated currents (Destexhe and Sejnowski, 1995).

This hypothesis was tested experimentally using dual intracellular recordings of pairs of connected thalamic (Kim et al., 1997) or cortical neurons (Thomson and Destexhe, 1999). In the thalamus, it was shown that evoking single spikes in RE cells does not evoke any detectable  $\text{GABA}_B$  component in the IPSP of the target TC cell, whereas evoking large burst discharges evokes strong  $\text{GABA}_B$ -mediated IPSPs (Kim et al., 1997), exactly like the model prediction. In neocortex, the same paradigm was observed in single-axon inhibitory connections that contained  $\text{GABA}_B$  receptors (Thomson and Destexhe, 1999). In this case, the cortical interneuron had to discharge at least three spikes at high frequency (around 100 Hz) in order to evoke a detectable  $\text{GABA}_B$  component in the target pyramidal cell, and that the response saturates for more than 10 presynaptic spikes (Figure 13.17).

A computational model of GABA release, diffusion and uptake similar to that of Destexhe and Sejnowski (1995) was investigated based on data from the neocortex (Thomson and Destexhe, 1999). As in the thalamic model, extracellular accumulation of GABA alone could not account for the non-linear relationship between spike number and IPSP amplitude (see details in Thomson and Destexhe, 1999). Different kinetic models were considered for how G-proteins activate  $\text{K}^+$  channels, including a kinetic model using four G-protein binding sites (see Figure 13.17B2) and an allosteric model (see Figure 13.17B3). All models fit to experimental data predicted an optimum of  $n = 4$  G-protein binding sites on  $\text{K}^+$  channels, consistent with the tetrameric structure of  $\text{K}^+$  channels (Hille, 2001).

Finally, it was found recently that the antiepileptic drug vigabatrin strongly affects spike-and-wave discharges in rats (Bouwman et al., 2003). This drug increases GABA concentrations by inhibiting GABA transaminase, one of the major enzymes implicated in GABA degradation. In particular, Bouwman et al. (2003) demonstrated that vigabatrin decreases the frequency of spike-and-wave discharges (from 7.5 Hz to 5.6 Hz), as well as prolongs the duration of seizures (from 1.04 s to 1.52 s). This effect occurs presumably through boosting of both  $\text{GABA}_A$  and  $\text{GABA}_B$  responses and is in agreement with predictions of the model (see Figure 3 in Destexhe, 1999).

### INCONSISTENCIES OF THE MODEL AND OPEN QUESTIONS

A number of experimental observations are not consistent with the present model. First, an apparent intact cortical inhibition was reported in cats treated with penicillin (Kostopoulos et al., 1983). However, this study did not distinguish between  $\text{GABA}_A$  and  $\text{GABA}_B$ -mediated inhibition. In the present model, even when  $\text{GABA}_A$  was antagonized, IPSPs remained of approximately the same size because cortical interneurons fired stronger discharges (see Figure 13.12C) and led to stronger  $\text{GABA}_B$  currents. There was a compensation effect between  $\text{GABA}_A$  and  $\text{GABA}_B$ -mediated IPSPs (not shown), which may lead to an apparent preservation of cortical inhibition. Indeed, an impaired intracortical inhibition was reported in the WAG/Rij genetic model of absence epilepsy in rats (Luhmann et al., 1995).

Second, some  $\text{GABA}_A$  agonists, like barbiturates, may increase the frequency of seizures (Vergnes et al., 1984), possibly through interactions with  $\text{GABA}_A$  receptors in TC cells (Hosford et al., 1997). A similar effect was seen in the model (Destexhe, 1998), but this effect was weak. More accurate simulation of these data would require modeling the variants of

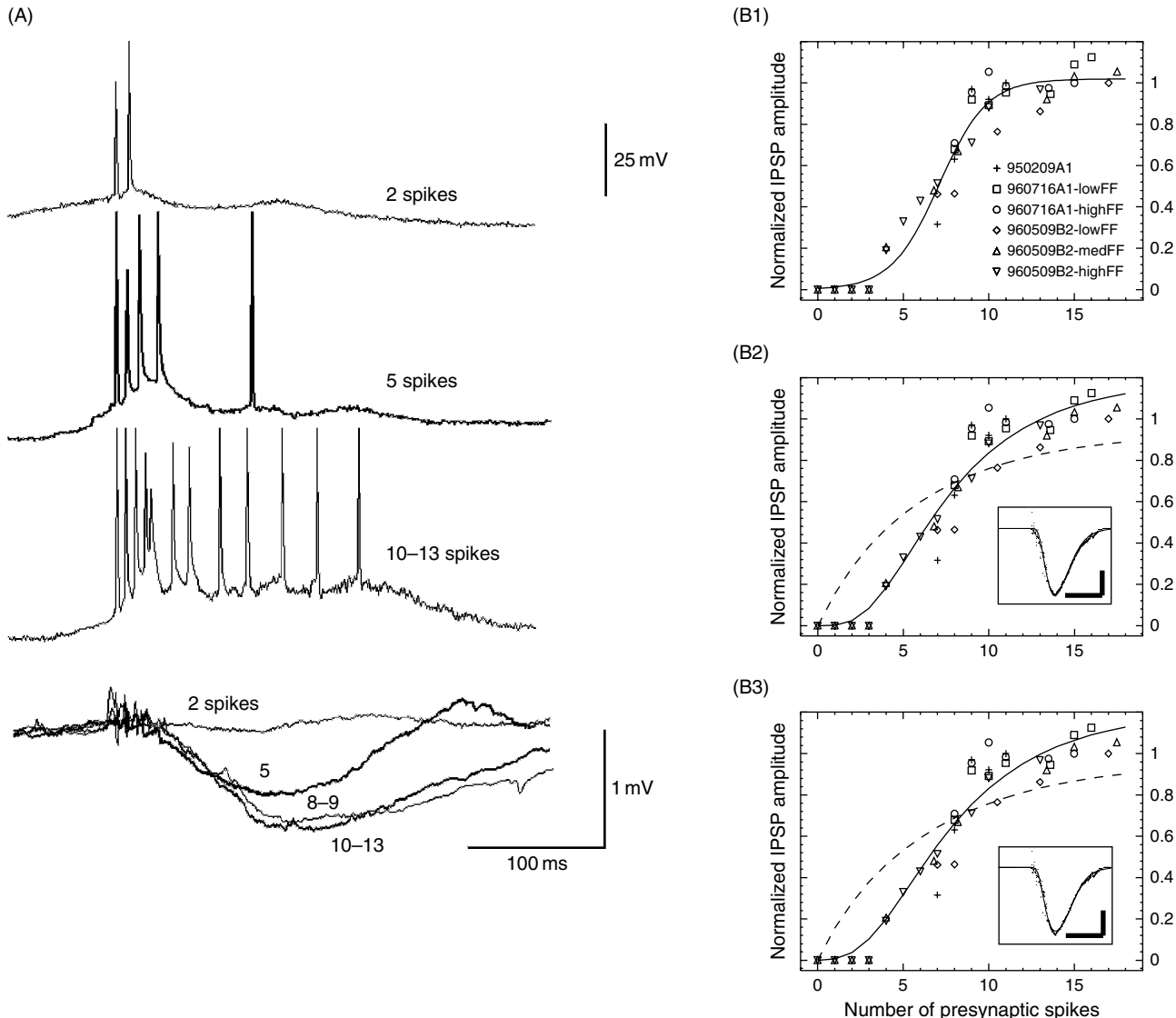


**FIGURE 13.17** Slow IPSPs in cerebral cortex are dependent on the number of presynaptic spikes. (A) Dual intracellular recordings in rat cerebral cortex *in vitro*. The presynaptic cell elicited slow bicuculline-resistant IPSPs in the postsynaptic cell. The top traces show different patterns of presynaptic activity evoked by current injection and the bottom traces show the simultaneously-recorded (presumably GABA<sub>B</sub>-mediated) slow IPSPs in the postsynaptic cell. (B) Nonlinear dependence of slow IPSP amplitude on the number of presynaptic spikes. The symbols indicate the normalized IPSP amplitudes for different experiments involving the same postsynaptic membrane potential and the same presynaptic firing frequency. The smooth curve is the best sigmoidal curve ( $1/(1 + \exp[-(x - x_0)/K])$ ) fit to the spike number/IPSP amplitude plot and yielded an optimal fit for  $x_0 = 7.1$  and  $K = 1.4$  (units of number of spikes). (B2) Same data shown with a kinetic model of GABA<sub>B</sub> responses involving multiple G-protein binding sites on K<sup>+</sup> channels (continuous line,  $n = 4$  binding sites; dashed line,  $n = 1$  binding site). The inset shows the best fit of the  $n = 4$  model to a slow IPSP obtained with 10 presynaptic spikes. (B3) Same fit as in (B2) but using an allosteric model for the K<sup>+</sup> channel regulation by G-proteins. In this case,  $n = 4$  binding sites also gave the best fits to the experimental data. Figure modified from Thomson and Destexhe, (1999).

GABA<sub>A</sub> receptor types in different cells to address how the threshold for spike-and-wave discharges is affected by various types of GABAergic conductances.

Third, an effect which was not incorporated here is the possible presence of GABA receptors in the presynaptic terminal (Waldmeier and Baumann, 1990; Sperk et al., 2004). Such inhibition of synaptic release could mediate various effects, such as dis-inhibition at GABAergic terminals, or presynaptic inhibition of excitatory transmission (assuming that GABA could act on presynaptic excitatory terminals via spillover). Although, the evidence discussed here all points to postsynaptic mechanisms, a presynaptic contribution cannot be ruled out and should be examined by future models.

Finally, it was shown that in the Wag-Rij rat genetic model of absence epilepsy, the seizure seems to start in a focus located in somatosensory cortex (Meeren et al., 2002). This observation is not necessarily inconsistent with the present thalamocortical model. It is conceivable that a given cortical area may have higher excitability and starts the seizure within the loop defined with its associated thalamic nuclei and later spreads to the whole thalamocortical system, even if some areas are not hyperexcitable (or less hyperexcitable). These points should be considered in future models.

## CONCLUSIONS: A CORTICOthalAMIC MECHANISM FOR ABSENCE SEIZURES

### A THALAMOCORTICAL LOOP MECHANISM FOR ABSENCE SEIZURES

The mechanism proposed for absence seizures can be summarized as follows. During sleep spindles, the oscillation is generated by intrathalamic interactions (TC-RE loops) and is reinforced by thalamocortical loops, as suggested in a previous model (Destexhe et al., 1998a). The combined action of intrathalamic and thalamocortical loops provides RE cells with moderate excitation, which evokes GABA<sub>A</sub>-mediated IPSPs in TC cells and sets the frequency to ~10 Hz. During spike-and-wave seizures, due to increased cortical excitability, corticothalamic feedback becomes strong enough to force prolonged burst discharges in RE cells which, in turn, evoke IPSPs in TC cells dominated by the GABA<sub>B</sub> component. In this case, the prolonged inhibition sets the frequency to ~3 Hz and the oscillation is generated by a thalamocortical loop in which the thalamus is intact (see details in Destexhe, 1998). Therefore, if the cortex is inactivated during spike-and-wave, this model predicts that the thalamus should resume generating spindle oscillations, as observed experimentally in cats treated with penicillin (Gloor et al., 1979).

Figure 13.18 shows the phase relations between the different cell types in this corticothalamic model of spike-and-wave seizures. High-frequency discharges generated ‘spike’ components in the field potentials, whereas ‘wave’ components

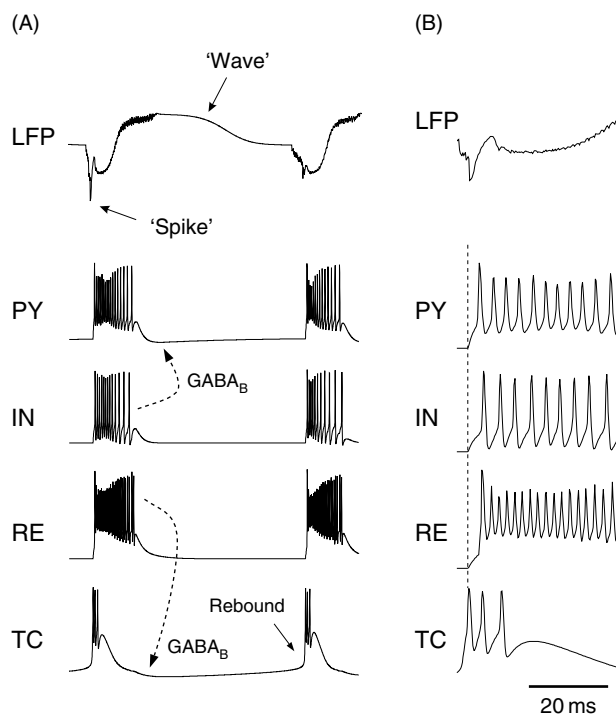


**FIGURE 13.18** Phase relationships during simulated spike-and-wave discharges. (A) Local field potentials (LFP) and representative cells of each type during spike-and-wave oscillations. *Spike*: all cells displayed prolonged discharges in synchrony, leading to spiky field potentials. *Wave*: the prolonged discharge of RE and IN neurons evoked maximal GABA<sub>B</sub>-mediated IPSPs in TC and PY cells respectively (dashed arrows), stopping the firing of all neuron types during a period of 300–500 ms, and generating a slow positive wave in the field potentials. The next cycle restarted due to the rebound of TC cells following GABA<sub>B</sub> IPSPs (arrow). (B) Phase relationships in the thalamocortical model. TC cells discharged first, followed by PY, RE and IN cells. The initial negative peak in the field potentials coincided with the first spike in TC cells before PY cells started firing, and was generated by thalamic EPSPs in PY cells. Modified from Destexhe, (1998).

were generated by  $\text{GABA}_B$  IPSPs in PY cells due to the prolonged firing of cortical interneurons. The hyperpolarization of PY cells during the ‘wave’ also contained a significant contribution from the voltage-dependent  $\text{K}^+$  current ( $I_M$  in the model), which was maximally activated due to the prolonged discharge of PY cells during the ‘spike’. The ‘wave’ component in this model is therefore due to two types of  $\text{K}^+$  currents, one intrinsic and the other  $\text{GABA}_B$ -mediated. The relative contribution of each current to the ‘wave’ depends on their respective conductance values (see details in Destexhe, 1998).

The ‘spike’ component was generated by a concerted prolonged discharge of all cell types. However, the discharges were not perfectly in phase, as indicated in Figure 13.18B. There was a significant phase advance of TC cells, as observed experimentally (Inoue et al., 1993; Seidenbecher et al., 1998). This phase advance was responsible for the initial negative spike in the field potentials, which coincided with the first spike in the TC cells (see Figure 13.18B, dashed line). This feature implements the precedence of EPSPs over IPSPs in the PY cell in order to generate spike-and-wave complexes. These simulations therefore suggest that the initial spike of spike-and-wave complex is due to thalamic EPSPs that precede other synaptic events in PY cells (Destexhe, 1998). Thalamic EPSPs may also trigger an initial avalanche of discharges due to pyramidal cell firing, before IPSPs arise, which would also result in a pronounced negative spike component in field potentials.

### CORTICAL VERSUS THALAMOCORTICAL SEIZURES

The models investigated here displayed oscillations with spike-and-wave field potentials arising either from intracortical mechanisms or from thalamocortical loops. As outlined above, the two types of seizures display fundamental differences. First, the oscillation frequency is slower in intracortical seizures compared to thalamocortical seizures (1.8–2.5 Hz compared to 2–4 Hz; Steriade and Contreras, 1998; Figure 13.19). The same was observed in the models (1.3 Hz in Figure 13.10 compared to 2–4 Hz in Figure 13.12; see Figure 13.19C and details in Destexhe, 1998; Destexhe et al., 2001). This effect was due in the intracortical model to the relatively small conductance of  $I_T$  in pyramidal cells, which gave rise to a significant delay before rebound and consequently a slower oscillation frequency. Second, the ‘spike’ component is less prominent in intracortical spike-and-wave complexes (compare C and D in Figure 13.8), which was also reproduced by the models (Figure 13.19C). In the thalamocortical model, the pronounced negative ‘spike’ was due to thalamic EPSPs that preceded other EPSPs in pyramidal cells (see Figure 13.8B in Destexhe, 1998). These events were of course absent in the intracortical model, leading to a less prominent negative ‘spike’ component, in agreement with Figure 13.8C.

In both cases, the negative ‘spike’ component was due to the EPSPs from the initial discharge of excitatory neurons (and thalamic EPSPs if applicable). The slow positive ‘wave’ was mediated by  $\text{GABA}_B$  IPSPs and voltage-dependent  $\text{K}^+$  currents. In both cases, the oscillation was generated by similar mechanisms based on rebound firing following  $\text{K}^+$ -mediated hyperpolarizing events (see above).

The coexistence of two different seizure mechanisms (intracortical versus corticothalamic) should be investigated by future models and experimental studies. No intracellular recording has been made so far during intracortical spike-and-wave seizures and may bring important information regarding the possible similarities – or differences – with thalamocortical seizures. The two models of intracortical and thalamocortical seizures should also be integrated into the same network, to study under which conditions intracortical loops prevail over corticothalamic loops, which may help to explain the rich variety of paroxysmal patterns observed experimentally.

In conclusion, we have presented here a corticothalamic mechanism for absence seizure generation (Destexhe, 1998, 2006; Destexhe and Sejnowski, 2001) and described the essential biophysical and functional ingredients implicated in this mechanism. Such a corticothalamic scheme differs from previous proposals. Similarly to Gloor’s ‘corticorectal’ scheme (Gloor, 1968), this mechanism postulates an increased cortical excitability. However, instead of considering that spike-and-wave arises from the abnormal cortical response to normal afferent thalamocortical inputs (Gloor, 1968), the present mechanism points to the reverse pathway, corticothalamic feedback. An exceedingly strong action of the cortex to the thalamus can switch thalamic circuits into a hypersynchronized oscillatory mode and entrains the whole thalamocortical system into a slow spike-and-wave oscillation. Thus, the primary deficit is cortical, which is consistent with the finding that absence seizures in rats start in cortex (Meeren et al., 2002). In a corticothalamic mechanism, however, cortical excitability needs not to be uniform across all layers, but may be local to deep layers (those projecting to thalamus). This also differs from Gloor’s mechanism, which would primarily postulate an increased excitability of superficial layers. This difference constitutes a strong prediction which should be tested by future experiments.

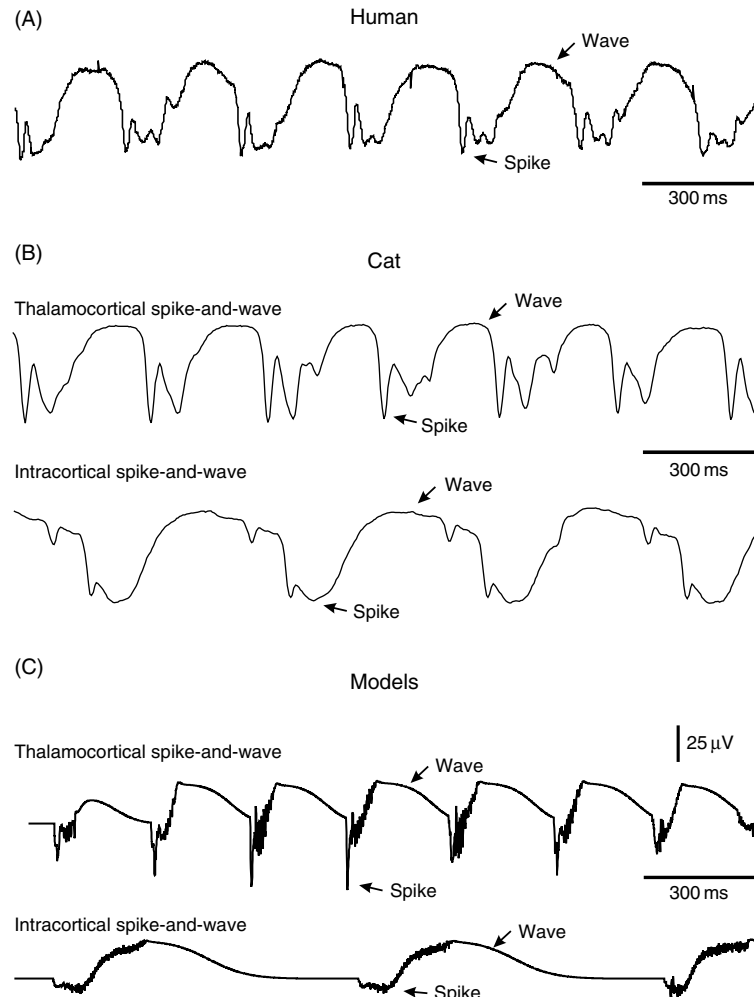


**FIGURE 13.19** Comparison of the morphology of spike-and-wave complexes in experiments and models. (A) EEG during a human absence seizure. Same data as in Figure 13.1, replotted at higher resolution. (B) Local field potential (LFP) measurements in cats in two different experimental models of spike-and-wave seizures following cortical injection of bicuculline. Top: seizure obtained in the intact thalamocortical system; Bottom: seizure in athalamic cat (data replotted from Figure 13.8B and C, respectively). (C) Simulated LFPs in models of spike-and-wave seizures. Top: thalamocortical model (replotted from Figure 13.12); Bottom: intracortical model (replotted from Figure 13.10). In each case, the spikes and the waves are indicated (see original figures for references).

#### ACKNOWLEDGMENTS

This chapter is dedicated to the memory of Mircea Steriade. Part of this research was supported by the MRC of Canada, the FRSQ of Québec, the European Community, the HFSP program and CNRS (France). All simulations were performed using NEURON (Hines and Carnevale, 1997). Supplementary information, such as program codes and computer-generated animations of network activity, are available at <http://cns.iaf.cnrs-gif.fr>

#### REFERENCES

- Avoli, M. and Gloor, P. (1981). The effect of transient functional depression of the thalamus on spindles and bilateral synchronous epileptic discharges of feline generalized penicillin epilepsy. *Epilepsia* 22:443–452.
- Avoli, M. and Gloor, P. (1982). Role of the thalamus in generalized penicillin epilepsy: observations on decorticated cats. *Exp Neurol* 77:386–402.
- Avoli, M., Gloor, P., Kostopoulos, G. and Gotman, J. (1983). An analysis of penicillin-induced generalized spike and wave discharges using simultaneous recordings of cortical and thalamic single neurons. *J Neurophysiol* 50:819–837.
- Bal, T. and McCormick, D.A. (1996). What stops synchronized thalamocortical oscillations? *Neuron* 17:297–308.

- Bal, T., von Krosigk, M. and McCormick, D.A. (1995). Synaptic and membrane mechanisms underlying synchronized oscillations in the ferret LGNd *in vitro*. *J Physiol* 483:641–663.
- Bal, T., Debay, D. and Destexhe, A. (2000). Cortical feedback controls the frequency and synchrony of oscillations *in* the visual thalamus. *J Neurosci* 20:7478–7488.
- Blumenfeld, H. and McCormick, D.A. (2000). Corticothalamic inputs control the pattern of activity generated in thalamocortical networks. *J Neurosci* 20:5153–5162.
- Bouwman, B.M., van den Broek, P.L., van Luijtelaar, G. and van Rijn, C.M. (2003). The effects of vigabatrin on type II spike wave discharges in rats. *Neurosci Lett* 338:177–180.
- Burke, W. and Sefton, A.J. (1966). Inhibitory mechanisms in lateral geniculate nucleus of rat. *J Physiol* 187:231–246.
- Buzsaki, G., Bickford, R.G., Ponomareff, G., Thal, L.J., Mandel, R. and Gage, F.H. (1988). Nucleus basalis and thalamic control of neocortical activity in the freely moving rat. *J Neurosci* 8:4007–4026.
- Charpier, S., Leresche, N., Deniau, J.M., Mahon, S., Hughes, S.W. and Crunelli, V. (1999). On the putative contribution of GABA(B) receptors to the electrical events occurring during spontaneous spike and wave discharges. *Neuropharmacology* 38:1699–1706.
- Coenen, A.M. and Van Luijtelaar, E.L. (2003). Genetic animal models for absence epilepsy: a review of the WAG/Rij strain of rats. *Behav Genet* 33:635–655.
- Connors, B.W. and Gutnick, M.J. (1990). Intrinsic firing patterns of diverse neocortical neurons. *Trends Neurosci* 13:99–104.
- Contreras, D. and Steriade, M. (1995). Cellular basis of EEG slow rhythms: a study of dynamic corticothalamic relationships. *J Neurosci* 15:604–622.
- Contreras, D. and Steriade, M. (1996). Spindle oscillation in cats: the role of corticothalamic feedback in a thalamically-generated rhythm. *J Physiol* 490:159–179.
- Contreras, D., Curró Dossi, R. and Steriade, M. (1993). Electrophysiological properties of cat reticular thalamic neurones *in vivo*. *J Physiol* 470:273–294.
- Contreras, D., Destexhe, A., Sejnowski, T.J. and Steriade, M. (1996). Control of spatiotemporal coherence of a thalamic oscillation by corticothalamic feedback. *Science* 274:771–774.
- Contreras, D., Destexhe, A. and Steriade, M. (1997). Intracellular and computational characterization of the intracortical inhibitory control of synchronized thalamic inputs *in vivo*. *J Neurophysiol* 78:335–350.
- Crunelli, V. and Leresche, N. (2002). Childhood absence epilepsy: genes, channels, neurons and networks. *Nat Rev Neurosci* 3:371–382.
- Danober, L., Deransart, C., Depaulis, A., Vergnes, M. and Marescaux, C. (1998). Pathophysiological mechanisms of genetic absence epilepsy in the rat. *Prog. Neurobiol* 55:27–57.
- Davies, C.H., Davies, S.N. and Collingridge, G.L. (1990). Paired-pulse depression of monosynaptic GABA-mediated inhibitory postsynaptic responses in rat hippocampus. *J Physiol* 424:513–531.
- de la Peña, E. and Geijo-Barrientos, E. (1996). Laminar organization, morphology and physiological properties of pyramidal neurons that have the low-threshold calcium current in the guinea-pig frontal cortex. *J Neurosci* 16:5301–5311.
- Deschénes, M. and Hu, B. (1990). Electrophysiology and pharmacology of the corticothalamic input to lateral thalamic nuclei: an intracellular study in the cat. *Eur J Neurosci* 2:140–152.
- Destexhe, A. (1992). Nonlinear dynamics of the rhythmical activity of the brain (in French). Doctoral dissertation. Université Libre de Bruxelles, Brussels.
- Destexhe, A. (1998). Spike-and-wave oscillations based on the properties of GABA<sub>B</sub> receptors. *J Neurosci* 18:9099–9111.
- Destexhe, A. (1999). Can GABA<sub>A</sub> conductances explain the fast oscillation frequency of absence seizures in rodents? *Eur J Neurosci* 11:2175–2181.
- Destexhe, A. (2000). Modeling corticothalamic feedback and the gating of the thalamus by the cerebral cortex. *J Physiol (Paris)* 94:391–410.
- Destexhe, A. (2006). Spike-and-wave oscillations. In: *Scholarpedia, encyclopedia of computational Neuroscience* (E. Izhikevich, ed.). URL: [http://www.scholarpedia.org/article/Spike-and-Wave\\_Oscillations](http://www.scholarpedia.org/article/Spike-and-Wave_Oscillations).
- Destexhe, A. and Sejnowski, T.J. (1995). G-protein activation kinetics and spill-over of GABA may account for differences between inhibitory responses in the hippocampus and thalamus. *Proc Natl Acad Sci USA* 92:9515–9519.
- Destexhe, A. and Sejnowski, T.J. (2001). Thalamocortical assemblies. Oxford University Press, Oxford.
- Destexhe, A. and Sejnowski, T.J. (2002). The initiation of bursts in thalamic neurons and the cortical control of thalamic sensitivity. *Phil Trans Roy Soc Lond Ser B* 357:1649–1657.
- Destexhe, A., Babloyantz, A. and Sejnowski, T.J. (1993a). Ionic mechanisms for intrinsic slow oscillations in thalamic relay neurons. *Biophys J* 65:1538–1552.
- Destexhe, A., McCormick, D.A. and Sejnowski, T.J. (1993b). A model for 8–10 Hz spindling in interconnected thalamic relay and reticularis neurons. *Biophys J* 65:2474–2478.
- Destexhe, A., Contreras, D., Sejnowski, T.J. and Steriade, M. (1994a). A model of spindle rhythmicity in the isolated thalamic reticular nucleus. *J Neurophysiol* 72:803–818.
- Destexhe, A., Mainen, Z.F. and Sejnowski, T.J. (1994b). An efficient method for computing synaptic conductances based on a kinetic model of receptor binding. *Neural Comput* 6:14–18.
- Destexhe, A., Bal, T., McCormick, D.A. and Sejnowski, T.J. (1996a). Ionic mechanisms underlying synchronized oscillations and propagating waves in a model of ferret thalamic slices. *J Neurophysiol* 76:2049–2070.
- Destexhe, A., Contreras, D., Steriade, M., Sejnowski, T.J. and Huguenard, J.R. (1996b). *In vivo, in vitro* and computational analysis of dendritic calcium currents in thalamic reticular neurons. *J Neurosci* 16:169–185.
- Destexhe, A., Neubig, M., Ulrich, D. and Huguenard, J.R. (1998). Dendritic low-threshold calcium currents in thalamic relay cells. *J Neurosci* 18:3574–3588.
- Destexhe, A., Contreras, D. and Steriade, M. (1998a). Mechanisms underlying the synchronizing action of corticothalamic feedback through inhibition of thalamic relay cells. *J Neurophysiol* 79:999–1016.
- Destexhe, A., Mainen, Z.F. and Sejnowski, T.J. (1998b). Kinetic models of synaptic transmission. In: *Methods in neuronal modeling*, 2nd edn (C. Koch and I. Segev, eds) pp. 1–26. MIT Press, Cambridge.
- Destexhe, A., Contreras, D. and Steriade, M. (2001). LTS cells in cerebral cortex and their role in generating spike-and-wave oscillations. *Neurocomputing* 38:555–563.

- Dutar, P. and Nicoll, R.A. (1988). A physiological role for GABA<sub>B</sub> receptors in the central nervous system. *Nature* 332:156–158.
- Fisher, R.S. and Prince, D.A. (1977a). Spike-wave rhythms in cat cortex induced by parenteral penicillin. I. Electroencephalographic features. *Electroencephalogr Clin Neurophysiol* 42:608–624.
- Fisher, R.S. and Prince, D.A. (1977b). Spike-wave rhythms in cat cortex induced by parenteral penicillin. II. Cellular features. *Electroencephalogr Clin Neurophysiol* 42:625–639.
- Foehring, R.C., Lorenzon, N.M., Herron, P. and Wilson, C.J. (1991). Correlation of physiologically and morphologically identified neuronal types in human association cortex in vitro. *J Neurophysiol* 66:1825–1837.
- Friedman, A. and Gutnick, M.J. (1987). Low-threshold calcium electrogenesis in neocortical neurons. *Neurosci Lett* 81:117–122.
- Gibbs, J.W., Berkow-Schroeder, G. and Coulter, D.A. (1996). GABA<sub>A</sub> receptor function in developing rat thalamic reticular neurons: whole cell recordings of GABA-mediated currents and modulation by clonazepam. *J Neurophysiol* 76:2568–2579.
- Gloor, P. (1968). Generalized cortico-reticular epilepsies. Some considerations on the pathophysiology of generalized bilaterally synchronous spike and wave discharge. *Epilepsia* 9:249–263.
- Gloor, P. and Fariello, R.G. (1988). Generalized epilepsy: some of its cellular mechanisms differ from those of focal epilepsy. *Trends Neurosci* 11:63–68.
- Gloor, P., Quesney, L.F. and Zumstein, H. (1977). Pathophysiology of generalized penicillin epilepsy in the cat: the role of cortical and subcortical structures. II. Topical application of penicillin to the cerebral cortex and subcortical structures. *Electroencephalogr Clin Neurophysiol* 43:79–94.
- Gloor, P., Pellegrini, A. and Kostopoulos, G.K. (1979). Effects of changes in cortical excitability upon the epileptic bursts in generalized penicillin epilepsy of the cat. *Electroencephalogr Clin Neurophysiol* 46:274–289.
- Golomb, D., Wang, X.J. and Rinzel, J. (1996). Propagation of spindle waves in a thalamic slice model. *J Neurophysiol* 75:750–769.
- Golshani, P., Liu, X.B. and Jones, E.G. (2001). Differences in quantal amplitude reflect GluR4-subunit number at corticothalamic synapses on two populations of thalamic neurons. *Proc Natl Acad Sci USA* 98:4172–4177.
- Hamill, O.P., Huguenard, J.R. and Prince, D.A. (1991). Patch-clamp studies of voltage-gated currents in identified neurons of the rat cerebral cortex. *Cerebr Cortex* 1:48–61.
- Hersch, S.M. and White, E.L. (1981). Thalamocortical synapses on corticothalamic projections neurons in mouse SmI cortex: electron microscopic demonstration of a monosynaptic feedback loop. *Neurosci Lett* 24:207–210.
- Hille, B. (2001). Ionic channels of excitable membranes, 3rd edn. Sinauer Associates, Sunderland.
- Hines, M.L. and Carnevale, N.T. (1997). The NEURON simulation environment. *Neural Comput* 9:1179–1209.
- Hodgkin, A.L. and Huxley, A.F. (1952). A quantitative description of membrane current and its application to conduction and excitation in nerve. *J Physiol* 117:500–544.
- Hosford, D.A., Clark, S., Cao, Z. et al. (1992). The role of GABA<sub>B</sub> receptor activation in absence seizures of lethargic (lh/lh) mice. *Science* 257:398–401.
- Hosford, D.A., Wang, Y. and Cao, Z. (1997). Differential effects mediated by GABA<sub>A</sub> receptors in thalamic nuclei of lh/lh model of absence seizures. *Epilepsy Res* 27:55–65.
- Huguenard, J.R. and Prince, D.A. (1994a). Clonazepam suppresses GABA<sub>B</sub>-mediated inhibition in thalamic relay neurons through effects in nucleus reticularis. *J Neurophysiol* 71:2576–2581.
- Huguenard, J.R. and Prince, D.A. (1994b). Intrathalamic rhythmicity studied *in vitro*, nominal T-current modulation causes robust anti-oscillatory effects. *J Neurosci* 14:5485–5502.
- Huntsman, M.M., Porcello, D.M., Homanics, G.E., DeLorey, T.M. and Huguenard, J.R. (1999). Reciprocal inhibitory connections and network synchrony in the mammalian thalamus. *Science* 283:541–543.
- Inoue, M., DuySENS, J., Vossen, J.M.H. and Coenen, A.M.L. (1993). Thalamic multiple-unit activity underlying spike-wave discharges in anesthetized rats. *Brain Res* 612:35–40.
- Jasper, H. and Kershman, J. (1941). Electroencephalographic classification of the epilepsies. *Arch Neurol Psychiatr* 45:903–943.
- Kim, U., Bal, T. and McCormick, D.A. (1995). Spindle waves are propagating synchronized oscillations in the ferret LGNd *in vitro*. *J Neurophysiol* 74:1301–1323.
- Kim, U., Sanchez-Vives, M.V. and McCormick, D.A. (1997). Functional dynamics of GABAergic inhibition in the thalamus. *Science* 278:130–134.
- Kim, D., Song, U., Keum, S. et al. (2001). Lack of the burst firing of thalamocortical relay neurons and resistance to absence seizures in mice lacking the  $\alpha_{1G}$  T-type  $\text{Ca}^{2+}$  channels. *Neuron* 31:35–45.
- Kostopoulos, G., Gloor, P., Pellegrini, A. and Gotman, J. (1981a). A study of the transition from spindles to spike and wave discharge in feline generalized penicillin epilepsy: microphysiological features. *Exp Neurol* 73:55–77.
- Kostopoulos, G., Gloor, P., Pellegrini, A. and Siatitsas, I. (1981b). A study of the transition from spindles to spike and wave discharge in feline generalized penicillin epilepsy: EEG features. *Exp Neurol* 73:43–54.
- Kostopoulos, G., Avoli, M. and Gloor, P. (1983). Participation of cortical recurrent inhibition in the genesis of spike and wave discharges in feline generalized epilepsy. *Brain Res* 267:101–112.
- Liu, X.B., Honda, C.N. and Jones, E.G. (1995a). Distribution of four types of synapse on physiologically identified relay neurons in the ventral posterior thalamic nucleus of the cat. *J Comp Neurol* 352:69–91.
- Liu, X.B., Warren, R.A. and Jones, E.G. (1995b). Synaptic distribution of afferents from reticular nucleus in ventroposterior nucleus of the cat thalamus. *J Comp Neurol* 352:187–202.
- Liu, Z., Vergnes, M., Depaulis, A. and Marescaux, C. (1991). Evidence for a critical role of GABAergic transmission within the thalamus in the genesis and control of absence seizures in the rat. *Brain Res* 545:1–7.
- Liu, Z., Vergnes, M., Depaulis, A. and Marescaux, C. (1992). Involvement of intrathalamic GABA<sub>B</sub> neurotransmission in the control of absence seizures in the rat. *Neuroscience* 48:87–93.
- Luhmann, H.J., Mittmann, T., van Luijtelaar, G. and Heinemann, U. (1995). Impairment of intracortical GABAergic inhibition in a rat model of absence epilepsy. *Epilepsy Res* 22:43–51.
- Lüthi, A. and McCormick, D.A. (1998). Periodicity of thalamic synchronized oscillations: the role of  $\text{Ca}^{2+}$ -mediated upregulation of  $I_h$ . *Neuron* 20:553–563.

- Lüthi, A. and McCormick, D.A. (1999). Modulation of a pacemaker current through  $\text{Ca}^{2+}$ -induced stimulation of cAMP production. *Nat Neurosci* 2:634–641.
- Lytton, W.W., Contreras, D., Destexhe, A. and Steriade, M. (1997). Dynamic interactions determine partial thalamic quiescence in a computer network model of spike-and-wave seizures. *J Neurophysiol* 77:1679–1696.
- Marcus, E.M. and Watson, C.W. (1966). Bilateral synchronous spike wave electrographic patterns in the cat: interaction of bilateral cortical foci in the intact, the bilateral cortical-callous and adiencephalic preparations. *Arch Neurol* 14:601–610.
- McCormick, D.A. and Hashemiyoon, R. (1998). Thalamocortical neurons actively participate in the generation of spike-and-wave seizures in rodents. *Soc Neurosci Abstr* 24:129.
- McCormick, D.A., Wang, Z. and Huguenard, J. (1993). Neurotransmitter control of neocortical neuronal activity and excitability. *Cerebr Cortex* 3:387–398.
- McLachlan, R.S., Avoli, M. and Gloor, P. (1984). Transition from spindles to generalized spike and wave discharges in the cat: simultaneous single-cell recordings in the cortex and thalamus. *Exp Neurol* 85:413–425.
- Meeren, H.K., Pijn, J.P., Van Luijtelaar, E.L., Coenen, A.M. and Lopes da Silva, F.H. (2002). Cortical focus drives widespread corticothalamic networks during spontaneous absence seizures in rats. *J Neurosci* 22:1480–1495.
- Nunez, P.L. (1981). Electric fields of the brain. The neurophysics of EEG. Oxford University Press, Oxford.
- Otis, T.S., Dekoninck, Y. and Mody, I. (1993). Characterization of synaptically elicited  $\text{GABA}_B$  responses using patch-clamp recordings in rat hippocampal slices. *J Physiol* 463:391–407.
- Pellegrini, A., Musgrave, J. and Gloor, P. (1979). Role of afferent input of subcortical origin in the genesis of bilaterally synchronous epileptic discharges of feline generalized epilepsy. *Exp Neurol* 64:155–173.
- Pinault, D., Leresche, N., Charpier, S. et al. (1998). Intracellular recordings in thalamic neurones during spontaneous spike and wave discharges in rats with absence epilepsy. *J Physiol* 509:449–456.
- Pollen, D.A. (1964). Intracellular studies of cortical neurons during thalamic induced wave and spike. *Electroencephalogr Clin Neurophysiol* 17:398–404.
- Prevett, M.C., Duncan, J.S., Jones, T., Fish, D.R. and Brooks, D.J. (1995). Demonstration of thalamic activation during typical absence seizures during  $\text{H}_2^{15}\text{O}$  and PET. *Neurology* 45:1396–1402.
- Puigcerver, A., Van Luijtelaar, E.J.L.M., Dringenburg, W.H.I.M. and Coenen, A.L.M. (1996). Effects of the  $\text{GABA}_B$  antagonist CGP-35348 on sleep-wake states, behaviour and spike-wave discharges in old rats. *Brain Res Bull* 40:157–162.
- Ralston, B. and Ajmone-Marsan, C. (1956). Thalamic control of certain normal and abnormal cortical rhythms. *Electroencephalogr Clin Neurophysiol* 8:559–582.
- Roy, J.P., Clercq, M., Steriade, M. and Deschênes, M. (1984). Electrophysiology of neurons in lateral thalamic nuclei in cat: mechanisms of long-lasting hyperpolarizations. *J Neurophysiol* 51:1220–1235.
- Sanchez-Vives, M.V. and McCormick, D.A. (1997). Functional properties of perigeniculate inhibition of dorsal lateral geniculate nucleus thalamocortical neurons in vitro. *J Neurosci* 17:8880–8893.
- Seidenbecher, T., Staak, R. and Pape, H.C. (1998). Relations between cortical and thalamic cellular activities during absence seizures in rats. *Eur J Neurosci* 10:1103–1112.
- Slaght, S.J., Leresche, N., Deniau, J.-M., Crunelli, V. and Charpier, S. (2002). Activity of thalamic reticular neurons during spontaneous genetically determined spike and wave discharges. *J Neurosci* 22:2323–2334.
- Smith, K.A. and Fisher, R.S. (1996). The selective  $\text{GABA}_B$  antagonist CGP-35348 blocks spike-wave bursts in the cholesterol synthesis rat absence epilepsy model. *Brain Res* 729:147–150.
- Snead, O.C. (1992). Evidence for  $\text{GABA}_B$ -mediated mechanisms in experimental generalized absence seizures. *Eur J Pharmacol* 213:343–349.
- Soltesz, I. and Crunelli, V. (1992).  $\text{GABA}_A$  and pre- and post-synaptic  $\text{GABA}_B$  receptor-mediated responses in the lateral geniculate nucleus. *Prog Brain Res* 90:151–169.
- Sperk, G., Furtinger, S., Schwarzer, C. and Pirker, S. (2004). GABA and its receptors in epilepsy. *Adv Exp Med Biol* 548:92–103.
- Staak, R. and Pape, H.C. (2001). Contribution of GABA(A) and GABA(B) receptors to thalamic neuronal activity during spontaneous absence seizures in rats. *J Neurosci* 21:1378–1384.
- Steriade, M. (1974). Interneuronal epileptic discharges related to spike-and-wave cortical seizures in behaving monkeys. *Electroencephalogr Clin Neurophysiol* 37:247–263.
- Steriade, M. (2003). Neuronal substrates of sleep and epilepsy. Cambridge University Press, Cambridge.
- Steriade, M. and Contreras, D. (1995). Relations between cortical and thalamic cellular events during transition from sleep patterns to paroxysmal activity. *J Neurosci* 15:623–642.
- Steriade, M. and Contreras, D. (1998). Spike-wave complexes and fast components of cortically generated seizures. I. Role of neocortex and thalamus. *J Neurophysiol* 80:1439–1455.
- Steriade, M., Wyzinski, P. and Apostol, V. (1972). Corticofugal projections governing rhythmic thalamic activity. In: *Corticothalamic projections and sensorimotor activities* (T.L. Frigyesi, E. Rinik and M.D. Yahr, eds) pp. 221–272. Raven Press, New York.
- Steriade, M., Jones, E.G. and Llinás, R.R. (1990). Thalamic oscillations and signalling. John Wiley & Sons, New York.
- Steriade, M., McCormick, D.A. and Sejnowski, T.J. (1993). Thalamocortical oscillations in the sleeping and aroused brain. *Science* 262:679–685.
- Suffczynski, P., Kalitzin, S. and Lopes Da Silva, F.H. (2004). Dynamics of non-convulsive epileptic phenomena modeled by a bistable neuronal network. *Neuroscience* 126:467–484.
- Thomson, A.M. and Destexhe, A. (1999). Dual intracellular recordings and computational models of slow IPSPs in rat neocortical and hippocampal slices. *Neuroscience* 92:1193–1215.
- Timofeev, I., Bazhenov, M., Sejnowski, T.J. and Steriade, M. (2002). Cortical hyperpolarization-activated depolarizing current takes part in the generation of focal paroxysmal activities. *Proc Natl Acad Sci USA* 99:9533–9537.
- Traub, R.D. and Miles, R. (1991). Neuronal networks of the hippocampus. Cambridge University Press, Cambridge.
- Tsakiridou, E., Bertolini, L., de Curtis, M., Avanzini, G. and Pape, H.C. (1995). Selective increase in T-type calcium conductance of reticular thalamic neurons in a rat model of absence epilepsy. *J Neurosci* 15:3110–3117.

- Vergnes, M. and Marescaux, C. (1992). Cortical and thalamic lesions in rats with genetic absence epilepsy. *J Neural Transmiss* 35(Suppl.):71–83.
- Vergnes, M., Marescaux, C., Micheletti, G., Depaulis, A., Rumbach, L. and Warter, J.M. (1984). Enhancement of spike and wave discharges by GABA mimetic drugs in rats with spontaneous petit-mal-like epilepsy. *Neurosci Lett* 44:91–94.
- von Krosigk, M., Bal, T. and McCormick, D.A. (1993). Cellular mechanisms of a synchronized oscillation in the thalamus. *Science* 261:361–364.
- Waldmeier, P.C. and Baumann, P.A. (1990). Presynaptic GABA receptors. *Ann NY Acad Sci* 604:136–151.
- Wallenstein, G.V. (1994). The role of thalamic  $I_{GABA}$  in generating spike-wave discharges during petit mal seizures. *Neuroreport* 5:1409–1412.
- Wang, X.J., Golomb, D. and Rinzel, J. (1995). Emergent spindle oscillations and intermittent burst firing in a thalamic model: specific neuronal mechanisms. *Proc Natl Acad Sci USA* 92:5577–5581.
- White, E.L. and Hersch, S.M. (1982). A quantitative study of thalamocortical and other synapses involving the apical dendrites of corticothalamic cells in mouse SmI cortex. *J Neurocytol* 11:137–157.
- Williams, D. (1953). A study of thalamic and cortical rhythms in petit mal. *Brain* 76:50–69.

# 14

## MECHANISMS OF GRADED PERSISTENT ACTIVITY: IMPLICATIONS FOR EPILEPSY

ERIK FRANSÉN

### ABSTRACT

One major topic in epilepsy is factors contributing to neuronal excitability. In this work, we consider depolarizing sources from cationic currents. These ion channels of the TRP-type are permeable to Na, K and sometimes Ca, and show a slow time dynamics. They can therefore provide the dendrites with integrative properties over seconds and perhaps even minutes. This makes them powerful as integrators of synaptic input. Further, their activation depends to a large degree on intracellular calcium. They may therefore during seizures become strongly activated and thereby further contribute to epileptogenic activity directly by depolarization and indirectly by their calcium permeability. Cationic currents are widely distributed throughout the nervous system, including cortical, cerebellar and subcortical neurons. In this chapter, we describe our work in entorhinal cortex and, specifically, the plateau firing characteristics found in pyramidal cells of layer V. These cells show persistent action potential firing at plateaus, which may last over 10 minutes. Intriguingly, these plateaus are graded in that input, synaptic or by current injection, can shift them up and down in frequency. After our original finding, graded plateaus have been found also in perirhinal cortex and amygdala. Functionally, cationic neuronal integrator capacity has been shown to be involved in sensory-motor integration and may in our case be involved in e.g. path integration. Finally, anticonvulsants like lamotrigine and phenytoin have been found to reduce depolarizations involving cationic currents. Cation currents may therefore be targets in treatments of epilepsy.

### INTRODUCTION

While exploring its environment, an animal faces patterns of input over time scales from seconds to minutes. To process this information, it needs to integrate sensory inputs and produce motor outputs on the corresponding time scale. Neurons, on the other hand, show membrane integration constants of synaptic input on the order of 10 ms. The nervous system uses basically two strategies to bridge from milliseconds to seconds and minutes, intrinsic neuronal and network synaptic. Using interconnected networks of neurons, transient input may circulate in the network thus producing persistence. Theoretical work on so-called attractor networks have, however, shown that the conditions for reliably circulating activities in neural circuits are not as general as may intuitively be thought (see e.g. Fransén and Lansner, 1995). Activity may cease for a number of reasons. By combining sustained network activity with neural intrinsic properties enabling neurons to integrate inputs over time scales exceeding the membrane time constant, activity may be very reliable and stable. One such intrinsic mechanism is slow cationic ion channels located in the dendrites. These channels, voltage gated and/or calcium activated, can produce long-lasting depolarizations of the neuron. Every mechanism, however, works as a dual-sided sword. The long activation times enabling powerful integration also produces a potential risk of hyperexcitability if input frequencies become high and excitation overrides inhibitory mechanisms. In this work, we will describe how slow cationic ion channels can contribute to integration and also discuss how these properties relate to excitability and epileptogenesis.

Experimental data from entorhinal (EC) cortical slices and computational modeling have demonstrated that intrinsic properties in single neurons are sufficient to generate graded persistent spiking activity (Egorov et al., 2002; Fransen et al., 2006). In the initial study, we showed how repetitive application of a brief input (current injection or synaptic stimulation) to a cell can be effective in producing a graded series of self-sustained stable levels of firing frequency (Figure 14.1).

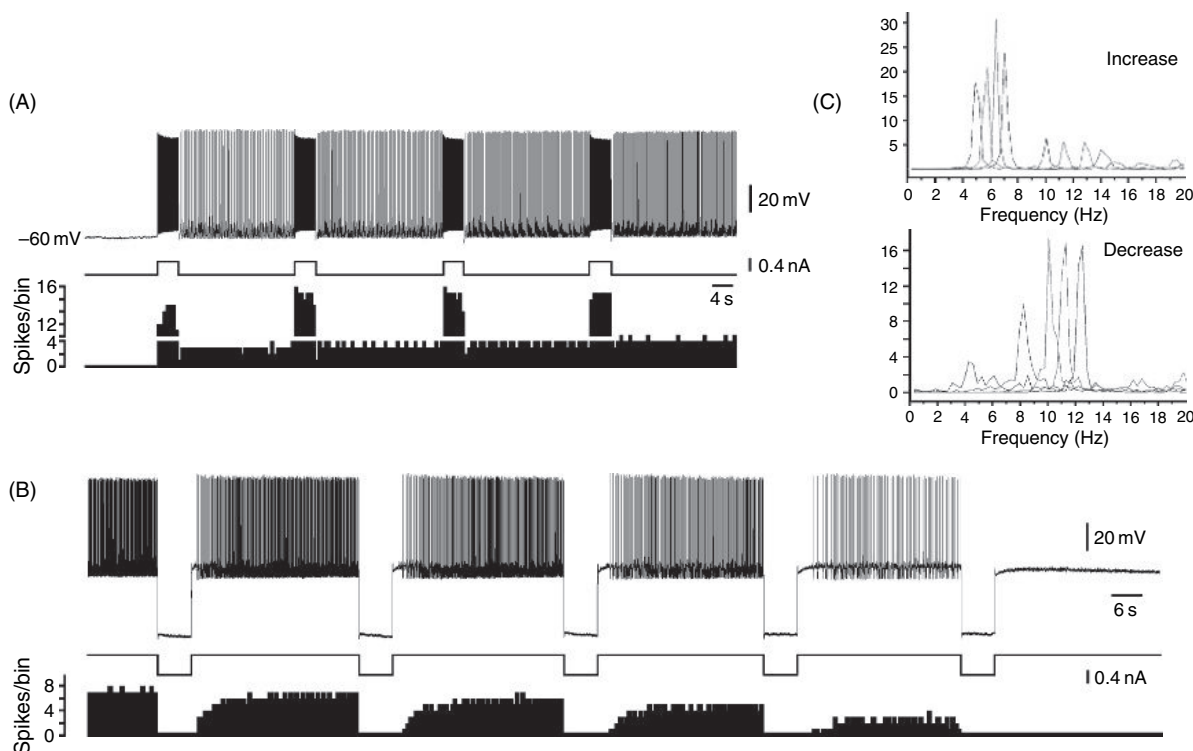


**FIGURE 14.1** Experiment showing graded levels in a layer V EC cell. (A) Increasing stable levels following depolarizing current injections. Top trace shows soma membrane potential. Middle trace shows applied current injection. Bottom trace shows frequency histogram. (B) Decreasing stable levels following hyperpolarizing current injections. Top and bottom traces as in (A). (C) Frequency of stable levels. Top diagram shows frequencies during stable levels following depolarizing pulses and bottom diagram shows decreases following hyperpolarizing pulses.

The firing frequency of the cell at any given level depends on the previous history of the input that is being applied, both in terms of its duration and amplitude, as well as on its pattern of occurrence. Importantly, the stable levels have been observed sustained for up to 13 minutes. Graded firing has since then also been observed in basolateral amygdala (Egorov et al., 2006) as well as perirhinal cortex (Leung et al., 2006). The pharmacological analysis of the phenomenon has revealed dependence on a cationic current (CAN), a calcium-dependence (presumed to act on the calcium sensitive cationic current) and a dependence on activation of muscarinic receptors or metabotropic glutamate receptors (presumed also to act on the CAN current). In the initial studies, carbachol, a cholinergic agonist, was used in the bath medium. But, important to note is that in the study by Egorov in amygdala, they were able to show that endogenous acetylcholine (ACh), released by activation of cholinergic fibers from nucleus basalis of Meynert, was sufficient to permit the graded levels. For the case of entorhinal cortex, there are cholinergic projections to the hippocampal formation from e.g. septal nuclei (Alonso et al., 1995).

Cation channels are not only present in entorhinal cortex neurons, but are found in many cortical and subcortical regions (Moran et al., 2004; von Bohlen und Halbach et al., 2006). In this work, we will focus on the channels belonging to the transient receptor potential (TRP)-type which can be voltage and/or calcium gated, permeable to sodium and potassium and sometimes also calcium, and which are modulated by a number of intracellular messengers and activated by several receptors, e.g. muscarinic and metabotropic glutamate.

Graded persistent spiking information has been demonstrated in systems such as the oculomotor system (Robinson, 1972), the head direction system (Taube and Bassett, 2003) and the somatosensory system (Romo et al., 1999), and also been reviewed by Frank and Brown (2003) and Major and Tank (2004). It is not clear in these systems whether the origin of storage of graded information is exclusively at the network level or whether it may involve single cell properties (Delgado-Garcia et al., 2006). Several models representing graded spiking information have been based on a network of cells interacting (Seung et al., 2000, Goldman et al., 2002, Koulakov et al., 2002, Brody et al., 2003, Miller et al., 2003). As mentioned above, our recent evidence of intrinsic mechanisms for graded cellular spiking activity points to a potential role of intrinsic mechanisms. In particular, these mechanisms could enhance the information storage capacity of cortical circuits by allowing maintenance of graded information. However, the intracellular mechanisms for maintaining

graded spiking activity remain to be determined. In the work presented here, we have utilized computational modeling to elucidate possible cellular mechanisms involved in graded spiking phenomena. This modeling has focused on studying functional requirements of biochemical pathways which could potentially be involved and qualitatively to evaluate the resulting model.

The involvement of cationic currents in integrator-like activity has been reported for several systems ranging from sensory-motor integration in the reticulospinal neurons in the lamprey (Viana Di Prisco et al., 2000) integrating cutaneous input and transforming this into a motor command, sensory motor adaptation in medullary pacemaker nucleus neurons (Oestreich et al., 2006) where pulse counting over several minutes leads to changes in electromotor output (the jamming avoidance response) and climbing-fiber potentiation of parallel-fiber inputs to cerebellar Purkinje cells (Batchelor and Garthwaite, 1997) with an integration window of 1–2 minutes.

The very long integration time window of cationic currents also leads to a potential excitability risk. Cationic currents have been implicated in how seizure-like events are sustained during epileptiform discharges in neocortical slices (Schiller, 2004). Entorhinal cortical slices have also been shown to produce epileptiform activity following application of cholinergic agonists (Dickson and Alonso, 1997). Cations are therefore targets of anticonvulsants. The antiepileptic drug, lamotrigine, reduces a cellular depolarization associated with a cationic current (Xiong et al., 2001). Similarly, the anticonvulsant, phenytoin, suppresses depolarizations caused by a cationic current (Kang et al., 1998). Finally, cationic currents have also been shown to be involved in muscarinically induced gamma oscillations in hippocampus CA3 (Fisahn et al., 2002). Thus, both the property of long integration times and of increased synchronicity imposes potential risks in relation to epilepsy-related activity.

#### GRADED SPIKING ACTIVITY VERSUS PLATEAU POTENTIALS

Some types of neurons, for instance spinal motoneurons, display plateau potentials. When stimulated by depolarizing current injections they subsequently maintain firing in the absence of synaptic or current injection input. This firing is of the all-or-none type and the frequency is thus more or less constant and fixed for a particular neuron. When stimulated to spike at an intermediate frequency, the cell will either increase its frequency to the plateau potential frequency, or it will cease firing. It can thus be said to have two stable points of frequency, 0 and  $f_{plateau}$ . Depolarizing plateaus are, by definition, enhancing the excitability. They may therefore be involved in excitability aspects of epileptogenesis. In the presence of cholinergic agonists, depolarizing plateau potentials have been observed in for instance entorhinal cortex (Dickson and Alonso, 1997; Shalinsky et al., 2002). In the slices, activity may also develop into epileptiform activity (Dickson and Alonso, 1997). A cationic current appears to be involved in this activity (Klink and Alonso, 1997).

Our data point to a fundamentally different case. EC layer V neurons can sustain a range of frequencies within an interval, in that any frequency within this interval is stable. Moreover, we do not observe that the neuron drifts up or down following the stimulation, which would be one indication if the cell had a limited number of discrete multiple stable points and was transiently moving to one of those following stimulation. Also, we do not observe that the cell returns to the same frequency values when graded levels are decreased following a series of increases, which also would be indicative of multiple fixed stable points.

Several cell models of graded firing levels have been published (Durstewitz, 2003; Loewenstein and Sompolinsky, 2003; Teramae and Fukai, 2005). Our model differs fundamentally from the first two models which both build on the concept of a line attractor (we will return to the concept of a line attractor in the next section). A line attractor is fundamentally unstable to noise or stimulus distractors and therefore needs additional means of stabilization. We build on the concept of a point attractor which is inherently stable, and which point of stability can be moved due to input. Durstewitz proposed balancing of currents across a range of membrane potentials. That model would require co-alignment of the two balancing curves over a range of voltage as well as very fine tuning of their voltage dependence. Our model does not depend on a delicate balance of conductances. Lowenstein and Sompolinsky (2003) focused on the interaction of multiple dendritic compartments of tonically maintained calcium concentration. But their model would suffer from variations in calcium concentration due, for instance, to calcium inactivation or desensitization effects which are prevalent in the calcium pathways. In their case of tonic fluxes of calcium (Ca), it is also conceivable that interference with calcium stores would lead to effects on stability or gradedness. We have shown experimentally that stable graded levels persist for block of calcium stores (Fransén et al., 2006). This also argues against the model by Teramae et al., which builds on a non-linear interaction with internal stores to maintain graded levels (Teramae and Fukai, 2005). Our model focuses on effects which are resistant to small-scale variations in calcium concentration and does not build on tonic activity in calcium processes.

## CONCEPTUAL MODEL

The model will be described first conceptually and then we will describe its detailed implementation. We will start the description of the stable level by listing the requirements of the model that we derived from analysis of the original experimental data (Egorov et al., 2002; Alonso, unpublished data). The motivation behind compiling this list was to use it to evaluate different hypotheses and models. Line attractor activity can be produced by a number of different models, more details may therefore provide valuable means of differentiating between these.

1. The phenomena is Ca-dependent and an intermediate level of Ca-concentration sustained by spiking is required for the maintenance of a stable level. Since: (a) intracellular Ca chelation blocks the phenomenon (Egorov et al., 2002); (b) blocking spikes with TTX causes plateaus to decay, and (c) blocking intracellular stores with thapsigargin or CPA does not affect the phenomenon (Fransén et al., 2006).
2. A high level of Ca-concentration<sup>1</sup> is required for induction of a stable level. (Egorov et al., 2002 Figures 1b left, 1c left, 2a).
3. A low *value*<sup>1</sup> of Ca-concentration is required for reduction of stable level. A 20 mV hyperpolarization lasting less than 2 s is always ineffective in reducing a stable level (Egorov et al., 2002, Figure 2c).
4. There is a neutral interval in Ca-concentration. There is noise tolerance, first natural noise (fluctuations in membrane potential as well as variable rates during stable levels) (Egorov et al., 2002, Figure 2a,c). Second, tolerance to distractor stimulation (Egorov et al., 2002, Supp Figure B).
5. There is stability for many minutes despite presumed slow changes in ionic conductances and in Ca-related processes (Egorov et al., 2002).
6. There is a maximal (saturated) level of plateau firing frequency level (Egorov et al., 2002).
7. From (4) and (5) we infer that there is stability for slow changes and noise and distractors. This cannot be obtained with reversible processes since they have monotonous sensitivity curves and curves with more than one inflection point is unlikely.

### Graded stable intrinsic spiking activity

We start by considering the situation at stable firing. At stable firing, hyperpolarizing currents are equal and opposing depolarizing currents. A small perturbation to a higher potential (or higher [Ca]) leads to increased hyperpolarizing and/or decreased depolarizing currents, and vice versa for a shift to a lower potential. Thus, considering limitations on the kinetics of e.g. Ca-related compounds or the cationic current, perfect balance may not be true at all moments, but on the scale of one or a few action potentials it will be. As a comparison, for a regular neuron which is not stable but shows transient firing returning back to resting potential following a depolarizing current injection, the hyperpolarizing currents dominate, at least on average and in the long run.

Further, for a bistable cell, like a spinal motoneuron, showing a plateau potential following a depolarizing current injection, there is one point in potential above which depolarizing currents dominate producing the plateau, and below which hyperpolarizing currents dominate returning the cell back to resting potential. A further discussion of the differences between graded levels and plateau potentials follows below.

In Figure 14.2, we illustrate different types of stability conditions by a particle-in-a-box model. The system strives to attain the nearest lowest point while influenced by the control parameter (indicated by the arrow). The control parameter corresponds in our case to calcium concentration which affect the CAN channel state. In (A) there is only one stable value. In (B), a line attractor, there is an arbitrary number of values, i.e. graded value, but none of them are stable. In (C), there is a fixed number of stable points. This leads to restrictions on how close stable points can be found and still be stable. Specifically, after a pulse, one would not see a stereotyped transient decay where a specific amount of the initial amplitude decays down to the stable level as observed in the experiments. Instead, depending on where the initial point starts in relation to the fixed set of stable points, some decays would be large whereas others would be small. Also, the stable values would have specific points and could not be arbitrarily close, so in an experiment with increased as well as decreased stable levels, one would never see relatively closely spaced stable levels, but always with a minimum of separation. In (D), there is one stable point which can be shifted, corresponding to the model presented in this work. The position is in our case controlled by the balance of phosphorylation and dephosphorylation acting on the CAN current (we will get back to this in the section about detailed implementation). Stability is controlled separately by the balance between the CAN current and outward currents (see Figure 14.4A).

<sup>1</sup> The amplitude of the stimulus required to elicit a stable level depends on the pulse length, the longer the pulse, the lower the amplitude required.

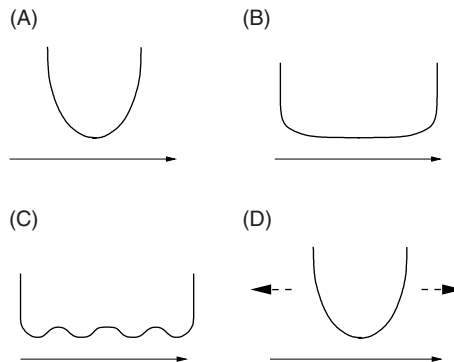


**FIGURE 14.2** Stability of graded levels. (A) Fixpoint attractor. Only one stable value, but displays stability to noise. Arrow indicates direction of increasing control parameter, i.e. membrane potential or calcium concentration. The system is assumed to attain the lowest point on the curve as seen in a local neighborhood. (B) Line attractor. Infinite number of values, but unstable to noise. (C) Multiple fixpoint attractors. Multiple stable values which are stable to noise, but discretely spaced. (D) Movable fixpoint attractor. The position of the point of stability can attain an arbitrary value, thus giving infinite number of stable values which are stable to noise.

The stability of the model providing tolerance to distractors also results in robustness to variations in activity. Irregularities during e.g. epileptiform activity would thereby be smoothed-out adding further to the persistence of epileptogenic activity.

### Induction of a new level

Induction of a stable graded level appears to involve a threshold as there always is a minimal time and/or minimal amplitude of the stimulation (Egorov et al., 2002; Figure 1b,c,d). Further, the presence of stability to noise during the stable levels as well as stability to distractor inputs (Egorov et al., 2002) also point to the presence of a threshold in the induction process. Thus, if the applied depolarizing current is sufficient in strength or duration, membrane potential and firing frequency increase to the new steady-state. In this work, we are assuming this change in depolarizing strength comes from a phosphorylation process of the channel. At high levels of intracellular calcium the channel goes to the high conductance state, and at low levels of calcium to the low conductance state (we will return to the low and high conductance states related to the phosphorylated and dephosphorylated states in the section on detailed implementation below).

As discussed above, experimental results indicated the presence of a threshold for induction of a change of the graded level. In Figure 14.3 we illustrate different possibilities. In (A), we illustrate the effect of a system displaying one fixed threshold. This can only provide two levels and transitions between these occur at the same point, the point of the threshold. With multiple thresholds, as in (B), there could be several levels. The biochemical implementation of such a multithreshold

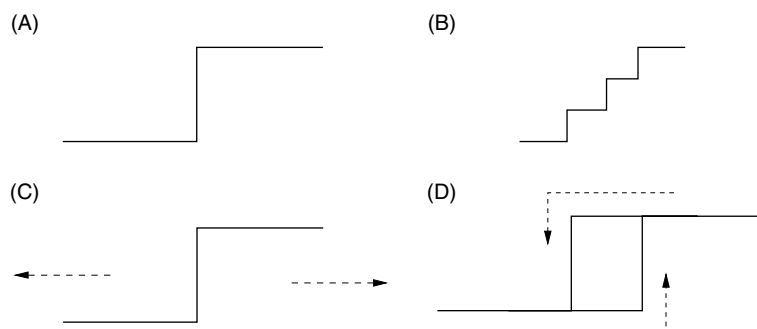


**FIGURE 14.3** Induction of stable levels. (A) One fixed threshold. This provides only two stable levels and the point of transition from one to the other is the same. (B) Multiple thresholds. The biochemical implementation of multiple stable points seems unclear and probably requires a complex biochemical network. As in (A), the transition points are the same going up and down. (C) Movable fixed threshold. This produces an arbitrary number of stable levels, but as in (B) the biochemical implementation is unclear and presumably complex, and as in (A) and (B) transitions points up and down are the same. (D) Separate thresholds. With separate thresholds for up and down transitions the system possesses hysteresis. With a neutral region it can attain graded levels as one fraction of the system can be maintained in the upper at the same time as the other fraction is maintained at the lower level.

system is, however, unclear. If the single threshold as in (A) could be moved, as in (C), there could be multiple levels. As in (B), the implementation of this is unclear as the threshold would have to move coordinately along with the change of level for the threshold to be located at the ‘next’ higher (or lower) transition point. Only in Figure 14.3D, with separate up and down transition points and a neutral region, can we have multiple stable levels and provide noise and distractor tolerance as well as explain the threshold for induction of changes of stable levels. With this type, we have the property of hysteresis. With a set of components each of which is either on the upper or lower curve (but still on the same point on the x-axes), graded information can be stored (Lisman and Goldring, 1988).

A high Ca level for induction and an intermediate Ca level for maintenance of a stable level could indicate hysteresis in the system. Indeed, considering the step-up experiments (Egorov et al., 2002; Fransén et al., 2006), a pulse that induces a change in level consists of a pre-pulse current, a pulse current and a post-pulse current. The pre- and post-currents are identical, but the pre- and post-potentials are not, thus showing that the system has not returned to its pre-pulse state. If a hyperpolarizing pulse follows the depolarizing pulse, the system may return to the state before the two pulses. This behavior would be typical of a system displaying hysteresis. Hysteresis is a characteristic feature of bistable systems.

Increased intracellular calcium levels have been discussed in relation to epilepsy (Delorenzo et al., 2005). As induction depends on calcium, elevated calcium levels would lead to facilitated induction and thereby increased cation depolarization of the cell.

#### DETAILED IMPLEMENTATION

In the following, we will describe how the conceptual model outlined above may be implemented. As above, we start by considering stability.

We have hypothesized that the CAN channel is under metabolic dynamic control by two competing processes that for simplicity, we will denote phosphorylation and dephosphorylation (Fransén et al., 2006). This means stabilizing a phosphorylated state of the channel or an associated regulatory protein. The mechanism of the model presented here could be implemented in a number of different ways. In the model presented here, we assume the phosphorylation increases the Ca-sensitivity of the  $I_{CAN}$  current and/or channel open time (Inoue et al., 1994; Walters et al., 1998).

Stability due to balancing currents is shown in Figure 14.4A. We suggest that the point of intersection is moved as a consequence of a current injection or synaptic input, resulting in a new stable point as the CAN current either increases (direction indicated by higher percent figures) or decreases (direction indicated by lower percent figures). If  $I_{CAN}$  and  $I_{K(AHP)}$  become co-aligned (by slanting of either one, the mechanism suggested by Durstewitz (2003)), a line attractor is possible.

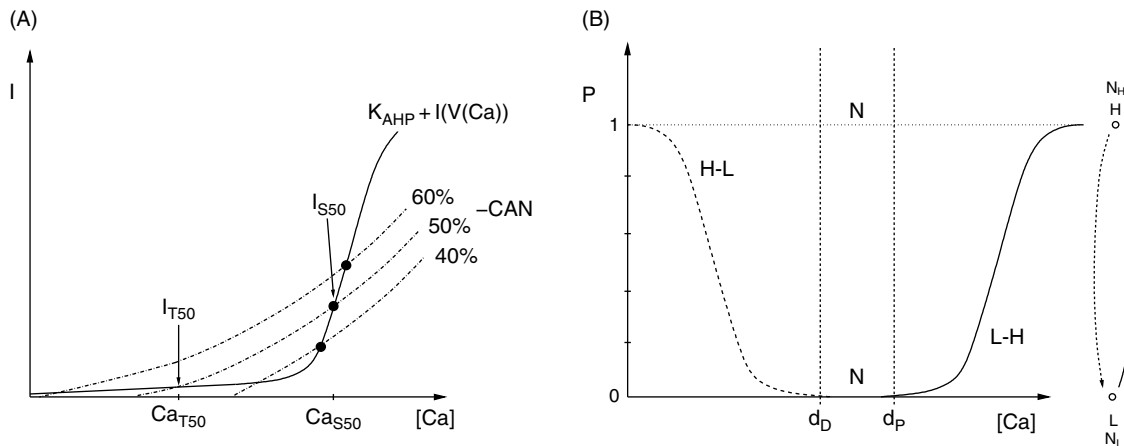


**FIGURE 14.4** (A) Balancing currents. The two opposing calcium dependent currents CAN and  $K_{AHP}$  are plotted showing the magnitude of the currents at stable firing. The intersection points symbolize three such stable levels. L, direction of larger proportion of low conductance channels. H, direction of larger proportion of high conductance channels. Percentages indicate the proportion of high conductance channels of  $I_{CAN}$ . (B) Single channel transition probabilities. Left:  $P_H$ , probability of channel to be in the high conductance state. L-H, transition probability from low to high conductance state. H-L, transition probability from high to low, both functions of intracellular calcium concentration (or an interrelated product). N, neutral calcium concentration region. Right: Single channel state. L, low conductance state. H, high conductance state. N, number of channels in respective state.

However, stability is lost as the restoring current (the difference between  $I_{CAN}$  and  $I_{K(AHP)}$ ) vanishes. For weak restoring currents one would observe large amplitude oscillations around a central point, something not observed experimentally.

Note that, for low proportions of  $I_{CAN}$  there may not be any stability if the curve of  $I_{CAN}$  stays below that of  $I_{K(AHP)}$  for all values. Also, for high percentages there may at high levels of [Ca] be no region where  $I_{K(AHP)}$  exceeds  $I_{CAN}$ , resulting in activity going to the maximal (saturated) level of firing.

Next we discuss the implementation of changes of levels. This is continued in the section on the intracellular signalling network below. In Figure 14.4B we show in detail the transition probability of a channel from its low conductance state to its high conductance state illustrated in the far right side of the figure. The total conductance of the ion channel  $G = g_L * N_D + g_H * N_H$ , where  $g_s$  denote single channel conductances and  $N_s$  denote number of channels. When  $N_x$  are large numbers, transitions appear graded. At any moment, each channel is either in its high or low conductance state. The transition probabilities are continuous entities, but the states for the channel are either low or high, so the average conductance constitutes the macroscopic conductance. The curves indicate the transition probability and, when a channel changes, its transition probability follows the other curve.

### MODEL OF LAYER V PRINCIPAL CELL

Graded firing rates were modeled in a compartmental biophysical simulation of an entorhinal cortex layer V principal neuron (Fransén et al., 2006). This simulation was based on a previously published model of the pyramidal-like cell of EC layer II (Fransén et al., 2002) which includes the following currents:  $Na$ ,  $NaP$ ,  $Ca_L$ ,  $K_{dr}$ ,  $K_C$ ,  $K_{AHP}$ ,  $K_M$ . To address the properties of layer V neurons, modifications were made to the previous simulation. The following modifications were made:

1. addition of a transient potassium current  $K_A$ , modeled according to Traub et al. (1991)
2. replacing the non-specific muscarinically activated calcium sensitive current  $I_{NCM}$  with an  $I_{CAN}$  current that does not show Ca down regulation. This was, as in Fransén et al. (2002) modeled according to Traub et al. (1991)
3. addition of a biochemical pathway connecting  $I_{CAN}$  to spike related Ca influx, as described in detail below.

### Intracellular signalling pathway

Experimental observations point to the involvement of intracellular calcium from e.g. high threshold calcium channels, as well as activation of a cationic current. The full signalling mechanism from intracellular calcium to cationic current is, as yet, unknown. The components of this biochemical pathway are schematically depicted in Figure 14.5 and it includes as a starting point the high threshold Ca-current and as an end point  $I_{CAN}$ . The crucial functional component of our model shown in Figure 14.5 is a calcium concentration controlling the production and break-down of a reactant X which, in turn, determines the balance between the low and high states of the  $I_{CAN}$  current.

The influx of calcium through the high threshold calcium channel  $Ca_L$  changes intracellular calcium concentration  $[Ca]_{PD}$  which is regulated through pumping and buffering processes modeled according to Traub et al. (1991) and McCormick and Huguenard (1992).  $[Ca]_{PD}$  has a linear rise of Ca proportional to the  $Ca_L$  current and a time constant. The time constant of cytosolic Ca for entorhinal layer II stellate cells and layer III pyramidal cells is on the order of 5 s (Gloveli et al., 1999), a value comparable to those derived from Ca-diffusion simulations of a cell of comparable size (Yamada et al., 1989), where a time constant of around 5 s was also found for the core volume. However, to represent Ca in the volume most immediately

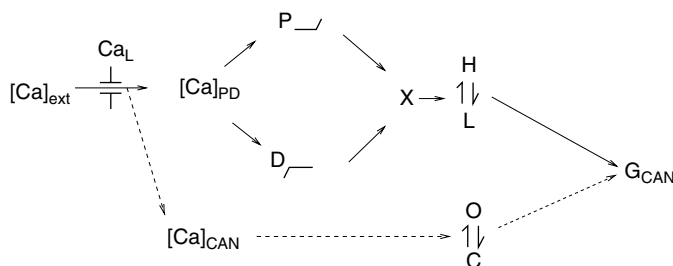


**FIGURE 14.5** Biochemical pathway. Influx of calcium via a high threshold calcium current  $Ca_L$  affects both the CAN current conductance  $G_{CAN}$  directly (dashed pathway, open state O and closed state C) and indirectly via the phosphorylation-dephosphorylation pathway (solid arrow to  $[Ca]_{PD}$ ). Phosphorylation P and dephosphorylation D affect, via regulatory product X, the balance of high conductance state CAN channels H and low conductance L respectively.

near the membrane, we have used a shorter time constant of 250 ms, in agreement with the simulation findings of Yamada et al. Thus, the slow kinetics of our system is not primarily determined by the time constant of the Ca concentration. Instead, it arises from the regulation of  $I_{CAN}$  by the intracellular calcium  $[Ca]_{CAN}$  as well as by the two pathways described in the following. We start by induction of an increase. When the calcium concentration  $[Ca]_{PD}$  crosses a threshold, it can increase the  $I_{CAN}$  current via production of a compound X resulting in an increase in the concentration [X]. This pathway operates only when  $[Ca]_{PD}$  is above the threshold  $[Ca]_{ThP}$ . The product X controls the balance between hypothetical kinases and phosphatases which, in turn, controls the balance between a phosphorylated state and an unphosphorylated state of the  $I_{CAN}$  channel. Thus, an increase in [X] causes a graded increase in the number of channels  $I_{CAN}$  in a high conductance state, thereby causing a graded increase in firing frequency. Next we describe the induction of a decrease. When the calcium concentration  $[Ca]_{PD}$  falls below a threshold it can decrease  $I_{CAN}$  current via breakdown of compound X, resulting in a reduction in the concentration [X],  $[X] \geq 0$ . This pathway operates only when  $[Ca]_{PD}$  is below a threshold  $[Ca]_{ThD}$ . A decrease in [X] causes a graded decrease in the number of individual  $I_{CAN}$  channels in a high conductance state and, thereby, causes a graded decrease in firing frequency. Importantly, in the interval of  $[Ca]_{PD}$  between  $[Ca]_{ThD}$  and  $[Ca]_{ThP}$  there is no change in [X]. This allows the graded levels to remain stable despite small variations in membrane potential (or brief large-scale changes) and small variations in intracellular calcium concentration. Therefore, the graded levels only shift when there are large-scale changes in intracellular calcium,  $[Ca]_{PD}$ , passing either threshold.

As noted above, the concentration [X] regulates the conductance of  $I_{CAN}$ . This was implemented in the model by changing the effective CAN channel current dependent on the level of [X]. This describes the transition between the channel state producing a low charge transfer to the state producing a high charge transfer and it is meant to encompass processes such as changes in single channel conductance or channel open time. For the modification depending on [X], we use the model for concentration dependence of the Ca-dependent potassium current in Traub et al. (1991). This modification was added to the maximal conductance of the low state of  $I_{CAN}$ . The transition between low and high conductance was modeled according to Traub et al. (1991) where the gating particle represents how many channels are in the low and high conductance states (0 represents all CAN channels in the low state and 1 represents the case where the maximal possible number of CAN channels are in the high state). Due to the general Ca-sensitivity of the cation channel, the conductance of  $I_{CAN}$  will also depend on  $[Ca]_{CAN}$  as described in Fransén et al. (2002) (Figure 14.5 dashed pathway) and was modeled similarly as the calcium dependent K-current in Traub et al. (1991).

The pathway model components should not be studied in isolation, they only have a meaning as a whole and do not necessarily by themselves correspond to specific parts of the biochemical pathway. The order of the components does likewise not necessarily correspond to any order in the real system. This type of modeling is analogous to how the alphas and betas of the H-H equations model the potential barrier of the membrane without making claims regarding the internal charge distribution in the channel.

As in Fransén et al. (2002), the  $Ca^{2+}$  diffusion and buffering was modeled according to previous techniques (Traub et al., 1991; McCormick and Huguenard, 1992). To take into account the differences in distances and diffusion constants for the calcium influencing each of the different currents, the calcium kinetics was modeled separately for each case, consistent with separate calcium compartments and reaction pathways within the cell. In addition, until calcium-clamp data exist on the individual currents, it is not possible to separate the kinetics of the calcium concentration from the kinetics of the channel itself. Therefore, the models of the concentration and of the individual currents should be seen as a unit.

## RESULTS

Consistent with experimental observations (Egorov et al., 2002), plateau duration depends both on stimulus magnitude as well as stimulus duration. Figure 14.6A can be compared to (C) showing experimental data reported in Egorov et al. (2002) and (B) can be compared to experimental data in (D), both (A) and (B) showing the same qualitative changes of duration as in experiments (C) and (D). Note specifically that both the property of a lower point below which no sustained activity is produced and an upper point above which only sustained activity exists is produced.

Next, we show a simulation performed to demonstrate the various aspects of the phenomenon. As can be seen in Figure 14.7, all the requirements are fulfilled. We show in sequence, two upward transitions displaying stable spiking activity, one transition downward, tolerance to distracting inputs, followed by two transitions downward. The model proposed displays some features that were listed in the previous section describing observed features, but which were not part of the model construction process.

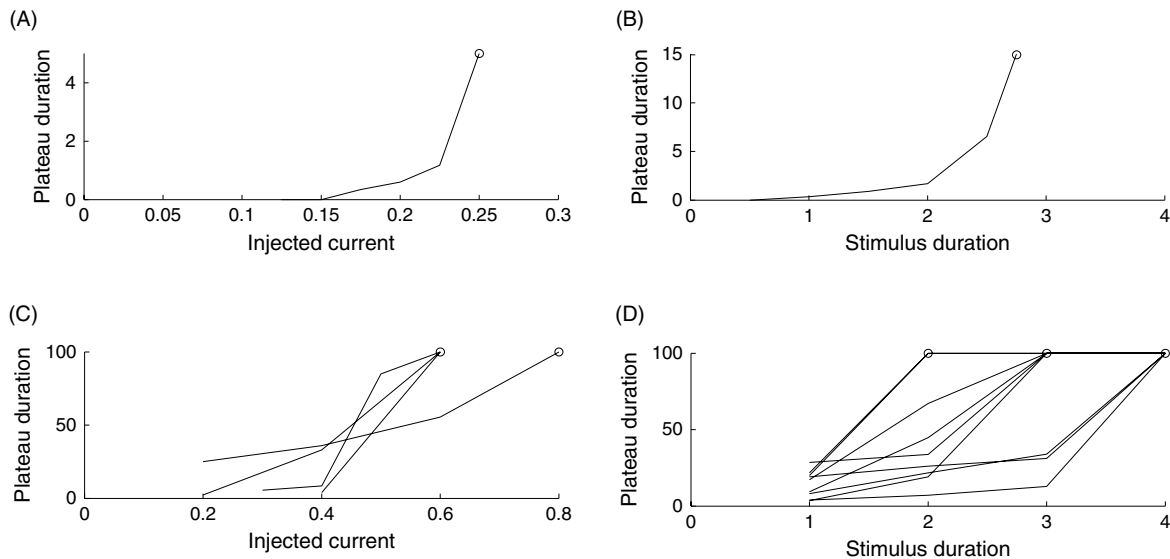


**FIGURE 14.6** Induction of a stable plateau. (A) Simulation showing how plateau duration depends on magnitude of injected current. The circled point represents stable persistent activity. (B) Simulation showing how plateau duration depends on duration of injected current. (C) Experimental data showing how plateau duration depends on magnitude of injected current. (D) Experimental data showing how plateau duration depends on duration of injected current.

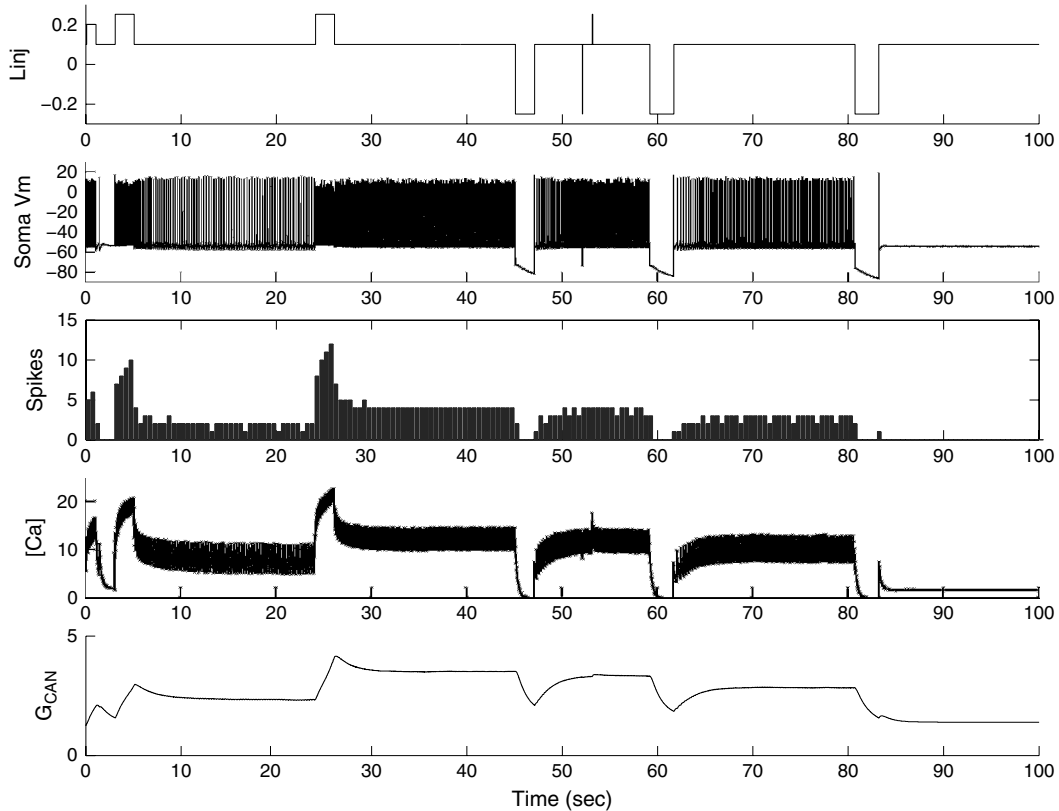


**FIGURE 14.7** Simulation of stable levels. In the figure we plot from top: the current injection  $\text{Inj}$  (nA), soma membrane potential  $V_m$  (mV), spike histogram, calcium concentration (arbitrary units) affecting the balance, and cationic current conductance  $G_{CAN}$  ( $S/m^2$ ).

First, the model shows increasing frequencies during the stimulation, which is correct. (See Egorov et al., 2002 Figure 1a left where the threshold to spike steadily increases. See also Egorov et al., 2002 Figure 1a right where blockage of the muscarinic action by atropine displays a flat threshold, i.e. no acceleration of spiking.) Secondly, the model also shows decaying membrane potential during hyperpolarizing current injections (Egorov et al., 2002 Figure 2c), consistent with the notion of a closing current. Thirdly, the model produces a peak in  $I_{CAN}$  (data not shown) that lags the stimulation pulse as well as the Ca concentration. That is consistent with Egorov et al. (2002 Figure 1d, middle pulse), where some spikes are produced with a delay after the stimulation associated spikes have ended. Fourthly, and most importantly, the model produces a transient small decrease to steady-state frequency following a step-up pulse (see Figure 14.7 third trace). Thus, at the end of the stimulation pulse, the cell does not immediately attain the stable graded frequency. Finally, the model produces a transient increase in frequency following a step-down pulse (see Figure 14.7 third trace).

Figure 14.8 shows phase plane plots of data from Figure 14.7. In (A), we show how calcium concentration interacts with the membrane potential during a stable level followed by a change to a new stable level, corresponding to the time interval 20–34 s. In (B), we show the conductance of the cationic current versus the calcium concentration during the same time interval as in (A). Note that the cationic current increases relatively shortly after the onset of the current injection as the cationic current is calcium sensitive. This does, however, not immediately lead to an increase in the high conductance state conductance as can be seen in (D). In (C), we show the conductance of the cationic current versus the calcium concentration during the subsequent time interval 34–52 when there is a change to a new lower level. Note that the decreased level of calcium quickly affects the conductance of the cationic current as the current is calcium sensitive. This does, however, not immediately lead to a decrease in the high conductance state conductance as can be seen in (D). In (D), we show the conductance of the high-conductance state of the cationic current versus a low-pass filtered calcium concentration. The time interval of the curve is that of (B) and (C). The arrows 1, 3, 5 indicate stable levels before the upward shift, after the upward shift, and after the downward shift. The stars indicate the level of the second change to a lower level around 60 s and later around 82 s. Note how calcium initially increases during the depolarizing current injection

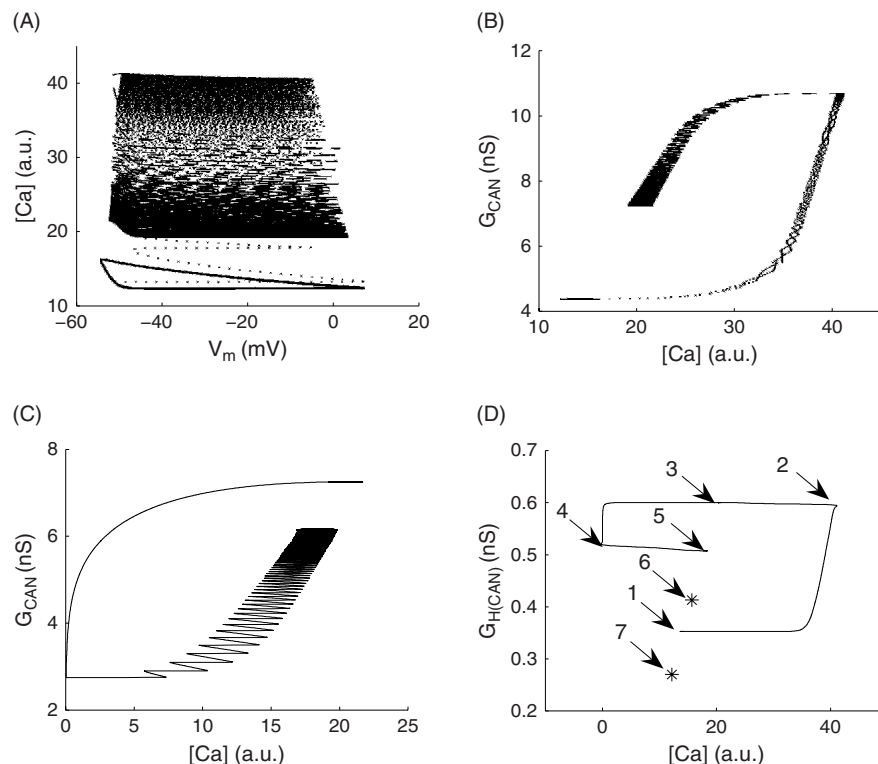


**FIGURE 14.8** Phase plane plot. (A) Calcium concentration versus soma membrane potential for time interval 20–34 s. Solid line indicates stable starting and ending level. Dotted line indicates time during depolarizing current injection. Dashed line indicates transient decay following end of current injection. (B) Effect of depolarizing pulse at 26 seconds. Conductance of cationic current versus calcium concentration. Line marks as in A. (C) Effect of hyperpolarizing pulse at 47 seconds. (D) Downward arrows 1, 3, 5, 6, 7 indicate points of stable levels. Note how they indicate existence of an isocline. Arrows 2 and 4 indicate end of stimulation pulse.

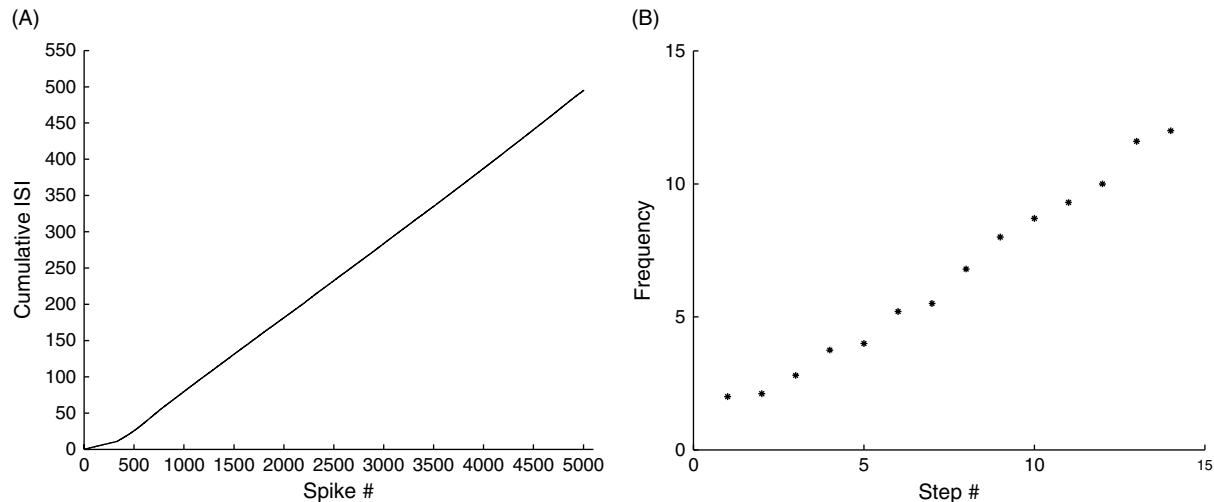


**FIGURE 14.9** (A) Stability of firing at plateau. Cumulative inter-spike interval (ISI) plot for a simulation of 6 minutes plateau activity, similar to Fransén et al. (2006, Figure 1C2). Firing frequency was 8.6 Hz. The initial smaller slope comes from the stimulation period with a frequency of about 30 Hz. (B) Continuum of levels. Simulation data of the frequency during plateaus after 13 different depolarizing current injections, similar to Fransén et al. (2006, Figure 1B2).

without an immediate change in cationic high conductance state due to the neutral region of the P- and D- pathways. The arrows 2 and 4 indicate the end of current injections. Note that the current keeps changing after this point due to the slow kinetics of the channel.

In Figure 14.9A, the stability of the firing is shown for data from a 6 minute simulation comprising more than 3200 spikes, to be compared to the experimental data in Fransén et al. (2006, Figure 1C2). In (B), we show the ability to generate a continuum of graded levels, corresponding to the experimental data shown in Fransén et al. (2006, Figure 1B1).

#### SEMI-STABLE MODEL

The possibility that a graded stable level could be achieved by a balance of currents was evaluated by excluding the key change of  $I_{CAN}$  conductance state from low to high. As predicted, a model based only on a balance between the  $I_{CAN}$  and the K(AHP) currents will not be truly stable. The model will appear stable for finite time and for cases with limited membrane potential interval, i.e. small changes in stable level (Figure 14.10). To get stable graded spiking, this type of balance means that the two curves in Figure 14.4B do not just intersect, but perfectly overlap over an interval of calcium. Outside the perfect overlap there will be an accelerating drift towards either higher or lower frequencies.

The two currents  $I_{CAN}$  and K(AHP) can, in principle, balance perfectly at one Ca-level. At a significant change in Ca, either due to changes in firing frequency, or possibly indirectly due to a change in internal calcium dynamics, the system will be unlikely to have a perfect balance. This will result either in a negative feedback returning the cell to resting potential if K(AHP) dominates, or depolarize the cell to a high saturated firing frequency if  $I_{CAN}$  dominates. As discussed above, a similar situation is presented in Durstewitz (2003) where an ADP-current is balancing against the neurons f-I curve, a situation which is not likely to be stable.

#### MODEL PREDICTIONS

A key assumption in the model is that the calcium concentration must cross above or below the transition points for de/phosphorylation to occur. This provides the robustness to noise, prevents drifting and prevents positive feedback from leading to saturated firing frequency or termination of firing. Experimental support of existence of this kind of mechanism comes from synaptic plasticity. Two different transition points for opposing processes separated by a neutral region have been reported for the induction of long-term potentiation and depression of synaptic transmission at higher and lower levels of calcium respectively (Cho et al., 2001), see also the discussion of ‘no man’s land’ by Lisman (2001).

Experimentally, the induction of a stable plateau is calcium dependent (Egorov et al., 2002). Figure 14.10 shows in the model how blocking of the calcium current prevents induction of a stable level following the first stimulation. A subsequent

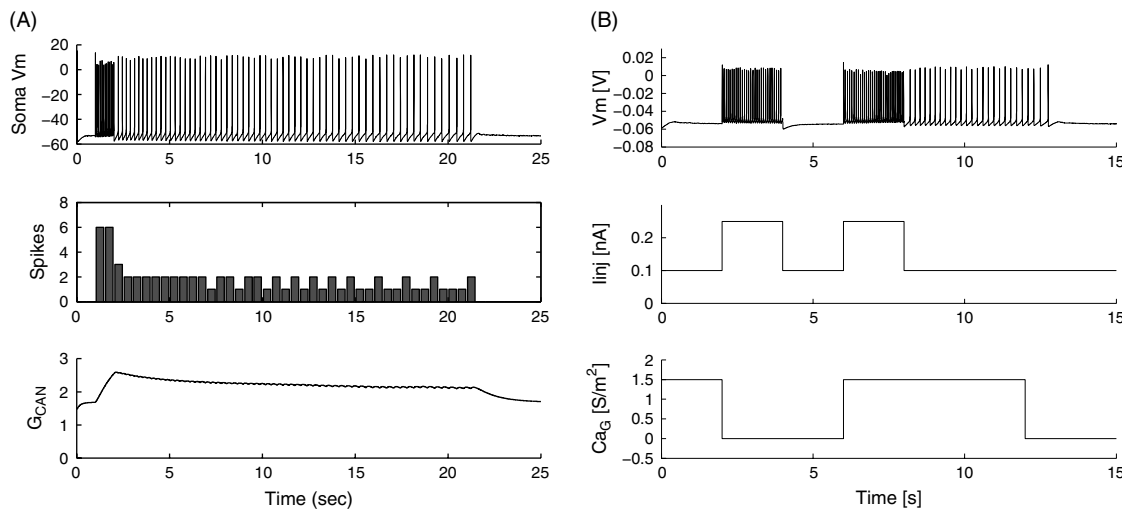


**FIGURE 14.10** (A) Semi-stable activity. By balancing inward and outward currents graded levels can be achieved. These are only semi-stable and for any precision in the balancing of the currents, there will be a maximal time of relative stability. The model shown is stable for less than 5 seconds. Further, the frequency interval within which the level is stable is limited. Note that between 2.5 and 7 s, the frequency diagram appears flat, while the conductance of  $I_{CaN}$  continuously decreases. (B) Calcium dependence. Soma membrane potential, injected current and calcium channel conductance is plotted over time. From left to right, blocking the calcium current prevents induction of a stable level. Unblocking of the calcium current leads to induction of a plateau which, however, is ended when the calcium current is blocked during the plateau.

unblocking of the calcium current leads to a stable level. We further predict that if calcium is blocked during the plateau, the plateau is ended, as indicated in the figure around 12 seconds.

## DISCUSSION

We have shown how a cationic current of the TRP-type may be involved in generating intrinsic stable persistent firing. The mechanism provides a way to integrate input over time scales of several minutes. Due to this persistence of the firing, the mechanism provides a powerful property to the neuron affecting excitability not only of the neuron itself but also of the network it is part of. Whereas the isolated neuron saturates its firing due to the graded activity at some 13 Hz, an extensive network where all cells individually are depolarized to fire at this rate may run into epileptogenic activity.

Cationic currents have been implicated in how seizure-like events are sustained during epileptiform discharges in neocortical slices (Schiller, 2003). In the presence of cholinergic agonists, cation-dependent depolarizing plateau potentials and epileptiform activity have also been observed in entorhinal cortex (Dickson and Alonso, 1997). Factors modulating the conductance of these cation channels may therefore be of relevance for hyperexcitability. TRP channels are modulated by a number of signalling substances and supranormal activity of enhancing factors or subnormal activity of suppressive factors may thus play a role in epileptogenesis. The antiepileptic drug, lamotrigine reduces a cellular depolarization associated with a cationic current (Xiong et al., 2001). Similarly, the anticonvulsant, phenytoin, suppresses depolarizations caused by a cationic current (Kang et al., 2004).

Due to the slow kinetics of cations, they may facilitate the persistence of epileptiform activity and provide depolarizations that bridge short epochs of lower activity that otherwise could have ended the epileptiform activity. Furthermore, hippocampal depolarizing plateaus depend on suppression of inhibition (Fraser et al., 2001). With compromised inhibition, not only the direct loss of hyperpolarizing factors could result, but also increased plateau potentials and thereby increased excitability and spiking.

Moreover, group I metabotropic activation has been implicated in epileptogenesis (Wong et al., 1999; Chuang et al., 2001) and one possible target of this mGluR activation could be cationic TRP channels which are known to be mGluR activated (Gee et al., 2003). Finally, it has been suggested that elevated levels of calcium is one of the key mechanisms in epileptogenesis (Delorenzo et al., 2005). Due to their strong modulation by calcium, increased levels of calcium could result in increased activation of cationic currents and thereby increased excitability.

### GRADED STORAGE BY MULTIPLE BINARY ELEMENTS

In the past, work on storage of information has concentrated on changes of synaptic function. Several of these hypotheses concern the issue of how information can be reliably stored for very long time periods.

A single switch can only store a binary value, on or off. Using a population of switch-like components, each of which can only take either of two states, one can obtain a graded storage by switch-like components. This was used by Lisman and Goldring (1988) for synaptic long-term plasticity. As will be discussed below, it has also been used by Koulakov et al. (2002) in the context of graded activity in networks. Biochemical switches have been discussed in relation to long-term potentiation (LTP), e.g. Lisman and Fallon (1999), for instance a second messenger switch involving MAPK and a kinase switch where the kinase autophosphorylates. As storage is viewed as permanent, they commonly do not contain a reversible mechanism, as is present in our system. Further, these models are not dependent on any maintenance level, as opposed to our situation. The phosphorylated/non-phosphorylated state of a channel as in our model is also a binary state, but in the presence of many channels it will look graded and continuous. A switch-like activation of principal dendrites was suggested by Connors (2002) and Heckman et al. (2003) to account for the cellular stable graded levels discussed in the present work. That model would give the neuron the maximal number of stable levels as it has principal dendrites. We have, however, shown that a cell can have many closely spaced stable levels, indicating a continuum of stable levels (Fransén et al., 2006).

### GRADED INTRINSIC SPIKING ACTIVITY

The main focus in the above mentioned models has thus been on the construction of a stable structure, and less work has been devoted to the opposite, how long-term depression (LTD) would lead to a controlled opposite change or breakdown of stable structures. In our case, this is an intimate part of the system. There is a distinct difference between systems that implement truly irreversible storage and systems that are reversible. An irreversible system could explain either the step-up experiments or the step-down experiments, but not both. Further, in our case, the two opposing mechanisms are not simply in equilibrium, as that would not give the tolerance to noise and distractors seen. The processes must be separately controlled, either by separate mechanisms, or separation of the dynamic range for the levels of the controlling substance. With an (additional) intermediate neutral interval, within which noise and distractors would appear, a stable system could exist, as will be discussed below.

#### Channel hysteresis

Hysteresis is a property of a system which shows up as a dependence on the (previous) history of the system. For neurons, hysteresis is common in the sense that, from resting, a cell will display a threshold for spiking when subjected to a current injection. At one point of current amplitude the cell will start spiking. If the current is held constant, the cell may continue to fire. For increased amplitude the cell will usually increase its firing rate. If the amplitude of the current is lowered, some neurons may continue to fire even below the lowest amplitude that initially was necessary to initiate spiking. Eventually, at one point the firing will cease, thus defining one higher point for transition from resting to spiking and one lower point for transition from spiking to resting. In the interval between these points, the state of the neuron, whether it fires or not, will depend on its previous history. This property gives a form of memory and a form of noise tolerance and has therefore been used in man-made controllers like thermostats as well as in models of memory (Koulakov et al., 2002).

Cationic channels can in themselves show hysteresis regarding the activating parameter (Kaestner et al., 2000; Xu et al., 2002; Männikkö et al., 2005). This property could explain the step-up and step-down experiments and the higher threshold for induction of a stable level and a lower threshold for maintenance. But it does not explain the resistance to distractors seen in our experiments. Channel hysteresis can thus not by itself explain the data. If there additionally were a Ca buffer in the Ca concentration which activates the  $I_{CAN}$  current, slow changes might be filtered out. Such a buffer would have to be regulated to the stable level at hand and thus only react on changes from a given baseline. Large changes would saturate the buffer and lead to changes in  $I_{CAN}$  current, consistent with experiments. The regulation could be based on the buffer capacity staying proportional to the average Ca-level. Changes of buffer capacity would have to be triggered by changes in the average Ca. To stay proportional, the sensors of Ca concentration initiating the change could show desensitization to the present level and thus only respond to changes. As in the model by Durstewitz (2003), the problem is how two curves can have the same shape to follow each other over an extended parameter interval, a problem further discussed in the following paragraph.

### Balancing of conductances

To have a stable firing, outward and inward currents must balance. This can be the case at one specific frequency if the sum of the inward currents intersects the sum of the outward currents for that frequency. Two curves can be made to intersect at one specific point by a combination of translation and rotation. What is required for a balance over and extended interval of firing frequencies, is not only as suggested by Durstewitz, that the ADP-current and the f-I curve are aligned and intersect, but also that the shape (i.e. voltage or calcium sensitivity) of the two curves is matching. If they are not, they will not overlap for an extended range of frequencies. How to construct the shapes of these curves using a learning/modification rule is not addressed in that work. Further, that work suggests that as the two curves get better and better aligned at a specific firing frequency, the fluctuations around the stable point should get larger and larger, something we have not observed experimentally.

As above, we turn to the issue of stability to distractors. Stability to distractors and noise could be obtained if an sAHP current is relatively faster and has a lower [Ca] sensitivity than the  $I_{CAN}$  current, and the  $I_{CAN}$  current has a threshold for activation for [Ca]. After a change in potential, the sAHP will dominate due to its faster kinetics, providing the system with a negative feedback. For induction of a new stable level, the stimulation time must be larger than the sAHP time in order for the slower  $I_{CAN}$  current to dominate. But, the remaining problem is how slow drifts could be tolerated permitting stable activity for 10s of minutes. We do not want to assume processes that have time constants of this order of magnitude. A calcium buffer could take care of smaller amounts of Ca originating from 'drift' sources. However, as the level of stable activity is shifted up or down, the capacity of the buffer would have to change accordingly.

### Diffusion models

For time periods that are moderately long, systems have been constructed that can store a graded level that depends on the amplitude of the input (Okamoto and Ichikawa, 1994). This model does not, however, have a threshold on the input and will thus be sensitive to distractors. In models of LTP which are confined to describing a spine, there may not be much need to discuss gradients and diffusion but, on the other hand, to discuss occupation numbers (Lisman and Goldring, 1988). Our work concerns the dendrite and we will thus assume large numbers of molecules. Due to likely compartmentalizations within the cell and dendrite, there may be diffusion along gradients of Ca and of buffers of Ca. Consistent with this, some models with stable activity build on diffusion of some of the reactants (Okamoto and Ichikawa, 1994).

Using multicompartmental representation of dendritic branches containing voltage-dependent  $\text{Ca}^{2+}$  channels, Loewenstein and Sompolsky (2003) have produced multiple stable graded levels of firing of an isolated neuron. The model builds on Ca-diffusion and on Ca-release from internal stores. As discussed by Wang and Major (2003), the major drawback is how this mechanism could be implemented with known properties of calcium release, buffering and extrusion. Specifically, they point to problems like Ca-inactivation and diffusion of the receptor disturbing the stability of the Ca-fronts, as this model builds on the presence of a stable and continuous calcium concentration over the entire stable period. Thus, albeit this model fulfills the functional requirements of multiple stable graded levels and shows tolerance to noise, its central assumptions of continuous calcium and calcium-related product flux is not supported experimentally. As pointed out, most of these components show the opposite characteristic, inactivation, effectively opposing stability of the suggested type.

### LINE ATTRACTORS

When a system can only stably maintain one value it is said to display point attractor dynamics. When it can maintain any value between two endpoints in an interval, the system is said to display line attractor dynamics. A shiftable point attractor as we have used is not a line attractor. We have separated the mechanisms of changing the stable level (shifting) from stability of the point attractor. Thereby the problems of stability of the line attractor while providing a means of graded change.

A line attractor mechanism in a cell can work as an analog memory of displacements along the neutral region (Malmgren H, personal communication). At the same time, it will not posses any robustness to noise or presence of drift. Noise will generate a random walk along the line which can be arbitrarily far from a starting point (the expectation value). A drift will be integrated and memorized positions will be mixed with drifts of unknown amplitude and duration. A line attractor in its pure form will therefore only work in mathematically ideal systems and not in a living cell.

Our data show how a single neuron in the absence of synaptic input can sustain stable graded firing. Other models of graded activity, however, build on interactions in a network. Recent work in the goldfish oculomotor system (Seung et al., 2000) extends previous work on that system in mammalian systems (Cannon et al., 1983). This work demonstrates line attractor dynamics dependent upon synaptic connectivity between neurons. This synaptic mechanism for attractor

dynamics differs from the intrinsic cellular mechanism described here. This network property demonstrates stability after modification of the synaptic connections and the stability of the system can be perturbed experimentally, causing drifts in the neuronal activity. A key problem with this type of network is that the synaptic conductances have to be tuned quite precisely to support stable network activity. One solution was to include bistable dendrites (Goldman et al., 2002).

The sensitivity to precise synaptic tuning was addressed by Koulakov et al. (2002) and discussed in Brody et al. (2003). In Koulakov et al., the authors suggest two mechanisms, both producing hysteresis, which effectively solves this problem. The general approach using hysteresis is very similar to the one suggested by Lisman (1985) and Lisman and Goldring (1988) for long-term synaptic plasticity. One mechanism relies on the bistability of strongly connected recurrent networks, the other on the bistability of the voltage dependence of the NMDA receptor. Recently, it has been shown in the oculomotor system that the function may involve single cell properties in the form of cation channels (Delgado-Garcia et al., 2004). It is thus possible that the function involves a combination of cellular and network mechanisms.

### FUNCTIONAL ROLE OF CATIONS

As reviewed in the introduction, cationic currents are involved in several processes which may be labeled sensory-motor integration. If cognitive mnemonic processes were to be included in a generalized 'motor' term, this notion of sensory-motor integration may apply also to entorhinal cortex. It then supplies the 'sensory' input to hippocampus and receives back the 'motor' product of hippocampus. More specifically, input to EC layer V cells comes from presubiculum/post-subiculum cortices (van Haeften et al., 2000) which contain head direction cells that display persistent firing encoding directional heading (Taube et al., 1990). Persistent activity by the EC layer V cells could thus be important for complex aspects of trajectory encoding by 'place cells', which are present in EC layer V (Frank et al., 2000). In primates, spatial memory representations may also be provided by 'spatial view' cells which have been recorded both in the hippocampus and parahippocampal region (including the EC) and which display persistent firing coding for the allocentric position in the space being viewed (Georges-Francois et al., 2000). Moreover, EC layer V gives rise to feedback cortical projections and lesions of the EC have been shown to prevent inferotemporal neurons from representing associations between visual stimuli (Higushi and Miyashita, 1996). In humans, pharmacological cholinergic suppression has furthermore been shown to reduce persistent activity in the parahippocampal region (Schön et al., 2005) and persistent activity in this region during a working memory task has been shown to correlate to subsequent long-term memory recall (Schön et al., 2004). Cation channels are not only present in entorhinal cortex neurons, but are found in many cortical and subcortical regions (Moran et al., 2004; von Bohlen und Halbach et al., 2006). They can therefore be assumed to contribute to memory and integrative neural function in general and be involved in neural dysfunction such as epilepsy.

### ACKNOWLEDGMENTS

This work was done in collaboration with Angel Alonso, Alexei Egorov and Babak Tahvildari at McGill University and Michael Hasselmo at Boston University. Angel Alonso passed away during the final stages of the revision of the work, 7/6/2005, and we are indebted to him for his friendship and scientific knowledge and skillfulness.

This article was previously published in *Neuron*, 49, Fransén, Tahvildari, Egorov, Hasselmo, Alonso, Mechanisms of graded persistent cellular activity of entorhinal cortex layer V neurons, 735–746, Copyright Elsevier Inc. (2006).

### REFERENCES

- Alonso, J.R. and Amaral, D.G. (1995). Cholinergic innervation of the primate hippocampal formation. I. Distribution of choline acetyltransferase immunoreactivity in the *Macaca fascicularis* and *Macaca mulatta* monkeys. *J Comp Neurol* 355:135–170.
- Batchelor, A.M. and Garthwaite, J. (1997). Frequency detection and temporally dispersed synaptic signal association through a metabotropic glutamate receptor pathway. *Nature* 385:74–77.
- Brody, C.D. Romo, R. and Kepes, A. (2003). Basic mechanisms for graded persistent activity: discrete attractors, continuous attractors, and dynamic representations. *Curr Opin Neurobiol* 13:204–13211.
- Cannon, S.C., Robinson, D.A. and Shamma, S. (1983). A proposed neural network for the integrator of the oculomotor system. *Biol Cybern* 49:127–136.
- Cho, K., Aggleton, J.P., Brown, M.W. and Bashir, Z.I. (2001). An experimental test of the role of postsynaptic calcium levels in determining synaptic strength using perirhinal cortex of rat. *J Physiol* 532(2):459–466.
- Chuang, S.C., Bianchi, R., Kim, D., Shin, H.S. and Wong, R.K. (2001). Group 1 metabotropic glutamate receptors elicit epileptic form discharges in the hippocampus through PLCbeta signaling. *J Neurosci* Aug 15 (21):6387–6394.

- Connors, B.W. (2002). Single-neuron mnemonics. *Nature* 420:133–134.
- Delgado-Garcia, J.M., Yajeya, J. and Navarro-Lopez Jde D. (2006). A cholinergic mechanism underlies persistent neural activity necessary for eye fixation. *Prog Brain Res* 154:211–224.
- Delorenzo, R.J., Sun, D.A. and Deshpande, L.S. (2005). Cellular mechanisms underlying acquired epilepsy: the calcium hypothesis of the induction and maintenance of epilepsy. *Pharmacol Ther* 105:229–266.
- Dickson, C.T. and Alonso, A. (1997). Muscarinic induction of synchronous population activity in the entorhinal cortex. *J Neurosci* 17:6729–6744.
- Durstewitz, D. (2003). Self-organizing neural integrator predicts interval times through climbing activity. *J Neurosci* 23:5342–5353.
- Egorov, A.V., Hamam, B.N., Fransen, E., Hasselmo, M.E. and Alonso, A.A. (2002). Graded persistent activity in entorhinal cortex neurons. *Nature* 420:173–178.
- Egorov, A.V., Unsicker, K. and von Bohlen und Halbach, O. (2006). Muscarinic control of graded persistent activity in lateral amygdala neurons. *Eur J Neurosci* 24:3183–3194.
- Fisahn, A., Yamada, M., Duttaroy, A. et al. (2002). Muscarinic induction of hippocampal gamma oscillations requires coupling of the M1 receptor to two mixed cation currents. *Neuron* 33:615–624.
- Frank, L.M., Brown, E.N. and Wilson, M. (2000). Trajectory encoding in the hippocampus and entorhinal cortex. *Neuron* 27:169–178.
- Frank, L.M. and Brown, E.N. (2003). Persistent activity and memory in the entorhinal cortex. *Trends Neurosci* 26:400–401.
- Fransén, E. and Lansner, A. (1995). Low spiking rates in a population of mutually exciting pyramidal cells. *Network* 6:271–288.
- Fransén, E., Alonso, A.A. and Hasselmo, M.E. (2002). Simulations of the role of the muscarinic-activated calcium-sensitive nonspecific cation current INCM in entorhinal neuronal activity during delayed matching tasks. *J Neurosci* 22:1081–1097.
- Fransén, E., Tahvildari, B., Egorov, A.V., Hasselmo, M.E. and Alonso, A.A. (2006). Mechanism of graded persistent cellular activity of entorhinal cortex layer V neurons. *Neuron* 49:735–746.
- Fraser, D.D., Doll, D. and MacVicar, B.A. (2001). Serine/threonine protein phosphatases and synaptic inhibition regulate the expression of cholinergic-dependent plateau potentials. *J Neurophysiol* 85:1197–1205.
- Gee, C.E., Benquet, P. and Gerber, U. (2003). Group I metabotropic glutamate receptors activate a calcium-sensitive transient receptor potential-like conductance in rat hippocampus. *J Physiol* 546(3):655–664.
- Georges-Francois, P., Rolls, E.T. and Robertson, R.G. (1999). Spatial view cells in the primate hippocampus: allocentric view not head direction or eye position or place. *Cereb Cortex* 9:197–212.
- Gloveli, T., Egorov, A.V., Schmitz, D., Heinemann, U. and Muller, W. (1999). Carbachol-induced changes in excitability and  $[Ca^{2+}]_i$  signalling in projection cells of medial entorhinal cortex layers II and III. *Eur J Neurosci* 11(10):3626–3636.
- Goldman, M.S., Levine, J.H., Major, G., Aksay, E., Tank, D.W. and Seung, H.S. (2002). Dendritic bistability increases the robustness of persistent neural activity in a model oculomotor neural integrator. *Soc Neurosci Abstr* 32:266.14.
- Heckman, C.J., Lee, R.H. and Brownstone, R.M. (2003). Hyperexcitable dendrites in motoneurons and their neuromodulatory control during motor behaviour. *TINS* 26:688–695.
- Higuchi, S. and Miyashita, Y. (1996). Formation of mnemonic neuronal responses to visual paired associates in inferotemporal cortex is impaired by perirhinal and entorhinal lesions. *Proc Natl Acad Sci USA* 93:739–743.
- Inoue, R., Waniishi, Y., Yamada, K. and Ito, Y. (1994). A possible role of tyrosine kinases in the regulation of muscarinic receptor-activated cation channels in guinea pig ileum. *Biochem Biophys Res Commun* 203:1392–1397.
- Kaestner, L., Christophersen, P., Bernhardt, I. and Bennekou, P. (2000). The non-selective voltage-activated cation channel in the human red blood cell membrane: reconciliation between two conflicting reports and further characterisation. *Bioelectrochemistry* 52:117–125.
- Kang, Y., Okada, T. and Ohmori, H. (1998). A phenytoin-sensitive cationic current participates in generating the afterdepolarization and burst afterdischarge in rat neocortical pyramidal cells. *Eur J Neurosci* 10:1363–1375.
- Klink, R. and Alonso, A. (1997). Ionic mechanisms of muscarinic depolarization in entorhinal cortex layer II neurons. *J Neurophysiol* 77:1829–1843.
- Koulakov, A.A., Raghavachari, S., Kepcs, A. and Lisman, J.E. (2002). Model for a robust neural integrator. *Nat Neurosci* 5:775–782.
- Leung, V.L., Zhao, Y. and Brown, T.H. (2006). Graded persistent firing in neurons of rat perirhinal cortex. *Soc Neurosci Abstr* 32:636.18.
- Lisman, J.E. (1985). A mechanism for memory storage insensitive to molecular turnover: a bistable autophosphorylating kinase. *Proc Natl Acad Sci USA* 82:3055–3050.
- Lisman, J.E. (2001). Three  $Ca^{2+}$  levels affect plasticity differently: the LTP zone, the LTD zone and no man's land. *J Physiol* 532(2):285.
- Lisman, J.E. and Fallon, J.R. (1999). What maintains memories? *Science* 283:339–340.
- Lisman, J.E. and Goldring, M.A. (1988). Feasibility of long-term storage of graded information by the  $Ca^{2+}$ /calmodulin-dependent protein kinase molecules of the postsynaptic density. *Proc Natl Acad Sci USA* 85:5320–5324.
- Loewenstein, Y. and Sompolinsky, H. (2003). Temporal integration by calcium dynamics in a model neuron. *Nat Neurosci* 6:961–967.
- Major, G. and Tank, D. (2004). Persistent neural activity: prevalence and mechanisms. *Curr Opin Neurobiol* 14:675–684.
- Männikkö, R., Pandey, S., Larsson, H.P. and Elinder, F. (2005). Hysteresis in the voltage dependence of HCN channels: conversion between two modes affects pacemaker properties. *J Gen Physiol* 125:305–326.
- McCormick, D.A. and Huguenard, J.R. (1992). A model of the electrophysiological properties of thalamocortical relay neurons. *J Neurophysiol* 68:1384–1400.
- Miller, P., Brody, C.D., Romo, R. and Wang, X.J. (2003). A recurrent network model of somatosensory parametric working memory in the prefrontal cortex. *Cereb Cortex* 13:1208–1218.
- Moran, M.M., Xu, H. and Clapham, D.E. (2004). TRP ion channels in the nervous system. *Curr Opin Neurobiol* 14:362–329.
- Oestreich, J., Dembrow, N.C., George, A.A. and Zakon, H.H. (2006). A 'sample-and-hold' pulse-counting integrator as a mechanism for graded memory underlying sensorimotor adaptation. *Neuron* 49:577–588.
- Okamoto, H. and Ichikawa, K. (1994). Model for an enzymatic reaction-diffusion system realizing storage of graded information. *Phys Rev E Stat Phys Plasmas Fluids Relat Interdiscip Topics* 50:1704–1707.
- Robinson, D.A. (1972). On the nature of visual-oculomotor connections. *Invest Ophthalmol* 11:497–503.

- Romo, R., Brody, C.D., Hernandez, A. and Lemus, L. (1999). Neuronal correlates of parametric working memory in the prefrontal cortex. *Nature* 399:470–473.
- Schiller, Y. (2004). Activation of a calcium-activated cation current during epileptiform discharges and its possible role in sustaining seizure-like events in neocortical slices. *J Neurophysiol* 92:862–872.
- Schön, K., Hasselmo, M.E., Lopresti, M.L., Tricarico, M.D. and Stern, C.E. (2004). Persistence of parahippocampal representation in the absence of stimulus input enhances long-term encoding: a functional magnetic resonance imaging study of subsequent memory after a delayed match-to-sample task. *J Neurosci* 24:11088–11097.
- Schön, K., Atri, A., Hasselmo, M.E., Tricarico, M.D., LoPresti, M.L., Stern, C.E. (2005). Scopolamine reduces persistent activity related to long-term encoding in the parahippocampal gyrus during delayed matching in humans. *J Neurosci* 25:9112–9123.
- Seung, H.S., Lee, D.D., Reis, B.Y. and Tank, D.W. (2000). Stability of the memory of eye position in a recurrent network of conductance-based model neurons. *Neuron* 26:259–271.
- Shalinsky, M.H., Magistretti, J., Ma, L. and Alonso, A.A. (2002). Muscarinic activation of a cation current and associated current noise in entorhinal-cortex layer-II neurons. *J Neurophysiol* 88:1197–1217.
- Taube, J.S. and Bassett, J.P. (2003). Persistent neural activity in head direction cells. *Cereb Cortex* 13:1162–1172.
- Taube, J.S., Muller, R.U. and Ranck, J.B. Jr (1990). Head-direction cells recorded from the postsubiculum in freely moving rats. I. Description and quantitative analysis. *J Neurosci* 10:420–435.
- Teramae, J.-N. and Fukai, T. (2005). A cellular mechanism for graded persistent activity in a model neuron and its implications in working memory. *J Comp Neurosci* 18:105–121.
- Traub, R.D., Wong, R.K.S., Miles, R. and Michelson, H. (1991). A model of a CA3 pyramidal neuron incorporating voltage-clamp data on intrinsic conductances. *J Neurophysiol* 66:635–650.
- van Haeften, T., Wouterlood, F.G. and Witter, M.P. (2000). Presubicular input to the dendrites of layer-V entorhinal neurons in the rat. *Ann NY Acad Sci* 911:471–473.
- Viana Di Prisco, G., Pearlstein, E., Le Ray, D., Robitaille, R. and Dubuc, R. (2000). A cellular mechanism for the transformation of a sensory input into a motor command. *J Neurosci* 20:8169–8176.
- von Bohlen and Halbach, O., Hinz, U., Unsicker, K. and Egorov, A.V. (2005). Distribution of TRPC1 and TRPC5 in medial temporal lobe structures of mice. *Cell Tissue Res* 322:201–206.
- Walters, R.J., Kramer, R.H. and Nawy, S. (1998). Regulation of cGMP-dependent current in bipolar cells by calcium/calmodulin-dependent kinase. *Vis Neurosci* 15:257–261.
- Wang, S.S. and Major, G. (2003). Integrating over time with dendritic wavefronts. *Nat Neurosci* 6:906–908.
- Wong, R.K., Bianchi, R., Taylor, G.W. and Merlin, L.R. (1999). Role of metabotropic glutamate receptors in epilepsy. *Adv Neurol* 79:685–698.
- Xiong, Z.G., Chu, X.P. and MacDonald, J.F. (2001). Effect of lamotrigine on the  $\text{Ca}^{(2+)}$ -sensing cation current in cultured hippocampal neurons. *J Neurophysiol* 86:2520–2526.
- Xu, H., Ramsey, I.S., Kotecha, S.A. et al. (2002). TRPV3 is a calcium-permeable temperature-sensitive cation channel. *Nature* 418:181–186.
- Yamada, W., Koch, C. and Adams, P. (1989). Multiple channels and calcium dynamics. In: *Methods in neuronal modeling: From synapses to networks*. (C. Koch and I. Segev, eds) pp. 97–134. MIT Press, Cambridge.

# 15

## SMALL NETWORKS, LARGE NETWORKS, EXPERIMENT AND THEORY – CAN WE BRING THEM TOGETHER WITH OSCILLATIONS, HETEROGENEITY AND INHIBITION?

FRANCES K. SKINNER AND ERNEST HO

### ABSTRACT

We propose a ‘design’ and ‘discover’ approach to obtain cellular-based mechanisms in biological networks. Three ideas toward developing objective methods in this approach are presented in the context of synchronous output in inhibitory networks. In the first idea, we suggest using maximal heterogeneities for which synchronous output occurs in two-cell networks to compare single compartment models, thus obtaining optimal parameter sets. In the second idea, we suggest using results from analyses of heterogeneous two-cell networks to constrain larger network dynamics since quantitative linkages occur between two-cell and N-cell network dynamics. Finally, in our third idea, we propose that it is possible to develop quantitative relationships between synaptic parameters estimated from model networks and from experimental data since parameter changes are correctly captured in spike-free model networks and pseudo-biological data. Although many more steps need to be taken, we believe that the presented ideas represent a framework on which to test and build.

Any understanding of epilepsy will need to encompass an understanding of the dynamics of brain networks. However, the highly non-linear nature of brain dynamics makes understanding difficult and even more so if a cellular-based understanding is sought. From an epilepsy perspective, a cellular-based understanding is desirable to allow for the development and design of new drugs and therapeutic targets as well as a better understanding of the workings of existing drugs.

There are many reasons that achieving an understanding will be difficult. One major reason is that brain dynamics need to be understood in some reasonably well-defined behavioral context and it is not obvious how best to relate such contexts to network state(s) and whether network states can be well-defined. Therefore, while it is clear that non-linearity prevents experimental approaches alone from being enough to provide us with an understanding, it is not clear how computational and modeling efforts will fill the gap. Models incorporating various levels of detail are used for a variety of reasons (such as the availability of experimental data, computational ease and analytical possibilities). Simply consider the different levels of models possible and being used to represent a single neuron (e.g. see Herz et al., 2006).

A reasonable place to focus in trying to understand brain dynamics is rhythmic output since it is well recognized that different rhythmic frequencies are associated with different behavioral states. Moreover, there is much evidence to support the critical involvement of oscillations in information processing (Engel et al., 2001). In general, there are networks of interneurons, or inhibitory GABAergic cells, in the hippocampus and neocortex that have been shown to be responsible for the generation and control of several population rhythms by molding the temporal output of excitatory neurons (Buzsáki and Chrobak, 1995). Specifically, spontaneous and robust population oscillations are expressed in intact and thick slice

*in vitro* hippocampal preparations (Wu et al., 2002, 2005a, 2005b) and these oscillations are critically dependent on inhibitory coherence and interactions. Furthermore, similar frequency and pharmacological profiles suggest that these *in vitro* rhythms might form the basis of *in vivo* rhythms in the behaving animal. Such experimental studies provide the motivation for us to work toward the development of direct links between cellular-based models and experimental data.

In this chapter, we describe our developing approach to ‘design’ model networks and ‘discover’ biologically-relevant mechanisms incorporated within them. This approach derives from the simple fact that it is impossible to know the importance or critical aspect of various biological (cellular, intrinsic and synaptic) details in the absence of some defined context. It is always a balance. Therefore, we need objective methods to compare different models and to compare model and experimental data in clearly defined situations.

By ‘design’ and ‘discover’, we mean the following. We invoke some underlying mechanism(s) of how the network output could be produced (design stage). We would first build smaller networks to allow a cellular perspective to be included and we would use ideas and insight from experimental work and modeling studies. Importantly, we would take advantage of theory and mathematical techniques in analyzing and understanding the dynamics of these smaller networks. We would then build larger networks using the understanding achieved in the smaller networks and constrain network parameter characteristics by developing direct links with the experimental data. If the resulting network output compares favorably with the experimental network output in various scenarios, then the underlying mechanism(s) giving rise to the output could be considered biologically plausible for the network output (discover stage). In other words, it would be a designed discovery of the workings of biological networks in particular contexts.

Along these lines, we present three ideas that we have considered toward having objective methods in our developing approach. They all rely on heterogeneity and have been developed using inhibitory network models. These ideas are developed in the context of spike synchrony being important for the particular network output. We first describe an idea of how two-cell network models could be compared in terms of producing synchronous output. Next, we show that two-cell network model parameters have meaning as far as predicting patterned output in larger N-cell networks. Finally, we describe how model network characteristics might be constrained by simulating virtual networks to represent experimental recordings and comparing estimated synaptic conductances.

#### IDEA 1: USING HETEROGENEITY TO COMPARE SINGLE COMPARTMENT NEURONAL MODELS

Any neuronal model is never complete in its intrinsic biological details – there are details about the neuron’s morphology, its particular array of membrane ion channels, as well as its subcellular composition and so on. It is clear that intrinsic details as expressed in particular neuronal models affect the output of a network in which it is embedded. Furthermore, these details often affect the output in unexpected and non-intuitive ways because of the inherent non-linearity in biological systems (e.g. see Kepler et al., 1990, Skinner et al., 1999). In essence, the interaction of intrinsic and synaptic details needs to be considered. However, trying to include too many details in a neuronal network model turns the model into an experiment itself, albeit an easily manipulated one. From a purely experimental point of view, one could use pharmacological means to establish the importance of various biological details in producing rhythmic population output (e.g. contribution of particular cell types, ion channels and synaptic receptors). But without knowing the mechanism(s) that generate the network output in the first place, one cannot uncover critical interactions between various intrinsic and synaptic details and so ultimately predict and control network output.

We propose using heterogeneity to determine an optimal set of model parameters for synchronous rhythms to emerge in two-cell networks. In our previous work, we considered inhibitory networks and used single compartment representations for the individual neurons (Skinner et al., 2005a, 2005b), but our idea would be equally applicable to excitatory networks or inhibitory/excitatory network combinations. Although there are various ways in which to incorporate heterogeneity in network models, arguably, the most reasonable way (in terms of biological interpretation) is by varying the injected current level to each cell in its single compartment model representation. The straightforward interpretation of this would be that there is variability in the afferent drive to each cell, which certainly is the case biologically. Alternatively, there can be variability in intrinsic ion channel properties or in synaptic strengths and time constants, but assigning a biological interpretation would be less straightforward. For example, variability in ion channels could be due to different membrane distributions and conditions affecting the opening and closing kinetics of the channels.

Using a single compartment neuronal model developed by Wang and Buzsáki (1996) to represent a hippocampal interneuron, we examined two-cell inhibitory network models in which heterogeneity was incorporated in the injected

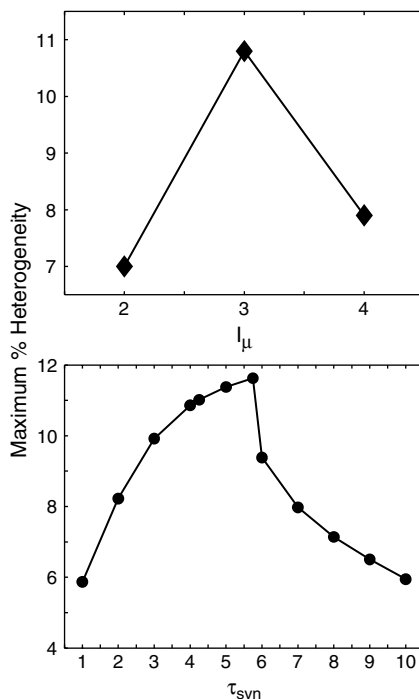


**FIGURE 15.1** Maximal heterogeneities and optimal parameter sets. Plots show the non-monotonic dependence of the maximal percent (%) heterogeneity for variation in two different parameters, the mean input current (top) and the synaptic decay time constant,  $\tau_{\text{syn}}$  (bottom). Units for input current and time constant are  $\mu\text{A}/\text{cm}^2$  and ms respectively. For the top plot, synaptic conductance is  $0.25 \text{ mS}/\text{cm}^2$  and  $\tau_{\text{syn}}$  is 4 ms. For the bottom plot, mean input current is  $3 \mu\text{A}/\text{cm}^2$  and synaptic conductance is  $0.25 \text{ mS}/\text{cm}^2$ . See Appendix 15.1 for equations and definition of % heterogeneity.

current levels. We found that optimal parameter sets could be obtained (Skinner et al., 2005b). By optimal parameter sets, we mean sets of parameters that maximize the amount of heterogeneity that the two-cell network can have and still express (near) synchronous output. In other words, how different do the firing frequencies of the two cells need to be before they can no longer exhibit synchronous firing. This is sensible to consider from a biological viewpoint since the mathematical models are neuronal caricatures and, if one is to argue for the model output having biological meaning and interpretation in terms of the patterns it expresses, one naturally would like the patterns to be as robust as possible. The model equations and heterogeneity definition are given in Appendix 15.1.

Two particular examples are shown in Figure 15.1. In Figure 15.1(top), we see that the maximal percent heterogeneity occurs at a mean injected current around  $3 \mu\text{A}/\text{cm}^2$ , as determined from several simulations. As such, we can consider this mean injected current value as an optimal parameter value for synchronous output in inhibitory networks when the synaptic parameters are as given (see Figure 15.1 caption). More exact parameter values can be obtained using bifurcation analysis and numerical continuations (Skinner et al., 2005a, 2005b). These mathematical techniques allow one to examine the limits of particular solutions (such as near synchronous behaviors) and thus obtain precise parameter values. See Appendix 15.1 for a brief description of these techniques. In Figure 15.1(bottom), we show a precise optimal time constant parameter value of 5.75 ms, as obtained from bifurcation analyses and numerical continuations. Considering synaptic time constant, conductance and mean injected current parameter variations simultaneously, we found that an optimal set of parameters to be mean injected current of  $3 \mu\text{A}/\text{cm}^2$ , synaptic conductance of  $0.25 \text{ mS}/\text{cm}^2$  and synaptic time constant of 5.75 ms. With these values, the maximal heterogeneity is about 12% and the result is about a 90 Hz network frequency (near-synchronous firing) in which the phase lag between the firing of the two cells is about 10% (Skinner et al., 2005b).

In summary, our idea is to use heterogeneity to compare various neuronal models and obtain optimal parameter sets. This provides a way to evaluate quantitatively the importance of various intrinsic cellular details in producing synchronous output. This is useful from two considerations. First, from an experimental point of view, one can evaluate how much difference is brought about by, say, using two rather than one delayed type potassium rectifier currents (Lien et al., 2002) in hippocampal neuron models, or whether adding a synaptic delay, as done in the network models of Bartos et al. (2001), significantly changes the optimal parameter values. In other words, we can evaluate detailed differences in

biophysical-based models. Second, from a computational viewpoint, if one finds similar optimal parameter sets for various neuronal models representing a particular neuron, a minimal (reduced) mathematical model of the particular neuron which produces similar dynamics could be developed and used in larger network models.

Since the optimal parameter sets give rise to particular network dynamics, it might be possible to use this idea to compare different brain regions. This might be particularly helpful when considering values for the optimal injected current levels. For example, if synaptic time constant and conductance values are measured in different regions where synchronous inhibitory network output is considered to be important, optimal mean input currents for these different regions could be obtained for the given measured synaptic parameters. These optimal values used in the network models result in particular network frequencies. This is already a possibility to consider since Bartos et al. (2002) found differences in synaptic time constants and peak synaptic conductances in DG (dentate gyrus), CA3 and CA1 regions of hippocampus. Although it would certainly be a leap to consider that such resulting frequencies represent some preferred frequency for different brain regions, it at least allows us to move beyond just using measured experimental values in various models with various levels of detail, to evaluating and quantifying the importance of such measured differences. We need to do this in some fashion to avoid us all being buried in our individual and immense oceans of experimental and model detail.

Finally, we note that the injected current parameter is taken to represent the afferent input and is not easily assessed experimentally. This is because it represents summation of synaptic and background activities along dendritic and axonal trees of the cell and whose effect depends on the integrative properties of the particular cell and the network in which it resides. Moreover, one would expect it to vary dynamically in different network states. However, in using a single compartment model representation, we collapse such aspects into the injected current parameter. While this greatly simplifies several biological details, it does not ignore them entirely. However, in moving to a more detailed compartmental model representation for the single cell, many more model parameters and choices are required and model comparisons become more complex. Thus, single compartment model representations could provide essential guides in network mechanism considerations.

#### IDEA 2: USING TWO-CELL NETWORK MODEL PARAMETERS TO CONSTRAIN AND PREDICT N-CELL NETWORK MODEL OUTPUTS

In our first idea, we proposed using heterogeneity to obtain optimal parameter sets and so compare neuronal models with different biophysical details. We used bifurcation analyses and numerical continuations to obtain precise parameter values for which near-synchronous patterns occurred. These techniques also allow one to ascertain parameter ranges in which there is overlap of different dynamical outputs – for example, multistability of near-synchronous and antiphase firing states. (See further description in Appendix 15.1.) This would be virtually impossible to do using simulations alone. On the other hand, using these mathematical techniques to analyze larger networks is virtually impossible – even with two cells it can be challenging to analyze the network model in certain cases.

Therefore, in our second idea, we propose to use parameter values obtained in two-cell networks to predict some of the network dynamics that would occur in larger networks. Assuming that one has a single compartment neuronal model with an appropriate level of biophysical detail, and that one has used it in a two-cell network model to determine parameter values for which different dynamical patterns (say, near-synchronous, antiphase and so on) are present, one could set up larger N-cell networks to determine whether similar dynamical patterns occur. In Skinner et al. (2005a) we have shown that this is possible in a surprisingly precise fashion. We generated 20-, 50- and 100-cell inhibitory networks with all-to-all coupling architecture. The heterogeneity of these larger networks is described by randomly choosing the level of current injected into each cell up to a specified maximum amount. Maximal synaptic conductances were normalized for the size of the network (i.e. simply dividing the conductance value used in the two cell network by N) so that a cell in an N-cell network would have the same net maximal conductance as that of the two-cell network. Equation details are provided in Appendix 15.1. We found that when we constrained the maximum heterogeneity used in the N-cell networks to be within the range for which near-synchronous output was obtained in the two-cell network, coherent output was obtained in the N-cell network. We also found that optimal parameter values as described in our first idea were preserved. However, one needs to be careful in considering optimal parameter sets in the larger networks as one needs to use a measure of coherence of some sort (rather than simply considering near-synchronous patterns) and values for coherence measures are biased due to bin size and frequency. In other words, the network patterning needs to be taken into consideration in developing appropriate coherence measures.

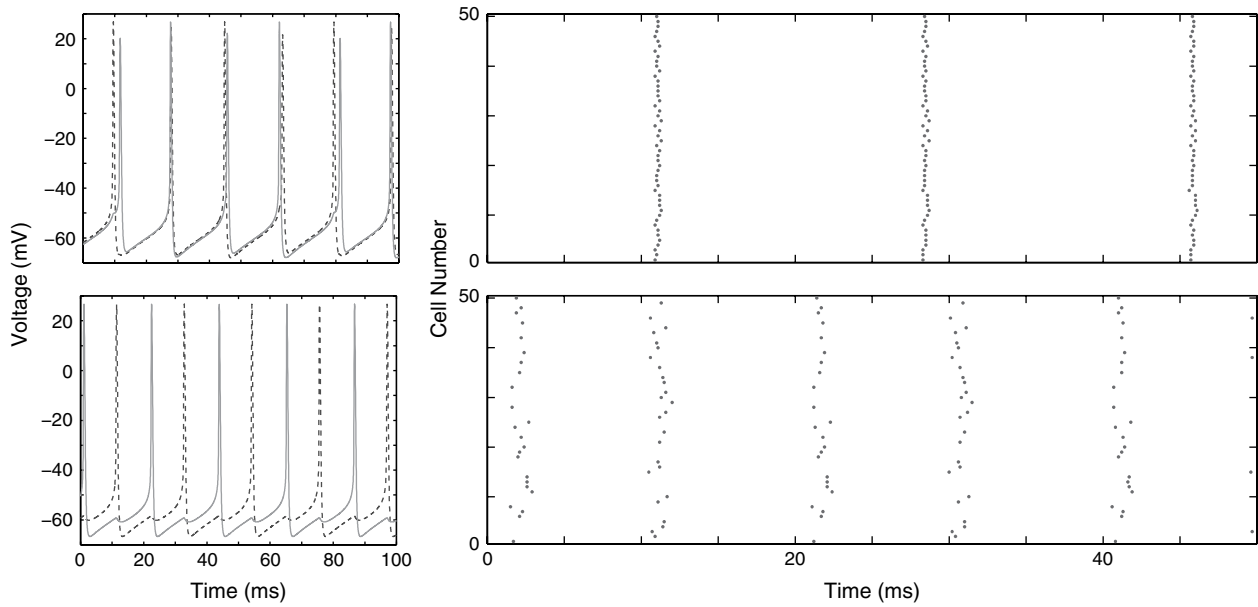


**FIGURE 15.2** Two- to N-cell network output correspondence. The two plots on the left side show voltage recordings from two cells coupled in a mutual inhibitory fashion. Bistable (near-synchronous and near-antiphase firing) output is present with the output recordings from the two cells shown by solid and dashed lines. This behavior is bistable in that it is produced using the same set of parameters, only the initial conditions are different. Input currents to the two cells are 1.0 and  $1.01\mu\text{A}/\text{cm}^2$  respectively (1.2% heterogeneity), synaptic conductance is  $0.25\text{ mS}/\text{cm}^2$  and  $\tau_{\text{syn}}$  is 1 ms. Equations and other parameter values are given in Appendix 15.1. The two plots on the right hand side are raster plots from two 50-cell network simulations. For the upper case, the raster plot shows correspondence with two-cell network outputs exhibiting near-synchronous behavior (e.g. see top left plot). For the lower case, the correspondence is with two-cell network outputs exhibiting near-antiphase firing (e.g. see bottom left plot). The parameters used in the 50-cell network simulations are the same as the two-cell model, but with the maximal synaptic conductance normalized for the network size, and with heterogeneity being randomly chosen up to a 4% maximum heterogeneity (see text).

Most interestingly, we found that parameter values of the two-cell networks in which multistability was found gave rise to distinct network patterns in the larger networks. We specifically chose synaptic conductance and time constant values that we knew produced multistability in two-cell networks and performed several N-cell simulations using different initial conditions. Although each N-cell simulation did not have an identical amount of overall heterogeneity because the amount injected into each cell was random, each N-cell simulation did have a maximum allowable amount of heterogeneity. In Figure 15.2, we show an example of how the two-cell output could predict the possible N-cell patterning. On the left, we show output from a two-cell network exhibiting bistable behavior – the top left shows near-synchronous firing and the bottom left shows near-antiphase firing. On the right side of Figure 15.2, we show raster plots from two 50-cell simulations in which the maximum amount of heterogeneity was fixed and the parameter values were the same as for the two-cell networks. For this chosen maximal amount of heterogeneity, we know that it is possible to obtain either near-synchronous or near-antiphase patterning in the two-cell networks depending on the initial conditions used. The 50-cell simulations show the emergence of corresponding patterns – those due to near-synchrony (top, right) or those due to near-antiphase firing (bottom, right), when different initial conditions are used.

In summary, our work has shown that quantitative linkages occur between two-cell and N-cell network dynamics. In particular, multistable patterns in the two-cell system are manifest as different and distinct coherent patterns in the larger networks for the same parameter sets (example shown in Figure 15.2). Therefore, mathematical analyses performed on two-cell networks can be viewed as quantitative predictors of N-cell network dynamics. We do not expect that all possible N-cell network dynamics would be predicted from two-cell analyses. However, since the two-cell analyses allow us to evaluate the contribution of biophysical detail (see Idea 1 above), predictions of the dependence of at least some large network dynamics on biophysical detail might be possible. Furthermore, by determining basins of attraction for different two-cell network dynamic states, it might be possible to estimate the probability of obtaining the different patterns in the larger networks. We are encouraged by this work as it suggests that insight that one obtains on critical biophysical parameters and potential mechanisms from two-cell analyses and experimental observations can be translated to larger

networks – performing ‘designed’ simulations with thousands of cells so as to approach biological numbers will allow us potentially to understand and predict the importance of various biophysical/cellular details in large networks.

### IDEA 3: ESTIMATING SYNAPTIC PARAMETERS FROM ACTUAL AND VIRTUAL MODEL NETWORKS

In this third idea, we consider how we might link network model characteristics to experimental data. This is no small task as network models are generated at many different levels of detail and acquiring experimental data for several details simultaneously may not be possible. A critical aspect in network considerations is the balance between excitation and inhibition (e.g. Shu et al., 2003) and, as usual, the context of the situation should be clear to attach any potential meaning and interpretation to parameter values. For example, one can estimate synaptic conductances from voltage-clamp data during UP states (persistent network activities) in ferrets (Haider et al., 2006). Means and standard deviations are obtained by performing multiple sets of voltage clamp measurements.

Another method to estimate synaptic conductances which uses current clamp data has been developed. This method is based on fitting analytic expressions of sub-threshold membrane potential ( $V_m$ ) distributions ( $D$ ) of conductance-based models to distributions obtained from experimental intracellular recordings (Rudolph et al., 2004). These distributions are necessarily affected by the network in which the cell (from which the intracellular recording is obtained) is embedded. Minimally, one requires current clamp recordings at two different injected current levels to obtain both mean and variance estimates of synaptic conductances. This is useful not only because it uses current clamp data, which are technically easier to acquire, but also because an estimate of the variance does not require multiple measurements. However, from a practical point of view, one would want to have current clamp data from several injected current levels to allow error estimates for means and variances to be obtained. Also, since sub-threshold fluctuations are used, spikes have to be removed from the intracellular recordings. Furthermore, from theoretical perspectives, improved analytic representations for sub-threshold fluctuations might need to be considered (Richardson and Gerstner, 2006). In summary, this  $V_mD$  method provides a way to characterize synaptic background activities during different network states. As such, it could provide a way to constrain model network characteristics.

We propose that we can develop quantitative relationships between synaptic parameters estimated from model networks and experimental data. For the experimental data, synaptic estimates obtained via the  $V_mD$  method must be made in the absence of spikes. For the model networks, we make the following assumption. Given a network patterning associated with a particular context, this patterning is not fixed and the variable patterning can be captured by averaging across many deterministic network simulations in which the initial conditions (i.e. the history of input characteristics which affects initial network states) and heterogeneity is varied. The representation of heterogeneity in the model would depend on the specifics associated with the model network detail and design. Ideally, one should associate it with some experimental measurement. Since ‘spike-free’ data are used experimentally, we need to develop relationships under similar conditions in the model networks.

Using 50-cell heterogeneous, inhibitory networks as described in the second idea above, we performed several simulations with different initial conditions and random heterogeneity up to a fixed maximal amount. For each simulation, one can extract the total synaptic conductance value onto a given cell in the network. This value depends on what’s happening in the rest of the network (i.e. its state or context). From several simulations, one can obtain a distribution and obtain a mean and variance for the synaptic conductance. In a model network, one can simply extract the synaptic conductance without worrying about removing the spikes. Any change in model parameters would obviously result in different extracted values. What is not obvious is whether appropriate synaptic parameters would be extracted if ‘spike-free’ model data are used to develop the distributions and obtain means and variances of the synaptic conductance. In other words, would changes in synaptic model parameters give rise to appropriately changed values of synaptic conductance means and variances?

In Skinner (2007), we found that it is possible to obtain synaptic distributions that can be distinguished for different model network characteristics (synaptic conductance and time constant) even when spikes are removed. This is illustrated in Figure 15.3. In the top part of the figure, we show the total synaptic current onto a given cell, as averaged from two hundred 50-cell network simulations. The left and right cases refer to different parameter sets only in terms of the maximal inhibitory synaptic conductance values – on the left it is smaller than on the right (see details in Appendix 15.1 and figure caption). Two observations can be made. First, the synaptic current onto a given cell is smaller, as might be expected, when a smaller maximal conductance is used in the network simulations. Second, on average, for these parameter sets, the

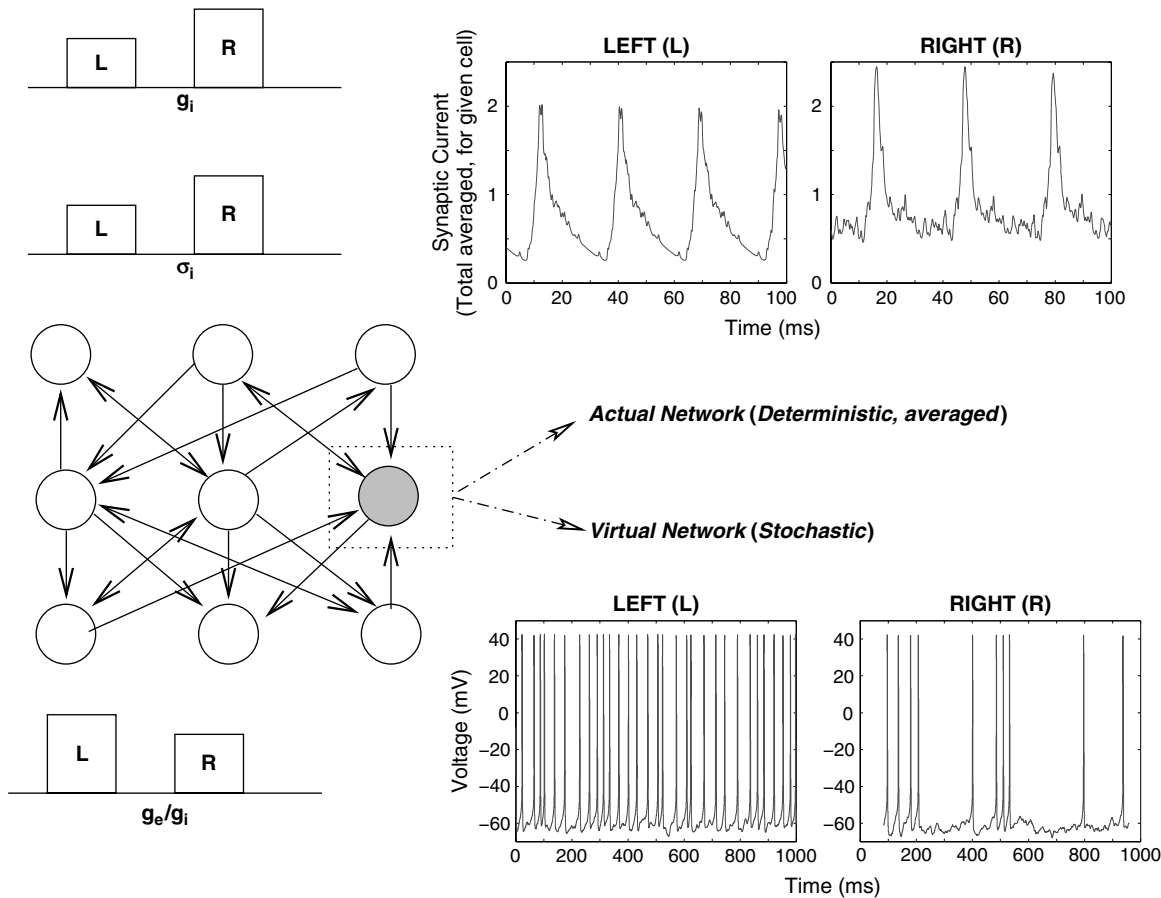


**FIGURE 15.3** Synaptic parameter estimations from model networks. The top part of the figure corresponds to simulations from 50-cell inhibitory networks. The plots show the total synaptic current onto a given cell, as averaged over 200 (deterministic) simulations. The irregular-looking output is due to the heterogeneity of the network, different initial conditions and multistability occurring in the 200 simulations. For the left plot, a smaller inhibitory conductance ( $0.0035 \text{ mS/cm}^2$ ) relative to the right plot ( $0.005 \text{ mS/cm}^2$ ) is used, all other parameters being the same. This model parameter difference is present when extracted from synaptic distributions obtained from the many deterministic simulations after spike removal, (see details in text). The bottom part of the figure corresponds to simulations of a single neuron model with stochastic synapses (i.e. a pseudo-biological cell in a virtual network). The plots show output (with zero injected DC current) for two different virtual network situations. The left plot has a smaller mean inhibitory conductance ( $0.1 \text{ mS/cm}^2$ ) relative to the right plot ( $0.125 \text{ mS/cm}^2$ ) and the variances and mean excitatory conductance are the same. Equations and other parameters are given in Appendix 15.1. Estimations of mean excitatory to inhibitory conductances using the VmD method, as illustrated on the left, change appropriately with those of the actual model parameters. Note that the left side of the figure shows schematics and are not meant to represent actual values. However, actual representative model output is shown on the right side of the figure.

network produces population rhythms (as reflected in the synaptic currents) and they have slightly faster frequencies for the smaller maximal inhibitory conductance shown on the left plot on the top.

For each of the 200 network simulations, spikes are removed from a given cell's individual recording using a spike removal protocol that detects the spike peak and then ignores synaptic input to the given cell 3.0 ms before and 8.5 ms after the peak. Synaptic input for the rest of the time (i.e. 'spike-free' time with respect to the given cell) is summated for all the other cells contributing to synaptic input to the given cell. From log-logistic fits performed on the resulting distributions, means (variances) of  $0.036 (4.07 \times 10^{-6})$  and  $0.028 (1.21 \times 10^{-6})$  are obtained for the top right and left examples respectively. As schematically illustrated on the top left, the extracted inhibitory conductance is smaller for the left example as it should be. Details associated with spike removal protocols can be adjusted and require consideration given spike details (intrinsic properties) and network states. We note that absolute synaptic conductance values should not be focused on as they are affected by the particular spike removal protocol used. For example, see Skinner (2007) where a spike cutoff at different voltage values is considered. However, regardless of the specifics associated with spike removal protocols, one consistently obtains extracted synaptic conductance values that are in accordance with model network

parameter changes. We did not explicitly model excitatory conductances in these simulations. However, if one assumes that the excitatory conductance can be represented by the heterogeneous (excitatory) injected current levels, then the ratio of excitatory to inhibitory conductance also changes appropriately since the maximal heterogeneity was not different in the left and right sets of network simulation examples shown in Figure 15.3.

As a precursor to dealing with experimental data directly, we used a neuron model with stochastic synapses to represent a biological neuron in a virtual network as might be recorded experimentally. Using these ‘noisy’ models also allows us to develop an appreciation for the limitations associated with the VmD method. Equations used for this model are given in Appendix 15.1. The bottom of Figure 15.3 shows voltage recordings from the stochastic neuron model at a given injected current level ( $0 \mu\text{A}/\text{cm}^2$ ) for two different inhibitory conductance values – all other model parameters are the same. This and another current level ( $0.25 \mu\text{A}/\text{cm}^2$ ) are used to obtain estimates via the VmD method. As schematized on the left, the balance between excitatory and inhibitory conductances as estimated using the VmD method are appropriate given the actual values used in the virtual network model. Specifically, the estimated ratios are 0.23 and 0.21 for the bottom left and right respectively, and the values of the ratios used in the stochastic model are 0.20 (left) and 0.16 (right). We note that while the estimated ratios obtained are found to be appropriate for various injected current levels used, the absolute values of the separate inhibitory and excitatory conductance estimates obtained are not always appropriate. Further investigations are ongoing.

Overall, we have shown that synaptic estimates obtained from actual and virtual networks do change appropriately in the face of spike removal when model synaptic parameter values are changed. The ability for our synaptic estimates to distinguish between model parameter changes means that we can associate synaptic parameter values (i.e. network characteristics) extracted from model networks with experimental data. In this way, we can develop quantitative relationships as proposed and thus constrain our model network characteristics, ensuring that they relate to experimental estimates. It is important to note that the extracted synaptic parameter values represent averages for the particular network state or context from which it is taken. With enough data, however, one could compare averages in different network states. However, determining the mechanism(s) underlying the network dynamics is a separate and additional consideration, and this is where the model networks with their invoked cellular-based underlying mechanism(s) would contribute. At least with such matching of conductance ratios as proposed in this third idea, we have some linkage of model networks (which encompass their necessarily simplified neuronal representation for the single cell) with the data. Such developed and constrained network models have a higher probability of capturing an understanding of the dynamics underlying different network states from a cellular-based perspective in biological systems.

Thus, once we have our larger network models with some cellular-based understanding of network dynamics based on its linkage to the two-cell situation, we can manipulate network characteristics to ensure an association with the experimental data as described above – this gives a direct link to the data by ensuring that synaptic balances are constrained appropriately.

#### DISCUSSION, SUMMARY AND CONCLUSIONS

The complexity of brain networks makes their output challenging to interpret and the underlying mechanisms giving rise to a variety of dynamics difficult to understand. While we undoubtedly need a multipronged approach to tackle the challenge of understanding epilepsy (e.g. see Suffczynski et al., 2005; Traub et al., 2005; Wendling et al., 2005), we also need to make links between various network models such that comparisons and constraints at different levels can be made.

In our developing approach described in this chapter, we have presented three ideas toward a consideration of making links. These ideas have been presented in the context of synchronous output in inhibitory networks, now known to be an essential aspect in many population rhythms. The seminal work by Wang and Rinzel (1992) used a two-cell inhibitory network to show that synchrony was possible in purely inhibitory networks, provided that appropriate balances between intrinsic and synaptic properties were present. This mechanism has been invoked and shown to explain the output obtained from large networks (Traub et al., 1996; Wang and Buzsáki, 1996). In our first idea, we suggested using heterogeneity in injected current levels to individual cells in a two-cell network to allow comparisons between models with varying amounts of biophysical detail. We note that while theoretical mechanisms determined using two-cell networks can provide a basis for understanding the dynamics in larger networks, this cannot be assumed at the outset. Thus, in our second idea, we showed that it is possible to predict larger network dynamics using parameter constraints determined using two-cell networks. Using such parameter constraints in much larger networks so as to investigate clustering and other dynamics investigated theoretically (e.g. see Golomb et al., 2001) would provide further insight. Finally, in our third idea, we propose

developing relationships between synaptic parameters estimated from model networks and from experimental data. We have shown that this proposal is not unreasonable given that we can obtain appropriate synaptic ratio estimates under conditions of spike removal, as would be required in estimating synaptic conductances from current clamp experimental data via the VmD method. We have performed preliminary applications of the VmD method to experimental data involving population oscillations (Wu et al., 2005a, 2005b) and obtained synaptic estimates that exhibit significant differences in different network states (Ho et al., 2006).

Therefore, in our overall approach, we envisage going back and forth between doing two-cell mathematical analyses, performing large network simulations, developing appropriate representations for individual neuronal models and estimating synaptic parameters from experimental data. Although there are many more steps to be taken, we think that our overall approach represents a framework of ideas on which to test and build. We think this because robust population oscillations dependent on inhibitory coherence are present in hippocampal preparations (Wu et al., 2002) and unbiased characterizations of these rhythms have been developed (Gillis et al., 2005). Furthermore, because hippocampal networks exhibit epileptic seizures under various conditions, we have an opportunity – an opportunity to make links as described by our above ideas and possibly uncover critical balances and workings of brain networks that give rise to epileptic seizures.

## APPENDIX 15.1

### NETWORK MODELS AND DEFINITION OF HETEROGENEITY

A single compartment model developed by Wang and Buzsáki (WB) (1996) represents the intrinsic properties of a hippocampal interneuron cell. The equations for each cell are given by:

$$\begin{aligned} C \frac{dV}{dt} &= I_{app} - g_{Na} m_\infty^3 h (V - V_{Na}) - g_K n^4 (V - V_K) \\ &\quad - g_L (V - V_L) \\ \frac{dh}{dt} &= \phi(\alpha_h(V)(1-h) - \beta_h(V)h) \\ \frac{dn}{dt} &= \phi(\alpha_n(V)(1-n) - \beta_n(V)n) \end{aligned}$$

where  $V$  is the cell membrane voltage in mV,  $h$  is the inactivation of the sodium current,  $n$  is the activation of the potassium current and  $t$  is time in ms.  $m_\infty$  is the steady-state activation of the sodium current and is given by:  $m_\infty = \alpha_m / (\alpha_m + \beta_m)$ , where  $\alpha_m(V) = -0.1(V + 35)/(\exp(-0.1(V + 35)) - 1)$ ,  $\beta_m(V) = 4 \exp(-(V + 60)/18)$ .  $\alpha_h(V) = 0.07 \exp(-(V + 58)/20)$ ,  $\beta_h(V) = 1/(\exp(-0.1(V + 28)) + 1)$ ,  $\alpha_n(V) = -0.01 \exp(-(V + 34)/\exp(-0.1(V + 34)) - 1)$ ,  $\beta_n(V) = 0.125 \exp(-(V + 44)/80)$ ,  $\phi = 5$ . Maximal sodium,  $g_{Na}$ , potassium,  $g_K$ , and leak,  $g_L$ , conductances are: 35, 9 and 0.1 mS/cm<sup>2</sup> respectively. Reversal potentials,  $V_{Na}$ ,  $V_K$ ,  $V_L$ , are 55, -90 and -65 mV respectively, and the capacitance,  $C$ , is 1  $\mu$ F/cm<sup>2</sup>.

Mutually inhibitory two-cell networks are formed via synapses that are described by first order kinetics. The inhibitory synaptic current,  $I_{syn}$ , which would be added to the current balance equation of the postsynaptic cell, is given by:

$$I_{syn} = g_{syn} s (V - V_{syn})$$

where

$$\begin{aligned} \frac{ds}{dt} &= \alpha T(V_{pre})(1-s) - s/\tau_{syn} \\ T(V_{pre}) &= \frac{1}{1 + \exp(-V_{pre}/2)} \end{aligned}$$

and  $V_{pre}$  is the voltage of the presynaptic cell,  $g_{syn}$  is the maximal inhibitory synaptic conductance,  $V_{syn} = -75$  mV is the synaptic reversal potential,  $\alpha = 6.25 \text{ ms}^{-1}$  is the rate constant of the synaptic activation and  $\tau_{syn}$  is the synaptic decay time constant.

$I_{app}$  represents the applied or external drive to the cell, or the injected current into the cell, and this parameter is used to introduce heterogeneity into the system.

For the two-cell networks, the external drive to cell 1 or 2 is:

$$\begin{aligned} I_{app,1} &= I_\mu - \epsilon \quad \text{or} \\ I_{app,2} &= I_\mu + \epsilon \end{aligned}$$

respectively, so that their external drives differ by  $2\epsilon$ . We define the percent heterogeneity, %Het, as:

$$\% \text{Het} = \frac{(I.F. \text{ at } I_{app,2}) - (I.F. \text{ at } I_{app,1})}{I.F. \text{ at } I_{app,2}} \times 100\%$$

where *I.F.* is the intrinsic frequency of the isolated cell.

For the described 50-cell networks, the  $I_{app}$ s are randomly chosen in the interval  $[-\% \text{Het}, +\% \text{Het}]$ . In the all-to-all coupled network simulations,  $g_{syn}$  values are normalized so that each presynaptic cell ‘delivers’ a maximal inhibition of  $g_{syn}/N$ .

Network simulations are performed using our in-house software, NNET, which is described in Murray (2004). Integration of the system of differential equations is done using either CVODE or Runge-Kutta methods, and using a tolerance of  $10^{-6}$  or less and a stepsize of 0.01 ms.

#### DESCRIPTION OF BIFURCATION ANALYSIS AND NUMERICAL CONTINUATION

A dynamical systems approach for studying non-linear ordinary differential equations involves bifurcation analyses, in which the dependence of solutions to the differential equations on various parameters is examined. Solutions include steady states and oscillations. A well-known feature of a non-linear system is its ability to express multiple stable solutions, i.e. multistability. For a fixed set of parameters, one can determine equilibrium points for the system. For example, voltage (V) values that do not change with time ( $dV/dt = 0$ ) and so on. It is the stability of these equilibrium points that determines the particular solution(s) that the system expresses (steady states, oscillations etc.). A dynamical system is said to undergo a bifurcation if the qualitative dynamics of the system are different above and below a particular value of a parameter. The value where the change occurs is called a bifurcation value. For example, the WB model has an  $I_{app}$  bifurcation value close to  $0.2 \mu\text{A/cm}^2$  in that below this value, the model system expresses a steady-state voltage output and, above this value, the model system produces an oscillatory output, i.e. repetitive firing. There are different types of bifurcations and knowing the specific type of bifurcation allows one to predict the presence of multistable patterns. Because it is hardly ever possible to perform stability calculations analytically, numerical techniques must be used. A numerical continuation refers to using numerical approaches to find equilibrium points and periodic solutions and to examine how their stability changes as parameters are varied. Although challenging to set up and run, numerical continuations have the advantage over numerical simulations of easily finding multistability and finding highly accurate bifurcation values. Numerical solutions from simulations can only produce stable solutions. If multistability is present, the solution produced depends on the initial conditions used.

#### EQUATIONS FOR NEURON MODEL WITH STOCHASTIC SYNAPSES

$$\begin{aligned} C_m \frac{dV}{dt} &= -I_{Na} - I_K - I_{syn} - I_t + I_{ext} \\ I_K &= g_K n^4 (V - E_K) \\ I_{Na} &= g_{Na} m^3 h (V - E_{Na}) \\ I_t &= g_L (V - E_L) \\ I_{syn} &= g_i (V - E_i) + g_e (V - E_e) \\ \frac{dg_i}{dt} &= \frac{1}{\tau_i} (g_{i0} - g_i) + \sqrt{\frac{2\sigma_i^2}{\tau_i}} \chi_i \\ \frac{dg_e}{dt} &= \frac{1}{\tau_e} (g_{e0} - g_e) + \sqrt{\frac{2\sigma_e^2}{\tau_e}} \chi_e \\ \frac{dn}{dt} &= \frac{1}{\tau_n} (n_\infty - n) \end{aligned}$$

$$\begin{aligned}
\frac{dh}{dt} &= \frac{1}{\tau_h} (h_\infty - h) \\
m &= \frac{1}{1 + e^{-0.08(V+26)}} \\
n_\infty &= \frac{1}{1 + e^{-0.045(V+10)}} \\
h_\infty &= \frac{1}{1 + e^{0.13(V+38)}} \\
\tau_n &= 0.5 + \frac{2}{1 + e^{0.045(V-50)}} \\
\tau_h &= \frac{0.6}{1 + e^{-0.12(V+67)}}
\end{aligned}$$

where  $\chi_{i,e}$  are independent Gaussian white noise processes,  $C_m$  is the membrane capacitance,  $I_{K,Na,l,syn}$  are the potassium, sodium, leak and synaptic current respectively,  $g_{e,i}$  are the excitatory and inhibitory conductances respectively.  $n$ ,  $m$ ,  $h$  are the various gating variables.  $g_{e0,i0}$ ,  $n_\infty$ ,  $h_\infty$  are equilibrium values of various conductances or gating variables.

#### PARAMETERS USED IN THE STOCHASTIC SIMULATIONS

Area = 15 000  $\mu\text{m}^2$ ,  $\tau_e = 2.7$  ms,  $\tau_i = 10.5$  ms,  $g_{e0} = 0.02$  mS/cm $^2$ ,  $g_L = 0.015$  mS/cm $^2$ ,  $E_e = 0$ ,  $E_i = -75$  mV,  $E_l = -65$  mV,  $g_{Na} = 30$  mS/cm $^2$ ,  $g_K = 20$  mS/cm $^2$ ,  $E_{Na} = 45$  mV,  $E_K = -80$  mV,  $\sigma_e = 0.007$  mS/cm $^2$ ,  $\sigma_i = 0.015$  mS/cm $^2$ .

XPPAUT (Ermentrout 2002) is used to integrate the equations using an Euler integration routine with 0.02 ms stepsize.

#### ACKNOWLEDGMENTS

This work was supported by NSERC of Canada. We would like to thank Dr Liang Zhang for his motivation and collaboration over the years. We would also like to thank Dr Sue Ann Campbell for her help and collaboration with bifurcation analysis and numerical continuation studies that have contributed to this work. Finally, FKS would like to thank all past and present lab members for discussions and interactions that have contributed to the various ideas presented in this work.

#### REFERENCES

- Bartos, M., Vida, I., Frotscher, M., Geiger, J.R.P. and Jonas, P. (2001). Rapid signaling at inhibitory synapses in a dentate gyrus interneuron network. *J Neurosci* 21:2687–2698.
- Bartos, M., Vida, I., Frotscher, M. et al. (2002). Fast synaptic inhibition promotes synchronized gamma oscillations in hippocampal interneuron networks. *Proc Natl Acad Sci USA* 99:13222–13227.
- Buzsáki, G. and Chrobak, J.J. (1995). Temporal structure in spatially organized neuronal ensembles: a role for interneuronal networks. *Curr Opin Neurobiol* 5:504–510.
- Engel, A.K., Fries, P. and Singer, W. (2001). Dynamic predictions: oscillations and synchrony in top-down processing. *Nat Rev Neurosci* 2:704–716.
- Ermentrout, G.B. (2002). Simulating, analyzing, and animating dynamical systems: a guide to XPPAUT for researchers and students. SIAM, Philadelphia.
- Gillis, J.A., Luk, W.P., Zhang, L. and Skinner, F.K. (2005). Decomposing rhythmic hippocampal data to obtain neuronal correlates. *J Neurosci Meth* 147(2):99–113.
- Golomb, D., Hansel, D. and Mato, G. (2001). Mechanisms of synchrony of neural activity in large networks. In: *Handbook of biological physics*, Vol. 4 (S. Gielen, M. Moss, eds) pp.887–968. Elsevier Science B.V., Amsterdam.
- Haider, B., Duque, A., Hasenstaub, A.R. and McCormick, D.A. (2006). Neocortical network activity in vivo is generated through a dynamic balance of excitation and inhibition. *J Neurosci* 26:4535–4545.
- Herz, A.V.M., Gollisch, T., Machens, C.K. and Jaeger, D. (2006). Modeling single-neuron dynamics and computations: a balance of detail and abstraction. *Science* 314:80–85.
- Ho, E.C., Zhang, L. and Skinner, F.K. (2006). Characterizing synaptic background activities in in vitro hippocampal circuits. Program No. 539.7 Neuroscience Meeting Planner. Society for Neuroscience, Atlanta, GA. Online.
- Kepler, T.B., Marder, E. and Abbott, L.F. (1990). The effect of electrical coupling on the frequency of model neuronal oscillations. *Science* 248:83–85.
- Lien, C.C., Martina, M., Schultz, J.H., Ehmke, H. and Jonas, P. (2002). Gating, modulation and subunit composition of voltage-gated K(+) channels in dendritic inhibitory interneurons of rat hippocampus. *J Physiol* 538:405–419.
- Murray, P.A. (2004). Capturing details of short-term synaptic plasticity in simple schemes. Master's Thesis, University of Toronto.
- Richardson, M.J.E. and Gerstner, W. (2006). Statistics of subthreshold neuronal voltage fluctuations due to conductance-based synaptic shot noise. *Chaos* 16:026106.

- Rudolph, M., Piwkowska, Z., Badoual, M., Bal, T. and Destexhe, A. (2004). A method to estimate synaptic conductances from membrane potential fluctuations. *J Neurophysiol* 91:2884–2896.
- Shu, Y., Hasenstaub, A. and McCormick, D.A. (2003). Turning on and off recurrent balanced cortical activity. *Nature* 423:288–293.
- Skinner, F.K. (2007). Toward direct links between model networks and experimental data. *Neurocomputing* in press.
- Skinner, F.K., Zhang, L., Perez Velazquez, J. and Carlen, P. (1999). Bursting in inhibitory interneuronal networks: a role for gap-junctional coupling. *J Neurophysiol* 81:1274–1283.
- Skinner, F.K., Bazzazi, H. and Campbell, S.A. (2005a). Two-cell to N-cell heterogeneous, inhibitory networks: precise linking of multistable and coherent properties. *J Comput Neurosci* 18:343–352.
- Skinner, F.K., Chung, J.Y.J., Ncube, I., Murray, P.A. and Campbell, S.A. (2005b). Using heterogeneity to predict inhibitory network model characteristics. *J Neurophysiol* 93:1898–1907.
- Suffczynski, P., Lopes da Silva, F., Parra, J., Velis, D. and Kalitzin, S. (2005). Epileptic transitions: model predictions and experimental validation. *J Clin Neurophysiol* 22:288–299,342.
- Traub, R.D., Whittington, M.A., Colling, S., Buzsáki, G. and Jefferys, J. (1996). Analysis of gamma rhythms in the rat hippocampus in vitro and in vivo. *J Physiol* 493:471–484.
- Traub, R.D., Contreras, D. and Whittington, M.A. (2005). Combined experimental/simulation studies of cellular and network mechanisms of epileptogenesis in vitro and in vivo. *J Clin Neurophysiol* 22:330–342.
- Wang, X.J. and Buzsáki, G. (1996). Gamma oscillation by synaptic inhibition in a hippocampal interneuronal network model. *J Neurosci* 16:6402–6413.
- Wang, X.J. and Rinzel, J. (1992). Alternating and synchronous rhythms in reciprocally inhibitory model neurons. *Neural Comput* 4:84–97.
- Wendling, F., Hernandez, A., Bellanger, J.-J., Chauvel, P. and Bartolomei, F. (2005). Interictal to ictal transition in human temporal lobe epilepsy: insights from a computational model of intracerebral EEG. *J Clin Neurophysiol* 22:343–356.
- Wu, C., Luk, W.P., Gillis, J., Skinner, F.K. and Zhang, L. (2005a). Size does matter: generation of intrinsic network rhythms in thick mouse hippocampal slices. *J Neurophysiol* 93(4):2302–2317.
- Wu, C., Nassiri Asl, M., Gillis, J., Skinner, F.K. and Zhan, L. (2005b). An in vitro model of hippocampal sharp waves: regional initiation and intracellular correlates. *J Neurophysiol* 94(1):741–753.
- Wu, C.P., Shen, H., Luk, W.P. and Zhang, L. (2002). A fundamental oscillatory state of isolated rodent hippocampus. *J Physiol* 540:509–527.

This page intentionally left blank

PART

IV

---

## HOMEOSTASIS AND EPILEPSY

---

This page intentionally left blank

# 16

## STABILITY AND PLASTICITY IN NEURONAL AND NETWORK DYNAMICS

ASTRID A. PRINZ

### ABSTRACT

The brain is able to learn, store memories and adapt to changes in the environment. These forms of neuronal plasticity are thought to be based on cellular and synaptic mechanisms such as long-term potentiation and depression. On the other hand, the brain – being the central control organ of behavior – needs to perform its function reliably, which requires mechanisms such as synaptic scaling and homeostatic regulation to ensure that neuronal circuits operate in a functional dynamic range at all times. Do plasticity and stability mechanisms coexist in the same neuronal circuits? How do they interact, and do they interfere with each other's function? Could the cellular and synaptic mechanisms that support plasticity and stability in intact neuronal circuits play a role in neurological disorders such as epilepsy, in which network stability appears to be lost? The present chapter examines experimental evidence and results from computational modeling to address these and other questions and speculates on possible links between plasticity and stability mechanisms and seizure-like brain activity.

### INTRODUCTION

The nervous system is facing two seemingly contradictory challenges. It must perform its sensory, motor, cognitive and emotional functions reliably, which requires neuronal network stability, but it also needs to be able to learn and adapt to changes in the body it resides in and in its environment, which requires network plasticity. In this chapter, I will review recent work on the mechanisms that underlie plasticity and stability of neuronal systems and will speculate how these mechanisms might be involved in normal and in seizure-like network activity.

Plasticity and stability mechanisms seem to be operating both within the synapses in a neuronal network and in its component neurons. In the following two sections, I will focus on cellular and synaptic mechanisms, respectively, while the fourth section will describe how both types of mechanisms are thought to interact at the network level. It has been suggested that the same mechanisms that allow a healthy neural circuit to learn and maintain stable function may also be involved in the loss of network stability in seizure-prone brains that have, through some insult, been perturbed far away from a stable equilibrium point (also see Chapter 26 for this notion). The final section will summarize recent ideas about the possible involvement of plasticity and stability mechanisms in neurological disorders such as epilepsy.

### CELLULAR HOMEOSTASIS MECHANISMS

Neuronal networks are composed of neurons, so it seems natural to assume that stable and robust network function calls for the necessary, although not necessarily sufficient, prerequisite that the individual nerve cells constituting the network also function robustly. Homeostatic regulation is a form of negative feedback that allows a neuron to compensate for changes in its membrane properties and electrical activity in a way that returns neuronal activity to a functional target pattern and is thought to be at the basis of stable neuronal activity. Before I describe two forms of cellular homeostatic regulation, namely activity-dependent and activity-independent regulation, I will discuss recent experimental and computational studies that address how tightly neuronal properties need to be constrained in order to achieve functional neuron behavior.

### NEURONAL SOLUTION SPACES

The spontaneous electrical activity of an isolated neuron and how it responds to synaptic inputs from other neurons in the network is shaped by the complex interplay of the ion currents in the neuron's membrane. In order for a neuron to perform its function properly, do parameters such as the maximal conductances, voltage-dependences and temporal dynamics of its membrane currents have to be closely tuned to specific values, or can functional neuron behavior be achieved with more widely varying ranges of parameter values? This question has recently been addressed in a number of computational studies that explore the parameter spaces of model neurons to determine what regions of parameter space generate a desired model neuron behavior – such a region is called the 'solution space' for that behavior.

Systematic computational exploration of the parameter space of a single-compartment model of neurons in the stomatogastric ganglion (STG) of crustaceans allowed six different values for each of the eight maximal membrane conductances of the neuron, resulting in a total of  $6^8$  or approximately 1.7 million different simulations (Prinz et al., 2003). Almost two-thirds of these 1.7 million conductance combinations generated rhythmic bursting behavior and a subset of nine of those bursting model versions closely matched the rhythmic pacemaker activity observed in the pyloric pacemaker kernel of crustaceans in terms of burst period, duration and duty cycle and phase response and slow wave characteristics. Figure 16.1A shows one of the nine models thus identified, along with a voltage recording from the biological pacemaker it was intended to mimic. Maximal membrane conductances of the nine models that form the pacemaker solution space are tabulated in Figure 16.1B, which shows that each maximal conductance varies over a two- to fivefold range within the solution space. Functional pacemaker behavior of the stomatogastric model neuron can thus arise from widely differing parameter combinations, suggesting that individual neurons indeed have extended solution spaces at their disposal rather than having to tune each cellular parameter to a unique value. The flexibility that comes along with this choice of functional parameter combinations may be an important factor in the robustness of neuronal function, because parameter perturbations, if small enough or in an insensitive direction, will not necessarily move the neuron out of its solution space.

Do biological neurons actually use different solutions to achieve the same electrical behavior? Voltage clamp experiments on synaptically isolated pyloric neurons suggest that they do (Golowasch et al., 1999a; Goldman et al., 2001). This is illustrated in Figure 16.1C, which shows maximal conductances for three membrane currents recorded from pacemaker and other identified pyloric neurons in the crab stomatogastric ganglion. Although these neurons perform very stereotypical pattern-generating functions, the same maximal conductances vary several-fold between different animals, leading to similar standard deviation per mean values as in the computational model pacemakers. Similarly, recordings from cerebellar Purkinje neurons show similar burst profiles in neurons with different amplitudes of sodium and calcium currents (Swensen and Bean, 2005). Different animals thus appear to have found different solutions to the same challenge. More recently, differences in ion channel expression levels between stomatogastric neurons of the same type in different animals have

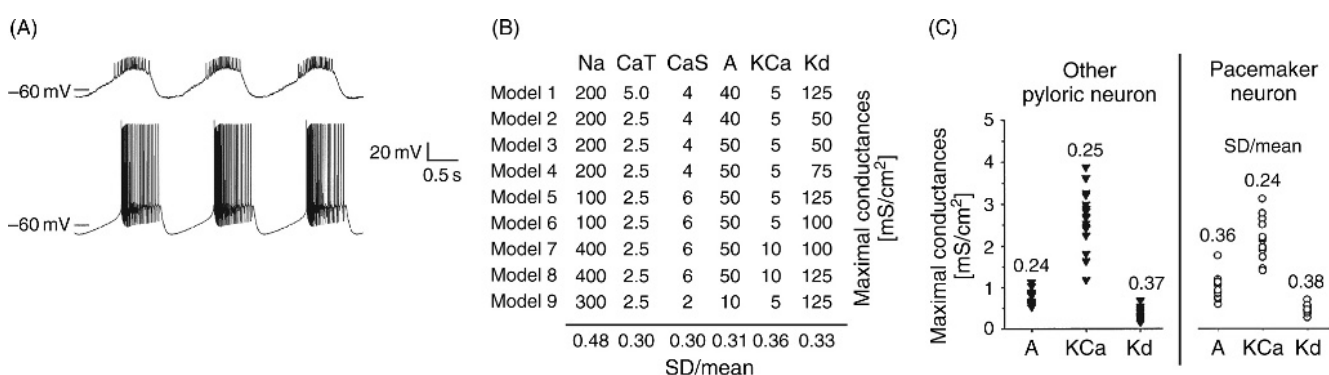


**FIGURE 16.1** Single neuron solution spaces. (A) Voltage trace recorded from a biological pyloric pacemaker neuron (top) and simulated voltage trace from one of nine model pacemaker neurons (bottom). Note that overshooting spikes in the model are due to use of a single compartment model, whereas spike initiation occurs far from the soma in the electrotonically extended biological neuron. (B) Maximal conductances of selected membrane currents in the nine model pacemakers. Membrane currents are:  $I_{Na}$ : fast Na current,  $I_{CaT}$  and  $I_{CaS}$ : fast and slow transient Ca currents,  $I_A$ : transient K current,  $I_{Kca}$ : Ca-dependent K current,  $I_{Kd}$ : delayed rectifier K current. Bottom row gives the standard deviation over the mean for each column. (C) Maximal conductances of three K currents recorded in pacemaker (right) and other identified pyloric neurons (left). Each data point within a group comes from the same identified neuron in a different animal. Numbers above each group of data points give the standard deviation over the mean. From Prinz et al. (2003); Golowasch et al. (1999a); Goldman et al. (2000) with permission.

also been demonstrated at the mRNA level (Schulz et al., 2006a). The same study showed that mRNA expression levels are closely correlated to the amplitudes of experimentally measurable currents in the neuronal membrane, which means that variability of membrane properties between neurons of the same type can be studied with the available repertoire of molecular techniques in the future.

Robustness of neuronal behavior to parameter variations, sometimes even over orders of magnitude, has also been observed in systematic parameter space explorations of multicompartment olfactory bulb granule and mitral cell models (Bhalla and Bower, 1993), in models of bursting leech heart interneurons generated with evolutionary algorithms (Tobin and Calabrese, 2006; Tobin et al., 2006) and in stochastic searches of the parameter spaces of a variety of Hodgkin-Huxley type model neurons from different systems (Foster et al., 1993; Goldman et al., 2001).

An issue closely related to the question whether extended solution spaces can contribute to robustness of neuron function is whether those solution spaces are contiguous in parameter space or whether they are scattered into multiple disconnected ‘solution islands’. Successful homeostatic regulation of cellular parameters to stabilize neuron function would seem to be harder to achieve in the latter, disconnected scenario. Fortunately, solution spaces of model neurons appear to be generally well behaved (Prinz et al., 2003) in that parameter combinations that generate similar behavior are located in contiguous regions of parameter space (Achard and De Schutter, 2006; Taylor et al., 2006), although those regions are not always convex (Golowasch et al., 2002) and can have complex structure (Achard and De Schutter, 2006).

To summarize, exploration of model parameter spaces and experimental measurements of conductance variability in biological neurons indicate that nerve cells can achieve similar function on the basis of different cellular properties, suggesting that neuronal properties do not need to be fine-tuned to unique parameter combinations. Such extended solution spaces make neuronal output less sensitive to parameter fluctuations and thus contribute to functional neuron robustness.

The finding that multiple solutions can generate similar, functional neuron output also has important implications for the way we study neuronal activity and its sensitivity to changes in the underlying conductance parameters. Computational sensitivity analysis often proceeds by first constructing a ‘canonical’ model neuron and then varying its parameters one at a time while monitoring the effects on the model’s activity. However, the results of such studies can strongly depend on where in solution space the canonical model was located (Goldman et al., 2000; Calabrese and Prinz, in press). When trying to understand how the behavior of a neuron depends on its membrane conductances and other cellular properties, it may thus be more appropriate to think of, and examine, entire solution spaces and their shape and extent in parameter space rather than focusing on a single ‘canonical’ model that may not represent the full repertoire of solutions available to a biological neuron. This cautionary remark is further supported by the fact that the construction of canonical models from experimental observations in a population of neurons often proceeds by separately averaging each cellular parameter (for example, the maximal conductance of a membrane current) over the experimental population. Because solution spaces are often non-convex, such averaging can result in a ‘canonical’ model that, although arising from averages over the parameters of points in solution space, is not itself inside the solution space (Golowasch et al., 2002).

## ACTIVITY-DEPENDENT REGULATION

How does a biological neuron ensure that it functions properly at all times, or in other words, that its combination of membrane parameters always stays inside the solution space? The naïve notion that the maximal conductances and dynamic properties of all ionic currents in a neuron’s membrane could simply be hard-wired in the cell’s genome in a way that guarantees functional behavior is obviously impractical and too rigid, because it would leave the neuron unable to adapt to perturbations or changes in its network environment. The above discussion of solution spaces suggests that what really characterizes a neuron type is its electrical activity and behavior in the network, as opposed to the particular combination of membrane properties that underlies that activity (Foster et al., 1993; Liu et al., 1998). Distinguishing neurons by their activity patterns and response properties has certainly long been one method by which electrophysiologists categorize different neuron types. The idea that what defines the identity of a given biological neuron type is a certain target activity pattern, rather than a specific molecular make-up, is at the basis of the concept of activity-dependent homeostatic regulation (Marder and Prinz, 2002). Activity-dependent homeostatic regulation refers to a negative feedback system through which a neuron can sense deviations of its electrical activity from a desired pattern due to some perturbation. The neuron is then thought to be able to compensate for the perturbation by adjusting its cellular properties in a way that will restore target activity (Figure 16.2). The intracellular calcium concentration and its dynamics are thought to play an important role in

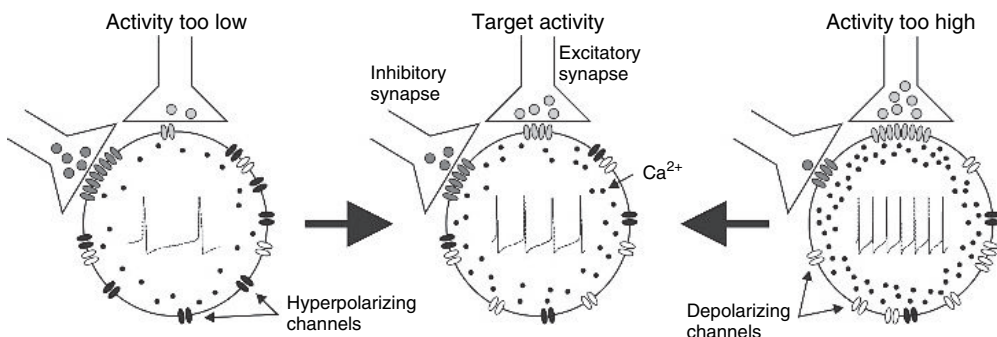


**FIGURE 16.2** Basic idea of activity-dependent homeostatic regulation. A neuron can sense if its activity falls below a target level (left) by detecting the accompanying decrease in intracellular calcium concentration. It can return its activity to the target level by increasing depolarizing currents such as inward membrane currents or excitatory synaptic currents and decreasing hyperpolarizing currents such as outward membrane currents and inhibitory synaptic currents, and vice versa if the activity rises above the target level (right). From Marder and Prinz, 2002, with permission.

connecting changes in electrical activity to downstream changes in cellular properties, because the calcium concentration correlates well with electrical activity (Ross, 1989) and because calcium is involved in numerous intracellular signaling cascades (Berridge et al., 2003).

### Experimental evidence

Some of the earliest evidence for activity-dependent homeostatic regulation of intrinsic neuronal properties came from experiments on cultured lobster stomatogastric neurons (Turrigiano et al., 1994). When newly isolated in culture, these neurons are silent, but proceed to adjust their excitability over the course of several days to restore the bursting activity pattern they normally express *in vivo* in response to rhythmic synaptic drive. This adjustment of firing properties is activity-dependent, because artificially stimulating a cultured neuron to induce the target burst pattern reverses the transition from silence to bursting activity. The presence of a calcium buffer in the stimulated neurons blocks the activity-dependent regulation of intrinsic properties, showing that calcium plays an important role in activity-dependent homeostatic regulation (Turrigiano et al., 1994; Golowasch et al., 1999a). In visual cortical neurons of the rat, the downstream effects of activity-dependent changes in calcium concentration are thought to be mediated through the protein kinase A (PKA) pathway (Cudmore and Turrigiano, 2004).

The major changes underlying activity-dependent homeostatic regulation in cultured lobster neurons were upregulation of inward currents and downregulation of outward currents to increase excitability (see Figure 16.2) and vice versa to achieve a decrease in excitability (Turrigiano et al., 1995). Similarly, cultures of postnatal rat cortical neurons show upregulated amounts of sodium current and downregulation of TEA-sensitive potassium and A-type potassium current in response to several days of activity-deprivation, whereas calcium currents and a persistent potassium current in the same preparation were unaffected (Desai et al., 1999).

However, the effects of increased or decreased electrical activity on membrane conductances of different types of neurons are not always as clear-cut as in the experiments described above, or as simple as illustrated in Figure 16.2. For example, in isolated crab stomatogastric neurons the sum of the delayed rectifier potassium and the calcium-dependent potassium current  $I_{KCa}$  was downregulated by rhythmic burst activity, but another potassium current – the transient current  $I_A$  – was simultaneously upregulated (Golowasch et al., 1999a). Furthermore, whereas downregulation of  $I_{KCa}$  contributed to a decrease in excitability in these crab STG neurons, it caused increased excitability in mouse vestibular nucleus neurons that had been exposed to periods of synaptic inhibition or direct membrane hyperpolarization (Nelson et al., 2003). More recently, the spontaneous and stimulation-induced excitability changes observed in cultured crab stomatogastric neurons were shown to be based on regulation of a high-threshold potassium and a calcium current, but the same stimulation protocol was found to induce different excitability changes in different neurons (Haedo and Golowasch, 2006). In rat hippocampal neurons, theta-burst firing induced a decrease in neuronal excitability through upregulation of yet another target current, the hyperpolarization-activated inward cation current  $I_h$  (Fan et al., 2005). The details and molecular mechanisms of activity-dependent homeostatic regulation thus can differ significantly between different neuron types and no single unifying regulation scheme has yet been identified.

### Computational models

Because little is known about the molecular mechanisms and detailed dynamics that underlie activity-dependent homeostatic regulation of neuronal properties, the few existing models of cellular regulation assume abstract activity sensors that monitor intracellular calcium and directly regulate the maximal conductances of membrane currents, without specifying any actual molecular players or pathways. Nonetheless, these models have demonstrated that activity-dependent homeostasis and self-assembly of neuronal models is possible and have provided some insight into the constraints inherent to such regulatory mechanisms.

The first model (to our knowledge) of activity-dependent regulation of neuronal membrane properties assumed a simple regulation scheme similar to the one illustrated in Figure 16.2, in which inward and outward currents of a conductance-based single-compartment STG model neuron were regulated in opposite directions depending on a single calcium-based activity sensor (LeMasson et al., 1993). Despite its relative simplicity, this regulation strategy was able to restore the target bursting activity in response to a variety of model perturbations, such as changes in extracellular ion concentrations or varied stimulation protocols. When applied to each individual compartment of a multicompartment CA1 pyramidal cell model (Siegel et al., 1994), the same strategy resulted in physiologically realistic spatial distributions of one sodium and two potassium channels in different branches of the neuron's dendritic tree. These branch-specific distributions were influenced by the local synaptic input density and could act to restore homeostatically the neuron to its optimal firing range after synapses are modified by 'Hebbian' mechanisms such as long-term potentiation or depression (see below).

Homeostatic regulation mechanisms that depend on a single activity-sensor have the problem that the sensor output depends non-uniquely on the neuron's electrical activity. For example, a slowly bursting and a fast-spiking neuron might generate similar average numbers of spikes per time interval and thus similar average intracellular calcium concentrations, such that a regulation mechanism dependent on the concentration alone would be unable to distinguish the two behaviors, and preferentially to restore one over the other. However, biological neurons contain a multitude of intracellular signaling and regulatory cascades, many of which involve calcium (Carafoli and Klee, 1999). These complex biochemical networks thus contain the potential for multiple calcium-based activity-sensors operating on different time-scales and with different sensitivities for calcium concentration and thus electrical activity. This reasoning led to the latest-generation cellular model of activity-dependent homeostatic conductance regulation (Liu et al., 1998). This model contains three calcium sensors, one responding to calcium dynamics on the time-scale of spikes, one at the time-scale of bursts and one responding to the long-term average of the calcium concentration. These sensors influence the maximal conductances of the eight membrane currents in the model neuron through a complex regulation scheme that goes far beyond the simple idea illustrated in Figure 16.2 and is successful at stabilizing and restoring many types of target activity in the face of a wide range of simulated perturbations.

### ACTIVITY-INDEPENDENT REGULATION

Although activity-dependent regulation of neuronal properties has been demonstrated in a variety of systems (see above), biological neurons appear not to rely on it exclusively for homeostasis. Additional constraints on the cellular parameter combinations that occur in biological neurons come from the fact that some neuronal properties are coregulated in an activity-independent manner (Marder and Prinz, 2003). In the pyloric dilator (PD) neuron of the lobster stomatogastric ganglion, massive overexpression of the *shal* gene, which encodes the transient potassium current  $I_A$ , did not lead to the expected changes in neuronal firing properties, but instead was compensated for by proportional upregulation of the hyperpolarization-activated current  $I_h$  (MacLean et al., 2003). This coregulation is thought to be activity-independent, because it also occurs in response to overexpression of a non-functional mutant version of *shal* that does not lead to insertion of current-conducting channels into the neuronal membrane. Interestingly, the coregulation does not work both ways, as overexpression of the  $I_h$  channel gene does not lead to an increase in  $I_A$  current (Zhang et al., 2003). The same uni-directional coregulation has, in the meantime, also been found in pyloric neurons other than PD (MacLean et al., 2005), including neuron types that use activity-independent regulation for some membrane currents and activity-dependent mechanisms for others (see above).

In cerebellar Purkinje neurons, a similar homeostatic compensation effect occurs between a sodium current and the balance of calcium currents and calcium-dependent potassium currents in the case of acute sodium channel blocking and in double-knockouts of the sodium channel gene (Swensen and Bean, 2005), although in this system it remains to be determined whether the compensatory current up- or downregulations are activity-dependent or independent. Furthermore, the detailed molecular mechanisms of activity-independent homeostatic regulation of neuronal properties are as yet unknown.

From the perspective of stabilizing neuronal function, what are the respective advantages and disadvantages of activity-dependent versus activity-independent regulation mechanisms? It would appear that activity-independent coregulation of membrane currents at a fixed ratio reduces the extent of parameter space that a neuron has at its disposal. Such constraints on the parameter combinations accessible to a neuron could be a disadvantage if the neuron is exposed to extreme perturbations, because they limit the range of possible homeostatic responses. On the other hand, constraining the accessible parameter space of a neuron could be beneficial in the sense that it might prevent homeostatic regulation from failing in the way described below.

## SYNAPTIC MECHANISMS OF PLASTICITY AND STABILITY

### SYNAPTIC PLASTICITY

It has long been recognized that the synapses between neurons are dynamic and can undergo changes in their strength and dynamics. This synaptic plasticity is thought to underlie learning and memory and has thus received much attention. Perhaps the best-studied forms of synaptic plasticity are long-term potentiation (LTP) and long-term depression (LTD), i.e. long-lasting enhancements or reductions in synaptic efficacy. Because the mechanisms, characteristics and function of synaptic plasticity are diverse in different systems (Malenka and Bear, 2004) and reviewing them would far exceed the scope of this section, we will very narrowly focus on the properties of LTP and LTD that are most relevant to the relationship between neuronal network plasticity and stability.

Synaptic plasticity is known to depend on the relative timing between pre- and postsynaptic action potentials, such that a presynaptic spike preceding a postsynaptic spike within a certain time window will tend to elicit LTP, whereas a postsynaptic spike followed by a presynaptic spike will tend to depress the synapse (Ganguly et al., 2000). This spike timing-dependent plasticity (Dan and Poo, 2006) is intriguing, because it provides a possible physiological mechanism for the form of causality-dependent learning postulated by Hebb (Hebb, 1949).

Hebbian learning, including Hebbian-type LTP and LTD, is essentially a positive feedback mechanism, because synapses that were previously strong enough to participate repeatedly in making the postsynaptic neuron fire will be strengthened further, whereas synapses that were weak to begin with will tend to become further depressed over time (Miller, 1996). This positive feedback makes Hebbian learning prone to instabilities in the form of runaway excitation resulting in seizure-like network activity, or in the form of largely inactive networks (Desai, 2003). Preventing these instabilities requires constraints on the strength and potentiation of synapses (Miller and Mackay, 1994) and, in subsequent sections, I will discuss how synaptic and intrinsic homeostatic mechanisms might be able to provide such constraints.

Beyond its possible involvement in network instabilities, another feature of synaptic plasticity that relates to the stabilizing homeostatic mechanisms described above is that its induction and maintenance are calcium-dependent processes (Cavazzini et al., 2005). The same signal – intracellular calcium and its dynamics – that plays a crucial role in activity-dependent homeostatic regulation of cellular properties is thus also involved in synaptic plasticity and it is interesting to speculate how two seemingly antagonistic processes can be regulated through interlinked molecular pathways.

### SYNAPTIC SCALING

The synaptic plasticity mechanisms described above are thought to be the basis of nervous system plasticity and learning, but can also lead to potentially catastrophic network instabilities. Are there synaptic homeostasis mechanisms in place that, together with the cellular homeostasis mechanisms described in the previous section, can counterbalance the destabilizing trend of synaptic plasticity and the positive feedback loops it involves? Recent work suggests that at least one such synaptic mechanism, synaptic scaling, is present in a variety of systems. Synaptic scaling is a slow process in which the strengths of synapses impinging onto a neuron are scaled by a common multiplicative factor in a way that adjusts the total synaptic drive to match the neuron's dynamic range while preserving the relative strengths of the synapses and thus, presumably, the memory traces left by previous learning events mediated by LTP or LTD (Turrigiano, 1999; Turrigiano and Nelson, 2000).

While operating on a slower time scale than correlation-based learning mechanisms such as LTP and LTD, synaptic scaling is thought to involve some of the same molecular players as those mechanisms (Turrigiano and Nelson, 2000) and has been suggested to support the competition between synapses onto the same neuron that is one of the critical features of Hebbian learning (Feldman, 2002). Apart from operating on different time scales, synaptic plasticity and synaptic scaling

have also been speculated to be operating in the same circuits at different phases of the circadian cycle, with Hebbian learning mostly taking place during wakefulness and synaptic scaling being one of the beneficial effects of sleep (Tononi and Cirelli, 2003). Based on this hypothesis, it is tempting to assume a link between network plasticity and stability mechanisms and sleep or mood disorders (Tononi and Cirelli, 2006).

### PLASTICITY AND STABILITY AT THE NETWORK LEVEL

In the previous sections, I described cellular homeostasis mechanisms and synaptic plasticity and stability phenomena. In neuronal networks, where multiple or many neurons contact each other through synapses, how do these cellular and synaptic mechanisms interact to determine overall network behavior and stability? Before I turn to experimental and theoretical evidence that addresses this question, I will again (as above for individual neurons) examine how tightly network parameters have to be regulated to achieve stable and functional network output.

### SOLUTION SPACES OF NEURONAL NETWORKS

Using a computational parameter exploration strategy similar to the one described above for single neuron models, we recently examined the 10-dimensional synapse strength and cellular parameter space of a three-cell, seven-synapse model of the crustacean pyloric pattern-generating network (Prinz et al., 2004). We found that, just as in the case of individual neurons, similar network output could arise from widely different combinations of underlying cellular and synaptic properties. This suggests that neuronal networks may have extended solution spaces at their disposal rather than having to fine-tune their components to narrow value ranges. Multiple possible solutions that can generate the same behavior may contribute to network stability, because a neural system with multiple possible solutions is less vulnerable to loss of function due to small changes in parameters than a narrowly tuned system.

Evidence that biological networks actually employ different solutions to achieve the same output comes from several sources. The voltage clamp characterizations of neurons in pyloric circuits that were described in above and Figure 16.1C (Golowasch et al., 1999a; Goldman et al., 2001) and the gene expression studies also described there (Schulz et al., 2006a) show that pyloric circuits in different animals differ significantly in their cellular parameters. Furthermore, pyloric network phase relationships have been shown to be relatively insensitive to the strengths and temporal dynamics of important synapses in the circuit (Rabbah and Nadim, 2005). And, finally, the recovery experiments described below (Luther et al., 2003) show that pyloric circuits are able to generate similar rhythmic output in the presence or absence of neuromodulators and the membrane and synaptic currents that they sustain, again confirming that circuits can generate similar output from different network properties.

In spite of the direct evidence for inter-animal variability of network parameters cited above, the notion of similar network output from different network properties is not undisputed. A recent publication describes experiments in which pyloric networks in different animals react similarly to application of pharmacological blockers of individual membrane currents such as the transient potassium current  $I_A$  or of synapse types such as cholinergic or glutamatergic synapses (Szücs and Selverston, 2006). The authors argue that blocking membrane or synaptic currents in networks that operate with different combinations of underlying parameters should unmask differences in the remaining currents and thus lead to different behaviors of the manipulated circuits. Following this line of argument, the fact that all circuits reacted similarly to pharmacological manipulation would imply that pyloric circuits do, in fact, have tightly regulated cellular and synaptic properties. Further experimental and computational work will be required to reconcile these results with the direct evidence for circuit parameter variability cited above.

### NETWORK-LEVEL HOMEOSTATIC REGULATION

#### Experimental evidence

In the stomatogastric system, the most direct evidence for homeostatic regulation at the network level stems from recovery experiments in which a rhythmically active STG preparation is deprived of the neuromodulatory inputs that sustain the rhythm (Luther et al., 2003). This manipulation leads to acute silencing of the pyloric rhythm but, over the course of one or several days, the STG circuits are able to reconfigure themselves – whether through activity-dependent or activity-independent regulation or both is currently unknown – to once again generate an (albeit slower) pyloric rhythm in the continued absence of neuromodulatory input. In the recovered circuit, the strength of inhibitory synapses and the amplitudes

of the delayed rectifier and calcium dependent potassium currents in pacemaker neurons are significantly smaller than in the intact circuit, whereas the amplitude of the hyperpolarization-activated current is significantly larger (Thoby-Brisson and Simmers, 2002), suggesting that both synaptic and intrinsic processes contribute to the recovery. Interestingly, this slow recovery process involves silent periods interrupted by so-called ‘bouts’ of rhythmic activity, as if during homeostatic regulation the circuit was entering and exiting parameter space regions of pyloric-like activity (also see Figure 16.3). This transient occurrence of different types of neuronal and network activity is reminiscent of the activity patterns generated during activity-dependent homeostatic regulation in the cellular model (Liu et al., 1998) described above.

Action of both intrinsic and synaptic homeostasis mechanisms simultaneously in the same network has also been observed in organotypic rat hippocampal slices (Karmarkar and Buonomano, 2006). Manipulations of network activity in both directions in these slices induced compensatory changes in the effectiveness of inhibitory connections at suppressing action potentials and in the intrinsic excitability of hippocampal neurons. However, the authors observed that intrinsic and synaptic homeostatic plasticity occurred with different temporal profiles, suggesting different underlying mechanisms, and went on to speculate that, in the hippocampus, synaptic forms of homeostatic plasticity may only be engaged if intrinsic excitability changes alone are not sufficient to stabilize network activity.

In the tadpole optic tectum, cell-intrinsic homeostatic upregulation of a voltage-dependent sodium current increases neuronal excitability to compensate for the reduction of excitatory synaptic drive that results from several hours of visual stimulation (Aizenman et al., 2003). The combined compensatory changes in excitability and synaptic excitation, besides stabilizing network activity, also lead to increased sensitivity of the retinotectal system to burst stimuli and decreased sensitivity to background activity. Thus, homeostatic regulation at the network level can be beneficial beyond simply stabilizing network activity.

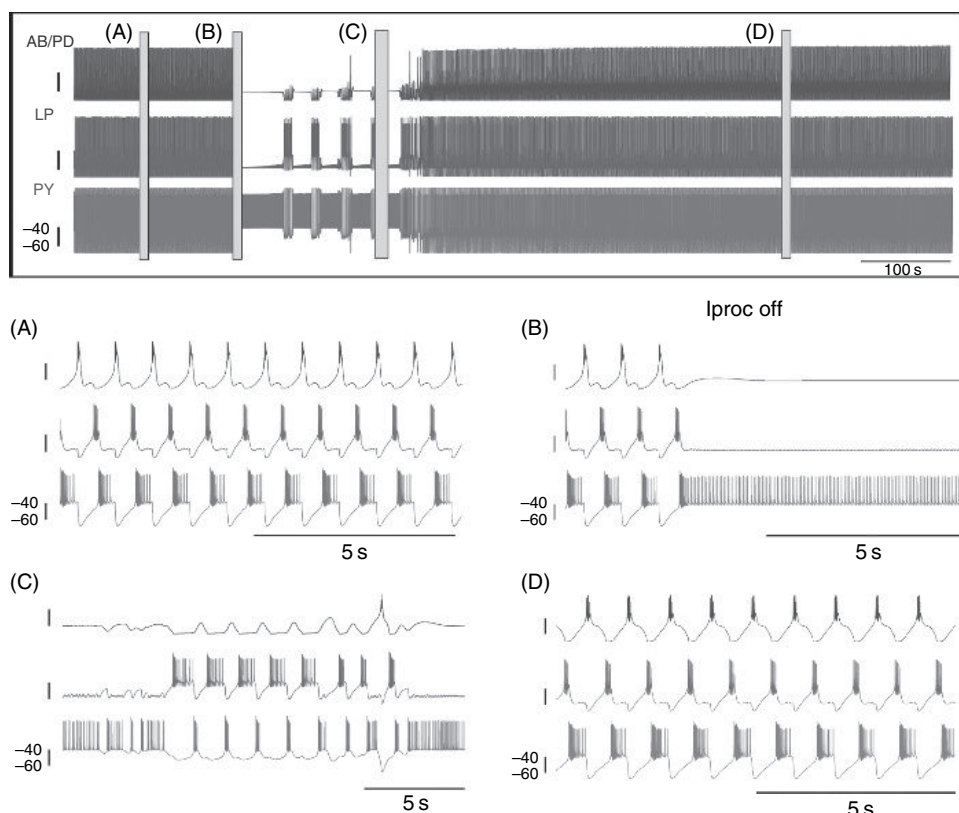


**FIGURE 16.3** Homeostasis in a pyloric network model based on constrained regulation of cellular properties. Top: Voltage traces from the three neurons (AB: anterior burster, LP: lateral pyloric neuron, PY: pyloric neuron) in a pyloric circuit model before and after simulated deafferentation at time B. A–D: Network activity before (A), and immediately after (B) deafferentation simulated by switching off the neuromodulatory current  $I_{\text{proc}}$ , during bouting activity (C), and after recovery of rhythmic activity (D) in the continued absence of the neuromodulatory current. The initially rhythmic network loses rhythmicity upon deafferentation, goes through bouts of activity, and eventually recovers by reconfiguring its cellular properties. LeDoux and Marder, unpublished data. (See Plate 9 in color plate section.)

Synaptic scaling, which had previously been demonstrated mostly in cultured networks (O'Brien et al., 1998; Turrigiano et al., 1998), has now also been shown to act as a mechanism of network homeostasis *in vivo* (Feldman, 2002). In the developing rat visual cortex, brief periods of monocular deprivation by TTX (tetrodotoxin) injection into one eye lead to compensatory scaling of excitatory synapses in principal neurons (Desai et al., 2002), although that scaling is layer-specific and dependent on the developmental stage. In the embryonic chick spinal cord, suppression of the spontaneous network activity thought to be involved in network maturation leads to an upregulation of AMPAergic miniature postsynaptic currents, thus increasing the excitability of the cord (Gonzalez-Islas and Wenner, 2006). Interestingly, GABAergic currents, which at the developmental stage used in these experiments are excitatory, were also upregulated. This indicates that mechanisms of homeostatic synapse regulation may have evolved to scale synapses in the direction appropriate to their electrophysiological function (i.e. excitatory versus inhibitory) at each developmental stage, regardless of the transmitter's function in the adult.

### Computational models

Network-level homeostatic regulation has been computationally modeled in a variety of contexts. Interestingly, homeostatic regulation mechanisms have been found not only to lead to network stability, but also potentially to support important network-level phenomena such as working memory, circuit and map self-organization, and learning.

In a model of spatial working memory in hippocampal networks, synaptic scaling was found to solve a long-standing problem in working memory models, namely that spatial information can be stably stored in highly homogeneous network models, but rapidly decays if physiologically realistic cellular and synaptic heterogeneity is included in the model (Renart et al., 2003). Synaptic scaling was shown to preserve cellular and spatial tuning curve heterogeneity while generating functional homogeneity, such that spatial memories can be stably encoded in biologically realistic model networks.

Models of self-organizing cortical map formation during development also long had to make an artificial assumption, namely that synaptic weight normalization counteracts the otherwise unchecked growth of synaptic weights during the Hebbian learning that underlies map formation. Again, the implementation of synaptic scaling in models of map formation was able to replace the physiologically unfounded weight normalization mechanism and led to robust map formation (Sullivan and de Sa, 2006a, 2006b). The role of synaptic scaling as a physiologically well-founded normalization mechanism that successfully replaces previous synaptic weight correction assumptions appears to be a recurrent theme in neuronal network modeling, as it was also used in models of associative memory storage (Chechik et al., 2001). Furthermore, implementing synaptic scaling in a neuronal network model has been shown to support physiologically realistic avalanches of electrical activity by ensuring that the network is stabilized at its critical point, i.e. in a state where the average number of neurons excited after a given neuron fires is close to 1 (Hsu and Beggs, 2006). Network criticality in this sense prevents information loss due to excessive spread or dampening of excitation, thus by supporting network criticality, synaptic scaling can contribute to optimal information throughput in a network.

The examples cited above suggest that, in large cortical and memory networks, homeostatic mechanisms such as synaptic scaling can counteract the destabilizing effects of plasticity mechanisms such as Hebbian learning and can thus preserve network stability while allowing network plasticity. In the smaller pattern-generating networks of invertebrates, which are not typically known for pronounced plasticity through mechanisms like LTP and LTD, homeostatic regulation mechanisms appear to serve the more conventional role of network stabilization – crucial for pattern generating circuits that underlie vital behaviors such as breathing – and potentially contributes to circuit self-assembly. Self-assembly of two-cell and three-cell pattern-generating networks – the latter inspired by the crustacean pyloric circuit – on the basis of activity-dependent regulation of inhibitory synapse strength has been demonstrated in network models that use the pre- and postsynaptic calcium concentrations as tuning signals for synapse modification (Soto-Trevino et al., 2001). These models were successful at achieving the desired rhythmic network activity for the vast majority of random initial network conditions tested, suggesting that simple activity-dependent synapse regulation rules can provide a powerful means for self-assembling and stabilizing functional networks.

All the models of network homeostasis described thus far rely on the activity-dependent regulation of synaptic properties and appear to be largely successful. Can similarly robust network regulation be achieved on the basis of cell-intrinsic, rather than synaptic, regulation mechanisms? A model of activity-dependent regulation of a calcium current and a potassium current in each cell of a three-cell model of the pyloric network was able to reproduce the recovery from deafferentation of the pyloric rhythm described above and enabled self-assembly of the rhythmically active pyloric circuit from different, not rhythmically active, initial conditions (Golowasch et al., 1999b). However, that model regulated the maximal conductances for only two of six membrane currents present in each model neuron, and did so in a highly constrained manner that kept the sum of the two regulated maximal conductances in each neuron constant.

It appears that the situation is more complicated for intrinsic regulation mechanisms that affect a large number of cellular parameters, which would seem realistic based on the experimental data described above. A recent attempt at achieving stable network-level homeostatic regulation by implementing the successful calcium-based cellular regulation model from (Liu et al., 1998) in all three cells of a model pyloric network led to unstable network activity and failure to generate pyloric-like rhythmic activity (Prinz, 2006). This model, which successfully stabilizes electrical activity in isolated neuron models and was described above, regulates seven membrane conductances through three different calcium sensors. The fact that this model works at the cellular but fails at the network level suggests that the synaptic interactions between the self-regulating neurons in the network introduce instabilities in the regulation mechanism and that regulation within each cell may have to be constrained to ensure network stability. This assumption is corroborated by the successful replication of the pyloric rhythm recovery experiments described above by a cell-based regulation mechanism that uses regulation strategies inspired by (Liu et al., 1998), but restricts regulation to just three slow currents in each cell, namely the inactivating potassium current  $I_A$ , the calcium-dependent potassium current  $I_{KCa}$ , and the hyperpolarization-activated current  $I_h$  (E. LeDoux and E. Marder, unpublished results). Successful network stabilization by this constrained regulation model is illustrated in Figure 16.3 and replicates the bursting activity observed during rhythm recovery in biological recovery experiments (Thoby-Brisson and Simmers, 2002; Luther et al., 2003).

The simulations described above suggest that homeostatic regulation of network activity based on intrinsic regulation of cellular properties is a complex process prone to instabilities if not properly constrained. Do biological networks that undergo activity-dependent regulation of cellular properties show evidence of such stabilizing constraints? New experimental evidence from the crustacean pyloric network suggests that such constraints may in fact be in place (Schulz et al., 2006b). These experiments demonstrate that the mRNA expression levels of different ion channels in pyloric cells are correlated, which suggests that, rather than exploring the full parameter space theoretically accessible to homeostatically regulating neurons, the regulation mechanism seems to be constrained by correlated expression of subsets of membrane currents, as described above for the currents  $I_A$  and  $I_h$  in the pyloric dilator neurons (MacLean et al., 2003). Furthermore, which types of ion channels were expressed in a correlated manner varied from cell type to cell type, indicating that the regulation mechanism and its constraints are cell-type specific and may define the electrical identity of a cell in the network (Schulz et al., 2007).

### IMPLICATIONS FOR EPILEPSY AND CONCLUSIONS

The previous sections have shown that experimental evidence and computational modeling studies support a role of synaptic and intrinsic homeostasis mechanisms in stabilizing cellular and network activity while allowing network plasticity through mechanisms such as LTP and LTD. But we have also seen that, if not properly constrained, homeostatic regulation can lead to network instability and dysfunction. It is tempting to speculate that failure or malfunction of regulation mechanisms that normally support stable network function in the intact and healthy brain (Debanne et al., 2003) could contribute to network instabilities such as over-excitation or seizure-like activity in diseased or injured brain structures (see also Chapter 26). For example, exposure to a single episode of status epilepticus leads to activity-dependent upregulation of T-type calcium currents in a rat model of epilepsy, which in turn increases the tendency to burst firing in hippocampal pyramidal neurons that is thought to contribute to the development of a chronic epileptic condition (Su et al., 2002). Beyond epilepsy, synaptic scaling in response to increased activity has also been implicated as a possible mechanism for the onset of Alzheimer's disease (Chang et al., 2006). It remains to be seen whether understanding how and why regulation mechanisms that work properly at the single-cell level fail to stabilize network activity will bring us closer to an understanding of the mechanisms of network stability and robustness operating in biological circuits, and to understanding how these stability mechanisms fail in neurological disorders.

### ACKNOWLEDGMENTS

I thank Erwan LeDoux for graciously providing me with Figure 16.3 and Eve Marder for useful discussions. Support from the Burroughs Wellcome Fund and the Alfred P. Sloan Foundation is also acknowledged.

## REFERENCES

- Achard, P. and De Schutter, E. (2006). Complex parameter landscape for a complex neuron model. *PLoS Comput Biol* 2:794–804.
- Aizenman, C.D., Akerman, C.J., Jensen, K.R. and Cline, H.T. (2003). Visually driven regulation of intrinsic neuronal excitability improves stimulus detection in vivo. *Neuron* 39:831–842.
- Berridge, M.J., Bootman, M.D. and Roderick, H.L. (2003). Calcium signalling: dynamics, homeostasis and remodelling. *Nat Rev Mol Cell Biol* 4:517–529.
- Bhalla, U.S. and Bower, J.M. (1993). Exploring parameter space in detailed single neuron models – simulations of the mitral and granule cells of the olfactory-bulb. *J Neurophysiol* 69:1948–1965.
- Calabrese, R.L. and Prinz, A.A. (in press). Realistic modeling of small neuronal networks. In: Computational modeling methods for neuroscientists (E. De Schutter, ed.). MIT Press, Cambridge.
- Carafoli, E. and Klee, C. (1999). Calcium as a cellular regulator. Oxford University Press, New York.
- Cavazzini, M., Bliss, T. and Emptage, N. (2005). Ca<sup>2+</sup> and synaptic plasticity. *Cell Calcium* 38:355–367.
- Chang, E.H., Savage, M.J., Flood, D.G. et al. (2006). AMPA receptor downscaling at the onset of Alzheimer's disease pathology in double knockin mice. *Proc Natl Acad Sci USA* 103:3410–3415.
- Chechik, G., Meilijson, I. and Ruppin, E. (2001). Effective neuronal learning with ineffective Hebbian learning rules. *Neural Comput* 13:817–840.
- Cudmore, R.H. and Turrigiano, G.G. (2004). Long-term potentiation of intrinsic excitability in LV visual cortical neurons. *J Neurophysiol* 92:341–348.
- Dan, Y. and Poo, M.M. (2006). Spike timing-dependent plasticity: from synapse to perception. *Physiol Rev* 86:1033–1048.
- Debanne, D., Daoudal, G., Soudet, V. and Russier, M. (2003). Brain plasticity and ion channels. *J Physiol Paris* 97:403–414.
- Desai, N.S. (2003). Homeostatic plasticity in the CNS: synaptic and intrinsic forms. *J Physiol Paris* 97:391–402.
- Desai, N.S., Rutherford, L.C. and Turrigiano, G.G. (1999). Plasticity in the intrinsic excitability of cortical pyramidal neurons. *Nat Neurosci* 2:515–520.
- Desai, N.S., Cudmore, R.H., Nelson, S.B. and Turrigiano, G.G. (2002). Critical periods for experience-dependent synaptic scaling in visual cortex. *Nat Neurosci* 5:783–789.
- Fan, Y., Fricker, D., Brager, D.H. et al. (2005). Activity-dependent decrease of excitability in rat hippocampal neurons through increases in I-h. *Nat Neurosci* 8: 1542–1551.
- Feldman, D.E. (2002). Synapses, scaling and homeostasis in vivo. *Nat Neurosci* 5:712–714.
- Foster, W.R., Ungar, L.H. and Schwaber, J.S. (1993). Significance of conductances in Hodgkin-Huxley models. *J Neurophysiol* 70:2502–2518.
- Ganguly, K., Kiss, L. and Poo, M.M. (2000). Enhancement of presynaptic neuronal excitability by correlated presynaptic and postsynaptic spiking. *Nat Neurosci* 3:1018–1026.
- Goldman, M.S., Golowasch, J., Marder, E. and Abbott, L.F. (2000). Dependence of firing pattern on intrinsic ionic conductances: sensitive and insensitive combinations. *Neurocomputing* 32:141–146.
- Goldman, M.S., Golowasch, J., Marder, E. and Abbott, L.F. (2001). Global structure, robustness, and modulation of neuronal models. *J Neurosci* 21:5229–5238.
- Golowasch, J., Abbott, L.F. and Marder, E. (1999a). Activity-dependent regulation of potassium currents in an identified neuron of the stomatogastric ganglion of the crab *Cancer borealis*. *J Neurosci* 19:RC33.
- Golowasch, J., Casey, M., Abbott, L.F. and Marder, E. (1999b). Network stability from activity-dependent regulation of neuronal conductances. *Neural Comput* 11:1079–1096.
- Golowasch, J., Goldman, M.S., Abbott, L.F. and Marder, E. (2002). Failure of averaging in the construction of a conductance-based neuron model. *J Neurophysiol* 87:1129–1131.
- Gonzalez-Islas, C. and Wenner, P. (2006). Spontaneous network activity in the embryonic spinal cord regulates AMPAergic and GABAergic synaptic strength. *Neuron* 49:563–575.
- Haedo, R.J. and Golowasch, J. (2006). Ionic mechanism underlying recovery of rhythmic activity in adult isolated neurons. *J Neurophysiol* 96:1860–1876.
- Hebb, D.O. (1949). The organization of behavior: a neuropsychological theory. Wiley, New York.
- Hsu, D. and Beggs, J.M. (2006). Neuronal avalanches and criticality: a dynamical model for homeostasis. *Neurocomputing* 69:1134–1136.
- Karmarkar, U.R. and Buonomano, D.V. (2006). Different forms of homeostatic plasticity are engaged with distinct temporal profiles. *Eur J Neurosci* 23:1575–1584.
- LeMasson, G., Marder, E. and Abbott, L.F. (1993). Activity-dependent regulation of conductances in model neurons. *Science* 259:1915–1917.
- Liu, Z., Golowasch, J., Marder, E. and Abbott, L.F. (1998). A model neuron with activity-dependent conductances regulated by multiple calcium sensors. *J Neurosci* 18:2309–2320.
- Luther, J.A., Robie, A.A., Yarotsky, J., Reina, C., Marder, E. and Golowasch, J. (2003). Episodic bouts of activity accompany recovery of rhythmic output by a neuromodulator- and activity-deprived adult neural network. *J Neurophysiol* 90:2720–2730.
- MacLean, J.N., Zhang, Y., Johnson, B.R. and Harris-Warrick, R.M. (2003). Activity-independent homeostasis in rhythmically active neurons. *Neuron* 37:109–120.
- MacLean, J.N., Zhang, Y., Goeritz, M.L. et al. (2005). Activity-independent coregulation of I-A and I-h in rhythmically active neurons. *J Neurophysiol* 94:3601–3617.
- Malenka, R. C. and Bear, M.F. (2004). LTP and LTD: an embarrassment of riches. *Neuron* 44:5–21.
- Marder, E. and Prinz, A.A. (2002). Modeling stability in neuron and network function: the role of activity in homeostasis. *Bioessays* 24:1145–1154.
- Marder, E. and Prinz, A.A. (2003). Current compensation in neuronal homeostasis. *Neuron* 37:2–4.
- Miller, K.D. (1996). Synaptic economics: competition and cooperation in synaptic plasticity. *Neuron* 17:371–374.
- Miller, K.D. and Mackay, D.J.C. (1994). The role of constraints in Hebbian learning. *Neural Comput* 6: 100–126.
- Nelson, A.B., Krispel, C.M., Sekirnjak, C. and du Lac, S. (2003). Long-lasting increases in intrinsic excitability triggered by inhibition. *Neuron* 40:609–620.
- O'Brien, R.J., Kamboj, S., Ehlers, M.D., Rosen, K.R., Fischbach, G.D. and Huganir, R.L. (1998). Activity-dependent modulation of synaptic AMPA receptor accumulation. *Neuron* 21:1067–1078.

- Prinz, A.A. (2006). Toward models of activity-dependent homeostatic network regulation based on cellular regulation mechanisms. Program No. 649.1. 2006 Neuroscience Meeting Planner. Society for Neuroscience, Atlanta. Online.
- Prinz, A.A., Billimoria, C.P. and Marder, E. (2003). Alternative to hand-tuning conductance-based models: construction and analysis of databases of model neurons. *J Neurophysiol* 90: 3998–4015.
- Prinz, A.A., Bucher, D. and Marder, E. (2004). Similar network activity from disparate circuit parameters. *Nat Neurosci* 7:1345–1352.
- Rabbah, P. and Nadim, F. (2005). Synaptic dynamics do not determine proper phase of activity in a central pattern generator. *J Neurosci* 25:11269–11278.
- Renart, A., Song, P.C. and Wang, X.J. (2003). Robust spatial working memory through homeostatic synaptic scaling in heterogeneous cortical networks. *Neuron* 38:473–485.
- Ross, W.N. (1989). Changes in intracellular calcium during neuron activity. *Annu Rev Physiol* 51:491–506.
- Schulz, D.J., Goaillard, J.M. and Marder, E. (2007). Quantitative expression profiling of identified neurons reveals cell-specific constraints on highly variable levels of gene expression. *PNAS* 104(32):13187–13191.
- Schulz, D.J., Goaillard, J.M. and Marder, E. (2006a). Variable channel expression in identified single and electrically coupled neurons in different animals. *Nat Neurosci* 9:356–362.
- Schulz, D.J., Baines, R.A., Hempel, C.M., Li, L., Liss, B. and Misonou, H. (2006b). Cellular excitability and the regulation of functional neuronal identity: from gene expression to neuromodulation. *J Neurosci* 26:10362–10367.
- Siegel, M., Marder, E. and Abbott, L.F. (1994). Activity-dependent current distributions in model neurons. *Proc Natl Acad Sci USA* 91:11308–11312.
- Soto-Trevino, C., Thoroughman, K.A., Marder, E. and Abbott, L.F. (2001). Activity-dependent modification of inhibitory synapses in models of rhythmic neural networks. *Nat Neurosci* 4:297–303.
- Su, H., Sochivko, D., Becker, A. et al. (2002). Upregulation of a T-type Ca<sup>2+</sup> channel causes a long-lasting modification of neuronal firing mode after status epilepticus. *J Neurosci* 22:3645–3655.
- Sullivan, T.J. and de Sa, V.R. (2006a). Homeostatic synaptic scaling in self-organizing maps. *Neural Netw* 19:734–743.
- Sullivan, T.J. and de Sa, V.R. (2006b). A self-organizing map with homeostatic synaptic scaling. *Neurocomputing* 69:1183–1186.
- Swensen, A.M. and Bean, B.P. (2005). Robustness of burst firing in dissociated Purkinje neurons with acute or long-term reductions in sodium conductance. *J Neurosci* 25:3509–3520.
- Szücs, A. and Selverston, A.I. (2006). Consistent dynamics suggests tight regulation of biophysical parameters in a small network of bursting neurons. *J Neurobiol* DOI 10.1002/neu.20325.
- Taylor, A.L., Hickey, T.J., Prinz, A.A. and Marder, E. (2006). Structure and visualization of high-dimensional conductance spaces. *J Neurophysiol* 96:891–905.
- Thoby-Brisson, M. and Simmers, J. (2002). Long-term neuromodulatory regulation of a motor pattern-generating network: maintenance of synaptic efficacy and oscillatory properties. *J Neurophysiol* 88:2942–2953.
- Tobin, A.E. and Calabrese, R.L. (2006). Endogenous and half-center bursting in morphologically inspired models of leech heart interneurons. *J Neurophysiol* 96:2089–2106.
- Tobin, A.E., Van Hooser, S.D. and Calabrese, R.L. (2006). Creation and reduction of a morphologically detailed model of a leech heart interneuron. *J Neurophysiol* 96:2107–2120.
- Tononi, G. and Cirelli, C. (2003). Sleep and synaptic homeostasis: a hypothesis. *Brain Res Bull* 62:143–150.
- Tononi, G. and Cirelli, C. (2006). Steep function and synaptic homeostasis. *Sleep Med Rev* 10:49–62.
- Turrigiano, G., Abbott, L.F. and Marder, E. (1994). Activity-dependent changes in the intrinsic properties of cultured neurons. *Science* 264:974–977.
- Turrigiano, G.G. (1999). Homeostatic plasticity in neuronal networks: the more things change, the more they stay the same (21:221, 1998) (22:280, 1999). *Trends Neurosci* 22:416–416.
- Turrigiano, G.G. and Nelson, S.B. (2000). Hebb and homeostasis in neuronal plasticity. *Curr Opin Neurobiol* 10:358–364.
- Turrigiano, G.G., LeMasson, G. and Marder, E. (1995). Selective regulation of current densities underlies spontaneous changes in the activity of cultured neurons. *J Neurosci* 15:3640–3652.
- Turrigiano, G.G., Leslie, K.R., Desai, N., Rutherford, L.C. and Nelson, S.B. (1998). Activity-dependent scaling of quantal amplitude in neocortical neurons. *Nature* 391:892–896.
- Zhang, Y., Oliva, R., Gisselmann, G., Hatt, H., Guckenheimer, J. and Harris-Warrick, R.M. (2003). Overexpression of a hyperpolarization-activated cation current (I<sub>h</sub>) channel gene modifies the firing activity of identified motor neurons in a small neural network. *J Neurosci* 23:9059–9067.

# 17

## HOMEOSTATIC PLASTICITY AND POST-TRAUMATIC EPILEPTOGENESIS

MAXIM BAZHENOV, ARTHUR R. HOUWELING, IGOR TIMOFEEV  
AND TERRENCE J. SEJNOWSKI

### ABSTRACT

Within 24 hours following head injury, up to 80% of patients with penetrating wounds display clinical seizures. Such acute seizures often initiate epileptogenesis – the subthreshold processes that lead to spontaneous, recurring seizures and ultimately to epilepsy. The mechanisms operating in this model of post-traumatic epileptogenesis are not well understood. We hypothesize that homeostatic plasticity, which is thought to maintain a set-point level of activity in the cortex, may fail to control ‘normal’ excitability in heterogeneous networks consisting of subpopulations of neurons with different levels of activity – conditions found in traumatized cortex. This may create an unstable balance of excitation and inhibition and lead to paroxysmal seizures. In this chapter, we discuss how this and other mechanisms may contribute to epileptogenesis after brain trauma and we propose interventions that could prevent seizures.

### INTRODUCTION

Within 24 hours up to 80% of patients with penetrating head wounds display clinical seizures (Kollevold, 1976; Dinner, 1993). Following the Vietnam and Croatia wars, approximately 50% of patients with penetrating cranial wounds developed epilepsy characterized by recurring seizures 10–15 years later (Salazar et al., 1985; Marcikic et al., 1998). What causes epilepsy in patients with penetrating brain wounds? What are the mechanisms of trauma-related epileptogenesis?

Chronically isolated slabs of neocortex, produced by gray and white matter lesions, develop chronic hyperexcitability and focal epileptogenesis (Sharpless and Halpern, 1962; Echlin and Battista, 1963; Prince, 1999). A few days after isolation, spontaneous bursts of activity appear which occur more frequently during subsequent days and weeks (Grafstein and Sastry, 1957; Sharpless and Halpern, 1962; Burns and Webb, 1979) while field potentials display slow waves at frequencies around 1 Hz (Echlin and Battista, 1963). At the same time, the isolated cortex develops an increased susceptibility to experimentally induced epileptiform activity (Grafstein and Sastry, 1957; Sharpless and Halpern, 1962; Echlin and Battista, 1963), similar to the phenomenon of disuse supersensitivity encountered in peripheral structures after deprivation of afferent inputs (Sharpless, 1969). In slices of chronically (>1–2 weeks) isolated cortex, electrical stimulation may evoke ‘epileptiform’ burst discharges (Prince and Tseng, 1993) that are initiated in layer 5 (Hoffman et al., 1994) and resemble in some ways the upstates of the slow (<1 Hz) oscillation in cortical slices (Sanchez-Vives and McCormick, 2000) and naturally sleeping cats (Steriade et al., 2001). Similar burst discharges are observed in lesioned organotypic hippocampal slice cultures (McKinney et al., 1997) and cell cultures subjected to chronic blockade of activity (Furshpan and Potter, 1989; Ramakers et al., 1990; Van Den Pol et al., 1996; Rutherford et al., 1997). The mechanisms underlying epileptogenesis in chronically isolated neocortex are unclear. Previous proposals involve the sprouting of new excitatory connections (Purpura and Housepian, 1961; Salin et al., 1995; McKinney et al., 1997), decreases in synaptic inhibition (Ribak and Reiffenstein, 1982) and increases of NMDA currents and pyramidal cell excitability (Bush et al., 1999).

Neuronal activity of acutely isolated cortex is strongly reduced (Burns, 1951; Sharpless and Halpern, 1962; Timofeev et al., 2000). Evidence from *in vitro* and *in vivo* studies suggests that chronic blockade of activity may modify synaptic

strengths and intrinsic neuronal excitability by activating homeostatic plasticity processes (Turriano, 1999; Desai et al., 2002) that upregulate depolarizing influences on excitatory neurons (such as inward ionic currents and glutamatergic synaptic conductances) and downregulate hyperpolarizing influences (such as outward ionic currents and GABAergic synaptic conductances). Homeostatic plasticity, which is thought to maintain a set-point level of activity in the cortex, may fail to control 'normal' excitability in heterogeneous networks consisting of subpopulations of neurons with different levels of activity – conditions found in traumatized cortex (Topolnik et al., 2003b). This may create an unstable balance of excitation and inhibition and lead to paroxysmal seizures. In this chapter, we explore how this and other mechanisms may contribute to epileptogenesis after brain trauma.

### SHIFT OF BALANCE BETWEEN EXCITATION AND INHIBITION AS SEIZURE TRIGGERING FACTOR

It is widely accepted that the development of epileptiform activity results from a shift in the balance between excitation and inhibition towards excitation (Dichter and Ayala, 1987; Galarreta and Hestrin, 1998; Nelson and Turriano, 1998). A well-known experimental manipulation to elicit acute seizures consists of reducing inhibition (Matsumoto and Ajmone-Marsan, 1964a, 1964b; Prince, 1978; Gutnick et al., 1982; Chagnac-Amitai and Connors, 1989a, 1989b; Steriade et al., 1998; reviewed in McNamara, 1994; Traub et al., 1996; Timofeev and Steriade, 2004). Increased inhibition and decreased excitation may also lead to a functional imbalance in cortical circuits; however, their role in seizure initiation is poorly understood. By increased 'inhibition' we mean either increased synaptic inhibition or 'disfacilitation', i.e. a temporal absence of recurrent network activity. By decreased 'excitation' we mean decreased neuronal activity in afferent structures or decreased synaptic excitation. Any of these factors may create conditions favorable to seizure generation.

One of the initiating factors for seizure generation may be a functional heterogeneity in cortical networks, such as the presence of two or more different cortical regions with relatively high and low levels of synaptic activity. Transitory or persistent reduction in synaptic activity within some cortical foci may increase the sensitivity of cortical neurons in those foci by homeostatic mechanisms (Abbott et al., 1997; Desai et al., 1999a, 1999b). Therefore, the synaptic inputs from cortical regions exhibiting moderate or high levels of activity would lead to an increased responsiveness in those cortical areas where the sensitivity is increased.

There are two lines of evidence suggesting a role for disfacilitation through deafferentation as an important factor in eliciting seizures. One is that seizures occur most often during slow-wave sleep (SWS) or during transitions from waking to SWS (see Steriade, 2003; Timofeev and Steriade, 2004). The state of SWS is characterized by the presence of long-lasting periods of disfacilitation associated with neuronal hyperpolarization (Timofeev et al., 2001). During periods of disfacilitation, synapses are likely to be released from a steady depression (Galarreta and Hestrin, 1998) which strengthens synaptic transmission and could contribute to the onset of seizures. The other evidence is based on penetrating wounds or acute experimental deafferentation, which have been described as strong epileptogenic factors (Kollevold, 1976; Dinner, 1993; Prince et al., 1997; Topolnik et al., 2003a, 2003b; Jacobs and Prince, 2005; Jin et al., 2005). In such conditions, some of the axons impinging onto postsynaptic neurons are damaged and not functioning normally. The partial deafferentation may enhance the effectiveness of the remaining synaptic inputs by homeostatic mechanisms. Thus, both factors, the sleep-related disfacilitation and the traumatic deafferentation, increase the probability of seizures via a similar mechanism of an increased effectiveness of synaptic transmission (Crochet et al., 2005; Li et al., 2005). The increased effectiveness of synaptic transmission may depend on increased levels of extracellular  $\text{Ca}^{2+}$  concentration, as reported during silent periods of network activities (Massimini and Amzica, 2001; Crochet et al., 2005) and on synaptic facilitation that follows periods of neuronal silence (Galarreta and Hestrin, 1998). Increased levels of extracellular  $\text{Ca}^{2+}$  increase the intrinsic excitability of cortical neurons and convert some neurons to burst firing (Boucetta et al., 2003). Synaptic excitability is also enhanced by trauma-related increases in glutamate levels (Sakowitz et al., 2002). In acute trauma-related seizures, however, other factors could promote seizures. These factors primarily depend on increases in extracellular levels of  $\text{K}^+$  (Moody et al., 1974) that lead to enhanced intrinsic excitability of neurons (Traynelis and Dingledine, 1988; McNamara, 1994; Topolnik et al., 2003b).

Thus, the appearance of inhomogeneous levels of excitability via overexcitation or blockage of inhibition (as following repetitive sensory or electrical stimulation, or focal injection of inhibition blockers) as well as disfacilitation or deafferentation (sleep or trauma) could be epileptogenic factors.

### LONG-LASTING HOMEOSTATIC ALTERATIONS OF EXCITABILITY AND CHRONIC EPILEPTOGENESIS

Evidence from *in vitro* studies suggests that chronic blockade of activity may modify synaptic strengths and intrinsic neuronal excitability. After a few days of pharmacological blockade of activity in cortical cell cultures, the amplitudes of mEPSCs (excitatory postsynaptic conductances) and EPSCs in pyramidal cells increase (Turrigiano et al., 1998; Watt et al., 2000) as well as release probabilities (Murthy et al., 2001). Conversely, prolonged enhanced activity levels induced by blockade of synaptic inhibition or elevated  $[K^+]_o$ , reduce the size of mEPSCs (Lissin et al., 1998; Turrigiano et al., 1998; Leslie et al., 2001). Similar activity-dependent changes in mEPSC size have been observed in spinal cell cultures (O'Brien et al., 1998). Synaptic scaling occurs in part postsynaptically by changes in the number of open channels (Turrigiano et al., 1998; Watt et al., 2000), although all synaptic components may increase (Murthy et al., 2001) including numbers of postsynaptic glutamate receptors (Rao and Craig, 1997; Lissin et al., 1998; O'Brien et al., 1998; Liao et al., 1999). There is a similar regulation of NMDA (N-methyl-D-aspartate) currents by activity (Watt et al., 2000; see, however, Lissin et al., 1998). Interestingly, mIPSCs (inhibitory postsynaptic conductances) are scaled down with activity blockade in the opposite direction to excitatory currents. This effect is reversible (Rutherford et al., 1997) and is accompanied by a reduction in the number of open GABA<sub>A</sub> channels and GABA<sub>A</sub> receptors clustered at synaptic sites (Kilman et al., 2002). In addition, intrinsic excitability is regulated by activity. After chronic activity blockade, Na<sup>+</sup> currents increase and K<sup>+</sup> currents decrease in size, resulting in an enhanced responsiveness of pyramidal cells to current injections (Desai et al., 1999a). These observations suggest the existence of a fundamental mechanism, termed 'homeostatic plasticity' (Turrigiano, 1999), that controls the levels of neuronal activity, possibly firing rates (Turrigiano et al., 1998; Murthy et al., 2001). Recent evidence indicates that some of these processes may also occur *in vivo* (Desai et al., 2002).

Homeostatic plasticity is usually considered as a gain control mechanism serving a 'positive' function in regulating neuronal activity (Wierenga et al., 2005). Indeed, under certain conditions, changes in synaptic and intrinsic excitability can compensate for a range of network activity changes and restore the 'original' level of activity (Houweling et al., 2005). What happens when the brain undergoes severe alterations of intrinsic properties or connectivity patterns following changes of neuronal activity levels? Such a condition may occur after trauma when a population of neurons is partially deafferented and thus underexcited, inducing homeostatic plasticity that upregulates depolarizing currents in excitatory cells and downregulates hyperpolarizing currents. Recent modeling studies suggest that homeostatic synaptic plasticity after a severe deafferentation of cortex can trigger homeostatic plasticity leading to a development of paroxysmal activities (Houweling et al., 2005).

Chronic exposure to tetrodotoxin (TTX) reduces epileptogenesis in chronically (10–15 days) isolated cortex (Graber and Prince, 1999, 2004). It is possible, however, that in these experiments TTX blocked all residual neuronal activity after deaffermentation and homeostatic plasticity somehow requires a minimal amount of spontaneous firing. TTX can block neuronal activity in the intact tissue around the undercut tissue, so that the deafferented neurons did not receive the cortical input needed to initiate epileptiform activity *in vivo*. Additional factors may also contribute to the epileptogenesis in chronically injured neocortex, such as axonal sprouting (Salin et al., 1995) and increased input resistances (Prince and Tseng, 1993).

### PARTIAL CORTICAL DEAFFERENTATION PROMOTES DEVELOPMENT OF PAROXYSMAL ACTIVITY *IN VIVO*

Over the past several years, we have investigated electrographical activities induced by cortical partial deafferentation (Topolnik et al., 2003a, 2003b; Nita et al., 2006a, 2006b). This partial deafferentation was achieved by means of cortical undercut. The undercut cortex (Figure 17.1A) was produced by large white matter transections below the suprasylvian gyrus (13–15 mm posteroanteriorly, 3–4 mm mediolaterally and 3–4 mm deep). A knife was inserted into the posterior part of the suprasylvian gyrus, perpendicularly to its surface at a depth of 3–4 mm, then rotated 90° and advanced rostrally along the gyrus parallel to its surface for a total distance 13–15 mm, then moved back, rotated 90° and removed from the same place where it entered the cortex. Thus, the white matter below the posterior part of the gyrus was transected, creating conditions of partial cortical deafferentation.

### ACUTE DEAFFERENTATION *IN VIVO*

Under ketamine-xylazine anesthesia, the EEG from the cortical depth exhibited a spontaneous slow oscillation (<1 Hz) (see Figure 17.1B, left panel – Control). Immediately after the undercut of the suprasylvian gyrus (earliest measurements were

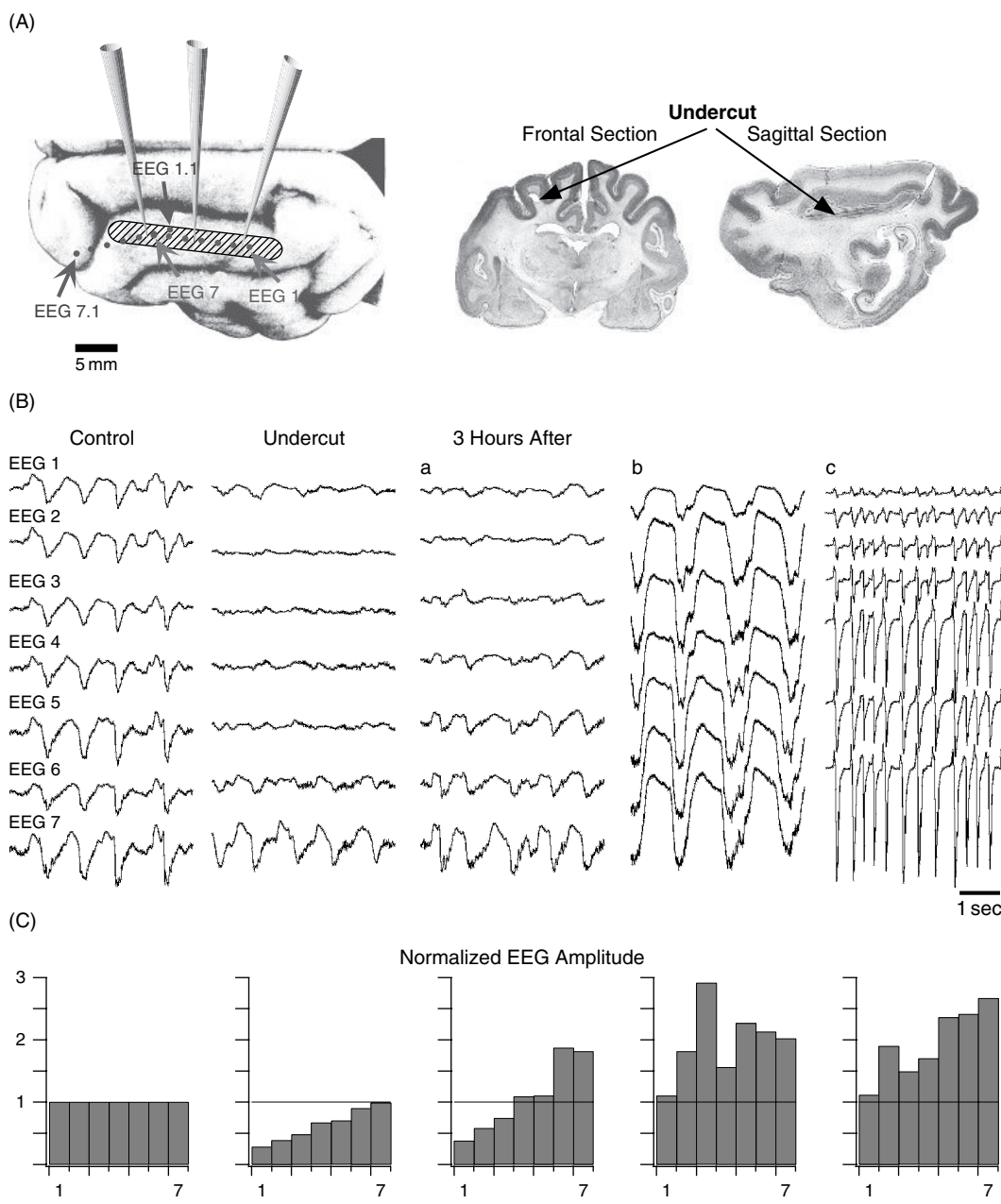


**FIGURE 17.1** Slow oscillation in intact suprasylvian gyrus is modified by cortical undercut. (A) Position of EEG arrays of electrodes and of intracellular pipettes and histology of the undercut suprasylvian gyrus. Upper panel: dorsal view of the left hemisphere. The zone of undercut is tentatively indicated by shaded area. Blue points show the generally used position of EEG electrodes (EEG1–EEG7) along the suprasylvian gyrus. Red points show the second position of EEG electrodes (EEG1.1–EEG7.1) in the postcruciate gyrus and anterior part of suprasylvian gyrus. Position of pipettes is schematically indicated. Bottom panel shows frontal and parasagittal section of the left hemisphere from two different cats showing the extent of the undercut (indicated by arrows). (B) Field potential recordings (EEG) from the intact cortex (left panel – Control), undercut suprasylvian gyrus, immediately after the undercut (middle panel – Undercut) and 3 hours later (three right panels; a, b and c, three different animals). Position of EEG electrodes was indicated in (A) by blue points. (C) depicts normalized EEG amplitude (vertical axis) of the corresponding EEG from different sites (horizontal axis). Mean EEG amplitude for each electrode in control was taken as 1. EEG1 – field potential recording from the posterior part of the suprasylvian gyrus, EEG7 – recording from the anterior part of this gyrus. Note the decreased EEG amplitude immediately after the undercut and partial recovery or increase in the amplitude 3 hours later, especially during the paroxysmal activity. From Topolnik et al., 2003a, with permission. (See Plate 10 in color plate section.)

obtained 5 min following the undercut), the amplitude of EEG waves was reduced, especially in the posterior and middle parts of the suprasylvian gyrus where the degree of deafferentation was maximal (see Figure 17.1B,C, middle panel – Undercut). The EEG activity in this partially deafferented cortex remained markedly decreased up to 1–2 hours. In a few experiments, surviving spindles (7–14 Hz) could be observed in the anterior part (electrodes 6–7) of the undercut cortex (see Plate 10–3 hours after), probably because some thalamocortical connections remained intact in those areas. Two to three hours after the undercut, the activity in the undercut cortex reorganized and increased amplitude of EEG waves in the middle and anterior parts of the suprasylvian gyrus could be detected (see Figure 17.1B,C, panels indicating 3 hours after; a, b and c, three different animals). Forty percent of the animals demonstrated paroxysmal-like activity or clear-cut electrographic seizures. By paroxysmal-like activity we mean high-amplitude slow waves with the morphological features of interictal spikes. Their amplitude was at least twice as high as during the normal slow oscillation (see Figure 17.1B,C, 3 hours after). In approximately 50% of cases, electrographic seizures developed progressively from the slow oscillation, although in the other half of the cases seizures started suddenly. The paroxysmal activities were variable in their electrographic patterns. In different experiments we observed interictal spikes, sharp waves (see Plate 10B,C – upper right panel), spike-wave (SW) and polyspike-wave (PSW) complexes at 2–3 Hz and fast runs at 10–15 Hz. Following cortical undercut, the field potential activities with increased amplitude were also found in barbiturate anesthetized cats, but these did not evolve into full-blown seizures. Recording of paroxysmal activity from the intact neighboring cortical areas revealed that electrographic seizures were always initiated in the intact cortical regions surrounding the undercut (Topolnik et al., 2003a).

The observed changes at EEG level were from modifications in the intrinsic and synaptic excitability of affected neurons. The proportion of intrinsically-bursting neurons in both relatively intact and partially deafferented regions increased about 35–40% as opposed to 15% in intact cortex of anesthetized cats (Figure 17.2). Similar bursting patterns were observed in response to depolarizing current pulses and during spontaneous transition from silent to active network states, which

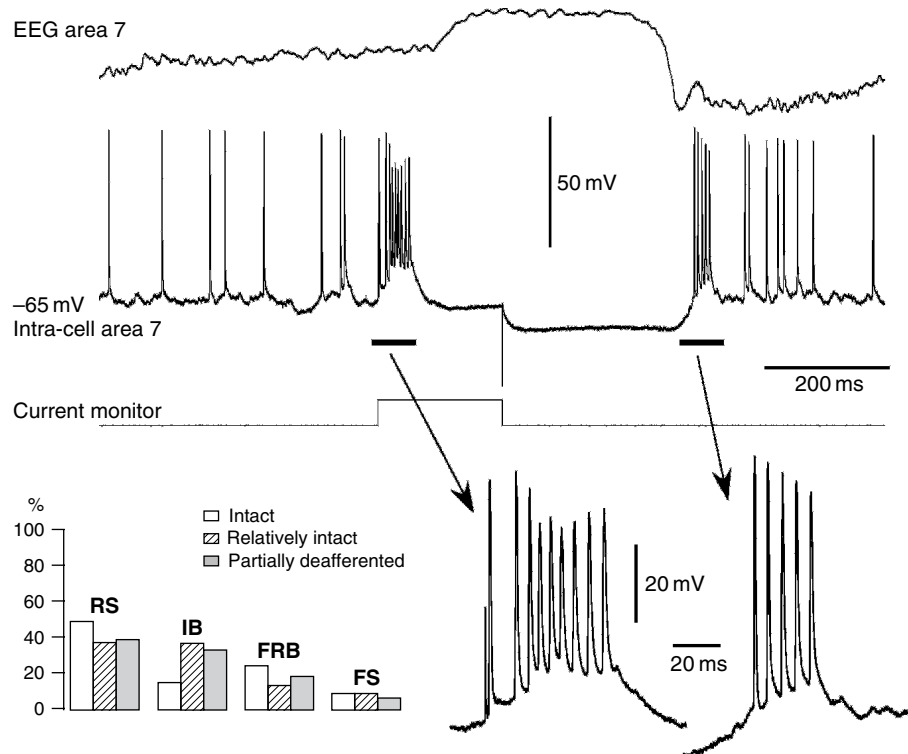
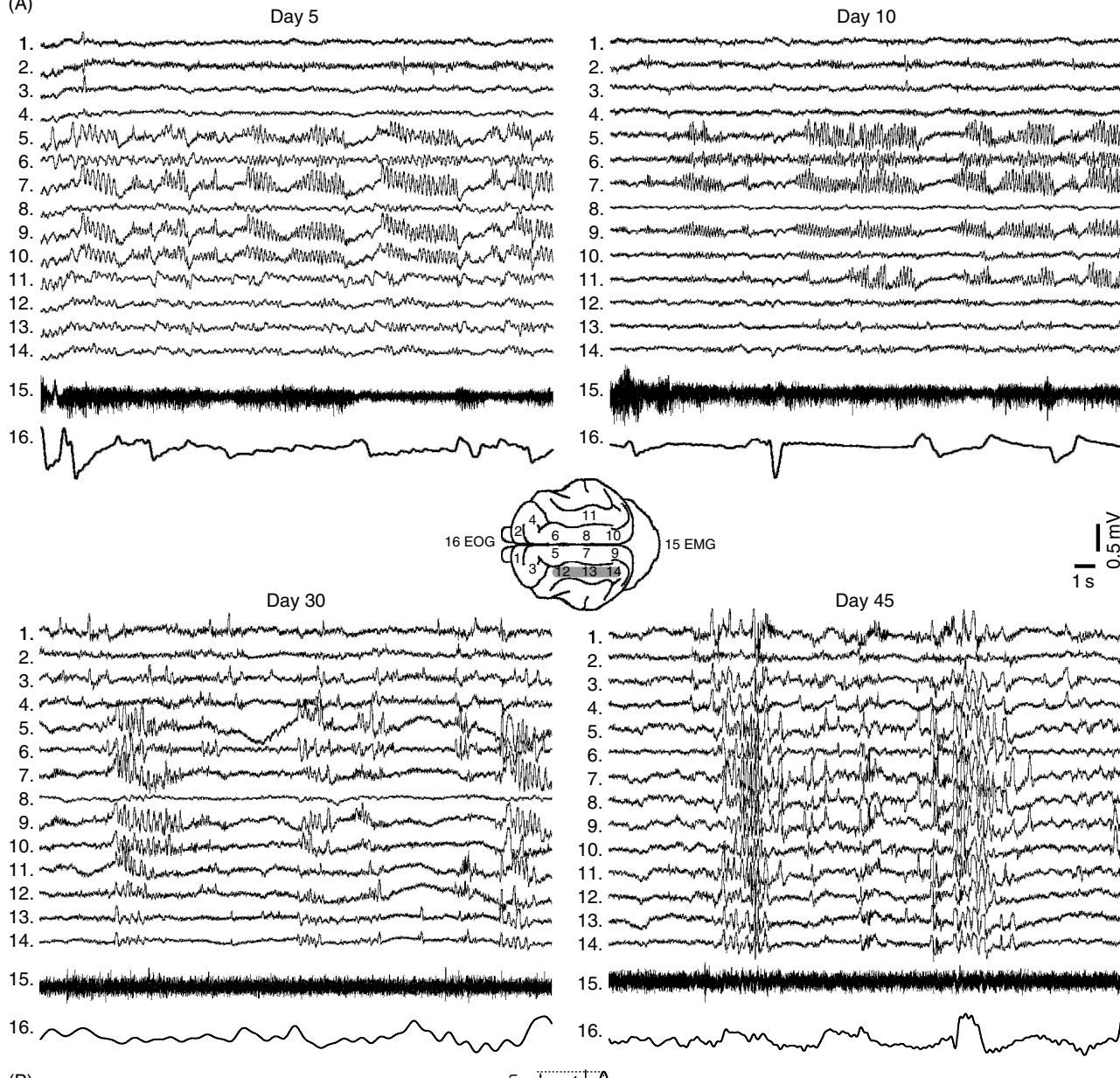
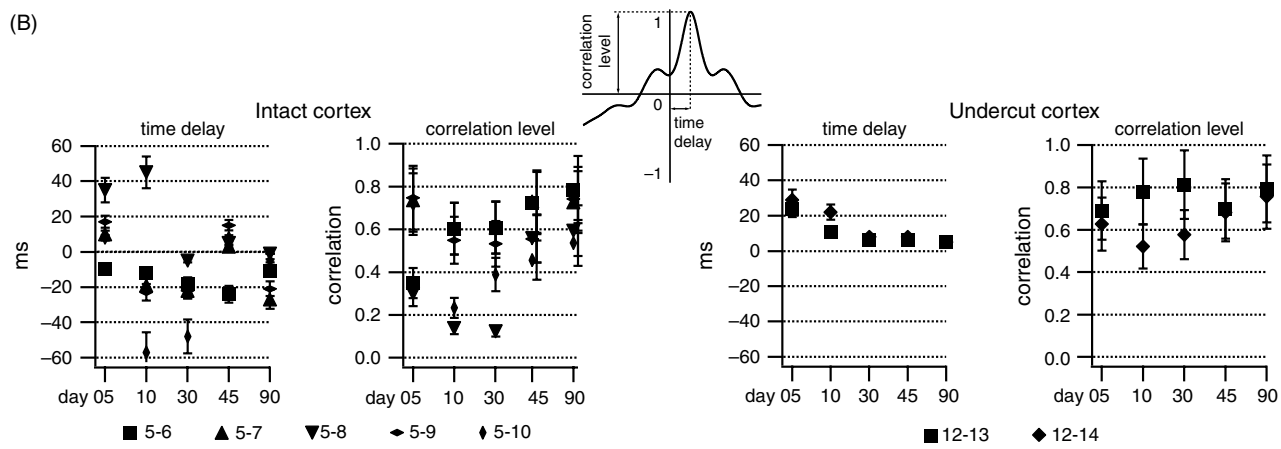


**FIGURE 17.2** Burst firing of neurons in the undercut cortex. Upper panel: a fragment of depth-EEG and intracellular recording during slow oscillation from cortical neuron showing single-spike and bursting behavior. During active network states (leftmost and rightmost parts of the panel), the neuron fires single spikes or occasionally spike-doublets. Upon direct intracellular depolarization with current pulse the neuron fires spike burst, typical for intrinsically-bursting neurons. Very similar burst is also fired by the same neuron during spontaneous transition from silent to active network states. The bursts are expanded as indicated by arrows. Bottom left histogram shows the proportion of different types of neurons in intact, relatively intact and partially deafferented cortex. RS: regular-spiking; IB: intrinsically-bursting; FRB: fast-rhythmic-bursting; FS: fast-spiking firing patterns.

(A)



(B)



correspond to transition from depth-negative to depth-positive EEG waves (Figure 17.2). Multiple factors could account for such increase in the proportion of intrinsically-bursting neurons. Among them the most important are:

1. more hyperpolarizing levels of the membrane potentials of cortical neurons (Topolnik et al., 2003b) which increase the bursting in neocortical neurons (Timofeev et al., 2000)
2. reduction of modulatory, in particular cholinergic, inputs due to cutting of cholinergic axons (acetylcholine abolishes bursting firing in intrinsically bursting neurons (Wang and McCormick, 1993)
3. increase in  $[K^+]$ , which in some neurons favors transition of regular-spiking to intrinsically-bursting firing pattern (Jensen et al., 1994; Jensen and Yaari, 1997).

The postsynaptic impact of a burst is larger than the postsynaptic impact of single spikes (Lisman, 1997; Timofeev et al., 2000), which increases the excitability of the undercut cortex and could contribute to the onset of seizures. The other factors contributing to the increase of synaptic excitability were the increase in instantaneous firing rates on regular-spiking neurons and the increase in the number of neurons revealing depolarizing sag at the onset of silent network states, which was likely mediated by H-current (Topolnik et al., 2003b).

The increased synaptic excitability could be indirectly estimated from the changes in the amplitude of evoked potentials in relatively intact and partially deafferented cortical regions elicited by intracortical electrical stimulation (see Figure 8 in Topolnik et al., 2003b). Following partial cortical deafferentation, the amplitude of evoked potentials increased in both relatively intact and partially deafferented regions, but the increase in the relatively intact areas was at least twofold larger.

#### LONG-TERM EFFECT OF DEAFFERENTATION IN VIVO

Following cortical undercut, the first seizures started 2–3 hours after the knife penetration (see above). One of the experimental artifacts that could contribute to the development of these seizures is the presence of ketamine-xylazine anesthesia. This type of anesthesia elicits paroxysmal activities in about 30% of cats (Steriade et al., 1998) and these seizures were present in over 40% of cats with acute undercut (Topolnik et al., 2003a). In chronic experiments, in which the synchronizing patterns of paroxysmal activities were studied for a period from 3 days to 5 weeks, the paroxysmal discharges were present in virtually all cats (Nita et al., 2006b).

In order to avoid the influence of this anesthesia on development of paroxysmal activities, we performed experiments with chronic undercut and the recordings were performed from non-anesthetized, head restrained cats. Multisite electrographic recordings revealed the presence of electrographic paroxysmal discharges in all experimental animals (Nita et al., 2006a). However, the patterns of these activities were not constant and developed with time (studied period 5–120 days). This evolution is depicted during the waking state in Figure 17.3A. As in data obtained under acute conditions, the paroxysmal activities on the fifth to tenth recording day were exclusively present over areas *around* the undercut cortex, especially in the marginal gyrus of the ipsilateral hemisphere (electrodes 5, 7 and 9 during days 5 and 10 in Figure 17.3A). On day 10, the paroxysmal discharges spread to some homotopic marginal foci of the contralateral hemisphere (lead 10 on day 5, Figure 17.3A). Besides the marginal gyrus, paroxysmal activity was also detected *around* the undercut, within the most posterior part of the suprasylvian gyrus. During later stages, all cats exhibited a tendency toward generalization over the whole cortical surface; the deafferented suprasylvian gyrus displayed this type of generalized paroxysmal activity only after 30–40 days (day 45 in Figure 17.3A). Average time delays and peak level of cross-correlograms computed between different cortical EEG electrodes from day 5 to day 90 (Figure 17.3B) indicated that, in the undercut, the propagation of 4 Hz activities typically had an anteroposterior pattern, while in the intact cortex, seizures started around the deafferented cortex (electrodes 7 and 9) with a more heterogeneous dynamics. A tendency toward faster propagation (smaller time-lags between electrodes) and increased correlation, both in the intact and the undercut cortex, was observed with time from day 5 to day 90.

In all studied animals ( $n = 9$ ) with the chronic undercut, we did not observe major behavioral seizures; however, in three animals abnormal tail myoclonus and/or body jerks were seen 1–4 months after the undercut. These observations suggest

**FIGURE 17.3** Topographic distributions of ictal events over the cortical surface from day 5 to day 45 during wake. (A) Polygraphic recordings in chronic cat with deafferented left suprasylvian gyrus (depicted as a gray box) indicate that paroxysmal activities are present initially in the cortical areas adjacent to the deafferented cortex and they display a tendency toward generalization in time over the whole cortical surface. (B) Average time delays and peak level of cross-correlograms performed between different cortical EEG electrodes from day 5 to day 90 in 3 different experimental animals. In the intact cortex, electrode 5 was taken as reference, while in the undercut the reference was the electrode 12. In the undercut, the propagation of 4 Hz activities regularly displayed an anteroposterior pattern, while in the intact cortex, seizures started around the deafferented cortex (electrodes 7 and 9). Data indicate a tendency toward faster propagation and increased correlation with time both in the intact and the undercut cortex. From Nita et al. (2006a), with permission.

that seizure activity progressively develops in the traumatized brain. Initially recorded local electrographic seizures become generalized after several weeks from the undercut, but this electrographic activity does not cause behavioral seizures. One or several months later, the initial signs of behavioral seizures become apparent.

### MODELING OF HOMEOSTATIC SYNAPTIC PLASTICITY PROCESSES LEADING TO EPILEPTOGENESIS

We hypothesized that the post-traumatic epileptogenesis in chronically isolated neocortex results from homeostatic plasticity (a mechanism generally assumed to stabilize neuronal activity) induced by low neuronal activity after deafferentation. To test this hypothesis, we constructed computer models of neocortex incorporating a biologically-based homeostatic plasticity rule that operates to maintain firing rates (Houweling et al., 2005). The cortical network model consisted of 5000 cortical pyramidal neurons and 1250 interneurons and deafferentation consisted of removing the extrinsic excitatory inputs from all the cells (Houweling et al., 2005). After deafferentation, homeostatic upregulation of excitatory synapses on pyramidal cells, either with or without concurrent downregulation of inhibitory synapses or upregulation of intrinsic excitability, initiated slowly repeating burst discharges that closely resembled the epileptiform burst discharges recorded in chronically isolated neocortex. These burst discharges lasted a few hundred milliseconds, propagated at 1–3 cm/s and consisted of large (10–15 mV) intracellular depolarizations topped by a small number of action potentials (Houweling et al., 2005).

#### NETWORK MODEL DESIGN

The responses of neocortical pyramidal cells (PY) and interneurons (IN) were simulated using Hodgkin-Huxley-style reduced two-compartment models (Mainen and Sejnowski, 1996). The axosomatic compartment contained a leak current  $I_{leak}$  and fast Na<sup>+</sup> and K<sup>+</sup> currents for action potential generation,  $I_{Na}$  and  $I_K$ . The dendritic compartment contained  $I_{leak}$ ,  $I_{Na}$ , a high-voltage activated Ca<sup>2+</sup> current  $I_{Ca}$ , a slow non-inactivating K<sup>+</sup> current  $I_M$  and a Ca<sup>2+</sup>-activated K<sup>+</sup> current  $I_{KCa}$ . A persistent Na<sup>+</sup> current  $I_{NaP}$  (Golomb and Amitai, 1997) was added to the dendritic compartment of PY cells. Maximal conductance values ( $\bar{g}$ ) and descriptions of currents were identical to those in Mainen and Sejnowski (1996), except for  $\bar{g}_{NaP} = 0.07 \text{ mS/cm}^2$  and  $\bar{g}_{Ca} = 0.01 \text{ mS/cm}^2$ . The leak reversal potential of each cell was drawn from a normal distribution with mean  $-70 \text{ mV}$  and standard deviation  $\sigma = 4 \text{ mV}$ . All simulations used NEURON (Hines and Carnevale, 1997).

Synaptic connections between cells were both sparse and local, i.e. each cell connected with a probability of 20% to cells within a radius of 5% of the size of the network. We also considered networks with dense local connectivity (100% connection probability within the synaptic footprint) and networks with sparse all-to-all connectivity. On average, each PY cell connected to 100 ( $\pm 9$ ) PY cells with AMPA and NMDA synapses and to 25 ( $\pm 4$ ) IN cells with AMPA synapses, and each IN cell connected to 100 ( $\pm 9$ ) PY cells and 25 ( $\pm 4$ ) IN cells with GABA<sub>A</sub> synapses. All synapses contacted the dendritic compartments. The synaptic footprint shape was square, i.e. synaptic conductance values of a particular type were the same for different pairs of connected cells. NMDA current was included at PY-PY synapses with a ratio of NMDA:AMPA peak current of 0.15 (in zero Mg<sup>2+</sup>) in agreement with experimental values of 0.1–0.2 (Spruston et al., 1995; McAllister and Stevens, 2000). AMPA and GABA<sub>A</sub> receptor-mediated currents were represented by an instantaneous increase in synaptic conductance  $g$  followed by exponential decay:

$$\frac{dg}{dt} = -\frac{g}{\tau} + \bar{g} \sum_i D_i \delta(t - t_i) \quad (1)$$

$$I = g(V - E) \quad (2)$$

Here,  $\bar{g}$  is the maximal conductance increase per synaptic event,  $t_i$  is the time of the  $i$ -th synaptic event,  $\delta(t)$  is the delta function,  $D_i$  is a depression variable representing the fraction of available ‘synaptic resources’ for release at  $t_i$  (see below),  $I$  is the synaptic current,  $V$  is the membrane potential and  $E$  is the synaptic reversal potential. The time constant of decay  $\tau$  was 5 ms for both AMPA and GABA<sub>A</sub> currents and the reversal potentials were 0 and  $-70 \text{ mV}$  respectively. The NMDA current was modeled as a difference of two exponentials, with time constants of rise ( $\tau_1$ ) and decay ( $\tau_2$ ) of 2 and 80 ms respectively (see also Wang, 1999):

$$\frac{dc_1}{dt} = -\frac{c_1}{\tau_1} + \bar{c} \sum_i D_i \delta(t - t_i), \quad \frac{dc_2}{dt} = -\frac{c_2}{\tau_2} + \bar{c} \sum_i D_i \delta(t - t_i) \quad (3)$$

$$I = (c_2 - c_1)(V - E)/(1 + \exp(-0.062V)/3.57) \quad (4)$$

The NMDA current, with synaptic conductance  $c_2 - c_1$ , had a time-to-peak of  $\sim 8$  ms and a maximal conductance increase per synaptic event proportional to  $\bar{c}$ . The last term in Equation (4) represents the voltage-dependent  $Mg^{2+}$  block of the NMDA current (Jahr and Stevens, 1990).

A small amount of short-term synaptic depression was incorporated at PY-PY synapses (Abbott et al., 1997; Tsodyks and Markram, 1997):

$$\frac{dD}{dt} = \frac{1-D}{\tau_D} - U \sum_i D_i \delta(t - t_i) \quad (5)$$

with  $U = 0.05$  and  $\tau_D = 750$  ms, which depressed EPSPs at firing rates of 5 Hz to approximately 86% of the maximal size.  $D_i$  is value of  $D$  immediately before the  $i$ th event. In the intact cortex model, each PY and IN cell received AMPAergic synaptic input from extrinsic afferents, modeled as an independent Poisson process with a rate of 1000 Hz and an average synaptic conductance of  $G_{ex-PY}$  and  $G_{ex-IN}$ , respectively.

### ASYNCHRONOUS NETWORK STATE AND ACUTE EFFECTS OF DEAFFERENTATION

Our model of intact cortex consisted of 5000 PY and 1250 IN cells, with local (within 10% of the size of the network) but sparse (20% connection probability) synaptic connections between all cell types (Houweling et al., 2005). Extrinsic afferent synapses (e.g. from the thalamus and other cortical areas) provided glutamatergic inputs to both PY and IN cells. The values of the synaptic parameters in the model were constrained using the following assumptions:

1. the network activity is characterized by minimal correlations of the spike discharges of neighboring neurons (Noda and Adey, 1970)
2. spontaneous firing rates of neurons are low, with mean firing rate of around 5–20 Hz (Hobson and McCarley, 1971; Sanseverino et al., 1973; Legendy and Salzman, 1985; Steriade et al., 2001)
3. synaptic activity makes up a large fraction of the input conductance of cells *in vivo* (Paré et al., 1998).

An asynchronous network state was obtained only when the average conductance  $G$  of recurrent synapses was smaller than that of extrinsic synapses:  $G_{PY-PY} < G_{ex-PY}$  and  $G_{PY-IN} < G_{ex-IN}$ . With  $G_{PY-PY}/(G_{PY-PY} + G_{ex-PY}) = G_{PY-IN}/(G_{PY-IN} + G_{ex-IN}) = 0.25$ , the network settled into asynchronous firing at rates close to 5 Hz (PY cells) and 10 Hz (IN cells) and input resistances of about 40% of those of isolated cells (Figure 17.4A).

Deafferentation consisted of removing the extrinsic excitatory inputs from all PY and IN cells. Immediately after deafferentation, the average membrane potential of PY cells dropped from  $-62.2 \pm 1.6$  mV to  $-69.2 \pm 4.3$  mV, which closely resembled measured values in awake (Steriade et al., 2001) and deafferented cortex (Timofeev et al., 2000). Deafferentation also dramatically reduced the firing rates of PY and IN cells to on average 0.7 and 0.2 Hz, respectively (Figure 17.4B). A small fraction of PY (13%) and IN (6%) cells was spontaneously active due to variability in leak current reversal potential ( $E_{leak}$ ) values. The size of individual EPSPs in PY cells was approximately 0.3 mV.

### HOMEOSTATIC PLASTICITY MODELING

Chronic activity blockade in culture systems sets into action a variety of homeostatic processes. These processes include upregulation of synaptic efficacy between PY cells, downregulation of inhibitory synaptic strength on PY cells and enhancement of intrinsic excitability of PY cells by changes in  $Na^+$  and  $K^+$  current densities. In particular, after two days of activity blockade mEPSCs are upregulated by 60–100% (Rutherford et al., 1998; Turrigiano et al., 1998; Watt et al., 2000) and evoked EPSCs by 150–200% (Turrigiano et al., 1998), with a similar upregulation for AMPA and NMDA components (Watt et al., 2000) and mIPSCs are downregulated by 40–60% (Rutherford et al., 1998; Kilman et al., 2002).

We assumed that the homeostatic regulation of synaptic and/or intrinsic conductances controlled the average firing rate  $F$  of PY cells (Turrigiano et al., 1998; Murthy et al., 2001). Because the time scale of homeostatic plasticity is very slow compared to that of neuronal integration and network states depended only on peak synaptic conductances, average firing rate was measured every 20 seconds and conductances were updated in the model by adding (or subtracting) a small constant value until a steady state was reached with  $F$  equal to the target average firing rate ( $T$ ). This method provides a correct development of network activity states (as long as  $F \leq T$ ) without explicit knowledge of the homeostatic synaptic

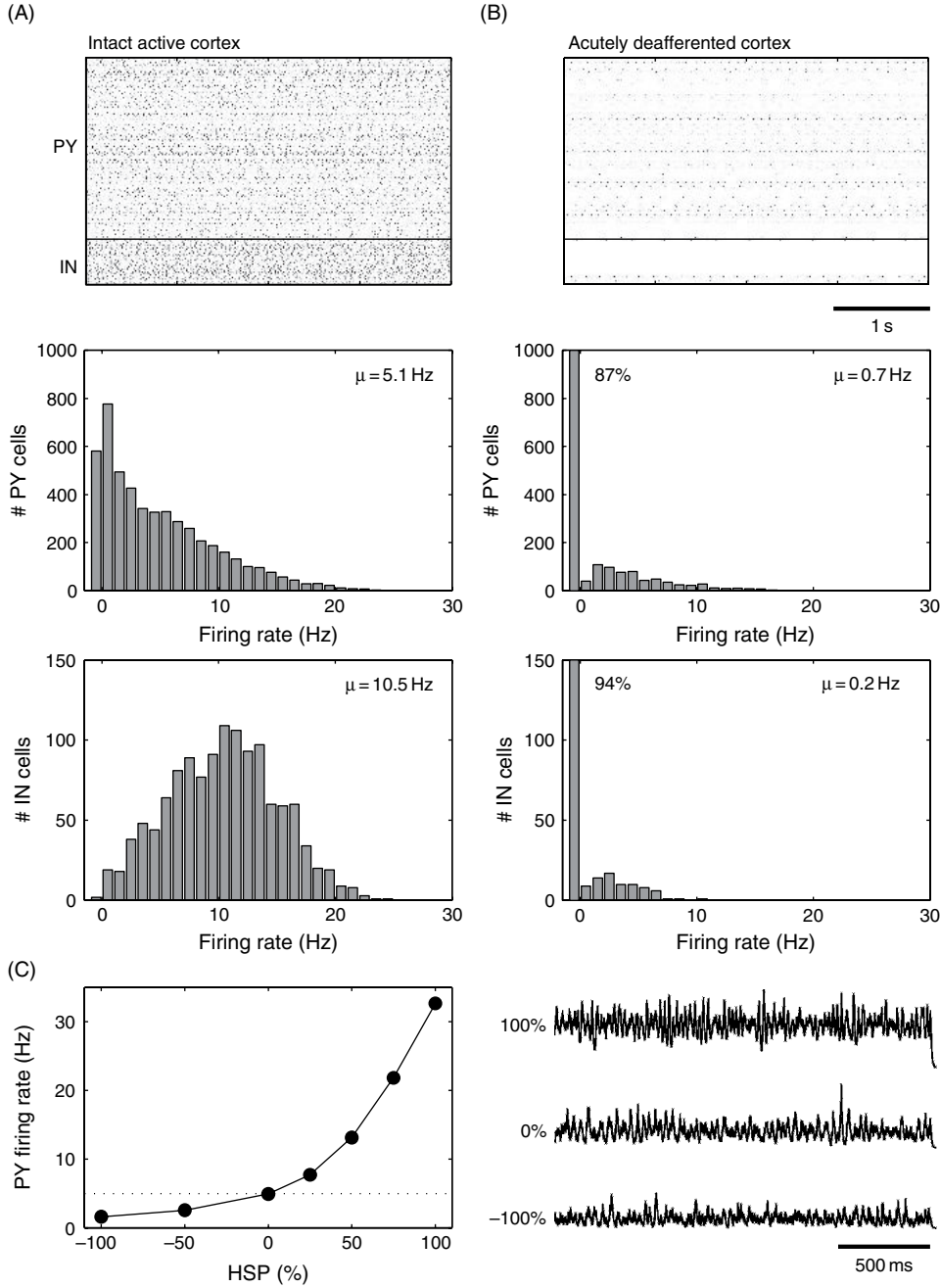


**FIGURE 17.4** Computer model of intact and acutely deafferented cortex models. Each dot represents the spike from a single model neuron. Each line in the raster plot is from a single neuron. The PY cells are in the top part of the diagram and the IN cells are shown in the bottom part. The spike rasterplots are shown for (A) intact cortex and (B) acutely deafferented cortex. The corresponding firing rate histograms are shown below. (C) Synaptic scaling in intact cortex modulated the average firing rate of PY cells while maintaining a low-amplitude irregular LNP. The LNPs are scaled by the reverse of the square root of their means for comparison purposes. The simulations in (C) were performed in a network with 500 PY and 125 IN cells and sparse all-to-all synaptic connectivity. Adapted from Houweling et al. (2005), with permission.

plasticity (HSP) rate functions, although it does not provide the time course of homeostasis. We assumed that a  $k\%$  increase in  $\bar{g}_{PY-PY}$  occurs concurrently with a  $0.5k\%$  decrease in  $\bar{g}_{IN-PY}$ :

$$\frac{1}{\bar{g}_{IN-PY}(t=0)} \frac{d\bar{g}_{IN-PY}}{dt} = -0.5 \frac{1}{\bar{g}_{PY-PY}(t=0)} \frac{d\bar{g}_{PY-PY}}{dt}, F \leq T$$

This constant relationship is predicted from the exponential time course of homeostatic regulation in silenced cell cultures (Murthy et al., 2001).

### LONG-TERM EFFECTS OF HOMEOSTATIC SYNAPTIC PLASTICITY IN DEAFFERENTED CORTEX

We hypothesized that the strongly reduced levels of neuronal activity in deafferented cortex activated homeostatic synaptic plasticity. To test this hypothesis we examined a simple phenomenological model of homeostatic plasticity (see above). The homeostasis rule assumes that homeostatic plasticity occurs whenever the average firing rate of PY cells,  $F$ , drops below a target firing rate,  $T$ , which was set at the average firing rate of PY cells in intact cortex, 5 Hz, so that intact cortex is at steady state. We first focused on the synaptic homeostatic processes. Homeostatic synaptic plasticity involved the regulation, in opposite directions, of PY-PY and IN-PY synaptic strengths. We assumed that a  $k\%$  increase in PY-PY peak conductance occurred in the same amount of time as a  $0.5k\%$  decrease in IN-PY conductance. Thus, in close agreement with observations in cell cultures after two days of activity blockade (Rutherford et al., 1997, 1998; Turrigiano et al., 1998; Watt et al., 2000; Kilman et al., 2002), a 100% upregulation of PY-PY synaptic strength was accompanied by a 50% downregulation of IN-PY synaptic strength, which is designated an HSP value of 100%.

To understand the effect of homeostatic rules in the intact cortex model (without deafferentation), we scaled PY-PY and IN-PY synaptic strengths (in opposite directions). Synaptic scaling modulated firing rates while maintaining network activity characterized by a low-amplitude irregular LNP (see Figure 17.4C).

In the deafferented cortex, homeostatic synaptic plasticity had initially little effect on network activity. Up to 60% HSP, firing rates were similar to those in the acutely deafferented network (Figure 17.5A). PY cells fired at an average rate of 0.9 Hz and IN cells at 0.3 Hz. After 63% HSP, the spontaneous activity of the network changed in a qualitative manner (Figure 17.5B). Occasionally, locally generated spike bursts propagated through the network. These burst discharges were approximately 200–400 ms in duration and involved multiple spikes in PY and IN cells (Figure 17.5B). Bursts were generated by network interactions because none of the cells possessed intrinsic bursting mechanisms (all PY cells were of the regular-spiking type). As the average number of spikes per PY cell measured over long periods of time (1.4 Hz) was still below the homeostasis target frequency of 5 Hz, further HSP increased the occurrence of network bursts (Figure 17.5C, 65% HSP). Eventually, a steady state was reached where bursts repeated at frequencies of about 0.5 Hz and the average PY cell firing rate (5.0 Hz) equaled the homeostasis target firing rate (Figure 17.5D, 72% HSP). The amounts of HSP needed to reach steady state in four different simulations (with different seeds of the random number generator) were 65%, 69%, 70% and 71% (mean 69.4%). Note that our approach does not provide the time course of homeostasis, which requires an exact description of how the rates of homeostatic plasticity depend on average firing rate  $F$ , target firing rate  $T$  and conductance values  $\bar{g}_j$ .

Inspection of the local average membrane potentials (of 500 PY cells, corresponding to one synaptic footprint) during a spontaneous paroxysmal burst revealed the presence of large-amplitude multiphasic activity on top of a strong depolarization (Figure 17.6A). The appearance of these local average membrane potentials was similar to the paroxysmal field potentials recorded in slices of chronically deafferented cortex (Prince and Tseng, 1993; Hoffman et al., 1994). Membrane potentials of individual PY and IN cells showed a similar depolarization, lasting 200–400 ms and carrying a variable number of action potentials (Figure 17.6B). The observation that IN cells are active during these paroxysmal bursts is in agreement with recordings of pyramidal cells in slices of chronically isolated cortex, which revealed large amplitude IPSCs in voltage-clamp (Salin et al., 1995; Li and Prince, 2002) and IPSP-like hyperpolarizing potentials in current-clamp (Prince and Tseng, 1993).

The frequency at which bursts repeated, the number of spikes in bursts and the speed of burst propagation all increased in the course to steady state (see Figure 17.6C). The average number of spikes per cell during a burst more than doubled from PY  $4.5 \pm 1.8$  (SD) and IN  $2.5 \pm 1.4$  at 47% HSP to PY  $10.9 \pm 2.4$  and IN  $6.5 \pm 2.3$  at 72% HSP. To obtain a measure for burst duration, we determined for each PY cell the time interval between the first and the last spike during a burst. Using this measure, average burst duration increased from  $146 \pm 51$  ms at 47% HSP to  $251 \pm 40$  ms at 72% HSP (not shown). The velocity of burst propagation, measured in synaptic footprints (SF) per second, increased from  $8.9$  SF/s at 47% HSP to  $30.1$  SF/s at 72% HSP. If one synaptic footprint is taken to be 1 mm, these velocities become 0.89 and 3.01 cm/s, respectively. Paroxysmal bursts in slices of chronically deafferented cortex were reported to propagate at a similar range of speeds of 1–5 cm/s (Prince and Tseng, 1993; Hoffman et al., 1994).

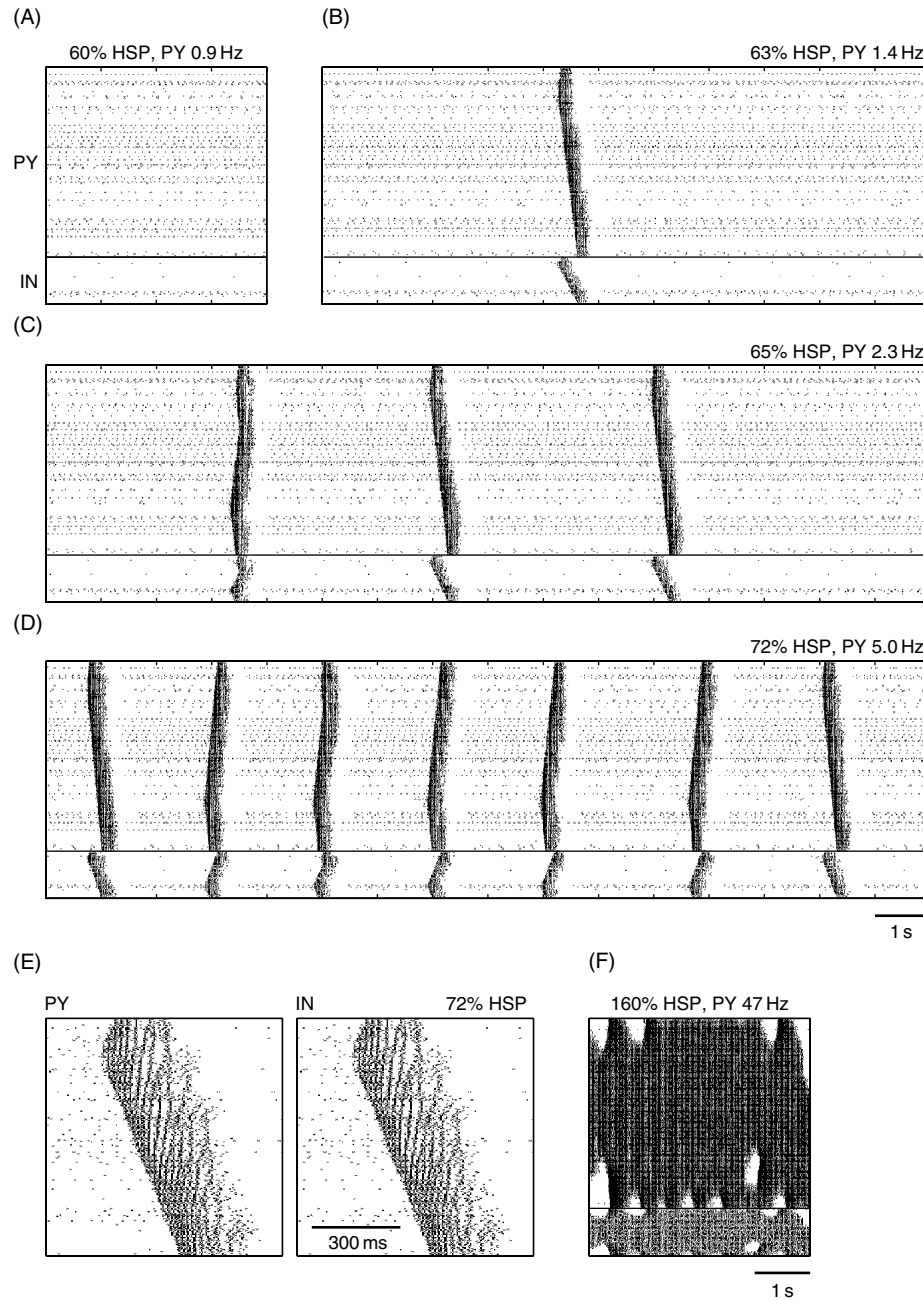


**FIGURE 17.5** Computer model of propagating burst discharges in deafferented cortex after homeostatic synaptic plasticity. Each dot represents the spike from a single model neuron. Each line in the raster plot is from a single neuron. The PY cells are in the top part of the diagram and the IN cells are shown in the bottom part. These spike rasterplots show network activity after (A) 60% HSP, (B) 63% HSP, (C) 65% HSP and (D) 72% HSP. After 72% HSP a steady state was reached for which PY cells fired on average 5.0 Hz. (E) An expanded plot of spontaneous burst at 72% HSP. (F) Large amount of homeostatic synaptic plasticity could result in sustained activity in parts of the network (1000 PYs – 250 INs; dense local synaptic connectivity). Adapted from Houweling et al. (2005), with permission.

#### EFFECT OF INTRINSIC AND SYNAPTIC CURRENTS AND SPONTANEOUS ACTIVITY

Increasing  $\bar{g}_{\text{KCa}}$  or the parameter  $U$  of short-term synaptic depression decreased burst duration and the number of spikes per burst (Figure 17.7A, left and middle-left). A complete block of  $I_{\text{KCa}}$  ( $\bar{g}_{\text{KCa}} = 0$ ) or short-term synaptic depression ( $U = 0$ ) caused burst discharges to sustain indefinitely. NMDA current at PY-PY synapses modulated burst duration and number of spikes in a similar manner (Figure 17.7A, middle-right). Interestingly, blocking NMDA current approximately halved

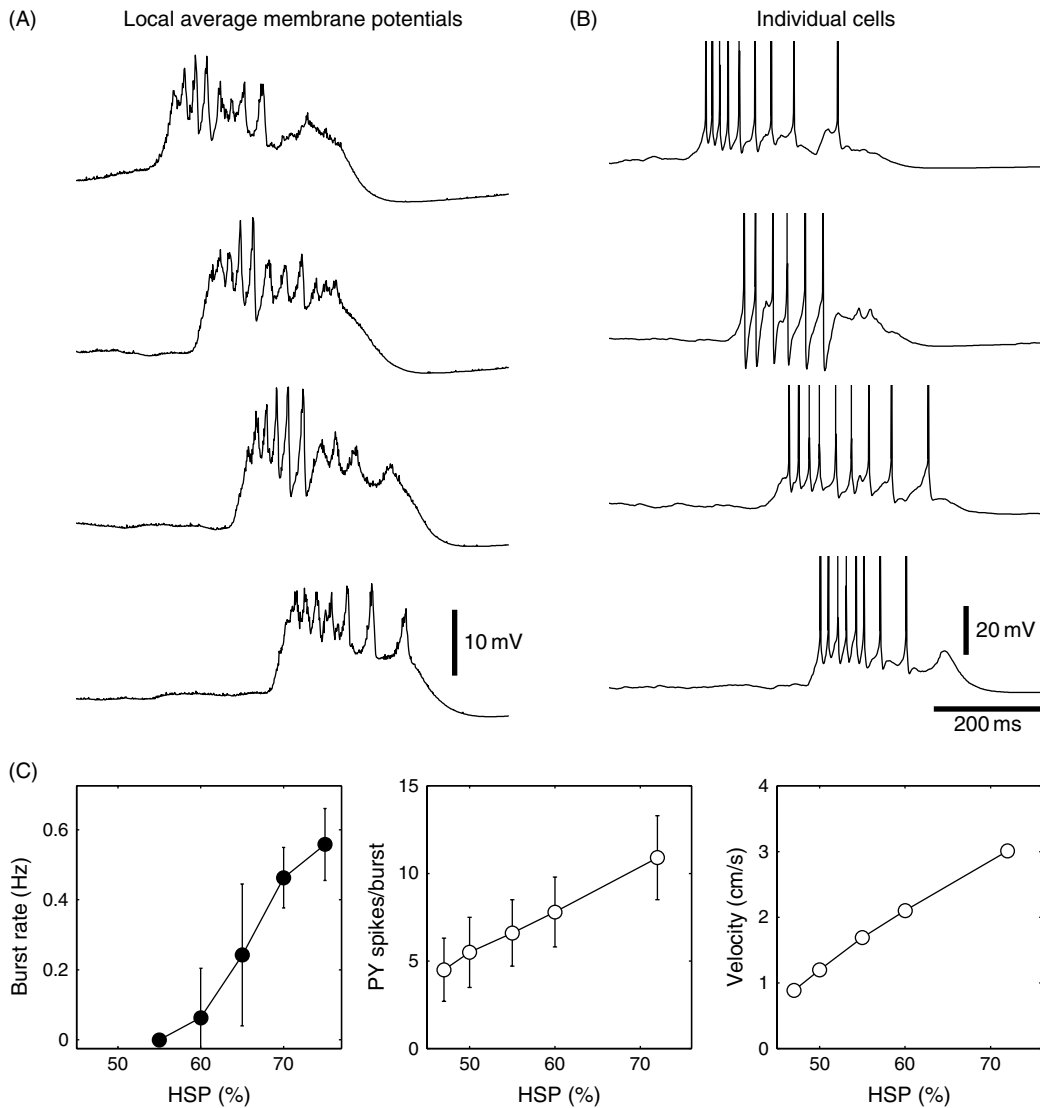


**FIGURE 17.6** Properties of paroxysmal bursts in chronically deafferented cortex. (A) Average PY cell membrane potentials at four locations (20–40–60–80% along the length of the network) during a spontaneous paroxysmal burst that occurred after 70% HSP. (B) Membrane potentials of three PY cells and one IN cell (second from top) at each of the four locations. (C) Rate at which bursts repeated, average number of PY cell spikes per burst and speed of burst propagation as a function of the amount of HSP. Number of spikes per burst and burst velocity were measured from evoked burst discharges in a model with reduced spontaneous activity. Adapted from Houweling et al. (2005), with permission.

the number of spikes per burst in networks at 70% HSP, but completely blocked burst discharges at low HSP values ( $\leq 56\%$ ). Addition of electrical synapses between IN cells had no effect on our burst measures, even for very high coupling conductances (Figure 17.7A, right). In these simulations, each IN cell was electrically coupled to, on average, 10 neighboring IN cells (randomly chosen within the synaptic footprint) and the average summated coupling conductance ( $g_{GAP}$ ) that each cell received was of the same order of magnitude as the leak conductance of individual IN cells (Amitai et al., 2002).

The frequency at which bursts repeated depended not only on the amount of HSP, but also on the spontaneous firing rates of PY cells. In the model of acutely deafferented cortex, a small fraction of cells (13%) was spontaneously active due to variability in  $E_{leak}$  values. We assessed the role of spontaneously active cells in triggering paroxysmal bursts using a different model of spontaneous activity. In this model, the variability in  $E_{leak}$  values was reduced ( $\sigma = 2 \text{ mV}$ ) to eliminate almost all spontaneous activity. Instead, each cell received glutamatergic inputs from a set of additional PY cells that were modeled as independent Poisson processes. One additional PY cell was placed at each PY location with efferent synaptic connections that were the same as those of the regular PY cell. The firing rate of the added PY cells influenced the rate at

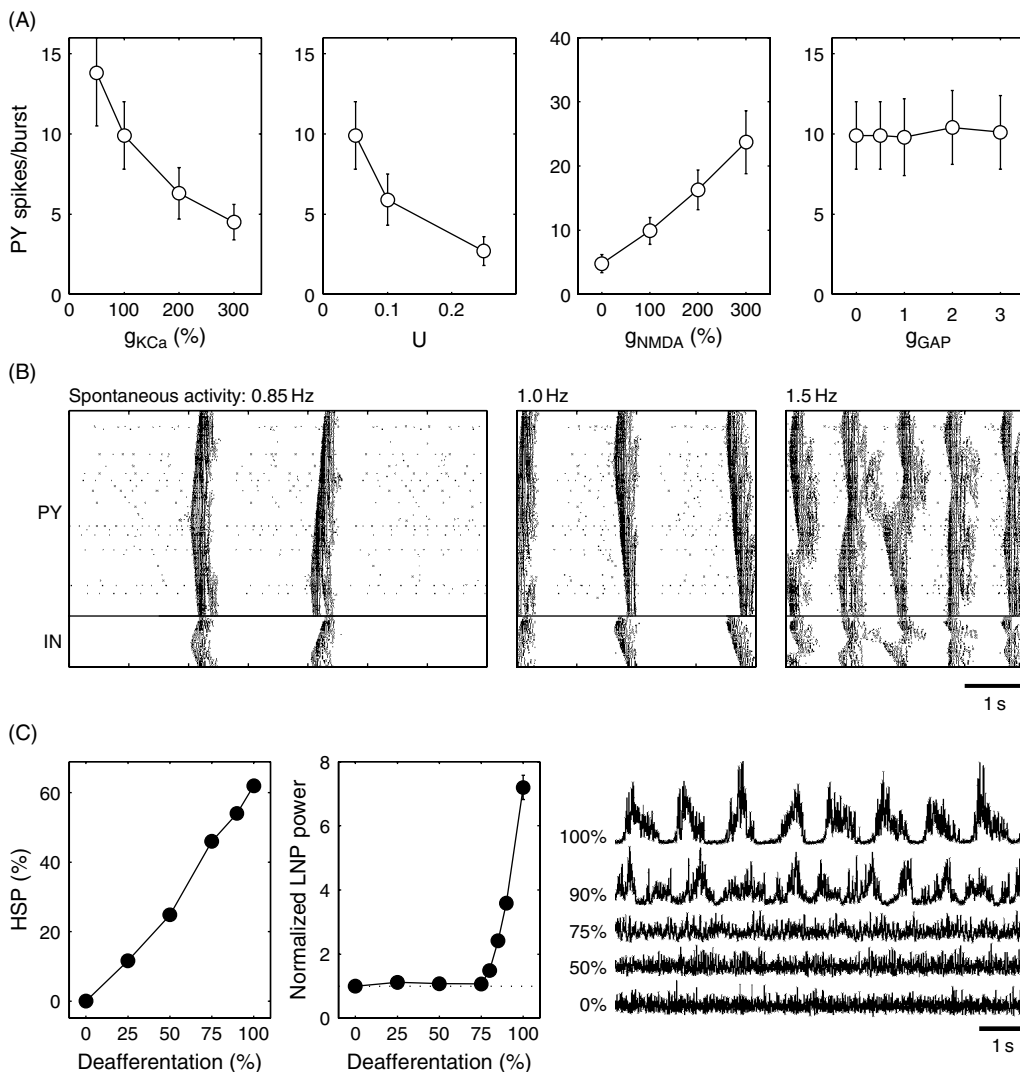


**FIGURE 17.7** Parameter dependence of burst discharges and role of spontaneous activity. (A) Dependence of the average number of PY spikes per burst on  $\bar{g}_{\text{KCa}}$ , parameter  $U$  of short-term synaptic depression,  $\bar{g}_{\text{PY-PY,NMDA}}$  and the summated electrical coupling conductance  $g_{\text{GAP}}$ . The values of  $\bar{g}_{\text{KCa}}$  and  $\bar{g}_{\text{PY-PY,NMDA}}$  are expressed as a percentage of their default values and that of  $g_{\text{GAP}}$  as a fraction of the leak conductance of individual IN cells. Burst discharges were evoked after 70% HSP. (B) Spike rasterplots of paroxysmal activity in the chronically deafferented cortex after 70% HSP. Spontaneously active cells generated Poisson-distributed random spike trains at rates of 0.85 Hz, 1.0 Hz and 1.5 Hz. (C) Homeostatic synaptic plasticity restores low-amplitude irregular network activity after partial deafferentation. The amount of HSP that was required to restore the average PY cell firing rate to 5 Hz (left) in networks that were partially deprived of afferents and the resulting average network activity computed over all PY cells (right). For each block of 100 PY cells the power of average network activity was computed. The middle panel plots the average power over all 10 blocks normalized with respect to that of intact cortex. The simulations in partially deafferented cortex were performed in networks with 1000 PY and 250 IN cells and dense local synaptic connections. Adapted from Houweling et al. (2005), with permission.

which paroxysmal events were generated (see Figure 17.7B). In a network that had been subjected to steady-state amounts of HSP, bursts appeared when the spontaneous firing rate was larger than about 0.8 Hz. Because of the random spontaneous activity, bursts were initiated at multiple locations in the network. When the spontaneous firing rate was 1.5 Hz, paroxysmal bursts repeated at regular intervals of about 1 s.

#### ONLY NEARLY COMPLETE DEAFFERENTATION LEADS TO NETWORK BURSTING ACTIVITY

Because cortical trauma may not necessarily lead to complete (100%) deafferentation, we systematically varied the degree of deafferentation and studied the effects of homeostatic synaptic plasticity. Surprisingly, only nearly complete deafferentation

resulted in slow bursting activity (see Figure 17.7C). When the model was deprived of only a fraction (<80%) of extrinsic inputs, homeostatic synaptic plasticity restored a low-amplitude irregular LNP similar to that of intact cortex. Homeostatic upregulation of the remaining extrinsic synapses on PY cells (not modeled here) may also contribute to restoring an asynchronous network state. These results indicate that only after severe deafferentation homeostatic synaptic plasticity is unable to restore an asynchronous state and periodic bursting occurs.

### ALTERNATIVE MODELS

To test the robustness of our main result further, we constructed a set of active cortex models with different physiological properties (Houweling et al., 2005): all synapse types display strong short-term depression (STD) with  $U = 0.25$  (model 1); none of the synapses display STD (model 2); none of the synapses display STD and PY cells lack  $I_{KCa}$  (model 3); PY cells lack  $I_{KCa}$  (model 4); PY-PY synapses lack an NMDA component (model 5); the NMDA:AMPA ratio at PY-PY synapses is 0.3 instead of 0.15 (model 6); each IN cell is electrically coupled to on average 10 neighboring IN cells randomly chosen within the synaptic footprint (the average summated coupling conductance that each cell receives equals the leak conductance of individual IN cells) (model 7); IN cells fire at 5 Hz instead of 10 Hz (model 8); PY cells fire at 10 Hz (homeostasis target firing rate  $T = 10$  Hz) and IN cells at 20 Hz (model 9). Two other models assumed different contributions of synaptic activity to input conductances:  $\bar{g}_{IN-PY}$  and  $\bar{g}_{IN-IN}$  were either doubled (model 10) or halved (model 11). A final set of models considered different values of  $r_{PY} = G_{PY-PY}/(G_{PY-PY} + G_{ex-PY})$  and  $r_{IN} = G_{PY-IN}/(G_{PY-IN} + G_{ex-IN})$  in the default model:  $r_{PY} = r_{IN} = 0.1$  (model 12),  $r_{PY} = r_{IN} = 0.4$  (model 13) and  $r_{PY} = 0.25$  and  $r_{IN} = 0.125$  (model 14).

The amount of HSP that was required to reach the homeostasis target firing rate after deafferentation varied between the models (Figure 17.8, top panel). In particular, models 3, 10, 13 and 14 required smaller amounts (~40% HSP) than the default model (~60% HSP, model 0), whereas model 12 required twice the amount. Nevertheless, homeostatic synaptic plasticity restored bursting states in all models except model 3, although with differences in frequency, intensity and duration of burst discharges (Figure 17.8, LNP traces). The results of model 3 indicate that either STD or  $I_{KCa}$  was required in PY cells to develop bursting. Two other interesting observations were made:

1. In model 2, burst discharges propagated for short distances only and the average firing rate  $F$  varied sharply with small changes in the amount of HSP in the steady state.
2. In model 12, even very large HSP values (up to 200%) failed to restore firing rates in fully deafferented cortex because of the small  $\bar{g}_{PY-PY}$  values (results are shown in partially (90%) deafferented cortex).

The sparseness of synaptic connections and the size of unitary EPSCs and IPSCs did not affect burst discharge properties (as long as total conductance values remained unchanged). The amount of HSP required to evoke bursts, their duration, number of spikes per cell and speed of propagation were similar in models with twofold changes in sparseness and/or number of synaptic connections per cell. A gaussian synaptic footprint shape ( $\sigma = 0.4$  radius of connectivity) instead of the default square footprint did not affect burst properties except that propagation was slower (1.72 cm/s versus 2.83 cm/s at 70% HSP). In models with dense local synaptic connections (1000 PY and 250 IN cells), relatively large HSP values ( $\geq 53\%$ ) were required to evoke propagating burst discharges compared to the sparse default model ( $\geq 47\%$ ), but all other burst measures were similar. Also, burst discharges sometimes failed to propagate at HSP values of 53–61%, which was never observed in the sparse model (at HSP values  $\geq 47\%$ ). Surprisingly, the amount of HSP to reach the homeostasis target firing rate was lower in the dense model than in the sparse model (63% versus 69%).

Besides glutamatergic inputs, cholinergic and other neuromodulatory inputs may contribute to the spontaneous firing of cells in intact cortex. Activation of cholinergic synapses increases firing rates of pyramidal neurons by decreasing an M-type  $K^+$  current and a  $Ca^{2+}$ -activated  $K^+$  current (McCormick, 1992). In large burst-firing layer 5 pyramidal cells, ACh causes an additional decrease in resting  $K^+$  conductance. The excitability of cortical interneurons is differentially regulated by ACh, causing depolarization in some GABAergic subtypes while hyperpolarization in others (Kawaguchi, 1997; Xiang et al., 1998). Cholinergic effects may be incorporated in our active cortex model by reducing  $\bar{g}_M$ ,  $\bar{g}_{KCa}$  and  $\bar{g}_{K,leak}$  in PY (and IN) cells and reducing extrinsic glutamatergic excitation to keep firing rates fixed. The resulting deafferented model, deprived of both extrinsic glutamatergic and cholinergic inputs, is identical to the default deafferented model. Thus, our results do not depend on the exact implementation of cholinergic effects on intrinsic neuronal excitability.

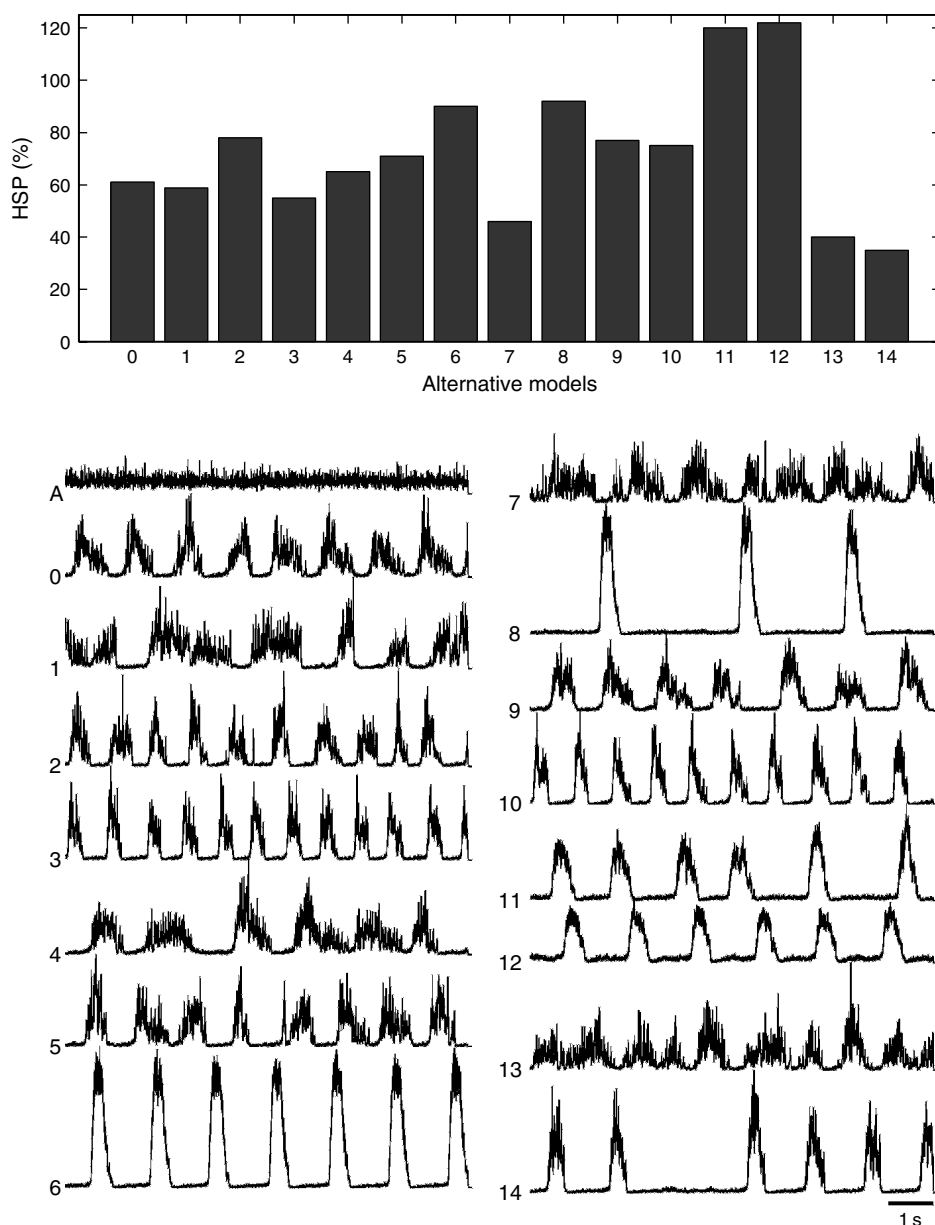


**FIGURE 17.8** Effects of homeostatic synaptic plasticity after deafferentation in models with different physiological properties. The amount of HSP that was required to restore the average PY cell firing rate in various alternative models (top). For each model the resulting LNP (computed over all PY cells) is shown. For comparison, model 0 is the default model and trace A is the LNP in its intact cortex. These simulations were performed in networks with 1000 PY and 250 IN cells and dense local synaptic connections. Adapted from Houweling et al. (2005), with permission.

#### OTHER FACTORS PROMOTING EPILEPTOGENESIS

Rearrangement of neuronal circuitry may be another factor contributing to the epileptogenesis in chronically injured neocortex. A recent study in young mesial temporal lobe epileptic patients (3–10 years old) demonstrated an enhanced glutamate receptor subunit profile, suggesting that dendritic changes precede axonal sprouting (Lynd-Balta et al., 2004). Long-term hyperexcitability and mossy fiber sprouting were observed after head trauma in hippocampus (Santhakumar et al., 2001) and computer studies revealed that even weak mossy fiber sprouting results in the spread and sustenance of seizure-like activity in a population of neurons (Santhakumar et al., 2005). There is evidence for sprouting of layer 5 pyramidal cell axons and formation of new synapses in chronically isolated cortex (Salin et al., 1995). It is not known,

however, whether new synapses are formed predominantly on pyramidal cells, which would create an enhanced recurrent excitatory circuit such as after mossy fiber sprouting in a model of temporal lobe epilepsy (Buckmaster et al., 2002). In computer studies, new synapses between pyramidal cells support epileptogenesis, but not when an equal number of new synapses was added from pyramidal cells to interneurons (Houweling et al., 2005). It is possible that axonal sprouting and the formation of new synapses is a secondary effect induced by paroxysmal activity. Indeed, the axonal sprouting of corticostriatal neurons after ischemic cortical lesions was shown to depend on synchronous neuronal activity in perilesion neocortex (Carmichael and Chesselet, 2002). Axonal sprouting is possibly the primary factor leading to an increase in the number and efficiency of physiologically identified synaptic contacts during the several weeks that follow the undercut (Avramescu and Timofeev, 2006).

## CONCLUSION

Penetrating wounds can lead to epileptogenesis and chronic seizures. The mechanisms of trauma-induced epileptogenesis are not clear. We proposed that the deafferentation triggers homeostatic plasticity mechanisms that enhance both intrinsic and synaptic excitability. The neurons in deafferented areas receive less synaptic inputs compared to adjacent intact cortex. Initially, this would hyperpolarize the deafferented cells leading to a low overall neuronal activity in these areas. According to our main hypothesis, homeostatic plasticity will then significantly increase the sensitivity of the partially deafferented neurons to the remaining synaptic inputs. Activation of these synaptic inputs upregulated by homeostatic plasticity could then cause the development of neocortical seizures within or close to the deafferented region.

Usually, antiepileptic drug therapy (for other than petit mal seizures) is aimed at increasing inhibitory activities and reducing the efficiency of sodium currents (Brodie and French, 2000; Kwan and Brodie, 2000; Brodie and Kwan, 2001). Both these measures decrease cortical excitability and, therefore, potentiate homeostatic plasticity. As a result the types of drugs applied have to be changed with certain periodicity and still some forms of epilepsy remain drug resistant. If the hypothesis that homeostatic plasticity may be a leading factor in the trauma-induced epileptogenesis is correct, then the treatment should instead be designed to reduce the homeostatic mechanisms. This could be accomplished by the use of locally applied drugs enhancing excitability of traumatized cortex and/or local electrical stimulation with properties that would not induce kindling.

## ACKNOWLEDGMENTS

This study was supported by National Institute on Deafness and Other Communication Disorders, National Institutes of Health (Grant R01 DC006306), Canadian Institutes of Health Research (Grant MOP- 37862, MOP-67175) and Natural Science and Engineering Research Council of Canada. I.T. is Canadian Institutes of Health Research scholar.

## REFERENCES

- Abbott, L.F., Varela, J.A., Sen, K. and Nelson, S.B. (1997). Synaptic depression and cortical gain control. *Science* 275:220–224.
- Amitai, Y., Gibson, J.R., Beierlein, M. et al. (2002). The spatial dimensions of electrically coupled networks of interneurons in the neocortex. *J Neurosci* 22:4142–4152.
- Avramescu, S. and Timofeev, I. (2006). Synaptic synchrony modulation following cortical injury. Society for Neuroscience Washington, DC.
- Boucetta, S., Crochet, S. and Timofeev, I. (2003). Effects of extracellular Ca<sup>2+</sup> concentration on firing properties of cortical neurons. In SFN annual meeting, Program No. 791.796. New Orleans.
- Brodie, M.J. and French, J.A. (2000). Management of epilepsy in adolescents and adults. *Lancet* 356:323–329.
- Brodie, M.J. and Kwan, P. (2001). The star systems: overview and use in determining antiepileptic drug choice. *CNS Drugs* 15:1–12; discussion 13–15.
- Buckmaster, P.S., Zhang, G.F. and Yamawaki, R. (2002). Axon sprouting in a model of temporal lobe epilepsy creates a predominantly excitatory feedback circuit. *J Neurosci* 22:6650–6658.
- Burns, B.D. (1951). Some properties of isolated cerebral cortex in the unanaesthetized cat. *J Physiol (Lond)* 112:156–175.
- Burns, B.D. and Webb, A.C. (1979). The correlation between discharge times of neighbouring neurons in isolated cerebral cortex. *Proc R Soc Lond B Biol Sci* 203:347–360.
- Bush, P.C., Prince, D.A. and Miller, K.D. (1999). Increased pyramidal excitability and NMDA conductance can explain posttraumatic epileptogenesis without disinhibition: a model. *J Neurophysiol* 82:1748–1758.
- Carmichael, S.T. and Chesselet, M.F. (2002). Synchronous neuronal activity is a signal for axonal sprouting after cortical lesions in the adult. *J Neurosci* 22:6062–6070.

- Chagnac-Amitai, Y. and Connors, B.W. (1989a). Horizontal spread of synchronized activity in neocortex and its control by GABA-mediated inhibition. *J Neurophysiol* 61:747–758.
- Chagnac-Amitai, Y. and Connors, B.W. (1989b) Synchronized excitation and inhibition driven by intrinsically bursting neurons in neocortex. *J Neurophysiol* 62:1149–1162.
- Crochet, S., Chauvette, S., Boucetta, S. and Timofeev, I. (2005). Modulation of synaptic transmission in neocortex by network activities. *Eur J Neurosci* 21:1030–1044.
- Desai, N.S., Rutherford, L.C. and Turrigiano, G.G. (1999a). Plasticity in the intrinsic excitability of cortical pyramidal neurons. *Nat Neurosci* 2:515–520.
- Desai, N.S., Nelson, S.B. and Turrigiano, G.G. (1999b). Activity-dependent regulation of excitability in rat visual cortical neurons. *Neurocomputing* 26–27:101–106.
- Desai, N.S., Cudmore, R.H., Nelson, S.B. and Turrigiano, G.G. (2002). Critical periods for experience-dependent synaptic scaling in visual cortex. *Nat Neurosci* 5:783–789.
- Dichter, M.A. and Ayala, G.F. (1987). Cellular mechanisms of epilepsy: a status report. *Science* 237:157–164.
- Dinner, D. (1993). Posttraumatic epilepsy. In: *The treatment of epilepsy: principles* (E. W., ed.) pp. 654–658. Lea & Fibinger, Philadelphia.
- Echlin, F.A. and Battista, A. (1963). Epileptiform seizures from chronic isolated cortex. *Arch Neurol* 9:154–170.
- Furshpan, E.J. and Potter, D.D. (1989). Seizure-like activity and cellular damage in rat hippocampal neurons in cell culture. *Neuron* 3:199–207.
- Galarreta, M. and Hestrin, S. (1998). Frequency-dependent synaptic depression and the balance of excitation and inhibition in the neocortex. *Nat Neurosci* 1:587–594.
- Golomb, D. and Amitai, Y. (1997). Propagating neuronal discharges in neocortical slices: computational and experimental study. *J Neurophysiol* 78:1199–1211.
- Graber, K.D. and Prince, D.A. (1999). Tetrodotoxin prevents posttraumatic epileptogenesis in rats. *Ann Neurol* 46:234–242.
- Graber, K.D. and Prince, D.A. (2004). A critical period for prevention of posttraumatic neocortical hyperexcitability in rats. *Ann Neurol* 55:860–870.
- Grafstein, B. and Sastry, P.B. (1957). Some preliminary electrophysiological studies on chronic neuronally isolated cerebral cortex. *Electroencephalogr Clin Neurophysiol Suppl* 9:723–725.
- Gutnick, M.J., Connors, B.W. and Prince, D.A. (1982). Mechanisms of neocortical epileptogenesis in vitro. *J Neurophysiol* 48:1321–1335.
- Hines, M.L. and Carnevale, N.T. (1997). The NEURON simulation environment. *Neural Comput* 9:1179–1209.
- Hobson, J.A. and McCarley, R.W. (1971). Cortical unit activity in sleep and waking. *Electroencephalogr Clin Neurophysiol* 30:97–112.
- Hoffman, S.N., Salin, P.A. and Prince, D.A. (1994). Chronic neocortical epileptogenesis in vitro. *J Neurophysiol* 71:1762–1773.
- Houweling, A.R., Bazhenov, M., Timofeev, I., Steriade, M. and Sejnowski, T.J. (2005). Homeostatic synaptic plasticity can explain post-traumatic epileptogenesis in chronically isolated neocortex. *Cereb Cortex* 15:834–845.
- Jacobs, K.M. and Prince, D.A. (2005). Excitatory and inhibitory postsynaptic currents in a rat model of epileptogenic microgyria. *J Neurophysiol* 93:687–696.
- Jahr, C.E. and Stevens, C.F. (1990). Voltage dependence of NMDA-activated macroscopic conductances predicted by single-channel kinetics. *J Neurosci* 10:3178–3182.
- Jensen, M.S. and Yaari, Y. (1997). Role of intrinsic burst firing, potassium accumulation, and electrical coupling in the elevated potassium model of hippocampal epilepsy. *J Neurophysiol* 77:1224–1233.
- Jensen, M.S., Azouz, R. and Yaari, Y. (1994). Variant firing patterns in rat hippocampal pyramidal cells modulated by extracellular potassium. *J Neurophysiol* 71:831–839.
- Jin, X., Huguenard, J.R. and Prince, D.A. (2005). Impaired Cl<sup>-</sup>extrusion in layer V pyramidal neurons of chronically injured epileptogenic neocortex. *J Neurophysiol* 93:2117–2126.
- Kawaguchi, Y. (1997). Selective cholinergic modulation of cortical GABAergic cell subtypes. *J Neurophysiol* 78:1743–1747.
- Kilman, V., van Rossum, M.C. and Turrigiano, G.G. (2002). Activity deprivation reduces miniature IPSC amplitude by decreasing the number of postsynaptic GABA(A) receptors clustered at neocortical synapses. *J Neurosci* 22:1328–1337.
- Kollevold, T. (1976). Immediate and early cerebral seizures after head injuries. Part I. *J Oslo City Hosp* 26:99–114.
- Kwan, P. and Brodie, M.J. (2000). Early identification of refractory epilepsy. *N Engl J Med* 342:314–319.
- Legendy, C.R. and Salcman, M. (1985). Bursts and recurrences of bursts in the spike trains of spontaneously active striate cortex neurons. *J Neurophysiol* 53:926–939.
- Leslie, K.R., Nelson, S.B. and Turrigiano, G.G. (2001). Postsynaptic depolarization scales quantal amplitude in cortical pyramidal neurons. *J Neurosci* 21:RC170.
- Li, H. and Prince, D.A. (2002). Synaptic activity in chronically injured, epileptogenic sensory-motor neocortex. *J Neurophysiol* 88:2–12.
- Li, H., Bandrowski, A.E. and Prince, D.A. (2005). Cortical injury affects short-term plasticity of evoked excitatory synaptic currents. *J Neurophysiol* 93:146–156.
- Liao, D., Zhang, X., O'Brien, R., Ehlers, M.D. and Huguenard, R.L. (1999). Regulation of morphological postsynaptic silent synapses in developing hippocampal neurons. *Nat Neurosci* 2:37–43.
- Lisman, J.E. (1997). Bursts as a unit of neural information: making unreliable synapses reliable. *Trends Neurosci* 20:38–43.
- Lissin, D.V., Gomperts, S.N., Carroll, R.C. et al. (1998) Activity differentially regulates the surface expression of synaptic AMPA and NMDA glutamate receptors. *Proc Natl Acad Sci USA* 95:7097–7102.
- Lynd-Balta, E., Pilcher, W.H. and Joseph, S.A. (2004). AMPA receptor alterations precede mossy fiber sprouting in young children with temporal lobe epilepsy. *Neuroscience* 126:105–114.
- Mainen, Z.F. and Sejnowski, T.J. (1996). Influence of dendritic structure on firing pattern in model neocortical neurons. *Nature* 382:363–366.
- Marcikic, M., Melada, A. and Kovacevic, R. (1998). Management of war penetrating craniocerebral injuries during the war in Croatia. *Injury* 29:613–618.
- Massimini, M. and Amzica, F. (2001). Extracellular calcium fluctuations and intracellular potentials in the cortex during the slow sleep oscillation. *J Neurophysiol* 85:1346–1350.
- Matsumoto, H. and Ajmone-Marsan, C. (1964a). Cortical cellular phenomena in experimental epilepsy: interictal manifestations. *Exp Neurol* 9:286–304.
- Matsumoto, H. and Ajmone-Marsan, C. (1964b). Cortical cellular phenomena in experimental epilepsy: ictal manifestations. *Exp Neurol* 9:305–326.

- McAllister, A.K. and Stevens, C.F. (2000). Nonsaturation of AMPA and NMDA receptors at hippocampal synapses. *Proc Natl Acad Sci USA* 97:6173–6178.
- McCormick, D.A. (1992). Neurotransmitter actions in the thalamus and cerebral cortex and their role in neuromodulation of thalamocortical activity. *Prog Neurobiol* 39:337–388.
- McKinney, R.A., Debanne, D., Gahwiler, B.H. and Thompson, S.M. (1997). Lesion-induced axonal sprouting and hyperexcitability in the hippocampus *in vitro*: implications for the genesis of posttraumatic epilepsy. *Nat Med* 3:990–996.
- McNamara, J.O. (1994). Cellular and molecular basis of epilepsy. *J Neurosci* 14:3413–3425.
- Moody, W.J., Futamachi, K.J. and Prince, D.A. (1974). Extracellular potassium activity during epileptogenesis. *Exp Neurol* 42:248–263.
- Murthy, V.N., Schikorski, T., Stevens, C.F. and Zhu, Y. (2001). Inactivity produces increases in neurotransmitter release and synapse size. *Neuron* 32:673–682.
- Nelson, S.B. and Turrigiano, G.G. (1998). Synaptic depression: a key player in the cortical balancing act. *Nat Neurosci* 1:539–541.
- Nita, D.A., Cisse, Y., Timofeev, I. and Steriade, M. (2006a). Waking-sleep modulation of paroxysmal activities induced by partial cortical deafferentation. *Cereb Cortex* 10:1093/cercor/bhj1145.
- Nita, D.A., Cisse, Y., Timofeev, I. and Steriade, M. (2006b). Increased propensity to seizures after chronic cortical deafferentation *in vivo*. *J Neurophysiol* 95:902–913.
- Noda, H. and Adey, W.R. (1970). Firing of neuron pairs in cat association cortex during sleep and wakefulness. *J Neurophysiol* 33:672–684.
- O'Brien, R.J., Kamboj, S., Ehlers, M.D., Rosen, K.R., Fischbach, G.D. and Huganir, R.L. (1998). Activity-dependent modulation of synaptic AMPA receptor accumulation. *Neuron* 21:1067–1078.
- Paré, D., Shink, E., Gaudreau, H., Destexhe, A. and Lang, E.J. (1998). Impact of spontaneous synaptic activity on the resting properties of cat neocortical pyramidal neurons *in vivo*. *J Neurophysiol* 79:1450–1460.
- Prince, D.A. (1978). Neurophysiology of epilepsy. *Annu Rev Neurosci* 1:395–415.
- Prince, D.A. (1999). Epileptogenic neurons and circuits. *Adv Neurol* 79:665–684.
- Prince, D.A. and Tseng, G.F. (1993). Epileptogenesis in chronically injured cortex: *in vitro* studies. *J Neurophysiol* 69:1276–1291.
- Prince, D.A., Jacobs, K.M., Salin, P.A., Hoffman, S. and Parada, I. (1997). Chronic focal neocortical epileptogenesis: does disinhibition play a role? *Can J Physiol Pharmacol* 75:500–507.
- Purpura, D.P. and Housepian, E.M. (1961). Morphological and physiological properties of chronically isolated immature neocortex. *Exp Neurol* 4:377–401.
- Ramakers, G.J., Corner, M.A. and Habets, A.M. (1990). Development in the absence of spontaneous bioelectric activity results in increased stereotyped burst firing in cultures of dissociated cerebral cortex. *Exp Brain Res* 79:157–166.
- Rao, A. and Craig, A.M. (1997). Activity regulates the synaptic localization of the NMDA receptor in hippocampal neurons. *Neuron* 19:801–812.
- Ribak, C.E. and Reiffenstein, R.J. (1982). Selective inhibitory synapse loss in chronic cortical slabs: a morphological basis for epileptic susceptibility. *Can J Physiol Pharmacol* 60:864–870.
- Rutherford, L.C., DeWan, A., Lauer, H.M. and Turrigiano, G.G. (1997). Brain-derived neurotrophic factor mediates the activity-dependent regulation of inhibition in neocortical cultures. *J Neurosci* 17:4527–4535.
- Rutherford, L.C., Nelson, S.B. and Turrigiano, G.G. (1998). BDNF has opposite effects on the quantal amplitude of pyramidal neuron and interneuron excitatory synapses. *Neuron* 21:521–530.
- Sakowitz, O.W., Unterberg, A.W. and Stover, J.F. (2002). Neuronal activity determined by quantitative EEG and cortical microdialysis is increased following controlled cortical impact injury in rats. *Acta Neurochir Suppl* 81:221–223.
- Salazar, A.M., Jabbari, B., Vance, S.C., Grafman, J., Amin, D. and Dillon, J.D. (1985). Epilepsy after penetrating head injury. I. Clinical correlates: a report of the Vietnam Head Injury Study. *Neurology* 35:1406–1414.
- Salin, P., Tseng, G.-F., Hoffman, S., Parada, I. and Prince, D.A. (1995). Axonal sprouting in layer V pyramidal neurons of chronically injured cerebral cortex. *J Neurosci* 15:8234–8245.
- Sanchez-Vives, M.V. and McCormick, D.A. (2000). Cellular and network mechanisms of rhythmic recurrent activity in neocortex. *Nat Neurosci* 3:1027–1034.
- Sanseverino, E.R., Agnati, L.F., Maioli, M.G. and Galletti, C. (1973). Maintained activity of single neurons in striate and non-striate areas of the cat visual cortex. *Brain Res* 54:225–242.
- Santhakumar, V., Ratzliff, A.D., Jeng, J., Toth, Z. and Soltesz, I. (2001). Long-term hyperexcitability in the hippocampus after experimental head trauma. *Ann Neurol* 50:708–717.
- Santhakumar, V., Aradi, I. and Soltesz, I. (2005). Role of mossy fiber sprouting and mossy cell loss in hyperexcitability: a network model of the dentate gyrus incorporating cell types and axonal topography. *J Neurophysiol* 93:437–453.
- Sharpless, S.K. (1969). Isolated and deafferented neurons: diffuse supersensitivity. In: *Basic mechanisms of the epilepsies* (H.W.A. Jasper and A. Pope, eds), pp. 329–348. Little Brown, Boston.
- Sharpless, S.K. and Halpern, L.M. (1962). The electrical excitability of chronically isolated cortex studied by means of permanently implanted electrodes. *Electroencephalogr Clin Neurophysiol* 14:244–255.
- Spruston, N., Schiller, Y., Stuart, G. and Sakmann, B. (1995). Activity-dependent action potential invasion and calcium influx into hippocampal CA1 dendrites. *Science* 268:297–300.
- Steriade, M. (2003). *Neuronal substrates of sleep and epilepsy*. Cambridge University Press, Cambridge.
- Steriade, M., Amzica, F., Neckelmann, D. and Timofeev, I. (1998). Spike-wave complexes and fast components of cortically generated seizures. II. Extra- and intracellular patterns. *J Neurophysiol* 80:1456–1479.
- Steriade, M., Timofeev, I. and Grenier, F. (2001). Natural waking and sleep states: a view from inside neocortical neurons. *J Neurophysiol* 85:1969–1985.
- Timofeev, I. and Steriade, M. (2004). Neocortical seizures: initiation, development and cessation. *Neuroscience* 123:299–336.
- Timofeev, I., Grenier, F., Bazhenov, M., Sejnowski, T.J. and Steriade, M. (2000). Origin of slow cortical oscillations in deafferented cortical slabs. *Cereb Cortex* 10:1185–1199.
- Timofeev, I., Grenier, F. and Steriade, M. (2001). Disfacilitation and active inhibition in the neocortex during the natural sleep-wake cycle: An intracellular study. *Proc Natl Acad Sci* 98:1924–1929.

- Topolnik, L., Steriade, M. and Timofeev, I. (2003a). Partial cortical deafferentation promotes development of paroxysmal activity. *Cereb Cortex* 13:883–893.
- Topolnik, L., Steriade, M. and Timofeev, I. (2003b). Hyperexcitability of intact neurons underlies acute development of trauma-related electrographic seizures in cats *in vivo*. *Eur J Neurosci* 18:486–496.
- Traub, R.D., Borck, C., Colling, S.B. and Jefferys, J.G. (1996). On the structure of ictal events *in vitro*. *Epilepsia* 37:879–891.
- Traynelis, S.F. and Dingledine, R. (1988). Potassium-induced spontaneous electrographic seizures in the rat hippocampal slice. *J Neurophysiol* 59:259–276.
- Tsodyks, M.V. and Markram, H. (1997). The neural code between neocortical pyramidal neurons depends on neurotransmitter release probability. *Proc Natl Acad Sci USA* 94:719–723.
- Turrigiano, G.G. (1999). Homeostatic plasticity in neuronal networks: the more things change, the more they stay the same. *Trends Neurosci* 22:221–227.
- Turrigiano, G.G., Leslie, K.R., Desai, N.S., Rutherford, L.C. and Nelson, S.B. (1998). Activity-dependent scaling of quantal amplitude in neocortical neurons. *Nature* 391:892–896.
- Van Den Pol, A.N., Obrietan, K. and Belousov, A. (1996). Glutamate hyperexcitability and seizure-like activity throughout the brain and spinal cord upon relief from chronic glutamate receptor blockade in culture. *Neuroscience* 74:653–674.
- Wang, X.J. (1999). Synaptic basis of cortical persistent activity: the importance of NMDA receptors to working memory. *J Neurosci* 19:9587–9603.
- Wang, Z. and McCormick, D.A. (1993). Control of firing mode of corticotectal and corticopontine layer V burst-generating neurons by norepinephrine, acetylcholine, and 1S,3R-ACPD. *J Neurosci* 13:2199–2216.
- Watt, A.J., van Rossum, M.C., MacLeod, K.M., Nelson, S.B. and Turrigiano, G.G. (2000). Activity coregulates quantal AMPA and NMDA currents at neocortical synapses. *Neuron* 26:659–670.
- Wierenga, C.J., Ibata, K. and Turrigiano, G.G. (2005). Postsynaptic expression of homeostatic plasticity at neocortical synapses. *J Neurosci* 25:2895–2905.
- Xiang, Z., Huguenard, J.R. and Prince, D.A. (1998). Cholinergic switching within neocortical inhibitory networks. *Science* 281:985–988.

PART

V

---

MECHANISMS OF  
SYNCHRONIZATION

---

This page intentionally left blank

# 18

## SYNCHRONIZATION IN HYBRID NEURONAL NETWORKS

JOHN A. WHITE AND THEODEN I. NETOFF

### ABSTRACT

We explore how phase-response techniques from the mathematical discipline of non-linear dynamics can be applied in cellular electrophysiological experiments. These techniques are a powerful tool for studying synchronization under normal conditions, as well as in pathological conditions like epilepsy. Applying phase-response methods in principal cells of the entorhinal cortex, we show that layer 2 spiny stellate cells synchronize strongly via mutual excitation. Layer 3 pyramidal cells also synchronize via mutual excitation, but less strongly. The inwardly rectifying cation conductance  $g_H$  is a crucial determinant of the ability of interconnected excitatory networks to synchronize. Manipulation of  $g_H$  experimentally can lead to opposing effects on excitability and synchronization. We discuss these results in the context of animal models of epilepsy.

### INTRODUCTION: SYNCHRONIZED ACTIVITY IN THE HIPPOCAMPAL FORMATION

The brain exhibits a number of EEG rhythms, generated by synchronous neuronal activity, that appear in particular behavioral contexts. Local rhythmic activity is particularly prominent in the hippocampal formation. This structure, which exhibits mainly feedforward excitatory connections, is crucial for learning and memory associated with episodes in one's own life (Squire and Zola-Morgan, 1991; Cohen and Eichenbaum, 1993; Eichenbaum, 1997) and a site of critical neuropathologies in Alzheimer's disease (Hyman et al., 1984; Van Hoesen and Hyman, 1990) and temporal lobe epilepsy (Wieser, 1983). The data that we will show are from layers 2–3 of the entorhinal cortex (EC). These neurons are responsible for delivering input from the neocortex to three subfields of the hippocampus proper: the dentate gyrus, region CA3 and region CA1.

During periods of attentiveness or intentional movement, the rat hippocampal EEG is dominated by a 4–12 Hz rhythm called the *theta rhythm* (Bland and Colom, 1993; O'Keefe, 1993), which is the product of synchronous oscillatory activity in several interconnected brain regions, including the hippocampus and EC (Bland and Colom, 1993). Closely associated with the theta rhythm is the *gamma rhythm* (Chrobak and Buzsáki, 1998a, 1998b), generated by bursts of 30–80 Hz coherent activity within each cycle of the theta rhythm. Figure 18.1A shows a recording from a putative inhibitory interneuron in EC, along with simultaneous recordings of the local gamma and theta rhythms. As a population, interneurons in EC and hippocampus fire coherently at gamma frequencies (Figure 18.1B). Putative excitatory cells in region CA1 fire high frequency bursts, 'clocked' by the theta rhythm; thus, their interspike interval histograms show power at frequencies greater than 100 Hz and near 10 Hz (Figure 18.1B). Excitatory cells in the superficial EC fire with interspike intervals that are dominated by the theta rhythm.

The theta and gamma rhythms are linked to the memory-related functions of the hippocampal region by several lines of evidence. For example, such coherent activity arises when animals are in states of active locomotion and information acquisition (Bland and Colom, 1993; Buzsáki, 2002). Disabling coherent theta activity leads to severe memory impairment (Stewart and Fox, 1990; Squire and Zola-Morgan, 1991). Theta-patterned activity induces long-term changes in synaptic efficacy thought to be linked to memory formation in the hippocampus (Larson and Lynch, 1986; Christie and Abraham, 1992). In the EC and hippocampus, the outcome of synaptic plasticity experiments depends critically on fine differences

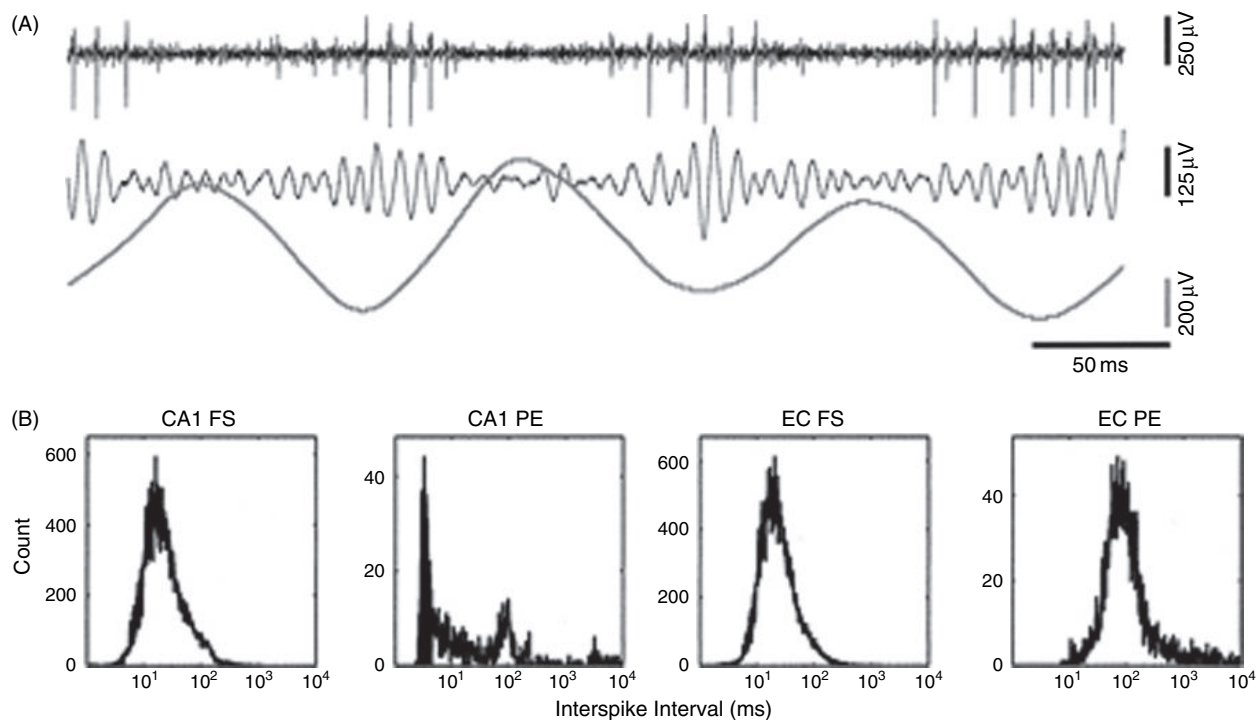


**FIGURE 18.1** Neurons in the hippocampal formation show synchronized pseudo-periodic firing. (A) The top trace shows a single-unit recording of a putative fast-spiking interneuron in the entorhinal cortex (EC). The middle and bottom traces, recorded at the same time as the single-unit recording, show local field potentials, filtered to emphasize the 30–80 Hz gamma rhythm (middle trace) and 4–12 Hz theta rhythm (bottom trace). The consistent phase relationship between these three levels of activity arises because the gamma and theta rhythms are generated by synchronized activity from single neurons. Adapted from Chrobak and Buzsáki (1998b). Used with permission. Copyright 1998 by the Society for Neuroscience. (B) Different populations show synchronization at different frequencies, as reflected in their interspike interval (ISI) distributions. Putative CA1 pyramidal cells (CA1 PE) fire in high-frequency bursts, modulated by the 10 Hz ( $10^2$  ms ISI) theta rhythm. Putative excitatory cells from EC (EC PE) fire at theta frequencies. Adapted from Frank et al. (2001). Used with permission.

in spike timing (Zhou et al., 2005; Wittenberg and Wang, 2006). Computational models incorporating nested theta-gamma oscillations are well-suited to associative and sequence-learning tasks (Wallenstein et al., 1998; Jensen and Lisman, 2005).

The tendency of neurons in the hippocampal formation to fire coherently, and to re-wire in response to coherent pre- and postsynaptic activity, may be a double-edged sword, making this structure a particularly common epileptic focus (Ben-Ari and Represa, 1990; Leite et al., 2005). In this chapter, we will describe how techniques from the mathematical discipline of *non-linear dynamics* can be applied to study normal and abnormal synchronous activity. Our work suggests that levels of cellular excitability and network synchronization can be manipulated independently, with implications for understanding epilepsy.

## RESULTS

### FACTORS CONTRIBUTING TO SYNCHRONIZED ACTIVITY IN THE HIPPOCAMPAL FORMATION

Three potential factors may contribute to synchronized neuronal activity in hippocampus:

- *External pacing.* The hippocampal/entorhinal theta rhythm has components that are sensitive and resistant to the metabotropic cholinergic antagonist atropine. Both components are diminished by lesioning or disrupting activity in the medial septum/diagonal band of Broca (MS/DB), suggesting that the MS/DB ‘paces’ the theta rhythm in the hippocampal formation (Petsche et al., 1962; Bland and Colom, 1993; Buzsáki, 2002). The MS/DB contains both cholinergic and GABAergic neurons that project to the hippocampal formation. The GABAergic neurons phase lock with the theta rhythm (Borhegyi et al., 2004; Simon et al., 2006), implying that phasic GABAergic drive contributes

to the atropine-resistant portion of the theta rhythm. Because cholinergic neurons in MS/DB do not seem to phase lock to the theta rhythm (Simon et al., 2006), and because muscarinic effects are too slow to ‘pace’ the theta rhythm, it seems unlikely that external pacing drives the atropine-sensitive portion of the theta rhythm.

- *Cellular properties.* Although the pacemaker hypothesis of hippocampal theta is appealing, abundant evidence from slice work demonstrates that both atropine-sensitive and atropine-resistant theta can be generated by local mechanisms in the absence of any phasic external input (e.g. MacVicar and Tse, 1989; Williams and Kauer, 1997; Gillies et al., 2002). At least two cell types within the hippocampal formation are biophysically constrained to generate subthreshold oscillations and tonic firing within the theta range of frequencies: glutamatergic spiny stellate cells of the EC layer 2 (Alonso and Llinas, 1989; Alonso and Klink, 1993) and GABAergic *oriens-lacunosum-moleculare* (O-LM) interneurons of the hippocampus (Maccaferri and McBain, 1996).
- *Network properties.* Of course, intrinsic theta oscillators cannot synchronize without interacting, typically via ionotropic chemical synaptic transmission. The details of the synaptic interaction matter a great deal. For example, both modeling and dynamic clamp studies demonstrate that stellate cells are prone to synchronization via mutual excitation (Acker et al., 2003; Netoff et al., 2005b). Although many classes of inhibitory interneurons can synchronize via mutual inhibition (Sohal and Huguenard, 2005), O-LM cells apparently cannot synchronize in this manner (Netoff et al., 2005b; Rotstein et al., 2005); more complex schemes seem necessary to explain how O-LM cells pace a local theta rhythm in hippocampal slices (Gillies et al., 2002; Rotstein et al., 2005).

### PHASE-RESPONSE TECHNIQUES

In *phase-response techniques*, the researcher models the effects of synaptic inputs simply in terms of how these inputs modify the timing of subsequent action potentials in the postsynaptic neuron. These techniques have a well-developed theoretical background (e.g. Kuramoto, 1984; Kopell, 1988; Ermentrout and Kopell, 1991; Hansel et al., 1995; Glass, 2001; Winfree, 2001), but here we will focus on experimental applications.

Application of phase-response techniques is made much simpler if three verifiable assumptions hold. First, most formulations require that the postsynaptic neuron be firing periodically. Second, it is helpful to assume that the synaptic input alters the firing period for only one cycle, although effects of longer cellular ‘memories’ can be accounted for (Oprisan and Canavier, 2001). Third, phase-response techniques generalize far more easily if one can assume synaptic inputs are ‘weak’ which implies that timing perturbations scale with synaptic amplitude and the effects of multiple inputs per cycle can be calculated easily (Kuramoto, 1984; Kopell, 1988; Ermentrout and Kopell, 1991; Hansel et al., 1995; Netoff et al., 2005a).

### LAYER 2 STELLATE CELLS OF ENTORHINAL CORTEX (EC) ARE WELL-ADAPTED TO SYNCHRONIZE VIA MUTUAL EXCITATION

We first applied phase-response methods in recordings from two neuronal types that fire preferentially within the 4–12 Hz theta range: EC layer 2 stellate cells and hippocampal O-LM interneurons (see above). Figure 18.2 shows an example phase-response curve, generated by delivering artificial excitatory postsynaptic conductances (EPSPs) to a stellate cell. For this neuron, ‘early’ EPSPs (i.e. EPSPs that arrived soon after the most recent postsynaptic action potential) have, on average, no effect on spike timing. The amount of scatter in responses to early EPSPs derives from the inherent jitter in interspike intervals around their average (Netoff et al., 2005b). In contrast to early EPSPs, late EPSPs consistently advance the timing of the next postsynaptic action potential.

Phase-response methods allow for easy predictions of how simple networks should behave. These predictions are straightforward to state in mathematical terms (Acker et al., 2003). Intuitively, one can understand predictions from phase-response measurements by considering a network of two stellate neurons interconnected via mutual excitation and each described adequately by Figure 18.2. If such a network is started in a near-synchronous (but not identically synchronous state), the *leading cell* would initially receive synaptic inputs just after it spikes; such inputs, from the left-hand side of the phase-response curve, would have little effect on spike timing on the average. In contrast, the *following cell* would receive inputs just before it spikes, on the right-hand side of the curve, that would advance spike timing in the following cell substantially. Because the following cell is, on average, advanced more than the leading cell, interconnected cells with this phase-response relationship would be expected to synchronize stably. The same result is obtained more formally using mathematical analysis (Acker et al., 2003) or stochastic simulation techniques (Netoff et al., 2005a, 2005b).

Figure 18.3 shows histograms of time differences ( $\Delta t$ ) in networks constructed from two interconnected stellate cells. The solid lines represent predictions made from phase-response measurements. For these predictions, we measured the

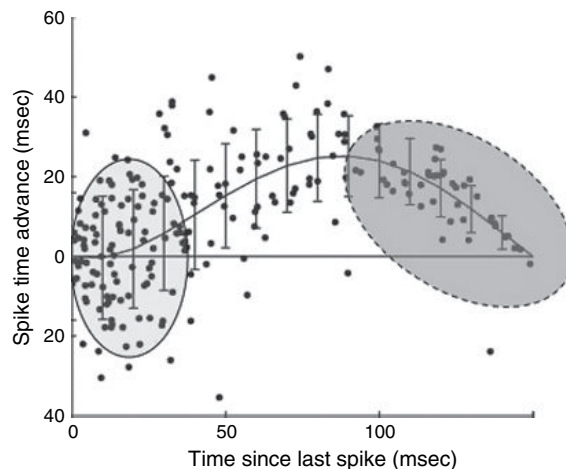


**FIGURE 18.2** Phase-response curve from a layer 2 stellate cell of the entorhinal cortex. A phase-response curve, showing the amount that an artificial EPSP arriving at a particular time during the firing cycle (x axis) advances the timing of the next postsynaptic action potential (y axis) in a periodically firing layer 2 stellate neuron. Early inputs (light gray oval with solid outline) have little effect (on average) on spike timing. Late inputs (dark gray oval with dashed outline) lead to substantial advances in timing of the next spike. As discussed in the text, this type of phase-response relationship supports synchronization via mutual excitation.

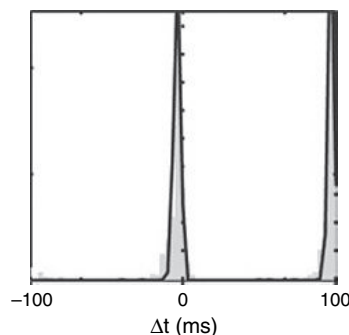


**FIGURE 18.3** Synchronization histograms of predicted and observed time differences in two-cell networks. The histogram shows counts of  $\Delta t$ , the time difference between spikes in two stellate cells connected by mutual excitation. The tight distribution near  $\Delta t = 0$  indicates near-synchronous firing. The gray bars show data from a hybrid neural network, constructed by connecting two recorded stellate cells via artificial AMPAergic synapses under dynamic clamp. The black lines show predictions from stochastic simulations derived from the phase-response curves of the two neurons. The agreement between theory and experiment is excellent.

phase-response curve for each cell, fit a polynomial to the data and estimated the standard deviation as a function of input timing, then ran stochastic simulations to generate the histogram. The gray bars represent experimental data collected by connecting the two cells under dynamic clamp via virtual AMPAergic synapses. The agreement between predicted and observed behaviors is very close. For this case, mutual excitation generates synchronization at  $\Delta t = 0$ . This behavior holds very consistently for stellate cells (Netoff et al., 2005b).

As simple as phase-response measurements and observed behaviors in two-cell networks are, they are predictive of behavior in large networks, as long as those networks have all-to-all or some other form of simple connectivity (White et al., 1998).

#### THE INWARD RECTIFYING CONDUCTANCE $G_H$ PROMOTES SYNCHRONY IN LAYER 3 PYRAMIDAL CELLS OF EC

In more recent experiments, we have begun examining phase-response relationships in layer 3 pyramidal cells of the EC. These neurons give less consistent results than layer 2 stellate cells. In the example shown in Figure 18.4 for control conditions (solid line), the phase-response curve predicts poor synchronization relative to that seen in Figure 18.3.

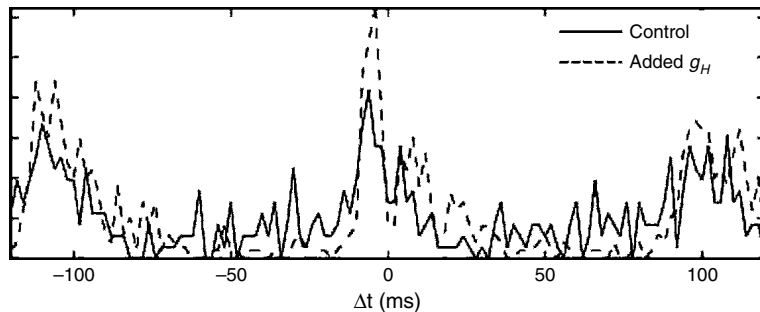


**FIGURE 18.4** Synchronization histograms for layer 3 pyramidal cells under control conditions and with increased  $g_H$ . Histograms of the spike time difference  $\Delta t$  for hybrid networks constructed from pairs of layer 3 pyramidal cells of EC, taken from hundreds of consecutive firing cycles. In control conditions (solid line), the cells synchronize somewhat weakly. Using the dynamic clamp system to increase  $g_H$ , the conductance underlying the slow inward rectifying current (dashed line), increases the tendency to synchronize.

In 6 total recordings, we saw synchronization in pyramidal cells that was consistently worse than in stellate cells. In some cases (not shown), pyramidal cells showed no synchronization at all when connected via mutual excitation.

Layer 3 cells express the HCN channels that give rise to the slow, inwardly rectifying cation conductance  $g_H$ . For a week after kainite-induced seizures,  $g_H$  is decreased and layer 3 neurons are hyperexcitable (Shah et al., 2004). Based on findings that blocking  $g_H$  tends to increase excitability (Fan et al., 2005), Shah and colleagues suggested that the decrease in  $g_H$  is an underlying cause of the post-seizure hyperexcitability. However, other studies have shown that blocking  $g_H$  has anti-convulsant effects (Kitayama et al., 2003; Gill et al., 2006), suggesting that the decrease in  $g_H$  could be a feedback mechanism intended to mitigate seizures. We sought to cast light on this issue by exploring the effects of  $g_H$  on neuronal synchronization in these cells. To do this, we used a dynamic clamp system (Dorval et al., 2001) to add to the density of  $g_H$  (Figure 18.4; we added to  $g_H$  rather than subtracting from it because adding to a conductance is more straightforward experimentally). In five out of six cases, this manipulation increased the propensity of pyramidal cells to synchronize. We quantified the effect in terms of changes in the width of the histograms like those in Figure 18.4 and found that increasing  $g_H$  increases the propensity to synchronize (i.e. narrows the spike time difference histogram) with high significance (t-test,  $n=6$ ,  $P < 0.01$ ). These preliminary data suggest that changes in the density of  $g_H$  lead to somewhat paradoxical effects: changes that decrease excitability increase the propensity for excitation-based synchronization and vice-versa.

## DISCUSSION

In the results reported here, we demonstrate the utility of phase-response methods in studying neuronal synchronization. These methods work well because their main underlying assumptions hold. In particular, timing effects of synaptic inputs are mainly confined to the next postsynaptic spike. Timing effects largely scale with synaptic input amplitude. Finally, spike-timing effects of multiple inputs per cycle can be predicted from responses to single inputs per cycle (Netoff et al., 2005a).

We applied phase-response techniques in two neuronal populations in the medial entorhinal cortex: layer 2 stellate cells and layer 3 pyramidal cells. Stellate cells are well suited to synchronize via mutual AMPAergic excitation; responses of pyramidal cells are more variable from recording to recording. Increasing  $g_H$ , the conductance of the inwardly rectifying slow cation conductance, increased the tendency of pyramidal cells to synchronize via mutual excitation.

Our results above may have implications regarding disparate changes in  $g_H$  seen in different models of epilepsy. As mentioned, after kainate-induced seizures,  $g_H$  decreases in EC layer 3 pyramidal cells (Shah et al., 2004). This change in  $g_H$  would be expected to increase cellular excitability (Shah et al., 2004; Fan et al., 2005), but our results imply that this change would also decrease the tendency of the cells to synchronize via mutual excitation, at least at low frequencies. Thus, our results may help explain the finding that increasing excitability by blocking  $g_H$  can have anti-epileptic effects (Kitayama et al., 2003; Gill et al., 2006). In another model of epilepsy (Chen et al., 2001),  $g_H$  increases, a change that would be expected to decrease excitability but potentially increase the tendency to synchronize. Our results point to the possibility that attempts to control single-neuron excitability via mechanisms of cellular homeostasis may lead to disruptions at the network level that would be difficult to detect at the cellular level.

The approach we take here is useful but of course over-simplified. Phase-response-related techniques can be extended to account for more realistic interactions including multiple populations of excitatory and inhibitory neurons (Rotstein et al., 2005; Pervouchine et al., 2006). Future efforts will extend our work on putative mechanisms of epilepsy to more complex networks.

## REFERENCES

- Acker, C.D., Kopell, N. and White, J.A. (2003). Synchronization of strongly coupled excitatory neurons: relating network behavior to biophysics. *J Comput Neurosci* 15:71–90.
- Alonso, A. and Llinas, R.R. (1989). Subthreshold Na<sup>+</sup>-dependent theta-like rhythmicity in stellate cells of entorhinal cortex layer II. *Nature* 342:175–177.
- Alonso, A. and Klink, R. (1993). Differential electroresponsiveness of stellate and pyramidal-like cells of medial entorhinal cortex layer II. *J Neurophysiol* 70:128–143.
- Ben-Ari, Y. and Represa, A. (1990). Brief seizure episodes induce long-term potentiation and mossy fibre sprouting in the hippocampus. *Trends Neurosci* 13:312–318.
- Bland, B.H. and Colom, L.V. (1993). Extrinsic and intrinsic properties underlying oscillation and synchrony in limbic cortex. *Prog Neurobiol* 41:157–208.
- Borhegyi, Z., Varga, V., Szilagyi, N., Fabo, D. and Freund, T.F. (2004). Phase segregation of medial septal GABAergic neurons during hippocampal theta activity. *J Neurosci* 24:8470–8479.
- Buzsáki, G. (2002). Theta oscillations in the hippocampus. *Neuron* 33:325–340.
- Chen, K., Aradi, I., Thon, N., Eghbal-Ahmadi, M., Baram, T.Z. and Soltesz, I. (2001). Persistently modified h-channels after complex febrile seizures convert the seizure-induced enhancement of inhibition to hyperexcitability. *Nat Med* 7:331–337.
- Christie, B.R. and Abraham, W.C. (1992). Priming of associative long-term depression in the dentate gyrus by theta frequency synaptic activity. *Neuron* 9:79–84.
- Chrobak, J.J. and Buzsáki, G. (1998a). Operational dynamics in the hippocampal-entorhinal axis. *Neurosci Biobehav Rev* 22:303–310.
- Chrobak, J.J. and Buzsáki, G. (1998b). Gamma oscillations in the entorhinal cortex of the freely behaving rat. *J Neurosci* 18:388–398.
- Cohen, N.J. and Eichenbaum, H. (1993). Memory, amnesia, and the hippocampal system. MIT Press, Cambridge.
- Dorval, A.D., Christini, D.J. and White, J.A. (2001). Real-time linux dynamic clamp: a fast and flexible way to construct virtual ion channels in living cells. *Annals Biomed Engineering* 29:897–907.
- Eichenbaum, H. (1997). How does the brain organize memories? *Science* 277:330–332.
- Ermentrout, G.B. and Kopell, N. (1991). Multiple pulse interactions and averaging in systems of coupled neural oscillators. *J Math Biol* 29:195–217.
- Fan, Y., Fricker, D., Brager, D.H. et al. (2005). Activity-dependent decrease of excitability in rat hippocampal neurons through increases in I(h). *Nat Neurosci* 8:1542–1551.
- Frank, L.M., Brown, E.N. and Wilson, M.A. (2001). A comparison of the firing properties of putative excitatory and inhibitory neurons from CA1 and the entorhinal cortex. *J Neurophysiol* 86:2029–2040.
- Gill, C.H., Brown, J.T., Shiyji, N. et al. (2006). Inhibition of Ih reduces epileptiform activity in rodent hippocampal slices. *Synapse* 59:308–316.
- Gillies, M.J., Traub, R.D., LeBeau, F.E. et al. (2002). A model of atropine-resistant theta oscillations in rat hippocampal area CA1. *J Physiol* 543:779–793.
- Glass, L. (2001). Synchronization and rhythmic processes in physiology. *Nature* 410:277–284.
- Hansel, D., Mato, G. and Meunier, C. (1995) Synchrony in excitatory neural networks. *Neural Comput* 7:307–337.
- Hyman, B.T., Van Hoesen, G.W., Damasio, A.R. and Barnes, C.L. (1984). Alzheimer's disease: cell-specific pathology isolates the hippocampal formation. *Science* 225:1168–1170.
- Jensen, O. and Lisman, J.E. (2005). Hippocampal sequence-encoding driven by a cortical multi-item working memory buffer. *Trends Neurosci* 28:67–72.
- Kitayama, M., Miyata, H., Yano, M. et al. (2003). Ih blockers have a potential of antiepileptic effects. *Epilepsia* 44:20–24.
- Kopell, N. (1988). Toward a theory of modelling central pattern generators. In: Neural control of rhythmic movements in vertebrates (A.H. Cohen, S. Rossignol and S. Grillner, eds) pp. 369–413. Wiley, New York.
- Kuramoto, Y. (1984). Chemical oscillations, waves, and turbulence. Springer-Verlag, Berlin.
- Larson, J. and Lynch, G. (1986). Induction of synaptic potentiation in hippocampus by patterned stimulation involves two events. *Science* 232:985–988.
- Leite, J.P., Neder, L., Arisi, G.M., Carlotti, C.G. Jr, Assirati, J.A. and Moreira, J.E. (2005). Plasticity, synaptic strength, and epilepsy: what can we learn from ultrastructural data? *Epilepsia* 46 Suppl 5:134–141.
- Maccaferri, G. and McBain, C.J. (1996). The hyperpolarization-activated current (Ih) and its contribution to pacemaker activity in rat CA1 hippocampal stratum oriens-alveus interneurons. *J Physiol* 497 (Pt 1):119–130.
- MacVicar, B.A. and Tse, F.W. (1989). Local neuronal circuitry underlying cholinergic rhythmical slow activity in CA3 area of rat hippocampal slices. *J Physiol* 417:197–212.
- Netoff, T.I., Acker, C.D., Bettencourt, J.C. and White, J.A. (2005a). Beyond two-cell networks: experimental measurement of neuronal responses to multiple synaptic inputs. *J Comput Neurosci* 18:287–295.
- Netoff, T.I., Banks, M.I., Dorval, A.D. et al. (2005b). Synchronization in hybrid neuronal networks of the hippocampal formation. *J Neurophysiol* 93:1197–1208.
- O'Keefe, J. (1993). Hippocampus, theta, and spatial memory. *Curr Opin Neurobiol* 3:917–924.
- Oprian, S.A. and Canavier, C.C. (2001). Stability analysis of rings of pulse-coupled oscillators: the effect of phase resetting in the second cycle after the pulse is important at synchrony and for long pulses. *Diff Equ Dyn Sys* 9:243–258.
- Pervouchine, D.D., Netoff, T.I., Rotstein, H.G. et al. (2006). Low-dimensional maps encoding dynamics in entorhinal cortex and hippocampus. *Neural Comput* 18:2617–2650.

- Petsche, H., Stumpf, C. and Gogolak, G. (1962). The significance of the rabbit's septum as a relay station between the midbrain and the hippocampus. I. The control of hippocampus arousal activity by the septum cells. *Electroencephalogr Clin Neurophysiol* 14:202–211.
- Rotstein, H.G., Gillies, M.J., Acker, C.D. et al. (2005). Slow and fast inhibition and an h-current interact to create a theta rhythm in a model CA1 interneuron network. *J Neurophysiol* 94:1508–1517.
- Shah, M.M., Anderson, A.E., Leung, V., Lin, X. and Johnston, D. (2004). Seizure-induced plasticity of h channels in entorhinal cortical layer III pyramidal neurons. *Neuron* 44:495–508.
- Simon, A.P., Poindessous-Jazat, F., Dutar, P., Epelbaum, J. and Bassant, M.H. (2006). Firing properties of anatomically identified neurons in the medial septum of anesthetized and unanesthetized restrained rats. *J Neurosci* 26:9038–9046.
- Sohal, V.S. and Huguenard, J.R. (2005). Inhibitory coupling specifically generates emergent gamma oscillations in diverse cell types. *Proc Natl Acad Sci USA* 102:18638–18643.
- Squire, L.R. and Zola-Morgan, S. (1991). The medial temporal lobe memory system. *Science* 253:1380–1386.
- Stewart, M. and Fox, S.E. (1990). Do septal neurons pace the hippocampal theta rhythm? *Trends Neurosci* 13:163–168.
- Van Hoesen, G.W. and Hyman, B.T. (1990). Hippocampal formation: anatomy and the patterns of pathology in Alzheimer's disease. *Prog Brain Res* 83:445–457.
- Wallenstein, G.V., Eichenbaum, H. and Hasselmo, M.E. (1998). The hippocampus as an associator of discontiguous events. *Trends Neurosci* 21:317–323.
- White, J.A., Chow, C.C., Ritt, J., Soto-Trevino, C. and Kopell, N. (1998). Synchronization and oscillatory dynamics in heterogeneous, mutually inhibited neurons. *J Comput Neurosci* 5:5–16.
- Wieser, H.G. (1983). *Electroclinical features of the psychomotor seizure*. Butterworths, London.
- Williams, J.H. and Kauer, J.A. (1997). Properties of carbachol-induced oscillatory activity in rat hippocampus. *J Neurophysiol* 78:2631–2640.
- Winfree, A.T. (2001). *The geometry of biological time*, 2nd edn. Springer Verlag, New York.
- Wittenberg, G.M. and Wang, S.S. (2006). Malleability of spike-timing-dependent plasticity at the CA3-CA1 synapse. *J Neurosci* 26:6610–6617.
- Zhou, Y.D., Acker, C.D., Netoff, T.I., Sen, K. and White, J.A. (2005). Increasing Ca<sup>2+</sup> transients by broadening postsynaptic action potentials enhances timing-dependent synaptic depression. *Proc Natl Acad Sci USA* 102:19121–19125.

# 19

## COMPLEX SYNAPTIC DYNAMICS OF GABAERGIC NETWORKS OF THE HIPPOCAMPUS

GIANMARIA MACCAFERRI

### ABSTRACT

The purpose of this chapter is to illustrate with two specific examples some of the advantages and of the limits of an integrated computational modeling/experimental approach in the investigation of complex problems related to epileptiform activity and network dynamics of the hippocampus *in vitro*. In more detail, this chapter will focus on some critical properties of chemical and electrical synaptic connectivity that ultimately affect GABAergic networks and thus shape epileptiform bursting. The first example will discuss the role of cell type-specific GABAergic input as a critical determinant of network-driven spike timing in pyramidal cells versus interneurons. The second example will illustrate the gap junction-mediated spreading of synaptic potentials in interneuronal networks and will address the necessary conditions for effective propagation and its consequences in specific models of network activity.

### INTRODUCTION

The purpose of this chapter is to illustrate with two specific examples some of the advantages and of the limits of an integrated computational modeling/experimental approach in the investigation of complex problems related to epileptiform activity and network dynamics of the hippocampus *in vitro*. In more detail, this chapter will focus on some critical properties of chemical and electrical synaptic connectivity that ultimately affect GABAergic networks and thus shape epileptiform bursting.

### EPILEPSY AND GABAERGIC INTERNEURONS OF CORTICAL CIRCUITS

Despite the overwhelming majority of the cellular elements of mammalian cortical networks is composed by excitatory neurons releasing glutamate as main neurotransmitter, a significant minority (~15%) releases gamma-aminobutyric acid (GABA). GABAergic interneurons innervate a large number of postsynaptic target cells (Freund and Buzsaki, 1996) and hence, despite their relative small number, can exert profound effects in shaping the dynamics of the network. The first role to be historically attributed to GABAergic interneurons was the dampening of local circuit excitability (Schwartzkroin, 1986) via feedback (Andersen et al., 1963; Dingledine and Langmoen, 1980) or feedforward (Alger and Nicoll, 1982; Pouille and Scanziani, 2001) circuits. Thus, it is not surprising that interneurons are essential players in the dynamic regulation of many network states related to different brain activities. Disruption of this delicate tuning may be catastrophic and lead to pathological discharges characterized by network hyperexcitability and hypersynchronicity. Lack of excitatory input onto interneurons and/or activity-dependent depression of GABAergic input (Miles and Wong, 1987a; Thompson

and Gahwiler, 1989a, 1989b; Sloviter, 1991; Bekenstein and Lothman, 1993; Schwartzkroin, 1994; Staley et al., 1995; Isokawa, 1996; Doherty and Dingledine, 2001; Chen et al., 2007; but see also Bernard et al., 1998) have been repeatedly proposed as mechanisms potentially contributing to epileptiform discharges *in vitro* or *in vivo*. Furthermore, a fraction of GABAergic inhibition appears intrinsically altered in human tissue surgically removed from adult epileptic patients so that instead of reducing, it conversely enhances excitability (Cohen et al., 2002). The resetting of GABA-mediated inhibition to early developmental stages, when it generates depolarization and excitation (Ben-Ari et al., 1997) has been proposed as a possible mechanism (Cohen et al., 2003). It is not surprising that several drugs impacting GABAergic synaptic transmission are widely used in the therapy of epilepsy and other neurological and psychiatric disorders (Baldessarini, 2005; Baldessarini and Tarazi, 2005; McNamara, 2005). Thus, understanding the molecular mechanism and the network organization mediating the functions of GABAergic interneurons in the developing and adult brain holds the promise for fruitful discoveries both at the level of basic science and novel antiepileptic strategies (Dzhala et al., 2005).

### **NETWORK ORGANIZATION: FROM INDIVIDUAL INTERNEURONS TO GABAERGIC NETWORKS**

In contrast to the relative anatomical and functional homogeneity of hippocampal principal neurons, GABAergic interneurons display a staggering level of heterogeneity on both levels (Freund and Buzsaki, 1996). Only in the last decades has this heterogeneity of subtypes begun to be matched with specific electrophysiological and molecular properties thanks to experiments performed *in vitro* from biocytin filled cells connected pairs (Buhl et al., 1994; Miles and Poncer, 1996; Miles et al., 1996; Maccaferri et al., 2000). Thus, a constantly growing number of morpho-functionally defined GABAergic cell types has been classified thanks to the combination of a variety of technical approaches based on electrophysiology, anatomy and molecular biology (Maccaferri and Lacaille, 2003). Although this line of research is far from being completed, an additional level of complexity has been raised by the issue of their network organization, which is mediated by both chemical and electrical synapses. Indeed, cell type-specificity of the connectivity mediated by chemical versus electrical synapses seems to exist. With a few important exceptions that will not be mentioned here (for details, see Friend and Buzsaki, 1996), GABAergic neurons of cortical circuits may target both principal neurons and other interneurons via symmetrical GAD-positive chemical synapses (Freund and Buzsaki, 1996). Because of the high degree of synaptic divergence, a relatively small number of interneurons can provide powerful GABAergic inhibition to a much larger number of pyramidal cells.

In the case of electrical synapses, different rules seem to apply. Parallel work in the hippocampus and neocortex has revealed that, in most cases, only similar types of GABAergic interneurons are electrically coupled via gap junctions (Galarreta and Hestrin, 1999, 2002; Gibson et al., 1999; Venance et al., 2000; Bartos et al., 2001, 2002; Price et al., 2005; for a review see Hestrin and Galarreta, 2005, but see also Zsiros and Maccaferri, 2005 and Simon et al., 2005) and significant mixed interneuron-pyramidal cell coupling is present only transiently during early stages of development (Meyer et al., 2002).

In this chapter, we will try to address two issues related to interneuronal network organization and their impact on epileptiform discharges. First, we will address the role of fast GABAergic (i.e. mediated by GABA<sub>A</sub> receptors) input on pyramidal cells as a potential factor modulating pyramidal cell-specific spike timing during synchronized epileptiform activity. We will then continue in the second part of the chapter by discussing the role of electrical coupling as a factor modulating divergence and active population recruitment in GABAergic networks during epileptiform synchronization. The two subjects we have selected are certainly biased by our scientific interests, but they also appear to us as particularly suited illustrative examples of work that can benefit from the integration of an experimental/computational approach.

### **CELL TYPE-SPECIFIC GABAERGIC INPUT MODULATES SPIKE TIMING DURING HIPPOCAMPAL EPILEPTIFORM ACTIVITY**

#### **SPIKE TIMING: GENERALITIES**

For the purpose of this chapter, we will refer to ‘spike timing’ as the temporal aspect of the initiation of a synaptically triggered action potential. Two main factors define spike timing: the latency required to initiate an action potential and the temporal precision of the process, which can result in different degrees of temporal fidelity of action potential occurrence. The precise timing of occurrence of an action potential in a neuron of the brain has been proposed to carry information.

Despite an initial intense debate (for example, see Shadlen and Newsome, 1994 and Softky, 1995), information theory, experimental data and theological arguments converge in suggesting various advantages of a neuronal code taking into account the precise timing of spike generation, when compared to a code transferring information based only on average firing rates (Konig et al., 1996; Borst and Theunissen, 1999). Experimental evidence obtained in both hippocampal interneurons and pyramidal cells has suggested that both types of cells, under the appropriate conditions, may act as coincidence detectors of synchronous synaptic input and hence produce particularly precise spike timing. Although this tendency may be especially strong in many types of interneurons (Fricker and Miles, 2001; Jonas et al., 2004) when compared to pyramidal cells [because of intrinsic factors such as the fast kinetics of their AMPA receptors (Geiger et al., 1997) and the activation of potassium currents during synaptic input (Fricker and Miles, 2000)], a high degree of spike timing precision can be achieved also in pyramidal cells when feedforward inhibitory mechanisms are fully operative (Pouille and Scanziani, 2001) or depending on specific stimulus properties (Axmacher and Miles, 2004). Furthermore, experimental work *in vitro* has also shown that the precise relationship between postsynaptic spike timing and presynaptic input in cortical neurons can carry information in terms of long-term bidirectional synaptic plasticity at both glutamatergic (Magee and Johnston, 1997; Markram et al., 1997, for a review see Dan and Poo, 2006) and GABAergic synapses, (Holmgren and Zilberman, 2001). Given that synaptic plasticity at excitatory and inhibitory synapses in large populations of neurons has been linked to the synchronization and the emergence of epileptiform bursting in the hippocampus (Miles and Wong, 1987a; Bains et al., 1999), the precise temporal relationships between firing patterns observed in pyramidal cells and interneurons may be of significance for the maintenance of specific synaptic weights linked to active networks states.

In this particular example, we have selected a relatively simple, but explosive network state such as the epileptiform burst. This type of network state is reflected in electroencephalographic recordings from epileptic patients by interictal spikes, which are markers of epilepsy (Pedley, 1984). Interictal spikes have been proposed to be generated by the spontaneous burst firing of CA3 pyramidal neurons, which are anatomically and physiologically well suited to recruit an explosive response because of their powerful excitatory recurrent collateral system (Miles and Wong, 1983; Traub and Miles, 1991; Bains et al., 1999; Menendez de la Prida et al., 2006). Indeed, a particularly interesting consideration is that the circuitry of the hippocampus has an intrinsic tendency towards the generation of synchronized population activity, which is tightly controlled by GABAergic inhibition (Miles and Wong, 1987b). A similar type of epileptiform activity involving the entire network or only a partial fraction of its population can be maintained and recorded in hippocampal slices exposed to elevated external potassium (for a review on the elevated potassium model of epilepsy see McBain et al., 1993, for a review on additional models see Wilson and Bragdon, 1993).

When examined, spike timing during epileptiform bursting recorded in pyramidal cells and interneurons in slices appears to follow the apparently counterintuitive principle that interneurons fire before pyramidal cells, as shown in Figure 19.1. However, the same observation is also compatible with burst being stochastically initiated by the intrinsic bursting properties of a few excitatory pyramidal neurons (Wong and Prince, 1978) and then propagated in a cascade of events to other pyramidal cells and GABAergic interneurons (Traub and Miles, 1991; Menendez de la Prida et al., 2006). In this case, cell type-specific differences in spike-timing properties (Fricker and Miles, 2000; Maccaferri and Dingledine, 2002) would be crucial in determining the relative timing of action potentials in the cells recruited with the progression of the burst cycle. In their seminal monographic book summarizing many years of research, Traub and Miles (1991) constructed a network model of the CA3 hippocampus, which could reproduce synchronized bursting and maintain the experimentally-observed temporal relationships of spike timing between pyramidal cell sand interneurons (Figure 19.1). Analysis of the firing pattern of the cells of the model indicated that a burst cycle initiated by the intrinsic properties of a few ancestral excitatory pyramidal neurons may lead to the partial or total recruitment of the network and produce the experimentally observed cell type-specific spike timing. In this seminal work, inhibitory cells were functionally divided into cells targeting the perisomatic area as opposed to the dendritic tree of pyramidal neurons. This functional distinction was later validated by following work *in vitro* showing separate roles for perisomatic and dendritic inhibition with respect to the control of fast, sodium-based versus slow, calcium-based action potentials, respectively (Miles et al., 1996). It is now established that perisomatic and dendritic GABAergic input are the result of the activity of a complex population of different interneurons subtypes (Freund and Buzsaki, 1996).

#### COMPUTATIONAL MODELING AND SYNAPTIC DYNAMICS OF SYNCHRONIZED BURSTING

Although cell type-specific differences in intrinsic properties and excitatory stimulus characteristics can result in cell type-specific spike timing (Fricker and Miles, 2000; Maccaferri and Dingledine, 2002; Axmacher and Miles, 2004), the possibility that synaptic inhibitory mechanisms can also play a role cannot be ruled out. As mentioned above, the integration

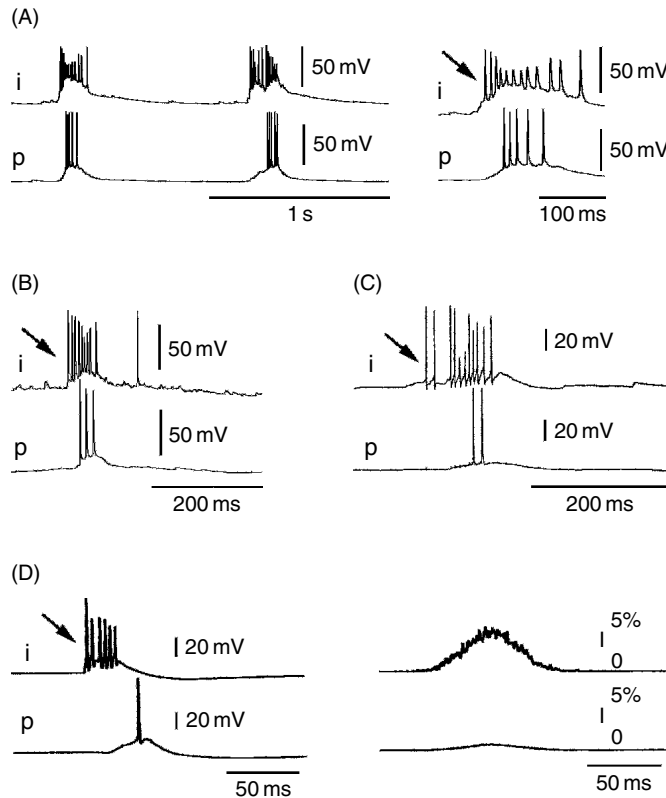


**FIGURE 19.1** Spike timing in interneurons and pyramidal cells during synchronized activity in different experimental models of epilepsy *in vitro* and in computer-generated simulations. (A) Simultaneous whole-cell patch-clamp recordings obtained from a hippocampal interneuron (i) and a CA3 pyramidal cell (p) exposed to elevated potassium conditions. Note the synchronized spontaneous bursting in the two neurons. The inset to the right shows a time-expanded view of a burst cycle. Notice that the first action potential in the interneuron (arrow) precedes firing activity in the pyramidal cell. Modified from Aradi and Maccaferri (2004) (Copyright 2004 by the Society for Neuroscience). (B) Similar spike-timing dynamics recorded in a CA1 interneuron (i) and pyramidal cell (p) in slices exposed to 0  $Mg^{2+}$  and low concentrations of 4-AP. Notice that the cell type-specificity of spike timing is maintained and that the interneuron fires first (arrow). Modified from Ziburkus et al. (2006) (Copyright 2006 by the American Physiological Society). (C) A similar example from human epileptic hippocampal tissue. The arrow highlights the first action potential in the interneuron (i). Notice the relatively delayed firing in the pyramidal cell (p). Modified with permission from Schwartzkroin and Haglund (1986). Copyright Blackwell Publishing, 1986. (D) Spike timing during spontaneous synchronous oscillatory activity in a model network. Notice the resemblance to the recordings in A, B and C. The model reproduces the early firing in the interneuron model cell (i) compared to the model pyramidal cell (p). In this case, the type of activity shown by the model network was associated with the recruitment of a small percentage of the overall interneuronal and pyramidal cell populations, as shown in the right plots. Modified from Traub and Miles (1991). Figure 7.7, page 166. Copyright Cambridge University Press 1991. Reprinted with permission of Cambridge University Press.

of all these components (intrinsic properties, synaptic excitation and inhibition) along the progressive development of an oscillatory burst cycle will determine spike timing in the recruited population of neurons. The study by Aradi and Maccaferri (2004) analyzed in detail the synaptic mechanisms that contribute to the difference in spike timing between a selected group of hippocampal interneurons (Maccaferri, 2005) and CA3 pyramidal cells in the elevated potassium model of epilepsy *in vitro* (McBain et al., 1993). Raising the extracellular concentration of potassium to 8.5 mM generates synchronized synaptic activity that is reflected in bursting activity of both pyramidal cells and interneurons (McBain, 1995). Interestingly, as already mentioned, firing in interneurons appears to lead firing in pyramidal cells (Aradi and Maccaferri, 2004). This type of stereotyped spike timing is potentially indicative of some type of preserved emergent property of the network, because it can be observed in various other experimental models of epilepsy. For example, Ziburkus and colleagues (2006) observed very similar dynamics in bursting slices after application of the potassium channel blocker 4-aminopyridine (4-AP, Avoli et al., 1988). Furthermore, this type of activity was originally recognized in human epileptic and primate non-epileptic neocortical tissue displaying spontaneous synchronous activity by Schwartzkroin and Haglund (1986). Figure 19.1 shows experimental traces of epileptiform bursting recorded by different groups in the rodent and human hippocampus under a variety of experimental conditions and a simulation from the work of Traub

and Miles (1991). Despite all the experimental differences, cell type-specific spike timing appears surprisingly preserved. How to interpret this apparent stereotyped result? Being aware of the enormous diversity of interneurons (Freund and Buzsaki, 1996), it is difficult to think that interneuron heterogeneity would not result in temporal variability of interneuronal firing pattern. Recent work *in vivo*, for example, has shown that different classes of hippocampal interneurons display cell type-specific firing patterns during different brain network states (Klausberger et al., 2003, 2004, 2005). Therefore, it is important to consider that this apparently stereotyped result may be the consequence of some powerful pyramidal cell-specific property that may overcome the variability of the interneuronal population. For example, a strong pyramidal cell-specific inhibitory input at the beginning of a burst cycle could produce a significant delay of spike initiation compared to interneurons.

In our study (Aradi and Maccaferri, 2004), a combination of experimental and computational modeling techniques was employed to address this issue. In order to explore the effect of fast GABAergic inhibition on CA3 pyramidal cells bursting, we first recorded experimentally the time course of isolated excitatory and fast synaptic conductances (gEPSC and gIPSC, respectively) during a burst cycle in pyramidal neurons and interneurons. Excitatory and inhibitory components were dissected out by voltage-clamping the two distinct cell types at the estimated reversal potential for fast GABAergic and glutamatergic input, respectively. As shown in Figure 19.2, the dynamics of the excitatory burst synaptic conductances were very similar in pyramidal cells and interneurons. In contrast, the dynamics of fast GABAergic currents active during a burst displayed cell type-specificity on two levels. First, the ratio between inhibition and excitation (evaluated as charge transfer of the inhibitory and excitatory burst currents) was much smaller in interneurons compared to pyramidal cells (Aradi and Maccaferri, 2004). This finding by itself suggests that the relative weakness of fast inhibition may act as a potential reason for the apparent different spike timing and excitability of interneurons versus pyramidal cells during a synchronous burst. In addition, the kinetics of the fast GABAergic burst conductance (gIPSC<sub>Pyr</sub>) recorded in pyramidal cells was different when compared to interneurons (gIPSC<sub>Int</sub>, Figures 19.2 and 19.3). Synaptic inhibition during a burst would initiate earlier in pyramidal cells, thus suggesting that fast GABAergic input at the beginning of a burst cycle slows down the initiation of pyramidal cells firing.

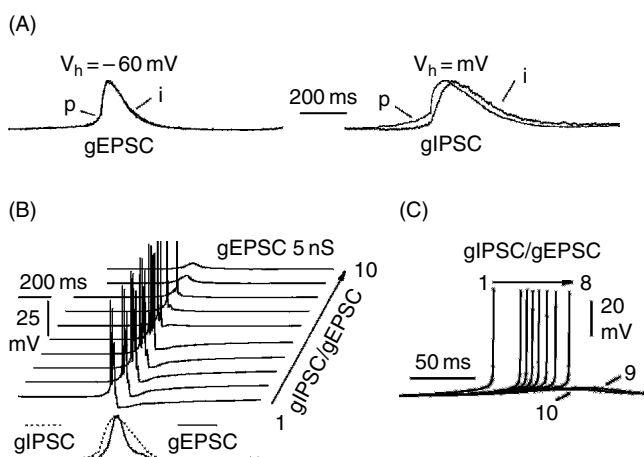


**FIGURE 19.2** Cell type-specific dynamics of GABA<sub>A</sub> receptor-mediated-inhibition during a burst cycle. (A) Experimentally-derived waveforms of the excitatory and fast inhibitory conductances (gEPSC and gIPSC; left and right panels, respectively) recorded in voltage-clamp in interneurons (i) and pyramidal cells (p) during a burst cycle. Waveforms have been normalized and superimposed to highlight the different kinetics. gEPSCs were recorded at the estimated reversal potential for fast inhibition ( $V_{holding} = -60$  mV), whereas gIPSCs were recorded at the assumed reversal potential for glutamatergic excitatory input ( $V_{holding} = 0$  mV). Waveforms are the averages of several experiments. Notice the similarity of the kinetics of gEPSC recorded in interneurons and pyramidal cells, in contrast to the earlier activation of gIPSC in pyramidal cells, when compared to interneurons. (B) Injection of gEPSC and gIPSC derived from pyramidal neurons in slices into a simulated pyramidal cell: notice that increasing gIPSC (from 1 to 10 nS) while keeping the same gEPSC value (5 nS) results in weaker bursting activity until only subthreshold responses are obtained. The kinetics of the inhibitory (gIPSC) and excitatory (gEPSC) conductances are shown for reference below the simulations. (C) Spike timing of the first action potential in the burst depends on the level of inhibition relative to excitation. Traces are simulated responses of the model cell to a gEPSC of 5 nS paired with a gIPSC ranging from 5 to 50 nS. For clarity, only the upstroke of the first spike is shown. Modified from Aradi and Maccaferri (2004). Copyright 2004 by the Society for Neuroscience.

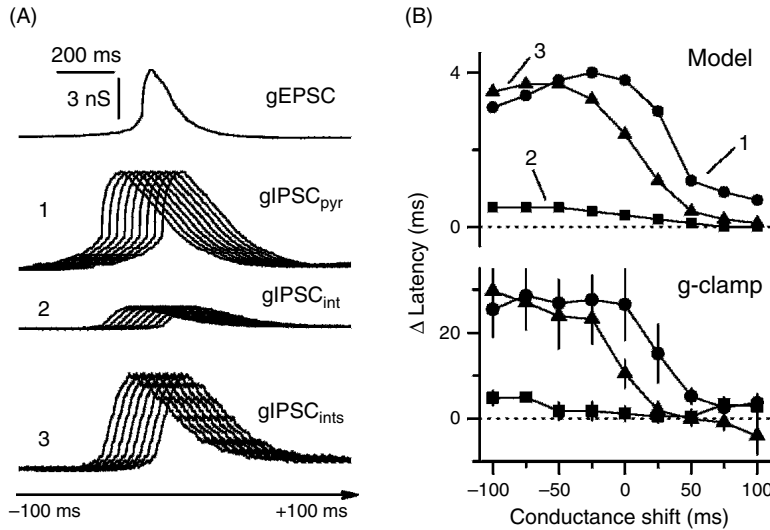


**FIGURE 19.3** Modeling predicts qualitatively, but not quantitatively the effect of cell type-specific fast inhibition during a burst cycle. (A) Conductance waveforms of excitatory input (gEPSC derived from pyramidal cell recordings, see also Figure 19.2A) and shifting GABA<sub>A</sub> receptor-mediated inhibition derived from pyramidal cell (gIPSC<sub>pyr</sub>) and interneuron (gIPSC<sub>int</sub>) recordings. gIPSC<sub>pyr</sub> and gIPSC<sub>int</sub> maintain the ratio reflected by the experimentally measured charge transfer to the recorded currents (Aradi and Maccaferri, 2004). gIPSC<sub>ints</sub> reflect the scaling of gIPSC<sub>int</sub> to maintain the same area ratio as gIPSC<sub>pyr</sub>/gEPSC. (B) Upper plot: injecting gEPSC and shifting gIPSC<sub>pyr</sub> (1), gIPSC<sub>int</sub> (2) and gIPSC<sub>ints</sub> (3) in a model cell results in different timing of the first spike of the simulated burst. Spike timing is quantified in the plot as the latency relative to the first action potential of a burst generated by the sole injection of gEPSC. Different spike timing due to the injection of cell type-specific gIPSCs are clearly visible. Notice the very weak effect of gIPSC<sub>int</sub> and the differential modulation generated by gIPSC<sub>pyr</sub> and gIPSC<sub>ints</sub>. Lower plot: experimental approach using dynamic clamp. The same set of conductances is injected in a CA3 pyramidal cell of a hippocampal slice. Note the very similar qualitative result, but the stronger modulation achieved by gIPSC<sub>pyr</sub> and gIPSC<sub>ints</sub>, much more in agreement with experimental results shown in Figure 19.1. Modified from Aradi and Maccaferri (2004). Copyright 2004 by the Society for Neuroscience.

If this effect was really critical, two key points of this interpretation should be verified. First, reducing gIPSC<sub>pyr</sub>, while maintaining constant gEPSC should affect spike timing in pyramidal cells. Second, if gIPSC<sub>int</sub> were to be substituted for gIPSC<sub>pyr</sub> in pyramidal cells during a burst, then their spike timing should be anticipated, similarly to that observed in interneurons. Because of the constraints imposed to an experimental approach by the nature of the slice preparation, we tested these hypotheses by taking advantage of computational modeling. The multicompartmental model of a bursting CA3 pyramidal cell (Traub and Miles, 1991) was used with a few modifications. The model cell was endowed with 19 compartments and 6 different voltage-gated conductances. Details of the model cell compartmentalization and conductance kinetics can be found in Traub and Miles (1991). Additional adjustments were made in order to make the simulation results more similar to the experimental records and are detailed in Aradi and Maccaferri (2004). Simulations were performed using NEURON 5.4 software (Hines and Carnevale, 1997) running on a Linux OS computer. As shown in Figure 19.2, injections of different levels of inhibition relative to excitation were associated with different bursting strength and spike timing with respect to initiation of the burst cycle. Thus, the first key point of our interpretation was verified.

Next, we addressed the significance of the cell type-specificity of gIPSC by observing the effect of changing the properties of the injected inhibitory conductance from gIPSC recorded from pyramidal cells (gIPSC<sub>pyr</sub>) to gIPSC derived from interneurons (gIPSC<sub>int</sub>). As shown in Figure 19.3, the injection of a shifting gIPSC<sub>pyr</sub> waveform resulted in modulation of spike timing within the burst cycle, whereas very little, if any, modulation followed the injection of gIPSC<sub>int</sub>. Scaling gIPSC<sub>int</sub> to the same area of gIPSC<sub>pyr</sub> yet did not reproduce spike-timing modulation produced by gIPSC<sub>pyr</sub>, indicating that even the cell type-specific kinetics of gIPSC had by itself significant effects. Repeating the same experiment in a slice using dynamic clamp (g-clamp) techniques (Prinz et al., 2004) yielded a qualitative similar result. However, g-clamp experiments matched the experimental results much better from a quantitative point of view. In more detail, the injection of a shifting inhibitory conductance to the model cell could modulate spike timing only of a few milliseconds, whereas dynamic-clamp performed on real pyramidal cells revealed modulation of tens of milliseconds, which was much more adherent to the experimental results observed during spontaneous epileptiform activity (see for example, Figure 19.1A).

Thus, computational modeling was an excellent predictor of spike-timing modulation by cell type-specific inhibitory conductances, but only on a qualitative, rather than quantitative level.

The cell type-specificity of fast GABAergic input during a burst cycle opens the questions of what cellular/molecular mechanisms may underlie the reported differences. Although at present no firm answer has been provided, two potential mechanisms have been proposed. First, the flurry of GABAergic activity in the initial part of a bursting cycle, which is specific to pyramidal cells may be the result of cell type-specific input from a subpopulation of interneurons, such as, for example axo-axonic cells, which target preferentially excitatory cells, when compared to other interneurons (Somogyi et al., 1983). Consistently, axo-axonic cells fire immediately before a highly synchronized sharp wave cycle in the CA1 hippocampus *in vivo* (Klausegger et al., 2003). Alternatively, cell type-specific suppression of the initial GABAergic input in interneurons, but not in pyramidal cells could be the result of specific expression of receptors modulating inhibitory input. Kogo and colleagues (2004) have described depression of GABAergic input in stratum oriens horizontal interneurons mediated by group III metabotropic glutamate receptors. If these receptors were to be activated during synchronized bursting, then a cell type-specific mechanism of suppressing GABAergic input to interneurons would be potentially available. These hypotheses need to be tested in the future, and remain at present only speculative.

In conclusion, this first example highlights some of the advantages of combining experimental and computational modeling approaches in the study of complex network dynamics. In general, questions regarding the role of different types of conductances (intrinsic or synaptic) during a specific type of network activity are very complicated to study with a purely experimental approach. The reason is that the experimental evaluation of the role played by a particular ionic channel in a dynamic state is usually assessed by its pharmacological modulation, most often by application of an antagonist on the *entire circuit* (the slice *in vitro*). If the conductance is indeed involved in the generation of the selected dynamic state, then its pharmacological blockade will be bound to lead to a different dynamic state of the network. For example, the comparison of bursts generated in the presence versus in the absence of fast GABAergic input after bath application of a GABA<sub>A</sub> receptor antagonists suffers from the fact that bursts are generated by completely different network states, as demonstrated by the finding that blockade of GABA<sub>A</sub> receptors in the elevated potassium model of epilepsy changes the frequency of spontaneous bursts (Rutecki et al., 1985; Korn et al., 1987; Staley et al., 1998). Therefore, although this type of pharmacological experiment is important for establishing that the chosen conductance participates in the regulation of the selected network activity, it does not explain what its direct role is. Again, going back to the previous example, are the changes observed in bursts recorded in the presence versus in the absence of the drug due to blockade of fast inhibition or simply reflective of a novel dynamic network state that implies different burst-shaping mechanisms? Comparisons of bursts recorded in control versus pharmacological blockade of GABA<sub>A</sub> receptor-mediated inhibition will be affected by secondary effects due to the fact that:

1. Events will initiate at a different phase of the burst hyperpolarization (Alger and Nicoll, 1980; Chamberlin and Dingledine, 1989).
2. Different bursting frequency will be associated with different short-term plasticity (Salin et al., 1996) and hence release probability of glutamate at the recurrent collateral synapses (Staley et al., 1998).
3. Blockade of GABA<sub>A</sub> receptors in the entire population may interfere with GABA<sub>B</sub> receptor-mediated inhibition in pyramidal cells (Lopantsev and Schwartzkroin, 1999, 2001) and interneurons (Traub and Miles, 1991; Miles and Wong, 1983; Scanziani, 2000).
4. Before reaching a new steady state, GABA<sub>A</sub> receptor blockade results in irregular network hyper-excitability (Aradi and Maccaferri, 2004) that can trigger activity-dependent long-term changes of inhibitory or excitatory synaptic transmission (Bains et al., 1999; Chevaleyre and Castillo, 2003).

Thus, a purely experimental approach based on the bath application of GABA<sub>A</sub> receptor antagonists cannot prove that changes in spontaneous bursts are the direct result of the elimination of fast inhibitory conductances, because a lot of secondary effects may have taken place.

The computational approach shown in the examples illustrated above (see Figures 19.2 and 19.3) has the advantage of assessing the role of fast GABAergic inhibition in a scenario where everything else is maintained unchanged. The excitatory conductance injected in the simulation or in the dynamic clamp experiment was indeed derived from experimental control conditions and maintained unaltered when changes in the GABA<sub>A</sub> conductance were studied. Thus, in the absence of an effective drug that can be loaded in the recording electrode and quickly and selectively block GABA<sub>A</sub> receptor-mediated currents in a single cell (without affecting the rest of the network), a combined experimental/computational approach can provide insights otherwise unattainable. We will now proceed to the second example, which is related to some aspects of interneuronal connectivity that are mediated by electrical coupling.

## ELECTRICAL COUPLING AND PROPAGATION OF POSTSYNAPTIC CURRENTS AND POTENTIALS IN GABAERGIC NETWORKS

### GENERALITIES ON GAP JUNCTION MEDIATED-COUPLING IN GABAERGIC NETWORKS OF THE HIPPOCAMPUS

Not too many years ago, neuroscience textbooks reported that gap junctions are relatively rare between adult mammalian neurons. This view has now radically changed. Great advances in the study of electrical coupling in cortical networks have come as the result of technical developments allowing the simultaneous recording from multiple neurons in '*in vitro*' slices (Miles and Poncer, 1996). These experimental arrangements provide an excellent model to study the connectivity of specific brain regions. Work from several laboratories in the neocortex and hippocampus (for a review of work in the neocortex see Hestrin and Gallarreta, 2005, for work in the hippocampus, see Venance et al., 2000; Bartos et al., 2001, 2002; Meyer et al., 2002; Zhang et al., 2004, Price et al., 2005; Zsiros and Maccaferri, 2005, Zsiros et al., 2007) has shown directly by paired recordings that GABAergic inhibitory neurons are electrically coupled. Moreover, electrical synapses of cortical network have been shown to play an important role for synchronization of GABAergic networks (Galarreta and Hestrin, 1999, 2002; Gibson et al., 1999; Bartos et al., 2001; Szabadics et al., 2001; Blatow et al., 2003; Chu et al., 2003; Galarreta et al., 2004; Simon et al., 2005).

Despite the relatively large amount of experimental work highlighting gap junctions as essential elements of GABAergic networks promoting synchrony, the detailed assessment of the role of electrical coupling in network dynamics remains a complicated task to be evaluated experimentally. Apart from the technical difficulties related to paired recording in a slice, the lack of specific gap junction blockers has made a purely experimental approach particularly challenging. Therefore, it is not surprising, that a lot of work has also investigated these issues by taking advantage of computational modeling techniques. Simulations of pairs of neurons connected by gap junctions have been performed by different laboratories using a variety of model cells. Because of the lack of detailed structural and electrical properties of interneurons, model cells of early work represented neurons without references to specific cortical interneuron subtypes. The effect of gap junctions was initially evaluated by simulations studying small networks formed by two electrically coupled cells, in the absence of chemical synaptic connectivity (Sherman and Rinzel, 1992). Despite difference in the structure of the model cells used, a fundamental theme seemed to suggest that the strength of electrical coupling may be a critical determinant of synchrony and result in in phase or out of phase firing. This type of result would predict that modulation of the junctional conductance in neuronal networks could have profound effects on their synchronization. Furthermore, the level of coupling can change the firing pattern on both a quantitative and qualitative level. Sherman and Rinzel (1992) showed that bursting can be increased in its duration in pairs of electrically coupled model cells and the firing frequency of tonically active cells can be modulated. Perez-Velazquez and colleagues (2001) took advantage of the injection of artificial junctional conductances in pairs of uncoupled cells to study the effect of electrical coupling on the firing activity of neurons with similar and different intrinsic properties. Their results showed that naturally non-bursting neurons can acquire a bursting phenotype, when coupled to intrinsically bursting neurons, thus highlighting a potential role for gap junctions in the determination of intrinsic firing properties. More recent work has taken advantage of model cells incorporating specific intrinsic conductances resulting from experimental work in selected interneuronal subpopulations (Nomura et al., 2003; Saraga et al., 2006). Furthermore, the effect of electrical coupling has been explored on subthreshold oscillatory activity, similar to rhythms that are believed to be physiologically relevant *in vivo* (Traub et al., 2003). This modeling work has highlighted an important modulating role exerted by dendritic gap junctions between interneurons on gamma oscillations. An additional mechanism performed by electrical coupling in GABAergic networks, which may affect population activity is the functional enhancement of synaptic divergence (Figure 19.4). Gap junction-mediated spreading of synaptic potentials would boost synaptic divergence in GABAergic networks and potentially favor the recruitment of a large number of elements of the network. The propagation of postsynaptic potentials generated by chemical neurotransmission via gap junctions was predicted or even directly shown at invertebrate and non-cortical synapses (for example, Decima, 1969; Martin and Pilar, 1963; Zipser and Bennett, 1976; Marder and Eisen, 1984; Slesinger and Bell, 1985; Pereda et al., 1995; for a review of electrical coupling in the mammalian brain see Connors and Long, 2004, for a general review see Bennett, 1977). However, most of those studies were focused on antidromic transmission from postsynaptic sites to presynaptic terminals. In contrast, mammalian GABAergic cortical networks are believed to be coupled by gap junctions located at somatic or dendritic sites (Kosaka and Hama, 1985; Fukuda and Kosaka, 2000; Szabadics et al., 2001; Simon et al., 2005; Fukuda et al., 2006).

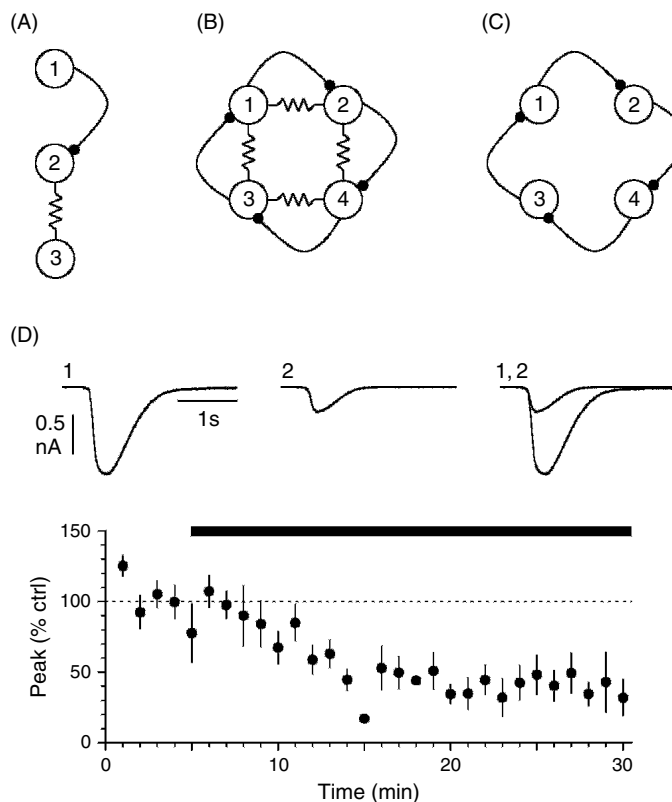


**FIGURE 19.4** Simplified schematic cartoons illustrating the proposed extension of synaptic divergence introduced by electrical coupling in GABAergic networks. (A) In a simple polysynaptic chain of three neurons direct neurotransmitter release from neuron 1 to neuron 2 can generate a postsynaptic potential in neuron 3, which is not directly innervated by neuron 1. (B) During network synchronization, electrical coupling may serve as a recurrent circuit extending excitatory GABAergic input. Notice, for example, that the chemical postsynaptic potential generated by neuron 1 onto neuron 2 can be propagated also to neuron 4 and back to neuron 1, despite the lack of direct chemical connectivity. Similar observations extend to the rest of the network. (C) The same network in the absence of gap junctions. Propagation of postsynaptic potentials is strictly determined by the anatomical chemical connectivity. The experimental comparison of network synchronization in stratum lacunosum-moleculare interneurons in scenarios reflected by (B) versus (C) is addressed experimentally in panel D. (D) The gap junction uncoupler carbenoxolone depresses epileptiform GABAergic postsynaptic currents recorded directly in stratum-lacunosum moleculare interneurons. Application of the drug (100  $\mu$ M, black bar) strongly reduces the network-driven epileptiform PSC recorded from slices exposed to 4-aminopyridine. Blockers of ionotropic glutamatergic synaptic transmission present throughout. Holding potential was  $-60$  mV. Insets show average traces in control conditions (1), in the presence of the drug (2) and superimposed (1, 2). Modified from Zsiros et al. (2007). Copyright Blackwell Publishing, 2007.

#### STRATUM LACUNOSUM-MOLECULARE INTERNEURONS, GAP JUNCTIONS AND THE 4-AMINOPYRIDINE MODEL OF EPILEPSY *IN VITRO*

There are specific conditions that would make the spreading of neurotransmitter-generated postsynaptic events via gap junctions particularly pertinent for the study of epileptiform activity. In the following example, we will illustrate gap junction-mediated propagation of postsynaptic GABAergic activity in a particular subpopulation of interneurons, which are strongly electrically coupled (Price et al., 2005; Zsiros and Maccaferri, 2005, Zsiros et al., 2007). Interestingly, these types of interneurons have been shown to react with an all or none response to exogenous GABA application in the 4-aminopyridine model of epilepsy *in vitro* (Perkins, 2002), suggesting the possibility that spreading of excitation via gap junction-mediated propagation of GABAergic synaptic input may contribute to the rapid recruitment of the network during an epileptiform cycle. Thus, under this scenario, electrical coupling between elements of the GABAergic network would act as an additional excitatory circuit contributing to the recruitment of the entire connected population, as shown in the cartoon of Figure 19.4. Consistently, in the presence of 4-aminopyridine, epileptiform activity can be recorded in stratum lacunosum-moleculare interneurons in the presence of blockers of glutamatergic ionotropic synaptic transmission (Zsiros et al., 2007) and it occurs simultaneously to large GABAergic currents which have a depolarized reversal potential ( $\sim -35$  mV, Zsiros et al., 2007). Application of the gap-junction uncoupler carbenoxolone has been shown by different

groups to affect 4-AP-induced epileptiform activity in the hippocampus *in vitro* (Ross et al., 2000; Lamsa and Taira, 2003). In more detail, the role of gap junction-mediated propagation of GABAergic synaptic potential in stratum lacunosum-moleculare interneurons was directly tested by carbenoxolone application while monitoring GABAergic network currents recorded directly in interneurons, as shown in Figure 19.4 (Zsiros et al., 2007).

However, a more detailed study of the gap junction-mediated propagation of synaptic activity during highly synchronized epileptiform network states is very difficult because direct postsynaptic events (generated by neurotransmitter release) and propagated events are supposed to occur at the same time on the same neuron. Furthermore, as previously mentioned, no gap junction-specific blocker exists and carbenoxolone may suffer from unspecific effects. Therefore, separating the contribution of these two synaptic pathways is very challenging. In contrast, distinguishing unambiguously direct from propagated input may be facilitated by taking into account asynchronous network states such as spontaneous background synaptic noise in quiescent slices. We used this approach to investigate the dynamics between chemical input and gap junction-mediated electrical coupling in a simple model network of two multipolar neurons connected by a junctional conductance ( $G_j = 2 \text{ nS}$ ) and receiving GABA<sub>A</sub> receptor mediated inputs (Zsiros et al., 2007). Simulations were performed using the NEURON 5.4 software (Hines and Carnevale, 1997) running on Linux. The model cells were constructed to resemble multipolar interneurons of stratum lacunosum-moleculare described in Zsiros and Maccaferri (2005). For simplicity purposes, the model neuron structure was simplified to a soma and four dendrites. Voltage-activated Na<sup>+</sup>, delayed rectifier K<sup>+</sup>, and A-type K<sup>+</sup> channels (the kinetics of the channels were taken from Aradi and Holmes, 1999 and Yamada et al., 1989) were included in the model cells. In more detail, the morphological and biophysical parameters were as follows:

1. soma: diameter = 15 μm, number of compartments = 2, maximal conductance values for gNa = 150 mS/cm<sup>2</sup>, gK-DR = 40 mS/cm<sup>2</sup>, gKA = 2.55 mS/cm<sup>2</sup>
2. dendrites: length = 100 μm, diameter: proximal = 1.5 μm, distal = 0.2 μm, number of compartments = 20, maximal conductance values for gNa = 13 mS/cm<sup>2</sup>, gK-DR = 4 mS/cm<sup>2</sup>.

Resting membrane potential was set at -65 mV and membrane specific capacitance was 3 μF/cm<sup>2</sup>.

The reason for the use of a relatively high value of specific capacitance was to compensate for the oversimplified anatomical structure of the model, which includes only four dendrites and hence is likely to underestimate the global membrane capacitance of the neuron. Nevertheless, this approach produces DC and spike coefficient coupling that are similar to that reported experimentally in the literature (Zsiros et al., 2007) and is more conservative with regard to propagation of events via gap junctions when compared to the more standard value of specific capacitance such as 1 μF/cm<sup>2</sup> (Zsiros et al., 2007). The input resistance for these model neurons was similar to that reported for anatomically identified multipolar neurogliaform cells of stratum lacunosum moleculare (Price et al., 2005). Further details can be found in Zsiros et al. (2007). In order to design an experimental protocol that could dissociate direct synaptic input from gap junction-propagated events, we began by running a set of simulations as shown in Figure 19.5. The rationale underlying the simulation is that manipulations of GABA<sub>A</sub> receptor reversal potential restricted in a cell recorded under voltage-clamp conditions should affect only the direct, but not the electrical coupling-propagated synaptic input. The simulation shown in Figure 19.5 predicted that direct chemical input on the recorded cell could be dissociated from the propagated input by voltage-clamping at an intermediate potential between the different reversal potentials. As shown in Figure 19.5, cell 1 was supposed to be recorded with a chloride-loaded solution setting EGABA<sub>A</sub> to ~0 mV, whereas EGABA<sub>A</sub> in the coupled cell was supposed to be closer to physiological values recorded in hippocampal interneurons with non-invasive techniques (Lamsa and Taira, 2003, Vida et al., 2006). The result of the simulation predicted that voltage-clamp recordings at a membrane potential intermediate between EGABA<sub>A</sub> in cell 1 and cell 2 would differentiate direct from propagated chemical input because of the different polarities of the recorded events. However, the model cells used suffered from an oversimplification of their structure and from many assumptions relative to their intrinsic properties, which have not been characterized in detail. This prediction was tested experimentally and confirmed by recording spontaneous synaptic activity at -15 mV from stratum lacunosum-moleculare interneurons, in the presence of blockers of ionotropic glutamatergic and GABA<sub>B</sub> receptor-mediated synaptic transmission. As shown in Figure 19.5, spontaneous events of different polarities (i.e. outward and inward) could be clearly identified. Furthermore, the pharmacological analysis of outward events revealed that they were sensitive to both GABA<sub>A</sub> receptor blockers and a gap junction uncoupler such as carbenoxolone, whereas inward events were only sensitive to GABA<sub>A</sub> receptor antagonists, but not to a gap junction uncoupler (Zsiros et al., 2007). Thus, a combination of computational modeling techniques and experimental recordings suggests that gap junction-mediated propagation of synaptic events can break down the privacy of chemical synaptic communication in GABAergic networks of the hippocampus even at the level of individual events. Nevertheless, the observed propagated events were a small

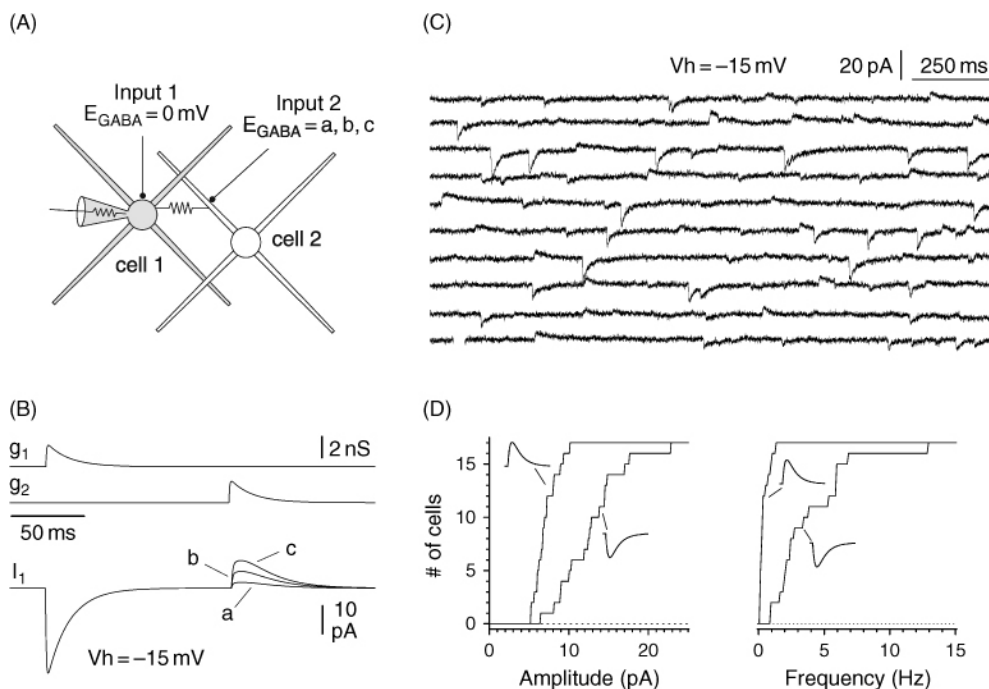


**FIGURE 19.5** Propagation of GABA<sub>A</sub> receptor-mediated currents in a two cell-network: simulations and experimental testing of the predictions. (A) Cartoon of the general properties of two simplified model interneurons (cell 1, and cell 2) connected by a gap junction (2 nS) and receiving independent GABAergic input (input 1, and input 2). Model neurons had only four dendrites (100  $\mu\text{M}$  length, thickness proximal  $\rightarrow$  distal 1.5  $\rightarrow$  0.2  $\mu\text{m}$ , twenty compartments) extending from the soma (diameter 15  $\mu\text{m}$ , two compartments). (B) Sequential activation of the synaptic conductances gated by input 1 ( $g_1$ ) and input 2 ( $g_2$ ) in the model cells. Simulated voltage-clamp conditions in model cell 1 ( $V_{\text{holding}} = -15 \text{ mV}$ ), generated currents with opposite polarities (input 1  $\rightarrow$  inward and input 2  $\rightarrow$  outward).  $E_{\text{GABA}}$  was set to 0 mV for cell 1, whereas three different  $E_{\text{GABA}}$  values were tested for cell 2 ( $a = -50 \text{ mV}$ ,  $b = -60 \text{ mV}$ ,  $c = -70 \text{ mV}$ ). (C) Experimental testing of the model predictions. Upper panel: spontaneous events recorded from a stratum lacunosum-moleculare interneuron held at  $-15 \text{ mV}$ . As predicted by the model, both inward and outward postsynaptic currents can be distinguished. (D) Basic properties of spontaneous events separated by their polarity. Cumulative distribution graphs of the amplitude and frequency of observed events are shown in the left and right panel, respectively. Distributions for inward and outward events are indicated by the appropriate polarity symbol. Excitatory synaptic transmission and slow inhibition were blocked pharmacologically. Modified with permission from Zsiros et al. (2007). Copyright Blackwell Publishing, 2007.

fraction of the overall recorded spontaneous activity, suggesting that not every synaptic event can spread across coupled cells.

This aspect was investigated in the model network by varying the position of the chemical input with respect to the site of the gap junction. As shown in Figure 19.6, events that originate close to the gap junction site propagate strongly compared to distal events, which may suffer severe attenuation and not reach the detection threshold in the coupled cell. Thus, a set of favorable conditions seems to be required for electrical coupling-mediated propagation of synaptic input. Interestingly, structural evidence for chemical synapses located strategically close to the gap junction has been reported in dendrites of hippocampal interneurons (Fukuda and Kosaka, 2000). The other prediction of the simulations is that significant kinetic filtering should occur in propagated events. The comparison of the kinetics of outward versus inward events confirmed these expectations (Zsiros et al., 2007).

Although the illustrated experiments and simulations highlight the potential for propagation of synaptic input via gap junctions, they also indicate that favorable conditions must be met. In particular, this type of mechanism will be more significant when synaptic input will be strongly synchronized such as during epileptiform activity. Epileptiform network synchronization based on the propagation of excitatory GABAergic currents in interneuronal networks has been suggested to operate in patients affected by Taylor's type focal cortical dysplasia (Taylor et al., 1971; Avoli, 1996; D'Antuono et al., 2004). Hyperexcitability and hypersynchronicity of GABAergic networks could contribute to bridge brain regions affected by loss of glutamatergic connections such as mesial limbic structures of temporal lobe epilepsy patients with Hammon's horn sclerosis (Gloor, 1991). In such a scenario, electrical coupling of GABAergic networks could play an important role.

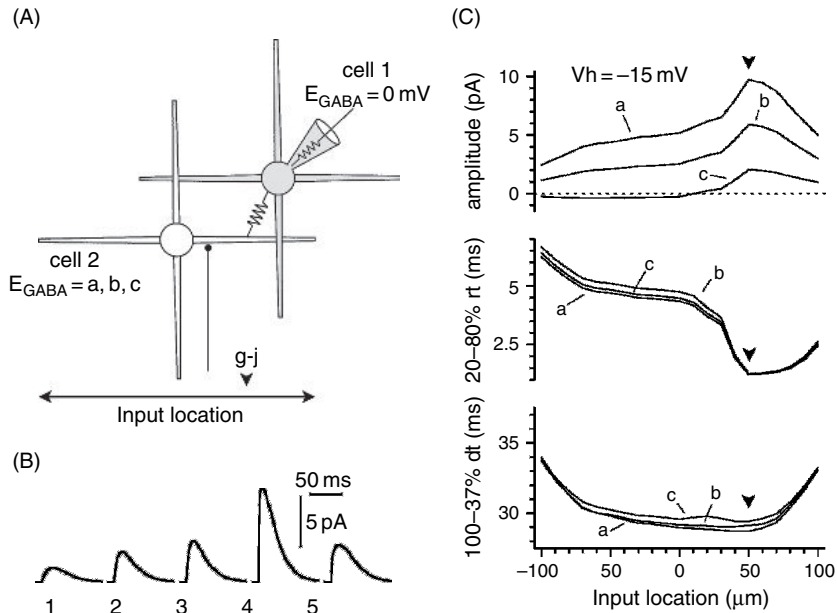


**FIGURE 19.6** Modeling the location-dependency of the properties of the propagated events. Conditions were identical to Figure 19.4A. (A) Schematic of the two cell-network: the gap junction is maintained at a fixed dendritic position (+50 μm, downward arrowhead) along the horizontal dendritic axis (from left to right: ±100 μm), whereas the location of chemical input in cell 2 is moved along the dendrite (double arrow). (B) Simulated gap junction-propagated events as they would be recorded on cell 1 are plotted against the different locations of synaptic input in cell 2 (1 = −100 μm, 2 = −60 μm, 3 = soma, 4 = +50 μm, 5 = +100 μm).  $E_{GABA}$  was set to 0 mV in cell 1 and −60 mV in cell 2. (C) Summary graphs highlighting the location-dependency of the propagated events amplitudes (top panel), 20–80% rise times (middle panel), and 100–37% decay times (bottom panel). Plots were derived from simulations with  $E_{GABA}$  in cell 1 set at 0 mV, and in cell 2 set at −70 mV, −60 mV and −50 mV (indicated as a, b and c respectively). Modified with permission from Zsiros et al. (2007). Copyright Blackwell Publishing, 2007.

#### GENERAL CONCLUSIONS AND FUTURE APPROACHES

In conclusion, we hope to have provided two simple examples of how a combination of computational modeling and experimental recordings may be a useful approach to gain insights into questions that are not easy to be tested experimentally, such as synaptic dynamics signaling in GABAergic networks of the hippocampus.

We would draw two main conclusions from these examples. First, even a simplified model of a cell or of a network can be useful and produce results very similar to what an experimental approach might reveal. However, these insights need to be taken with a lot of care. It is very important to point out that qualitative predictions may not be accurate quantitatively.

Currently, the constant cooperation between experimentalist and modelers is generating models of networks of the brain that are very detailed in the quantitative structure of the underlying cellular circuits. If the rate of growth of hardware computational power will continue at similar pace in the next decades, we should expect very realistic models of elementary network structures of specific brain areas (Markram, 2006). The power of these very detailed models will lie in making predictions at a much higher level than the one shown in this chapter. The side-to-side collaboration between experimental and computational neuroscientist is bound to produce in the future new discoveries that hopefully will identify novel points of intervention for the cure of neurological diseases of the brain network, such as epilepsy.

#### ACKNOWLEDGMENTS

The work carried out in this laboratory and reviewed here was performed in collaboration with Drs I. Aradi and V. Zsiros and was supported by National Institute of Mental Health (MH067561).

## REFERENCES

- Acsady, L., Katona, I., Martinez-Guijarro, F.J., Buzsaki, G. and Freund, T.F. (2000). Unusual target selectivity of perisomatic inhibitory cells in the hilar region of the rat hippocampus. *J Neurosci* 20:6907–6919.
- Alger, B.E. and Nicoll, R.A. (1980). Epileptiform burst afterhyperpolarization: calcium-dependent potassium potential in hippocampal CA1 pyramidal cells. *Science* 210:1122–1124.
- Alger, B.E. and Nicoll, R.A. (1982). Feed-forward dendritic inhibition in rat hippocampal pyramidal cells studied in vitro. *J Physiol* 328:105–123.
- Andersen, P., Eccles, J.C. and Loynan, Y. (1963). Recurrent inhibition in the hippocampus with identification of the inhibitory cell and its synapse. *Nature* 198:540–542.
- Aradi, I. and Holmes, W.R. (1999). Role of multiple calcium and calcium-dependent conductances in regulation of hippocampal dentate granule cell excitability. *J Comput Neurosci* 6:215–235.
- Aradi, I. and Maccaferri, G. (2004). Cell type-specific synaptic dynamics of synchronized bursting in the juvenile CA3 rat hippocampus. *J Neurosci* 24:9681–9692.
- Artola, A., Brocher, S. and Siger, W. (1990). Different voltage-dependent thresholds for inducing long-term depression and long-term potentiation in slices of rat visual cortex. *Nature* 347: 69–72.
- Avoli, M. (1996). GABA-mediated synchronous potentials and seizure generation. *Epilepsy* 37:1035–1042.
- Avoli, M., Perreault, P., Olivier, A. and Villemure, J.G. (1988). 4-Aminopyridine induces a long-lasting depolarizing GABAergic potential in human neocortical and hippocampal neurons maintained. *Neurosci Lett* 94:327–332.
- Axmacher, N. and Miles, R. (2004). Intrinsic cellular currents and the temporal precision of EPSP-action potential coupling in CA1 pyramidal cells. *J Physiol* 555:713–725.
- Bains, J.S., Longacher, J.M. and Staley, K.J. (1999). Reciprocal interactions between CA3 network activity and strength of recurrent collateral synapses. *Nat Neurosci* 2:720–726.
- Baldasseroni, R.J. (2005) Drug therapy of depression and anxiety disorders. In: Goodman and Gilman's the pharmacological basis of therapeutics, 11th edn (L. Brunton, J. Lazo, K. Parker, eds) pp. 429–460. McGraw-Hill, New York.
- Baldasseroni, R.J. and Tarazi, F.I. (2005). Pharmacotherapy of psychosis and mania. In: Goodman and Gilman's the pharmacological basis of therapeutics, 11th edn (L. Brunton, J. Lazo, K. Parker, eds) pp. 461–500. McGraw-Hill, New York.
- Bartos, M., Vida, I., Frotscher, M., Geiger, J.R. and Jonas, P. (2001). Rapid signaling at inhibitory synapses in a dentate gyrus interneuron network. *J Neurosci* 21:2687–2698.
- Bartos, M., Vida, I., Frotscher, M. et al. (2002). Fast synaptic inhibition promotes synchronized gamma oscillations in hippocampal interneuron networks. *Proc Natl Acad Sci USA* 99:13222–13227.
- Bekenstein, J.W. and Lothman, E.W. (1993). Dormancy of inhibitory interneurons in a model of temporal lobe epilepsy. *Science* 259:97–100.
- Ben-Ari, Y., Khazipov, R., Leinekugel, X., Caillard, O. and Gaiarsa, J.L. (1997). GABA, NMDA and AMPA receptors: a developmentally regulated ‘ménage à trois’. *Trends Neurosci* 20:523–529.
- Bennett, M.V.L. (1977). Electrical transmission: a functional analysis and comparison to chemical transmission. In: *Handbook of physiology*, volume I Cellular biology of neurons (E. Kandel, ed.) pp. 357–416. American Physiological Society, Bethesda.
- Bernard, C., Esclapez, M., Hirsch, J.C. and Ben-Ari, Y. (1998). Interneurons are not so dormant in temporal lobe epilepsy: a critical reappraisal of the dormant basket cell hypothesis. *Epilepsy Res* 32:93–103.
- Blatow, M., Rozov, A., Katona, I. et al. (2003). A novel network of multipolar bursting interneurons generates theta frequency oscillations in neocortex. *Neuron* 38:805–817.
- Borst, A. and Theunissen, F.E. (1999). Information theory and neural coding. *Nat Neurosci* 2:947:957.
- Buhl, E.H., Halasy, K. and Somogyi, P. (1994). Diverse sources of hippocampal unitary inhibitory postsynaptic potentials and the number of synaptic release sites. *Nature* 369:823–828.
- Chamberlain, N.L. and Dingledine, R. (1989). Control of epileptiform burst rate by CA3 hippocampal cell afterhyperpolarization in vitro. *Brain Res* 492:337–346.
- Chen, K., Neu, A., Howard, A.L. et al. (2007). Prevention of plasticity of endocannabinoid signaling inhibits persistent limbic hyperexcitability caused by developmental seizures. *J Neurosci* 27:46–58.
- Chevaleyre, V. and Castillo, P.E. (2003). Heterosynaptic LTD of hippocampal GABAergic synapses: a novel role of endocannabinoids in regulating excitability. *Neuron* 38:461–472.
- Chu, Z., Galarreta, M. and Hestrin, S. (2003). Synaptic interactions of late-spiking neocortical neurons in layer 1. *J Neurosci* 23:96–102.
- Cobb, S.R., Buhl, E.H., Halasy, K., Paulsen, O. and Somogyi, P. (1995). Synchronization of neuronal activity in hippocampus by individual GABAergic interneurons. *Nature* 378:75–78.
- Cohen, I., Navarro, V., Clemenceau, S., Baulac, M. and Miles, R. (2002). On the origin of interictal activity in human temporal lobe epilepsy in vitro. *Science* 298:1418–1421.
- Cohen, I., Navarro, V., Le Duigou, C. and Miles, R. (2003). Mesial temporal lobe epilepsy: a pathological replay of developmental mechanisms? *Biol Cell* 95:329–333.
- Connors, B.W. and Long, M.A. (2004). Electrical synapses in the mammalian brain. *Annu Rev Neurosci* 27:393–418.
- Dan, Y. and Poo, M.M. (2006). Spike timing-dependent plasticity: from synapse to perception. *Physiol Rev* 86:1033–1048.
- D'Antuono, M., Louvel, J., Kohling, R. et al. (2004). GABA<sub>A</sub> receptor-dependent synchronization leads to ictogenesis in the human dysplastic cortex. *Brain* 127:1626–1640.
- Decima, E.E. (1969). An effect of postsynaptic neurons upon presynaptic terminals. *Proc Natl Acad Sci USA* 63:58–64.
- Dingledine, R. and Langmoen, I.A. (1980). Conductance changes and inhibitory actions of recurrent IPSPs. *Brain Res* 185:277–287.
- Doherety, J. and Dingledine, R. (2001). Reduced excitatory drive onto interneurons in the dentate gyrus after status epilepticus. *J Neurosci* 27:25929–25938.

- Dzhala, V.I., Talos, D.M., Sdrulla, D.A. et al. (2005). NKCC1 transporter facilitates seizures in the developing brain. *Nat Med* 11:1205–1213.
- Freund, T. and Buzsaki, G. (1996). Interneurons of the hippocampus. *Hippocampus* 6:347–470.
- Frick, D. and Miles, R. (2000). EPSP amplification and the precision of spike timing in hippocampal neurons. *Neuron* 28:559–569.
- Frick, D. and Miles, R. (2001). Interneurons, spike timing, and perception. *Neuron* 32:771–77.
- Fukuda, T. and Kosaka, T. (2000). Gap junctions linking the dendritic network of GABAergic interneurons in the hippocampus. *J Neurosci* 20:1519–1528.
- Fukuda, T., Kosaka, T., Singer, W. and Galuske, R.A.W. (2006). Gap junctions among dendrites of cortical GABAergic neurons establish a dense and widespread intercolumnar network. *J Neurosci* 26:3434–3443.
- Galarreta, M. and Hestrin, S. (1999). A network of fast-spiking cells in the neocortex connected by electrical synapses. *Nature* 402:72–75.
- Galarreta, M. and Hestrin, S. (2002). Electrical and chemical synapses among parvalbumin fast-spiking GABAergic interneurons in adult mouse neocortex. *Proc Natl Acad Sci USA* 99:12438–12443.
- Galarreta, M., Erdelyi, F., Szabo, G. and Hestrin, S. (2004). Electrical coupling among irregular-spiking GABAergic interneuron expressing cannabinoid receptors. *J Neurosci* 24:9770–9778.
- Geiger, J.R.P., Lubke, J., Roth, A., Frotscher, M. and Jonas, P. (1997). Submillisecond AMPA receptor-mediated signaling at a principal neuron interneuron synapse. *Neuron* 18:1009–1023.
- Gibson, J.R., Beierlein, M. and Connors, B.W. (1999). Two networks of electrically coupled inhibitory neurons in neocortex. *Nature* 402:75–79.
- Gloor, P. (1991). Mesial temporal sclerosis: historical background and an overview from a modern perspective. In: *Epilepsy surgery* (H. Luders, ed.) pp. 689–703. Raven Press, New York.
- Hestrin, S. and Galarreta, M. (2005). Electrical synapses define networks of neocortical GABAergic neurons. *Trends Neurosci* 28:304–309.
- Hines, M.L. and Carnevale, N.T. (1997). The NEURON simulation environment. *Neuronal Comput* 9:1179–1209.
- Holmgren, C.D. and Zilberman, Y. (2001). Coincident spiking activity induces long-term changes in inhibition of neocortical pyramidal cells. *J Neurosci* 21:8270–8277.
- Isokawa, M. (1996). Decrement of GABA<sub>A</sub> receptor-mediated inhibitory postsynaptic currents in dentate granule cells in epileptic hippocampus. *J Neurophysiol* 75:1901–1908.
- Jonas, P., Bischofberger, J., Fricker, D. and Miles, R. (2004). Interneuron diversity series: fast in, fast out – temporal and spatial signal processing in hippocampal interneurons. *Trends Neurosci* 27:30–40.
- Klausberger, T., Magill, P.J., Marton, L.F. et al. (2003) Brain-state and cell-type-specific firing of hippocampal interneurons in vivo. *Nature* 421:844–848.
- Klausberger, T., Marton, L.F., Baude, A., Roberts, J.D., Magill, P.J. and Somogyi, P. (2004). Spike timing of dendrite-targeting bistratified cells during hippocampal network oscillations in vivo. *Nat Neurosci* 7:41–47.
- Klausberger, T., Marton, L.F., O'Neill, J. et al. (2005). Complementary roles of cholecystokinin- and parvalbumin-expressing GABAergic neurons in hippocampal network oscillations. *J Neurosci* 25:9782–9793.
- Kogo, N., Dalezios, Y., Capogna, M., Ferraguti, F., Shigemoto, R. and Somogyi, P. (2004). Depression of GABAergic input to identified hippocampal interneurons by group III metabotropic glutamate receptors in the rat. *Eur J Neurosci* 19:2727–2740.
- Konig, P., Engel, A.K. and Singer, W. (1996). Integrator or coincidence detector? The role of the cortical neuron revisited. *Trends Neurosci* 19:130–137.
- Korn, S.J., Giacchino, J.L., Chamberlin, N.L. and Dingledine, R. (1987). Epileptiform burst activity induced by potassium in the hippocampus and its regulation by GABA-mediated inhibition. *J Neurophysiol* 57:325–340.
- Kosaka, T. and Hama, K. (1985). Gap junctions between non-pyramidal cell dendrites in rat hippocampus (CA1 and CA3 regions): a combined Golgi-electron microscope study. *J Comp Neurol* 231:150–161.
- Lamsa, K. and Taira, T. (2003). Use-dependent shift from inhibitory to excitatory GABA<sub>A</sub> receptor action in SP-O interneurons in the rat hippocampal CA3 area. *J Neurophysiol* 90:1983–1995.
- Larkum, M.E., Zhu, J.J. and Sakmann, B. (1999). A new cellular mechanism for coupling inputs arriving at different cortical layers. *Nature* 398:338–341.
- Lopatsev, V. and Schwartzkroin, P.A. (1999). GABA<sub>A</sub>-dependent chloride influx modulates GABA<sub>B</sub>-mediated IPSPs in hippocampal pyramidal cells. *J Neurophysiol* 82:1218–1223.
- Lopatsev, V., Schwartzkroin PA (2001). GABA<sub>A</sub>-dependent chloride influx modulates reversal potential of GABA<sub>B</sub>-mediated IPSPs in hippocampal pyramidal cells. *J Neurophysiol* 85:2381–2387.
- Maccaferri, G. (2005). Stratum oriens horizontal interneurone diversity and hippocampal network dynamics. *J Physiol* 562:73–80.
- Maccaferri, G. and Dingledine, R. (2002). Control of feedforward dendritic inhibition by NMDA receptor-dependent spike timing in hippocampal interneurons. *J Neurosci* 22:5462–5472.
- Maccaferri, G. and Lacaille, J.C. (2003). Interneuron diversity series: hippocampal interneuron classifications – making things as simple as possible, not simpler. *Trends Neurosci* 26:564–571.
- Maccaferri, G., Roberts, D.B.J., Szucs, P., Cottingham, C.A. and Somogyi, P. (2000). Cell surface domain specific postsynaptic currents evoked by identified GABAergic neurons in rat hippocampus in vitro. *J Physiol* 524:91–116.
- Magee, J.C. and Johnston, D. (1997). A synaptically controlled, associative signal for Hebbian plasticity in hippocampal neurons. *Science* 275:209–213.
- Marder, E. and Eisen, J.S. (1984). Electrically coupled pacemaker neurons respond differently to same physiological inputs and neurotransmitters. *J Neurophysiol* 51:1362–1374.
- Markram, H. (2006). The blue brain project. *Nat Review Neurosci* 7:153–160.
- Markram, H., Lubke, J., Frotscher, M. and Sakmann, B. (1997). Regulation of synaptic efficacy by coincidence of postsynaptic APs and EPSPs. *Science* 275:213–215.
- Martin, A.R. and Pilar, G. (1963). Dual mode of synaptic transmission in the avian ciliary ganglion. *J Physiol* 168:443–463.
- McBain, C.J. (1995). Hippocampal inhibitory neuron activity in the elevated potassium model of epilepsy. *J Neurophysiol* 73:2853–2863.
- McBain, C.J., Traynelis, S.F. and Dingledine, R. (1993). High potassium-induced synchronous bursts and electrographic seizures. In: *Epilepsy: models, mechanisms and concepts* (P.A. Schwartzkroin, ed.) pp. 437–461. Cambridge University Press, Cambridge.
- McNamara, J.O. (2005). Pharmacotherapy of the epilepsies. In: *Goodman and Gilman's the pharmacological basis of therapeutics*, 11th edn (L. Brunton, J. Lazo, K. Parker, eds) pp. 501–527. McGraw-Hill, New York.

- Menendez de la Prida, L., Huberfeld, G., Cohen, I. and Miles, R. (2006). Threshold behavior in the initiation of hippocampal population burst. *Neuron* 49:131–142.
- Meyer, A.H., Katona, I., Blatow, M., Rozov, A. and Monyer, H. (2002). *in vivo* labeling of parvalbumin-positive interneurons and analysis of electrical coupling in identified neurons. *J Neurosci* 22:7055–7064.
- Miles, R. and Wong, R.K.S. (1983). Single interneurons can initiate synchronized population discharge in the hippocampus. *Nature* 306:371–373.
- Miles, R. and Wong, R.K.S. (1987a). Latent synaptic pathways revealed after tetanic stimulation in the hippocampus. *Nature* 329:724–726.
- Miles, R. and Wong, R.K.S. (1987b). Inhibitory control of local excitatory circuits in the guinea-pig hippocampus. *J Physiol* 388:611–629.
- Miles, R. and Poncer, J.-C. (1996). Paired recordings from neurons. *Curr Opin Neurobiol* 6:387–394.
- Miles, R., Toth, K., Gulyas, A.I., Hajos, N. and Freund, T.F. (1996). Differences between somatic and dendritic inhibition in the hippocampus. *Neuron* 16:815–823.
- Nomura, M., Fukai, T. and Aoyagi, T. (2003). Synchrony of fast-spiking interneurons interconnected by GABAergic and electrical synapses. *Neural Comput* 15:2179–2198.
- Pedley, T.A. (1984). Epilepsy and the human electroencephalogram. In: *Electrophysiology of epilepsy* (P.A. Schwartzkroin and ?? Wheal, eds) pp. 1–30. Academic Press, London.
- Pereda, A.E., Bell, T.D. and Faber, D.S. (1995). Retrograde synaptic communication via gap junctions coupling auditory afferents to the Mauthner cell. *J Neurosci* 15:5943–5955.
- Perez-Velazquez, J.L., Carlen, P.L. and Skinner, F.K. (2001). Artificial electrotonic coupling affects neuronal firing patterns depending upon cellular characteristics. *Neuroscience* 103:841–849.
- Perkins, K.L. (2002). GABA application to hippocampal CA3 or CA1 stratum lacunosum-moleculare excites and interneuron network. *J Neurophysiol* 87:1404–1414.
- Pouille, F. and Scanziani, M. (2001). Enforcement of temporal fidelity in pyramidal cells by somatic feed-forward inhibition. *Science* 293:1159–1163.
- Price, C.J., Cauli, B., Kovacs, E.R. et al. (2005). Neurogliaform neurons form a novel inhibitory network in the hippocampal CA1 area. *J Neurosci* 25:6775–6786.
- Prinz, A.A., Abbott, L.F. and Marder, E. (2004). The dynamic clamp comes of age. *Trends Neurosci* 27:218–224.
- Ross, F.M., Gwyn, P., Spanswick, D. and Davies, S.N. (2000). Carbenoxolone depresses spontaneous epileptiform activity in the CA1 region of rat hippocampal slices. *Neuroscience* 100:789–796.
- Rutecki, P.A., Lebeda, F.J. and Johnston, D. (1985). Epileptiform activity induced by changes in extracellular potassium in the hippocampus. *J Neurophysiol* 54:1363–1374.
- Salin, P.A., Scanziani, M., Malenka, R.C. and Nicoll, R.A. (1996). Distinct short-term plasticity at two excitatory synapses in the hippocampus. *Proc Natl Acad Sci USA* 93:13304–13309.
- Saraga, F., Leo, N. and Skinner, F.K. (2006). Distal gap junctions and active dendrites can tune network dynamics. *J Neurophysiol* 95:1669–1682.
- Scanziani, M. (2000). GABA spillover activates postsynaptic GABA(B) receptors to control rhythmic hippocampal activity. *Neuron* 25:673–681.
- Schwartzkroin, P.A. (1986). Regulation of excitability in hippocampal neurons. In: *The hippocampus*, Vol 3 (R.L. Isaacson and K.H. Pribram, eds), pp. 113. Plenum, New York.
- Schwartzkroin, P.A. (1994). Cellular electrophysiology of human epilepsy. *Epilepsy Res* 17:185–192.
- Schwartzkroin, P.A. and Haglund, M.M. (1986). Spontaneous rhythmic synchronous activity in epileptic human and normal monkey temporal lobe. *Epilepsia* 27:523–533.
- Shadlen, M.N. and Newsome, W.T. (1994). Noise, neuronal codes, and cortical organization. *Curr Opin Neurobiol* 4:569–579.
- Sherman, A. and Rinzel J (1992). Rhythmic effects of weak electrotonic coupling in neuronal models. *Proc Natl Acad Sci USA* 89:2471–2474.
- Simon, A., Szabolcs, O., Molnar, G., Szabadics, J. and Tamas, G. (2005). Gap junctional coupling between neurogliaform cells and various interneuron types in the neocortex. *J Neurosci* 25:6278–6285.
- Slesinger, P. and Bell, C.C. (1985). Primary afferent fibers conduct impulses in both directions under physiological stimulus conditions. *J Comp Physiol* 157:15–22.
- Sloviter, R.S. (1991). Permanently altered hippocampal structure, excitability, and inhibition after experimental status epilepticus in the rat: the ‘dormant basket cell’ hypothesis and its possible relevance to temporal lobe epilepsy. *Hippocampus* 1:41–66.
- Sofky, W.R. (1995). Simple codes vs. efficient codes. *Curr Opin Neurobiol* 5:239–247.
- Somogyi, P. and Klausberger, T. (2005). Defined types of cortical interneurone structure and space and spike timing in the hippocampus. *J Physiol* 562:9–26.
- Somogyi, P., Nunzi, M.G., Gorio, A. and Smith, A.D. (1983). A new type of specific interneuron in the monkey hippocampus forming synapses exclusively with the axon initial segment of pyramidal cells. *Brain Res* 259:137–142.
- Staley, K.J., Soldo, B.L. and Proctor, W.R. (1995). Ionic mechanisms of neuronal excitation by inhibitory GABA(A) receptors. *Science* 269:977–981.
- Staley, K.J., Longacher, M., Bains, J.S. and Yee, A. (1998). Presynaptic modulation of CA3 network activity. *Nat Neurosci* 1:201–209.
- Szabadics, J., Lorincz, A. and Tamas, G. (2001).  $\beta$  and  $\gamma$  frequency synchronization by dendritic GABAergic synapses and gap junctions in a network of cortical interneurons. *J Neurosci* 21:5824–5831.
- Taylor, D.C., Falconer, M.A., Bruton, C.J. and Corsellis, J.A. (1971). Focal dysplasia of the cerebral cortex in epilepsy. *J Neurol Neurosurg Psychiatr* 34:369–387.
- Thompson, S.M. and Gähwiler, B.H. (1989a). Activity-dependent disinhibition. I. Repetitive stimulation reduces IPSP driving force and conductance in the hippocampus *in vitro*. *J Neurophysiol* 61:501–511.
- Thompson, S.M. and Gähwiler, B.H. (1989b). Activity-dependent disinhibition. II. Effects of extracellular potassium, furosemide, and membrane potential on ECl- in hippocampal CA3 neurons. *J Neurophysiol* 61:512–523.
- Traub, R.D. and Miles, R. (1991). *Neuronal networks of the hippocampus*. Cambridge University Press, Cambridge.
- Traub, R.D., Pais, I., Bibbig, A. et al. (2003). Contrasting roles of axonal (pyramidal cell) and dendritic (interneuron) electrical coupling in the generation of neuronal network oscillations. *Proc Natl Acad Sci USA* 100:1370–1374.

- Tsubokawa, H. and Ross, W.N. (1996). IPSPs modulate spike backpropagation and associated  $\{\text{Ca}^{2+}\}$  changes in the dendrites of hippocampal CA1 pyramidal neurons. *J Neurophysiol* 76:2896–2906.
- Venance, L., Rozov, A., Blatow, M., Burnashev, N., Feldmayer, D. and Monyer, H. (2000). Connexin expression in electrically coupled postnatal rat brain neurons. *Proc Natl Acad Sci USA* 97:10260–10265.
- Vida, I., Bartos, M. and Jonas, P. (2006). Shunting inhibition improves robustness of gamma oscillations in hippocampal interneuron networks by homogenizing firing rates. *Neuron* 49:107–117.
- Wilson, W.A. and Bragdon, A. (1993). Brain slice models for the study of seizures and interictal spikes. In: *Epilepsy: models, mechanisms and concepts* (P.A. Schwartzkroin, ed.) pp. 371–387. Cambridge University Press, Cambridge.
- Wong, R.K.S. and Prince, D.A. (1978). Participation of calcium spikes during intrinsic burst firing in hippocampal neurons. *Brain Res* 159:385–390.
- Yamada, W.M., Koch, C. and Adams, P.R. (1989). Multiple channels and calcium dynamics. In: *Methods in neuronal modeling: from synapses to networks* (C. Koch C and I. Segev, eds) pp. 97–134. MIT Press, Cambridge.
- Zhang, X.L., Zhang, L. and Carlen, P.L. (2004). Electrotropic coupling between stratum oriens interneurones in the intact *in vitro* mouse juvenile hippocampus. *J Physiol* 558:825–839.
- Ziburkus, J., Cressman, J.R., Barreto, E. and Schiff, S.J. (2006). Interneuron and pyramidal cell interplay during *in vitro* seizure-like events. *J Neurophysiol* 95:3948–3954.
- Zipser, B. and Bennett, M.V.L. (1976). Responses of cells of posterior lateral line lobe to activation of electroreceptors in a Mormyrid fish. *J Neurophysiol* 39:693:712.
- Zsiros, V. and Maccaferri, G. (2005). Electrical coupling between interneurons with different excitable properties in stratum lacunosum-moleculare of the juvenile CA1 rat hippocampus. *J Neurosci* 25:8686–8695.
- Zsiros, V., Aradi, I. and Maccaferri, G. (2007). Propagation of postsynaptic currents and potentials via gap junctions in GABAergic networks of the rat hippocampus. *J Physiol* 578:527–544.

# 20

## EXPERIMENTAL AND THEORETICAL ANALYSES OF SYNCHRONY IN FEEDFORWARD NETWORKS

ALEX. D. REYES

### ABSTRACT

A hallmark of neural activity during a seizure is the appearance of synchronous events throughout the brain. Synchrony, however, is not exclusively found during a seizure but seems to be ubiquitous under normal conditions and, indeed, may be crucial for information processing. This chapter focuses on recent experimental and theoretical studies of synchrony in feedforward neural networks. This network is the backbone for information transfer in the brain given that signals must be propagated from neuron to neuron, from one nucleus to another, and from one brain region to another. Epileptiform activity may represent an aberrant manifestation of functional synchrony. If so, then understanding the mechanism by which synchrony propagates normally through a neural network might provide clues as to how the synchrony becomes pathological and may suggest preventive measures. As in feedforward networks, epileptiform activity originates from a focal point and then spreads rapidly in a stereotypic manner through a sequence of cortical areas. The simplicity of the feedforward network means that both experimental and rigorous theoretical approaches can be used to derive very general principles, which may then be applied to the study of epilepsy.

### INTRODUCTION

#### SYNCHRONY IN THE NORMAL BRAIN

There is a wealth of electrophysiological evidence suggesting that synchronous firing of neurons is present in the normal functioning brain. Recordings in awake animals reveal synchronous discharges occur, e.g. when animals are exploring space (Csicsvari et al., 1999), performing olfactory discrimination (Stopfer et al., 1997; Martin et al., 2004), motor (Riehle et al., 1997; Hatsopoulos, 1998), visual (Azouz and Gray, 1999, 2003) and memory-related (Sakurai and Takahashi, 2006; Uhlhaas and Singer, 2006) tasks. Synchrony is also postulated to play an important role in generating stereotypical firing patterns in cortex (Ikegaya et al., 2004). Convincing evidence for the presence of synchrony also comes from recent intracellular recordings *in vivo* (Azouz and Gray, 2003; Ikegaya et al., 2004; Bruno and Sakmann, 2006). These experiments reveal the presence of very large voltage transients whose amplitudes often exceed 10 mV, far greater than the 0.3–1 mV unitary synaptic potentials documented between two connected neurons (Markram et al., 1997; Reyes et al., 1998; Reyes and Sakmann, 1999). Therefore, the large transients are likely to be due to the summation of many unitary events that occur synchronously.

Although synchrony is prevalent, its function is still hotly debated. Synchrony has been postulated to be the substrate for encoding precise timing of action potentials that is necessary for pattern formation (Abeles, 1991) or for ‘binding’ activities of neurons that encode distinct features of a stimulus (Engel and Singer, 2001; Singer, 2001; but see Shadlen and Movshon, 1999). Intracellular recordings *in vivo* reveal that stimulus driven activity is often associated with the appearance or increase in the frequency of synchronous potentials. Experiments with the iteratively constructed networks (see below) suggest that synchrony is crucial for the propagation of information about input rate (Reyes, 2003). In the absence of synchrony, the firing rate ( $F$ ) at successive layers ( $L$ ) can be described by:  $F_{L+1} = kF_L$  where  $k$  is a constant

whose value depends on several parameters including the number of presynaptic inputs, the size of synaptic currents and the input-output transfer function of each neuron. Thus,  $F$  is preserved across layers only if the various parameters are such that  $k = 1$ ; otherwise  $F$  will either die out ( $k < 1$ ) or blow up ( $k > 1$ ). In the synchronous mode, where frequency is encoded as the inverse of the time between synchronous events,  $F$  is propagated more reliably because the large transient potentials are considerably less sensitive to potential variability across layers.

### SYNCHRONY DURING SEIZURES

Electroencephalographic (EEG) recordings in patients reveal stereotypical firing patterns during a seizure (see McCormick and Contreras, 2001 for a review). EEG recordings detect the *net* transmembrane current generated by the synaptic activity of a large population of synchronously firing neurons; waveforms from neurons firing asynchronously cancel out. During a seizure, EEG records are characterized by high frequency discharges (tonic) followed by lower frequency transients (clonic). In between seizures are interictal discharges, which consist of brief (100–200 ms) depolarizations that occur periodically. The waveforms are mediated by network synaptic interactions.

Epileptiform activity resembling that observed *in vivo* can be induced in the *in vitro* brain slice preparation. Seizures are commonly generated in the slice by increasing the overall excitability of the neural network. Methods for this include bathing the slice in high  $K^+$  solutions, blocking GABA<sub>A</sub>-mediated inhibitory inputs, blocking  $K^+$  channels with 4-aminopyridine (4-AP) and removing  $Mg^{2+}$  to unveil the N-methyl-D-aspartate (NMDA) components of glutamatergic synapses. Under these conditions, field potential recordings reveal several phases that correspond approximately to those observed in patients: sustained transients during the seizure (ictal) followed by briefer transients (interictal) (Avoli et al., 1996). Intracellular recordings reveal that neurons exhibit large, sustained depolarizations during the ictal phase, characterized by bursts of action potentials riding upon an underlying depolarization (Miles and Wong, 1983; Lopantsev and Avoli, 1998a; McCormick and Contreras, 2001). As will be shown below, these are ideal conditions for spreading synchronous firing in feedforward networks.

*In vitro* recordings indicate that several cortical areas are activated in a feedforward manner. In a slice preparation containing hippocampus and entorhinal cortex (Avoli et al., 1996; Nagao et al., 1996), pharmacologically induced epileptiform activity progresses sequentially from entorhinal cortex to CA3 and then to CA1 of the hippocampus. Moreover, within entorhinal cortex, epileptiform activity originates from layer V and then propagates to the upper layers (Avoli et al., 1996; Jones and Lambert, 1990). The corticothalamic loop, which may provide a feedback regenerative process important for sustaining epileptiform discharges (McCormick and Contreras, 2001), can also be thought of as a feedforward circuit consisting of alternating layers of cortical and thalamic neurons.

In summary, there is strong evidence for spread of synchrony in a feedforward manner during a seizure. An important question is therefore why synchrony that is present during normal brain function becomes uncontrolled during a seizure.

## SYNCHRONY IN FEEDFORWARD NETWORKS

### RECONSTRUCTING NETWORKS *IN VITRO*

It is very difficult to examine signal processing in cortex, which consists of several classes of pyramidal cells and excitatory and inhibitory interneurons. It is not possible at the moment to monitor the activities of all the cells during e.g. sensory stimulation, nor is it possible to stimulate, under well-controlled conditions, specific neural populations in a manner similar to what would occur under natural conditions.

To circumnavigate these problems, an iterative procedure was developed which essentially permits the reconstruction of the firing of thousands of neurons within a network from the activity of a single recorded neuron (Reyes, 2003). The technique is a hybrid of experiments in brain slices and computer simulations and offers advantages of both. As with simulations, it is possible to vary systematically parameters to explore synchrony under a variety of conditions. However, the networks are effectively comprised of real neurons, rather than simplified models with many assumed parameters. Moreover, the technique allows us to input specific patterns and monitor the associated activities of all the neurons in the network.

Most networks, including those with recurrent excitation and/or feedback inhibition, can be reconstructed *in vitro* using the iterative procedure (Reyes, 2005). However, it is more informative at this stage first to consider a simple feedforward network. Once the general principles are understood with theoretical analyses (see below), the complexity of the network can be gradually increased to resemble the circuitry in cortex (see below).

### Iterative procedure

To construct neural networks using the iterative procedure, whole-cell (or intracellular) recording is first established in a neuron. The general strategy is to simulate the activities of neurons in the first layer, use these to generate inputs which will then be delivered to the recorded neuron several times (once for each neuron in the layer) to recreate the firings of neurons in the second layer. The firings of the recorded neuron are then used to calculate inputs that are again delivered to the recorded neuron (which now represents a neuron in the third layer). This procedure is iterated until the activities of the entire network are reconstructed. The detailed procedure is as follows.

The network shown in Figure 20.1A consists of  $m$  layers, each with  $w$  neurons. The network is sparsely connected so that each neuron has a 0.1 probability of being connected to a neuron in the next layer. The recorded neuron is defined

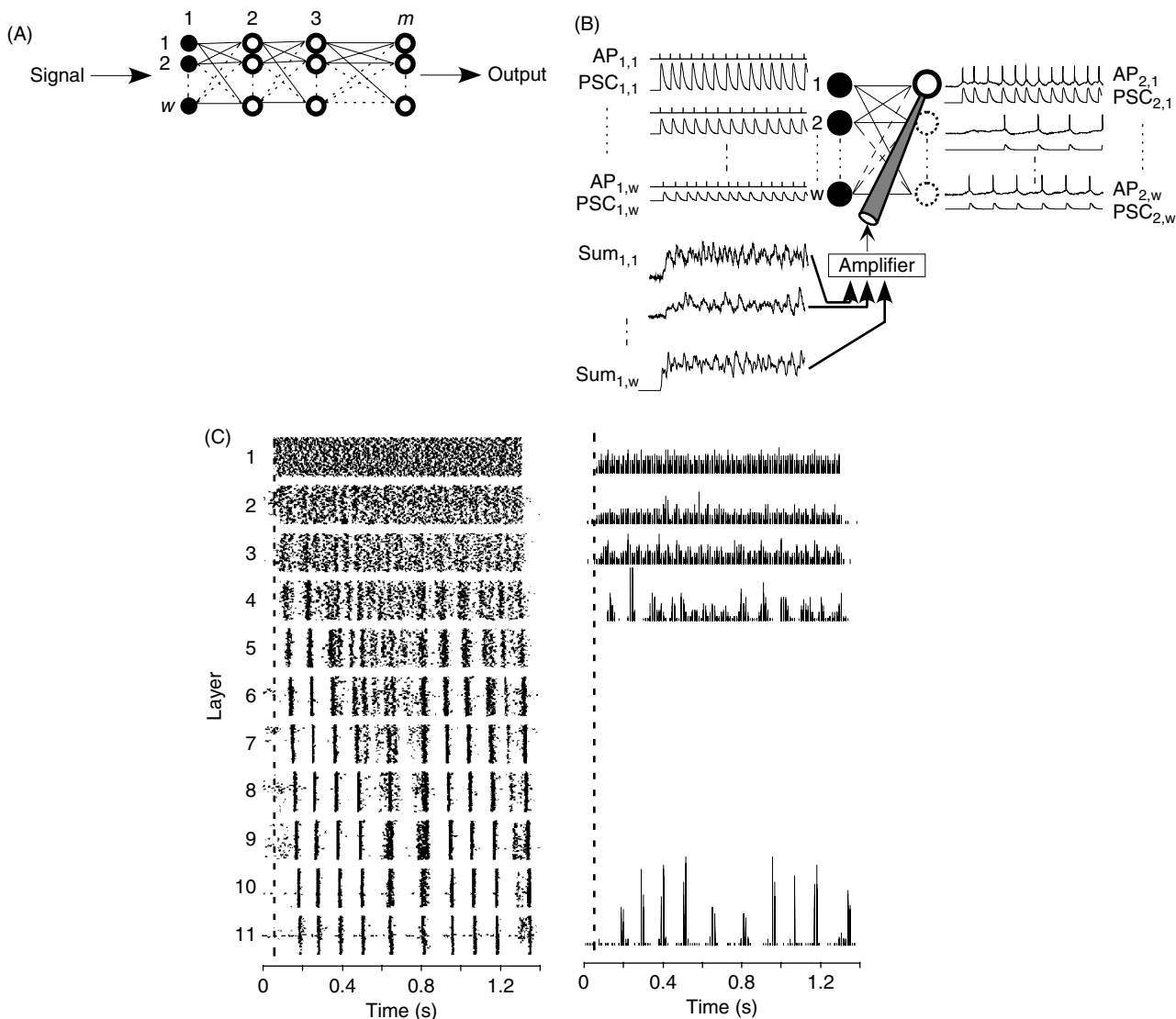


**FIGURE 20.1** Synchrony in *in vitro* feedforward networks. (A) Schematic of a feedforward network consisting of  $m$  layers with  $w$  neurons per layer. (B) Protocol for reconstructing the firing of the neurons in the feedforward network (see text for details). The first layer of neurons is simulated. The spikes are used to calculate synaptic currents (PSCs), which are then injected into the recorded neuron. In the first iteration, the recorded neuron is in the second layer. The neuron is stimulated a total of  $w$  times, with each spike train representing the firing of a neuron in the second layer. The amplitudes and latencies of the synaptic currents are randomized. The resultant spike trains are then used to generate synaptic currents, which are re-injected back to the neuron  $w$  more times. This reconstructs the firing of neurons in the third layer. This iterative procedure is repeated until the firing of all  $m$  layers are re-constructed. (C) Dot rasters of neurons in each layer of an 11-layer network (left). Associated poststimulus time histograms are shown on right. From Reyes (2003).

to be in the second layer (Figure 20.1B). The activities of the  $w$  neurons in the first layer are simulated and are made to fire repetitively and asynchronously with respect to each other. Each spike produces a transient that resembles unitary excitatory postsynaptic current (PSC). The amplitude and latency of the PSCs are randomized according to experimentally measured distributions (Markram et al., 1997; Reyes et al., 1998; Reyes and Sakmann, 1999). A subset (10% to reflect the 0.1 connection probability between pyramidal cells) of the trains are chosen at random and summed. The resultant waveform ( $\text{sum}_{1,1}$ , Figure 20.1B) therefore represents the net synaptic current that the layer 1 neurons' combined activity would generate in a layer 2 neuron. This waveform is then injected into the recorded neuron to evoke repetitive firing ( $\text{AP}_{2,1}$ ) in one of the cells in the second layer.

Because the network is assumed to be homogeneous, all cells within a layer are identical and differ only in their inputs from the previous layer. Therefore, to replicate the activity of another cell (dashed circles) in layer 2, a new current trace ( $\text{sum}_{1,2}$ ) is calculated and injected into the pyramidal neuron once again to evoke repetitive firing ( $\text{AP}_{2,2}$ ). The firing is equivalent to another cell in the layer firing. To complete the first iteration, this process is repeated  $w - 1$  times, once for each neuron in layer 2. To propagate the signal into the third layer, the procedure is repeated except that simulated layer 1 AP trains are replaced with the evoked 'layer 2' AP trains. The summed current is injected into the neuron and the resultant firing is equivalent to that of a cell in the third layer. The pyramidal neuron is once again stimulated  $w - 1$  times to complete the second iteration. This procedure is iterated  $m - 1$  times, once for each layer. In this manner, the signal introduced in the first layer could be systematically traced through the network.

#### DEVELOPMENT OF SYNCHRONY

The most salient feature of activity in the feedforward network is synchrony. In every case examined, synchrony developed by layers 2–3, even though the neurons in the first layer were made to fire asynchronously. Figure 20.1C shows dot rasters, where each row of dots represents a train of APs in a given cell, and the population poststimulus histograms (PSTHs) for each layer of an 11-layer network. In layer 1, the dots in the raster are distributed uniformly and the histogram is flat, reflecting the fact that the simulated neurons fired asynchronously with respect to each other. In layer 2, which is constructed from the activity of real neurons, the dots begin to cluster and the histograms begin to develop peaks indicating that the neurons have started to fire synchronously. With each passing layer, the clustering and histogram peaks become sharper eventually to reach steady-state values.

The development of synchrony is not strongly dependent on the architecture of the network and is indeed robust under a wide variety of configurations. Changing the statistics of the input (from repetitive firing to a Poisson process) or decreasing the connection probability (from 0.1 to 0.01) had little effect on the development of synchrony. To eliminate the possibility that synchrony arose because the network behavior was reconstructed from the activity of only one cell, simultaneous recordings were from up to four cells to make the network more heterogeneous. The neurons were chosen so that their input resistances and firing responses were different: some fired repetitively with different degrees of adaptation, while others fired repetitive bursts. Increasing heterogeneity qualitatively changed the firing patterns but failed to eliminate synchrony. Synchrony also persisted when a random DC bias was introduced from trial to trial to simulate different initial conditions, the PSCs exhibited frequency-dependent changes in amplitudes, and slow NMDA-like PSCs were used.

Synchrony also persisted in the presence of background synaptic noise. The rationale for adding noise to the input is to increase the variability in the timing of action potentials across neurons in a layer. Under *in vivo* conditions, synaptic noise is composed of both excitatory and inhibitory inputs. Inhibitory neurons were incorporated into the iteratively constructed network either by using some of the spike trains of the recorded pyramidal neuron to represent those of inhibitory neurons or to record simultaneously from a pyramidal neuron and an inhibitory interneuron. Excitatory and inhibitory postsynaptic potentials were evoked in the recorded cell by using a dynamic clamp circuit to inject current (Reyes, 2003). Dynamic clamp accurately reproduces the conductance changes caused by synaptic input. Initially, levels of excitatory and inhibitory inputs were adjusted to be in the 'balanced' configuration so that the mixed input increased the variance but not the mean of the injected current. The problem was that firing was difficult to evoke under the balanced configuration because the associated conductances limited the amplitude of the voltage fluctuations; threshold was rarely crossed. Increasing the number of inputs was ineffective because the total conductance of the cell also increased. Similar observations were made during injection of Poisson distributed barrages of excitatory and inhibitory conductances under dynamic clamp (Chance et al., 2002).

Alternatively, the background noise can be injected in current clamp rather than dynamic clamp mode. In current clamp mode, the conductance changes associated with synaptic input are neglected so that the magnitude of the injected current can be arbitrarily large. Injecting noise did reduce synchrony (Reyes, 2003) but only at levels that probably cannot be achieved under physiological conditions (Chance et al., 2002).

Preliminary results with simulations suggest that adding feedback inhibition or recurrent excitation does not remove synchrony (Cateau and Reyes, 2003). In fact, under certain conditions, feedback enhances synchrony. Feedback effectively adds temporal structure to the input due to the fact that there is a fixed latency determined by the axonal length and synaptic delays.

In summary, the experiments show that any network with more than three layers will likely give rise to synchronous firing. It should be noted that inputs were artificially made asynchronous; synchrony will develop faster if the inputs are already partially correlated.

### MODELING FEEDFORWARD NETWORKS

The *in vitro* experiments suggest that synchrony is the default state of the feedforward network. In order to devise ways of minimizing synchrony and perhaps, also the rapid spread of epileptiform activity, it is important first to understand the underlying mechanisms that give rise to synchrony. Many of the important principles can be readily understood intuitively with a ‘toy’ model. A more formal model that uses tools from non-equilibrium statistical physics will be presented below.

### TOY MODEL

The development of synchrony in the feedforward networks can in part be explained by two simple phenomena. The first is that with any stimulus, neurons that receive common depolarizing inputs will tend to fire closely in time after the stimulus onset. Stimulus-evoked excitatory inputs into all neurons cause their membrane potential to rise from rest (or any initial conditions) and reach threshold at a rate determined by the membrane time constant. This can be seen readily by modeling the first layer as a network of unconnected leaky integrate-and-fire (LIF) neurons. Numerical simulations of an LIF neuron for a step current give an exponentially rising voltage. Upon reaching threshold, an ‘action potential’ occurs and the membrane potential is reset back to near rest. Figure 20.2A (left) shows the firing of representative neurons in a layer in response to a current step. Independent noise is added to each neuron to produce variability in spike times. The population PSTH, compiled by summing the individual spike trains, shows a peak shortly after the current step onset followed by progressively smaller peaks. The peak indicates that the spike times tend to cluster at a certain time window; had the spikes occurred randomly with respect to each other, the histograms would be flat.

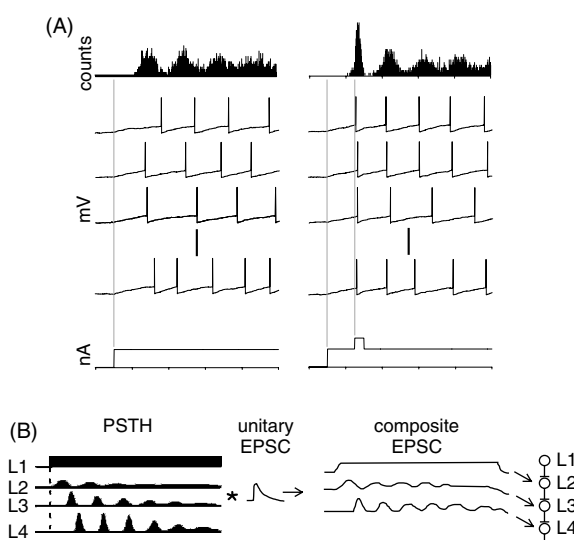


**FIGURE 20.2** Mechanisms underlying the development of synchrony. (A, left) Firing simulated with leaky integrate-and-fire neurons. A step of current was injected to each neuron (bottom trace). Noise was added to the voltage to increase spike time variability. The poststimulus time histogram (PSTH) is shown on top. Right, when a brief current transient was added to the step, the peaks in the poststimulus time histogram became taller and narrower. (B) Schematic showing the relation between the PSTH (left) in a given layer and the composite synaptic current that is delivered to the next layer of neurons (right). The composite current is obtained by convolving the PSTH with the unitary postsynaptic current.

The second phenomenon is that any transients in the current will tend to synchronize the cells. As described previously (Perkel et al., 1967; Mainen and Sejnowski, 1995), transient inputs will increase the temporal precision of spikes. This effect can be seen by adding a ‘bump’ to the step of current (see Figure 20.2A, right). The added pulse causes the membrane potential to rise rapidly to threshold, effectively constricting the distributions of the spikes. The result is that the peaks of the PSTH become narrower and larger. The sharpening of the peaks is magnified if the amplitude and/or rate of rise of the bumps are increased.

These two phenomena provide important clues as to why synchrony increases in successive layers. In the experiments, neurons in the first (simulated) layers were made to fire asynchronously with respect to each other. The resultant PSTH is therefore uniform (see Figure 20.2B). The total input,  $I_i(t)$ , to the second layer is essentially the PSTH filtered by the unitary excitatory postsynaptic current (uEPSC). Mathematically, this is equivalent to convolving the PSTH with the uEPSC:

$$I_i(t) = \int PSTH_{i-1}(t) * uEPSC(t - \tau) d\tau \quad (1)$$

Because the PSTH is uniform, the total synaptic current in layer 2 resembles a DC step. As a result, the first phenomenon dictates that the spikes will cluster after a short delay and the PSTH will have peaks. These spikes in turn provide inputs into the third layer. Performing the convolution again shows that the net current into layer 3 neurons will have ‘bumps’. Because of the second phenomenon, the resultant PSTHs in layer 3 will have peaks that are narrower and taller. These changes in the PSTHs proceed in successive layers until steady-state synchrony is reached. Note, however, that the toy model, unlike the experiments, predicts that synchrony will decrease with time after the stimulus onset. This discrepancy is examined in greater detail in the next section.

Synchrony propagation was investigated more formally by Diesmann et al. (1999) and by Cateau and Fukai (2001) using idealized state-space analyses. In these modeling studies, the authors delivered a packet of input to the first layer. The packet consisted of spikes that were Gaussian distributed in time. The authors varied the width of the packet (1 standard deviation) and the area (= number of spikes) and examined how the packet propagated through the layers. They ran simulations using different initial values of area and width and then traced the changes in values in a plot of area versus width (idealized state-space graph). There were only two possibilities. If the packet width was sufficiently narrow and the area sufficiently large, the packet propagated successfully. As with the toy model, the packet systematically narrowed to a steady value. In other words, there was an attractor in the state-space graph. On the other hand, if the packet width was broad or the area small so that the initial values were far from the attractor, the packet degraded with successive layers and failed to propagate.

In summary, neurons in a given population will tend to respond within a finite time window after the stimulus onset. This onset synchrony, and the associated peaks that come afterward, provide the seed for synchrony in the next layers. As will be argued below, the onset synchrony is difficult to eliminate under physiological conditions.

### FOKKER-PLANCK FORMULATION

To uncover the basic laws that govern the development of synchrony, it is useful to use analyses developed in the physical sciences for analyzing the behavior of large systems of randomly forced particles. Recently, Fokker-Planck equations (FPEs; see Gardiner, 2003) have been applied to the study of feedforward networks (Cateau and Fukai, 2001; Cateau and Reyes, 2005; Doiron et al., 2006). FPEs were originally used by physicists to describe Brownian motion and other diffusive systems. The FPE provides a compact expression that essentially relates the properties of idealized individual neuron models to the behavior of the entire network. Also, from a practical viewpoint, a well-coded FPE program is considerably faster than numerical simulations of large networks of LIF neurons. FPEs may be adapted to neural networks as follows.

For simplicity, each neuron in a layer is modeled as a leaky integrate and fire (LIF) process:

$$\tau_m \frac{dV}{dt} = -V + R_m I_{syn}(t) \quad (2)$$

where  $V$  is voltage,  $\tau_m$  is the membrane time constant and  $R_m$  is the membrane resistance. Each  $i^{\text{th}}$  neuron receives a net synaptic input,  $I_{syn}(t)$ . As a first approximation, the individual synaptic events that comprise  $I_{syn}$  are assumed to be Poisson so that the mean and variance are equal and vary with the input rate.  $I_{syn}$  may therefore be described in terms of a diffusion approximation (Gerstein and Mandelbrot, 1964) as:

$$I_{syn}(t) = \alpha N \lambda + \alpha \sqrt{N \lambda} \xi(t) \quad (3)$$

where  $N$  is the number of presynaptic cells,  $\alpha$  is the total charge produced in the postsynaptic cell by a single presynaptic input (modeled as a  $\delta$ -function),  $\lambda$  is the input rate, and  $\zeta$  is the Gaussian white noise term. The first term on the right may be interpreted as the mean synaptic current arriving from neurons in the previous layer and the second term, the fluctuations around the mean.

The evolution of membrane potential of each neuron with time is described by Equation 2. The FPE in turn gives the probability distribution,  $P(V,t)$ , of membrane potentials of all the neurons in a layer in a slice of time. Figure 20.3A

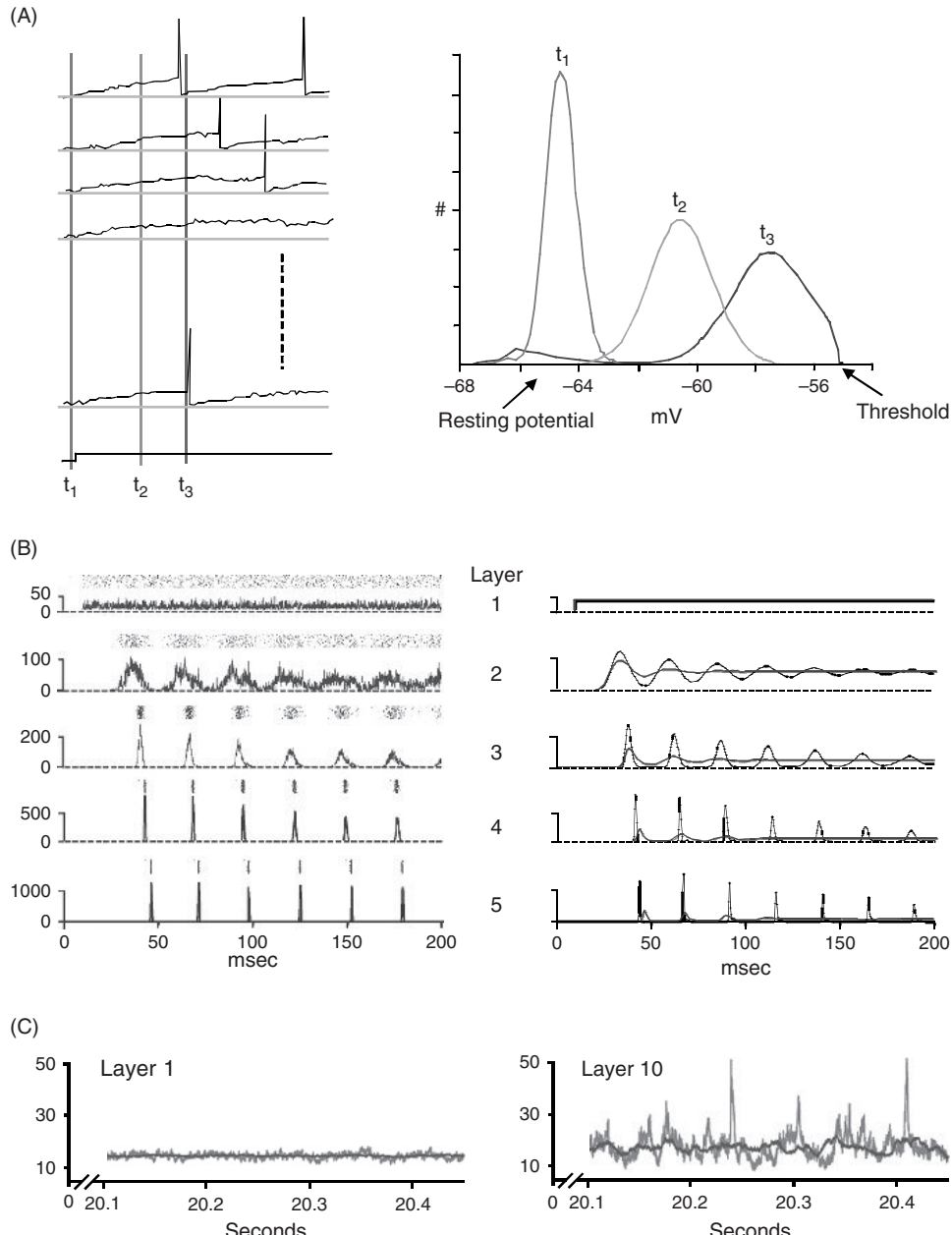


**FIGURE 20.3** Fokker-Planck analysis of feedforward networks. (A, left) Firing of a population of leaky integrate-and-fire neurons in response to a current step with Gaussian white noise. Right, distributions of membrane potentials taken through 3 time points (vertical lines on left). (B) Poststimulus time histograms obtained with a feedforward network of leaky integrate and fire neurons. Right, prediction generated with a Fokker-Planck equation assuming that the neurons were Poisson processes (blue). Note that unlike the simulations and experiments, the predicted histogram flattens out by  $100$  ms, indicating asynchronous firing. Fit to the simulations was improved by relaxing the Poisson assumption (black). From Cateau and Reyes, 2006. (C) Poststimulus time histograms obtained when finite size effect perturbations are taken into account. Synchronous firing persisted when few, larger inputs were used (red). In contrast, asynchrony developed when there were many, small inputs (blue). From Doiron et al., 2006. (See Plate 11 in color plate section.)

(left) shows representative membrane potentials of several LIF neurons in a given layer in response to a step of current. Each neuron receives the same mean current but they do not have identical membrane potentials because of independent sources of noise. Prior to the onset of the stimulus ( $t_1$ ), the membrane potentials are distributed normally around the resting potential of the neurons (see Figure 20.3A, right, red). Just past the input onset ( $t_2$ ), the membrane potentials have begun rising and the mean of the distribution shifts rightward toward threshold (green). Note the change in the shape of the distribution. Later in time ( $t_3$ ), the membrane potentials of a fraction of the neurons have crossed threshold (blue). For simplicity, the action potentials are assumed to be instantaneous and are not registered in the distribution. Hence, the spike reset mechanism forces the distribution to be zero at threshold. After crossing threshold, the membrane potential of the neurons resets and a small peak appears near resting potential. Importantly, the portion of the distribution that crosses threshold gives the firing rate of the population at a given time.

The general FPE is:

$$\frac{\partial P(V, t)}{\partial t} = -a(V, t) \frac{\partial P(V)}{\partial v} + \frac{b^2(V, t)}{2} \frac{\partial^2 P(V)}{\partial V^2} \quad (4)$$

where  $P(V, t)$  is the distribution of the membrane potential ( $V$ ) at a given slice in time (see Figure 20.3A). The term  $a$  is the drift term and describes the effects of deterministic forces (i.e. mean synaptic input) on the membrane potential of the population of neurons. The term  $b$  is the diffusion term and describes the effects of fluctuating inputs that are statistically identical but statistically independent across the population.

The drift and diffusion terms for the neurons in a given layer can be obtained by combining and re-arranging Equations 2 and 3 to get a stochastic differential equation:

$$\frac{dV}{dt} = \left( -\frac{V}{\tau_m} + \frac{\alpha R_m}{\tau_m} (N\lambda) \right) + \frac{\alpha R_m}{\tau_m} \sqrt{N\lambda} \xi(t) \quad (5)$$

The first term on the right gives the drift term and the second term gives the diffusion term of the FPE:

$$\frac{\partial P(V, t)}{\partial t} = - \left( \frac{V}{\tau_m} - \frac{\alpha R_m}{\tau_m} N\lambda \right) \frac{\partial P(V)}{\partial V} + \frac{N\lambda}{2} \left( \frac{\alpha R_m}{\tau_m} \right)^2 \frac{\partial^2 P(V)}{\partial V^2} + J_v(t) \delta(v - V_{reset}) \quad (6)$$

$$\int_{-\infty}^{\infty} P(V, t) dV = 1 \quad (7)$$

where  $V_{reset}$  of the flux term corresponds to the depth of the afterhyperpolarization. The flux term has the form:

$$J_V(t) = -\frac{N\lambda}{2} \left( \frac{\alpha R_m}{\tau_m} \right)^2 \frac{\partial P(V)}{\partial V} \Big|_{v=\theta} \quad (8)$$

The flux term at each time point can be used to construct the PSTH for a given layer. The PSTH, which has units of rate ( $= \lambda$ ), can in turn be used to calculate the drift and diffusion terms for the next layer. The FPE can be solved numerically (Cateau and Reyes, 2005; Doiron et al., 2006) with the boundary condition that  $P=0$  at threshold (reflecting the fact that  $V$  is immediately reset to near rest after a threshold crossing).

The FPE as formulated captures some but not all of the important features of synchrony in feedforward networks. Figure 20.3B shows a simulation of a feedforward network of LIF neurons (left) and the PSTHs calculated with the FPE (right, blue) using Equation 6. The FPE-calculated PSTHs, like the simulations, show a gradual development of synchrony in successive layers. However, one major difference is that the peaks of the FPE-calculated PSTH becomes progressively broader with time and eventually flatten out. In contrast, the peaks of the simulated and experimentally determined PSTHs remain robust for the duration of the stimulus.

That the FPE does not fully describe the experimental and simulated data is surprising. *A priori*, the network should behave as a dissipative system and eventually reach equilibrium which, in this case, is asynchrony. The peak at the onset of the stimulus, as argued above, is intuitively clear. However, a reasonable expectation might be that at longer times, the onset synchrony will be ‘forgotten’ due to cumulative effects of noise. For example, autocorrelation of spike trains *in vivo* or *in vitro* typically exhibit sharp peaks near the origin and progressively broader and flatter peaks later in time (Cateau and Reyes, 2006). This suggests that synchrony in feedforward networks cannot be simply described as a dissipative process; there are other mechanisms that prevent the network from reaching equilibrium.

The discrepancy arises from at least two sources. First, the assumption that the firing of presynaptic neurons, and the associated synaptic currents in their targets, are Poisson processes is incorrect. Neurons are not memory-less but rather tend to fire periodically, as would be expected because neurons have finite membrane time constants and various time-dependent conductances. Indeed, the autocorrelation of spike trains are not  $\delta$ -functions but rather have troughs on either side of a central peak. It has recently been proven that non-Poisson nature of spiking is preserved even when the activities of an arbitrarily large population of neurons are summed (Cateau and Reyes, 2006; Lindner, 2006). When the Poisson assumption is relaxed, the theory agrees better with the experiments but still shows asynchrony in the large time limit (Cateau and Reyes, 2006). Second, the FPE as formulated in Equation 6 does not take into account for so-called finite size effects. The synaptic potentials are not infinitesimally small so that the histograms in e.g. layer 1 are not smooth but have fluctuations. These fluctuations occur throughout the stimulus and provide ‘seeds’ for synchrony (in a manner similar to the bumps in the toy model) in the next layer. When the FPE is modified to account for these phenomena, the resultant histograms match the experimental data more accurately and synchrony now persists for all time (Doiron et al., 2006). Figure 20.3C shows that the PSTH obtained with the equivalent of few ( $N = 500$ ) synaptic inputs (red) produced synchrony at long times after the stimulus onset whereas many ( $N = 10\,000$ ) but small synaptic inputs produced a flat PSTH (blue).

In summary, an important implication of the FPE analyses is that once synchrony develops in a particular layer, the network never reaches an equilibrium state where neurons are firing asynchronously. There are ‘forcing’ functions which are inherent within the network that maintain synchrony for long periods of time.

### STRATEGIES FOR ELIMINATING SYNCHRONY

The models suggest that the strategy for reducing synchrony is first to eliminate the tendency of neurons to fire at a fixed delay after the stimulus onset. This tendency causes a peak in the PSTH, which though broad, provides the seed for stronger synchrony in deeper layers. Once a critical number of spikes occurs together in a sufficiently short period of time, full-scale synchrony develops. Secondly, the tendency of neurons to fire at a fixed interspike interval must be reduced. Because neurons tend to fire repetitively, the appearance of the first peak means that there will tend to be another peak approximately one interspike interval ( $= 1/\text{avg. firing rate}$ ) later. Finally, the finite size effects must be reduced. As discussed above, the finite size effects are largely responsible for maintaining synchrony at long times after the stimulus onset.

A completely flat population PSTH occurs when the distribution of spike times for neurons in a layer is uniform. At the onset of the stimulus (for simplicity a step), the membrane potential rises exponentially towards threshold. Thus, the probability that the spike will occur say 3–4 membrane time constants later is much higher than at the start. After spikes occur, the probabilities are again low but will rise back up again (if the stimulus is sustained) and the cycle repeats. Forcing the population spikes to occur randomly is tantamount to making the spiking probability distribution uniform for the entire duration of the stimulus. This is remarkably difficult to accomplish under biological conditions.

One possibility is to make the network functionally more heterogeneous by increasing the distributions of initial conditions of the neurons within a layer. For example, imparting a different subthreshold membrane potential to each neuron would, in principle, cause neurons within a layer to fire spikes at different times with respect to each other (Reyes, 2003). An important restriction is that the distribution of membrane potentials must be uniform across all neurons in a layer. Any peaks in the distribution (as would occur with a Gaussian or Gamma distribution) will cause the population of neurons to fire at a preferred time interval; neurons whose membrane potentials fall e.g. within one standard deviation of the Gaussian will dominate the PSTH. A similar restriction applies to spontaneously active neurons: the distribution of firing frequencies must be uniform.

A second possibility is to increase heterogeneity by e.g. widening the range of membrane properties of the neurons. This was attempted in the experiments but perhaps not enough heterogeneity could be achieved with four types of neurons in the network (see above; Reyes, 2003). The tricky part is choosing a distribution of membrane properties that will produce uniform spiking probabilities. For example, simulations with LIFs indicate that increasing heterogeneity by varying the membrane time constants requires that some neurons have very short time constants (to produce spikes immediately at the start of the stimulus) and some to have very long time constants (to produce spikes at later times). Whether the range of passive (or active) properties of neurons or whether the uniform distribution of these parameters is biologically realistic is unclear.

Eliminating the finite size effects may not be feasible under physiological conditions. This would essentially entail making the amplitude of the synaptic potentials infinitesimally small and the number of presynaptic inputs infinitely large

(Doiron et al., 2006). On the average, the amplitude of EPSPs recorded between pyramidal neurons in rat cortex is about 300 µV to 1 V (Markram et al., 1997; Reyes et al., 1998; Reyes and Sakmann, 1999). Even synaptic inputs located distally in the dendrite could produce a measurable potential at the soma owing to active dendritic conductances that boost the EPSPs (Oviedo and Reyes, 2002, 2005).

The best way of removing synchrony is by introducing background synaptic noise. If the noise is sufficiently large, then the effects of the membrane trajectory both at the stimulus onset and during repetitive firing are reduced substantially. Noise increases the spiking variability of each neuron in the network much more effectively than increasing the heterogeneity or adding feedback, mainly because it causes the neurons to be independent of each other and removes the memory (thereby eliminating peaks following onset synchrony). In the limit, the spikes essentially become Poisson processes. However, the noise amplitude has to be comparable to the difference between resting membrane potential and threshold, which range from 10 to 20 mV. Increasing the variability of the input without changing the mean requires simultaneously increasing the rates of excitatory and inhibitory inputs. As discussed above, producing large amplitude noise may not be possible because the associated increase in synaptic conductance severely limits the amplitude of the fluctuations. *In vivo* recordings do reveal large transients but these, as argued above, are likely to be due to synchronous arrival of inputs. Perhaps a more compelling argument against large amplitude noise is that it would obscure the intended signal, thereby substantially crippling the ability of the network to propagate information.

#### CONTROLLING THE SPREAD OF SYNCHRONY WITH INHIBITION

Experiments, simulations and theoretical analyses suggest that synchronous firing in feedforward networks is strong and robust under a very wide range of conditions. This raises an obvious question that may have direct implication for epilepsy: what is preventing the synchrony from spreading throughout the cortex? Working under the premise that synchrony is unavoidable and may indeed be necessary for propagating signals, then epilepsy may be viewed as resulting from some malfunction in the ability of the network to control synchrony.

To gain some insights as to how synchrony can spread uncontrollably, the feedforward network must be modified to include realistic connection patterns between neurons in cortex (Marchetti and Reyes, 2004). Holmgren et al. (2003) determined the connection probabilities between pyramidal neurons and between pyramidal and local interneurons in an *in vitro* slice preparation of the rat somatosensory cortex. The study involved painstakingly performing simultaneous whole-cell recording from two neurons and then determining the probability of connection as a function of distance between the cells. An important finding was that pyramidal cells are much more likely to form synaptic connections with interneurons than with each other. On the basis of this study, the connection probability distributions shown in Figure 20.4A were used in the networks. For pyramidal-pyramidal connections, the probability distribution is approximately Gaussian with a peak value of 0.1. In comparison, the pyramidal-interneuron probability distribution is approximately uniform (at least in the limited range examined) with a value of approximately 0.6. Thus, inhibitory neurons, though making up only 20–25% of neurons in cortex, make connections with many of their neighbors within at least 100 µm radius. The connections between pyramidal cells and inhibitory interneurons within and across layers were randomly determined from these distributions. Within each layer, there were recurrent excitatory connections as well as inhibitory feedback. Importantly, the connection scheme effectively set up a lateral inhibitory circuit across layers.

Neurons were modeled using quadratic-integrate-and-fire (QIFs) processes. QIF neurons can be modified so as to produce spiking patterns that resemble those of pyramidal neurons, interneurons or bursting neurons (Izhikevich, 2004). However, for simplicity, the networks were constructed with excitatory and inhibitory neurons that have identical properties. The excitatory and inhibitory synaptic conductances were adjusted to produce EPSPs and IPSPs with amplitudes of approximately 0.5 to 1 mV (see Figure 20.4B, upper traces). Instead of activating the entire first layer as above, stimuli are delivered only to a subset (25%) of the neurons in the center of the first layer.

As with the uniformly connected network above, synchrony developed in the deeper layers. One difference is that the dot rasters tended to be ‘C’-shaped. This occurs because neurons at the edge of the stimulus receive less input from the previous layer. Note that neurons at the edge do not fire as synchronously as those in the center.

Preliminary observations suggest that inhibition plays an important role in decreasing the spread of synchrony laterally within each layer (Figure 20.4B, first column). In the control network with both excitatory and inhibitory neurons, the activities in successive layers are confined to a narrow band that matched the extent of the activated neurons in the first layer (dashed lines). When inhibition was removed, the activities in successive layers spread beyond the narrow band (second column).

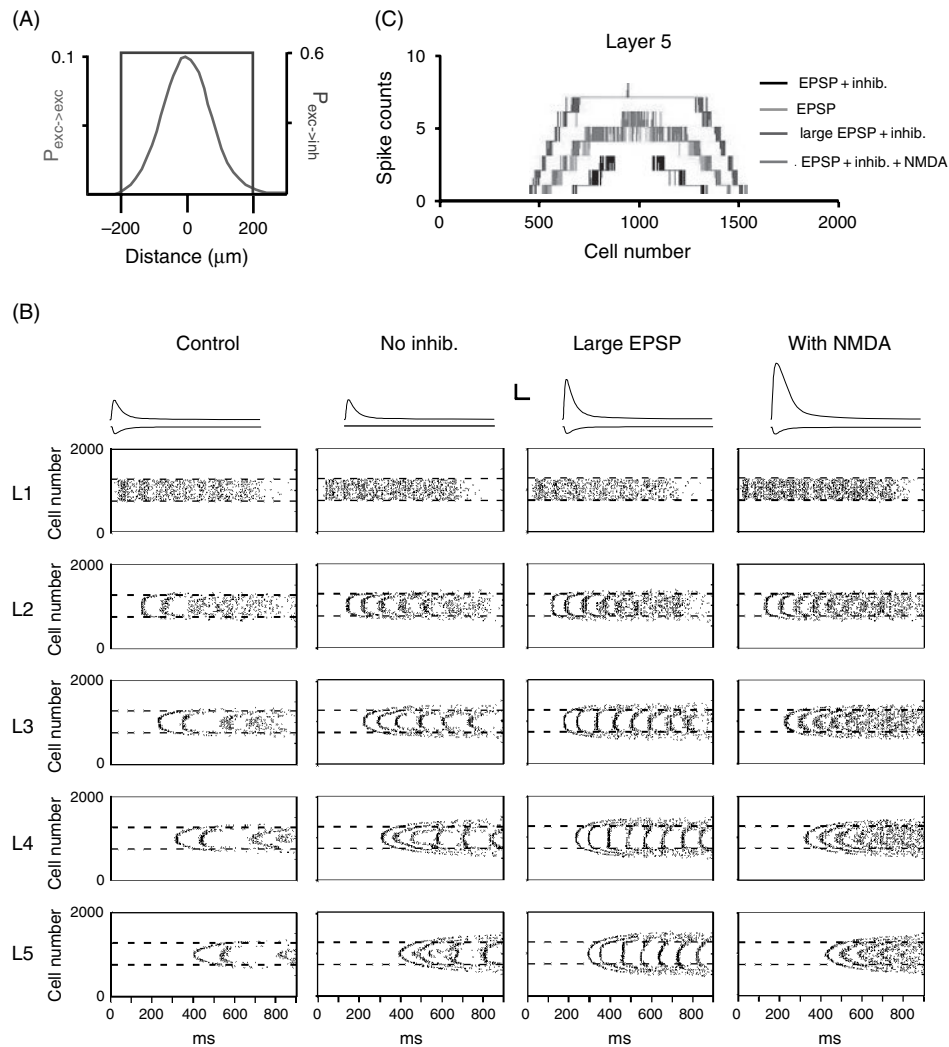


**FIGURE 20.4** Spread of synchrony. (A) Probability distributions for connections between pyramidal cells (blue) and between pyramidal cells and inhibitory cells (red) as a function of distance. (B) Dot rasters for 5 layered feedforward networks of quadratic-integrate-and-fire neurons (columns) under 4 configurations (rows). First column: control condition was with excitatory and inhibitory neurons with the connection schemes in (A) (see text). Second column: network with only excitatory neurons. Third column: similar to control network except the amplitude of the excitatory input was doubled. Fourth column: similar to control except an NMDA component was added to the excitatory input. The horizontal dashed lines demarcate the boundary of the activated neurons in layer 1. Scale bars for synaptic potentials: 0.5 mV, 20 ms. (C) Total number of action potentials (ordinate) fired by cells (abscissa) in layer 5 under the 4 conditions. Note that the spread of activity in the non-control conditions was substantially greater than in the control network. (See Plate 12 in color plate section.)

#### PATHOLOGICAL SYNCHRONY

Synchrony seems to play an important role in signal processing in the normal brain as long as it is confined and controlled. One may imagine many feedforward networks where synchrony exists among neurons within each network but not across networks. Pathology may occur if significant synchrony develops across networks, i.e. when it becomes unbounded. The fact that the tendency to synchronize is so powerful suggests that the nervous system may be teetering on the verge of full-blown synchrony. Small irregularities in the synaptic mechanisms or neural architecture may be all that is needed as a trigger.

Unbounded synchrony may occur when the excitatory/inhibitory ratio increases. A combination of decreased inhibition or increased excitation can attenuate the effectiveness of inhibition at the periphery. As shown above, removing inhibition increases the lateral spread of synchrony. This effect can be enhanced in the control network by doubling the amplitude

of the EPSPs (see Figure 20.4B, third column). Similarly, adding a slow NMDA-like component to the EPSP increases the spread, although the effect appears to be mainly due to the increase in amplitude rather than the longer time course (fourth column). Comparison of the number of action potentials generated by cells in layer 5 shows that increasing the excitatory/inhibitory ratio produces substantially more spread than in the control network (see Figure 20.4C).

Perhaps not surprisingly, the conditions that lead to increased synchrony in feedforward networks are very similar to those that are used in animal models to induce epileptic discharges. Blocking GABA-A receptors with bicuculline and picrotoxin is often used to generate spontaneous depolarizing after hyperpolarization. The protocol for kindling, which involves repetitive stimulation of afferents, is very similar to the protocol for inducing long-term potentiation of excitatory synapses in *in vitro* slice preparations. Unblocking of NMDA receptor mediated potentials by removal of Mg<sup>2+</sup> would also increase the overall amplitude of EPSPs. The potassium channel blocker 4-AP has the dual effect of increasing the amplitude of EPSPs and depolarizing the cell.

## SUMMARY

The default state of feedforward networks is synchronous firing. Even when the input to the first layer is asynchronous, synchrony develops within 2–3 layers. Several factors contribute to synchrony. First, neurons tend to fire at a fixed delay after the stimulus onset, thereby causing a peak in the PSTH. Second, because neurons tend to fire repetitively (i.e. they are non-Poisson processes), multiple peaks form after the onset peak. Third, finite size effects of the networks ensure that synchrony is maintained for all time: theoretical analyses suggest that the neurons within any given layer never reach equilibrium such that there is no asynchronous state. Synchrony is robust and persists for a wide range of network configuration. In the normal brain, it is conceivable that there are many feedforward networks where neurons within but not across networks fire synchronously. Synchrony does not spread owing to the presence of inhibitory neurons. Under pathological conditions, such as when there is a shift in the excitatory/inhibitory ratio, synchrony spreads uncontrollably. Many of the manipulations that promote seizures also facilitate the spread of synchrony in feedforward networks. Much can indeed be learned about the spread of epileptiform activity by studying of simple feedforward networks.

## REFERENCES

- Abeles, M. (1991). *Corticonics*. Cambridge University Press, Cambridge.
- Avoli, M., Barbarosie, M., Lucke, A., Nagao, T., Lopantsev, V. and Kohling, R. (1996). Synchronous GABA-mediated potentials and epileptiform discharges in the rat limbic system *in vitro*. *J Neurosci* 16:3912–3924.
- Azouz, R. and Gray, C.M. (1999). Cellular mechanisms contributing to response variability of cortical neurons *in vivo*. *J Neurosci* 19:2209–2223.
- Azouz, R. and Gray, C.M. (2003). Adaptive coincidence detection and dynamic gain control in visual cortical neurons *in vivo*. *Neuron* 37:513–523.
- Bruno, R.M. and Sakmann, B. (2006). Cortex is driven by weak but synchronously active thalamocortical synapses. *Science* 312:1622–1627.
- Cateau, H. and Fukai, T. (2001). Fokker-Planck approach to the pulse packet propagation in synfire chain. *Neural Netw* 14:675–685.
- Cateau, H. and Reyes, A.D. (2003). Modulation of synchrony duration in multilayer neural networks by feedback: stochastic analyses. *Soc. Neurosci. Abst.* 305.2
- Cateau, H. and Reyes, A.D. (2006). Relation between single neuron and population spiking statistics and effects on network activity. *Phys Rev Lett* 96:058101.
- Chance, F.S., Abbott, L.F. and Reyes, A.D. (2002). Gain modulation from background synaptic input. *Neuron* 35:773–782.
- Csicsvari, J., Hirase, H., Czurko, A., Mamiya, A. and Buzsaki, G. (1999). Oscillatory coupling of hippocampal pyramidal cells and interneurons in the behaving rat. *J Neurosci* 19:274–287.
- Diesmann, M., Gewaltig, M.O. and Aertsen, A. (1999). Stable propagation of synchronous spiking in cortical neural networks. *Nature* 402:529–533.
- Doiron, B., Rinzel, J. and Reyes, A.D. (2006). Stochastic synchronization in finite size spiking networks. *Phys Rev E (rapid comm.)* 74.
- Engel, A.K. and Singer, W. (2001). Temporal binding and the neural correlates of sensory awareness. *Trends Cogn Sci* 5:16–25.
- Gardiner, C. (2003). *Handbook of stochastic methods*, 3rd edn. Springer, Berlin.
- Gerstein, G.L. and Mandelbrot, B. (1964). Random walk models for the spike activity of a single neuron. *Biophys J* 4:41–68.
- Harris, K.D., Hirase, H., Leinekugel, X., Henze, D.A. and Buzsaki, G. (2001). Temporal interaction between single spikes and complex spike bursts in hippocampal pyramidal cells. *Neuron* 32:141–149.
- Hatsopoulos, N., Ojakangas, C.L., Paninski, L. and Donoghue, J.P. (1998). Information about movement direction obtained from synchronous activity of motor cortical neurons. *Proc Natl Acad Sci* 95:15706–15711.
- Holmgren, C., Harkany, T., Svensenfors, B. and Zilberman, Y. (2003). Pyramidal cell communication within local networks in layer 2/3 of rat neocortex. *J Physiol* 551:139–153.
- Ikegaya, Y., Aaron, G., Cossart, R. et al. (2004). Synfire chains and cortical songs: temporal modules of cortical activity. *Science* 304:559–564.
- Izhikevich, E.M. (2004). Which model to use for cortical spiking neurons? *IEEE Trans Neural Netw* 15:1063–1070.

- Jones, R.S. and Lambert, J.D. (1990). Synchronous discharges in the rat entorhinal cortex in vitro: site of initiation and the role of excitatory amino acid receptors. *Neuroscience* 34:657–670.
- Lindner, B. (2006). Superposition of many independent spike trains is generally not a Poisson process. *Phys Rev E Stat Nonlin Soft Matter Phys* 73:022901.
- Lopantsev, V. and Avoli, M. (1998a). Laminar organization of epileptiform discharges in the rat entorhinal cortex in vitro. *J Physiol* 509 (Pt 3):785–796.
- Lopantsev, V. and Avoli, M. (1998b). Participation of GABA<sub>A</sub>-mediated inhibition in ictallike discharges in the rat entorhinal cortex. *J Neurophysiol* 79:352–360.
- Mainen, Z.F. and Sejnowski, T.J. (1995). Reliability of spike timing in neocortical neurons. *Science* 268:1503–1506.
- Marchetti, C. and Reyes, A.D. (2004). Using lateral inhibition to control signal flow in iteratively constructed networks. *Soc Neurosci Abst* 30(9.3).
- Markram, H., Lubke, J., Frotscher, M., Roth, A. and Sakmann, B. (1997). Physiology and anatomy of synaptic connections between thick tufted pyramidal neurones in the developing rat neocortex. *J Physiol* 500 (Pt 2):409–440.
- Martin, C., Gervais, R., Hugues, E., Messaoudi, B. and Ravel, N. (2004). Learning modulation of odor-induced oscillatory responses in the rat olfactory bulb: a correlate of odor recognition? *J Neurosci* 24:389–397.
- McCormick, D.A. and Contreras, D. (2001). On the cellular and network bases of epileptic seizures. *Annu Rev Physiol* 63:815–846.
- Miles, R. and Wong, R.K. (1983). Single neurones can initiate synchronized population discharge in the hippocampus. *Nature* 306:371–373.
- Nagao, T., Alonso, A. and Avoli, M. (1996). Epileptiform activity induced by pilocarpine in the rat hippocampal-entorhinal slice preparation. *Neuroscience* 72:399–408.
- Oviedo, H. and Reyes, A.D. (2005). Variation of input-output properties along the somatodendritic axis of pyramidal neurons. *J Neurosci* 25:4985–4995.
- Oviedo, H. and Reyes, A.D. (2002). Boosting of neuronal firing evoked with asynchronous and synchronous inputs to the dendrite. *Nature Neurosci* 5:261–266.
- Perkel, D.H., Gerstein, G.L. and Moore, G.P. (1967). Neuronal spike trains and stochastic point processes. II. Simultaneous spike trains. *Biophys J* 7:419–440.
- Reyes, A. and Sakmann, B. (1999). Developmental switch in the short-term modification of unitary EPSPs evoked in layer 2/3 and layer 5 pyramidal neurons of rat neocortex. *J Neurosci* 19:3827–3835.
- Reyes, A., Lujan, R., Rozov, A., Burnashev, N., Somogyi, P. and Sakmann, B. (1998). Target-cell-specific facilitation and depression in neocortical circuits. *Nat Neurosci* 1:279–285.
- Reyes, A.D. (2003). Synchrony-dependent propagation of firing rate in iteratively constructed networks in vitro. *Nat Neurosci* 6:593–599.
- Reyes, A.D. (2005). In vitro reconstruction of auditory receptive fields: role of feedforward/back inputs. *Soc Neurosci Abst* 31(615.9).
- Riehle, A.G.S., Diesmann, M. and Aertsen, A. (1997). Spike synchronization and rate modulation differentially involved in motor cortical function. *Science* 278:1950–1953.
- Sakurai, Y. and Takahashi, S. (2006). Dynamic synchrony of firing in the monkey prefrontal cortex during working-memory tasks. *J Neurosci* 26:10141–10153.
- Shadlen, M.N. and Movshon, J.A. (1999). Synchrony unbound: a critical evaluation of the temporal binding hypothesis. *Neuron* 24:67–77, 111–125.
- Singer, W. (2001). Consciousness and the binding problem. *Ann NY Acad Sci* 929:123–146.
- Stopfer, M., Bhagavan, S., Smith, B.H. and Laurent, G. (1997). Impaired odour discrimination on desynchronization of odour-encoding neural assemblies. *Nature* 390:70–74.
- Uhlhaas, P.J. and Singer, W. (2006). Neural synchrony in brain disorders: relevance for cognitive dysfunctions and pathophysiology. *Neuron* 52:155–168.

# 21

## MODULATION OF SYNCHRONY BY INTERNEURONS: INSIGHTS FROM ATTENTIONAL MODULATION OF RESPONSES IN THE VISUAL CORTEX

PAUL H.E. TIESINGA AND CALIN I BUIA

### ABSTRACT

Strongly recurrent excitatory networks are often implicated in epilepsy, but they are also used in the cortex to select and amplify weak sensory inputs. How can cortical networks quickly modulate their firing rate and synchrony while preventing global synchrony and high sustained firing rates that are characteristic of epileptic states? We study this problem within the context of attentional modulation of synchrony in the primary visual cortex.

Many neurons in the visual cortex are orientation-selective, increase their firing rate with contrast and are modulated by attention. In the ring model (Somers et al., 1995) for the visual cortex, orientation selectivity arises via strong recurrent excitatory connections and is controlled by a single type of interneuron (the simple interneurons). We did not find parameter settings for which synchrony in the standard ring model could be modulated independently from firing rate. Only when a second type of interneuron (the complex interneurons), with properties similar to those found recently in cat primary visual cortex (Hirsch et al., 2003), was included did the network behave appropriately. A critical feature in the model was that complex interneurons projected to simple interneurons but that the simple interneurons did not project back to them. In order to prevent epileptic states in the network, the complex interneurons had to project to the excitatory cells as well as receive inputs from them. The network was switched from the non-attended state to the attended state by increasing the depolarization of the complex interneurons. The model reproduced the following experimental results: (1) the gamma-frequency range coherence between the estimated local field potential (eLFP) and spike trains of excitatory cells was higher in the attended state than in the non-attended state, but the firing rates of the excitatory cells did not vary between states (Fries et al., 2001); (2) the gamma-frequency-range power in the eLFP increased with contrast (Henrie and Shapley, 2005).

The model was developed for the visual cortex, but it could provide insight into how to modulate synchrony and firing rate independently, and in a controlled fashion, in other brain areas. As such, it suggests that in order to improve the effectiveness of pharmacological therapies for epilepsy it may be necessary to target specific types of interneurons.

### INTRODUCTION

During epilepsy, neurons fire synchronously at high rates over long periods of time. Increased excitability of principal neurons, strong recurrent excitatory connections and pathologies of interneuron networks are all factors in the development of epileptic seizures (Traub and Miles, 1991). Networks with strong recurrent excitatory connections also perform an

important function in the cortex: they amplify and select features in the sensory input (Douglas et al., 1995; Douglas and Martin, 2004). Recent theoretical and experimental studies (reviewed in Salinas and Sejnowski, 2001), suggest that firing rate and synchrony are independent channels for information processing and that they can be modulated independently. We study how cortical circuits can independently modulate their firing rate and their degree of synchrony in a model for attentional modulation of responses in the primary visual cortex.

Inhibitory interneurons make up 15–20% of all cortical neurons and have been classified into distinct groups based on their morphology, the complement of calcium-binding proteins they express and their physiological properties (Markram et al., 2004; Soltesz, 2006). Recent work suggests that interneurons play a direct role in cortical information processing. For instance, in the ring model (Ben-Yishai et al., 1995; Somers et al., 1995), orientation-selectivity emerges in part because inhibitory neurons sharpen the weakly orientation-tuned inputs that cortical neurons receive from the lateral geniculate nucleus (LGN), whereas recent models suggest that attention may be mediated by the synchrony of inhibitory neurons (Fries et al., 2001; Bichot et al., 2005; Tiesinga et al., 2005; Buia and Tiesinga, 2006). It is not clear whether both attention and sharpening of tuning are achieved by the same class of interneurons because it has not yet been possible to link conclusively the classification of interneurons to their function in the cortical circuit. We use computational models to investigate what types of interneurons are necessary for attentional modulation of orientation-selective neurons in layer 4 of the visual cortex. Our hypothesis is that spatial attention is mediated by a depolarization of interneurons which, in turn, synchronize the cortical network (Buia and Tiesinga, 2006). In our simulations, synchrony could not be modulated effectively in a ring model containing only simple inhibitory cells. However, when the network included complex inhibitory cells projecting to simple inhibitory cells, synchrony could be modulated effectively. Evidence for complex and simple inhibitory cells was recently obtained in the visual cortex of the anesthetized cat using intracellular recordings (Hirsch et al., 2003). In addition, anatomical studies have revealed evidence for various kinds of complex-like inhibitory neurons projecting preferentially to other inhibitory neurons (Gonchar and Burkhalter, 1999, 2003) and receiving top-down inputs from other cortical areas or from neurons in the basal forebrain (Freund and Meskenaite, 1992).

In the study of epilepsy and the development of therapies for it, the high firing rate and synchrony of epileptic states are often viewed as a single issue. In the circuit proposed here, firing rate and synchrony can be modulated independently using two different types of interneurons. The resulting insights might be helpful for developing more effective pharmacological therapies that target a specific subpopulation of interneurons (Soltesz, 2006) and have less adverse effects on the cognitive skills of the patient.

## METHODS

### CORTICAL MODELS

The ring model consisted of  $N_c = 21$  columns, each comprised of 21 inhibitory and 84 excitatory cells (total: 1764 excitatory cells, 441 inhibitory cells). These numbers are representative for a hypercolumn in cat visual cortex (Somers et al., 1995). The preferred orientation varied smoothly from column to column; for the  $i^{th}$  column it was  $(180 \text{ degrees}) (i - 1)/N_c$  (Figure 21.1A). Since the left-most column and the right-most column have similar orientation preferences, the model is referred to as a ring model. The LGN was represented using 1681 ON and 1681 OFF cells laid out on two overlapping 41 by 41 grids spanning 8 by 8 degrees of the visual field with a center to center spacing of 0.2 degrees in both the x as well as the y direction (Figure 21.1B and C). The grids of ON and OFF cells were fully overlapping. The LGN inputs to each cortical neuron came from three rectangular subfields, each 1 by 3 degrees in size, with their long axis oriented along the preferred orientation of the neuron (Figure 21.1B and C). The OFF, ON and OFF subfields were arranged from left to right with their long axes parallel and with a center-to-center distance of 1 degree. For each cortical neuron, an appropriate number (see Table 21.1) of LGN-OFF cells were randomly selected out of the area covered by the OFF subfield (Figure 21.1C) and were connected to the neuron. A similar procedure was applied to the LGN-ON cells, which were selected out of the ON subfield (Figure 21.1B).

The relative probability  $P$  for a connection between a presynaptic neuron  $i$  (preferred orientation:  $\theta_i$ ) and a postsynaptic neuron  $j$  (preferred orientation:  $\theta_j$ ) depended on the difference between their preferred orientations,  $P = f(\theta_i - \theta_j, \sigma, mr)$ . Here,  $f(x, \sigma, mr) = \exp(-x^2/2\sigma^2)$  for  $|x| < mr$  and  $f = 0$  for  $|x| \geq mr$ ,  $\sigma$  is the orientation tuning width and  $mr$  stands for maximum range and is the orientation difference beyond which no connections are made. For each cortical neuron,

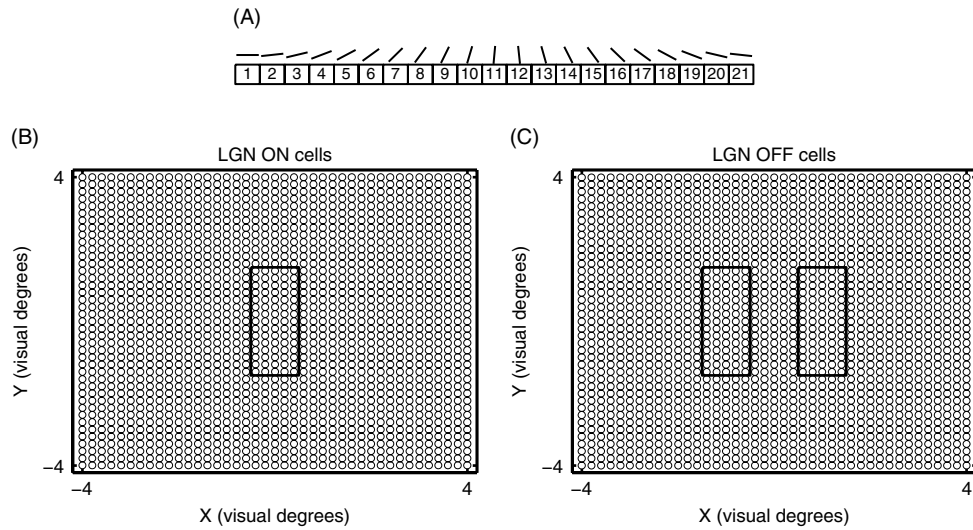


**FIGURE 21.1** Generation of orientation selectivity in the LGN to cortex projection. (A) There were 21 columns with excitatory and inhibitory neurons, whose preferred orientation smoothly varied from horizontal (0 degrees) via vertical (90 degrees) to almost 180 degrees. The preferred orientation of the rightmost column is close to that of the leftmost columns, hence these can be identified as neighbors, giving the model a ring architecture. (B,C) There were 1681 LGN-ON and 1681 LGN-OFF cells laid out on a 41 by 41 grid spanning 8 by 8 visual degrees. An excitatory cortical cell with a receptive field center at  $X = 0$  and  $Y = 0$  and a preferred orientation of 90 degrees, would receive inputs from 12 ON cells located in the rectangle in (B) and inputs from 12 OFF cells located in either of the rectangles shown in (C). These rectangles (subfields) were rotated and shifted appropriately for a neuron with a different receptive field center and preferred orientation.

**TABLE 21.1** The parameter settings for synaptic connections in the standard ring model

Type	Unitary strength ( $\mu\text{S}/\text{cm}^2$ )	Number of synapses	Syn. time constant (ms)	Mean of conduction delay (ms)	Std of conduction delay (ms)	$\sigma$ (rad)	mr (rad)
LGN -> E	14	12	5	10	5	—	—
LGN -> SI	8	8	5	5	3	—	—
E -> E	6	36	5	3	1	0.1	0.7
E -> SI	3	56	5	3	1	0.1	0.7
SI -> E	12	24	10	3	1	1	1.5
SI -> SI	5	8	10	3	1	1	1.5

an appropriate number of presynaptic neurons were chosen with relative probability  $P$  and connected to the neuron. The values used for the model are summarized in Table 21.1.

For the ‘complex’ version of the model, referred to as the complex ring model, 11 inhibitory cells with complex receptive fields (RFs) were added to each column. These cells were labeled by the preferred orientation of the column to which they were assigned. They received LGN inputs from ON and OFF cells in a 3 by 3 degree area centered on the neuron’s receptive field center (Figure 21.2B). The intracortical connections between complex and simple cells did not depend on the difference between the preferred orientation of the pre- and postsynaptic neuron (formally:  $\sigma = \infty$  and  $mr = \pi/2$ ). There was an asymmetry in the connection between inhibitory neurons with a simple receptive field (SI) and those with a complex receptive field (CI). Most inhibitory inputs to CI cells came from other CI cells, but a significant fraction of inhibitory inputs to SI cells came from CI cells (Table 21.2). The excitatory cells received inputs from both CI and SI cells.

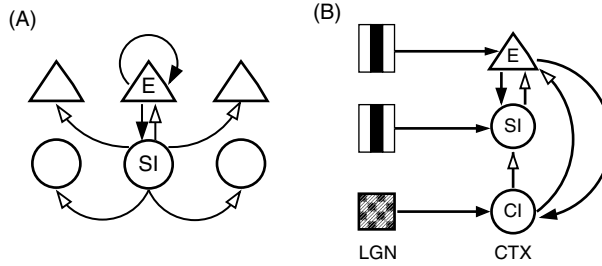


**FIGURE 21.2** The local circuit. (A) The standard ring model consisted of simple excitatory (E) and inhibitory (SI) cells, each with a receptive field comprised of parallel subfields arranged in an OFF-ON-OFF configuration. The excitatory cells only projected to other excitatory and inhibitory cells with a similar orientation preference (filled arrows), whereas the inhibitory neurons projected to other neurons with orientation preferences in a broader range around that of the home-column (open arrows). (B) In the modified network an additional inhibitory cell type (CI) with complex receptive field characteristics was introduced. Only the numerically dominant projections are shown in the graph. These neurons received inputs from LGN-ON and LGN-OFF cells with overlapping receptive fields centers. The CI cells projected to the simple excitatory and inhibitory cells, regardless of their preferred orientation. A CI cell received excitatory inputs with equal probability from all preferred orientations. Only a few SI cells provided inputs to the CI cells.

**TABLE 21.2** The parameter settings for the complex ring model. The conduction delays and the synaptic time constants are as in Table 21.1

Type	Unitary strength ( $\mu\text{S}/\text{cm}^2$ )	Number of synapses on target	$\sigma$ (rad)	$mr$ (rad)
LGN ->E	14	12	—	—
LGN ->SI	8	8	—	—
LGN ->CI	8	4 ON, 2 OFF	—	—
E ->E	6	36	0.1	0.7
E ->SI	1	56	0.1	0.7
E ->CI	1	56	$\infty$	$\pi/2$
SI ->E	20	19.6	1	1.5
CI ->E	20	4.4	$\infty$	$\pi/2$
SI ->SI	4	26.25	1	1.5
SI ->CI	4	0.76	$\infty$	$\pi/2$
CI ->SI	4	13.75	$\infty$	$\pi/2$
CI ->CI	4	39.24	$\infty$	$\pi/2$

#### CALCULATION OF LGN SPIKE TRAINS USED AS INPUT TO THE CORTICAL NEURONS

The LGN cells were represented by non-separable spatiotemporal filters, which were defined in terms of a Gaussian spatial filter:

$$F(x, y|\sigma, K) = (K/2\pi\sigma^2) \exp(-(x^2 + y^2)/2\sigma^2)$$

and an alpha-type temporal filter:

$$G(t|\tau) = (1/\tau) \exp(-t/\tau).$$

Specifically,

$$F_{st} = F(x, y|\sigma_c, K_c)G(t, \tau_c) - F(x, y|\sigma_s, K_s)G(t - \delta, \tau_s)$$

Here,  $x$  and  $y$  are defined with respect to the receptive field center of the LGN cell. Parameters values are  $K_c/K_s = 17/16$ ,  $\sigma_c = 0.17$  deg,  $\sigma_s = 0.53$  deg,  $\tau_c = 10$  ms,  $\tau_s = 20$  ms and the delay between the surround and center response is  $\delta = 3$  ms. The firing rate of the ON cells is:

$$R_{ON}(t) = [R_0 + c_{lin}F_{sc}(F_{st} * s)]_+$$

and for the OFF cells it is:

$$R_{OFF}(t) = [R_0 - c_{lin} F_{sc}(F_{st} * s)]_+$$

In these expressions  $R_0 = 15\text{Hz}$  is the baseline firing rate of thalamic neurons (Somers et al., 1995),  $c_{lin}$  is the *linear* contrast, a scaling factor between 0 and 1 (0 and 100%),  $s$  is the stimulus waveform (see below),  $F_{st} * s$  is the scalar filter output determined as a sum across space and a convolution in time,  $F_{sc}$  is a scaling factor such that  $F_{sc}(F_{st} * s)$  is 50 Hz during the sustained part of the response to the vertical bar stimulus (see below), and  $[x]_+$  denotes rectification. The spike trains for LGN neurons are obtained as a Poisson process with a time-varying rate given by  $R_{ON}(t)$  or  $R_{OFF}(t)$  for ON and OFF cells, respectively. The filter is 64 ms long (sampling rate is 1 kHz), shifting the stimulus onset in the filtered temporal waveform by 32 ms. Hence, in combination with the 5–10 ms axonal conduction delay (see Table 21.1), stimulus-onset reached cortical neurons after a 40 ms delay.

### STIMULUS GENERATION

The stimulus was represented as a spatiotemporal waveform  $s(x,y,t)$ , with a pixel value of zero representing the gray background. A vertical bar of 1 by 3 degrees was generated by setting the values of  $s(x,y,t)$  equal to one for  $t_1 < t < t_2$ ,  $-0.5 \text{ degrees} < x < 0.5 \text{ degrees}$  and  $-1.5 \text{ degrees} < y < 1.5 \text{ degrees}$  during either a 300 ms long period starting at  $t_1 = 250$  or 400 ms, or a 600 ms period starting at  $t_1 = 800$  ms. We used a temporal resolution of 1 ms and a spatial resolution of 0.1 degrees for the stimulus matrix.

### NEURON AND SYNAPSE MODELS

The neurons were represented by Hodgkin-Huxley-style models. For the inhibitory neuron, we used the model in Wang and Buzsaki (1996) and for the excitatory neuron, we used the model in Golomb and Amitai, (1997) and Golomb (1998). The AMPA-type excitatory and fast GABA-type inhibitory synapses were also taken from Golomb and Amitai (1997) and Golomb (1998). The implementation details and equations for the cell and synapse model were given in a previous publication and are not repeated here (Buia and Tiesinga, 2005; Buia and Tiesinga, 2006). The only single-neuron parameters varied during the course of the simulations reported here are the level of depolarizing current  $I_{Cl}$ ,  $I_{SI}$  and  $I_E$  to the complex inhibitory, simple inhibitory and excitatory neurons, respectively, and for the excitatory cells, the maximum conductance  $g_{Kslow}$  (standard value  $0.075 \text{ mS/cm}^2$ ) of slow potassium current responsible for adaptation (Golomb and Amitai, 1997; Golomb, 1998) and the decay time of the corresponding kinetic variable (standard value:  $\tau_z = 75 \text{ ms}$ ). NMDA synapses were implemented according to Golomb and Amitai (1997) and Golomb (1998) with a time-scale of 149 ms. We fixed their unitary strength to 32% of the strength of the AMPA conductance.

### CALCULATED QUANTITIES

Spike times were determined as the times the voltage crossed 0 mV from below. The firing rate was the number of spikes produced during the stimulus period divided by its duration. The rates were averaged across all neurons of a given type (excitatory, simple inhibitory, complex inhibitory) in a column. A tuning curve was constructed by plotting this firing rate as a function of the preferred orientation of the column. We performed the same analysis on the synaptic inputs that a cortical neuron receives from LGN neurons and other cortical neurons.

For spectral analysis we used the multitaper routines implemented in the Chronux MATLAB toolbox (Mitra and Pesaran, 1999; Jarvis and Mitra, 2001). First, a spike-time histogram was constructed for each neuron type by calculating the number of spikes in a 1 ms wide bin. Histograms were normalized by the number of neurons and the bin width in seconds, yielding the time-varying average firing rate expressed in Hz. The power spectrum density of the histograms was calculated using the Chronux routine *mtspectrumpb* with a spectral bandwidth  $NW = 3$ , averaged over 5 tapers. In this routine, the length of the time series was increased to twice the next integer power of two by zero-padding. Two types of coherencies were calculated using the routine *coherencypb* with the same parameter values as used for the power spectrum. The coherence between histograms of two different types of neurons was calculated. In addition, the coherence between the histogram of the complex inhibitory cells and the spike train of an excitatory neuron was determined and averaged across 100 spike trains randomly picked among the 1764 excitatory cells (we excluded spike trains with no spikes, since these led to division by zero errors).

## RESULTS

The standard ring model produced an orientation selective response. The rastergram and histogram for the excitatory and inhibitory cells are shown in Figure 21.3A and B, respectively. The mean firing rate of a column in response to a vertical bar is shown as a function,  $f_{population}(\theta_p)$ , of its preferred orientation  $\theta_p$  (Figure 21.3C, D). Experimentally, an orientation tuning curve,  $f_{neuron}(\theta_s)$ , is obtained by presenting stimuli of different orientation  $\theta_s$  to a single neuron with a specific preferred orientation. Because of the ring symmetry and the fact that here the firing rate of a neuron only depends on the absolute value of the difference between its preferred orientation and the stimulus orientation, these tuning functions are directly related to each other according to the mathematical identity

$$f_{neuron}(\theta_s|\theta_p) = f(|\theta_s - \theta_p|) = f_{population}(\theta_p|\theta_s).$$

The tuning function for excitatory neurons was sharper (half width at half height (HWHH) was 15 degrees) than that for inhibitory neurons (HWHH=20 degrees). The tuning functions were approximately contrast-invariant. Contrast in the simulations is a linear scaling factor between zero and one, with zero yielding a baseline rate of 15 Hz for all the LGN cells, and one corresponding to the LGN-ON cells firing at 65 Hz in response to a 1 by 3 degrees bar covering their entire RF. This does not take into account the non-linearity of the contrast response function of LGN neurons (Cheng et al., 1995). These non-linearities can be accounted for by an appropriate scaling of the x-coordinate in our graphs. However, plotting linear contrast makes it easier to distinguish the non-linearity due to cortical dynamics from that due to the LGN input. Furthermore, the experimental LGN curves were obtained in response to gratings rather than the bars used here and thus may only be qualitatively correct.

We added the complex inhibitory cells to the network without altering the strength of the recurrent excitatory connections. However, in order to obtain contrast-invariant orientation tuning it was necessary to change the other connections (compare Table 21.1 with 21.2). Briefly, the number of inhibitory synapses received by each inhibitory neuron was increased from 8 to 40, the total strength of recurrent inhibition was increased by a factor four, and the unitary strength of the excitatory synapse to inhibitory neurons was halved. The resulting network activity for the non-attended condition is shown in Figure 21.4. There were three obvious changes compared to Figure 21.3. First, the tuning was less sharp (Figure 21.4D, HWHH=17 degrees for excitatory cells and 20.5 degrees for inhibitory cells). Second, the contrast sensitivity had decreased (Figure 21.4D), as responses above 10 Hz were only obtained for contrast values of 30% and higher, compared with 12% for the standard ring model. Third, the maximum rate of inhibitory neurons had decreased from 90 Hz to

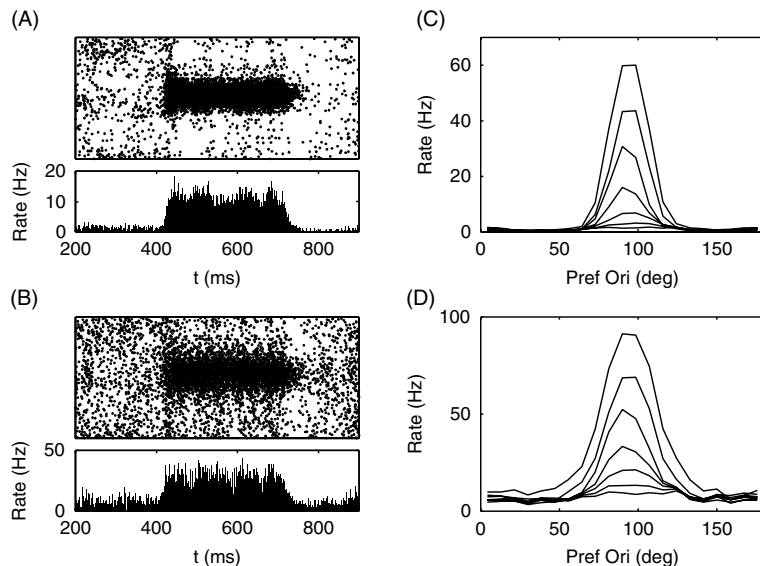


**FIGURE 21.3** Orientation-selective response of the standard ring model to a vertical bar. A 1 by 3 degree vertical bar was presented at full contrast between 400 ms and 700 ms. (A,B) In each panel, (top) the rastergram and (bottom) the histogram are shown for all the (A) excitatory and (B) inhibitory neurons. (C,D) The mean firing rate during the stimulus period as a function of the preferred orientation of the column, averaged across all (C) excitatory and (D) inhibitory neurons in the column. From bottom to top, the tuning curves are for 0, 5, 10, 15, 25, 50 and 100% linear contrast. The driving currents (expressed in  $\mu\text{A}/\text{cm}^2$ ) were  $I_E = -0.6$ ,  $I_{SI} = -0.1$ .

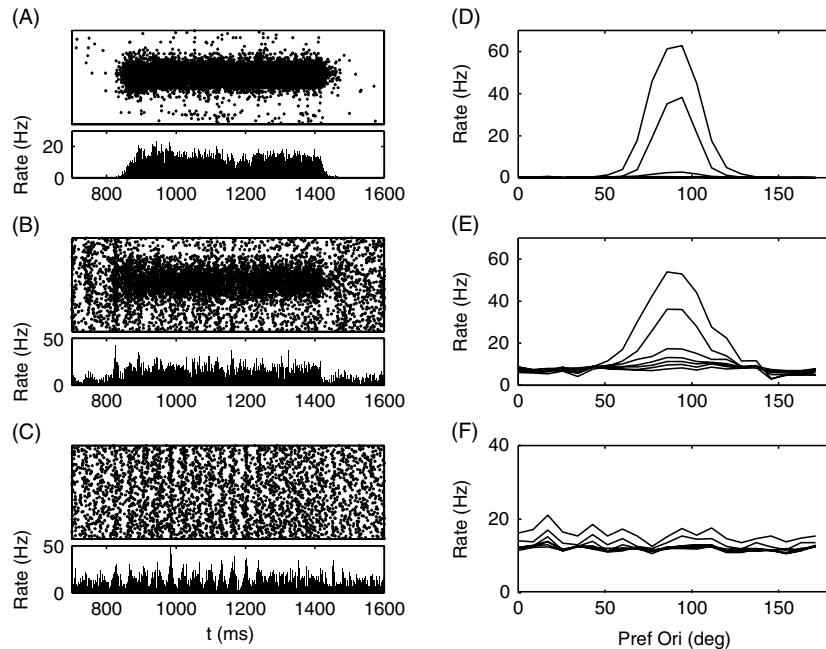


**FIGURE 21.4** The response of the complex ring model in the non-attended condition. A vertical bar was presented at full contrast between 800 and 1400 ms. (A–C) We show (top) the rastergram and (bottom) the histogram averaged across (A) excitatory cells, (B) simple inhibitory cells and (C) complex inhibitory cells. (D–F) The firing rate in response to a vertical bar as a function of the preferred orientation of the column for (D) excitatory cells, (E) simple inhibitory cells and (F) complex inhibitory cells. From bottom to top, the tuning curves are for 0, 5, 10, 15, 25, 50 and 100% linear contrast. The driving currents (expressed in  $\mu\text{A}/\text{cm}^2$ ) were  $I_E = -0.6$ ,  $I_{SI} = 0.1$ ,  $I_{CI} = 0.4$ .

50 Hz (Figure 21.4E). The complex cells were not orientation-selective and their firing rate varied only weakly with contrast (Figure 21.4F). For a 100% contrast stimulus (Figure 21.4C), the complex cells were weakly synchronized with an oscillation frequency of about 28 Hz. For lower contrast, the complex cells were not synchronized (see below and Figure 21.8). When the CI network is in the non-attended condition, an increase in the level of depolarizing current or in the amount of excitatory inputs will synchronize it (see Tiesinga and Sejnowski, 2004).

To mimic the effects of attention, the depolarizing current to the CI cells was increased from  $I_{CI} = 0.4$  to  $0.9 \mu\text{A}/\text{cm}^2$  (Figure 21.5). The CI neurons were synchronized in the prestimulus period and remained synchronized during the stimulus presentation (Figure 21.5C). In response to the oriented stimulus, the excitatory and simple inhibitory cells increased their rate and became synchronized. The orientation tuning functions (Figure 21.5D) were virtually identical to those in the non-attended condition (see Figure 21.4D).

The effect of attention on the contrast response functions (CRFs) was determined for neurons whose preferred orientation matched the stimulus orientation (Figure 21.6A–C). For contrasts up to 48% (at a firing rate of 36.2 Hz), the firing rate of the excitatory cells increased non-linearly with contrast (Figure 21.6A). For higher contrast, the rate of increase of the firing rate with contrast leveled off, yielding approximately 64 Hz at 100% contrast. Note that for even higher LGN firing rates, corresponding to contrast values larger than 100%, the firing rate still increased with contrast. The CRF in the attended condition is almost the same: the difference can be described as a small leftward shift of 5% with respect to the curve in the non-attended condition. The CRF of the SI cells was reduced in the attended condition compared with the non-attended condition (Figure 21.6B). The firing rate of the CI cells was only weakly contrast dependent but was significantly increased with attention (Figure 21.6C).

The excitatory firing rate was not altered by attention because of the balance between two effects. The increased firing rate of CI cells *increases* the amount of inhibition the excitatory cells receive directly from CIs, but it also decreases the firing rate of SI cells, which *decreases* the amount of SI inhibition to the excitatory cells. The overall effect is not straightforward because the degree of synchrony of the inhibitory inputs also varied, which by itself, even in the absence of any rate changes, could modulate the postsynaptic neuron's firing rate (see Tiesinga et al., 2005). The precise balance depends on how much of the inhibitory input to the SI cells comes from the CI cells. For the present parameter setting, 34% comes from CI cells (see Table 21.2). When the fraction of inputs coming from the CI cells was increased, the firing rate of the excitatory cells increased significantly with attention. This parameter setting may thus be more appropriate for cortical

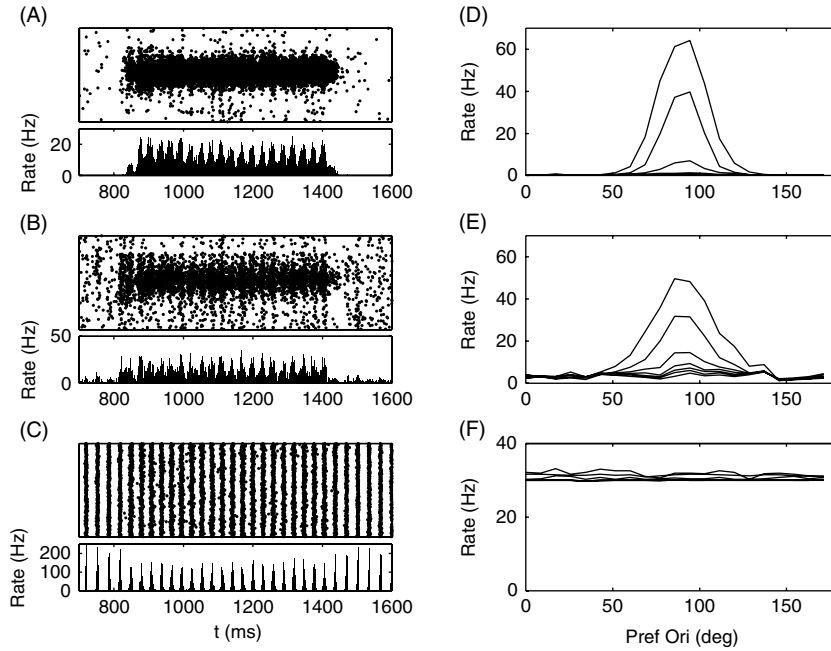


**FIGURE 21.5** The response of the complex ring model in the attended condition. A vertical bar was presented at full contrast between 800 and 1400 ms. The panels are as in Figure 21.4. The driving currents (expressed in  $\mu\text{A}/\text{cm}^2$ ) were  $I_E = -0.6$ ,  $I_{SI} = 0.1$ ,  $I_{CI} = 0.9$ .

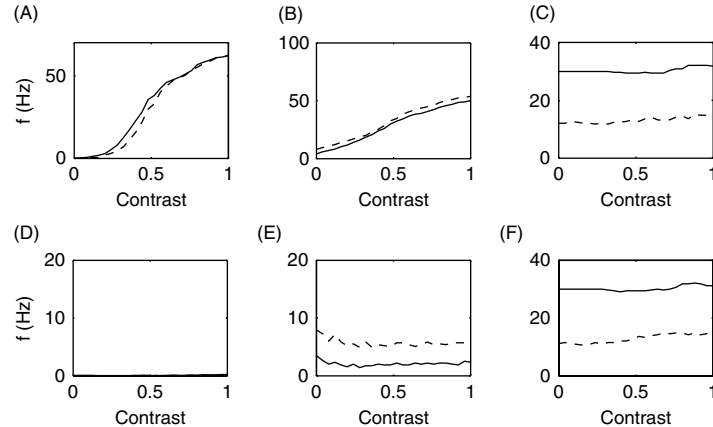


**FIGURE 21.6** Attentional modulation of the contrast response functions. We show the CRF of neurons in the column (A–C) whose preferred orientation matched the stimulus orientation and (D–F) whose preferred orientation was orthogonal to the stimulus orientation. The CRFs were averaged across (A,D) all excitatory neurons, (B,E) simple inhibitory neurons and (C,F) complex inhibitory neurons. The responses are shown for a network in the attended (solid lines) and in the non-attended condition (dashed lines).

areas downstream of V1. In order to obtain reasonable firing rates (to prevent epileptic states), the CI cells should receive sufficiently strong excitatory inputs and project strong enough inhibition back to the excitatory cells (results not shown).

The non-linearity present in the CRF for low contrast depends on the strength of recurrent excitation. For low contrast, the firing rate elicited in response to the stimulus grew *over time*, because of the recurrent excitation, to reach its maximum 100 ms or more after response onset. For this range of contrast values, the CRF increased steeply with contrast. For higher contrast, or a higher unitary strength of excitatory synapses, the firing rate reached its maximum value sooner *in time*. The leveling-off of the rate of increase of the CRF was associated with the firing rate reaching its maximum value shortly after response onset and a change in the dynamics of the interneurons. Specifically, in the attended state, the complex interneurons increased their firing rate and oscillation frequency but their precision was decreased (see below). In the non-attended state, the simple inhibitory cells increased their firing rate.

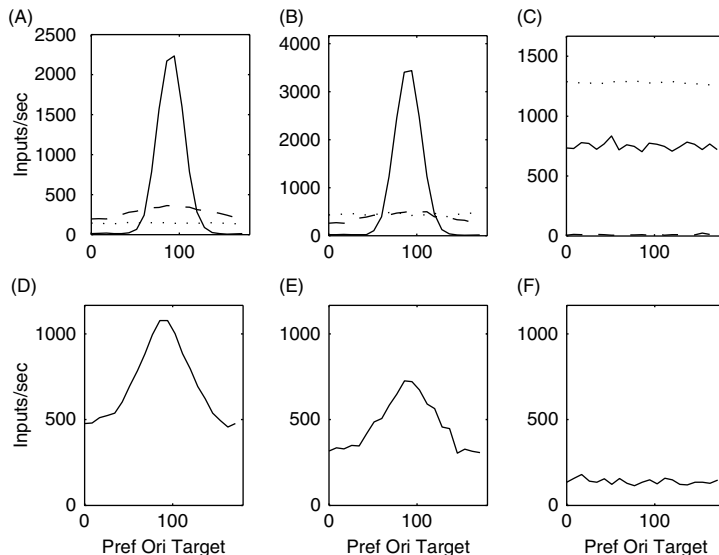


**FIGURE 21.7** Tuning of the synaptic inputs to cortical neurons in response to the presentation of a vertical bar. We show the rate of inputs to (A) excitatory, (B) simple inhibitory and (C) complex inhibitory neurons from excitatory (solid lines), simple inhibitory (dashed lines) and complex inhibitory neurons (dotted lines) as a function of the neuron's preferred orientation. The responses were averaged across all neurons of a specific type in each column. In the bottom three graphs the LGN inputs to (D) excitatory, (E) simple inhibitory and (F) complex inhibitory neurons are shown.

Figure 21.6D–F shows the CRF for neurons that prefer a horizontal orientation, which is orthogonal to the presented stimulus orientation. The excitatory cells did not fire for any value of the contrast (see Figure 21.6D), whereas the simple inhibitory cells fired, but their firing rate decreased as a function of contrast (see Figure 21.6E). In the attended condition, their CRF was shifted downward by approximately 4 Hz compared with the non-attended condition. The complex cells labeled as preferring horizontal behaved exactly the same as the ones shown in Figure 21.6C because they were not orientation selective.

We studied the tuning of synaptic drives from the LGN, SI, CI and E populations by calculating for a given stimulus orientation the rate of inputs to a neuron as a function of its preferred orientation (Figure 21.7). Like the orientation tuning curves discussed before, these curves can be reinterpreted as the input rate to one specific column as a function of stimulus orientation. The excitatory neurons received moderately tuned input from the LGN (Figure 21.7D), sharply tuned input from other excitatory neurons (Figure 21.7A, solid line) and weakly tuned input from simple inhibitory cells (Figure 21.7A, dashed line). The input from complex inhibitory cells was not orientation-tuned (Figure 21.7A, dotted line). The simple inhibitory cells received similarly tuned inputs (Figure 21.7B and E), except that the rate of the LGN inputs was lower because fewer LGN neurons project to the interneurons (see Table 21.2), whereas the rate of excitatory inputs was higher. The inhibitory inputs from complex cells dominated those coming from the simple inhibitory cells. None of the synaptic inputs to complex cells were orientation-tuned (Figure 21.7C and F).

We estimated the temporal modulation of synchrony using a multitaper spectrogram of the spike-time histogram of the E, SI and CI populations. The LFP is hypothesized to reflect the synaptic currents to neurons in the neighborhood of the electrode (Liu and Newsome, 2006). Hence, when the spike time histograms for each population are filtered by the corresponding synaptic time constants and added together with the appropriate weights, they might behave similarly to the LFP. We therefore refer to the (unfiltered) spike time histogram as the estimated LFP, eLFP for short. In the non-attended condition (Figure 21.8A), complex cells show power in the frequency range between 22 and 28 Hz which grows in amplitude and frequency as a function of contrast. The corresponding oscillations are only visible in the spike-time histogram for the 100% contrast stimulus (Figure 21.4C). Power at this frequency was absent or barely detectable in the simple inhibitory and excitatory cells (Figure 21.8B). In the attended state (Figure 21.8C and D), the complex cells were synchronized during the entire period, including when there was no stimulus present. During stimulus presentation the synchrony was maintained but, for higher contrast, the oscillation frequency increased whereas its power decreased slightly (Figure 21.8C). The simple inhibitory and excitatory cells followed the CI generated rhythm when they spiked, i.e. during the stimulus period. The gamma-frequency range power in the eLFP thus increased with contrast (Figure 21.8D).

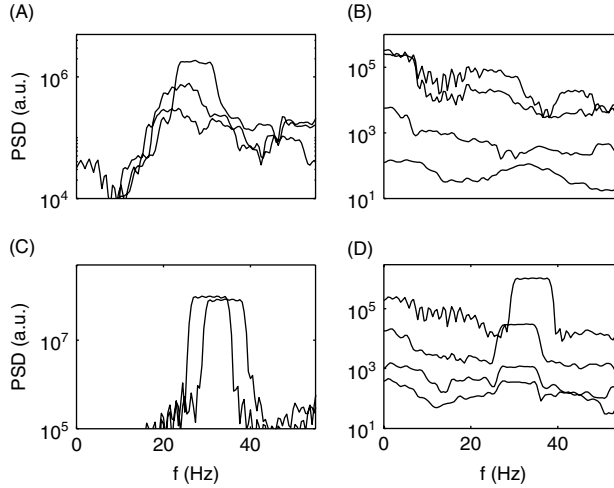


**FIGURE 21.8** Gamma-frequency-range power in the estimated local field potential increased with contrast. We show the power spectrum density of the spike-time histogram (eLFP) of the (A,C) complex inhibitory neurons and (B,D) excitatory neurons in the (A,B) non-attended state and (C,D) attended state. In each panel, power spectra are shown for different values of the contrast: (A), from bottom to top, 0, 35 and 100%; (B), from bottom to top, 0, 25, 50 and 100%; (C), left 0% and right 100%; (D) from bottom to top, 0, 10, 25 and 100%. The results are for a complex ring model in the attended state (as in Figure 21.5). The power spectrum was calculated across 600 samples of the spike-time histogram with a 1 ms time resolution and averaged across 5 tapers with a bandwidth of NW = 3.

The coherence between the excitatory and inhibitory population was quantified using the multitaper coherency (Mitra and Pesaran, 1999; Jarvis and Mitra, 2001). We calculated the coherencies between the spike-time histograms (not shown) as well as between the excitatory spike trains and the eLFP of the CI cells (Figure 21.9). The latter measure is similar to the spike field coherence used in Fries et al. (2001). The coherence is a complex quantity – its absolute value represents the strength of the coherence (Figure 21.9A and C) and its phase is proportional to the delay between the activity of the two populations (Figure 21.9B and D). During the stimulus period in the attended state, the coherence showed a clear peak for frequencies between 28 and 40 Hz (Figure 21.9A) with the CIs lagging the excitatory neurons, as is indicated

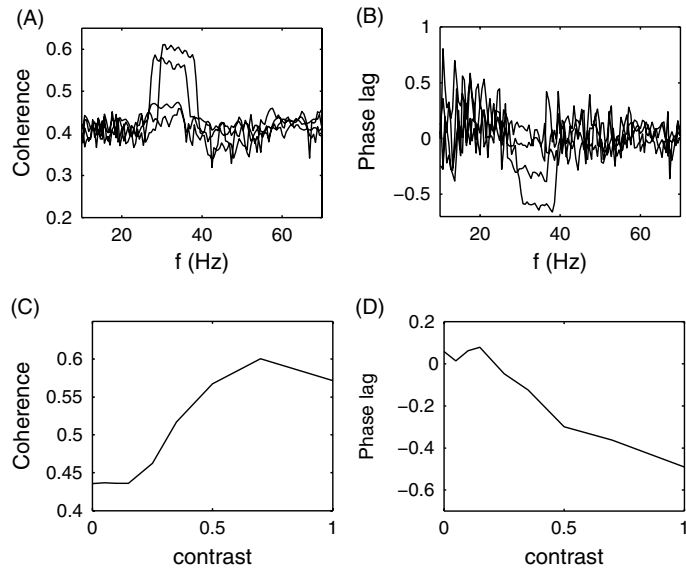


**FIGURE 21.9** The gamma-frequency-range coherence between the estimated local field potential and the excitatory neurons increased with contrast. The (A) coherence and (B) relative phase between the spike-time histogram of inhibitory neurons and the spike trains of excitatory neurons as a function of frequency. A negative phase means that the excitatory neurons are ahead of the inhibitory neurons. The (C) coherence and (D) relative phase in the 28 to 36 Hz frequency band is plotted as a function of stimulus contrast. The results are for a complex ring model in the attended state (as in Figure 21.5) and are averaged across a hundred spike trains of excitatory neurons. The coherence was calculated across 600 samples of the spike-time histogram with a 1 ms time resolution and averaged across 5 tapers with a bandwidth of NW = 3.

by the negative phase (Figure 21.9B). The coherence grew with contrast, leveling off at 70% contrast (Figure 21.9C). Likewise, the phase lag increased, becoming more negative with contrast (Figure 21.9D). In the non-attended state, the level of coherence was not significant when tested at a *P*-value of 0.05. However, in the 22–32 Hz frequency range, there was coherence between the eLFPs of the excitatory and CI neurons (not shown).

Is it possible to obtain synchrony modulation without adding complex cells to the network? Theoretical and computational studies have identified two different ways of obtaining synchronous oscillations in the gamma frequency range (Wang and Buzsaki, 1996; White et al., 1998; Brunel, 2000; Tiesinga et al., 2001; Aradi and Soltesz, 2002; Bartos et al., 2002; Borgers and Kopell, 2003, 2005; Brunel and Wang, 2003; Hansel and Mato, 2003; Vida et al., 2006). In the first one, ‘PING’ (Borgers and Kopell, 2003), a synchronous volley of spikes from excitatory cells elicits a volley of spikes from the inhibitory cells, which shuts down the network for approximately a gamma period, 25 ms, after which the cycle starts anew. For this rhythm to be stable, the inhibitory cells should not be able to spike before the synchronous excitatory volley arrives (Borgers and Kopell, 2005). In the network studied here, excitatory and inhibitory cells are both driven by almost simultaneous LGN inputs that can make them spike even without intracortical excitation, suggesting that the PING mechanism might not be effective in this network architecture. In the second one, ‘ING’, the inhibitory network synchronizes by way of mutual inhibition (Wang and Buzsaki, 1996). This rhythm requires about one hundred neurons and a high degree of interconnectedness (Wang and Buzsaki, 1996; Golomb and Hansel, 2000). Furthermore, it can only exist when the random background activity (noise) and the degree of heterogeneity (differences in intrinsic excitability) are small enough (Wang and Buzsaki, 1996; White et al., 1998; Tiesinga and Jose, 2000). It is the heterogeneity that posed the main problem in our explorations of the standard ring model. In Figure 21.7B and D, the rates of intracortical and LGN inputs to interneurons are shown. The interneurons whose preferred orientation matched the stimulus orientation received much stronger inputs from the excitatory neurons and LGN neurons than did those whose preferred orientation was different from the stimulus orientation. The intracortical connections contributed more to the heterogeneity than the LGN inputs. We explored how far we could get, using only simple cells, towards our goal of finding a network that is synchronous in the prestimulus period and remains synchronous after the onset of the stimulus. The number of inhibitory cells was tripled to 63 per column and the number of inhibitory synapses onto each interneuron was increased to 128. Since the intracortical inputs caused the most heterogeneity, the intracortical connections were either made independent of the difference in orientation preference between the presynaptic cell and the postsynaptic cell or their unitary strength was reduced. In addition, the unitary strength of the thalamocortical synapses was reduced slightly. We found three ways in which the increase in heterogeneity associated with stimulus onset could be absorbed by the network without losing synchrony. First, the network could increase its oscillation frequency (Figure 21.10A). Second, it could decrease the latency of the interneurons whose preferred orientation matched that of the stimulus without changing the firing rate (Figure 21.10B). Third, it could increase the number of spikes the interneuron produces on each cycle without changing the oscillation (Figure 21.10C). The parameter settings are summarized in Table 21.3.

In case 1 (see Figure 21.10A), the interneurons received a large depolarizing drive and the mutual inhibition was strong. As a result, the interneurons could synchronize without strong LGN inputs. The intracortical connections were made untuned, i.e. the connection probability did not depend on the difference in preferred orientation between the presynaptic neuron and the postsynaptic neuron. When the vertical bar came on, it increased the rate of the interneurons with a preferred orientation close to 90 degrees. These neurons led the oscillation, thus increasing its frequency. Because of the strong mutual inhibition, the interneurons with preferred orientations farther from 90 degrees remained entrained to the sped-up rhythm, but they occasionally skipped a cycle. The modulation of interneuron firing rate with preferred orientation was weak: the dynamic range – the difference between the highest and lowest firing rate – was about 15 Hz. This modulation was on top of a high baseline rate of about 46 Hz. The dynamic range of the excitatory neurons was similar, around 18 Hz, with a baseline rate of 2.5 Hz.

For case 2 (see Figure 21.10B), the interneurons still received a large depolarizing current, but now the excitatory neurons also received a depolarizing current. The intracortical connections were made orientation-selective again, but the strength of all intracortical connections was reduced except for the strength of the mutual inhibition, which was kept the same. For these parameters, the excitatory neurons fired at a high rate even before stimulus onset and the network was synchronized. When the vertical bar came on, it increased the firing rate of the excitatory neurons with an orientation preference close to 90 degrees. However, because the strength of the excitatory synapses on the interneurons was weak, the stimulus onset did not increase interneuron firing rate, rather it decreased the spiking latency of interneurons preferring vertical bars compared with those that preferred different orientations. The inhibitory cells were not orientation-selective in the classical sense since their firing rate did not change with stimulus orientation. The dynamic range of the excitatory neuron was similar to that in case 1, about 24 Hz, but it sat on top of a much higher baseline rate of 35 Hz.

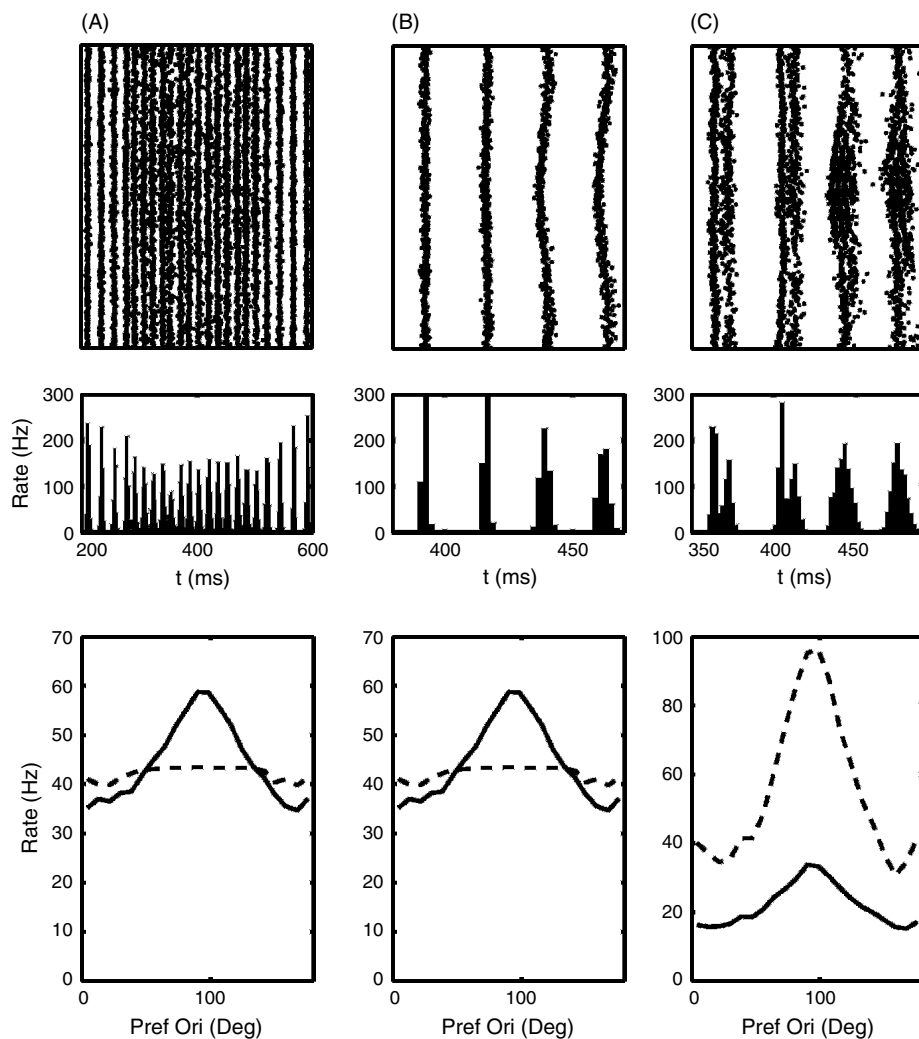


**FIGURE 21.10** Alternative mechanisms for obtaining synchrony modulations in the standard ring model. In each panel, we show (top) the rastergram, (middle) the histogram of simple inhibitory cells and (bottom) the firing rate in response to a vertical bar as a function of the preferred orientation for excitatory (solid lines) and simple inhibitory cells (dashed lines). We present simulations for three cases, when stimulus presentation increased the oscillation frequency (A), reduced the latency (B), or increased the number of spikes per cycle (C) of neurons with a preferred orientation that matched the stimulus orientation. The parameter values are listed in Table 21.3.

**TABLE 21.3** Parameters for the simulations shown in Figure 21.10. The parameters are as in the standard ring model, except that there were 63 inhibitory cells (increased from 21) and each inhibitory cell received 128 inhibitory synapses. The thalamocortical synapses onto excitatory cells had a unitary strength of  $12 \mu\text{S}/\text{cm}^2$ , those on inhibitory cells were  $7 \mu\text{S}/\text{cm}^2$

	E to E ( $\mu\text{S}/\text{cm}^2$ )	E to I ( $\mu\text{S}/\text{cm}^2$ )	I to E ( $\mu\text{S}/\text{cm}^2$ )	I to I ( $\mu\text{S}/\text{cm}^2$ )	Current to E ( $\mu\text{A}/\text{cm}^2$ )	Current to I ( $\mu\text{A}/\text{cm}^2$ )
Figure 21.10A	2	20	5	3	0	2
Figure 21.10B	1.2	1	2	3	1.1	2
Figure 21.10C	2	20	5	3	0.7	0.5

For case 3 (see Figure 21.10C), the depolarizing current to excitatory and inhibitory neurons was reduced. The unitary strengths of the intracortical connections were returned to their values for case 1, but they remained orientation-selective as in case 2. Before stimulus onset, the excitatory and inhibitory neurons were synchronized with an oscillation frequency of about 25 Hz. The excitatory neurons fired one spike on each cycle and led the interneurons, which fired two spikes on each cycle. When the vertical bar stimulus came on, the interneurons with an orientation preference close to 90 degrees increased their firing rate and spiked three times on each cycle, whereas the interneurons preferring orthogonal orientations reduced their rate to about one spike per cycle. The oscillation frequency increased slightly to 28.6 Hz. The excitatory neurons preferring vertical stimuli also increased their firing rate, but they still spiked at most once on each oscillation cycle. The dynamic range of the interneurons was large, 66 Hz, on top of a baseline rate of about 31 Hz, whereas the excitatory neurons had a small dynamic range of about 19 Hz on top of a 15 Hz baseline.

The outcome of this exploration is that it is possible to modulate synchrony. However, it is not possible, at the same time, to sharpen significantly the orientation tuning of cortical neurons compared with that of the LGN inputs by way of recurrent excitation and to have a large dynamic range of the firing rate.

## DISCUSSION

The simulations reported here were primarily directed at determining the dynamics of non-pathological cortical networks in response to sensory stimulation. Therefore, parameter values were chosen such that the maximum firing rate was less than 100 Hz in response to stimulus presentation, the background rate was a few Hertz and there was no global synchrony among the excitatory neurons. Nevertheless, our studies provide insight into preventing the high sustained firing rates and global synchrony that occur during epilepsy. In order to modulate firing rate and synchrony independently, two types of interneurons were required. The first type, SI, prevents runaway excitation because it is strongly driven by the excitatory neurons and, in return, it provides strong inhibition to the excitatory neurons. The model network goes into a high firing rate state, even in the absence of sensory stimulation, when either the synaptic strength of inhibition, the excitability of interneurons or the strength of excitatory synapses onto SI is reduced (results not shown). The second type, CI, generates synchrony. The CI neurons inhibit the SI neurons. Hence, in order to prevent epileptic states due to reduced SI inhibition, the CI neurons also need to project to the excitatory cells and receive inputs from them (results not shown). In the hippocampus, which is often a generator of epileptic seizures, there are also many distinct types of interneurons (Freund and Buzsaki, 1996; Somogyi and Klausberger, 2005; Soltesz, 2006). In order to develop effective and safe pharmacological therapies for epilepsy, further research is necessary, but the present study suggests some new avenues. For instance, should receptors on interneurons involved in firing rate regulation be targeted? This would allow synchrony to be generated and various cognitive functions (Buzsaki, 2006) that depend on synchrony to be spared. Or should the receptors on synchrony-generating interneurons be targeted? This would allow the balance between excitation and inhibition to be maintained without leading to homeostatic changes in intrinsic excitability that would otherwise occur. We conclude by discussing the link between the model proposed here and experimental observations on attentional modulation of responses in the primary visual cortex.

Multiple features of a visual stimulus are represented in the neural activity which it elicits in the visual pathway. These features include orientation, luminance contrast and whether the stimulus is in the focus of spatial attention. The most frequently used measure of neural activity is firing rate. Consider an orientation-selective neuron that has a baseline rate of 5 Hz, and which responds to a stimulus that matches its preferred orientation with 30 Hz if the stimulus is at 50% contrast and with 60 Hz if it is at 100% contrast. If a rate of 25 Hz is measured, what could the stimulus have been? It could have been a high contrast stimulus with an orientation different from the neuron's preferred orientation, or a low contrast stimulus with the neuron's preferred orientation, or a low contrast stimulus that was in the focus of attention. Or it could be that no stimulus was presented at all, but that the neuron's baseline firing rate increased because of general arousal. How does the visual system disambiguate the different possible meanings of such a firing rate response? And, are the changes in activity due to stimulus identity, stimulus strength and the focus of attention generated by distinct circuitry? The answer to the first question is that the population activity must be used, with the identity of the neurons that are most strongly activated and the degree of coherence/correlation between them being the most significant aspect of the population activity. So far, electrophysiological recordings in non-human primates have only offered a glimpse of the richness of the population response. Nevertheless, it has become clear that in the primary visual cortex of anesthetized macaque monkeys the LFP power in the gamma-frequency range increases with contrast (Henrie and Shapley, 2005), whereas the gamma-frequency-band coherence between a neuron's spike train and the LFP increases with attention (Fries

et al., 2001; Bichot et al., 2005). Thus, stimulus strength and the focus of attention modulate neural correlations (Salinas and Sejnowski, 2001). There is no definite answer to the second question, primarily because there is a lack of models and experiments that have addressed the issue of how attention, contrast and stimulus identity interact. This study is our first attempt to resolve this issue.

Our goal was to determine how the effects of attention could be incorporated in a model that produces contrast-invariant orientation-selective responses. The model needed to reproduce the following observations. First, contrast-invariant orientation tuning curves should have a half width at half height between 10 and 30 degrees (Gur et al., 2005). Second, the power of the local field potential (LFP) in the gamma-frequency should increase with contrast (Henrie and Shapley, 2005). Third, the width of the orientation curve should not change with attentional condition (McAdams and Maunsell, 1999). Fourth, attention should induce only small changes in the firing rate of neurons responding to a simple stimulus (McAdams and Reid, 2005). Fifth, attention should modulate the power of the LFP, as well as the coherence of spike trains with the LFP, in the gamma-frequency range (Fries et al., 2001; Bichot et al., 2005; Taylor et al., 2005). We show that it is easiest to assume the existence of interneurons with complex receptive field characteristics that are weakly or not at all orientation-selective and that show a modest increase in firing rate with contrast, but that are strongly modulated by attentional state. We have not conclusively shown that similar dynamics could not be achieved using only excitatory and inhibitory cells with simple receptive field characteristics, but so far we have not been successful in finding such a network that behaves appropriately. The reason for this is that the inhibitory neurons had to serve two functions. They needed to sharpen orientation-selectivity and they needed to synchronize. Synchrony develops in interneuron networks when:

1. there are enough interneurons, about one hundred (Wang and Buzsaki, 1996)
2. they are well connected, about sixty synapses per neuron (Wang and Buzsaki, 1996)
3. the level of background activity, noise, is low enough (Tiesinga and Jose, 2000)
4. the degree of heterogeneity is low enough (Wang and Buzsaki, 1996; White et al., 1998).

Not only does the variability in intrinsic properties of neurons contribute to the heterogeneity, but the inhomogeneous activation of neurons also contributes because of their different preferred orientations. Our solution was to assign a different interneuron to each function. In experiments, two types of interneurons were found in layer 4 of cat primary visual cortex in approximately equal proportions (Hirsch et al., 2003). One had a simple receptive field and was orientation-selective, whereas the other had a complex receptive field and was not orientation-selective. In a recent model, these complex interneurons were shown to be useful for contrast-invariant orientation tuning (Lauritzen and Miller, 2003). The question remains whether these complex interneurons also exist in layer 4 of primate visual cortex. The mechanism proposed here predicts that there is a pool of interneurons with complex RF characteristics that increases their rate with attention and another pool of interneurons with simple RFs that decreases their rate with attention.

We studied the behavior of the model in two operating regimes. In the first, the activity before stimulus onset was asynchronous, but the onset of a sufficiently high contrast stimulus led to weak synchronous oscillations in the spike-time histogram of complex inhibitory cells. Hence, the gamma-frequency power in the eLFP associated with the CI cells increased with stimulus contrast, consistent with the previously mentioned experimental results (Henrie and Shapley, 2005). We propose that this parameter setting represents the non-attended state. In the second, the complex cell activity was synchronous before and also during stimulus presentation, but the oscillation frequency increased during the stimulus presentation when the contrast was high enough. The excitatory cells were also synchronized. Their rate was low for low contrast, but it increased with contrast. As a result, the coherence between excitatory activity and the eLFP (from CI cells) increased with contrast. We propose that this parameter setting represents the attended state. The network can be switched from the non-attended to attended state solely by increasing the drive to the complex interneurons. This drive could be supplied by various subcortical (Freund and Meskenaite, 1992) and cortical feedback projections (Gonchar and Burkhalter, 1999, 2003).

The preceding discussion has focused on the modulation of synchrony by attention. In cortical areas V2, V4 and MT, changes of firing rate with spatial attention have been reported (Luck et al., 1997; McAdams and Maunsell, 1999; Treue and Maunsell, 1999; Reynolds et al., 2000; Williford and Maunsell, 2006). In V1, no clear evidence for firing rate changes with attention have been found when using simple stimuli (McAdams and Reid, 2005; but see Roelfsema et al., 2004; Khayat et al., 2006). However, attention may cause changes in synchrony in V1, which could lead to firing rate increases downstream (Tiesinga, 2004). Hence, our parameter settings for the V1 model were chosen such that there was little change in the CRF of excitatory neurons whose preferred orientation matched the stimulus orientation. This was achieved by tuning the number of synapses from CI to SI cells such that the increase in inhibition from CI cells to the excitatory cells with attention was balanced by the decrease in inhibition from SI cells. An increase in excitatory activity with attention,

as is observed in V4, can be obtained in this type of network by decreasing the fraction of synapses on SI neurons coming from CI cells.

We used the ring model to generate orientation selective neurons. The ring model has experimental support (Tsodyks et al., 1999; Kenet et al., 2003) and has been used previously in large-scale model simulations (Somers et al., 1995). There are alternative models, some of which require strong recurrent excitation and inhibition (McLaughlin et al., 2000; Marino et al., 2005), others of which are based primarily on the selectivity of thalamic inputs (Troyer et al., 1998; Ferster and Miller, 2000). The actual situation may lie between these two extreme cases (Monier et al., 2003; Teich and Qian, 2006). We have chosen the ring model as the first case to study, but it is of interest to determine how the considerations presented here apply to the alternative models.

Experiments with multielectrode arrays in awake behaving primates are presently being conducted in a number of labs, making it possible to record from multiple neurons simultaneously during an attention-demanding task. The model can potentially be useful for these experiments since it predicts how the coherence between neurons changes with attention and contrast and how it depends on the difference in stimulus preference between the neurons.

#### ACKNOWLEDGMENT

This work was supported in part by start-up funds from the University of North Carolina at Chapel Hill and by the Human Frontier Science Program.

#### REFERENCES

- Aradi, I. and Soltesz, I. (2002). Modulation of network behaviour by changes in variance in interneuronal properties. *J Physiol* 538:227–251.
- Bartos, M., Vida, I., Frotscher, M. et al. (2002). Fast synaptic inhibition promotes synchronized gamma oscillations in hippocampal interneuron networks. *Proc Natl Acad Sci USA* 99:13222–13227.
- Ben-Yishai, R., Bar-Or, R.L. and Sompolinsky, H. (1995). Theory of orientation tuning in visual cortex. *Proc Natl Acad Sci USA* 92:3844–3848.
- Bichot, N.P., Rossi, A.F. and Desimone, R. (2005). Parallel and serial neural mechanisms for visual search in macaque area V4. *Science* 308:529–534.
- Borgers, C. and Kopell, N. (2003). Synchronization in networks of excitatory and inhibitory neurons with sparse, random connectivity. *Neural Comput* 15:509–538.
- Borgers, C. and Kopell, N. (2005). Effects of noisy drive on rhythms in networks of excitatory and inhibitory neurons. *Neural Comput* 17:557–608.
- Brunel, N. (2000). Dynamics of sparsely connected networks of excitatory and inhibitory spiking neurons. *J Comput Neurosci* 8:183–208.
- Brunel, N. and Wang, X.J. (2003). What determines the frequency of fast network oscillations with irregular neural discharges? I. Synaptic dynamics and excitation-inhibition balance. *J Neurophysiol* 90:415–430.
- Buia, C.I. and Tiesinga, P.H.E. (2005). Rapid temporal modulation of synchrony in cortical interneuron networks with synaptic plasticity. *Neurocomputing* 65:809–815.
- Buia, C. and Tiesinga, P. (2006). Attentional modulation of firing rate and synchrony in a model cortical network. *J Comput Neurosci* 20:247–264.
- Buzsaki, G. (2006). *Rhythms of the brain*. Oxford University Press, New York.
- Cheng, H., Chino, Y.M., Smith, E.L. 3rd, Hamamoto, J. and Yoshida, K. (1995). Transfer characteristics of X LGN neurons in cats reared with early discordant binocular vision. *J Neurophysiol* 74:2558–2572.
- Douglas, R.J. and Martin, K.A. (2004). Neuronal circuits of the neocortex. *Annu Rev Neurosci* 27:419–451.
- Douglas, R.J., Koch, C., Mahowald, M., Martin, K.A. and Suarez, H.H. (1995). Recurrent excitation in neocortical circuits. *Science* 269:981–985.
- Ferster, D. and Miller, K.D. (2000). Neural mechanisms of orientation selectivity in the visual cortex. *Annu Rev Neurosci* 23:441–471.
- Freund, T.F. and Buzsaki, G. (1996). Interneurons of the hippocampus. *Hippocampus* 6:347–470.
- Freund, T.F. and Meskenaite, V. (1992). gamma-Aminobutyric acid-containing basal forebrain neurons innervate inhibitory interneurons in the neocortex. *Proc Natl Acad Sci USA* 89:738–742.
- Fries, P., Reynolds, J.H., Rorie, A.E. and Desimone, R. (2001). Modulation of oscillatory neuronal synchronization by selective visual attention. *Science* 291:1560–1563.
- Golomb, D. (1998). Models of neuronal transient synchrony during propagation of activity through neocortical circuitry. *J Neurophysiol* 79:1–12.
- Golomb, D. and Amitai, Y. (1997). Propagating neuronal discharges in neocortical slices: computational and experimental study. *J Neurophysiol* 78:1199–1211.
- Golomb, D. and Hansel, D. (2000). The number of synaptic inputs and the synchrony of large, sparse neuronal networks. *Neural Comput* 12:1095–1139.
- Gonchar, Y. and Burkhalter, A. (1999). Connectivity of GABAergic calretinin-immunoreactive neurons in rat primary visual cortex. *Cereb Cortex* 9:683–696.
- Gonchar, Y. and Burkhalter, A. (2003). Distinct GABAergic targets of feedforward and feedback connections between lower and higher areas of rat visual cortex. *J Neurosci* 23:10904–10912.
- Gur, M., Kagan, I. and Snodderly, D.M. (2005). Orientation and direction selectivity of neurons in V1 of alert monkeys: functional relationships and laminar distributions. *Cereb Cortex* 15:1207–1221.
- Hansel, D. and Mato, G. (2003). Asynchronous states and the emergence of synchrony in large networks of interacting excitatory and inhibitory neurons. *Neural Comput* 15:1–56.

- Henrie, J.A. and Shapley, R. (2005). LFP power spectra in V1 cortex: the graded effect of stimulus contrast. *J Neurophysiol* 94:479–490.
- Hirsch, J.A., Martinez, L.M., Pillai, C., Alonso, J.M., Wang, Q. and Sommer, F.T. (2003). Functionally distinct inhibitory neurons at the first stage of visual cortical processing. *Nat Neurosci* 6:1300–1308.
- Jarvis, M.R. and Mitra, P.P. (2001). Sampling properties of the spectrum and coherency of sequences of action potentials. *Neural Comput* 13:717–749.
- Kenet, T., Bibitchkov, D., Tsodyks, M., Grinvald, A. and Arieli, A. (2003). Spontaneously emerging cortical representations of visual attributes. *Nature* 425:954–956.
- Khayat, P.S., Spekreijse, H. and Roelfsema, P.R. (2006). Attention lights up new object representations before the old ones fade away. *J Neurosci* 26:138–142.
- Lauritzen, T.Z. and Miller, K.D. (2003). Different roles for simple-cell and complex-cell inhibition in V1. *J Neurosci* 23:10201–10213.
- Liu, J. and Newsome, W.T. (2006). Local field potential in cortical area MT: stimulus tuning and behavioral correlations. *J Neurosci* 26:7779–7790.
- Luck, S.J., Chelazzi, L., Hillyard, S.A. and Desimone, R. (1997). Neural mechanisms of spatial selective attention in areas V1, V2, and V4 of macaque visual cortex. *J Neurophysiol* 77:24–42.
- Marino, J., Schummers, J., Lyon, D.C. et al. (2005). Invariant computations in local cortical networks with balanced excitation and inhibition. *Nat Neurosci* 8:194–201.
- Markram, H., Toledo-Rodriguez, M., Wang, Y., Gupta, A., Silberberg, G. and Wu, C. (2004). Interneurons of the neocortical inhibitory system. *Nat Rev Neurosci* 5:793–807.
- McAdams, C.J. and Maunsell, J.H. (1999). Effects of attention on orientation-tuning functions of single neurons in macaque cortical area V4. *J Neurosci* 19:431–441.
- McAdams, C.J. and Reid, R.C. (2005). Attention modulates the responses of simple cells in monkey primary visual cortex. *J Neurosci* 25:11023–11033.
- McLaughlin, D., Shapley, R., Shelley, M. and Wielaard, D.J. (2000). A neuronal network model of macaque primary visual cortex (V1): orientation selectivity and dynamics in the input layer 4Calpha. *Proc Natl Acad Sci USA* 97:8087–8092.
- Mitra, P.P. and Pesaran, B. (1999). Analysis of dynamic brain imaging data. *Biophys J* 76:691–708.
- Monier, C., Chavane, F., Baudot, P., Graham, L.J. and Fregnac, Y. (2003). Orientation and direction selectivity of synaptic inputs in visual cortical neurons: a diversity of combinations produces spike tuning. *Neuron* 37:663–680.
- Reynolds, J.H., Pasternak, T. and Desimone, R. (2000). Attention increases sensitivity of V4 neurons. *Neuron* 26:703–714.
- Roelfsema, P.R., Lamme, V.A. and Spekreijse, H. (2004). Synchrony and covariation of firing rates in the primary visual cortex during contour grouping. *Nat Neurosci* 7:982–991.
- Salinas, E. and Sejnowski, T.J. (2001). Correlated neuronal activity and the flow of neural information. *Nat Rev Neurosci* 2:539–550.
- Soltesz, I. (2006). Diversity in the neuronal machine. Oxford University Press, New York.
- Somers, D.C., Nelson, S.B. and Sur, M. (1995). An emergent model of orientation selectivity in cat visual cortical simple cells. *J Neurosci* 15:5448–5465.
- Somogyi, P. and Klausberger, T. (2005). Defined types of cortical interneurone structure space and spike timing in the hippocampus. *J Physiol* 562:9–26.
- Taylor, K., Mandon, S., Freiwald, W.A. and Kreiter, A.K. (2005). Coherent oscillatory activity in monkey area V4 predicts successful allocation of attention. *Cereb Cortex* 15:1424–1437.
- Teich, A.F. and Qian, N. (2006). Comparison among some models of orientation selectivity. *J Neurophysiol* 96:404–419.
- Tiesinga, P., Fellous, J.-M., Salinas, E., Jose, J. and Sejnowski, T. (2005). Inhibitory synchrony as a mechanism for attentional gain modulation. *J Physiol (Paris)* 98:296–314.
- Tiesinga, P.H.E. (2004). Chaos-induced modulation of reliability boosts output firing rate in downstream cortical areas. *Phys Rev E* 69:031912.
- Tiesinga, P.H.E. and Jose, J.V. (2000). Robust gamma oscillations in networks of inhibitory hippocampal interneurons. *Netw-Comput Neural Syst* 11:1–23.
- Tiesinga, P.H.E. and Sejnowski, T.J. (2004). Rapid temporal modulation of synchrony by competition in cortical interneuron networks. *Neural Comput* 16:251–275.
- Tiesinga, P.H.E., Fellous, J.M., Jose, J.V. and Sejnowski, T.J. (2001). Computational model of carbachol-induced delta, theta, and gamma oscillations in the hippocampus. *Hippocampus* 11:251–274.
- Traub, R.D. and Miles, R. (1991). Neuronal networks of the hippocampus. Cambridge University Press, Cambridge.
- Treue, S. and Maunsell, J.H. (1999). Effects of attention on the processing of motion in macaque middle temporal and medial superior temporal visual cortical areas. *J Neurosci* 19:7591–7602.
- Troyer, T.W., Kruckowski, A.E., Priebe, N.J. and Miller, K.D. (1998). Contrast-invariant orientation tuning in cat visual cortex: thalamocortical input tuning and correlation-based intracortical connectivity. *J Neurosci* 18:5908–5927.
- Tsodyks, M., Kenet, T., Grinvald, A. and Arieli, A. (1999). Linking spontaneous activity of single cortical neurons and the underlying functional architecture. *Science* 286:1943–1946.
- Vida, I., Bartos, M. and Jonas, P. (2006). Shunting inhibition improves robustness of gamma oscillations in hippocampal interneuron networks by homogenizing firing rates. *Neuron* 49:107–117.
- Wang, X.J. and Buzsaki, G. (1996). Gamma oscillation by synaptic inhibition in a hippocampal interneuronal network model. *J Neurosci* 16:6402–6413.
- White, J.A., Chow, C.C., Ritt, J., Soto-Trevino, C. and Kopell, N. (1998). Synchronization and oscillatory dynamics in heterogeneous, mutually inhibited neurons. *J Comput Neurosci* 5:5–16.
- Williford, T. and Maunsell, J.H. (2006). Effects of spatial attention on contrast response functions in macaque area V4. *J Neurophysiol* 96:40–54.

PART

VI

---

INTERICTAL TO ICTAL TRANSITIONS

---

This page intentionally left blank

# 22

## CELLULAR AND NETWORK MECHANISMS OF OSCILLATIONS PRECEDING AND PERHAPS INITIATING EPILEPTIC DISCHARGES

ROGER D. TRAUB, DIEGO CONTRERAS AND MILES A. WHITTINGTON

### ABSTRACT

A rational approach to the prevention and treatment of epilepsy requires several types of information: (1) How do neurons behave during the seizure itself? (2) Are neurons doing something unusual prior to a seizure, recognition of which would provide useful warning? (3) What factors predispose the brain to engage in such unusual activities? – either *long-standing* structural or molecular abnormalities, or *recent, perhaps transient* fluctuations in neuronal environment or conditions – changes in neuromodulation or pH, perhaps. Many physiological studies have addressed the first of these questions, the intra-seizure activities of neurons. In this chapter, we shall concentrate on the second and third questions. We review data indicating that, in diverse seizure models, very fast oscillations ('VFO', >70 Hz) in neuronal network activity constitute the initial pre-seizure event; and indicating further that VFO is generated, in part, because gap junctions exist between the axons of principal cortical neurons (pyramidal cells, dentate granule cells, spiny stellate cells). Gap junctions between the axons of principal, i.e. excitatory, neurons act as an efficient means of spreading action potentials from neuron to neuron, and thus of amplifying (a) *synaptic* excitation (by *orthodromic* propagation of action potentials), (b) the effects of ectopically generated spontaneous axonal action potentials, which can propagate through the axonal plexus, and (c) the tendency of neurons to generate bursts (because of *antidromic* propagation of action potentials, which are then able to activate intrinsic membrane currents). Gap junction-mediated VFO is facilitated by alkalosis (which opens gap junctions), as well as by enhanced neuronal excitability; and VFO could, in turn, initiate seizures by a variety of use-dependent alterations in synaptic efficacy.

### INTRODUCTION

We shall assume that the reader is familiar with the critical role played by recurrent synaptic excitation in most types of epileptogenesis (Johnston and Brown, 1981; Traub and Wong, 1982; Lee and Hablitz, 1989; Traub and Miles, 1991; Traub et al., 1993). Building on this base, the chapter then will consist of four sections.

First, we will illustrate examples and review literature demonstrating that field potential oscillations – at frequencies from ~20 Hz to >100 Hz – occur prior to the onset of electrographic seizures in humans and experimental animals, and *in vitro* as well. Indeed, such an oscillatory 'preface' to epileptogenesis may be universal, perhaps demonstrable clinically and experimentally, if only one could record from enough intracortical sites – although this notion still remains a hypothesis. The pre-seizure oscillations may well play a causal role in starting the seizure. It is just as important, then, to investigate the physiological mechanisms and anatomical substrates of the pre-seizure oscillations as the corresponding mechanisms and substrates of seizures themselves. The oscillations may turn out to be a therapeutic target; the anatomical substrate may be amenable to prevention. We hope that these considerations will motivate the reader to grapple with the challenging issues to follow.

Second will come physiological and anatomical background, wherein we discuss the evidence for gap junction-mediated electrical coupling between principal cell axons and we discuss the mechanisms of very fast network oscillations (>70 Hz, VFO) that depend on, or are influenced by, gap junctions between principal cells. We emphasize that oscillations, occurring at the frequencies observed prior to seizures, cannot be understood without taking into account gap junctions at distinctive cellular locations and the diverse physiological effects such gap junctions can exert. We shall also present some examples of VFO occurring in conjunction with epileptiform events.

Third, we shall consider an *in vitro* model, in which epochs of gamma oscillations, lasting seconds, alternate with brief epileptiform bursts lasting hundreds of milliseconds. Whether such a clock-like alternation occurs *in vivo* is problematic, although PLEDs (periodic lateralized epileptiform discharges) (Walsh and Brenner, 1987) conceivably could be related, as could periodic ~1 Hz EEG spikes that occur in Creutzfeldt-Jakob disease (Wieser et al., 2006) or herpes simplex encephalitis (Lai and Gragasin, 1988); to our knowledge, no one has determined whether fast oscillations are present between the synchronized discharges. The *in vitro* model is illustrative of basic principles that may apply to the case where fast oscillations lead into a ‘full-blown’ seizure: transient depression of excitatory postsynaptic conductances (EPSPs) in interneurons, and enhancement of EPSPs in pyramidal cells that occurs during the course of a gamma oscillation epoch.

Fourth, we will address the problem of how very fast oscillations (sometimes lasting >10 s) can occur prior to sustained electrographic seizure activity. The solution to this problem is not yet experimentally available, but enough is known that, using network models, we can present some reasonable possibilities. Specifically, we illustrate a hypothesis as to how the kinetics of the M type of K<sup>+</sup> current, along with the size of EPSCs and IPSCs (respectively, excitatory and inhibitory postsynaptic conductances) in pyramidal cells, can together determine how a network of layer 5 pyramidal neurons, and interneurons, will behave: whether it generates beta2 (20–30 Hz), VFO or a seizure discharge.

#### THE ASSOCIATION OF VERY FAST OSCILLATIONS (VFO) WITH EPILEPTIFORM ACTIVITY

Perhaps the first experimental demonstration of VFO coexisting with an epileptiform event came from the examination of paroxysmal field potentials in disinhibited hippocampus *in vitro* (Prince, 1968; Dichter and Spencer, 1969; Schwartzkroin and Prince, 1977): the field potentials had a comb shape, with a clear superimposed very fast oscillation riding on a slower event lasting tens of milliseconds. Since then, VFO in association with epileptiform events have been observed in a number of contexts. The following citations are far from complete:

1. superimposed on epileptiform field potentials *in vitro*, seizure burst complexes *in vivo*, and interictal spikes *in vivo*, as well as in the midst of seizure discharges (Schwartzkroin and Prince, 1977; Wong and Traub, 1983; Grenier et al., 2001, 2003; Traub et al., 2001; Jirsch et al., 2006)
2. in pathological tissue capable of epileptogenesis, not necessarily with a seizure following immediately (Bragin et al., 1999; Worrell et al., 2004; M. Vyskocilova, personal communication)
3. prior to electrographic seizure, in depth and subdural recordings in humans, in cat neocortex *in vivo*, and also in *in vitro* models (Fisher et al., 1992; Traub et al., 2001; Grenier et al., 2003; Worrell et al., 2004 Akiyama et al., 2005; Khosravani et al., 2005). Oscillations of ~50–60 Hz in association with seizures have even been observed in scalp recordings in small children (Kobayashi et al., 2004)
4. immediately following an electrographic seizure (Bragin et al., 1997; Traub et al., 2001).

It is not known if the mechanisms of VFO occurring before, during and after a seizure are the same. Our hypothesis is, however, that the mechanisms of the VFO *per se* are indeed the same, or at least similar, in these three contexts, but that the VFO that occurs prior to a seizure is of particular significance, as this VFO may – by its very occurrence – tend to produce plastic changes in the neuronal tissue that help to initiate the seizure.

Figure 22.1 shows an example of an electrographic seizure in a 13-month-old child with a right subfrontal cortical dysplasia who had, prior to surgery, intractable focal motor and secondarily generalized seizures. The EEG data were recorded with a subdural grid. Figure 22.1A illustrates electrographic seizure activity involving all the derivations, but with initial very fast, low amplitude activity in selected derivations (e.g. G11, G13, G21–G23). Figure 22.1B shows data recorded with a different technique, better illustrating the initial VFO at 70–90 Hz. VFO was also superimposed on both interictal spikes and within-seizure burst complexes (Figure 22.1C), as has been observed repeatedly by many investigators (e.g. see also Pais et al., 2003). The localized nature of the VFO, as compared with electrographic seizure activity proper, is consistent with data of Bragin et al. (1999) demonstrating the patchy nature of tissue giving rise to abnormal very fast activity.

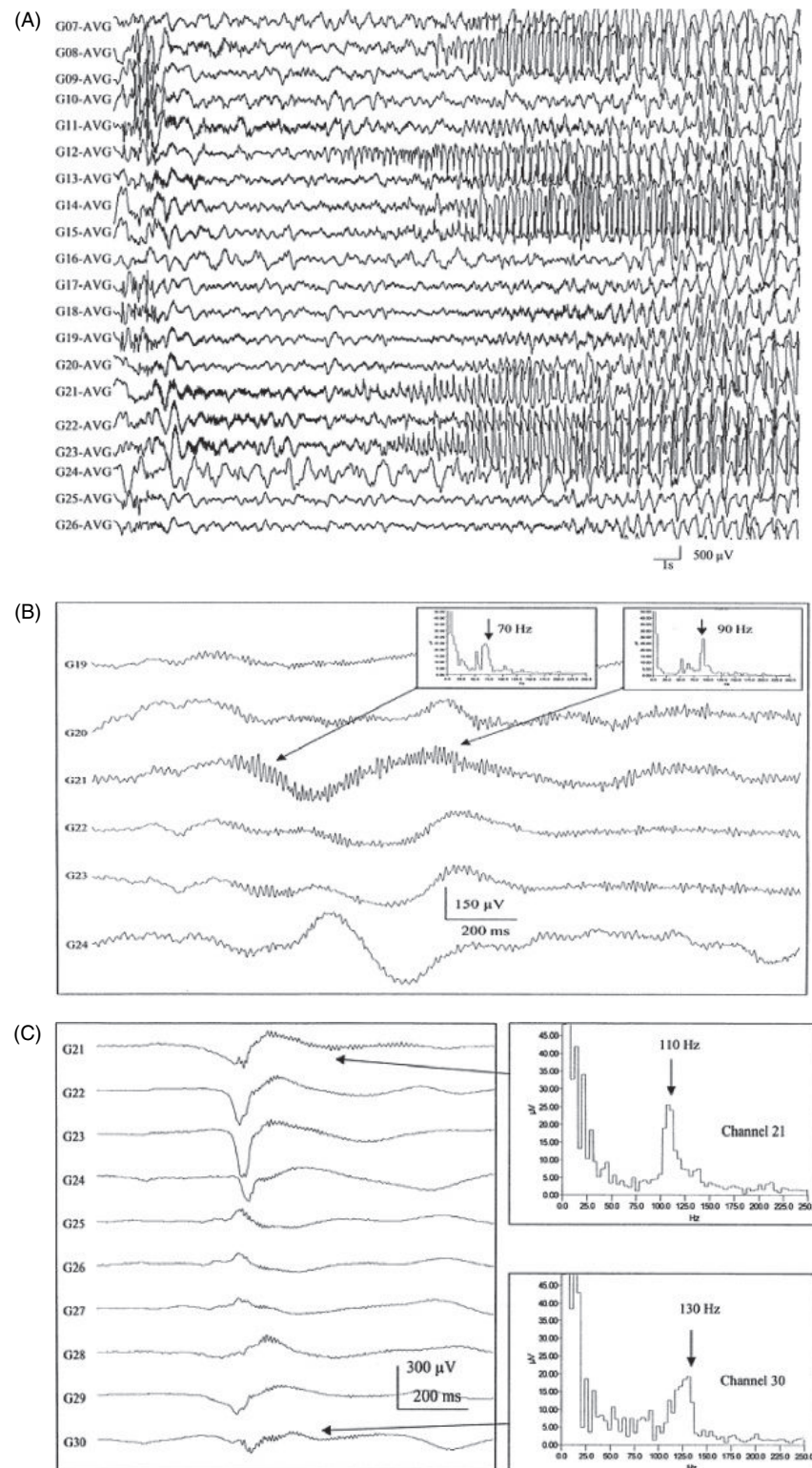


**FIGURE 22.1** Very fast oscillations (VFO) recorded in subdural grid EEG signals, prior to and during seizures in a 13-month old child with a right frontal subcortical dysplasia. (A) Widespread electrographic seizure activity is preceded by low-amplitude VFO in selected derivations, including G21–G23. (B) A different recording technique shows the pre-seizure VFO at 70–90 Hz. (C) 110–130 Hz low-amplitude EEG oscillations also occur during and immediately following burst complexes during the seizure itself. From Traub et al. (2001), with permission.

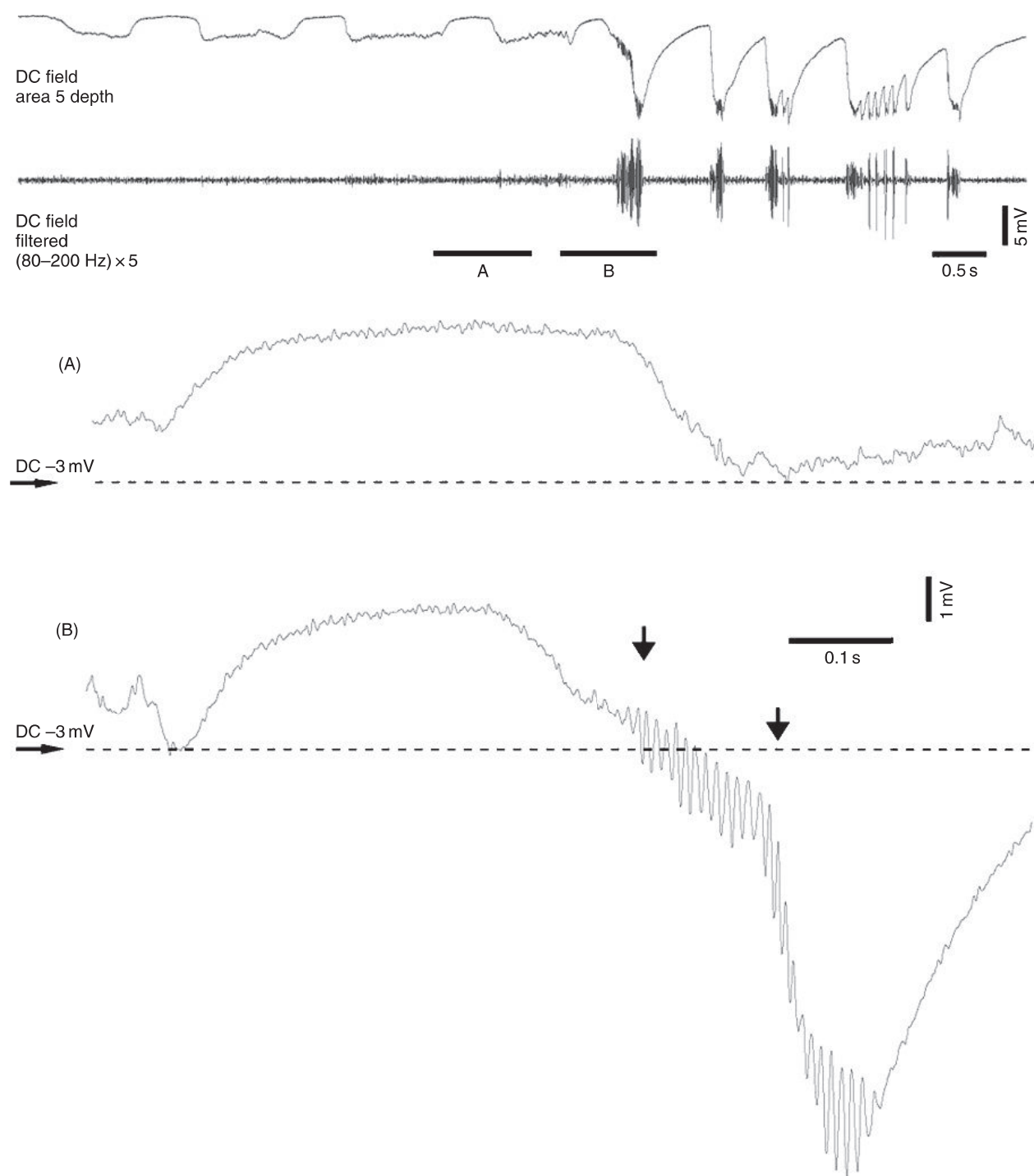


FIGURE 22.2 Brief  $\sim$ 100 Hz VFO prior to and during an epileptic discharge, in a ketamine-xylazine anesthetized cat. Upper traces show intracortical EEG, beginning with several waves of the slow oscillation (Steriade et al., 1993) and then several seconds of electrographic seizure activity. The expanded portion 'A' shows a wave of the slow oscillation. The expanded portion 'B' shows the termination of the slow wave transforming into VFO that continues into the first EEG 'spike'. From Grenier et al. (2003), with permission.

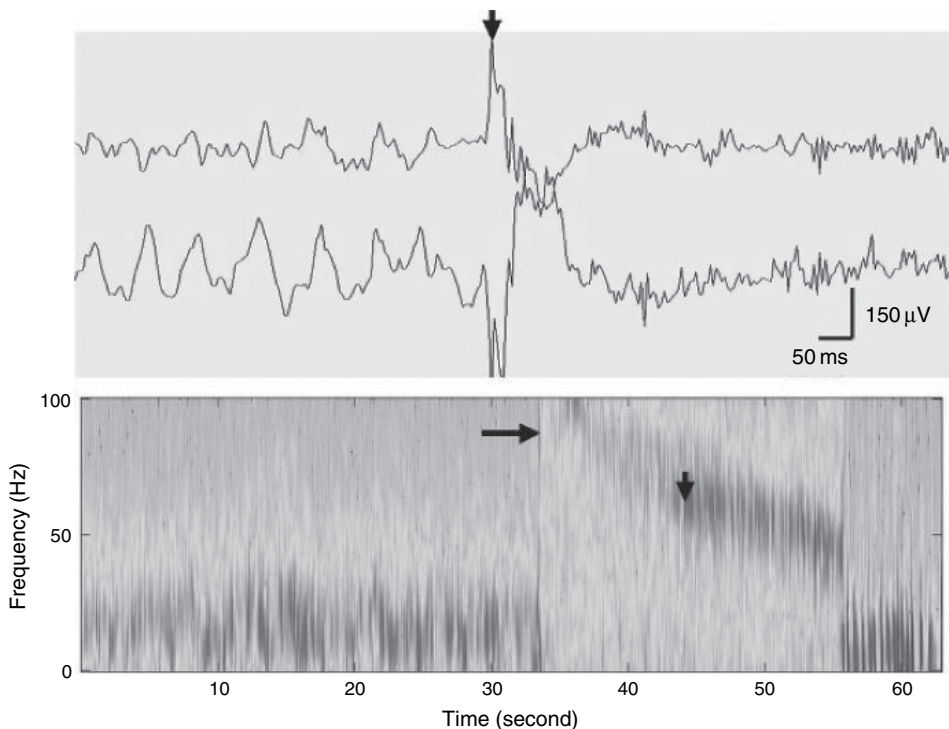
From the EEG data, one cannot be certain if the VFO arose from within the cortical dysplasia itself, or originated in nearby tissue whose characteristics might somehow have been altered by the dysplasia.

Figure 22.2 illustrates a brief interval of VFO (<200 ms) leading immediately into an electrographic seizure. The data were recorded with an intracortical electrode in a cat under ketamine-xylazine anesthesia; this preparation has been useful in the study of both the slow oscillation of sleep (Steriade et al., 1993) and a variety of spontaneous, cortically originating, electrographic seizure patterns (Steriade and Contreras, 1998; Steriade et al., 1998a). The data in Figure 22.2 show both the slow oscillation, at the start, and also part of a seizure. As shown here, and is true consistently, the seizure begins with VFO, ~100 Hz, at the tail end of a cortical slow wave; VFO can also occur at intervals in the midst of a seizure (Grenier et al., 2001, 2003).

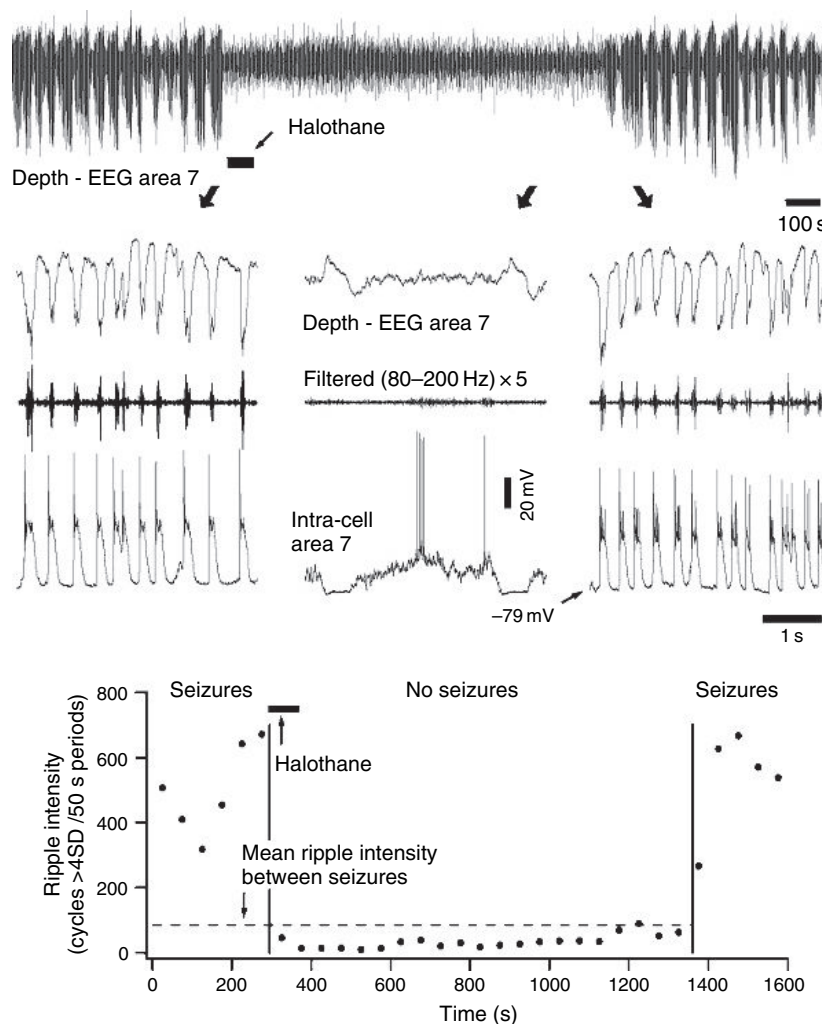
Figure 22.3 illustrates further human data: another example of VFO superimposed on a burst and also of VFO that is sustained for approximately 10 seconds prior to clinical seizure onset. Any account of the physiology of VFO must, therefore, explain not only the brief VFO such as seen in Figure 22.3, but also VFO that can persist for a relatively extended interval (Worrell et al., 2004).

Figure 22.4 provides indirect evidence that gap junctions may be critically involved in the genesis of VFO *in vivo*, something that might have been suspected from the high frequency of the oscillations alone. The data again derive from the ketamine-xylazine anesthetized cat with spontaneous electrographic seizures (Grenier et al., 2003). When the gap junction-blocking anesthetic halothane was administered ‘on top of’ the ketamine-xylazine, electrographic seizure activity was reversibly suppressed but, in addition, VFO (called ‘ripples’ in the figure) was also reversibly suppressed. Such data suggest as well that there might be a causal relationship between VFO and seizure activity.

We are motivated, therefore, to analyze *in vitro* models of VFO that involve gap junctions, in order to work out detailed cellular mechanisms. There is an essential interplay between network simulations and the *in vitro* studies.



**FIGURE 22.3** Demonstration of ~10 seconds of intracranial fast EEG oscillation prior to first motor evidence of ictal motor activity. This patient had seizures of frontal lobe onset. The upper traces show VFO in association with an EEG spike: compare Figure 22.1C and Figure 22.2. The color-coded time frequency plot below shows fast activity, beginning at ~90 Hz (horizontal arrow), that lasts about 15 seconds up to the first evident motor activity (vertical arrow). From Worrell et al. (2004), with permission. (See Plate 13 in color plate section.)



**FIGURE 22.4** In a ketamine-xylazine anesthetized cat, the gap junction-blocking anesthetic halothane suppresses VFO ('ripples') and also suppresses seizures. The uppermost traces show, on a very slow time scale, EEG seizure activity, followed by the reversible suppression of this seizure activity by halothane. The middle traces show, on a shorter time scale, EEG and intracellular records from pre-halothane and post-halothane portions of the data (note the repeating epileptiform bursts), along with corresponding records from the halothane interval (without epileptiform bursts). The graph below quantitates the suppression of VFO during the time when seizures are suppressed. From Grenier et al. (2003), with permission.

#### EVIDENCE FOR ELECTRICAL COUPLING BETWEEN AXONS, MEDIATED BY GAP JUNCTIONS, AND ITS LIKELY ROLE IN EPILEPTIFORM ACTIVITY AS WELL AS A VARIETY OF NETWORK OSCILLATIONS

The notion that gap junctions existed between the axons of pyramidal cells and that such gap junctions were critical for VFO, derived from the work of Draguhn et al. (1998), who showed that ~200 Hz network oscillations occurred spontaneously in hippocampal slices bathed in low-calcium media that blocked chemical synaptic transmission. (This and related work is reviewed in Traub et al. (2002).) The ~200 Hz oscillations were potentiated, and respectively suppressed, by pH and pharmacological manipulations expected to open (respectively close) gap junctions. The intracellular data demonstrated that population spikes were coincident with either full action potentials or with spikelets (fast prepotentials) in a pyramidal neuron. The action potentials appeared to be antidromic, because of either an inflection on the rising phase or even a notch prior to the action potential. Simulations of two coupled pyramidal cells indicated that electrical coupling between soma or dendrites did not lead to potentials that resembled the experimentally recorded spikelets, but rather to much slower potentials that reflected low-pass filtering by the gap junction. On the other hand, the simulation data suggested that electrical coupling between axons *could* replicate the experimental data, because spikelets were shown

to arise when an axonal spike conducted decrementally to the soma, blocking in the proximal axon. The idea was that a spike in one axon could cross the putative axonal gap junction to induce a spike in a coupled axon and the latter could conduct retrograde to give either a full antidromic spike, perhaps with an inflection or a notch, if invasion of the soma were to be delayed, or a spikelet, if the antidromically conducted action potential did not invade the soma fully.

Thus, the key experimental predictions were these: the existence of electrical coupling between axons; the ability of spikes to cross the gap junction; the critical contribution of active axonal membrane properties in producing the spikelet; and the origin of spikelets in axons, rather than dendrites. (Experimental support for this latter concept further derives from simultaneous somatic/dendritic recordings in the same CA1 pyramidal cell: an apical dendritic spike does *not* generate a spikelet at the soma, but rather a much slower potential (Gasparini et al., 2004).)

Schmitz et al. (2001) then provided experimental support for these predictions. Recording mainly from CA1 pyramidal neurons *in vitro*, in low-calcium media that blocked synaptic transmission, Schmitz and colleagues evoked spikelets by stimulating extracellularly in stratum oriens, the region of local axonal collateralization of the pyramidal neurons. Such spikelets had the following properties:

1. they followed stimulation 1:1 at frequencies up to 500 Hz without failure
2. they were conducted antidromically along the axon, as shown by simultaneous recording of soma and axon
3. they required active membrane properties, because the spikelets were blocked by intracellular application of QX314
4. they were suppressed by gap junction blockade, either via intracellular acidification or via carbenoxolone. (Controls were performed with carbenoxolone to ensure that action potential properties were not being affected.)

Hence, the electrophysiological and pharmacological data were consistent with the existence of gap junctions on the axons of CA1 pyramidal neurons. Schmitz et al. (2001) additionally were able to show dye-coupling between CA1 pyramidal neurons, with the site of coupling between axons, as identified by light microscopic criteria. This was possible in four instances and the site of coupling was approximately 50–150 µm from the soma.

What about ultrastructure of the putative axonal gap junctions? The gap junctions in question are unlikely to be mediated by what appears to be the most common neuronal connexin, connexin36, as very fast oscillations occur in low-calcium media in mice with connexin36 knocked out (Hormuzdi et al., 2001). The molecular nature of the putative gap junctions is not known, although pannexins are a possibility (Bruzzone et al., 2003). Searching for axonal gap junctions with immunological methods is therefore somewhat problematic. Conventional transmission electron microscopy may provide information.

Assuming that axonal gap junctions between principal neurons actually exist – how is one to account for the properties of very fast oscillations: their existence and their frequency, for example? Let us consider three possible models of VFO in gap junctionally connected networks and the means by which they might be conceptually, and experimentally, distinguished (some of the these issues will be revisited later in this chapter, as well).

1. Coupled oscillators. In this model, each cell is presumed to be capable of oscillating at very fast frequency on its own, whether or not the gap junctions are open, and the intrinsic frequencies of the oscillators should be similar to each other. Manipulations that alter the intrinsic oscillation frequency will, of course, correspondingly alter the network frequency. Network frequency should not depend on the number of gap junctions, once there is enough coupling to synchronize the system. Neurons in the medullary pacemaker nucleus of electric fish may function as electrically coupled oscillators, although oscillation frequency does slow with carbenoxolone (Moortgat et al., 2000). Of course, myocardial cells function as electrically coupled oscillators.
2. Percolation (Traub et al., 1999). Here, we imagine that the neurons are not intrinsic oscillators, but instead imagine that, in the absence of coupling, each neuron sits quietly except for a low rate of randomly occurring spontaneous action potentials. We suppose further that coupling is strong enough that if one cell fires, its coupled neighbors are also forced to fire – unless they have fired within the last few milliseconds. If the coupling topology is sparse, say in the form of a random graph (as in Figure 22.5, see also Erdős and Rényi (1960)) or a locally random graph, such a system generates oscillations of an interesting sort: the period is determined by network topology, rather than by the time course of membrane currents (Traub et al., 1999; Lewis and Rinzel, 2000). Besides the notion mentioned above that uncoupled cells are mostly quiet albeit excitable. Experimental predictions are (a) that the network frequency increases as connectivity increases; but (b) that once connectivity is too great, oscillation becomes impossible, as all cells fire continuously at near maximal rates. This model has been proposed to account for the oscillations recorded by Draguhn et al. (1998), as well as those seen in a putatively isolated axonal plexus (Traub et al., 2003b).
3. A combination of percolation with a slower membrane refractoriness, where the percolation through the network occurs faster than the duration of the refractoriness. This model can be best explained by analogy with a model of

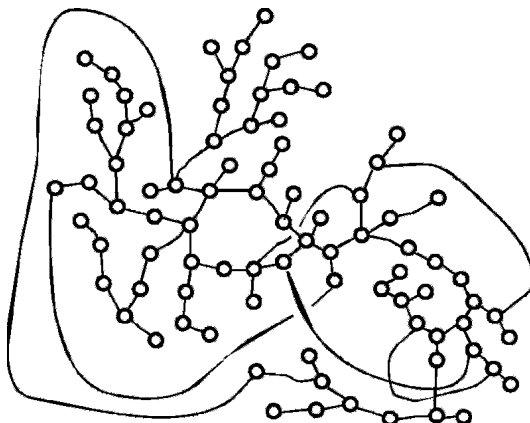


**FIGURE 22.5** The large cluster of a random graph, in which each node (here depicted as a circle) is coupled to 1.6 other nodes, on average.

repeating bursts in the disinhibited CA3 region *in vitro*, bursts that are synchronized (primarily) by recurrent synaptic excitation, but that recur at intervals of several seconds (Figure 22.6; Traub and Wong, 1982; Miles and Wong, 1983, 1986; Traub et al., 1993; reviewed in Traub and Miles, 1991). Provided that the population of pyramidal neurons is not too refractory, an individual synchronized burst can be triggered by bursting in a single pyramidal neuron, that forces bursting in at least some of its synaptically connected followers, which in turn trigger bursting in many of their followers, and so forth. Thus, the synchronization process is a type of percolation; it lasts tens of milliseconds or so, given the time it takes for bursting to propagate from cell to cell, and the overall synaptic connectivity (which defines how many steps there are before all of the cells are recruited). Once all the cells are bursting, however, a much slower process then takes over, consisting of one or more slow K<sup>+</sup> conductances, depletion of glutamate, or other slow processes. These then persist for some seconds before the next percolation can take place.

In analogous fashion, suppose we have a collection of pyramidal neurons that are strongly coupled electrically through their axons, where the cells are individually mostly quiet and there is a membrane refractoriness that lasts 5–10 ms. Now, if some of the cells start to fire, they quickly induce firing in the other cells via the gap junctions, in a process taking just a few milliseconds. Once all the cells have fired, however, intrinsic refractoriness sets in, and percolation cannot restart for 5–10 ms. Fast percolation and slower refractoriness alternate as in the synchronized burst model, but everything has been sped up. In this way, we can imagine that a population VFO could be generated, with the property that uncoupling the gap junctions causes the firing rates of the neurons to be vastly reduced. This is our prediction as to how pre-seizure VFO works in cortex (see also later on).

To recapitulate: the conceptual difference between model 2 (percolation) and model 3 (percolation + refractoriness) is this. In model 2, the period is determined by network topology and not by the time course of intrinsic membrane conductances. In model 3, the period is determined primarily by membrane refractoriness, with network topology playing a secondary role – because the percolation process is presumed fast relative to the refractoriness. Experimental distinction between the two models is, however, not straightforward. For example, it is not possible to manipulate network topology experimentally in a controlled manner and, furthermore, intrinsic membrane currents that may influence the refractory period, on the time scale of a VFO period, have not yet been identified definitively.

We shall now consider three cases in which the model suggests how axonal electrical coupling could account for certain aspects of experimental epileptogenesis.

In 1982, Traub and Wong proposed a model that could explain a number of aspects of epileptogenesis in the disinhibited CA3 region *in vitro* (Figure 22.6): the fact that a small, localized stimulus would evoke a synchronized burst only after a latency of 100 ms or so and the fact that prior to bursting in most cells, there was little evidence of synaptic activity during the latent period, even though there was a large EPSP during the burst itself. The model explained these observations as caused by exponential growth of bursting in a relatively sparsely synaptically connected network of pyramidal cells, with two key properties: each pyramidal cell was connected to more than one other postsynaptic cell and a burst in a single presynaptic cell could evoke a burst in a postsynaptic cell. These properties were later confirmed experimentally, as was the prediction that an epileptiform synchronized burst could be triggered by a burst in a single pyramidal neuron (Miles and Wong, 1983, 1986).

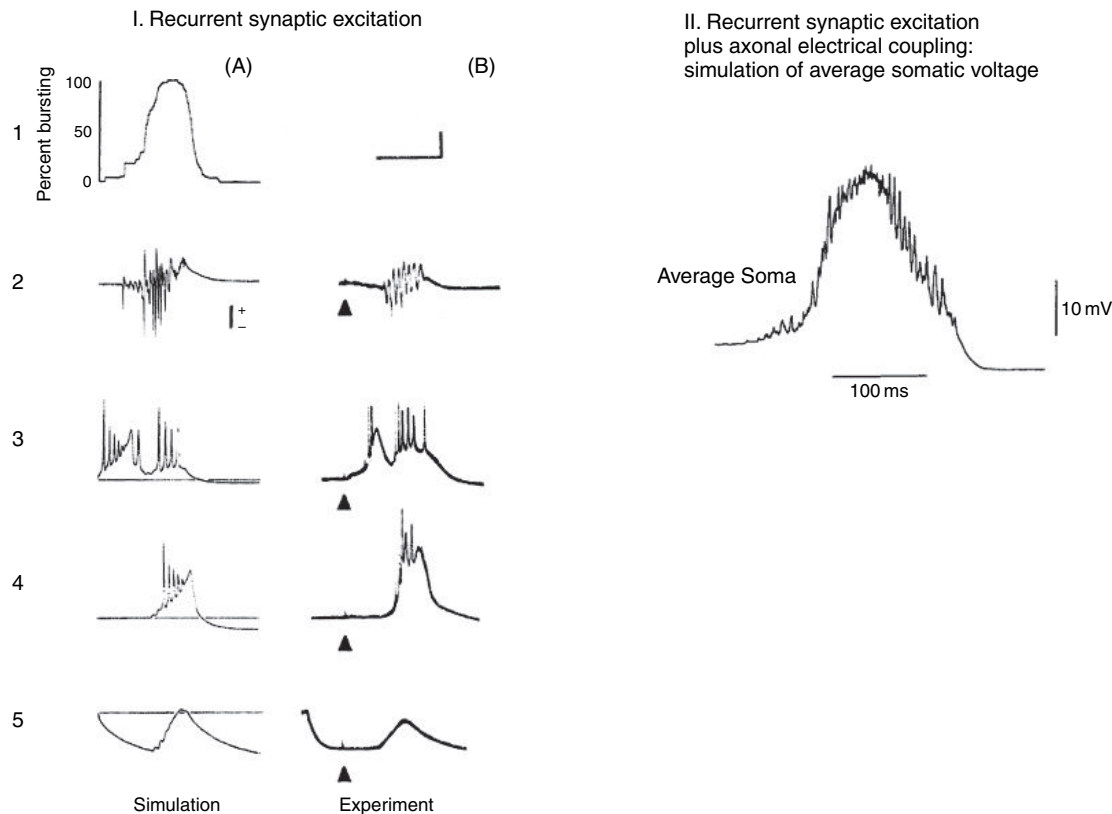


**FIGURE 22.6** In the disinhibited hippocampal CA3 region *in vitro*, the primary mechanism of synchronization of bursting activity is by recurrent excitatory chemical synapses; electrical coupling between pyramidal cells may, however, be responsible for the VFO superimposed on an epileptiform burst. I Experiment (B, right) shows stratum pyramidale field potential (line 2) in a disinhibited hippocampal slice, CA3 region, following a small localized extracellular stimulus (arrowhead); note the latency of tens of milliseconds prior to the epileptiform field potential, as well as the comb-shaped appearance of the latter, due to a superimposed very fast oscillation. Line 3 shows an intracellularly recorded burst in a pyramidal cell that happens to burst early on and then generates a second burst. Line 4 shows a more typical pyramidal cell that has negligible depolarization during the latent period, but then bursts during the field event. Line 5 shows the same cell as in line 4, hyperpolarized with current injection so as to prevent firing: this reveals the large EPSP during the field event, but no apparent activity during the latent period. A network model with 100 pyramidal neurons (A, left column) produces exactly these features under conditions of (a) intrinsic bursting; (b) sparse recurrent excitatory connections; (c) the synaptic connections have the property that a burst in one cell can induce a burst in follower cells. The combination of sparseness with connection strength accounts for the growth of synchronization, the long latent period and the absence of synaptic inputs in most cells during the latent period. However, this model does not generate a very fast oscillation superimposed on the epileptiform field potential. Scale bars: 50 ms (simulation), 60 ms (experiment); 4 mV (B2), 25 mV (A3, A4, A5), 20 mV (B3, B4, B5). II A simulation was performed according to the principles of I, but with more pyramidal neurons and with axonal electrical coupling. The synchronized epileptiform burst now has a superimposed very fast oscillation. Data in I appeared originally in Traub and Wong (1982); data in II appeared originally in Traub et al. (1999). This figure was reproduced from Traub et al. (2005b), with permission.

The 1982 model did not, however, account for another feature of the experimental data: the comb-shaped appearance of the epileptiform field potential, i.e. for the superimposed VFO (Figure 22.6-I, line 2). This issue was re-examined later (Traub et al., 1999), in which axonal gap junctions were added to a network model of pyramidal cells interconnected by recurrent chemical excitatory synapses. The later model showed that axonal coupling would produce the superimposed VFO and there was another interesting effect as well: that synchronization could take place with weaker chemical synapses, provided the electrical coupling was present between the axons – the axonal coupling acting as an additional pathway (besides the synapses) for firing to spread from neuron to neuron. To date, however, so far as we are aware, the specific predictions of the 1999 model have not been verified experimentally.

Pais et al. (2003) observed spikelets in hippocampal pyramidal neurons, prior to synchronized bursts – bursts which also depended on synaptic excitation. Subsequently, in an extremely detailed network model of a neocortical column (Traub et al., 2005a), it was predicted that spikelets would occur in neocortical pyramidal cells as well, prior to an epileptiform synchronized burst, as a result of electrical coupling between the axons (Figure 22.7). Fast potentials, some of which could be spikelets, are indeed recorded in neurons *in vivo*, prior to (and also during) synchronized bursts (Figure 22.7). Both

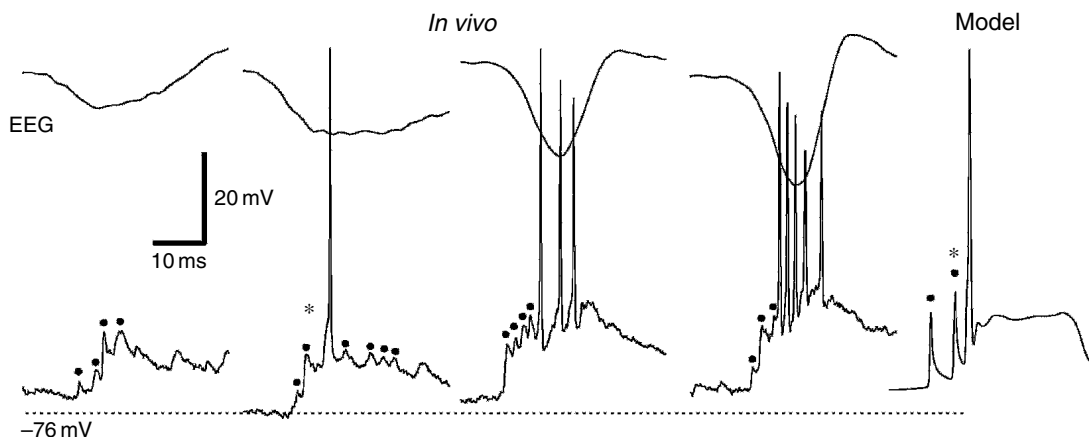


**FIGURE 22.7** During epileptiform events in rat neocortex *in vivo*, both spikelets and antidromic-appearing action potentials occur. The ‘EEG’ was recorded in the vicinity of the intracellularly recorded neuron (lower traces). Some of the brief small depolarizations (dots) resemble spikelets. Some of the action potentials (e.g. \*) have a pronounced inflection on the rising phase, as would be expected for an antidromic spike. The model trace (right) is from a layer 5 tufted pyramidal cell during a large neocortical network simulation of an epileptiform burst. Here, it can be shown directly that both the spikelets and the action potential are axonally initiated. From Traub et al. (2005a), with permission.

in experiment and in the model, some of the action potentials (e.g. as marked with asterisks in Figure 22.7) are strongly inflected on their rising phases, suggestive of an antidromic origin. In the model, it is possible to show that such action potentials, and the spikelets as well, do actually originate in axons. Such a demonstration is, of course, quite difficult to perform *in vivo*, however.

Spikelets are also observed in superficial neocortical pyramidal neurons, both in experiment and in a network model, during persistent gamma oscillations (Cunningham et al., 2004a). The experimental and the simulated gamma each depend on gap junctions and in the simulations one can show that at least some of the gap junctions need to be located on pyramidal cell axons. This has not been proven experimentally to date; it is the case, however, that pannexin2 mRNA is found in rat auditory cortex neurons of layers 2–6 (Cunningham et al., 2004a).

We have discussed above (see Figure 22.6) the superimposition of VFO on top of an epileptiform burst in the hippocampus *in vitro*. Figure 22.8 illustrates a corresponding superimposition in a striking comparison of experimental and network model data. The network model, used also in Figure 22.7, contained 3560 ‘neurons’ of diverse morphologies and firing patterns, corresponding to layer 5 tufted intrinsically bursting pyramids, layer 2/3 regular spiking pyramids, spiny stellate cells in layer 4 and a variety of other cell types; each model contained dozens of axonal/somatic/dendritic compartments and 11 sorts of intrinsic membrane conductance (Traub et al., 2005a). Chemical synapses in the model were present, activating AMPA, NMDA and GABA<sub>A</sub> types of postsynaptic receptors. There were dendritic gap junctions present between homologous types of interneurons (Gibson et al., 1999), as well as axonal gap junctions between homologous types of principal neurons within a layer (Gutnick et al., 1985): that is to say, for example, layer 2/3 pyramids could couple to other layer 2/3 pyramids, but not to any other type of neuron.

The simulation in the left of Figure 22.8 illustrates a spontaneous ‘interictal’ synchronized burst under conditions when GABA<sub>A</sub> receptors were blocked, when layer 4 spiny stellate cells were interconnected by voltage- and magnesium-independent NMDA receptors (Fleidervish et al., 1998) – which have the effect of producing a prolonged depolarization in these cells – and when gap junctions were present in some neocortical layers. The experiment was performed in rat auditory cortex, *in vitro*, bathed in kainate, and with GABA<sub>A</sub> receptors blocked by picrotoxin. [Abbreviations: L 2/3 = layer 2/3; RS = regular spiking; IB = intrinsic bursting.]

What is most relevant about the data in Figure 22.8, for purposes of this chapter, is the correspondence between model and experiment of the very fast oscillation following the burst. In the model at least, this depended on gap junctions, particularly in layer 4, but not in layer 5 (the latter were not present in the simulation of Figure 22.8, although they were in other simulations that demonstrated VFO associated with synchronized bursts). Yet, as we shall see later on, another cortical network phenomenon – the beta2 oscillation – exists which appears to depend on gap junctions between layer 5 pyramidal neurons. Our model prediction, then, is that the VFO depends on gap junctions between principal neurons, but the precise morphological substrate and identity of participating principal neurons, remains to be defined in detail, not just with dye coupling, but with ultrastructure as well.

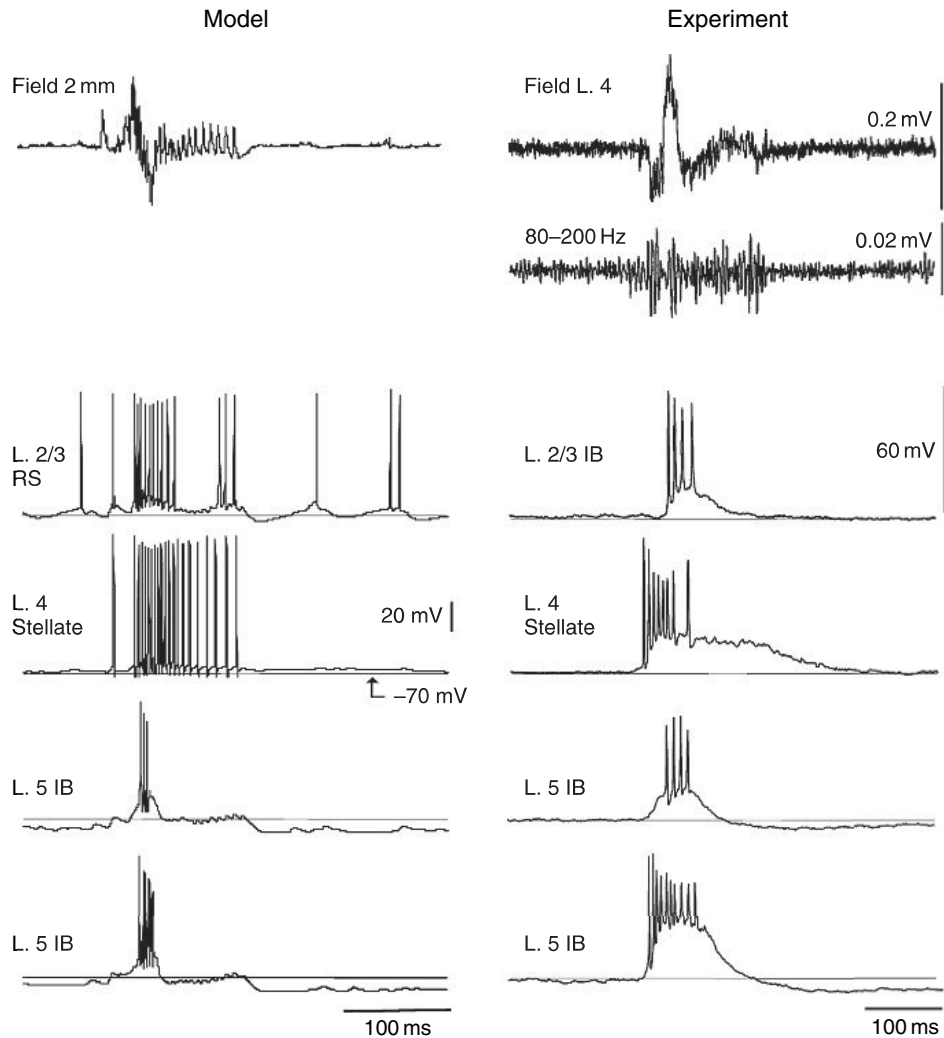


**FIGURE 22.8** Very fast oscillations during and after an epileptiform burst in neocortex occur *in vitro*, as well as *in vivo* (c.f. Traub et al., 2001). The model data are from a large neocortical network simulation, in which layer 4 spiny stellate cells were interconnected by voltage- and magnesium-independent NMDA receptors (Fleidervish et al., 1998); in addition to conventional types of chemical synaptic interactions, there were axonal gap junctions between superficial pyramidal cells, spiny stellate cells and layer 6 pyramidal cells. A synchronized epileptiform burst occurs, but note the prominent very fast oscillation in the field, as well as the prolonged firing of the layer 4 spiny stellate neuron. Experimental data show epileptiform activity in rat auditory cortex *in vitro*, bathed in kainate and picrotoxin. Note the similar very fast oscillatory activity in the field, as well as the prolonged depolarization in the layer 4 stellate neuron. More recent physiological data (e.g. Figure 22.10) indicate that electrical coupling between layer 5 pyramids also contributes to network activity; such coupling was not present in the model shown here, so that this issue requires further examination. From Traub et al. (2005a), with permission.

**AN *IN VITRO* EPILEPSY MODEL, IN WHICH EPOCHS OF GAMMA OSCILLATION ALTERNATE WITH EPILEPTIFORM BURSTS – THE TRANSITION MEDIATED BY TIME-DEPENDENT FLUCTUATIONS IN EPSP SIZE IN PYRAMIDAL CELLS AND INTERNEURONS**

We begin this section with a brief discussion of ‘persistent’ gamma (30–70 Hz) oscillations *in vitro*, a remarkable experimental phenomenon first observed in slices of hippocampus (Fisahn et al., 1998; reviewed in Traub et al., 2004), entorhinal cortex (Cunningham et al., 2004b) and superficial layers of neocortex (Cunningham et al., 2004a; Roopun et al., 2007). These gamma oscillations are induced by bath application of a drug, such as carbachol, kainate or the metabotropic glutamate receptor agonist DHPG and they derive their name because they can persist robustly for as long as the slice

remains viable, sometimes many hours. Persistent gamma tends to coexist with non-harmonic higher frequency oscillations (Traub et al., 2001, 2003b; Cunningham et al., 2004b), providing one of the important clues to the cellular mechanisms – clues which, we believe, are also important for epileptogenesis.

While the mechanistic details of persistent gamma differ somewhat between hippocampus, entorhinal cortex and neocortex, certain principles apply to each of them:

1. phasic excitation of interneurons, by AMPA receptors, is required, at least in most instances (Fisahn et al., 1998)
2. GABA<sub>A</sub> receptors are required (Fisahn et al., 1998)
3. gap junctions are required, in at least two different ways. Knock-out of connexin36, which virtually eliminates electrical coupling between interneurons, reduces gamma power by roughly 50%, but does not entirely suppress persistent gamma (Hormuzdi et al., 2001). Nevertheless, carbenoxolone does entirely suppress gamma (Pais et al., 2003); we interpret these data – and a network model is consistent – to mean that it is the electrical coupling between principal cell axons that is most critical for persistent gamma (Traub et al., 2003c)
4. Consistent with (3) is the observation that kainate, at high concentrations, induces persistent gamma in CA1 minislices, in which bursts of field VFO alternate with silent gamma periods, while a cut just below stratum pyramidale (leaving the isolated stratum oriens that contains the pyramidal cell axonal plexus without the somata) converts the pattern to continuous VFO. This behavior was predicted by our network model (Traub et al., 2003b)
5. the firing of pyramidal cell somata, on average, leads the firing of interneurons by a few milliseconds (Fisahn et al., 1998), however, pyramidal cell somata fire at much lower rates than do interneurons
6. EPSCs in pyramidal cells are small (Fisahn et al., 1998; Mann et al., 2005).

We have been able to synthesize the above listed data in a network model of pyramidal cells (with axons, soma and dendrites) and fast-spiking perisomatic region-contacting interneurons (along with other interneurons which are, however, less critical) (Traub et al., 2000). The essential idea is to have gap junctions between the proximal axons of the pyramidal neurons, a location consistent with the dye coupling data of Schmitz et al. (2001). In addition, recurrent excitation between the pyramidal cells must be kept small, again consistent with the data. What can then happen is this: suppose IPSCs in the pyramidal cells are, collectively, small and that there are occasional spontaneous action potentials in the pyramidal cell axonal plexus. By a percolation process, the axonal plexus starts to generate VFO, as described in the previous section. The action potentials in the pyramidal cell axon plexus propagate orthodromically (and antidromically to cause occasional antidromic spikes and spikelets) – orthodromically to pyramidal cells, producing little effect, because we assume these EPSCs to be small and orthodromically to interneurons, causing them to fire. The recurrent inhibition thus produced is ‘felt’ by the axonal gap junctions, in the form of shunting and hyperpolarization because, as noted above, the gap junctions are located not too far from the somata. Thus the VFO is terminated for a gamma period and the cycle can restart.

In this way, the model accounts for:

1. bursts of VFO, alternating with quiet periods that have the duration of a gamma oscillatory period
2. low firing rates of pyramidal cell somata, with higher firing rates in the interneurons
3. the phase relations of pyramidal cells versus interneurons
4. the pharmacological sensitivities of persistent gamma, with the requirements for synaptic excitation and inhibition, as well as gap junctions.

The model even accounts for the modulatory effects of gap junctions between interneurons (Hormuzdi et al., 2001; Traub et al., 2003c). When applied to the neocortex, however, the model needed an additional tweak. In order to ensure that regular-spiking pyramidal neurons fired at low rates, as seen experimentally, we found it necessary to incorporate a small subpopulation of fast rhythmic bursting (FRB, chattering) pyramidal neurons (Cunningham et al., 2004a); the physiological data support both the existence and the necessity of such a subpopulation.

What is most important for understanding the next two figures are these two facts:

1. It is well-known from a large amount of data that synchronized bursting is favored by strong recurrent excitation between principal neurons and by disinhibition (reviewed in Traub and Miles, 1991).
2. Drug-induced gamma oscillations are favored by the *opposite* scenario – weak recurrent excitation between pyramidal cells and strong recurrent inhibition – provided that axonal gap junctions are present.

There are thus two regimes in the ‘parameter space’, supporting two entirely different types of network behavior.

The next two figures illustrate an experimental demonstration that cycling between these two regimes can occur, with gamma alternating with synchronized bursts. Such a phenomenon was described first in connexin36 knockout mice (Pais

et al., 2003), in which, notably, the gap junction blocker carbenoxolone suppressed both the synchronized bursts, as well as the gamma oscillation. The experimental model described below, however, uses slices from wild-type mice.

The field potential recordings in Figure 22.9 show the basic phenomenology of gamma epochs, lasting seconds, that alternate with epileptiform synchronized bursts (Traub et al., 2005b). Note that the gamma oscillation is suppressed just after the bursts, most probably in part because of large after hyperpolarizations that develop in the pyramidal cells. We developed a network model that might account for the gamma/burst cycling, based on two simple ideas. The model started

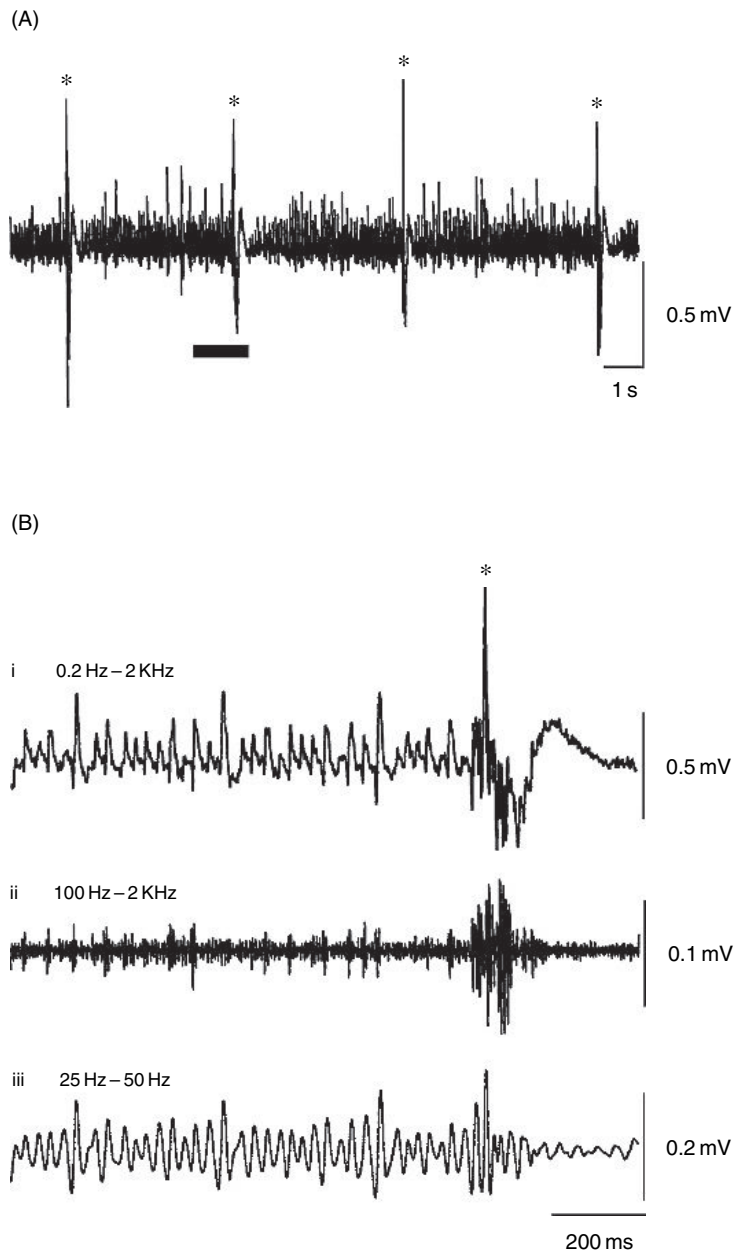


**FIGURE 22.9** Synchronized epileptiform bursts (\*) alternate with gamma oscillations in rat hippocampal CA3 region, *in vitro*, bathed in the metabotropic glutamate receptor agonist DHPG ((S)-3,5-dihydroxyphenylglycine, 20  $\mu$ M). (A) Field potential data showing the synchronized bursts (\*) at intervals of several seconds, with field oscillations between them. (B) Faster sweeps of the field potential data, filtered in different ways. Broadband data (i) and 25–50 Hz filtering (iii) show gamma oscillation preceding the burst, but attenuated following the burst. Very fast oscillations (ii) occur concurrently with gamma (c.f. Traub et al., 2003b), but especially just before and during the burst. From Traub et al. (2005b), with permission.

with the model of gamma oscillations as described above, with gap junctions between axons, weak recurrent excitation between pyramidal cells, and strong synaptic excitation of interneurons. We then made two postulates:

1. that there was use-dependent habituation (or attenuation) of EPSCs in interneurons, followed by recovery
2. that there was a rapid use-dependent habituation of EPSCs in pyramidal cells (Bains et al., 1999), with slower (seconds long) recovery.

With proper choice of the time constants, such a model would indeed cycle between gamma and synchronized bursts (Traub et al., 2005b).

Figure 22.10 provides experimental support for the postulates we made: EPSPs do, indeed, virtually disappear after a synchronized burst and increase during the gamma epoch and EPSPs in interneurons depress over the course of the gamma epoch, especially toward the end.

The possible clinical and physiological significance of these data are as follows: we have shown that VFO can precede seizure activity, and have suggested that the VFO may actually play a role in causing the seizure. If plastic changes in synaptic strengths occur during gamma, a plasticity that favors epileptogenesis, then perhaps similar plastic changes take place during VFO. In the final section of this chapter, we provide a hypothesis as to how pre-seizure VFO comes about in the cortex. Experimental testing of the hypothesis, and analysis of the proposed within-VFO synaptic plasticity, await further studies.

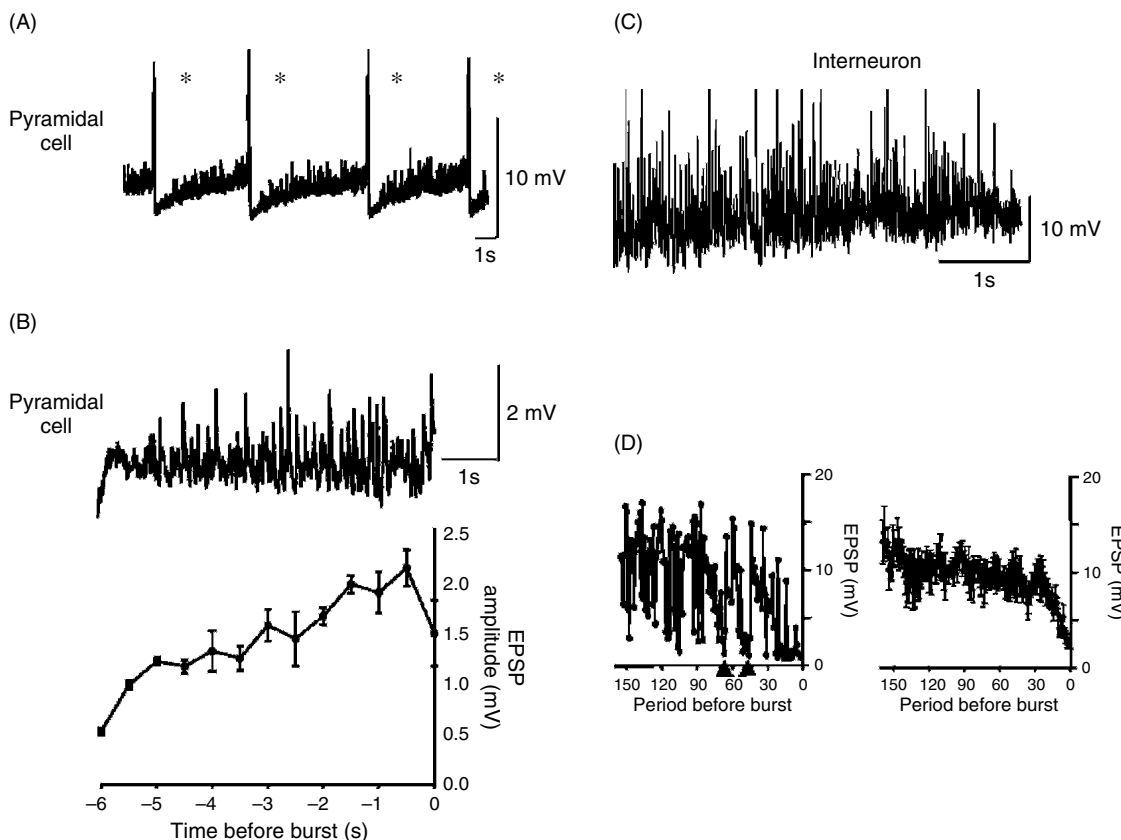


**FIGURE 22.10** During the between-burst gamma epochs induced by DHPG (Figure 22.8), EPSPs in pyramidal cells increase in amplitude, while EPSPs in interneurons diminish. (A) Intracellular recording of repeating bursts (\*) in a CA3 pyramidal cell, with  $-0.1\text{ nA}$  current injection to give mean resting membrane potential of  $-70\text{ mV}$ . (B) High-pass filtered ( $>0.5\text{ Hz}$ ) data, showing EPSPs. Graph below is pooled data (3 interburst intervals from each of 5 pyramidal cells), showing increase in mean EPSP size during the interburst interval. (C) EPSPs in a fast-spiking s. pyramidale interneuron (injected with  $-0.2\text{ nA}$  current, to give a mean resting membrane potential of  $-70\text{ mV}$ ), during the interburst interval. Action potentials attenuated. (D) Left shows EPSPs in the interneuron plotted as a function of gamma period, working backward from burst initiation. Right shows pooled data (mean  $\pm$  standard error) from 5 burst intervals. Note the sudden decline in EPSP amplitude in the  $\sim 25$  gamma periods ( $\sim 750\text{ ms}$ ) prior to the burst. From Traub et al. (2005), with permission.

**A PRIMARILY GAP-JUNCTION-MEDIATED BETA OSCILLATION IN LAYER 5 OF SOMATOSENSORY CORTEX *IN VITRO* AND HYPOTHESES ON VFO AND SEIZURE GENERATION SUGGESTED THEREBY: A ROLE FOR M-CURRENT KINETICS AS WELL AS GAP JUNCTIONS?**

There is considerable evidence that neocortical epileptiform events are often initiated in layers 4 and 5 (Chatt and Ebersole, 1982; Hoffman et al., 1994; Castro-Alamancos, 2000). Network oscillations in populations of layer 5 pyramidal neurons may therefore be of relevance to epileptogenesis, especially when the oscillations involve gap junctions. Here, we shall describe one such oscillation.

Application of submicromolar concentration of kainate to rat somatosensory cortex slices leads to something quite remarkable, the simultaneous occurrence of two distinct oscillations: gamma frequency in superficial layers and beta2 (20–30 Hz) in deep layers (Roopun et al., 2007). These oscillations are mechanistically distinct, as each proceeds independently of the other after a cut through layer 4 that separates superficial from deep layers. Evidently, the deep oscillation does not require much, if any, apical dendritic electrogensis. Intracellular recordings demonstrate that it is only the layer 5 intrinsically bursting (IB) pyramidal cells that participate. We have analyzed the deep-layer beta2 oscillation with a detailed network model, as well as with *in vitro* experiments.

As illustrated in Figure 22.11, layer 5 IB cells often exhibit large numbers of spikelets, in addition to single action potentials (and sometimes bursts), with notches on the rising phase, and with prominent afterdepolarizations. In the model, such electrogensis results from antidromically conducted axonal spikes that sometimes decrement on somatic invasion, due to the impedance load of the soma/dendrites. To date, it has not been possible to confirm the antidromic origin of the spikelets by direct experiment. The model activity is basically driven by the electrically coupled axonal plexus of the layer 5 pyramidal cells, under conditions when action potentials can cross from axon to axon. The model further predicts that the oscillation period is determined by the M conductance in pyramidal neurons, and experiments with the M conductance blocker linopirdine are consistent with this prediction (Figure 22.11C).

Additional experiments, both in brain slices and with the computer, show that gap junctional coupling is crucial for beta2 oscillations, which collapses in the presence of carbenoxolone (Roopun et al., 2007). Remarkably, carbenoxolone does not render the neurons inexcitable: they continue to fire normal-appearing action potentials, just fewer of them and not rhythmically. The conclusion is that the beta2 oscillation is an emergent phenomenon and does not simply represent the coupling of intrinsic neuronal oscillators – in contrast, say, to the situation in the medullary pacemaker nucleus of electric fish (Moortgat et al., 2000) – although gap junction blockers do lower the frequency of the fish pacemaker nucleus.

Further experiments have shown that AMPA and NMDA receptors are not required for the *in vitro* beta2 oscillation and that GABA<sub>A</sub> receptors are probably not critically involved, as concentrations of the GABA<sub>A</sub> receptor blocker gabazine, which suppress coexisting gamma in superficial cortical layers, leave the layer 5 beta2 oscillation intact. The role of gap junctions in the rhythm is therefore truly vital. We emphasize that the high incidence of spikelets in pyramidal cells is extremely suggestive that the requisite gap junctions are located in axons, but that morphological proof of this is still pending.

Could the experimental *in vitro* beta2 (20–30 Hz) oscillation, illustrated in Figure 22.11, be relevant to epileptogenesis? Several reasons suggest that it might be: first, oscillations at similar frequency occur in human corticospinal tract neurons, which are pyramidal neurons lying in layer 5 (Toyoshima and Sakai, 1982), just as are the neurons participating in the *in vitro* beta2. The human beta is coherent with muscle electrical activity (EMG) (Baker et al., 1997, 1999), indicating that the *in vitro* oscillation could correspond to *in vivo* neuronal activities of functional relevance.

Second, during ‘up states’ of the slow oscillation of sleep (Steriade et al., 1993) and its *in vitro* correlate (Cunningham et al., 2006), gamma and beta oscillations occur (Steriade et al., 1995; Steriade et al., 1998b).

Finally, as shown in Figure 22.3 above (Grenier et al., 2003), VFO (at ~100 Hz) can occur at the tail end of an *in vivo* up state, just prior to an epileptiform burst – as if there were a conversion of the gamma/beta (superimposed on the up state) into VFO. Some, as yet unidentified, cellular or biochemical event occurring during the up state, we hypothesize, predisposes the neurons to switch from beta or gamma into VFO.

We see as well from Figure 22.11C that the *in vitro* beta2 oscillation is gated by the M-current, a voltage-dependent non-inactivating K<sup>+</sup> current in neurons mediated by heteromeric KCNQ2/3 K<sup>+</sup> channels (Prole and Marrion, 2004). As shown in Figure 22.11C, oscillation frequency declines as M-conductance, g<sub>K(M)</sub>, is decreased over a certain range; in simulations, decreasing M-conductance below a critical value leads to abrupt cessation of beta2 and its replacement by a gap-junction dependent network oscillation at 140 Hz or above. Such fast activity occurs in neocortical slices under rather special conditions (M.A. Whittington and A. Roopun, unpublished data), but the network oscillation produced (in

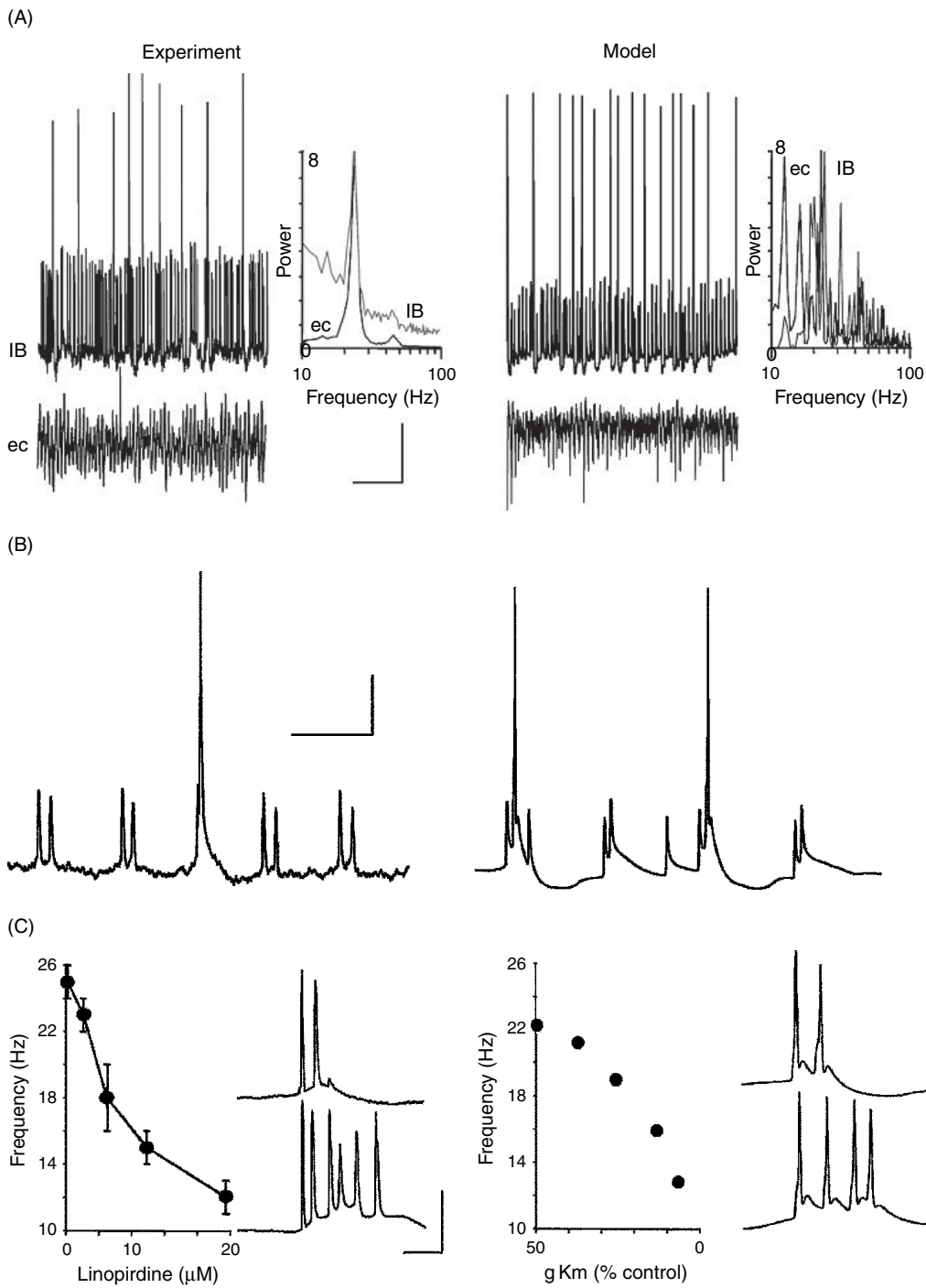
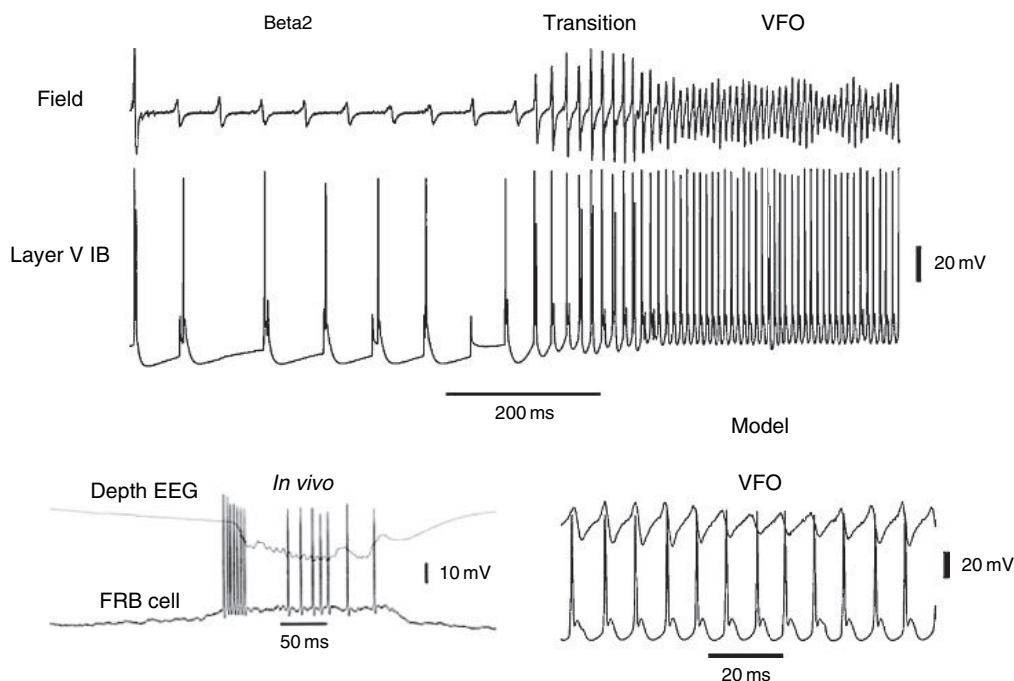


**FIGURE 22.11** Kainate (400 nM) induces a beta2 ( $\sim 25$  Hz) population rhythm in layer 5 intrinsically bursting pyramidal neurons *in vitro*, with prominent spikelets. The rhythm period is determined by the M type of  $K^+$  conductance and the oscillation can be accounted for with a network model of pyramidal neurons electrically coupled via their axons. (A) (Left panel) 2.5 second example trace from an electrophysiologically and anatomically identified layer V intrinsically bursting (IB) cell reveals combinations of spikelets, single spikes and spike-bursts at beta2 frequencies (mean RMP  $-55$  mV), coherent with the local field (ec, extracellular). Power spectra (inset) show the frequency content of concurrently recorded IB cell (IB) and layer V field (ec). (Right panel) Field and tufted IB cell data are accurately predicted from antidromic spiking in a network model that includes 2000 IB pyramidal cells, electrically coupled through their axons, along with other model neurons. Scale bars 10 mV (experiment intracellular), 100  $\mu$ V (experiment field), 15 mV (model intracellular), 500 ms. (B) Expanded timescale examples of layer V IB cell activity during field beta2 rhythms. Note the spikelets that can occur in pairs as well as the notch on the rising phase of the action potentials (arising from axonal spiking in the model, antidromically conducted). Scale bars (experiment) 10 mV, 15 mV (model), 10 ms. (C) Beta2 frequency is correlated with  $g_{K(M)}$ -mediated control of burst duration. Left panel shows mean peak frequency ( $n = 5$ ) of layer V field potentials. The decrease in population frequency with M-current reduction (linopirdine 0–20  $\mu$ M) was accompanied by increased IB cell burst duration and slowing of the population frequency. Examples shown with 2 and 20  $\mu$ M linopirdine. Right panel shows peak population frequency of model IB cells using different  $g_{K(M)}$  from 50% to 5% of control. Example bursts were taken with IB cell  $g_{K(M)} = 50\%$  and 5% of control. Scale bars (experiment) 30 mV, (model) 40 mV, 10 ms. From Roopun et al. (2007), with permission.

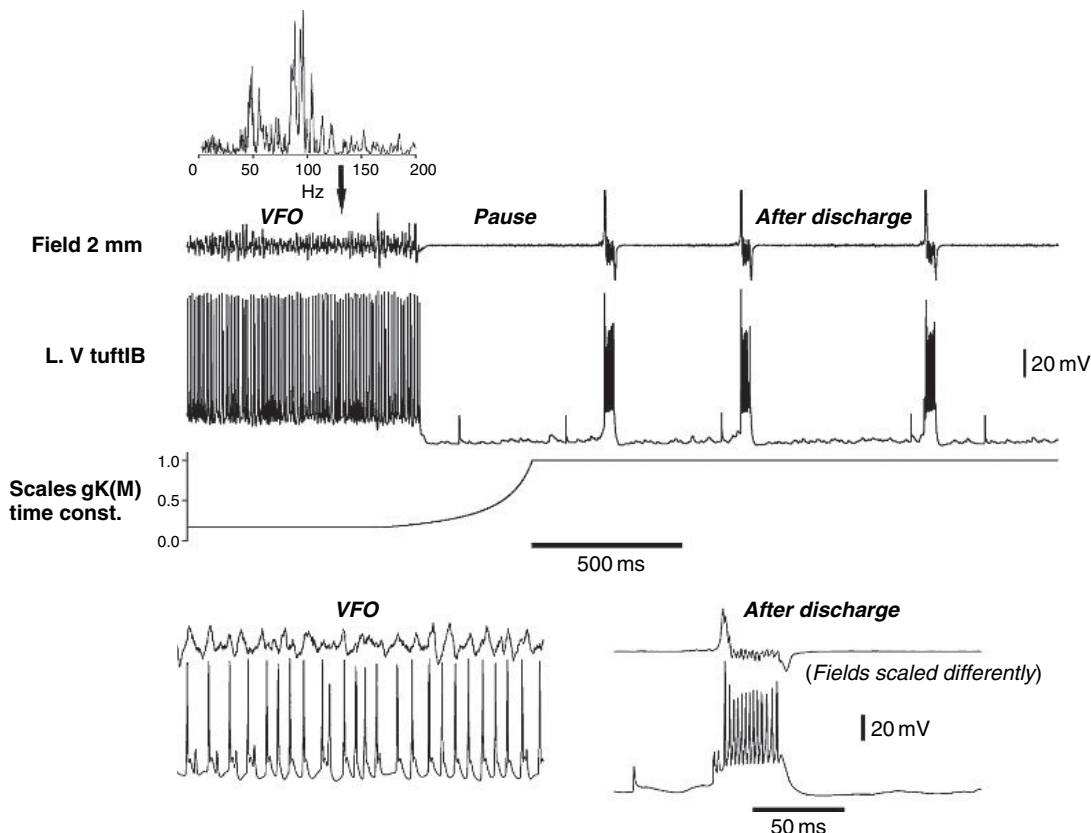
the model) by near complete block of M-conductance is rather faster than the ~70–110 Hz recorded *in vivo* and in an experimental model of the VFO → seizure transition (Traub et al., 2001). For this reason, we have examined other types of manipulation of the M conductance, such as activation/deactivation kinetics. (In our model, the conductance is simulated with Hodgkin-Huxley-like kinetics and does not inactivate (Traub et al., 2005a).)

Figure 22.12 shows that, at least in principle, speeding up of the kinetics of the M conductance could be responsible, in part anyway, for a transition from beta2 to VFO. This network simulation was run with chemical synapses blocked and also with block of high-threshold  $g_{Ca}$  and the  $Ca^{2+}$ -gated slow AHP conductance, thereby reducing the number of contributory parameters.  $g_{K(M)}$  was partially reduced, so that network beta was stable, as the left part of the figure demonstrates. Then, over a 250 ms interval, the kinetics of the M conductance were sped up sixfold (by multiplying the  $g_{K(M)}$  rate functions by a parameter that rises linearly over time from 1.0 to 6.0); simultaneously, the layer 5 IB neurons were depolarized by apical dendritic current injection. The effect is to convert the M conductance from a medium-duration AHP conductance into a conductance with time constants closer to those of the  $K^+$  channels that repolarize action potentials. This allows VFO to occur (shown in the right side of the simulation, ~125 Hz, detail in lower right inset), in a way that is stable and presumably could go on indefinitely: recall the ~10 s of pre-seizure VFO in the human EEG data of Figure 22.3 (Worrell et al., 2004). Both depolarization of the neurons and speeding up of M conductance were required for the transition to VFO. In addition, axonal gap junctions were required (in simulations, we emphasize) for the network VFO.

Is a speed-up of M-current kinetics something that could plausibly occur in real brain tissue? It has been shown that KCNQ2/3 channel kinetics are influenced by pH, with acidosis slowing kinetics and presumably alkalosis speeding them up (Prole et al., 2003). A similar effect of pH has been reported for the kinetics of KCNQ1, a channel which contributes to  $I_{Ks}$  in myocardial cells (Peretz et al., 2002). Unfortunately, at least so far as we are aware, the time course of pH fluctuations during the slow oscillation are not known (but see de Curtis et al., 1998). One parameter which *almost certainly does* fluctuate during the slow oscillation is intracellular ATP concentration, at least in an *in vitro* model, because up states are terminated by activation of an ATP-gated potassium channel (Cunningham et al., 2006). We therefore suggest the



**FIGURE 22.12** In network simulations of deep neocortical layers, a transition from beta oscillation to VFO (~125 Hz) can occur as  $g_{K(M)}$  kinetics are sped up, along with dendritic depolarization. This simulation was run with a program similar to that used in Figure 22.10. Chemical synapses were blocked, as were high-threshold calcium currents and slow AHP currents in layer 5 IB pyramidal cells.  $g_{K(M)}$  was reduced 50%. Under these conditions, a network beta oscillation occurs, similar to Figure 22.10. Over a 250 ms interval, the kinetics of the M-current in IB neurons were sped up sixfold, while depolarizing currents were ramped up in the middle apical dendrites (to a maximum of 3.6 nA). These manipulations caused a transition to network VFO, shown in more detail in the lower right inset. Lower left inset shows VFO in the field and in a fast-rhythmic bursting (FRB) neuron *in vivo* for comparison (from Steriade et al., 1998, with permission). R.D. Traub, A. Roopun and M.A. Whittington, unpublished data.



**FIGURE 22.13** In network simulations, returning  $g_{K(M)}$  kinetics to control values converts VFO to an epileptiform discharge, when AHP currents, recurrent excitation and disinhibition are present. In this simulation, high-threshold calcium currents and slow AHP currents in layer 5 IB pyramidal cells are at control values. Recurrent synaptic excitation (mediated by AMPA receptors) is present and GABA receptors were blocked. There was no tonic dendritic depolarization.  $g_{K(M)}$  kinetics in IB neurons begin with time constants 1/6 H control values, leading to network VFO (field power spectrum shown in upper inset). After  $g_{K(M)}$  kinetics are returned to control values, VFO is replaced by seizure-like activity. Details of the firing patterns are shown in insets below. R.D. Traub, A. Roopun and M.A. Whittington, unpublished data.

hypothesis that ATP depletion might speed up kinetics of the M conductance, and thereby predispose neuronal networks to produce VFO, especially when they are depolarized strongly as occurs during the up states (see Figure 22.2).

Now let us consider the transition from VFO to seizure. The simulation in Figure 22.13 was of the same network as used for Figure 22.12, but with the following conductances back in the picture: high-threshold  $g_{Ca}$  and the  $Ca^{2+}$ -gated slow AHP conductance, as well as recurrent synaptic excitation (but not synaptic inhibition). No tonic depolarizing currents were used, because calcium currents and synaptic excitation are sufficient to keep the pyramidal neurons depolarized enough for VFO ( $\sim 90$  Hz) to occur, when  $g_{K(M)}$  kinetics are fast enough – as shown in the left part of the figure and the lower left inset. Now, when  $g_{K(M)}$  kinetics are returned back to their original value, an afterdischarge occurs, facilitated by the recurrent synaptic excitation and gated by  $g_{K(M)}$  and  $g_{K(AHP)}$ .

To summarize the last two figures, leaving out the effects of the AHP conductance: we expect beta2 to occur in layer 5 if M conductances are slow and recurrent excitation is small; VFO to occur if M conductances are fast and recurrent excitation either large or small (provided the neurons are depolarized enough); and a seizure to occur if M conductances are slow and recurrent excitation is large. Further experiments are required to test this predicted form of the ‘phase space’.

## CONCLUSION

Epileptiform activity is often – and perhaps virtually always – preceded by very fast neuronal network oscillations, VFO. The most plausible hypothesis for VFO, at least at the moment, is that it depends upon electrical interactions between

principal, excitatory neurons that are mediated by gap junctions between the respective axons. Gap junction opening alone, however, may not fully explain how VFO comes about: transient alterations in the kinetics of one or more types of K<sup>+</sup> channels could also be required. Nor do we mean to diminish the critical roles played by recurrent synaptic excitation and, perhaps, synaptic disinhibition (reviewed in Traub and Miles, 1991).

A more precise experimental analysis of the origins of VFO and its transition into epileptiform activity, is essential, and not only for our basic understanding: first, of course, is the definition of specific targets for therapeutic intervention. Second, and perhaps of more fundamental significance in the long term, is that such an analysis will suggest detailed questions that can be approached with molecular biological techniques, questions that relate to how and why tissue becomes epileptogenic in the first place.

#### ACKNOWLEDGMENTS

This chapter is dedicated to the memories of the late Eberhard H. Buhl and Mircea Steriade. We thank Andrea Bibbig, Mark Cunningham, Farid Hamzei-Sichani, Nancy Kopell, Fiona E.N. LeBeau and Hannah Monyer for helpful discussions. Supported by the Wellcome Trust, the MRC (UK) and NIH/NINDS.

#### REFERENCES

- Akiyama, T., Otsubo, H., Ochi, A. et al. (2005). Focal cortical high-frequency oscillations trigger epileptic spasms: confirmation by digital video subdural EEG. *Clin Neurophysiol* 116:2819–2825.
- Bains, J.S., Longacher, J.M. and Staley, K.J. (1999). Reciprocal interactions between CA3 network activity and strength of recurrent collateral synapses. *Nat Neurosci* 2:720–726.
- Baker, S.N., Olivier, E. and Lemon, R.N. (1997). Coherent oscillations in monkey motor cortex and hand muscle EMG show task-dependent modulation. *J Physiol.* 501:225–241.
- Baker, S.N., Kilner, J.M., Pinches, E.M. and Lemon, R.N. (1999). The role of synchrony and oscillations in the motor output. *Exp Brain Res* 128:109–117.
- Bragin, A., Penttonen, M. and Buzsáki, G. (1997). Termination of epileptic afterdischarge in the hippocampus. *J Neurosci* 17:2567–2579.
- Bragin, A., Engel, J. Jr, Wilson, C.L., Fried, I. and Matherne, G.W. (1999). Hippocampal and entorhinal cortex high-frequency oscillations (100–500 Hz) in human epileptic brain and in kainic acid-treated rats with chronic seizures. *Epilepsia* 40:127–137.
- Bruzzone, R., Hormuzdi, S.G., Barbe, M.T., Herb, A. and Monyer, H. (2003). Pannexins, a family of gap junction proteins expressed in brain. *Proc Natl Acad Sci USA* 100:13644–13649.
- Castro-Alamancos, M.A. (2000). Origin of synchronized oscillations induced by neocortical disinhibition in vivo. *J Neurosci* 20:9195–9206.
- Chatt, A.B. and Ebersole, J.S. (1982). The laminar sensitivity of cat striate cortex to penicillin induced epileptogenesis. *Brain Res* 241:382–387.
- Cunningham, M.O., Whittington, M.A., Bibbig, A. et al. (2004a). A role for fast rhythmic bursting neurons in cortical gamma oscillations in vitro. *Proc Natl Acad Sci USA* 101:7152–7157.
- Cunningham, M.O., Halliday, D.M., Davies, C.H., Traub, R.D., Buhl, E.H. and Whittington, M.A. (2004b). Coexistence of gamma and high-frequency oscillations in the medial entorhinal cortex in vitro. *J Physiol* 559:347–353.
- Cunningham, M.O., Pervouchine, D., Racca, C. et al. (2006). Neuronal metabolism governs cortical response state. *Proc Natl Acad Sci USA* 103:5597–5601.
- De Curtis, M., Manfridi, A. and Biella, G. (1998). Activity-dependent pH shifts and periodic recurrence of spontaneous interictal spikes in a model of focal epileptogenesis. *J Neurosci* 18:543–7551.
- Dichter, M. and Spencer, W.A. (1969). Penicillin-induced interictal discharges from the cat hippocampus. I. Characteristics and topographical features. *J Neurophysiol* 32:649–662.
- Draguhn, A., Traub, R.D., Schmitz, D. and Jefferys, J.G.R. (1998). Electrical coupling underlies high-frequency oscillations in the hippocampus in vitro. *Nature* 394:189–192.
- Erdős, P. and Rényi, A. (1960). On the evolution of random graphs. *Publ Math Institut Hungar Acad Sci* 5:17–61.
- Fisahn, A., Pike, F.G., Buhl, E.H. and Paulsen, O. (1998). Cholinergic induction of network oscillations at 40 Hz in the hippocampus in vitro. *Nature* 394:186–189.
- Fisher, R.S., Webber, W.R.S., Lesser, R.P., Arroyo, S. and Uematsu, S. (1992). High-frequency EEG activity at the start of seizures. *J Clin Neurophysiol* 9:441–448.
- Fleidervish, I.A., Binshtok, A.M. and Gutnick, M.J. (1998). Functionally distinct NMDA receptors mediate horizontal connectivity within layer 4 of mouse barrel cortex. *Neuron* 21:1055–1065.
- Gasparini, S., Migliore, M. and Magee, J.C. (2004). On the initiation and propagation of dendritic spikes in CA1 pyramidal neurons. *J Neurosci* 24:11046–11056.
- Gibson, J.R., Beierlein, M. and Connors, B.W. (1999). Two networks of electrically coupled inhibitory neurons in neocortex. *Nature* 402:75–79.
- Grenier, F., Timofeev, I. and Steriade, M. (2001). Focal synchronization of ripples (80–200 Hz) in neocortex and their neuronal correlates. *J Neurophysiol* 86:1884–1898.
- Grenier, F., Timofeev, I. and Steriade, M. (2003). Neocortical very fast oscillations (ripples, 80–200 Hz) during seizures: intracellular correlates. *J Neurophysiol* 89:841–852.

- Gutnick, M.J., Connors, B.W. and Prince, D.A. (1982). Mechanisms of neocortical epileptogenesis in vitro. *J Neurophysiol* 48:1321–1335.
- Gutnick, M.J., Lobel-Yaakov, R. and Rimon, G. (1985). Incidence of neuronal dye-coupling in neocortical slices depends on the plane of section. *Neuroscience* 15:659–666.
- Hoffman, S.N., Salin, P.A. and Prince, D.A. (1994). Chronic neocortical epileptogenesis in vitro. *J Neurophysiol* 71:1762–1773.
- Hormuzdi, S.G., Pais, I., LeBeau, F.E., Towers, S.K., Rozov, A., Buhl, E.H., Whittington, M.A. and Monyer, H. (2001). Impaired electrical signaling disrupts gamma frequency oscillators in connexin-36 deficient mice. *Neuron* 31:487–495.
- Jirsch, J.D., Urrestarazu, E., LeVan, P., Olivier, A., Dubeau, F. and Gotman, J. (2006). High-frequency oscillations during human focal seizures. *Brain* 129:1593–1608.
- Johnston, D. and Brown, T.H. (1981). Giant synaptic potential hypothesis for epileptiform activity. *Science* 211:294–297.
- Khosravani, H., Pinnegar, C.R., Mitchell, J.R., Bardakjian, B.L., Federico, P. and Carlen, P.L. (2005). Increased high-frequency oscillations precede in vitro low-Mg seizures. *Epilepsia* 46:1188–1197.
- Kobayashi, K., Oka, M., Akiyama, T. et al. (2004). Very fast rhythmic activity on scalp EEG associated with epileptic spasms. *Epilepsia* 45:488–496.
- Lai, C.W. and Gragasin, M.E. (1988). Electroencephalography in herpes simplex encephalitis. *J Clin Neurophysiol* 5:87–103.
- Lee, W.-L. and Hablitz, J.J. (1989). Involvement of non-NMDA receptors in picrotoxin-induced epileptiform activity in the hippocampus. *Neurosci Lett* 107:129–134.
- Lewis, T.J. and Rinzel, J. (2000). Self-organized synchronous oscillations in a network of excitable cells coupled by gap junctions. *Netw Comput Neural Syst* 11:299–320.
- Mann, E.O., Suckling, J.M., Hajos, N., Greenfield, S.A. and Paulsen, O. (2005). Perisomatic feedback inhibition underlies cholinergically induced fast network oscillations in the rat hippocampus in vitro. *Neuron* 45:105–117.
- Miles, R. and Wong, R.K.S. (1983). Single neurones can initiate synchronized population discharge in the hippocampus. *Nature* 306:371–373.
- Miles, R. and Wong, R.K.S. (1986). Excitatory synaptic interactions between CA3 neurones in the guinea-pig hippocampus. *J Physiol* 373:397–418.
- Moortgat, K.T., Bullock, T.H. and Sejnowski, T.J. (2000). Precision of the pacemaker nucleus in a weakly electric fish: network versus cellular influences. *J Neurophysiol* 83:971–983.
- Pais, I., Hormuzdi, S.G., Monyer, H. et al. (2003). Sharp wave-like activity in the hippocampus in vitro in mice lacking the gap junction protein connexin 36. *J Neurophysiol* 89:2046–2054.
- Peretz, A., Schottelndreier, H., Aharon-Shamgar, L.B. and Attali, B. (2002). Modulation of homomeric and heteromeric KCNQ1 channels by external acidification. *J Physiol* 45:751–766.
- Prince, D.A. (1968). The depolarization shift in 'epileptic' neurons. *Exper Neurol* 21:467–485.
- Prole, D.L. and Marrion, N.V. (2004). Ionic permeation and conduction properties of neuronal KCNQ2/KCNQ potassium channels. *Biophys J* 86:1454–1469.
- Prole, D.L., Lima, P.A. and Marrion, N.V. (2003). Mechanisms underlying modulation of neuronal KCNQ2/KCNQ3 potassium channels by extracellular protons. *J Gen Physiol* 122:75–793.
- Roopun, A., Middleton, S.J., Cunningham, M.O. et al. (2007). A beta2-frequency (20–30 Hz) oscillation in non-synaptic networks of somatosensory cortex. *Proc Natl Acad Sci USA*.
- Schmitz, D., Schuchmann, S., Fisahn, A. et al. (2001). Axo-axonal coupling: a novel mechanism for ultrafast neuronal communication. *Neuron* 31:831–840.
- Schwartzkroin, P.A. and Prince, D.A. (1977). Penicillin-induced epileptiform activity in the hippocampal in vitro preparation. *Ann Neurol* 1:463–469.
- Steriade, M. and Contreras, D. (1998). Spike-wave complexes and fast components of cortically generated seizures. I. Role of neocortex and thalamus. *J Neurophysiol* 80:1439–1455.
- Steriade, M., Nuñez, A. and Amzica, F. (1993). Intracellular analysis of relations between the slow (<1 Hz) neocortical oscillation and other sleep rhythms of the electroencephalogram. *J Neurosci* 13:3266–3283.
- Steriade, M., Amzica, F. and Contreras, D. (1995). Synchronization of fast (30–40 Hz) spontaneous cortical rhythms during brain activation. *J Neurosci* 16:392–417.
- Steriade, M., Amzica, F., Neckelmann, D. and Timofeev, I. (1998a). Spike-wave complexes and fast components of cortically generated seizures. II. Extra- and intracellular patterns. *J Neurophysiol* 80:1456–1479.
- Steriade, M., Timofeev, I., Dürmüller, N. and Grenier, F. (1998b). Dynamic properties of corticothalamic neurons and local cortical interneurons generating fast rhythmic (30–40 Hz) spike bursts. *J Neurophysiol* 79:483–490.
- Toyoshima, K. and Sakai, H. (1982). Exact cortical extent of the origin of the corticospinal tract (CST) and the quantitative contribution to the CST in different cytoarchitectonic areas. A study with horseradish peroxidase in the monkey. *J Hirnforsch* 23:257–269.
- Traub, R.D. and Miles, R. (1991). Neuronal networks of the hippocampus. Cambridge University Press, New York.
- Traub, R.D. and Wong, R.K.S. (1982). Cellular mechanism of neuronal synchronization in epilepsy. *Science* 216:745–747.
- Traub, R.D., Miles, R. and Jefferys, J.G.R. (1993). Synaptic and intrinsic conductances shape picrotoxin-induced synchronized after-discharges in the guinea-pig hippocampal slice. *J Physiol* 461:525–547.
- Traub, R.D., Schmitz, D., Jefferys, J.G.R. and Draguhn, A. (1999). High-frequency population oscillations are predicted to occur in hippocampal pyramidal neuronal networks interconnected by axoaxonal gap junctions. *Neuroscience* 92:407–426.
- Traub, R.D., Bibbig, A., Fisahn, A., LeBeau, F.E.N., Whittington, M.A. and Buhl, E.H. (2000). A model of gamma-frequency network oscillations induced in the rat CA3 region by carbachol in vitro. *Eur J Neurosci* 12:4093–4106.
- Traub, R.D., Whittington, M.A., Buhl, E.H. et al. (2001). A possible role for gap junctions in generation of very fast EEG oscillations preceding the onset of, and perhaps initiating, seizures. *Epilepsia* 42:153–170.
- Traub, R.D., Draguhn, A., Whittington, M.A. et al. (2002). Axonal gap junctions between principal neurons: a novel source of network oscillations, and perhaps epileptogenesis. *Rev Neurosci* 13:1–30.
- Traub, R.D., Cunningham, M.O., Gloveli, T. et al. (2003b). GABA-enhanced collective behavior in neuronal axons underlies persistent gamma-frequency oscillations. *Proc Natl Acad Sci USA* 100:11047–11052.

- Traub, R.D., Pais, I., Bibbig, A. et al. (2003c). Contrasting roles of axonal (pyramidal cell) and dendritic (interneuron) electrical coupling in the generation of gamma oscillations in the hippocampus in vitro. *Proc Natl Acad Sci USA* 100:1370–1374.
- Traub, R.D., Bibbig, A., LeBeau, F.E.N., Buhl, E.H. and Whittington, M.A. (2004). Cellular mechanisms of neuronal population oscillations in the hippocampus in vitro. *Ann Rev Neurosci* 27:247–278.
- Traub, R.D., Contreras, D., Cunningham, M.O. et al. (2005a). Single-column thalamocortical network model exhibiting gamma oscillations, sleep spindles and epileptogenic bursts. *J Neurophysiol* 93:2194–2232.
- Traub, R.D., Pais, I., Bibbig, A. et al. (2005b). Transient depression of excitatory synapses on interneurons contributes to epileptiform bursts intermixed with gamma oscillations in the mouse hippocampal slice. *J Neurophysiol* 94:1225–1235.
- Walsh, J.M. and Brenner, R.P. (1987). Periodic lateralized epileptiform discharges – long-term outcome in adults. *Epilepsia* 28:533–536.
- Wieser, H.G., Schindler, K. and Zumsteg, D. (2006). EEG in Creutzfeldt-Jakob disease. *Clin Neurophysiol* 117:935–951.
- Wong, R.K.S. and Traub, R.D. (1983). Synchronized burst discharge in disinhibited hippocampal slice. I. Initiation in CA2-CA3 region. *J Neurophysiol* 49:442–458.
- Worrell, G.A., Parish, L., Cranstoun, S.D., Jonas, R., Baltuch, G., and Litt, B. (2004). High-frequency oscillations and seizure generation in neocortical epilepsy. *Brain* 127:1496–1506.

# 23

## TRANSITION TO ICTAL ACTIVITY IN TEMPORAL LOBE EPILEPSY: INSIGHTS FROM MACROSCOPIC MODELS

F. WENDLING AND P. CHAUVEL

### ABSTRACT

Temporal lobe epilepsy (TLE) is one of the most common forms of partial epilepsy. It is characterized by recurrent seizures originating from one or several areas of the temporal cortex and propagating through interconnected neuronal networks within and outside the temporal lobe. Although there is current evidence that seizures are related to abnormal excessive firing and synchronization of neurons, little is known about the precise basic mechanisms underlying human epileptic seizures and mechanisms of transitions from normal to paroxysmal activity. This chapter presents some insights into transition mechanisms to ictal activity in human TLE that can be drawn from a macroscopic modeling approach that developed over the three past decades. The term ‘macroscopic’ relates to the modeling level. Indeed, relevant variables in considered models describe the average activity of interconnected subpopulations of principal neurons and interneurons without explicit representation of mechanisms lying at the level of single cells, conversely to biologically-inspired detailed models. Although macroscopic, these models rely on neurophysiological data and have two essential features. First, their parameters relate to excitatory and inhibitory processes taking place in the considered neuronal tissue. Second, the temporal dynamics of their output is analogous to a field activity, allowing for direct comparison with real electroencephalographic signals recorded with intracerebral electrodes (depth-EEG, stereotaxic method) during presurgical evaluation of patients candidate to epilepsy surgery. The chapter provides a historical perspective about macroscopic models and describes their theoretical bases. A model-based interpretation of depth-EEG signals recorded during the transition to ictal activity is illustrated and discussed.

### INTRODUCTION

Epilepsy is a common neurological disorder that affects 1% of the world population, defined by the occurrence of recurrent seizures (Engel et al., 1989). Under certain (unknown) conditions, abnormal synchronization between local or remote neuronal populations results in the outburst of a seizure. According to the regional or distributed mode of topographic organization, epilepsies are named partial (focal) or generalized.

Temporal lobe epilepsy (TLE) is one of the most common forms of partial epilepsy. It is characterized by recurrent seizures originating in one or several anatomic divisions of the temporal lobe and propagating through interconnected neuronal networks within or outside the temporal region.

The typology of TLEs depends on the involvement of temporal lobe structures (Commission on Classification and Terminology of the International League Against Epilepsy, 1989; Williamson et al., 1998). The first and most common subtype is called medial TLE (MTLE) because of primary participation of medial (limbic) temporal structures. The second subtype is referred to as lateral TLE (LTLE). In this case, temporal neocortex was shown to be involved at seizure onset (Ebner, 1994; Burgerman et al., 1995; Walczak, 1995; Bartolomei et al., 1999, 2001).

Over the last decade, the extensive study of MTLE has resulted in the description of the so-called ‘MTLE syndrome’ (French et al., 1993; Wieser et al., 1993; Williamson et al., 1993). It is characterized by a significant atrophy of medial

(limbic) structures, particularly the hippocampus and parahippocampal areas, in which sclerosis can be detected by magnetic resonance imaging (MRI).

Drug therapy is often inefficient in patients with TLE and surgical excision of the epileptogenic region and/or seizure propagation pathways remains the only way to stop or reduce significantly the frequency of seizures. However, the rate of surgical failure in this population is far from negligible (Engel et al., 1993; French et al., 1993; Wieser et al., 1993; Williamson et al., 1993), suggesting that the precise identification of brain structures that belong to the epileptogenic zone as well as the understanding of seizure-triggering mechanisms still constitutes an essential step for improving the surgical outcome or for developing new therapeutic strategies like electrical stimulations (Morrell, 2006). Indeed, although there is currently strong evidence that seizures are related to abnormal excessive firing and synchronization of neurons, little is known about the precise basic mechanisms underlying human epileptic seizures and mechanisms of transitions from normal to paroxysmal activity. This crucial but still unsolved issue is discussed in a recent article (Lopes da Silva et al., 2003). Authors present epilepsy as a dynamical disease and classify dynamical processes leading to seizure generation in three categories referred to as 'routes to seizure'.

The first route would consist of progressive changes occurring in the epileptogenic region that may be seen as parameter changes in a system formed by networks of neuronal populations. Deformations of the system attractor induced by such changes would lead the system from normal to ictal activity. The second route would correspond to a bifurcation in a system in which two states, normal and paroxysmal, coexist for the same parameter setting. External inputs or internal random perturbations of the system would trigger sharp transition from normal to epileptic behavior. Finally, the third route would consist in a mixture of the two aforementioned scenarios in which gradual parameter variations of the system facilitate the abrupt transition from operational normal state to ictal state.

This categorization may be seen as an oversimplification of the very complex mechanisms that lead a region of the brain to generate an abnormal epileptic activity. However, it is conceptually interesting since it is a way to look at epileptogenic regions as dynamical systems (presumably highly non-linear) whose state-space trajectories are governed by neurophysiologically-relevant parameters.

In this chapter, we present various macroscopic models of such dynamical systems in the context of MTLE. Here, the term 'macroscopic' relates to the level of modeling. Indeed, these models consider the average activity of interconnected subpopulations of principal neurons and interneurons without explicit representation of mechanisms lying at the level of single cells, conversely to detailed models. Although macroscopic, these models rely on neurophysiological data and have two essential features. First, their parameters relate to excitatory and inhibitory processes taking place in the considered neuronal tissue. Second, the temporal dynamics of their output (analogous to a field activity) can be directly compared to those reflected in real electroencephalographic signals recorded with intracerebral electrodes during presurgical evaluation of patients candidate to epilepsy surgery. Consequently, they allow for model-based interpretation of such signals.

The main objective of this chapter is to present some insights into transition mechanisms to ictal activity in human TLE that can be drawn from this modeling approach. The chapter is organized as follows. The next section gives a brief historical background on neuronal population models and presents some general features. Electroencephalographic signals recorded during the transition from interictal to ictal activity are described next along with the recording technique namely stereoelectroencephalography (SEEG). These signals constitute input data to models presented in the following section which starts from the description of a generic model of neuronal population used to interpret transition from normal background activity to spiking activity. This section follows with the presentation of a second model adapted to the organization of neurons and interneurons in the hippocampus and emphasizes on the capacity of this model to explain typical activities recorded from this structure in patients with MTLE like fast onset activity lying in the EEG low gamma frequency band. After discussion of presented results, the chapter ends with main conclusions and perspectives related to modeling approaches aimed at improving our understanding of basic processes underlying epileptic behavior.

## NEURONAL POPULATION MODELS

### GENERAL OVERVIEW

Computational models developed in the field of epilepsy are complementary to experimental models of epilepsy. They provide an efficient way to integrate new and detailed knowledge coming from neurobiological research not only to explain experimental findings but also to generate experimentally testable hypotheses. Targeted mechanisms lie at the subcellular, neuronal or network level depending on the scale of representation and on the nature of the experimental data under study.

Readers may refer to Suffczynski et al. (2006b) for more detailed review about computational models used in the study of brain activity.

As far as interpretation of epileptic phenomena reflected by field activity recordings is concerned, two complementary approaches were developed over the past decades. In the first one, referred to as ‘detailed’, single neurons are accurately modeled regarding their structural components (dendrites, soma, axon) and functional properties such as passive or active channels. Neuronal networks are then built from the interconnection of a sufficiently large number (i.e. several thousands) of principal neurons and different types of interneurons with appropriate synaptic interactions. In these networks, the summated postsynaptic potentials of pyramidal cell membranes that correspond to the field activity can be studied as a function of various parameters such as the types of neurons introduced in the network, network size, connectivity patterns and conduction delays. This approach has been extensively developed by Traub and collaborators since the early 1980s (Traub, 1979, 1982; Traub and Llinas, 1979) who studied some spatial and temporal properties of the activity in simulated patch of neuronal tissue. Insights about tissue excitability, role of interneurons and factors leading to hypersynchronization have been put in evidence and confronted to real observations. The use of such models has explained some basic mechanisms by which synchronized activity emerges. In particular, these models are able to generate activity patterns, in realistic networks, that closely mimic epileptic activity recorded *in vitro* as well as different types of electroencephalographic (EEG) activity seen in patients.

In the second approach, referred to as ‘macroscopic’ or ‘lumped’, a higher level of organization, i.e. the neuronal population level, is considered. It starts from the fact that neurons form populations and that the EEG is a reflection of ensemble dynamics rising from macroscopic statistical interactions between interconnected neuronal subpopulations (pyramidal cells and interneurons). The macroscopic modeling approach has developed since the 1960s. It conceptually differs from the detailed approach briefly described above in the sense that it emphasizes the properties of populations of cells instead of those of individual neurons. In considered populations, cells are assumed to be spatially close and their interconnections are assumed to be random but dense enough so that the probability for any two cells in the population to be connected (either directly or via interneurons) is high. Based on these assumptions, population models represent the temporal dynamics of the aggregates while the spatial interactions between cells are neglected. This implies that the relevant variable of these models is not the single spike but rather the spike frequency, or firing-rate, computed from the total current delivered by synaptic inputs (which sum linearly according to the mean-field approximation) into the soma. During the past decades, this class of models has been used in numerous theoretical and experimental studies, mainly related to interpretation of neurophysiological data. A short bibliographical overview is given below.

#### BACKGROUND: FROM PIONEER TO MORE RECENT WORKS

Pioneer works on models of localized populations of neurons started in the early 1970s with Wilson and Cowan (Wilson and Cowan, 1972) who put the theoretical bases of these models. Authors started from works of Mountcastle (Mountcastle, 1957) and Hubel and Wiesel (Hubel and Wiesel, 1963, 1965) who brought physiological evidence for the existence of such populations: a high degree of local redundancy is present within relatively small volumes of cortical tissue as many cells have nearly identical responses to an identical stimulus. They also used a crucial assumption considered, at that time, as an axiom: all neural processes depend upon the interaction of excitatory and inhibitory cells. Therefore, they considered a population as being composed of two subpopulations, one excitatory and the other one inhibitory and proposed an approach based on two variables, namely  $E(t)$  and  $I(t)$ , representing the proportion of excitatory and inhibitory cells firing per unit time respectively. This two-variable approach was fundamentally different from those used in other studies on neural populations as the treatment of inhibition arises from exclusively inhibitory neurons. It allowed authors to derive the general non-linear differential equations governing the population temporal dynamics using a sigmoid function for each subpopulation response. Simple and multiple hysteresis phenomena and limit cycle activities represented in the model were then studied from phase plane analysis and results provided a physiological basis for oscillatory characteristics observed in particular EEG rhythms.

Following the same approach, Freeman and colleagues developed a comprehensive model of the olfactory system from the early 1960s (Freeman, 1963, 1968, 1973). Based on histological and physiological analytic methods conducted in animal models (cat), their model reproduces the global organization of the olfactory system. Its structure includes the olfactory receptor neurons (model input) as well as main components like the olfactory bulb (OB), the anterior olfactory nucleus (AON) and the prepyriform cortex (PC). Each part (OB, AON and PC) contains four subsets of cells (two excitatory and two inhibitory). The first key feature of Freeman’s model is that these subsets are ‘lumped’ representations of aggregates of strongly interconnected neurons which have, on average, similar properties such as a common sign of output (i.e. they are

either all excitatory or all inhibitory). Each subset is referred to as ‘neural mass’ or ‘neuron population’. The second key feature is that the dynamics of each subset are simply described by a second order non-linear ordinary differential equation (ODE) representing conversion operations between the population average postsynaptic potential (‘wave’) and the density of action potentials (‘pulse’) fired by local neurons. Despite the fact that the three main components of the model (AON, OB and PC) are strongly interactive, the activity of each part differs in its time series (which can be assimilated to EEG signals) from those of the others. For time constants fixed at physiologically determined values in the pulse-wave conversion, for gain constants fixed at a common value in the wave-pulse sigmoidal relationship and for appropriate setting of connection strengths between nodes within the AON, OB, and PC, Freeman and colleagues empirically showed that the model produces realistic EEG signals that approximate those experimentally recorded in the same structures (Freeman, 1987).

Similar ideas developed at the same time by Lopes da Silva and collaborators (Lopes da Silva et al., 1974, 1976) led to the development of a lumped-parameter population model able to explain the alpha rhythm of the EEG observed in dogs. The model was based on two interacting populations of neurons representing a subset of excitatory thalamocortical relay cells (TCR) and a subset of inhibitory interneurons (IN) connected to the former subset through a negative feedback loop. In each population, the conversion between the mean membrane potential and the average density of action potentials (APs) fired by the population is represented by a non-linear function (sigmoid shape), whereas conversion from presynaptic density of APs into mean postsynaptic potential is described by a linear transfer function. Interaction between the two populations is adjusted by coupling constants representing the average number of synaptic contacts between the two cell types. This model was shown to generate oscillations ranging from 8 to 11 Hz and closely resembling cortical alpha rhythm for physiologically-relevant model parameters. It allowed authors to formulate a general conclusion about the bandpass linear filter behavior of neural networks that explains output signals, such as alpha rhythmic activity observed in EEG, as linearly filtered noise.

These studies can be considered as the first attempts to formalize neurophysiological facts into computational models in order to describe and explain the links between activity in populations of neurons composed of interconnected subpopulations and field potentials measured from such populations. In particular, proposed models revealed the intimate relationships that exist between postsynaptic potentials generated from neuronal populations and oscillatory dynamics reflected in EEG signals. Another interesting feature is the generality of the concepts utilized in this modeling approach that has been adapted by many successive studies dealing with generation of EEG activity under various conditions (normal or pathologic).

Starting with Wilson and Cowan’s works, Zetterberg and colleagues (Zetterberg et al., 1978) designed a model including both positive and negative feedback loops and studied its performances in terms of stability. Interestingly, they imitated both background EEG activity and certain types of paroxysmal activity and reached a conclusion that epileptic spikes are generated by populations of neurons that operate close to instability.

Works were also pursued on the thalamocortical model developed in Lopes da Silva’s group. In particular, mechanisms of transition between normal EEG activity (i.e. non-epileptiform) and epileptiform paroxysmal activity were investigated based on relevant experimental and clinical data. Model predictions were compared with results obtained in different types of epilepsy, including patients with absence seizures and allowed for generation of hypotheses about pathophysiological mechanisms of ictal transitions (Suffczynski et al., 2001, 2006a). The lumped parameter model of alpha rhythm generation they proposed was also the starting point in the design of a model of cortical column used to simulate visual evoked potentials computed from spontaneous EEG signals (Jansen et al., 1993; Jansen and Rit, 1995). An interesting feature of this study is that the authors proposed a simplified generic model for cortical activity generation that was studied and extended by Wendling et al. (Wendling et al., 2000, 2002, 2005) in the context of model-based interpretation of intracerebral EEG signals in epilepsy. These works are developed below after description of electrophysiological patterns of transition to ictal activity recorded in human TLE using stereoelectroencephalography (see below). Finally, it is also important to underline that neural mass models have been recently used in studies dealing with connectivity among cortical regions and with impact of model parameters on the power spectrum of surface EEG or MEG signals (David and Friston, 2003; David et al., 2004; Zavaglia et al., 2006).

#### TRANSITION TO ICTAL ACTIVITY IN HUMAN TLE: DESCRIPTION OF ELECTROPHYSIOLOGICAL DATA OBTAINED FROM INTRACEREBRAL RECORDING

Investigation methods used in partial epilepsies are aimed at anatomically defining the epileptogenic zone (Chauvel et al., 1987; Bartolomei et al., 1999, 2001). Among these methods, stereoelectroencephalography (SEEG) permits direct recording of electrical activity from brain structures potentially involved in the epileptogenic zone. It provides electrophysiological

markers of epileptic activities (interictal and ictal) in the form of time series signals with excellent temporal resolution. Below is a section which aims at providing the reader with a detailed description of electrophysiological recordings performed in patients with TLE. Described signals will be further interpreted using neuronal population models. This description is preceded by a short introduction about the SEEG recording technique.

### **RECORDING TECHNIQUE: STEREOELECTROENCEPHALOGRAPHY (SEEG)**

Bancaud and Talairach introduced the term ‘stereo electroencephalography’ in 1962 to emphasize this recording of electrical activity within the intracranial space rather than from the surface, and the need for stereotaxic determination of the anatomical structures involved. The method has at its core the ‘anatomical-electro-clinical correlation’: this close observation of clinical features (including the order in which they occurred) and their relation to the regions primarily and secondarily involved in the epileptic discharge, allows a temporo-spatial profile of the seizure’s origin and propagation patterns to be built up and the corresponding anatomical structures to be defined, thus aiding the decision regarding surgical cortectomy to be performed. This approach is characterized by an individually tailored exploration and surgical decision for each patient’s particular epilepsy. The anatomical-electro-clinical correlation is considered absolutely fundamental to the SEEG method and remains today one of the factors distinguishing SEEG from other means of depth recording.

The SEEG for the first time has provided the possibility of a three-dimensional electrophysiological ‘view’ of brain structures, permitting study of the intracranial space rather than being limited to the cortical surface. The attempt to reconstruct a three-dimensional topography remains in contrast to the main existing neurophysiological method of presurgical exploration based on electrocorticography (ECOG) like subdural grid recording. The SEEG has been therefore developed in part with the aim of overcoming certain limitations linked with the 2-D and surface features of ECOG recording. The SEEG allows intracranial exploration (with recording of ictal events) to be carried out in a separate phase prior to the resective surgical procedure.

With the advent of SEEG, the seizure itself, rather than the interictal activities, has become the main marker of the epileptogenic process in human drug-resistant epilepsies, hence the concept of the epileptogenic zone (EZ). Fundamental to the original concept of the EZ was the idea of a region of brain involved in the primary organization of the ictal discharge, rather than a ‘focus’: the EZ is seen as a set of interconnected regions or systems. The EZ is recognized to be a separate entity from the region of maximal interictal spikes (irritative zone, IZ; relations between interictal and ictal activities are developed below) and also from the region of structural abnormality if present (lesional zone, LZ). These three regions are recognized to overlap to a greater or lesser degree; at the extremes being completely contiguous or, on the other hand, completely separate, which remains one of the most important observations arising from Bancaud and Talairach’s studies of patients with cerebral tumours and other lesions (Bancaud, 1980). Indeed, this concept remains very relevant in today’s era of neuroimaging where even subtle lesions can be identified by MRI techniques but their relevance to the production of seizures remains to be determined (Koepp and Woermann, 2005). Determining these three zones and their relations, in order to identify correctly the most appropriate surgical resection for a particular patient, therefore requires a three-dimensional approach to intracranial exploration, for which the SEEG is ideally adapted.

### **DESCRIPTION OF ELECTROPHYSIOLOGICAL PATTERNS RECORDED DURING TRANSITION TO ICTAL ACTIVITY**

Data shown in this section were recorded in patients undergoing presurgical evaluation of drug-resistant TLE. All patients had a comprehensive evaluation including detailed history and neurological examination, neuropsychological testing, routine MRI study and scalp EEG. SEEG recordings were performed during long-term video-EEG monitoring (5–8 days) using intracerebral multiple lead electrodes placed intracranially according to Talairach’s stereotactic method (see above). SEEG is always carried out as part of normal clinical care of patients who give informed consent in the usual way. Patients are informed that their data may be used for research purposes. The positioning of electrodes is determined in each patient from available non-invasive information and hypotheses about the localization of his/her epileptogenic zone. Implantation accuracy is peroperatively controlled by telemetric X-ray imaging. A postoperative computed tomography (CT) scan without contrast product is then used to verify both the absence of bleeding and the precise 3-D location of each electrode contact. After SEEG exploration, intracerebral electrodes are removed and an MRI is performed on which the trajectory of each electrode remains visible. Finally, a CT-scan/MRI data fusion is performed to locate anatomically each contact along each electrode trajectory. All patients had electrodes positioned in temporal region. Signals were recorded on a DeltamedTM system on a maximum number of channels equal to 128. They were sampled at 256 Hz and recorded to

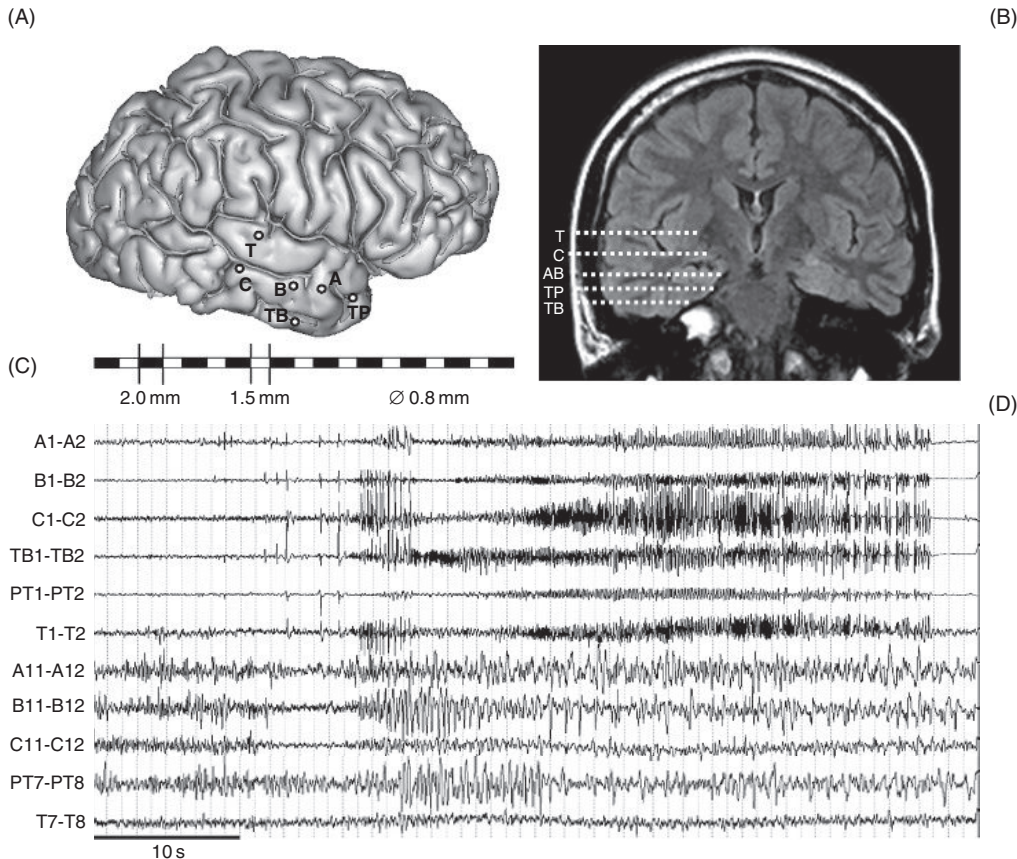


**FIGURE 23.1** SEEG exploration in patient with medial temporal lobe epilepsy. (A) Intracerebral implantation scheme defined from non-invasive data (scalp EEG, semiology, medical imaging). Electrodes are identified by one or two capital letters: A, B and C (medial contacts: amygdala, anterior part of hippocampus, posterior part of hippocampus; lateral contacts: middle temporal gyrus from anterior to posterior part), T (medial contacts: insula; lateral contacts: superior temporal gyrus), TB (medial contacts: entorhinal cortex; lateral contacts: temporo-basal cortex), TP (temporal pole). (B) Electrode trajectories reported on MRI data (coronal view). (C) Intracerebral electrodes are composed of 10–15 cylindrical contacts (length: 2 mm, diameter: 0.8 mm, 1.5 mm apart). Contacts are numbered from 1 to 10 or 15 depending on the number per electrode. Low weight numbers (1, 2, 3, . . .) correspond to deepest contacts. (D) Example of SEEG recording (bipolar signals) performed during transition to seizure activity.

hard disk (16 bits/sample) using no digital filter. The only filter present in the acquisition procedure is a hardware analog high-pass filter (cut-off frequency equal to 0.16 Hz) used to remove very slow variations that sometimes contaminate the baseline. An example of intracerebral SEEG exploration in TLE is given in Figure 23.1.

### Interictal activity

The number of seizures recorded during presurgical evaluation (over the period corresponding to video-EEG monitoring) is generally limited (in the order of 5 to 20, on average). Outside seizure periods, intracerebral signals reflect background EEG activity often mixed with paroxysmal transient events commonly referred to as ‘interictal spikes’. The relationship between interictal and ictal activity is an essential and unresolved question in epileptology which is beyond the scope of this chapter. Our experience shows that there is a high variability in the morphology and in the spatio-temporal organization of interictal spikes, from patient to patient with TLE (Bourien et al., 2005). Nevertheless, in patients with MTLE (i.e. when lateral neocortical structures are not, or just secondarily, involved during seizures), some general features may be described. High amplitude spikes generally last for a few hundreds of milliseconds. They always involve limbic structures, mainly the hippocampus and the entorhinal cortex. Implication of the amygdala is also relatively frequent conversely to lateral structures of the temporal lobe which are more rarely involved. This is illustrated in Figure 23.2A–C in a patient showing abundant interictal spiking in limbic structures while the middle temporal gyrus (from anterior to posterior part) exhibits almost normal background activity. The occurrence frequency of epileptic spikes is extremely varying in time and may depend on the vigilance state of the patient. Periods with no spikes, with infrequent sporadic spikes or with sustained discharges of spikes can be observed (Figure 23.2A–C). Although clear evidence has not been brought yet, qualitative

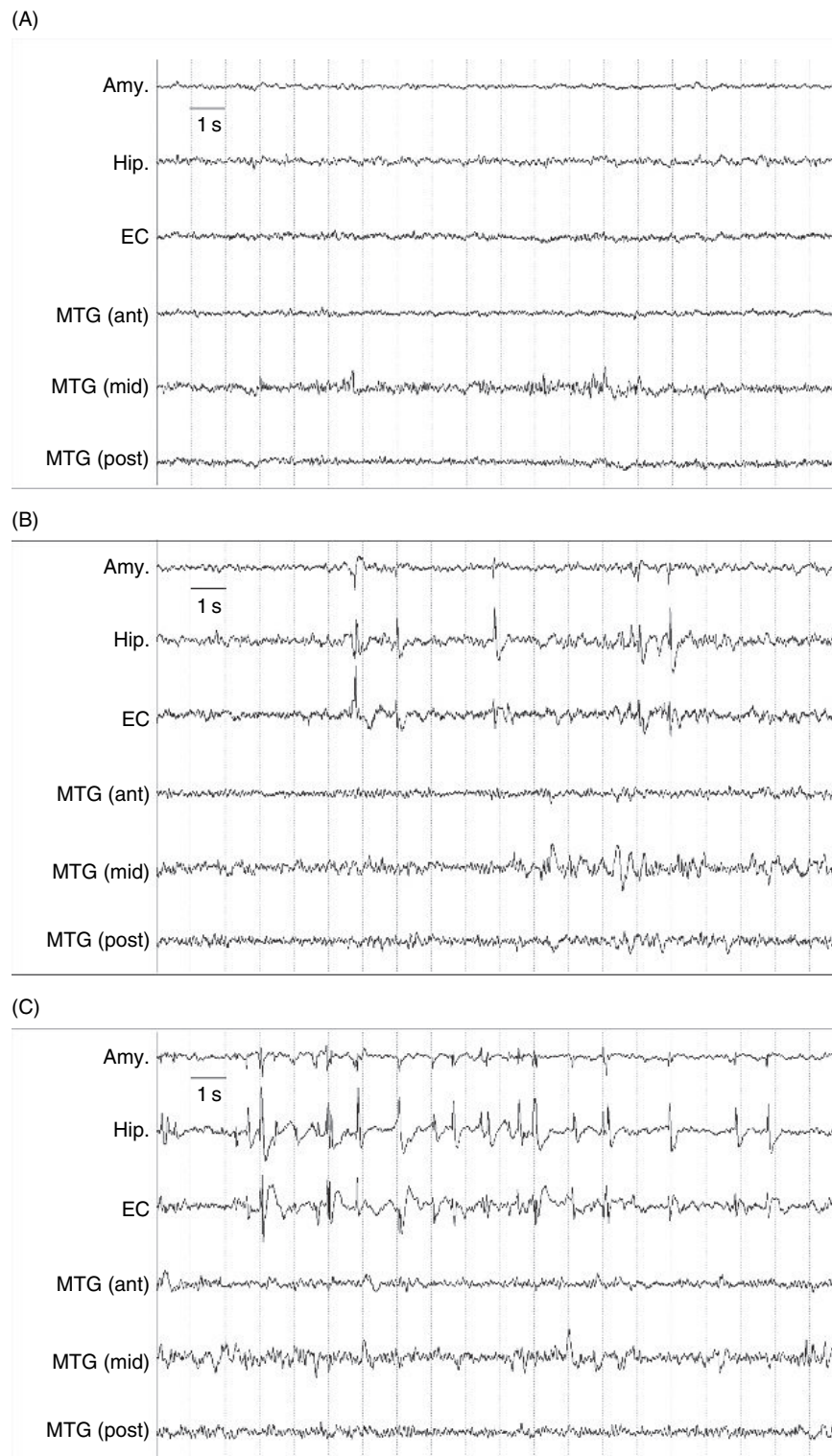


FIGURE 23.2 Example of interictal activity recorded in a patient with medial TLE (SEEG signals). See text for detailed description.

visual inspection of recordings often shows increased occurrence frequency and spatial organization of interictal spikes before seizures. This effect is explained by increased ratio between excitation and inhibition parameters across structures in computational models presented below.

### Transition from interictal to ictal activity

#### *Limbic structures*

Intracerebral EEG signals recorded during the transition from interictal to ictal activity are generally complex as they exhibit non-stationary properties. In other words, their frequency content evolves as a function of time. Nevertheless, they can generally be considered as piecewise-stationary. Transitions between stationary segments can be more or less abrupt.

In TLE, and particularly in MTLE, the onset of seizure is generally characterized by the appearance of a fast activity (also referred to as rapid discharge) in mesial structures like hippocampus, entorhinal cortex and amygdala, which are always recorded during SEEG exploration. This fast onset activity dramatically differs from interictal background activity recorded far from seizure (in time) with a re-distribution of the energy of intracerebral EEG signals towards higher frequency bands. The duration of fast onset activity may vary from patient to patient with an average value equal to 8 seconds, approximately. As illustrated in Figure 22.3, which shows intracerebral EEG signals recorded from hippocampus in three patients with MTLE, the transition from interictal activity to ictal activity may vary from patient to patient. In the first case (patient 1, Figure 22.3A), the transition to fast onset activity is relatively abrupt without the appearance of high amplitude spikes during the period that just precedes fast oscillations (referred to as the pre-onset period). In the second case (patient 2, Figure 23.3C), the transition from interictal to ictal activity is characterized by the emergence of a low-frequency high-amplitude rhythmic spiking activity followed by the rapid discharge. In the third case (patient 3, Figure 23.3E), the transition to ictal activity is marked by the appearance of a narrow frequency band activity (alpha-like, i.e. about 10–12 Hz, Figure 23.3F) during the pre-onset period. The two first patterns are those which are most often observed. They correspond to two main patterns already reported in previous studies (Engel et al., 1989; Spencer et al., 1992; Velasco et al., 2000; Bartolomei et al., 2004). Spectral features of the fast onset activity are quite reproducible from patient to patient. As shown by normalized power spectral densities (PSDs) given in Figure 23.3B,D and F, the dominant frequency ranges from 20 Hz to 30 Hz which corresponds to high beta and low gamma frequency bands of the EEG (Table 23.1).

As the seizure develops, the fast onset activity gradually slows down and a transition to an ictal narrowband activity ranging from 5 to 10 Hz (mostly within the EEG theta band) is often observed. As illustrated in Figures 23.3B,D and F, PSDs show that spectral features of this ictal activity is reproducible among patients. Usually, this narrowband activity changes into a slower (around 3 Hz) activity before seizure termination. This late ictal activity essentially consists in high amplitude rhythmic spikes spreading in multiple areas in the temporal lobe and beyond.

#### *Neocortical structures*

Electrophysiological patterns of transition to ictal activity in lateral neocortical temporal lobe structures differ from those observed in medial structures. During the pre-onset phase (just before seizure), spiking activity is usually not recorded. The appearance of a fast activity at seizure onset strongly depends on the type of epilepsy and, more particularly, on the extension of the epileptogenic zone to temporal neocortical structures. Fast oscillations (gamma band of the EEG) are rarely observed in neocortical structures in medial TLE. They are more commonly recorded in lateral TLE (Bartolomei et al., 1999), although this is not a general feature. The fact that rapid discharges are less frequent in TLE also contrasts with what is commonly observed in frontal lobe epilepsies (FLE). Indeed, in FLE, fast oscillations and very fast oscillations (EEG gamma band and beyond) are very often recorded at seizure onset (Bancaud et al., 1973; Allen et al., 1992; Traub et al., 2001; Wendling et al., 2003; Worrell et al., 2004; Jirsch et al., 2006). Intracerebral SEEG signals recorded from neocortical structures (middle temporal gyrus, MTG, from anterior to posterior part) and hippocampus during the transition to seizure in three patients with medial TLE are shown in Figure 23.4. As illustrated in Figure 23.4A, neocortex is not involved in patient 1 as revealed by visual inspection of SEEG signals that do not exhibit changes as the seizure develops in hippocampus. The PSD computed on the signal from the middle part of the MTG is also very similar to that computed during interictal background activity in the same structure (Figure 23.4B). In patients 2 and 3, a similar electrophysiological pattern is observed, just after seizure onset. This pattern consists in a flattening (reduction of the signal amplitude with respect to that measured during the pre-onset phase) followed by a high amplitude theta-like activity (around 3 Hz, Figure 23.4D and F).

In the following section, the interpretation of intracerebral EEG dynamics and transitions described above is based on macroscopic physiological models of EEG generation (neuronal population models).

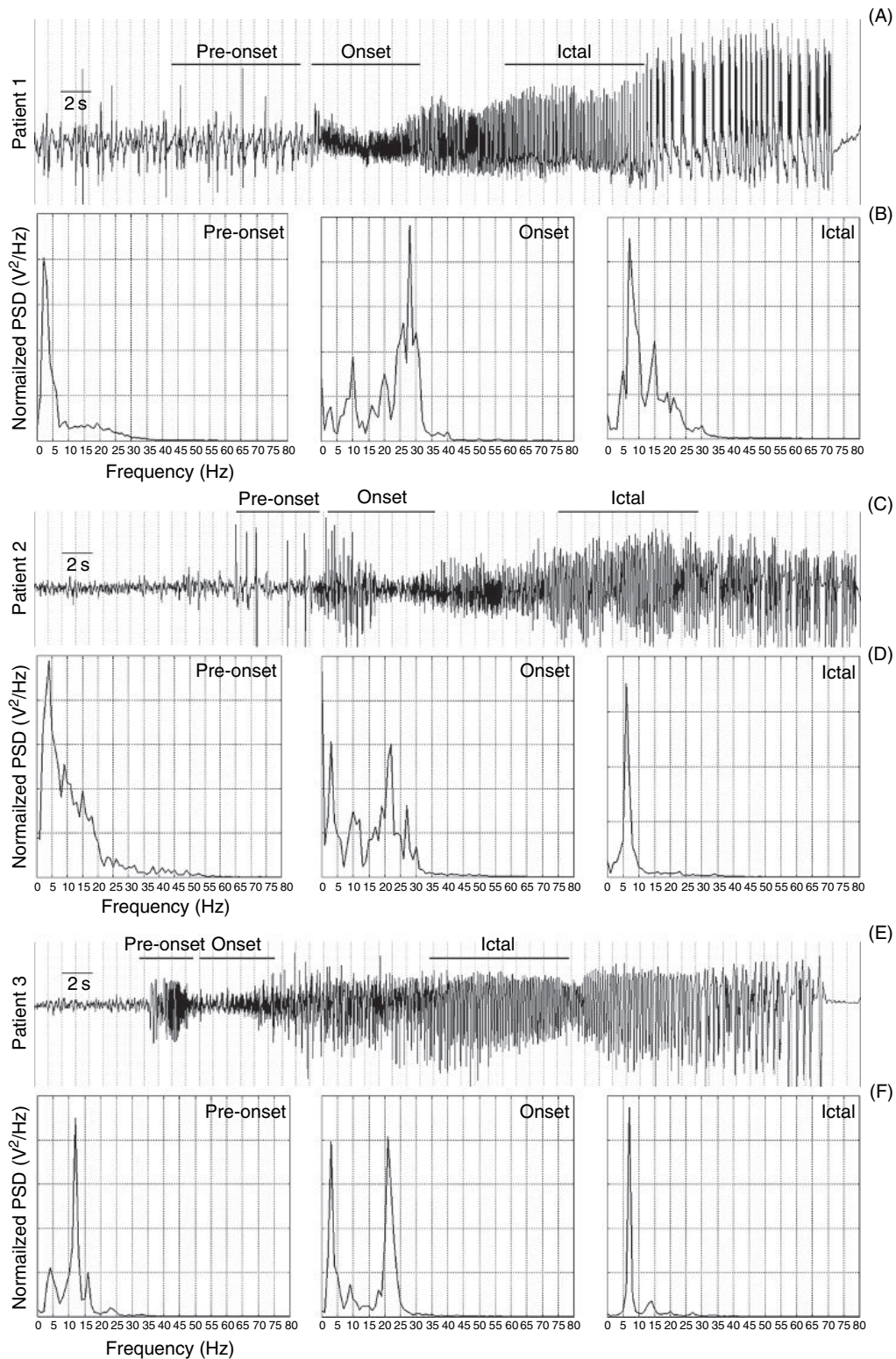
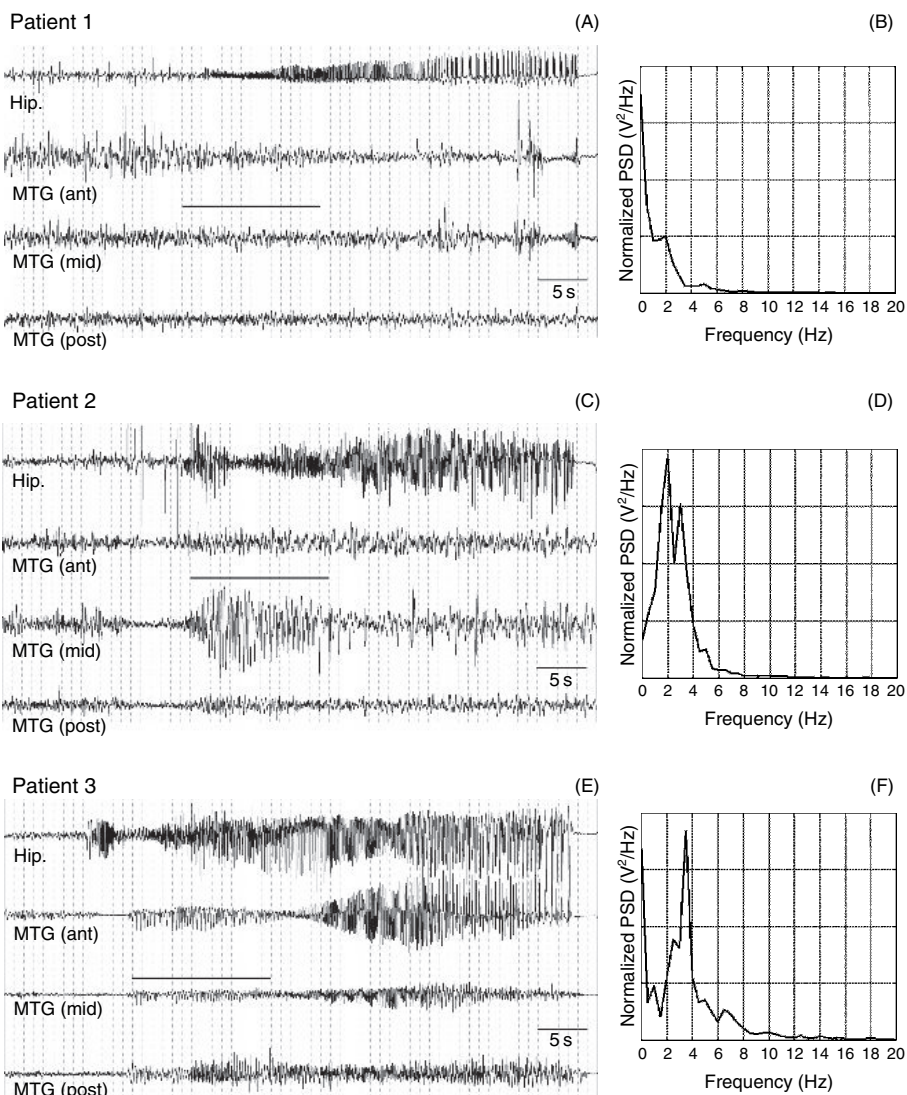


FIGURE 23.3 (A,C and E) Examples of SEEG signals recorded from the anterior part of the hippocampus in three patients with MTLE during the transition from interictal activity to ictal activity. (B,D and F) Normalized power spectral density computed on segments of activity selected during pre-onset, onset and ictal phases. Major changes are observed in the frequency content of signals. See text for detailed description.

**TABLE 23.1** EEG frequency bands referred to in this chapter. Lower and upper values of each band were obtained from Niedermeyer and Lopes Da Silva (1998)

Frequency band	Range (Hz)
Theta ( $\theta$ )	$3.5 \leq f < 7.4$
Alpha ( $\alpha$ )	$7.4 \leq f < 12.4$
Beta ( $\beta$ )	$12.4 \leq f < 24$
Gamma ( $\gamma$ )	$24 \leq f < 80$



**FIGURE 23.4** (A,C and E) Examples of SEEG signals recorded from the anterior part of the hippocampus and from lateral neocortex (MTG: middle temporal gyrus) in three patients with MTLE during the transition from interictal activity to ictal activity. Seizures begin in medial temporal lobe structures. (B,D and F) Normalized power spectral density (PSD) computed signal recorded from MTG (middle part) at seizure onset. They reveal the appearance of a neocortical theta activity in patients 2 and 3 conversely to patient 1 for whom activity stays normal. See text for detailed description.

## INTERPRETATION OF INTRACEREBRAL EEG SIGNALS RECORDED DURING THE TRANSITION TO SEIZURE USING NEURONAL POPULATION MODELS

As described above, two different modeling approaches were carried out to study the activity in neural populations along with its relation to the observed EEG. The first one is based on networks built with a large number of elementary cells to represent both the spatial and temporal properties of the activity in a given neuronal system. The second one is a lumped-parameter approach lying at the level of neuronal populations and able to represent the generation of spontaneous EEG.

This second approach is developed in the present section. It starts from a model initially developed by Lopes Da Silva et al. (1974, 1976) for alpha rhythm generation, formally studied by Zetterberg et al. (1978) for stability and more recently redesigned by Jansen et al. (1993, 1995) to represent the generation of evoked potentials in the visual cortex.

The objectives of this section are:

1. to present the general features of neuronal population models through the description of a simple generic model
2. to show how the capabilities of this model can be extended such that it can generate multivariate EEG signals from multiple coupled neural populations
3. to describe some alterations of model parameters that make the model produce signals that qualitatively resemble real SEEG signals recorded on multiple channels during interictal or ictal periods
4. to show that simulations can be used to interpret real signals.

The section is organized as follows. In the first part, the generic model and the extension to multiple populations are presented. Signals simulated from various scenarios (taking into account general hypotheses related to ictogenesis) are qualitatively compared to real SEEG signals. These results are then discussed. They show that the behavior of the model seems particularly relevant: although precise waveform fit is not the primary intent, simulated epileptiform signals strongly resemble those recorded before and during seizures. However, they also show that certain types of activity cannot be simulated. In particular, fast activities encountered in MTLE are not represented in this first model. This inconsistency points towards necessary model improvement and introduces the next section in which an extension of the model is described in order to represent faster oscillations generated in the hippocampus. For this second model, examples of simulated signals are shown. Comparison with real SEEG signals recorded from human hippocampus reveals that the model can generate very realistic epileptiform activities. This result consists in a first step of model validation. The second step is detailed next and provides results about the identification of model parameters from two different approaches. These results show that dynamics and transitions of dynamics observed in intracerebral EEG can be related to excitation/inhibition-related modifications that take place at the level of subpopulations of neurons. The discussion that follows is aimed at describing what insights into possible pathophysiological mechanisms involved during the transition from interictal to ictal activity in human hippocampus can be gained from such a modeling approach.

### GENERIC MODEL OF NEURONAL POPULATION

#### Model presentation

At the level of the single cell, synaptic activation of a neuron causes changes in membrane conductance which leads to the generation of primary currents through the membrane and causes a variation of the postsynaptic membrane potential (i.e. an excitatory or inhibitory postsynaptic potential, EPSP or IPSP). EPSPs cause active sinks at the level of apical dendrites, while IPSPs create active source at the soma. In both cases, extracellular currents (volume currents flowing in the surrounding medium) oriented in the same direction are generated and a dipolar source-sink configuration with the same polarity is created (Lopes da Silva, 2002).

At the level of neuronal assemblies, these extracellular currents can only be measured at a distance from the sources when neurons are well organized both in space and in time (columnar organization of pyramidal cells in some neocortical areas, for instance). Indeed, these currents sum up when parallel-oriented neurons activate quasi-synchronously. This principle allows us to consider the neuronal population as a whole and to represent its average electrical contribution by an equivalent current dipole whose time-varying moment depends on the time variations of average postsynaptic potentials generated at the population level. These variations, or temporal dynamics, directly reflect in intracerebral EEG signals recorded from macroscopic electrodes like those used for SEEG exploration (see Figure 23.1). This is also the reason why it is commonly accepted that EEG primarily is a reflection of summated postsynaptic potentials of activated pyramidal cells.

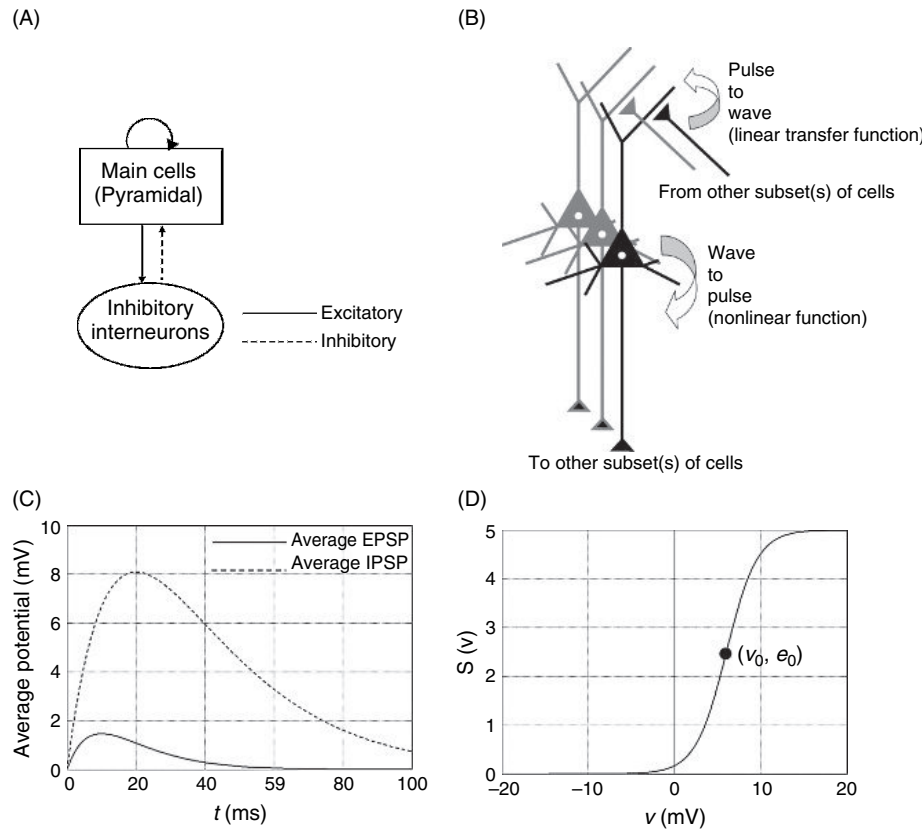


**FIGURE 23.5** (A) Structure of the generic neuronal population model representing a cluster of neurons composed of two subsets: main cells (i.e. pyramidal cells) and local interneurons (i.e. other non-pyramidal cells, stellate or basket cells). Pyramidal cells receive excitatory input from other pyramidal cells (collateral excitation) or inhibitory input from interneurons. These latter cells receive excitatory input only from pyramidal cells. (B) Each subset is characterized by two functions, respectively named as the ‘pulse-to-wave’ function and the ‘wave-to-pulse function’. The former changes presynaptic information (average density of afferent action potentials) into postsynaptic information (average excitatory or inhibitory postsynaptic membrane potential, respectively EPSP or IPSP). The latter relates the average level of membrane potential of the neurons to an average pulse density of potentials fired by these neurons. (C) Impulse response of the ‘pulse-to-wave function’ approximating actual average excitatory (dotted line) or inhibitory (solid line) postsynaptic potentials. (D) Shape of the ‘wave-to-pulse’ function. Non-linear sigmoid shape accounts for the integrating action that takes place at the soma (threshold and saturation effects).

In the simplest form of the neuronal population model, a cluster of neurons is considered. As displayed in Figure 23.5a, this cluster contains two subsets. The first subset is composed of the principal cells (i.e. pyramidal cells). The second subset is composed of local interneurons (i.e. other non-pyramidal cells, stellate or basket cells). Pyramidal cells receive excitatory input from other pyramidal cells (collateral excitation) or inhibitory input from interneurons. These latter cells receive excitatory input only from pyramidal cells.

As illustrated in Figure 23.5B, each subset is characterized by two functions, respectively named as the ‘pulse-to-wave function’ and the ‘wave-to-pulse function’ by Freeman (Freeman, 1992). The former is a linear transfer function that changes presynaptic information (i.e. the average density of afferent action potentials) into postsynaptic information (i.e. an average excitatory or inhibitory postsynaptic membrane potential, respectively EPSP or IPSP). The latter is a static non-linear function that relates the average level of membrane potential of the neurons in the considered subset to an average pulse density of potentials fired by these neurons. This non-linear function mimics the integrating action that takes place at the soma (threshold and saturation effects).

As detailed in Jansen and Rit (1995), the linear transfer function can be represented by a second order lowpass filter  $H(s) = G/(s + g)^2$  (where  $s$  is the Laplace variable). The shape of the impulse response of this filter was shown to approximate that of actual postsynaptic potentials (van Rotterdam et al., 1982). Consequently, the impulse response of the linear transfer function is given by  $h_e(t) = u(t) \cdot A a t e^{-at}$  in the excitatory case, and by  $h_i(t) = u(t) \cdot B b t e^{-bt}$  in the

inhibitory case, where  $u(t)$  is the Heaviside function (see Figure 23.5C) and where  $G = A$  or  $G = B$  and  $g = a$  or  $g = b$ , depending on the excitatory or inhibitory case.

Quantities  $A/a^2$  and  $B/b^2$  are the static gains of filters  $h_e$  and  $h_i$ . Lumped parameters  $a$  and  $b$  (expressed in  $s^{-1}$ ) are linked to the membrane average time constant that is itself related to the kinetics of synaptic transmission (mainly glutamatergic and gabaergic) and the average distributed delays in the dendritic tree. Given time constants  $1/a$  and  $1/b$ , parameters  $A$  and  $B$  can be used to adjust the sensitivity of excitatory and inhibitory synapses, respectively.

The static non-linear function is represented by the sigmoid function

$$S(v) = \frac{2e_0}{1 + e^{r(v_0 - v)}}$$

where  $2e_0$  is the maximum firing rate,  $v_0$  is the postsynaptic potential corresponding to a firing rate of  $e_0$  and  $r$  is the steepness of the sigmoid (see Figure 23.5D).

Figure 23.6A provides a block diagram representation of the neuronal population model displayed in Figure 23.5A. Basically, the model can be viewed as a non-linear feedback system driven by a noise input  $p(t)$  that globally represents the average density of afferent action potentials from neighboring or distant populations. The middle branch of the diagram corresponds to the subset of pyramidal cells that receives both positive (excitatory) feedback from other pyramidal cells (upper branch) and negative (inhibitory) feedback from interneurons (lower branch). Interactions between cells are summarized in the model by four connectivity constants,  $C_1$  to  $C_4$ , which account for the average number of synaptic contacts. The schematic description given in Figure 23.6A allows for derivation of ordinary differential equations that

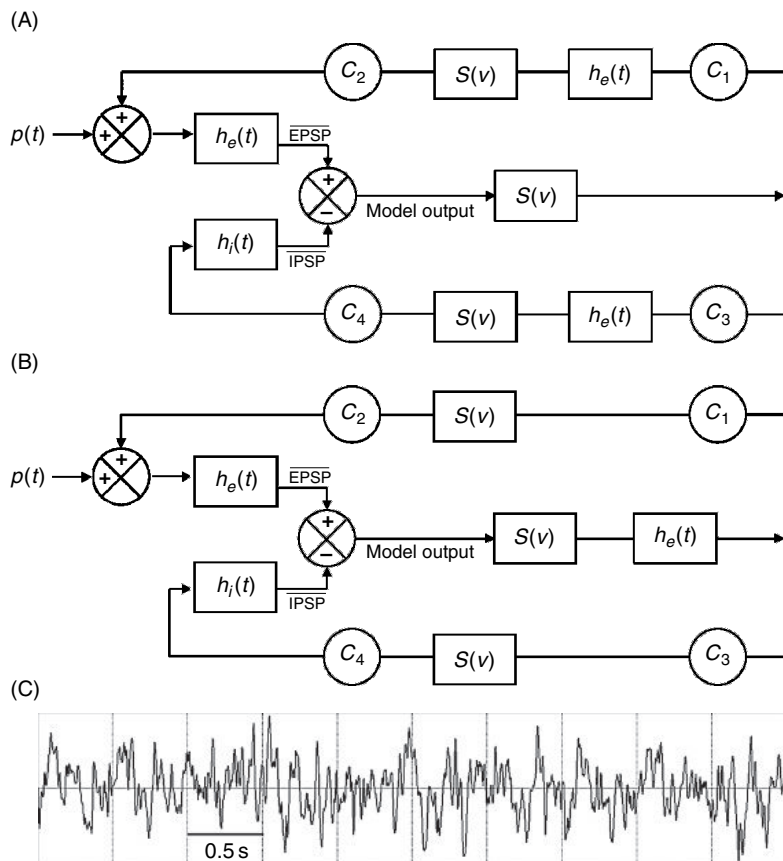


**FIGURE 23.6** Block diagram representation of the neuronal population model displayed in Figure 23.5A. The model can be viewed as a non-linear feedback system driven by a noise input  $p(t)$  that globally represents the average density of afferent action potentials from neighboring or distant populations. Representations in (A) and (B) are equivalent. (C) Example of simulated background activity. See Table 23.2 for model parameters.

govern the model. Both impulse responses  $h_e(t)$  and  $h_i(t)$  introduce a pair of first order ordinary differential equation of the form:

$$\begin{aligned}\dot{z}(t) &= z_1(t) \\ \dot{z}_1(t) &= Gg x(t) - 2g z_1(t) - g^2 z(t)\end{aligned}$$

where  $G = A$  or  $G = B$  and  $g = a$  or  $g = b$ , depending on the excitatory or inhibitory case, and where  $x(t)$  and  $z(t)$  are the respective input and output signals of the linear transfer functions. Taking into account the fact that the model presented in Figure 23.6A is equivalent to that shown in Figure 23.6B, which is actually the reduced model proposed by Jansen and Rit (1995), we obtain the following set of six differential equations for the model (two differential equations per ‘ $h$  function’):

$$\begin{cases} \dot{y}_0(t) = y_3(t) \\ \dot{y}_3(t) = AaS(y_1 - y_2) - 2ay_3(t) - a^2y_0(t) \\ \dot{y}_1(t) = y_4(t) \\ \dot{y}_4(t) = Aa \{ p(t) + C_2S[C_1y_0(t)] \} - 2ay_4(t) - a^2y_1(t) \\ \dot{y}_2(t) = y_5(t) \\ \dot{y}_5(t) = Bb \{ C_4S(C_3y_0(t)) \} - 2by_5(t) - b^2y_2(t) \end{cases}$$

This set of equation is solved by numerical integration methods (Euler, fixed step method, for example). Special attention must be paid to its stochastic nature due to noise input  $p(t)$ . In linear mode, alpha-like rhythms are produced by the model. However, as mentioned in Jansen and Rit (1995), experiments conducted by the authors showed that ‘the model is capable of much more complex behavior when it is allowed to operate in a non-linear mode’. Our results are in agreement with these previous studies: as shown below, the alteration of some parameters leads the model to produce signals that strongly resemble those recorded with intracerebral electrodes, interictally or ictally.

### Extension to multiple coupled populations

In order to explore the hypothesis that visual evoked potentials are due to an interaction between cortical columns, Jansen and co-workers proposed a model in which two populations were coupled.

In the context of epilepsy, as shown in the description of electrophysiological patterns recorded in patients with TLE (see above), multiple brain sites are often involved in the generation and the propagation of epileptic activities. The purpose of this section is to establish the general expression of the set of ordinary differential equations (ODEs) that describe a model of multiple ( $N \geq 2$ ) coupled populations.

Pyramidal cells are excitatory neurons that project their axons to other areas of the brain. To account for this organization, the average pulse density of action potentials from the main cells of one population can be used as an excitatory input to another population of neurons. However, as neuronal populations belong to distinct and distant cerebral areas, new parameters must be introduced that take into account the different ways of connecting populations and the delays associated with these connections. As shown in Figure 23.7, a gain constant  $K^{ij}$  is used to define the degree of coupling between population  $i$  and population  $j$  while a filter with an impulse response  $h_d(t)$  is used to model the delay associated with connections from population  $i$ . For simplicity,  $h_d(t)$  can be chosen as being similar to  $h_e(t)$ , i.e.  $h_d(t) = u(t) \cdot Aa_d t e^{-a_d t}$ , but with a different time constant ( $a_d \neq a$ ). This transfer function introduces a new second order equation that splits into two first order ordinary differential equations. Hence, the model is described by a set of eight ODEs per population (the six previous equations describing the intra-population behavior and two new equations describing the output of a given population):

$$\begin{cases} \dot{y}_0^n(t) = y_3^n(t) \\ \dot{y}_3^n(t) = AaS[y_1^n(t) - y_2^n(t)] - 2ay_3^n(t) - a^2y_0^n(t) \\ \dot{y}_1^n(t) = y_4^n(t) \\ \dot{y}_4^n(t) = Aa \left\{ p^n(t) + C_2S(C_1y_0^n(t)) + \sum_{i=1, N, i \neq n} K^i y_6^i(t) \right\} - 2ay_4^n(t) - a^2y_1^n(t) \\ \dot{y}_2^n(t) = y_5^n(t) \\ \dot{y}_5^n(t) = Bb \{ C_4S(C_3y_0^n(t)) \} - 2by_5^n(t) - b^2y_2^n(t) \\ \dot{y}_6^n(t) = y_7^n(t) \\ \dot{y}_7^n(t) = Aa_d S(y_1^n(t) - y_2^n(t)) - 2a_d y_7^n(t) - a_d^2 y_6^n(t) \end{cases}$$

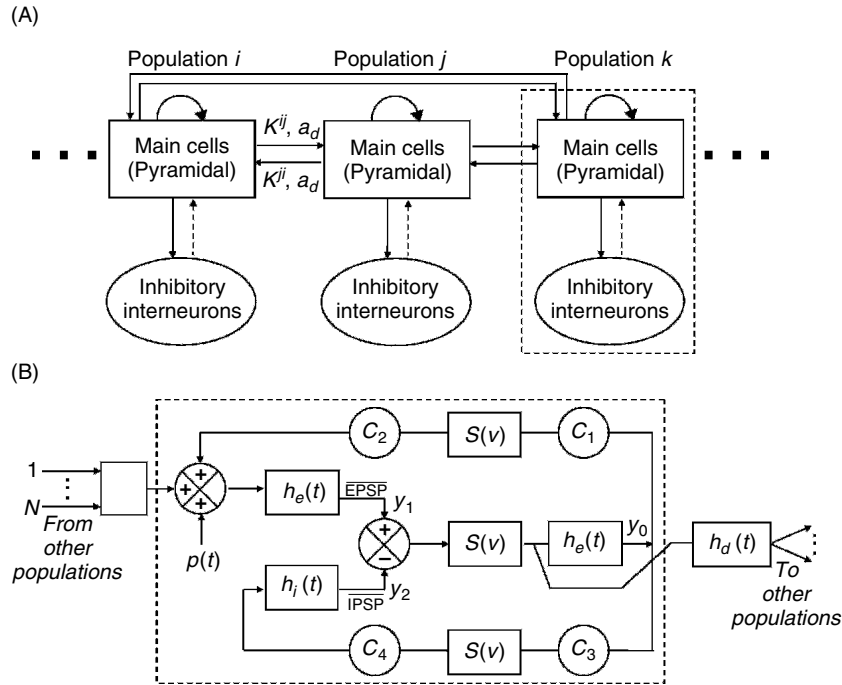


FIGURE 23.7 Model extension for description of multiple coupled populations. See text for detailed description.

Here, superscript  $n$  denotes the population under consideration; population  $n$  receives afferent information from populations  $i$ ,  $i = 1 \dots N$ ,  $i \neq n$ , as well as from the neighborhood (pulse density  $p^n(t)$ ). As shown in Figure 23.7B, quantity  $y_0^n(t)$  is the output of the EPSP transfer function  $h_e$  (from considered pyramidal cells to other pyramidal cells and to inhibitory interneurons);  $y_1^n(t)$  and  $y_2^n(t)$  are the respective outputs of EPSP and IPSP transfer functions  $h_e$  and  $h_i$  (from other pyramidal cells and inhibitory interneurons to considered pyramidal cells); and  $y_0^n(t)$  is the output of the EPSP transfer function  $h_d$ . For writing simplicity, superscript index  $n$  is not added to local parameters  $A, B, a, b, a_d, C1$  to  $C4$ . However, these parameters may depend on population  $n$  and may vary from one population to another. One can also notice here that for  $N = 2$  populations, the obtained set of  $2 \times 8 = 16$  differential equations is equivalent to that established by Jansen et al. (1995).

## Results

All parameters in the model have a physiological basis. The interpretation and value of parameters is summarized in Table 23.2. Although the number of parameters in macroscopic models is relatively low compared to detailed models, there still exists a high number of possibilities to alter and combine these parameters. We chose to restrain the study of model parameters by taking into account some hypotheses about general macroscopic mechanisms of epilepsy. In the neuronal population model, parameters may be adjusted at the level of each population and at the level of connections between populations. This is of interest in the context of epileptic signals analysis, since particular hypotheses related to the local balance of excitation and inhibition and to the degree/direction of couplings, may be explored using the model. Indeed, the balance between excitation and inhibition is at the center of numerous studies demonstrating that interictal or ictal spike discharges (on the EEG) in focal seizures originate in an area of the cortex that is excessively excitable (review in Dichter, 1997). This increased excitability may be due to increased excitation, decreased inhibition, or both (Prince, 1993). In the model, the balance between excitation and inhibition within each population is primarily influenced by parameters  $A$  and  $B$  as they determine the amplitude of the average postsynaptic potential, excitatory and inhibitory, respectively. Thus, the ratio  $A/B$  can be used to control the ‘degree of excitability’ of the modeled population of neurons and directly influences the dynamics of simulated signals, as illustrated hereafter.

A Gaussian white noise was used as the model input  $p(t)$ . For a mean and variance corresponding to a rate ranging from 60 to 120 pulses per second, the model produces a signal spontaneous EEG activity when other parameters of the model are set to standard values (see Table 23.2). As shown in Figure 23.8A, this signal reflects a ‘normal’ background

**TABLE 23.2** Parameters, interpretation and values used in the generic model of neuronal population (adapted from Jansen and Rit, 1995)

Parameter	Interpretation	Value
<i>A</i>	Average excitatory synaptic gain	$3.25\text{ mV}$
<i>B</i>	Average inhibitory synaptic gain	$22\text{ mV}$
<i>1/a</i>	Time constant of average excitatory postsynaptic potentials	$a = 100\text{ s}^{-1}$
<i>1/b</i>	Time constant of average inhibitory postsynaptic potentials	$b = 50\text{ s}^{-1}$
<i>1/a<sub>d</sub></i>	Time constant of the filter used to model the time delay associated to connections from considered population	$a_d = a/3 = 33\text{ s}^{-1}$
<i>c<sub>1</sub>, c<sub>2</sub></i>	Average number of synaptic contacts in the feedback excitatory loop	$C_1 = C, C_2 = 0.8C$ (with $C = 135$ )
<i>c<sub>3</sub>, c<sub>4</sub></i>	Average number of synaptic contacts in the slow feedback inhibitory loop	$C_3 = C_4 = 0.25C$
<i>v<sub>0</sub>, e<sub>0</sub>, r</i>	Parameters of the asymmetric sigmoid function <i>S</i> (transforming an average PSP into an average density of action potentials)	$v_0 = 6\text{ mV}, e_0 = 2.5\text{ s}^{-1}, r = 0.56\text{ mV}^{-1}$
<i>p(t)</i>	Excitatory input noise (positive mean gaussian white noise)	mean = $90\text{ pulses.s}^{-1}$ , sd = $30\text{ pulses.s}^{-1}$

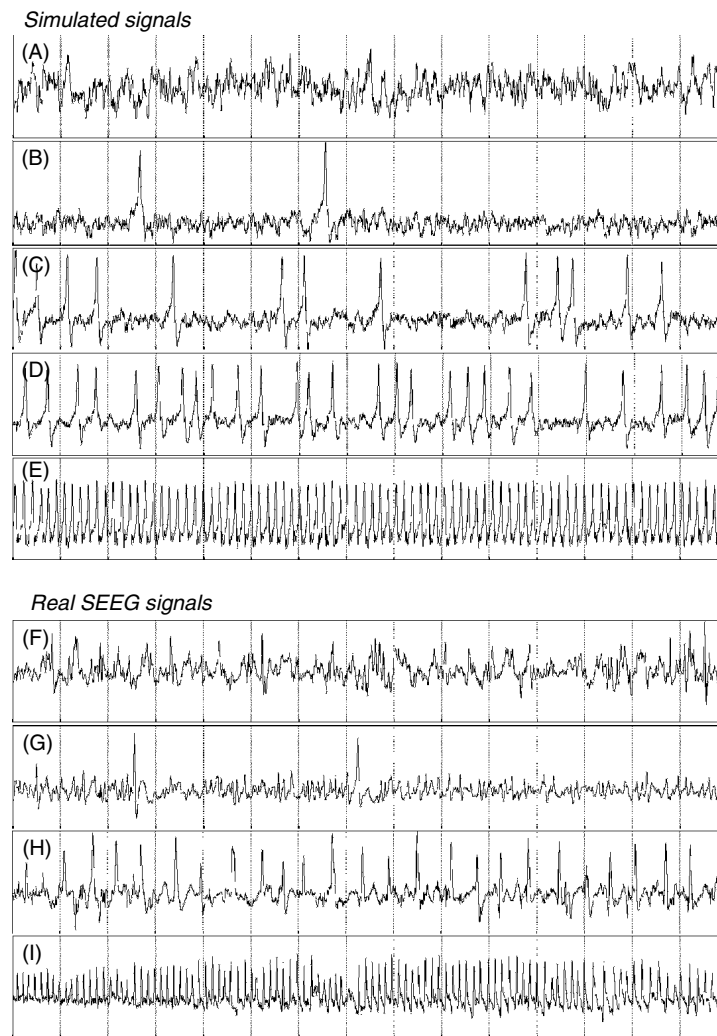


**FIGURE 23.8** Simulated signals (top) and real SEEG signals (bottom). Starting from a 'normal EEG' (A), the progressive increase of the excitation/inhibition ratio makes the model generate sporadic spikes (B) which appear more frequently (C and D) before changing into a rhythmic discharge of spikes (E). Simulated signals resemble real SEEG signals recorded before (F and G) and during (H and I) a seizure recorded from neocortical structure (middle temporal gyrus). From Wendling et al. (2000).

activity similar to that reflected by real SEEG signals recorded from electrodes implanted in neocortical structures during interictal periods (Figure 23.8F). Starting from this point, increase of the balance between excitation and inhibition can be analyzed in the model by progressively increasing the value of parameter  $A$  (synaptic gain in the excitatory loop) for constant parameter  $B$  (synaptic gain in the inhibitory loop), or vice-versa (decrease of  $B$  for constant  $A$ ). As illustrated in Figures 23.3B–E, this parameter change leads the model to generate spikes that appear sporadically ( $A = 3.4$  for constant  $B = 22$ ), then frequently ( $A = 3.6$ ) and finally rhythmically ( $A = 3.8$ ). The average frequency of this rhythmic discharge of spikes also increases with  $A$  and stays into theta band of the EEG (from 3 to 7 Hz). For higher values of  $A$ , the model switches from spiking activity to quasi-sinusoidal activity (alpha-like around 9–10 Hz).

The visual inspection of simulated signals shows that real waves are quite accurately reproduced by the model. Indeed, as described above and as depicted in Figure 23.8G–I, electrophysiological patterns recorded in human temporal brain structures often reflect sporadic spikes (before seizures) that gradually change into rhythmic discharges of spikes during the transition to ictal activity. Transition between spiking and quasi-sinusoidal activity is also illustrated in Figure 23.9 for both real and simulated signals.

This behavior of the model is summarized in Figure 23.10 which shows a bifurcation diagram obtained from plotting maximal positive and negative values of the amplitude of the simulated signal as a function of parameter  $B$  for constant parameter  $A$  ( $A = 5$ ). In this diagram, decreasing values of  $B$  (from 50 to 1, right to left on the  $B$  axis) correspond to increasing values of the  $A/B$  ratio (i.e. degree of excitability). Qualitatively, it shows that the model operates between two states. The former is stable (stable point) and corresponds to a state for which either normal background activity (when  $B$  goes from 50 to 30) or sporadic spikes (when  $B$  goes from 30 to 22) are produced. The latter is an unstable state for which sustained spiking ( $B:22$  to 11) or alpha-like ( $B:11$  to 8) activity is produced by the model. As an interesting model behavior, background EEG activity is produced for very low level of inhibition ( $B:8$  to 1).

So far as interactions between neuronal subsets are concerned, numerous studies have identified possible mechanisms leading to hyperexcitability like changes in excitatory and inhibitory neurotransmission functions or like the existence or development of recurrent excitatory circuits. These circuits may play a role in the production of epileptic activities (Jefferys, 1990; review in McNamara, 1994; Wilson et al., 1998). Other studies reported that abnormally strengthened connections may be implied in the production of epileptic activity (Chauvel et al., 1987; Gloor, 1990; Fish et al., 1993). The way circuits are built also seems to be important. For example, Buchanan et al. (Buchanan and Bilkey, 1997) underlined that some structures which reciprocally connect with others may play a role in epileptogenesis. In the model, the connectivity constants  $K^{ij}$  can be used to interconnect populations in uni- or bi-directional ways and to adjust the ‘degree of coupling’ between populations. In Figure 23.11, the effect of increasing parameter  $K^{ij}$  is illustrated on a simple example in which

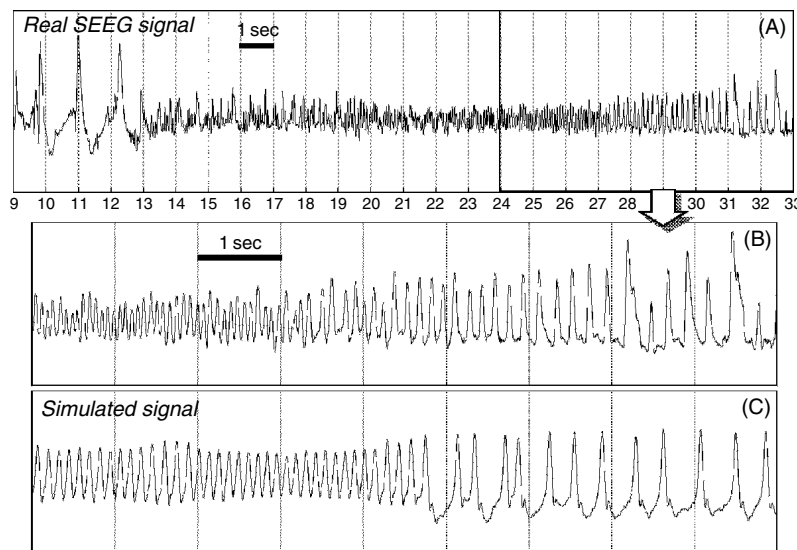


**FIGURE 23.9** Comparison between real activity and simulated activity. (A) Transition of activity in a real SEEG signal recorded from mesial structures (amygdala) at the beginning of a temporal lobe seizure. (B) Zoom on the transition between quasi-sinusoidal activity and spiking activity. (C) Spontaneous transition occurring in the simulated signal when the excitation/inhibition ratio is adjusted, in the model, at the frontier between two types of activities. From Wendling et al. (2000).

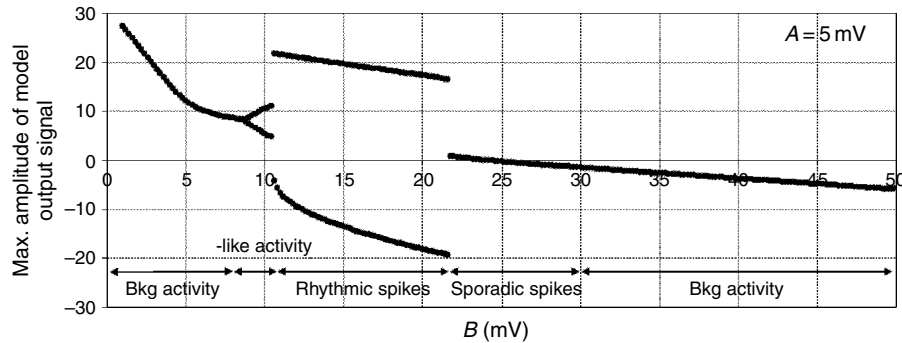


**FIGURE 23.10** Behavior of the generic neuronal population summarized by the bifurcation diagram obtained from plotting maximal positive and negative values of the amplitude of output simulated signal as a function degree of excitability. Decreasing values of parameter  $B$  (i.e. inhibition) correspond to increasing values of the excitation/inhibition ratio in the model. See text for details.

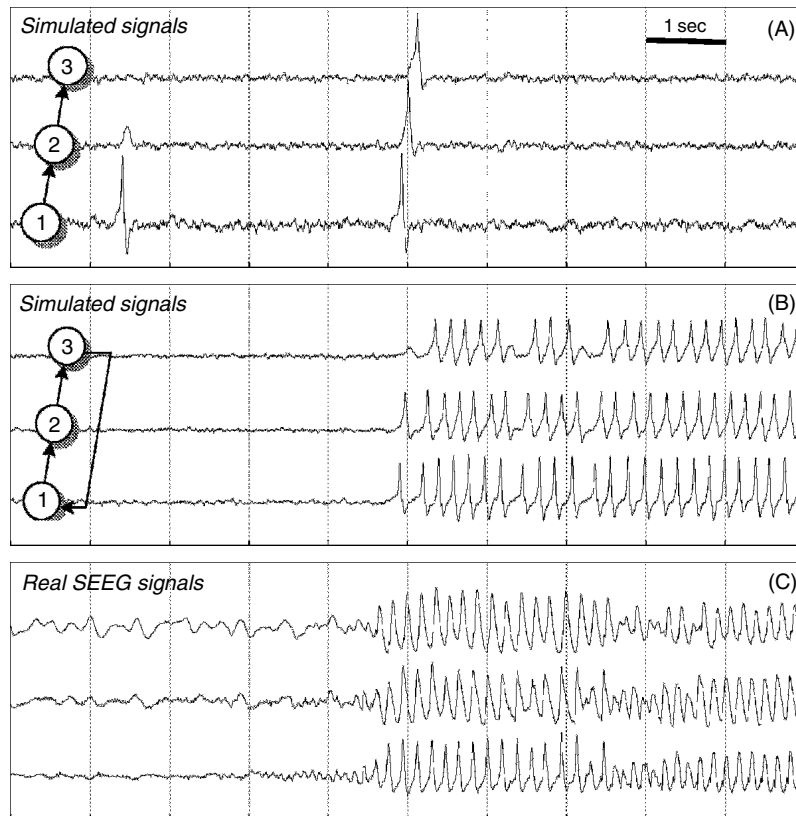


**FIGURE 23.11** Influence of the coupling mode in the model of coupled populations. Population 1 was made hyperexcitable by increasing its excitation/inhibition ratio. (A) For unidirectional coupling between population 1 and population 2 and between population 2 and population 3, sporadic spikes originating from population 1 propagate to population 2 and then from population 2 to population 3. (B) Introduction of a recurrent connection is a sufficient condition to make the model generate sustained discharges of spikes that resemble those reflected in real SEEG signals during the propagation of ictal activity to neocortex in temporal lobe seizures (C). From Wendling et al. (2000).

three populations are considered. The first one is rendered more excitable by increasing its  $A/B$  ratio (generation of sporadic spikes). Parameters of the two other populations are set to standard values. For null degree of coupling between these three populations, resulting signals correspond to normal background activity with epileptic spikes appearing randomly in the first population and to normal background activity only for the two other populations. When parameters  $K^{12}$  and  $K^{23}$  (unidirectional coupling from population 1 to population 2 and unidirectional coupling from population 2 to population 3)

are increased, propagation of spikes from population 1 to population 2 and population 3 are simulated (Figure 23.11a). As expected, spikes in populations 2 and 3 are delayed with respect to that generated in population 1.

To end with, the effect of recurrent coupling is illustrated in Figure 23.11B where population 3 is connected to population 1 (non-zero parameter  $K^{31}$ ). In this case, the model behavior changes dramatically as a different type of activity is produced. Indeed, the only introduction of this recurrent connection in the model is a sufficient condition for sporadic spikes to change into sustained discharges of spikes that involve the three populations. Interestingly, simulated signals closely resemble observed SEEG signals during seizure spread in neocortical structures in TLE (see Figure 23.11C and Figure 23.4C and E).

## Discussion

In the section above, two macroscopic models (single neuronal population and multiple coupled populations) have been presented. Results show that the generation of epileptiform EEG signals from such models is essentially obtained by increasing the excitation/inhibition ratio or by introducing recurrent couplings that are actually excitatory. Simulated signals reflect activities (sporadic epileptic spikes, rhythmic spikes, quasi-sinusoidal discharges) that closely resemble those recorded from cerebral structures with intracerebral electrodes (i.e. SEEG exploration) during the transition to seizure as well as during ictal periods. This is particularly true for neocortical structures as fast onset activity met in the hippocampus at seizure onset is not represented in the model. Apart from this limitation, which is thoroughly dealt with in the next section, these results are in accordance with hypotheses about the causes of hyperexcitability of the epileptic tissue that have been largely discussed during the past decades (Jefferys, 2003). Numerous studies showed that epileptic activities result from a collective behavior of neuronal assemblies which synchronize to produce bursts of spikes at the cellular level and spikes (sporadic or sustained bursts) on the EEG. In Lopes da Silva et al. (1994), the authors bring evidence that local neuronal networks behave as non-linear dynamic systems and show, through paired-pulse experiments, that ‘the excitation/inhibition ratio increases in the course of the establishment of a kindled epileptogenic focus’. In Zetterberg et al. (1978), the authors study a single population model whose structure is close to the population model presented here. They noticed that the model was able to generate epileptiform activities (spikes) that are ‘borderlike cases between normal background activity and seizure activity’. Results presented here corroborate this study as sporadic epileptic spikes constitute a transient activity between background activity and ictal spiking activity obtained for increased excitation.

Modeling at the neuronal population level appears to be well suited to the nature of real observations. Indeed, macroelectrodes, which are used for SEEG explorations, record the field activity (intracerebral EEG signal) rising from large assemblies of cells which precisely corresponds to one of the different outputs in neuronal populations models. Models of this class also include parameters directly related to excitation, inhibition or couplings between neuronal assemblies. These features are still considered as essential in the study of epileptic processes.

## MODEL OF HIPPOCAMPUS ACTIVITY

Interestingly, the model presented in the previous section cannot generate certain types of epileptic activity. In particular, fast activity encountered at the onset of seizures in limbic structures is not represented in the model (see Figure 23.3). This limitation or inconsistency points towards necessary improvement of the model in order to interpret intracerebral EEG signals recorded from medial structures of the temporal lobe. This is the objective of this section that describes how neuronal population models can be adapted to specific brain structures based on available data about the organization of subsets of neurons and interneurons within considered structures. This adaptation is detailed for the hippocampus and is followed by the presentation of two procedures aimed at identifying model parameters from real SEEG signals. Analysis of identified parameters allows for interpretation of macroscopic mechanisms leading to ictal activity in human hippocampus (discussion section).

### Model presentation

High-frequency oscillations (gamma band of the EEG and beyond) originating from one or several brain regions constitute a characteristic electrophysiological pattern in focal seizures of human epilepsy and have been reported in several clinical studies (Bragin et al., 1999; Traub et al., 2001; Wendling et al., 2003; Worrell et al., 2004; Jirsch et al., 2006). The regions they originate from are generally considered to be epileptogenic, as shown above in the description of electrophysiological patterns of transition to seizure recorded from limbic structures in patients with mesial TLE. In the hippocampus, although fast onset activities can be well characterized from a signal content standpoint, little is known about underlying mechanisms

involved in their generation. Some studies revealed that oscillations of gamma frequency are linked to the behavior of inhibitory interneurons in hippocampal networks ('inhibition-based rhythms') (Jefferys and Whittington, 1996). Some results also showed that two types of GABA<sub>A</sub> inhibitory postsynaptic currents (IPSCs) may play a crucial role in the formation of nested theta/gamma rhythms in hippocampal pyramidal cells (White et al., 2000). Other studies reported that these two types of inhibition (which depend on the location of synapses/receptors, in part) are present in the CA1 subfield of the hippocampus and that they are probably involved in epileptic processes in a different way. Particularly, in experimental focal models (kainate or pilocarpine-treated rat), it has been shown that GABAergic inhibition is impaired, but not uniformly: dendritic inhibition is reduced whereas somatic inhibition is preserved due to selective survival of perisomatic inhibitory interneurons (Houser and Escalapez, 1996; Cossart et al., 2001).

From these experimental results, a neuronal population model for hippocampus activity can be designed based on neuronal organization and connectivity of the CA1 region. As shown in Figure 23.12A, it includes three subsets of neurons, namely the main cells (i.e. pyramidal cells), the dendritic-projecting inhibitory interneurons (GABA<sub>A,slow</sub> receptors) and the somatic-projecting inhibitory interneurons (GABA<sub>A,fast</sub> receptors). The model accounts for collateral excitatory connections

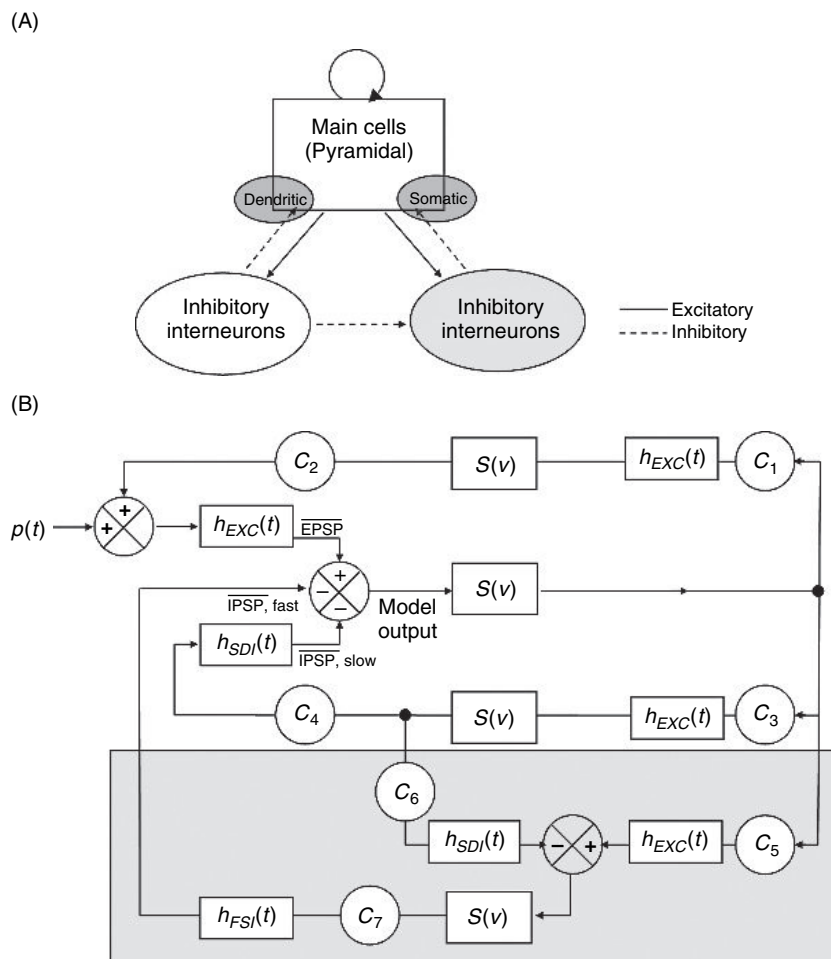


**FIGURE 23.12** Neuronal population model based on the cellular organization of the hippocampus. (A) Schematic representation. A whole population of neurons is considered inside which a subset of principal cells (pyramidal cells) project to and receive feedback from other local cells. Input to interneurons is excitatory (AMPA receptor-mediated). Feedback to pyramidal cells is either excitatory (recurrent excitation) or inhibitory (dendritic-projecting interneurons with slow synaptic kinetics – GABA<sub>A,slow</sub> – and somatic-projecting interneurons (gray color) with faster synaptic kinetics – GABA<sub>A,fast</sub>). As described in Banks et al. (2000), dendritic interneurons project to somatic ones. (B) Corresponding block diagram representation. The introduction of an additional subset of interneurons with fast synaptic kinetics adds a fast feedback inhibitory loop (gray rectangle) to the generic model. The three main parameters of the model respectively correspond to the average excitatory synaptic gain (EXC), to the average slow inhibitory synaptic gain (SDI) and to the average fast inhibitory synaptic gain (FSI). See Table 23.3 for other model parameters.

from pyramidal cells to pyramidal cells (Thomson and Radpour, 1991; Whittington et al., 1997). Pyramidal cells receive two types of GABA receptor mediated currents: slow dendritic and faster perisomatic inhibitory postsynaptic currents (IPSCs). As previously proposed (Miles et al., 1996; Banks et al., 1998; White et al., 2000), these two types of IPSCs are generated by two separate classes of interneurons (possibly basket cells and dendrite-projecting interneurons respectively called, for simplicity,  $GABA_{A,\text{fast}}$  interneurons and  $GABA_{A,\text{slow}}$  interneurons). In addition, as demonstrated in Banks et al. (2000),  $GABA_{A,\text{slow}}$  cells inhibit not only pyramidal cells but also  $GABA_{A,\text{fast}}$  interneurons. All interneurons receive excitatory input (AMPA and NMDA receptor-mediated) from pyramidal cells. From this functional organization of interacting subsets of principal cells and interneurons, the block diagram representation of the model shown in Figure 23.1B can be built. As depicted, the structure of the hippocampus model differs from that of the model described above. The main difference is the additional subset of cells (Figure 23.12A, gray ellipse) representing inhibitory interneurons that target pyramidal cells in the perisomatic region (presence of  $GABA_{A,\text{fast}}$  receptors). The consequence is a new feedback loop with a faster time constant (Figure 23.12B, gray rectangle) in the model structure.

Besides this difference, both models share common features of neuronal population models. The influence from neighboring or more distant populations is represented by an excitatory input  $p(t)$  (modeled by a positive mean Gaussian white noise) that globally describes the average density of afferent action potentials. In each subset of cells, a linear transfer function (second order as above) is used to transform the average presynaptic density of afferent action potentials (the input) into an average postsynaptic membrane potential (the output). This transfer function models synaptic transmission in a simplified way but still takes into account both the amplitude and kinetics of synaptic responses. Its impulse response:

$$h_{EXC}(t) = \frac{EXC}{\tau_E} \cdot t \cdot e^{-t/\tau_E}, \quad h_{SDI}(t) = \frac{SDI}{\tau_D} \cdot t \cdot e^{-t/\tau_D} \quad \text{and} \quad h_{FSI}(t) = \frac{FSI}{\tau_S} \cdot t \cdot e^{-t/\tau_S}$$

respectively determines the excitatory, dendritic inhibitory and somatic inhibitory average postsynaptic membrane potential (Figure 23.13). Lumped parameters EXC, SDI and FSI define the amplitude of the average postsynaptic membrane potential. Lumped parameters  $\tau_E$ ,  $\tau_D$  and  $\tau_S$  are time constant parameters that account for both the average decay time of sPSP and average distributed delays in the dendritic tree. In each subset, in turn, a static non-linear function (asymmetric sigmoid curve  $S(v) = 2e_0/[1 + e^{r(v_0-v)}]$ ) is used to model threshold and saturation effects in the relationship between the average postsynaptic potential and the average pulse density of action potentials fired by the neurons in a given subset. Interactions between main cells and local neurons are summarized in the model by connectivity constants (C1 to C7) which account for the average number of synaptic contacts.

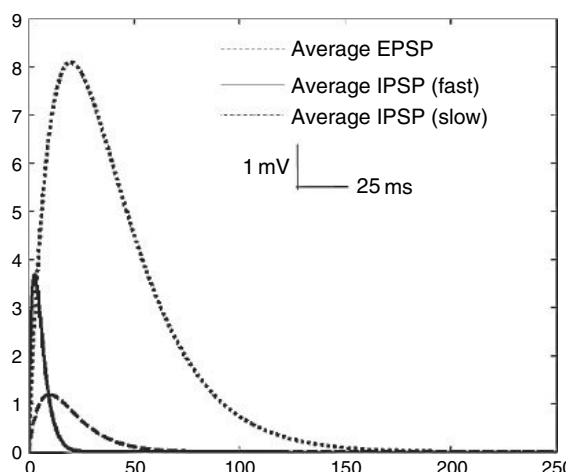


FIGURE 23.13 Time-course of average postsynaptic membrane potentials: excitatory, slow inhibitory and fast inhibitory respectively corresponding to impulse responses of functions  $h_{EXC}(t)$ ,  $h_{SDI}(t)$  and  $h_{FSI}(t)$  in which parameters EXC, SDI and FSI (synaptic gains) are set to standard values (see Table 23.3).

**TABLE 23.3** Parameters, interpretation and values in the model of neuronal population adapted to hippocampus

Parameter	Interpretation	Value
<i>EXC</i>	Average excitatory synaptic gain	$3.25\text{ mV}$
<i>SDI</i>	Average inhibitory synaptic gain (slow dendritic inhibition loop)	$22\text{ mV}$
<i>FSI</i>	Average inhibitory synaptic gain (fast somatic inhibition loop)	$20\text{ mV}$
$\tau_E$	Time constant of average excitatory postsynaptic potentials	$\tau_E = 10\text{ ms}$
$\tau_D$	Time constant of average inhibitory postsynaptic potentials	$\tau_D = 35\text{ ms}$
$\tau_S$	Time constant of the filter used to model the time delay associated to connections from considered population	$\tau_S = 5\text{ ms}$
$C_5, C_6$	Average number of synaptic contacts in the fast feedback inhibitory loop	$C_5 = C_6 = 0.1C$
$C_7$	Average number of synaptic contacts in the connection between slow and fast inhibitory interneurons	$C_7 = 0.8C$
$C_1, C_2, C_3, C_4, v_0, e_0, r, p(t)$	See Table 23.2	See Table 23.2

Finally, using the same procedure as in the previous model, a reduced set of 10 first order ordinary differential equations (two differential equations per ‘*h* function’) can be derived from the block diagram representation:

$$\begin{cases} \dot{y}_0(t) = y_5(t) \\ \dot{y}_5(t) = EXC.aS(y_1(t) - y_2(t) - y_3(t)) - 2ay_5(t) - a^2y_0(t) \\ \dot{y}_1(t) = y_6(t) \\ \dot{y}_6(t) = EXC.a \{p(t) + C_2S[C_1y_0(t)]\} - 2ay_6(t) - a^2y_1(t) \\ \dot{y}_2(t) = y_7(t) \\ \dot{y}_7(t) = SDI.bC_4S[C_3y_0(t)] - 2by_7(t) - b^2y_2(t) \\ \dot{y}_3(t) = y_8(t) \\ \dot{y}_8(t) = FSI.gC_7S[C_5y_0(t) - C_6y_4(t)] - 2gy_8(t) - g^2y_3(t) \\ \dot{y}_4(t) = y_9(t) \\ \dot{y}_9(t) = SDI.b[S(C_3y_0(t)] - 2by_9(t) - b^2y_4(t) \end{cases}$$

with  $a = 1/\tau_E$ ,  $b = 1/\tau_D$  and  $g = 1/\tau_S$ .

This set must be solved by numerical integration methods adapted to its stochastic nature (random noise input  $p(t)$ ). Model parameter values are given in Table 23.3.

### Results obtained from identification of model parameters

In the model, three key parameters, namely EXC, SDI and FSI, are directly related to excitatory and inhibitory synaptic interactions between subsets of cells. The goal of this section is to interpret, with respect to the temporal evolution of these three parameters, real EEG signals recorded from human hippocampus during the transition to seizure. As illustrated in Figure 23.14, the modification of these parameters shows that strikingly realistic activities are produced by the model when compared to real SEEG signals (see description above). High similarities between simulated and real signals are observed not only in the temporal dynamics, but also in the spectral content of signals, quantified by the PSD. The model produces five different types of activity. Type 1 and type 2 (Figure 23.14A and B) respectively correspond to normal background activity and sporadic spikes as observed in real signals during interictal or pre-onset periods. Type 3 (Figure 23.14C) is a faster activity (beta and low gamma frequency bands) similar to fast onset activity generally observed in hippocampus at the beginning of seizures. Type 4 (Figure 23.14D) is a narrow band activity (quasi-sinusoidal) with a dominant frequency around 9 Hz. In hippocampus, this ictal activity generally follows fast onset activity. Finally, type 5 (Figure 23.14E) corresponds to a sustained spiking activity in the theta frequency band (3–4 Hz). In real recordings, rhythmic spikes can be observed during pre-onset periods as well as during ictal periods, generally before seizure termination.

This first step shows that described classes of activity depend on the three main parameters of the model (EXC, SDI and FSI). These parameters respectively correspond to excitatory, slow inhibitory and fast inhibitory synaptic gains in feedback loops from interneurons to pyramidal cells and in the control of fast inhibitory interneurons by slow ones.

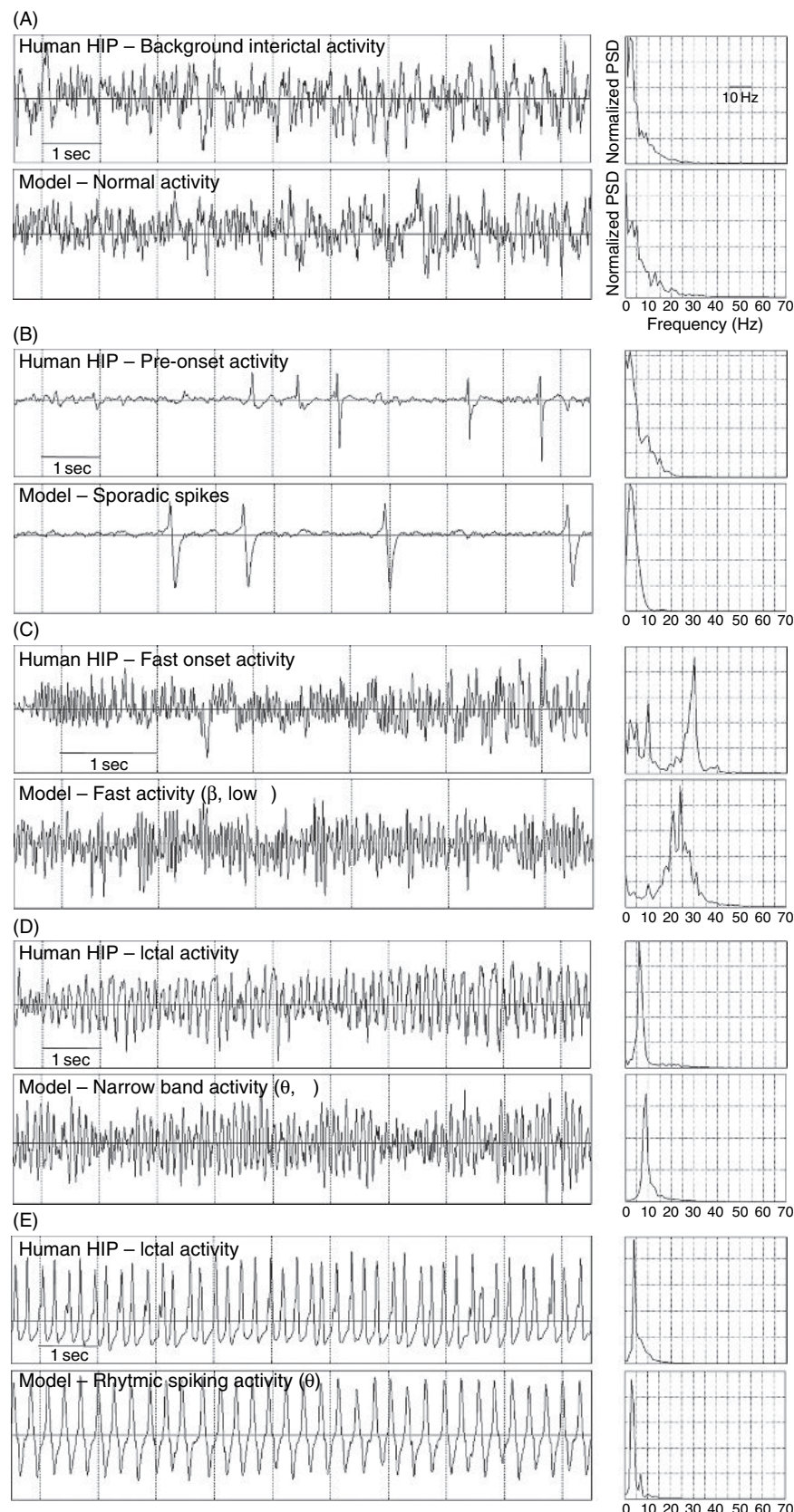


**FIGURE 23.14** Comparison between real activities recorded in human hippocampus and simulated activities produced by the model. (A) Normal background activity, (B) sporadic spikes, (C) fast onset activity generally observed in hippocampus at the beginning of seizures, (D) narrow band activity (quasi-sinusoidal) and (E) sustained spiking activity.

In a second step, dynamical changes observed in real signals (during transition to seizure activity) can be interpreted in terms of time variation of these excitation-/inhibition-related parameters. This step requires a parameter sensitivity study of the model that is detailed in Wendling et al. (2002). In brief, it uses an exhaustive procedure aimed at uncovering from simulations disjoint regions in the space of free parameters, each region being associated with a particular type of model activity. As the parameter space is of dimension 3, the plane (SDI, FSI) is explored by varying SDI and FSI values, step-by-step, for given values of parameter EXC. The signal that is simulated for each triplet (EXC, SDI, FSI) is automatically classified among the five classes of activity described above. Finally, the association of a specific color to each class of activity allows for graphical representation of results in the form of colored diagrams, referred to as ‘activity maps’. These results are displayed in Figure 23.15. They summarize the behavior of the model as a function of variations of parameters EXC, SDI and FSI. They were obtained from 9000 simulations of 10 seconds of activity (SDI = 1.50, FSI = 1.30 for EXC = 2, 3, 4, 5, 6 and 7).

From global analysis, several remarks can be made on activity maps. For low excitation (low values of parameter EXC), the model generates only normal EEG activity. Other types of activity appear for increased excitation. In particular, regions corresponding to fast activity and to rhythmic spiking activity expand as parameter EXC increases. The region associated with sporadic spikes is quite narrow and is at the border between normal and spiking activity, as expected. Activity maps also reveal that the transition to fast ictal activity observed in human hippocampus corresponds, in the model, to a shift from right to left along the SDI axis (blue region to yellow region), denoting a decrease of dendritic inhibition.

Activities reflected in real signals as well as transitions between activities encountered in real cases can be interpreted as possible paths connecting corresponding colored regions on activity maps elaborated from the model. An example is illustrated in Figure 23.15, where a candidate path is reported on the fourth map. This path is consistent with the typical sequence of activities reflected in real SEEG signals during the transition to seizure: normal background activity (1), sporadic spikes (2), rhythmic spikes (3), fast activity (4), ictal activity (5), as shown in Figure 23.16A. It also provides parameter variations. The initial step (1) corresponds to increased EXC parameter with respect to normal value and to standard SDI and FSI values. It is followed by three consecutive drops of dendritic inhibition with constant somatic inhibition (2, 3, 4) and by a re-increase of dendritic inhibition with decreased somatic inhibition (5). These gain profiles (Figure 23.16B) are then used in the model to simulate the time-series signal shown in Figure 23.16C. As expected, the gradual decrease of the slow inhibition level leads the model to generate sporadic spikes followed by sustained spikes comparable to those observed during the interictal to pre-onset phase in human hippocampus. Then, the third decrease leads the model to generate fast activity (beta and low gamma bands) similar to that observed at seizure onset. Finally, the slower narrow band activity (5–10 Hz) is observed when fast inhibition weakens and slow inhibition re-increases. Power spectral densities computed on real and simulated signals are compared in Figure 23.15D. They show that spectral contents of real and simulated signals are close over considered pseudo-stationary periods.

Results presented above were confirmed by a recent study in which model parameters EXC, SDI and FSI were directly identified from real signals in five patients with mesial TLE. An example is given in Figure 23.17. Readers may refer to Wendling et al. (2005) for detailed information. In brief, the identification procedure used optimization algorithms to minimize a spectral distance between real and simulated signals. The model was found to generate very realistic signals for automatically identified parameters. The evolution of model parameters was found to be consistent with results presented in this section and also reproducible among patients, as shown in Table 23.4. Results demonstrated that the transition from interictal to ictal activity cannot be merely explained by an increase in excitation and a decrease in inhibition, but rather by time-varying ensemble interactions between pyramidal cells and interneurons with slow and fast GABA<sub>A</sub> receptor kinetics. In particular, the identification procedure reveals an increase of excitation during the pre-onset period (10–50 seconds before seizure onset), an abrupt drop of dendritic inhibition at seizure onset with a crucial role of perisomatically projecting interneurons in the generation of fast onset activity.

## Discussion

On the basis of experimental data about cellular organization in the hippocampus, a physiologically relevant neuronal population model was elaborated. Main features include an excitatory loop as well as two parallel inhibitory circuits that represent the two separate populations of GABAergic interneurons that contact anatomically segregated postsynaptic receptors (dendritic/somatic region, GABA<sub>A,slow</sub>/GABA<sub>A,fast</sub>). The model can accurately reproduce various types of signal dynamics recorded in human hippocampus over interictal and ictal periods, qualitatively and quantitatively. This result, in line with other research studies conducted over the past decades, shows that macroscopic models can be specifically adapted to brain structures. Following this idea, a model lying at the same level was recently proposed for the entorhinal cortex by our group and was experimentally evaluated in an isolated brain preparation (Labyt et al., 2006).

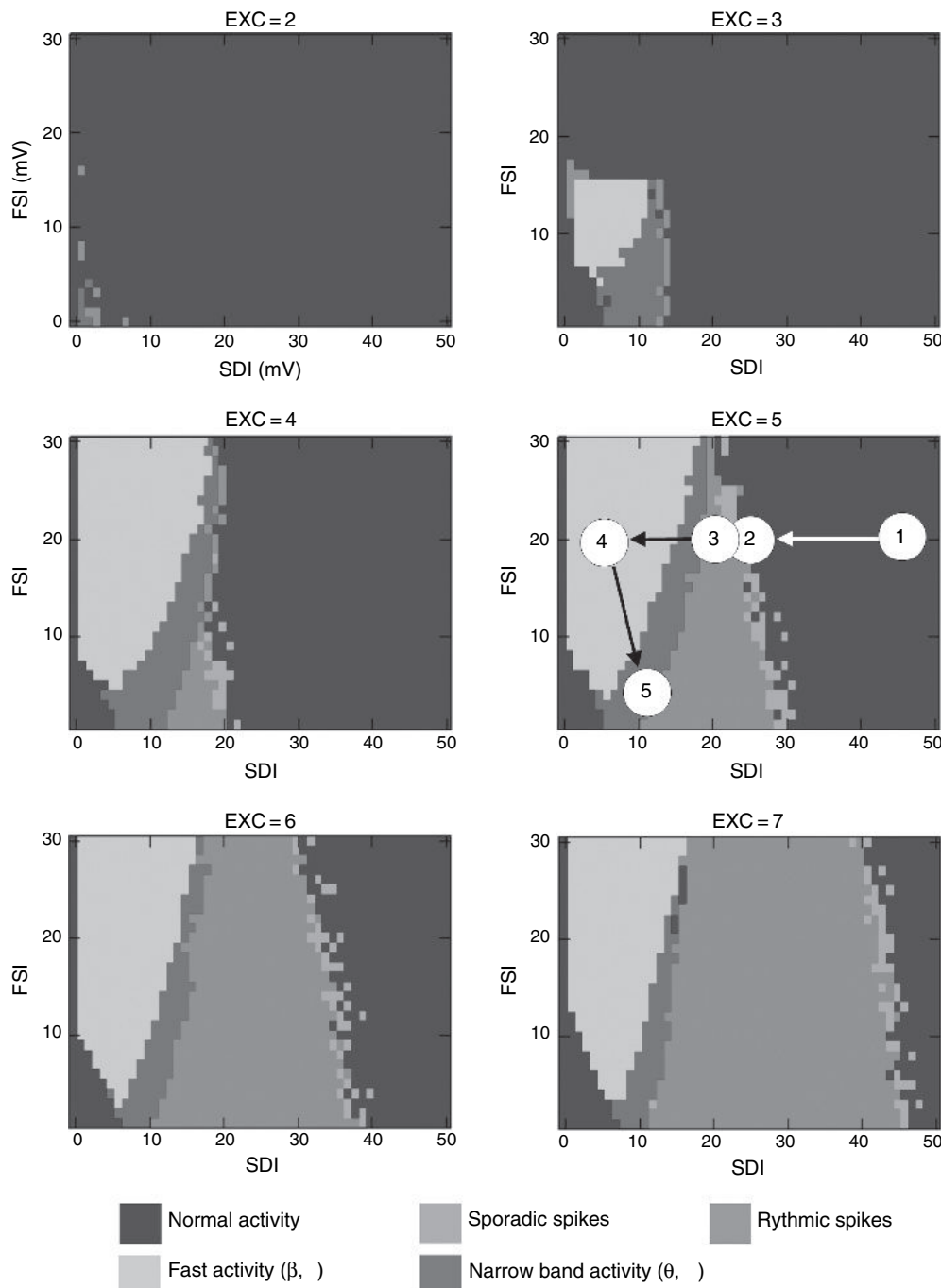


**FIGURE 23.15** Activity maps describing the behavior of the hippocampus model as a function of variations of parameters EXC, SDI and FSI. On the fourth map, a candidate path is reported, consistent with the typical sequence of activities reflected in real SEEG signals during the transition to seizure: normal background activity (1), sporadic spikes (2), rhythmic spikes (3), fast activity (4) and ictal activity (5). This path provides a way to identify parameter variations for which dynamics and transitions observed in real signals are reproduced by the model. See text for interpretation of identified parameters. See also Figure 23.16. (See Plate 14 in color plate section.)

For the hippocampus, identification procedures lead to reproducible modifications of model parameters related to excitation, slow dendritic inhibition and fast somatic inhibition over interictal, pre-onset, onset and ictal periods. In the following, these results are discussed with respect to current hypotheses about possible mechanisms involved in epileptogenesis or ictogenesis.

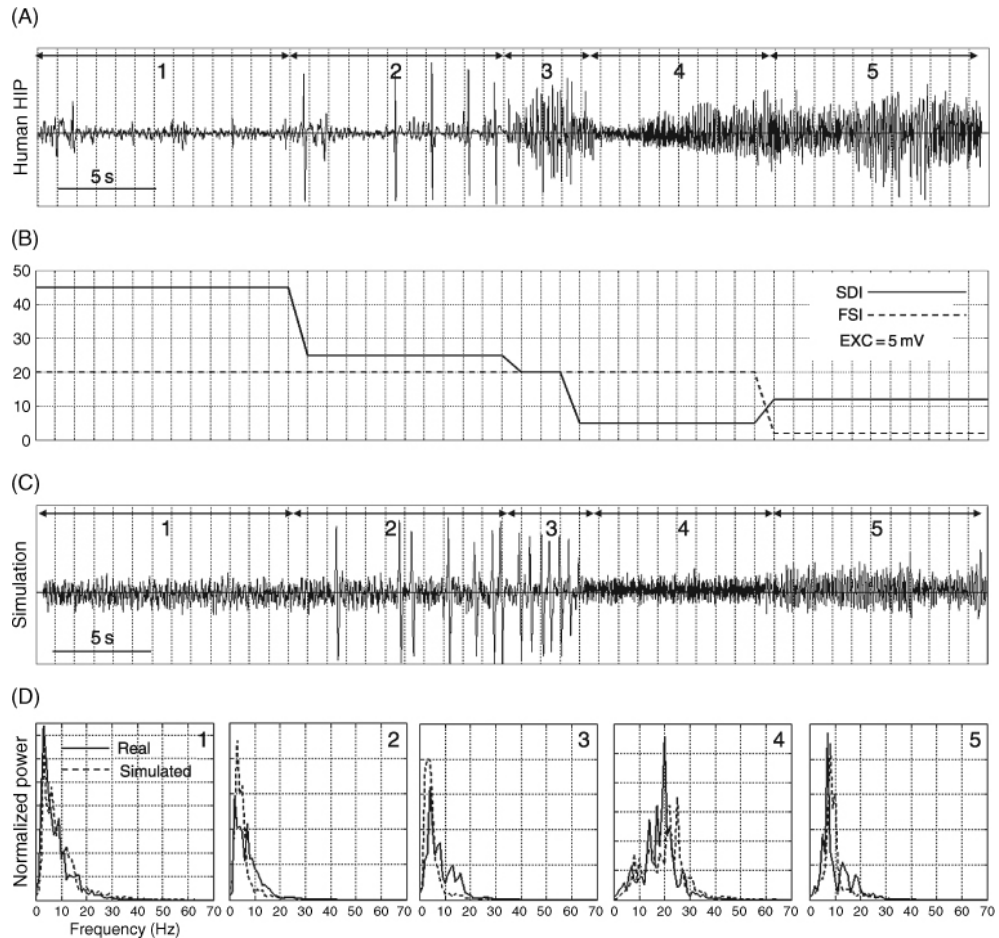


**FIGURE 23.16** Model-based interpretation of SEEG signals during the transition to seizure in TLE. (A) Intracerebral recording in human hippocampus. Five phases (1 to 5) are distinguished according to the pseudo-stationary nature of the activities reflected by the signal: interictal activity (1), high-amplitude spikes during preonset period (2, 3), fast activity (4) at seizure onset and quasi-sinusoidal ictal activity (5). (B) Evolution of slow and fast inhibition parameters (SDI, FSI) defined from a candidate path (see Plate 14) and used in the model to simulate a time-series signal (C). (D) Dynamics reflected in the simulated signal and transitions of dynamics match those observed. (E) Normalized power spectral densities of real (solid line) and simulated (dotted line) signals.

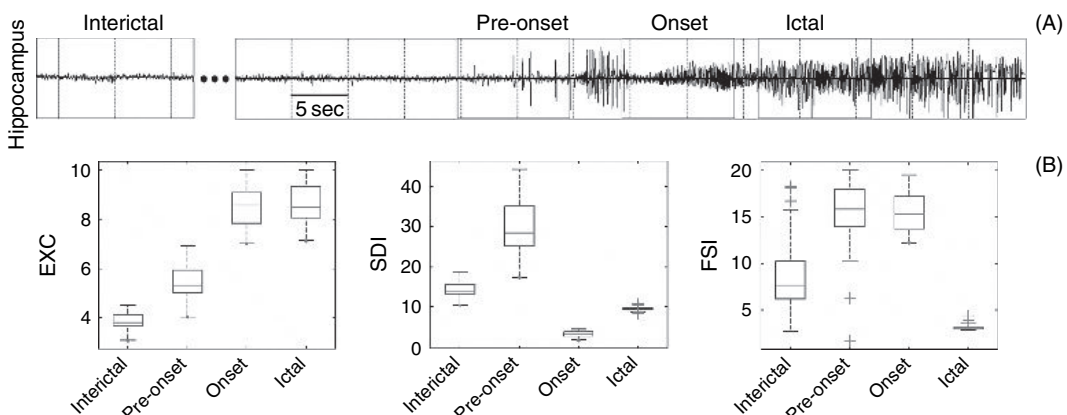


**FIGURE 23.17** Parameter identification results using a procedure based on evolutionary algorithms (see Wendling et al., 2005 for details). (A) Visually selected segments of EEG signals during transition to seizure recorded from hippocampus in a patient with medial TLE. (B) Boxplots are calculated from 30 independent realizations of the identification process for each segment of real activity. Results show the stability of the identified solutions and depict a global tendency in the evolution (as a function of time) of the main model parameters (EXC, SDI and FSI). (See Plate 15 in color plate section.)

**TABLE 23.4** Results obtained from a parameter identification procedure based on evolutionary algorithms about the evolution of EXC, SDI, FSI parameters of the hippocampus model (see Wendling et al., 2005 for details). Parameter evolution with respect to the type of transition is indicated by arrows (significant increase: ‘↗’, significant decrease: ‘↘’, no significant change: ‘↔’). Similar changes found in the five studied cases (patients with mesial TLE) are highlighted (gray color).

	EXC			SDI			FSI		
	interICTAL to preONSET	preONSET to ONSET	ONSET to ICTAL	interICTAL to preONSET	preONSET to ONSET	ONSET to ICTAL	interICTAL to preONSET	preONSET to ONSET	ONSET to ICTAL
Patient 1	↗	↗	↔	↗	↘	↗	↗	↔	↗
Patient 2	↗	↗	↗	↗	↘	↗	↔	↔	↗
Patient 3	↔	↗	↗	↗	↘	↗	↔	↔	↗
Patient 4	↔	↗	↔	↗	↘	↗	↔	↔	↗
Patient 5	↗	↗	↔	↗	↘	↗	↔	↔	↗

Regarding increased excitation from interictal to pre-onset and ictal activity, enhanced excitability may be caused by intrinsic and/or extrinsic factors. In the present study, parameter changes may only be related to intrinsic mechanisms, although exogenous factors, such as the enhancement of the direct entorhinal cortex input to CA1, can play a role in excitability changes in the hippocampus, as reported in Wu and Leung (2003). Results suggest that average excitatory synaptic gain in feedback loops that link pyramidal cells to local cells increases within the considered neuronal population during the transition from interictal to ictal activity. Several studies performed in experimental models of focal epilepsy (Bernard et al., 2001; Gorter et al., 2002) or performed in slices from human brain (Schwartzkroin, 1994) have already demonstrated that epileptic discharge patterns are correlated with prolonged and/or enhanced EPSPs. However, very few studies have attempted to relate them to gradual changes observed at the EEG level during the transition to seizure, as done here through the model of hippocampus. Indeed, excitation enhancement constitutes a necessary condition in the model to explain the appearance of interictal sporadic spikes. The excitation level must also stay high to get fast oscillations and theta-like ictal activity on simulated EEGs.

So far as decrease of slow dendritic inhibition at seizure onset is concerned, it can be hypothesized that a point is reached where inhibitory interneurons cannot compensate anymore for the increased excitation and where provided inhibition collapses due to a ‘fatigue process’. This hypothesis relates to the concept of ‘fragile inhibition’ proposed by Wu and Leung (2001). From a current source density analysis of the dentate gyrus (DG) in the kainic acid (KA) model of temporal lobe epilepsy, authors showed that the relatively strong inhibition in the DG of KA-treated rats can breakdown readily in the presence of a low dose of GABA<sub>A</sub> receptor antagonist. They concluded that the compensatory inhibition in the brain in animals and humans with temporal lobe seizures is vulnerable, although underlying mechanisms have not been clearly identified.

The generation of fast oscillations is explained, in the model, by the presence of a fast feedback inhibitory loop which is necessary to reproduce rapid discharges observed in the hippocampus at seizure onset. This result suggests that observed fast oscillations are mainly related to the activity of inhibitory interneurons targeting pyramidal cells in their perisomatic region (presence of GABA<sub>A</sub> receptor with faster kinetics). This hypothesis of EEG fast oscillations related to fast inhibitory interneurons is supported by several other studies on normal neuronal tissue. In Penttonen et al. (1998), results suggested that high frequency oscillations may reflect rhythmic postsynaptic potentials in hyperpolarized pyramidal cells brought about by rhythmically discharging somatic-projecting interneurons. White et al. (2000) also ended with the conclusion that GABA<sub>A,slow</sub> and GABA<sub>A,fast</sub> interneurons exist as two different populations and that both play a role in the generation of theta and gamma rhythms (CA1 region) using a combined computational/experimental approach (detailed model and experimental data obtained from hippocampal slices in rats). More recently, similar findings were reported by Hajos and colleagues (Hajos et al., 2004) who performed current source density analysis in the rat intact hippocampus during awake, attentive behavior. Their results support the hypothesis that gamma oscillations are explained by a synaptic feedback model that primarily involves pyramidal cells and perisomatic-projecting inhibitory interneurons.

After seizure onset, a rhythmic activity (quasi-sinusoidal or spiking, generally in the theta band) is typically observed in recorded EEG signals as the seizure develops and generally involves other mesial structures. In the model presented in this section, hypotheses about interactions between populations distributed over distant brain structures are not taken into

account. However, regarding ictal activity in the hippocampus, two remarks can be made. First, the transition from rapid to rhythmic theta-like activity is explained, in the model, by the exhaustion of fast inhibitory processes. Second, seizure activity seems to correspond to a situation where inhibition level is globally reduced compared to excitation.

### GENERAL CONCLUSION

In this chapter, neurophysiologically relevant computational models were described and used to generate hypotheses about the possible mechanisms involved in the transition from interictal to ictal EEG activity. These models consist in macroscopic representations of neuronal populations composed of principal cells and interneurons that interact through either excitatory or inhibitory connections. The first generic model of EEG generation we presented was shown to produce paroxysmal signals that qualitatively compare to those recorded in epileptic patients using intracerebral electrodes. However, this model was also shown to be incomplete as the fast activity often observed in brain structures at seizure onset was not represented. Such inconsistencies are often encountered in the process of modeling and point towards necessary model improvements. As fast activity is generally observed in mesial TLE at the beginning of ictal periods, we focused on the hippocampus and proposed an extension to the first model based on the CA1 subfield macroscopic neuronal organization (subsets of neurons and topology).

In this new model, parameter identification procedures led to results demonstrating that the transition from interictal to ictal activity can be explained by time-varying synaptic interactions between pyramidal cells and interneurons with slow and fast GABA<sub>A</sub> kinetics. In particular, the model predicts an abrupt drop of dendritic inhibition at seizure onset when fast oscillations appear in recorded EEG with a crucial role of perisomatically projecting interneuronal populations.

This computational modeling approach offers the unique opportunity to relate typical electrophysiological patterns – recorded with SEEG electrodes during the transition from interictal to ictal activity in the human hippocampus – to ictogenesis mechanisms. As in any model, some assumptions are made and lead to necessary simplifications of real systems under study. Regarding the models described in this chapter, the major simplification relates to the macroscopic level that does not allow for interpretation of observed signals at microscopic level (i.e. cellular or subcellular). However, in the context of intracerebral EEG signals interpretation, macroscopic representation offers at least two advantages. First, the neuronal population level is well adapted to the nature of clinical observations: simulated signals can be directly compared with real intracerebral EEG signals recorded with macroelectrodes in human drug-resistant partial epilepsies. Second, neuronal population models allowed us to investigate ensemble interactions between main cells and interneurons within the hippocampal formation and to study the relationship between their time course on the one hand, and transitions of temporal dynamics observed in real EEG signals, on the other hand.

Interestingly, this modeling approach conducted on human data led to results that corroborated experimental findings obtained in animal models. This is a unique feature of models that can also be seen as a way to establish bridges between clinical and basic research in epilepsy. The evaluation and the validation of computational models still remains a key issue in modeling studies. In this perspective, combined theoretical/experimental approaches can confirm predictions from proposed models and thus increase confidence in these models. They offer an optimal framework for model validation procedures that can, in turn, motivate the design of new experiments in order either to refute hypotheses or discern between competing ones. Advances in epilepsy research will certainly come from this combination between modeling and experimentation, but also from strong interaction with clinical data as the primary objective is still to progress in the understanding of human epilepsies.

### REFERENCES

- Allen, P.J., Fish, D.R. and Smith, S.J. (1992). Very high-frequency rhythmic activity during SEEG suppression in frontal lobe epilepsy. *Electroencephalogr Clin Neurophysiol* 82(2):155–159.
- Bancaud, J. (1980). Surgery of epilepsy based on stereotactic investigations – the plan of the SEEG investigation. *Acta Neurochir Suppl (Wien)* 30:25–34.
- Bancaud, J., Talairach, J., Geier, S. and Scarabin, J. (1973). *EEG et SEEG dans les tumeurs cérébrales et l'épilepsie*. Edifor, editor. Paris.
- Banks, M.I., Li, T.B. and Pearce, R.A. (1998). The synaptic basis of GABA<sub>A</sub>,slow. *J Neurosci* 18(4):1305–1317.
- Banks, M.I., White, J.A. and Pearce, R.A. (2000). Interactions between distinct GABA(A) circuits in hippocampus. *Neuron* 25(2):449–457.
- Bartolomei, F., Wendling, F., Vignal, J.P. et al. (1999). Seizures of temporal lobe epilepsy: identification of subtypes by coherence analysis using stereo-electro-encephalography. *Clin Neurophysiol* 110(10):1741–1754.

- Bartolomei, F., Wendling, F., Bellanger, J.J., Regis, J. and Chauvel, P. (2001). Neural networks involving the medial temporal structures in temporal lobe epilepsy. *Clin Neurophysiol* 112(9):1746–1760.
- Bartolomei, F., Wendling, F., Regis, J., Gavaret, M., Guye, M. and Chauvel, P. (2004). Pre-ictal synchronicity in limbic networks of mesial temporal lobe epilepsy. *Epilepsy Res* 61(1–3):89–104.
- Bernard, C., Marsden, D.P. and Wheal, H.V. (2001). Changes in neuronal excitability and synaptic function in a chronic model of temporal lobe epilepsy. *Neuroscience* 103(1):17–26.
- Bourien, J., Bartolomei, F., Bellanger, J.J., Gavaret, M., Chauvel, P. and Wendling, F. (2005). A method to identify reproducible subsets of co-activated structures during interictal spikes. Application to intracerebral EEG in temporal lobe epilepsy. *Clin Neurophysiol* 116(2):443–455.
- Bragin, A., Engel, J. Jr, Wilson, C.L., Fried, I. and Buzsaki G. (1999). High-frequency oscillations in human brain. *Hippocampus* 9(2):137–142.
- Buchanan, J.A. and Bilkey, D.K. (1997). Transfer of epileptogenesis between perirhinal cortex and amygdala induced by electrical kindling. *Brain Res* 771(1):71–79.
- Burgerman, R.S., Sperling, M.R., French, J.A., Saykin, A.J. and O'Connor, M.J. (1995). Comparison of mesial versus neocortical onset temporal lobe seizures: neurodiagnostic findings and surgical outcome. *Epilepsia* 36(7):662–670.
- Chauvel, P., Buser, P., Badier, J.M., Liegeois-Chauvel, C., Marquis, P. and Bancaud, J. (1987). {The ‘epileptogenic zone’ in humans: representation of intercritical events by spatio-temporal maps}. *Rev Neurol (Paris)* 143(5):443–450.
- Commission on Classification and Terminology of the International League Against Epilepsy (1989). Proposal for revised classification of epilepsies and epileptic syndromes. *Epilepsia* 30(4):389–399.
- Cossart, R., Dinocourt, C., Hirsch, J.C. et al. (2001). Dendritic but not somatic GABAergic inhibition is decreased in experimental epilepsy. *Nat Neurosci* 4(1):52–62.
- David, O. and Friston, K.J. (2003). A neural mass model for MEG/EEG: coupling and neuronal dynamics. *Neuroimage* 20(3):1743–1755.
- David, O., Cosmelli, D. and Friston, K.J. (2004). Evaluation of different measures of functional connectivity using a neural mass model. *Neuroimage* 21(2):659–673.
- Dichter, M.A. (1997). Basic mechanisms of epilepsy: targets for therapeutic intervention. *Epilepsia* 38 Suppl 9:S2–6.
- Ebner, A. (1994). Lateral (neocortical) temporal lobe epilepsy. In: *Epileptic seizures and syndromes* (P. Wolf, ed.) pp. 375–382. John Libbey and Co, London.
- Engel, J. Jr, Babb, T.L. and Crandall, P.H. (1989). Surgical treatment of epilepsy: opportunities for research into basic mechanisms of human brain function. *Acta Neurochir Suppl (Wien)* 46:3–8.
- Engel, J., VanNess, P., Rasmussen, T. and Ojemann, L. (1993). Outcome with respect to epileptic seizures. In: *Surgical treatment of the epilepsies*, 2nd edn (J. Engel, ed.) pp. 609–622. Raven Press, New York.
- Fish, D.R., Gloor, P., Quesney, F.L. and Olivier, A. (1993). Clinical responses to electrical brain stimulation of the temporal and frontal lobes in patients with epilepsy. Pathophysiological implications. *Brain* 116 ( Pt 2):397–414.
- Freeman, W.J. (1963). The electrical activity of a primary sensory cortex: analysis of EEG waves. *Int Rev Neurobiol* 5:53–119.
- Freeman, W.J. (1968). Patterns of variation in waveform of averaged evoked potentials from prepyriform cortex of cats. *J Neurophysiol* 31(1):1–13.
- Freeman, W.J. (1973). A model of the olfactory system. In: *Neural modeling* M.A.B. Brazier, D.O. Walter and D. Schneider, eds) pp. 41–62. University of California, Los Angeles.
- Freeman, W.J. (1987). Simulation of chaotic EEG patterns with a dynamic model of the olfactory system. *Biol Cybern* 56(2–3):139–150.
- Freeman, W.J. (1992). Tutorial on neurobiology: from single neurons to brain chaos. *Int J Bifurcation Chaos* 2(3):451–482.
- French, J.A., Williamson, P.D., Thadani, V.M. et al. (1993). Characteristics of medial temporal lobe epilepsy: I. Results of history and physical examination. *Ann Neurol* 34(6):774–780.
- Gloor, P. (1990). Experiential phenomena of temporal lobe epilepsy. Facts and hypotheses. *Brain* 113 ( Pt 6):1673–1694.
- Gorter, J.A., van Vliet, E.A., Aronica, E. and Lopes da Silva, F.H. (2002). Long-lasting increased excitability differs in dentate gyrus vs. CA1 in freely moving chronic epileptic rats after electrically induced status epilepticus. *Hippocampus* 12(3):311–324.
- Hajos, N., Palhalmi, J., Mann, E.O., Nemeth, B., Paulsen, O. and Freund, T.F. (2004). Spike timing of distinct types of GABAergic interneuron during hippocampal gamma oscillations in vitro. *J Neurosci* 24(41):9127–9137.
- Houser, C.R. and Esclapez, M. (1996). Vulnerability and plasticity of the GABA system in the pilocarpine model of spontaneous recurrent seizures. *Epilepsy Res* 26(1):207–218.
- Hubel, D.H. and Wiesel, T.N. (1963). Shape and arrangement of columns in cat's striate cortex. *J Physiol* 165:559–568.
- Hubel, D.H. and Wiesel, T.N. (1965). Receptive fields and functional architecture in two nonstriate visual areas (18 and 19) of the cat. *J Neurophysiol* 28:229–289.
- Jansen, B.H. and Rit, V.G. (1995). Electroencephalogram and visual evoked potential generation in a mathematical model of coupled cortical columns. *Biol Cybern* 73(4):357–366.
- Jansen, B.H., Zouridakis, G. and Brandt, M.E. (1993). A neurophysiologically-based mathematical model of flash visual evoked potentials. *Biol Cybern* 68(3):275–283.
- Jefferys, J.G. (1990). Basic mechanisms of focal epilepsies. *Exp Physiol* 75(2):127–162.
- Jefferys, J.G. (2003). Models and mechanisms of experimental epilepsies. *Epilepsia* 44 Suppl 12:44–50.
- Jefferys, J.G. and Whittington, M.A. (1996). Review of the role of inhibitory neurons in chronic epileptic foci induced by intracerebral tetanus toxin. *Epilepsy Res* 26(1):59–66.
- Jirsch, J.D., Urrestarazu, E., LeVan, P., Olivier, A., Dubeau, F. and Gotman, J. (2006). High-frequency oscillations during human focal seizures. *Brain* 129(Pt 6):1593–1608.
- Koepf, M.J. and Woermann, F.G. (2005). Imaging structure and function in refractory focal epilepsy. *Lancet Neurol* 4(1):42–53.
- Labey, E., Uva, L., de Curtis, M. and Wendling, F. (2006). Realistic modeling of entorhinal cortex field potentials and interpretation of epileptic activity in the guinea pig isolated brain preparation. *J Neurophysiol* 96(1):363–377.
- Lopes da Silva, F. (2002). Electrical potentials. In: *Encyclopedia of the human brain*, vol. 2 (V.S. Ramachandran, ed.) pp. 147–67. New York.

- Lopes da Silva, F.H., Hoeks, A., Smits, H. and Zetterberg, L.H. (1974). Model of brain rhythmic activity. The alpha-rhythm of the thalamus. *Kybernetik* 15(1):27–37.
- Lopes da Silva, F.H., Pijn, J.P. and Wadman, W.J. (1994). Dynamics of local neuronal networks: control parameters and state bifurcations in epileptogenesis. *Prog Brain Res* 102:359–370.
- Lopes da Silva, F.H., van Rotterdam, A., Barts, P., van Heusden, E. and Burr, W. (1976). Models of neuronal populations: the basic mechanisms of rhythmicity. *Prog Brain Res* 45:281–308.
- Lopes da Silva, F.H., Blanes, W., Kalitzin, S.N., Parra, J., Suffczynski, P. and Velis, D.N. (2003). Dynamical diseases of brain systems: different routes to epileptic seizures. *IEEE Trans Biomed Eng* 50(5):540–548.
- McNamara, J.O. (1994). Cellular and molecular basis of epilepsy. *J Neurosci* 14(6):3413–3425.
- Miles, R., Toth, K., Gulyas, A.I., Hajos, N. and Freund, T.F. (1996). Differences between somatic and dendritic inhibition in the hippocampus. *Neuron* 16(4):815–823.
- Morrell, M. (2006). Brain stimulation for epilepsy: can scheduled or responsive neurostimulation stop seizures? *Curr Opin Neurol* 19(2):164–168.
- Mountcastle, V.B. (1957). Modality and topographic properties of single neurons of cat's somatic sensory cortex. *J Neurophysiol* 20(4):408–434.
- Niedermeyer, E. and Lopes Da Silva, F. (eds) (1998). *Electroencephalography: basic principles, clinical applications, and related fields*. Lippincott, Williams & Wilkins.
- Penttonen, M., Kamondi, A., Acsady, L. and Buzsaki, G. (1998). Gamma frequency oscillation in the hippocampus of the rat: intracellular analysis *in vivo*. *Eur J Neurosci* 10(2):718–728.
- Prince, D. (1993). Basic mechanisms of focal epileptogenesis. In: *Epiletogenic and excitotoxic mechanisms* (G. Avanzini, R. Fariello, U. Heinemann and R. Mutani, eds) pp. 17–27. John Libbey & Company Ltd, London.
- Schwartzkroin, P.A. (1994). Cellular electrophysiology of human epilepsy. *Epilepsy Res* 17(3):185–192.
- Spencer, S.S., Guimaraes, P., Katz, A., Kim, J. and Spencer, D. (1992). Morphological patterns of seizures recorded intracranially. *Epilepsia* 33(3):537–545.
- Suffczynski, P., Kalitzin, S., Pfurtscheller, G. and Lopes da Silva, F.H. (2001). Computational model of thalamo-cortical networks: dynamical control of alpha rhythms in relation to focal attention. *Int J Psychophysiol* 43(1):25–40.
- Suffczynski, P., Lopes da Silva, F.H., Parra, J. et al. (2006a). Dynamics of epileptic phenomena determined from statistics of ictal transitions. *IEEE Trans Biomed Eng* 53(3):524–532.
- Suffczynski, P., Wendling, F., Bellanger, J.-J. and Da Silva, F.H.L. (2006b). Some insights into computational models of (patho)physiological brain activity. *Proc IEEE* 94(4):784–804.
- Thomson, A.M. and Radpour, S. (1991). Excitatory connections between CA1 pyramidal cells revealed by spike triggered averaging in slices of rat hippocampus are partially NMDA receptor mediated. *Eur J Neurosci* 3(6):587–601.
- Traub, R.D. (1979). Neocortical pyramidal cells: a model with dendritic calcium conductance reproduces repetitive firing and epileptic behavior. *Brain Res* 173(2):243–257.
- Traub, R.D. (1982). Simulation of intrinsic bursting in CA3 hippocampal neurons. *Neuroscience* 7(5):1233–1242.
- Traub, R.D. and Llinas, R. (1979). Hippocampal pyramidal cells: significance of dendritic ionic conductances for neuronal function and epileptogenesis. *J Neurophysiol* 42(2):476–496.
- Traub, R.D., Whittington, M.A., Buhl, E.H. et al. (2001). A possible role for gap junctions in generation of very fast EEG oscillations preceding the onset of, and perhaps initiating, seizures. *Epilepsia* 42(2):153–170.
- van Rotterdam, A., Lopes da Silva, F.H., van den Ende, J., Viergever, M.A. and Hermans, A.J. (1982). A model of the spatial-temporal characteristics of the alpha rhythm. *Bull Math Biol* 44(2):283–305.
- Velasco, A.L., Wilson, C.L., Babb, T.L. and Engel, J. Jr (2000). Functional and anatomic correlates of two frequently observed temporal lobe seizure-onset patterns. *Neural Plast* 7(1–2):49–63.
- Walczak, T.S. (1995). Neocortical temporal lobe epilepsy: characterizing the syndrome. *Epilepsia* 36(7):633–635.
- Wendling, F., Bellanger, J.J., Bartolomei, F. and Chauvel, P. (2000). Relevance of nonlinear lumped-parameter models in the analysis of depth-EEG epileptic signals. *Biol Cybern* 83(4):367–378.
- Wendling, F., Bartolomei, F., Bellanger, J.J. and Chauvel, P. (2002). Epileptic fast activity can be explained by a model of impaired GABAergic dendritic inhibition. *Eur J Neurosci* 15(9):1499–508.
- Wendling, F., Bartolomei, F., Bellanger, J.J., Bourien, J. and Chauvel, P. (2003). Epileptic fast intracerebral EEG activity: evidence for spatial decorrelation at seizure onset. *Brain* 126(Pt 6):1449–1459.
- Wendling, F., Hernandez, A., Bellanger, J.J., Chauvel, P. and Bartolomei, F. (2005). Interictal to ictal transition in human temporal lobe epilepsy: insights from a computational model of intracerebral EEG. *J Clin Neurophysiol* 22(5):343–356.
- White, J.A., Banks, M.I., Pearce, R.A. and Kopell, N.J. (2000). Networks of interneurons with fast and slow gamma-aminobutyric acid type A (GABA $A$ ) kinetics provide substrate for mixed gamma-theta rhythm. *Proc Natl Acad Sci USA* 97(14):8128–8133.
- Whittington, M.A., Traub, R.D., Faulkner, H.J., Stanford, I.M. and Jefferys, J.G. (1997). Recurrent excitatory postsynaptic potentials induced by synchronized fast cortical oscillations. *Proc Natl Acad Sci USA* 94(22):12198–12203.
- Wieser, H., Engel, J., Williamson, P., Babb, T. and Gloor, P. (1993). Surgically remediable temporal lobes syndromes. In: *Surgical treatment of the epilepsies*, 2nd edn (J. Engel Jr, ed.) pp. 49–63. Raven Press, New York.
- Williamson, P.D., French, J.A., Thadani, V.M. et al. (1993). Characteristics of medial temporal lobe epilepsy: II. Interictal and ictal scalp electroencephalography, neuropsychological testing, neuroimaging, surgical results, and pathology. *Ann Neurol* 34(6):781–787.
- Williamson, P.D., Thadani, V.M., French, J.A. et al. (1998). Medial temporal lobe epilepsy: videotape analysis of objective clinical seizure characteristics. *Epilepsia* 39(11):1182–1188.
- Wilson, C.L., Khan, S.U., Engel, J. Jr, Isokawa, M., Babb, T.L. and Behnke, E.J. (1998). Paired pulse suppression and facilitation in human epileptogenic hippocampal formation. *Epilepsy Res* 31(3):211–230.
- Wilson, H.R. and Cowan, J.D. (1972). Excitatory and inhibitory interactions in localized populations of model neurons. *Biophys J* 12(1):1–24.
- Worrell, G.A., Parish, L., Cranstoun, S.D., Jonas, R., Baltuch, G. and Litt, B. (2004). High-frequency oscillations and seizure generation in neocortical epilepsy. *Brain* 127(Pt 7):1496–1506.

- Wu, K. and Leung, L.S. (2001). Enhanced but fragile inhibition in the dentate gyrus in vivo in the kainic acid model of temporal lobe epilepsy: a study using current source density analysis. *Neuroscience* 104(2):379–396.
- Wu, K. and Leung, L.S. (2003). Increased dendritic excitability in hippocampal ca1 in vivo in the kainic acid model of temporal lobe epilepsy: a study using current source density analysis. *Neuroscience* 116(2):599–616.
- Zavaglia, M., Astolfi, L., Babiloni, F. and Ursino, M. (2006). A neural mass model for the simulation of cortical activity estimated from high resolution EEG during cognitive or motor tasks. *J Neurosci Methods*.
- Zetterberg, L.H., Kristiansson, L. and Mossberg, K. (1978). Performance of a model for a local neuron population. *Biol Cybern* 31(1):15–26.

# 24

## UNIFIED MODELING AND ANALYSIS OF PRIMARY GENERALIZED SEIZURES

P.A. ROBINSON, M. BREAKSPEAR AND J.A. ROBERTS

### ABSTRACT

This chapter reviews progress on physiologically-based mean-field modeling of cortical activity that has resulted in unified understanding of onsets and dynamics of primary generalized epileptic seizures. This approach treats the cortex as a continuous medium for the propagation of electrical activity, incorporating key anatomy and physiology such as separate neural populations, membrane biophysics, axonal propagation and delays, non-linear firing behavior and corticothalamic feedback. Analysis has demonstrated its validity for a wide range of measures of healthy states and has yielded specific predictions of seizure phenomena, including many properties of primary generalized seizures. Study of the model's linear instabilities and non-linear bifurcation properties has enabled the dynamics of the generalized absence and tonic-clonic seizures to be interrelated at a fundamental level. Its predictions have been confirmed by quantitative comparison with electrophysiological data.

### INTRODUCTION

Primary generalized seizures are pathological brain rhythms that involve all cortical regions and are associated with a gross disruption of cognition. The two main generalized seizures in humans are absence (petit mal) and tonic-clonic (grand mal). Tonic-clonic seizures are associated with markedly different pre- and post-ictal electroencephalograms (EEGs) and dynamically evolving waveforms that occur within each seizure. Subjects are typically awake and conscious prior to the seizure, but are unconscious post-ictally. In contrast, absence seizures have similar pre- and post-ictal EEG and a well-structured periodic spike and slow-wave shape which slows slightly during the seizure but does not significantly change form. Remarkably, cognitive function is usually only minimally disrupted after the seizure.

Seizure activity and EEG potentials often used to track it aggregate the behavior of large numbers of neurons. An effective way to model these large populations is to use a mean-field approach, in which individual spike times are ignored in favor of tracking firing rates averaged over sub-mm scales (Wilson and Cowan, 1973; Lopes da Silva et al., 1974; Nunez, 1974, 1995; Freeman, 1975; Jirsa and Haken, 1996; Wright and Liley, 1996; Robinson et al., 1997, 2001, 2002, 2004, 2005; Breakspear et al., 2006). This necessarily simplifies the physiology to model phenomena at multiple spatial and temporal scales simultaneously, but incorporates an increasing variety of physiological and anatomical effects. These include separate excitatory and inhibitory neural populations, synaptic and dendritic dynamics, membrane biophysics, non-linear threshold firing behavior, axonal propagation and delays, boundary conditions and discrete brain structures such as the thalamus.

Mean-field models have yielded a range of experimentally verified predictions for phenomena including steady-state firing rates, basic properties of waves of cortical electrical activity, EEG spectra, evoked response potentials, correlation and coherence properties of EEGs and spatial EEG structure (Wilson and Cowan, 1973; Lopes da Silva et al., 1974; Nunez, 1974, 1995; Freeman, 1975; Jirsa and Haken, 1996; Wright and Liley, 1996; Robinson et al., 1997, 2001, 2002, 2004, 2005; Breakspear et al., 2006) and these phenomena have been found to be reproduced using model parameters that are consistent with independent physiological and anatomical measures (Robinson et al., 2004). In the present context, predictions of the stability boundaries of the model are of particular interest, with Robinson et al. (2002), Lopes da Silva et al. (2003) and Breakspear et al. (2006) having argued that these represent the onsets of seizures via a transition from stable linear dynamics via linear instability to non-linear behavior.

In this chapter, we review recent studies of the mechanisms underlying the onset, evolution and termination of primary generalized seizures in a unified way using a physiologically-based model of the brain's dynamics and illustrate the resulting agreement with data. In doing this, we discuss the model's stability properties and bifurcations where the model undergoes a sudden change in dynamics such as a switch from steady state to periodic behavior (Abraham and Shaw, 1992). Non-linear instabilities and bifurcations in large-scale neural activity may be of special significance to brain dynamics: depending on the context, timing and extent, such phenomenon may be either adaptive – allowing flexible switches in cognition or behavior (Wright et al., 1985; Kelso et al., 1992; Daffertshofer et al., 2000; Fuchs et al., 2000; Friston, 2000; Breakspear, 2002; Freeman and Rogers, 2002; Breakspear et al., 2003, 2004) – or disruptive, such as at the onset of a generalized seizure (Arnhold et al., 1999; Robinson et al., 2002; Stam and van Dijk, 2002). Understanding such instabilities provides a window on the neurophysiological processes occurring in neural systems since they involve dynamical processes with strong feedback and non-linearity (Crevier and Meister, 1998; Izhikevich, 2001). A bifurcation from linear to non-linear brain dynamics also renders data analysis methods based on stochastic linear theory problematic. Hence elucidation of bifurcations in large-scale neuronal systems has cognitive, physiological and methodological significance for neuroscience.

Several empirical studies have concluded that large-scale electrical activity in the healthy human brain is, indeed, predominantly a linear/stochastic phenomenon with intermittent instances of weakly non-linear fluctuations in the alpha band (8–13 Hz) (e.g. Stam et al., 1999; Breakspear and Terry, 2002): as mentioned above, the non-linear neural model employed in the present study is able to predict and explain a variety of resting and sleeping state EEG properties when evolving in a stable, weakly damped linear regime (Robinson et al., 2001, 2004). This view of only occasional and weak non-linearity also finds strong support in the success of classic functional neuroscience algorithms which are rooted in a stochastic/linear framework (Friston et al., 1994). In contrast, clinical research suggests that several pathological processes, such as seizures (Andrzejak et al., 2001) and abnormal rhythms in pathological states (Stam et al., 1997; Stam and Pritchard, 1999) have a strong non-linear component. Robinson et al. (2002) argued that the transition from resting-state to seizure activity results from a linear instability that leads to oscillations in electric activity, whereas different types of seizures may be viewed as bifurcations between distinct types of non-linear dynamics (see also Wendling et al., 2002; Lopes da Silva et al., 2003; Perez Velazquez et al., 2003; Kramer et al., 2005; Liley and Bojak, 2005; Wilson et al., 2006).

In the next section of this chapter, we provide a brief overview of the model used in the work we review here, before outlining its stability properties. We then explain how the model has been applied to analyze the dynamics and bifurcation properties of absence and tonic-clonic seizures with comparison to EEG data. We then discuss how the two generalized seizures have been interrelated in this unified perspective and a summary appears in the final section.

## CORTICOthalamic MODEL

Large-scale neural activity arises from interactions between several neural populations, notably excitatory and inhibitory cortical and thalamic neurons. The corticothalamic model used in the work reviewed here is based upon the evolution of several dynamical variables in each of these populations. Each represents the local mean value of a physiological quantity at position  $\mathbf{r}$  in these neural systems, averaged over a small patch ( $\sim 0.3$  mm) of surrounding neuropil, thereby making the model a *continuum* or *mean-field* model (e.g. Wilson and Cowan, 1973; Nunez, 1974, 1995; Lopes da Silva et al., 1974; Freeman, 1975; Jirsa and Haken, 1996; Robinson et al., 1997, 2001, 2002, 2004, 2005; Breakspear et al., 2006).

## GENERAL MODEL

The dynamical variables for each neural population are the local mean cell-body potential  $V_a$ , the rate of neural firing  $Q_a$ , and the propagating field of spikes in axons  $\phi_a$ . The subscript  $a$  refers to the neural population ( $e$  = excitatory cortical;  $i$  = inhibitory cortical;  $s$  = specific thalamic nucleus;  $r$  = thalamic reticular nucleus;  $n$  = inputs from the brainstem). The mean firing rates  $Q_a$  are related to the potentials  $V_a$  according to the sigmoid activation function  $Q_a(\mathbf{r}, t) = S[V_a(\mathbf{r}, t)]$  where  $S$  is a smooth sigmoidal function that increases from 0 to  $Q_{\max}$  as  $V_a$  increases from  $-\infty$  to  $\infty$ . The function  $S$  is modeled as:

$$S(V_a) = \frac{Q_{\max}}{1 + \exp \left[ -\pi(V_a - \theta)/\sigma\sqrt{3} \right]}, \quad (1)$$

where  $\theta$  is the mean neural firing threshold,  $\sigma$  is the standard deviation of this (approximately normally distributed) threshold and  $Q_{\max}$  is the maximum firing rate.

Neurons firing at a rate  $Q_a$  generate an outward propagating mean field of activity  $\phi_a$  in their axons. Assuming that the ensemble of axons originating at a given location projects isotropically on average, this field approximately obeys the damped wave equation (Nunez, 1995; Jirsa and Haken, 1996; Robinson et al., 1997)

$$D_a \phi_a(\mathbf{r}, t) = Q_a(\mathbf{r}, t), \quad (2)$$

where the spatio-temporal differential operator  $D_a$  is

$$D_a = \frac{1}{\gamma_a^2} \left[ \frac{\partial^2}{\partial t^2} + 2\gamma_a \frac{\partial}{\partial t} + \gamma_a^2 - v_a^2 \nabla^2 \right]. \quad (3)$$

The parameter  $\gamma_a = v_a/r_a$ , where  $r_a$  and  $v_a$  are the characteristic range and conduction velocity of axons of type  $a$ , governs the dispersion of propagating waves, and  $\nabla^2$  is the Laplacian operator. It is important to note that there is no implication that propagation in any single axon is governed by a damped wave equation. This type of equation has been derived from a variety of perspectives, starting from differential, integrodifferential, or Green-function forms that incorporate various anatomical and physiological characteristics (Nunez, 1995; Jirsa and Haken, 1996; Robinson et al., 1997), and, more recently, from synaptic current based neural models (Coombes et al., 2003).

The system of equations is closed by introducing the effect of incoming axonal inputs to neurons at  $\mathbf{r}$  from other neural populations. The cell body potential  $V_a$  results after postsynaptic potentials have been filtered in the dendritic tree, then summed. For excitatory and inhibitory neurons within the cortex, this is modeled using a second order delay-differential equation (Robinson et al., 1997, 2001),

$$D_\alpha V_a(\mathbf{r}, t) = \nu_{ae} \phi_e(\mathbf{r}, t) + \nu_{ai} \phi_i(\mathbf{r}, t) + \nu_{as} \phi_s(\mathbf{r}, t - t_0/2), \quad (4)$$

where  $a = e, i$  and the temporal differential operator

$$D_\alpha = \frac{1}{\alpha\beta} \frac{\partial^2}{\partial t^2} + \left( \frac{1}{\alpha} + \frac{1}{\beta} \right) \frac{\partial}{\partial t} + 1, \quad (5)$$

incorporates lowpass filtering of incoming signals due to synaptic and dendritic dynamics. The quantities  $\alpha$  and  $\beta$  are the inverse decay and rise times of the cell body potential produced by an impulse at a dendritic synapse. Input from the thalamus to the cortex is delayed in Equation (4) by a propagation time  $t_0/2$ . For neurons within the specific and reticular nuclei of the thalamus, cortical input is time-delayed, so

$$D_\alpha V_a(\mathbf{r}, t) = \nu_{ae} \phi_e(\mathbf{r}, t - t_0/2) + \nu_{as} \phi_s(\mathbf{r}, t) + \nu_{ar} \phi_r(\mathbf{r}, t) + \nu_{an} \phi_n(\mathbf{r}, t), \quad (6)$$

where  $a = s, r$ . The synaptic strengths are given by  $\nu_{ab} = N_{ab} s_b$  where  $N_{ab}$  is the mean number of synapses from neurons of type  $b$  to type  $a$  and  $s_b$  is the strength of the response to a unit signal from neurons of type  $b$ . The final term on the right represents input from other structures projecting to the thalamus, such as the brainstem and retina. To simulate experimental time series, this term is approximated by random fluctuations about a constant mean; however, in analyses of bifurcations in the model these fluctuations are omitted. The signal  $\phi_n$  can also incorporate specific stimuli, of interest in studies of photic entrainment, seizure initiation by stimuli, and elsewhere.

The above model equations involve a range of physiological parameters, which have been found to be consistent with independent physiological measurements (Robinson et al., 2004), and whose default values are given in Table 24.1 (Robinson et al., 2002; Breakspear et al., 2006). A schematic of the model is shown in Figure 24.1.

### GLOBAL (SPATIALLY INVARIANT) MODEL

A full non-linear analysis of the model is non-trivial. However, in certain circumstances, particularly in generalized seizures, brain activity is dominated by very large scale – or even whole-brain – processes, in which case the dynamical variables do not depend greatly on  $\mathbf{r}$ . This ‘global model’ can be studied by setting the spatial gradient term in Equation (3) to zero, yielding

$$D_a = \frac{1}{\gamma_a^2} \left[ \frac{\partial^2}{\partial t^2} + 2\gamma_a \frac{\partial}{\partial t} + \gamma_a^2 \right]. \quad (7)$$

TABLE 24.1 Parameter values employed in the present study

Quantity	Value for absence seizure	Value for tonic-clonic seizure	Unit	Meaning
$Q_{\max}$	250	250	$s^{-1}$	Maximum firing rate
$\theta$	15	15	mV	Mean neuronal firing threshold
$\sigma$	6	6	mV	Threshold standard deviation
$\gamma_e$	100	100	$s^{-1}$	Axonal temporal damping rate
$\alpha$	50	60	$s^{-1}$	Inverse decay time of cell body potential
$\beta$	200	240	$s^{-1}$	Inverse rise time of cell body potential
$t_0$	80	80	ms	Corticothalamic loop propagation time
$v_{ee}$	1.0	1.2	mV s	Excitatory intracortical connection strength
$-v_{ei}$	1.8	1.8	mV s	Inhibitory intracortical connection strength
$v_{es}$	3.2	1.4	mV s	Connection strength of specific thalamic nuclei to cortex
$v_{se}$	4.4	1.0	mV s	Connection strength of cortex to specific thalamic nuclei
$-v_{sr}$	0.8	1.0	mV s	Connection strength of reticular to specific thalamic nuclei
$v_{sn} \phi_n$	2.0	1.0	mV	Brainstem input to specific thalamic nuclei
$v_{re}$	1.6	0.2	mV s	Connection strength of cortex to thalamic reticular nucleus
$v_{rs}$	0.6	0.2	mV s	Connection strength of specific to reticular thalamic nuclei

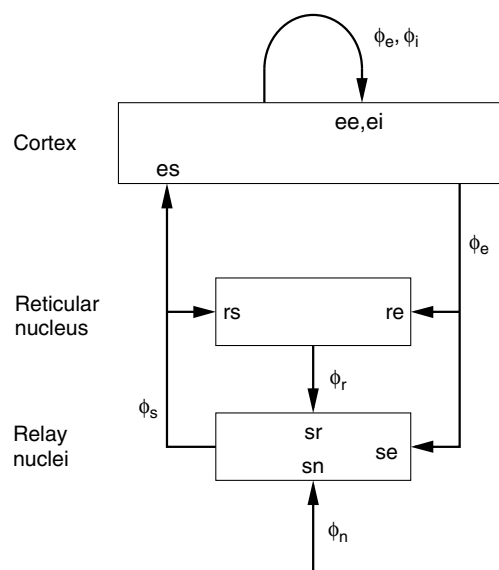


FIGURE 24.1 Schematic of principal neural fields and loops in the corticothalamic model. Fields include  $e$  = excitatory cortical;  $i$  = inhibitory cortical;  $s$  = specific thalamic nucleus;  $r$  = thalamic reticular nucleus;  $n$  = brainstem input. Connectivity and loops include intracortical ( $ee$ ,  $ei$ ), corticothalamic ( $re$ ,  $se$ ,  $es$ ), intrathalamic ( $sr$ ,  $rs$ ) and ascending noise ( $sn$ ).

The variables  $V_a$ ,  $Q_a$ , and  $\phi_a$  now depend only on  $t$ . If intracortical connectivities are assumed to be proportional to the numbers of synapses involved, this implies  $V_i = V_e$  and  $Q_i = Q_e$  (Wright and Liley, 1996; Robinson et al., 1997). The smallness of  $r_i$  and the thalamic nuclei allow us to set  $\gamma_c \approx \infty$ ,  $c = i, r, s$ , yielding the local approximation from Equations (2) and (7),  $\phi_c(t) = S[V_c(t)]$ . These steps yield a set of eight first order delay-differential equations, which permit computationally efficient study of large-scale brain dynamics. From Equations (2) and (4)–(7), these are

$$\frac{d\phi_e(t)}{dt} = \dot{\phi}_e(t), \quad (8)$$

$$\frac{d\dot{\phi}_e(t)}{dt} = \gamma_e^2 \{S[V_e(t)] - \phi_e(t)\} - 2\gamma_e \dot{\phi}_e(t), \quad (9)$$

$$\frac{dV_e(t)}{dt} = \dot{V}_e(t), \quad (10)$$

$$\frac{d\dot{V}_e(t)}{dt} = \alpha\beta \{\nu_{ee}\phi_e(t) + \nu_{ei}S[V_e(t)] + \nu_{es}S[V_s(t-t_0/2)] - V_e(t)\} - (\alpha + \beta)\dot{V}_e(t), \quad (11)$$

$$\frac{dV_s(t)}{dt} = \dot{V}_s(t), \quad (12)$$

$$\frac{d\dot{V}_s(t)}{dt} = \alpha\beta \{\nu_{se}\phi_e(t-t_0/2) + \nu_{sr}S[V_r(t)] + \nu_{sn}\phi_n(t) - V_s(t)\} - (\alpha + \beta)\dot{V}_s(t), \quad (13)$$

$$\frac{dV_r(t)}{dt} = \dot{V}_r(t), \quad (14)$$

$$\frac{d\dot{V}_r(t)}{dt} = \alpha\beta \{\nu_{re}\phi_e(t-t_0/2) + \nu_{rs}S[V_s(t)] - V_r(t)\} - (\alpha + \beta)\dot{V}_r(t), \quad (15)$$

which can be readily integrated numerically (Robinson et al., 2002; Breakspear et al., 2006). Note that the above approximations mean that the cortical inhibitory (*i*) quantities do not have to be tracked separately, but the effects of these neurons are retained in the above analysis.

#### STEADY STATES, LINEAR PROPERTIES AND STABILITY

Setting all spatial and temporal derivatives in the above equations to zero determines global (spatially invariant) corticothalamic steady states when the system is driven by a constant stimulus. A single, stable low firing rate solution is found, which corresponds to the normal state (Robinson et al., 1997). Other steady states are either unstable or correspond to near-maximal firing rates ( $Q_a \approx Q_{\max}$ ).

Small perturbations relative to steady states (e.g. due to stimuli) can be treated using linear analysis, which shows that these perturbations obey a linear wave equation (Nunez, 1974, 1995; Jirsa and Haken, 1996; Robinson et al., 1997). A central result is the linear transfer function that relates cortical activity to stimuli, often expressed in Fourier form (Robinson et al., 1997, 2001, 2004, 2005). These linear approaches have been employed to explain resting state EEG temporal (Robinson et al., 1997, 2002, 2004) and spatial (O'Connor et al., 2002) spectra, as well as a variety of evoked responses, and coherence and correlation properties of the EEG, including the effects of volume conduction and instrumental properties (Robinson et al., 2004, 2005). Inversion of fits of the model to spectra has also been shown to yield estimates of some physiological parameters by a new non-invasive route (Robinson et al., 2004; Rowe et al., 2004).

Studying the linear stability of the model permits mapping of the boundary which marks the transition between steady state behavior and non-linear dynamics. This boundary is the locus where waves have exactly zero linear damping, or equivalently where an eigenvalue associated with the fixed point crosses the imaginary axis, thereby rendering the system linearly unstable. Systematic analysis for realistic parameter ranges reveals a small number of key instabilities which constrain the way non-linear oscillations arise (Robinson et al., 2002). As well as the theta ( $\sim 3$  Hz) and alpha ( $\sim 10$  Hz) instabilities discussed in most detail here, slow wave ( $< 1$  Hz) and spindle ( $\approx 12$ – $15$  Hz) instabilities also arise. The occurrence of only a small number of instabilities has shown that it is possible to study the dynamics and stability of the brain in a low-dimensional space. Indeed, formal analysis of low frequency instabilities shows that three variables  $x$ ,  $y$ , and  $z$  – parameterizing corticocortical, corticothalamic and intrathalamic instability, respectively – encapsulate the

main effects that govern where the model loses linear stability at low frequencies (Robinson et al., 2002). These combine dynamic variables and state parameters and are defined by (Robinson et al., 2002)

$$x = G_{ee}/(1 - G_{ei}), \quad (16)$$

$$y = \frac{G_{ese} + G_{esre}}{(1 - G_{srs})(1 - G_{ei})}, \quad (17)$$

$$z = -G_{srs}\alpha\beta/(\alpha + \beta)^2, \quad (18)$$

where the gain  $G_{ab} = \rho_a \nu_{ab}$  is the differential response in neurons  $a$  to unit input from neurons  $b$ , sigmoid slope  $\rho_a = dS(V_a)/dV_a$ , with the definitions  $G_{ese} = G_{es}G_{se}$ ,  $G_{esre} = G_{es}G_{sr}G_{re}$ , and  $G_{srs} = G_{sr}G_{rs}$  made for convenience. Here these parameters define a coordinate transformation of the dynamical variables  $V_a(t)$ . The parameters  $x$ ,  $y$  and  $z$  give a measure of the feedbacks in the model:  $x$  describes purely cortical feedback,  $y$  describes feedbacks via the two corticothalamic loops (i.e. via the specific nuclei and via both the reticular and specific nuclei) and  $z$  describes feedback within the intrathalamic loop between reticular and specific nuclei. Thus  $x$ ,  $y$  and  $z$  relate to cortical, corticothalamic and intrathalamic linear stability, respectively.

The above variables enable visualization of where in parameter space the model becomes linearly unstable. Figure 24.2 shows the approximate instability boundary in this reduced space. Inside the tent-shaped surface is the stable zone of the model, where healthy non-seizure states lie. Points outside are associated with non-linear oscillations or divergence to near-maximal firing rate regimes (Robinson et al., 1997, 2002). The tent-shaped boundary corresponds to where the fixed points lose linear stability, leading to bifurcations. The various parts of the boundary (each shaded differently in Figure 24.2) correspond to the various instabilities mentioned in the previous paragraph. As the boundary is approached from within, the peak in the linear spectrum that corresponds to incipient instability sharpens and increases in amplitude, as do its harmonics, while measures of non-linear behavior begin to show sporadic increases (Robinson et al., 2002; Breakspear et al., 2006). These results are consistent with time series analyses of healthy, resting state EEG. These show only occasional occurrence of non-linear oscillations, which have a peak frequency in the alpha range during resting, awake EEG (Stam et al., 1999; Breakspear, 2002; Breakspear and Terry, 2002) and in the delta range (1–2 Hz) during non-rapid-eye-movement sleep (Terry et al., 2004).

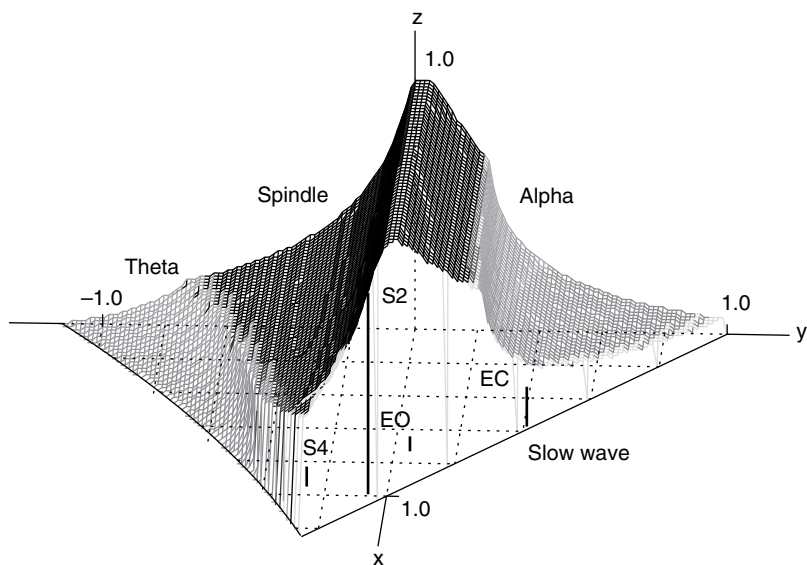


**FIGURE 24.2** Linear stability zone for the corticothalamic model in the reduced  $xyz$  space. The shaded surface represents the values at which the system loses instability at theta (light gray at left), spindle (dark gray) and alpha frequencies (light gray at right), with the front right-hand face left transparent as it corresponds to a slow-wave (non-oscillatory) instability. Within the tent are shown representative values for eyes closed, eyes open and sleep stages 2 and 4. The present study concerns the onset of non-linear oscillations as the system passes outside of the stability zone.

## ABSENCE SEIZURES

This section reviews what happens when the system exits the stability zone through the theta boundary at the left of Figure 24.2, leading to non-linear oscillations at 3–4 Hz, which have been identified with absence seizures (Robinson et al., 2002; Breakspear et al., 2006). Analysis of the model is reviewed first, then comparisons of its predictions with EEG data.

### MODEL ABSENCE SEIZURE

As mentioned above, Robinson et al. (2002) identified generalized absence seizures with crossings of the theta boundary at the left of Figure 24.2. For a system started with parameters in the unstable zone, they showed that the frequency and waveforms were consistent with the main features of absence seizures, estimated the period analytically to be

$$T \approx 2t_0 + 6/\alpha + 6/\beta + 4/\gamma_e, \quad (19)$$

and that instability is favored for high  $\gamma_e$ , which is consistent with childhood onset, where  $\gamma_e$  rises with increasing myelination of cortical axons.

Here, we describe recent simulations of the ~3 Hz theta instability in more detail (Breakspear et al., 2006). These were carried out by choosing physiologically plausible parameters which place the system in the vicinity of the 3 Hz instability boundary (Robinson et al., 2002) as given in Table 24.1. The quantity  $\nu_{se}$  was then increased to push the system to instability, after which it was decreased again to return it to the steady state.

In Figure 24.3A, we show a schematic of how the overall maximums and minimums in each cycle of the time series of  $\phi_e$  depend on  $\nu_{se}$  after any transients. A single value indicates a stable fixed point, while three values indicate a stable limit cycle with outer values (solid curve) as turning points, and an unstable fixed point at the middle value (dashed). This is related to, but not identical to a standard bifurcation diagram; we term it a bifurcation diagram for brevity. The parameter  $\nu_{se}$  was chosen to be varied because of its simple physical meaning and the prior implication of excitatory corticothalamic feedback in the pathophysiology of generalized tonic-clonic (Zifkin and Dravet, 1997; McCormick and Contreras, 2001) and absence (Destexhe and Sejnowski, 2001; McCormick and Contreras, 2001; Meeren et al., 2002) seizures. The macroscopic excitatory fields  $\phi_e$  are plotted as these best represent the cortical correlate of scalp potentials up to a linear transformation of the amplitudes (Nunez, 1995). Specifically, scalp potential is proportional to the cortical potential, which is proportional to the mean cellular membrane currents which are, in turn, proportional to the firing rates. Hence, apart from a dimensional constant of proportionality and the effects of volume conduction, scalp EEG signals correspond closely to  $\phi_e$  (Nunez, 1995; Robinson et al., 2004; Nunez and Srinivasan, 2006).

Figure 24.3A shows that as  $\nu_{se}$  increases, a supercritical Hopf bifurcation to periodic dynamics occurs with an initial instability at  $\nu_{se} \approx 1.8$  mV s. Exemplar time series, with added system and measurement noise are given in Figure 24.3B and C, where  $\nu_{se}$  was dynamically ramped from the linearly stable (weakly damped) region ( $\nu_{se} = 1.6$  mV s) to linear instability ( $\nu_{se} = 5.3$  mV s) and back again. The onset and termination of the seizure, in Figure 24.3B and C, respectively, exhibit a number of key phenomena:

1. Shortly after the onset of ramp-up of  $\nu_{se}$  at  $t = 5$  s periodic oscillations of growing amplitude appear in the field potentials.
2. After a few cycles the waveform becomes less sinusoidal, with spike and slow-wave oscillations appearing. These correspond to increased presence of harmonics in  $\phi_e$ , as seen in the dynamic spectrum in Figure 24.3D, which is dominated by the 3 Hz oscillation and its harmonics. These oscillations continue throughout the seizure, with amplitude modulated by the combined effects of system and measurement noise.
3. During ramp-down of  $\nu_{se}$  at  $t = 20$  s the amplitude of the spike and wave oscillations diminishes and the spikes disappear at approximately  $t = 21.5$  s.
4. Finally, remaining oscillations are damped away and the system returns *directly* to the pre-ictal EEG state, governed by stable damped stochastic fluctuations. This is reflected in the dynamic spectrum, which shows very similar pre- and post-ictal spectra.

Figure 24.3E shows the limit-cycle trajectory of the seizure in the reduced xyz space discussed above. As expected, the trajectory lies outside the tent-shaped stability zone. Because the seizure corresponds to limit-cycle dynamics, it can be embedded in this three-dimensional space without crossing of the orbits. This indicates that, during seizure, a dynamical system of reduced dimensionality should be able to describe the dynamics – or, equivalently, a relatively small number of

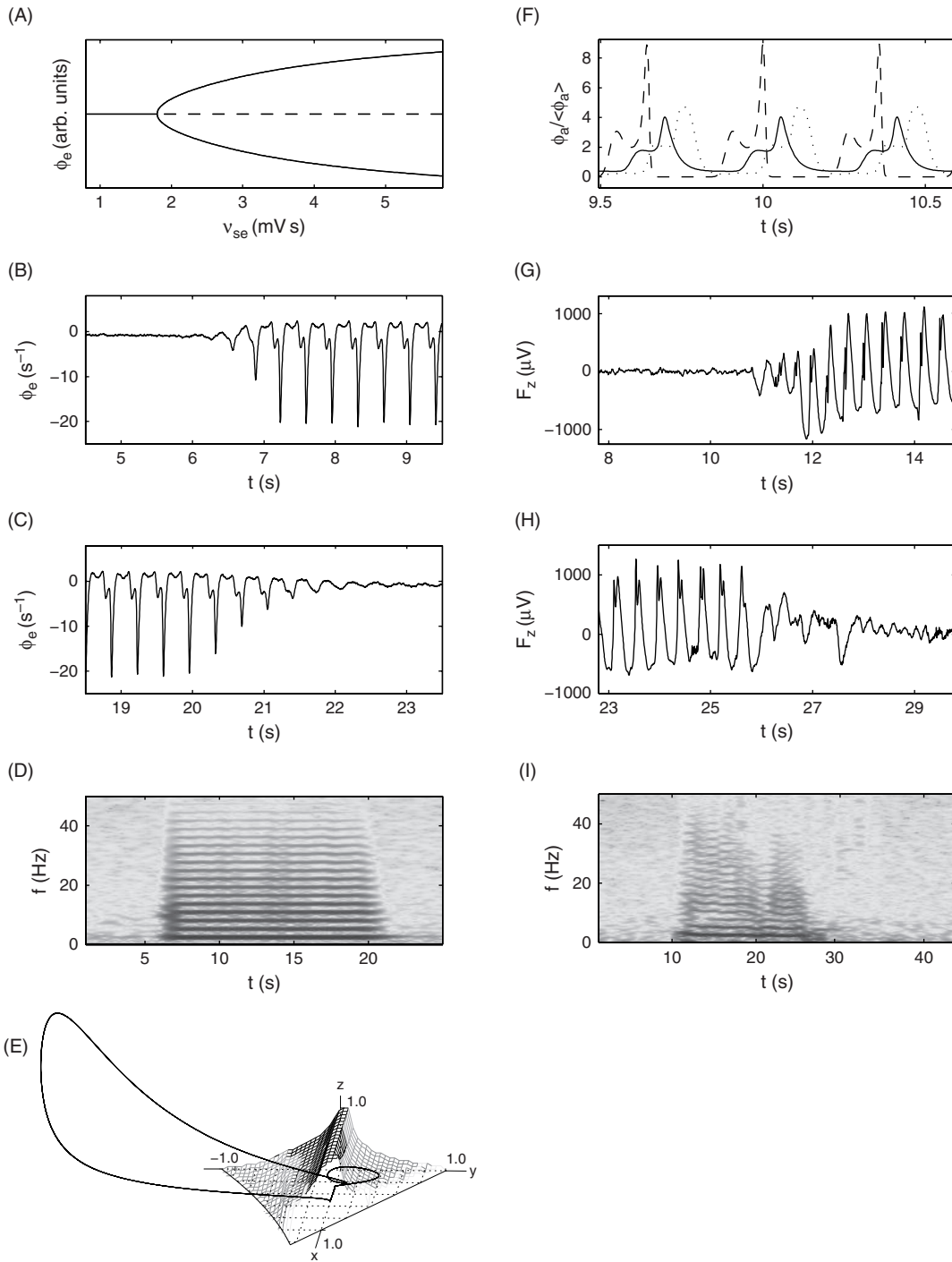


**FIGURE 24.3** Simulated and clinical absence seizures, with simulated  $\phi_e$  filtered and inverted for comparison with clinical data. (A) Schematic bifurcation diagram for the simulations. Horizontal straight line shows stable (solid) and unstable (dashed) fixed point. Solid curve represents stable limit-cycle turning points. (B) Simulated time series of seizure onset in cortical excitatory field  $\phi_e$ . (C) End of simulated seizure. (D) Dynamic spectrum of simulated  $\phi_e$  (filtered). (E) Seizure plotted within the phase space spanned by the stability parameters  $x$ ,  $y$ , and  $z$ . (F) Dynamics of the excitatory cortical  $\phi_e$  (solid), specific thalamic  $\phi_s$  (dashed), and reticular thalamic  $\phi_r$  (dotted) activities, rescaled against their mean values. (G) Onset of clinical seizure. (H) End of clinical seizure. (I) Dynamic spectrum of clinical seizure.

physiological processes may be involved in seizure onset and maintenance. At the start of the seizure, the trajectory spirals outward from the seizure initiation point (not shown); at the end it spirals back into a fixed point inside the stability zone.

Figure 24.3F shows the three principal fields  $\phi_a$  ( $a = e, r, s$ ) during seizure, each normalized by its mean, to illustrate the underlying mechanism of waveform generation. The peak of  $\phi_s$  at  $t \approx 10.0$  s is chosen as the starting point for convenience. This is entirely arbitrary, since the periodic dynamics imply that the waveforms have no particular beginning or end but are an emergent feature of the *entire* corticothalamic system. When  $\phi_s$  (dashed line) peaks,  $\phi_e$  (solid) is at an intermediate value, and  $\phi_r$  (dotted) is low; the thalamus is in its positive-feedback, excitatory state. The reticular nucleus responds immediately to the high activity from the specific nuclei, in addition to inputs that left the cortex a time  $t_0/2$  earlier. This sudden increase in  $\phi_r$  suppresses  $\phi_s$  rapidly and the thalamus switches to its negative-feedback, inhibitory state ( $t \approx 10.05$  s). A time  $t_0/2$  later, the peak in activity from the specific nuclei reaches the cortex, and  $\phi_e$  rises accordingly, with the peak slightly broadened by synaptic rise and decay times. Another  $t_0/2$  later, the spike in activity from the cortex reaches the thalamus, exciting the reticular nucleus and hence further suppressing the specific nuclei ( $t \approx 10.10$  s). This represents negative corticothalamic feedback, and the response of  $\phi_r$  results in a further broadening of the signal. With near silence in the specific nuclei, the cortical neurons relax. At  $t_0/2$  later there are no inputs to the reticular nucleus and hence it too relaxes, leading to a period of near silence in all three fields ( $t \approx 10.20$  s). In the meantime, the specific nuclei have been receiving the external input stimulus  $\phi_n$ , which is sufficient to cause them to reactivate once the reticular nucleus has been suppressed, so  $\phi_s$  rises. This corresponds to the thalamus switching back to its positive-feedback state. Immediately,  $\phi_r$  responds slightly, enough to subdue growth of  $\phi_s$ , but not before the increased activity is substantial enough to excite  $\phi_e$  a time  $t_0/2$  later back to the original intermediate value. Meanwhile, the specific nuclei have been receiving external stimuli continuously, and so while  $\phi_r$  is still low they are able to fire, completing a full cycle ( $t \approx 10.35$  s). The delicate balance of this process highlights the sensitivity of the shape of the waveform to changes in the various parameters. Indeed, a variety of spike and wave and polyspike morphologies is possible under modest changes in parameters. This may explain the varied morphologies observed in clinical absence seizure EEG recordings. It is also consistent with a previous study of absence seizures employing autoregressive non-linear signal analysis methods which showed that similar combinations of time-delayed non-linear (quadratic) terms could explain a variety of spike and wave morphologies (Schiff et al., 1995). Analysis of the above sequence yielded the estimate Equation (19) for the seizure period (Robinson et al., 2002).

### COMPARISON WITH ABSENCE SCALP EEG DATA

Breakspear et al. (2006) compared the above model dynamics with scalp EEG data obtained from adolescent epileptic patients of the Department of Neurology, Westmead Hospital, Sydney, by standard methods detailed in their paper, including use of the 10–20 international system for electrode placement, a data collection rate of 200 samples per second, and filtering with a 70 Hz low-pass third order Butterworth filter.

Figure 24.3G and H shows the onset and termination of a typical clinical seizure, revealing an approximately symmetrical appearance. The occurrence of simple periodic oscillations near the instability boundary, and spike and wave oscillations further from it, are clearly visible. Non-linear analysis confirmed an initial outward spiral onto the limit cycle and an inward spiral to a fixed point at termination. The spectrum of this seizure in Figure 24.3I is dominated by the 3 Hz spike and wave morphology, including both 3 Hz and its harmonics. Notably, the post-ictal spectrum returns rapidly to its relatively featureless pre-ictal form. All these features match the predictions for the model seizure in the previous subsection (Breakspear et al., 2006).

### TONIC-CLONIC SEIZURES

This section reviews what happens when the system exits the stability zone through the alpha boundary at the right of Figure 24.2, leading to non-linear oscillations at around 10 Hz, which have been identified with tonic-clonic seizures (Robinson et al., 2002; Breakspear et al., 2006). Analysis of the model is reviewed first, then comparisons of its predictions with EEG data.

### MODEL TONIC-CLONIC SEIZURE

As mentioned above, Robinson et al. (2002) identified generalized tonic-clonic seizures with crossings of the alpha boundary at the left of Figure 24.2, or possibly with crossing of the spindle boundary. For a system started with parameters in the unstable zone near the alpha boundary, they showed that the frequency and initial waveform were consistent with the

main features, but that spike-wave behavior, seen late in some seizures, was not reproduced. Their earlier work (Robinson et al., 2001) implies the period to be

$$T \approx t_0 + 1/\alpha + 1/\beta. \quad (20)$$

They found that instability is favored for high  $\gamma_e$ , which is consistent with childhood onset, where  $\gamma_e$  rises with increasing myelination of cortical axons and also accords with the rarity of seizures in patients with demyelinating diseases (Niedermeyer and Lopes da Silva, 1999).

Simulated instability at approximately 10 Hz was achieved by increasing  $\nu_{se}$ , starting at a state close to the alpha instability boundary (Breakspear et al., 2006). The schematic bifurcation diagram is given in Figure 24.4A, showing a region of bistability from  $\nu_{se} \approx 0.928$  mV s to  $\nu_{se} \approx 1.035$  mV s. Seizure onset and termination are shown in Figure 24.4B and C. The system is initialized in the linearly stable zone at  $\nu_{se} = 1.025$  mV s, close to the linear instability. As  $\nu_{se}$  was increased to  $\nu_{se} = 1.0425$  mV s the system bifurcated from the fixed point at  $\nu_{se} \approx 1.035$  mV s, where the fixed point becomes an unstable spiral. The orbits then grew exponentially in amplitude toward a large-amplitude attractor (arrow 1). When  $\nu_{se}$  is subsequently decreased, the system cannot return immediately to the fixed point once  $\nu_{se}$  falls below 1.035 mV s, but rather tracks back through parameter space on the large amplitude attractor (arrow 2) until  $\nu_{se} < 0.928$  mV s, when there is no longer a stable limit-cycle attractor and the orbits collapse back onto the fixed point (arrow 3). Although the system is then back on the fixed point attractor, it has reached this state in quite a different (more strongly damped) region than its initial configuration; to return to the original state,  $\nu_{se}$  must be increased again to  $\nu_{se} = 1.025$  mV s, whence the system exhibits hysteresis.

The above loop creates distinctive features seen in the dynamic spectrum in Figure 24.4D. Prior to seizure onset, the spectrum displays the characteristic alpha peak of resting state EEG, whose power increases just prior to, and after instability onset when the orbits grow exponentially toward the large-amplitude attractor (Robinson et al., 2002; Breakspear et al., 2006). This power is particularly strongly expressed during the seizure. Because of the non-linear nature of the oscillations, harmonics (at 20 Hz, 30 Hz, etc.) are evident. Due to bistability, this pattern remains evident even when  $\nu_{se}$  drops below its initial value. Once  $\nu_{se} < 0.928$  mV s, there is no longer a stable limit-cycle attractor, but a stable fixed point exists, to which the system returns. However, because of the strong damping in this region, the overall power is much diminished at  $41 \text{ s} < t < 50 \text{ s}$ , with power across all frequencies lower and the alpha peak absent. The alpha peak returns when  $\nu_{se}$  is restored to its initial value of 1.025 mV s. An additional feature of the spectral plot in Figure 24.4D during the seizure, most notable at higher frequencies (e.g. between 40 and 50 Hz) is the existence of subharmonics at approximately 1/3 and 2/3 of the fundamental frequency; similar subharmonics are also visible in the experimental dynamic spectrum shown in Figure 1 of Schiff et al. (2000).

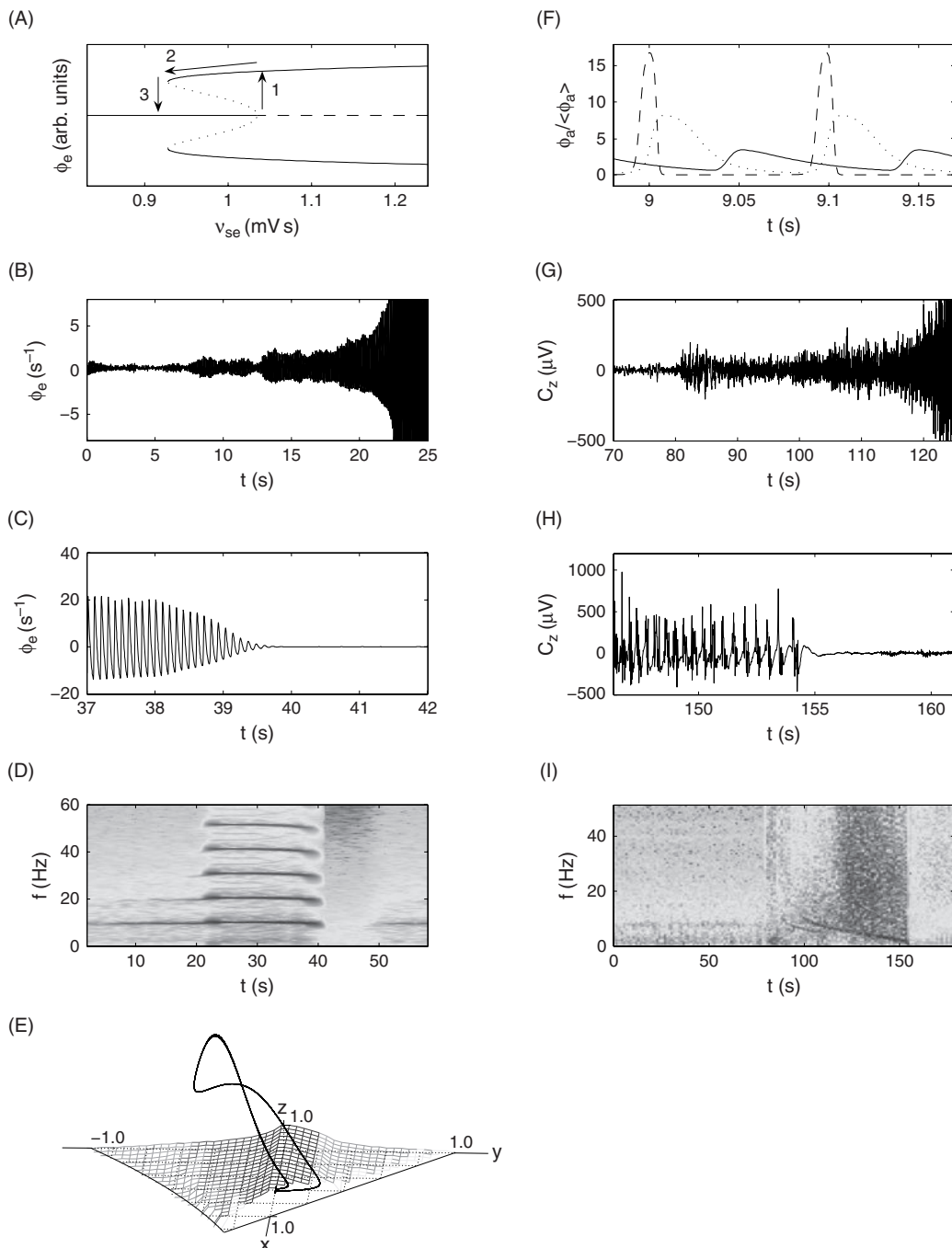
Figure 24.4E shows the large amplitude attractor that occurs when  $\nu_{se}$  is increased past instability. In this frame, all system and parameter noise has been removed, revealing the underlying periodic limit-cycle attractor.

Figure 24.4F shows the dynamics of the three principal fields  $\phi_a$  ( $a = e, r$ , and  $s$ ) during the modeled seizure. As in the analysis of the absence seizure, the peak of  $\phi_s$  is arbitrarily chosen as a starting point (e.g.  $t \approx 9.1$  s). While  $\phi_s$  is at its maximum,  $\phi_e$  is decreasing. The high activity in the specific nuclei – in addition to the high  $\phi_e$  that occurred a time  $t_0/2$  earlier ( $t \approx 9.05$  s) – induces a rise in activity  $\phi_r$  of the reticular nucleus. The subsequent peak in  $\phi_r$ , which is broadened by synaptic rise and decay times, in turn suppresses the specific nuclei. The spike from the relay nuclei reaches the cortex  $t_0/2$  later ( $t \approx 9.15$  s), eliciting a peak in  $\phi_e$ . Another  $t_0/2$  after the cortex is excited, the  $\phi_e$  activity reactivates the thalamus and the cycle continues.

### COMPARISON WITH SCALP EEG DATA

Breakspear et al. (2006) compared the above predictions with generalized tonic-clonic seizure scalp EEG data from pharmacoresistant epileptic patients whose antiepileptic drugs were tapered down. Bipolar voltage signals were stored at 102.4 samples per second after 1–50 Hz bandpass filtering.

Figure 24.4G and H shows the onset and termination of a typical generalized tonic-clonic seizure. After onset, exponential growth of orbit amplitude is visible, as in the model. Comparing onset with termination reveals a number of features. First, in contrast to the absence seizure, the waveform changes markedly prior to termination – suggesting non-stationarity of the dynamics. The frequency has fallen and the waveform has spike and slow waves. Second, abrupt seizure termination is visible, and third, post-ictal EEG suppression can be seen. The marked temporal asymmetry of each oscillation visible just prior to seizure termination is a classic feature of non-linear dynamics (Stam et al., 1998). Non-linear signal analysis



**FIGURE 24.4** Simulated and clinical tonic-clonic seizures, with simulated  $\phi_e$  filtered and inverted for comparison with clinical data. (A) Schematic bifurcation diagram for the simulations. Horizontal straight line shows stable (solid) and unstable (dashed) fixed point. Curves represent stable (solid) and unstable (dotted) limit-cycle turning points. Arrows mark sequence of events described in the text. (B) Simulated time series of seizure onset in cortical excitatory field  $\phi_e$ . (C) End of simulated seizure. (D) Dynamic spectrum of simulated  $\phi_e$  (filtered). (E) Seizure plotted within the phase space spanned by the stability parameters  $x$ ,  $y$  and  $z$ . (F) Dynamics of the excitatory cortical  $\phi_e$  (solid), specific thalamic  $\phi_s$  (dashed), and reticular thalamic  $\phi_r$  (dotted) activities, rescaled against their mean values. (G) Onset of clinical seizure. (H) End of clinical seizure. (I) Dynamic spectrum of clinical seizure.

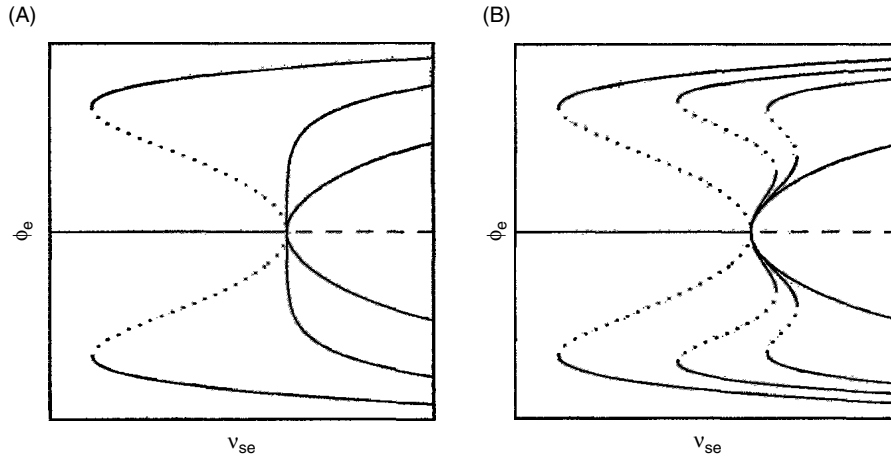
measures showed increases during those parts of the seizure where electromyelographic (EMG) contamination was not overwhelming (Breakspear et al., 2006).

Figure 24.4I shows the dynamic spectrum for the experimental data. As with the simulated seizure, increased power in the 10 Hz frequency peak coincides with the seizure onset ( $t \approx 90$  s). A peak persists throughout the seizure, although its frequency falls considerably. At  $t \approx 100$  s, two such peaks are visible. In comparison, the single peak frequency of the model seizure falls only marginally prior to the seizure termination (see Figure 24.4D), a point we discuss further below. Of particular note is that, as with the model seizure, the experimental spectrum shows a marked post-ictal suppression of power across all frequencies (at  $t \approx 155$  s). As discussed above, this is the critical fingerprint of traversing the bistable 10 Hz bifurcation diagram. Such a feature is also reflected in the highly asymmetrical character of both the modeled and experimental seizures. Another critical feature of the spectrum is the extremely strong increase in broad spectrum (10–50 Hz) power from  $t \approx 120$  s until seizure termination. Given that this is a scalp EEG recording, such power contains EMG contamination corresponding to the motor output of the seizure. It is thus probable that harmonic structure is obscured by the high amplitude noise, as harmonics are observed in intracranial recordings (Schiff et al., 2000). By comparison, no such EMG effect occurs in absence activity, so there the signal-noise ratio is more favorable. The second low frequency peak seen in the empirical data (see Figure 24.4I) at  $t \approx 100$  s does not permit such a straightforward explanation. Possible explanations include two sequential crossings of the instability boundary at slightly different regions due to rapidly changing parameter values, or the secondary excitation of a mode not captured by the present model. Further modeling and empirical study is required to establish the significance of this second peak and, if robust, seek a valid explanation for its origin.

In the model seizure presented above, only the parameter  $\nu_{se}$  was varied. It is probable that, during a lengthy seizure, other physiological parameters will vary as a consequence of the abnormally high activity and/or hypoxia resulting from disruptions to normal respiration and increased oxygen demand. Other parameters may also be varied by regulatory mechanisms to terminate the seizure (Engel et al., 1997; McCormick and Contreras, 2001). One parameter that would likely vary is the corticothalamic delay term  $t_0$ , as this depends upon axonal delays, which may be lengthened by both sustained high activity (Poolos et al., 1987) and hypoxia – leading to changes in ion concentration and diminished presynaptic neurotransmitter supply. The total transit time for a complete seizure also depends upon the membrane time constants  $\alpha$  and  $\beta$  – which would also be affected by these factors. For example, increased (inhibitory) influence of  $GABA_B$  would decrease  $\alpha$  and  $\beta$ , increasing the round-trip time. In an illustrative simulation, Breakspear et al. (2006) showed that an increase in the corticothalamic loop delay  $t_0$  could reproduce the decreasing trends in frequency seen in Figure 24.4I, but noted that other parameter variations may also be involved. Breakspear et al. (2006) found that introducing a second parameter non-stationarity also increased the non-stationarity of the seizure waveform, so that a spike and slow wave morphology was observed. Similar variations may also account for frequency decreases in absence seizures, typically roughly from 4 Hz to 3 Hz.

#### UNIFIED PERSPECTIVE ON GENERALIZED SEIZURES

Figures 24.3A and 24.4A illustrate local bifurcations obtained by varying the single parameter  $\nu_{se}$ . Each can be thought of as a one-dimensional cross-section through the global bifurcation set spanned by all the model's free parameters. The shapes of the two local diagrams have suggested that they may be related through an 'unfolding' of the bistability region of Figure 24.4A into the Hopf bifurcation of Figure 24.3A, as illustrated in the sequence of curves in Figure 24.5A. In this case, the region of bistability contracts until the fixed point became unstable to the left (rather than the right) of the onset of the large amplitude oscillations of Figure 24.4A. Plotting a series of such diagrams for points intermediate between the parameters of Figures 24.3 and 24.4, Breakspear et al. (2006) demonstrated that the actual situation is as shown schematically in Figure 24.5B. Rather than there being a continuous transition from one stable limit cycle to the other, there is a region of coexistence in which both types of limit cycles can exist simultaneously. The stability diagram in Figure 24.2 provides an alternative means of visualizing the situation, in that the surfaces corresponding to the alpha and theta instabilities intersect in xyz space *outside* the stability zone. This implies that both seizure types may coexist in the same region of parameter space. This is consistent with clinical findings that patients with absence seizures are more likely than average additionally to have tonic-clonic seizures and vice versa (Stefan and Snead, 1997; Zifkin and Dravet, 1997; Robinson et al., 2002). Robinson et al. (2002) also noted that a similar intersection between the spindle and theta instability surfaces toward the left of Figure 24.2 was consistent with experimental observations relating to the co-occurrence of 3 Hz and 10–15 Hz activity in animal preparations, and penicillin-induced transformations between these regimes.



**FIGURE 24.5** Schematic topology of global bifurcation diagram, showing transition from supercritical (innermost curves) to subcritical (outermost curves) bifurcation. Horizontal straight line shows stable (solid) and unstable (dashed) fixed point. Curves represent stable (solid) and unstable (dotted) limit-cycle turning points. (A) Simple transition with no coexistence of stable low- and high-amplitude limit-cycle attractors. (B) Transition with coexistence of stable low- and high-amplitude limit-cycle attractors.

#### SUMMARY AND CONCLUSION

This chapter reviews some aspects of recent physiologically-based mean-field modeling of brain activity that has yielded a unified explanation of the main features of the two major human generalized seizures in a framework that also captures a variety of normal behaviors and other phenomena. It is based on the premise that seizures arise when corticothalamic dynamics lose linear stability in specific regions of parameter space.

The model predicts a  $\sim 3$  Hz linear instability, leading to a continuous bifurcation from healthy resting EEG to absence (circa 3 Hz) seizure, yielding time series with periodic spike-and-wave morphology similar to scalp EEG data taken from absence seizures. Moreover, the nature of the bifurcation yields the symmetrical on-off character that is also found in the EEG data.

In contrast, tonic-clonic ( $\sim 10$  Hz) seizures show a discontinuous transition from damped (fixed point) dynamics to large-amplitude non-linear oscillations, associated with bistable behavior and hysteresis. This yielded time series realizations compatible with tonic-clonic seizures. Once the seizure commences, the system displays high amplitude periodic oscillations and it is necessary to traverse parameter space to a location beyond the onset point of the seizure before a stable linear regime re-emerges. This hysteresis is consistent with the differences between pre- and post-ictal EEG spectra and cognition that characterize tonic-clonic seizures. The sensitivity of instability to axonal propagation is consistent with childhood onset (increasing myelination) and the rarity of seizures in patients with demyelinating diseases.

A criticism of many physiologically-based models of neural activity is that their numerous parameters undermine their explanatory power. While this is an important consideration, a number of features of the present model are relevant in this regard. First, it has relatively few parameters and was not originally formulated to generate seizure waveforms, but rather to incorporate the key features of corticothalamic dynamics underlying temporal and spatial EEG generation in healthy states – when the activity turns out to be weakly damped and non-linearities are weak (Robinson et al., 1997, 2001, 2002; O'Connor et al., 2002). In the model, as clinically, seizures arise from resting EEG states when, due to a change in underlying physiology, the system passes a critical threshold (Robinson et al., 1997, 2002). The behavior of the model's dynamical variables during non-linear dynamics has permitted prediction of real physiological outcomes, which have been verified against physiological data. In the linearly stable zone, but near instability, EEG spectral peaks corresponding to the incipient instability are enhanced and non-linear measures show sporadic enhancements due to fluctuations toward instability, consistent with previous nonlinear analyses of resting EEG data (Stam et al., 1999; Breakspear and Terry, 2002; Robinson et al., 2002; Breakspear et al., 2006). Third, there are no free parameters in the sense that they have all been constrained by independent experimental estimates and matched against a large database of EEG spectra (Robinson et al., 2004). In the simulations, previously published parameters were used, not ones tuned to yield a particular outcome for seizures. Fourth, numerical simulations have yielded a number of phenomena which lend themselves to potential refutation, such as the periodic nature of the absence seizures, the spectral properties of pre- and post-ictal EEG, and the involvement of thalamic nuclei.

The role of the thalamus in absence seizures remains incompletely understood. Steriade and Contreras (1995) found that 40% of thalamocortical neurons discharge spike-bursts in close relation to those in depth cortical recordings. Moreover, these spikes progressed to full synchrony as the seizure progressed. Steriade and Contreras (1998) described 3 Hz spike-wave seizures following thalamectomy but they noted that these did not have the same global (cortex-wide) properties as those when the thalamus was intact, nor did they have the classic absence waveform (cf. Figures 4 and 10 of their paper). Whereas such data were acquired from fully anesthetized cats, PET (Prevett et al., 1995) and fMRI (Aghakhani et al., 2004) studies from human subjects with ‘naturally occurring’ absence epilepsy show involvement of the thalamus during absence seizures. Meeren et al. (2002) found that cortical and thalamic sites interact bidirectionally during seizures in a rat genetic model of absence epilepsy. Destexhe and Sejnowski (2001) provide further extensive discussion and references regarding the role of the thalamus in absence seizures.

It should be noted that the corticothalamic model employed above does not explicitly include  $\text{Ca}^{2+}$  T-channels within the thalamus. Such channels will need to be incorporated to model the sensitivity of absence seizures to T-channel blockade with ethosuximide, for example. T-channels, which show a refractory period following sustained bursting, have been incorporated into related neural population models of 3 Hz absence seizures (Destexhe and Sejnowski, 2001) and are likely to strengthen 3 Hz oscillations when incorporated into mean-field modeling, an innovation that is currently under way. Destexhe and Sejnowski (2001) treated axonal propagation times as negligible, so there was no time-delay corresponding to the quantity  $t_0$  of our model. In comparison, the presence of time-delayed corticothalamic feedback is a crucial ingredient in EEG spectra and the absence waveform observed. In fact, qualitatively similar spike-wave oscillations can be generated by our model with a variety of time-delayed feedback loops which differ in detail from those presented above. This is particularly interesting, since it is known experimentally that absence seizures can arise as a result of changes in a number of different pathways. Thus, although there are differences from the Destexhe and Sejnowski model, both emphasize the increased excitatory loops between the cortex and the specific and reticular nuclei of the thalamus underlying the generalized seizures. The work of Destexhe and Sejnowski (2001) shows that at least some types of experimentally observed spikes can be generated without time-delayed loops, which may explain certain purely cortical spikes (McCormick and Contreras, 2001). This possibility does not contradict the present model, since there is no reason why more than one spike-wave generation mechanism cannot be present in the brain. The corticothalamic model presented here has the advantage of making a wide set of testable predictions about both the spatial and temporal distribution of activity during seizures.

To illustrate the effect of hypoxia and neural fatigue on the modeled tonic-clonic seizure, the corticothalamic conduction delay was increased in some simulations (Breakspear et al., 2006). This had the effect of lowering the peak seizure frequency, imparting the ‘chirp’ property observed in the clinical recordings (Schiff et al., 2000). It is also probable that other physiological processes would also be affected by the impact of a tonic-clonic seizure. For example, active inhibitory mechanisms are likely to involve an increase in the number of activated GABA receptors, which corresponds to an increase in synaptodendritic rise and decay times in our model. These mechanisms need to be investigated further in future work, which could also study the manipulation of other model parameters. Such work, together with the incorporation of other physiological mechanisms, such as T-channels, is likely to improve further the match between the model seizure properties and the those of clinical seizures. Mismatches between a model and the observed phenomena are to be expected whenever relevant physiological mechanisms are omitted as they indicate precisely where the model requires refinement. Another direction we mention for future work is to investigate the spindle and slow-wave boundaries of the stability zone in Figure 24.2 in more detail: spindle instability, for example, may account for subtypes of generalized tonic-clonic seizures and its intersection with the theta instability is also likely to lead to rich dynamics (Robinson et al., 2002). Finally, we note that retention of the  $\nabla^2$  term in Equation (3), neglected in the present chapter, will enable spatial phenomena such as focal and secondarily generalized seizures to be treated in the same framework.

#### ACKNOWLEDGMENTS

We thank J.-W. Kim, S. Rodriguez and J. Terry for their comments. This work was supported by the Australian Research Council. Parts of the text and figures have been adapted from Robinson et al. (2002), published by the American Physical Society, and Breakspear et al. (2006), published by Oxford University Press.

## REFERENCES

- Abraham, R.H. and Shaw, C.D. (1992). Dynamics – the geometry of behavior. Addison-Wesley, Redwood City.
- Aghakhani, Y., Bagshaw, A.P., Bénar, C.G. et al. (2004). fMRI activation during spike and wave discharges in idiopathic generalized epilepsy. *Brain* 127:1127–1144.
- Andrzejak, R.G., Lehnertz, K., Mormann, F., Rieke, C., David, P. and Elger, C.E. (2001). Indications of nonlinear deterministic and finite-dimensional structure in time series of brain electrical activity: dependence on recording region and brain state. *Phys Rev E* 64:061907.
- Arnhold, J., Grassberger, P., Lehnertz, K. and Elger, C.E. (1999). A robust method for detecting interdependencies: application to intracranially recorded EEG. *Physica D* 134:419–430.
- Breakspear, M. (2002). Nonlinear phase desynchronization in human electroencephalographic data. *Hum Brain Mapp* 15:175–198.
- Breakspear, M. and Terry, J.R. (2002). Detection and description of non-linear interdependence in normal multichannel human EEG. *Clin Neurophysiol* 113:735–753.
- Breakspear, M., Terry, J.R. and Friston, K.J. (2003). Modulation of excitatory synaptic coupling facilitates synchronization and complex dynamics in a biophysical model of neuronal dynamics. *Netw Comput Neural Syst* 14:703–732.
- Breakspear, M., Williams, L.M. and Stam, C.J. (2004). A novel method for the topographic analysis of neural activity reveals formation and dissolution of ‘dynamic cell assemblies’. *J Comput Neurosci* 16:49–68.
- Breakspear, M., Roberts, J.A., Terry, J.R., Rodrigues, S., Mahant, N. and Robinson, P.A. (2006). A unifying explanation of primary generalized seizures through nonlinear brain modeling and bifurcation analysis. *Cereb. Cortex* 16:1296–1313.
- Coombes, S., Lord, G.J. and Owen, M.R. (2003). Waves and bumps in neuronal networks with axo-dendritic synaptic interactions. *Physica D* 178:219–241.
- Crevier, D.W. and Meister, M. (1998). Synchronous period-doubling in flicker vision of salamander and man. *J Neurophysiol* 79:1869–1878.
- Daffertshofer, A., Peper, C.E., Frank, T.D. and Beek, P.J. (2000). Spatio-temporal patterns of encephalographic signals during polyrhythmic tapping. *Hum Mov Sci* 19:475–498.
- Destexhe, A. and Sejnowski, T.J. (2001). Thalamocortical assemblies. Oxford University Press, Oxford.
- Engel, J. Jr, Dichter, M.A. and Schwartzkroin, P.A. (1997). Basic mechanisms of human epilepsy. In: *Epilepsy: a comprehensive textbook* (J. Engel Jr and T.A. Pedley, eds). Lippincott-Raven, Philadelphia.
- Freeman, W.J. (1975). Mass action in the nervous system. Academic Press, New York.
- Freeman, W.J. and Rogers, L.J. (2002). Fine temporal resolution of analytic phase reveals episodic synchronization by state transitions in gamma EEGs. *J Neurophysiol* 87:937–945.
- Friston, K.J. (2000). The labile brain. I. Neuronal transients and nonlinear coupling. *Philos Trans R Soc Lond B* 355:215–236.
- Friston, K.J., Jezzard, P. and Turner, R. (1994). Analysis of functional MRI time-series. *Hum Brain Mapp* 1:153–171.
- Fuchs, A., Mayville, J.M., Cheyne, D., Weinberg, H., Deecke, L. and Kelso, J.A.S. (2000). Spatiotemporal analysis of neuromagnetic events underlying the emergence of coordinative instabilities. *Neuroimage* 12:71–84.
- Izhikevich, E.M. (2001). Synchronization of elliptic bursters. *SIAM Rev* 53:315–344.
- Jirsa, V.K. and Haken, H. (1996). Field theory of electromagnetic brain activity. *Phys Rev Lett* 77:960–963.
- Kelso, J.A.S., Bressler, S.L., Buchanan, S. et al. (1992). A phase transition in human brain and behaviour. *Phys Lett A* 169:134–144.
- Kramer, M.A., Kirsch, H.E. and Szeri, A.J. (2005). Pathological pattern formation and cortical propagation of epileptic seizures. *JR Soc Interface* 2:113–127.
- Liley, D.T.J. and Bojak, I. (2005). Understanding the transition to seizure by modeling the epileptiform activity of general anesthetic agents. *J Clin Neurophysiol* 22:300–313.
- Lopes da Silva, F., Blanes, W., Kalitzin, S.N., Parra, J., Suffczynski, P. and Velis, D.N. (2003). Epilepsies as dynamical diseases of brain systems: basic models of the transition between normal and epileptic activity. *Epilepsia* 44(Suppl. 12):72–83.
- Lopes da Silva, F.H., Hoeks, A., Smits, H. and Zetterberg, L.H. (1974). Model of brain rhythmic activity. The alpha-rhythm of the thalamus. *Kybernetik* 15:27–37.
- McCormick, D.A. and Contreras, D. (2001). On the cellular and network bases of epileptic seizures. *Annu Rev Physiol* 63:815–846.
- Meeren, H.K.M., Pijn, J.P.M., Van Luijtelaar, E.L.J.M., Coenen, A.M.L. and Lopes da Silva, F.H. (2002). Cortical focus drives widespread corticothalamic networks during spontaneous absence seizures in rats. *J Neurosci* 22:1480–1495.
- Niedermeyer, E. and Lopes da Silva, F.H. (eds) (1999). *Electroencephalography: basic principles, clinical applications, and related fields*, 4th edn. Williams & Wilkins, Baltimore.
- Nunez, P.L. (1974). The brain wave equation: a model for the EEG. *Math Biosci* 21:279–297.
- Nunez, P.L. (1995). *Neocortical dynamics and human EEG rhythms*. Oxford University Press, Oxford.
- Nunez, P.L. and Srinivasan, R. (2006). *Electrical fields of the brain*. Oxford University Press, New York.
- O’Connor, S.C., Robinson, P.A. and Chiang, A.K.I. (2002). Wave-number spectrum of electroencephalographic signals. *Phys Rev E* 66:061905.
- Perez Velazquez, J.L., Cortez, M.A., Snead, O.C. III and Wennberg, R. (2003). Dynamical regimes underlying epileptiform events: role of instabilities and bifurcations in brain activity. *Physica D* 186:205–220.
- Poolos, N.P., Mauk, M.D. and Kocsis, J.D. (1987). Activity-evoked increases in extracellular potassium modulate presynaptic excitability in the CA1 region of the hippocampus. *J Neurophysiol* 58:404–416.
- Prevett, M.C., Duncan, J.S., Jones, T., Fish, D.R. and Brooks, D.J. (1995). Demonstration of thalamic activation during typical absence seizures using H<sub>2</sub>(<sup>15</sup>O) and PET. *Neurology* 45:1396–1402.
- Robinson, P.A., Rennie, C.J. and Wright, J.J. (1997). Propagation and stability of waves of electrical activity in the cerebral cortex. *Phys Rev E* 56:826–840.
- Robinson, P.A., Rennie, C.J., Wright, J.J., Bahramali, H., Gordon, E. and Rowe, D.L. (2001). Prediction of electroencephalographic spectra from neurophysiology. *Phys Rev E* 63:021903.
- Robinson, P.A., Rennie, C.J. and Rowe, D.L. (2002). Dynamics of large-scale brain activity in normal arousal states and epileptic seizures. *Phys Rev E* 65:041924.

- Robinson, P.A., Rennie, C.J., Rowe, D.L. and O'Connor, S.C. (2004). Estimation of multiscale neurophysiologic parameters by electroencephalographic means. *Hum Brain Mapp* 23:53–72.
- Robinson, P.A., Rennie, C.J., Rowe, D.L., O'Connor, S.C. and Gordon, E. (2005). Multiscale brain modelling. *Philos Trans R Soc Lond B* 360:1043–1050.
- Rowe, D.L., Robinson, P.A. and Rennie, C.J. (2004). Estimation of neurophysiological parameters from the waking EEG using a biophysical model of brain dynamics. *J Theor Biol* 231:413–433.
- Schiff, N.D., Victor, J.D., Canel, A. and Labar, D.R. (1995). Characteristic nonlinearities of the 3/s ictal electroencephalogram identified by nonlinear autoregressive analysis. *Biol Cybern* 72:519–526.
- Schiff, S.J., Colella, D., Jacyna, G.M. et al. (2000). Brain chirps: spectrographic signatures of epileptic seizures. *Clin Neurophysiol* 111:953–958.
- Stam, C.J. and Pritchard, W.S. (1999). Dynamics underlying rhythmic and non-rhythmic variants of abnormal, waking delta activity. *Int J Psychophysiol* 34:5–20.
- Stam, C.J. and van Dijk, B.W. (2002). Synchronization likelihood: an unbiased measure of generalized synchronization in multivariate data sets. *Physica D* 163:236–251.
- Stam, C.J., van Woerkom, T.C.A.M. and Keunen, R.W.M. (1997). Non-linear analysis of the electroencephalogram in Creutzfeldt-Jakob disease. *Biol Cybern* 77:247–256.
- Stam, C.J., Pijn, J.P.M. and Pritchard, W.S. (1998). Reliable detection of nonlinearity in experimental time series with strong periodic components. *Physica D* 112:361–380.
- Stam, C.J., Pijn, J.P.M., Suffczynski, P. and Lopes da Silva, F.H. (1999). Dynamics of the alpha rhythm: evidence for non-linearity? *Clin Neurophysiol* 110:1801–1813.
- Stefan, H. and Snead, O.C. III (1997). Absence seizures. In: *Epilepsy: a comprehensive textbook* (J. Engel Jr and T.A. Pedley, eds). Lippincott-Raven, Philadelphia.
- Steriade, M. and Contreras, D. (1995). Relations between cortical and thalamic cellular events during transition from sleep patterns to paroxysmal activity. *J Neurosci* 15:623–642.
- Steriade, M. and Contreras, D. (1998). Spike-wave complexes and fast components of cortically generated seizures. I. Role of neocortex and thalamus. *J Neurophysiol* 80:1439–1455.
- Terry, J.R., Anderson, C. and Horne, J.A. (2004). Nonlinear analysis of EEG during NREM sleep reveals changes in functional connectivity due to natural aging. *Hum Brain Mapp* 23:73–84.
- Wendling, F., Bartolomei, F., Bellanger, J.J. and Chauvel, P. (2002). Epileptic fast activity can be explained by a model of impaired GABAergic dendritic inhibition. *Eur J Neurosci* 15:1499–1508.
- Wilson, H.R. and Cowan, J.D. (1973). A mathematical theory of the functional dynamics of cortical and thalamic nervous tissue. *Kybernetik* 13:55–80.
- Wilson, M.T., Sleigh, J.W., Steyn-Ross, D.A. and Steyn-Ross, M.L. (2006). General anesthetic-induced seizures can be explained by a mean-field model of cortical dynamics. *Anesthesiology* 104:588–593.
- Wright, J.J. and Liley, D.T.J. (1996). Dynamics of the brain at global and microscopic scales: neural networks and the EEG. *Behav Brain Sci* 19:285–320.
- Wright, J.J., Kydd, R.R. and Lees, G.J. (1985). State-changes in the brain viewed as linear steady-states and non-linear transitions between steady-states. *Biol Cybern* 53:11–17.
- Zifkin, B. and Dravet, C. (1997). Generalized convulsive seizures. In: *Epilepsy: a comprehensive textbook* (J. Engel Jr and T.A. Pedley, eds). Lippincott-Raven, Philadelphia.

# 25

## A NEURONAL NETWORK MODEL OF CORTICOTHALAMIC OSCILLATIONS: THE EMERGENCE OF EPILEPTIFORM ABSENCE SEIZURES

PIOTR SUFFCZYSKI, STILIYAN KALITZIN AND F.H. LOPES DA SILVA

### ABSTRACT

It is currently believed that the mechanisms underlying spindle oscillations during sleep appear to be related to those that generate spike-and-wave (SW) discharges. The mechanisms of transition between these two types of oscillatory activity are not well understood. In order to provide insight into the dynamics of the neuronal networks leading to seizure generation in rat epilepsy models, we developed a computational model of thalamocortical circuits based on relevant (patho)physiological data. The model is constructed at the macroscopic level but with some neuronal mechanisms included since such an approach allows investigation of dynamical properties of the system and the role played by different cellular and network mechanisms in the process of seizure generation, both at short and long time scales. The main results are the following. (1) SW discharges represent bifurcations that occur in a bistable neuronal network. (2) Lengths of paroxysmal and normal epoch have exponential distribution, indicating that transitions between these two stable states occur randomly over time with constant probabilities. These probabilities can be controlled by a number of model parameters. (3) The probabilistic nature of onset of paroxysmal activity leads us to reject a possibility of prediction of its occurrence. (4) The bistable nature of the dynamical system allows that an ictal state may be aborted by a single counter-stimulus. Model results are shown to be consistent with many experimental data of rat models of absence epilepsy and model predictions are suggested to substantiate further the proposed dynamical mechanisms of seizure generation.

### INTRODUCTION

Absence seizures are paroxysmal losses of consciousness of abrupt onset and offset, accompanied by bilaterally synchronous spike-and-wave (SW) discharges in the EEG (Snead et al., 1999). It is currently considered that the mechanisms underlying SW discharges may be related to the thalamocortical mechanisms of sleep spindle generation. Spindles are defined as waxing and waning waves between 7 and 14 Hz, grouped in sequences that last for 1.5–2 seconds and that recur periodically with a slow rhythm of 0.1–0.2 Hz (Steriade et al., 1990). The thalamic origin of the spindle waves is well known (reviewed in Steriade and Deschenes, 1984). It is currently considered that spindle oscillations result from reciprocal interactions between thalamocortical relay (TC) and thalamic reticular nucleus (RE) cells. The RE cells receive excitatory input from TC cells and project back to relay nuclei via inhibitory synapses. TC cells can fire occasional rebound bursts of spikes following recovery from hyperpolarization induced by inhibitory postsynaptic potentials (IPSPs) of RE origin. RE cells tend to fire bursts of action potentials in response to excitation from thalamocortical and corticothalamic cells. In both types of cells, the ability to generate bursts is provided by a low-threshold ( $I_T$ ) calcium current (Jahnsen and Linas, 1984a, 1984b). The cellular mechanisms for the generation of spindle oscillations during sleep appear to be related to those for the generation of the spike-and-wave (SW) complexes that are associated with absence (petit mal) epileptic seizures.

This was put in evidence in ferret geniculate slices by the effect of the pharmacological block of GABA<sub>A</sub> receptors that results in the transformation of spindle waves into 3 Hz 'paroxysmal' activity. The latter is suppressed by GABA<sub>B</sub> receptor antagonists (von Krosigk et al., 1993; Bal et al., 1995a, 1995b). It should be noted that inhibitory postsynaptic potentials mediated by GABA<sub>A</sub> have time to peak about 20–25 ms, while those mediated by GABA<sub>B</sub> receptors have more prolonged duration between 150 and 300 ms (Bal et al., 1995a). Therefore the activation of GABA<sub>B</sub> receptors results in a slowing of the reverberatory activity between thalamocortical and thalamic reticular neurons. Although this activity *in vitro* may differ from that observed during absence seizure (Steriade and Contreras, 1998; Castro-Alamancos, 1999), the activation of GABA<sub>B</sub> receptors in the thalamic relay nuclei seems to be essential in both cases. In animals with genetic absence epilepsy, thalamic injection of selective agonists of GABA<sub>B</sub> receptors results in spike-and-wave discharges, whereas administration of GABA<sub>B</sub> receptor antagonists diminishes the occurrence of SW in a dose-dependent manner (Liu et al., 1992). The long duration of GABA<sub>B</sub> receptor mediated hyperpolarization is effective in removing the inactivation of the low-threshold calcium current. Therefore, activation of the GABA<sub>B</sub> receptors results in rebound bursts of action potentials in a large proportion of thalamocortical neurons. These facilitated TC cells discharges strongly excite RE cells, which can result in the generalization of paroxysmal activity.

Despite the fact that cellular and network mechanisms underlying spindle and SW rhythmicity are clarified to a large extent, the mechanisms that are responsible for the spontaneous transition between normal spindle and paroxysmal SW oscillations are not well understood. We assumed that a computational model investigating the dynamical aspects of seizure generation would be a valuable contribution. A number of detailed, distributed models of thalamic and thalamocortical networks were recently developed (e.g. Wang et al., 1995; Golomb et al., 1996; Destexhe 1998, 1999). These models give insight into some basic neuronal mechanisms, but to simulate a transition from normal to pathological behavior, usually, external change of some essential parameters is required. However, the mechanisms controlling these parameter changes are often beyond the scope of the model. Thus, the main aim of the present study is to find out the mechanisms responsible for spontaneous (i.e. not triggered by parameter change from outside) transitions from normal activity to paroxysmal SW discharges. This aspect of the dynamical process responsible for seizure generation has, to the best of our knowledge, not been addressed in a computational model of absence epilepsy and therefore the present model provides a novel contribution.

In this study, we approach the given problem at the intermediate level between the microscopic and macroscopic levels. That is, we do not simulate the explicit behavior of individual neurons but rather model the populations of interacting neurons integrating neuronal and network properties. The rationale for such a modeling level was to take advantage of the lumped modeling approach (see Chapter 23) but, at the same time, to include some essential processes at the level of neurons' membrane that are responsible for burst generation in thalamic cells.

In the present study, we focus on the SW activity that is recorded from a genetic animal model of absence epilepsy, namely the WAG/Rij (Wistar albino Glaxo from Rijswijk) rat model (van Luijtelaar and Coenen, 1986; Coenen et al., 1992), that has similar characteristics to the GAERS (generalized absence epilepsy) rats of Strasbourg (Marescaux et al., 1992; Danober et al., 1998). The main reason to choose these animal data for constructing the computational model is that rat experimental data at the cellular and network levels are available, in contrast to the human case.

## MATERIALS AND METHODS

### MODEL STRUCTURE

The model of thalamocortical network is an extended version of the lumped model initially proposed by Lopes da Silva et al. (1974). Lumped model means that we do not simulate single cells in a distributed network but rather we take a spatial average over a population and deal only with temporal dynamics of the mean values of the underlying statistical process. The model of Lopes da Silva was based on two interacting populations of neurons, namely excitatory cells of main population that projected to the interneurons while the latter fed back on the main cells, inhibiting them with fast GABA<sub>A</sub> receptor mediated inhibitory postsynaptic potentials (IPSPs). Each population was described by the time courses of postsynaptic potentials and sigmoid transfer function, which was used to simulate the conversion between the mean membrane potential of a neuronal population and the mean firing rate (number of pulses per second (pps)) of the population. This negative feedback system may be viewed as the basic mechanism responsible for the generation of EEG rhythmic activity within the alpha frequency range. That is, such a module produces rhythmic activity in between 8 and 13 Hz when submitted to a random input, as shown in a number of studies (Lopes da Silva et al., 1974; Zetterberg et al., 1978; Nunez, 1995).

We made a number of extensions and added new features to the above described model. The present model is advanced with respect to its precursor in three main points:

1. It consists of two lumps, cortical and thalamic ones, that are mutually interconnected.
2. The transformation between mean membrane potential and firing rate in the thalamic populations takes into account the low-threshold  $I_T$  calcium current that underlies burst firing in the thalamic cells.
3. In addition both fast  $GABA_A$ - and slow  $GABA_B$ -receptor mediated inhibitions are included.

The schematic diagram of the model is shown in Figure 25.1. It consists of four neuronal populations of cells (PY: pyramidal cells, IN: cortical interneurons, TC: thalamocortical cells, RE: reticular cells of the thalamus). Each element of the model is outlined below. Parameter values are given in Suffczynski et al. (2004). The Simulink model (version 6.2) and its full description is available at [www.eeg.pl](http://www.eeg.pl)

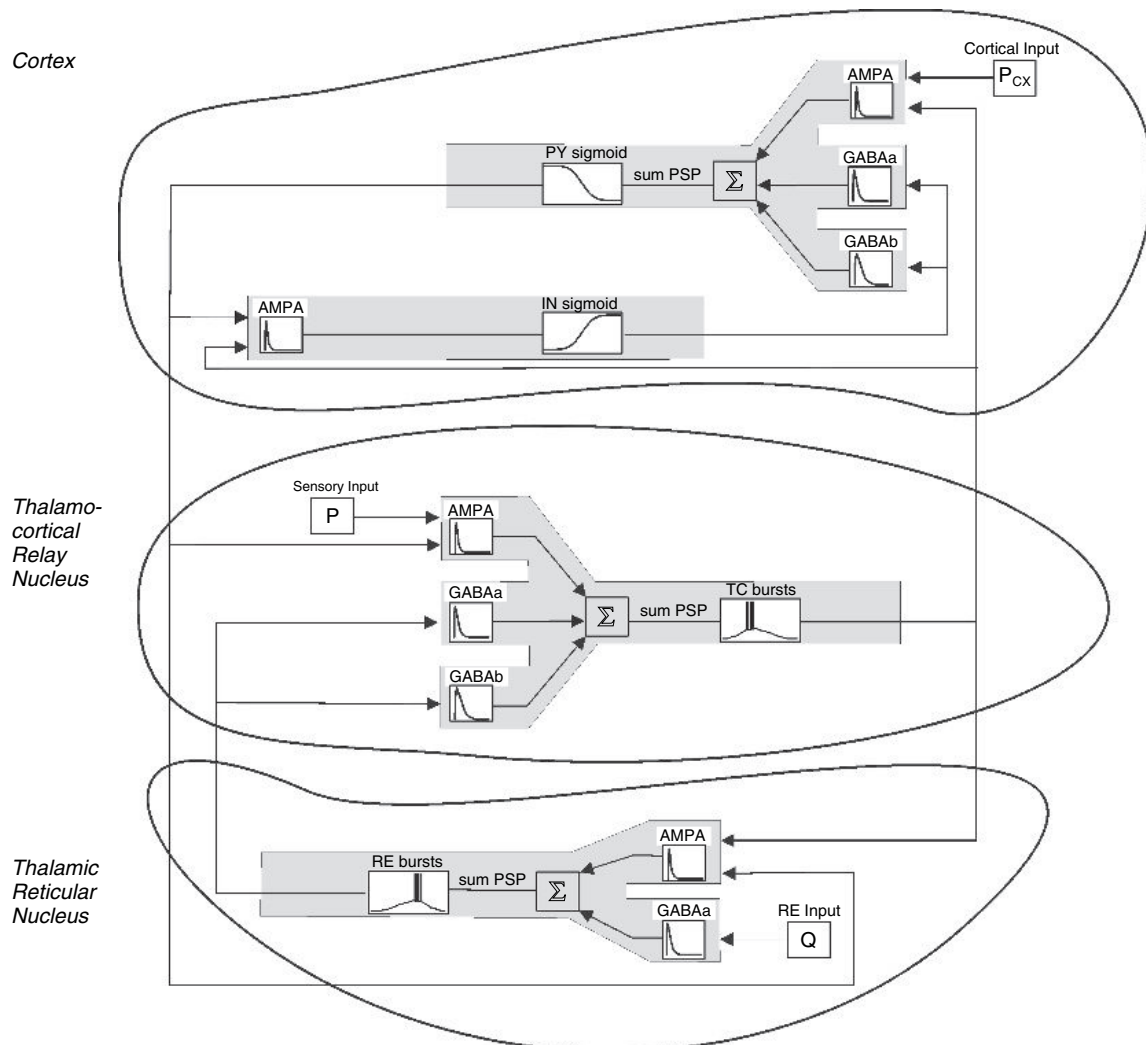


**FIGURE 25.1** Model diagram. A model of thalamocortical network consisting of four neuronal populations – pyramidal cells (PY) and interneurons (IN) in the cortex interconnected with thalamocortical relay cells (TCR) and reticular cells (RE) in the thalamus. Synaptic AMPA and  $GABA_A$  and  $GABA_B$  currents are assumed to contribute to mean membrane potential. Changes of mean membrane potential are transformed into firing densities. In both cortical populations, the transformations between mean membrane potential and firing density are described by sigmoidal functions, while in thalamic ones, low-threshold calcium currents responsible for burst firing is taken into account. The model receives external cortical input  $P_{Cx}$ , sensory input  $P$  and inhibitory input  $Q$ . The output of the model is a mean membrane potential in the PY population.

## SYNAPTIC TRANSMISSION

To simulate the time evolution of the mean membrane potential in the population we used the general equation:

$$C_m \frac{dV}{dt} = -\sum I_{syn} - g_{leak}(V - V_{leak}) \quad (1)$$

$$I_{syn} = g_{syn}(V - V_{syn}) \quad (2)$$

where  $V$  is the mean membrane potential,  $C_m$  is the membrane capacitance,  $g_{leak}$  is the leak current conductance,  $g_{syn}$  is the synaptic current conductance,  $V_{leak}$  and  $V_{syn}$  are the reversal potentials of leak current and synaptic current, respectively. Synaptic conductances were modeled by convolving an incoming action potential sequence, i.e. firing density ( $F(t)$ ) with a synaptic impulse response function ( $h_{syn}(t)$ ):

$$g_{syn}(t) = \int_{-\infty}^t h_{syn}(t - \tau) F(\tau) d\tau \quad (3)$$

$$h_{syn}(t) = A [\exp(-a_1 t) - \exp(-a_2 t)], \quad a_2 > a_1 \quad (4)$$

where  $A$ ,  $a_1$ ,  $a_2$  are an amplitude, rise and delay times, respectively. We also assumed that the amplitude of the GABA<sub>B</sub> postsynaptic current increases non-linearly with the firing density of the RE and IN populations (Kim et al., 1997). Therefore, GABA<sub>B</sub> current was of the form:

$$I_{GABAB} = g_{GABAB}(t) B(F)(V - V_{GABAB}) \quad (5)$$

$$B(F) = \left\{ 1 + \exp \left[ (F - \Theta_B) / \sigma_B \right] \right\}^{-1} \quad (6)$$

where  $F$  denotes mean firing rate,  $\theta_B$  is the threshold for GABA<sub>B</sub> receptor activation and  $\sigma_B$  is the slope parameter.

## MEAN MEMBRANE POTENTIAL TO FIRING RATE CONVERSION

Conversions from mean membrane potential ( $V$ ) to mean firing rates ( $F$ ) in cortical populations were of the sigmoidal form (Lopes da Silva et al., 1974; Freeman, 1975):

$$F(V) = G_s / (1 + \exp [(V - \Theta_s) / \sigma_s]) \quad (7)$$

where  $G_s$  is the maximal firing rate, and  $\theta_s$ ,  $\sigma_s$  are the threshold and slope parameter, respectively.

Conversions from mean membrane potential to pulse densities in thalamic populations took into account the burst firing of thalamic cells that occurs at the hyperpolarized membrane potential levels of these cells. The pulse densities associated with burst firing ( $F_B$ ) of the thalamic populations are:

$$F_B(V) = G_B m_{inf}(V) n(V) \quad (8)$$

$$n(V) = \int_{-\infty}^t h_n(t - \tau) n_{inf}(V) d\tau \quad (9)$$

$$h_n(t) = N [\exp(-n_1 t) - \exp(-n_2 t)], \quad n_2 > n_1, N = n_1 n_2 / (n_2 - n_1) \quad (10)$$

where  $G_B$  is the maximal firing rate during a single burst, variables  $n_{inf}(V)$  and  $m_{inf}(V)$  are static sigmoidal functions of the form of Equation (6) that express the fractions of cells in which  $I_T$  current is de-inactivated and activated, respectively and Equations (9, 10) describe time delay of  $I_T$  inactivation.

## CONNECTIVITY

The coupling constants  $c_1-c_{13}$  represented the number of synaptic contacts that any cell in one population receives on average from cells of other populations. For the purpose of investigating temporal dependencies between cortical and thalamic activities, we introduced explicit time delays in both thalamocortical and corticothalamic projections.

## MODEL'S INPUTS AND OUTPUT

The TC population received an external excitatory input  $P$  that represents glutamatergic sensory inputs. This was modeled as a random signal (Gaussian white noise) with a DC component. The PY population received cortical excitatory input  $P_{CY}$  that stands for the glutamatergic input from other pyramidal cells, not included in the lump. This was also modeled as a random signal with a DC offset. Finally, the RE population received an inhibitory DC offset signal  $Q$  representing the inhibitory bias from the neighboring RE cells. The output of the model,  $V_{CY}$ , was the mean membrane potential of the pyramidal cell population and simulates what is generally measured by recording local field potentials.

## RESULTS

### DIFFERENT TYPES OF MODEL BEHAVIOR

The model may exhibit two qualitatively different types of behavior, such as seen in the experimental animals (WAG/Rij and GAERS). Depending on the model parameters, the inputs and the initial conditions, the output signal may display a waxing and waning ‘spindle-like’ oscillation having a spectrum with a peak at approximately 11 Hz or a high amplitude ‘seizure-like’ oscillation at a frequency around 9 Hz. We refer to the former behavior as ‘normal on-going’ activity while to the latter as paroxysmal activity.

For the reference set of parameters, the model is in a bistable regime where it may generate both spindle and paroxysmal oscillations and spontaneous transitions between these two types of behavior. The model output in this regime is shown in Figure 25.2, upper panel. The lower panel depicts corresponding power spectra.

Spindle activity in the model is generated by the cyclical interaction between the TC and RE populations. Inhibitory postsynaptic potentials of RE origin facilitate the generation of rebound low threshold spikes in the TC population, which in turn activate GABAergic RE neurons. The dominant spindle frequency ( $\approx 11$  Hz) of this rhythmic activity is largely determined by the time courses of both excitatory and inhibitory postsynaptic currents and membrane time constant ( $C_m/g_{leak}$ ) and to a lesser degree by other factors like the characteristics of LTS spikes, synaptic coupling constants and sensory input level. Thalamic generated spindle activity induces activity of the same frequency in the cortical populations. During normal activity, the thresholds for the activation of  $GABA_B$  receptors in TC and PY cells are not reached. When one of these thresholds is surpassed, it is possible to trigger  $GABA_B$  receptor mediated IPSPs, which results in the sudden transition of the model’s behavior from ‘normal on-going’ spindle activity to ‘seizure-like’ 9 Hz high amplitude oscillations.

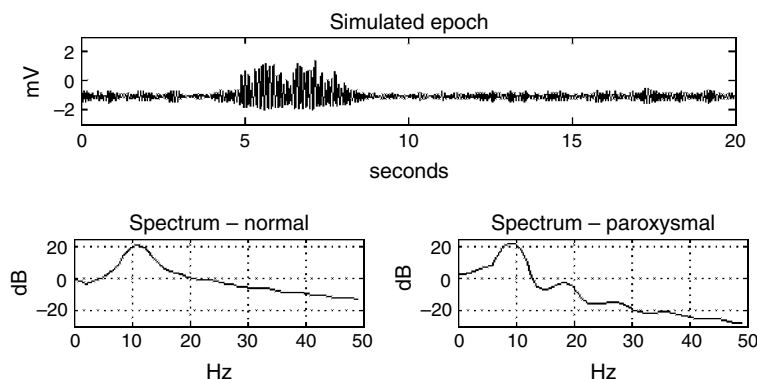


**FIGURE 25.2** Upper panel: 20 seconds of a simulation with the occurrence of a spontaneous paroxysmal episode. Lower panel: power spectra of signals simulated by the model. Spectrum of normal activity has dominant peak around 11 Hz while that of paroxysmal activity has peak around 9 Hz. Adapted from Neuroscience 126(2), Suffczynski, P., Kalitzin S. and Lopes da Silva, F.H., Dynamics of non-convulsive epileptic phenomena modeled by a bistable neuronal network, 467–484. Copyright (2004), with permission from Elsevier.

### BIFURCATION ANALYSIS

First, we should note that spontaneous onset and cessation of paroxysmal activity in the model, such as shown in Figure 25.2, cannot be explained by deterministic (e.g. intermittent) dynamics. This was put in evidence by the simulation with variance of noise inputs equal to zero. Under such conditions, the model exhibited either a constant output, or a periodic 9 Hz oscillation, depending on the initial conditions, but it did not exhibit transitions from one state to another. The mechanism of these transitions becomes clear while analyzing bifurcation diagrams.

In Figure 25.3A we show the two-dimensional bifurcation diagram for the reference set of parameters as a function of constant (noise free) cortical input  $P_{Cx}$ . Its three-dimensional version is presented in Figure 25.3B. In the bifurcation analysis, the noise component was removed from the inputs to keep the illustration simple. The bifurcation diagram was constructed by first increasing and subsequently decreasing the values of  $P_{Cx}$ , the arrows along the diagram follow changes of system's output as the cortical input increases and decreases. The changes in  $P_{Cx}$  were made step-wise and allowed the system to reach its stationary behavior. Figure 25.3A reveals that there are two types of activity possible: an equilibrium point corresponding to 'normal on-going' activity (solid line) and a limit cycle corresponding to paroxysmal oscillations (open circles mark its minimal and maximal amplitude). Figure 25.3A reveals further that the transition between the 'normal on-going' and the paroxysmal activity modes occurs when the cortical input  $P_{Cx}$  increases beyond the bifurcation point at  $P_{Cx}^{bif}$ . This is a typical bifurcation of the subcritical Hopf kind (Glass and Mackey, 1988). As the cortical input is subsequently decreased there is a jump from large amplitude limit cycle oscillations back to equilibrium state but this takes place at a value of  $P_{Cx}^*$  which is less than  $P_{Cx}^{bif}$ . This is a manifestation of hysteresis. For  $P_{Cx}^* < P_{Cx} < P_{Cx}^{bif}$ , there are two coexisting states: normal and paroxysmal. These two dynamical states are locally stable in the sense that, under

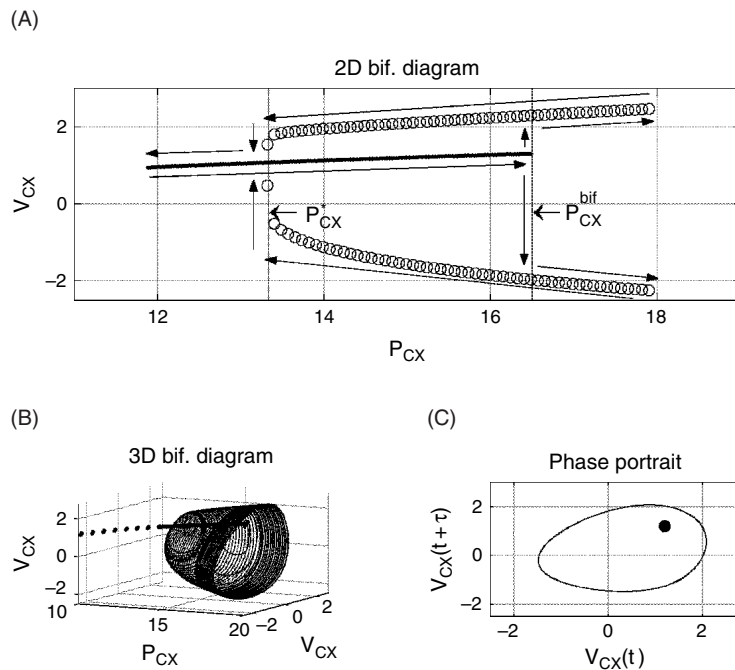


**FIGURE 25.3** (A) Two-dimensional bifurcation diagram showing amplitude of the mean membrane potential in the pyramidal cells population ( $V_{Cx}$  in mV) along the y-axis as a function of increasing and decreasing cortical input ( $P_{Cx}$  in pulses per second (pps)) along the x-axis. Arrows along the bifurcation diagram depict changes of  $V_{Cx}$  as  $P_{Cx}$  increases and decreases. To read a bifurcation diagram, fix the  $P_{Cx}$  at a particular value and mentally draw a vertical line at that value. Each crossing of this line with a curve in the diagram corresponds to a point attractor (thick line) or a limit cycle (open circles denote maxima and minima of an oscillation). Point attractor corresponds to normal activity while limit cycle corresponds to paroxysmal activity. For increasing  $P_{Cx}$  the transition from point attractor to limit cycle occurs at point  $P_{Cx}^{bif}$ . For  $P_{Cx} > P_{Cx}^{bif}$  only paroxysmal behavior is possible. For decreasing  $P_{Cx}$  the transition from limit cycle to point attractor occurs at point  $P_{Cx}^*$ . For  $P_{Cx} < P_{Cx}^*$  only normal behavior is possible. For  $P_{Cx}^* < P_{Cx} < P_{Cx}^{bif}$  the system possesses bistable dynamics: the normal state coexists with the paroxysmal oscillatory state. (B) Three-dimensional bifurcation diagram of the system constructed using delay embedding with cortical input  $P_{Cx}$  along the x-axis, model's output  $V_{Cx}$  along the y-axis and delayed ( $\tau = 40$  ms) version of model's output  $V_{Cx}$  along the z-axis. (C) Phase portrait of the system, obtained by taking a cross-section of figure in (B) for  $P_{Cx} = 15$  pps, showing coexistence of a point attractor (black dot) with a limit cycle (thin line). Reprinted from Neuroscience 126(2), Suffczynski, P., Kalitzin S. and Lopes da Silva, F.H., Dynamics of non-convulsive epileptic phenomena modeled by a bistable neuronal network, 467–484. Copyright (2004), with permission from Elsevier.

small perturbations of finite-time duration, the system recovers to its original state. Therefore, we can call such a system a bistable system. The coexistence of two attractors can be seen also in the phase space plot in Figure 25.3C, which is a cross-section of the bifurcation diagram shown in Figure 25.3B.

In the absence of noise, the normal and paroxysmal attractors correspond to equilibrium point and limit cycle, respectively. When random input fluctuations are introduced to the system, the perturbations of the steady state give rise to small amplitude rhythmic (spindle-like) activity, while perturbations of the limit cycle result in amplitude modulation of the SW oscillations (both rhythms can be seen in Figure 25.2). Spontaneous (i.e. noise induced) transitions between normal and paroxysmal state occur as follows. Let us assume that the system, initially in the normal stable state, is in the bistable domain and that all parameters, including the DC levels of the inputs, are constant. If the (randomly fluctuating) value of  $P_{Cx}$  becomes greater than  $P_{Cx}^{bif}$ , the system undergoes a transition to the paroxysmal state and remains there (because this is a stable state too) until the value of  $P_{Cx}$  becomes smaller than  $P_{Cx}^*$ , bringing the system back to its initial normal state.

The dynamical scenario of transitions between normal and paroxysmal states was described above using the bifurcation diagram in Figure 25.3, which was made for only one control parameter and for only one system's variable (model output). A more complete bifurcation analysis that would take into account other parameters and system's variables and simultaneous variation of two or more control parameters lies beyond the scope of this chapter. However, the following general conclusion can be formulated. The occurrence of paroxysmal activity in the model is governed by a random process, i.e. both the onset and cessation of paroxysms occur randomly over time with certain probabilities. Accordingly, the distribution of the duration of paroxysmal and normal epochs can be predicted to be exponential (Doob, 1953). Therefore, the construction of histograms of the durations of paroxysmal and normal epochs from simulated and experimental time series offers a way to verify these theoretical predictions regarding the dynamics of the process leading to spontaneous paroxysmal discharges. An exponential distribution of lengths of paroxysmal and normal epochs would favor the scenario presented above; different kinds of distributions may indicate that other mechanisms have to be taken into consideration.

#### DISTRIBUTIONS OF PAROXYSMAL AND NORMAL EPOCHS DURATION

To verify the theoretical prediction of the model, we first constructed duration histograms of paroxysmal and normal epochs from the simulated signals. The detection method is described in Suffczynski et al. (2004). The histograms of duration of paroxysmal and normal epochs detected during 24 hours of simulated time, for a reference set of parameters, are shown in Figure 25.4, upper panel. The histograms were fitted with an exponential function using *expfit* procedure in Statistical

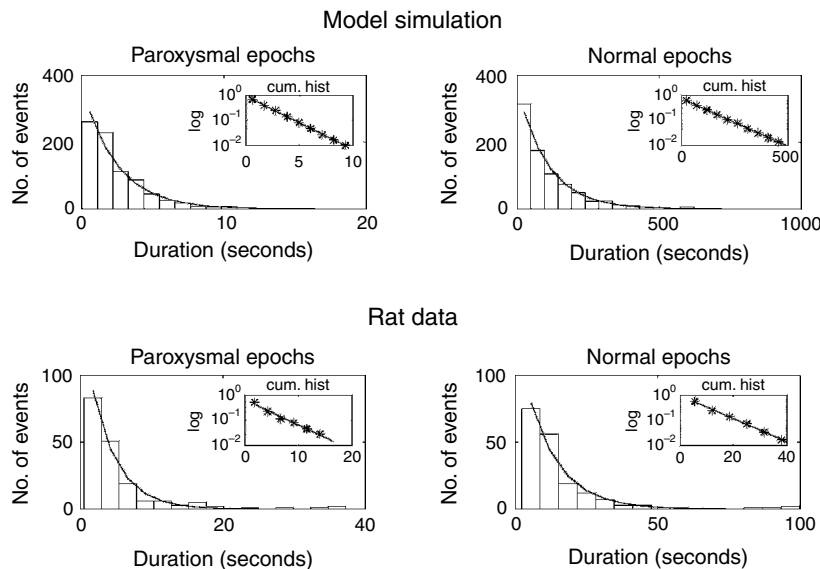


**FIGURE 25.4** Distributions of lengths of normal and paroxysmal epochs obtained using the model (upper panel) and of real EEG signal recorded from the rat (lower panel). On each plot an exponential function fitted to the histogram is shown. Model histograms were obtained by simulating 24 hours of activity using the reference parameters. Histograms of rat were obtained from 30 min recording of EEGs of WAG/Rij rats after administration of high dose of vigabatrine. Inset in each graph shows cumulative histogram on a logarithmic scale. In all our graphs shown, straight line fits well histogram points (\*) indicating exponential distribution. Reprinted from Neuroscience 126(2), Suffczynski, P., Kalitzin S. and Lopes da Silva, F.H., Dynamics of non-convulsive epileptic phenomena modeled by a bistable neuronal network, 467–484. Copyright (2004), with permission from Elsevier.

Toolbox in Matlab and the fitted curves are shown on the graphs indicating that the distributions are well described by exponential function. Additionally, in each panel, an inset shows the cumulative histogram on a logarithmic scale. Straight line fitting well cumulative histograms confirms exponential law.

An example of experimental distributions, with fitted exponential functions is shown in Figure 25.4, lower panel. These distributions were derived from data of WAG/Rij rat six hours after administration of vigabatrin (500 mg/kg). Vigabatrin is a GABA transaminase inhibitor and leads to increased GABA concentration. Increased GABA-mediated inhibition significantly enhances the incidence of paroxysms in WAG/Rij rats and therefore enables obtention of better statistics of the results (details on drug action and data acquisition are given in Bouwnan et al., 2003). Good quality fits of the experimental distributions by the exponential functions and linearity of cumulative histograms on a logarithmic scale, confirm the model's prediction.

### DEPENDENCE OF PAROXYSMS DURATION ON MODEL PARAMETERS

Exponential distributions are characterized by a single variable, the distribution mean. In this section, the dependence of the mean duration of normal and paroxysmal epochs on model parameters is analyzed. Other quantifiers such as total paroxysmal duration or paroxysm incidence can be derived from these two quantifiers. The quantifiers chosen in this study have straightforward interpretation. The first one tells how long one can expect a paroxysm to last on average and therefore it corresponds to the probability of termination of a paroxysmal epoch. The second quantifier tells, once a paroxysm has finished, how long we can expect to wait for the next one to occur and therefore it corresponds to probability of initiation of seizure-like activity.

For the analysis of the dependence of the model's behavior on parameters, we selected six out of 65 model parameters. We selected the parameters that are either assumed to play a role in the pathophysiology of absence seizures in animals and humans, or are assumed to be targets of antiepileptic drugs, or are associated with seizure activation methods (sleep, hyperventilation). We varied one parameter at a time while all others were kept constant. For each parameter setting we simulated 24 hours of activity and created duration histograms from detected paroxysmal and normal epochs. The histograms were fitted with exponential distributions and the distributions' means were calculated. Each parameter (except cholinergic modulation) was manipulated such that the system's behavior varied from at least one paroxysmal event during 24 hours of activity to a state of continuous paroxysmal activity. The influence of a cholinergic neuromodulatory input originating from the brainstem mesencephalic cholinergic neurons was investigated by applying additional DC offset simultaneously to membrane potential in the TC and RE populations. This offset was varied in the range  $-4$  to  $4$  mV in the TC and in the range  $8$  mV to  $-8$  mV in the RE population ( $+1$  mV shift in TC corresponded to  $-2$  mV shift in RE). This is justified taking into account that acetylcholine released by cholinergic pathways decreases a potassium conductance in the TC cells that brings about depolarization of the TC population, while it increases a potassium conductance in the RE neurons and thus induces hyperpolarization of the RE population (McCormick and Prince, 1986, 1987). Results of the analysis are summarized in Figure 25.5.

For each parameter, two panels are presented where the mean duration of paroxysmal epochs (left panel) and of normal epochs (right panel) are shown. The change of a parameter is given in percentage of the corresponding reference value. An increase of the duration of paroxysms and a decrease of the intervals between paroxysms can result from a series of factors: a reduction of cortical GABA<sub>A</sub> inhibition (see Figure 25.5A, left panel), reduction of intra-RE GABA<sub>A</sub> inhibition (see Figure 25.5E, left panel), withdrawal of thalamic cholinergic modulation (see Figure 25.5F, left panel), an increase of the slope of the sigmoid in the cortical interneuronal population (see Figure 25.5B, left panel), an increase of burst firing in the RE or TC populations (see Figure 25.5C, D, left panel). The mean paroxysmal epoch duration is always monotonic function of parameter change. In some plots, this dependence is linear on a logarithmic scale (see Figure 25.5C,E) indicating that, in these cases, the mean epochs duration has exponential dependence on the varied parameter. The local slope of the graph is related to the sensitivity of the system to a change of the given parameter. From Figure 25.5A,B, it follows that the system is most sensitive to cortical GABA<sub>A</sub> inhibition and to the slope of the sigmoid in the population of cortical interneurons, since in these graphs the operating range along the x-axes are the smallest while the range of the y-axes are comparable to the other graphs.

Another important parameter in the model is the noise level. We analyzed the model's performance by varying the variance of one noise source (cortical input  $P_{Cx}$ ) while assuming that the other noise source (sensory input  $P$ ) had a variance equal to zero. The results are summarized in Figure 25.6 where, in the left column, phase portraits of the system are presented and, in the right column, model outputs are shown. The phase portraits were created by plotting the mean membrane potential of the population of interneurons ( $V_{Int}$ ) versus that of pyramidal cells population ( $V_{Cx}$ ). Three panels

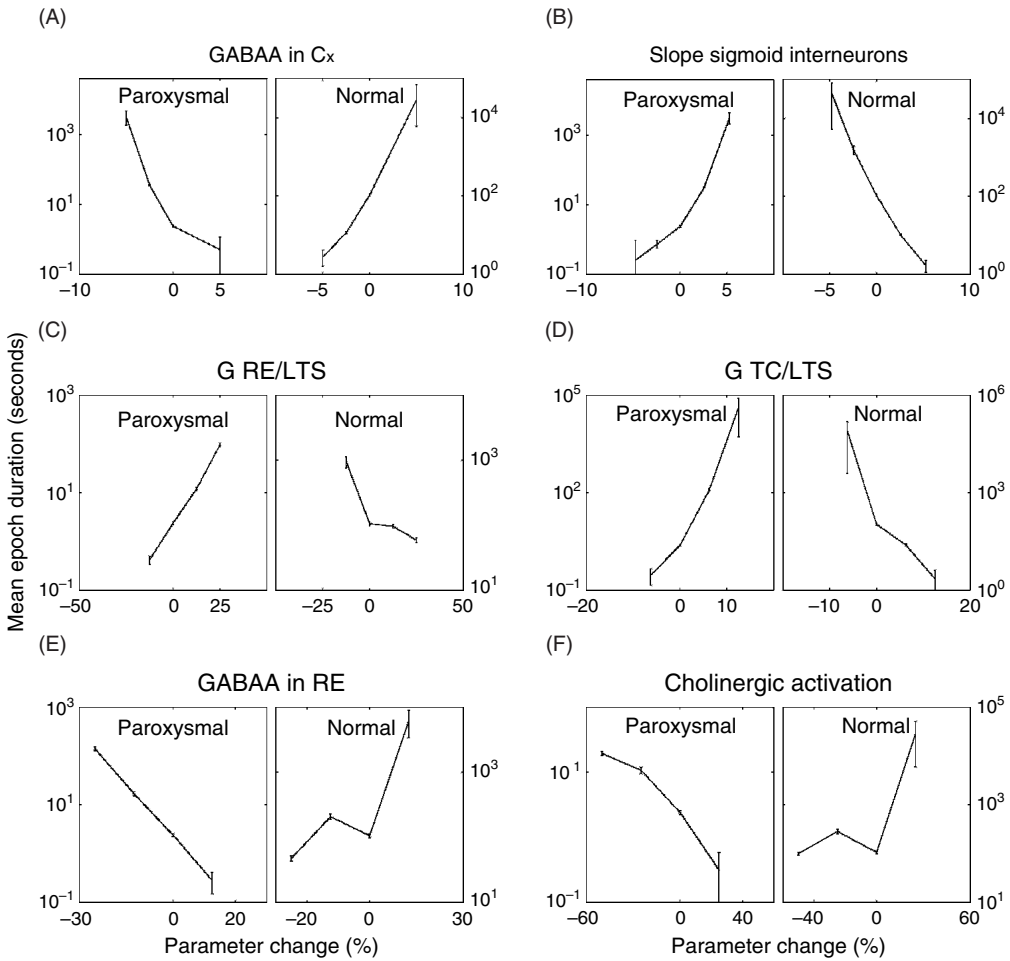


**FIGURE 25.5** Dependence of a mean duration of normal and paroxysmal epochs on the model parameters. For each parameter the mean duration of paroxysmal epochs is shown on the left panel while that of normal epochs is shown on the right panel. In all graphs, the x-axis denotes the relative parameter change in percentage around its reference value, while the y-axis denotes the mean epoch duration, in seconds, on a logarithmic scale. Reprinted from Neuroscience 126(2), Suffczynski, P., Kalitzin S. and Lopes da Silva, F.H., Dynamics of non-convulsive epileptic phenomena modeled by a bistable neuronal network, 467–484. Copyright (2004), with permission from Elsevier.

from top to bottom correspond to low, moderate and high levels of noise, respectively. For low levels of noise, the system is in a normal state and produces only normal activity of small amplitude. For intermediate levels of noise, the system can exhibit both normal and paroxysmal types of activity and spontaneous transitions between them. For high levels of noise, the normal and the paroxysmal states are merged, i.e. the output signal exhibits large temporal variation in amplitude and it is not possible anymore to distinguish epochs of normal and paroxysmal activity.

#### CORTICOTHALAMIC TIME DEPENDENCIES

In order to establish time dependencies between cortical and thalamic modules during both normal and paroxysmal activity, we measured phase differences of the signals generated in PY and TC cell populations during both types of activity. The results for the reference set of parameters are shown in Figure 25.7A. During normal activity, the phase differences at the dominant frequency exhibit large variations, while during paroxysmal activity the phase differences at the dominant frequency are much more stable indicating phase-locking between thalamic and cortical activity. Despite that phase-locking was found to be present during all paroxysmal epochs investigated, the value of the phase difference was dependent on model parameters. An example of phase difference dependence on parameter  $c_2$  (number of RE > TC GABA<sub>A</sub> connections) is shown in Figure 25.7B. Positive values of phase difference denote that the cortical signal precedes the thalamic one, while negative phase differences denote the opposite. An increase of parameter  $c_2$ , which is equivalent to an increase of

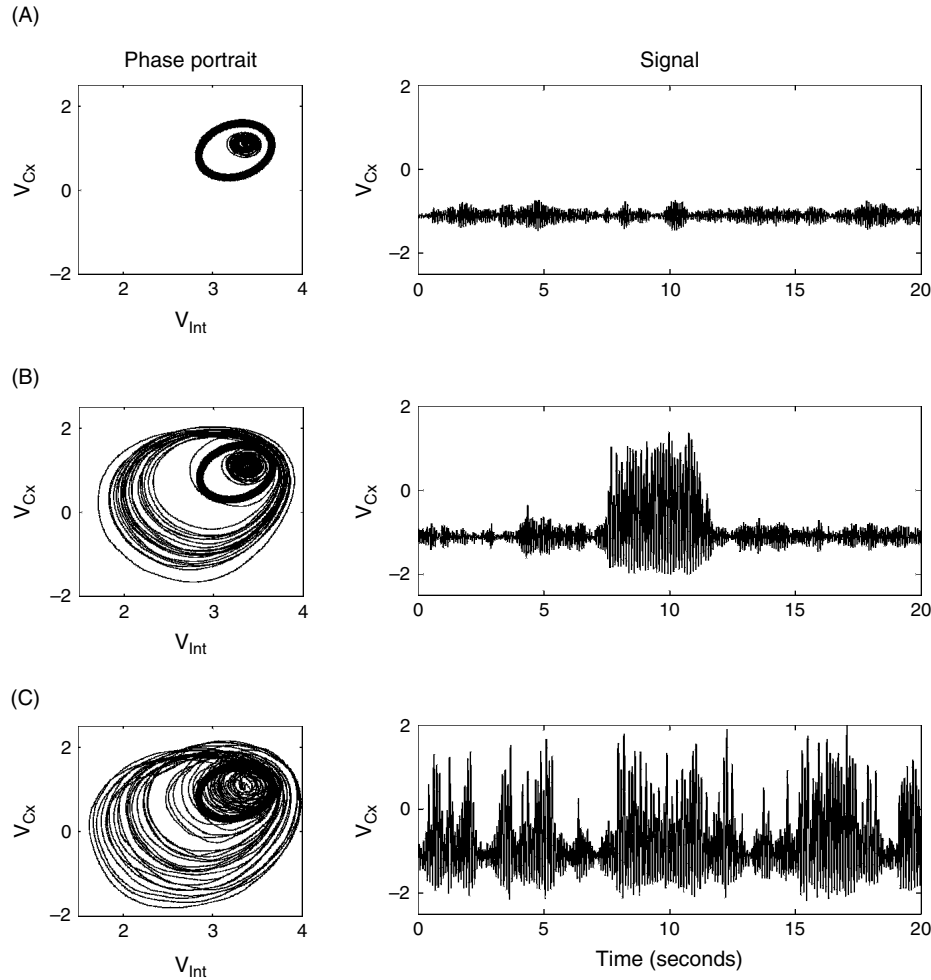


**FIGURE 25.6** Dependence of model behavior on the level of noise. Upper, middle and lower panels correspond to the following values of the standard deviation of cortical input noise: 4 pps, 6 pps and 12 pps, respectively. Standard deviation of sensory input noise was set to 0 in all simulations. For each noise level a two-dimensional phase portrait (left column) and simulated output signal epoch (right column) are presented. The phase portraits were obtained by plotting the mean membrane potential of the population of interneurons ( $V_{Int}$ ) versus that of pyramidal cells population ( $V_{Cx}$ ). Thin lines denote system's trajectory, thick lines denotes hypothetical separatrix separating normal state (within separatrix) from paroxysmal one (outside separatrix). Note different kinds of system's behavior depending on the relative size of fluctuations around normal state and the size of the separatrix.

the strength of GABA<sub>A</sub> inhibition on TC cells, changes the value of the phase difference from  $\approx +0.9$  rad to  $\approx -1.7$  rad. Taking into account that with an increase of  $c_2$ , the dominant frequency of a paroxysmal epoch increases also (from 9 to 11 Hz), the range of phase differences in Figure 25.7B corresponds to time range from  $\approx +15$  ms (cortex ‘leading’) to  $\approx -24$  ms (thalamus ‘leading’).

#### COUNTER-STIMULATION

There is a general interest to develop methods able to control the occurrence or the evolution of seizures. There are theoretical predictions that in bistable systems where a limit cycle coexists with a steady state, a perturbation delivered to the limit cycle may annihilate the oscillation (Glass and Mackey, 1988). Since our analysis presented above showed that the model, as well as some real epileptic systems, exhibits bistability properties, we investigated, using the model, how a paroxysmal oscillation could be aborted. A paroxysmal oscillation was triggered by a pulse of 40 pps (pulses per second) amplitude, 10 ms duration delivered to the cortical input around second 1.5. If no stimulation was applied afterwards, the paroxysmal discharge continued as time progressed (Figure 25.8A). However, a well-timed counter-stimulation pulse of either positive (Figure 25.8B) or negative (Figure 25.8C) polarity delivered to the cortical input was able to abort the paroxysmal oscillation.

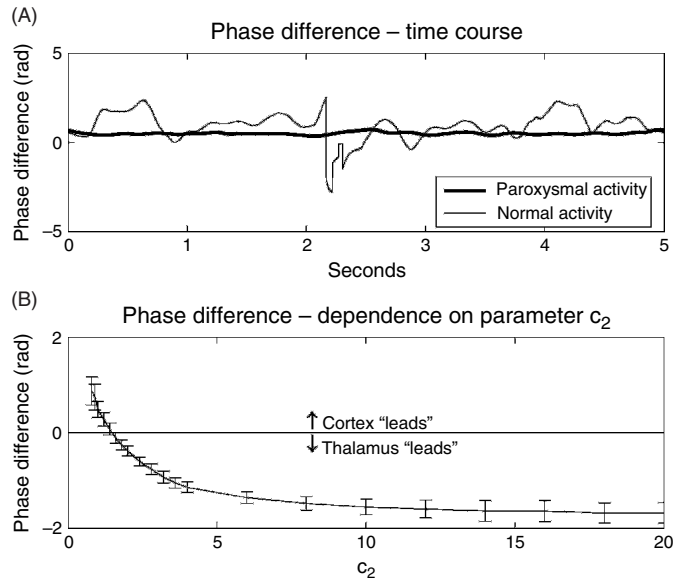


**FIGURE 25.7** Phase difference between mean membrane potentials of cortical PY and thalamic TC populations. (A) Time course of phase difference for representative epochs of normal (thin line) and paroxysmal (thick line) activity. (B) Dependence of phase difference during paroxysmal activity on parameter  $c_2$ . For each fixed value of the parameter  $c_2$  paroxysmal epoch was simulated. The mean and error of the mean of the phase difference during whole epoch were calculated using Gabor transforms of original signals (see Kalitzin et al., 2005a for details of the method). Note that for values of  $c_2$  smaller than 1.4 the paroxysmal activity of the cortex leads the activity of the thalamus while for  $c_2$  larger than 1.4 the opposite occurs.

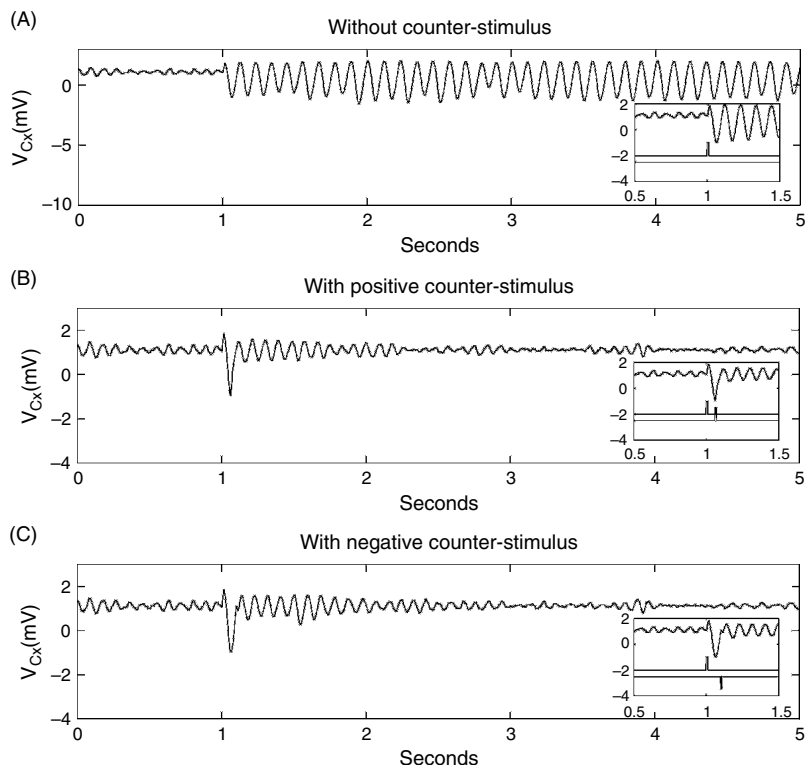


**FIGURE 25.8** Counter stimulation phenomenon. (A) The paroxysmal oscillations initiated by the triggering pulse are prolonged and there is no counter stimulation pulse applied. (B) The positive counter stimulation pulse delivered 62 ms after the trigger stops paroxysmal discharge. (C) The negative counter stimulation pulse delivered 95 ms after the trigger stops paroxysmal discharge. The insets display the output signal and both triggering and counter stimulation pulses in an extended time scale. They show that the positive critical stimulus effective in annihilation of the paroxysmal rhythm was delivered when the PY population was maximally inhibited while negative critical pulse was delivered during the raising slope of the PY population mean voltage.

## DISCUSSION

### BASIC PROPERTIES OF THE MODEL

We constructed a model of interconnected thalamic and cortical populations with parameters directly related to synaptic and cellular properties in order to investigate the mechanisms of generation of synchronized oscillations in a thalamocortical neuronal network, using animal data obtained in rat genetic models of absence (WAG/Rij and GAERS) as the basic experimental data to be modeled. The simulation studies of the dynamical behavior of the model and of its sensitivity to a number of basic parameters led to the following main results:

1. Paroxysmal discharges characterized by 9 Hz large amplitude oscillations represent bifurcations that occur in a neuronal network with bistability properties. This means that two stable states coexist, one corresponding to the ‘normal on-going’ EEG activity and the other to the paroxysmal oscillations, and that the system may undergo transitions from one state to another. These transitions can emerge spontaneously and are not induced by any parameter changes.
2. The distributions of lengths of paroxysmal and ‘normal on-going’ epoch are exponential, indicating that transitions between these two stable states occur randomly over time and that the probabilities for the transition between both states can be defined.
3. Probabilities of transitions between ‘normal on-going’ neuronal activity and paroxysmal oscillations depend on a number of model parameters; therefore decreases or increases of these probabilities can be achieved in a not unique way.
4. Activities in thalamic and cortical modules are phase-locked during paroxysmal events. Phase difference can be both positive and negative, depending on parameters.
5. Paroxysmal oscillations can be annihilated by a well-timed pulse
6. Since random fluctuations in control parameters and/or dynamic variables can lead to the sudden onset of large amplitude paroxysmal activity, this implies that the occurrence of this type of phenomenon is unpredictable per definition.

### TIME DISTRIBUTIONS OF PAROXYSMAL EVENTS

Here we discuss how our model results compare with experimental findings on rat models of absence epilepsy. The proposed scenario of transitions occurring randomly in time in a bistable network (points 1, 2) cannot be verified in a real system on the basis of single event analysis. However, the distribution of event duration over a long time of observation can offer a way for testing the model predictions. Therefore, it is interesting to compare model data with those obtained experimentally. The histograms of duration of experimental ictal and in-between ictal activity in WAG/Rij rats after administration of vigabatrin have exponential shape (see Figure 25.4, lower panel) providing an example of the real system in which seizure initiation and termination are random processes with constant probabilities over time. Other examples from various epileptic systems, including human experimental data, can be found in Suffczynski et al. (2005, 2006). In a number of cases, the null hypothesis of bistable system with fixed probability of transitions could not be rejected. However, we also found evidence for modulation of transition probabilities by specific neuronal processes that were not included in the present model.

### SENSITIVITY OF MODEL PERFORMANCE TO PARAMETERS: GABA<sub>A</sub> INHIBITION, INTERNEURONAL SYNCHRONIZATION AND CALCIUM CURRENTS

Parameter analysis of the model network revealed that seizure duration is most sensitive to:

1. cortical GABA<sub>A</sub> inhibition (see Figure 25.5A)
2. to the slope of the sigmoid transfer function of cortical interneurons (see Figure 25.5B)
3. to changes of the Ca<sup>2+</sup> currents, particularly in RE neurons (see Figure 25.5C).

We examine next a number of experimental findings that are in line with these three predictions of the model. Concerning the former, this is consistent with many experimental data obtained in animal models of absence epilepsy.

1. Investigations of the primary abnormalities underlying non-convulsive generalized seizures in GAERS rats revealed, among others, an impairment of GABA-mediated transmission in the neocortex (Avanzini et al., 1996). Similarly, the cortical hyperexcitability in WAG/Rij rats was demonstrated to be due to a decrease in GABA-mediated inhibition (Luhmann et al., 1995). Injection of GABA<sub>A</sub> antagonists such as penicillin or bicuculline to the cortex produced SWD discharges in cats (Gloor et al., 1990; Steriade and Contreras, 1998). Powerful control of cortical excitability by intracortical GABA<sub>A</sub> inhibition was also demonstrated *in vivo* and in a modeling study by Contreras et al. (1997).
2. The critical dependence of paroxysmal activity on the slope of the sigmoid transfer function of cortical interneurons does not have a straightforward interpretation. We may state that an increase of the slope of the sigmoid transfer function is directly related to narrowing the distribution of firing thresholds in a population and thus it represents an increased synchrony in that population. We hypothesize that the slope parameter may mimic the strength of gap-junctional connections within a population of interneurons. Therefore, it may be of interest to note that (a) it was proposed by Velazquez and Carlen (2000) that hyperventilation, which reduces blood CO<sub>2</sub> levels and causes alkalosis, may rapidly enhance gap-junctional communication and neural synchrony and (b) anatomical data indicate that gap junctions in the neocortex are specifically formed among inhibitory cells (Galarreta and Hestrin, 2001). In the light of these two statements, our modeling results showing that an increase of a parameter characterizing synchrony within interneuronal population has a powerful effect on paroxysmal activity may be related to the effect of hyperventilation, which is a well-known method of absence seizure activation in human patients.
3. A decrease of a calcium current in the RE population (i.e. a decrease of parameter  $G_{RE}$ ) was found to decrease seizure duration and increase intervals between seizures (see Figure 25.5C). Our model results are compatible with the experimental findings in epileptic GEARS rats. Tsakiridou et al. (1995) has demonstrated that in these epileptic animals the low-threshold ( $I_T$ ) calcium conductance in the reticular nucleus neurons is elevated in comparison to non-epileptic controls. In the same strain of epileptic rats, a pharmacological reduction of a burst firing in reticular nucleus, attributed to a decrease of the  $I_T$  calcium current and consequent decrease of calcium dependent potassium current, resulted in a decrement of paroxysmal discharge duration, measured over fixed time (Avanzini et al., 1992). Thomas and Grisar (2000) put forward an interesting hypothesis that increased synchrony of the thalamic network due to an increase of  $I_T$  current conductance in the RE neurons may be related rather to phase-shift in the activity of the TC and RE neurons than to increase of the amplitude of LTS in RE cells, since the latter was unaffected by  $I_T$  conductance changes. We also found in our model that an increase of  $I_T$  current in the RE population changes the phase relation between TC and RE neurons, increasing the network synchrony as indicated by the enhancement of the peak in the power spectrum of the thalamic signals.

#### SIMULATION OF EFFECTS OF ANTI-EPILEPTIC DRUGS (AED)

The model allowed also to investigate the mechanism by which antiepileptic drugs may affect the threshold for seizure occurrence. The most selective anti-absence drug, ethosuximide, is believed to exert its antiepileptic effect by antagonizing the burst firing in the TC neurons either by decreasing the  $I_T$  current (Coulter et al., 1989, 1990, 1991) or, as a more recent study suggests, by acting on the non-inactivating Na<sup>+</sup> current and on a Ca<sup>2+</sup>-activated K<sup>+</sup> current (Leresche et al., 1998). In our model, a reduction of the amplitudes of LTS generated in the TC population (reflected on parameter  $G_{TC}$ ) results in a decrease of paroxysm duration and an increase of in-between seizure interval (see Figure 25.5D). The effect of benzodiazepines, such as clonazepam, is related to specific cellular targets within the thalamic networks. Indeed, the RE and TC neurons do not have the same kind of GABA<sub>A</sub> receptors; those of the former have molecular subunits with binding sites for benzodiazepines, in contrast to the latter. Thus, these anti-absence drugs are believed to enhance GABA<sub>A</sub>-mediated inhibition within the reticular nucleus (Huguenard and Prince, 1994) but not in TC cells and, in this way, to suppress GABA-mediated inhibition of RE to TC neurons and thus prevent absence seizures. This hypothesis is confirmed by our model since an increase of inhibitory strength between RE cells (reflected on parameter  $Q$ ) decreases RE output and antagonizes paroxysmal activity (see Figure 25.5E), while an increase of GABA<sub>A</sub>-mediated inhibition in TC neurons has the opposite effect (not shown).

#### SIMULATIONS OF AROUSAL AND TRANSITION WAKEFULNESS-SLEEP

Our results are also consistent with clinical observations that absence seizures most often develop during sleep (Kellaway, 1985). In the model, we found (see Figure 25.5F) that a decrease of cholinergic activation from the brainstem, which

mainly underlies the transition from the waking state to sleep (McCormick and Bal, 1997), facilitates the generation of paroxysmal activity. The latter result is also in line with the fact that paroxysmal discharges in GAERS occurred primarily when attention and activity were reduced (Snead et al., 1999) and with the anti-burst action of cholinergic thalamic input as proposed by Buzsáki et al. (1990).

### **INFLUENCE OF THE NOISE LEVEL**

The transitions in the model are induced by fluctuation, therefore, the relative size of fluctuations with respect to size of basins of normal and paroxysmal attractors has profound consequences in observed model behavior. It was also hypothesized that this feature may discriminate between normal and epileptic brain (Lopes da Silva et al., 2003). When fluctuations are much smaller than the basin of attractor of normal activity, the system's trajectory stays confined within that basin and the system never switches to paroxysmal activity (see Figure 25.6A). With increased size of fluctuations, the trajectory may cross the separatrix (a line separating basins of attraction) occasionally, giving rise to paroxysmal episodes (see Figure 25.6B). For large fluctuations the trajectory switches back and forth between the two attractors and the two types of activity become merged (see Figure 25.6C). Such behavior has been observed e.g. in WAG/Rij rats after high doses of vigabatrin (Bouwman, personal communication).

### **DOES THE CORTEX OR THE THALAMUS LEAD DURING PAROXYSMAL EVENTS?**

A long-lasting controversy has existed whether the 'pacemaker' of SW oscillations associated with absence seizures in humans is located in cortical, thalamic or the thalamocortical network. The present model is able to generate paroxysmal activity in isolated cortical, thalamic or interconnected thalamocortical networks (Suffczynski et al., 2004). This points to the possibility that SW generation is not a homogeneous phenomenon and that both thalamus and cortex alone, as well as the full thalamocortical system are able to sustain SW oscillation. We also analyzed phase relations between cortical and thalamic neuronal signals during normal and paroxysmal activity. Phase differences between the PY and TC cells during normal activity exhibited large temporal variation, while during paroxysmal behavior the phase relation was much more stable (see Figure 25.7). These results are in agreement with Meeren et al. (2002) who investigated time delays between functionally related cortical and thalamic neuronal signals in WAG/Rij rats. They reported large variation of time delays in the activity preceding the onset of a seizure and a decrease of this variation during the seizure. Finally, we should note that phase relations do not necessarily provide causal relationships between activities in the structures involved in the oscillation. As we have shown, both negative and positive phase relations between thalamus and cortex may exist during limit-cycle oscillation involving these two interconnected structures. We found that whether these phase relations are positive or negative may depend on parameter  $c_2$ , i.e. on the number of RE > TC GABA A connections.

### **CAN PAROXYSMAL OSCILLATIONS BE ABORTED?**

In a bistable system where a stable steady state coexists with a stable limit cycle, the transitions between the two can be triggered by a single pulse. In addition, the oscillation may be terminated if a brief stimulus of sufficient magnitude is delivered at a critical phase of the oscillation (so called 'black hole' perturbation, Glass and Mackey, 1980). Also, as predicted by the theory (Murray, 2004), two such 'black holes' should exist. The results of the present model confirm these theoretical predictions. As shown in Figure 25.8, both positive and negative stimulus can be applied to abort the oscillation indicating that two A detailed analysis of the effective pulse parameters can be found in Suffczynski et al. (2004). These results may be verified experimentally, although one should bear in mind that the model is spatially localized, while real neural networks are spatially distributed which imposes some limitations on the above model predictions.

### **CAN ABSENCE SEIZURES BE PREDICTED?**

Recently, there is a growing interest whether changes in brain dynamics preceding a seizure exist and are detectable. The model can help to understand whether the occurrence of absence seizures may be predicted some time in advance or not. The fact that we found that random fluctuations can be responsible for the sudden onset of the paroxysmal oscillations implies that the occurrence of these seizures cannot be predicted since fluctuations of the input are unpredictable by definition. This conclusion is consistent with classic clinical observations in humans as expressed by Lennox and Lennox (1960): 'If warning occurs, the diagnosis of petit mal may be questioned'. This is, however, in contrast with Rogowski

et al. (1981), who reported the possibility of predicting absence seizures by several seconds. While the possibility of prediction of the exact timing of absence seizures is rejected by our model, quantifying the probability for an instantaneous seizure transition, e.g. by indirect measuring some control parameters might be a realistic option (Kalitzin et al., 2005b).

#### ACKNOWLEDGMENTS

Piotr Suffczynski was sponsored by Lopes da Silva Fellowship from Stichting Epilepsie Instellingen Nederland.

#### REFERENCES

- Avanzini, G., de Curtis, M., Marescaux, C., Panzica, F., Spreafico R. and Vergnes, M. (1992). Role of the thalamic reticular nucleus in the generation of rhythmic thalamo-cortical activities subserving spike and waves. *J Neural Transm (Suppl)* 35:85–95.
- Avanzini, G., de Curtis, M., Franceschetti S., Sancini G. and Spreafico R. (1996). Cortical versus thalamic mechanisms underlying spike and wave discharges in GAERS. *Epilepsy Res* 26(1):37–44.
- Bal, T., von Krosigk, M. and McCormick, D.A. (1995a). Synaptic and membrane mechanisms underlying synchronized oscillations in the ferret LGNd in vitro. *J Physiol Lond* 483:641–663.
- Bal, T., von Krosigk, M. and McCormick, D.A. (1995b). Role of the ferret perigeniculate nucleus in the generation of synchronized oscillations in vitro. *J Physiol Lond* 483:665–685.
- Bouwman, B., van den Broek, P.L.C., van Luijtelaar, E.L.J.M. and van Rijn, C.M. (2003). The effects of vigabatrin on type II spike wave discharges in rats. *Neurosci Lett* 338(3):177–180.
- Castro-Alamancos, M.A. (1999). Neocortical synchronized oscillations induced by thalamic disinhibition in vivo. *J Neurosci* 19(18):1–7.
- Buzsáki, G., Smith, A., Berger, S., Fisher, L. J. and Gage, F.H. (1990). Petit mal epilepsy and parkinsonian tremor: hypothesis of a common pacemaker. *Neuroscience* 36(1):1–14.
- Coenen, A.M.L., Drinkenburg, W.H.I.M., Inoue, M. and van Luijtelaar, E.L.J.M. (1992). Genetic models of absence epilepsy, with emphasis on the WAG/Rij strain of rats. *Epilepsy Res* 12:75–86.
- Contreras, D., Destexhe, A. and Steriade, M. (1997). Intracellular and computational characterization of the intracortical inhibitory control of synchronized thalamic inputs in vivo. *J Neurophysiol* 78:335–350.
- Coulter, D.A., Huguenard, J.R. and Prince, D.A. (1989). Characterization of ethosuximide reduction of low-threshold calcium current in thalamic neurons. *Ann Neurol* 25:582–593.
- Coulter, D.A., Huguenard, J.R. and Prince, D.A. (1990). Differential effects of petit mal anticonvulsants and convulsants on thalamic neurones: calcium current reduction. *Br J Pharmacol* 100:800–806.
- Coulter, D.A., Huguenard, J.R. and Prince, D.A. (1991). Mechanism of block of thalamic ‘T’-type  $\text{Ca}^{2+}$  channels by petit mal anticonvulsants. *Exp Brain Res* 20:201–204.
- Danober, L., Deransart, C., Depaulis, A., Vergnes, M. and Marescaux, C. (1998). Pathophysiological mechanisms of genetic absence epilepsy in the rat. *Prog Neurobiol* 55:27–57.
- Destexhe, A. (1998). Spike-and-wave oscillations based on the properties of  $\text{GABA}_B$  receptors. *J Neurosci* 18:9099–9111.
- Destexhe, A. (1999). Can  $\text{GABA}_A$  conductances explain the fast oscillation frequency of absence seizures in rodents? *Eur J Neurosci* 11:2175–2181.
- Doob, J.L. (1953). *Stochastic Processes*. John Wiley & Sons: New York.
- Freeman, W.J. (1975). Mass action in the nervous system. Academic Press, New York.
- Galarreta, M. and Hestrin, S. (2001). Electrical synapses between  $\text{GABA}$ -releasing interneurons. *Nat Rev Neurosci* 2:425–433.
- Glass, L. and Mackey, M.C. (1988). From clocks to chaos: the rhythms of life. Princeton University Press, Princeton.
- Gloor, P., Avoli, M. and Kostopoulos, G. (1990). Thalamocortical relationships in generalized epilepsy with bilaterally synchronous spike-and-wave discharge. In: ‘Generalized epilepsy, neurobiological approaches’ (M. Avoli, P. Gloor, G. Kostopoulos and R. Naquet, eds) pp. 190–212. Birkhäuser, Boston.
- Golomb, D., Wang X.-J. and Rinzel, J. (1996). Propagation of spindle waves in a thalamic slice model. *J Neurophysiol* 75(2):750–769.
- Huguenard, J.R. and Prince, D.A. (1994). Clonazepam suppresses  $\text{GABA}_B$  mediated inhibition in thalamic relay neurons through effect in nucleus reticularis. *J Neurophysiol* 71:2576–2581.
- Jahnsen, H. and Llinas, R.R. (1984a). Electrophysiological properties of guinea-pig thalamic neurons, an in vitro study. *J Physiol (Lond)* 349:205–226.
- Jahnsen, H. and Llinas, R.R. (1984b). Ionic basis for the electroresponsiveness and oscillatory properties of guinea-pig thalamic neurones in vitro. *J Physiol (Lond)* 349:227–247.
- Kalitzin, S.N., Derchansky, M., Velis, D.N., Parra, J., Carlen, P.L. and Lopes da Silva, F.H. (2005a). Amplitude and phase synchronization in a model of temporal lobe epilepsy. The 3rd European Medical and Biological Engineering Conference, November 20–25, 2005, Prague, Czech Republic, IFMBE Proc. 11(1).
- Kalitzin, S.N., Velis, D.N., Suffczynski, P., Parra, J. and Lopes da Silva, F.H. (2005b). Intermittent electrical brain-stimulation paradigm for estimating the seizure onset site and the time to ictal transition in temporal lobe epilepsy. *Clin Neurophysiol* 116:718–728.
- Kellaway, P. (1985). Sleep and epilepsy. *Epilepsia* 26:15–30.
- Kim, U., Sanchez-Vives, M.V., McCormick, D.A. (1997). Functional Dynamics of GABAergic Inhibition in the Thalamus. *Science* 278, 130–134.
- Lennox, W.G. and Lennox, M.A. (1960). *Epilepsy and related disorders*, Vol. 1. Little, Brown and Co., Boston.

- Leresche, N., Parri, H.R., Erdemli, G. et al. (1998). On the action of the anti-absence drug ethosuximide in the rat and cat thalamus. *J Neurosci* 18(13):4842–4853.
- Liu, Z., Vergnes, M., Depaulis, A. and Marescaux, C. (1992). Involvement of intrathalamic GABA<sub>B</sub> neurotransmission in the control of absence seizures in the rat. *Neuroscience* 48:87–93.
- Lopes da Silva, F.H., Hoeks, A., Smits, H. and Zetterberg, L.H. (1974). Model of brain rhythmic activity. the alpha-rhythm of the thalamus. *Kybernetik* 15:27–37.
- Lopes da Silva, F.H., Blanes, W., Kalitzin, S.N., Parra, J., Suffczynski, P. and Velis, D.N. (2003). Dynamical diseases of brain systems: different routes to epileptic seizures. *IEEE Trans Biomed Eng* 50(5):540–548.
- Luhmann, H.J., Mittmann, T., van Luijtelaar, E.L.J.M. and Heinemann, U. (1995). Impairment of intracortical GABAergic inhibition in a rat model of absence epilepsy. *Epilepsy Res* 22:43–51.
- Marescaux, C., Vergnes, M. and Depaulis, A. (1992). Genetic absence epilepsy rat from Strasbourg – a review. *J Neural Transm (Suppl)* 35:37–69.
- McCormick, D.A. and Bal, T. (1997). Sleep and arousal: thalamocortical mechanisms. *Ann Rev Neurosci* 20:185–215.
- McCormick, D.A. and Prince, D.A. (1986). Acetylcholine induces burst firing in thalamic reticular neurones by activating a potassium conductance. *Nature* 319:402–405.
- McCormick, D.A. and Prince, D.A. (1987). Actions of acetylcholine in the guinea-pig and cat medial and lateral geniculate nuclei in vitro. *J Physiol (Lond)* 392:147–165.
- Meeren, H.K.M., Pijn, J.M.P., Van Luitelaar, E.L.J.M., Coenen, A.M.L. and Lopes da Silva, F.H. (2002). Cortical focus drives widespread corticothalamic networks during spontaneous absence seizures in rats. *J Neurosci* 22:1480–1495.
- Murray, J.D. (2004). Mathematical biology I. Springer, New York.
- Nunez, P.L. (1995). Neocortical dynamics and human EEG rhythms. Oxford University Press, New York.
- Rogowski, Z., Gath, I. and Bentel, E. (1981). On the prediction of epileptic seizures. *Biol Cybern* 42:9–15.
- Snead, C.O., Depaulis, A., Vergnes, M. and Marescaux, Ch. (1999). Jasper's basic mechanisms of the epilepsies. In: Advances in neurology, Vol. 79 (A.V. Delgado-Escueta, W.A. Wilson, R.W. Olsen and R.J. Porter, eds) pp. 253–279. Lippincott Williams and Wilkins, Philadelphia.
- Steriade, M. and Contreras, D. (1998). Spike-wave complexes and fast components of cortically generated seizures. I. Role of neocortex and thalamus. *J Neurophysiol* 80:1439–1455.
- Steriade, M. and Deschenes, M. (1984). The thalamus as a neuronal oscillator. *Brain Res. Rev.* 8, 1–63.
- Steriade, M., Gloor, P., Llinas, R.R., Lopes de Silva, F.H. and Mesulam, M.M. (1990). Report of IFCN Committee on basic mechanisms. Basic mechanisms of cerebral rhythmic activities. *Electroencephalogr Clin Neurophysiol* 76(6):481–508.
- Suffczynski, P., Kalitzin, S. and Lopes da Silva, F.H. (2004). Dynamics of non-convulsive epileptic phenomena modeled by a bistable neuronal network. *Neuroscience* 126(2):467–484.
- Suffczynski, P., Lopes da Silva, F.H., Parra, J., Velis, D. and Kalitzin, S. (2005). Epileptic transitions – model predictions and experimental validation. *J Clin Neurophysiol* 22(5): 288–299.
- Suffczynski, P., Lopes da Silva, F.H., Parra, J. et al. (2006) Dynamics of epileptic phenomena determined from statistics of ictal transitions. *IEEE Trans Biomed Eng* 53(3):524–532.
- Thomas, E. and Grisar, T. (2000). Increased synchrony with increase of a low-threshold calcium conductance in a model thalamic network: a phase-shift mechanism. *Neural Comput* 12(7):1553–1571.
- Tsakiridou, E., Bertolini, L., De Curtis, M., Avanzini, G. and Pape, H.C. (1995). Selective increase in T-type calcium conductance of reticular thalamic neurons in a rat model of absence epilepsy. *J Neurosci* 15:3110–3117.
- van Luijtelaar, E.L.J.M. and Coenen, A.M.L. (1986). Two types of electrocortical paroxysms in an inbred strain of rats. *Neurosci Lett* 70:393–397.
- Velazquez, J.L.P. and Carlen, P.L. (2000). Gap junctions, synchrony and seizures. *Trends Neurosci* 23:68–74.
- von Krosigk, M., Bal, T. and McCormick, D.A. (1993). Cellular mechanisms of a synchronized oscillation in the thalamus. *Science* 261:361–364.
- Wang, X.-J., Golomb, D. and Rinzel, J. (1995). Emergent spindle oscillations and intermittent burst firing in a thalamic model: specific neuronal parameters. *Proc Natl Acad Sci USA* 92:5577–5581.
- Wendling, F., Bartolomei, F., Bellanger, J.J. and Chauvel, P. (2002). Epileptic fast activity can be explained by a model of impaired GABAergic dendritic inhibition. *Eur J Neurosci* 15: 499–508.
- Zetterberg, L.H., Kristiansson, L. and Mossberg, K. (1978). Performance of the model for a local neuron population. *Biol Cybern* 31:15–26.

# 26

## EXTRACELLULAR POTASSIUM DYNAMICS AND EPILEPTOGENESIS

FLAVIO FRÖHLICH, IGOR TIMOFEEV, TERRENCE J. SEJNOWSKI  
AND MAXIM BAZHENOV

### ABSTRACT

Extracellular ion concentrations change as a function of neuronal activity and represent important factors influencing the dynamic state of a population of neurons. In particular, relatively small changes in extracellular potassium concentration ( $[K^+]$ )<sub>o</sub>) mediate substantial changes in neuronal excitability and intrinsic firing patterns. While experimental approaches are limited in their ability to shed light on the dynamic feedback interaction between ion concentration and neural activity, computational models and dynamic system theory provide powerful tools to study activity-dependent modulation of intrinsic excitability mediated by extracellular ion concentration dynamics. In this chapter, we discuss the potential role of extracellular potassium concentration dynamics in the generation of epileptiform activity in neocortical networks. Detailed bifurcation analysis of a model pyramidal cell revealed a bistability with hysteresis between two distinct firing modes (tonic firing and slow bursting) for mildly elevated  $[K^+]$ <sub>o</sub>. In neocortical network models, this bistability gives rise to previously unexplained slow alternating epochs of fast runs and slow bursting as recorded *in vivo* during neocortical electrographic seizures in cats and in human patients with the Lennox-Gastaut syndrome. We conclude that extracellular potassium concentration dynamics may play an important role in the generation of seizures.

### INTRODUCTION

Epilepsy is one of the most common neurological disorders. Close to 5% of people in the world may have at least one seizure in their lifetime. At any time, 50 million people have epilepsy, especially in childhood, adolescence and old age. In developed countries, the annual incidence of epilepsy is estimated at 50 per 100 000 of the general population. Studies in developing countries, however, suggest that this figure is nearly double at 100 per 100 000 people. Up to 30% of people with epilepsy may not respond to pharmacological treatment (<http://www.who.int/mediacentre/factsheets/fs165/en>). These data illustrate that not enough is known about the mechanisms of epileptogenesis to treat it effectively. For the development of more effective antiepileptic drugs, it is therefore essential to better understand the underlying causes of the different forms of epileptic brain activity. Due to the complexity of neural dynamics, computational models with biological plausibility have become an important tool to study the epileptic brain.

While changes in the ionic composition of the extracellular milieu clearly modulate cortical network dynamics, experiments have only had limited success in providing a mechanistic understanding of ion concentration dynamics and epileptogenesis. In this chapter, we show how recent computational models of cortical circuits with extracellular potassium concentration ( $[K^+]$ )<sub>o</sub>) dynamics help to overcome these previous limitations and contribute towards a more refined and experimentally testable theory of  $[K^+]$ <sub>o</sub> dynamics and epilepsy. We first set the grounds by discussing the cortical origin of neocortical paroxysmal oscillations, *in vivo* and *in vitro* experiments concerning  $[K^+]$ <sub>o</sub> dynamics, and the cortical network model with  $[K^+]$ <sub>o</sub> dynamics. Then, we describe single cell dynamics including detailed bifurcation analysis of a novel bistability with hysteresis between tonic spiking and slow bursting mediated by  $[K^+]$ <sub>o</sub>. Next, we extend the model to the network level and describe mechanisms underlying slow state transitions between two distinct oscillatory firing modes (slow bursting and fast run). The transitions between episodes of slow bursting and fast run observed in the model exhibit the same qualitative features as those recorded *in vivo* during neocortical electrographic seizures in cat and in human patients with the Lennox-Gastaut syndrome. Then, we show mechanisms of seizure cessation. We conclude by discussing the novel insights derived from computational models and the potential implications for clinical research.

### CORTICAL ORIGIN OF PAROXYSMAL OSCILLATIONS GENERATED WITHIN THE THALAMOCORTICAL SYSTEM

The origin of seizures that accompany various types of epileptic activities is unclear. Here we focus on neocortical seizures. The etiologies of epilepsies with cortical seizures include cortical dysplasia, traumatic injury and other idiopathic causes (Stafstrom, 2005). Anesthetized or naturally sleeping and awake cats exhibit seizures with transitions between periods of spike-wave complexes (2–3 Hz) and fast runs (10–15 Hz) (Steriade and Contreras, 1995; Steriade et al., 1998; Timofeev and Steriade, 2004). Similar transitions are observed in the electroencephalogram (EEG) of patients with the Lennox-Gastaut syndrome, a severe epileptic encephalopathy with neocortical seizures characterized by epochs of both slow spike or polyspike waves (SW/PSW) at 1.5–2.5 Hz and 10–20 Hz paroxysmal fast activity (Niedermeyer, 2002; Markand, 2003). Usually, the SW-PSW complexes of electrographic seizures correspond to clonic components of seizure, while the runs of fast spikes correspond to tonic components of seizures (Niedermeyer, 1999a,b).

Intracellular *in vivo* recordings reveal the physiology of neocortical seizures. During SW discharges, cortical neurons are depolarized and fire spikes during depth-negative (EEG spike) components and are hyperpolarized during depth-positive (EEG wave) components. A typical electrographic seizure consisting of SW-poly-SW (PSW) complexes recurring with frequencies of 1–3 Hz and fast runs with oscillation frequencies of 8–14 Hz is shown in Figure 26.1. The seizure starts with SW-PSW discharges. Epochs of fast run lasting several seconds interrupt the SW-PSW complexes. The seizure terminates with an epoch of SW discharges with decreasing frequency.

Recent experimental studies strongly suggest that both seizures with EEG pattern of the Lennox-Gastaut syndrome and spike-wave EEG complexes at around 3 Hz, as in petit-mal epilepsy, originate in neocortex (Pinault et al., 1998;

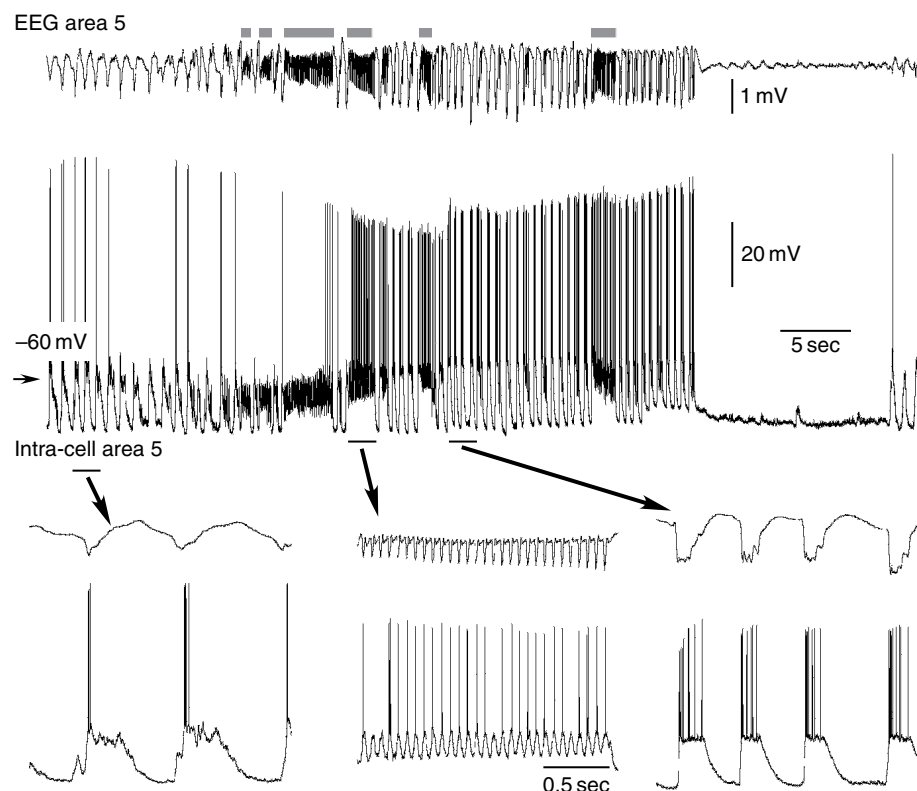


**FIGURE 26.1** Electrographic seizure composed of spike-wave complexes and runs of fast paroxysmal spikes. Upper panel shows depth EEG and intracellular activity during normal slow oscillation and its transformation to paroxysmal activity composed of fast runs and spike-wave complexes. Thick gray lines indicate periods of fast runs. The other periods of the seizure are spike-wave complexes. Three expanded fragments indicated by horizontal bars and arrows show (from left to right) a period of slow oscillation, a paroxysmal fast run and a period of spike-wave discharges. From Frohlich et al. (2006), with permission. Copyright 2006 Society for Neuroscience.

Steriade et al., 1998; Steriade and Contreras, 1998; Timofeev et al., 1998; Steriade, 2003; Timofeev and Steriade, 2004). The cortical origin is established by the following facts:

1. the presence of focal paroxysms both in neuronal pools within cortical depth (oscillations do not even reach the cortical surface (Steriade, 1974)) and in isolated cortical slabs *in vivo* (Timofeev et al., 1998)
2. the induction of neocortical seizures by infusion of the GABA<sub>A</sub>-receptor antagonist bicuculline in neocortex of ipsilaterally thalamectomized cats (Steriade and Contreras, 1998)
3. the absence of SW seizures after intrathalamic injections of bicuculline *in vitro* (Bal et al., 1995) and *in vivo* (Ajmone-Marsan and Ralston, 1956; Steriade and Contreras, 1998; Castro-Alamancos, 1999)
4. hyperpolarization of the vast majority of thalamocortical (TC) neurons without action potentials during paroxysmal discharges recorded in corresponding cortical areas (Steriade and Contreras, 1995; Pinault et al., 1998; Timofeev et al., 1998; Steriade and Timofeev, 2001; Timofeev and Steriade, 2004).

Fast runs also originate in neocortex. Fast runs and spindles, which originate in thalamus, share similar frequencies and duration. This could suggest that both paroxysmal fast runs and spindles are caused by similar mechanisms and that therefore fast runs originate in the thalamus. However, experiments demonstrated that during fast runs:

1. TC neurons display excitatory postsynaptic potentials (EPSPs) that rarely lead to action potential generation (Timofeev et al., 1998)
2. no rebound Ca<sup>2+</sup> spikes triggered by inhibitory postsynaptic potentials (IPSPs) occur
3. EPSPs in TC neurons follow cortical neurons, whereas the Ca<sup>2+</sup> spike bursts in TC neurons precede cortical depolarizing potentials during spindles (see Figure 11 in Timofeev et al., 1998).

Furthermore, runs of fast paroxysmal EEG spikes were recorded in isolated neocortical slabs (Timofeev et al., 1998). In sum, these observations support the cortical origin of fast runs.

This section has summarized the substantial experimental evidence for the cortical origin of neocortical seizures both for spike-wave and for fast run episodes. In the next section, we discuss experimental evidence for the role of extracellular ion concentration dynamics in epileptogenesis.

## CHANGES IN THE EXTRACELLULAR MILIEU AND EPILEPTOGENESIS

The role and significance of extracellular potassium concentration [K+]<sub>o</sub> dynamics in the central nervous system has been subject of considerable debate over the past decades. In this section, we summarize findings from both *in vivo* and *in vitro* experiments. We suggest that oversimplified assumptions and experimental difficulties have left most of the crucial questions about [K+]<sub>o</sub> dynamics and epileptogenesis unanswered. We conclude this section by explaining how detailed computational models of neural circuits and the interstitial space can provide clarifying insights into the role of [K+]<sub>o</sub> in epileptogenesis.

*In vivo* measurement with potassium-selective microelectrodes have established that [K+]<sub>o</sub> is modulated in an activity-dependent way. Visual stimulation and electrical activation of afferent pathways transiently increased [K+]<sub>o</sub> in cat lateral geniculate nucleus of the thalamus (Singer and Lux, 1973). Paired [K+]<sub>o</sub> and extracellular single unit recordings in cat striate cortex showed tight correlations (Singer and Lux, 1975). In cat somatosensory cortex, moving a brush across the contralateral forepaw increased [K+]<sub>o</sub> (Heinemann et al., 1977). A number of studies consistently showed that [K+]<sub>o</sub> changes dramatically during epileptic activity in cortex and spinal cord. Dual neuron-glia intracellular recordings from cortical suprasylvian association areas 5 and 7 of cats under ketamine-xylazine anesthesia revealed phasic negative events in glial membrane potential that were related to the onset of the paroxysmal depolarizing shifts in neurons (Amzica and Steriade, 2000). Although early studies used glia cell recordings and loading of the brain with radioactive labeled potassium (Grossman and Hampton, 1968; Fertziger and Ranck, 1970; Sypert and Ward, 1971; Dichter et al., 1972), later studies used potassium-selective microelectrodes (Lux and Neher, 1973) to show modulation of [K+]<sub>o</sub> during seizures and activity evoked by electrical stimulation in cortex (Hotson et al., 1973; Prince et al., 1973; Futamachi et al., 1974; Moody et al., 1974; Sypert and Ward, 1974; Lothman et al., 1975; Heinemann and Lux, 1977; Heinemann et al., 1977). Based on the measured increase in [K+]<sub>o</sub> during seizures, [K+]<sub>o</sub> was initially suggested to be the primary cause for both seizure initiation and termination (Fertziger and Ranck, 1970). According to this potassium accumulation hypothesis, an initial increase in [K+]<sub>o</sub> causes an increase in excitability which in turn further promotes [K+]<sub>o</sub> accumulation. Due to the

regenerative nature of this mechanism,  $[K+]_o$  will eventually sufficiently increase to silence the neurons ('cathodal block') which will result in seizure termination.

Many other studies, however, found little evidence in support of the potassium accumulation hypothesis. Rather, in apparent contradiction to the potassium accumulation hypothesis, most *in vivo* studies reported an absence of a  $[K+]_o$  threshold for seizure initiation (e.g. Futamachi et al., 1974), a delayed rise of  $[K+]_o$  following a paroxysmal increase in neural firing (e.g. Heinemann et al., 1977) and a decrease in  $[K+]_o$  during clonic phases of epileptic fits (e.g. Sypert and Ward, 1974). We propose that the rejection of the potassium accumulation hypothesis was mostly based on oversimplified assumptions and indirect conclusions. Specifically, a critical point for the initiation of the positive feedback loop between neural activity and increase in  $[K+]_o$  can exist in absence of a unique, experimentally determinable threshold value since other factors are likely to modulate excitability. Therefore, the threshold value could differ from experiment to experiment. Moreover, a spatial mismatch between origin of the seizure and the potassium-selective microelectrode can further complicate the establishment of a causal link between  $[K+]_o$  and epileptogenesis. Most importantly, the *in vivo* studies discussed above did not permit experiments which required the control of  $[K+]_o$ .

In contrast to the *in vivo* situation, the acute slice preparation provided the opportunity to at least partially control  $[K+]_o$ , and therefore to test more directly for a causal role between increase in  $[K+]_o$  and epileptogenesis. A series of studies, mostly in hippocampal slices, showed that an increase in  $[K+]_o$  can indeed lead to various interictal and ictal phenomena. Here, we discuss a few examples illustrating some key insights from *in vitro* studies. A threshold in  $[K+]_o$  for triggering non-synaptic paroxysmal events in hippocampus CA1 by locally applied  $K^+$  and progressive increase in  $[K+]_o$  before onset of a spontaneous seizure-like event suggest a causal role of  $[K+]_o$  (Yaari et al., 1986). Spontaneous synaptic epileptiform activity with  $K^+$ -dependent frequency modulation occurred in CA3 hippocampal slice in elevated  $[K+]_o$  (Rutecki et al., 1985).  $[K+]_o$  increased during the tonic phase and decreased during the clonic phase of ictal events in hippocampal slices (Jensen and Yaari, 1997). CA1 pyramidal cells switched from tonic firing to bursting in response to depolarizing current injections when  $[K+]_o$  was artificially increased (Jensen et al., 1994). However, although these studies suggest a potential causal role of  $[K+]_o$  and provide important insight into cellular mechanisms, it is unclear how the observed phenomena translate to the intact brain.

Increase in extracellular  $[K+]_o$  can potentially be a result of deficits in the potassium regulatory system. Indeed, hippocampal tissue from human patients with temporal lobe epilepsy exhibited impairment of glial inward-rectifying  $K^+$ -channels responsible for  $K^+$  uptake (Hinterkeuser et al., 2000; Kivi et al., 2000). On the other hand, recordings in rat hippocampal slices revealed that the regulation of  $[K+]_o$  is not impaired after injury and it was suggested that the larger  $[K+]_o$  increase evoked by neuronal activity is a consequence, rather than the primary mechanism underlying post-traumatic hyperexcitability (Santhakumar et al., 2003).

Although it remains mostly unclear how the above-described limitations of *in vivo* and *in vitro* experiments can be overcome, recent computational models of cortical circuits and ion concentration dynamics in the interstitial space allow us for the first time to address crucial questions concerning how  $[K+]_o$  shapes cortical dynamics. In this chapter, we summarize our results that address the role of  $[K+]_o$  in mediating sustained oscillatory activity in the absence of external input. Although the original question about the causal role of  $[K+]_o$  for seizure initiation remains unanswered for the time being, results from computational models illustrate that the initial hypothesis of a positive feedback mechanism leading to seizures by a global loss of stability (potassium accumulation hypothesis) needs substantial refinement. Specifically, our computational models reconcile intracellular recordings of neocortical seizure with the previously neglected findings that  $[K+]_o$  increases during the tonic and decreases during the clonic phase both *in vivo* (Sypert and Ward, 1974) and *in vitro* (Jensen and Yaari, 1997) and that the firing pattern of pyramidal cells depends on  $[K+]_o$  (Jensen et al., 1994).

## MODEL DESCRIPTION

In order to investigate the interaction of extracellular potassium concentration  $[K+]_o$  dynamics and the firing behavior of networks of cortical neurons, a computational network model of synaptically coupled cortical pyramidal cells and inhibitory interneurons was devised. In the model, each cell was surrounded by an extracellular compartment endowed with potassium concentration regulation mechanisms (Bazhenov et al., 2004; Frohlich et al., 2006). This section describes the computational model of individual cells, the synaptic coupling and the extracellular ion concentration dynamics.

### SINGLE CELL MODEL

Each model neuron was endowed with both intrinsic and synaptic currents and consisted of an axo-somatic compartment with membrane voltage  $V_S$  described by

$$g(V_S - V_D) = -I_S^{\text{int}},$$

and a dendritic compartment with membrane voltage  $V_D$  with

$$C_m \frac{dV_D}{dt} = -g_L(V_D - E_L) - g(V_D - V_S) - I_D^{\text{int}} - I^{\text{syn}}$$

where  $g$  is the coupling conductance between the two compartments,  $I_S^{\text{int}}$  and  $I_D^{\text{int}}$  are the intrinsic currents in the respective compartments,  $C_m$  is the membrane capacitance,  $g_L$  and  $E_L$  are the conductance and reversal potential of the leak current, respectively (Mainen and Sejnowski, 1996; Frohlich and Bazhenov, 2006). The axo-somatic capacitance was approximated by zero for computational efficiency (Mainen and Sejnowski, 1996). The ratio of dendritic to axo-somatic surface area  $r$  was chosen to reproduce regular spiking ( $r=165$ ) and fast-spiking ( $r=50$ ) firing behavior for pyramidal cells (PYs) and inhibitory interneurons (INs), respectively. Intrinsic ionic currents were modeled with a set of Hodgkin-Huxley type conductances. Fast inactivating  $\text{Na}^+$  channels (high and low density in axo-somatic and dendritic compartment, respectively) and fast delayed rectifier  $\text{K}^+$  channels (axo-somatic compartment) mediated action potentials. Persistent sodium conductance  $G_{\text{NaP}}$ , slow voltage-gated  $\text{K}^+$  conductance  $G_{\text{Km}}$ , slow calcium-activated  $\text{K}^+$  conductance  $G_{\text{KCa}}$ , high-threshold  $\text{Ca}^{2+}$  conductance  $G_{\text{Ca}}$ , and hyperpolarization-activated depolarizing conductance  $G_h$  were included in the dendritic compartment and  $\text{K}^+$  leak conductance  $G_L$  was introduced in both axo-somatic and dendritic compartments (Timofeev et al., 2000; Frohlich and Bazhenov, 2006).

### SYNAPTIC DYNAMICS

Synaptic transmission was modeled by first-order kinetics of neurotransmitter binding and unbinding to postsynaptic receptors (Destexhe et al., 1994). With rectangular neurotransmitter concentration time-courses, the time-course of the fraction of open-receptors  $[O](t)$  after a presynaptic action potential equaled a single exponential. All synaptic currents  $I_{\text{syn}}$  were described by

$$I_{\text{syn}} = g_{\text{syn}}[O](V - E_{\text{syn}})$$

where  $g_{\text{syn}}$  is the maximal conductance (total synaptic conductances:  $g_{\text{AMPA(PY-PY)}}=0.15 \mu\text{S}$ ,  $g_{\text{NMDA(PY-PY)}}=0.01 \mu\text{S}$ ,  $g_{\text{AMPA(PY-IN)}}=0.07 \mu\text{S}$ ,  $g_{\text{NMDA(PY-IN)}}=0.008 \mu\text{S}$ ,  $g_{\text{GABA(IN-PY)}}=0.05 \mu\text{S}$ ) and  $E_{\text{syn}}$  the reversal potential ( $E_{\text{AMPA}}=0 \text{ mV}$ ,  $E_{\text{NMDA}}=0 \text{ mV}$ ,  $E_{\text{GABA(A)}}=-75 \text{ mV}$ ). Dependence of NMDA receptors on postsynaptic membrane voltage  $V_{\text{post}}$  was modeled by  $1/(1+\exp(-(V_{\text{post}}-V_{\text{th}})/\sigma))$  with  $V_{\text{th}}=-25 \text{ mV}$  and  $\sigma=12.5 \text{ mV}$ .

Excitatory synapses included short-term depression described by a depression variable  $D \leq 1$  which was multiplied with the maximal synaptic conductance after each presynaptic spike (Tsodyks and Markram, 1997; Markram et al., 1998).  $D$  was adjusted with factor  $R=0.93$  (7% resources per action potential) from its previous value  $D_i$  after a presynaptic spike at time  $t_i$  with recovery time constant  $\tau=700 \text{ ms}$ :

$$D = 1 - (1 - D_i R) \exp(-(t - t_i)/\tau).$$

The network dynamics discussed here resulted from the simulation of networks with various sizes. All networks, however, exhibited a similar structure consisting of a one-dimensional layer of pyramidal cells and a one-dimensional layer of inhibitory interneurons. In case of a very small network (e.g. 5 PYs and 1 IN), network connectivity was global, such that each cell projected to all other cells. Specifically, each PY cell was connected to every other PY cell by excitatory synapses (AMPA and NMDA). The IN received excitatory input from all PY cells (AMPA and NMDA) and inhibited all PY cells ( $\text{GABA}_A$ ). For larger networks, the synaptic connectivity was local with synaptic footprints few neurons wide. For example, in the network model composed of two one-dimensional layers formed by 60 PYs and 15 INs respectively, each PY was connected to five neighboring PYs on either side, each PY excited three consecutive INs and each IN inhibited a total of eleven neighboring PYs. For all networks, the unitary conductance impinging on a given neuron was scaled by the total number of inputs.

## POTASSIUM DYNAMICS

In the model, each neuron was surrounded by an extracellular compartment endowed with potassium regulation mechanisms.  $[K+]_o$  was computed for both the dendritic ( $[K+]_{o(D)}$ ) and the somatic compartment ( $[K+]_{o(S)}$ ) of each cell. Processes affecting  $[K+]_{o(D,S)}$  were channels permeable to  $K^+$ ,  $K^+$  pumps, glial  $K^+$  uptake (buffering)  $G$ , and lateral diffusion current  $I_{\text{Diff}}$ :

$$d[K+]_{o(D,S)}/dt = (k/Fd)I_{\Sigma K} + G + I_{\text{Diff}(DS,SD)}$$

where  $k = 10$  is a conversion factor,  $F = 96489 \text{ C/mol}$  is the Faraday constant, and  $d$  is the ratio of the volume of the extracellular compartment to the surface area. The total potassium current  $I_{\Sigma K}$  is the sum of all potassium currents (fast rectifying  $I_K$ , calcium-activated  $I_{KCa}$ , voltage-dependent non-inactivating  $I_{Km}$ , and leak current  $I_L$ ) and the current  $I_{Kpump}$  mediated by  $K^+$  pumps:

$$I_{\Sigma K} = I_K + I_{KCa} + I_{Km} + I_L + I_{Kpump}$$

The  $K^+$  pump current  $I_{Kpump}$  was an inward current with a sigmoid dependence on the ratio of steady-state  $[K+]_{o(eq)} = 3.5 \text{ mM}$  to current  $[K+]_o$  and saturated at  $I_{max}$ , which was chosen to balance  $K^+$  leak current (dendritic compartment  $I_{max} = 5 \mu\text{A}/\text{cm}^2$ , somatic compartment  $I_{max} = 40 \mu\text{A}/\text{cm}^2$ )

$$I_{Kpump} = I_{max}/(1 + ([K+]_{o(eq)}/[K+]_o))^2.$$

Glial  $K^+$  buffering current  $G$  was described by a free buffer (total buffer  $[B]_{max} = 500 \text{ mM}$ ) with concentration  $[B]$ , which bound and unbound from  $K^+$  with according on- and off-rates  $k_1 = 0.008$  and

$$k_2 = k_1/(1 + \exp(([K+]_o - [K+]_{o(th)})/-1.15))$$

governed by first order kinetics

$$d[B]/dt = k_1([B]_{max} - [B]) - k_2[K+]_o[B], \quad G = k_1([B]_{max} - [B])/k_{IN} - k_2[K+]_o[B].$$

Threshold concentrations  $[K+]_{o(th)}$  (15 mM for somatic compartment, 9 mM for dendritic compartment) and  $k_{IN} = 1.1$  were chosen such that  $[K+]_o$  equilibrated both for silent and for tonic firing mode (Bazhenov et al., 2004).

Diffusion currents between dendritic and axo-somatic compartments  $I_{\text{Diff}(DS,SD)}$  were given by

$$I_{\text{Diff}(DS,SD)} = D([K+]_{o(D,S)} - [K+]_{o(S,D)})/\Delta x^2,$$

where  $D = 4 \cdot 10^{-6} \text{ cm}^2/\text{s}$  was the diffusion constant and  $\Delta x = 100 \mu\text{m}$  corresponded to the distance between the centers of the two compartments. In a subset of simulations, lateral diffusion between compartments corresponding to neighboring neurons was introduced

$$I_{\text{Diff(lateral)}} = D([K+]_{o(+)} - 2[K+]_o + [K+]_{o(-)})/\Delta x^2$$

where  $[K+]_{o(+)}$  and  $[K+]_{o(-)}$  represented the potassium concentration in the two neighboring compartments.

Any changes in  $[K+]_o$  affected the reversal potential for all  $K^+$  currents. The Nernst equation was used to compute the reversal potential for  $K^+$  conductances

$$E_K = 26.64 \text{ mV} \ln([K+]_o/[K+]_i).$$

The reversal potential for  $G_h$  and  $G_L$ , both ion channels permeable to several ion types, were updated according to the Goldman-Hodgkin-Katz equation using the different ionic concentrations ( $[Na^+]_o = 130 \text{ mM}$ ,  $[Na^+]_i = 20 \text{ mM}$ ,  $[Cl^-]_o = 130 \text{ mM}$ ,  $[Cl^-]_i = 8 \text{ mM}$ ) and degrees of permeability:

$$E_h = 26.64 \text{ mV} \ln([K+]_o + 0.2[Na^+]_o)/([K+]_i + 0.2[Na^+]_i)$$

$$E_L = 26.64 \text{ mV} \ln([K+]_o + 0.085[Na^+]_o + 0.1[Cl^-]_i)/([K+]_i + 0.085[Na^+]_i + 0.1[Cl^-]_o).$$

### SINGLE CELL DYNAMICS MEDIATED BY ELEVATED EXTRACELLULAR K<sup>+</sup>

This section describes the dynamics of the above introduced model cortical pyramidal cell surrounded by an extracellular compartment endowed with potassium regulation mechanisms. We first describe the behavior of the model cell in response to a transient increase in extracellular K<sup>+</sup> concentration elicited by suprathreshold step depolarization. Then, we use bifurcation analysis to show the [K+]<sub>o</sub> dependence of the different firing patterns.

#### TRANSIENT OSCILLATION TRIGGERED BY INCREASE OF EXTRACELLULAR K<sup>+</sup> CONCENTRATION

The pyramidal cell (PY) model ( $G_{Ca} = 0.022 \text{ mS/cm}^2$ ,  $G_h = 0.1 \text{ mS/cm}^2$ ) showed oscillatory firing outlasting the stimulation with a suprathreshold DC pulse of 10 second duration (Figure 26.2A) (Timofeev et al., 2000; Bazhenov et al., 2004; Frohlich and Bazhenov, 2006; Frohlich et al., 2006). Directly after stimulation, the neuron fired bursts with a frequency of 2–3 Hz and a pronounced after-hyperpolarization at the end of each burst. After about 10 seconds of bursting, there was

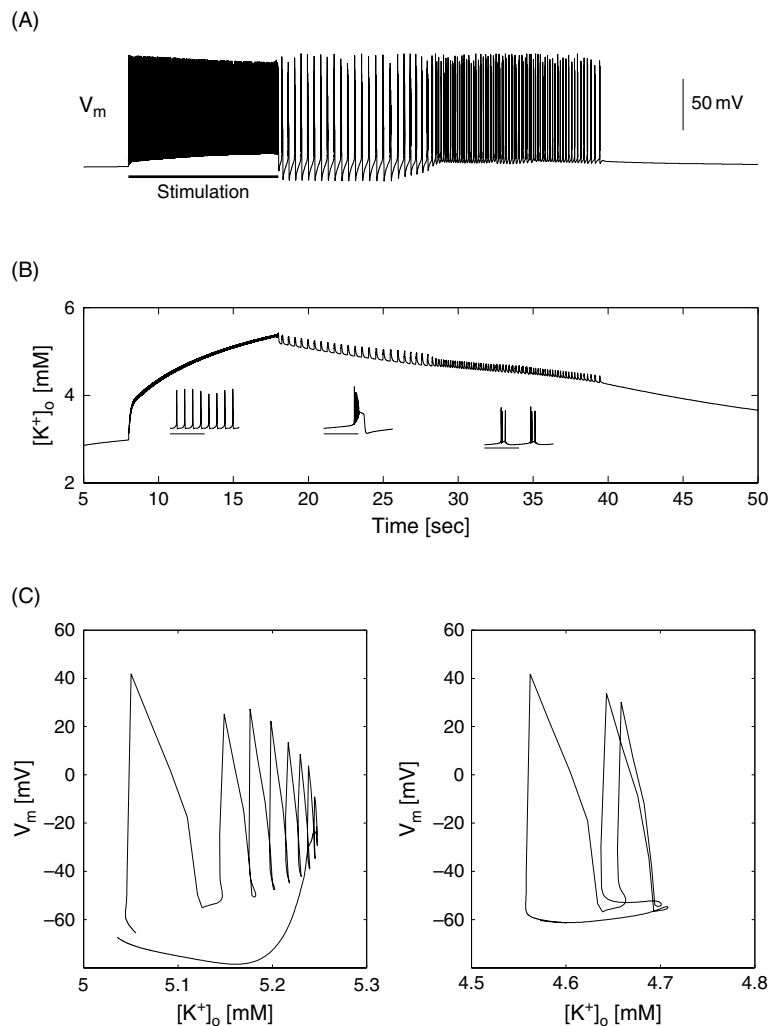


**FIGURE 26.2** Single PY neuron stimulated with suprathreshold DC current pulse of 10 second duration (Bazhenov et al., 2004). (A) Membrane voltage time course. The neuron exhibited high frequency firing during stimulation, switched first to bursting directly after stimulation (slow bursting, pronounced after hyperpolarization, duration about 10 seconds) and then to fast run (higher frequency, no after hyperpolarization, duration about 10 seconds) before returning back to its resting state. (B) Extracellular potassium concentration [K+]<sub>o</sub> increased during stimulation and gradually returned to baseline after stimulation. The insets illustrate the different oscillatory firing modes (calibration bars: 50 ms, 200 ms, 200 ms, respectively). (C) Phase plane plots showing membrane voltage as a function of [K+]<sub>o</sub> for slow bursting (left panel) and fast run (right panel).

a sharp transition to another oscillatory regime consisting of spike triplets at a higher frequency than the previous bursts. During this so-called fast run, no after-hyperpolarization was observed. About 10 seconds later, the neuron turned silent again and the membrane voltage eventually returned to the resting potential before stimulation.

During initial stimulation, the high frequency firing of the neuron (see Figure 26.2B, left inset) caused an increase in  $[K^+]_o$ . In this condition, active and passive mechanisms decreasing the excess potassium were not sufficient to keep the potassium concentration near steady-state level. After stimulation,  $[K^+]_o$  decreased during both bursting (see Figure 26.2B, middle inset) and fast run (see Figure 26.2B, right inset) until it reached baseline again. Potassium efflux was mainly mediated by the fast delayed-rectifier (41% and 43% for bursting and fast run, respectively) and the leak conductance (43% and 56%, respectively). Each burst was accompanied by a noticeable change in  $[K^+]_o$  (see Figure 26.2C, left panel). In fast run,  $[K^+]_o$  changed only marginally during a triplet of spikes (see Figure 26.2C, right panel). This model of an isolated single cell surrounded by a spatially limited extracellular compartment showed that the cell was in different firing regimes as a function of  $[K^+]_o$ . Since there was no  $K^+$  diffusion, increase in  $[K^+]_o$  may be stronger and longer lasting in this model than *in vitro* or *in vivo*. To investigate how these transitions between silent state, bursting mode and fast run depend on  $[K^+]_o$ , the  $K^+$  regulation mechanism was switched off and  $[K^+]_o$  was treated as a constant (bifurcation analysis).

### CO-EXISTENCE OF SLOW BURSTING AND TONIC FIRING

In this section, we treat  $[K^+]_o$  as a parameter to determine the firing behavior of the cell as a function of  $[K^+]_o$ . Therefore, all mechanisms controlling  $[K^+]_o$  evolution in the model were blocked and the firing behavior was analyzed for different fixed values of  $[K^+]_o$  within the physiological range (Frohlich et al., 2006). Specifically, we focused on the occurrence of different stable firing modes as a function of parameter  $[K^+]_o$ .

First, we discuss the stable fixed points of the system. For very low  $[K^+]_o$ , the neuron was at rest. For increasing  $[K^+]_o$ , the resting potential became more depolarized as the driving force for potassium decreased. For  $[K^+]_o = 4.85 \text{ mM}$ , the silent state lost stability by means of a saddle-node bifurcation (Type I neural oscillator (Rinzel and Ermentrout, 1989; Ermentrout, 1996), fixed point bifurcations in Figure 26.3A). At  $[K^+]_o = 9.46 \text{ mM}$ , a new stable state corresponding to a depolarized state with spike inactivation ( $V_m = -26.3 \text{ mV}$ ) appeared by means of a subcritical Andronov-Hopf bifurcation (Figure 26.3A).

In order to characterize further the transition between tonic firing and slow bursting, we computed a Poincaré cross-section by calculating the values of intracellular calcium concentration  $[Ca^{2+}]_i$  each time the membrane potential crossed the threshold  $V_m = -20 \text{ mV}$ ; these values were plotted as a function of  $[K^+]_o$  (see Figure 26.3B). In such a representation, periodic oscillations (corresponding to limit cycles) are represented as points defined by a threshold crossing of a trajectory. This approach allows the graphical representation of changes in the nature of an oscillatory (firing) behavior as a function of a parameter. For a given value of  $[K^+]_o$ , tonic spiking is represented by a single point on this Poincaré cross-section since  $[Ca^{2+}]_i$  assumes the same value at  $V_m = -20 \text{ mV}$  for every spike. During a burst, however,  $[Ca^{2+}]_i$  increases after each spike of a given burst. Therefore, a burst appears as a vertical group of points each representing a single spike. In other words, a set of parallel horizontal lines in the Poincaré cross-section (see Figure 26.3B) delimits a range of  $[K^+]_o$  values for which bursting occurs.

For determining the Poincaré cross-section,  $[K^+]_o$  was gradually increased and decreased to reveal the complete tonic firing and slow bursting region, respectively. We found a bistability between tonic firing and slow bursting, which was associated with a hysteresis (evident by comparison of top and bottom plots in Figure 26.3B). For increasing  $[K^+]_o$ , the cell stayed in tonic firing until slow bursting with spike inactivation became the only stable state at  $[K^+]_o = 6.40 \text{ mM}$ . Decreasing  $[K^+]_o$  caused the cell to stay in slow bursting mode until tonic firing was the only stable state at  $[K^+]_o = 5.75 \text{ mM}$ . For increasing  $[K^+]_o$  (see Figure 26.3B, top), the tonic firing region consisted of three subregions with single spikes, spike doublets and single spikes, respectively. Note that the left region with single spikes existed only in the case of a non-zero hyperpolarization-activated depolarizing conductance ( $G_h = 0.05 \text{ mS/cm}^2$ ). For decreasing  $[K^+]_o$  (see Figure 26.3B, bottom) two distinct bursting regimes – with and without spike inactivation – were found (see Figure 26.3C).

### MECHANISM OF BURST GENERATION

To study the bursting dynamics in the model, we used fast-slow analysis by choosing a state variable with dynamics on the time-scale of individual bursts in the complete system and treating it as a parameter of the resulting reduced system for a fixed value of  $[K^+]_o$  (Frohlich and Bazhenov, 2006). Here, the calcium-activated potassium conductance  $g_{KCa}$ , with a time scale at least as slow as the slow  $[Ca^{2+}]_i$  dynamics, was chosen as the slow variable. The conductance  $g_{KCa}$

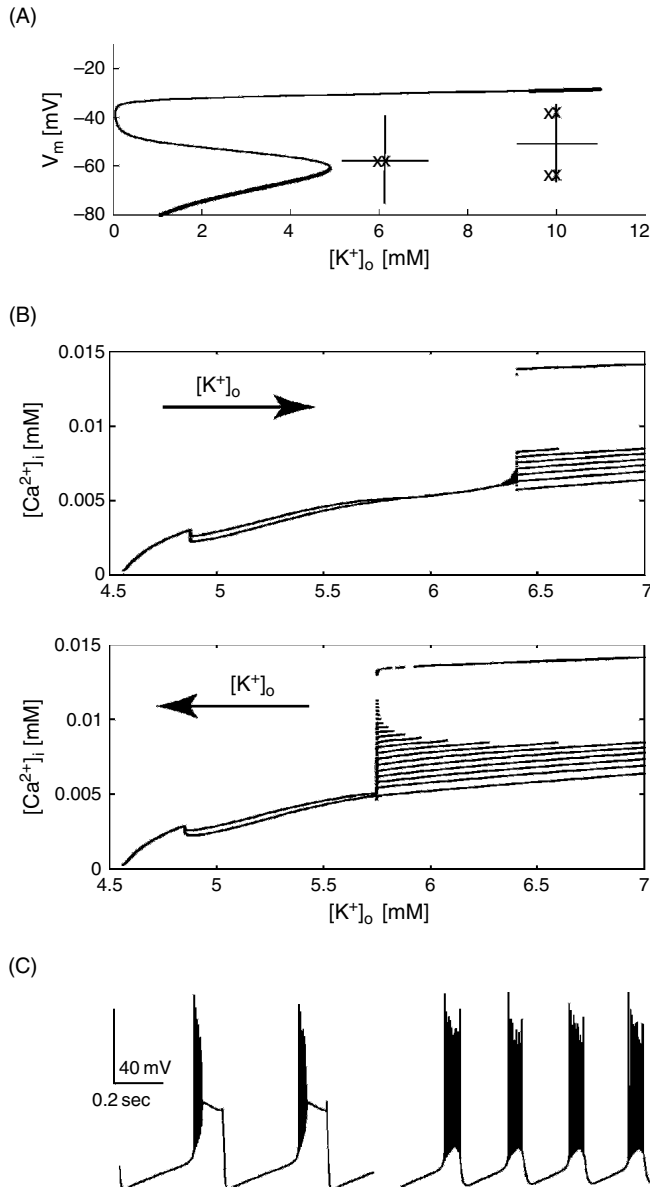


**FIGURE 26.3** (A) Stable fix points corresponding to rest and the depolarized state are connected via unstable fix points. Transition from silent to tonic firing is a saddle-node bifurcation. Transition from slow bursting to depolarized is a Andronov-Hopf bifurcation. Insets illustrate eigenvalues at bifurcation points. (B) Poincaré cross-section for gradually increasing (top) and decreasing (bottom)  $[K^+)_o$ . Tonic firing corresponds to a single point, spike doubles to two points and bursting to a series of points in the Poincaré cross-section for a given value of  $[K^+)_o$ . Bistability between tonic firing and bursting for  $[K^+)_o$  between 5.75 and 6.4 mM. (C) Left: bursting with spike inactivation for  $[K^+)_o = 6.00$  mM (slow bursting branch,  $[K^+)_o$  decreasing). Right: bursting without spike inactivation for  $[K^+)_o = 5.75$  mM (slow bursting branch,  $[K^+)_o$  decreasing). Adapted from Frohlich et al. (2006), with permission. Copyright 2006 Society for Neuroscience.

terminates bursts after sufficient calcium influx via the high-threshold calcium conductance, which was activated during the depolarized membrane state of each burst.

We here consider the case of  $[K^+)_o = 5.9$  mM which is within the bistable region (see Figure 26.3B). Although a conductance reflecting an assembly of ion channels cannot be negative, we included  $g_{KCa} < 0$  to capture the entire bifurcation structure of the system. The bifurcation plot in Figure 26.4 shows the dendritic membrane voltage values that correspond to fixed points of the reduced system as a function of  $g_{KCa}$ . Similarly, for all limit cycles, maximum and minimum dendritic membrane voltages of the oscillatory trajectory are plotted. The fixed points of the reduced system follow a z-shaped line as a function of  $g_{KCa}$  (Figure 26.4, top panels). The two arms of stable fixed points,  $P_s^d$  and

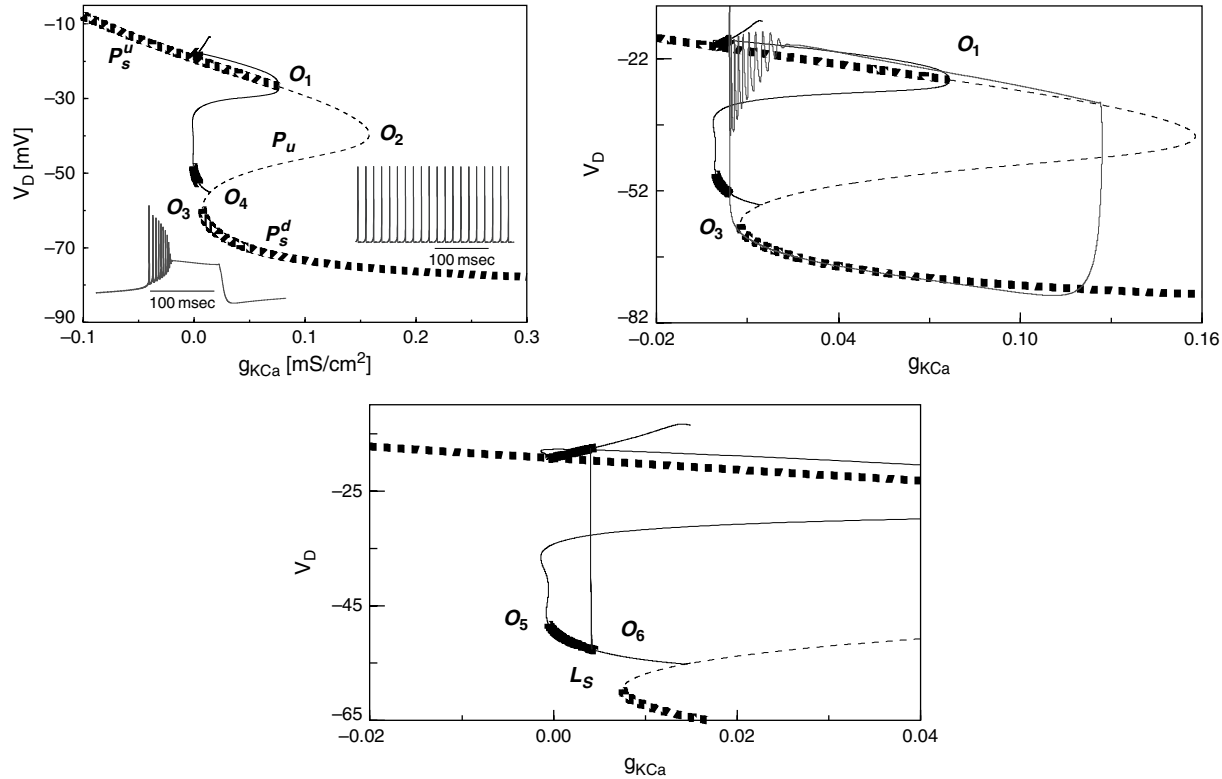


**FIGURE 26.4** Bifurcation diagram of the reduced system for  $[K^+}_o = 5.9\text{ mM}$ . Top left panel: Stable fixed points  $P_s^u$  and  $P_s^d$  (thick dashed line) are connected by the branch of unstable fixed points  $P_u$  (thin dashed line). Solid lines indicate stable (thick) and unstable (thin) limit cycles.  $O_1$  Andronov-Hopf;  $O_2$  and  $O_3$ , fold;  $O_4$ , saddle homoclinic orbit bifurcation points. Insets show bursting and tonic spiking patterns in the complete system with freely running  $g_{KCa}$ . Top right and bottom panels: enlarged region of interest.  $O_5$ , Neimark-Sacker and  $O_6$ , period doubling bifurcation points.  $L_s$  indicates stable limit cycles. Projection of the phase trajectory for the complete system during bursting mode (solid line, middle panel) and tonic firing (solid vertical line, bottom panel). Adapted from Frohlich and Bazhenov, (2006), with permission. Copyright 2006 by the American Physical Society.

$P_s^u$ , are connected by a branch of unstable fixed points. Importantly, for  $g_{KCa}$  between 0.007 and 0.076 mS/cm<sup>2</sup>, both stable states coexist.  $P_s^u$  loses stability by a subcritical Andronov-Hopf bifurcation at  $O_1$ .  $P_s^d$  coalesces with the unstable fixed point in a saddle-node bifurcation at  $O_3$ . In the following, we explain how this bifurcation landscape of fixed points in the reduced system explains the oscillatory bursting behavior in the complete system (Figure 26.4, top left panel).

During the hyperpolarized phase in between bursts, the system follows  $P_s^d$  and conductance  $g_{KCa}$  decreases since calcium removal mechanisms reduce intracellular calcium concentration. Eventually,  $P_s^d$  loses stability at the saddle-node bifurcation point  $O_3$  causing a transition into the basin of attraction of  $P_s^u$ . The trajectory rotates several times around the stable focus  $P_s^u$ , but never quite reaches it. The rapid sequence of action potentials at the onset of burst is mediated by the trajectory approaching the stable fixed point. The decaying amplitude of the transient oscillations corresponds to the decreasing spike amplitude in the membrane voltage time-course during a burst. As the system approaches  $P_s^u$ , no more action potentials occur and the membrane voltage remains depolarized. In this depolarized state with spike inactivation, intracellular Ca<sup>2+</sup> concentration increases due to the activation of the high-threshold Ca<sup>2+</sup> conductance which mediates calcium influx. As a consequence,  $g_{KCa}$  increases which eventually leads to a loss of stability of  $P_s^u$  at  $O_1$ , forcing the trajectory back to  $P_s^d$ . In summary, bursting in the complete system corresponds to periodic transitions between two stable fixed points in the reduced system (point-point bursting mechanism (Izhikevich, 2007)).

#### MECHANISM OF TONIC SPIKING

In the previous section, we discussed the bifurcation landscape responsible for burst generation. We now turn our attention to tonic firing (see Figure 26.4, bottom panel). In the bifurcation diagram of the reduced model, tonic spiking corresponds to a limit cycle. Stability of the limit cycle in the reduced system is therefore necessary for occurrence of tonic firing. Whether tonic firing is stable in the full model depends on the value of  $g_{KCa}$  for which the limit cycle is stable in the

reduced system. Specifically, the value of  $g_{\text{KCa}}$  needs to be such that the corresponding intracellular calcium concentration can be achieved and maintained during tonic firing. Here, the bifurcations of the limit cycles in the reduced model are analyzed (again for  $[K+]_o = 5.9 \text{ mM}$ ). In the bifurcation plot, the small-amplitude unstable limit cycle which arises at  $O_1$  folds around at  $g_{\text{KCa}} = -0.001 \text{ mS/cm}^2$  leading to the coexistence of a small- and a large-amplitude unstable limit cycle. Before merging with the unstable fixed point  $P_u$  in a saddle homoclinic orbit bifurcation at point  $O_4$ , the unstable limit cycle with larger amplitude in the  $V_D$  dimension becomes stable in a narrow range of  $g_{\text{KCa}}$  between  $-0.0005$  and  $0.0045 \text{ mS/cm}^2$ . This stable region is delimited by a subcritical Neimark-Sacker bifurcation on the lower end (bifurcation point  $O_5$ ) and a period-doubling bifurcation on the upper end (bifurcation point  $O_6$ ). In the complete system,  $g_{\text{KCa}}$  is small during tonic firing since  $g_{\text{Ca}}$ , which causes calcium influx, is in average only weakly activated. Also,  $g_{\text{KCa}}$  is bounded by zero on the left side since an ionic conductance cannot become negative. Therefore,  $g_{\text{KCa}}$  is sufficiently constrained in the full system to fit the window of values for which a stable limit cycle was found in the reduced system. This limit cycle mediating tonic spiking dynamics coexists with the previously discussed periodic orbit mediating bursting. Therefore, the complete model of a cortical pyramidal cell exhibits bistability between slow bursting and tonic firing for elevated  $[K+]_o$ .

For values of  $[K+]_o$  outside the region of hysteresis, the complete system displayed only tonic spiking or bursting dynamics (see Figure 26.3B). Bifurcation analysis for low values of  $[K+]_o < 5.75 \text{ mM}$  revealed that the vicinity of the saddle-node point  $O_3$  (see Figure 26.4, top left panel) no longer belongs to the basin of attraction of the upper stable fixed point  $P_s^u$  (Frohlich and Bazhenov, 2006). Therefore, for initial conditions on the low stable branch of fixed points  $P_s^d$ , the system reaches the saddle-node bifurcation point and moves to the stable limit cycle, mediating firing with spike doublets. Conversely, for high values of  $[K+]_o > 6.4 \text{ mM}$ , only bursting is stable in the complete system. The limit cycle corresponding to tonic spiking was found in the reduced system with  $g_{\text{KCa}}$ , however, it became unstable in the complete system (Frohlich and Bazhenov, 2006). Hence, tonic firing does not exist as a stable state for sufficiently elevated  $[K+]_o$ .

### NETWORK DYNAMICS MEDIATED BY ELEVATED EXTRACELLULAR $K^+$

In the previous sections, we have presented an in-depth analysis of the model of a single cortical pyramidal cell surrounded by an extracellular compartment with potassium concentration dynamics. The bistability with hysteresis between tonic firing and slow bursting did not affect the spiking activity of a single pyramidal cell challenged by an increase in  $[K+]_o$  since in either of the two firing regimes  $[K+]_o$  decreased and only transient oscillations occurred. This is different in case of a network of neurons with  $[K+]_o$  dynamics as we will show in this section.

### SLOW STATE TRANSITIONS

In the single cell model, the after-discharge following stimulation was of finite length since  $[K+]_o$  eventually returned to its baseline value. Here, we now discuss the slow dynamics in case of model cells interconnected with synapses to form cortical network models. First, we analyze the behavior of a small compact network which consists of five pyramidal cells (PYs) and one inhibitory interneuron (IN) with global connectivity. Such a small circuit is a direct extension of the single cell model due to its compact nature. Second, we show that our findings generalize to larger networks with more localized synaptic connectivity patterns. These larger networks exhibited not only very similar temporal dynamics but, additionally, also spatial patterning of the oscillatory activity.

Key difference between the single cell and the small network case is the duration of the  $K^+$  mediated oscillatory dynamics. In case of a single cell, the transient firing exhibits patterning into two distinct epochs (slow bursting and fast run) before returning to the silent state. Conversely, in case of the network, we found indefinitely lasting oscillatory dynamics patterned into epochs of slow bursting and fast run. The slow state transitions between the two oscillatory modes occurred on the time-scale of seconds. Essentially, the slow dynamics are mediated by the above discussed bistability between tonic firing and slow bursting, which is maintained in the network model (Figure 26.5A). Specifically, bifurcation analysis for the network revealed a similar structure of  $[K+]_o$  dependent firing modes (silence, fast run, slow bursting, depolarized locked state) exhibiting bistability with hysteresis for transitions between the different oscillatory firing types. In contrast to the single cell, however,  $[K+]_o$  increased during fast run in the complete model with  $[K+]_o$  as a dynamics variable. This key difference is responsible for the persistent nature of the oscillatory firing in the network model. While the cells were in fast run,  $[K+]_o$  increased up to the level where fast run loses stability and the cells were forced to switch to slow bursting (upper end point of hysteresis). During slow bursting, however,  $[K+]_o$  decreased. Because of the bistability with hysteresis, the cells stayed in slow bursting until the lower endpoint of the hysteresis was reached where the slow bursting mode loses stability and is replaced by fast run.

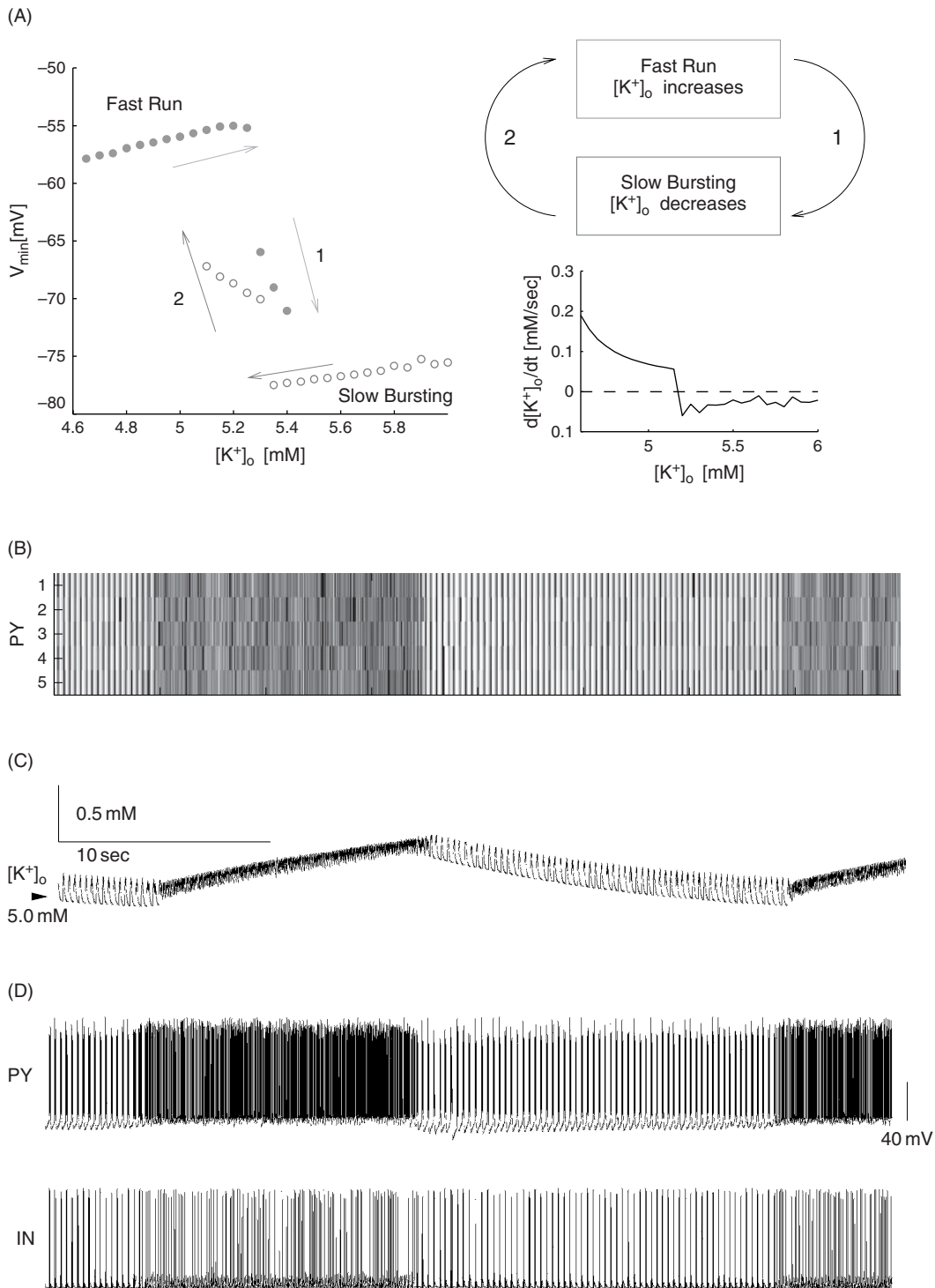


**FIGURE 26.5** Globally connected network with five PY cells and one IN. (A) Left: bifurcation analysis (minimum of membrane voltage): hysteresis between fast run and slow bursting for  $[K^+]$  between 5.0 and 5.4 mM. Circles denote stable limit cycle oscillations. Top right: schematic of slow periodic network dynamics. Bottom right: averaged  $[K^+]$  gradient as a function of  $[K^+]$ . (B–D) Slow transitions after initial brief increase in  $[K^+]$ . (B) Network activity of PY cells (40 seconds duration) shows alternating epochs of fast run and slow bursting. (C)  $[K^+]$  increased during fast run and decreased during slow bursting. Upper switching point for transition from fast run to slow bursting and lower switching point for transition from slow bursting to fast run correspond to hysteresis endpoints in (A). (D) Membrane voltage time course of PY cell (top trace) and IN (bottom trace). From Frohlich et al. (2006), with permission. Copyright 2006 Society for Neuroscience.

At this point, the network has gone through an epoch of fast run followed by an epoch of slow bursting (Figure 26.5B). The nature of the hysteresis forces the network to stay in the bistable region leading to an infinite sequence of such alternating epochs of slow bursting and fast run (Figure 26.5C,D).

Since the network connectivity was found to be critical for the slow state transitions to occur, simulations for a range of excitatory and inhibitory coupling strengths were used to determine the conditions that the synaptic coupling strengths need to fulfill for the slow state transitions to occur. Simulations sampling all pairs of excitatory (lateral recurrent excitation) and inhibitory (inhibition mediated by interneurons) coupling strengths for a range of 80% to 120% of the original values used in the model revealed that the occurrence of slow state transitions is a robust phenomenon at a broad range of coupling strengths, as long as synaptic excitation and inhibition are scaled such that the balance between excitation and inhibition is maintained (Figure 26.6). An unbalanced increase in excitation favored the occurrence of slow bursting, resulting in an increase in the duration of slow bursting epochs and an increase in the width of the hysteresis between slow bursting and fast run (Figure 26.6A). The latter phenomenon was caused by a lowering of the  $[K^+]_o$  threshold for which the network switched from slow bursting to fast run (lower endpoint of hysteresis, Figure 26.6B). Conversely, an unbalanced increase in synaptic inhibition caused an increase in the duration of the epochs of fast run by narrowing the width of hysteresis through increase of  $[K^+]_o$  threshold for transition from slow bursting to fast run (lower endpoint of hysteresis). In cases

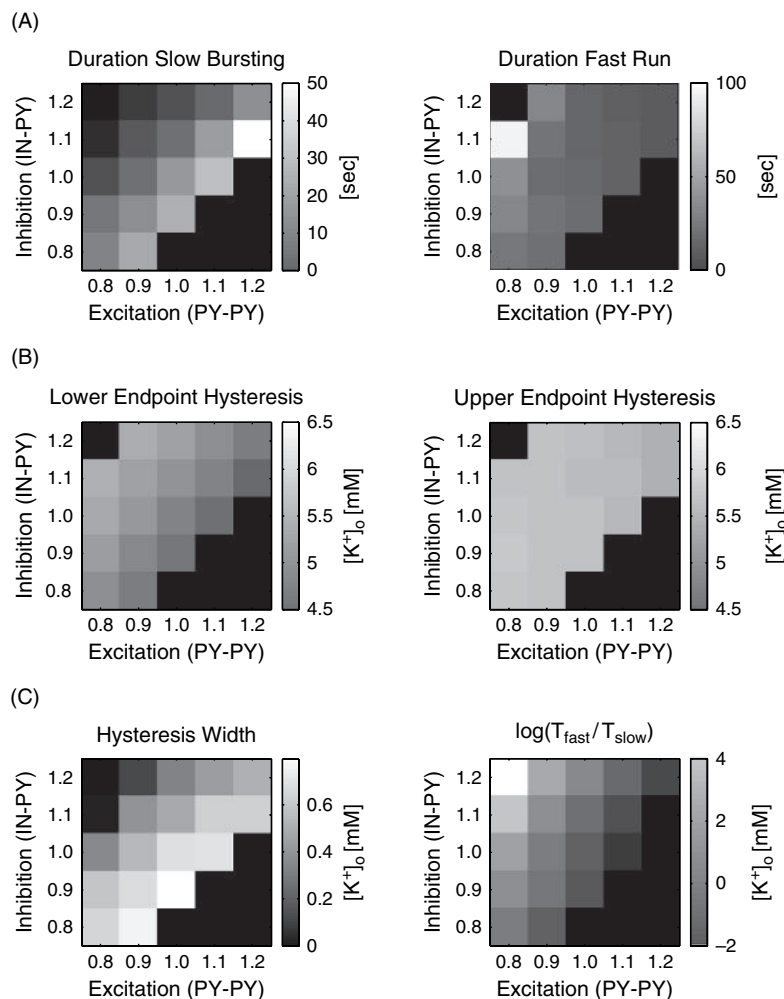


**FIGURE 26.6** Quantification of periodic slow transitions between slow bursting and fast run as a function of excitatory and inhibitory coupling. Balanced excitation and inhibition causes alternating epochs of slow bursting and fast run. (A) Left: duration of epochs of slow bursting. Right: duration of epochs of fast run. Values determined from simulation of 400 s of activity. (B) Lower (left) and upper (right) endpoint of hysteresis. (C) Width of hysteresis (right) and logarithmic ratio of duration of fast run and slow bursting (right) as a function of synaptic excitation and inhibition. Top left corner corresponds to regime with exclusive fast run, whereas bottom right corner denotes the regime with exclusive slow bursting. Adapted from Frohlich et al. (2006), with permission. Copyright 2006 Society for Neuroscience.

of strongly unbalanced excitation and inhibition, no state transitions were found. For strong excitation and weak inhibition, bursting followed by silence occurred. Quite the opposite was observed for weak excitation and strong inhibition; the network displayed activity similar to fast run without exhibiting any slow state transitions and never returned to the silent state. In summary, balanced excitation and inhibition was found to be crucial for the occurrence of patterned oscillatory network activity in network models of cortical circuits with potassium dynamics.

The resulting slow state transitions are an interesting phenomenon for a series of reasons. First, the model exhibits slow dynamics in absence of any process with an explicit slow time-scale. The transitions occur on a time-scale of seconds (larger network with local synaptic connectivity shown in Figure 26.7), whereas the slowest processes in the

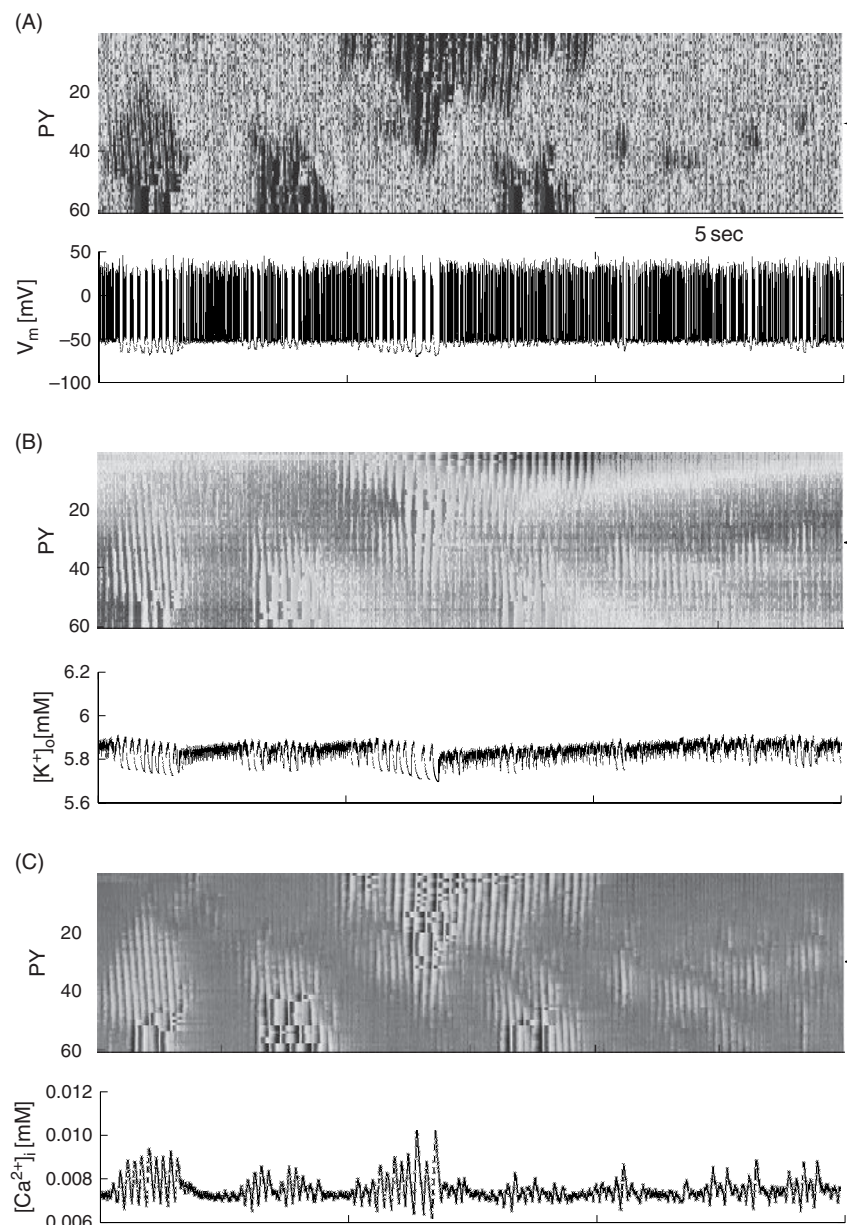


**FIGURE 26.7** Large network (60 PY cells and 15 INs) with local synaptic connectivity. (A) PY cell activity as a function of time (top panel). Time-course of  $V_m$  for PY 30 (bottom panel, arrow in top panel). Cells switched between bursting and fast run as in the case of the small network. Due to the local synaptic connectivity, the activity pattern exhibited complex spatial structure. (B)  $[K^+]_o$  in extracellular compartments surrounding PY cells as a function of time (top panel). Time-course of  $[K^+]_o$  for PY 30 (bottom panel, arrow in top panel). (C) Intracellular calcium  $[Ca^{2+}]_i$  in PY cells as a function of time. Time-course of  $[Ca^{2+}]_i$  for PY 30 (bottom panel, arrow in top panel). From Frohlich et al. (2006), with permission. Copyright 2006 Society for Neuroscience.

model have time-constants of at most a few hundred milliseconds. Rather, the slow dynamics emerge from the interaction of fast processes increasing and decreasing  $[K^+]_o$ . Very slow evolution of  $[K^+]_o$  is the net effect of this push and pull dynamics close to the equilibrium (where the  $[K^+]_o$  gradient is zero). Second, the model predicts specific  $[K^+]_o$  gradients during the two oscillatory phases: positive in case of fast run and negative in case of slow bursting. This matches the experimental *in vivo* (Sypert and Ward, 1974) and *in vitro* (Jensen and Yaari, 1997) finding of increasing and decreasing  $[K^+]_o$  during tonic and clonic components of seizures. Third, these slow transitions closely resemble the patterned activity during electrographic seizure in cat *in vivo* (see Figure 26.1) and clinical seizures in patients suffering from the Lennox-Gastaut syndrome. The mechanism underlying this patterning of oscillatory firing has so far remained elusive. Our network model including extracellular potassium dynamics provides a novel mechanistic explanation for these slow state transitions.

### FAILURE OF $K^+$ REGULATORY SYSTEM LEADS TO PAROXYSMAL OSCILLATIONS

The previous section established that extracellular potassium concentration dynamics can explain slow state transitions between two distinct oscillatory firing modes resembling neocortical paroxysmal activity *in vivo*. Experimental evidence suggests that, in certain epileptic brains, the potassium regulatory system exhibits deficits. Post-traumatic hippocampal glia cells failed to maintain  $K^+$  homeostasis in the extracellular space (D'Ambrosio et al., 1999) leading to increased  $[K^+]_o$  and afterdischarges during stimulation *in vitro* (but see Santhakumar et al., 2003). Hippocampal tissue from human patients with temporal lobe epilepsy exhibited impairment of glial inward-rectifying  $K^+$ -channels responsible for  $K^+$  uptake (Hinterkeuser et al., 2000; Kivi et al., 2000).

Here, the computational model of a cortical circuit with extracellular potassium dynamics is used to test the hypothesis that such deficits in the mechanisms responsible for  $[K^+]_o$  homeostasis can lead to paroxysmal oscillations. Specifically, the following two cases are investigated: (1) blocking of potassium pumps and (2) blocking of glial cell buffering.

#### Role of $K^+$ pump

In the case of a single model PY cell surrounded by an extracellular compartment endowed with glial buffering of excess potassium but no  $K^+$  pump for active reuptake, random external synaptic input led to bursting at a range of slow frequencies accompanied by a moderate increase in  $[K^+]_o$  (Figure 26.8A). In a network (100 PYs and 20 INs), initial random firing increased in frequency for cells which lacked a functioning  $K^+$  pump. As a result,  $K^+$  further increased, effectively mediating a positive feedback loop. After a few seconds, the network started to burst at slow frequency with neighboring groups of neurons bursting in synchrony (Figure 26.8B). These bursting oscillations were persistent even after removal of the external input. Hence, the potassium regulation system found a new equilibrium state in the absence of potassium pumps.  $[K^+]_o$  converged to an elevated value for which any further increase in  $[K^+]_o$  by bursting was balanced by glial potassium buffering.

#### Role of $K^+$ buffering

In the absence of glial buffering, a single model neuron fired bursts with spike inactivation and pronounced after-hyperpolarization (see Figure 26.8C). The long depolarized phase during the burst allowed substantial potassium outflow, which rapidly accumulated in the extracellular compartment due to the absence of glial buffering. The resulting depolarization of the potassium reversal potential weakened the calcium-activated potassium current, which mediates burst termination. Eventually, the cell became locked in the depolarized state where no more spiking occurred due to substantial inactivation of the transient voltage-gated sodium channels and no more hyperpolarization occurred since the calcium-activated potassium current was too weak to repolarize the neuron.

In the network case, cells without glial buffering in their extracellular space exhibited a transient phase of slow bursting oscillation before  $[K^+]_o$  was sufficiently elevated for the cells to switch to the depolarized state with spike-inactivation (see Figure 26.8D, top panel). Adding lateral diffusion of potassium changed the qualitative nature of the dynamics (see Figure 26.8D, middle and bottom panel). The potassium accumulating in the extracellular compartments with no glial buffering diffused into compartments with intact glial buffering and therefore lower  $[K^+]_o$ . As a consequence, the whole network exhibited slow bursting, even in the absence of external input. No more long-lasting depolarization was observed. In summary, impairment of the glial buffering system had a dramatic effect on the network dynamics and can explain paroxysmal bursting.

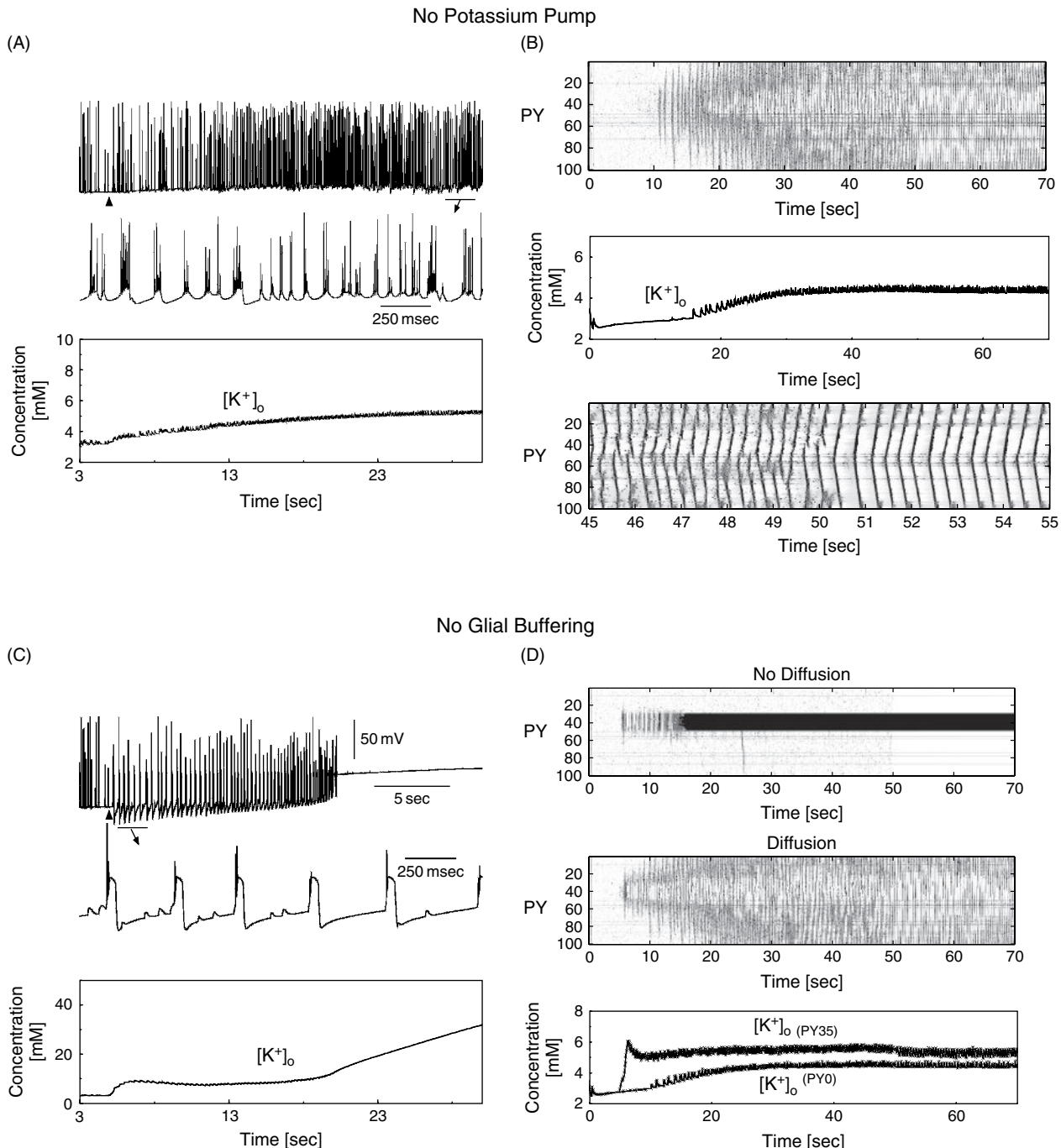


**FIGURE 26.8** Effect of glial buffering and  $K^+$  pump on a neuron activity. (A) Following block of  $K^+$  pump (arrowhead),  $[K^+]_o$  increased and led to fast bursting in single cell model. (B) Blocking the  $K^+$  pump at  $t = 5$  s led to increase of  $[K^+]_o$  and bursting. Oscillations continued after removing random external input at  $t = 50$  s. A group of cells with  $I_h$  led the network oscillations. (C) Blocking glial  $K^+$  uptake system transformed random firing maintained by random external stimulation into periodic bursting and eventually led to permanent spike inactivation. (D) Glial buffering system was blocked in a group of cells (no. 30–50) at  $t = 5$  s. Top: low-frequency bursting was found in this group and was followed by permanent spike inactivation at about  $t = 20$  s. Middle and bottom: when lateral (between cell) diffusion of  $K^+$  was introduced to the model, the cells outside the group also increased firing. After external random input to the network was removed at  $t = 50$  s, the network displayed periodic oscillations at about 3 Hz. Adapted from Bazhenov et al. (2004), used with permission. Copyright 2004 the American Physiological Society.

### TERMINATION OF PAROXYSMAL OSCILLATIONS BY SHIFTING BALANCE OF EXCITATION AND INHIBITION

Little is known about seizure cessation (Timofeev and Steriade, 2004). Although the network model with extracellular potassium dynamics discussed above explains initiation and maintenance of neocortical electrographic seizures characterized by alternating epochs of fast run and slow bursting, little has been said about possible mechanisms leading to termination of patterned paroxysmal oscillations – seizure cessation. Here, two different mechanisms that both cause a shift in balance between synaptic excitation and inhibition resulting in seizure cessation are described. Both mechanisms are based on the previously discussed finding that persistent oscillations only occurred in case of balanced excitation and inhibition. In case of scaled-up excitation without counterbalance by increased inhibition, the model exhibited only a single epoch of slow bursting during which  $[K^+]_o$  decreased. As a consequence, the network returned to the silent state without a single episode of fast run. Therefore, any activity-dependent mechanism which shifts the balance between excitation and inhibition towards more excitation can potentially terminate the oscillations. To confirm this hypothesis, the network model with extracellular potassium dynamics was refined by adding slow, activity-dependent modulation of synaptic currents.

#### Synaptic plasticity

In the first case, ‘slow synaptic depression’ similar to the standard model of use-dependent short-term depression (STD) was used for both the excitatory (recurrent excitation among pyramidal cells) and the inhibitory (inhibition onto pyramidal cells) synaptic conductances (Figure 26.9). However, parameters were different from the STD model. The recovery time-scale was

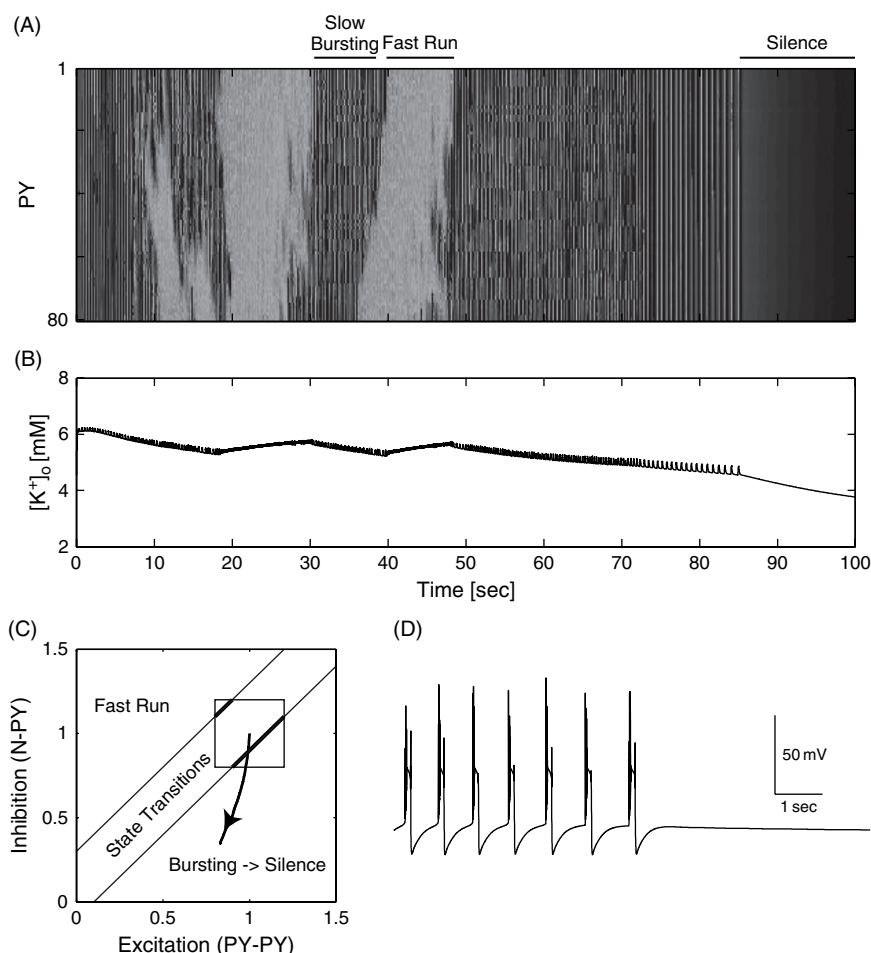


**FIGURE 26.9** Patterned cortical network oscillations of finite length for slow depression of synaptic transmission. (A) Activity of all 80 PYs as a function of time. (B) Extracellular potassium concentration time-course (C) Phase-space representation of normalized synaptic coupling strength. Dynamic change in balance between excitation and inhibition (line with arrowhead). Arrowhead indicates direction of time. Diagonal lines delimit the region for which alternating epochs of fast run and slow bursting may occur infinitely. The box corresponds to the values of synaptic coupling strengths for which we found persistent oscillations in a small network with the same dynamics (Frohlich et al., 2006). (D) Time-course of membrane voltage before termination of oscillations shows slow bursting.

set to a very slow value such that there was no effective recovery on the time-course of an individual seizure ( $\tau = 1000$  s) and the fraction of synaptic resources used per presynaptic action potential was several magnitudes smaller in comparison to STD. As a result, both excitation and inhibition decreased during the paroxysmal oscillatory activity. When the rates were chosen such that inhibition decreased faster than excitation, a net shift in balance between synaptic excitation and inhibition occurred. In the case of parameters causing a fast divergence from the balanced condition, no epoch of fast run occurred. In the limit, this corresponds to the previously discussed, static case where too strong excitatory coupling would not permit slow state transitions. If, however, the values were chosen such that divergence from the balanced condition occurred at a slower speed, which allowed the occurrence of few slow state transitions before the region of approximately balanced synaptic excitation and inhibition was left, the model exhibited both maintenance of patterned oscillatory activity and termination on a time-scale comparable to the paroxysmal events observed *in vivo*. This shows that a shift in balance between excitation and inhibition permits seizure cessation in the model. However, it is not trivial to match the relatively simple slow depression mechanism in the model with actual physiological processes. Although it is known that plasticity on multiple time-scales occurs during seizure-like events, more experimental evidence is required to fully justify the choice of depression mechanisms and parameters.

### Intracellular chloride accumulation

In the model, synaptic inhibition is mediated by receptor channels which activate upon binding to GABA. The inhibitory current is mediated by chloride ions. Chloride has a higher extracellular than intracellular concentration. *In vivo* recordings

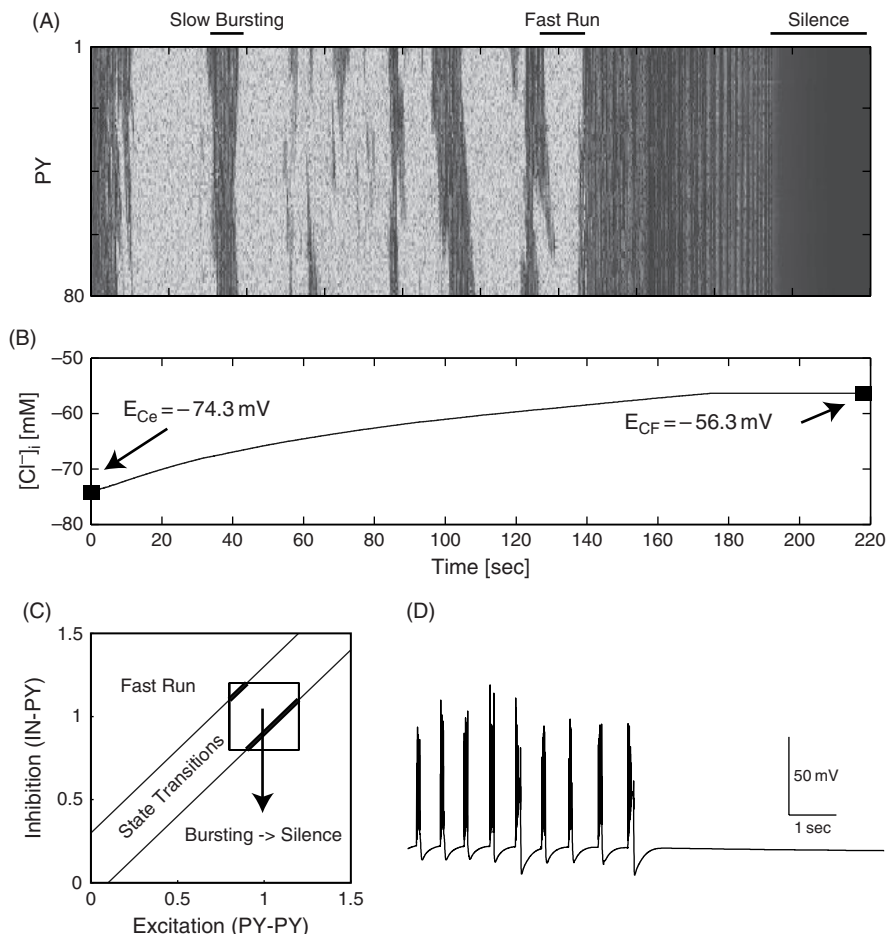


**FIGURE 26.10** Patterned cortical network oscillations of finite length for dynamically updated intracellular chloride concentration. (A) Activity of all 80 PYs as a function of time. (B) Intracellular chloride concentration time-course. Corresponding reversal potentials are shown for the onset and the end of oscillations. (C) Symbolic phase-space representation of dynamic change in balance between excitation and inhibition (line with arrowhead). Arrowhead indicates direction of time. Diagonal lines delimit the region for which alternating epochs of fast run and slow bursting may occur infinitely. (D) Time-course of membrane voltage before termination of oscillations.

measuring the reversal potential of inhibitory currents showed that the reversal potential for chloride mediated inhibition depolarized from  $-69.7$  to  $-54.2$  mV during seizures (Timofeev et al., 2002). Activity-dependent accumulation of intracellular chloride is the most likely candidate mechanism underlying this shift in reversal potential. In the model, chloride accumulation mediated by inhibitory currents reproduces the depolarization of the reversal potential (Figure 26.10). Similarly to the previous case where synaptic plasticity mediated divergence away from balanced excitation and inhibition, intracellular chloride accumulation caused a selective decrease in inhibition by reduction of the corresponding driving force. This activity-dependent decrease in inhibition caused seizure termination in the model. In summary, an additional state equation, which modeled the intracellular chloride accumulation closely, reproduced the experimentally determined depolarization of the corresponding reversal potential and caused seizure cessation.

## CONCLUSION

Over the past decades, computational models of neurons and networks of neurons have provided significant insight into how the nervous system functions. The efforts discussed in this chapter contribute to the relatively young field of mathematical and computational modeling of pathological brain states. The work presented here is focused on the investigation of the mechanism underlying neocortical paroxysmal oscillations. Although an increase in intrinsic excitability via increase in extracellular potassium concentration had been implicated in epileptogenesis for decades, little about the resulting dynamics had been established. Most commonly, increase in  $[K^+]_o$  has been associated with a positive feedback mechanism eventually leading to depolarization with spike inactivation by some form of global loss of stability (potassium accumulation hypothesis).

We have found that extracellular potassium dynamics explains slow state transitions between two metastable oscillatory states, fast run and slow bursting. Bifurcation analysis has helped to understand the underlying dynamics in terms of the newly discovered bistability between tonic firing and slow bursting in the model cortical neuron. Our potassium model of neocortical epilepsy reproduces the main features of paroxysmal cortical activity characterized by alternating epochs of slow bursting and fast run as observed in human patients with the Lennox-Gastaut syndrome.

We conclude by suggesting that:

1.  $[K^+]_o$  dynamics mediate slow transitions between SW discharges and fast runs in cortical seizures
2.  $[K^+]_o$  increases during tonic discharges and decreases during clonic discharges
3. pyramidal cells fire either tonically or in slow bursts depending on  $[K^+]_o$
4. slow state transitions between tonic and clonic activity occur in conditions of balanced excitation and inhibition
5. a shift in the balance between synaptic excitation and inhibition towards more excitation mediates seizure cessation
6. cortical tonic-clonic seizures end with a clonic epoch. The last prediction has been observed *in vivo* (I. Timofeev, unpublished observation).

The hypotheses derived from our modeling work need to be tested by new experiments to further investigate the role of extracellular potassium dynamics in seizure initiation, maintenance and termination. We hope that these studies will eventually contribute to the development of new clinical methods of prevention and intervention in patients suffering from epilepsy.

## ACKNOWLEDGMENT

This study was supported by National Institute on Deafness and Other Communication Disorders, National Institutes of Health (Grant R01 DC006306), Canadian Institutes of Health Research (Grant MOP-37862, MOP-67175) and Natural Science and Engineering Research Council of Canada. I.T. is Canadian Institutes of Health Research scholar.

## REFERENCES

- Ajmone-Marsan, C. and Ralston, B. (1956). Thalamic control of certain normal and abnormal cortical rhythms. *Electroencephalogr Clin Neurophysiol Suppl* 8:559–582.  
 Amzica, F. and Steriade, M. (2000). Neuronal and glial membrane potentials during sleep and paroxysmal oscillations in the neocortex. *J Neurosci* 20:6648–6665.

- Bal, T., von Krosigk, M. and McCormick, D.A. (1995). Synaptic and membrane mechanisms underlying synchronized oscillations in the ferret lateral geniculate nucleus in vitro. *J Physiol* 483 (Pt 3):641–663.
- Bazhenov, M., Timofeev, I., Steriade, M. and Sejnowski, T.J. (2004). Potassium model for slow (2–3 Hz) in vivo neocortical paroxysmal oscillations. *J Neurophysiol* 92:1116–1132.
- Castro-Alamancos, M.A. (1999). Neocortical synchronized oscillations induced by thalamic disinhibition in vivo. *J Neurosci* 19:RC27.
- D'Ambrosio, R., Maris, D.O., Grady, M.S., Winn, H.R. and Janigro, D. (1999). Impaired K(+) homeostasis and altered electrophysiological properties of post-traumatic hippocampal glia. *J Neurosci* 19:8152–8162.
- Destexhe, A., Mainen, Z.F. and Sejnowski, T.J. (1994). Synthesis of models for excitable membranes, synaptic transmission and neuromodulation using a common kinetic formalism. *J Comput Neurosci* 1:195–230.
- Dichter, M.A., Herman, C.J. and Selzer, M. (1972). Silent cells during interictal discharges and seizures in hippocampal penicillin foci. Evidence for the role of extracellular K<sup>+</sup> in the transition from the interictal state to seizures. *Brain Res* 48:173–183.
- Ermentrout, B. (1996). Type I membranes, phase resetting curves, and synchrony. *Neural Comput* 8:979–1001.
- Fertziger, A.P. and Ranck, J.B. Jr (1970). Potassium accumulation in interstitial space during epileptiform seizures. *Exp Neurol* 26:571–585.
- Frohlich, F. and Bazhenov, M. (2006). Coexistence of tonic firing and bursting in cortical neurons. *Phys Rev E Stat Nonlin Soft Matter Phys* 74.
- Frohlich, F., Bazhenov, M., Timofeev, I., Steriade, M. and Sejnowski, T.J. (2006). Slow state transitions of sustained neural oscillations by activity-dependent modulation of intrinsic excitability. *J Neurosci* 26:6153–6162.
- Futamachi, K.J., Mutani, R. and Prince, D.A. (1974). Potassium activity in rabbit cortex. *Brain Res* 75:5–25.
- Grossman, R.G. and Hampton, T. (1968). Depolarization of cortical glial cells during electrocortical activity. *Brain Res* 11:316–324.
- Heinemann, U. and Lux, H.D. (1977). Ceiling of stimulus induced rises in extracellular potassium concentration in the cerebral cortex of cat. *Brain Res* 120:231–249.
- Heinemann, U., Lux, H.D. and Gutnick, M.J. (1977). Extracellular free calcium and potassium during paroxysmal activity in the cerebral cortex of the cat. *Exp Brain Res* 27:237–243.
- Hinterkeuser, S., Schroder, W., Hager, G. et al. (2000). Astrocytes in the hippocampus of patients with temporal lobe epilepsy display changes in potassium conductances. *Eur J Neurosci* 12:2087–2096.
- Hotson, J.R., Sypert, G.W. and Ward, A.A. Jr (1973). Extracellular potassium concentration changes during propagated seizures in neocortex. *Exp Neurol* 38:20–26.
- Izhikevich, E.M. (2007). *Dynamical systems in neuroscience: the geometry of excitability and bursting*. MIT Press: Cambridge MA.
- Jensen, M.S. and Yaari, Y. (1997). Role of intrinsic burst firing, potassium accumulation, and electrical coupling in the elevated potassium model of hippocampal epilepsy. *J Neurophysiol* 77:1224–1233.
- Jensen, M.S., Azouz, R. and Yaari, Y. (1994). Variant firing patterns in rat hippocampal pyramidal cells modulated by extracellular potassium. *J Neurophysiol* 71:831–839.
- Kivi, A., Lehmann, T.N., Kovacs, R. et al. (2000). Effects of barium on stimulus-induced rises of [K+]o in human epileptic non-sclerotic and sclerotic hippocampal area CA1. *Eur J Neurosci* 12:2039–2048.
- Lothman, E., Lamanna, J., Cordingley, G., Rosenthal, M. and Somjen, G. (1975). Responses of electrical potential, potassium levels, and oxidative metabolic activity of the cerebral neocortex of cats. *Brain Res* 88:15–36.
- Lux, H.D. and Neher, E. (1973). The equilibration time course of (K<sup>+</sup>)<sub>0</sub> in cat cortex. *Exp Brain Res* 17:190–205.
- Mainen, Z.F. and Sejnowski, T.J. (1996). Influence of dendritic structure on firing pattern in model neocortical neurons. *Nature* 382:363–366.
- Markand, O.N. (2003). Lennox-Gastaut syndrome (childhood epileptic encephalopathy). *J Clin Neurophysiol* 20:426–441.
- Markram, H., Pukas, D., Gupta, A. and Tsodyks, M. (1998). Potential for multiple mechanisms, phenomena and algorithms for synaptic plasticity at single synapses. *Neuropharmacology* 37:489–500.
- Moody, W.J., Futamachi, K.J. and Prince, D.A. (1974). Extracellular potassium activity during epileptogenesis. *Exp Neurol* 42:248–263.
- Niedermeyer, E. (1999a). Abnormal EEG patterns: epileptic and paroxysmal. In: *Electroencephalography: basic principles, clinical applications, and related fields* (E. Niedermeyer and F. Lopes de Silva F, eds), pp. 235–260. Williams & Wilkins, Baltimore.
- Niedermeyer, E. (1999b). Epileptic seizure disorders. In: *Electroencephalography: basic principles, clinical applications, and related fields* (E. Niedermeyer and F. Lopes de Silva F, eds), pp. 476–585. Williams & Wilkins, Baltimore.
- Niedermeyer, E. (2002). Lennox-Gastaut syndrome. Clinical description and diagnosis. *Adv Exp Med Biol* 497:61–75.
- Pinault, D., Leresche, N., Charpier, S. et al. (1998). Intracellular recordings in thalamic neurones during spontaneous spike and wave discharges in rats with absence epilepsy. *J Physiol* 509 (Pt 2):449–456.
- Prince, D.A., Lux, H.D. and Neher, E. (1973). Measurement of extracellular potassium activity in cat cortex. *Brain Res* 50:489–495.
- Rinzel, J. and Ermentrout, B. (1989). Analysis of neural excitability and oscillations. In: *Methods in neuronal modeling* (C. Koch and I. Segev, eds). MIT Press, Cambridge.
- Rutecki, P.A., Lebeda, F.J. and Johnston, D. (1985). Epileptiform activity induced by changes in extracellular potassium in hippocampus. *J Neurophysiol* 54:1363–1374.
- Santhakumar, V., Voipio, J., Kaila, K. and Soltesz, I. (2003). Post-traumatic hyperexcitability is not caused by impaired buffering of extracellular potassium. *J Neurosci* 23:5865–5876.
- Singer, W. and Lux, H.D. (1973). Presynaptic depolarization and extracellular potassium in the cat lateral geniculate nucleus. *Brain Res* 64:17–33.
- Singer, W. and Lux, H.D. (1975). Extracellular potassium gradients and visual receptive fields in the cat striate cortex. *Brain Res* 96:378–383.
- Stafstrom, C.E. (2005). Neurons do the wave (and the spike!) during neocortical seizures. *Epilepsy Curr* 5:69–71.
- Steriade, M. (1974). Interneuronal epileptic discharges related to spike-and-wave cortical seizures in behaving monkeys. *Electroencephalogr Clin Neurophysiol* 37:247–263.
- Steriade, M. (2003). *Neuronal substrates of sleep and epilepsy*. Cambridge University Press, Cambridge.
- Steriade, M. and Contreras, D. (1995). Relations between cortical and thalamic cellular events during transition from sleep patterns to paroxysmal activity. *J Neurosci* 15:623–642.

- Steriade, M. and Contreras, D. (1998). Spike-wave complexes and fast components of cortically generated seizures. I. Role of neocortex and thalamus. *J Neurophysiol* 80:1439–1455.
- Steriade, M. and Timofeev, I. (2001). Corticothalamic operations through prevalent inhibition of thalamocortical neurons. *Thalamus related syst* 1:225–236.
- Steriade, M., Amzica, F., Neckelmann, D. and Timofeev, I. (1998). Spike-wave complexes and fast components of cortically generated seizures. II. Extra- and intracellular patterns. *J Neurophysiol* 80:1456–1479.
- Sypert, G.W. and Ward, A.A. Jr (1971). Unidentified neuroglia potentials during propagated seizures in neocortex. *Exp Neurol* 33:239–255.
- Sypert, G.W. and Ward, A.A. Jr (1974). Changes in extracellular potassium activity during neocortical propagated seizures. *Exp Neurol* 45:19–41.
- Timofeev, I. and Steriade, M. (2004). Neocortical seizures: initiation, development and cessation. *Neuroscience* 123:299–336.
- Timofeev, I., Grenier, F. and Steriade, M. (1998). Spike-wave complexes and fast components of cortically generated seizures. IV. Paroxysmal fast runs in cortical and thalamic neurons. *J Neurophysiol* 80:1495–1513.
- Timofeev, I., Grenier, F., Bazhenov, M., Sejnowski, T.J. and Steriade, M. (2000). Origin of slow cortical oscillations in deafferented cortical slabs. *Cereb Cortex* 10:1185–1199.
- Timofeev, I., Grenier, F. and Steriade, M. (2002). The role of chloride-dependent inhibition and the activity of fast-spiking neurons during cortical spike-wave electrographic seizures. *Neuroscience* 114:1115–1132.
- Tsodyks, M.V. and Markram, H. (1997). The neural code between neocortical pyramidal neurons depends on neurotransmitter release probability. *Proc Natl Acad Sci USA* 94:719–723.
- Yaari, Y., Konnerth, A. and Heinemann, U. (1986). Nonsynaptic epileptogenesis in the mammalian hippocampus in vitro. II. Role of extracellular potassium. *J Neurophysiol* 56:424–438.

# 27

## SLOW WAVES ASSOCIATED WITH SEIZURE ACTIVITY

ANATOL BRAGIN AND JEROME ENGEL JR

### ABSTRACT

Slow waves with a period less than 1 second often occur in conjunction with faster brain waves that include theta, beta, gamma, ripples and fast ripples. While a number of studies provide evidence that propose functional roles for theta, beta and gamma activity, there are relatively fewer studies on slow waves and their potential role during these complex patterns of brain activity. This chapter describes the occurrence of slow waves during three phases of seizure activity: the initiation of seizures, accumulation of extracellular potassium during seizures and spreading depression following seizures. It is proposed that during each of these phases the mechanisms underlying the generation of slow waves are different and these mechanisms of slow wave generation may have distinct functional roles that contribute to seizure activity.

### INTRODUCTION

The occurrence of specific patterns of electrical activity can characterize different types of brain activity and, in epilepsy, may indicate different mechanisms triggering seizure activity. Understanding mechanisms responsible for generation of these patterns could lead to new approaches in treatment to prevent seizure occurrence. According to a recent ILAE (International League Against Epilepsy) report, there are more than 25 different types of seizures (Engel, 2006). So far, a significant progress has been made in understanding the mechanisms of generation of absence seizures with generalized spike-and-wave pattern (Prince et al., 1983; Huguenard, 2000; McCormick and Contreras, 2001; Steriade and Amzica, 2003; Timofeev and Steriade, 2004). Despite significant efforts by basic and clinical neuroscientists, however, mechanisms triggering other types of seizures are poorly understood.

This chapter will focus on the analysis of slow waves with durations of one second or more associated with different stages of seizures. These slow waves are a part of a complex pattern of brain electrical activity and other patterns of fast brain oscillations, such as theta, beta and gamma, ripples and fast ripples are superimposed on these slow waves. At present, there is much more information about the functional role of theta, beta and gamma activity than about the functional role of slow waves. On the basis of existing publications, at least three types of seizure-associated slow waves can be distinguished. The first occurs only at seizure onset; the second appears during seizure development and remains throughout the entire seizure; and the third appears at seizure termination.

We propose that seizure associated slow waves reflect three processes:

1. initiation of seizures
2. accumulation of extracellular potassium and changes in the pH of the extracellular space as a result of extensive neuronal discharges
3. occurrence and propagation of spreading depression when concentration of extracellular potassium reaches a certain critical level.

Potential mechanisms generating these waves and the need to consider the involvement of non-synaptic and non-neuronal processes, in addition to those of the neuronal networks, in attempting to understand the origin of certain types of slow waves will be discussed. Modeling of broad brain functions may require consideration of mechanisms of slow wave

generation due to non-synaptic processes and non-neuronal elements including glia-neuronal networks, during normal and pathological conditions.

#### SLOW WAVES THAT APPEAR AT SEIZURE ONSET (INITIAL SLOW WAVES: ISWs)

Seizure onset characterized by initial suppression of electroencephalography (EEG) amplitude and increase of EEG frequency is termed low-voltage fast (LVF) onset (Townsend and Engel, 1991; Spencer et al., 1992; Velasco et al., 2000; Lee et al., 2000). Intracranial recordings with amplifiers in the frequency band from 0.1 to 70 Hz, revealed the existence of initial slow waves (ISWs) in this type of seizure onset. These slow waves at the LVF seizure onset have been described in several publications for patients with temporal lobe and neocortical epilepsy (Spencer et al., 1992; Ikeda et al., 1996, 1997; King et al., 1997; Velasco et al., 2000; Hughes et al., 2005) and for patients with West syndrome (Kobayashi et al., 2005), however, there have been no detailed analyses of possible mechanism of their generation. Duration of ISWs varied between 0.3 s and 6.0 s (mean  $1.2 \pm 0.7$  SD) and maximum amplitude varied from 0.2 mV to 1.4 mV (mean  $0.6 \text{ mV} \pm 0.3$  SD).

An example of an ISW at seizure onset in a patient with mesial temporal lobe epilepsy is shown in Figure 27.1. It illustrates bipolar depth electrode recordings from 27 bilateral deep and superficial sites. At the seizure onset, a slow wave appeared in all recording sites within a period of less than 0.1 s with or without superimposed EEG spikes on the ascending or descending part of the slow wave, followed by a suppression of the EEG amplitude.

Inserts A and B in Figure 27.1 show axial magnetic resonance (MR) images and the location of electrode contacts. Inset C represents a sagittal MR image where numbers illustrate the distance between some of the recording sites. The distance between most frontal and posterior recording sites was about 180 mm and between deepest and superficial recording sites was about 50 mm. The synchronous appearance of ISW does not depend on the existence of this wave at the reference electrode. Figure 27.2 illustrates the same seizure in referential montage from different reference electrodes, FZ on the left and CZ on the right. It is clear from this figure that the pattern of ISW remains the same in all electrodes regardless of the

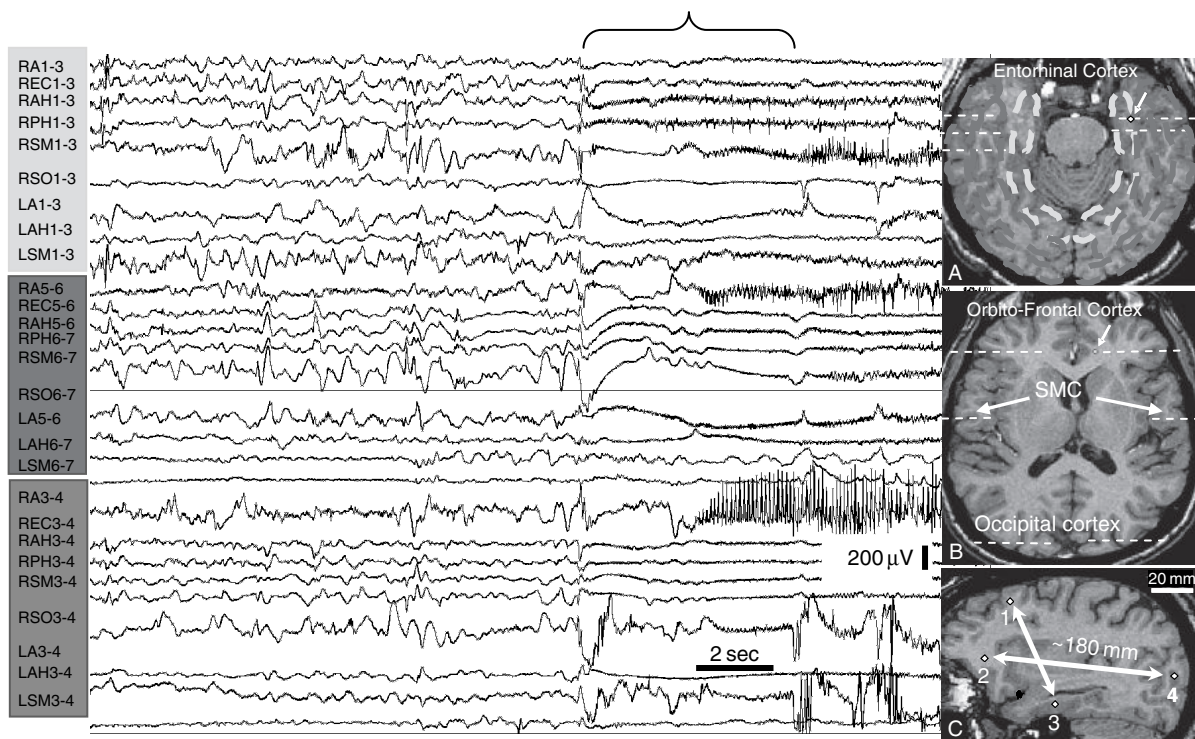


**FIGURE 27.1** Example of a seizure recorded in bipolar montage with initial slow wave at the onset, indicated by the bracket at the top. Yellow, red and blue colors indicate correspondingly mesial, medial and lateral locations of the recorded sites, illustrated on part (A) of MRI image. (B,C) Examples of MR images indicating the location of the recorded sites. (See Plate 16 in color plate section.)

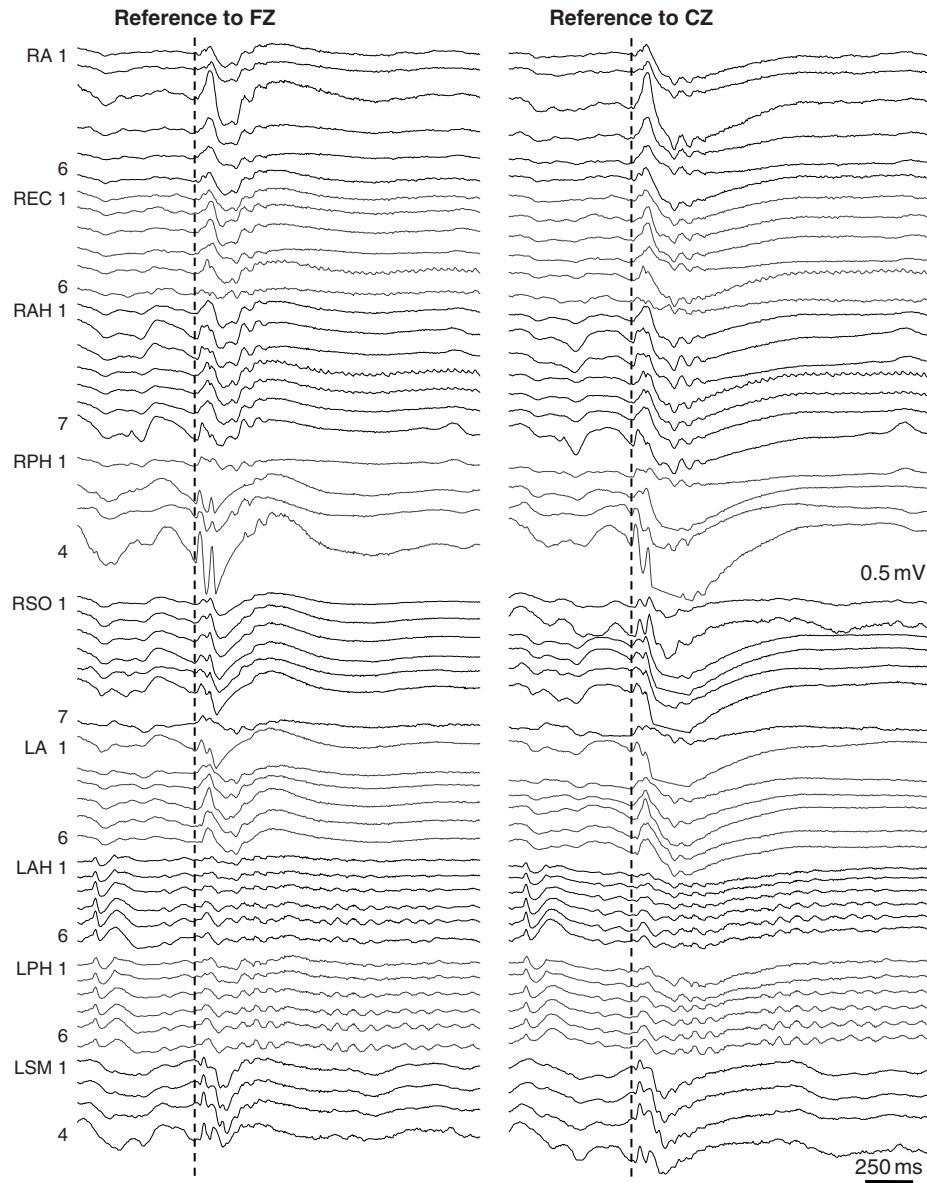


**FIGURE 27.2** Onset of seizure presented in Plate 16 recorded in relation to different reference electrodes: FZ on the left column and CZ on the right column. This figure illustrates that the synchrony and the shape of the ISW is not a result of a common potential generated in the area of the reference electrode.

area of the brain chosen as a reference. The spatio-temporal characteristics of ISWs were different from those of recorded interictal EEG spikes, which were more localized and of shorter duration (Bragin et al., 2005a).

Two types of ISWs were distinguished on the basis of voltage depth profiles. In 21% of patients, ISWs were positive at the deepest contacts, located in the amygdala, hippocampus or entorhinal cortex (ISWs1, Figure 27.3B). ISWs1 changed polarity at contact 2 and slowly decreased in amplitude towards the neocortex. In the remaining 79% of patients, the ISWs had negative amplitude at the deepest contacts. The amplitude of these ISWs was smallest in the deep brain areas and increased towards the superficial contacts, located in the neocortex (ISWs2). The maximum amplitude of the ISWs2 could be at recording site 4–5 (Figure 27.3C) or 6 (Figure 27.3D) and sharply decreased in the most superficial contact (Figure 27.3C and D). The identification of the recording sites in these patients on MRI showed that the abrupt decrease in amplitude of ISWs occurred in contacts located near the surface of the neocortex and the maximum amplitude of ISWs was in the white matter (Figure 27.3C and D). No change was observed in the polarity of ISWs at the border between gray and white matter, while some EEG interictal spikes did reverse polarity between gray and white matter.

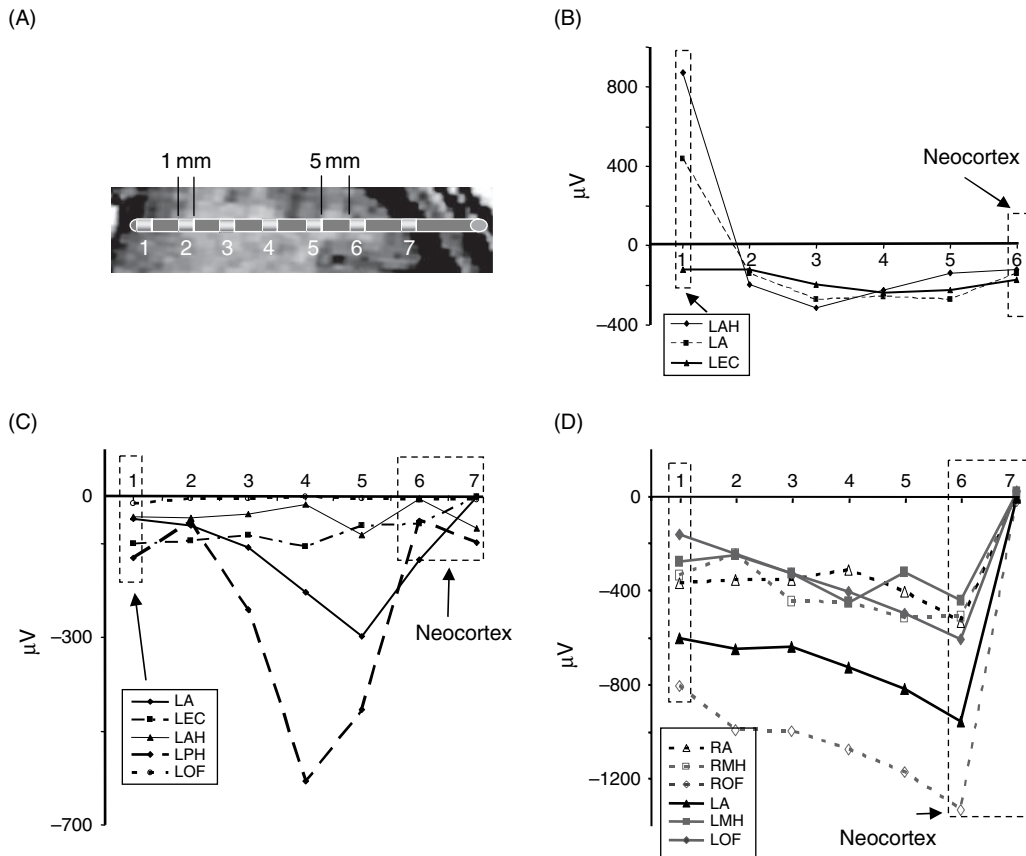


**FIGURE 27.3** (A) Schematic of the location of the recording electrodes. Voltage depth profiles of ISWs (B) with phase reversal, (C) without phase reversal with maximum amplitude in the white matter (electrodes nos 4–5). (D) Without phase reversal with maximum amplitude in the gray matter of neocortex.

There was a difference in electrographic patterns accompanying ISWs<sub>1</sub> and ISWs<sub>2</sub>. ISWs<sub>1</sub> were associated with an increase in amplitude of 10–20 Hz sinusoidal activity. This activity remained for 5–10 s and then decreased to a frequency of 2–5 Hz. In all seizures with ISWs<sub>1</sub>, EEG interictal spikes (IIS) were consistently riding on the ISWs<sub>1</sub>. ISWs<sub>2</sub> were associated with an increase in amplitude of gamma (20–60 Hz) activity and there were no IIS observed related to ISWs<sub>2</sub>.

#### SLOW WAVES THAT OCCUR DURING SEIZURE DEVELOPMENT

In experiments where brain electrical activity was recorded with direct current coupled amplifiers, waves of long duration, termed steady potentials, were discovered (Goldring and O’Leary, 1951). These steady potentials occurred during experimentally evoked seizures. In subsequent publications (O’Leary and Goldring, 1959/60, 1964; Goldring, 1963; Li and Salmoiraghi, 1963), the term steady potential was replaced by the term direct current shift (DC shift).

Later, some concerns were expressed regarding possible technical pitfalls of these earlier data (see Vanhatalo et al., 2005 for review). One was that, in these earlier studies, silver or stainless steel electrodes were used for recording. These electrodes can generate polarization potentials and fluctuation of these potentials could lead to erroneous conclusions. However, recently published data obtained with non-polarizable recording electrodes and stable DC amplifiers (Morrell and Nelson, 1987; Vanhatalo et al., 2002, 2003a,b,c; Voipio et al., 2003) confirmed the principal findings published in the 1950s and 1960s that electrical events in the frequency band lower than 1 Hz are real and have some important functional meaning in the interpretation of brain functions.

Ikeda et al. (Ikeda et al., 1996, 1999) have studied DC shift potentials recorded with subdural electrodes in patients with neocortical epilepsy. Ictal DC shifts were observed in 85% of all the recorded seizures. This DC shift usually was

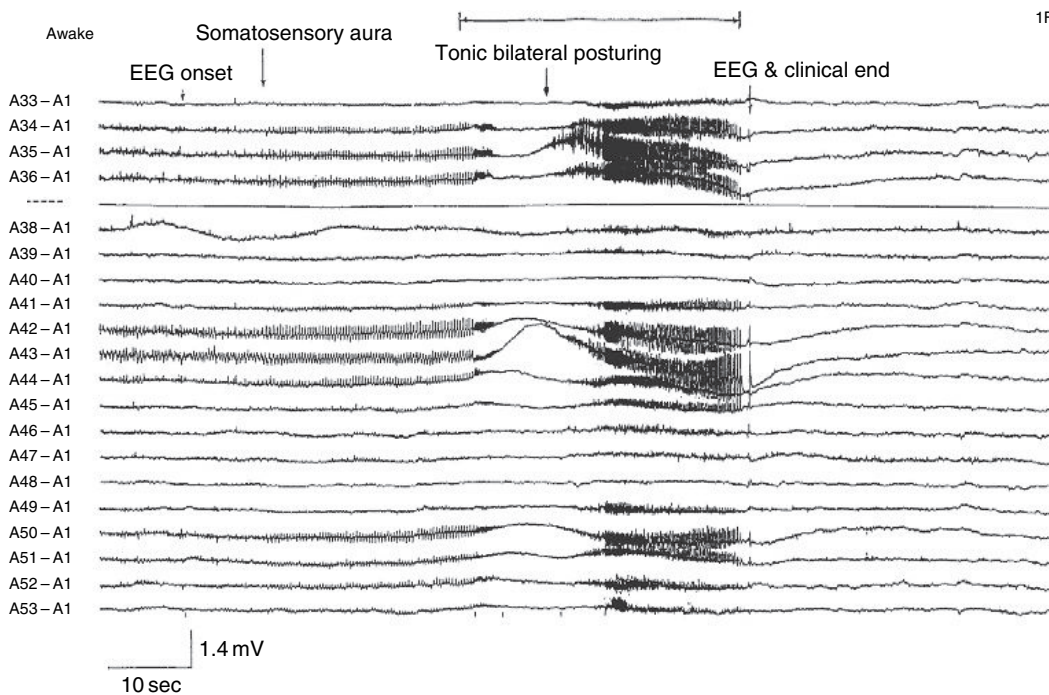


**FIGURE 27.4** A two-minute segment of a seizure outlined by a black horizontal bar at the top, with DC shift that slowly increases as the seizure progresses. (Modified with permission from Ikeda et al., 1996.)

accompanied by a suppression of amplitude of other EEG patterns (Figure 27.4). This suppression of EEG amplitude had a wide distribution, while the DC shift pattern was localized to just one or two electrodes, at which the conventional initial ictal EEG change was also observed. Surgical outcome after resection of the cortex, including the area showing the DC shift, resulted in seizure control. Therefore, the authors concluded that the ictal DC shift reflects the activity of the true ‘epileptogenic’ area, which conforms earlier data received by Morrell’s laboratory (Morrell and Nelson, 1987). Similar DC shifts were observed in recordings from scalp (Ikeda et al., 1997; Vanhatalo et al., 2003c). They were, like the subdurally recorded ones, mainly surface-negative in polarity, closely related to the electrodecremental pattern during seizure onset and consistent in their location. Although scalp-recorded DC shifts were detected mainly when seizures were clinically intense, no slow shifts were observed during small seizures. It was concluded that subdurally recorded ictal slow shifts could be clinically useful to help delineate an epileptogenic area for surgical resection.

Vanhatalo and his coauthors (Vanhatalo et al., 2002, 2003b; Voipio et al., 2003) reproduced these findings in patients with temporal lobe epilepsy. They showed that the majority of seizures were associated with negative DC shifts with amplitude 30–150 µV relative to vertex, beginning at the electrical seizure onset and lasting for the whole seizure. In all cases, the side of the DC shift was more clearly lateralized than the conventional scalp EEG.

#### SLOW WAVES AT SEIZURE TERMINATION

Seizures recorded with conventional clinical electrodes and amplifiers are often followed by depressed electrical activity, termed ‘post-ictal silence’ (Engel, 1989). A silent period was observed also at the termination of electrically induced afterdischarge (Leung, 1987; Bragin et al., 1997a). While recording with AC amplifiers, this silent period was accompanied by seizure termination slow waves (STSWs). The duration of the silent period varied between 4 and 60 seconds, while duration of slow waves recorded with AC-coupled amplifiers lasted for 1–4 seconds. The termination of spontaneous seizures or afterdischarges can occur simultaneously in many brain areas or separately in different areas. Several studies have specifically addressed the issue of the termination period in acute seizures, indicating that it is associated with spreading depression (SD) (Liberson and Cadilhac, 1953; Penfield and Jasper, 1954; Sypert and Ward, 1971; Heinemann et al., 1977; Haglund and Schwartzkroin, 1984; Somjen and Giacchino, 1985; Leung, 1987). SD and STSWs usually began

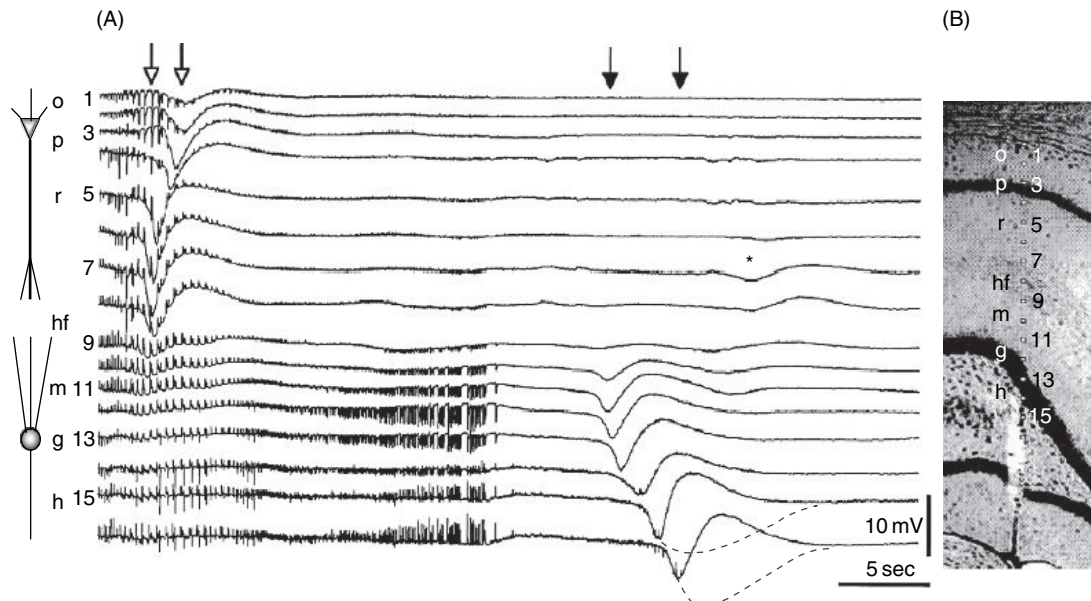


**FIGURE 27.5** (A) Seizure termination slow wave (STSW) in a rat associated with afterdischarge recorded by a 16-channel silicone probe with 100  $\mu\text{m}$  distance between recording sites. The early part of the afterdischarge is omitted to provide a better time resolution. Arrows above trace indicate the onset of large DC shifts recorded by AC-coupled amplifiers. The high frequency oscillation associated with the DC shift is not visible at this magnification and low sampling rate (200 Hz). The propagation speed of the DC front was 0.28 mm/s in the CA1 region (open arrows) and 0.12 mm/s in the dentate gyrus (filled arrows). Asterisk indicates a second wave of DC shift in the absence of neuronal activity. Dashed lines illustrate the real shape of the STSWs if it had been recorded by the DC amplifier. (B) Nissl stained brain section with silicon probe track *in situ* at its final recording position as seen during vibratome sectioning. Recording sites during the afterdischarge shown in (A) are marked by 1 to 16. *o*, CA1 stratum oriens; *p*, CA1 pyramidal layer; *r*, stratum radiatum; *hf*, hippocampal fissure; *m*, molecular layer; *g*, granule cell layer; *h*, hilus (Modified with permission from Bragin et al. 1997.)

earlier and were always of larger amplitude and longer duration in the layer of apical dendrites than in the pyramidal layer (Wadman et al., 1992; Herreras and Somjen, 1993; Bragin et al., 1997a). This is illustrated in Figure 27.5 in recordings with a multiple recording site silicon probe-oriented along the soma-dendritic axis. STSWs at the end of afterdischarge in the CA1 region occurred first at the level of the distal dendrites, i.e. around the hippocampal fissure (Figure 27.5, open arrows, electrode 8). The front of the STSW (i.e. the negative peak of the AC-coupled slow wave) moved toward the CA1 pyramidal cell layer at a velocity of 0.1–0.2 mm/s, as calculated from the time difference between the negative peaks of the slow waves and the distance between the recording sites in this and other animals. The wave sometimes failed to propagate across the cell body layers or was delayed by 3–5 s before invading the pyramidal layer and stratum oriens. In some cases, the STSWs crossed the hippocampal fissure and moved toward the granule cell layer at the same propagation velocity as in the CA1 stratum radiatum.

In the dentate gyrus/CA3c area, STSWs similarly occurred in the dendritic layer (see Figure 27.5 electrodes 9–16), which may occur independently of STSWs generated in the CA1 area and move through the granule layer towards the hilus.

Simultaneous extra- and intracellular recordings showed that as the soma became more depolarized during afterdischarge development, action potentials emanated from the depolarizing peaks of the fast oscillatory waves. After a series of fast action potentials, the membrane potential suddenly depolarized to between 230 and 210 mV, signaling the end of the extracellular STSW (Figure 27.6), however, neurons remained depolarized and membrane potential returned to the baseline over the time frame of 1–2 minutes (Figure 27.6A, right section). The afterdischarge-induced STSWs and intracellular depolarization could be mimicked by extracellular injection of KCl into the CA1 stratum radiatum (Figure 27.6C).

In summary, the onset of the sustained potential changes in the extracellular milieu at the end of the seizure or afterdischarge corresponded to a large intracellular depolarization of pyramidal cells and a consequent block of their firing.

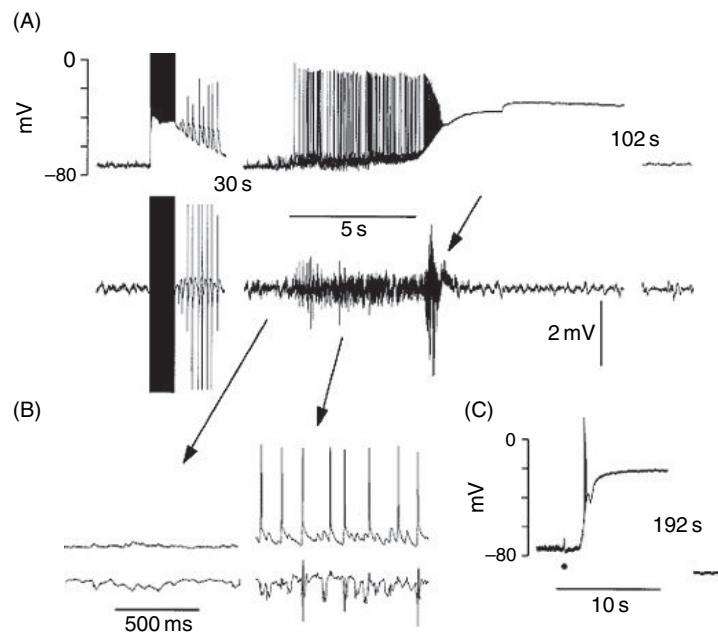


**FIGURE 27.6** Intracellular correlates of the seizure termination slow wave. (A) Afterdischarge induced by commissural stimulation in the urethane anesthetized rat recorded intracellularly (top trace) and field activity (bottom trace) recorded 0.5 mm posterior to the micropipette. Thirty seconds are omitted between traces (30 s). Note fast spike burst and depolarization block of the cell associated with extracellular STSW and the onset of the extracellular DC potential shift (arrow above field trace). Extracellular trace was wide-band-filtered (1 Hz to 5 kHz). Resting membrane potential was restored after 102 s (last trace segment). (B) Details of records in (A) (arrows) at faster speed. Note fast depolarizing potentials and action potentials during STSW. (C) Depolarization block could be mimicked by extracellular injection of KCl. Recovery occurred after 192 s. In other experiments, KCl induced fast field oscillations (STSW) and a 5–30 mV negative DC shift in the pyramidal cell layer (not shown). (Modified with permission from Bragin et al. 1997.)

#### POTENTIAL MECHANISMS OF SEIZURE ASSOCIATED SLOW WAVES

It is not clear at this moment whether slow waves that occur only at the seizure onset and those that gradually appear during seizure development or at seizure termination are generated by the same or different mechanisms. To the best of our knowledge there are no publications that have studied mechanisms of generation of these waves in the same experimental environment. The majority of existing publications are dedicated to the analysis of mechanism of DC shift during development of acutely evoked seizures and seizure termination. There are few data about ISW.

#### MECHANISMS GENERATING ISWs

One hypothesis explaining the occurrence of ISWs is that they reflect paroxysmal depolarization shifts (PDS) within recorded populations of neurons as a result of the synchrony of their discharges. PDS has been suggested to be a hallmark for epileptic activity in partial-onset seizures. This phenomenon initially was described during development of seizures induced by penicillin application (Matsumoto and Ajmone Marsan, 1964; Prince, 1968). PDS in these experiments were gigantic postsynaptic potentials (Johnston and Brown, 1981), followed by prolonged after hyperpolarization. In extracellular recordings, a correlate of the intracellular paroxysmal depolarization shift is a negative sharp wave (Matsumoto and Ajmone Marsan, 1964; Prince, 1968; Swann et al., 1993).

Two different types of ISWs associated with LVF ictal onset were distinguished on the basis of voltage depth profile analysis. The ISWs1 is local and generated within deep brain areas (amygdala, hippocampus, entorhinal cortex). This type of ISW contains EEG spikes on the ascending part. Accepting the point of view that interictal spikes reflect PDS (Ayala et al., 1973; de Curtis and Avanzini, 2001), we can assume that the spike component of ISWs1 could be PDSs. The descending part of ISWs1 could be a prolonged feedback inhibition, which is generated by intrinsic  $\text{Ca}^{2+}$ -gated  $\text{K}^+$  as well as  $\text{Cl}^-$  ( $\text{GABA}_A$ ) and  $\text{K}^+$  ( $\text{GABA}_B$ ) currents (see de Curtis and Avanzini, 2001 for review). One suggested reason

for the long inhibition is that the synchrony of the neuronal discharges during this particular event is unusually strong and causes stronger feedback discharges and triggers seizure activity.

In many cases, the amplitude of the EEG spike at the seizure onset is smaller than that of many previous IIS that did not trigger seizure activity (Bragin et al., 1997b, 2005b). However, the amplitude of the EEG signals does not always reflect the synchrony of neuronal discharges. It may be that the neurons have strong connections with remote areas so that synchrony of their discharges will not be detected by a given EEG electrode due to a rapid decay of the signal. We previously suggested and provided evidence for the existence of clusters of pathologically interconnected neurons (PIN clusters) within epileptic brain areas, which are characterized by strong local interneuronal connections (Bragin et al., 2000, 2004). The size of these clusters is on the order of several cubic millimeters and they generate bursts of population spikes as a result of hypersynchronous discharges of the principal cells. PIN clusters are diffusely distributed within the epileptic brain, forming a network of PIN clusters with strong connections. Due to the short duration of population spikes (5–20 ms) and the small size of the area generating synchronous discharges, the signal may have fast spatial decay of amplitude and the synchrony of PIN cluster discharges may not generate high amplitude field potential recorded by the EEG electrode. However, they could activate an interneuronal network forming strong feedback inhibition. The widely distributed interneuronal network would then generate a massive suppression of the activity of large populations of neurons. This massive feedback inhibition would be reflected by the occurrence of slow waves, which have long decay (200–500 ms) and are visible on recordings with conventional clinical electrodes. The activity of large populations of principal cells is suppressed during this inhibition. The seizure would then occur as a result of the rebound from this inhibition (Figure 27.7).

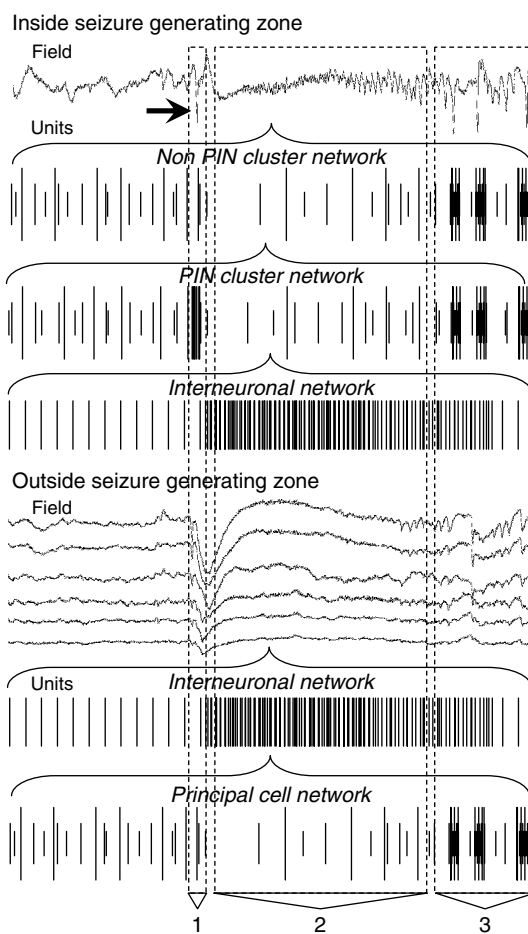


**FIGURE 27.7** A schematic illustrating possible mechanisms of seizure occurrence as a result of synchronous discharges of pathologically interconnected neuron clusters (PIN clusters). Lines with different amplitude indicate different neurons. Seizure starts with synchronous discharges of PIN cluster network, which is reflected by occurrence of interictal spike (1) (arrow). It is followed by an increased frequency of discharges of the interneuronal network inside and outside seizure generating zone with a parallel suppression of discharges of the principal cell network (2). EEG population spikes occur later as a result of rebound of principal cell network (3).

The occurrence of seizures as a result of release from strong inhibition has also been proposed by several other authors (Jones and Westbrook, 1997; Mody, 1998, 2005; Coulter, 1999; Andre et al., 2001; Dudek et al., 2002; Timofeev et al., 2002; Wendling et al., 2002; Freund, 2003).

The ISWs<sub>2</sub> has different voltage depth profiles than the ISWs<sub>1</sub>, with maximum amplitude within white matter or in neocortical areas. The absence of interictal spikes at the ISWs<sub>2</sub> onset and the difference in voltage depth profiles of ISWs<sub>2</sub> and the ISWs<sub>1</sub> indicate that these waves have different mechanisms of generation. It is not likely that the mechanism of generation of ISWs<sub>2</sub> is similar to the DC shift described during seizure development (Goldring, 1963; Ikeda et al., 1996, 1997; Vanhatalo et al., 2003c, 2005; Voipio et al., 2003) because this DC shift has negative polarity at the surface of the neocortex, while ISWs<sub>2</sub> has positive polarity. The duration of the DC shift varied from several seconds to several tens of seconds, while the mean duration of ISWs is around 2–3 s. According to existing data (Ikeda et al., 1996, 1999; Vanhatalo et al., 2003b), the DC shift is localized to certain brain areas (probably epileptogenic zones), while ISWs<sub>2</sub>s are generalized. The DC shift is associated with an increase in concentration of extracellular potassium. In order to evoke ictal activity, the extracellular concentration of potassium should increase 3–5 times: from 3 mM in normal CSF to 12–15 mM (see Somjen et al., 1985; Jefferys, 1995 for review). So far, there are no data indicating that potassium is accumulating in the extracellular space before a seizure onset, but it has been clearly shown that the concentration of extracellular potassium is increased during the seizure period.

The generalized ISWs<sub>2</sub> at seizure onset could indicate that the seizure began in an area distant from the recording sites and involved them simultaneously in the seizure activity. These could be thalamic or brainstem areas of the brain that have diffuse synaptic connections with the neocortex. However, the absence of phase reversal in the neocortex does support this suggestion.

Another suggestion is that seizures with ISWs<sub>2</sub> initial onset occur as a result of glutamate release from glial cells such as astrocytes. Some of the data presented here support this hypothesis, including the fact that the absence of phase reversal within neocortex and between neocortex and white matter indicates possible non-neuronal mechanisms of the generation of ISWs<sub>2</sub>. It has been shown that astrocytes can release glutamate in the extracellular space with synchronized discharges in neighboring neurons (Tian et al., 2005). It is known that astrocytes form a functional syncytium (Konietzko and Muller, 1994; Hansson and Ronnback, 1995; Rash et al., 1997) and release of glutamate may cover a broad brain volume. Perhaps ISWs<sub>2</sub> are generated by a diffuse glial network due to impairment of buffering function and release of glutamate in the extracellular space (D'Ambrosio et al., 1999; Amzica et al., 2002; Borges et al., 2003; Eid et al., 2004; Huang et al., 2004; Zhou and Sutherland, 2004; Kang et al., 2005; Rogawski, 2005; Tian et al., 2005). However, it is not clear what mechanisms are capable of triggering the broad astrocytes network release of glutamate. One could be an extensive reaction of astrocytes to fluctuation of metabolic supplies like glucose or oxygen. Glutamate can be released in the extracellular space when one of these supplies is altered, for a number of reasons.

#### MECHANISMS OF DC SHIFT DURING SEIZURE DEVELOPMENT

The DC shift might be accompanied by changes of several processes in the extraneuronal space:

1. increased concentration of extracellular potassium (see Prince, 1968; Dichter et al., 1972; Somjen et al., 1985; Somjen and Giacchino, 1985; Lux et al., 1986; Heinemann, 1987)
2. changes in the pH of extracellular and intracellular space (Siesjo et al., 1985; Xiong and Stringer, 2000)
3. glial cell dysfunction (Spencer et al., 1999; Gouder et al., 2004; Kang et al., 2005)
4. changes in blood-brain barrier (BBB) functions (Iijima et al., 1992; Vanhatalo et al., 2003c; Voipio et al., 2003).

The importance of each component is unclear. Most likely all of them are parts of the common complex process leading to the occurrence and termination of DC shift as a result of massive neuronal discharges.

#### EXTRACELLULAR POTASSIUM AND DC SHIFT

The extensive neuronal discharges result in an increase in the concentration of potassium in the extracellular space. One set of experimental data illustrating that DC shift during seizure activity reflects an increase in concentration of extracellular potassium has been discussed in several reviews (Prince, 1968; Somjen et al., 1985; Lux et al., 1986).

### EXTRACELLULAR AND INTRACELLULAR pH AND DC SHIFT

Hypersynchronized neuronal activity is also associated with accumulation of intracellular H<sup>+</sup> (Xiong et al., 2000). An initial alkalization in extracellular space in some brain areas like CA1 of hippocampus was reported during seizure activity, followed by prolonged acidification (Siesjo et al., 1985; Chesler and Kaila, 1992; Xiong and Stringer, 2000). In the dentate gyrus, only late acidification occurs at the termination of seizures (Xiong and Stringer, 2000). This acidification was interpreted to reflect spreading depression and fast transcellular Na<sup>+</sup>/H<sup>+</sup> exchange. Following cessation of seizure discharge, intracellular pH rapidly increased to normal and subsequently to supranormal values. The extracellular pH normalized at a surprisingly slow rate, with some acidosis persisting even after 45 minutes (Siesjo et al., 1985). Regional and subcellular pH dynamics are governed by the respective localization of glial cells, ligand-gated ion channels and extracellular and intracellular carbonic anhydrase (Chesler and Kaila, 1992).

### ROLE OF GLIAL CELLS

An increase in concentration of extracellular potassium during the ictal event indicates that glial cells are not capable of removing it from the extracellular space due to the impairment of glial cell buffering function in the epileptic brain. Three mechanisms that could be involved in the occurrence of the DC shift are:

1. impairment of the K<sup>+</sup> pump, leading to accumulation of potassium in the extracellular space
2. impairment of glutamate utilization by glial cells, leading to accumulation of glutamate in the extracellular space
3. release of glutamate by glial cells in response to some damaging factors (Spencer et al., 1999).

Increased extracellular potassium (up to several millivolts) would depolarize glial cells, resulting in relatively large amplitude DC shifts (Prince et al., 1973; Ransom and Goldring, 1973; Speckmann and Elger, 1999).

### BLOOD-BRAIN BARRIER AND DC SHIFT

Occlusion of the left middle cerebral artery in rats with duration between 1.2 and 3.7 minutes is followed by suppression of EEG amplitude and the occurrence of multiple DC shifts (Iijima et al., 1992). The number of these shifts declined after MK-801 injection, produced to a decrease in the volume of ischemically injured tissue. Anoxic depolarization producing slow DC shift is closely associated with a massive intracellular calcium elevation possibly due to activation of NMDA (N-methyl-D-aspartate) receptors (Heinemann et al., 1977). Vanhatalo and co-authors studied whether similar changes may also contribute to the generation of ictal DC shifts in the epileptic brain (Vanhatalo et al., 2003c). They showed that hemodynamic changes in the human brain are associated with marked DC shifts that cannot be accounted for by intracortical neuronal or glial currents. DC shifts were also elicited by changes in artificial ventilation, causing end-tidal CO<sub>2</sub> variations within a 2–5% range. Hypercapnia was consistently associated with negative scalp DC shifts, whereas hypocapnia induced positive scalp DC shifts in all electrodes referenced to the naseon (Nita et al., 2004).

### MECHANISMS OF STSWs GENERATION

At a certain concentration of extracellular potassium (9–12 mM), a spreading depression occurs and slowly propagates from the point of origin. Several features of the sustained potentials, associated with the termination of seizures, were identical to those of spreading depression (Leao, 1972).

The sustained potential after the afterdischarge was invariably initiated in the dendritic layers, around the hippocampal fissure. The front of the wave traveled very slowly (0.1–0.2 mm/s) in all directions, regardless of the anatomical connections of neurons. The wave spread toward the CA1 pyramidal layer and granule cell layer, as well as into the longitudinal axis, with a similar speed. Pyramidal cells discharged at a high frequency and time-locked to the local extracellular STSWs (Bragin et al., 1997a).

In recordings with DC-coupled amplifiers, the seizure (after discharge) terminates when extracellular concentration of potassium and/or acidification in the extracellular space reaches the ceiling level, where generation of neuronal action potentials is blocked by hyperdepolarization. Most likely, STSWs reflect spreading depression, which occurs when the concentration of extracellular potassium is further increased. Other mechanisms of seizure termination have, however, been described. (Lowenstein et al., 1999; Wallace et al., 2003).

## CONCLUSION

The above described data indicate that there are several mechanisms of generation of slow waves. Possible mechanisms of seizure associated slow waves are illustrated in Figure 27.8. We hypothesize that ISWs most likely reflect prolonged IPSPs. These IPSPs occur as a result of two triggers. The first trigger is hypersynchronous discharges of PIN clusters reflected by the occurrence of all IISs, which is followed by prolonged IPSPs generated by feedback of inhibitory interneuronal network. The second trigger is the release of glutamate from glial cells due to impairment of their buffering functions. In this case, interneurons, which have a lower threshold for spike generation than pyramidal cells (Alonso and Klink, 1993; Fricker et al., 1999; McBain et al., 1999), increase their discharge frequency. This is reflected by the occurrence of beta and gamma activity on the descending part of SASWs. In both cases, seizures occur as a result of the rebound from the massive inhibition produced by the interneuronal network and appear as synchronization of principal neurons in the large brain networks responsible for their clinical manifestation.

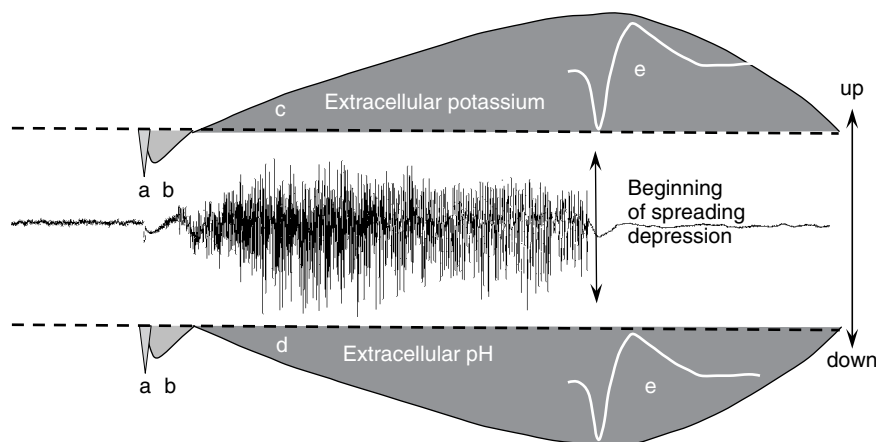


**FIGURE 27.8** The schematic of initiation, development and termination of seizure with indication of major components. (a) Interictal spike; (b) initial slow wave; DC shift is accompanied by an increase in concentration of extracellular potassium (c) decrease in extracellular pH (d) and (e) seizure termination slow wave.

The failure of glial cells to uptake extracellular potassium and glutamate during seizures leads to the accumulation of potassium in the extracellular space and acidification of the extracellular space (see Figure 27.8c,d). This process is reflected by the occurrence and increase in amplitude of the DC shift. When extracellular concentration of potassium reaches the level 12–15 mM, it blocks generation of action potentials and interrupts seizure activity. In AC recordings, it is reflected as the occurrence of slow wave at the seizure offset (Figure 27.8e) which is, in fact, a spreading depression wave generated initially in the dendritic layers and propagated from one area of the brain to another.

## REFERENCES

- Alonso, A. and Klink, R. (1993). Differential electroresponsiveness of stellate and pyramidal-like cells of medial entorhinal cortex layer II. *J Neurophysiol* 70:128–143.
- Amzica, F., Massimini, M. and Manfridi, A. (2002). Spatial buffering during slow and paroxysmal sleep oscillations in cortical networks of glial cells *in vivo*. *J Neurosci* 22:1042–1053.
- Andre, V., Marescaux, C., Nehlig, A. and Fritschy, J.M. (2001). Alterations of hippocampal GABAergic system contribute to development of spontaneous recurrent seizures in the rat lithium-pilocarpine model of temporal lobe epilepsy. *Hippocampus* 11:452–468.
- Ayala, G.F., Dichter, M., Gumnit, R.J., Matsumoto, H. and Spencer, W.A. (1973). Genesis of epileptic interictal spikes. New knowledge of cortical feedback systems suggests a neurophysiological explanation of brief paroxysms. *Brain Res* 52:1–17.
- Borges, K., Gearing, M., McDermott, D.L. et al. (2003). Neuronal and glial pathological changes during epileptogenesis in the mouse pilocarpine model. *Exp Neurol* 182:21–34.
- Bragin, A., Penttonen, M. and Buzsaki G (1997a). Termination of epileptic afterdischarge in the hippocampus. *J Neurosci* 17:2567–2579.

- Bragin, A., Wilson, C.L., Matherne, G.M. and Engel, J.J. (1997b). Generation of interictal spikes and spontaneous seizures in freely moving rats with chronic intrahippocampal KA-lesion. *Epilepsia* 38:205.
- Bragin, A., Wilson, C.L. and Engel, J. Jr (2000). Chronic epileptogenesis requires development of a network of pathologically interconnected neuron clusters: a hypothesis. *Epilepsia* 41:S144–152.
- Bragin, A., Wilson, C.L., Almajano, J., Mody, I. and Engel, J. Jr (2004). High-frequency oscillations after status epilepticus: epileptogenesis and seizure genesis. *Epilepsia* 45:1017–1023.
- Bragin, A., Wilson, C., Fields, T., Fried, I. and Engel, J.J. (2005a). Analysis of seizure onset on the basis of wideband EEG recordings. *Epilepsia* 46:59–63.
- Bragin, A., Azizyan, A., Almajano, J., Wilson, C.L. and Engel, J. (2005b). Analysis of chronic seizure onsets after intrahippocampal kainic acid injection in freely moving rats. *Epilepsia* 46:1592–1598.
- Chesler, M. and Kaila, K. (1992). Modulation of pH by neuronal activity. *Trends Neurosci* 15:396–402.
- Coulter, D.A. (1999). Chronic epileptogenic cellular alterations in the limbic system after status epilepticus. *Epilepsia* 40:S23–33.
- D'Ambrosio, R., Maris, D.O., Grady, M.S., Winn, H.R. and Janigro, D. (1999). Impaired K(+) homeostasis and altered electrophysiological properties of post-traumatic hippocampal glia. *J Neurosci* 19:8152–8162.
- de Curtis, M. and Avanzini, G. (2001). Interictal spikes in focal epileptogenesis. *Prog Neurobiol* 63:541–567.
- Dichter, M.A., Herman, C.J. and Selzer, M. (1972). Silent cells during interictal discharges and seizures in hippocampal penicillin foci. Evidence for the role of extracellular K<sup>+</sup> in the transition from the interictal state to seizures. *Brain Res* 48:173–183.
- Dudek, F.E., Hellier, J.L., Williams, P.A., Ferraro, D.J. and Staley, K.J. (2002). The course of cellular alterations associated with the development of spontaneous seizures after status epilepticus. *Prog Brain Res* 135:53–65.
- Eid, T., Thomas, M.J., Spencer, D.D. et al. (2004). Loss of glutamine synthetase in the human epileptogenic hippocampus: possible mechanism for raised extracellular glutamate in mesial temporal lobe epilepsy. *Lancet* 363:28–37.
- Engel, J. (2006) Report of the ILAE Classification Core Group doi:10.1111/j.1528–1167.2006.00215.x. *Epilepsia* 47:1558–1568.
- Engel, J.J. (1989). Seizures and epilepsy. F.A David, Philadelphia.
- Freund, T.F. (2003). Interneuron diversity series: rhythm and mood in perisomatic inhibition. *Trends Neurosci* 26:489–495.
- Fricker, D., Verheugen, J.A. and Miles, R. (1999). Cell-attached measurements of the firing threshold of rat hippocampal neurones. *J Physiol (Lond)* 517:791–804.
- Goldring, S. (1963). Negative steady potentials shifts which lead to seizure discharge. In: *Brain function*. UCLA forum med. sci. (M.A.B. Brazier, ed.) pp. 215–236. University of California Press, Los Angeles.
- Goldring, S. and O'Leary, J.L. (1951). Experimentally derived correlates between ECG and steady cortical potential. *J Neurophysiol* 14:275–288.
- Gouder, N., Scheurer, L., Fritschy, J.M. and Boison, D. (2004). Overexpression of adenosine kinase in epileptic hippocampus contributes to epileptogenesis. *J Neurosci* 24:692–701.
- Haglund, M.M. and Schwartzkroin, P.A. (1984). Seizure-like spreading depression in immature rabbit hippocampus in vitro. *Brain Res* 316:51–59.
- Hansson, E. and Ronnback, L. (1995). Astrocytes in glutamate neurotransmission. *Faseb J* 9:343–350.
- Heinemann, U. (1987). Changes in the neuronal micro-environment and epileptiform activity. In: *Current problems in epilepsy (3) The epileptic focus* (H.G. Wieser, E.J. Speckmann and J.J. Engel, eds) pp. 27–44: John Libbey & Company Ltd.
- Heinemann, U., Lux, H.D. and Gutnick, M.J. (1977). Extracellular free calcium and potassium during paroxysmal activity in the cerebral cortex of the cat. *Exp Brain Res* 27:237–243.
- Herreras, O. and Somjen, G.G. (1993). Propagation of spreading depression among dendrites and somata of the same cell population. *Brain Res* 610:276–282.
- Huang, Y.H., Sinha, S.R., Tanaka, K., Rothstein, J.D. and Bergles, D.E. (2004). Astrocyte glutamate transporters regulate metabotropic glutamate receptor-mediated excitation of hippocampal interneurons. *J Neurosci* 24:4551–4559.
- Hughes, J., Fino, J.J. and Patel, K. (2005). A newly described ictal pattern: the initial ictal slow shift. *Clin EEG Neurosci* 36:161–170.
- Huguenard, J.R. (2000). Circuit mechanisms of spike-wave discharge: are there similar underpinnings for centrot temporal spikes? *Epilepsia* 41:1076–1077.
- Iijima, T., Mies, G. and Hossmann, K.A. (1992). Repeated negative DC deflections in rat cortex following middle cerebral artery occlusion are abolished by MK-801: effect on volume of ischemic injury. *J Cereb Blood Flow Metab* 12:727–733.
- Ikeda, A., Terada, K., Mikuni, N. et al. (1996). Subdural recording of ictal DC shifts in neocortical seizures in humans. *Epilepsia* 37:662–674.
- Ikeda, A., Yazawa, S., Kunieda, T. et al. (1997). Scalp-recorded, ictal focal DC shift in a patient with tonic seizure. *Epilepsia* 38:1350–1354.
- Ikeda, A., Taki, W., Kunieda, T. et al. (1999). Focal ictal direct current shifts in human epilepsy as studied by subdural and scalp recording. *Brain* 122 (Pt 5):827–838.
- Jefferys, J.G. (1995). Nonsynaptic modulation of neuronal activity in the brain: electric currents and extracellular ions. *Physiol Rev* 75:689–723.
- Johnston, D. and Brown, T.H. (1981). Giant synaptic potential hypothesis for epileptiform activity. *Science* 211:294–297.
- Jones, M.V. and Westbrook, G.L. (1997). Shaping of IPSCs by endogenous calcineurin activity. *J Neurosci* 17:7626–7633.
- Kang, N., Xu, J., Xu, Q., Nedergaard, M. and Kang, J. (2005). Astrocytic glutamate release-induced transient depolarization and epileptiform discharges in hippocampal CA1 pyramidal neurons. *J Neurophysiol* 94:4121–4130.
- King, D., Spencer, S.S., McCarthy, G. and Spencer, D.D. (1997). Surface and depth EEG findings in patients with hippocampal atrophy. *Neurology* 48:1363–1367.
- Kobayashi, K., Oka, M., Inoue, T., Ogino, T., Yoshinaga, H. and Ohtsuka, Y. (2005). Characteristics of slow waves on EEG associated with epileptic spasms. *Epilepsia* 46:1098–1105.
- Konietzko, U. and Muller, C.M. (1994). Astrocytic dye coupling in rat hippocampus: topography, developmental onset, and modulation by protein kinase C. *Hippocampus* 4:297–306.
- Leao, A. (1972). Spreading depression In: *Experimental models of epilepsy: a manual for the laboratory worker* (D. Purpura, J. Penry, D. Tower, D. Woodbury and R. Walter, eds) pp. 174–196. Raven, New York.
- Lee, S.A., Spencer, D.D. and Spencer, S.S. (2000). Intracranial EEG seizure-onset patterns in neocortical epilepsy. *Epilepsia* 41:297–307.
- Leung, L.W. (1987). Hippocampal electrical activity following local tetanization. I. Afterdischarges. *Brain Res* 419:173–187.

- Li ,C. and Salmiraghi, G. (1963). Cortical steady potential changes: Extracellular microelectrode investigations. *Nature* 196:858–859.
- Liberson, W.T. and Cadilhac, J.G. (1953) Electroschock and rhinencephalic seizure states. *Confin Neurol* 13:278–286.
- Lowenstein, D.H., Bleck, T. and Macdonald, R.L. (1999). It's time to revise the definition of status epilepticus. *Epilepsia* 40:120–122.
- Lux, H.D., Heinemann, U. and Dietzel, I. (1986). Ionic changes and alterations in the size of the extracellular space during epileptic activity. *Adv Neurol* 44:619–639.
- Matsumoto, H. and Ajmone Marsan, C. (1964). Cortical interictal phenomena in experimental epilepsy: interictal manifestations. *Exp Neurol* 9:286–304.
- McBain, C.J., Freund, T.F. and Mody, I. (1999). Glutamatergic synapses onto hippocampal interneurons: precision timing without lasting plasticity. *Trends Neurosci* 22:228–235.
- McCormick, D.A. and Contreras, D. (2001). On the cellular and network bases of epileptic seizures. *Annu Rev Physiol* 63:815–846.
- Mody, I. (1998). Interneurons and the ghost of the sea. *Nat Neurosci* 1:434–436.
- Mody, I. (2005). Aspects of the homeostatic plasticity of GABA<sub>A</sub> receptor-mediated inhibition. *J Physiol* 562:37–46.
- Morrell, F. and Nelson, E. (1987). Epileptic foci: correlation between standing potential contour and histological abnormality. In: *Fundamental mechanisms of human brain* (J.J. Engel, ed.) pp. 187–199. Raven Press, New York.
- Nita, D.A., Vanhatalo, S., Lafortune, F.D., Voipio, J., Kaila, K. and Amzica, F. (2004). Nonneuronal origin of CO<sub>2</sub>-related DC EEG shifts: an in vivo study in the cat. *J Neurophysiol* 92:1011–1022.
- O'Leary, J.L. and Goldring, S. (1959/60). Slow cortical potentials. Their origin and contribution to seizure discharge. *Epilepsia* 1:561–574.
- O'Leary, J. and Goldring, S. (1964). D-C potentials of the brain. *Physiol Rev* 44:91–125.
- Penfield, W. and Jasper, H. (1954). *Epilepsy and the functional anatomy of the human brain*. Little, Brown and Company, Boston.
- Prince, D., Lux, H. and Neher, E. (1973). Measurement of extracellular potassium activity in cat cortex. *Brain Res* 50:489–495.
- Prince, D.A. (1968). The depolarization shift in 'epileptic' neurons. *Exp Neurol* 21:467–485.
- Prince, D.A., Connors, B.W. and Benardo, L.S. (1983). Mechanisms underlying interictal-ictal transitions. *Adv Neurol* 34:177–187.
- Ransom, B.R. and Goldring, S. (1973). Ionic determinants of membrane potential of cells presumed to be glia in cerebral cortex of cat. *J Neurophysiol* 36:855–868.
- Rash, J.E., Duffy, H.S., Dudek, F.E., Bilhartz, B.L., Whalen, L.R. and Yasumura, T (1997). Grid-mapped freeze-fracture analysis of gap junctions in gray and white matter of adult rat central nervous system, with evidence for a 'panglial syncytium' that is not coupled to neurons. *J Comp Neurol* 388:265–292.
- Rogawski, M.A. (2005). Astrocytes get in the act in epilepsy. *Nat Med* 11:919–920.
- Siesjo, B.K., von Hanwehr, R., Nergelius, G., Nevander, G. and Ingvar, M. (1985). Extra- and intracellular pH in the brain during seizures and in the recovery period following the arrest of seizure activity. *J Cereb Blood Flow Metab* 5:47–57.
- Somjen, G.G. and Giacchino, J.L. (1985). Potassium and calcium concentrations in interstitial fluid of hippocampal formation during paroxysmal responses. *J Neurophysiol* 53:1098–1108.
- Somjen, G.G., Aitken, P.G., Giacchino, J.L. and McNamara, J.O. (1985). Sustained potential shifts and paroxysmal discharges in hippocampal formation. *J Neurophysiol* 53:1079–1097.
- Speckmann, E. and Elger, C. (1999). Introduction of the neurophysiological basis of the EEG and DC potentials. In: *Electroencephalography: basic principles, clinical applications, and related fields* (E. Niedermeyer and F. Lopes da Silva, eds) pp. 15–27. Williams & Wilkins, Baltimore.
- Spencer, S.S., Guimaraes, P., Katz, A., Kim, J. and Spencer, D. (1992). Morphological patterns of seizures recorded intracranially. *Epilepsia* 33:537–545.
- Spencer, S.S., Kim, J., deLanterolle, N. and Spencer, D.D. (1999). Differential neuronal and glial relations with parameters of ictal discharge in mesial temporal lobe epilepsy. *Epilepsia* 40:708–712.
- Steriade, M. and Amzica, F. (2003). Sleep oscillations developing into seizures in corticothalamic systems. *Epilepsia* 44 Suppl 12:9–20.
- Swann, J.W., Smith, K.L. and Brady, R.J. (1993). Localized excitatory synaptic interactions mediate the sustained depolarization of electrographic seizures in developing hippocampus. *J Neurosci* 13:4680–4689.
- Sypert, G.W. and Ward, A.A. Jr (1971). Unidentified neuroglia potentials during propagated seizures in neocortex. *Exp Neurol* 33:239–255.
- Tian, G.F., Azmi, H., Takano, T. et al. (2005). An astrocytic basis of epilepsy. *Nat Med* 11:973–981.
- Timofeev, I. and Steriade, M. (2004). Neocortical seizures: initiation, development and cessation. *Neuroscience* 123:299–336.
- Timofeev, I., Grenier, F. and Steriade, M. (2002). The role of chloride-dependent inhibition and the activity of fast-spiking neurons during cortical spike-wave electrographic seizures. *Neuroscience* 114:1115–1132.
- Townsend, J.B. III and Engel, J. Jr (1991). Clinicopathological correlations of low voltage fast and high amplitude spike and wave mesial temporal stereoencephalographic ictal onsets. *Epilepsia* 32, Suppl. 3:21.
- Vanhatalo, S., Tallgren, P., Andersson, S., Sainio, K., Voipio, J. and Kaila, K. (2002). DC-EEG discloses prominent, very slow activity patterns during sleep in preterm infants. *Clin Neurophysiol* 113:1822–1825.
- Vanhatalo, S., Voipio, J., Dewaraja, A., Holmes, M.D. and Miller, J.W. (2003a). Topography and elimination of slow EEG responses related to tongue movements. *Neuroimage* 20:1419–1423.
- Vanhatalo, S., Holmes, M.D., Tallgren, P., Voipio, J., Kaila, K. and Miller, J.W. (2003b). Very slow EEG responses lateralize temporal lobe seizures: an evaluation of non-invasive DC-EEG. *Neurology* 60:1098–1104.
- Vanhatalo, S., Tallgren, P., Becker, C. et al. (2003c). Scalp-recorded slow EEG responses generated in response to hemodynamic changes in the human brain. *Clin Neurophysiol* 114:1744–1754.
- Vanhatalo, S., Voipio, J. and Kaila, K. (2005). Full-band EEG (FbEEG): an emerging standard in electroencephalography. *Clin Neurophysiol* 116:1–8.
- Velasco, A.L., Wilson, C.L., Babb, T.L. and Engel, J. Jr (2000). Functional and anatomic correlates of two frequently observed temporal lobe seizure-onset patterns. *Neural Plast* 7:49–63.
- Voipio, J., Tallgren, P., Heinonen, E., Vanhatalo, S. and Kaila, K. (2003). Millivolt-scale DC shifts in the human scalp EEG: evidence for a nonneuronal generator. *J Neurophysiol* 89:2208–2214.
- Wadman, W.J., Juta, A.J., Kamphuis, W. and Somjen, G.G. (1992). Current source density of sustained potential shifts associated with electrographic seizures and with spreading depression in rat hippocampus. *Brain Res* 570:85–91.

- Wallace, M.J., Blair, R.E., Falenski, K.W., Martin, B.R. and DeLorenzo, R.J. (2003). The endogenous cannabinoid system regulates seizure frequency and duration in a model of temporal lobe epilepsy. *J Pharmacol Exp Ther* 307:129–137.
- Wendling, F., Bartolomei, F., Bellanger, J.J. and Chauvel, P. (2002). Epileptic fast activity can be explained by a model of impaired GABAergic dendritic inhibition. *Eur J Neurosci* 15:1499–1508.
- Xiong, Z.-Q. and Stringer, J.L. (2000). Extracellular pH responses in CA1 and the dentate gyrus during electrical stimulation, seizure discharges, and spreading depression. *J Neurophysiol* 83:3519–3524.
- Xiong, Z.-Q., Saggau, P. and Stringer, J.L. (2000). Activity-dependent intracellular acidification correlates with the duration of seizure activity. *J Neurosci* 20:1290–1296.
- Zhou, J. and Sutherland, M.L. (2004). Glutamate transporter cluster formation in astrocytic processes regulates glutamate uptake activity. *J Neurosci* 24:6301–6306.

This page intentionally left blank

PART

VII

---

SEIZURE DYNAMICS

---

This page intentionally left blank

# 28

## DYNAMICS OF EPILEPTIC SEIZURES DURING EVOLUTION AND PROPAGATION

CHRISTOPHE C. JOUNY AND GREGORY K. BERGEY

### ABSTRACT

Epileptic seizures are rapidly evolving dynamic events which typically last less than two minutes. The need to understand better the dynamics of these transient events is important in part because of increased interest in responsive neurostimulation as potential therapy for epileptic seizures. The matching pursuit (MP) decomposition and Gabor atom density (GAD) are modern techniques which allow detailed time-frequency decomposition (MP) and quantification of complexity changes (GAD). This allows investigations of seizure onset, evolution and propagation of rapidly changing epileptic phenomena with a new perspective and a new level of precision. Using these methods has revealed increased complexity at the onset of many seizures and remarkable similarity of ictal onset patterns from multiple seizures from a single focus in a given patient. These methods can potentially provide insights into network mechanisms contributing to seizure generation and propagation. In this chapter, we illustrate the application of these techniques to partial seizures recorded from intracranial arrays in humans undergoing presurgical evaluations and demonstrate the possibility to identify specific ictal phases. Understanding these specific ictal dynamics can provide information that may assist seizure detection and understanding of the dynamics that contribute to propagation and seizure termination.

### INTRODUCTION

Epileptic seizures are transient phenomena, something that has been recognized since the time of Hughlings Jackson and before. Initially, observations focused on the clinical manifestations of partial and generalized tonic-clonic seizures. With the advent of the electroencephalogram (EEG) in 1929, one could study the interictal and ictal patterns suggestive of or characteristic of certain seizure types. Since routine EEGs only record ictal events in a small minority of patients, studies deal more with interictal patterns. With the growth of surgical therapy for intractable epilepsy, ictal recordings in epilepsy monitoring units became the gold standard for diagnosis and these events are now routinely available for study. Patients requiring intracranial monitoring with subdural strips or grids or depth electrode arrays, provide clear, usually artifact-free recordings of ictal events. However, presurgical evaluations, whether scalp or intracranial, appropriately have focused on localization of the seizure onset zone and correlations of these changes with any imaging abnormalities. There has been interest in studying whether certain ictal patterns are suggestive of specific regions of seizure onset (e.g. frontal neocortical versus mesial temporal) because this can assist in the detection and localization of the seizure onset for possible later surgery. In contrast, the dynamics and patterns of evolution of seizures remain relatively neglected because seizure evolution and propagation are not that important in the presurgical evaluations.

Understanding the dynamic evolution of epileptic seizures can provide insights into why seizures are indeed self-limited events, typically lasting less than 3 minutes in duration. While the rapid evolution and non-stationarity of the signal present challenges for analysis, tools exist which permit detailed decomposition of the ictal signal. Patients undergoing presurgical evaluations, particularly those requiring intracranial electrodes provide excellent data for these studies. The following discussion will address some of these studies and the dynamic ictal patterns observed. While it is recognized that such initial analyses are descriptive, such studies serve to determine the best methods for such analyses. In addition, this information can enhance studies of neural network modeling. Understanding why epileptic seizures stop after a brief

period can potentially provide insights into not only network behavior, but also can contribute to new responsive therapies developed to produce early seizure termination (Bergey et al., 2006).

The results presented here will be restricted to intracranial recordings (which facilitate accurate analysis) of partial seizures with or without secondary generalization. Primary generalized seizures represent an entirely different seizure dynamic reflecting different mechanisms of seizure generation and propagation and will not be discussed. Also, primary generalized seizures are not amenable to resective surgery so intracranial studies are not done in these patients.

## METHODS FOR ANALYSIS OF THE EEG

### FREQUENCY ANALYSIS

Analysis of EEG signals has been a very active arena for the testing and application of new methods of signal analysis. Such interest comes from the desire to understand better patterns of normal and abnormal brain activity. Initially, computational ability limited the analyses to either non-automated or computationally efficient methods. However, many of those methods have survived the modern era of computer analysis and have been used in even the most advanced devices due to their modest requirements for processing power and the already existing data from a large variety of clinical situations. Analyzing a background EEG signal presents many fewer challenges than does analysis of an epileptic seizure. Although all EEGs are typically composed of a number of component frequencies, many of these records have prolonged periods of relative stationarity. In contrast, the ictal EEG is a rapidly changing dynamical signal that poses a number of analytic challenges that make certain methods (e.g. linear or averaging) less than ideal.

The introduction of the Fast-Fourier transform (FFT) algorithm of Cooley and Tukey (Cooley and Tukey, 1965) represented a major advance in the ability to analyze EEG signals and methods based on FFT are still perhaps the most widely used. For the first time, the EEG signals could be decomposed into component frequencies and changes specific to selected frequency bands could be detected. Although visual characterization of EEG frequencies has been part of routine EEG interpretation since inception, FFT made this analysis objective, quantifiable and accessible. FFT is most appropriately applied to relatively stationary signals such as those during general anesthesia or during ICU recordings of background activity (e.g. slow activity). While short time FFT can be applied to ictal events, the method itself is not suited for detailed time analysis.

The EEG during sleep, including the various sleep stages is one that represents evolution of activity, albeit much more gradual and prolonged than that seen during seizures. EEG activity during sleep has been analyzed extensively and frequency bands from 0 to 40 Hz have been correlated with phases of sleep and sleep-related events. Each band of EEG frequencies has been analyzed and correlated with both visual analysis and with sleep stages. Furthermore, cortical and thalamocortical circuits involved in the generation of those frequencies have been investigated to determine if EEG signal frequency can be equated with specific cerebral activity and the location of such activity.

With increased and more readily available computational power, less computationally efficient methods of signal analysis have been applied. Numerous methods based on autoregressive modeling have provided considerable data from ictal EEGs (Franaszczuk et al., 1985; Gath et al., 1992; Franaszczuk and Bergey, 1999). Even more recently, methods based on non-linear dynamics (e.g. chaos) have been applied to the EEG (Stam, 2005). While the original hypothesis of finding a chaotic state in the brain failed, it has been replaced more recently with more realistic goals of detecting and characterizing the associated non-linear dynamics.

Current intracranial EEG (ICEEG) recordings with higher routine sampling rates allow investigation of higher frequencies. Accurate recording of high frequency activity (e.g. >200 Hz) requires not only appropriate sampling, but also special electrodes designed for this activity. There is a growing number of investigations regarding whether or not this activity is an important component of seizure initiation and of the evolutionary dynamic with early studies in 1992 (Allen et al., 1992; Fisher et al., 1992) and more recent studies utilizing instrumentation that facilitates exploration of higher frequency (Traub et al., 2001; Jirsch et al., 2006). However, the definition of high frequency activity is still variable among groups and results are often limited by the number of patients studied.

Early attempts to provide extended information or analysis in the time-frequency domain were limited by the requirements for stationarity of most methods and the problem of interference of the signal components (cross-terms). Zaveri et al., in 1992, described the maturity of the time-frequency analysis applied to EEG signals of seizures and the possible use of specially designed analysis with limited interference (Zaveri et al., 1992). However, probably due to the mathematical complexity of those methods, they were not developed further than the experimental stages. The introduction of the matching pursuit method provided a method that had no such requirements and was not affected by the cross-term problem.

### MATCHING PURSUIT AND GAD METHODS

Matching pursuit (MP) is an analysis based on the decomposition of a signal into simpler and smaller signal elements called atoms. The method was introduced by Mallat and Zhang in 1993 (Mallat and Zhang, 1993). Although various atoms can be used, the most common ones are based on the Gabor function, which is a Gaussian modulated oscillation. The MP method can be applied to any signal and has no requirements for stationarity of the signal. The MP pursuit algorithm is a significant improvement in time-frequency analysis combining some of the advantage of short-windowed Fourier transform and wavelet analysis. Basic windowed Fourier transform describes the signal in terms of atoms localized in frequency. Wavelet analysis offers decomposition in time and scale where frequency is only derived from the scale. The MP method can offer a more rich decomposition using time, frequency and scale parameters. To do so, MP uses a non-orthogonal dictionary of functions, without constraints on the scale and frequency parameters. We have utilized the MP method to explore the structure of EEG signals during epileptic seizures. The use of a largely redundant dictionary gives extended flexibility and the ability to provide a more detailed decomposition of the signal patterns in the time-frequency domain, something not available with most other methods.

Figure 28.1 shows an example of the various elements produced by the matching pursuit decomposition for an artificial signal that contains both fast transients and rhythmic activity. The signal consists of eight components of various durations but all of the same energy. They are ordered by octave from left to right. Octave is a parameter defining the repartition of the atom energy in the time-frequency domain. Low octave represents fast transient (spike-like) activity which is very short in time but has a large spectrum. High octave represents more sustained activity (e.g. spindle-like) (Figure 28.1 – octave 8) or even continuous activity represented by a Fourier function (Figure 28.1 – octave 12) which is a continuous event but constant or near constant in frequency. Gabor functions seem naturally suited for representation of EEG activities

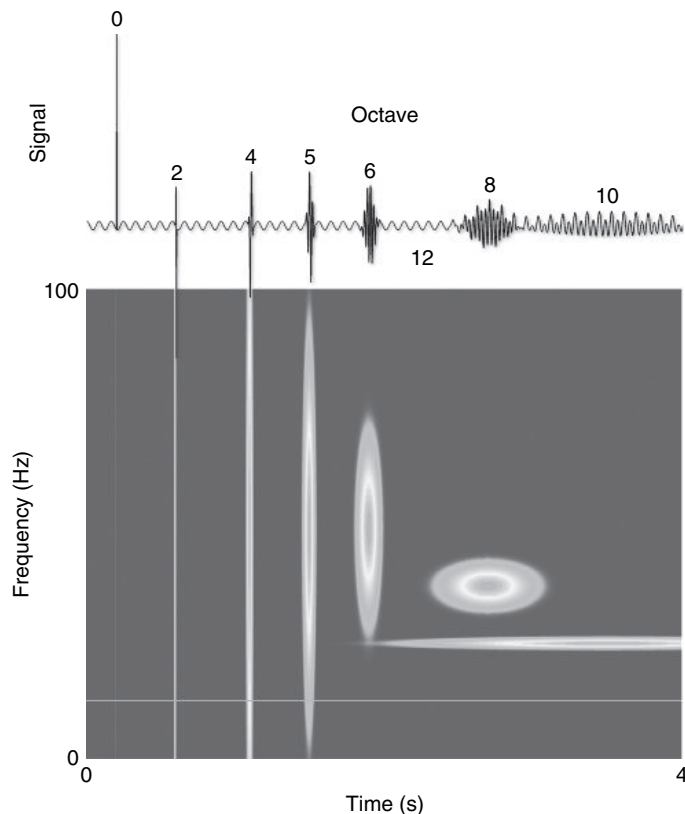


**FIGURE 28.1** Illustration of principle of matching pursuit decomposition. Shown on top is an artificial signal generated with 8 atoms (Gaussian modulated sinusoidal functions) of the same energy. The number above the signal indicates the octave for the atom associated, except for octave 12 which is a Fourier function (not localized in time). The lower panel is the time-frequency representation of those 8 atoms. A sharp transient with a low octave is very short in time but spread over large frequency spectrum. More sustained activity with higher octave is spread over longer time but has a narrower frequency spectrum.

and the MP decomposition has been described as an excellent method for the parametrization of the EEG (Durka and Blinowska, 2001).

Although the MP method requires long computations and is a single channel method, current computer processing power is more than adequate to handle intracranial recordings which can include 120 or more channels. The reconstruction of the time-frequency energy distribution is possible due to the properties of the decomposition (conservation of energy). When applied to the signal of a single channel EEG, the MP is applied on successive windows and repeated for the whole seizure. Time-frequency is reconstructed from the atoms from all the windows. This allows some high degree of filtering to target some specific activities. Multichannel analyses can be done by sequential MP decompositions for the channels of interest. One of the most appealing aspects of MP is that it is not limited to the analysis of stationary signals and can be appropriately applied to rapidly changing signals and, as such, is particularly well suited to analysis of epileptic seizures which are rapidly changing, time-limited phenomena.

Gabor atom density (GAD) was developed as an index to measure the complexity of the signal based on the MP decomposition (Jouny et al., 2003). For each window of analysis, GAD is derived from the number of atoms needed to represent the signal. Increased complexity is often associated with epileptic activity and GAD is used to measure the change of dynamic for each signal as well as for assessing the global change of propagation of epileptic activity.

## SEIZURE DYNAMICS

### CORRELATION OF DYNAMIC

An epileptic seizure is an evolving, dynamic process. While this is recognized by those who study seizures, detailed investigation of seizure dynamics has been neglected since, as mentioned, the most important considerations clinically are the focus of seizure origin and the clinical manifestations. The seizure itself is typically classified as an event and relatively little attention is directed to issues of composite frequencies, propagation or patterns of termination. Correlation between analyses of the EEG information with different aspect of the seizure has been reported by Pacia and Ebersole (Pacia and Ebersole, 1997) and by Spencer et al. (Spencer et al., 1992), but these reports deal mostly with the earlier period of the seizures and the correlation between the pattern of onset and the localization of the focus.

EEG activity results from synchronous neuronal activity, much of it due to normal cerebral function. Measured at the macroscopic level of the ICEEG, this represents the averaged activity of thousands of neurons in the underlying networks. Epileptic seizures are due to abnormal, increased synchronous firing of neuronal networks. This is manifest in the ictal EEG by high amplitude synchronous activity producing quasi-rhythmic EEG waveforms. Ictal activity is often described using the traditional EEG terminology that incorporates standard frequency bands (delta, theta, alpha, beta and gamma). The advantage of this terminology is that it facilitates description of the predominant component visible in the EEG signals by the neurologist. Higher frequency content is often grouped into a gamma band denomination or other variations. Lately, these very high frequencies have been classified as ripples and fast-ripples (Staba et al., 2002).

### PHASES OF A SEIZURE

As mentioned previously, the intrinsic dynamics of epileptic seizures have been relatively neglected because of the emphasis (directed by clinical needs for seizure localization) on ictal onset patterns. Indeed, with increasing computational ability, recent efforts have been extended to early seizure detection and attempts at seizure prediction have gathered lots of interest (Lehnertz and Litt, 2005), but not so much on the intrinsic seizure dynamics.

Fisch (1996) proposed a possible separation of the phases in generalized tonic-clonic seizures, but based the distinction on clinical signs more than EEG activity. He distinguished four phases for generalized tonic-clonic seizure plus three more if the seizure evolved from a partial seizure to a secondary generalized seizure. The full evolution of a partial seizure with secondary generalization is comprised of seven phases: premonitory phase, simple partial phase, complex partial phase, onset of generalization, immediate pre-tonic-clonic phase, tonic-clonic phase, immediate post-ictal phase and the post-ictal recovery phase.

These clinical signs are often easily observed and are important in classification of seizure semiology. At times, with complex partial seizures that do not secondarily generalize, the transition from ictal to post-ictal may be difficult to determine accurately even with ictal scalp recordings. Some seizures (e.g. frontal lobe complex partial seizures) may have a paucity of ictal findings on scalp EEG. Other seizures (e.g. tonic or atonic seizures) may have broad regional changes

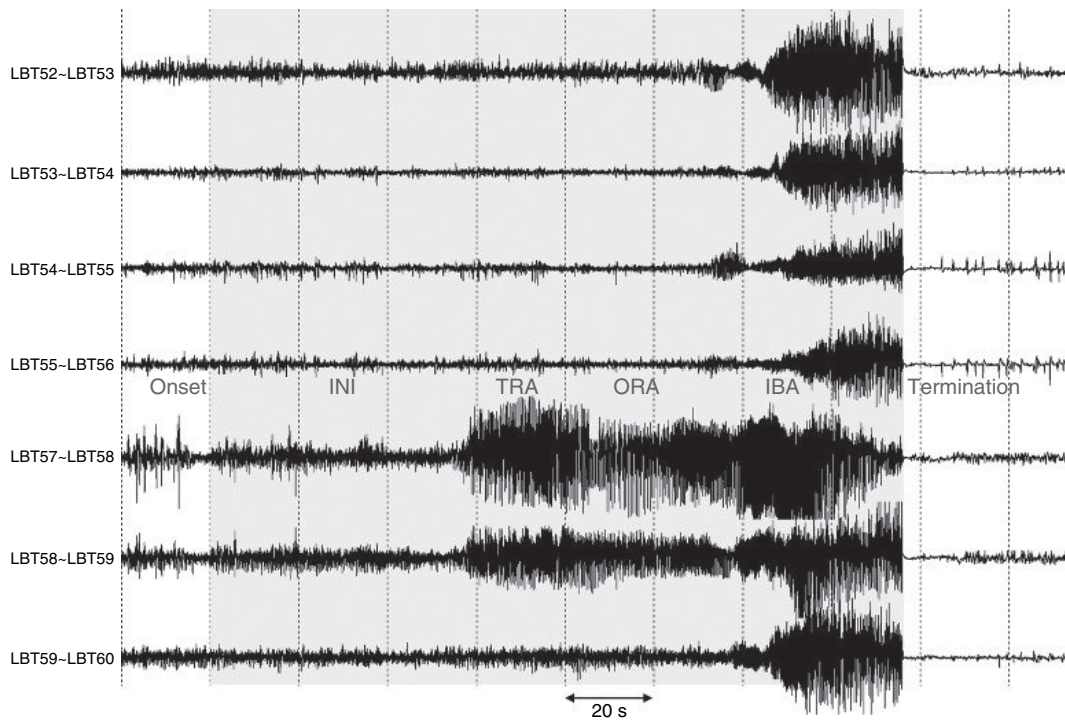


**FIGURE 28.2** Intracranial recordings of selective subdural grid contacts of a complex partial seizure from several electrodes close to the epileptic focus. LBT57-LBT58 is the electrode pair the closest to the focus. The different phases of the seizure are marked and detailed in Figure 28.3.

(electrodecremental) on scalp EEG that reveal little about the evolving seizure dynamics. At other times, in part depending upon the region of partial seizure onset, there may be dramatic EEG changes with few or only subtle clinical changes until further evolution (e.g. regional spread or secondary generalization) occurs.

Intracranial recordings with depth electrode arrays, subdural strips or subdural grids can provide the best assessment of ictal onset and evolution provided the regional of focal onset is sampled by the recording contacts. In our studies of complex partial seizures, we have been able to separate ictal evolution into several discrete periods. This separation is based on both the visual inspection of the intracranial ictal recordings, but also incorporates studies of spectral content and complexity. The original observations and MP analyses (Franaszczuk et al., 1998) were on mesial temporal onset complex partial seizures and, indeed, these seizures show the clearest evolution, but neocortical onset seizures share some similarities in their patterns of evolution. Figure 28.2 illustrates an example of a mesial temporal onset complex partial seizure with four phases lasting slightly over 150 seconds total duration.

Signals displayed here were recorded from electrodes which were over the left basal and mesial temporal regions (LBT). The two electrodes LBT57 and LBT58 were closest to the mesial temporal focus. The ICEEG shows the relatively slow evolution of epileptiform activity characteristic of mesial temporal lobe onset seizures. A more detailed view of the ICEEG for each phase is shown in Figure 28.3. This more clearly shows the patterns of rhythmic, quasi-rhythmic and periodic activity seen during seizure evolution.

#### INI: the initiation phase

The period of seizure initiation, even in mesial temporal onset seizures, can be the most variable in either pattern or duration. The initial appearance of the epileptiform activity over the focus and the initial evolution of activity at the focus occur during this phase. The pattern seen at onset can be influenced by location of seizure onset and the pathological substrate. Although there are diverse patterns of seizure onset, patterns of onset (like most seizure dynamics) tend to be very stereotyped for a given seizure focus in a given patient. This stereotyped nature facilitates tuning of seizure detection algorithms. Patterns that are commonly seen include low voltage fast activity (beta, gamma or higher), increased spiking (at times quasi-periodic) or rhythmic theta activity. Appreciating these onset patterns (and having appropriate sampling to detect them) is important for the clinician in identifying the seizure focus in presurgical evaluations. The emergence of changes in epileptiform activity from the background EEG, however, can be challenging at times, especially when the



**FIGURE 28.3** Different phases of a complex partial seizure. Each sample of intracranial EEG is 10 seconds long. Electrodes LBT57 and 58 were determined to be the closest to the focus. Five non-continuous periods are represented from top to bottom. INI: initiation phase of the seizure, dependent on the nature of the seizure and the localization. TRA: transition phase reflects the build up of the epileptic activity over the region of onset. ORA: the organized rhythmic activity phase is the central period of the seizure, exhibiting the most regular rhythmic pattern. IBA: the intermittent bursting activity marks the loss of coherency of the previous pattern and the epileptic activity is more and more interrupted by flat period of EEG. The termination is not a phase *per se* but more the delimitation of the end of epileptic activity.

region being sampled is highly epileptogenic even between seizures. Clinicians often use a reverse time approach consisting into going back in time from a period where the seizure is clearly occurring back to where this activity appeared or was at least significantly higher than the background level. This distinction clearly relies on the expertise of the reviewer. The INI phase can be a prolonged period or one lasting only a few seconds. GAD analysis (see below) can be helpful, particularly in those patients with active interictal activity, in that it can identify a complexity change at seizure onset that may not be apparent visually. Any claims of analyses that ‘predict’ seizures must first address whether the method is merely ‘detecting’ seizure onset earlier than is apparent from the initial visual EEG analysis (Jouny et al., 2005).

#### TRA: transition rhythmic activity

This phase is a transition from the period of initiation to the more organized rhythmic activity. Typically, this phase will be composed of mixed frequencies, including a build up of lower frequency activity and the signal is of higher complexity. There is some increase in amplitude of epileptiform activities and variable early local propagation.

### ORA: organized rhythmic activity

During this brief phase, ICEEG signals have a rhythmic or quasi-rhythmic pattern. Although this activity is transient, it is often the most visually distinctive because it is a signal with a predominant frequency of typically 4–15 Hz. With mesial temporal lobe onset partial seizures, this ORA is most commonly 5.3–8.4 Hz (Franceszczuk et al., 1998) and, indeed, this is a common finding in seizures either originating from the mesial temporal structures or with secondary mesial temporal generators. While visual analysis of this period can identify the rhythmic component, time-frequency decomposition of the signal can reveal much more detailed information. This is illustrated in Figure 28.4. Often the main activity is the predominant frequency (with associated harmonics) that accounts for most of the energy of the signal. GAD analysis confirms that the complexity of the ictal signal typically decreases during this period, reflecting the decreased number of component frequencies in the signal. Typically, this activity undergoes a monotonic decline in frequency prior to the onset of intermittent bursting activity. Indeed, if this decline were not present, one could speculate that seizure activity might be much more prolonged. Studies in neuronal cell and network models have provided one explanation for this monotonic decline in ORA (Kudela et al., 2003), while not excluding other alternative hypotheses. Kudela et al. suggest that changes in free intracellular calcium removal rates during bursting could result in the decline in ORA. Indeed, their models were very comparable to the ORA seen in actual intracranial ictal recordings from humans with mesial temporal lobe onset seizures.

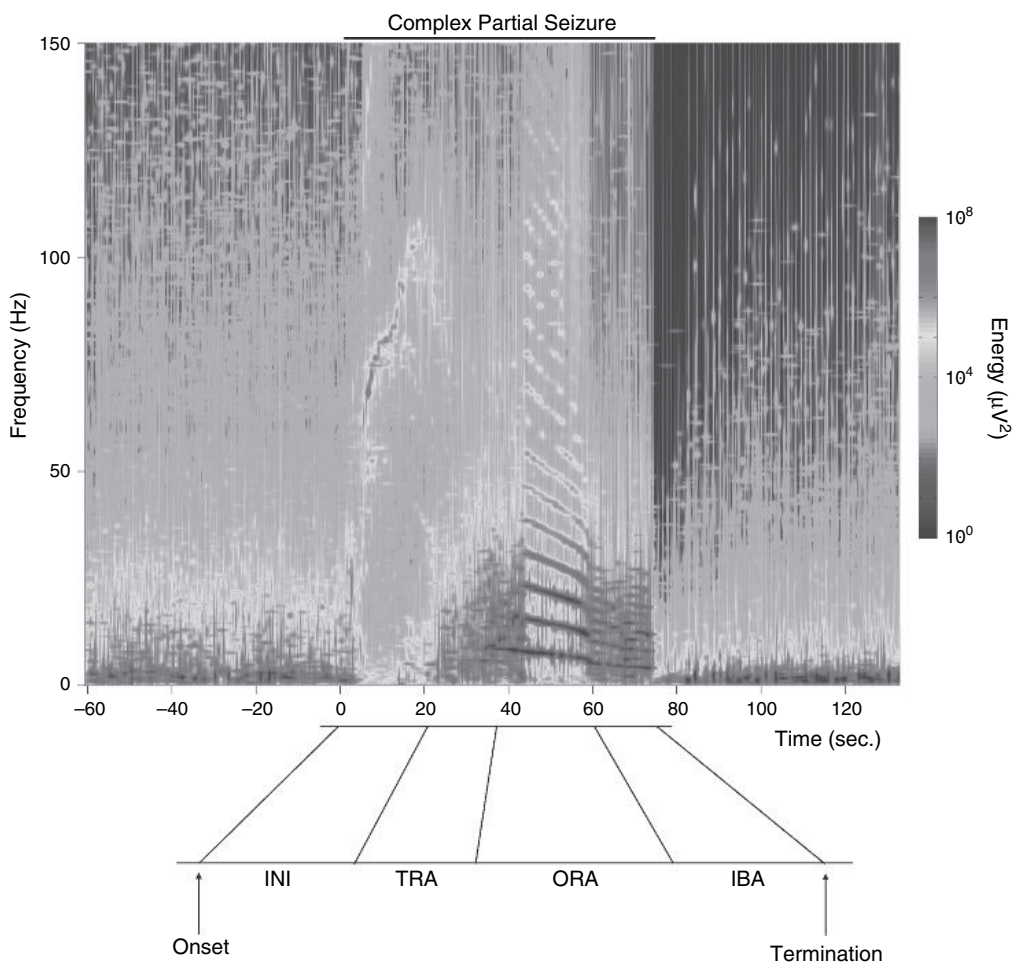


**FIGURE 28.4** The four phases of a partial seizure as seen on the time-frequency reconstruction of the energy of the ICEEG signal. Horizontal axis is time. Left axis is frequency. Color bar on the right is representing the scale of the energy representation. (See Plate 17 in color plate section.)

### **IBA: intermittent bursting activity**

As mentioned above, the period of ORA is a finite period and transitions into a period of intermittent bursting activity (IBA). While this pattern is seen in most seizures and most patients, on rare occasions, the seizure may terminate directly after the ORA period. The regular pattern of the ICEEG transitions to one of intermittent activity, a discontinuous pattern where bursts of epileptiform activity are interrupted by relative lack of activity. These electrodecremental intervals become longer and the bursting less frequent prior to seizure termination. The appearance of IBA is a reliable predictor of imminent seizure termination. This systematic evolution in itself is an indicator that the mechanisms underlying seizure activities are of a dynamic nature. Such intermittent bursting is also seen in *in vitro* neuronal systems exposed to convulsants (Macdonald and Barker, 1978), although the activity in these systems can be much more prolonged. This IBA pattern prior to the termination of partial seizures in human may reflect changes in network synchronization and the progressive inability of the network to sustain regional synchronized activity. The underlying cellular or synaptic mechanisms that contribute to the transition to and self-limited nature of IBA are not known.

Seizure termination is not a phase of the seizure *per se* but marks the end of the seizure. This period is characterized by generalized voltage depression, although this may be punctuated by some residual bursts of focal or regional activity. Some seizures have dramatic termination patterns with abrupt termination of all activities on all channels while other seizures have a less well-defined ending, with activity ending in some channels and persisting for some time in others (Afra et al., 2006).

The four main phases of a seizure, although common in MTLE patients, are not always observed. Short seizures, especially with neocortical onset, often present fewer phases and may only be composed of INI-TRA phases. Some seizures do not have an ORA and have only INI-TRA-IBA phases.

### **TIME-FREQUENCY APPROACH OF SEIZURE DYNAMIC**

Although electrical changes throughout the different phases of the seizure can be seen visually, these changes are more quantitative and distinctive on the time-frequency representations obtained from MP. The time-frequency change of ICEEG activity and the transition of phases are illustrated in Figure 28.4 for a seizure recorded in a different patient with neocortical onset seizures. Time zero marks the electrical onset of the seizure. The ICEEG signal prior to seizure onset has a typical 1/f frequency distribution. The amplitude is inversely related to the frequency. At onset, dramatic changes in the distribution of energy occur. Low frequency components almost completely disappear and, at the same time, high frequency components (30 Hz and over 60 Hz) appear. This corresponds to the INI phase of the seizure. The relation between those high-frequency features and the localization of the seizure onset is still a question prompting considerable investigation (Schiff et al., 2000; Worrell et al., 2004; Jirsch et al., 2006).

The following TRA phase appears then as a composite of mixed activity with energy spread over the spectrum but biased toward lower frequencies. No specific pattern is visible on the reconstruction during that period. The TRA phase is then followed by the ORA phase clearly identifiable with its predominant frequency and its numerous harmonics forming a 'ladder' on the time-frequency reconstruction.

The main component of the ORA is the predominant rhythmic activity with a declining trend. The more rhythmic the pattern, the more harmonics will be observed ranging from 3 to up to 20 and more. The number of harmonics is linked to the shape of the signal. When present, ORA always demonstrates a monotonic decline prior to transition to IBA.

The loss of rhythmicity of the ictal activity heralds the beginning of the next phase, IBA. Remnants of the main frequency component can still be seen in the reconstruction, but to a lesser extent and with much more overlapping activity. Spikes, which are decomposed into atoms represented as vertical lines on the energy reconstruction, represent the major part of the decomposition.

After termination the post-ictal ICEEG signal is clearly of very low energy, with possible occurrence of low frequency components with a slow gradual return to the 1/f signal distribution.

### **Seizures are stereotyped**

The MP method provides a detailed time-frequency decomposition of the ictal EEG signal. The composite frequencies illustrate the complexity of the EEG signal and synthetic complexity measures can facilitate monitoring of seizure evolution. Despite the irregular appearance of some seizures, epileptic events are often extremely stereotyped and can have similar patterns even over several minutes. The similarity of those patterns, while often apparent with visual inspection of the ictal EEG, is even more dramatic with the time-frequency representation of the energy of the seizure. Figure 28.5 shows

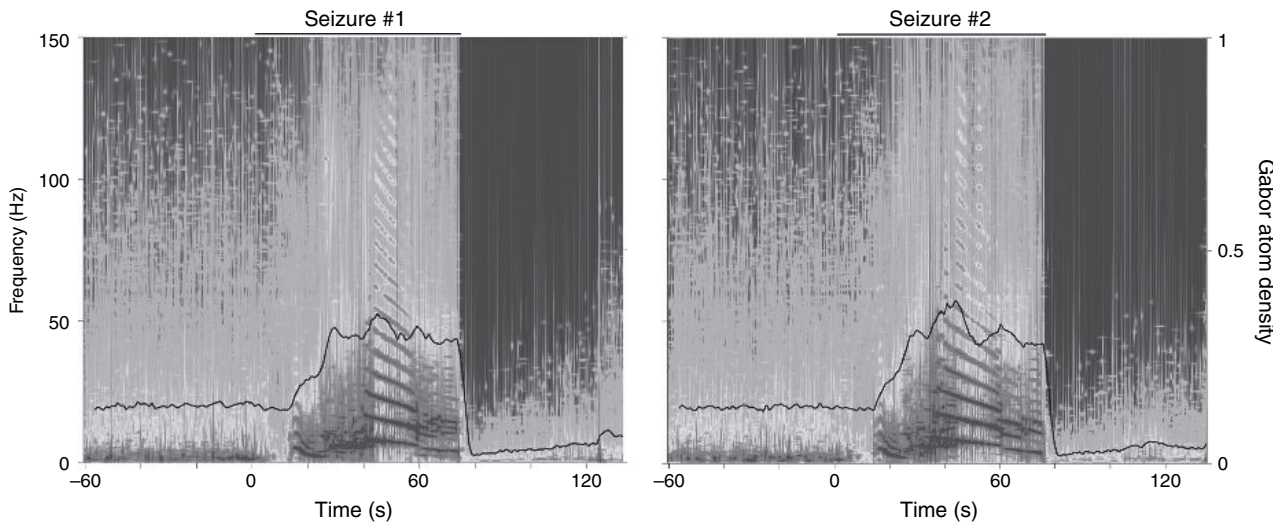


**FIGURE 28.5** Comparison of two time-frequency reconstructions for two different complex partial seizures from the same patient. The similarity of seizure evolution between two seizures translates into similar content in the time-frequency domain. Both seizures have identical spectral features and seizure phases: INI with low amplitude onset with rhythmic theta/delta, TRA, ORA, IBA and post-ictal depression. (See Plate 18 in color plate section.)

an example of two complex partial seizures from the same patient recorded 7 hours apart from each other. Both seizures exhibit similar dynamics and contain the same phases with extremely similar time-frequency compositions.

From each time-frequency reconstruction we can observe the electrodecremental onset visible by the lack of low frequency atoms shortly after the time zero, followed by an initiation period containing a main component whose frequency slightly rises then slowly declines toward the transition period. The main frequency of the ORA appears during the end of the TRA period and shows an almost linear decline throughout the phase. Lack of low frequency atoms and a large number of harmonics characterize the organized rhythmic aspect of the ICEEG during that phase. The following IBA phase, again similar in duration in both seizures, is the final phase of seizure evolution prior to termination.

The similarity of seizures as seen on time-frequency map is also readily visible when one compares the Gabor atom density of those seizures. GAD is a synthetic measure based on the MP decomposition. It quantifies the number of atoms needed to represent the ICEEG signal during a limited window of time and is a measure of the signal complexity (Jouny et al., 2003). A high complexity signal requires many atoms to be represented. A low complexity signal requires few. High complexity does not mean that there are generators for every component frequency. Ictal transition is frequently (very often, but not always) associated with increased complexity. Seizure termination, conversely, is typically associated with a decreased signal complexity, often below that seen at baseline in the pre-ictal state. Both seizures of Figure 28.5 have the signal complexity GAD represented as the black traces overlapping the time-frequency representation.

GAD plots indicate the composite complexity of the EEG signals and allow one to quantify more easily the changes of seizure dynamics over time. Figure 28.6 shows the juxtaposition of the GAD for several seizures recorded from the same patient. All seizures are aligned on time zero as the time of the onset. Two observations can be made from these plots. First, the similarity of the GAD plots reflects the stereotyped ictal dynamics. Second, differences between these seizures dynamics late in seizure evolution allows grouping of the events into subcategories of patterns of evolution. Five seizures have a GAD dynamic with a final increase (in complexity) toward the end, two seizures show the same duration of complexity increase but without a final incremental increase and one of the seizures terminates early. For this patient with relatively short seizures, all the seizures have very similar dynamics for the first 20 seconds and then diverge into three types of evolution. Within each type the dynamics remain remarkably consistent.

### Propagation is stereotyped

Just as the dynamics of the EEG signal at the focus allow comparisons of local seizure dynamics, propagation maps composed of the evolution of signal complexity for all channels allow one to assess propagation patterns. The MP method is a single channel method, but propagation maps can be constructed by juxtaposition of the GAD values for all channels. The representation may reflect grid architecture (e.g. contact 8 is next to 16 on the map, but far from contact 9 which

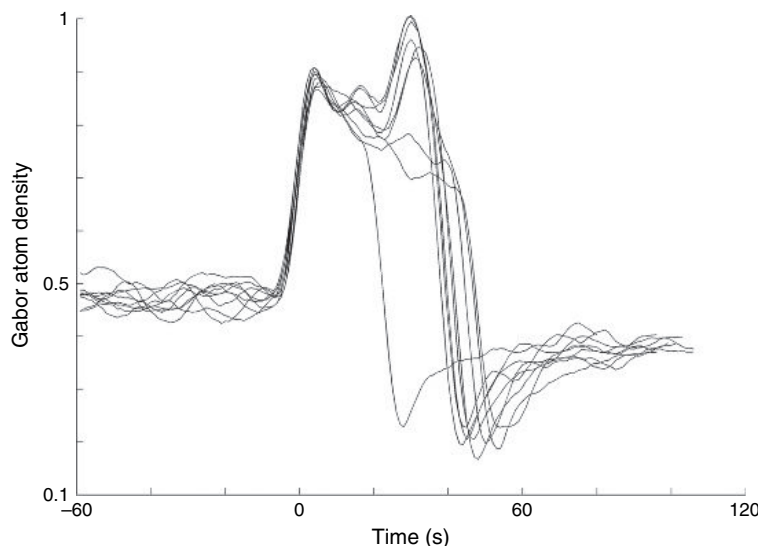


**FIGURE 28.6** Gabor atom density (GAD) for seven seizures from the same patient. Time zero is the onset of the seizures. The similarity of dynamic and the subdivision of dynamic patterns are visible on these seven seizures which show high similarity as well as three distinct subgroups of dynamic changes. Reproduced with permission from Clinical Neurophysiology, Vol. 114(3):426-437, Jouny, C.C., Franaszczuk, P.J. and Bergey, G.K. Characterization of epileptic seizure dynamics using Gabor atom density © 2003 International Federation of Clinical Neurophysiology.

is adjacent on the actual grid) but allows one to assess readily the extent of the propagation and the similarity between seizures. In some instances this may merely reflect propagation patterns that are apparent by visual inspection but, in many other instances, the GAD-based propagation maps reveal patterns that are difficult to determine from routine inspection. The display format of these maps greatly facilitates analyses of seizure propagation.

Figure 28.7 illustrates the propagation for two complex partial seizures from a patient with frontal lobe onset seizures. Each map contains the GAD for all channels recorded from the main frontal subdural grid and the additional subdural strips. With seizure onset in the middle of the frontal grid, the propagation pattern is one of a prolonged regional onset confined to the frontal grid. After 120 seconds there is further spread to involve additional frontal areas covered by the grid and also the adjacent temporal lobe (PT). The second partial seizure exhibits a very similar pattern of propagation and total seizure duration (around 4 minutes). The termination of the seizure is marked by the post-ictal depression represented

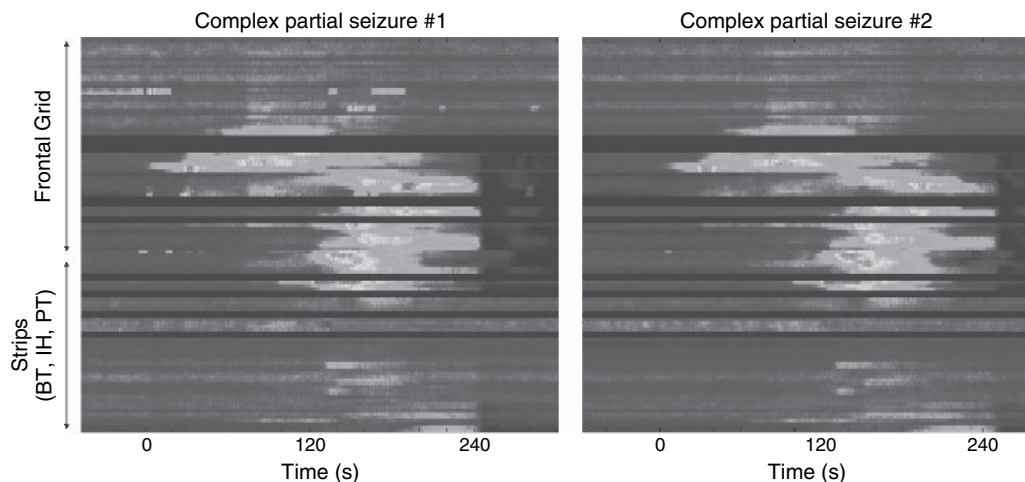


**FIGURE 28.7** Propagation maps for two complex partial seizures from the same patient. Time zero is the onset of the seizure. Blue represents low GAD value and red represents high GAD values. Two separate events recorded hours apart still exhibit highly similar dynamics. Onset location, timing of propagation pattern, seizure duration and pattern of termination are very similar. (See Plate 19 in color plate section.)

by large GAD decreases (deep blue) in all channels around 240 seconds. This post-ictal period represents a period of low complexity signal. Whether this represents desynchronized activity or the relative absence of activity is not established.

The similarity of patterns of propagation is consistent from seizure to seizure with some variations. This may reflect similar pathways of propagation in a given patient. Not all seizures from all patients have identical patterns. There is, however, a possibility to study the similarity or difference between propagation maps. This similarity of the dynamics of partial seizures from a given patient, although commonly acknowledged, has not been studied in any quantitative detail until such methods as the MP method made this possible. This similarity of pattern suggests a process that is more deterministic and less random than previously considered.

### Variations in propagation

Similarity of seizure dynamics can be shown by single channel time-frequency decompositions or complexity measures from selected channels. Similarities of seizures can also be shown by the GAD-based propagation maps. These maps reveal similar patterns of early regional propagation during complex partial seizures (CPS) and then dynamic differences when complex partial seizures secondarily generalize (CPS + 2<sup>nd</sup> GTC). It is of interest to compare the initial propagation pattern of CPS and CPS + 2<sup>nd</sup> GTC for seizures from the same patient. Partial seizures with secondary generalization begin with focal activity. Typically, there are not any early indications from the ICEEG, even with detailed time-frequency decompositions, that can distinguish which seizures will generalize until the generalization actually occurs. The comparison of propagation maps for a mesial temporal onset partial seizure and a partial seizure with secondary generalization can be seen in Figure 28.8. The recording array includes a left fronto-temporal grid and a series of strips over the basal temporal, occipital and parietal regions. The closest electrode to the focus was on the LBT strip. We can see during the complex partial seizure the involvement of these contacts close to the focus and then the spread to the contacts of the LFG strip very early in the seizure before subsequent broad regional spread involving the frontal grid.

In this patient, there are similarities between self-limited partial seizures and seizures that secondary generalize. During the first 40 seconds, seizure dynamics and regional propagation are similar for both the partial seizure without generalization and the seizure that subsequently generalizes. The early complexity changes are very similar for both seizures. There is nothing to distinguish the two seizures during this period. Of course, once the generalization occurs, the dynamic is altered in many of the channels, reflecting more extensive propagation and there is increased complexity in almost all channels. By 80 seconds after seizure onset, almost all electrodes recorded show increased complexity.

These representations of propagation maps facilitate assessment of similarities and differences of patterns of propagation. Comparison of the GAD measurements from the focus and from a remote location provides a different perspective. Figure 28.9 represents five complex partial seizures (CPS) and one complex partial seizure with secondary generalization (CPS + 2<sup>nd</sup> GTC) for the same patient. These seizures are the same as illustrated in Figure 28.6 where focal dynamics are compared, but here the GAD of a remote location during the GTC is also shown. The dynamic of the event is remarkably

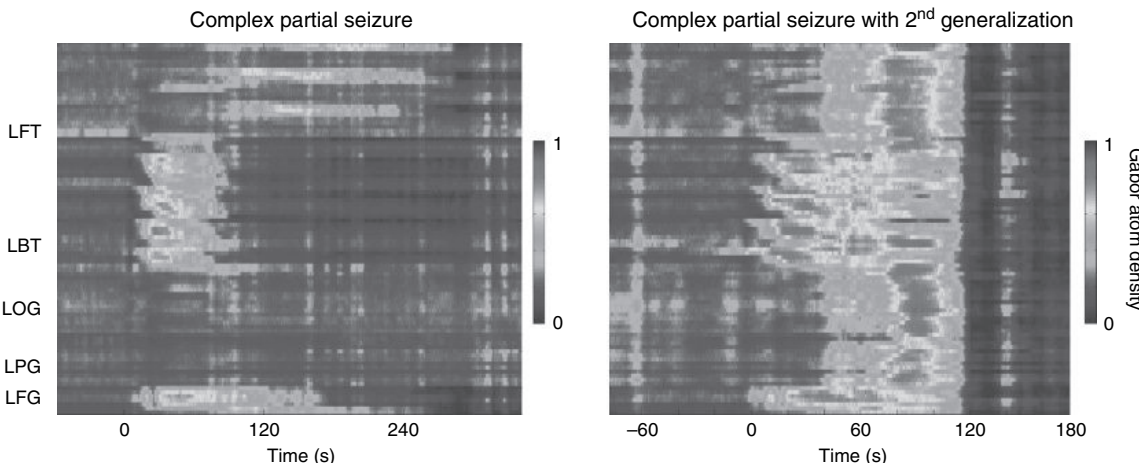


**FIGURE 28.8** Propagation maps for a complex partial seizure (left) and a complex partial seizure with secondary generalization (right). Time zero is the onset of the seizure. Blue represents low GAD value and red represents high GAD values. Both events appear to have similar dynamic and propagation during the early period of the seizure. (See Plate 20 in color plate section.)

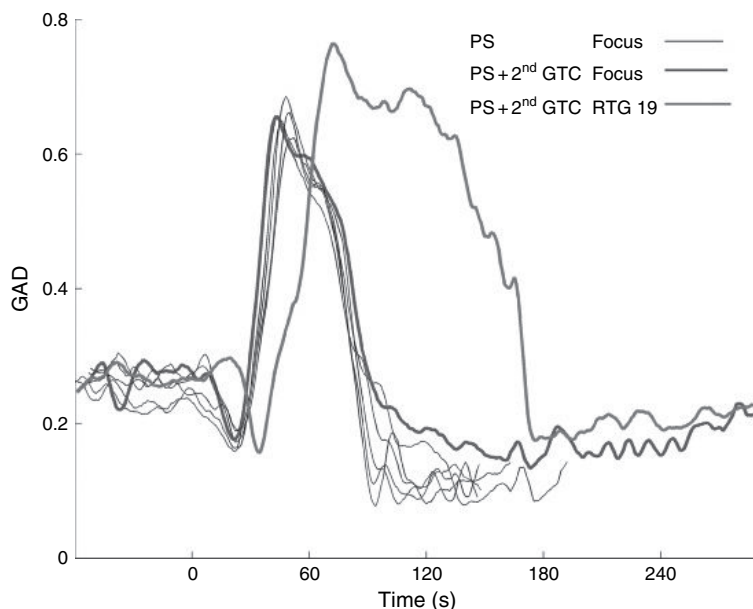


**FIGURE 28.9** GAD for five complex partial seizures (CPS) and one complex partial seizure with secondary generalization (CPS+2<sup>nd</sup> GTC) for the same patient. Black traces represent GAD for the focus during the CPS. Blue trace represents GAD for the focus during the GTCS. Orange trace represents GAD for a remote electrode (RTG19) during the GTCS. (See Plate 21 in color plate section.)

similar for all CPS (black traces); the CPS + 2<sup>nd</sup> GTC exhibit nearly identical patterns (blue trace) even toward the end of the event. Comparing the GAD for the remote location (orange trace), one can clearly recognize the GAD decrease which occurs around 15 seconds later at the remote location followed by the major GAD increase during the generalization of the seizure.

More importantly, one can see that the seizure dynamics at the focus are similar for CPS and the CPS + 2<sup>nd</sup> GTC, indicating that the generalization of the GTCS did not affect the dynamics at the focus. Although these are early results, similar observation suggests that the dynamics of secondary generalization might differ between mesial temporal onset seizure and neocortical onset seizure (Jouny et al., 2007).

#### RATIONALE FOR THE QUANTIFICATION OF SEIZURE DYNAMICS: POTENTIAL APPLICATIONS

The increased utilization of intracranial EEG monitoring in presurgical evaluations has provided detailed digitized continuous ictal and interictal records. Intracranial monitoring is typically done both better to localize the seizure focus and to map eloquent areas. As mentioned, the most important consideration in patient management is better to define the seizure focus; seizure dynamics and patterns of propagation are typically of secondary importance if they are considered at all. Examination of seizure dynamics and propagation patterns can, however, potentially provide important insights.

Seizures are self-limited events, lasting only about 3 minutes or less in most patients. While antiepileptic drugs (AEDs) may reduce the number of seizures a patient experiences and the number of secondarily generalized seizures, it is not clear that AEDs alter the dynamics of partial seizures. Preliminary data from patients undergoing AED withdrawal during epilepsy monitoring, has not demonstrated that drug withdrawal prolongs partial seizures (Adamolekun et al., 2004). This suggests that there may be an intrinsic focal seizure dynamic. This is further supported by the fact that seizure dynamics, particularly early in the seizure are often very stereotyped for all seizures from a given focus in a selected patient. This observation that has been suggested by visual analyses in the past can be quantitatively demonstrated by the time-frequency and complexity measures discussed above. Indeed, the newly developed GAD measure facilitates quantitative comparisons for either single channel or multichannel analyses.

This stereotyped onset pattern facilitates recognition of repetitive seizures. This is important for presurgical assessments, but also can be important in the application of responsive therapies (e.g. responsive neurostimulation) (Bergey et al., 2006)

where it may be critical accurately to detect seizures early (i.e. within seconds) of seizure onset so that therapy can be given before regional or bilateral propagation, when therapy may either be less effective or less beneficial. Whether the occurrence of seizures is random or non-random, these analyses of seizure dynamics and the similarity between events clearly illustrate that seizure evolution is very much a deterministic process that utilizes similar mechanisms of seizure generation and similar patterns of network involvement.

The fact that partial seizures are brief, self-limited events even without therapy suggests that there are neuronal or network factors that produce seizure termination. The appearance of an intermittent bursting pattern reliably predicts seizure termination. Understanding the intrinsic dynamics of seizures may allow development of more effective responsive stimulation parameters.

The degree of seizure propagation determines the clinical manifestations of a partial seizure. Seizures that remain confined to a discrete focus, hippocampal or other, may produce only brief simple partial seizures, including auras, or even just electrical events with no clinical manifestations. Limiting seizure propagation will therefore not just reduce secondarily generalized seizures, but also evolution of complex partial symptomatology.

The methods are now available for assessing seizure dynamics at the focus, patterns of propagation and patterns of termination. The GAD-based propagation maps allow one to assess the spatial propagation of epileptic activity and the ability to differentiate more quantitatively between events (either in the same patient or multiple patients). Time-frequency reconstructions using the matching pursuit method can be accurately applied to even rapidly changing signals to provide analyses with a new level of precision. Hopefully, analyses of human seizure dynamics will provide insights that can lead to methods that can facilitate seizure termination and analyses of onset and propagation patterns will help determine which patients, particularly those with non-lesional neocortical epilepsy, are the best candidates for resection.

## REFERENCES

- Adamolekun, B., Jouny, C.C., Franaszczuk, P.J. and Bergey, G.K. (2004). Does antiepileptic drug withdrawal affect seizure duration? *Epilepsia* 45(S7):58.
- Afra, P., Jouny, C.C., Franaszczuk, P.J. and Bergey, G.K. (2006). Partial seizure duration may influence patterns of seizure termination. *Epilepsia* 47(S4):48.
- Allen, P.J., Fish, D.R. and Smith, S.J. (1992). Very high-frequency rhythmic activity during SEEG suppression in frontal lobe epilepsy. *Electroencephalogr Clin Neurophysiol* 82(2):155–159.
- Bergey, G., Worrell, G., Chabolla, D. et al. (2006). Safety and preliminary efficacy of a responsive neurostimulator (RNS™) for the treatment of intractable epilepsy in adults. *Neurology* 66(Suppl 2):A387.
- Cooley, J.W. and Tukey, J.W. (1965) An algorithm for the machine calculation of complex Fourier series. *Math Comput* 19: 297–301.
- Durka, P.J. and Blinowska, K.J. (2001). A unified time-frequency parametrization of EEGs. *IEEE Eng Med Biol Mag* 20(5):47–53.
- Fisch, B.J. (1996). Generalized tonic-clonic seizures. In: *The treatment of epilepsy: principles and practice* (E.Wyllie, ed.) pp. 502–521. Williams & Wilkins, Cleveland.
- Fisher, R.S., Webber, W.R., Lesser, R.P., Arroyo, S. and Uematsu, S. (1992). High-frequency EEG activity at the start of seizures. *J Clin Neurophysiol* 9(3):441–448.
- Franaszczuk, P.J. and Bergey, G.K. (1999). An autoregressive method for the measurement of synchronization of interictal and ictal EEG signals. *Biol Cybern* 81(1):3–9.
- Franaszczuk, P.J., Bergey, G.K., Durka, P.J. and Eisenberg, H.M. (1998). Time-frequency analysis using the matching pursuit algorithm applied to seizures originating from the mesial temporal lobe. *Electroencephalogr Clin Neurophysiol* 106(6):513–521.
- Franaszczuk, P.J., Blinowska, K.J. and Kowalczyk, M. (1985). The application of parametric multichannel spectral estimates in the study of electrical brain activity. *Biol Cybern* 51(4):239–247.
- Gath, I., Feuerstein, C., Pham, D.T. and Rondouin, G. (1992). On the tracking of rapid dynamic changes in seizure EEG. *IEEE Trans Biomed Eng* 39(9):952–958.
- Jirsch, J.D., Urrestarazu, E., LeVan, P., Olivier, A., Dubeau, F. and Gotman, J. (2006). High-frequency oscillations during human focal seizures. *Brain* 129(Pt 6):1593–1608.
- Jouny, C.C., Franaszczuk, P.J. and Bergey, G.K. (2003). Characterization of epileptic seizure dynamics using Gabor atom density. *Clin Neurophysiol* 114(3):426–437.
- Jouny, C.C., Franaszczuk, P.J. and Bergey, G.K. (2005). Signal complexity and synchrony of epileptic seizures: is there an identifiable preictal period? *Clin Neurophysiol* 116(3):552–558.
- Jouny, C.C., Adamolekun, B., Franaszczuk, P.J. and Bergey, G.K. (2007). Intrinsic ictal dynamics at the seizure focus: effects of secondary generalization revealed by complexity measures. *Epilepsia* 48(2):297–304.
- Kudela, P., Franaszczuk, P.J. and Bergey, G.K. (2003). Reduction of intracellular calcium removal rate can explain changes in seizure dynamics: studies in neuronal network models. *Epilepsy Res* 57(2–3):95–109.
- Lehnertz, K. and Litt, B. (2005). The first international collaborative workshop on seizure prediction: summary and data description. *Clin Neurophysiol* 116(3):493–505.
- Macdonald, R.L. and Barker, J.L. (1978). Specific antagonism of GABA-mediated postsynaptic inhibition in cultured mammalian spinal cord neurons: a common mode of convulsant action. *Neurology* 28(4):325–330.

- Mallatm S,G, and Zhang, Z. (1993). Matching pursuit with time-frequency dictionaries. *IEEE Trans Biomed Eng* 41:3397–3415.
- Pacia, S.V. and Ebersole, J.S. (1997). Intracranial EEG substrates of scalp ictal patterns from temporal lobe foci. *Epilepsia* 38(6):642–654.
- Schiff, S.J., Colella, D., Jacyna, G.M. et al. (2000). Brain chirps: spectrographic signatures of epileptic seizures. *Clin Neurophysiol* 111(6):953–958.
- Spencer, S.S., Guimaraes, P., Katz, A., Kim, J. and Spencer, D. (1992). Morphological patterns of seizures recorded intracranially. *Epilepsia* 33:537–545.
- Staba, R.J., Wilson, C.L., Bragin, A., Fried, I. and Engel, J. Jr (2002). Quantitative analysis of high-frequency oscillations (80–500 Hz) recorded in human epileptic hippocampus and entorhinal cortex. *J Neurophysiol* 88(4):1743–1752.
- Stam, C.J. (2005). Nonlinear dynamical analysis of EEG and MEG: review of an emerging field. *Clin Neurophysiol* 116(10):2266–2301.
- Traub, R.D., Whittington, M.A., Buhl, E.H. et al. (2001). A possible role for gap junctions in generation of very fast EEG oscillations preceding the onset of, and perhaps initiating, seizures. *Epilepsia* 42(2):153–170.
- Worrell, G.A., Parish, L., Cranstoun, S.D., Jonas, R., Baltuch, G. and Litt, B. (2004). High-frequency oscillations and seizure generation in neocortical epilepsy. *Brain* 127(Pt 7):1496–506.
- Zaveri, H.P., Williams, W.J., Iasemidis, L.D. and Sackellares, J.C. (1992). Time-frequency representation of electrocorticograms in temporal lobe epilepsy. *IEEE Trans Biomed Eng* 39(5):502–509.

# 29

## ARE CORRELATION DIMENSION AND LYAPUNOV EXPONENTS USEFUL TOOLS FOR PREDICTION OF EPILEPTIC SEIZURES?

YING-CHENG LAI, IVAN OSORIO, MARK G. FREI  
AND MARY ANN F. HARRISON

### ABSTRACT

Epilepsy, a common neurological disorder, manifests with seizures that occur suddenly, cyclically but aperiodically, features that enhance its disabling power. That reliable prediction of seizures would considerably lessen this burden, explains the intense interest in fulfilling this valuable objective. Among the different tools applied thus far to this end, two fundamental quantities that characterize certain chaotic sets, the correlation dimension and the Lyapunov exponents have been the most used. The presumed non-linear behavior of neuronal networks that make up the brain, along with other properties, was deemed a valid rationale to applying these methods to the electroencephalogram (EEG) or electrocorticogram (ECOG) to predict seizures. The purpose of this chapter is to review a number of recent studies on the predictive powers of the correlation dimension and of the Lyapunov exponents. In particular, based on results from extensive analyses of clinical data and control studies, we shall demonstrate that the correlation dimension and the Lyapunov exponent do not reliably predict seizures and that their performance is not superior to that of random predictors. The fundamental relation between the fractal dimension and the Lyapunov exponents of a chaotic set, as given by the Kaplan-Yorke formula, implies that the Lyapunov exponents would have no predictive power for phenomena such as seizures. If heeded, this may have avoided the substantial but, thus far, fruitless efforts to pursue this research avenue. We propose that the largely ignored task of characterization of the dynamical properties and behavior of seizures should be the top priority of the epilepsy research community, replacing the prevailing approach of indiscriminately applying tools from non-linear dynamics or any other fields to the *prediction* of seizures. While serendipity may reward current seizure prediction attempts, fundamental advances in epileptology require the unraveling of the *laws* that govern seizure generation in epilepsy. The knowledge thus accrued, may provide answers to whether or not seizures are predictable. A positive answer would shape the approach to actual seizure prediction.

### INTRODUCTION

It has been recognized increasingly that epileptic seizures are a dynamic disease caused by a change in the state of the brain dynamical system (Schiff, 1998). For instance, it has been speculated since about one hundred years ago that synchronization may play an important role in seizure dynamics. In standard, comprehensive textbooks on neuroscience (Kandel et al., 1991), it is written that ‘large populations of neurons are activated synchronously during an epileptic seizure’. However, whether or not this is the case, is far from being settled. For example, a recent experimental study of synchronization between CA1 pyramidal neurons revealed that seizure-like events are associated with *desynchronization* (Netoff and Schiff, 2002).

From the standpoint of seizure prediction based on electroencephalogram (EEG) or electrocorticogram (ECoG) signals, the assumption that seizures are caused by synchronization among neurons has the practical implication that, during the seizure, the number of degrees of freedom of the underlying brain dynamical system may be reduced. Thus, if the dimension of the underlying brain dynamical system can be measured and if the dimension shows some systematic change during the time evolution toward seizure, its prediction may become possible. The development in non-linear dynamics of efficient methods for estimating dimensions from time series gives a further stimulus to the idea of predicting seizures based on calculating dimensions. This has indeed been practiced (Babloyantz and Destexhe, 1986; Mayer-Kress and Layne, 1987; Albano et al., 1988; Rapp et al., 1994; Lerner, 1996; Quyen et al., 1997; Lehnertz and Elger, 1998; Martinerie et al., 1998; Schiff, 1998; Osorio et al., 1998; Diambra and Malta, 1999; Hively et al., 2000; Quiroga et al., 2000; Andrzek et al., 2001; Porcher and Thomas, 2001), along with efforts to develop seizure prediction algorithms using other basic non-linear dynamics quantities such as the Lyapunov exponents (Iasemidis et al., 1990, 2001, 2003a,b; Iasemidis and Sackellares, 1991). Many of these studies claim that epileptic seizures can be predicted minutes (Iasemidis et al. 1990, Iasemidis and Sackellares, 1991) or even tens of minutes (Iasemidis et al., 2001, 2003a,b) in advance. There is one fundamental difficulty associated with seizure prediction claims based on dimensions or Lyapunov exponents: these quantities are useful primarily for low-dimensional, non-noisy systems, conditions that the human brain does not satisfy.

While early research suggested that the brain activity generating the EEG or ECoG signals could be described by low-dimensional dynamical systems (Babloyantz and Destexhe, 1986; Mayer-Kress and Layne, 1987; Albano et al., 1988; Rapp et al., 1994) re-examination of these results indicate a lack of low-dimensional dynamical structure in brain signals (Theiler, 1995; Theiler and Rapp, 1996; Frank et al., 1990; Ivanov et al., 1996; Jeong et al., 1999). In fact, typical EEG or ECoG signals are similar to stochastic systems that are infinite-dimensional dynamical systems. To try to measure the dimension of an infinite-dimensional system and use it to discern different states of the system is a highly questionable practice. Lyapunov exponents measure the exponential separation rates of initially close trajectories in the different eigenspaces riding with a typical trajectory and they are fundamentally related to the fractal dimensions (Kaplan and Yorke, 1979). So far, accurate estimates of Lyapunov exponents from time series can be obtained only for low-dimensional dynamical systems described by discrete-time maps. To calculate them based on time series from continuous-time, low-dimensional systems, even for the celebrated, three-dimensional Lorenz chaotic system (Lorenz, 1963; Kantz, 1994), remains problematic (Kantz and Schreiber, 1997), let alone for higher dimensional systems in the presence of noise. This indicates that Lyapunov exponents estimated from EEG or ECoG signals are difficult to interpret and to use them to distinguish seizure from preseizure state may be futile.

The technical materials of this review chapter are mostly based on our recent works (Osorio et al., 2001; Lai et al., 2002, 2003, 2004, 2005; Harrison et al., 2005). We shall first review the results of correlation dimension analysis from an extensive clinical data base: over 2000 total hours of continuous ECoG from 20 subjects with epilepsy (Harrison et al., 2005). In particular, sensitivity of the estimated dimension to properties such as the signal amplitude and autocorrelation will be examined, the effect of the embedding (necessary for estimating dimension from time series, to be described below) and the filtering method will be discussed and surrogate data analysis will be performed. The conclusion is that the correlation dimension has no predictive power for seizures. Next, we shall describe the fundamental relation between the fractal dimension and the Lyapunov exponents, as given by the Kaplan-Yorke formula (Kaplan and Yorke, 1979), and argue for the inability of Lyapunov exponents to predict seizures. We will then review the control studies based on non-stationary dynamical systems modeled by discrete-time maps and by continuous-time flows (Lai et al., 2003, 2004), for which the behavior of the Lyapunov exponents is known *a priori*, to show that the exponents have no predictive or even detective power for characteristic system changes – even when only an exceedingly small amount of noise is present. Supporting results from analysis of clinical ECoG data will also be discussed.

## CORRELATION DIMENSION, LYAPUNOV EXPONENTS AND THE KAPLAN-YORKE FORMULA

### CORRELATION DIMENSION

The geometry of an attractor in a non-linear system is characterized by the fractal-dimension spectrum (or the generalized dimensions) (Grassberger and Procaccia, 1983; Hentschel and Procaccia, 1983; Ott, 2002). To define the dimension spectrum, one covers the attractor using a uniform grid of boxes of size  $\varepsilon$  and calculates the frequencies of visit of a

typical trajectory to all non-empty boxes. Let  $\mu_i$  be the frequency of visit to (or the natural measure of) the  $i$ th box, from which the following summation can be performed:

$$I(q, \varepsilon) = \sum_{i=1}^{N(\varepsilon)} \mu_i^q, \quad (1)$$

where  $N(\varepsilon)$  is the number of boxes required to cover the attractor. The generalized dimensions are given by

$$D_q = \lim_{\varepsilon \rightarrow 0} \frac{1}{q-1} \frac{\ln I(q, \varepsilon)}{\ln \varepsilon}, \quad (2)$$

where  $D_0 \geq D_1 \geq D_2 \geq \dots$ . For  $q = 0$ , we have  $I(0, \varepsilon) = N(\varepsilon)$  so that Equation (2) gives the box-counting dimension  $D_0$ . Similarly, setting  $q = 1$  gives the information dimension  $D_1$  (Farmer et al., 1983). These two dimensions, while fundamental in non-linear dynamics, are difficult to calculate from time series because of the need to count boxes over a range of the box size. The dimension  $D_2$ , however, can be computed readily from time series (Grassberger and Procaccia, 1983; Hentschel and Procaccia, 1983) and, hence, it becomes the standard choice of dimension to be estimated in non-linear time-series analysis and in experimental chaos research. This is justified because, for typical dynamical systems, the values of these dimensions are close (Ott, 2002).

To see why  $D_2$  is particularly convenient for time-series analysis, note that  $\{\mu_i\}$  is a probability measure and, for  $q = 2$ , the sum  $I(q, \varepsilon)$  can be written as

$$I(q, \varepsilon) = \sum_{i=1}^{N(\varepsilon)} \mu_i^2 = \langle \mu_i \rangle,$$

which is the ensemble average of the probability measure  $\{\mu_i\}$ . Under the assumption of ergodicity, both the ensemble average and the measure itself can be replaced by time averages with respect to a typical trajectory on the attractor. Thus the sum  $I(q, \varepsilon)$  can be evaluated approximately by the following *correlation integral*:

$$C(N, \varepsilon) = \frac{1}{N(N-1)} \sum_{i \neq j} \Theta(\varepsilon - ||\mathbf{x}_i - \mathbf{x}_j||), \quad (3)$$

for  $N \rightarrow \infty$ , which is the fraction of pairs of points on the attractor within a hypersphere of radius  $\varepsilon$ . Consequently, the correlation dimension is given by

$$D_2 = \lim_{N \rightarrow \infty} \lim_{\varepsilon \rightarrow 0} \frac{\log C(N, \varepsilon)}{\log \varepsilon}. \quad (4)$$

For scalar time-series data, computations of the correlation can be carried out by first using the standard time-delay embedding method (Takens, 1981) to reconstruct an  $m$ -dimensional phase space variable

$$\mathbf{y}_i = [x_i, x_{i+\tau}, x_{i+2\tau}, \dots, x_{i+(m-1)\tau}], \quad (5)$$

where  $m$  is the embedding dimension and  $\tau$  is the time delay. In order to resolve the dynamics in the underlying system generating the scalar time series,  $m$  needs to be sufficiently large. In particular, if the measured data come from an attractor of box-counting dimension  $D_0$ ,  $m$  has to be at least more than  $2D_0$  (Sauer et al., 1991). The choice of  $\tau$  is mostly empirical. Since two adjacent components in  $\mathbf{y}_i$ , say  $x_i$  and  $x_{i+\tau}$ , are considered as independent coordinates, if  $\tau$  is too small, the components will be too correlated to be independent. If it is too large, the components are effectively random with respect to each other and so they cannot serve as coordinates either. Usually, the autocorrelation function of the scalar time series can be computed and  $\tau$  is chosen as the autocorrelation length (Kantz and Schreiber, 1997).

For a given value of the embedding dimension  $m$ ,  $D_2$  can be determined according to Equation (4). Since the intrinsic dimension of the underlying attractor is not known *a priori*, it is necessary systematically to increase  $m$  to calculate a number of values for  $D_2$ . Suppose the ‘real’ dimension value is  $\bar{D}_2$ , then the estimated value of  $D_2$  will increase with  $m$  for  $m \leq [\bar{D}_2]$ , where  $[\cdot]$  denotes the integer part. This can be understood by considering the simple example of a three-dimensional object. If one uses spaces of dimensions 1–3 to represent the object, one gets  $D_2 = 1, 2, 3$ , respectively. Only

when the space has dimension more than three, one gets the correct dimension value  $\bar{D}_2 = 3$ . This observation apparently holds for more complicated sets such as a chaotic attractor (Ding et al., 1993), where for an infinite, noiseless time series, the estimated dimension value  $D_2$  increases with  $m$  but plateaus for  $m \geq [\bar{D}_2] + 1$ . For finite and noisy time series, the value of  $m$  required for  $D_2$  to plateau is likely to be higher. For a completely stochastic system which is intrinsically infinitely dimensional, the estimated  $D_2$  will *never* plateau, no matter how large  $m$  is. This line of reasoning emphasizes the need to estimate  $D_2$  from a systematic set of  $m$  values. In this regard, the choice of  $m = 7$  used in EEG analysis in the Lyapunov-exponent literature (Iasemidis et al., 1990, 2001, 2003a,b; Iasemidis and Sackellares, 1991) does not appear to be justifiable, considering the noisy nature of EEG signals.

### LYAPUNOV EXPONENTS FROM TIME SERIES

The Lyapunov exponents characterize how a set of orthonormal, infinitesimal distances evolve under the dynamics. For an  $M$ -dimensional dynamical system, there are  $M$  Lyapunov exponents. Consider a dynamical system described by

$$\frac{d\mathbf{x}}{dt} = \mathbf{F}(\mathbf{x}), \quad (6)$$

where  $\mathbf{x} \in \mathbf{R}^M$  is an  $M$ -dimensional vector. Taking the variation of both sides of Equation (6) yields an equation governing the evolution of infinitesimal vector  $\delta\mathbf{x}$  in the tangent space at  $\mathbf{x}(t)$ ,

$$\frac{d\delta\mathbf{x}}{dt} = \frac{\partial \mathbf{F}}{\partial \mathbf{x}} \cdot \delta\mathbf{x}. \quad (7)$$

Solving for Equation (7) gives

$$\delta\mathbf{x}(t) = \mathbf{A}'\delta\mathbf{x}(0), \quad (8)$$

where  $\mathbf{A}'$  is a linear operator that evolves an infinitesimal vector from time 0 to time  $t$ . The mean exponential rate of divergence of the tangent vector is then given by

$$\lambda[\mathbf{x}(0), \delta\mathbf{x}(0)] = \lim_{t \rightarrow \infty} \frac{1}{t} \ln \frac{||\delta\mathbf{x}(t)||}{||\delta\mathbf{x}(0)||}, \quad (9)$$

where  $||\cdot||$  denotes the length of the vector with respect to a Riemannian metric. In typical situations there exists a set of  $d$ -dimensional basis vectors  $\{\mathbf{e}_i\}$  ( $i = 1, \dots, M$ ), in the following sense:

$$\lambda_i \equiv \lambda[\mathbf{x}(0), \mathbf{e}_i]. \quad (10)$$

These  $\lambda_i$ s define the Lyapunov spectrum, which can be ordered as

$$\lambda_1 \geq \lambda_2 \geq \dots \geq \lambda_M. \quad (11)$$

Values of  $\lambda_i$  do not depend on the choice of the initial condition  $\mathbf{x}(0)$ , insofar as it is chosen randomly in a proper phase-space region.

Computationally, there exist several methods for computing the Lyapunov spectrum from time series (Wolf et al., 1985; Sano and Sawada, 1985; Eckmann and Ruelle, 1985; Eckmann et al., 1986; Iasemidis et al., 1990; Brown et al., 1991). While details of these methods are different, they share the same basic principle. The key is to find approximate Jacobian matrices along a trajectory in the reconstructed,  $m$ -dimensional phase space by using the delay-coordinate embedding technique (Takens, 1981; Sauer et al., 1991). The matrices govern the evolution of infinitesimal vectors in the tangent space. Given a trajectory point  $\mathbf{x}_i$ , a point in a small  $\epsilon$ -neighborhood of  $\mathbf{x}_i$  can be located and how it evolves under dynamics can be monitored, which gives the time evolution of a small vector  $\delta\mathbf{x}_i$  at  $\mathbf{x}_i$  as

$$\delta\mathbf{x}_{i+1} \approx \mathbf{T}(\mathbf{x}_i) \cdot \delta\mathbf{x}_i,$$

where  $\mathbf{T}(\mathbf{x}_i)$  is the  $m \times m$  Jacobian matrix at  $\mathbf{x}_i$ . In order uniquely to determine the matrix,  $m$  independent, orthonormal vectors in the neighborhood of  $\mathbf{x}_i$  are required. Thus, it is necessary to collect a number of points around  $\mathbf{x}_i$ . After the Jacobian matrices are computed, a QR-decomposition procedure can be used to yield the spectrum of Lyapunov exponents (Eckmann and Ruelle, 1985; Eckmann et al., 1986).

Because the Jacobian matrices are meaningful only in the linear neighborhoods of trajectory points, the sizes of the neighborhoods must be small enough to ensure that the dynamics within are approximately linear. While smaller sizes in general can yield more accurate matrices, the length of the time series required will be greater. In particular, in order to have a fixed number of points in a small region, as its size  $\epsilon$  is decreased, the required length of the time series increases. Experience with time series from low-dimensional chaotic systems suggests that  $\epsilon$  should be about a few percent of the size of the attractor. That is, if the time series is normalized to the unit interval, the choice of  $\epsilon$  should be less than 5% (usually between 1% and 5%) but greater than the error due to the digitization precision of the data.

Another issue in the computation of Lyapunov exponents from time series is the inevitable occurrence of the *spurious* exponents. If the invariant set is  $d_0$ -dimensional, and an  $m$ -dimensional embedding space is used ( $m > 2d_0$ ), there will be  $m - d_0$  spurious Lyapunov exponents. For convenience, we call  $\lambda_i^e$  ( $i = 1, \dots, m$ ), all  $m$  exponents computed from time series, the *pseudo-Lyapunov spectrum*. For low-dimensional dynamical systems, *for some specific choice of  $m$* , and in a noise-free case, there are criteria for distinguishing the spurious exponents from the true ones (Sauer et al., 1998; Sauer and Yorke, 1999). For instance, for one-dimensional chaotic maps where there is a positive Lyapunov exponent  $\lambda > 0$ , the  $(m - 1)$  spurious exponents are  $2\lambda, \dots, m\lambda$ . For a two-dimensional map (or equivalently, a three-dimensional flow) where there is a positive and a negative exponent,  $\lambda_1 > 0 > \lambda_2$  and for  $m = 5$ , the pseudo-Lyapunov spectrum is:  $\lambda_1^e \approx 2\lambda_1$ ,  $\lambda_2^e \approx \lambda_1$ ,  $\lambda_3^e \approx \lambda_1 + \lambda_2$ ,  $\lambda_4^e \approx \lambda_2$ , and  $\lambda_5^e \approx 2\lambda_2$ . Unfortunately, at present there are no general criteria for determining the distribution of spurious Lyapunov exponents for an arbitrary system with arbitrary embedding dimension. The existing specific criteria can, however, be used to test whether the algorithm is coded correctly.

### KAPLAN-YORKE FORMULA

There exists a fundamental relation between the fractal dimension and the Lyapunov exponents of a dynamical system, the Kaplan-Yorke formula (Kaplan and Yorke, 1979). The implication is that if the fractal dimension has no predictive power for epileptic seizures, neither do the Lyapunov exponents. It is an elementary notion in non-linear dynamics that the information dimension is an upper bound for the correlation dimension. In typical situations, the values of these two dimensions are close. The information dimension  $D_I$  is conjectured by Kaplan and Yorke, (1979) to be the same as the Lyapunov dimension  $D_L$ , which is defined in terms of the Lyapunov spectrum, as follows:

$$D_L = J + \frac{\sum_{i=1}^J \lambda_i}{|\lambda_{J+1}|}, \quad (12)$$

where  $1 \leq J \leq d$  is an integer that satisfies

$$\sum_{i=1}^J \lambda_i > 0 > \sum_{i=1}^{J+1} \lambda_i.$$

The Kaplan-Yorke conjecture can be shown to be exact for random dynamical systems (e.g. deterministic system under noise) by Ledrappier (1981) and Young (1982). Since there is evidence (Osorio et al., 2001; Lai et al., 2002; Harrison et al., 2005) that  $D_2$  is ineffective for early detection of seizures, Equation (12) suggests that the Lyapunov exponents would not be useful for predicting seizure.

### INABILITY FOR CORRELATION DIMENSION TO PREDICT SEIZURES

#### EFFICIENT METHOD TO COMPUTE CORRELATION DIMENSION

Due to the extraordinarily large amount of clinical ECoG data to be analyzed, it is necessary to develop a computationally efficient method to compute the correlation integral and the dimension. Here we describe the method in Harrison et al. (2005).

For the correlation dimension computation, the quantity of interest is the scaling of the correlation sum with respect to  $\epsilon$ , meaning that the sum needs to be repeated for geometrically spaced values of  $\epsilon$ . Since a point pair within a hypersphere

of radius  $\epsilon_d$  is also within hyperspheres of radius  $\epsilon_{d+n}$ , where  $\epsilon_{d+n} > \epsilon_d$ , the correlation sum can be written as the sum of the fraction of point pairs between consecutive discrete values of  $\epsilon_d$  (Parker and Chua, 1989; Widman et al., 1998). This can be expressed as

$$\begin{aligned}\Delta C(N, d) &= F \sum_{k=W}^{N-1} \sum_{i=1}^{N-k} [\Theta(-\epsilon_{d-1} + \|\mathbf{x}_j - \mathbf{x}_i\|) \Theta(\epsilon_d - \|\mathbf{x}_j - \mathbf{x}_i\|)], \\ C(N, d) &= \sum_{i=1}^d \Delta C(N, i).\end{aligned}\quad (13)$$

For  $\epsilon_d = \epsilon_0 10^{d/r}$ , since  $\Theta(\epsilon_{d-1} - \|\mathbf{x}_j - \mathbf{x}_i\|) = 1$ , the indices of the corresponding  $\Delta C(N, d)$  bin are  $d = \text{int}(r \log_{10} \|\mathbf{x}_j - \mathbf{x}_i\| - r \log_{10} \epsilon_0)$ .

A number of additional improvements can be made to the basic correlation sum algorithm computed with time-delay vectors (Widman et al., 1998). For time-delay embedding, any given coordinate difference may appear in up to  $m$  different positions in point difference vectors. These redundant difference computations can be eliminated by first computing all the coordinate differences, storing them in an array and performing a table lookup to compute the interpoint differences. Additional speed improvement can be made by computing the maximal coordinate distance for each interpoint difference rather than the Euclidean distance. This is equivalent to changing the geometry of hyperspheres to hypercubes. Switching to the maximal norm also enables one to switch the order of operations of the logarithm and the maximum operators, since the logarithm preserves the sequence order of a set of numbers. This means that the logarithm can be performed at the time of the coordinate differences computation.

Application of the correlation sum to prediction requires that it be applied to a finite window  $X_i(j), j = 1, \dots, N$  of time-series data, and then re-applied to following windows  $X_k(j), j = 1, \dots, N$  of the same size, whose starting point is offset from the first  $X_k(1) > X_i(1)$ . To improve temporal resolution in this scheme of sliding windows, there may be overlap between the windows, i.e.  $X_k(j) - X_i(j) < N$ . In this case, some of the coordinate differences may be in common between adjacent windows. The limits of the coordinate difference array is depicted by the outer boundary of the shape shown in Figure 29.1, and the total number of coordinate differences in coordinate difference array  $D$  is

$$N_D = 1/2(N - W)^2 - 1/2(m - 1)^2\tau^2 + 1/2(N - W - (m - 1)\tau).$$

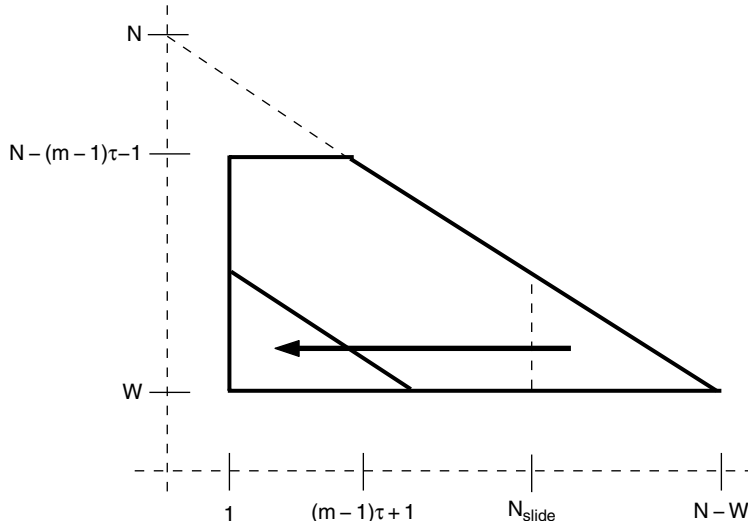


FIGURE 29.1 A schematic of the coordinate difference array. Coordinate differences from the  $i$ th window in the triangle at the right are copied into their corresponding positions into the triangle on the left in the  $(i+1)$ th window. The remainder of the array is filled with the new coordinate differences from the  $(i+1)$ th window.  $N$  is the number of data points per window,  $W$  is the Theiler correction,  $N_{slide}$  is the number of points between the right-hand indices of consecutive windows,  $m$  is the embedding dimension, and  $\tau$  is the delay time.

Let  $X_k(j) - X_i(j) = N_{slide}$ . The points in the coordinate difference array that are in common between the  $X_k$ th and  $X_{k+1}$ th windows are given by

$$[D(i, j), i = N_{slide} + 1, \dots, N - W, j = W, \dots, N - i],$$

which totals

$$N_{Dslide} = 1/2(N - W - N_{slide})(N - W - N_{slide} - 1)$$

points. In the  $X_{k+1}$ th window, the indices of the values correspond to  $[D(i, j), i = 1, \dots, N - W - N_{slide}, j = W, \dots, i]$ . These values are copied into their new positions in the array and only the remaining coordinate differences are recomputed.

### TECHNICAL ISSUES ASSOCIATED WITH COMPUTATION OF CORRELATION DIMENSION

Given a non-stationary time series, such as ECoG, various time-frequency-energy properties of the signal may vary from window to window. To assess the predictive power of the correlation dimension, it is necessary to remove these non-stationary effects prior to computation of the correlation integral-based measures, since these effects are more easily and accurately quantifiable by other measures from traditional statistical analysis. Thus, amplitude normalization is necessary. Another factor is the amount of autocorrelation in the data, which can lead to spurious estimate of the correlation dimension. These two issues will be discussed in relatively more detail. Other issues such as filtering of data in different frequency bands and different embedding schemes for reconstructing the phase space will be mentioned only briefly.

#### Amplitude normalization

The amplitude of an epileptic ECoG signal typically shows visible difference in the ictal phase from those in the inter-ictal and in the post-ictal phase. It has been observed (Osorio et al., 2001; Lai et al., 2002) that even simple changes in the signal amplitude can cause large changes in the correlation integral or dimension. For instance, consider two windows of ECoG recorded from the same subject, one during the inter-ictal state with amplitude  $A_1$ , and the other during a seizure or ictal state with amplitude  $A_2$ , where  $A_2 > A_1$ . The correlation integral depends on the number of point pairs separated by at most a distance  $\epsilon$ . Selecting one arbitrary point  $x_i$ , we draw a sphere of radius  $\epsilon$  around the point and count the number of point pairs enclosed by the sphere. In the inter-ictal window, the points are clustered into a far tighter group than in the seizure window, and the number of points within the *fixed* sphere of radius  $\epsilon$  is higher than that generated by the seizure data. This leads to a decrease in the correlation integral during the seizure relative to the inter-seizure state. If we make the simplistic assumption that the inter-seizure and seizure data are uniformly distributed in  $A_1$  and  $A_2$  respectively, the probability of a point pair being inside a ball of radius  $\epsilon$  is proportional to  $(\epsilon/A_1)^m$  during the inter-ictal period, and to  $(\epsilon/A_2)^m$  during the seizure period. The relative decrease in the correlation integral then would be on the order of  $(A_1/A_2)^m$ . While a realistic ECoG signal is not likely to follow a uniform distribution, it is apparent that the correlation integral is sensitive to changes in the signal amplitude.

For a non-periodic or quasiperiodic signal, there is no standard definition of the signal's amplitude. It is convenient to use rank order statistics to quantify the spread in the data,

$$A = (x_{p_1} - x_{p_2})/2, \quad (14)$$

where  $x$  is a window of the scalar time series, and  $p_1$  and  $p_2$  are percentile values of the ranked time series. If the original, unnormalized coordinate difference array is defined by  $[D = r \log_{10} ||x_i - x_{i+k}||; i = W, N - (m-1)\tau - 1; j = 1, N - i]$ , the amplitude-normalized coordinate difference array is  $D = r \log_{10} ||(x_i - x_{i+k})/A|| + K$ , where  $K$  is a constant identical for all data windows that shifts the coordinate differences back to the approximate dynamical range of the original values, so that they remain integers. For instance, in Harrison et al. (2005),  $K = r10 \log_{10} 2$  is chosen for data with 10 bits of precision. Coordinate differences in common between two adjacent windows due to window overlap can be renormalized as  $D_{j+1} = D_j + \log_{10} A_j - \log_{10} A_{j+1}$ .

For on-line amplitude normalization based on order statistics, each window can be subdivided into sections equal in size to the amount of overlap between windows with an additional section equivalent to the remaining amount for cases where the length of the window is not an integer multiple of the overlap between windows. These subdivisions are stored in a two-dimensional buffer that is circular in one dimension, individually sorted using a quick sort and then merged together with a merge sort. Then, order-statistics can be determined by the position in the ordered list. In this method, at most only two subdivisions need to be resorted in every window, resulting in a great reduction in the number of operations performed.

### Autocorrelation

An appreciable degree of autocorrelation typically arises as a result of oversampling of the data, as first observed in Theiler (1986). He also suggested an effective method to reduce the autocorrelation by removing time-delayed vector points that are too close to each other in the reconstructed phase space. In particular, let  $F_s$  be the sampling rate of the data and  $W$  be an integer threshold called the Theiler correction. Theiler showed that the effect of autocorrelation in the original data on the correlation dimension can be reduced drastically or even eliminated by removing vector points within the time  $t = W/F_s$ . Incorporating this correction and exploiting the fact that  $\|\mathbf{x}_i - \mathbf{x}_j\| = \|\mathbf{x}_j - \mathbf{x}_i\|$  yield the following standard Theiler-corrected form of the correlation sum:

$$C(N, \epsilon) = F \sum_{k=W}^{N-1} \sum_{i=1}^{N-k} \Theta(\epsilon - \|\mathbf{x}_i - \mathbf{x}_{i+k}\|), \quad (15)$$

where  $k = j - i$ , and

$$F = 1 / \left( \sum_{k=W}^{N-1} \sum_{i=1}^{N-k} 1 \right) = 2/(N^2 + N - 2WN - W - W^2).$$

### Filtering of data

The frequency band in which seizure activities typically occur is about 10–40 Hz (Osorio et al., 1998). The issue is thus whether band filtering of the ECoG data can affect the detective or predictive power of the correlation dimension. A detailed data analysis in Harrison et al. (2005) indicates that the finding of the lack of any predictive power of the correlation dimension holds, regardless of the way that the data are filtered.

### Embedding

In addition to time-delay embedding, there are alternate embedding schemes to reconstruct a vector phase space from scalar time series. A question is whether different embedding methods may affect the predictive power of the correlation dimension. Again, an extensive analysis (Harrison et al., 2005) indicates that different embedding schemes have no effect on the finding of the inability for the correlation dimension to predict seizures.

## EVIDENCE FOR LACK OF PREDICTIVE POWER OF CORRELATION DIMENSION FOR SEIZURES

### Data

The database used in Harrison et al. (2005) is as follows. Twenty ECoG data sets (anonymized data from a previous HSC-approved study) are selected from consecutive admissions of subjects with pharmaco-resistant seizures who underwent evaluation for epilepsy surgery at the University of Kansas Comprehensive Epilepsy Center. The data are recorded via depth electrodes (Ad-Tech), implanted stereotactically into the amygdalo-hippocampal region. Correctness of placement is assessed with magnetic resonance imaging (MRI). The signal is sampled at a rate of 240 Hz, amplified, passed through a 0.5–70 Hz analog band-pass filter, and digitized to 10 bits precision with 0.6  $\mu$ V/bit using commercially available devices (Nicolet, Madison WI). The recordings are deemed of good technical quality and suitable for analysis. Data sets are required to be at least 75 hours and no more than 125 hours long for each subject, and to contain a minimum of five seizures. For subjects with data longer than 125 hours, the first 125 hour segment of good quality data containing five typical seizures is chosen. The total number of hours of ECoG analyzed was 2347, with a median of 124 hours (mean 117 hours) per subject.

Seizure scoring is performed using a validated, generic, automated detection method (Osorio et al., 1998, 2002) and confirmed through visual review by an epileptologist, who determines false and true positives, as well as visually scoring electrographic onset times. Because the degree of seizure continuum varies, the discriminating statistic in this automated seizure detection algorithm (SDA) may oscillate above and below the preset, generic detection threshold. This can result in multiple, closely spaced detections that could be counted as separate seizures. To eliminate this complicating factor, detections are clustered together using a temporal criterion of 60 seconds, which is based on the distributions of durations of seizure discontinuities (Osorio et al., 2002).

After clustering, there is a median of 18 seizure detections (mean 48 detections) per subject. For purposes of parameter training and more detailed analysis of the behavior of the methods, a training data set is chosen consisting of 10 five-hour segments of data. Each segment contains at least one typical seizure chosen at random from the time series.

### Evidence of lack of determinism in epileptic ECoG data

After the correlation integral is computed, the  $\log C$  versus  $d$  curves for a systematic set of values of the embedding dimension can be normalized window-by-window for amplitude and the slopes of any linear scaling regions present in the data can be calculated. Figure 29.2A shows the curves for  $m = 1, \dots, 35$  for a typical window of inter-seizure data. In the

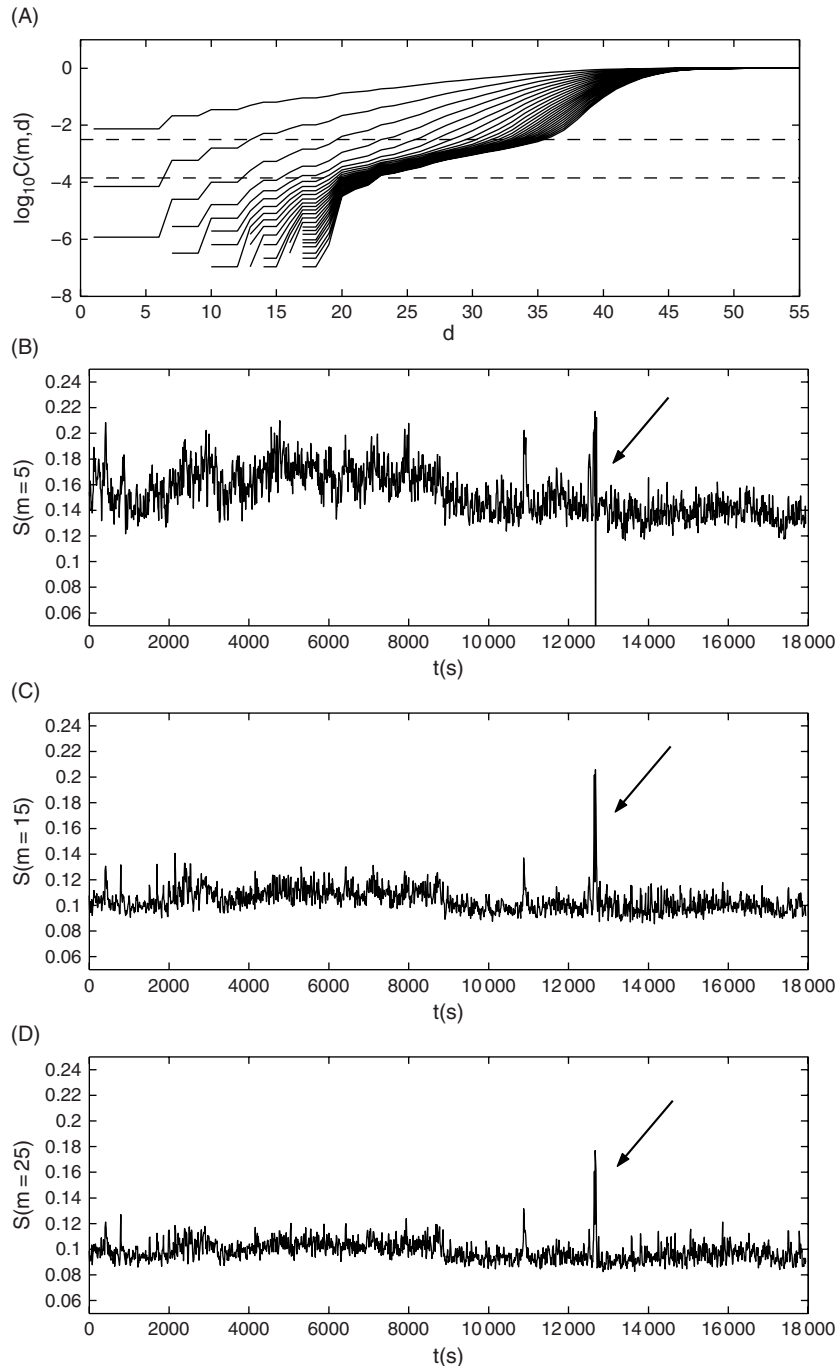


**FIGURE 29.2** (A) Anomalous slope ( $S$ ) of  $\log C(m, d)$  versus length scale parameter  $d$  for embedding dimension  $m = 1, \dots, 35$  for a typical window for inter-seizure data. There is a linear scaling region between the dashed lines. (B) For embedding dimension  $m = 5$ , the slope in the linear scaling region for a 5 hour segment of data with a seizure at  $t = 12675$ . (C) As in (B), but with  $m = 15$ . (D) As in (B), but with  $m = 25$ .

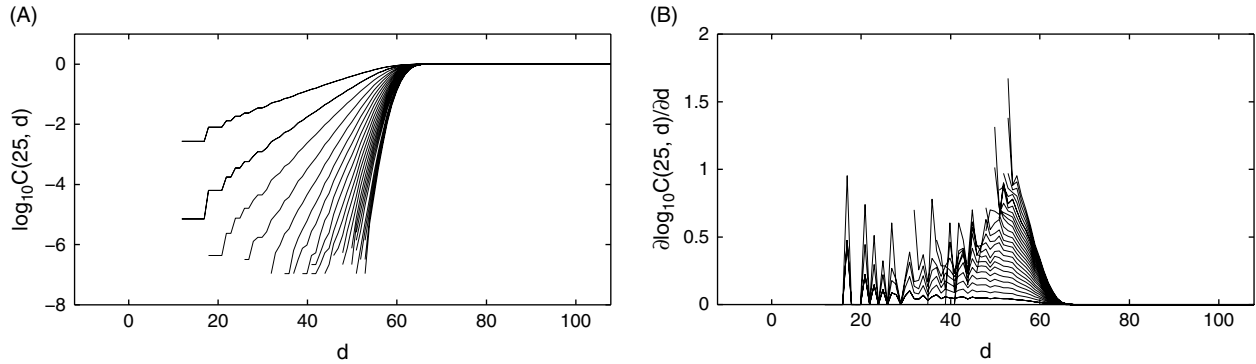


**FIGURE 29.3** (A) For  $m = 1, \dots, 25$ , the  $\log_{10} C$  versus  $d$  curves for a Theiler corrected window and (B) derivatives of the curves in (A), where  $C$  is the correlation integral,  $m$  is the embedding dimension, and  $d$  is a length scale parameter.

region  $\log C = [-3.85, -2.50]$ , the slopes of the curves reach a plateau as the value of  $m$  is increased. In Figure 29.2B–D, values of the slopes  $S$  in this scaling region are plotted for each window for  $m = [5, 15, 25]$ , respectively. A seizure (shown by the arrows) occurs at  $t = 12\,675$  s. The region with a plateau in the correlation dimension would suggest the presence of a low-dimensional, deterministic dynamical component, but this is nothing but an artifact due to the excessive autocorrelation in the data. As we have described, this anomalous scaling region can be eliminated by implementing the Theiler correction (Theiler, 1986), which omits point pairs from the correlation sum that are temporally separated by less than some time  $T$ . In Harrison et al. (2005),  $T$  is chosen to be the first zero of the autocorrelation function. When the correction procedure is performed in this manner, no linear scaling region is apparent up to embedding dimension  $m = 25$ , as is shown in Figure 29.3 for a non-seizure window, where we observe that the slope of the curve (i.e. approximate value of the correlation dimension) increases with the embedding dimension. In addition, the seizure discriminating ability of this window-by-window Theiler corrected method is either greatly reduced or non-existent for all of the training data. These results strongly suggest that the ECoG signals are entirely stochastic and neither the correlation integral nor the correlation dimension has any predictive power for seizures.

### Surrogate analysis

To test the null hypothesis that the observed dynamics of the ECoG are due to a linear Gaussian process, a surrogate data analysis is useful. Since the signal amplitude influences the value of the correlation integrals, it is convenient to choose the amplitude adjusted Fourier transform surrogate (Theiler et al., 1992). This surrogate specifically tests the null hypothesis that the observed time series is a monotonic non-linear transformation of a linear Gaussian process. Given an original scalar time series  $x$  of length  $N$ , one first generates a time series  $y$  also of length  $N$ , consisting of independently generated Gaussian random numbers. Gaussian time series  $y$  is then reordered so that the ranks of the elements match those of the original time series  $x$ . For example, if  $x_i$  is the  $p$ th largest value in  $x$ ,  $y$  is reordered so that  $y_i$  is the  $p$ th largest value in  $y$ . The Fourier transform is performed on  $y$ , and the phases are randomized by multiplying each complex amplitude by  $e^{i\phi}$ , where  $\phi$  is chosen uniformly and randomly from the interval  $[0, 2\pi]$ . Then, the inverse Fourier transform is taken to produce  $y'$ , and  $x$  is reordered so that the ranks of its elements match those of  $y'$ . This surrogate time series has the same amplitude distribution as the original time series.

A systematic approach to addressing whether the non-linear or the time-energy-frequency properties of the signal contribute to the predictability or detectability of seizures is to compute surrogate data window-by-window. The correlation integrals can then be computed for each window and be compared with the correlation integrals computed on the original data. Figure 29.4A depicts for one subject, the time series of the correlation dimension timelocked for a one hour segment containing two seizures (indicated by arrows). Figure 29.4B shows the same from the surrogate time series of the same data. Surrogate and original  $D_2$  time series are shown overlaid for  $m = 20$  in Figure 29.4C. The seizure discriminating ability is roughly the same in the surrogate and original time series for one seizure and is actually improved in the surrogate time series for the other seizure. No predictive ability is apparent in either. Since the seizure detection ability was preserved in the surrogate time series, the implication is that it is the time-frequency-energy properties of the signal that are responsible for the measure's seizure discriminating ability, not the lower-level dynamics of the brain.

Validation analysis on long ECoG time series yields the same finding (Harrison et al., 2005).

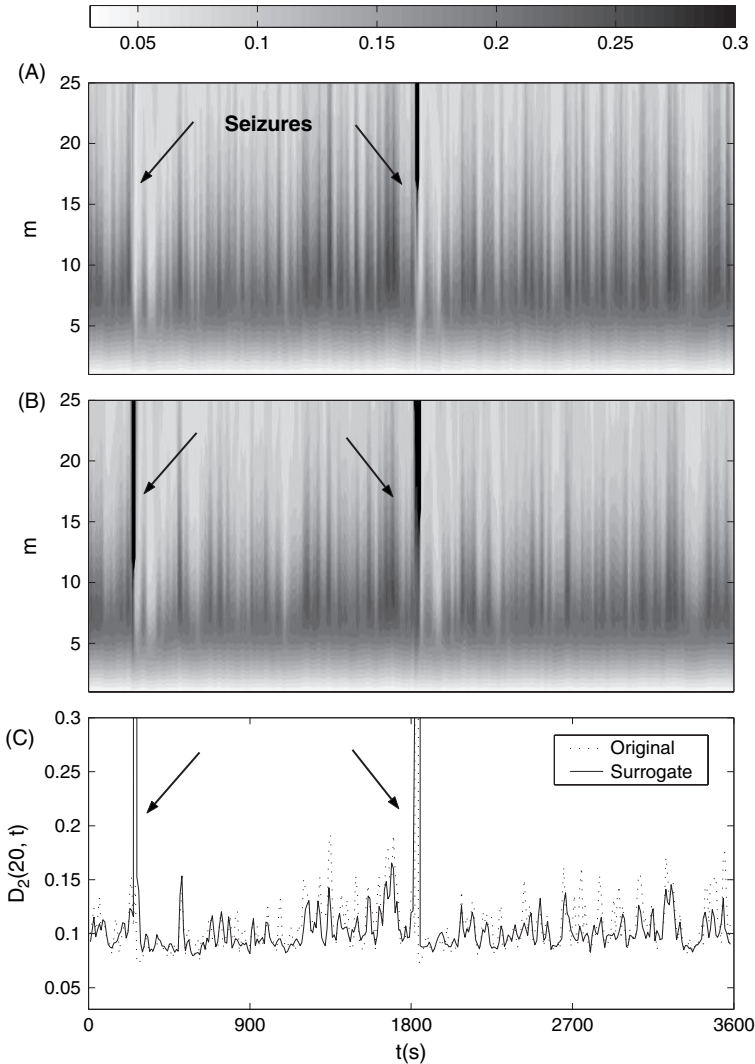


**FIGURE 29.4** For a 1-hour segment of data with two seizures taken from one subject 3, (A) the time series of correlation dimension  $D_2(m)$  for the original data, (B) the time series of  $D_2(m)$  for the surrogate data, and (C) a single time series at embedding dimension  $m = 20$  of the original and surrogate data, overlaid on the same axis. Since the seizure detection ability is approximately the same or is actually somewhat improved for the surrogate data versus the original, the implication is that the time-frequency-energy properties of the signal are what detects the seizure, rather than any possible change in the dynamical structure of the signal. Seizures occur at approximately 250 s and 1820 s.

#### LYAPUNOV EXPONENTS DO NOT PREDICT EPILEPTIC SEIZURES

In general, the Lyapunov exponents are more difficult to calculate from time series than the correlation dimension. They are also quite sensitive to noise. While the exponents can be defined for a finite-dimensional dynamical system, for a stochastic system their meaning is not as clear because, in principle, their number is infinite. A practical consequence is that, from a finite time series, the values of the exponents estimated from a finite-dimensional reconstructed phase space may depend on the length of the time series. For instance, for EEG or ECoG analysis, using moving windows of different length may yield different estimated values for the exponents. The consideration applies, of course, to all exponents including the maximum Lyapunov exponent, the one that current literature of seizure prediction focuses on (Iasemidis et al., 1990, 2001, 2003a,b; Iasemidis and Sackellares, 1991). As the EEG or ECoG time series are mostly stochastic, as well as non-stationary, using the exponents (or the maximum exponent) for detection or prediction does not seem to be sensible.

Suppose one insists on using the Lyapunov exponents to predict seizure. The question concerning the predictive power of the exponents must be addressed. Intuitively, since there is strong evidence that the correlation dimension has no predictive power for seizure (Harrison et al., 2005), the Kaplan-Yorke formula stipulates a fundamental lack of the predictive power for the exponents. A systematic way to address the predictive-power issue is to conduct a control study. That is, one can construct a ‘simple’ yet non-trivial dynamical system for which the behavior of the Lyapunov exponents is known and test the predictive power of the exponents calculated from moving-window time series. For this purpose, the control system should be non-stationary, noisy and exhibit a critical bifurcation at some time, after which the behavior of the system is characteristically different (to mimic a seizure). This approach has been taken recently (Lai et al., 2003, 2004, 2005). In particular, a two-dimensional chaotic map with a time-varying parameter  $p(t)$  has been constructed. The system is thus non-stationary and the range of the parameter variation is designed to contain a crisis at which the chaotic attractor suddenly increases its size. Assuming that starting from an initial value  $p_0$  the parameter varies slowly with time and passes through the critical point  $p_c$  at a later time and eventually comes back to  $p_0$ . A typical time series thus consists of segments of small-amplitude chaotic oscillations for  $p < p_c$  and a segment of large-amplitude oscillations for  $p \geq p_c$ , mimicking EEG or ECoG signals containing a seizure. Lyapunov exponents are then computed from a moving window over the time series to test whether the system change at  $p = p_c$  reflects itself in the computed time-varying exponents and whether this gradual parameter drift can be detected in advance of the crisis in order to predict the impending crisis event. Analysis and computations (Lai et al., 2003, 2004, 2005) indicate that there are two major factors that can prevent the exponents from being effective to predict characteristic system changes: statistical fluctuations and noise. As can be expected intuitively, even for low-dimensional, deterministic chaotic systems, the power of the Lyapunov exponents to detect parameter drift into crisis holds only in noiseless or extremely low-noise situations. In a realistic situation, especially in a system as high-dimensional and noisy as the brain, it appears unlikely that the Lyapunov exponents can be useful for predicting or even detecting epileptic seizures. All these factors suggest that the Lyapunov exponent should *never* be the choice for seizure prediction.

In the following, we shall review the main idea and finding of the control study for the predictive power of the Lyapunov exponents.

## CONTROL MODEL USING DISCRETE-TIME MAPS

### Model description

In Lai et al. (2003, 2004, 2005), the following IHJM (Ikeda-Hammel-Jones-Moloney) map (Ikeda, 1979; Hammel et al., 1985) is chosen, which is a paradigmatic model of low-dimensional chaotic systems:

$$z_{n+1} = A + Bz_n \exp \left[ ik - \frac{ip}{1 + |z_n|^2} \right], \quad (16)$$

where  $z \equiv x + iy$  is a complex dynamical variable, and  $A$ ,  $B$ ,  $k$  and  $p$  are parameters. To be concrete the first three parameters are set to be  $A = 0.85$ ,  $B = 0.9$  and  $k = 0.4$  (somewhat arbitrary), and  $p$  is assumed to vary with time. To mimic ECoG data with seizure (Nagai and Lai, 1995),  $p$  is chosen from an interval about the nominal value  $p_c \approx 7.27$ , at which there is an interior crisis (Grebogi et al., 1983). Specifically, for  $p \lesssim p_c$ , there is chaotic attractor of relatively small size in the phase space. At  $p = p_c$ , the small attractor collides with a pre-existing, non-attracting chaotic set (chaotic saddle) (Lai et al., 1993) to form a larger attractor. For  $p \gtrsim p_c$ , a trajectory spends most its time in the phase-space region where the original small attractor resides, with occasional visits to the region in which the original chaotic saddle lies. A typical time series then consists of chaotic behavior of smaller amplitude most of the time, with occasional, randomly occurring bursts of relatively larger amplitude. Assume  $p_0 \lesssim p_c$ , so that the system is in a pre-crisis state but it is about to undergo a crisis. Then, the parameter changes through the critical value  $p_c$ , after sometime it comes back to the original, pre-crisis value  $p_0$ . During the time interval in which the parameter changes, we expect to observe characteristically different behavior (e.g. random motion of larger amplitude). To be concrete, for the IHJM map we choose a time interval of 50 000 iterations, and assume the following variation of the parameter  $p$ :

$$p_n = \begin{cases} p_0, & n < t_i = 20000 \\ p_0 + n(p_1 - p_0)/5000, & t_i \leq n < t_m = 25000 \\ p_1 - n(p_1 - p_0)/5000, & t_m \leq n < t_f = 30000 \\ p_0, & n > t_f, \end{cases} \quad (17)$$

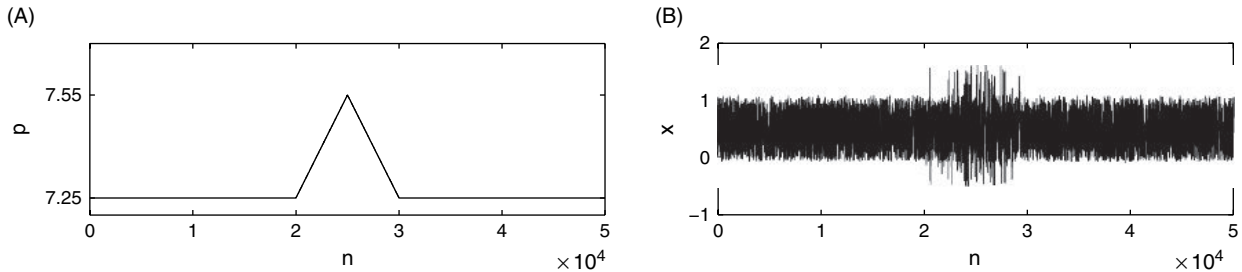


**FIGURE 29.5** For the IHJM map in Equation (16), (A) parameter variation as described by Equation (17) and (B) a typical time series which mimics a segment of ECoG data with a seizure.

where  $p_0 = 7.25$  and  $p_1 = 7.55$ , as shown in Figure 29.5A. A typical time series  $\{x_n\}$  is shown in Figure 29.5B, where we see a different behavior for  $20000 < n \leq 30000$  during which the parameter variation occurs. The time series in Figure 29.5B mimics a segment of ECoG data with a seizure. The average values of the two Lyapunov exponents in this ‘ictal’ phase are  $\lambda_1 \approx 0.42$  and  $\lambda_2 \approx -0.63$ .

### Can detectability be improved by increasing moving-window size?

A fundamental difficulty with Lyapunov exponents is that they, when computed in finite time, typically exhibit fluctuations even if the system equations are available. The situation becomes worse when the exponents are evaluated using finite time series in the presence of noise. One might hope to reduce the statistical fluctuations to enhance the detectability by increasing the length of the time series, or the size of the moving window. Unfortunately, the following reasoning and numerical evidence indicate that this is not the case.

If the number  $N$  of data points in the moving window is small, the computed pseudo-Lyapunov exponents will have large fluctuations, as exemplified in Figure 29.6A–F for  $m = 5$  and  $N = 630$ , where Figure 29.6A shows the non-stationary time series and Figure 29.6B–F are the evolutions of  $\lambda_i^e$  ( $i = 1, \dots, m$ ). Comparing with the asymptotic values of the two Lyapunov exponents ( $\lambda_1 \approx 0.42$  and  $\lambda_2 \approx -0.63$ ), the second and the fourth ( $\lambda_2^e$  and  $\lambda_4^e$ ) are approximately the true exponents, while the remaining are spurious ones. The vertical dashed line indicates  $t_i$ , the time when the control parameter  $p$  starts to change. The parameter change is somewhat reflected in  $\lambda_1^e$ . For the average change in  $\lambda_1^e$  to be

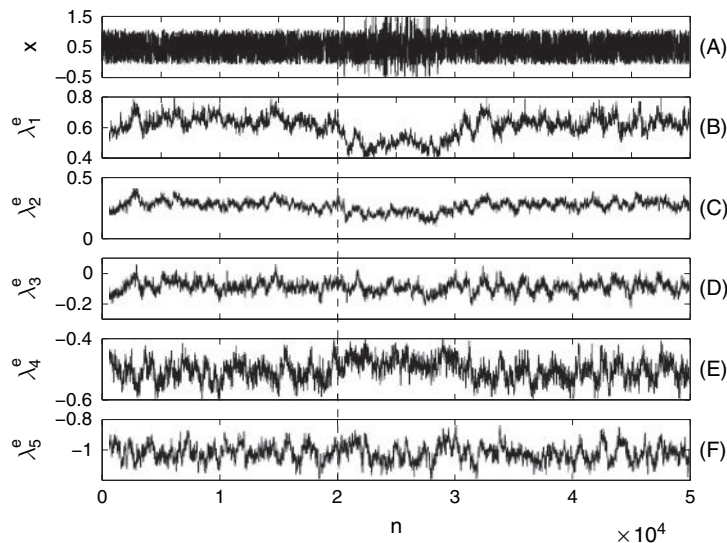


**FIGURE 29.6** For the IHJM map in Equation (16),  $m = 5$  and  $N = 630$ , (A) non-stationary time series, (B–F) temporal evolution of  $\lambda_i^e$  for  $i = 1, \dots, 5$ , respectively.

statistically significant, where the change should be greater than the average amount of fluctuation, the time required is about  $\Delta t_1 \approx 700$  after  $t_i$  for  $\lambda_1^e$ . One question is whether increasing  $N$  would help reduce  $\Delta t$ .

Consider the situation where  $N$  is large. Given this finite time  $N$ , one can imagine choosing a large number of initial conditions and computing the Lyapunov spectra for all the resulting trajectories of length  $N$ . The exponents computed in finite time are effectively random variables whose histograms can be constructed. For trajectories on a chaotic attractor, the typical distribution of a finite-time Lyapunov exponent  $\lambda_N$  is (Ott, 2002)

$$P(\lambda_N, N) \approx \left[ \frac{NG''(\bar{\lambda})}{2\pi} \right]^{1/2} \exp \left[ -\frac{N}{2} G''(\bar{\lambda})(\lambda - \bar{\lambda})^2 \right], \quad (18)$$

where  $\bar{\lambda}$  is the asymptotic value of  $\lambda_N$  in the limit  $N \rightarrow \infty$ , and  $G(x)$  is a function satisfying  $G(\bar{\lambda}) = 0$ ,  $G'(\bar{\lambda}) = 0$ , and  $G''(\bar{\lambda}) > 0$ . For large  $N$ , the standard deviation of  $\lambda_N$  is

$$\sigma_{\lambda_N} \sim \frac{1}{\sqrt{N}}. \quad (19)$$

If the moving time window is located completely in  $t < t_i$ , the average Lyapunov exponent is

$$\lambda_N = \frac{1}{N} \sum_{i=1}^N \lambda^{(1)}(i), \quad (20)$$

where  $\lambda^{(1)}(i)$  is the time-one Lyapunov exponent for  $t < t_i$ . Now consider a moving time window across the critical time  $t_i$ , where  $N_1$  points are before  $t_i$ ,  $N_2$  points are after, and  $N_1 + N_2 = N$ . The computed exponent is

$$\lambda'_N = \frac{1}{N} \left[ \sum_{i=1}^{N_1} \lambda^{(1)}(i) + \sum_{i=1}^{N_2} \lambda^{(2)}(i) \right], \quad (21)$$

where  $\lambda^{(2)}(i)$  is the time-one Lyapunov exponent for  $t > t_i$ . Let  $\bar{\lambda}^{(1)}$  and  $\bar{\lambda}^{(2)}$  be the asymptotic values of the Lyapunov exponent for  $t < t_i$  and  $t > t_i$ , respectively. If  $N_1 \gg 1$ ,  $N_2 \gg 1$ ,  $N_1 \sim N$ , and  $N_2 \sim N$ , one gets

$$\begin{aligned} \sum_{i=1}^N \lambda^{(1)}(i) &= N\bar{\lambda}^{(1)} + \mathcal{O}(1/\sqrt{N}), \\ \sum_{i=1}^{N_1} \lambda^{(1)}(i) &= N_1\bar{\lambda}^{(1)} + \mathcal{O}(1/\sqrt{N_1}) \approx N_1\bar{\lambda}^{(1)} + \mathcal{O}(1/\sqrt{N}), \\ \sum_{i=1}^{N_2} \lambda^{(2)}(i) &= N_2\bar{\lambda}^{(2)} + \mathcal{O}(1/\sqrt{N_2}) \approx N_2\bar{\lambda}^{(2)} + \mathcal{O}(1/\sqrt{N}), \end{aligned} \quad (22)$$

where  $\mathcal{O}(1/\sqrt{N})$  is a number on the order of  $1/\sqrt{N}$ . The change in the computed time- $N$  exponent is thus

$$\begin{aligned} \Delta\lambda_N = \lambda_N - \lambda'_N &\approx \frac{1}{N} [N\bar{\lambda}^{(1)} - N_1\bar{\lambda}^{(1)} - N_2\bar{\lambda}^{(2)}] \\ &+ \mathcal{O}(1/\sqrt{N}) = \frac{N_2}{N} (\bar{\lambda}^{(1)} - \bar{\lambda}^{(2)}) + \mathcal{O}(1/\sqrt{N}) \sim \frac{N_2}{N}. \end{aligned} \quad (23)$$

For the change in the Lyapunov exponent to be statistically significant and thus detectable, we require  $\Delta\lambda_N \gtrsim \sigma_{\lambda_N}$ , which gives the time required to detect the change,

$$\Delta t = N_2 \gtrsim \sqrt{N}. \quad (24)$$

Thus, increasing the size of the moving window in fact causes an increase in the time required to detect a change in the Lyapunov exponent. The increase is, however, incremental as compared to the increase in  $N$  and therefore may not be easily observed. In numerical experiments, no apparent decrease in  $\Delta t$  is observed (Lai et al., 2004) with increasing  $N$ . In particular, as  $N$  is increased, the level of fluctuations in the Lyapunov exponents is reduced but the detection time is not reduced.

### Predictive power of Lyapunov exponents

Imagine that the onset of seizure corresponds to the transition of the system through a critical state. In order to be able to predict the seizure in advance, it may be assumed that the state of system undergoes slow changes before seizure onset. The question is whether any state change before the critical point (onset of the seizure) can be detected through the pseudo-Lyapunov exponents. Motivated by this, the following situation has been considered (Lai et al., 2003; 2004). Say a critical event occurs in which the system bifurcates to a characteristically different state. However, before the event, the parameter changes smoothly toward the critical bifurcation, although perhaps not at the same rate as that at which it passes through the critical point. For example, the scheme of parameter change as shown in Figure 29.7A can be considered, where initially the parameter  $p$  is fixed at a constant value ( $p = 7.1$ ) below the critical point  $p_c$ . As  $p$  passes through  $p_c$  at about  $n \gtrsim 20000$ , a critical event (interior crisis) occurs. Before this,  $p$  is assumed to change at a slower rate for  $10000 < n < 20000$ . The entire time interval of interest is taken to be 40 000 iterations. If the time series before the critical point is measured, there is no apparent characteristic change, despite the slow change in parameter, as shown in Figure 29.7B. This setting represents an appropriate test bed for the predictive power of pseudo-Lyapunov exponents.

When  $N$  is small, the large fluctuations in the exponents render undetectable the slow parameter changes preceding the onset of crisis. This indicates that the crisis cannot be predicted when  $N$  is small. As  $N$  is increased, the fluctuations are reduced so that the system change preceding the crisis can be detected, as shown in the behaviors of  $\lambda_i^e$  in Figure 29.8(B–F), respectively, for  $m = 5$  and  $N = 3981$ . The change indeed can be detected at time  $n \gtrsim 10000$ , which precedes the crisis. *While this seems to indicate that the exponents have the predictive power for crisis, we find that the presence of small noise can wipe out this power completely.*

To simulate noise, terms  $D\xi_n^x$  and  $D\xi_n^y$  can be added to the  $x$ - and  $y$ -equations of the IHJM map, where  $D$  is the noise amplitude, and  $\xi_n^x$  and  $\xi_n^y$  are independent random variables uniformly distributed in  $[-1, 1]$ . Figure 29.9(B–F) and 29.10(B–F) show, for  $m = 5$  and  $N = 3981$ , the temporal evolutions of the five pseudo-Lyapunov exponents for  $D = 10^{-2.0}$  and  $D = 10^{-1.0}$ , respectively. Note that the range of the time series from the IHJM map is about 2.0, so these noise levels roughly correspond to 0.5% and 5% of the variation of the dynamical variable, which can be considered as small. There is a progressive deterioration of the predictive power of the exponents, as the parameter change preceding the crisis can no longer be detected at the noise level of about  $D = 10^{-2.0}$ . For relatively larger noise [ $D = 10^{-1.0}$  in Figure 29.10(B–F)], even the critical event (crisis) itself cannot be detected through the variation of these exponents. These results suggest that, in practical situations where small noise is inevitable, one should not expect the Lyapunov exponents computed from time series to have any predictive power, as it appears unlikely that their variations are statistically significant enough to allow for detection of system change preceding a critical event.

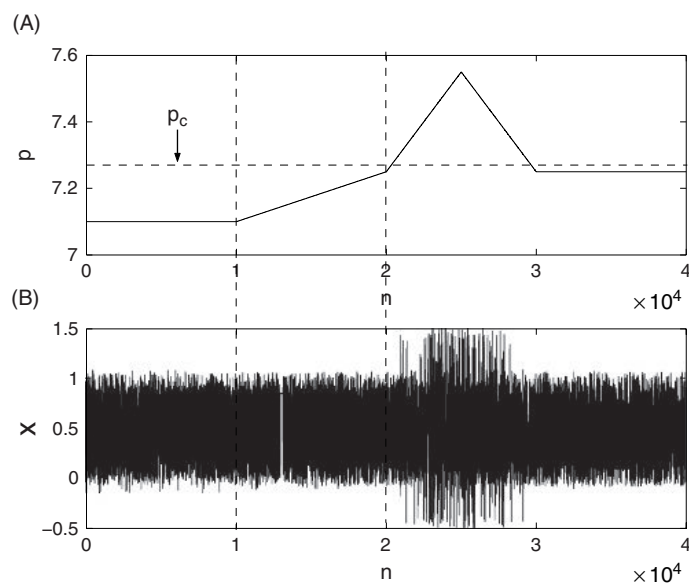


**FIGURE 29.7** Testing scheme for assessing the predictive power for critical event of Lyapunov exponents from time series, utilizing the IHJM map. (A) Parameter variation with time, where it changes slowly before the interior-crisis point and (B) a typical time series that shows no characteristic change before the crisis, despite the parameter change.

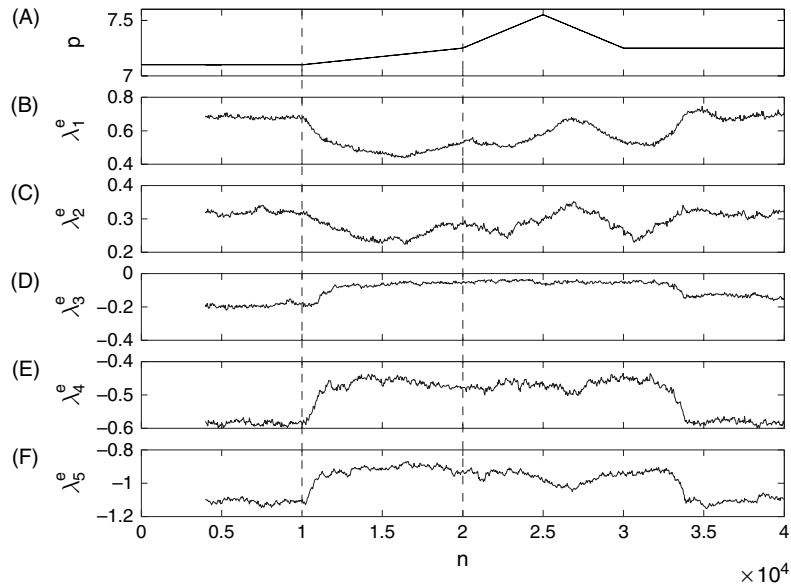


**FIGURE 29.8** (A) Scheme of parameter variation with time. (B–F) Temporal evolutions of  $\lambda_i^e$  ( $i = 1, \dots, 5$ ) for  $m = 5$  and  $N = 3981$ , in the absence of noise. In this case, the parameter change preceding the crisis can be detected through the pseudo-Lyapunov exponents.

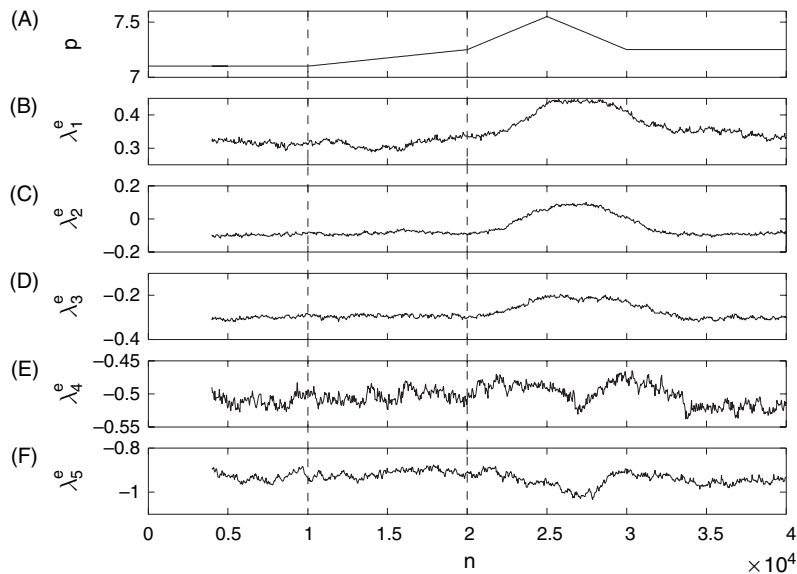


**FIGURE 29.9** (A) Scheme of parameter variation with time, (B–F) temporal evolutions of  $\lambda_i^e$  ( $i = 1, \dots, 5$ ) for  $m = 5$ ,  $N = 3981$ , and noise amplitude  $D = 10^{-2.0}$  (corresponding to about 0.5% of the amplitude of the measured data). At this noise level the crisis cannot be predicted in advance because the parameter change preceding the crisis cannot be detected.

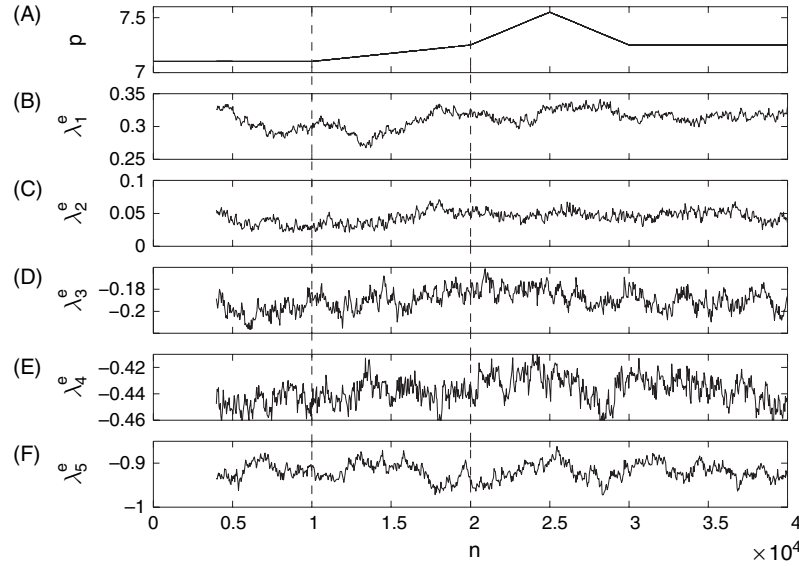


FIGURE 29.10 (A) Scheme of parameter variation with time, (B–F) temporal evolutions of  $\lambda_i^e$  ( $i = 1, \dots, 5$ ) for  $m = 5$ ,  $N = 3981$  and noise amplitude  $D = 10^{-1.0}$ . At this noise level, which is about 5% of the amplitude of the measured time series, even the crisis itself cannot be detected through the exponents.

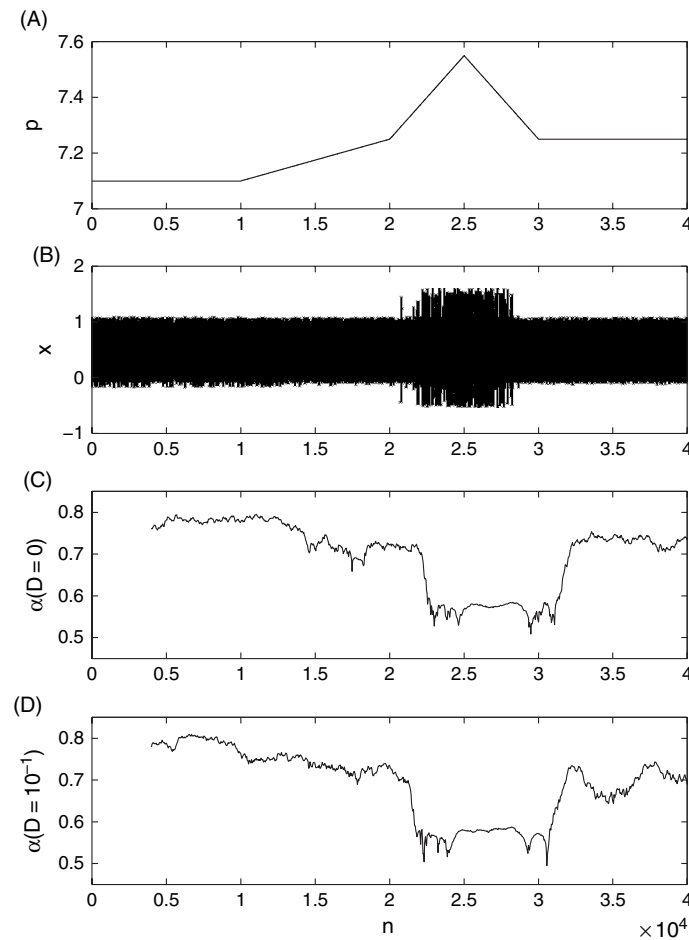


FIGURE 29.11 (A) Parameter variation in time, (B) time series of  $x$  in the absence of noise ( $D = 0$ ), (C) plot of  $\alpha$  computed in 4000 point windows, overlapped by 3960 points computed on the time series in (B), (D) the same as in (C) except that there is a noise of amplitude  $D = 10^{-1}$ .

### Comparison with autocorrelation

To provide a means for comparison of the Lyapunov exponents' predictive abilities, from time series  $x(t)$  an approximation of the decay of the autocorrelation envelope can be computed (Theiler, 1986),

$$\alpha = \frac{1}{M} \sum_{k=1}^M |R_k|^{1/k}, \quad (25)$$

where

$$R_\tau = \frac{\sum x(t)x(t+\tau)}{\sqrt{\sum x^2(t) \sum x^2(t+\tau)}}, \quad (26)$$

and  $M = 6$ . Using the same model as in Figure 29.7,  $\alpha$  has been computed (Lai et al., 2004) on sliding windows of length 4000 points with an overlap of 3960 points. The noise-free case is shown in Figure 29.11C. Both the parameter drift preceding the crisis and the crisis itself are clearly visible in the  $\alpha$  time series. In contrast to the Lyapunov exponents, the autocorrelation's ability to detect this drift appears robust even under moderate noise ( $D = 10^{-1}$ , or 5%), as shown in Figure 29.11D. For this noise value, the Lyapunov spectrum could not even detect the crisis as shown in Figure 29.10.

A comparison has been made between the detectability of the autocorrelation and the correlation dimension (Lai et al., 2002), with the result that the two measures tend to track each other in seizure, though neither demonstrated any predictive ability. Before and after the seizure, the value of the correlation dimension is approximately constant, but it fluctuates significantly during the seizure, due to a dramatic loss and gain of the autocorrelation, alternating in time. The implication, as in the present case, is that traditional analyses of stochastic processes or linear time-frequency analyses may be as effective (if not more effective) for seizure analysis with ECoG signals.

## CONTROL MODEL BASED ON CONTINUOUS-TIME FLOWS

### Model description

For a continuous-time system described by differential equations, the nature of bifurcation is an issue of concern. In particular, in the discrete-time map model, the critical event used to model seizure is interior crisis, which is a global bifurcation. One might argue that epileptic seizures may be a local bifurcation. Indeed, for an interior crisis, the properties of the attractor before the bifurcation are generally not affected by the fact that the crisis will happen. In addition, the sensitivity of the dynamical invariants of the attractor such as the dimensions, Lyapunov exponents, and entropies to the control parameter is about the same in the parameter regime before the crisis. For a local bifurcation, for instance, a Hopf bifurcation at which a stable steady state becomes unstable and a stable limit cycle is born, the Lyapunov exponent may be a stronger indicator for the bifurcation. To address these issues, we now consider a continuous-time model with a Hopf bifurcation and investigate the sensitivity of Lyapunov exponents to parameter changes in the presence of noise (Lai et al., 2004).

A convenient model for control study (Lai et al., 2004) is the following two-dimensional system for Hopf bifurcation, under white noise of amplitude  $D$ :

$$\begin{aligned} \frac{dx}{dt} &= -y + x[a(t) - x^2 - y^2] + D\xi_1(t), \\ \frac{dy}{dt} &= x + y[a(t) - x^2 - y^2] + D\xi_2(t), \end{aligned} \quad (27)$$

where  $a(t)$  is a control parameter that can vary with time and  $\xi_1(t)$  and  $\xi_2(t)$  are independent Gaussian random variables of zero mean and unit variance with the following properties:  $\langle \xi_1(t)\xi_1(t') \rangle = \delta(t-t')$ ,  $\langle \xi_2(t)\xi_2(t') \rangle = \delta(t-t')$ , and  $\langle \xi_1(t)\xi_2(t') \rangle = 0$ . When  $a(t)$  is constant, the stochastic processes  $x(t)$  and  $y(t)$  are stationary; otherwise they are non-stationary. For the deterministic system ( $D = 0$ ), if  $a < 0$ , the attractor of the system is a steady state defined by  $x = 0$  and  $y = 0$ . The Hopf bifurcation occurs at  $a_c = 0$  where for  $a > 0$ , the steady state becomes unstable and a limit-cycle attractor, given by  $x(t) = a \cos t$  and  $y(t) = a \sin t$ , becomes stable. The period of the oscillation ( $T_0 \equiv 2\pi$ ) thus defines the natural time scale of the system. To mimic a seizure, a time interval of 9000 cycles of oscillation is examined (Lai et al., 2004), which corresponds to actual time of  $T = 9000T_0$ , and this time is divided into three intervals:  $(0, T_1)$ ,  $(T_1, T_2)$ , and

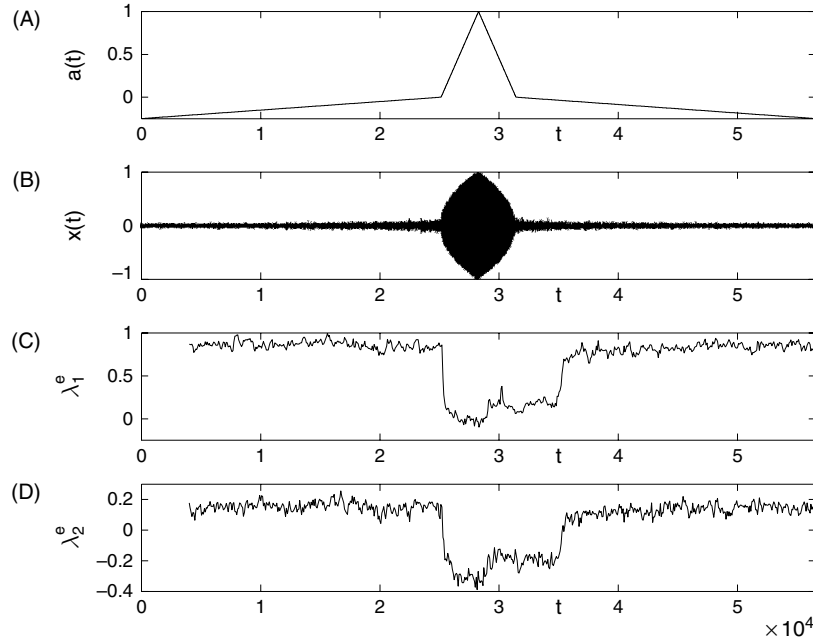


**FIGURE 29.12** For the non-stationary, continuous-time model Equation (27) with a local Hopf bifurcation under noise of amplitude  $D = 0.01$ , (A) the parameter variation, (B) the noisy time series  $x(t)$ , (C,D) the first two Lyapunov exponents computed from moving window over the time series, which appear to be able to detect the bifurcation.

$(T_2, T)$ . The parameter variations in these intervals are chosen such that in the first and third intervals the attractor of the system is the steady state ( $x = 0$  and  $y = 0$ ) but, in the middle interval, the attractor is the limit-cycle oscillator, as follows:

$$a(t) = \begin{cases} a_0 + (a_1 - a_0)t/T_1 & \text{for } 0 < t < T_1, \\ a_1 + 2(a_2 - a_1)(t - T_1)/(T_2 - T_1) & \text{for } T_1 < t < T_1 + (T_2 - T_1)/2, \\ a_2 - 2(a_2 - a_1)[t - T_1 - (T_2 - T_1)/2]/(T_2 - T_1) & \text{for } T_1 + (T_2 - T_1)/2 < t < T_2, \\ a_1 - (a_1 - a_0)(t - T_2)/(T - T_2) & \text{for } T_2 < t < T, \end{cases} \quad (28)$$

as shown in Figure 29.12A for  $a_0 = -0.25$ ,  $a_1 = 0.0$ ,  $a_2 = 1.0$ ,  $T_1 = 4000T_0$ , and  $T_2 = 5000T_0$ . A typical time series from this non-stationary system is shown in Figure 29.12B, where the noise amplitude is  $D = 10^{-2}$ . Analogous to the terms of epilepsy, the three intervals of time can be conveniently called pre-ictal, ictal and post-ictal phases, respectively. For the stationary system [ $a(t) = a = \text{constant}$ ], the theoretical values of the two Lyapunov exponents for  $a < 0$  are  $\lambda_1 = \lambda_2 = a < 0$ . After the limit-cycle attractor is born via the Hopf bifurcation at  $a_c$ , the exponents are  $\lambda_1 = 0$  and  $\lambda_2 = -2a < 0$ . Thus, for the non-stationary system as in Figure 29.12A and 29.12B, the theoretical value of the largest Lyapunov exponent is negative for the pre-ictal and post-ictal phases, while it is zero for the ictal phase.

#### Lack of predictive power of Lyapunov exponents for local bifurcation

To obtain time series from the model Equation (27), the standard second-order, Heun's method for solving stochastic differential equations (Kloeden and Platen, 1992) can be used. For the system in Figure 29.12A and B, the step size can be chosen to be  $h = 0.01$  in numerical integration and time series  $x(t)$  [or  $y(t)$ ] can be generated using the sampling interval of  $t_s = 40 h$ , corresponding to approximately 16 points per oscillating period. Lyapunov exponents are then computed from the time series using a moving time window of width  $\Delta t \approx 636T_0$ , spaced at  $t_w \approx 12.7T_0$ . The delay time used (Lai et al., 2004) is  $\tau \approx 0.95T_0$  (approximately one cycle of the natural oscillation) and the embedding dimension is chosen to be  $m = 3$  (considering that the steady-state and limit-cycle attractors are only zero- and one-dimensional, respectively). Due to noise, for the pre-ictal and post-ictal phases, the first two Lyapunov exponents from the moving windows are positive, which are spurious, as shown in Figure 29.12C and D. However, as indicated in these plots, in the ictal phase where, theoretically, the largest exponent is zero, the algorithm seems to be able to capture the correct value. There is thus a relatively sharp change in the estimated value of the exponents shortly after the onset of the ictal phase, indicating that the exponents are

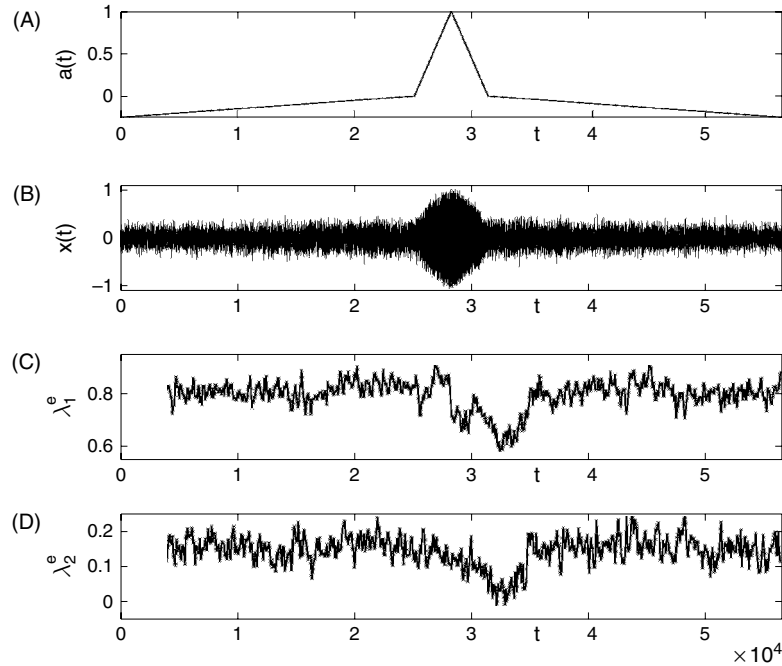


**FIGURE 29.13** (A–D) The same as in Figure 29.12(A–D), respectively, except that the noise level is now  $D = 0.1$ . The ability for the Lyapunov exponents to detect even this local bifurcation apparently deteriorates as compared with the case of lower noise in Figure 29.12.

capable of detecting the local, Hopf bifurcation in spite of the presence of noise. Note that, however, the noise level for Figure 29.12C and D are relatively small: about 1% of the amplitude of the oscillation in the ictal phase. As the time series becomes more noisy, as shown in Figure 29.13B for  $D = 0.1$  (about 10% of the oscillation in the ictal phase), the ability for the Lyapunov exponents to detect even this local bifurcation deteriorates, as shown in Figure 29.13C and D.

These results thus demonstrate that Lyapunov exponents from time series are capable of detecting simple, local bifurcations in the presence of noise. Nonetheless, this task of detection can also be accomplished by using measures from traditional stochastic analysis such as the autocorrelation. Taking into account the computational complexity, Lyapunov exponents are arguably disadvantageous for detection. On the other hand, ECoG signals typically come from a large number of neurons (approximately  $10^5$ – $10^8$  (Nunez, 1995). It may not be suitable to regard epileptic seizures as being caused by some local bifurcations. This again suggests that Lyapunov exponents are not useful for predicting or detecting seizures.

#### TESTS USING ECoG DATA

When computing the pseudo-Lyapunov exponents from epileptic ECoG time series, there are several computational parameters that can affect the results. These are: the length  $N$  of the moving window, the embedding dimension  $m$ , the delay time  $\tau$  and the size  $\epsilon$  of the linear neighborhood. Usually, the computed exponents are relatively robust against variations in  $\tau$  and  $\epsilon$ , insofar as they are chosen properly. The choice of the delay time  $\tau$  is quite straightforward. Given an ECoG signal  $x(t)$ , one chooses  $\tau$  such that  $R_\tau = 1/e$  (Theiler, 1986). For the available ECoG data,  $\tau = 1/12$  (seconds) is chosen. For  $\epsilon$ , computational results vary little when it is chosen to be around 0.02 (2% of the amplitude of the ECoG signal). It is thus convenient to fix  $\epsilon = 0.02$ . In Lai et al. (2004), the effects of varying the key parameters,  $N$  and  $m$ , have been examined.

Figure 29.14A shows, for  $m = 5$ , the segment of ECoG time series of 600 seconds containing a seizure, occurring at  $t \approx 300$  (seconds). Figure 29.14B–F shows, for a moving window of length  $\Delta t \approx 4.17$  seconds (corresponding to  $N = 1000$  data points), the five computed Lyapunov exponents versus time, where the time is recorded at the end of the window. All exponents exhibit significant fluctuations, which can be reduced as  $N$  is increased, as exemplified in Figure 29.15B–F for  $\Delta t \approx 131.8$  (seconds) (corresponding to  $N = 10^{4.5} = 31\,623$ ). Despite this reduction in the fluctuations of the pseudo-Lyapunov exponents, there is no indication that any statistically significant change in these exponents occurs before, during and after the seizure, suggesting that the computed exponents are not capable of distinguishing among pre-seizure, seizure and post-seizure phases, let alone being able to predict the occurrence of the seizure in advance.

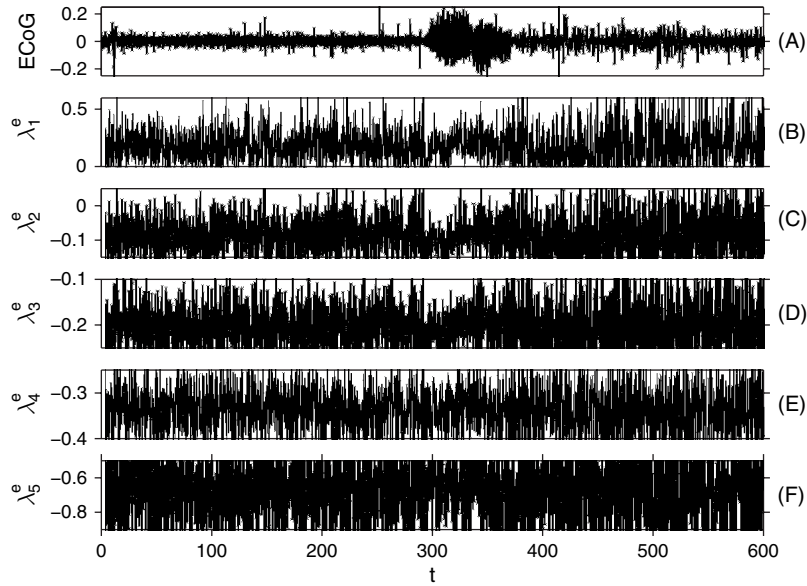


**FIGURE 29.14** (A) A segment of ECoG time series containing a seizure which starts at approximately  $t = 300$  (seconds) and lasts for about 80 (seconds). (B–F) For  $m = 5$  and  $\Delta t \approx 4.17$  (seconds) (corresponding to  $N = 1000$  data points), the five computed Lyapunov exponents versus time, where time is counted as the end of the moving window.

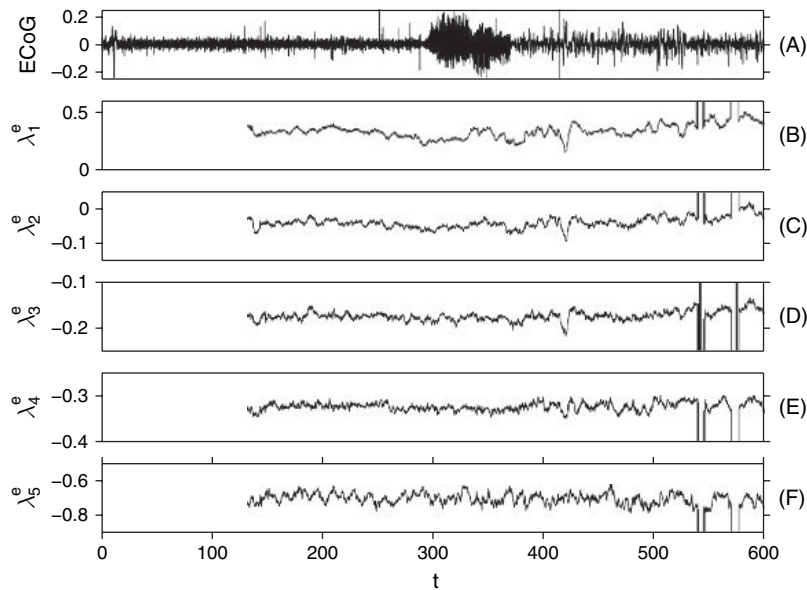


**FIGURE 29.15** (A) Segment of ECoG time series identical to that of Figure 29.14(A). (B–F) For  $m = 5$  and  $\Delta t \approx 131.8$  (seconds) (corresponding to  $N = 10^{4.5} = 31\,623$ ) the five computed Lyapunov exponents versus time.

## DISCUSSION

Prediction of epileptic seizures is an enormous challenge. Presently, there is little to no consensus on whether seizures are predictable to a degree useful for clinical application, or whether the methods that have been used are reliable. There is also no consensus on the existence of a pre-ictal state though there is speculation that such a state exists (Litt et al., 2001; Litt and Echauz, 2002; Litt and Lehnertz, 2002; Lehnertz et al., 2003; Iasemidis et al., 2003a). Our opinion is that a systematic and generally applicable methodology for seizure prediction is still lacking, despite existing claims to the

contrary. This is especially true when techniques designed for low-dimensional non-linear dynamical systems are used. Possible reasons for this are: (1) EEG or ECoG signals are complicated, non-linear, non-stationary, high-dimensional and noisy; (2) the techniques may not be sufficiently sensitive to discriminate random behaviors with subtle differences, though they are highly effective in distinguishing between regular and chaotic behaviors. From this viewpoint, it is uncertain whether non-linear-dynamics based techniques would perform better than the techniques from random signal processing or linear time-frequency-energy techniques. Prediction of seizures based on EEG or ECoG signals thus remains largely an open problem.

This chapter reviews recent progress on assessing the predictive powers of the correlation-dimension related measures and the Lyapunov exponents. In particular, there has been a comprehensive analysis of the correlation dimension and related measures based on extensive clinical ECoG data (Harrison et al., 2005). The result is the resounding finding that the correlation dimension and integrals do not predict epileptic seizures. By the fundamental relation between the fractal dimension and the Lyapunov exponents, the finding implies that the same can be expected for the Lyapunov exponents. This is consistent with a systematic control study (Lai et al., 2003, 2004) designed to address whether the Lyapunov exponents may have any predictive power for characteristic system changes.

### **Correlation dimension and related measures**

Retrospective studies with these measures yielded seizure prediction times on the order of 10 minutes (Martinerie et al., 1998; Elger and Lehnertz, 1998; Lehnertz and Elger, 1998). To assess the meaning of these claims, it is important to understand precisely what type of signal characteristics these measures are sensitive to, and also to validate the fundamental component of the methods, the correlation integral, on long time series. Preliminary analyses of short ECoG segments have been performed which elucidated the measures' dependence on amplitude and autocorrelation (Osorio et al., 2001; Lai et al., 2002). More recently, a systematic, large-scale study on correlation integral-based measures has been carried out (Harrison et al., 2005) that not only meticulously examined the sensitivity to the individual parameters and method variations, but also tested the method on long time series, including continuous computation on over 2000 hours of ECoG data. The main result is that seizure detection measures based on the correlation integral are sensitive to time-frequency-energy signal changes such as those quantified by autocorrelation and signal amplitude (Osorio et al., 2001; Lai et al., 2002). Window-by-window amplitude normalization and Theiler correction (Theiler, 1986) can eliminate these effects, but significantly reduce the ability of the measures to discriminate seizures from inter-seizure periods. This suggests that the seizure detection ability of the correlation-integral based measures is directly linked to the signal's variation in the time-frequency-energy characteristics rather than to any non-linear dynamics present in the ECoG. This is supported by results with surrogate data, which illustrate that the seizure detection ability is approximately equivalent for both original and shuffled data. In addition, no significant improvement in seizure detection or prediction ability is seen when the data are preprocessed through filtering to extract frequency bands that may be prominent in seizure or 'precursor' activity. Likewise, different embedding schemes did not substantially improve the measures' abilities to detect or predict seizures.

No evidence of prediction has been found on a timescale of 15–90 minutes before seizure onset, and on overlaid time series within a scale of 0–15 minutes before seizure; the only advanced warning is less than one minute prior to seizure for some seizures in some subjects. However, advanced warnings can be easily obtained through subject-tuning of an existing automated seizure detection algorithm (Osorio et al., 1998) which is far more computationally efficient than the correlation integral method. Furthermore, the correlation-dimension based method is far less specific in terms of false positives than the discriminating statistic used in the automated seizure detection algorithm, thus the correlation integral probably has little value as a seizure detector, let alone as a predictor.

### **Lyapunov exponents**

Lyapunov exponents are fundamental invariant quantities characterizing a dynamical system. To determine them from time series, when the underlying mathematical model is unknown, is one of the most challenging tasks in non-linear dynamics. While algorithms based on phase-space reconstruction by delay-coordinate embedding have existed for about two decades, issues such as the distribution of spurious exponents in low-dimensional chaotic systems (Sauer et al., 1998; Sauer and Yorke, 1999) and the accuracy of the estimated exponents (Kostelich, 2001) still need to be addressed.

There are two major factors that can prevent the Lyapunov exponents from being effective to predict characteristic system changes: *statistical fluctuations* and *noise*. In particular, the fluctuations in the finite-time Lyapunov exponents present a serious obstacle to their predictive power because any changes in the exponents must be larger than the fluctuations in order for them to be indicative of system changes. Increasing the size of a moving window will not decrease the detection time for system changes. This implies that any characteristic change of the system must be significant enough for it to be detected

through the Lyapunov exponents, regardless of the size of the finite data set contained in the moving window, insofar as it is statistically meaningful. While relatively small parameter changes in the system preceding a critical event can be detected through the changes in the Lyapunov exponents, this predictive power of the Lyapunov exponents can be ruined completely by noise with magnitude as small as less than 1% of the variation of the system variable. As the noise level is increased to about 5% of the variation, even the detective power of the exponents is lost. These results have been obtained in a control study using a class of non-stationary, noisy but low-dimensional chaotic maps (Lai et al., 2003, 2004). The brain dynamical systems responsible for the epileptic seizures are much more complicated than low-dimensional chaotic systems or even idealized high-dimensional systems such as coupled map lattices. In epilepsy, all information is from a few dozen probes, each sensing approximately  $10^5$ – $10^8$  neurons (Nunez, 1995), into the corresponding neuron ensemble in the brain about which relatively little is known. The signals so obtained (ECoG) are inevitably noisy. These considerations suggest a complete lack of any predictive or detective powers of the Lyapunov exponents for epileptic seizures.

Besides our work (Osorio et al., 2001; Lai et al., 2002, 2003, 2004; Harrison et al., 2005), a recent study (Mormann et al., 2006) examining the sensitivity and specificity of a large collection of measures used in the literature for seizure prediction finds that univariate measures, including many non-linear dynamical measures such as the correlation dimension, are inadequate for clinical applications. The message we wish to convey in this review chapter is: *the correlation dimension and the Lyapunov exponents should never be the choice for seizure prediction.*

Non-linear dynamics can advance our understanding (Larter et al., 1999; Robinson et al., 2002) of the spatiotemporal behavior of seizures but estimation of the correlation dimension or Lyapunov exponents for seizure prediction is of little value. Other approaches based on spatiotemporal information as can be offered by multichannel ECoG recordings, such as synchronization-based techniques (Quiroga et al., 2002a,b) that has been successful in detecting very subtle correlations between biomedical signals, deserve investigation (Tass et al., 1998; Lai et al., 2006). Characterization of the dynamical behavior of seizures, a largely ignored task, should be the top priority of the epilepsy research community, replacing the well motivated but blind approach of indiscriminately applying tools from non-linear dynamics or any other fields to the *prediction* of seizures. While serendipity may reward current seizure prediction attempts, fundamental advances in epileptology require the unraveling of the *laws* that govern seizure generation in epilepsy. The knowledge thus accrued, may provide answers to whether or not seizures are predictable.

#### ACKNOWLEDGMENT

This work was supported by NIH/NINDS under Grants No. 1R43NS43100-01 and 1R01NS046602-01.

#### REFERENCES

- Albano, A.M., Muench, J., Schwartz, C., Mees, A.I. and Rapp, P.E. (1988). Singulae-value decomposition and the Grassberger-Procaccia algorithm. *Phys Rev A* 38:3017–3026.
- Andrzejak, R.G., Lehnertz, K., Mormann, F., Rieke, C., David, P. and Elger, C.E. (2001). Indications of nonlinear deterministic and finite-dimensional structures in time series of brain electrical activity: dependence on recording region and brain state. *Phys Rev E* 64:061907.
- Babloyantz, A. and Destexhe, A. (1986). Low-dimensional chaos in an instance of epilepsy. *Proc Nat Acad Sci USA* 83:3513–3517.
- Brown, E., Bryant, P. and Abarbanel, H.D.I. (1991). Computing the Lyapunov spectrum of a dynamic system from an observed time series. *Phys Rev A* 43:2787–2806.
- Diambra L. and Malta, C.P. (1999). Nonlinear models for detecting epileptic spikes. *Phys. Rev. E* 59:929–937.
- Ding, M., Grebogi, C., Ott, E., Sauer, T. and Yorke, J.A. (1993). Plateau onset for correlation dimension: when does it occur? *Phys Rev Lett* 70:3872–3875.
- Eckmann, J.-P. and Ruelle, D. (1985). Ergodic theory of chaos and strange attractors. *Rev Mod Phys* 57:617–656.
- Eckmann, J.-P., Kamphorst, S.O., Ruelle, D. and Ciliberto, S. (1986). Liapunov exponents from time series. *Phys Rev A* 34:4971–4979.
- Elger, C.E. and Lehnertz, K. (1998). Seizure prediction by nonlinear time series analysis of brain electrical activity *Eur J Neurosci* 10:786–789.
- Farmer, J.D., Ott, E. and Yorke, J.A. (1983). The dimension of chaotic attractors. *Physica D* 7:153–180.
- Frank, G.W., Lookman, T. and Nerenberg, M.A.H. (1990). Recovering the attractor – a review of chaotic time-series analysis. *Can J Phys* 68:711–718.
- Grassberger, P. and Procaccia, I. (1983). Measuring the strangeness of strange attractors. *Physica D* 9:189–208.
- Grebogi, C., Ott, E. and Yorke, J.A. (1983). Crises, sudden changes in chaotic attractors, and transient chaos. *Physica D* 7:181–200.
- Hammel, S.M., Jones, C.K.R.T. and Moloney, J.V. (1985). Global dynamical behavior of the optical-field in a ring cavity. *J Opt Soc Am B* 2:552–564.
- Harrison, M.A.F., Osorio, I., Frei, M.G., Asuri, S. and Lai, Y.-C. (2005). Correlation dimension and integral do not predict epileptic seizures. *Chaos* 15:033106.
- Hentschel, H.G.E. and Procaccia, I. (1983). The infinite number of generalized dimensions of fractals and strange attractors. *Physica* 8D:435–444.
- Hively, L.M., Protopopescu, V.A. and Gailey, P.C. (2000). Timely detection of dynamical change in scalp EEG signals. *Chaos* 10:864–875.

- Iasemidis, L.D. and Sackellares, J.C. (1991). The evolution with time of the spatial distribution of the largest Lyapunov exponent on the human epileptic cortex. In: Measuring chaos in the human brain (D.W. Duke and W.S. Pritchard, eds) pp. 49–82. World Scientific, Singapore.
- Iasemidis, L.D., Sackellares, J.C., Zaveri, H.P. and Williams, W.J. (1990). Phase space topography and the Lyapunov exponent of electrocorticograms in partial seizures. *Brain Topograph* 2:187.
- Iasemidis, L.D., Pardalos, P.M., Sackellares, J.C. and Shiu, D.S. (2001). Quadratic binary programming and dynamical system approach to determine the predictability of epileptic seizures. *J Comb Optim* 5:9–26.
- Iasemidis, L.D., Shiu, D.S., Chaovatwongse, W. et al. (2003). Adaptive epileptic seizure prediction system. *IEEE Trans Biomed Eng* 50:616–627.
- Iasemidis, L.D., Pardalos, P.M., Shiu, D.S. et al. (2003). Prediction of human epileptic seizures based on optimization and phase changes of brain electrical activity. *Optimiz Meth Softw* 18:81–104.
- Ikeda, K. (1979). Multiple-valued stationary state and its instability of the transmitted light by a ring cavity system. *Opt Commun* 30:257–261.
- Ivanov, D.K., Posch, H.A. and Stumpf, C. (1996). Statistical measures derived from the correlation integrals of physiological time series. *Chaos* 6:243–253.
- Jeong, J., Kim, M.S. and Kim, S.Y. (1999). Test for low-dimensional determinism in electroencephalograms. *Phys Rev E* 60:831–837.
- Kandel, E.R., Schwartz, J.H. and Jessell, T.M. (1991). Principle of neural science. Appleton and Lange, Norwalk.
- Kantz, H. (1994). A robust method to estimate the maximal Lyapunov exponent of a time series. *Phys Lett A* 185:77–87.
- Kantz, H. and Schreiber, T. (1997). Nonlinear time series analysis. Cambridge University Press, Cambridge.
- Kaplan, J.L. and Yorke, J.A. (1979). Chaotic behavior of multidimensional difference equations. In: Functional differential equations and approximations of fixed points (lecture notes in mathematics 730, (H.-O. Peitgen and H.-O. Walter, eds) pp. 204–277. Springer, Berlin.
- Kloeden, P.E. and Platen, E. (1992). Numerical solution of stochastic differential equations. Springer-Verlag, Berlin.
- Kostelich, E.J. (2001). Bootstrap estimates of chaotic dynamics. *Phys Rev E* 64:016213.
- Lai, Y.-C., Grebogi, C., Yorke, J.A. and Kan, I. (1993). How often are chaotic saddles nonhyperbolic? *Nonlinearity* 6:779–797.
- Lai, Y.-C., Osorio, I., Harrison, M.A.F. and Frei, M.G. (2002). Correlation-dimension and autocorrelation fluctuations in epileptiform seizure dynamics. *Phys Rev E* 65:031921.
- Lai, Y.-C., Harrison, M.A.F., Frei, M.G. and Osorio, I. (2003). Inability of Lyapunov exponents to predict epileptic seizures. *Phys Rev Lett* 91:068102.
- Lai, Y.-C., Harrison, M.A.F., Frei, M.G. and Osorio, I. (2004). Control test for predictive power of Lyapunov exponents: their inability to predict epileptic seizures. *Chaos* 14:630–642.
- Lai, Y.-C., Harrison, M.A.F., Frei, M.G. and Osorio, I. (2005). Reply to comment on ‘Inability of Lyapunov exponents to predict epileptic seizures.’ *Phys Rev Lett* 94:019802.
- Lai, Y.-C., Frei, M.G. and Osorio, I. (2006). Detecting and characterizing phase synchronization in nonstationary dynamical systems. *Phys Rev E* 73:026214.
- Larter, R., Speelman, B. and Worth, R.M. (1999). A coupled ordinary differential equation lattice model for the simulation of epileptic seizures. *Chaos* 9:795–804.
- Ledrappier, F. (1981). Some relations between dimension and Lyapunov exponents. *Commun Math Phys* 81:229–238.
- Lehnertz K. and Elger, C.E. (1998). Can epileptic seizures be predicted – evidence from nonlinear time series analysis of brain electrical activity. *Phys Rev Lett* 80:5019–5022.
- Lehnertz, K., Mormann, F., Kreuz, T. et al. (2003). Seizure prediction by nonlinear EEG analysis. *IEEE Eng Med Biol Mag* 22:57–63.
- Lerner, D. (1996). Monitoring changing dynamics with correlation integrals: case study of an epileptic seizure. *Physica D* 97:563–576.
- Litt, B. and Echauz, J. (2002). Prediction of epileptic seizures. *Lancet Neurol* 1:22–30.
- Litt, B. and Lehnertz, K. (2002). Seizure prediction and the preseizure period. *Curr Opin Neurol* 15:173–178.
- Litt, B., Esteller, R., Echauz, J. et al. (2001). Epileptic seizures may begin hours in advance of clinical onset: a report of five patients. *Neuron* 30:51–64.
- Lorenz, E.N. (1963). Deterministic nonperiodic flow. *J Atmos Sci* 20:130–141.
- Martinierie, J., Adam, C., Quyen, M.L.V. et al. (1998). Epileptic seizures can be anticipated by nonlinear analysis. *Nat Med* 4:1173–1176.
- Mayer-Kress G. and Layne, S.P. (1987). Dimensionality of the human electroencephalogram. *Ann NY Acad Sci* 504:62–87.
- Mormann, F., Elger, C.E. and Lehnertz, K. (2006). Seizure anticipation: from algorithms to clinical practice. *Curr Opin Neurol* 19:187–193.
- Nagai Y. and Lai, Y.-C. (1995). Selection of desirable chaotic phase using small feedback control. *Phys Rev E* 51:3842–3848.
- Netoff, T.I. and Schiff, S.J. (2002). Decreased neuronal synchronization during experimental seizures. *J Neurosci* 22:7297–7307.
- Nunez, P. (ed.) (1995). In: Neocortical dynamics and human EEG rhythms pp. 3–67 and pp. 68–133. Oxford University Press, Oxford.
- Osorio, I., Frei, M.G. and Wilkinson, S.B. (1998). Real-time automated detection and quantitative analysis of seizures and short-term prediction of clinical onset. *Epilepsia* 39:615–627.
- Osorio, I., Harrison, M.A.F., Lai, Y.-C., and Frei, M.G. (2001). Observations on the application of the correlation dimension and correlation integral to the prediction of seizures. *J Clin Neurophys* 18:269–274.
- Osorio, I., Frei, M.G., Gifakis, J. et al. (2002). Performance reassessment of a real-time seizure-detection algorithm on long ECoG series. *Epilepsia* 43:1522–1535.
- Ott, E. (2002). Chaos in dynamical systems. Cambridge University Press, Cambridge.
- Parker, T.S. and Chua, L.O. (1989). Practical numerical algorithms for chaotic systems. Springer-Verlag, New York.
- Porcher, R. and Thomas, G. (2001). Estimating Lyapunov exponents in biomedical time series. *Phys Rev E* 64:010902.
- Quiroga, R.Q., Arnhold, J. and Grassberger, P. (2000). Learning driver-response relationships from synchronization patterns. *Phys Rev E* 61:5142–5148.
- Quiroga, R.Q., Kraskov, A., Kreuz, T. and Grassberger, P. (2002a). Reply to Comment on ‘Kullback-Leibler and renormalized entropies: applications to electroencephalograms of epilepsy patients.’ *Phys Rev E* 66:041903.
- Quiroga, R.Q., Kreuz, T. and Grassberger, P. (2002b). Event synchronization: a simple and fast method to measure synchronicity and time delay patterns. *Phys Rev E* 66:041904.
- Quyen, M.L.V., Martinierie, J., Adam, C. and Varela, F.J. (1997). Unstable periodic orbits in human epileptic activity. *Phys Rev E* 56:3401–3411.
- Rapp, P.E., Zimmerman, I.D., Vining, E.P., Cohen, N., Albano, A.N. and Jimenezmontano, M.A. (1994). The algorithmic complexity of neural spike trains increases during focal seizures. *J Neurosci* 14:4731–4739.

- Robinson, P.A., Rennie, C.J. and Rowe, D.L. (2002). Dynamics of large-scale brain activity in normal arousal states and epileptic seizures. *Phys Rev E* 65:041924.
- Sano, M. and Sawada, Y. (1985). Measurement of the Lyapunov spectrum from a chaotic time series. *Phys Rev Lett* 55:1082–1085.
- Sauer, T.D. and Yorke, J.A. (1999). Reconstructing the Jacobian from data with observational noise. *Phys Rev Lett* 83:1331–1334.
- Sauer, T.D., Yorke, J.A. and Casdagli, M. (1991). Embedology. *J Stat Phys* 65:579–616.
- Sauer, T.D., Tempkin, J.A. and Yorke, J.A. (1998). Spurious Lyapunov exponents in attractor reconstruction. *Phys Rev Lett* 81:4341–4344.
- Schiff, S.J. (1998). Forecasting brain storms. *Nat Med* 4:1117–1118.
- Takens, F. (1981). Detecting strange attractors in turbulence. In: *Dynamical systems and turbulence (lecture notes in mathematics)* (D. Rand and L.S. Young, eds.) pp. 366–381. Springer-Verlag, Berlin.
- Tass, P., Rosenblum, M.G., Weule, J. et al. (1998). Detection of n:m phase locking from noisy data: application to magnetoencephalography. *Phys Rev Lett* 81:3291–3294.
- Theiler, J. (1986). Spurious dimension from correlation algorithms applied to limited time-series data. *Phys Rev A* 34:2427–2432.
- Theiler, J. (1995). On the evidence for low-dimensional chaos in an epileptic electroencephalogram. *Phys Lett A* 196:335–341.
- Theiler, J. and Rapp, P.E. (1996). Re-examination of the evidence for low-dimensional, nonlinear structure in the human electroencephalogram. *Electroen Clin Neurol* 98:213–222.
- Theiler, J., Eubank, S., Longtin, A., Galdrikian, B. and Farmer, J.D. (1992). Testing for nonlinearity in time series: the method of surrogate data. *Physica D* 58:77–94.
- Widman, G., Lehnertz, K., Jansen, P., Meyer, W., Burr, W. and Elger, C.E. (1998). A fast general purpose algorithm for the computation of auto- and cross-correlation integrals from single channel data. *Physica D* 121:65–74.
- Wolf, A., Swift, J.B., Swinney, H.L. and Vastano, J.A. (1985). Determining Lyapunov exponents from a time series. *Physica D* 16:285–317.
- Young, L.-S. (1982). Dimension, entropy, and Lyapunov exponents. *Ergodic Theo Dynam Syst* 2:109.

# 30

---

## TOWARDS A DYNAMICS OF SEIZURE MECHANICS

---

STEVEN J. SCHIFF, JOHN R. CRESSMAN, ERNEST BARRETO  
AND JOKŪBAS ŽIBURKUS

### ABSTRACT

There is a wide variety of neuronal dynamics that are classified as seizures. We pose the hypothesis that, as in any description of the physics of ensembles, the macroscopic phenomena of a seizure need to be characterized in terms of the interactions between the relevant neuronal subtypes taking part in this process. As in many non-biological pattern formation processes, persistently active states, including seizures, may depend on the interplay between inhibitory interneurons and excitatory principal (pyramidal) cells. We discuss the characteristics of synchronization between interneurons and pyramidal cells in hippocampal seizures, using techniques to extract input synaptic currents from the output spikes recorded during intracellular recordings. We describe strategies to minimize the effect of spurious correlations due to shared frequencies and finite data sample lengths. We contrast these findings with the synchronization characteristics from human seizures and show how an adaptation of canonical linear discrimination can be used with metrics of synchrony features. We describe how interneuron depolarization block may be an integral component in orchestrating the time course of seizures and how gap junction connectivity may synchronize such depolarization block among interneurons. Searching for the universality that might underlie the variety of seizure dynamics in human epilepsy remains an important open challenge.

### INTRODUCTION

Despite a voluminous literature on the physiology of seizures, there remains no dynamical understanding of what a seizure is. Jackson (1890) proposed that epileptic seizures are due to an excessive discharge of neurons – a prescient conjecture stated prior to the firm evidence that the brain was made up of individual neurons rather than a syncytium. The more modern clinical literature is replete with vague descriptive terms such as paroxysmal, which offers us little in terms of the underlying physics of such phenomena. Long before the extraction of neuronal interactions became technically feasible in experiments, Penfield and Jasper (1954) described seizure dynamics as ‘hypersynchronous’ and the monolithic description of seizures as ‘synchronous’ neuronal discharge has entered our canon (Westbrook, 1991).

We pose the hypothesis that, as in any description of the physics of ensembles, the macroscopic (network) phenomena of a seizure need to be characterized in terms of the interactions between the relevant neuronal subtypes taking part in this process. A corollary to this hypothesis is that since there is a wide variety of clinical phenomena which are characterized as epileptic seizures in humans, ranging from brief absence episodes to full blown generalized tonic-clonic seizures, we anticipate that there will be a variety of dynamical interactions which constitute seizures. Searching for the universality that might underlie the variety of seizure dynamics in human epilepsy would be a major open challenge given these conjectures.

Are there many dynamical phenomena which we call seizures in humans? To our knowledge, we do not have suitable neuronal interaction data to characterize any human seizures. Such data require the recording of multiple individual neurons, of specific cell-type, during seizures – a very difficult technical challenge in the intact animal or human. Although recent work is progressing towards the ability to define more reliably neuronal subtype from extracellular recordings (Gold et al., 2006), at present, only intracellular data are suitable. While transgenic mice with fluorescent proteins associated

with promoter regions expressed heavily in particular neuronal subtypes are now becoming available, in general, we still require *post hoc* morphological and immunohistochemical analysis in order to identify neuronal subtypes with reasonable accuracy. These requirements presently restrict us to the use of animal experiments to inform us of possible mechanisms for human seizures.

Single neuron interactions are innumerable in the brain and punishing to acquire. An alternative is to make the case that interaction data from single neurons could be suitably lumped to form larger ideal neurons (perhaps through a renormalization strategy), or perhaps columnar structure would form such an organizational basis. But such a strategy has no supporting evidence at this time.

So we presently confine ourselves to examine, from the top down, both scalp and intracranial electroencephalograms (EEG) from human patients with a variety of epilepsies, as well as from the bottom up, rodent slice data where we can examine the functional interactions between neurons in great detail. We utilize slices because of our present need to impale specific neurons with micropipette electrodes. Although brain slices can be induced to demonstrate events which phenomenologically resemble the electrical manifestations of human seizures, we have at present no direct proof that such phenomena share the interaction physics with any known human epilepsy. Nevertheless, our findings in brain slices are disturbingly inconsistent with the dogma we have all been taught regarding seizure mechanisms. These data suggest that our present understanding of seizures may need to be re-evaluated.

### THE POSSIBLE ROLE OF INHIBITION

Another tenet of our understanding of seizures is that they constitute excessive excitation in the presence of relatively decreased inhibition. However, inhibition is retained in samples from human epileptics (Babb et al., 1989; During and Spencer, 1993; Menendez de la Prida et al., 2002) and interneuron activity appears essential for the generation of *in vitro* epileptiform activity in human (Cohen et al., 2002) and animal (Higashima et al., 1996; Avoli et al., 1996a; Lopantsev and Avoli, 1998; Perez-Velazquez and Carlen, 1999; Fujiwara-Tsukamoto et al., 2004) tissue.

In hippocampal slice work, there are many phenomena that are readily seen without active inhibition (or at least without fast GABA-A channels being active), including brief (<250 ms) population burst firing which may be periodic (Menendez de la Prida et al., 2006). Similarly, in neocortical slices, activation of such networks in the presence of GABA-A blockade can give strong periodic oscillations, phenomena replicated in excitatory computational models of cortex or more generic excitable media (Huang et al., 2004). Whether slower GABA-B synaptic effects play a role in the recovery mechanisms (Menendez de la Prida et al., 2006) in such wave phenomena remains an open question for now.

We will take the position that population bursts and wave phenomena in GABA-A disinhibition may be dynamically different from seizures in intact cortex where fast inhibition is active. Seizures generally contain higher frequencies than observed in GABA-A disinhibition and are often more long lasting than such population bursts and oscillatory waves. Sustaining such high frequency reverberant states may require high frequency inhibition.

Working memory has provided us with an archetype of a persistently active state. In the aftermath of a cue, neuronal networks remain active during a delay period (Funahashi et al., 1989). Computationally, such persistent activity can be produced through a relative balance of excitation and inhibition, although such reverberation may be sustained through asynchrony and quenched through synchronization (Gutkin et al., 2001). Further experiments of up and down states in cortex (Shu et al., 2003; Haider et al., 2006) have shown that the inhibitory and excitatory conductances maintain an impressive degree of balance despite large variations in cortical activity. In order to accomplish such persistent activity without fast inhibition, the cortex may need to organize activity in spatiotemporal wave patterns (Huang et al., 2004). How anatomically constrained waves in intact cortex relate to these slice data remains unclear (Rubino et al., 2006), although one clear difference is the higher frequency oscillations observed in intact cortex with GABA-A transmission intact.

### EXCITATORY NEURON INTERACTIONS IN SEIZURES

In 2002, we examined the evidence for synchronization between excitatory pyramidal cells in 4-aminopyridine (4AP) seizure-like events (SLEs) induced in hippocampal slices (Netoff and Schiff, 2002). Such cells were studied in current clamp mode with whole cell attached patch clamp technique, using an intracellular solution containing a compound to prevent spikes (QX-314). Unexpectedly, using linear and non-linear methods to detect synchronization, it was found that the synaptic currents impinging upon pairs of such neurons decreased during the initial stage of such SLEs (Figure 30.1).

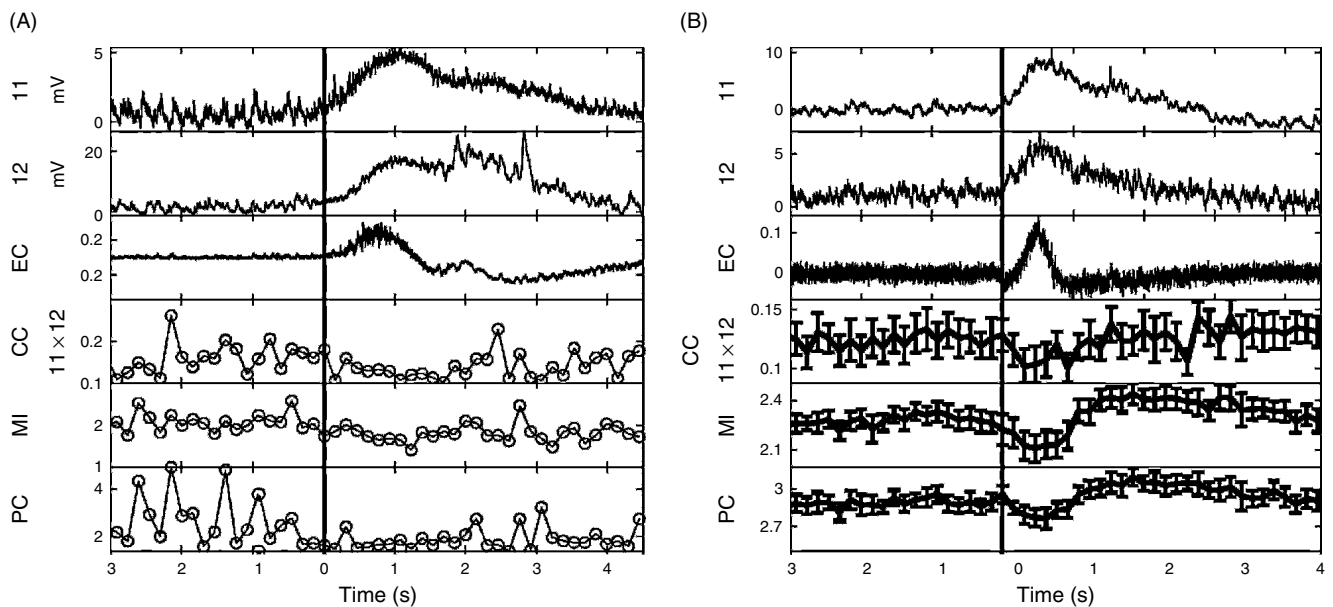


**FIGURE 30.1** Input synaptic currents to pyramidal cells during seizures. Dual whole cell impalements (I1 and I2) and extracellular (EC) recordings from pairs of pyramidal cells in hippocampal slices. The electrical seizure-like event starts at the heavy line. On the left is a single seizure, and on the right, the time locked averages from 26 consecutive seizures in a separate experiment. Shown are the results of cross-correlation (CC), mutual information (MI) and phase correlation (PC). Full details on calculating CC, MI and PC, along with their statistics, are described in Netoff and Schiff (2002). All of these measures inferring synchronization decrease following the onset of the seizures. After Netoff and Schiff. (2002) (reproduced with permission).

Synchronization increased towards the end of such events. Also unexpected was the finding that such SLEs were abolished in the presence of the GABA-A blocker picrotoxin (Netoff and Schiff, 2002).

#### HUMAN SEIZURE DYNAMICS

What about human seizures? One of the hallmarks of partial complex seizures with secondary generation are the clinical stages of the progression from partial, to generalized tonic, to clonic, followed by afterdischarges. These EEG patterns are accompanied by behavioral manifestations of such seizures. Nevertheless, there has been surprisingly little previous work quantifying the stages of seizures dynamically. In experimental kindled seizures, Racine (1972) described progressive changes in electrical seizure patterns corresponding to behavioral manifestations. In the tetanus toxin model of experimental seizures, a staging system has been devised for different segments of seizures based on EEG frequency (Finnerty and Jefferys, 2000). For the particular case of human status epilepticus, Treiman et al. (1990) defined a staging system. In all of the above, the classification of seizure stages was based upon qualitative assessments following visual inspection of behavior or EEG. The most quantitative approaches to segmentation of seizures that we are aware of (Wendling et al., 1996; Wu and Gotman, 1998) focused upon comparing the similarities (or dissimilarities) between different seizures.

To study better the dynamical evolution of such events, we examined a variety of human seizures recorded from both scalp and intracranial electrodes. We used six features of such multielectrode signals: total power, total correlation at both zero and arbitrary time lag, phase amplitude coherence and phase angle and amplitude dispersion. Using multivariate linear discrimination, we were able to show that almost all of these seizures had at least three dynamical stages that were statistically discriminable (Schiff et al., 2005). In our analysis, no consistent evidence of increased synchronization was evident within the initial or terminal phases of these seizures – synchronization was a prominent feature only once the seizure had passed through its initiation phase, and was a variable feature of seizure termination depending on subject (Figure 30.2). Although the scales of observation were vastly different, these human *in vivo* results showed a similar lack of synchronization during the initiation of such events as did our intracellular measures from slice work described above.

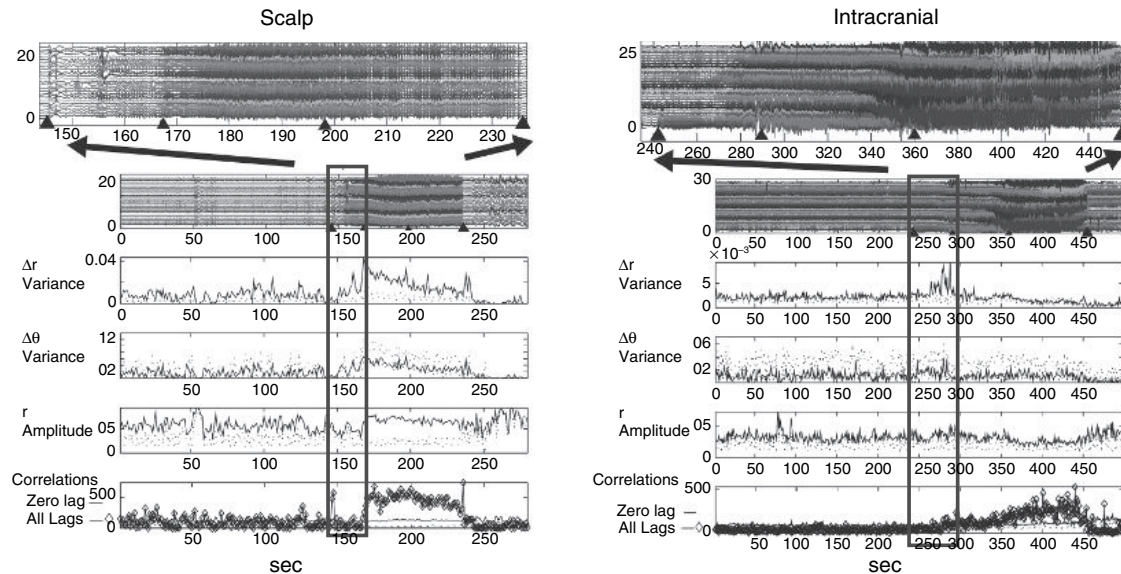


**FIGURE 30.2** Dynamical evolution of human seizures. On the left is shown an example of a human seizure recorded from scalp, and on the right, from intracranial electrodes. The dynamics were partitioned using an adaptation of multivariate linear discrimination (Schiff et al., 2005). Five separate measures inferring synchronization are shown: from a phase analysis, amplitude ( $r$ ) and angle ( $\theta$ ) magnitude and variance (dispersion), as well as cross-correlations shown for zero lag and at arbitrary lag. The initial stage of these seizures (red rectangles) shows no evidence of increased synchronization by any measure, whereas a consistent feature of both intracranial and extracranial seizure recordings is the statistically significant increase in correlations seen during the middle stage of these events. After Schiff et al., 2005 (reproduced with permission). (See Plate 22 in color plate section.)

Which leads us to ask – what about the relation between the excitatory and inhibitory (EI) neurons in creating such patterns?

#### EXCITATORY AND INHIBITORY INTERPLAY IN SEIZURE PATTERNS

There are a number of studies of *in vitro* intracellular excitatory-inhibitory (EI) interplay. These works focused primarily on stimulation-induced epileptiform activity (Perez-Velazquez and Carlen, 1999; Perez-Velazquez, 2003; Fujiwara-Tsukamoto et al., 2004). In these paradigms, tetanic stimulation replaced pre-ictal and ictal onset dynamics and the resulting after-discharges demonstrated synchronous activation of inhibitory and excitatory cells (Fujiwara-Tsukamoto et al., 2004). However, we know little about EI interactions and synchrony during spontaneous pre-ictal, ictal and post-ictal events.

Or at least we think that we know little. Forty-five years ago, Kandel and Spencer (1961) recorded from untyped cells in the hippocampus during seizures in animals and noted that some of these cells fired out of phase with the EEG, while others were in phase. Such findings were harbingers of what follows next.

To investigate EI, excitatory-excitatory (EE) and inhibitory-inhibitory (II) interactions in robust SLEs, we used a 4AP and decreased magnesium seizure model. Producing SLEs in brain slices is a bit *ad hoc* and there are many conditions for *in vitro* preparations that are intangible to identify and replicate. We fortuitously discovered that decreasing the  $Mg^{2+}$  concentration to 0.6 mM, although insufficient by itself to promote SLEs, had a profound affect on prolonging 4AP-induced SLEs. 4AP increases inhibitory and excitatory signaling (Avoli et al., 1988, 1996b; Somjen, 2004), while decreased  $Mg^{2+}$  partially removes N-methyl-D-aspartate (NMDA) receptor blockade and divalent charge screening. A similar strategy employs elevated potassium with decreased magnesium (Khosravani et al., 2003, 2005; Isaev et al., 2005). Traynelis and Dingledine (1988) demonstrated similarly prolonged seizures in a high  $K^+$  model (8.5 mM  $K^+$ , 1.5 mM  $Mg^{2+}$ ) and we suspect that differences in chamber design (interface versus submerged) or other unknown variables prevent our electrical seizures in high  $K^+$  or 4AP from such prolongation without decreasing  $Mg^{2+}$ .

Simultaneous dual and triple whole-cell recordings of inhibitory oriens interneurons and excitatory pyramidal cells, along with extracellular potential measurements, were performed in the CA1 of rat hippocampal slices. An extracellular

electrode was placed in the stratum pyramidale near the patched cells. A subset of experiments was performed after isolating CA1 ( $n = 13$ ) by making cuts from alveus to stratum moleculare lacunosum on each side of CA1.

Because we wanted to examine the interrelation between subthreshold inputs and suprathreshold output spikes from these neurons, we did not inhibit spike production as in Netoff and Schiff (2002). In what follows, all recordings are performed in current clamp.

Putative stratum oriens interneurons were distinguished from excitatory pyramidal cells using these criteria:

1. horizontal appearance and location of cell bodies using differential infrared contrast microscopy
2. membrane resting potential (pyramidal cells:  $V_m_{rest} = -67 \pm 0.8 \text{ mV}$ ,  $n = 40$ ; interneurons:  $V_m_{rest} = -62 \pm 1 \text{ mV}$ ,  $n = 15$ )
3. active membrane properties: spike height (pyramidal cells:  $80 \pm 5.2 \text{ mV}$ ; interneurons:  $68 \pm 2.9 \text{ mV}$ ) and spike width at half-height (pyramidal cells:  $1.4 \pm 0.1 \text{ ms}$ ; interneurons:  $1.1 \pm 0.2 \text{ ms}$ ) (Figure 30.3A)
4. post-hoc morphological reconstruction with *camera lucida* using biocytin histochemistry (Figure 30.3B).

Neurons filled with neurobiotin were processed using the modified biocytin histological methods of Horikawa and Armstrong (1988). To describe dominant currents and spike trains, the cells were held at  $-75 \text{ mV}$  and incremental ( $50\text{--}100 \text{ pA}$ ;  $500 \text{ ms}$ ) negative and positive square wave current pulses were injected (see Figure 30.3A). Oriens lacunosum moleculare (OLM) interneurons, following negative current pulses, exhibit a characteristic initial hyperpolarizing sag, an inward rectification and triangularly shaped afterhyperpolarizations as seen in Figure 30.3A (Maccaferri and McBain, 1996; Maccaferri and Lacaille, 2003). Most of our recorded interneurons resembled OLM cells in their membrane properties (Figure 30.3A) and horizontally oriented dendritic projections (Figure 30.3B). OLM cells also constitute the overwhelming majority of the oriens interneurons (Freund and Buzsaki, 1996; Somogyi and Klausberger, 2005).

For the entire duration of the experiments, the cells were held with bias currents no greater than  $-100 \text{ pA}$ . Only cells with input resistance greater than  $100 \text{ M}\Omega$  and access resistance of less than  $20 \text{ M}\Omega$  were included in the final analysis. Cells selected for patching were  $30\text{--}200 \mu\text{m}$  apart (average  $122 \mu\text{m}$ ).

SLEs appeared following  $100 \mu\text{M}$  bath-application of 4AP and raising the temperature to  $36^\circ\text{C}$ . Increasing concentrations of 4AP were used (up to  $200 \mu\text{M}$ ) if SLE formation was not observed within 20 min.

Alignment of the seizure start times was based on an identifiable feature of the extracellular recording – the fast positive extracellular shift (FPES,  $1\text{--}5 \text{ mV}$ , see Figure 30.4D). Oriens interneurons were targeted because of their importance and vulnerability in epilepsy (Oliva et al., 2002; Santhakumar and Soltezs, 2004; Sanon et al., 2005) and their role in network dynamics (Pike et al., 2000; Gillies et al., 2002). Seven of 12 interneurons that underwent depolarization block (DB) displayed OLM interneuron membrane characteristics and bipolar horizontal dendritic morphology (Maccaferri and McBain, 1996; Maccaferri and Lacaille, 2003).

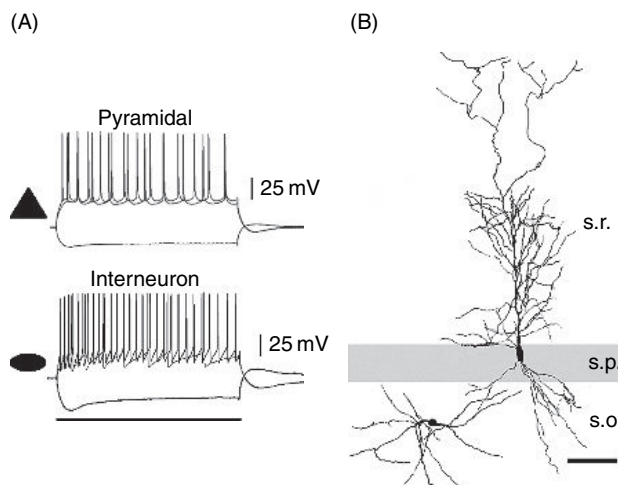


**FIGURE 30.3** Excitatory and inhibitory neurons. (A) Examples of pyramidal (triangle) and oriens interneuron (ellipse) membrane properties following 500 ms (scale bar) negative and positive current injections. (B) Camera lucida microscope drawings of the dendrites of the cells in (A). s.: stratum; o.: oriens; p.: pyramidale; r.: radiatum. Scale bar 50  $\mu\text{m}$ . The axon from the putative OLM interneuron is not well filled, but electrical characteristics and oriens location are highly consistent with the OLM subtype. After Ziburkus et al. (2006) (reproduced with permission).

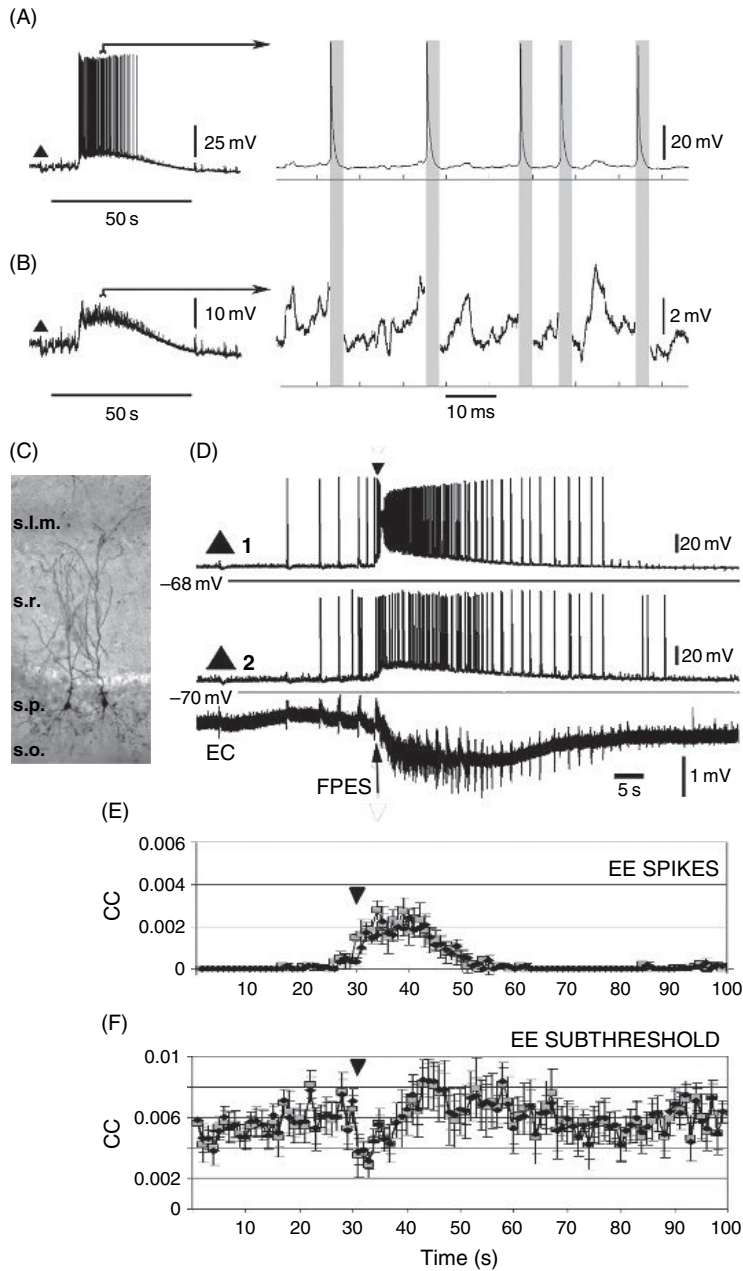


**FIGURE 30.4** Analysis of the SLEs in pyramidal cell pairs. (A) Left trace shows the complete voltage signal recorded from a pyramidal cell during SLE; right contains an expanded excerpt from the left. (B) Examples of the same signal as in (A) with the spikes removed (regions in gray boxes). The residual interspike voltage signal was used for subthreshold correlation analysis. (C) Photomicrograph of two neurobiotin filled pyramidal cells in the CA1. s.: stratum; l.m.: lacunosum moleculare; r.: radiatum; p.: pyramide; o.: oriens. (D) Whole-cell recordings from two pyramidal cells (triangles) and an extracellular electrode (EC). Following some pre-ictal spikes, pyramidal cells fire a prolonged burst of spikes riding on a wave of intracellular depolarization (ictal event), followed by post-ictal spikes of decaying frequency. The inverted triangle (at 30 s, D and E) is aligned with the FPES used to denote the start of the ictal events. (E and F) The cross-correlation (CC) between each pair was measured within one-second non-overlapping windows beginning 30 s before until 70 s after the FPES. Graphs of cross-correlation values for spikes (E) and subthreshold voltages (F). Black diamonds represent unweighted pooled and gray squares weighted resampled averages. ANOVA results for one-second windows showed that cross-correlation values for subthreshold voltages ( $df = 7199, F = 1.38, P = 0.0083$  for unweighted) and for the spikes ( $df = 7199, F = 14.72, P < 0.0001$ ) significantly changed across the evolution of SLEs. Tukey multiple comparison tests ( $P < 0.001$  for unweighted and  $P < 0.05$  for weighted averages) confirmed that correlation values at the start of the ictal event (inverted triangle mark) significantly decreased for the subthreshold voltages and increased for the spikes. After Ziburkus et al. (2006) (reproduced with permission).

To track the temporal evolution of EE and EI synchrony, two unbiased cross-correlations were calculated using subthreshold membrane potentials and spike times of pairs of neurons over discrete time windows. We use cross-correlation to infer the presence of synchronization (Netoff and Schiff, 2002). Dual correlation analyses allowed us to compare synchrony in subthreshold inputs and suprathreshold neuronal spike outputs. Alternate methods to achieve a similar analysis used median filters to remove spikes (Mooney et al., 2001; Buonomano, 2003), which alter the spectra and are less suitable for correlation measures.

For spike correlation, a simple threshold was used to identify discrete spike times. To measure subthreshold correlations, data between spike initiation and termination were discarded and correlations were performed using interspike data (Figure 30.4A and B). The spike data gaps were retained, leaving the time relationships among the residual subthreshold voltages unchanged. This subthreshold activity reflects synaptic network inputs to the cells, as well as intrinsic voltage-gated subthreshold responses. In contrast, spike cross-correlation reflects neuronal output. We applied an estimate of the expected cross-correlation variance given each time series' autocorrelation and time length (the expected cross-correlation given no functional communication between the cells, see Box and Jenkins, 1976). Only statistically significant correlations, greater than two standard deviations of the expected value, were included in the analysis.

To excise spikes, the times of spike initiation and termination were determined by measuring the slope of the membrane potential over a fraction of a millisecond. The slope threshold for spike initiation was set to a finite positive value, typically 25 mV/ms. The end slope was chosen to be zero, thus forcing the spike to end before any subsequent spikes would begin.

We will here focus on linear correlation in the time domain (cross-correlation). Correlation is used as an inference that there exists a functional relationship, synchrony, between two time series. All time series which share frequencies, and which are collected for finite time, have a non-zero measured cross-correlation, and we will use statistical measures below that to estimate how large a cross-correlation is expected for a given pair of time series based on their autocorrelations (we use a Bartlett estimator – see below). We also note that there is a significant literature on non-linear (generalized) synchrony, whose statistics are rather different and we have employed such tools in neuronal systems. The interested reader is referred to previous technical papers for further discussion of metrics and statistics for non-linear synchronization (Schiff et al., 1996; Netoff and Schiff, 2002; So et al., 2002; Netoff et al., 2004).

For subthreshold voltages, correlations were calculated within non-overlapping sliding time windows of 1 second. The continuous cross-correlation function,  $c_{i,j}(\tau)$ , for each pair of neurons  $i$  and  $j$  for each time window  $T$  was calculated using:

$$c_{i,j}(\tau) = \frac{\sum_{t=-T/2}^{T/2} x_i(t)x_j(t+\tau)}{\left( \sum_{t=-T/2}^{T/2} (x_i(t))^2 \right)^{1/2} \left( \sum_{t=-T/2}^{T/2} (x_j(t))^2 \right)^{1/2}}$$

where  $x(t)$  is the voltage (continuous with mean removed) at time  $t$  for channel  $i$  or  $j$ , and  $\tau$  is the time lag.

The absolute value of  $c_{i,j}(\tau)$  at each time lag was compared to the Bartlett estimator of cross-correlation standard error,  $\sigma_{i,j}$ , (Bartlett, 1946; Box and Jenkins, 1976):

$$\sigma_{i,j}^2(\tau) = \left| \frac{\sum_{\tau=-T/2}^{T/2} c_{i,i}(\tau)c_{j,j}(\tau)}{(T+1-\tau)} \right|$$

determined from the autocorrelation functions of each signal,  $c_{i,i}(\tau)$ ,  $c_{j,j}(\tau)$ , where  $|\cdot|$  indicates absolute value. The correlation value for each window was then determined by the sum,  $S$ , of the cross-correlation values greater than two times the standard error:

$$S = \sum_{\tau=-T/2}^{T/2} |c_{i,j}(\tau)| \theta(|c_{i,j}(\tau)| - 2\sigma_{i,j}(\tau))$$

where  $\theta$  is the Heaviside function (1 if  $|c_{i,j}(\tau)| - 2\sigma > 0$ , and 0 otherwise). This method reduces the spurious cross-correlation effects due to the magnitude of the autocorrelation of the individual signals and takes into account the finite nature of the short time series used.

For spikes, we binned the time series of spikes,  $s(t)$ , for each pair of neurons  $i$  and  $j$ , by discretizing time into  $N$  intervals of 10 ms. The point process correlation,  $p_{i,j}(\tau)$ , corrected for the expected product of the spike numbers  $n, m$  within  $-T/2 < t < T/2$  for neuron  $i$  and  $j$  respectively, is

$$p_{i,j}(\tau) = \frac{1}{nm} \left[ \sum_{t=-T/2}^{T/2} s_i(t)s_j(t+\tau) - \frac{nm}{N} \right]$$

(Brody, 1991). The spike rate correction compensates for the effects of increased correlations due to increased activity. As stated above, correlations in the individual signals can erroneously produce higher correlation values in the cross-correlation signal.

In order to account for this effect, we once again used a Bartlett estimator to determine the significance of  $p_{i,j}(\tau)$ . This point process estimator was calculated in the same manner as for the synaptic correlations, using the autocorrelation function

$$g_{i,i}(\tau) = \frac{1}{n^2} \left[ \sum_{t=-T/2}^{T/2} s(t)_i s(t+\tau)_i - \frac{n^2}{N} \right]$$

and the estimate of the point process standard error,  $\epsilon_{ij}$ , as

$$\epsilon_{i,j}^2(\tau) = \left| \frac{\sum_{\tau=-T/2}^{T/2} g_{i,i}(\tau) g_{j,j}(\tau)}{(T+1-\tau)} \right|$$

Averaged data representing spiking rates and cross-correlation values are reported as mean  $\pm$  standard deviation (s.d.). Analysis of variance (ANOVA) was used to determine whether the means of correlation measures from distinct SLE epochs were significantly different. Post-hoc Tukey multiple comparison tests (confidence limit  $P < 0.001$ ) were performed following ANOVA. Because the number of SLEs measured per cell pair was variable (5–18), we also recalculated averages by randomly resampling to equalize the number of SLEs compared from each pair. Both pooled and resampled averages are reported.

#### EXCITATORY AND INHIBITORY INTERPLAY DURING EPILEPTIFORM BURSTS

Shortly after application of 4AP we observed burst firing in EE and EI pairs. These events were network driven, as they were also reflected in the extracellular recordings (Figure 30.5A,B). Interneurons produced more spikes than pyramidal cells and often exhibited a short (up to 100 ms) depolarization block which coincided with burst firing in pyramidal cells (Figure 30.5C,D). These findings coupled with other recent reports (Aradi and Maccaferri, 2004) show that distinct timing interplay of inhibition and excitation might also exist during *in vitro* interictal-like burst firing events.

#### EXCITATORY AND INHIBITORY INTERPLAY DURING SEIZURES

Recurrent SLEs (>15 s ictal-like network events with extracellular potential shifts; see Figure 30.4D) were recorded in 30 neuronal pairs (18 dual and 4 triple) located in strata oriens and pyramidale, yielding over 250 SLEs for analysis (Ziburkus et al., 2006). Qualitatively analogous SLEs were observed in experiments in which the CA1 region was surgically isolated ( $n = 13$  cells), suggesting that the excitatory Schaeffer collateral pathway is not necessary for local network SLE generation in the CA1 (Barbarosie and Avoli, 1997; Netoff and Schiff, 2002).

Pyramidal cells ( $n = 35$ ) fired at lower rates than interneurons prior to SLEs. Consistent early features of SLEs were a burst of pyramidal cell spikes ( $\approx 1$ –3 s), coinciding with an FPES in the extracellular and intracellular potentials followed by a sustained negative extracellular shift (1–5 mV; see Figure 30.4D). When multiple FPESs were seen, the final one just before the slow negative extracellular potential shift was selected as the temporal anchor point for subsequent analysis.

Sub- and suprathreshold cross-correlation analyses of excitatory cell pairs ( $n = 15$ ) revealed qualitatively different results (see Figure 30.4E,F). Pyramidal cell spike output increased markedly during the SLEs ( $n = 15$  pairs, 148 SLEs)

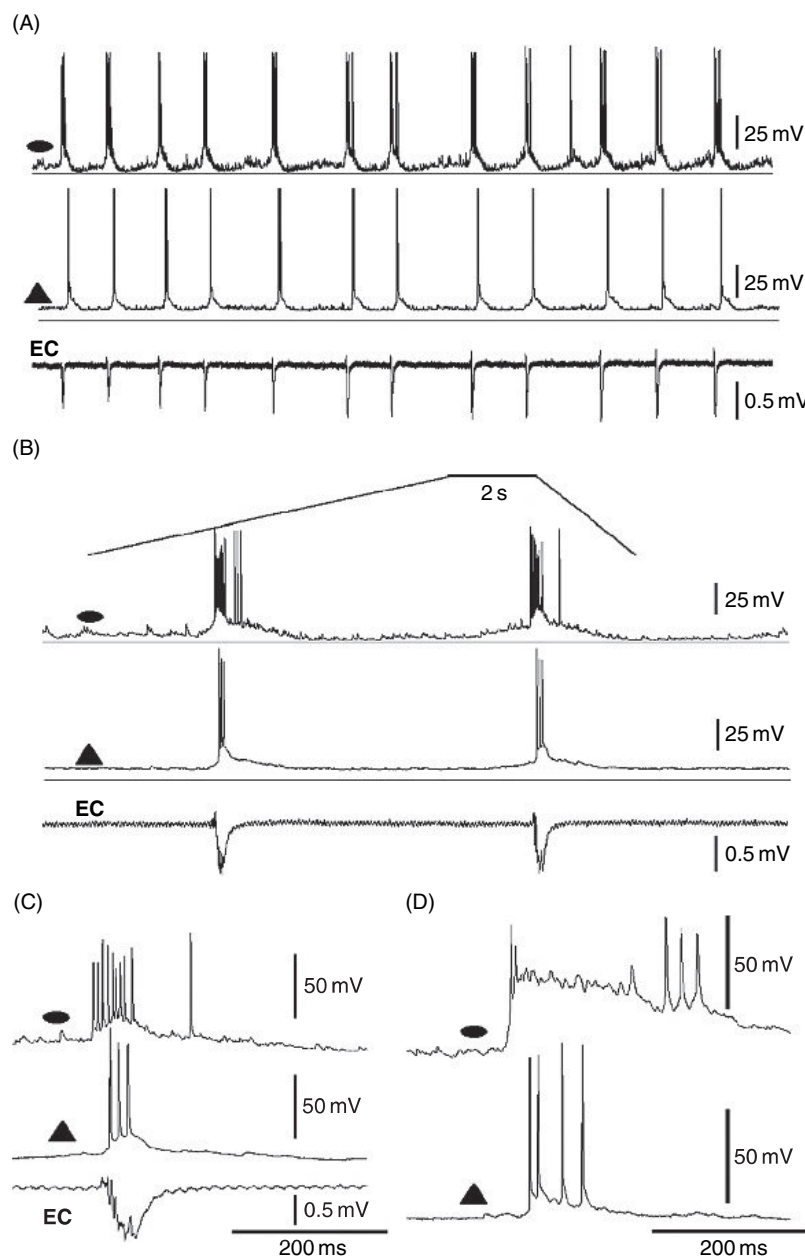


**FIGURE 30.5** EI interplay during interictal burst discharges. (A) Traces of three simultaneous recordings from an interneuron (ellipse, top), pyramidal cell (triangle, middle) and extracellular electrode (EC, bottom). (B) Expanded portion of the burst discharges from (A). (C) Single burst at expanded scale from (B). (D) Burst from a dual recording of an interneuron and pyramidal cell taken from another slice. Note that pyramidal cells fire most of their spikes in the middle of the time period of the interneuron paroxysmal depolarizing shift and burst discharge. The interneurons show a brief period of near spike inactivation in (C) and a longer inactivation in (D). After supplementary data Ziburkus et al. (2006) (reproduced with permission).

and showed a considerable increase in spike cross-correlation (see Figure 30.4E). In contrast, averaged subthreshold EE correlations ( $n = 15$  pairs; 148 SLEs) showed significantly decreased correlations at the start of the ictal-like event (see Figure 30.4F). This finding is consistent with previous results in which voltage-activated conductances during similar recordings were blocked (Netoff and Schiff, 2002).

In the presence of 4AP, oriens interneurons were more active and fired at higher frequencies than concurrently recorded pyramidal cells (Figure 30.6 and see Figure 30.7). During SLEs, the interneurons and pyramidal cells exhibited a robust spiking interplay (see Figure 30.7), which took place over substantially longer time scales compared to the interplay seen in interictal bursts (see Figure 30.5).

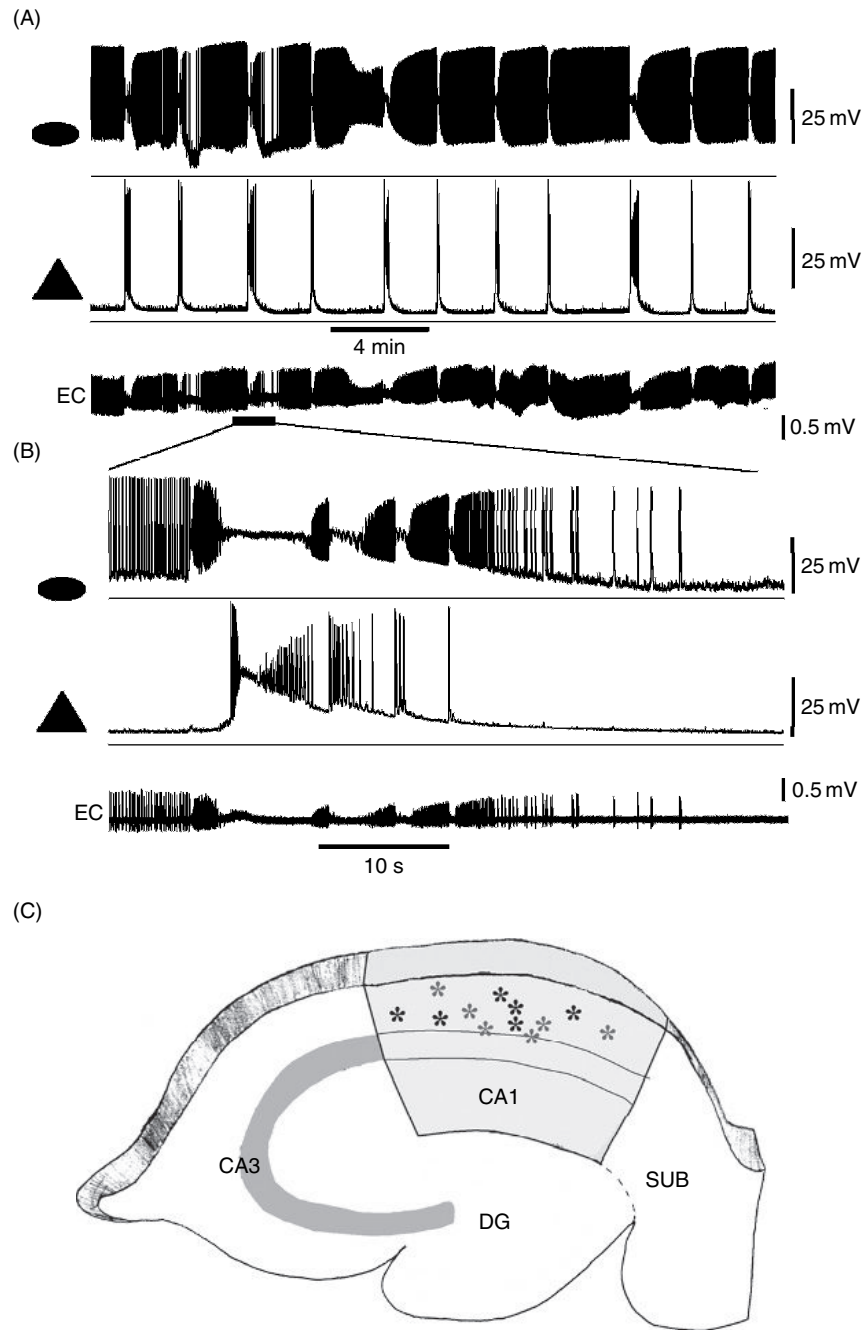


**FIGURE 30.6** EI interplay during SLEs. (A) Repetitive SLEs and EI interplay. The interneuron (ellipse) is more active in 4AP than the pyramidal (triangle) cell. EC denotes a fortuitous extracellular single unit recording of action potentials from the axon of this interneuron. The EC electrode was placed in oriens, about 75  $\mu$ m from the interneuron soma. Higher time scale magnification of data (not shown) revealed that the intracellularly recorded interneuron spikes corresponded precisely to each extracellularly recorded spike. (B) Expanded time base illustrating robust EI interplay during the SLEs. Note the cessation of axonal spikes in EC during interneuron DB. (C) Locations of interneurons exhibiting DB. Horizontal and rounded interneuron somata were mapped following neurobiotin histochemistry. Gray stars indicate interneurons that underwent DB in isolated CA1. After Ziburkus et al. (2006) (reproduced with permission).

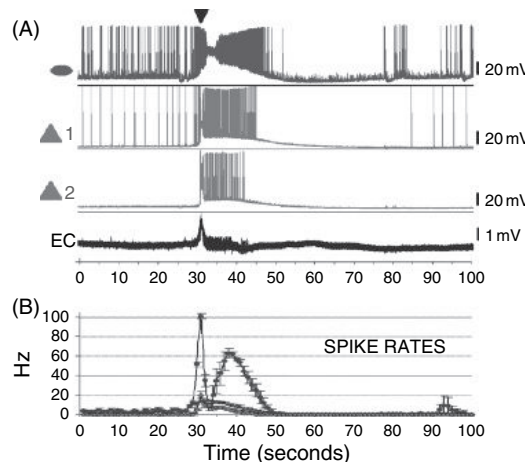


**FIGURE 30.7** EI spike interplay during SLEs. (A) Traces from simultaneous whole cell measurements from one interneuron (blue, ellipse) and two pyramidal cells (red, triangles) and an extracellular DC mode recording (EC). Inverted black triangle denotes the FPES. (B) Average spike rates of the three cells (interneuron, blue circles, pyramidal 1, red diamonds, pyramidal 2, red triangles). Note that the plot in (B) is an average ( $n = 8$  SLEs in the experiment) and hence is not precisely time locked to the single SLE example shown in (A). (See Plate 23 in color plate section.)

Interneuron firing rates peaked at 62 Hz just prior to entering into the long-lasting (5–40 s) DB within the ictal discharge. DB was characterized by transmembrane potential depolarization (to  $-40$  to  $-10$  mV) and the inactivation of action potential generating mechanisms (Bragin et al., 1997; Bikson et al., 2003; Somjen, 2004). DB was observed in 12 horizontal interneurons located in stratum oriens and the pyramidale-oriens layer border. For the cells that exhibited DB, the outline of the slices and stratum pyramidale were drawn using *camera lucida* and overlaid to the best fit (see Figure 30.6C). Depolarization block was rarely pronounced in pyramidal cells and, when observed, was significantly shorter (<2 s) than in interneurons. As seen in Figures 30.6 and Figure 30.7, pyramidal cells produced sustained barrages of spikes during interneuron DB, typically firing 6–15 spikes per second. Note the fortuitous extracellular single unit recording from the axon of the interneuron in Figure 30.6 (A and B), confirming cessation of inhibitory spiking during DB. SLE termination was accompanied by the return of interneuron activity as pyramidal cells became progressively quiescent.

Figure 30.7 shows an example of simultaneous EE and EI interactions during a triple whole-cell and extracellular recording of a spontaneous SLE and the respective average ( $n = 8$  SLEs) firing rates. This example illustrates that the firing rates of the two recorded pyramidal cells changed together, with peak firing rates at the onset and sustained high firing rates during the interneuron DB (Ziburkus et al., 2006).

Analysis of 102 SLEs from EI pairs are shown in Figure 30.8A–C ( $n = 12$  pairs). There was an increase in EI subthreshold correlations at the beginning and towards the end of the interneuron DB (Ziburkus et al., 2006). With resampling, the increase in subthreshold correlations towards the end of the SLEs was the most robust feature (see Figure 30.8A).

A significant increase in EI spike correlations was observed at the beginning (unweighted) and towards the end of the SLEs (weighted averages; about 45 seconds, see Figure 30.8B). These EI subthreshold and spike findings are consistent with the fact that pyramidal cells and interneurons were active together at the onset and offset of the depolarization block (Ziburkus et al., 2006).

The spike rate averages ( $n = 12$  pairs, 102 SLEs) in Figure 30.8C show a consistent robust sequence starting with intense interneuron firing, followed by a peak in pyramidal cell firing during interneuron DB and concluding with the return of intense inhibitory firing as pyramidal activity decays (Ziburkus et al., 2006). The terminal decay in pyramidal cell firing frequency is associated with the second peak and sustained firing in interneurons recovering from the block (about 35 seconds; see Figure 30.8C and inset).

Figure 30.9 shows an example of two interneurons participating in an SLE. Although spiking activity ceased as both interneurons entered DB, subthreshold correlation values nevertheless increased ( $n = 13$  SLEs, 3 pairs). The finding that pyramidal cell spike correlations are increased during interneuron DB (see Figure 30.3E) is consistent with synchronous excitation contributing to the subthreshold II correlations during their DB (Ziburkus et al., 2006). In contrast, the loss of inhibitory spike outputs is consistent with the decrease in EE subthreshold correlations during DB (see Figures 30.1 and 30.4F).

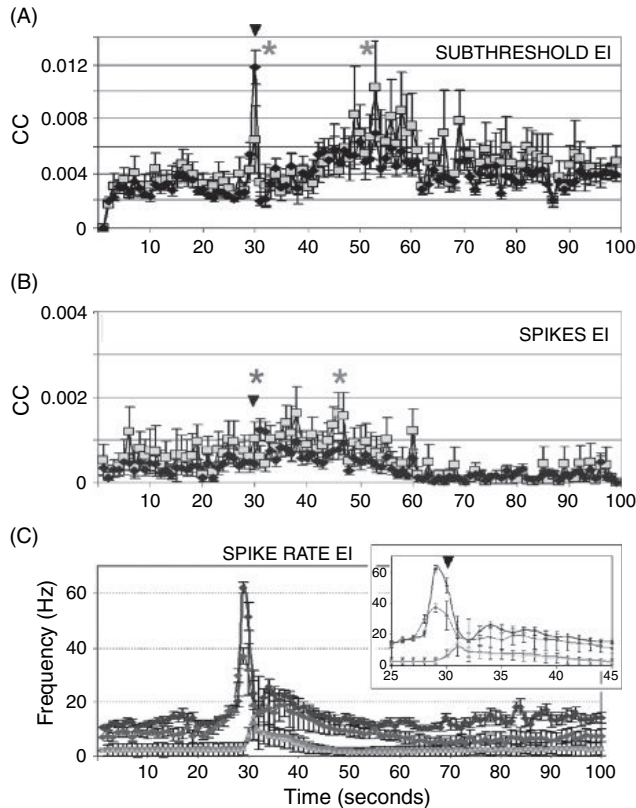


**FIGURE 30.8** EI correlations during SLEs. (A) EI cross-correlation (CC) averages. The means of EI subthreshold cross-correlation values were significantly different (ANOVA:  $df = 10199$ ,  $F = 4.27$ ,  $P < 0.0001$ ) at distinct SLE stages (Tukey multicomparison, green asterisks). Unweighted pooled subthreshold EI cross-correlation values (represented as black diamonds) peaked at the onset of SLEs, followed by a decrease and then a gradual increase towards the end of the SLEs (Tukey multiple comparison test,  $P < 0.001$ ). With weighted resampled averages (gray squares) the peak at the onset of SLEs was less prominent, but the significance of the increase in subthreshold EI correlations was retained ( $P < 0.05$ ). Inverted black triangles denote the FPES in (A, B, inset in C). (B) A significant increase in EI spike correlations was observed at the beginning (unweighted, blue asterisk) and following the DB in interneurons (weighted averages, green asterisk). (ANOVA,  $df = 10199$ ,  $F = 3.27$ ,  $P < 0.0001$ ; Tukey multiple comparison test,  $P < 0.001$  for unweighted (black diamonds) and  $P < 0.005$  for weighted resampled (gray squares) averages). (C) Cumulative average spike rates ( $n = 15$  oriens interneurons and  $n = 40$  pyramidal cells from pairs and single whole cell recordings). Note the peak of inhibitory spiking preceding the FPES (dark blue, I unweighted pooled; light blue, I weighted resampled). Excitatory firing rates increase as interneurons enter into the DB and decreased as interneurons exit the DB (red, unweighted pooled; orange, unweighted pooled). Inset shows average spike rates at expanded time scale. After Ziburkus et al. (2006) (reproduced with permission). (See Plate 24 in color plate section.)

#### GAP JUNCTIONS AND SEIZURES

Recent findings show that electrotonic coupling is present between oriens interneurons (Zhang et al., 2004) and that gap junctions connecting putative cortical interneurons increase synchrony (Merriam et al., 2005). To test whether 4AP seizures and DB are dependent on gap junction connectivity, we bath applied low concentrations (2–20  $\mu$ M) of carbenoxolone to cells exhibiting seizures (Figure 30.10,  $n = 4$  interneurons and  $n = 4$  pyramidal cells). Using these low concentrations of carbenoxolone, we were able to manipulate the length of depolarization block and SLE. The length of DB in interneurons decreased with increasing concentration of carbenoxolone in increments as small as 2  $\mu$ M (Figure 30.10A). In half of the slices, SLE could be blocked with 20  $\mu$ M carbenoxolone. However, in some cases to block completely SLE and neuronal hyperexcitability, higher carbenoxolone concentrations were needed (20–100  $\mu$ M;  $n = 4$ ). Following wash out of carbenoxolone ( $\sim 1$  hour,  $n = 2$ ), DB and recurring seizures (of shorter duration) returned. Thus, electrotonic coupling may play a role in the sequence of the EI interplay that we have here described (see supplementary data, Ziburkus et al., 2006).

The full spectrum of the effects of carbenoxolone is under scrutiny. In rat hippocampal glial-neuronal cocultures where only glial cells were electronically coupled, high concentrations (100  $\mu$ M) of carbenoxolone could directly affect neuronal excitability (Rouach et al., 2003). On the other hand, experiments in *in vitro* slice and intact hippocampal preparations

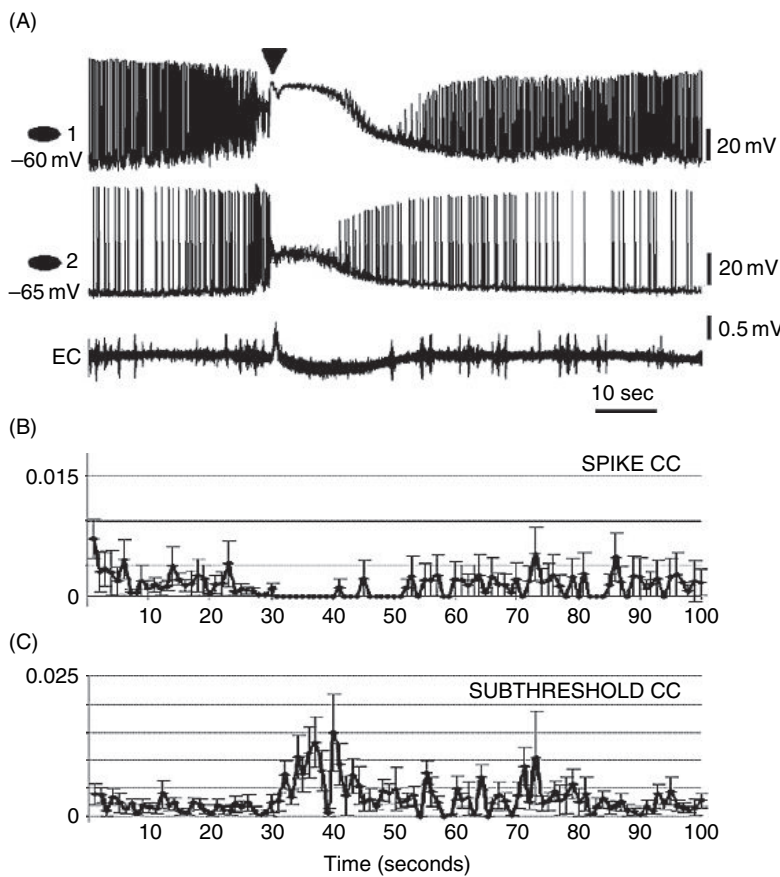


**FIGURE 30.9** II activity during SLEs. (A) Whole cell measurements from two oriens interneurons accompanied by the average cross-correlation (CC) measures of suprathreshold (B) and subthreshold (C) signals ( $n = 13$  SLEs, 3 pairs). Inverted triangle indicates the FPES. Note the clear loss of spiking and increase in subthreshold correlations during DB in II pairs (unweighted averages). After Ziburkus et al. (2006) (reproduced with permission).

showed minimal effects of carbenoxolone on intrinsic neuronal membrane properties (100–150  $\mu\text{M}$ ) and a potent effect on electronic coupling between OLM cells (Yang and Michelson, 2001; Zhang et al., 2004). We observed distinct effects with concentrations as low as 2  $\mu\text{M}$  and a clear concentration dependency between 2 and 20  $\mu\text{M}$ . Although further experiments with more specific neuronal gap junction blockers and recordings from electrically coupled cells will be required to establish more definitively the role of gap junctions in SLE, our results are highly suggestive that gap junction connectivity plays a role in DB and SLE.

## DISCUSSION

What are the dynamics of seizures? This chapter suggests that we are further from defining this than we had hoped. Certainly, there appears to be abundant evidence suggesting that a description of seizures as a straightforward increase in synchronization between neurons may be too simplistic.

Our fundamental finding from the study of seizures in brain slices is the discovery of an interleaved spiking pattern between pyramidal cells and interneurons during spontaneous seizure-like events. Our analysis of spike output between EI pairs revealed that pyramidal cells and interneurons became activated at different times during SLEs. Oriens interneurons were more active at SLE onset, followed by a period of DB during which pyramidal cells exhibited runaway excitation. SLE termination was characterized by the oriens interneurons emerging from DB into progressively more active spiking and the simultaneous gradual reduction of pyramidal cell spiking.

Note that although we most frequently observed a single sequence of interplay – excess inhibition followed by excess excitation followed by excess inhibition – at times an ongoing oscillation between these EI networks could be observed

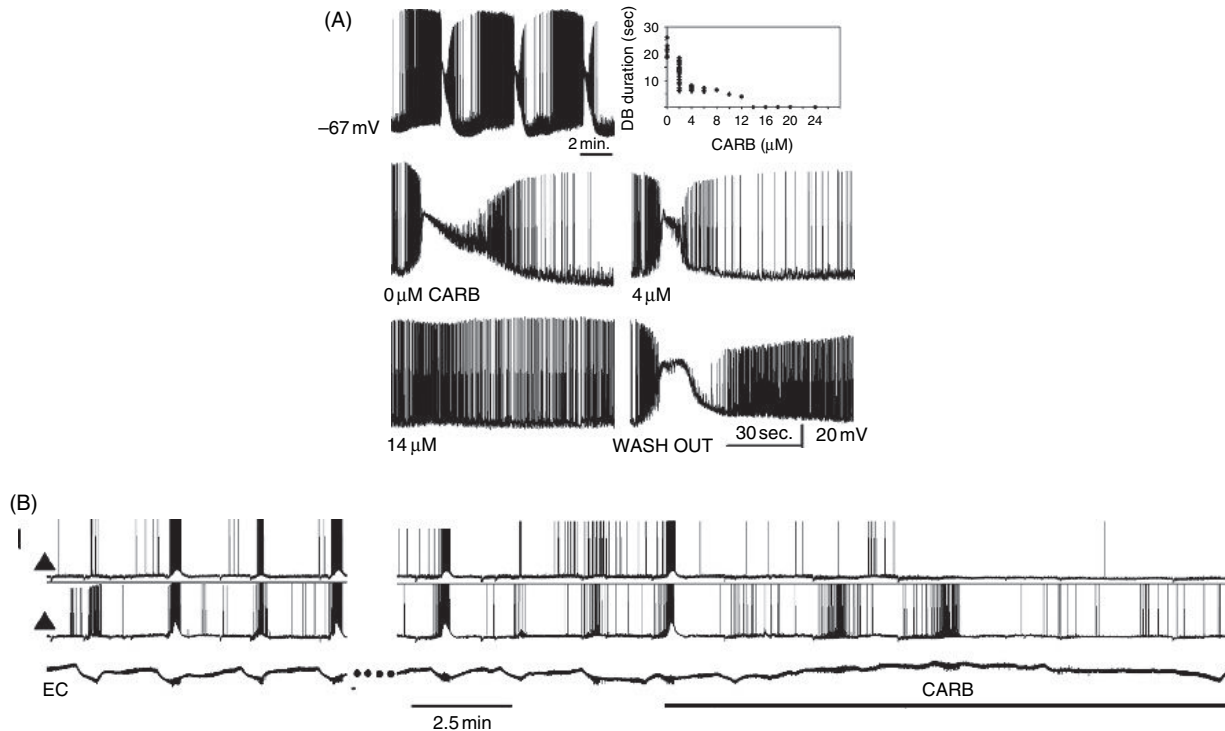


**FIGURE 30.10** Interneurons in DB and gap junctions. (A) Compressed data segment showing three recurring DBs during seizures in an oriens interneuron. Bath application of increasing carbamoloxolone (CARB) concentrations (2, 4, 6, 8, 10, 12, 14, 16, 20 and 24  $\mu\text{M}$ ) decreased the duration of the DB ( $n = 3$ ). Inset graph (top right) shows duration of DB (ordinate) for the same interneuron from which the example traces are taken. Complete seizure blockade was observed at 20  $\mu\text{M}$  ( $n = 4$ ). DB returned following a 60 minute washout. (B) Traces illustrate seizures recorded in EE pair in isolated CA1. 20  $\mu\text{M}$  carbamoloxolone blocked the seizures, but cells retained sub- and suprathreshold activity. Dots indicate a time gap in the tracing. After supplementary data Ziburkus et al. (2006) (reproduced with permission).

(see e.g. Figure 30.6B). A broader view of these observations would suggest that these seizures are an oscillation which emerges from fluctuations in network stability. In this view, the most common interplay we observed was a damped oscillation, but the degree of damping is not fixed.

Neuronal interplay and depolarization block may have been first observed in pioneering *in vivo* studies of single intracellular neocortical and hippocampal seizure recordings from untyped cells (Kandel and Spencer, 1961; Matsumoto and Marsan, 1964). More recently, a strong inhibitory component of seizures with increased inhibitory spiking before and after paroxysmal discharges was observed in single cell intracellular *in vivo* recordings from fast spiking putative interneurons (Timofeev et al., 2002). Additional recent *in vivo* observations have clearly shown that precisely interleaved activity of subpopulations of inhibitory cells coordinate physiologically normal hippocampal theta rhythms and sharp waves (Klausberger et al., 2003).

Examples of *in vitro* EI interplay have been observed in spontaneous population burst firing with elevated  $\text{K}^+$  (Aradi and Maccaferri, 2004). We have also observed similar burst firing interplay in our preparations (see Figure 30.5) and have observed that the spontaneous SLEs retained features of the burst EI interplay, but at the much longer time scale of seizures. This is in contrast to tetanically stimulated seizure-like after discharges that show an apparent EI synchronization (Perez-Velazquez and Carlen, 1999; Fujiwara-Tsukamoto et al., 2004). We are aware of no other observations of such EI interactions during spontaneous SLEs.

In our work we explicitly calculated the correlation between distinct neuronal subtypes. We found that correlations during SLEs depended qualitatively upon whether subthreshold or spike information was considered. During the SLE onset, we observed a decrease in the subthreshold input correlation among EE pairs. This finding is consistent with our previous work in which we pharmacologically suppressed active conductances (Netoff et al., 2002). EE spike output correlation, on the other hand, increased during SLEs. Similar increases in spike correlation were observed *in vivo* between nearby putative neocortical pyramidal cells (Timofeev et al., 2004).

It remains to be explained how hippocampal pyramidal cells, with sparse associational connections, exhibit prominent spike synchronization in the setting of decreased subthreshold correlations. It is possible that such spikes synchronize through their ephaptic electric fields (Traub et al., 1985a, 1985b) or through gap junction connectivity between the axons of pyramidal cells (Draguhn et al., 1998). These effects are likely to be more effective when interneurons coordinate their DB activity via their own gap junctions (Zhang et al., 2004), thus releasing the pyramidal cells from inhibition concurrently. Indeed, our data suggest that the gap junction blocker carbenoxolone blocks SLEs and, at low concentrations, shortens DB in interneurons (see Figure 30.10).

In contrast to EE, EI correlation was elevated at the beginning and end of SLEs. These findings are consistent with the fact that EI spike synchrony can only occur when both populations of cells are firing – at the beginning and towards the end of inhibitory DB. The loss of inhibitory spikes during DB is coincident with the simultaneous decrease in pyramidal cell subthreshold EE synchronization. Lastly, subthreshold II correlation increased while the interneurons in DB stopped firing and pyramidal cell spike correlation increased. We suggest that correlated EE spiking during interneuron DB delivers synchronous synaptic currents to interneurons at a time during which they are unable to respond by spiking.

Nonetheless, we are cautious in evaluating data following spike extraction. The residual subthreshold time series likely undersampled synaptic currents that are coincident with spike generation, potentially leading to a spurious decrease in subthreshold EE correlation. However, our results are consistent with earlier findings during active conductance blockade (Netoff et al., 2002). It may be possible that overestimation of correlation due to the presence of active membrane conductances, and underestimation through time series undersampling following spike extraction, may have partially offset each other.

Previous work has shown that following stimulation, chloride loading inside pyramidal cells causes inhibition to become excitatory (Fujiwara-Tsukamoto et al., 2004, 2006). It is possible that excessive inhibitory activity at the start of our SLEs became excitatory in its effects on pyramidal cells. Preliminary voltage clamp observations (Ziburkus et al., 2005, additional data unpublished) suggest that not only pyramidal cells but interneurons as well may have elevated intracellular chloride in this 4AP model.

Although seizures have traditionally been treated as monolithic entities – ictal versus non-ictal – there is little to support this notion. Our findings suggest that the interplay of cellular activity supports a natural partitioning of these *in vitro* SLEs into stages. If inhibitory and excitatory cell types fire at different times during seizures, then our findings suggest several novel therapeutic targets for seizure control, including blocking excessive inhibitory network activity and preventing depolarization block. The motif of excessive inhibition, subsequent inhibitory breakdown through DB and the concurrent increase in excitatory output could underlie some of the structured patterns seen in EEGs during seizures (Schiff et al., 2005). It remains a challenge to identify the relevant cellular mechanisms that underlie the evolution of endogenous seizure stages *in vivo*.

#### ACKNOWLEDGMENTS

We are grateful to B. Gluckman, T. Netoff, T. Sauer and S. Weinstein for their invaluable expertise. Supported by NIH grants R01MH50006 (SJS), K02MH01493 (SJS), K25MH01963 (EB), F32NS051072 (JRC), the Epilepsy Foundation (JZ) and the Pennsylvania Department of Community and Economic Development. This project is also funded, in part, by a grant with the Pennsylvania Department of Health using Tobacco Settlement Funds. The Department specifically disclaims responsibility for any analyses, interpretations or conclusions.

#### REFERENCES

- Aradi, I. and Maccaferri, G. (2004). Cell type-specific synaptic dynamics of synchronized bursting in the juvenile CA3 rat hippocampus. *J Neurosci* 24:9681–9692.
- Avoli, M., Perreault, P., Olivier, A. and Villemure, J.G. (1988). 4-Aminopyridine induces a long-lasting depolarizing GABAergic potential in human neocortical and hippocampal neurons maintained. *Neurosci Lett* 94:27–32.
- Avoli, M., Barbarosie, M., Lucke, A., Nagao, T., Lopantsev, V. and Kohling, R. (1996a). Synchronous GABA-mediated potentials and epileptiform discharges in the rat limbic system. *J Neurosci* 16:3912–3924.
- Avoli, M., Louvel, J., Kurcewicz, I., Pumain, R. and Barbarosie, M. (1996b). Extracellular free potassium and calcium during synchronous activity induced by 4-aminopyridine in the juvenile rat hippocampus. *J Physiol* 493:707–717.
- Babb, T.L., Pretorius, J.K., Kupfer, W.R. and Crandall, P.H. (1989). Glutamate decarboxylase immunoreactive neurons are preserved in human epileptic hippocampus. *J Neurosci* 7:2562–2574.
- Barbarosie, M. and Avoli, M. (1997). CA3-driven hippocampal-entorhinal loop controls rather than sustains limbic seizures. *J Neurosci* 17:9308–9314.

- Bartlett, M.S. (1946). On the theoretical specification of sampling properties of autocorrelated time series. *J Royal Stat Soc B*8:27.
- Bikson, M., Hahn, P.J., Fox, J.E. and Jefferys, J.G. (2003). Depolarization block of neurons during maintenance of electrographic seizures. *J Neurophysiol* 90:2402–2408.
- Box, G.E. and Jenkins, G.M. (1976). Time series analysis forecasting and control. Holden-Day, California.
- Bragin, A., Penttonen, M. and Buzsaki, G. (1997). Termination of epileptic afterdischarge in the hippocampus. *J Neurosci* 17:2567–2579.
- Brody, C.D. (1991). Correlations without synchrony. *Neural Comput* 11:1537–1551.
- Buonomano, D.V. (2003). Timing of neural responses in cortical organotypic slices. *Proc Natl Acad Sci* 100:4897–4902.
- Cohen, I., Navarro, V., Clemenceau, S., Baulac, M. and Miles, R. (2002). On the origin of interictal activity in human temporal lobe epilepsy. *Science* 298:1418–1421.
- Draguhn, A., Traub, R.D., Schmitz, D. and Jefferys, J.G.R. (1998). Electrical coupling underlies high-frequency oscillations in the hippocampus in vitro. *J Neurophysiol* 39:189–192. [???
- During, M. and Spencer, D.D. (1993). Extracellular hippocampal glutamate and spontaneous seizure in the conscious human brain. *Lancet* 341:1607–1610.
- Finnerty, G.T. and Jefferys, J.G. (2000). 9–16 Hz oscillation precedes secondary generalization of seizures in the rat tetanus toxin model of epilepsy. *J Neurophysiol* 83:2217–2226.
- Freund, T.F. and Buzsaki, G. (1996). Interneurons of the hippocampus. *Hippocampus* 6:347–470.
- Fujiwara-Tsukamoto, Y., Isomura, Y., Kaneda, K. and Takada, M. (2004). Synaptic interactions between pyramidal cells and interneurone subtypes during seizure-like activity in the rat hippocampus. *J Physiol* 557:961–979.
- Fujiwara-Tsukamoto, Y., Isomura, Y. and Takada, M. (2006). Comparable GABAergic mechanisms of hippocampal seizure-like activity in post-tetanic and low-Mg<sup>2+</sup> conditions. *J Neurophysiol* 95:2013–2019.
- Funahashi, S., Bruce, C.J. and Goldman-Rakic, P.S. (1989). Mnemonic coding of visual space in the monkey's dorsolateral prefrontal cortex. *J Neurophysiol* 61:331–349.
- Gillies, M.J., Traub, R.D., LeBeau, F.E. et al. (2002). A model of atropine-resistant theta oscillations in rat hippocampal area CA1. *J Physiol* 543:779–793.
- Gold, C., Henze, D.A., Koch, C. and Buzsaki G. (2006). On the origin of the extracellular action potential waveform: a modeling study. *J Neurophysiol* 95:3113–3128.
- Gutkin, B.S., Laing, C.R., Colby, C.L., Chow, C.C. and Ermentrout, G.B. (2001). Turning on and off with excitation: the role of spike-timing asynchrony and synchrony in sustained neural activity. *J Comput Neurosci* 11:121–134.
- Haider, B., Duque, A., Hasenstaub, A.R. and McCormick, D. (2006). Neocortical network activity in vivo is generated through a dynamic balance of excitation and inhibition. *J Neurosci* 26:4535–4545.
- Higashima, M., Kinoshita, H., Yamaguchi, N. and Koshino, Y. (1996). Activation of GABAergic function necessary for afterdischarge generation in rat hippocampal slices. *Neurosci Lett* 207:101–104.
- Horikawa, K. and Armstrong, W.E. (1988). A versatile means of intracellular labeling: injection of biocytin and its detection with avidin conjugates. *J Neurosci Methods* 25:1–11.
- Huang, X., Troy, W.C., Yang, Q., Ma, H., Laing, C.R., Schiff, S.J., Wu, J.Y. (2004). Spiral waves in disinhibited mammalian neocortex. *J Neurosci* 24:9897–9902.
- Isaev, D., Isaeva, E., Khazipov, R. and Holmes, G.L. (2005). Anticonvulsant action of GABA in the high potassium-low magnesium model of ictogenesis in the neonatal rat hippocampus in vivo and in vitro. *J Neurophysiol* 94:2987–2992.
- Kandel, E.R. and Spencer, W.A. (1961). Excitation and inhibition of single pyramidal cells during hippocampal seizure. *Exp Neurol* 4:162–179.
- Khosravani, H., Carlen, P.L. and Perez Velazquez, J.L. (2003). The control of seizure-like activity in the rat hippocampal slice. *Biophys J* 84:687–695.
- Khosravani, H., Pinnegar, C.R., Mitchell, J.R., Bardakjian, B.L., Federic, P. and Carlen, P.L. (2005). Increased high-frequency oscillations precede in vitro low-Mg<sup>2+</sup> seizures. *Epilepsia* 46:1188–1197.
- Klausberger, T., Magill, P.J., Marton, L.F. et al. (2003). Brain-state- and cell-type-specific firing of hippocampal interneurons in vivo. *Nature* 421:844–848.
- Lopantsev, V. and Avoli, M. (1998). Participation of GABA<sub>A</sub>-mediated inhibition in ictal-like discharges in the rat entorhinal cortex. *J Neurophysiol* 79:352–360.
- Maccaferri, G. and Lacaille, J.C. (2003). Interneuron diversity series: hippocampal interneuron classifications – making things as simple as possible, not simpler. *Trends Neurosci* 26:564–571.
- Maccaferri, G. and McBain, C.J. (1996). The hyperpolarization-activated current (I<sub>h</sub>) and its contribution to pacemaker activity in rat CA1 hippocampal stratum oriens-alveus interneurons. *J Physiol* 497:119–130.
- Matsumoto, H. and Marsan, C.A. (1964). Cortical cellular phenomena in experimental epilepsy: interictal manifestations. *Exp Neurol* 9:286–304.
- Menendez de la Prida, L., Benavides-Piccione, R., Sola, R. and Pozo, M.A. (2002). Electrophysiological properties of interneurons from intraoperative spiking areas of epileptic human temporal neocortex. *Neuroreport* 13:1421–1425.
- Menendez de la Prida, L., Huberfeld, G., Cohen, I. and Miles, R. (2006). Threshold behavior in the initiation of hippocampal population bursts. *Neuron* 49:131–142.
- Merriam, E.B., Netoff, T.I. and Banks, M.I. (2005). Bistable network behavior of layer I interneurons in auditory cortex. *J Neurosci* 25:6175–6186.
- Mooney, R., Hoes, W. and Nowicki, S. (2001). Auditory representation of the vocal repertoire in a songbird with multiple song types. *Proc Natl Acad Sci* 98:12778–12783.
- Netoff, T.I. and Schiff, S.J. (2002). Decreased neuronal synchronization during experimental seizures. *J Neurosci* 22:7297–7307.
- Netoff, T.I., Pecora, L.M. and Schiff, S.J. (2004). Analytical coupling detection in the presence of noise and nonlinearity. *Phys Rev E* 69:017201.
- Oliva, A.A. Jr, Lam, T.T. and Swann, J.W. (2002). Distally directed dendrotoxicity induced by kainic acid in hippocampal interneurons of green fluorescent protein-expressing transgenic mice. *J Neurosci* 22:8052–8062.
- Penfield, W. and Jasper, H. (1954). Epilepsy and the functional anatomy of the human brain. Little, Brown & Co., Boston.
- Perez-Velazquez, J.L. (2003). Bicarbonate-dependent depolarizing potentials in pyramidal cells and interneurons during epileptiform activity. *Eur J Neurosci* 18:1337–1342.
- Perez-Velazquez, J.L. and Carlen, P.L. (1999). Synchronization of GABAergic interneuronal networks during seizure-like activity in the rat horizontal hippocampal slice. *Eur J Neurosci* 11:4110–4118.

- Pike, F.G., Goddard, R.S., Suckling, J.M., Ganter, P., Kasthuri, N. and Paulsen, O. (2000). Distinct frequency preferences of different types of rat hippocampal neurones in response to oscillatory input currents. *J Physiol* 529:205–213.
- Racine, R.J., Gartner, J.G. and Burnham, W.M. (1972). Epileptiform activity and neural plasticity in limbic structures. *Brain Res* 47:262–268.
- Rouach, N., Segal, M., Koulakoff, A., Giaume, C. and Avignone, E. (2003). Carbenoxolone blockade of neuronal network activity in culture is not mediated by an action on gap junctions. *J Physiol* 553:729–745.
- Rubino, D., Robbins, K.A. and Hatsopoulos, N.G. (2006). Propagating waves mediate information transfer in the motor cortex. *Nature Neurosci* 9:1549–1557.
- Sanon, N., Carmant, L., Emond, M., Congar, P. and Lacaille, J.C. (2005). Short-term effects of kainic acid on CA1 hippocampal interneurons differentially vulnerable to excitotoxicity. *Epilepsia* 46:837–848.
- Santhakumar, V. and Soltesz, I. (2004). Plasticity of interneuronal species diversity and parameter variance in neurological diseases. *Trends Neurosci* 27:504–510.
- Schiff, S.J., So, P., Chang, T., Burke, R.E. and Sauer, T. (1996). Detecting dynamical interdependence and generalized synchrony through mutual prediction in a neural ensemble. *Phys Rev E* 54:6708–6724.
- Schiff, S.J., Sauer, T., Kumar, R. and Weinstein, S.L. (2005). Neuronal spatiotemporal pattern discrimination: the dynamical evolution of seizures. *NeuroImage* 28:1043–1055.
- Shu, Y., Hasenstaub, A. and McCormick, D.A. (2003). Turning on and off recurrent balanced cortical activity. *Nature* 423:288–293.
- So, P., Barreto, E., Josic, K., Sander, E. and Schiff, S.J. (2002). Limits to the experimental detection of nonlinear synchrony. *Phys Rev E* 5:046225.
- Somjen G.G. (2004). Ions in the brain. Oxford University Press, New York.
- Somogyi, P. and Klausberger, T. (2005). Defined types of cortical interneurone structure, space and spike timing in the hippocampus. *J Physiol* 562:9–26.
- Timofeev, I., Grenier, F. and Steriade, M. (2002). The role of chloride-dependent inhibition and the activity of fast-spiking neurons during cortical spike-wave electrographic seizures. *Neuroscience* 114:1115–1132.
- Timofeev, I., Grenier, F. and Steriade, M. (2004). Contribution of intrinsic neuronal factors in the generation of cortically driven electrographic seizures. *J Neurophysiol* 92:1133–1143.
- Traub, R.D., Dudek, F.E., Taylor, C.P. and Knowles, W.D. (1985a). Simulation of hippocampal afterdischarges synchronized by electrical interactions. *Neuroscience* 14:1033–1038.
- Traub, R.D., Dudek, F.E., Snow, R.W. and Knowles, W.D. (1985b). Computer simulations indicate that electrical field effects contribute to the shape of the epileptiform field potential. *Neuroscience* 15:947–958.
- Traynelis, S.F. and Dingledine, R. (1988). Potassium-induced spontaneous electrographic seizures in the rat hippocampal slice. *J Neurophysiol* 59:259–276.
- Treiman, D.M., Walton, N.Y. and Kendrick, C. (1990). A progressive sequence of electroencephalographic changes during generalized convulsive status epilepticus. *Epilepsy Res* 5:49–60.
- Wendling, F., Carrault, G. and Badier, J.M. (1997). Segmentation of depth-EEG seizure signals: method based on a physiological parameter and comparative study. *Ann Biomed Eng* 25:1026–1039.
- Westbrook, G.L. (1991). Seizures and epilepsy. In: *Principles of neural science* E.R. Kandel, T.M. Jessell and J.H. Schwartz, eds). McGraw-Hill, New York.
- Wu, L. and Gotman, J. (1998). Segmentation and classification of EEG during epileptic seizures. *Electroencephalogr Clin Neurophysiol* 106:344–356.
- Wyler, A.R., Ojemann, G.A. and Ward, A.A. (1982). Neurons in human epileptic cortex: correlation between unit and EEG activity. *Ann Neurol* 11:301–308.
- Yang, Q. and Michelson, H.B. (2001). Gap junctions synchronize the firing of inhibitory interneurons in guinea pig hippocampus. *Brain Res* 907:139–143.
- Zhang, X.-L., Zhang, L. and Carlen, P.L. (2004). Electrotonic coupling between stratum oriens interneuronones in the intact mouse juvenile hippocampus. *J Physiol* 558:825–839.
- Ziburkus, J., Cressman, J.R., Johnson, K.E. and Schiff, S.J. (2005). Inhibitory and excitatory interplay: neuronal conductance measures during in vitro seizures. *Epilepsia* 46(Suppl. 8):271–272.
- Ziburkus, J., Cressman, J.R., Barreto, E. and Schiff, S.J. (2006). Interneuron and pyramidal cell interplay during in vitro seizure-like events. *J Neurophysiol* 95:3948–3954.

PART

# VIII

---

## TOWARDS COMPUTER-AIDED THERAPY

---

This page intentionally left blank

# 31

## PRINCIPLES AND PRACTICE OF COMPUTER-AIDED DRUG DESIGN AS APPLIED TO THE DISCOVERY OF ANTI EPILEPTIC AGENTS

DONALD F. WEAVER

### ABSTRACT

Existing antiepileptic drug therapies are not effective in a substantial part of the patient population, indicating the pressing need for new therapeutics. This chapter discusses the principles and practice of modern computer-aided drug design as applied to the search for new drugs in epilepsy. In particular, focus will be on how application of computational advances can dramatically facilitate the implementation of the sequential approach of lead compound identification and optimization for the purpose of novel antiepileptic drug development.

### INTRODUCTION

The need to discover new therapeutics for the treatment of epilepsy persists as an ongoing neuropharmacological priority. Fortunately, over the coming decades, computational methods will herald substantial improvements in our ability to devise new therapies for epilepsy.

The search for improved anticonvulsant drugs clearly exemplifies the pressing need for new antiepileptic therapies. Existing anticonvulsant drugs are effective in only 65% of people with seizure disorders and the administration of such agents is associated with undesirable side-effects in more than 50% of those who receive them. Moreover, all of the currently available antiepileptic drugs are merely anticonvulsant agents (i.e. anti-seizure, ‘anti-ictogenic’ drugs) that symptomatically suppress the occurrence of seizures in people with already-established epilepsy; there are no truly disease-modifying ‘antiepileptogenic’ agents that prevent the onset of epilepsy after a brain insult or injury. Therefore, the need for new treatments for epilepsy (as either improved anti-ictogenic drugs or pioneering antiepileptogenic drugs) is apparent.

What is not apparent is actually how to discover these new drugs. Historically, anticonvulsant drugs have been discovered by serendipity. The anticonvulsant properties of phenobarbital, for example, were discovered by accident when it was used as a sleeping pill in people with epilepsy. Analogously, valproic acid was shown to have anticonvulsant effects when it was fortuitously employed as a solvent during the evaluation of other compounds as potential drugs for epilepsy.

Now that humankind has entered the 21st century, established methods for drug design are in place and are slowly supplanting the time-honoured tradition of serendipity (Nogradi and Weaver, 2005). The current approach to drug design has two sequential and equally important components:

1. Lead compound identification
  - By rational drug design, or
  - By high throughput screening
2. Lead compound optimization
  - By evaluation of a large number of analogs

Lead (pronounced ‘lēd’ [not ‘l[ē]d’]) compound identification is the process of finding a prototype molecule or family of molecules that can be used as a starting point in the design of a future drug. A lead compound is invariably an organic molecule that acts as a prototype drug around which future optimization is centered and focused. Identifying a lead compound is the key to starting the drug discovery engine. Although lead compound identification is a *sine qua non* of modern drug design, the process of lead compound identification is a non-trivial undertaking.

The first approach to lead compound identification is to use rational drug design. Rational drug design means that the drug designer knows the three-dimensional structure of a biological macromolecule (typically a protein, such as an enzyme) that is central to the underlying disease process and then insightfully engineers a small molecule to bind to the larger macromolecule in order to modify the macromolecule’s functional properties. This small molecule will become the lead compound or prototypic agent around which future drug optimization will be centered.

The second approach to lead compound identification is to perform high throughput screening. This means that the drug designer has access to an efficient and inexpensive *in vitro* assay (typically an enzymatic assay). Next, a library of structurally diverse molecules is screened against this assay. Using robotics, millions of compounds are experimentally tested in this *in vitro* assay (hence the name high throughput screening). If the library of compounds is sufficiently large and sufficiently diverse, odds are in favor of identifying at least one compound that works in the assay. The so-identified compound then becomes the lead compound or prototypic agent around which future drug optimization will be centered.

Once this prototype lead compound has been identified (by either rational design or high throughput screening), its structure can then be optimized to yield a final drug candidate. This optimization process typically involves the synthesis of hundreds, if not thousands, of analogs of the lead compound. Each one of these analogs is individually evaluated in appropriate biological models or assays in order to determine the one analog with optimal bioactivity. Thus, the optimization process is long and arduous.

Implementing the sequential approach of lead compound identification and optimization for the purpose of anticonvulsant drug design is of paramount importance to the future development of novel antiepileptic therapeutics. Thankfully, the efficiency of this implementation will be facilitated by the application of computational advancements. Computer-aided drug design is the process whereby these computational advances are aiding the design of future drugs and future anticonvulsants.

This chapter will address the principles and practice of computer-aided drug design as applied to the search for new therapeutics for epilepsy.

#### AN OVERVIEW OF COMPUTER-AIDED DRUG DESIGN FOR EPILEPSY

When confronted with the task of designing anticonvulsant drugs, it would be wonderful to have theoretical methods for predicting the properties of drug molecules – before actually having to prepare and test them. Computer-aided drug design (CADD) offers a powerful solution to this prediction dilemma (Stuper et al., 1979; Good, 1980; Cohen, 1983, 1985; Franke, 1984; Hopfinger, 1985; Burgen and Roberts, 1986; Lipinski, 1986; Marshall, 1987).

Designing drugs for epilepsy requires techniques for determining the geometry, conformation (shape) and electronic properties of both small molecules (i.e. anticonvulsant drug molecules with molecular weights less than 500 g/mol) and macromolecules (i.e. receptor proteins, such as neuronal ion channels). CADD is such a technique. CADD is an evaluation of the molecular properties and structures of a drug molecule and its receptor using three-dimensional visualization and representations; CADD is the application of the methods of modern molecular modeling to understanding drug action at the molecular and atomic level of structural refinement; CADD is the employment of computer-aided techniques within a high performance computing environment to design, discover and optimize bioactive molecules as putative drugs.

#### CADD – IDENTIFICATION OF LEAD COMPOUNDS BY RATIONAL DRUG DESIGN

CADD can be used to aid in the identification of a lead compound for epilepsy by rational drug design. CADD enables an improved understanding of the three-dimensional shape of a receptor protein and facilitates the design of drug molecules to bind with this receptor. Mechanics methods (e.g. quantum mechanics, molecular mechanics) combined with energy minimization methods (e.g. minimization algorithms, energy surface search algorithms) permit a rigorous three-dimensional understanding of a receptor and a drug. In turn, this rigorous understanding of molecular geometry enables rational drug design.

### CADD – IDENTIFICATION OF LEAD COMPOUNDS BY HIGH THROUGHPUT SCREENING

CADD can also be used to aid in the identification of a lead compound for epilepsy by high throughput screening. Rather than performing the entire process by experimental *in vitro* methods, the screening can be done *in silico* using virtual molecules. Using a computer model of the receptor and computer models of millions (billions?) of virtual drug molecules, it is possible to perform the screening *in silico*, prior to ever having to make a molecule. Mechanics methods and energy minimization methods are central to this high throughput *in silico* screening.

### CADD – OPTIMIZATION OF A LEAD COMPOUND

Finally, CADD can be used to facilitate the optimization of the lead antiepileptic compound. A specialized informatics method (a cheminformatics technique called quantitative structure-activity relationship (QSAR) study) permits the rapid identification of the molecular properties essential to a drug's bioactivity. The identification of these properties enables the subsequent optimization of the lead compound.

### KEY POINTS

1. Computer methods that enable a rigorous three-dimensional visualization of drug molecules and drug receptors can facilitate the design of a prototype antiepileptic drug by the process of rational drug design; where rational drug design implies that the drug designer understands epilepsy at some fundamental molecular level and uses this understanding to engineer insightfully an antiepileptic molecule using precise geometric calculations.
2. Computer methods can be used to evaluate the ability of billions of computer-generated virtual drug molecules to interact with a computer-generated model of an epilepsy-relevant receptor; this enables the identification of a prototype antiepileptic drug by the process called *in silico* high throughput screening.
3. Computer methods can be used to optimize a prototype antiepileptic drug using a numerical process called quantitative structure-activity relationship studies (QSAR).

### THE METHODS OF COMPUTER-AIDED DRUG DESIGN FOR EPILEPSY

In order to achieve the goal of computer-aided drug design for epilepsy, a number of mathematical methods and algorithms must be used.

#### MECHANICS METHODS: ASSIGNING AN ENERGY VALUE TO THE SHAPE OF AN ANTICONVULSANT DRUG MOLECULE OR DRUG RECEPTOR

The first and foremost goal of anticonvulsant CADD is to predict and determine the optimal geometry of anticonvulsant drug molecules and drug receptors. This is best achieved by using a 'mechanics' method that permits the geometry of a drug molecule or receptor molecule to be expressed as a function of energy. By minimizing this energy function, one can ascertain the optimal geometry of the molecule. Quantum mechanics and molecular mechanics are the dominant 'mechanics' methods in CADD.

#### Quantum mechanics

The Schrödinger equation is the centerpiece of molecular quantum mechanics (Szabo and Ostlund, 1996; Atkins, 1997; Simons and Nichols, 1997; Cook, 1998; House, 1998). In its simplest form, the Schrödinger equation may be represented as

$$H\Psi = E\Psi$$

where  $\Psi$  is the wavefunction,  $E$  is the energy of the system and  $H$  (the 'Hamiltonian operator') is a mathematical operator function. Once the wavefunction is known for a drug molecule, then any physical property may, in principle, be determined for that molecule.

The wavefunctions that satisfy Schrödinger's equation for a simple hydrogen atom are called orbitals; this hydrogenic atomic orbital is therefore the three-dimensional mathematical function from which one may calculate the energy and other properties of a single electron. For single atoms that contain multiple electrons (polyelectronic mono-atomic systems), the

wavefunction for the atom ( $\Psi$ ) is a product of one-electron wavefunctions ( $\chi_i$ ), one for each electron. For single molecules that contain multiple atoms (polyelectronic, polyatomic, molecular systems), the wave function for the molecule ( $\Psi$ ) is a product of one-electron wavefunctions ( $\varphi_i$ ) (where  $\varphi$  is a three-dimensional mathematical function representing the energy and properties of an individual electron within the molecule).

In CADD, the goal is to determine the wavefunction  $\Psi$  for the anticonvulsant drug molecule so that the optimal geometry and other properties of the drug may be calculated. Regrettably, Schrödinger's equation may only be exactly solved for the hydrogen atom – it is not possible to provide an exact mathematical solution for the wavefunction of an entire drug molecule of interest to the treatment of epilepsy. Accordingly, *molecular orbital calculations* that provide approximate, but not exact, solutions for the drug molecule wavefunction are employed.

In molecular orbital calculations, the molecular orbitals  $\varphi$  are represented as a linear combination of atomic orbital functions ( $\chi_i$ ). Molecular orbital calculations may be broadly divided into two types: *ab initio* and semi-empirical – *ab initio* calculations are the most accurate and thus are preferably used when determining the properties of an anticonvulsant drug molecule. The term *ab initio* is used universally for molecular orbital wavefunction calculations that explicitly consider all electrons within the drug molecule.

Quantum mechanics calculations provide high quality structural information about small molecules containing fewer than 60 atoms. Therefore, quantum mechanics calculations are useful for studying anticonvulsant drug molecules, but cannot be applied to larger molecules such as receptor proteins. Using widely available commercial computer programs (e.g. GAUSSIAN, GAMESS), it is possible to perform quantum mechanics calculations on a wide variety of anticonvulsant drug molecules.

### Molecular mechanics

Molecular mechanics is the other major mechanics method used when applying CADD to antiepileptic drug design. The term molecular mechanics refers to an empirically parameterized computational method that leads to accurate geometries and relative energies for different shapes of molecules (Burkert and Allinger, 1982; Kollman, 1987; Allinger, 1998). The essential idea of molecular mechanics is that a molecule is a collection of particles held together by elastic or harmonic forces (i.e. a molecule is composed of distensible balls (atoms) held together by compressible/stretchable springs (bonds)), which can be defined individually in terms of potential energy functions. The sum of these various potential energy equations comprises a multidimensional energy function termed the *force field*; the force field quantitatively describes the restoring forces acting on a molecule when the minimal potential energy is perturbed. The force field approach supposes that bonds have natural lengths and angles and that molecules relax their geometries to assume these values. Thus, molecular mechanics uses an empirically derived set of simple classical mechanical equations and is well suited to provide accurate *a priori* structures and energies for drugs, proteins or other receptor molecules of CADD interest.

The heart of molecular mechanics is the force field equation. A typical molecular mechanics force field is shown below:

$$\begin{aligned} V &= V_r + V_\theta + V_\omega + V_{inv} + V_{nb} + V_{hb} + V_{cross} \\ V_r &= \sum k_r (r - r_o)^2 \\ V_\theta &= \sum k_\theta (\theta - \theta_o)^2 \\ V_\omega &= \sum \frac{V_n}{2} (1 + \cos(n\phi - \gamma)) \\ V_{nb} &= \sum_{i < j} \left( \frac{A_{ij}}{r_{ij}^{12}} - \frac{B_{ij}}{r_{ij}^6} + \frac{q_i q_j}{\epsilon r_{ij}} \right) \\ V_{hb} &= \sum \left( \frac{C_{ij}}{r_{ij}^{12}} - \frac{D_{ij}}{r_{ij}^{10}} \right) \end{aligned}$$

or

$$V = \sum k_r (r - r_o)^2 + \sum k_\theta (\theta - \theta_o)^2 + \sum \frac{V_n}{2} (1 + \cos(n\phi - \gamma)) + \sum_{i < j} \left( \frac{A_{ij}}{r_{ij}^{12}} - \frac{B_{ij}}{r_{ij}^6} + \frac{q_i q_j}{\epsilon r_{ij}} \right) + \sum \left( \frac{C_{ij}}{r_{ij}^{12}} - \frac{D_{ij}}{r_{ij}^{10}} \right) + V_{cross}$$

where  $V_r$  represents bond length energies;  $V_\theta$  represents bond angle energies;  $V_\omega$  represents dihedral angle energies;  $V_{nb}$  represents non-bonded interaction energies (van der Waals and electrostatic);  $V_{hb}$  represents hydrogen bonding interactions.

Typically, the bond stretching and bending functions are derived from Hooke's law of harmonic potentials; a truncated Fourier series approach to the torsional energy permits accurate reproduction of conformational preferences.

The mathematics of molecular mechanics is thus rapid and trivial, which makes the technique ideal for the treatment of pharmaceutically relevant macromolecules.

Molecular mechanics calculations provide reasonable structural information about both small and large molecules, containing 10–10 000 atoms. Therefore, molecular mechanics calculations are useful for studying larger molecules such as receptor proteins. Using widely available commercial computer programs, it is possible to perform molecular mechanics calculations on a wide variety of anticonvulsant receptor molecules. The AMBER and CHARMM force fields are used for macromolecules such as peptides and nucleic acids.

### ENERGY MINIMIZATION METHODS: FINDING THE LOWEST ENERGY SHAPE OF A MOLECULE

#### Energy minimization algorithms

Whether one is using quantum mechanics or molecular mechanics, both approaches must be used in conjunction with an energy minimization algorithm (Clark, 1985; Leach, 1996; Jensen, 1999; Young, 2001). The two mechanics methods provide a single energy for a single given geometry of the molecule; i.e. they express geometry as a function of energy – this function defines an energy surface such that all possible geometries of the molecule are defined by a point on the energy surface. To obtain the optimal geometry, one must minimize the energy function (as defined by either the Schrödinger equation or a force field); i.e. one must find the lowest point or deepest well on the energy surface. This is a multidimensional problem complicated by the presence of many local energy troughs on the energy surface which are minima in a mathematical sense, but which are higher in energy than the one single global energy minimum. Many of the minimization algorithms in current use today are based on either a steepest descent method or a Newton-Raphson method, which require first and second derivative information about the energy surface, respectively.

#### Algorithms for searching the potential energy hypersurface

If the anticonvulsant drug molecule under study is 'large and floppy' (i.e. it is conformationally labile and exists in a family of low energy shapes), it is difficult to identify the lowest energy conformer using CADD calculations. For example, if the putative anticonvulsant agent being studied is a hexapeptide, it will exist in a multiplicity of low energy shapes; the hexapeptide's potential energy surface will have many, many low energy wells and trying to identify the global energy minimum (the lowest energy well) is a challenging task. Such energy surfaces (sometimes called hypersurfaces because of their seemingly infinite complexity) may have billions or trillions of low energy wells and trying to identify the single lowest energy well is computationally demanding. This problem is sometimes referred to as the multiple minima problem.

There exists a number of techniques for addressing the multiple minima problem when trying to identify the lowest energy conformer for a flexible drug or for a receptor protein (Clark, 1985; Leach, 1996; Jensen, 1999; Young, 2001). These CADD techniques enable one to 'search the conformational space' of the floppy drug molecule or protein under study. The Monte Carlo method was one of the first methods used to search conformational space (Rapaport, 1997). This method has been adapted from classical statistical mechanics. Using this method, random moves are made to the rotatable bonds of an isolated molecule. Then, using a sampling procedure, it is possible to generate a large number of suitable different conformations. The spectrum of acceptable conformations is then energy minimized (using a quantum mechanics or molecular mechanics approach, as discussed above) and ranked by energy. Although it is necessary to generate a large number of conformations, in principle it is possible, within a user-defined time-frame, to achieve a representative sample from low-energy conformational space.

A second widely used method for searching conformational space is through molecular dynamics calculations (Marcus, 1997; Rapaport, 1997; Balbuena and Seminario, 1999). A simple definition of molecular dynamics is that it simulates the motions of a system of atoms within a molecule with respect to the forces that are present and acting on the molecule. This collection of forces causes the system to change, but by collective motion of atoms over time, in a way that is described by integrating Newton's second law of motion ( $F = ma$ , where  $F$  is the force acting on an atom,  $m$  is its mass and  $a$  is its acceleration). If one can calculate the next configuration of the collection of atoms, it is possible to follow the evolution of the atomic movements within the molecule over time. By 'heating' the molecule and permitting it to cool, it is possible to explore the conformational space of the molecule, thereby identifying low energy shapes.

#### Combining mechanics methods with energy minimization methods

Understanding these basic principles is important because of the ever-increasing role of CADD in anticonvulsant drug design and discovery. The diverse concepts presented thus far may be summarized as follows. The 'mechanics' methods

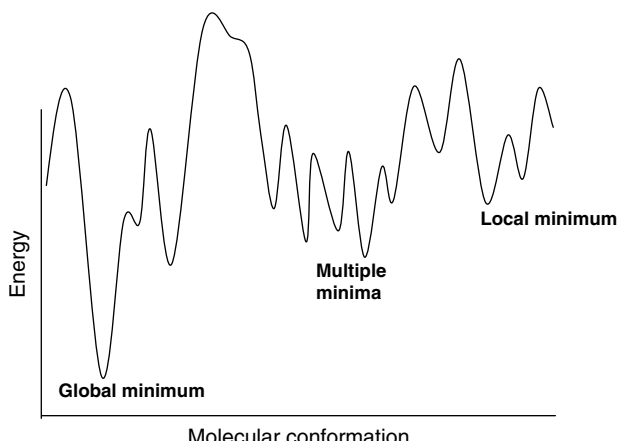


**FIGURE 31.1** Potential energy surface of a drug molecule. Since a biological molecule may exist in an extremely large variety of different shapes, the single energy values corresponding to each of these shapes define a surface (termed the potential energy hypersurface); the single energy values may be defined using either quantum mechanics or molecular mechanics. The potential energy hypersurface has many different minima. The lowest point on this surface (global minimum) is assumed to represent the most probable shape of the molecule. However, finding the lowest point on the surface is difficult. Methods such as Monte Carlo and molecular dynamics permit one to 'skip' across the potential energy hypersurface, thereby sampling it in a point-by-point fashion, which may identify a point (i.e. a single conformation of the molecule) that lies in a low energy region of the surface. Once a low energy region of the surface has been so-identified, then energy minimization algorithms (e.g. Newton-Raphson algorithm) may be used to 'fine tune' the geometry and conformation of the molecule to ensure that the lowest energy structure has been identified.

(quantum mechanics, molecular mechanics) provide a single value of energy for a single shape (conformation) of an anticonvulsant drug molecule or receptor molecule. Since a molecule may have an almost infinite variety of shapes, the infinite single energy values corresponding to these shapes define a surface (termed the potential energy hypersurface). The lowest point on this surface (global minimum) is assumed to represent the most probable shape of the molecule (Figure 31.1). However, finding the lowest point on the surface is difficult. Methods such as Monte Carlo and molecular dynamics permit one to 'skip' across the potential energy hypersurface, thereby sampling it in a point-by-point fashion, which may identify a point (i.e. a single conformation of the molecule) that lies in a low energy region of the surface. Once a low energy region of the surface has been so-identified, then energy minimization algorithms (e.g. Newton-Raphson algorithm) may be used to 'fine tune' the geometry and conformation of the molecule to ensure that the lowest energy structure has been identified.

### INFORMATICS METHODS

When performed on a large series of putative anticonvulsant molecules, quantum mechanics and molecular mechanics calculations produce a huge amount of data/information. Bioinformatics and cheminformatics are significant, new, rapidly evolving techniques focused upon the management of information (Bisby, 2000; Edwards et al., 2000; Lander and Weinberg, 2000; Pal, 2000; Jasny and Roberts, 2001). Bioinformatics and cheminformatics are exerting an important influence on the future of CADD calculations as applied to anticonvulsant drug design (Sugden and Pennisi, 2000; Thayer, 2000; Pollock and Safer, 2001; Sanchez, 2001; Watkins, 2001).

#### Bioinformatics

Bioinformatics refers to the tools and techniques (usually computational) for storing, handling and communicating the massive and seemingly exponentially increasing amounts of biological data emerging mainly from genomics research but also from other areas of biological research (Sugden and Pennisi, 2000; Thayer, 2000; Pollock and Safer, 2001; Sanchez, 2001; Watkins, 2001). Bioinformatics encompasses a diverse range of activities including data capture, automated data recording, data storage, data access, data analysis, data visualization and the use of search engines and query tools for probing multiple databases. Bioinformatics also endeavors to draw correlations between biological data from multiple sources in an attempt to identify novel information that may have utility in drug design; the use of bioinformatics in drug design is now ubiquitous and all pervasive.

## **Ceminformatics**

Ceminformatics is the chemistry equivalent to bioinformatics and involves the tools and techniques (usually computational) for storing, handling and communicating the massive and ever increasing amounts of data concerning molecular structures. Like bioinformatics, ceminformatics attempts to combine data from varying sources: molecular modelling studies, high-throughput screening, structure-based drug design studies, small molecule compound libraries and virtual chemical libraries.

Ceminformatics is used extensively in high throughput screening (HTPS) approaches to drug discovery. If an HTPS assay is available for a particular disorder (such as epilepsy), then it is possible to screen a large library of small molecule compounds through this screen to identify a potential lead candidate. A problem central to this approach is verifying that the library of small molecules possesses true molecular diversity and that the molecules contained within the library contain all possible functional groups displayed systematically in three-dimensional space.

When used in harmony, bioinformatics and ceminformatics are a powerful combination of computer intensive techniques which will grow in power over the coming decade as information handling technologies improve in sophistication.

## **Quantitative structure-activity relationship studies (QSAR)**

An important application of ceminformatics calculations to antiepileptic drug design is in the area of QSAR (Kirschner and Kowalski, 1978; Henry and Block, 1979; Chu, 1980; Mager, 1980; Kier and Hall, 1986). Over the past 30 years, QSAR has progressed from the simple regression equations, through 2D-QSAR, to modern 3D-QSAR methods. The applications of CADD calculations are well exemplified in 2D-QSAR studies. Typically, these studies start with 10–20 analogues of a bioactive lead anticonvulsant compound. These analogues range from biologically active to inactive. Each analogue, regardless of its bioactivity, undergoes extensive calculations and is described by a series of descriptors. Geometric descriptors reflect properties such as bond lengths, bond angles and interatomic distances within the analogue series. Electronic descriptors represent properties such as atomic charge densities and molecular dipoles. Topological descriptors encode aspects of molecular shape and branching. Physicochemical descriptors reflect properties related to the ability of the molecules to traverse biological barriers, such as the blood–brain barrier. These descriptors, especially the geometric and electronic descriptors, may be ascertained using quantum mechanics calculations. Once the descriptors have been determined, a data array is constructed with descriptors along one axis of the array and biological activity along the other axis of the array. Statistical methods are then used to search the array and to identify the minimal descriptor set capable of differentiating between biological activity and inactivity. As a corollary to this, it is possible to deduce the bioactive face of the molecule, where the bioactive face is a submolecular zone termed the ‘pharmacophore’.

## **KEY POINTS**

1. Quantum mechanics calculations are valuable CADD methods that enable rigorous geometry optimizations of ‘small’ anticonvulsant drug molecules containing fewer than 60 atoms.
2. Molecular mechanics calculations are valuable CADD methods that enable reasonable geometry optimizations of ‘large’ anticonvulsant receptor molecules containing thousands of atoms.
3. Mechanics methods (either quantum mechanics or molecular mechanics) when combined with energy surface search algorithms (e.g. Monte Carlo methods) and energy minimization methods (e.g. Newton-Raphson methods) enable the identification of low energy shapes for anticonvulsant drug molecules and drug receptors; in turn this facilitates drug design, especially by a rational drug design approach.
4. Informatics methods (such as the ceminformatics method termed quantitative-structure activity relationship studies (QSAR)) facilitate the discovery of new antiepileptic prototype drugs by *in silico* screening methods and the subsequent optimization of these prototype drugs.

## **APPLYING THE METHODS OF CADD TO ANTIPILEPTIC DRUG DESIGN: BASIC PRINCIPLES**

The methods described above can be used to identify lead compounds as prototypic antiepileptic agents and to optimize these prototype molecules.

## CADD AND ANTIEPILEPTIC LEAD COMPOUND IDENTIFICATION BY RATIONAL DRUG DESIGN

The concept of rational drug design implies that the drug designer understands epilepsy at some fundamental molecular level and that this understanding can be exploited for purposes of anticonvulsant drug design (Van de Waterbeemd, 1995). This involves the use of CADD to predict the structure of an epilepsy-relevant receptor protein and to use geometrical calculations to design a drug molecule to fit into that receptor.

### CADD and the prediction of an antiepileptic receptor structure

The most important potential application of CADD to the rational design of anticonvulsants is in the area of receptor structure prediction. In anticonvulsant drug design, most of these receptors are proteins, such as voltage gated ion channels (e.g. voltage gated  $\text{Na}^+$  channel, voltage gated  $\text{Ca}^{2+}$  channel), ligand gated ion channels (e.g. gamma-aminobutyric acid (GABA) channel, N-methyl-D-aspartate (NMDA) channel) or enzymes (e.g. GABA-transaminase). Predicting the structures of these protein receptors would greatly enhance the possibility of rational drug design.

Protein structure may be considered at multiple levels of refinement: primary structure refers to the amino acid sequence; secondary structure is defined by the local conformations induced by hydrogen bonding along the peptide backbone (e.g.  $\alpha$ -helix,  $\beta$ -sheet,  $\beta$ -turn); tertiary structure concerns the three-dimensional structure arising from hydrogen bonding, electrostatic interactions and other intramolecular interactions involving either side-chain or backbone functional groups; quaternary structure refers to the three-dimensional structure of proteins composed of more than one peptide chain. From this hierarchical system of structure arises the fundamental question (called the protein folding problem) in applying CADD to protein structure: does the primary amino acid sequence determine the three-dimensional structure of a protein and, if so, what are the rules which will permit us to predict tertiary structure with only a knowledge of primary structure? To date, the protein folding problem remains unsolved – we cannot predict the overall three-dimensional structure of a protein. This failing of CADD is a major impediment to successful rational drug design for epilepsy.

There have been multiple attempts to solve the protein folding problem. One method of attempting to predict three-dimensional structure is via sequence alignment and homology modeling. In this process, the calculations begin with the crystal structure of a known protein. Then, a protein with an unknown three-dimensional structure is ‘aligned’ with the structure of the known protein. Similar amino acids are aligned with each other; for example, a glutamate in one protein may be aligned with an aspartate in the other protein. Regions of the two proteins with similar amino acids are aligned against each other and are said to have sequence homology. The three-dimensional structure of the unknown protein is then set to be analogous to the three-dimensional structure of the known protein. Although useful, this procedure still does not solve the protein folding problem and it does require a similar protein with an experimentally solved structure.

### Using CADD to design drugs to fit receptors

Another important application of CADD to rational drug design is its use in *de novo* drug design of novel molecular shapes that will fit into a known receptor site. If the molecular structure of a receptor protein has been solved by experimental methods and if the location of a potential receptor site within this protein has been deduced, then it may be possible to design small molecules to fit into this receptor site. By identifying hydrogen bonding donors or acceptors and other points for intermolecular interactions on the receptor site, it is possible to design complementary molecules to fit into this site. Molecular mechanics and quantum mechanics are well suited to this task of designing new molecules as putative drugs.

A successful antiepileptic drug molecule is merely a collection of chemical functional groups appropriately positioned on the three-dimensional space of a hydrocarbon framework in a fixed geometrical relationship that enables a desirable interaction with a receptor macromolecule. When the medicinal chemist knows the *bioactive zone* of the receptor macromolecule, he or she identifies multiple functional groups within that bioactive zone. The selection of these receptor-based functional groups is a crucial step. Next, complementary functional groups capable of energetically favorable intermolecular interactions with the receptor-based functional groups are selected. These complementary functional groups will ultimately form part of the drug that is being designed and will constitute the pharmacophore. These drug-based functional groups are then ‘clicked together’ in three-dimensional space by being covalently attached to a relatively rigid hydrocarbon frame. The number of functional groups determines the number of contact points between the drug molecule and the receptor macromolecule. A *three-point pharmacophore* with have three different intermolecular interactions between the drug and the receptor. A large number of points of contact are unfavorable from a pharmacokinetic perspective, since the resulting increased polarity of the drug molecule tends to decrease the pharmacological half-life and decrease the ability of the drug to diffuse across membranes during its distribution throughout the body. In general, most neuroactive anticonvulsant drugs have 2–4 points of contact, while many non-neuroactive drugs have 3–6 points of contact.

Once the pharmacophore has been designed, the remainder of the molecular fragments (individually composed of inert bioinactive spacers, but collectively referred to as *molecular baggage*) are assembled. One of the primary goals of the molecular baggage component is to hold the pharmacophore in a desired conformation such that it can interact with its receptor.

### CADD AND LEAD ANTIPILEPTIC COMPOUND IDENTIFICATION BY *IN SILICO* HIGH THROUGHPUT SCREENING

Another important application of large-scale CADD calculations to drug molecule design concerns the process of docking simulation. Either molecular mechanics calculations or combined quantum mechanics/molecular mechanics calculations may be used to simulate a drug molecule interacting with a proposed receptor site in a macromolecule such as a protein.

When performed on a large scale, this facilitates lead compound identification by HTPS.

Using a computer model of a receptor and computer models of millions (billions?) of structurally diverse virtual drug molecules, it is possible to perform *in silico* screening. For example, if the crystal structure of an enzyme (e.g. GABA transaminase) were known and its active site were identified, *in silico* methods could be employed to screen billions of virtual molecules for their ability to dock with this site. If any of these molecules demonstrated an ability to bind with the active site, they could then be synthesized and evaluated *in vitro* as putative prototype enzyme inhibitors.

### CADD AND OPTIMIZING THE LEAD ANTIPILEPTIC COMPOUND

Once the lead compound has been identified, the next task is to optimize its structure; QSAR calculations facilitate this optimization. The purpose of such methods is to increase the probability of finding active compounds among those eventually synthesized, thus keeping synthetic and screening efforts within reasonable limits in relation to the success rate. There are three main classifications of QSAR methods: 1D-QSAR (1-dimensional QSAR; e.g. Hansch analysis); 2D-QSAR (2-dimensional QSAR; e.g. pattern recognition analysis); 3D-QSAR (3-dimensional QSAR; e.g. comparative molecular field analysis). Each method has its own strengths and weaknesses.

2D-QSAR is a widely used method for correlating activity and structure of neuroactive molecules. The first step in performing a 2D-QSAR is to select the *training set*. This is a subset of known and tested molecules that are diverse, in terms of both structure and bioactivity. Ideally, the compounds that are available cover the full spectrum of bioactivity, ranging from active (fully and partially, covering a 10<sup>3</sup>-fold range in receptor binding affinities) to inactive. It is difficult to determine what makes a molecule bioactive (or conversely what makes a molecule bioinactive) if all of the compounds tested have similar bioactivities. The more molecules the better, but a reasonable start can be made with as few as ten compounds. It is important not to use all available molecules, since another subset is held back and retained as a *test set*. This test set will ultimately be used to validate any prediction algorithm that is developed through the study of the training set.

Next, every molecule in the training set, regardless of its anticonvulsant pharmacological activity, is characterized by a series of *descriptors*. The geometric descriptors (bond lengths, bond angles, torsional angles, interatomic distances) reflect molecular geometry and are conceptually straightforward. Electronic descriptors (charge densities on atoms) reflect properties arising from variations in electron distribution throughout the drug molecule framework. Topological descriptors (graph theory indices (Randic indices, Kier-Hall indices), *ad hoc* indices (number of rings in the molecule) endeavor to describe molecular branching and complexity through the notion of *molecular connectivity*. The physicochemical descriptors (octanol-water partition coefficients (LogP, (LogP)<sup>2</sup>)) reflect the ability of the drug to partition itself into the lipid surroundings of the receptor microenvironment within brain.

All of these descriptors are calculated for every compound within the training set. Next a 2D data array is constructed. Along the vertical axis, all of the training set compounds are listed in descending order of bioactivity. Along the horizontal axis, all of the descriptors are arranged for every training set compound. This data array is then probed with statistical calculations to ascertain the minimum number of descriptors that differentiate active compounds from inactive compounds. In order to probe the data array, several methods are available. *Pattern recognition* and *cluster analysis*, two recent quantitative methods, make use of sophisticated statistics and computer software.

Once the data array has been probed and the minimum number of descriptors that differentiate activity from inactivity has been ascertained, a *prediction algorithm* is deduced. This algorithm attempts to quantify the bioactivity in terms of the relevant descriptors. The predictive usefulness of this algorithm is then validated by being applied to the test set compounds. If the prediction algorithm is sufficiently robust, it can be used to direct the syntheses of optimized compounds. In this way, QSAR calculations enable the optimization of a lead antiepileptic compound.

## KEY POINTS

1. Most receptor proteins worthy of being targeted for antiepileptic drug design are large transmembrane proteins. Because of the protein folding problem, current computer-assisted molecular design (CAMD) methods do not permit the development of computer models of sufficient accuracy to enable drug design.
2. Most anticonvulsant drugs are small molecules with molecular weights less than 500 g/mol; these compounds can be rigorously and meaningfully studied using CAMD techniques, such as molecular quantum mechanics methods.
3. If the structure of a drug receptor is known from experimental studies (i.e. X-ray crystallography) then current CAMD methods will permit the identification of a prototype drug by either rational drug design or *in silico* high throughput screening.
4. Once a prototype antiepileptic drug has been identified, current CAMD methods (such as QSAR) permit optimization of the lead compound.

### APPLYING THE METHODS OF CADD TO ANTICONVULSANT DRUG DESIGN: SPECIFIC EXAMPLES AND FUTURE CONSIDERATIONS

#### CADD AND MODELING ANTICONVULSANT RECEPTORS

Modern CADD calculations (particularly molecular mechanics calculations) are being used to develop *in silico* models of many of the proteins involved in the cortical hyperexcitability that mediates epileptogenesis. Since the aetiology and pathogenesis of epilepsy is neurochemically complex, many proteins are possible receptors for the design of anticonvulsant drugs. Some of the proteins studied using CADD include the following: voltage gated Na<sup>+</sup> channel, voltage gated K<sup>+</sup> channel, NMDA receptor, AMPA ( $\alpha$ -amino-3-hydroxy-5-methyl-4-isoxazolepropionic acid) receptor and the GABA-A receptor (Ban et al., 2004; Campagna-Slater and Weaver, 2007). These CADD studies have recently been reviewed by Li and Harte (2002).

One of the most recent CADD studies of an epilepsy-relevant receptor protein is a homology protein modeling study by Campagna-Slater and Weaver on the GABA-A receptor protein (Campagna-Slater and Weaver, 2007). The GABA-A ion channel protein is central to the mechanism of action of anticonvulsant drugs. Using CADD calculations, they constructed an *in silico* model of the alpha(1)beta(2)gamma(2) GABA-A ligand-gated ion channel protein. The cryo-electron microscopy structure of the nicotinic acetylcholine receptor (nAChR) from *Torpedo marmorata* and the X-ray crystal structure of the acetylcholine binding protein (AChBP) from *Lymnaea stagnalis* were used as starting templates for comparative homology modeling. Features of the modeling approach used in the development of this GABA-A model included:

1. multiple sequence alignment of members of the Cys-loop superfamily
2. the design and implementation of a quasi-*ab initio* loop modelling algorithm
3. expansion of the transmembrane domain (TMD) ion pore to model the open-state of the GABA-A channel
4. hydrophobicity analysis of the TMD to refine the structure in regions involved in general anaesthetic binding.

The final model of the alpha(1)beta(2)gamma(2) GABA-A protein agreed with available experimental data. Thus, an *in silico* model of the GABA-A channel has been created and is shown in Figure 31.2.

Although these computer models of proteins are elaborate, they are not yet sufficiently accurate to permit lead compound identification by either rational drug design or HTPS. Nevertheless, these models are useful in identifying protein regions that should be studied using experimental methods such as site-directed mutagenesis. In coming decades, there is room for optimism that computer generated theoretical models of proteins may be useful for the design of anticonvulsant drugs (Weaver, 2006).

#### CADD AND MODELING ANTICONVULSANT DRUGS

Modern CADD calculations (particularly quantum mechanics calculations) are being used to study smaller molecules such as anticonvulsant drugs (Weaver, 1996; Carter et al., 2003). Unlike the molecular mechanics calculations on large receptor proteins, these drug molecule calculations are highly accurate, rivalling high quality experimental studies. This accuracy is exemplified by a recent study of tricyclic anticonvulsant drugs.

Tricyclic molecules are frequently used to treat a diversity of disorders. As their name implies, tricyclic drugs contain three rings, fused together. Molecules belonging to this structural class are routinely used for the treatment of epilepsy

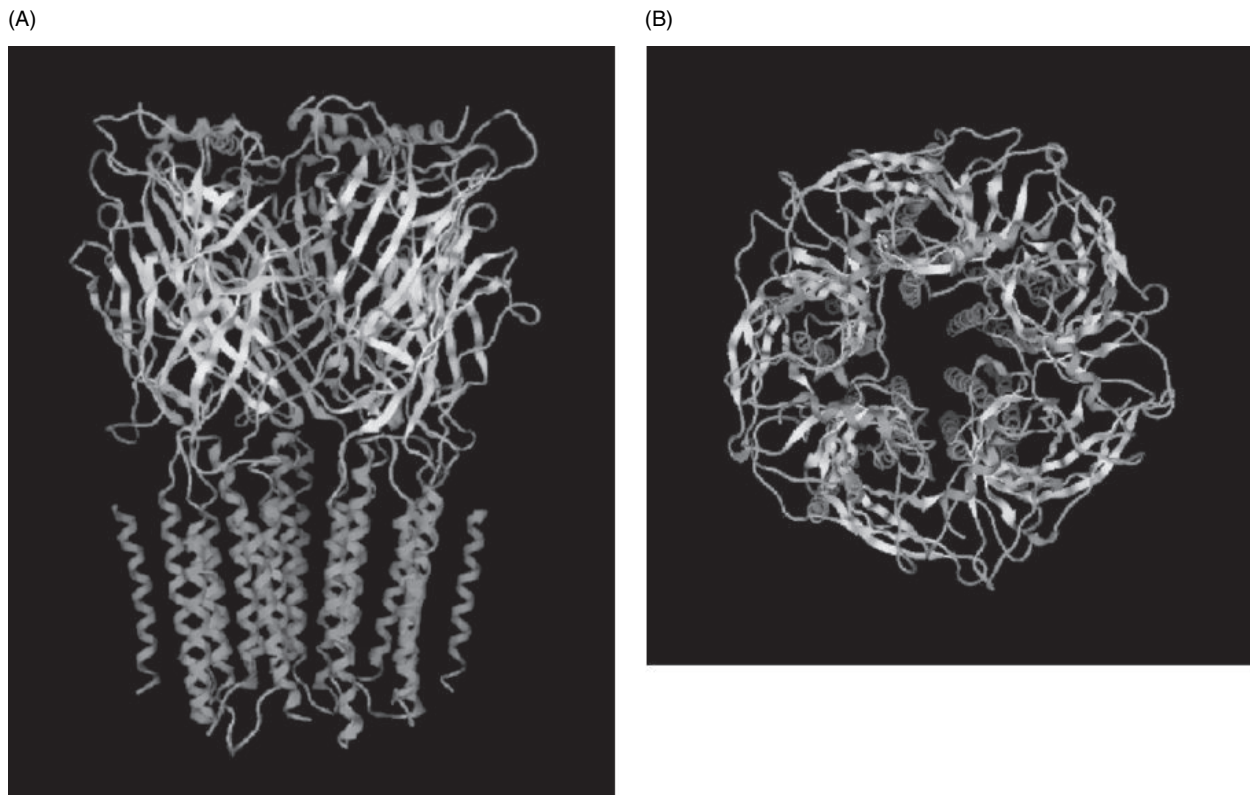


**FIGURE 31.2** Computer model of the GABA-A receptor protein. A computer model of the GABA-A receptor protein achieved using homology modeling in conjunction with molecular mechanics energy minimizations. The side-view (A) and top-view (B) of the protein are shown. Such theoretical models of protein structure have not yet reached the level of accuracy to permit rational drug design. (See Plate 25 in color plate section.)

(carbamazepine, oxcarbazepine) as well as psychosis (chlorpromazine), schizophrenia, depression (amitriptyline), headache, insomnia and chronic pain. In treating these many disorders, tricyclic drugs demonstrate an ability to bind to a plethora of different (and structurally quite distinct) receptors, including the voltage gated  $\text{Na}^+$  channel protein as well as multiple types of dopamine receptors, serotonin receptors and acetylcholine receptors.

The relationship between tricyclic structure and bioactivity can be assessed using CADD calculations. Employing quantum mechanics calculations, Marone et al. (1999) were able to quantify the spatial relationships ('butterfly angles') between the planes defined by the 'aromatic wings' of the tricyclic molecules. A series of angular descriptors can be used as measures of these spatial relationships; these descriptors can be accurately calculated using molecular orbital calculations. These angles and spatial relationships are shown in Figure 31.3. These high-level quantum mechanics calculations enable fundamental insights into the mechanism of action of anticonvulsant drugs.

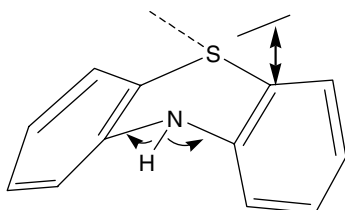


**FIGURE 31.3** Butterfly angles of a tricyclic drug. Many neuroactive drugs have a tricyclic structure. Some are anticonvulsants, while others are antidepressants or antipsychotics. The anticonvulsant tricyclics interact with the voltage gated  $\text{Na}$  channel protein. The angles formed between the various rings within these molecules define the receptor site with which the molecule interacts; these angles can be rigorously determined using quantum mechanics calculations.

### CADD AND ANTICONVULSANT QSAR STUDIES

Modern CADD calculations are being used to aid in the optimization of anticonvulsant drug molecules via QSAR studies. There have been QSAR studies on a variety of anticonvulsant molecule series, including barbiturates, hydantoins and ureides (Klopman and Contreras, 1985; Khalil and Weaver, 1990; Bikker et al., 1994; Knight and Weaver, 1998; Sutherland and Weaver, 2003; Jin et al., 2005). Recently, Sutherland et al. (2003, 2004a,b) reviewed the various QSAR methods available for studying anticonvulsants.

Sutherland et al. have also recently reported an extensive QSAR analysis on a large set of hydantoin derivatives with measured anticonvulsant activity in mice and rats (Sutherland and Weaver, 2003). The classification set comprised 287 hydantoins having maximal electroshock (MES) activity expressed in qualitative form. A subset of 94 hydantoins with MES ED<sub>50</sub> values was used for QSAR analysis. Numerical descriptors were generated to encode topological, geometric, electronic and physicochemical properties of molecules. Analyses were performed with training and test sets of diverse compounds selected using their representation in a principal component space. Cell and distance metric-based selection methods were employed in this process. For QSAR, a genetic algorithm (GA) was used for selecting subsets of 5–9 descriptors that minimize the root mean square error (rms) on the training sets. The most predictive models had rms errors of 0.86 ( $r^2 = 0.64$ ) and 0.73 ( $r^2 = 0.75$ ) ln(1/ED<sub>50</sub>) units on the cell and distance metric-derived test sets, respectively, and showed convergence in the selected descriptors. Classification models were developed using recursive partitioning (RP) and spline-fitting with a GA (SFGA). The most predictive RP and SFGA models had classification rates of 75% and 80% on the test sets; both methods produced models with similar discriminating features.

### SELECTING FUTURE TARGETS FOR CADD OF DRUGS FOR EPILEPSY

CADD offers powerful methods to facilitate drug design. However, in future, it will also be crucial to identify targets worthy of drug design (Weaver, 2003). Traditionally, anticonvulsant drug design has focused on ion channel proteins. Are these the best targets for future antiepileptic drug design?

The currently available anticonvulsant drugs, whether old or new, are little more than ‘symptomatic’ agents that suppress the symptoms of epilepsy (i.e. seizures) while failing to contend with the underlying pathological process that initially caused (or continues to cause) the predisposition to seizures (Weaver, 2003). Although the need to discover pioneering ‘curative’ therapeutics for epilepsy is clinically obvious, the direction to be pursued in the realization of such agents is not apparent. Central to the discovery of definitive therapeutics, which positively influence the natural history of epilepsy in a curative sense (and not merely mask the symptoms), will be the evolution of concepts concerning the pathogenesis of epilepsy and thus the related molecular targets for drug design.

A seizure is a single discrete clinical *event* caused by an excessive electrical discharge from a collection of neurons. Seizures are merely the symptom of epilepsy. Epilepsy, on the other hand, is a dynamic and frequently progressive *process* characterized by an underlying sequence of pathological transformations whereby normal brain is altered, becoming susceptible to spontaneous, recurrent seizures. Therefore, an important first step in this conceptual evolution of identifying new targets for drug design is differentiating between the notions of ‘ictogenesis’ and ‘epileptogenesis’ (Nogradi and Weaver, 2005).

Ictogenesis (the initiation and propagation of a seizure in time and space) is a rapid electrical/chemical event occurring over seconds or minutes. Ictogenesis involves excessive brain electrical discharges propagated by a cascade of chemical events initiated by the sequential opening of voltage gated Na<sup>+</sup> channels with subsequent involvement of K<sup>+</sup> channels and the Ca<sup>2+</sup> channel mediated release of neurotransmitters. The central role of the transmembrane voltage gated Na<sup>+</sup> channel in ictogenesis has resulted in the majority of the current anticonvulsant drugs (e.g. phenytoin, carbamazepine, lamotrigine) being targeted against this receptor site.

Epileptogenesis (the gradual process whereby normal brain is transformed into a state susceptible to spontaneous, episodic, time-limited recurrent seizures through the initiation and maturation of an ‘epileptogenic focus’) is a slow biochemical/histological process occurring insidiously over months to years. Epileptogenesis, unlike ictogenesis, is a gradual two-phase process showing dynamic changes over the course of time. This is a long, protracted process in which seizures may become more frequent, more severe, more refractory to treatment, or phenomenologically different in their clinical manifestations.

The cascade of histological/biochemical events that characterize epileptogenesis differ from those of ictogenesis. The macroscopic features of epileptogenesis include fibrous gliosis with cellular shrinkage and atrophy. Microscopically, there is neuronal loss affecting the pyramidal cell layers in the hippocampal subfields CA1, CA3 and in the dentate gyrus, but sparing the granule cells of the dentate gyrus. At the histological level, epileptogenesis involves cellular alterations (mesial

temporal sclerosis) in a variety of limbic brain structures. At the biochemical level, various theories of epileptogenesis have been put forth (Sutula et al., 1988, 1989; Sloviter, 1991; Beckenstein and Lothman, 1993; Lothman, 1996). The mossy fiber sprouting hypothesis postulates an upregulation of excitatory coupling between neurons mediated by N-methyl-D-aspartate (NMDA) glutamatergic receptors which are activated in chronic epileptic brain under circumstances that would not lead to activation in normal brain. In contrast, the dormant basket cell hypothesis suggests a downregulation of inhibitory coupling between neurons such that the connections which normally drive  $\gamma$ -aminobutyric acid (GABA) releasing inhibitory interneurons are disturbed thereby rendering them functionally dormant.

Although such glutamatergic and GABAergic processes are obvious participants in the molecular mechanism of epileptogenesis, there are other molecular claimants to the throne (Gall and Isackson, 1989; Shamovsky et al., 1998). For example, in the kindling animal model of epileptogenesis, neurotrophic peptides, such as nerve growth factor (NGF), play a facilitative role in hippocampal synaptic reorganization. Other molecular processes potentially involved in the excitotoxic cascade of epileptogenesis include cellular  $\text{Ca}^{2+}$  influx, apoptosis, nitric oxide synthase overproduction and free radical accumulation. Clearly, the future development of antiepileptic agents must exploit the full range of targets, extending from amino acid neurotransmitters to peptidic neuromodulators.

Future drugs for epilepsy must extend beyond the scope of simple ictogenesis and should encompass the greater mandate of epileptogenesis. Drug discovery and the identification of targets for rational drug design must take this into consideration.

## CONCLUSIONS

CADD calculations have, are, and will continue to revolutionize drug design of anticonvulsants. Until the dawning of the 20th century, it was believed that all reality was eminently describable through Newton's laws (Nogradi and Weaver, 2005). However, through the work of Bohr and others, it was eventually realized that classical Newtonian mechanics failed at the atomic level of reality. An alternative approach was needed for the quantitative evaluation of molecular phenomena. Molecular quantum mechanics was to be such an approach.

Over the past thirty years, two advances have enhanced the practical usefulness of molecular quantum mechanics:

1. The development of molecular mechanics, which incorporates quantum mechanical data into a simplified mathematical framework derived from the classical equations of motion to permit reasonable calculations on biomolecules of large size
2. The construction of 'super-computers' capable of performing the massive calculations necessary for considering very large biomolecules.

Accordingly, CADD has become an attainable goal and calculational computer modeling permits large molecules to be studied meaningfully.

Computer-assisted molecular design (CAMD) employs these powerful computational techniques to engineer molecules for desired receptor site geometries. CADD has gained widespread acceptance and is beginning to prove its usefulness in many realms of pharmacological endeavor. CADD enables rigorous modelling of drug molecules, of receptor macromolecules and of complex drug-receptor interactions. CADD has the potential profoundly to influence the future of antiepileptic drug design.

## ACKNOWLEDGMENTS

DFW acknowledges salary support from a Canada Research Chair, Tier 1, in neuroscience. Operating support from the Canadian Institutes of Health Research is also acknowledged.

## REFERENCES

- Allinger, N.L. (1998). Molecular mechanics. *Encycl Comput Chem* 2:1013.  
Atkins, P.W. and Friedman, R.S. (1997). Molecular quantum mechanics. Oxford University Press, Oxford.  
Balbuena, P., and Seminario, J. (1999). Molecular dynamics. Elsevier, Amsterdam.  
Ban, F., Kusalik, P. and Weaver, D. (2004). Density functional theory quantum mechanical investigations on the chemical basis of the selectivity filter of the transmembrane voltage gated K<sup>+</sup> channel. *J Am Chem Soc* 126: 4711–4716.

- Beckenstein, J. and Lothman, E.W. (1993). Dormancy of inhibitory interneurons in a model of temporal lobe epilepsy. *Science* 259:97–100.
- Bikker, J., Kubanek, J. and Weaver, D.F. (1994). Quantum pharmacologic studies applicable to the design of anticonvulsants: theoretical conformational analysis and structure-activity studies of barbiturates. *Epilepsia*. 35:411–425.
- Bisby, F.A. (2000). The quiet revolution: biodiversity informatics. *Science* 289:2309.
- Burgen, S.V. and Roberts, G.C.K. (eds) (1986). Molecular graphics and drug design. topics in molecular pharmacology, vol. 3. Elsevier, Amsterdam.
- Burkert, U. and Allinger, N. (1982). Molecular mechanics. American Chemical Society, Washington.
- Campagna-Slater, V. and Weaver, D.F. (2007). Molecular modelling of the GABA-A ion channel protein. *J Molec Graph Modelling* (in press).
- Carter, M., Stephenson, V. and Weaver, D. (2003). Are anticonvulsants ‘two-thirds’ of local anaesthetics: a quantum pharmacology study. *J Molec Struct: Theochem* 638:57–62.
- Chu, K.C. (1980). The quantitative analysis of structure–activity relationships. In: *The basis of medicinal chemistry*, Part 1, 4th edn (M.E. Wolff, ed.), pp. 393–418. Wiley-Interscience, New York.
- Clark, T. (1985). A handbook of computational chemistry. John Wiley and Sons, New York.
- Cohen, N.C. (1983). Towards the rational design of new leads in drug research. *Trends Pharmacol Sci* 4:503–506.
- Cohen, N.C. (1985). Drug design in three dimensions. In: *Advances in drug research*, vol. 14 (B. Testa, ed.) pp. 41–145. Academic Press, New York.
- Cook, D.B. (1998). Handbook of computational quantum chemistry. Oxford University Press, Oxford.
- Edwards, A., Arrowsmith, C. and des Pallieres, B. (2000). Proteomics: new tools for a new era. *Mod Drug Discov* 3:34.
- Franke, R. (1984). Theoretical drug design methods. Elsevier, Amsterdam.
- Gall, C. and Isackson, P. (1989). Limbic seizures increase neuronal production of messenger RNA for nerve growth factor in adult rat forebrain. *Science* 245:758–761.
- Good, P. (1980). Three-dimensional molecular modeling and drug design. *Science* 208:1425–1431.
- Henry, D.R. and Block, J.H. (1979). Classification of drugs by discriminant analysis using fragment molecular connectivity values. *J Med Chem* 22: 465–472.
- Hopfinger, A.J. (1985). Computer-assisted drug design. *J Med Chem* 28:1133–1139.
- House, J.E. (1998). Fundamentals of quantum mechanics. Academic Press, San Diego.
- Jasny, B.R. and Roberts, L. (2001). Unlocking the genome. *Science* 294:81.
- Jensen, F. (1999). Introduction to computational chemistry. John Wiley and Sons, New York.
- Jin, A., Kohn, H., Beguin, C., Andurkar, S., Stables, J. and Weaver, D.F. (2005). A quantitative structure-activity relationship study for alpha-substituted acetamido-n-benzylacetamide derivatives – a novel anticonvulsant drug class. *Can J Chem* 83:37–45.
- Khalil, M. and Weaver, D. (1990). A pattern recognition study of acyclic ureide anticonvulsants. *J Pharm Pharmacol* 42:349–351.
- Kier, L.B. and Hall, L.H. (1986). Molecular connectivity in structure-activity studies. Research Studies Press, Lechtworth.
- Kirschner, G.L. and Kowalski, B.R. (1978). The application of pattern recognition to drug design. In: *Drug design* vol. 9 (E.J. Ariëns, ed.) pp. 73–131. Academic Press, New York.
- Klopman, G. and Contreras, R. (1985). Use of artificial intelligence in structure-activity relationships of anticonvulsant drugs. *Mol Pharmacol* 27:86–93.
- Knight, J. and Weaver, D. (1998). A computational quantitative structure activity relationship study of carbamate anticonvulsants using quantum pharmacological methods. *Seizure* 7:347–354.
- Kollman, P. (1987). Molecular mechanics. *Ann Rev Phys Chem* 38:303.
- Lander, E.S. and Weinberg, R. (2000). Genomics: journey to the center of biology. *Science* 287:1777.
- Leach, A.R. (1996). Molecular modelling principles and applications. Longman, Harlow.
- Li, Y. and Harte, W.E. (2002). A review of molecular modelling approaches to pharmacophore models of ion channel modulators in the CNS. *Curr Pharm Des* 8: 99–110.
- Lipinski, C.A. (1986). Bioisosterism in drug design. *Annu Rep Med Chem* 21:283–291.
- Lothman, E.W. (1996). Basic mechanisms of seizure expression. *Epilepsy Res* S11:9–16.
- Mager, P.P. (1980). The MASCA model of pharmacochemistry I. Multi-variate statistics. In: In: *Drug design* vol. 9 (E.J. Ariëns, ed.) pp. 187–236. Academic Press, New York.
- Marcus, R.A. (1997). Molecular dynamics. *Adv Chem Phys* 101:391.
- Marshall, G.R. (1987). Computer-aided drug design. *Annu Rev Pharmacol Toxicol* 27:193–213.
- Marone, S., Rozas, I. and Weaver, D. (1999). Theoretical structural analyses of tricyclic neuroactive drugs: quantum pharmacologic descriptors for clustering anticonvulsant, antidepressant, and antipsychotic activities. *J Molec Struct: Theochem* 467:25–30.
- Nogrady, T. and Weaver, D.F. (2005). Medicinal chemistry: a molecular and biochemical approach, 3rd edn. Oxford University Press, New York.
- Pal, K. (2000). The keys to chemical genomics. *Mod Drug Discov* 3:46.
- Pollock, S. and Safer, H. (2001). Bioinformatics in the drug discovery process. *Ann Rep Med Chem* 36:201.
- Rapaport, D.C. (1997). The art of molecular simulation. Cambridge University Press, Cambridge.
- Sanchez, M. (2001). Bioinformatics: the wave of the future. *Biotechnol Focus* March:16.
- Shamovsky, I., Ross, G., Riopelle, R. and Weaver, D. (1998). Molecular modelling studies of a nerve growth factor receptor. *Can J Chem* 76:1389–1401.
- Simons, J. and Nichols, J. (1997). Quantum mechanics in chemistry. Oxford University Press, Oxford.
- Sloviter, R. (1991). Permanently altered hippocampal structure, excitability, and inhibition after experimental status epilepticus in the rat: the dormant basket cell hypothesis and its possible relevance to temporal lobe epilepsy. *Hippocampus* 1:41–66.
- Stuper, A.J., Brugger, W.E. and Jurs, P.C. (1979). Computer assisted studies of chemical structure and biological function. Wiley, New York.
- Sugden, A. and Pennisi, E. (2000). Bioinformatics and biodiversity. *Science* 289:2305.
- Sutherland, J. and Weaver, D.F. (2003). Development of quantitative structure-activity relationships and numerical classification models for anticonvulsant activities of hydantoin analogues. *J Chem Informat Comput Sci* 43:1028–1036.
- Sutherland, J., O’Brien, L.A. and Weaver, D.F. (2003). spline fitting with a genetic algorithm: a method for developing classification structure-activity relationships. *J Chem Informat Comput Sci* 43:1906–1915.

- Sutherland, J., O'Brien, L.A. and Weaver, D.F. (2004a). A comparison of methods for modelling quantitative-structure-activity relationships. *J Med Chem* 47:5541–5554.
- Sutherland, J., O'Brien, L.A. and Weaver, D.F. (2004b). Pruned receptor surface models and pharmacophores for 3D database searching. *J Med Chem* 47:3777–3787.
- Sutula, T., Xiao-Xian, H., Cavazos, J. et al. (1988). Synaptic reorganization in the hippocampus induced by abnormal functional activity. *Science* 239:1147–1150.
- Sutula, T., Cascino, G., Cavazos, J. et al. (1989). Mossy fiber synaptic reorganization in the epileptic human temporal lobe. *Ann Neurol* 26:321–330.
- Szabo, A. and Oslund, N. (1996). Modern quantum chemistry. Dover, New York.
- Thayer, A.M. (2000). Bioinformatics. *Chem Engin News* Feb 7:19.
- Van de Waterbeemd, H. (1995). Advanced computer assisted techniques in drug discovery. John Wiley and Sons, New York.
- Watkins, K.J. (2001). Bioinformatics. *Chem Engin News* Feb 19:29.
- Weaver, D.F. (1996). Applications of computer assisted quantum pharmacology calculations in devising anticonvulsant rational polypharmacy strategies. *Epilepsy Res Suppl* 11:95–111.
- Weaver, D.F. (2003). Epileptogenesis, ictogenesis and the design of future antiepileptic drugs. *Can J Neurol Sci* 30:4–7.
- Weaver, D.F. (2006). Designing future drugs for the treatment of intractable epilepsy. *Adv Neurol* 97:429–434.
- Young, D.C. (2001). Computational chemistry. John Wiley and Sons, New York.

# 32

## COMPUTATION APPLIED TO CLINICAL EPILEPSY AND ANTIEPILEPTIC DEVICES

JAVIER ECHAUZ, STEPHEN WONG, OTIS SMART, ANDREW GARDNER,  
GREGORY WORRELL AND BRIAN LITT

### ABSTRACT

More and more, computational neuroscientists are embracing opportunities to build anatomically accurate and clinically relevant models of functional networks in brain. One strong motivation for this trend is an explosion of venues for translating this work into clinical diagnostic and therapeutic devices. Epilepsy is one of the most active areas in translational neuroengineering, with two early devices currently in pivotal clinical trials, and a number of others close behind. The methods described in this chapter, used for this clinical translation, are not unique to epilepsy, but rather come from a collection of diverse fields in engineering, computer science and related disciplines. The themes are similar to those in other areas of engineering, including those used for industrial applications: condition signals for processing (e.g. noise reduction), extract quantitative features from the system, train and employ classifiers to perform decision tasks, and effect responses based upon classifier outputs. In this chapter, we describe several methods we have found useful for detecting, characterizing and tracking seizures and their generation in epileptic networks, and translating them into clinical devices. Rather than providing a comprehensive reference, this chapter is intended to convey an approach and a sampling of quantitative tools that can be creatively applied to the task at hand. This work must be put into the context of other important, related tasks, such as algorithm optimization, hardware development and implementation on implantable platforms that are required for clinical translation. On a personal note, this chapter is also about multidisciplinary collaboration between ‘technically literate’ physicians and engineers who model, build and deploy technologies that *do* things in the world we live in.

### INTRODUCTION

Computational neuroscience research in epilepsy encompasses a broad range of scales in space and time. Some of the most promising work in this area focuses on biophysically accurate models of circuits and synapses in brain that give rise to seizures. It is ultimately through work on this level, understanding interactions between cells and their simple functional aggregates, that the building blocks of clinical epilepsy must be understood, in order to develop optimal therapies. The complexity of human cortex, our limited knowledge of the fundamental cellular and network lesions that cause epilepsy, and limitations of memory, storage and computational power make the progress of this research slow, though its pace is accelerating. At the same time, there are pressing clinical needs that require practical solutions on a much larger scale. Rather than action potentials, gap junctions and individual ion channels, the clinical world relies on crude, smeared averages of postsynaptic potentials heavily filtered by skull, scalp, CSF and dura, to make life and death decisions. System behavior is measured on a gross spatial scale, far removed from the elegant microscopic behavior of individual and small aggregates of cells, which dictate its conduct.

Scalp electroencephalography (EEG), with its physiological noise and narrow bandwidth, was the language of most clinical epilepsy electrophysiology until approximately 60 years ago, when the first electrocorticographic (ECOG) records were made. Since that time, intracranial EEG (IEEG), obtained through subdural grids, strips and depth electrodes has become the standard for obtaining high fidelity, stable and relatively noise-free EEG recordings for localizing epileptic networks during evaluation for resective epilepsy surgery. The advantage of these types of recordings is that they have the capability better to transduce and localize epileptic and normal physiological activity, because they record much richer,

higher frequency activity from within the skull. In the modern era of epilepsy surgery, these recordings are required to investigate seizure generation, antiepileptic brain stimulation, and algorithms for localizing epileptic networks prior to surgical treatment of medically refractory seizures. More recently, it is becoming clear that even higher frequency recordings made from micro- and other novel network electrode configurations, may be required to address clinical questions.

At present, neural computation on a ‘clinical’ scale focuses on a number of basic questions for diagnostic and therapeutic applications. These questions include:

1. Where and when do seizures begin? This discussion has many facets, on multiple scales, but clinically revolves around seizure and ‘event’ detection. Seizure detection is a discipline that focuses on using quantitative features extracted from EEG signals to determine objectively when seizures ‘begin’. Clinicians know well, and recent quantitative work demonstrates, that when a seizure begins depends largely upon how closely one looks, and particularly upon the bandwidth of the recordings and spatial sampling (Worrell et al., 2004). Seizure detection algorithms are used clinically to alert staff when patients have seizures in epilepsy monitoring units, to trigger intervention in responsive implantable devices and to map epileptic networks. Multiple approaches have been used over the years for detecting seizures, including time, frequency and chaotic domain features, and machine learning methods (e.g. support vector machines (Gardner et al., 2006)).
2. Can seizures be predicted? Seizure ‘prediction’ refers to tracking the generation of seizures over time and identifying periods of time when the probability of EEG or clinical seizure onset is increased. While a number of quantitative algorithms and statistical methods for performing this task have been proposed, true prospective seizure prediction has yet to be convincingly demonstrated. A number of different approaches have been promoted over the past 10 years for analyzing these recordings. Our group has concentrated on using quantitative methods to follow basic neurophysiology in epilepsy to track seizure generation (Litt et al., 2001). A reasonable review of the state of the art of this topic can be found in the summary paper from the First International Collaborative Workshop on Seizure Prediction (Lehnertz and Litt, 2005) and a recent review in the journal *Brain* (Mormann et al., 2007). Recent progress in statistical methods for validating this process suggests that more definitive seizure prediction studies are imminent (Wong et al., 2007).
3. How, when and where should local therapy be delivered to arrest seizures? This question centers on the ability to localize seizure generation or onset, to find regions that appear to be critical to this process and to assess the efficacy of therapy once delivered to these regions. Computational components and support for this work includes the need to detect, localize and characterize statistics regarding specific neurophysiologic events associated with epileptic networks (e.g. fast ripples, chirps, ‘seizure precursors’, etc.), synchronizing stimulation or other interventions with particular characteristics of these events and assessing the response. Other approaches include automated methods for adjusting stimulation parameters and continuous closed loop control algorithms applied to pathologic intracranial EEG.
4. Are there models of seizures and brain stimulation, on a systems or ‘macro’ level that can be used to develop new treatment methods or test stimulation or other therapeutic paradigms? This question is assessed elsewhere in this volume, as well as below. The key here is the focus on models that approach the scale of clinical questions and treatments. Models of this nature are often somewhat less satisfying than more detailed, realistic cellular models, because of their simplicity and distance from ‘real’ neuroanatomy and neurophysiology. A central challenge to translating of basic modeling research to the clinical realm is developing models capable of accurately capturing system behavior that are at the same time relatable to basic cellular properties and interactions. These types of models can be used either for investigation of basic mechanisms or, more pertinent to this chapter, as test-beds for clinical diagnostic and therapeutic strategies.

These are only samples of the types of questions that are the focus of the work in our research group, encompassed under the heading of ‘computational neuroscience in epilepsy applied to clinical translation’.

#### CLINICAL DATA ACQUISITION

The core of computational work for clinical applications, other than modeling neuronal circuits, is acquired electrophysiological data. In our laboratory collaborations, these data are acquired from a variety of sources including neuronal cell cultures, hippocampal slice experiments, *in vivo* animal recordings and human data. The data themselves can take many forms, on a range of temporal and spatial scales, including scalp EEG, intracranial macro- and microelectrode data,

functional imaging data and digital images acquired from fast cameras recording cellular activity after exposure to voltage sensitive dyes. While some laboratories focus on scalp EEG data, our collaborative group has shied away from this, because of its limited bandwidth and because of the substantial physiological artifacts that contaminate such records. These artifacts include muscle, movement, line noise and artifacts from changing electrode position or impedance. Intracranial EEG data are much more artifact free, though transients due to capacitance in connecting cables can sometimes be an issue when patients move. Muscle and movement artifacts are otherwise not commonly a problem, because electrode contacts are firmly embedded in brain tissue or secured subdurally, far from muscle and other sources of noise. Because the tissue–electrode interface is very stable in intracranial electrodes, except those directly in contact with blood vessels or connective tissue, impedance is more stable over time and line noise is usually not a problem, as long as reference and ground electrodes are applied properly.

Concepts in clinical electrophysiology for epilepsy, for data acquired during evaluation of patients, are changing rapidly. Bandwidths of 0.1–70 Hz, which have typically been used for both scalp and intracranial recordings, are rapidly being abandoned in favor of higher bandwidth, on both sides of the spectrum. While the clinical utility of broader band recordings, particularly high frequency and DC signals, has yet to be proven, early studies clearly demonstrate findings not seen with standard clinical EEG. Seizure onsets are clearly seen earlier (Worrell et al., 2004) on both DC and high frequency recordings and the rationale for standard clinical filter settings for intracranial EEG is being challenged. How broadband is wide enough? This question has yet to be answered. There is great interest in waveforms such as ripples and fast ripples that must be sampled at over 1 kHz to be resolved properly, though the clinical utility of recording these waveforms has yet to be proven. While broad field DC shifts just prior to unequivocal seizure onset on clinical EEG are clear, when such recordings are made, their clinical utility is also unproven. The conclusion is that the best temporal resolution of brain activity in epilepsy electrophysiology is yet to be determined. It is a very active area of investigation and it is expected that better guidelines for such recordings will be in hand within the next several years.

Similarly, optimal spatial resolution of electrophysiology in clinical epilepsy recordings is in debate as well. Standard clinical electrodes, with platinum-iridium discs of 0.5 cm diameter, up to 1 cm apart (on center) and depth electrodes with cylindrical contacts approximately 3–5 mm in length and 1 cm apart on center (a variety of configurations are available) are actively being redesigned as well. Electrode manufacturers are scrambling to poll clinicians and researchers to determine ‘optimal’ electrode configurations, though this remains largely a research question, until clinical utility of higher resolution sensors is demonstrated. Hybrid electrodes that include microelectrode probes spanning from 6 to 40  $\mu\text{m}$  in diameter are now being custom designed and assembled for implantation within standard clinical macroelectrodes, so that field recordings can be supplemented by recordings of single and multiunit activity. Other centers are experimenting with research systems, such as ‘bed of nails’ microelectrodes, with very high spatial resolution over a limited area (e.g. 100 microelectrodes over 1  $\text{cm}^2$ ), which are placed in regions complementing placement of standard intracranial electrodes during invasive epilepsy monitoring. Again, while there appears to be a rich amount of detail available in looking at unit ensembles in limited regions, the clinical utility of these investigations remains unclear.

A central theme of the sections below is that the methods discussed are independent of the type of data input into feature extraction algorithms and classifiers. Even when imaging data are exchanged for electrophysiology, the methods remain largely the same, though sampling rates, sliding processing windows and the like must be changed appropriately. Interpretations of data analysis, of course, need to be scaled appropriately in light of the temporal and spatial scales of the data which are analyzed.

## COMPUTATIONAL ANALYSIS

Understanding biophenomena such as epileptic seizures and translating research into therapeutic devices ultimately means iterating analysis (a whole broken into parts) and synthesis (parts unified into a whole). The overarching problem is to synthesize a model  $M$  that ‘compresses’ all inputs  $I$  and paired outputs  $O$  observed in an experiment (e.g. a big data spreadsheet) into a function that summarizes how  $I$  morphs into  $O$ . The function/model  $M$  could be a non-linear regression, a seizure detector or predictor, a probability estimator, a ruleset, the vector field in the differential equations of motion of a dynamical network, etc. Analysis in this context could be a decomposition of data  $I$  or model  $M$  into parts that add up to the original (such as a Fourier series), or other projections not necessarily adding up such as arbitrary features. The  $M$  somehow captures a scientific target concept and ‘explains’ the data. It also suggests how to ‘predict’ and ‘control’ the underlying phenomenon. For example, predicting the next 100 solar eclipses is hard using Tycho Brahe’s massive data records, but easy starting from Newton’s and Kepler’s laws. There is a symmetry we seek to exploit using computational

methods of this chapter: (1) Given  $I$  and  $O$ , we can obtain  $M$  and thus *explain*, (2) given  $I$  and  $M$ , we can obtain  $O$  and thus *predict* and (3) given  $M$  and desired  $O$ , we can obtain  $I$  and thus hope to know what to do in order to *control* the phenomenon.

The methods described entail original and mainstream contributions in the field of computational intelligence, merging many years of advancements in engineering (e.g. systems theory, digital signal processing, neural networks, fuzzy logic, pattern recognition), statistics (e.g. descriptive and inferential, discriminant analysis, regression, density estimation, regularization, resampling, simulation), computer science (e.g. expert systems, machine learning, evolutionary computation) and mathematics (e.g. non-linear dynamics, theory of evidence, optimization). We will describe one major analysis and two synthesis problems, respectively: feature extraction (with instantaneous frequency as example feature), classification, and computer simulation of seizure and therapy using population models.

## FEATURE EXTRACTION

The inputs to decision support systems are *features* – quantitative or qualitative measures that distill raw data into relevant information for tasks such as classification, regression, density estimation and clustering. This is the least understood and most difficult part of the pattern recognition problem (Glorioso, 1975). Features can be univariate versus multivariate (e.g. single versus multiple channels of data fed in), scalar-valued versus vector-valued, single-natured versus multinatured (e.g. feature coordinate 1 = FFT amplitude in frequency bin 1, feature coordinate 2 = FFT amplitude in frequency bin 2, etc., versus feature coordinate 1 = energy, feature coordinate 2 = entropy, etc.). For our purposes, a feature is any transformation from a set of numbers to a scalar  $\varphi : \{R \times R \times \dots\} \rightarrow R$ , for example, from a big matrix containing a page of digitized EEG to one number representing the maximum absolute amplitude in that page. A *feature vector*, element of  $R^m$ , can be formed from  $m$  scalars regardless of where they came from.

### Data windowing

In general, the calculation of each feature vector coordinate at a given instant of time requires observation of a ‘window’ of the raw brain signals, opened to a certain extent spatially (multiple channels) and temporally (interval from a point in the past to the present time). For certain features computed recursively (e.g. an IIR filter output), this window is in effect semi-infinitely long but exponentially forgetful of the past. The observation window ‘slides’ across the time axis, typically with a fixed amount of advancement that creates a certain overlap between adjacent windows. Conversion of each data window into a feature vector thus creates a feature time series with built-in compression (going from a big data matrix to a small vector each time, but also skipping a number of time samples in between).

The shaded block in Figure 32.1 is a sliding *observation window* containing raw multichannel IEEG. Practical constraints put a limit on the extent and number of channels in this window. For seizure detection, the observation window should have enough temporal resolution at least to capture the seizure onset. For seizure prediction, the period of time from the right edge of this window to the last instant when seizure is still pharmacologically or electrically preventable defines a prediction window or horizon. In addition to the observation and prediction windows, we define a history window as a superset of the observation window. We distinguish multiple levels of features. Instantaneous features are computed from observation windows that are essentially 1.25 seconds or less in duration. Historical features span longer periods and are

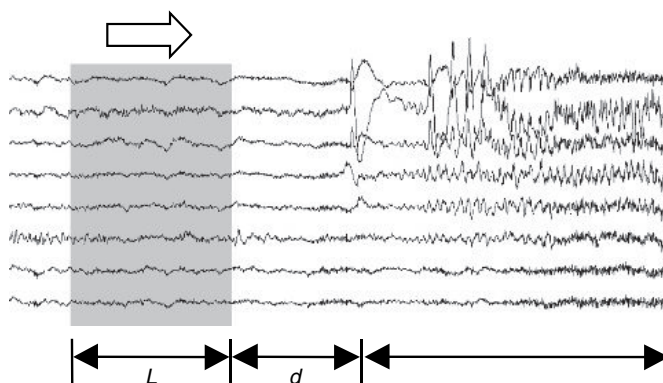


FIGURE 32.1 Sliding length- $L$  window for feature extraction. The next frame will advance  $d$  samples.

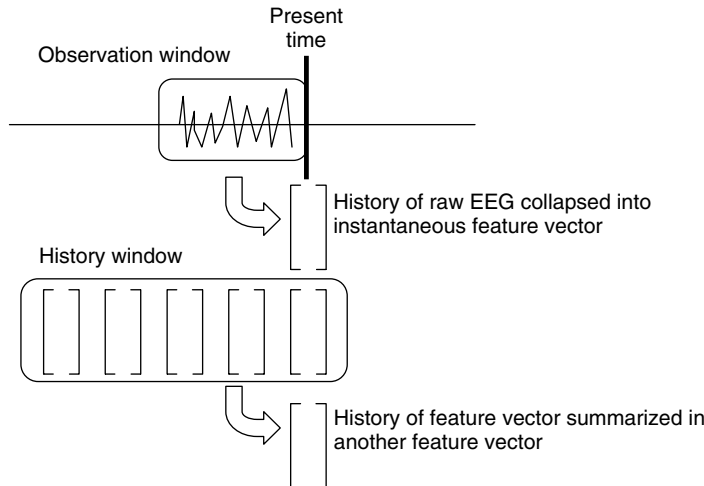


FIGURE 32.2 Windows for feature versus features of features.

based on the time *evolution* of instantaneous features, as shown in Figure 32.2. From a geometrical point of view, historical features are features of the trajectories of instantaneous features in feature space – they are ‘features of the features’. This process of nested feature compositions can be repeated *ad libitum* as long as there are enough buffered data to feed the feature extractors.

Instantaneous features in a library might include: auto-regressive coefficients, coherence, cross-covariance, correlation between entropies, energy, energy derivative, entropy, filtered amplitude squared, fractal dimension, fourth power indicator, mean frequency, non-linear decorrelation lag, non-linear energy operator, number of zero crossings, Pisarenko harmonic decomposition, power distribution in frequency bands, principal components, principal Lyapunov exponent, real cepstrum, spike (occurrence, amplitude, curvature), third-order spectrum, wavelet subband energy, wavelet compression coefficients and zero crossings of energy derivative. The raw signals themselves should be considered as instantaneous features in a special case of zero compression of information.

#### **Example: estimation of instantaneous frequency**

In order to illustrate feature extraction according to several useful methods, we shall use the chirp as model of time-varying parameters. Chirps are important spectrographic signatures of seizure onsets (Schiff et al., 2000). A general chirp is a function  $x(t) = A(t) \cos\{\varphi(t)\}$ , or its complex-valued version  $A(t) \exp\{j\varphi(t)\}$ . The *local* amplitude, phase and frequency are  $A(t)$ ,  $\varphi(t)$  and  $d\varphi(t)/dt$  respectively. The *instantaneous* amplitude, phase and frequency are  $|z(t)|$ ,  $\angle z(t)$ ,  $d\angle z(t)/dt$  respectively, where  $z(t)$  is the analytic signal of  $x(t)$ ,

$$z(t) = x(t) + jH\{x\}(t)$$

and  $H\{x\}(t)$  is the Hilbert transform (HT; also a function of time)

$$H\{x\}(t) = x(t) * 1/(\pi t)$$

where  $*$  denotes convolution, or

$$\text{real}(\text{IFFT}\{-j * \text{sgn}(\{1 : N/2 - N/2 : -1\}) * \text{FFT}(x)\})$$

for the power-of-2 length discrete-time version. (Note: MATLAB’s `hilbert(x)` is really the complexified analytic signal  $z = x + jH(x)$ ). When  $A(t)$  varies slowly compared to the oscillations  $\cos\{\varphi(t)\}$ , the local and instantaneous counterparts are approximately the same. For example, one type of AM demodulator is

$$A(t) \approx \sqrt{x^2(t) + H^2\{x\}(t)} = |z(t)|.$$

In the case of linear frequency modulation  $\varphi(t) = 2\pi f_o t + \pi\alpha t^2$  (instantaneous =  $2\pi f_o + \alpha t$ ), another parameter of interest is the chirp rate  $\alpha$ . In this section, we are interested in the more general, arbitrary changes in frequency  $\varphi'(t)$ (rad/s), or  $\varphi'(t)/(2\pi$  in Hz).

Methods for detecting chirps based on cross ambiguity function, Radon, chirplet, Hough continuous-time wavelet, and other transforms involve computation of multiple inner products (correlations) for which no fast algorithms are known. Here, we extract specifically the time-varying frequency component of a chirp using faster methods based on: spectrogram peak (FFT), Hilbert transform (HT), wavelet packets (WP), and line length (LL).

### Frequency feature from spectrogram peak (FFT)

The periodogram ( $|FFT|^2/N$ ) can be shown to be the optimal test statistic for detection of a sinusoid of unknown amplitude and phase in white Gaussian noise (Kay, 1998). When the frequency is also unknown, the test involves taking the maximum of the periodogram over all frequencies, thus an estimate of the frequency is the maximizer. When the time of arrival (onset) of the sinusoid is also unknown, the test involves taking the maximum over all delays as well. Therefore, the test is the same as tracking the maximum of a time-sliding periodogram (a spectrogram). The frequency estimate in Hz at every time  $n$  is

$$f_{\text{FFT}}[n] = \frac{F_s}{L_x} \arg \max_k |FFT\{\mathbf{x}[n]\}_k|^2$$

where  $F_s$  is the sampling frequency,  $L$  is the power-of-2 length of the data observation window,  $k$  indexes discrete frequencies from 0 to  $L - 1$ , and  $\mathbf{x}\{n\}$  is the current window of data  $\{x\{n-L+1\}, \dots, x\{n-2\}, x\{n-1\}, x\{n\}\}$ . Since the magnitude squared is monotonically increasing, squaring is not necessary, but can still be preferred to exploit the complex conjugate arithmetic  $FFT\{\cdot\}FFT^*\{\cdot\}$ .

In the case of colored noise, the signal is prewhitened (inverse filter from AR estimate, or even just the first difference) before periodogram computation. Furthermore, if the noise is non-Gaussian, a Rao detector applies a PDF-dependent non-linear limiting function before periodogram computation (and a post-normalization) which keeps the test optimal for a large class of non-Gaussian PDFs (Kay, 1998). (Note: MATLAB's default specgram is a Hanning-windowed sliding non-averaged periodogram.)

### Frequency feature from Hilbert transform (HT)

From the previous introduction, we see that one way to estimate frequency is numerically to differentiate the instantaneous phase obtained from Hilbert. We will take the instantaneous slope at the midpoint of each sliding window to obtain  $(\angle z)'/(2\pi)$  in Hz as

$$f_{\text{HT}}[n] \approx \frac{1}{2\pi} \frac{\Delta(\angle z_n[\lfloor L/2 \rfloor])}{\Delta t} = \frac{F_s}{2\pi} (\angle z_n[\lfloor L/2 \rfloor + 1] - \angle z_n[\lfloor L/2 \rfloor])$$

where  $\angle z_n[m](m \in \{1, 2, \dots, L\})$  is one of the  $L$  (unwrapped) instantaneous phases obtained from a length- $L_x$  data window right-aligned at time  $n$ , collectively given by

$$\angle \mathbf{z}_n = \arctan_2 \frac{H\{\mathbf{x}[n]\}}{\mathbf{x}[n]}$$

where  $\arctan_2(\cdot)$  returns angles of complex numbers (recognizes quadrants), with vector division taken pointwise. A disadvantage of the HT approach is that it can produce wild estimates (e.g. negative frequencies) when subjected to noise, so special handling is required when applying this method to EEG.

### Frequency feature from wavelet packets (WP)

A discrete wavelet transform (DWT) orthogonally decomposes a signal into an approximation signal (low-pass filtered version) plus details signal (remaining high-pass). The same split is applied to the approximation signal itself and this process is repeated at increasingly deeper levels (larger scales, lesser resolutions), resulting in a narrow tree structure of filter coefficients (or their reconstructed signal counterparts, which add up to the original). These coefficients can be interpreted as correlations between the original signal and dyadically scaled (stretched by factor  $2^{-j}$ ,  $j \in \mathbb{Z}$ ) and shifted (translated to position  $n2^j$ ,  $n \in \mathbb{Z}$ ) versions of a wavelet (and its associated scaling function). Due to a 'twin-scale' mathematical relation, one does not actually stretch and shift a wavelet (which is sometimes a fractal or a waveform in the limit so cannot even see it) to compute correlations – all is done efficiently using special pairs of FIR filters and downsamplings by 2 in a scheme known as fast wavelet transform (Mallat, 1988, exactly the same as 2-channel 'subband coding' or 'quadrature mirror filters' by Croisier et al., 1976). The computational complexity is  $O(N)$ .

The wavelet packet (WP) decomposition generalizes the DWT tree to its full breadth by allowing all of the detail signals to be split as well (Coifman and Wickerhauser, 1992). The computational complexity is now like an FFT,  $O(N \log N)$ . Whereas the wavelet underlying DWT oscillates a fixed, ‘small’ number of times, WPs induce a whole family of waveforms that oscillate at ‘all’  $2^{lev}$  bin frequencies in the interval  $(0, F_s/2)$  Hz (here the signal has been digitally sampled), where  $lev$  is the number of levels in the WP tree. Thus, WPs encode not only scale and time position, but also an actual measure of frequency relatable to an oscillation parameter  $osc$  of each WP. For example, at the terminal layer of a level-5 WP tree, there are  $2^5 = 32$  nodes (sets of WP coefficients) collectively forming the equivalent of a bank of bandpass filters. The terminal-node oscillations progress in paley order (mirror-image shufflings) for  $osc = 0, 1, 2, \dots, 2^{lev} - 1$ . For example,  $\text{paley\_order}(0:7) = [0\ 1\ 3\ 2\ 6\ 7\ 5\ 4]$  (this function is not part of the Wavelet Toolbox). Let us arrange the terminal-node coefficients into a  $2^{lev} \times L_c$  (=no. coefficients per node at level  $lev$ ) matrix  $\mathbf{C}$ . By indexing into the rows as  $\mathbf{C}(\text{paley\_order}(0:2^{lev}-1) + 1, :)$ , the natural frequency ordering (monotonically increasing) is restored in the vertical axis of an image of the coefficients, with bin-center frequencies in Hz:

$$f_{\text{bin}[k]} = \frac{F_s}{2} \frac{(k+0.5)}{2^{lev}}$$

for  $k = 0, 1, 2, \dots, 2^{lev} - 1$  (other frequency assignments such as bandpass filter centroids are not uniformly spaced).

The image of  $(|\cdot|, (\cdot)^2$ , or  $\log |\cdot|$  of) coefficients with frequencies in natural order is a kind of ‘spectrogram’, but the time axis still needs trimming. If the length of the original discrete-time signal is  $L_x$ , the length of the WP coefficients for every node at the 1<sup>st</sup> level is  $L_c[1] = \lfloor (L_x + L_f - 1)/2 \rfloor$ , where  $L_f$  is the length of the FIR filters used in decomposition. This is because the length of convolution is  $L_x + L_f - 1$ , but then downsampling by 2 keeps only the even-numbered indices of the result. These sets of coefficients become shorter ‘signals’ at each succeeding stage of decomposition (filter followed by  $\downarrow 2$ ). Thus, at the 2<sup>nd</sup> level,  $L_c[2] = \lfloor (L_c[1] + L_f - 1)/2 \rfloor$ . An upper bound on this sequence is  $L_x/2^{lev} + L_f(1/2 + 1/4 + \dots + 1/2^{lev})$ , so it approaches  $L_f$  as  $lev \rightarrow \infty$ . At each level, we are keeping only half as many coefficients ( $\sim L_x/2$  the 1<sup>st</sup> time) corresponding to the ‘signal of interest’, i.e. the central part of convolution that matches the time span of the original signal, while at the same time we are adding  $\sim L_f/2$  of ‘junk’ (convolution transitions) to both sides of the sequence. Thus, the time interval of interest has shrunk to length  $\sim L_x/2^{lev}$  at the terminal level. Of all the coefficients stored in matrix  $\mathbf{C}$ , we keep only the  $\lceil L_x/2^{lev} \rceil$  middle columns in the WP spectrogram image since they correspond to the original time interval. There is no point in going to levels deeper than  $\log_2 L_x$  since that would leave a single or no time point of the original time axis, while the deep-layer coefficients melt down to zero.

The frequency estimate in Hz at every time  $n$  can be obtained by peak-picking the WP spectrogram

$$f_{\text{WP}}[n] = f_{\text{bin}[k^*]}, \quad \text{where } k^* = \arg \max_k \mathbf{c}^2 \{\mathbf{x}[n]\}_k$$

where  $\mathbf{c}$  is the rightmost column of the centrally-kept part of  $\mathbf{C}$  (the one corresponding to time  $n$ ),  $k+1$  indexes its elements, and the square (or  $|\cdot|$ ) is taken pointwise. In practice, we take the max of the whole matrix to get the entire frequency profile inside the  $L_x$  window in a single snapshot. Unlike the sliding periodogram method, there is no need to slide a short window little by little in time since wavelets already account for signal non-stationarity. This could be implemented in a ‘non-overlapped sliding image’ scheme. However, note the single-shot WP spectrogram trade-off: *with more frequency bins we lose temporal resolution*. This is in contrast to the wavelet scalogram (contained in the lowpass branch of the WP tree), where the smaller scales (shallow layers) more densely cover the time axis with small shifts of a thin scaling and wavelet function. These scalograms do not look as appealing as WP for a chirp because of the non-uniform atom size associated to pseudofrequencies obtained from reciprocals of scale. The WP spectrogram time resolution could be increased with overlapping sliding windows, at CPU expense, but interpolation of the single-shot is probably a better compromise. Finally, we note that if the sampling frequency is high compared to the bandwidth of EEG, a lot of the WP frequency resolution is wasted by confining the EEG spectrum to just a few bins of the already coarse (e.g. 32) bank. Decimating the signal to a lower sampling rate makes more efficient use of the WP spectral resolution, possibly at expense of missing high-frequency transient events.

### Frequency feature from line length (LL)

Kircher and Raskin reported that ‘line length’, the sum of absolute differences between adjacent sample points, is a good measure of respiration suppression for use in computerized lie detection (Kircher and Raskin, 1988). In image processing, this feature is known as 1-D total variation, or  $L_1$  norm of a gradient. The Johns Hopkins University (JHU) disclosed

line length as one of the features for automatic seizure detection (Olsen et al., 1994). The JHU Applied Physics Lab also evaluated about 10 000 features and line length made it to their PolyScore lie detection system (which is identical to the EEG patent except the input is electrodermal). A variant of line length was implemented as Euclidean distances in Katz fractal dimension, and can be seen upsampled in Higuchi's method (Esteller, 2000). Line length (LL) is a universal seizure detector suitable for implantable medical devices (Esteller et al., 2001; Echauz et al., 2001).

Line length does simultaneous AM and FM demodulation, but how and under what conditions? Consider a sinusoid  $x(t) = A \cos\{2\pi ft\}$ , with frequency of oscillation  $f$  slow enough for the digitally sampled waveform still to 'look' like the sinusoid (up to  $\sim F_s/8$ , or  $4\times$  oversampling). The LL of this sinusoid over an observation window of length  $L$  is approximately the LL of one half-wave (sum of vertical segments from one extremum to the next =  $2A$ ) times the number of half-waves that fit in the length- $L$  window. Equivalently, that is  $2A$  times *twice* the number of full-waves that fit in the length- $L$  window ( $f$  such waves fit in  $F_s$  samples), so  $LL \approx (2A)(2)(fL/F_s) = (4L/F_s)Af$ . Thus, the LL of an oversampled sinusoid is proportional to its amplitude and frequency as claimed (and obeys homogeneity but not additivity). From this, the estimate of frequency in Hz is

$$f_{LL}[n] = \frac{F_s LL}{4AL}.$$

Note direct dependence on  $A$ , so for this estimate to work on a chirp, the amplitude has to vary very slowly compared to the oscillation.

### Quadratic chirp as seen by FFT, HT, WP and LL

The quadratic chirp signal obtained from the following MATLAB program will be used to illustrate the four methods discussed previously:

```
t = -2 : 0.001 : 2;
y = chirp(t,100,1,200,'q');
```

This signal has constant amplitude = 1 while its frequency chirps down from 500 to 100 Hz during times  $-2$  to  $0$  s, and then symmetrically up during  $0$  to  $2$  s. Here we have  $F_s = 1000$  Hz and  $L_x = 4001$ .

Figure 32.3A shows the output of the command specgram (y,256,1e3,256,255) which corresponds to  $L = 256$ ,  $F_s = 1000$  Hz, Hanning window and sliding window overlap = 255 (displacement one by one). The dark band is thick because this function plots  $\log|FFT|$ , not  $|FFT|^2$ . It does not correctly return a time vector corresponding to the original time axis and does not account for causality either, so imagine 255 time points before the left edge being blank for initial buffering, the first of them corresponding to time  $-2$  s.

Figure 32.3B shows the Hilbert-based estimate  $f_{HT}[n]$  with  $L = 256$ ,  $F_s = 1000$  Hz. The dashed line is the theoretically correct curve. The estimates are good, although our midpoint derivative method necessarily has a  $\sim L/2$ -point delay with respect to time  $n$  (this delay could seemingly disappear taking derivative at the right edge of the window).

Figure 32.3C shows the WP spectrogram with energies (squared) of all the terminal coefficients of a level-5 WP tree using the discrete Meyer wavelet (FIR filter length 62), applied in one shot to the entire signal of length  $L_x = 4001$ . The image matrix is formed by stacking the rows of WP coefficients in natural frequency ordering, each row representing one of 32 nodes, and keeping only the central  $\lceil 4001/32 \rceil = 126$  columns most closely matching the original time axis. It would seem there is no time delay because every time point has a shaded pixel in the image, but remember the entire signal had to be buffered in before producing the single image, so the delay would range from  $L_x$  for the leftmost time point to virtually zero for the rightmost (plus whatever the WP itself takes).

Figure 32.3D shows the line length estimate  $f_{LL}[n]$  with  $L = 256$ ,  $F_s = 1000$  Hz,  $A = 1$ . Since the length normalization ( $LL/L$ ) in the formula performs some kind of average over the whole observation window and the chirp is continuous, the frequency estimate corresponds to the theoretical one at some time delayed on average by  $L/2$  points (by mean value theorem it is somewhere between 0 and  $L$ ). We also note that values of true frequency larger than  $\sim F_s/8 = 125$  Hz get underestimated.

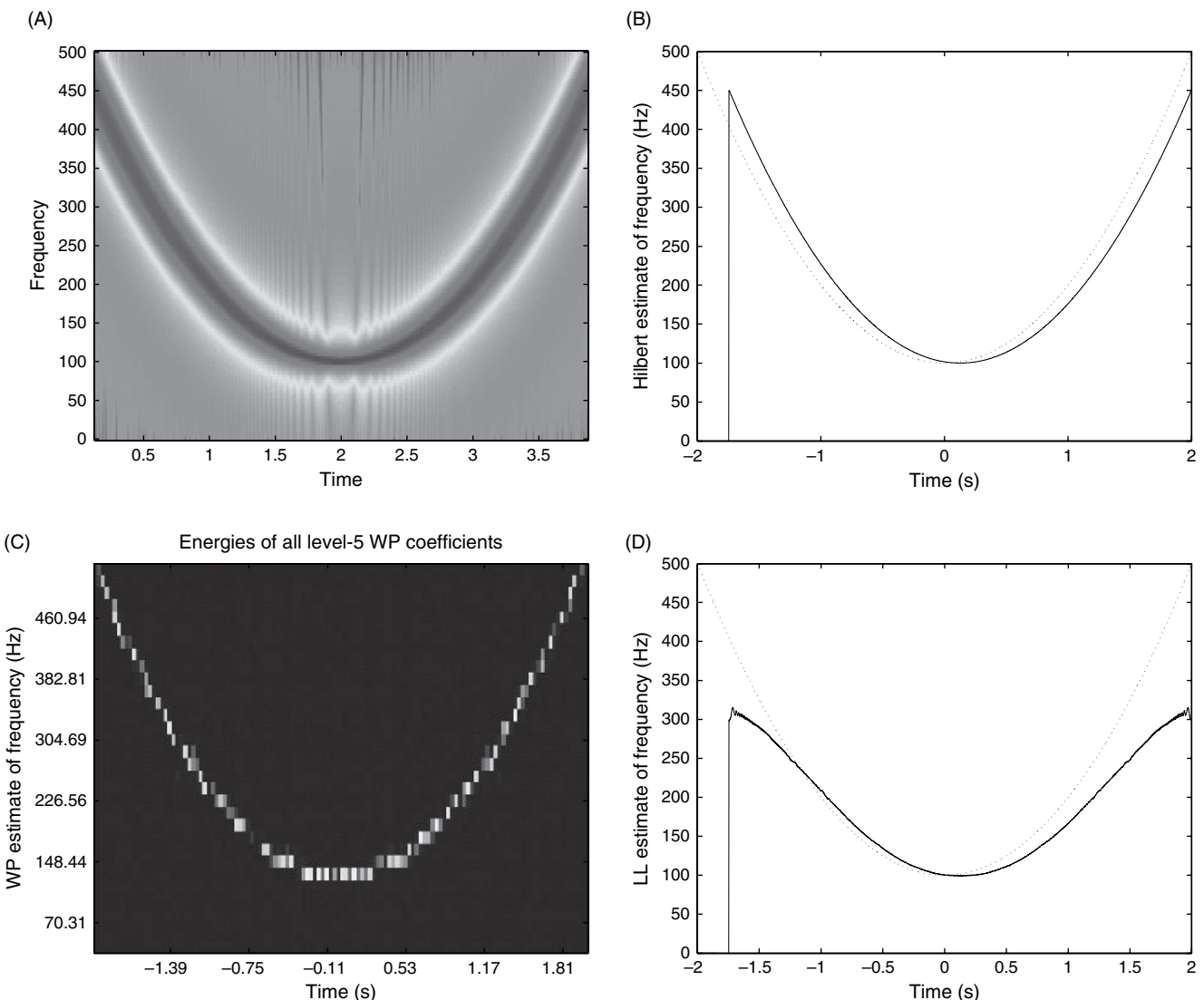


FIGURE 32.3 Instantaneous frequency extracted by (A) FFT, (B) HT, (C) WP, (D) LL.

#### AUTOMATED CLASSIFICATION AND DECISION SUPPORT

The job of a classifier is to categorize its input as belonging to 1 of  $K$  classes. Classification is a special case of regression in which the synthesized function is discontinuous and discrete-valued  $\hat{f} : \mathbb{R}^n \rightarrow \{C_1, C_2, \dots, C_K\}$  (Figure 32.4).

Detection is a special case of classification in which there are only  $K = 2$  output classes. The output labels of the classifier can be encoded as one of the integers in  $\{1, \dots, K\}$ , or can be spread into a decoder-style, 1-of- $K$  binary vector

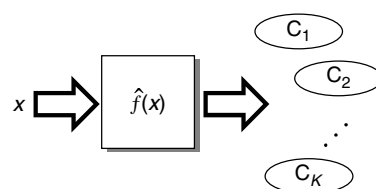


FIGURE 32.4 Classification: mapping from real-valued vector to discrete class labels.

$\{0010\dots0\}$ , where the 1 occurs at the  $i^{\text{th}}$  position corresponding to the  $i^{\text{th}}$  class. Two of the  $K$  classes can optionally be: outlier class – definitely not one of the recognized classes – and a doubt class – not sure which of the classes so no classification is issued (Ripley, 1996). Implementation approaches include:  $k$ -nearest neighbors (kNN), maximum selector of discriminant functions, decision trees, neural networks, fuzzy production rules, Holland's classifier systems, statistical pattern recognition, syntactic pattern recognition and support vector machines.

Classifiers can be created from data using any of the general classes of learning methods: supervised when classes  $C_i$  are known *a priori*, unsupervised when classes are not known *a priori*, thus starting with clustering and then applying the clusters in some decision rule, reinforcement learning when only a high-level ‘success’ versus ‘failure’ or a delayed performance metric is available and, more recently, a hybrid between unsupervised and supervised, one-class novelty detection, where training occurs using only one labeled class of data. The actual algorithms used to tune the classifier parameters include genetic algorithms, linear and non-linear regression using Newton methods, expectation-maximization and quadratic programming.

### Performance criteria

Some of the classification methods specifically optimize criteria such as Bayes error (minimum expected probability of error), maximum a posteriori (MAP) probability of the class given the feature vector, MAP under conditional independence (naive Bayes), maximum likelihood, maximum entropy, minimum error risk, maximum margin, etc. When applied to detection, all these optimality criteria correspond to different locations on the receiver operating characteristic (ROC) curve, which summarizes the trade-off between sensitivity and specificity of a detector. The performance of detectors is often framed in terms of mean detection latency, confusion matrix, sensitivity (recall), specificity, misclassification rate, positive predictive value (precision), negative predictive value, false positives per hour, extremal margin and others.

### Generalization performance over unseen, future data

During training and measurement of performance, it is crucial to understand that if the model is too complex, it can memorize peculiarities of data sparsity or irrelevant details about noise. If the model is too simple, it cannot even approximate noise-free training data. Thus, the right balance of model complexity is needed to achieve the best possible generalization performance. Several approaches exist to attempt to minimize the expected prediction error over future input data as opposed to the overoptimistic (on average) apparent error over the training set. These include: split sample (train versus hold-out test); group method of data handling (GMDH); cross validation to estimate nearly unbiased (though potentially highly variable in small samples) prediction error (Efron and Tibshirani, 1993); jackknife, bootstrap to estimate bias, variance, confidence intervals,  $P$ -values; Vapnik-Chervonenkis theory leading to support vector machines (SVMs) with built-in tight upper bound on future misclassification rate (Cherkassky and Mulier, 1998); and regularization formulas that approximate bias correction from a single data sample, including Akaike's final prediction error (FPE), an information criterion (AIC), Rissanen's minimum description length (MDL), Barron's predicted square error (PSE), Moody's generalized prediction error (GPE) and others. The latter regularization methods facilitate model selection (e.g. ‘size’ determination) with a variable structure (e.g. growing number of parameters) by adding a complexity term to the apparent error rate. This is similar to ridge regression in statistics, weight decay in artificial neural networks and the fact that most weights are set to zero during quadratic programming in SVMs. Another method to address generalization with a variable size structure is pruning, where instead of growing, a model starts with large structure and then weights or connections are eliminated. An example is optimal brain damage (OBD) in neural networks (Le Cun et al., 1990). Other methods address generalization with a fixed structure, including early stopping where training occurs until performance on a ‘validation’ or checking data set starts degrading, and jittering, where noise is artificially injected to the input data.

### Feature fusion as subset selection

Retrospective examination of features typically shows promise but no perfect consistency for any one feature working individually to discriminate between classes. Fusing features together can be motivated from many different points of view ranging from Dempster-Shafer theory to Bayesian reasoning. The unifying principle is that certain feature *combinations* exist that can work better together when fed to a classifier, than each one individually would suggest in a given problem. One approach to fusing features is to carry out feature *subset selection* from a given list of candidates.

Many of the  $N_f$  features in a feature library can be redundantly correlated to others, or be completely irrelevant for the particular classification task. Furthermore, the use of all features in this library is associated with a large computational burden on the learning and execution process. There are  $\binom{N_f}{n} = \frac{N_f!}{n!(N_f - n)!}$  possible ways of choosing  $n$ -dimensional

feature vectors from the universe of  $N_f$  features,  $n \leq N_f$ . This can grow so large as to preclude the possibility of exhaustive search. For example,  $\binom{30}{5}$ ,  $\binom{30}{10}$ ,  $\binom{100}{5}$ , and  $\binom{100}{10}$  are 142 506,  $30(10)^6$ ,  $75(10)^6$ , and  $1.7(10)^{13}$ , respectively. An expedient strategy to deal with this exponential explosion is to find the smallest feature subset that first ‘works’ through a forward sequential search. More recently, recursive feature elimination (RFE; backward elimination using SVM) (Guyon et al., 2002), where the worst feature is eliminated at each iteration forming nested subsets, and Corona (CORrelatiON as feAtures) (Yang et al., 2005), its improvement for multivariate time series such as EEG, have been shown to have built-in regularization and resist overfitting the training data.

### SIMULATION OF SEIZURES AND THERAPEUTIC INTERVENTIONS USING POPULATION MODELS

Computer simulation is an attractive tool that can accelerate the development of therapeutic devices. Such simulations can be run millions of times in order to explore network dynamics, effect of parameter changes in the system, the effect of therapeutic intervention, etc., without the cost or physical harm involved in experimental setups. Focusing on small details of the nervous system has produced some spectacular successes, but does not provide much information on processes such as memory or seizures, many of whose characteristics are emergent and are not understandable below the level of ensembles of neurons. When investigating the dynamics of epilepsy, the most appropriate level of description would seem to be a population or group of neurons (Larter et al., 2000) (in contrast to the level of compartmentalized models of neural networks). Other authors conclude that effective therapy should be aimed at desynchronizing populations rather than naively at the concept of excitation/inhibition balance (Ebersole and Milton, 2003). To test how epileptic activity is ‘sustained’, measurements have shown zero net phase lag, suggesting that seizures behave more like coupled oscillators than re-entrant loops or than projections from a discrete pacemaker (Jefferys, 2003). Computer simulation of seizure-like activity and therapeutic interventions in this section are presented based on the models of Suffczyński, Wendling and Tass.

#### **Suffczyński model**

Suffczyński et al. have developed a 16-dimensional state vector model in Simulink® (personal communication) that generates *spontaneous* seizure-like activity as shown in Figure 32.5.

The model has been extended using a 26-dimensional state vector that outputs spindles and spike-and-wave-like seizures that also match the exponential distribution obtained from a genetic rat model of such epileptic activity (Suffczyński et al., 2004).

#### **Wendling model**

Wendling et al. developed a 10-dimensional ordinary differential equations model of IEEG that produces 6 ‘photorealistic’ epileptic states (Wendling et al., 2000, 2002). This model evolved from the neurophysiologically plausible Freeman’s olfactory bulb model of EEG, Lopes da Silva’s model producing alpha rhythm EEG, Jansen’s extensions producing realistic visual evoked potentials, Wendling’s modifications producing intracranial patterns and Wendling’s final modification which

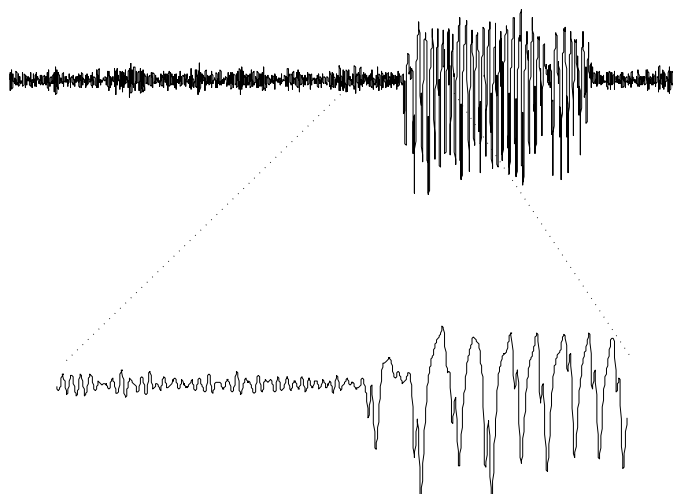
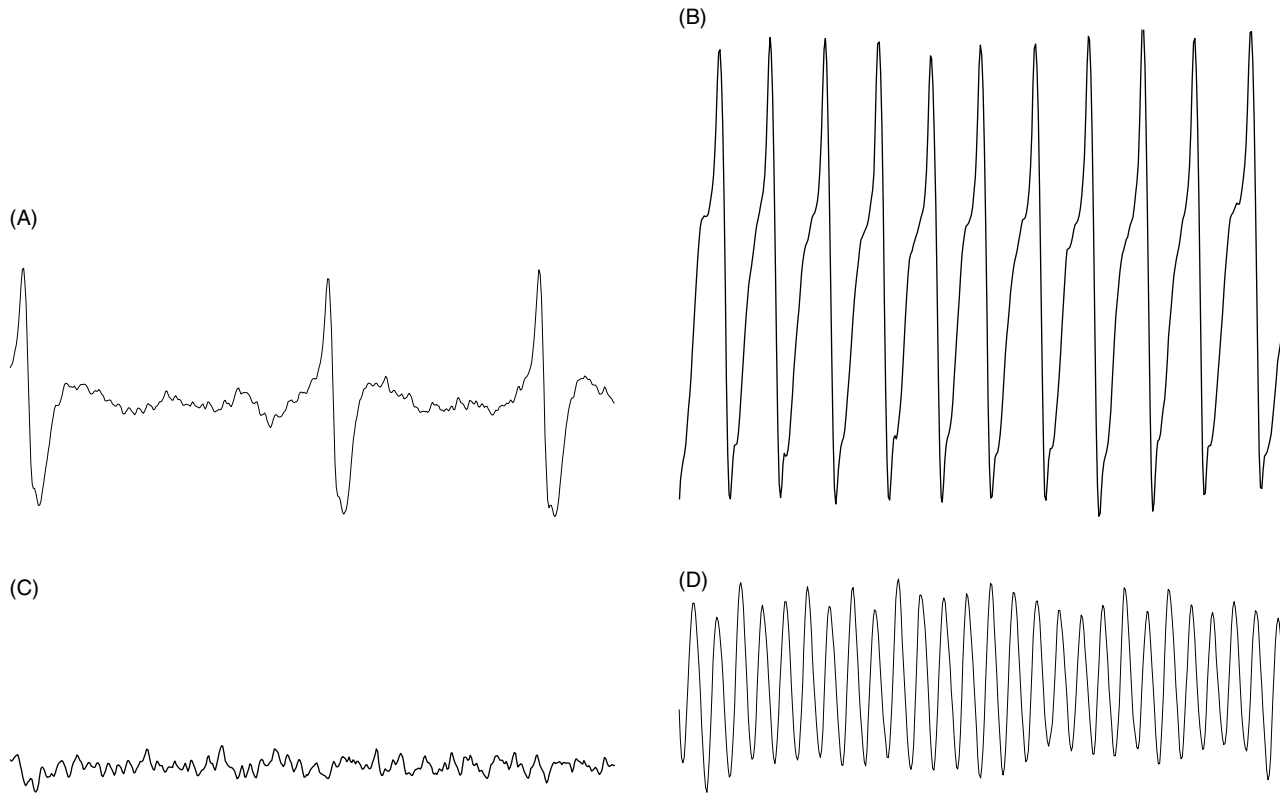


FIGURE 32.5 Spontaneous simulated seizure generated by the Suffczyński model.



**FIGURE 32.6** Four of the qualitative IEEG states produced by Wendling's model: (A) sporadic spiking, (B) rhythmic spiking, (C) low-voltage fast and (D) quasi-sinusoidal (seizure). The model also produces slow rhythmic and normal background activities, not shown here.

additionally produces low-voltage fast activity (beta buzz). Figure 32.6 shows four of the qualitative states produced by the model. The authors have shown examples of actual (human) IEEG clips possessing striking similarities to the morphologies produced by the computer simulations.

One attractive aspect of the Suffczyński model – spontaneity of seizure-like activity – is not directly available in Wendling's. Additional dynamical equations to drive the variation of the gain parameters would be needed (a transition to seizure can be constructed by manually changing these gains). A disadvantage of both Suffczyński's and Wendling's models is that external inputs are either not emphasized or are accommodated in terms of average pulse densities – positive quantities that do not model the bipolar nature of neurostimulation current. The Tass model, discussed next, specifically includes the effect of stimulation on network dynamics. Like Wendling's, the Tass model is perpetually in a given qualitative state of oscillation unless driven out of it by additional means. For Tass, this is accomplished by the influence of therapeutic intervention.

### Tass model

Tass has developed an infinite-dimensional model of desynchronization in the framework of stochastic phase resetting (Tass, 1999). Although initially motivated in the context of Parkinsonian tremor, the principles are fundamental and should be broadly applicable to other biological oscillations, including epileptic seizures. A phase oscillator continually sweeps angle from 0 to  $2\pi$  and repeats. In isolation, it will do this at a constant angular speed  $\Omega$ . Interconnected, phases can wax and wane to try to synchronize. The times of spiking/bursting of a neuron are represented each time a rotator up-crosses the  $+x$ -axis in the complex plane (amplitude information is discarded here). Think of the network as an infinite population of rotators whose collective synchronization depends on mutual coupling, noise and stimulation resetting influences and whose dynamics are given by a partial differential equation derived in the asymptotic limit from Winfree, Kuramoto and other prior models of oscillatory behavior.

The model output is the average number density  $n(\psi, t)$  – a time-varying PDF of phases (think of as ‘fraction’ of neurons firing at phase  $\psi$  at a given time  $t$ ). For numerical stability, the evolution of  $n(\psi, t)$  is solved as ordinary differential

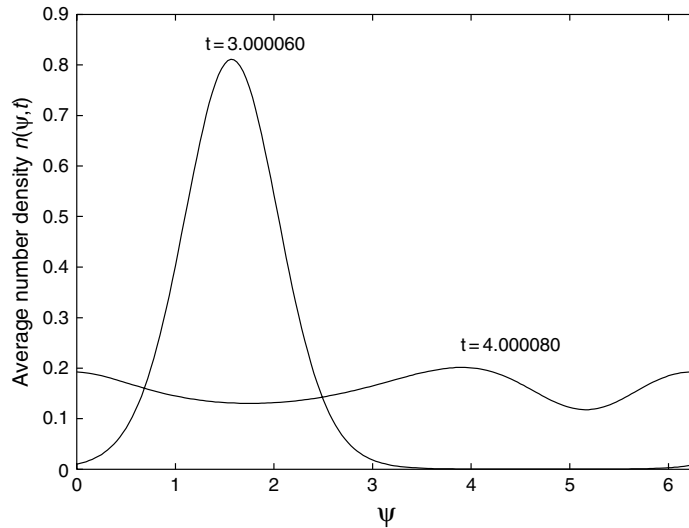


**FIGURE 32.7** Snapshots of the average number density at times  $t = 3$  (synchronized) and  $t = 4$  after continuous feedback stimulation (approaching fully desynchronized state  $1/(2\pi)$ ).

equations in the Fourier series domain using Euler or Runge-Kutta with 100 modes, so the infinite-dimensional state becomes a vector with 100 state variables (the Fourier coefficients of the PDF). Given an initial PDF  $n(\psi, 0)$ , depending on bifurcation parameters, the network will be either incoherent or attracted to a limit cycle which we associate to ‘seizure’. In the synchronized state, the *whole network acts like one giant oscillator* (Tass, 2001). At any given time, the network will show at least one preferred range of phases in the form of peakedness in the PDF. Extreme synchronization would be an impulse at a single phase, while complete desynchronization is the uniform distribution.

Figure 32.7 shows the PDFs at  $t = 3$  and  $t = 4$  corresponding to Figure 32.8C. Instead of a constant, we made stimulation intensity a function of time to allow for arbitrary control laws. In the simulations, the influence of stimulation had a single Fourier mode:  $I(t) \cos \psi$  (effect is singly-periodic with phase, and overall synchronization or desynchronization is encouraged or discouraged depending on timing and current  $I(t)$ ); rotators ‘self-oscillate’ with eigenfrequency  $\Omega = 2\pi$ ; Gaussian noise (which dampens synchronization) had variance 0.4; influence of mutual coupling also had a single Fourier mode:  $-K \sin \varphi$  with coupling constant  $K = 2\pi$ ; and initial phase distribution was a circularly periodic Gaussian with central location  $\pi/2$  and variance 0.6.

#### Biphasic pulse train stimulation versus continuous feedback

Tass first showed that this model can be desynchronized, via phase-resetting calibrations, using open-loop schemes: single pulse, periodic pulse train, double pulse, bipolar double pulse and coarse-grained schemes: ‘demand-controlled’ timing and duration (Tass, 1999, 2001, 2003; Tass and Majtanik, 2006) and, recently, calibration-free methods using multiple sites and delays feedback coordination (Hauptmann et al., 2005) but using a different model that lacks the attractive properties of Tass. Other calibration-free (in other words, practicable) methods exist, using closed-loop feedback as opposed to open-loop control, that easily desynchronize the network of phase oscillators.

In control systems parlance, the Tass system of equations is called ‘feedback linearizable’ (non-linearity can be cancelled and poles placed at any desired location), however, this leads to a complex-valued current  $I(t)$ , which has no physical meaning in this context. One way to desynchronize is by driving the ‘error’ signal  $(y(t) - y_{\text{desired}}) = (y(t) - \{0 + j0\}) = (\text{Re}\{y(t)\} - 0) + j(\text{Im}\{y(t)\} - 0)$  to zero, and for almost every point in the complex plane, the sum  $\text{Re}\{y(t)\} + \text{Im}\{y(t)\}$  provides a signed ‘corrective’ signal (this real-valued law still leaves a null space where desynchronization is not guaranteed, however, addition of integral control eliminates steady state error, while derivative control improves transient response). Remarkably, regulating just the 1<sup>st</sup> Fourier mode of  $n(\psi, t)$  to zero drives all other (infinitely many) modes of the phase distribution to zero, which is an illustration of Haken’s enslaving principle (at a phase transition and during further evolution, a few order parameters dominate all others (Haken, 1983)). Other optimal control laws desynchronize the network even faster.

In Figure 32.8, we compare the firing density of the network using a biphasic pulse train stimulation (an example of commonly used open-loop control) with typically chosen parameters (Figure 32.8A) versus a proportional closed-loop control law whose sole parameter is a gain (Figure 32.8C), both applied for 1 second between times  $t = 3$  and  $t = 4$ .

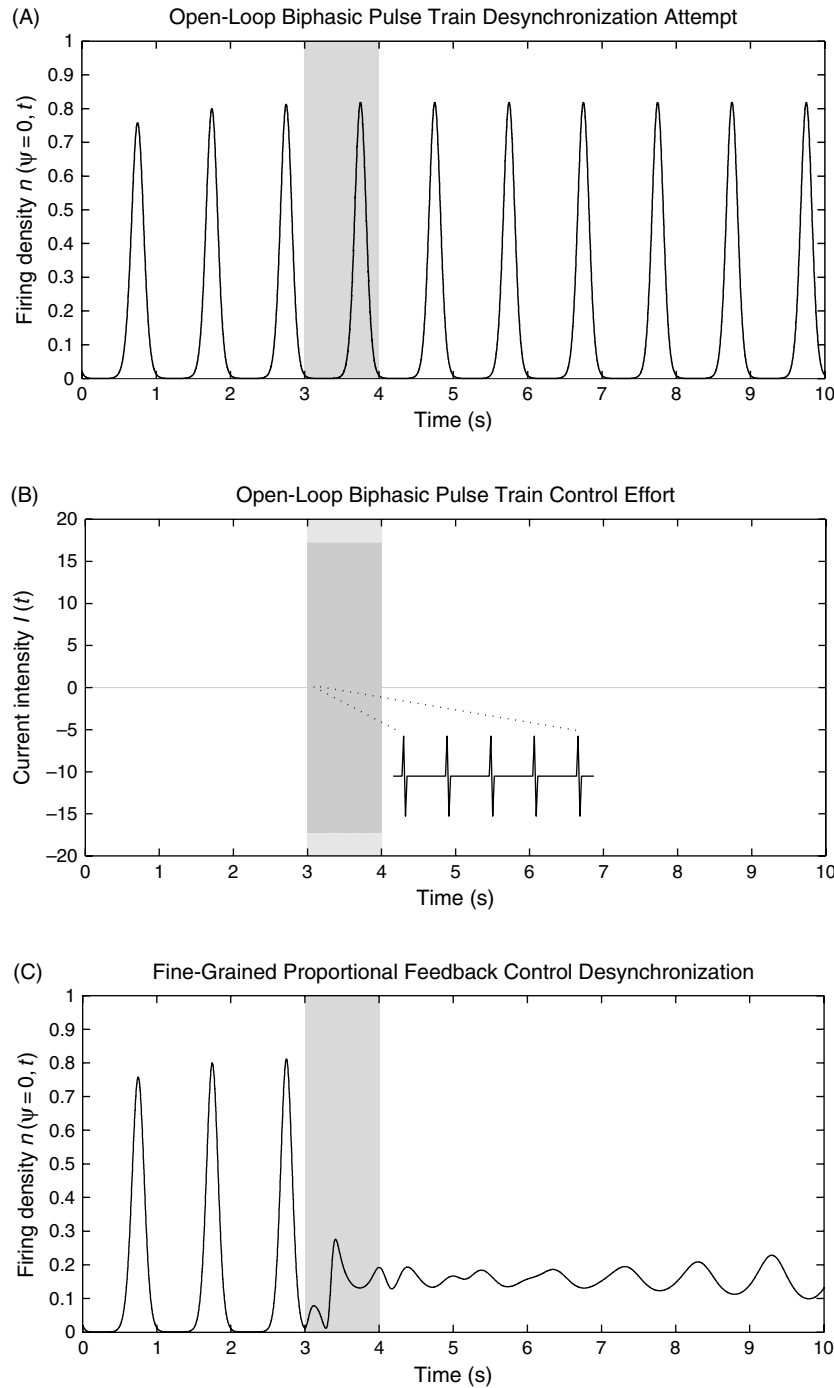


**FIGURE 32.8** (A) Open-loop biphasic pulse train control was applied between times  $t = 3$  and  $t = 4$ . Without the impractical calibration steps, this has no effect on firing density (except by lucky choice of timing, amplitude and duration), which continues to oscillate in its synchronized state. (B) Biphasic pulse train control effort has amplitude 17.15 (to make total energy expended equal to that of the control signal in (D)), 200 Hz frequency and 5% duty cycle per phase. In human trials, the burst duration can be shorter but can be reinitiated several times within the same seizure by automatic seizure detection. (C) Fine-grained closed-loop control was applied between times  $t = 3$  and  $t = 4$ . Firing density approaches its maximally desynchronized state value of  $1/(2\pi = 0.1592$  (uniform distribution of phases). Exact timing is irrelevant in achieving this here. In a few more seconds after stimulation stops, network will spiral back to its synchronized-state limit cycle. (D) Control effort  $I(t) = K_p(\text{Re}\{y(t)\} + \text{Im}\{y(t)\})$ , where  $K_p = 100$  and  $y(t) = 1^{\text{st}}$  Fourier mode of  $n(\psi, t)$  in the phase axis, cannot be any of the prescribed waveforms found in current devices. The time-varying intensity ('shape') is automatically determined from a measure of network state. Furthermore, the gain  $K_p$  is not a critical parameter in achieving desynchronization; for a wide range it only changes undershoot and settling time.

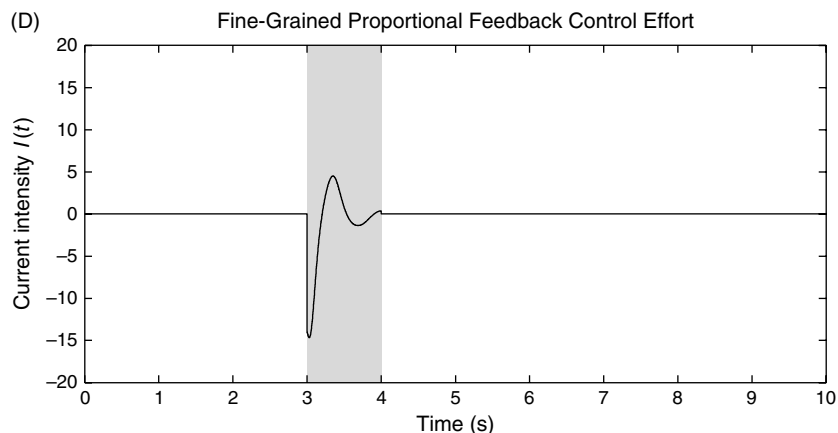


FIGURE 32.8 (Continued)

A key aspect of this method is that the signal being fed back to the controller is a measure of the distribution of phases in the network, not simply the firing density or EEG directly as in prior studies of feedback control (Mogul et al., 2005). Further extensions of this work show that the network can be desynchronized even without knowledge of the internal state variable (1<sup>st</sup> Fourier mode), which is crucial in a practical implementation, by applying delay embedding and extracting modes from a sliding-window FFT, at expense of additional delay in achieving the desired state.

## PRACTICAL APPLICATIONS

### SEIZURE DETECTION

EEG-based seizure detection, performed by human inspection, is a non-trivial pattern recognition task that requires advanced clinical training before adequate competence is achieved. Computational methods can greatly facilitate this task, especially when analyzing long-term EEG records. Detection algorithms are employed in closed-loop, implantable devices designed to deliver stimulation to abort evolving seizures (Echauz et al, 2001). Among other uses, seizure detection algorithms are being deployed in implanted devices for continuous monitoring to provide feedback regarding the efficacy of clinical interventions.

#### Singleton and multiple features

Electroencephalographers use several heuristics to identify seizures, such as rhythmic spiking, spatial spread, sudden change from the background and duration of 1–2 minutes. Nevertheless, the varied electrographic morphologies between seizures renders any single heuristic potentially fallible. For example, a prominent characteristic of a mesial temporal seizure may be rhythmic theta spiking in the temporal lobe, but if a similar pattern occurs during drowsiness with short duration, it is classified instead as wicket spikes. The constellation of multiple electrographic features, over any single feature alone, enables accurate diagnosis.

Current methods of automated seizure detection utilize such combinatoric approaches. Here, various computational features are first extracted from consecutive EEG data epochs with a sliding window paradigm to create feature profiles (Figure 32.9). Analogous to laboratory tests or physical exam maneuvers to identify the signs of a particular disease, each computational feature ideally measures orthogonal, or independent, characteristics of the EEG and has limited ability to distinguish between ictal and interictal segments. If the features are relatively simple, it is unlikely that any single feature will be able to distinguish all ictal data epochs from all interictal data epochs with sensitivities and specificities approaching that of a human expert.

Modern automated seizure detection algorithms typically integrate multiple features by plotting normalized feature values in a multidimensional feature space (Figure 32.10). In this geometric representation, meaningful relationships can be easily visualized and quantitated among the EEG data epochs. Epochs from similar events such as seizures would presumably have similar feature values and lie in close proximity to each other within this space. In this manner, automated seizure

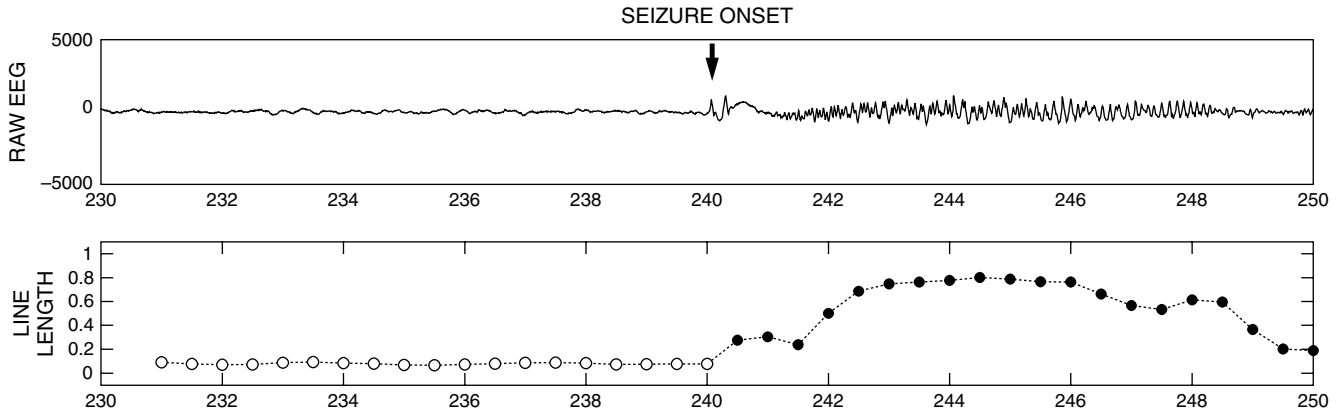


**FIGURE 32.9** The top panel shows a 20-second clip (with the x-axis in seconds) of a seizure onset from a single channel of intracranial EEG. The bottom panel shows its normalized line length feature representation, generated by a sliding window paradigm from consecutive 1-second data epochs overlapping by a half-second. Interictal points are denoted by hollow gray circles, while ictal data epochs are represented by black dots. In these limited data, the line length feature shows good discriminatory value between the interictal and ictal segments.

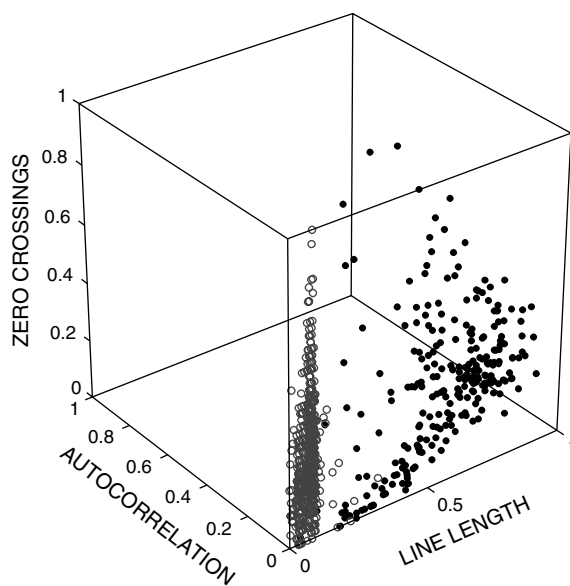


**FIGURE 32.10** Feature profile representations of the seizure seen in previous figure (this time containing 8 minutes worth of points and the entire seizure) have been plotted against each other in a normalized, 3-dimensional feature space. Each 3-D point (line length, autocorrelation and zero crossings) is derived from a single epoch of EEG data. In this geometrical representation, the task for a classifier is to find regions of feature space that separate seizure epochs (black dots) from interictal epochs (hollow gray circles).

detection is reformulated to a problem of identifying seizure and non-seizure regions in a multidimensional space. This task is relegated to computational algorithms generically referred to as classifiers. In statistical and machine learning parlance, the process of learning decision boundaries from labeled training examples is considered a supervised learning problem (Hastie et al., 2003). Once the boundaries between events and non-events in feature space are delineated, classification of future segments of EEG can be performed by plotting their feature values in this space and observing on which side of the boundary they lie.

As we have described it so far, any calculation performed on EEG data can potentially be a feature. However, the utility of a single feature in event detection can be described by its ability to distinguish events from non-events. If the features themselves possess excellent discriminatory power, the classifier's subsequent task can be as simple as finding a hyperplane in the multidimensional feature space. On the other hand, if the features have limited discriminatory power, the burden falls upon the classifier to find more complex boundaries between ictal and interictal segments. For example,

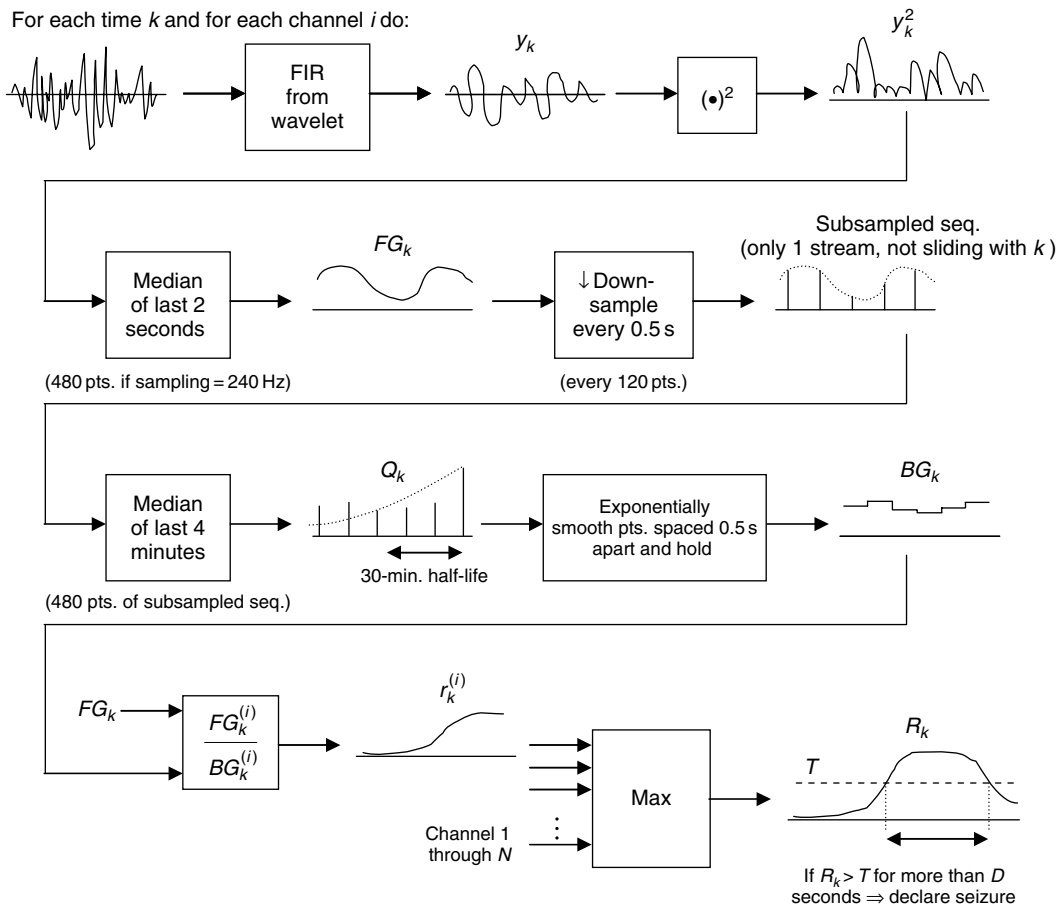


FIGURE 32.11 Block diagram of the Osorio-Frei seizure detection algorithm.

consider the output from a complex feature that has built-in morphology detection (such as the number of repetitive spikes) versus a simple feature whose output is the kurtosis of the histogram of values within a data epoch. In this case, a simple classifier algorithm, such as linear regression (which finds hyperplanes), may perform well if the spike detector feature is included, but fail to produce good results if the kurtosis feature is substituted in its place. On the other hand, a support vector machine or neural network classifier may discover complex non-linear classification boundaries for the second case, producing roughly equal classification performance in both cases despite unequal performance at the single feature level.

EEG features are labeled in the literature as univariate (calculated from only one channel of EEG) or multivariate (calculated from 2 or more channels of EEG, e.g. channel cross-correlation). An example of a successful univariate seizure detection algorithm is the one developed by Osorio and Frei (Osorio et al., 1998), shown in Figure 32.11.

The typical features that have been implemented historically include calculations based on time-frequency representations of EEG, such as Fourier, wavelet and Gabor atomic decompositions. Typical classifier algorithms that have been implemented in the literature include artificial neural networks, support vector machines and  $k$ -nearest neighbors. A whole host of additional classifier algorithms can be adapted to the task, including clustering algorithms, Bayesian networks, boosted decision trees, etc. The makers of Insight, an established seizure detection software, recently published their algorithm with a neural network classifier and Gabor atomic decomposition as features. In addition, statistical calculations (e.g. variance, skewness, kurtosis) and other calculations such as RMS amplitude, zero crossings and line length have been utilized. This multiple feature/classifier framework can be scalable and recursive. For example, the outputs from multiple classifier schemes, over a variety of time scales, can be utilized as the primary input features for a meta-classifier. In this manner, the process of pattern recognition can proceed towards increasingly abstract percepts.

Figure 32.12 shows a typical output from a classification system adapted for seizure detection. In this case, a clustering algorithm was used for classification. The number of centroids was pre-specified and their coordinates were found from the data with the expectation-maximization (EM) algorithm. The centroids were assigned a shade of color. Feature points that

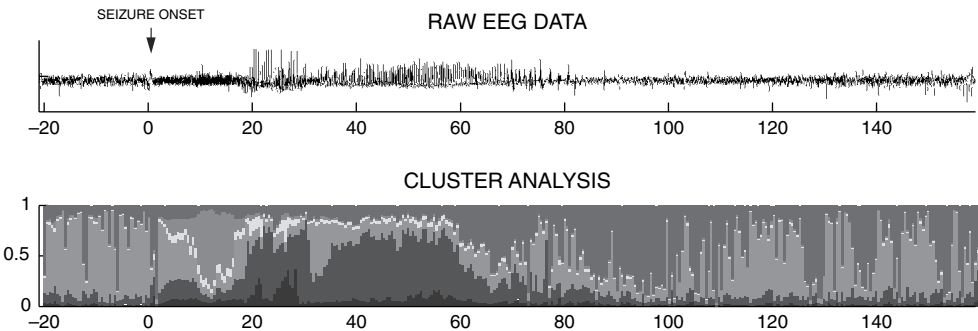


**FIGURE 32.12** Cluster analysis of a hippocampal seizure recorded from an intracranial electrode. The bottom panel shows a normalized measure of the inverse of the distance of a particular EEG data epoch in feature space from centroids found via a clustering algorithm. The six centroids used in this particular analysis are distinguished by different shades. The closer in proximity an EEG data epoch's feature space representation is to a particular centroid, the larger the vertical bar of shade at that time point. The dominant centroid around  $t = 10$  seconds can be used to trigger early seizure occurrence.

reside in close proximity to a particular centroid were assigned a higher probability of belonging to that cluster, reflected by the height of the bar associated with that centroid's shade (bottom panel). A decision rule that could be fashioned for seizure detection in this example is when the probability is maximal for the dominant centroid around  $t = 10$  in the figure.

An important distinction in seizure detection exists between patient-independent and patient-specific detection methods (Shoeb et al., 2004; Wilson, 2004). In the former paradigm, the training examples given to the classifier are comprised of seizures from multiple patients. In the latter, the training examples are obtained from the same patient that subsequent seizure detection is to be performed upon. In general, patient-specific methods are significantly superior to patient-independent methods, despite much lower quantities of training data (Shoeb et al., 2004). This is an intuitive finding because seizures are typically highly stereotyped electrographic events in any particular individual, but much more variable across subjects. The main limitation is that a prior seizure may not be available for training and finding one currently requires verification from a human expert.

### Novelty detection using support vector machines

Support vector machines (SVMs) possess many desirable properties that make them popular in machine learning applications – low-to-moderate computational complexity, a globally optimal training technique, strong theoretical generalization properties and easy interpretability. These are evident in two of the more commonly cited SVM applications: real-time face detection using simple histograms (Osuna et al., 1997) and text categorization using sparse, high-dimensional feature vectors (Joachims et al., 1998). Many of the applications of SVMs to biomedical engineering problems have focused on image processing tasks. Some examples include: classification of blood cells by shape, color and texture features, and medical image segmentation under shape deformation.

The basic idea behind the SVM is to find a hyperplane in a feature space that ‘optimally’ separates two classes. Many other linear learning machines have been considered for this task (e.g. the Perceptron, Fisher’s discriminant, least squares, ridge regression, etc.), but the SVM yields a unique solution that can be shown to yield the tightest upper bound to the expected risk of misclassifying unseen examples (Vapnik, 1999). In other words, SVM attempts to find the best *non-overtrained* classifier assuming that the lowest-capacity classifier is the best generalizer for the problem at hand, which is usually the case in practice (a counterexample is the celebrated 2-D two-spiral data set, where SVM ‘refuses’ to place boundaries along edges of the spirals, despite *that* being in fact the structure of all future data). Training algorithms involve the solution of a well-known optimization problem – constrained quadratic programming – that is computationally efficient and yields global solutions.

Extensions to the basic SVM provide rich, non-linear decision surfaces by first mapping the inputs into a higher-dimensional feature space and performing a linear separation in that feature space. This seems at first counterintuitive because of the ‘curse of dimensionality’: (1) transforming the input data to a higher-dimensional space can be computationally expensive and (2) a sparse representation in a high-dimensional feature space increases the potential for under- and overfitting. The first problem is addressed by the well-known kernel trick (e.g. computing inner product of high-dimensional vectors as inner product of low-dimensional input vectors via kernel such as  $(\langle \mathbf{x}, \mathbf{c} \rangle + 1)^d$ ); the second

by the use of the structural risk minimization (SRM) implicit in the SVM formulation (Cristianini and Shawe-Taylor, 2000). The  $v$ -SVM improves the basic SVM by changing the definition (and hence interpretation) of the penalty parameter for misclassification. Whereas the classic SVM algorithm requires the specification of a non-intuitive misclassification penalty,  $C \in \{0, \infty\}$ , the interpretation of  $v \in \{0, 1\}$  is straightforward: (1) it specifies the expected fraction of misclassified instances and (2) it affects the number of support vectors returned by the algorithm. This allows for precise and intuitive control over classification accuracy and computational complexity.

The solution that Schölkopf et al. arrived at, the 1-class  $v$ -SVM (referred to throughout this section as the 1-class SVM), was inspired by Ben-David's previous work on density estimation in learning and its use for novelty detection was introduced (Schölkopf et al., 1999). An advantage of the novelty detection framework for seizure analysis is that it requires only baseline data for training – no seizure data are necessary for detector training, especially when recordings are artifact-free or artifacts are included in the baseline training set.

We now illustrate application of 1-class SVM to seizure detection. A benchmark 3-dimensional feature vector will be used, consisting of logarithmically-scaled variants of line length, energy, and Teager energy:

$$\begin{aligned} LL'[n] &= \log \left( \frac{1}{N} \sum_{m=n-N+1}^n |x[m] - x[m-1]| \right) \\ E'[n] &= \log \left( \frac{1}{N} \sum_{m=n-N+1}^n x^2[m] \right) \\ TE'[n] &= \log \left( \frac{1}{N} \sum_{m=n-N+1}^n (x^2[m-1] - x[m]x[m-2]) \right) \end{aligned}$$

where  $x[m](m \in \mathbb{Z})$  is a physiological time series and  $N$  is the window length. The default window size is fixed at 1.0 seconds. Window overlap is chosen to be 50% of the window length which corresponds to an overlap time of 0.5 seconds. All features vectors can be normalized to the range  $\{0, 1\}$ .

Two-class approaches assume that both positive and negative examples cluster in specific ways. It is not clear that this is true (consider the question, ‘how many measurably distinct pre-ictal states does the EEG exhibit?’). The two-class approach implies a characteristic time horizon for prediction. For example, when considering ‘preseizure’ versus ‘seizure’ segments, do ‘preseizure’ data begin 1-minute prior to onset? 5-minutes? 20-minutes? Are all seizures preceded by stereotypical precursors beginning precisely 1- or 5- or 20-minutes prior to onset, or is it possible that these precursors are stochastically distributed? Baseline brain electrical activity was regarded as the positive, or *normal*, class. It was hypothesized that feature vectors corresponding to artifact- or seizure-related frames were distributed differently in feature space and that seizure events would be detected as novelties. The data are first mapped into a feature space using an appropriate kernel function and then maximally separated from the origin using a hyperplane. The hyperplane parameters are determined by solving a quadratic programming problem:

$$\min \left( \frac{1}{2} \|\mathbf{w}\|^2 + \frac{1}{vl} \sum_{i=1}^l \xi_i - \rho \right)$$

subject to  $\min(\mathbf{w} \cdot \Phi(x_i)) \geq \rho - \xi_i, i = 1, 2, \dots, l$   $\xi_i \geq 0$ , where  $\mathbf{w}$  and  $\rho$  are hyperplane parameters,  $\Phi$  is the map from the input space to feature space,  $v$  is the asymptotic fraction of outliers (novelties) allowed,  $l$  is the number of training instances and  $\xi$  is a slack variable. Figure 32.13 shows the geometry of the single-class SVM in feature space: hyperplane normal to  $\mathbf{w}$  and  $\xi$  penalizing misclassifications.

The implementation of the 1-class SVM algorithm requires the following model parameter specifications: kernel function, kernel parameters, outlier fraction and separating point in feature space. The kernel function encodes prior information about the problem (e.g. distance or similarity measures). The most common kernel function used is the radial basis function which is described by a single parameter, the kernel width,  $\gamma$ . The outlier fraction should incorporate prior knowledge regarding the frequency of novelty occurrences (i.e. seizing frequency); a nominal value used here is  $v = 0.1$ , indicating that approximately 10% or less of the entire data is estimated to be novel.

A simple sequential hypothesis test can be used to control the rate of false alarms. This test is simply an estimate of the probability that IEEG exhibits novel behavior for a frame. For a sequence of  $N$  observations of the 1-class SVM

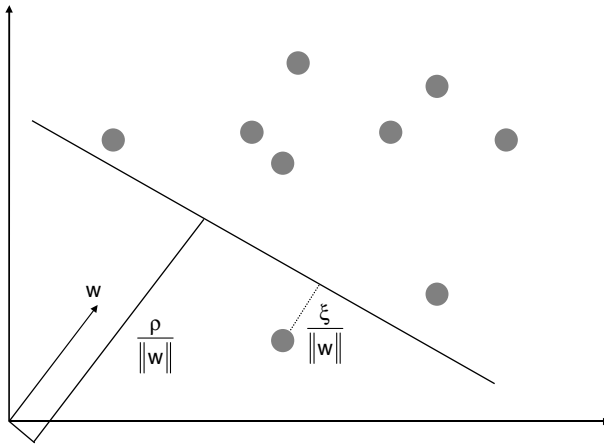


FIGURE 32.13 Geometry of 1-class novelty detection in feature space.

output,  $y \in \{-1, +1\}$ , under the assumption that outputs are identically independently distributed, the maximum likelihood estimate of the probability that a novelty event occurred is given by:

$$\begin{aligned}\hat{p} &= P(\text{novelty} | y_1, y_2, \dots, y_N) \\ &= \frac{N_-}{N} = \frac{1}{2} \left( 1 - \frac{1}{N} \sum_{i=1}^N y[i] \right)\end{aligned}$$

where  $N_-$  is the number of negatives. A decision function for declaring frames as baseline or novelty can be constructed by thresholding:

$$w[k] = \text{sgn} \left( p - \frac{1}{2} \left( 1 - \frac{1}{N} \sum_{i=k-N+1}^k y[i] \right) \right)$$

where  $w\{k\}$  is the  $k$ -th frame label (novelty =  $-1$  or baseline =  $+1$ ),  $y\{i\}$  is the  $i^{\text{th}}$  frame classifier output,  $N$  is the number of classifier outputs considered, and  $p$  is a user-specified threshold. There is a similarity between this formulation of novelty detection and statistical process control (SPC). The basic idea of SPC is that by monitoring a process parameter or statistic with respect to a set of thresholds known as control limits, one can sort out variability due to common causes (considered statistically ‘stable’ or ‘in control’) from variability due to special causes (considered ‘abnormal’). Persistent deviations of the parameter outside of its control limits, for example the count of consecutive violations from one group of frames to the next, signal a developing change in the process and an alarm should be issued.

It has been observed during experiments that the detector tends to generate novelty events (i.e. ‘fire’) in bursts. To improve interpretability, a refractory parameter  $T$  can be used, which introduces a *non-retriggerable one-shot persistence* behavior in the detection output. The refractory parameter specifies an interval during which the detector, if triggered, maintains its state and ignores subsequent triggers.

The default system was validated using leave-one-out cross validation on randomly chosen 15-minute baselines for training and unseen seizure epochs for testing, with respect to four performance metrics: sensitivity, early-detection fraction, mean detection latency and false positive rate (reported per hour). The early-detection fraction (ED) is a measure of the ability of the detector to predict, at least on a short-time basis, an impending seizure onset. It is computed as:

$$ED = \frac{TP|_{\tau<0}}{TP|_{\tau<0} + TP|_{\tau \geq 0}}$$

where  $TP$  is the number of true positives. The Gaussian radial basis function ( $\gamma = 1.0$ ) was selected as the kernel function, the outlier fraction ( $v = 0.1$ ) was chosen to be consistent with the estimated class fraction for the novelty class, the novelty

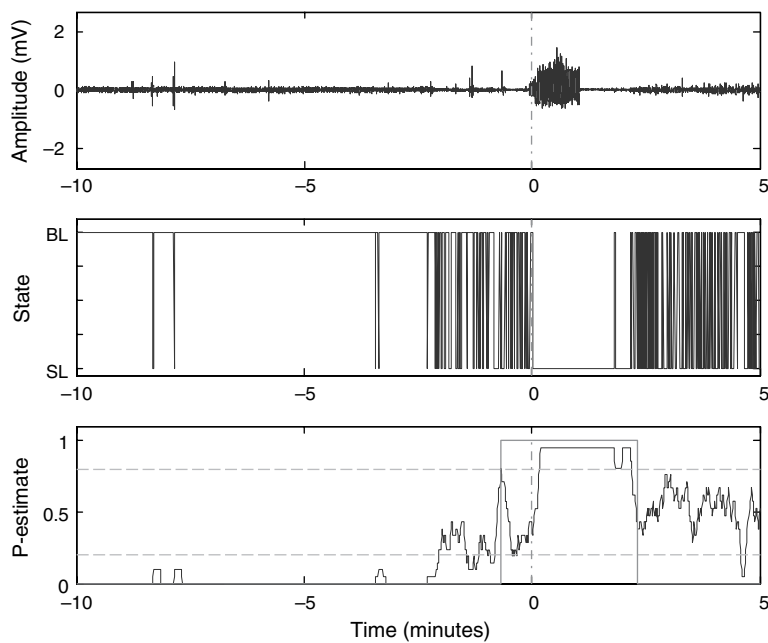


**FIGURE 32.14** An example of an early detection ( $-40\text{ s}$ ). (Top) IEEG signal, (middle) framewise output of the novelty detector,  $z$ , (bottom) probability estimate of being in the novelty state. The indicator function represents the output of the novelty detection system with non-retriggerable one-shot persistence.

detection threshold was set ( $p = 0.8$ ) to produce a low false alarm rate and the number of frames used to estimate  $p$  was fixed ( $N = 20$ ). An example of early detection using the above methodology is shown in Figure 32.14.

For a persistence setting of  $T = 180$  seconds, the static detector achieved 100% sensitivity,  $-7.08$  mean detection latency and 41% early detection fraction at 1.57 FPh. The system as presented has five major parameters of interest:  $\Pi = (\nu, \gamma, p, N, T)$ . These results demonstrated that the novelty detector robustly detects seizures for the default model parameters  $\Pi = (0.1, 1.0, 0.8, 20, 180)$ . Optimal detector model parameters were additionally determined by genetic algorithm (GA) optimization with floating-point chromosome. The best solution found was (0.073, 0.3, 0.59, 38, 192). An online version of this algorithm was also implemented. The 1-class SVM was retrained every epoch on feature vectors derived from the previous epoch using the GA-optimal parameters. The system was evaluated over a net total of 93 seizures spanning 1077 hours of recordings. This simple online adaptation scheme achieved 97.85% sensitivity,  $-13.3\text{ s}$  mean latency and 40% early detection fraction, at 1.74 FPh, thus making it an attractive alternative to state-of-the-art detection and early prediction systems (Gardner, 2004).

## TRACKING PATHOLOGIC ACTIVITY IN EPILEPTIC NETWORKS

### High-frequency epileptiform oscillations

In analyzing electroencephalogram electrodes implanted for presurgical evaluation, investigators have observed normal and abnormal oscillations. The epilepsy literature focuses on abnormal oscillations that are separated by their dominant frequencies and reportedly generated by epileptic networks as pathological activity. Bragin and Engle (Bragin et al., 1999a, 1999b, 2002a,b, 2004) refer to ripples (200 Hz) and fast ripples (500 Hz) from microelectrode recordings; Worrell et al. (2004) identify lower frequency pathological oscillations (60–100 Hz), referred to as high frequency epileptiform oscillations (HFOs) in epileptic patients; and Jirsch et al. (2006) discovered distinct epileptic oscillations localized to areas of seizure onset and spread in depth macro-electrode recordings. These investigations represent converging evidence that link pathological high frequency oscillations (HFOs) within the IEEG to the localization, generation and propagation of epileptic seizures. Furthermore, these findings suggest that HFOs may possess a key role in the generation and spread of epileptic seizures, further our understanding of the dynamics of epilepsy, elucidate the formation of epileptic networks and facilitate the most effective means to disrupt epileptic seizures.

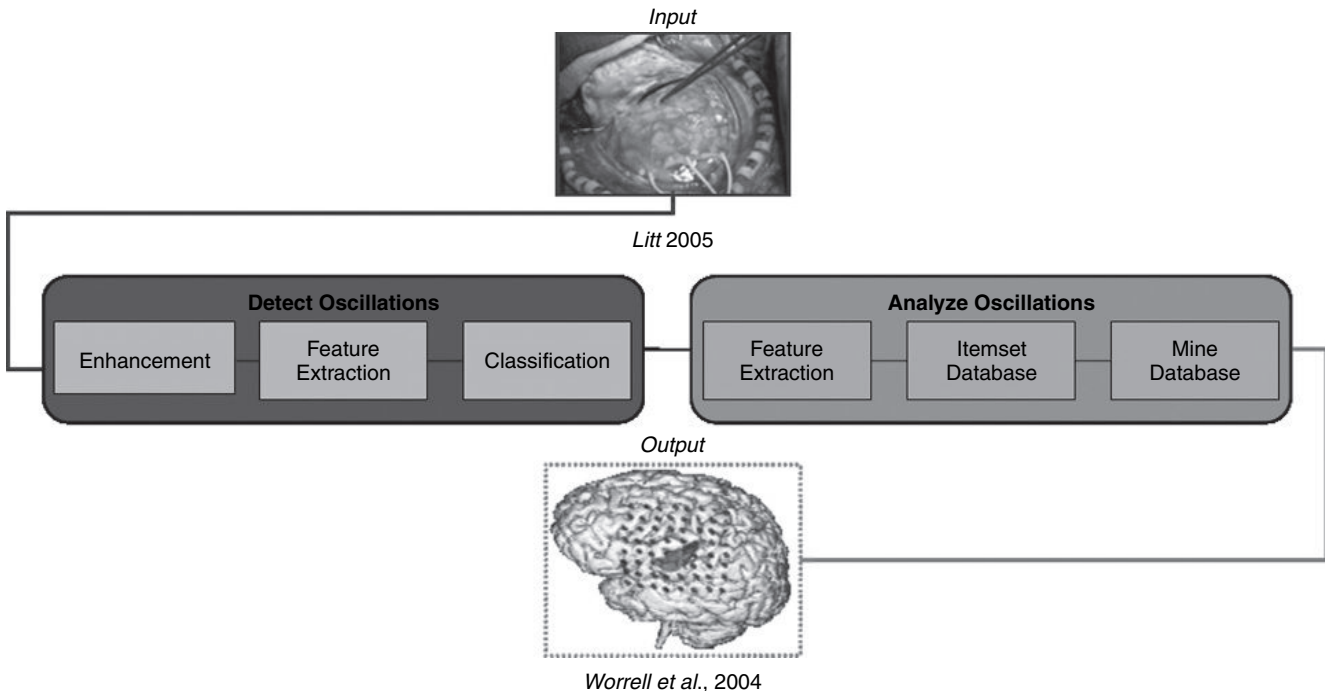


**FIGURE 32.15** The two-stage methodology for mapping epileptic networks based on detecting concentrations of pathological activity, such as HFOs. The key to the stage of detection (left) and analysis (right) is the extraction of features that discern pathological activity from non-pathological activity before a decision is made in detecting moments of time when, and clustering locations where, epileptic oscillations occur.

An important need in the investigation of HFOs is the development of reliable automated algorithms to detect and cluster (or map) pathological activity that is presumably generated by epileptic networks. These algorithms can supply an overall system to track the spatial and temporal evolution of the abnormal electrographic signatures. Designing an automatic detector involves an architecture using the traditional modules of pattern classification: signal enhancement, feature extraction and classification (Duda et al., 2000). Whereas the most appropriate technique for mapping (e.g. self-organized maps, fuzzy clustering) requires further investigation, mining appears to be the most appropriate framework. Figure 32.15 shows a block diagram of one such system we have studied (Smart, 2005).

Although there are no accepted benchmarks for the automatic detection of high-frequency oscillations, most proposed methods extract one (Khalilov et al., 2005; Gardner et al., 2007) or two physics-based features (e.g. short-time line length, short-time energy) for classification. However, the choice of these features is very subjective, primarily relying on the notion that the HFOs are brief sinusoidal fluctuations with additive noise (background) in the electrographic recordings, and ignores projected performance in detection. Nonetheless, these methods show the promise for automatic detection of pathological activity in EEG. On the other hand, evolutionary algorithms (e.g. genetic programming (GP), particle swarm optimization (PSO), grammatical evolution (GE)) offer automated objective techniques for feature selection and combination or altogether deriving a feature. That is, an evolutionary algorithm (EA) can be used to compute an optimal, *artificial feature* for extraction. The feature is optimal in the sense that EA maximizes an objective function which measures the performance of a feature in distinguishing a pathological HFO from non-pathological activity and artificial because the EA returns a computer-crafted result that might not have a physical meaning, as perhaps expected (or desired) by the user of the algorithm. This idea has been successful (Firpi et al., 2007; Smart et al., 2007) in the detection of HFOs and may be improved by exploring alternative evolutionary algorithms. Figure 32.16 conveys the value of using an artificial feature.

Automatically mapping concentrations of pathological activity can be framed as a problem in *frequent itemset mining* (FIM), which is often referred to as data mining. The application complements the detector by processing with features the output of the detector, which is executed across long-duration multielectrode EEG recordings with bursts of pathological HFOs. Essentially, the technique to map the epileptic activity parallels pattern classification where the detector can be

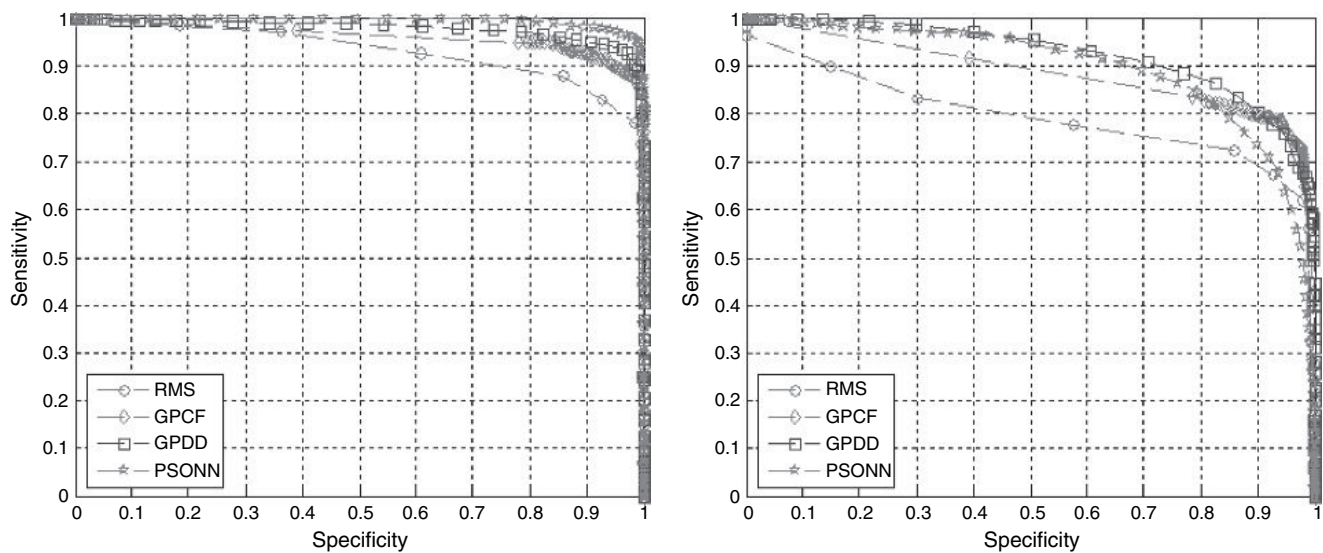


**FIGURE 32.16** Receiver operating characteristic (ROC) curves for a detector of HFEOs based upon three different approaches to compute an artificial feature (squares, diamonds, stars) and an energy feature (circles) in two human subjects. In each of the two cases, the detection of HFEOs is projected to be better with an artificial feature as evinced by the area underneath the ROC curves.

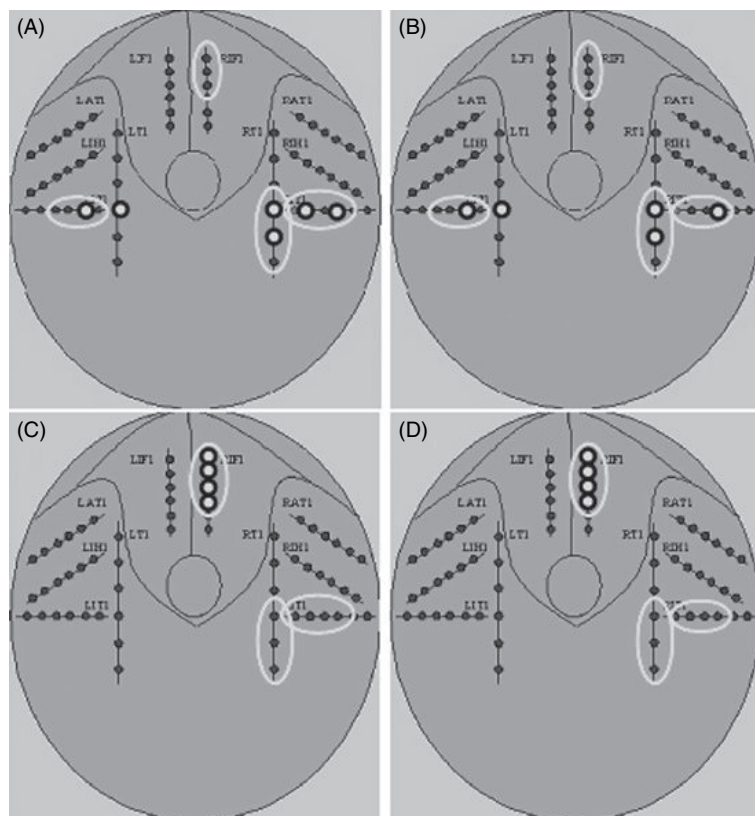


**FIGURE 32.17** Mapping of putative epileptic networks based on frequent concentrations of pathological high frequency oscillations (i.e. HFEOs) in two interictal records for Patients X (A,B) and Y (C,D). It is interesting to observe that HFEOs concentrate (dots) in or near seizure onset zones (ovals).

viewed as a sort of ‘signal enhancement’ stage and feature extraction now discriminates regions, rather than moments of time, of pathologic activity relative to non-pathologic activity. The ultimate aim in applying FIM to the detected HFO events is to discover objectively a pattern (if any) involving the occurrence of a particular HFO (e.g. HFOs, fast ripples, sharp waves) within the recordings. Obviously, to perform this task with statistical rigor and reproducibility is impractical for humans, especially since the duration of the HFOs is on the order of only milliseconds to a few seconds. However, FIM provides a computationally efficient solution for such a difficult problem: finding the most informative grouping of channels from many possible combinations – a total of  $\sum_{n=1}^{n=32} \binom{32}{n} = 4,294,967,295$  in the case of 32 electrodes, of putatively associated electrodes. A few examples of FIM for two epilepsy patients with pathologic HFOs prior to seizure onset are illustrated in Figure 32.17.

By combining the abovementioned techniques in pattern classification and statistical clustering, studying large volumes of data for possible patterns is enabled, however, human participation is not eliminated. Instead, incorporating evolutionary algorithms for detection and frequent itemset mining for clustering EEG electrodes can lead experts to make more effective decisions about localizing epileptic seizures, describing epileptic syndromes and designing therapy for patients with epilepsy.

## APPLICATION TO ANTIEPILEPTIC SEVICES

### Vagus nerve and anterior nucleus of the thalamus stimulation

There are a number of devices, currently in clinical trials, that have the capability to utilize some of the computational approaches detailed above after implantation in individuals with epilepsy. The vagus nerve and anterior thalamic nucleus stimulation (ANTs) devices are two such examples. The vagus nerve stimulator is the first implantable device approved for the treatment of medically refractory epilepsy in humans. It is an ‘open loop’ device, meaning that its outputs are not determined by any particular signal inputs, but rather only to a scheduled duty cycle that is programmed into the device. Clinical trials demonstrate that most patients get a modest reduction in the number of seizures, after the device stimulation has been appropriately titrated, and that less than one patient in ten is rendered seizure-free by the therapy (Fisher et al., 1997). This device consists of an IPG (implantable pulse generator) implanted beneath the collar bone on the left side and a stimulating electrode wrapped around the vagus nerve in the neck. The device stimulates this nerve at programmed intervals, with preprogrammed intensity, duration and frequency. The mechanism of its antiepileptic effects is unknown, though it has been speculated to work through thalamic networks.

The application of computational neurophysiology to this device is the potential to couple it to seizure detection or prediction algorithms, in order to make it responsive to impending seizures or early seizure onset. Interest in doing this is fueled by reports suggesting that seizures can be aborted early when triggering stimulation of the vagus nerve at the time immediately around seizure onset. Patients are supplied with a strong magnet, which they wear on a wrist band, and instructed to hold it over the device when they feel a seizure coming on. This triggers immediate stimulation through the device, which can theoretically stop or prevent a clinical event. While the clinical efficacy of responsive vagus nerve stimulation has not been demonstrated in a controlled clinical trial, to our knowledge, several groups are actively involved developing this ‘closed loop’, or responsive technology to augment the current device.

The anterior thalamic nucleus stimulation device is one that is currently being tested in a pivotal clinical trial in the USA as of this writing. Similar to the vagus nerve stimulator, this device is ‘open-loop’, meaning that stimulation is not based upon any input signals or responsive logic. Stimulation electrodes are implanted bilaterally in the brain in the anterior thalamic nucleus on each side, stereotactically, through a small quarter-inch-sized (6.3 mm) burr hole in each side of the head (Kerrigan et al., 2004). Early attempts at coupling this device to automated seizure detection algorithms have not shown clear efficacy in responsively stopping seizures, though there is interest in perfecting such technology for larger clinical trials that might adequately test this hypothesis (Osorio et al., 2005).

### Responsive and pre-emptive neurostimulation

In *responsive* neurostimulation (Bergey et al., 2002), direct electrical brain stimulation is automatically triggered upon detection of electrographic seizure in order to diminish or arrest aberrant electrical activity and clinical manifestations. When detection sensitivity is increased to a point of hyperdetection, triggering on numerous epileptiform events whether or not they are seizures, this form of therapy becomes a type of *pre-emptive* neurostimulation (Goodman et al., 2005). The latter has been demonstrated to be well tolerated during clinical trials and appears to normalize background EEG

and reduce seizure frequency in some patients (Worrell et al., 2005). Some of the concepts of this chapter, multivariate feature extraction and resampling statistics to assess generalizability of an implied single-threshold classifier, are applied to pre-emptive stimulation versus non-stimulation data obtained during feasibility trials in humans of NeuroPace's external neurostimulation (eRNS) device (Murro et al., 2003; Kossoff et al., 2004).

Spreading seizures often display synchronization across channels. We introduce the mean of absolute correlation coefficients across all pairings of channels as a global measure of gain-independent similarity among waveforms within an electrocorticogram (ECOG). A correlation coefficient for a pair of channels is the normalized sample covariance of the waveforms  $x(t)$  and  $y(t)$ :

$$C_{xy} = \langle(x - m_x)(y - m_y)\rangle / (s_x s_y)$$

where  $m$  and  $s$  are the amplitude mean and standard deviation across the duration of each waveform, and  $\langle \cdot \rangle$  is the mathematical expectation (here, sample mean). Absolute values  $|C_{xy}|$  account for phase reversals in negatively correlated activity. The global correlation (GC) measure

$$GC = \frac{1}{N_{ch}(N_{ch}-1)} \sum_i |C_{xy}^{(i)}|$$

is asymptotically Gaussian for randomly correlated pairs, with mean 0.5 and variance  $1/\{12N_{ch}(N_{ch}-1)\}$  where  $N_{ch}$  is the number of channels.

A total of 9736 electrographic events in 35 eRNS patients were analyzed with respect to the post-event global correlation (2-second ECoG snippet from  $t = +2$  to  $+4$  s where onset = 0), relative to its pre-event counterpart (2-second ECoG snippet from  $t = -2$  to 0 s) and, furthermore, with respect to the class of event: stimulated (STIM) versus non-stimulated (NoSTIM). The definition and timing of these classes of data are shown in Figure 32.18. ‘Event’ was either a stimulation burst ‘leader’ (the first within an episode) or a non-stimulated detection not near a stimulation.

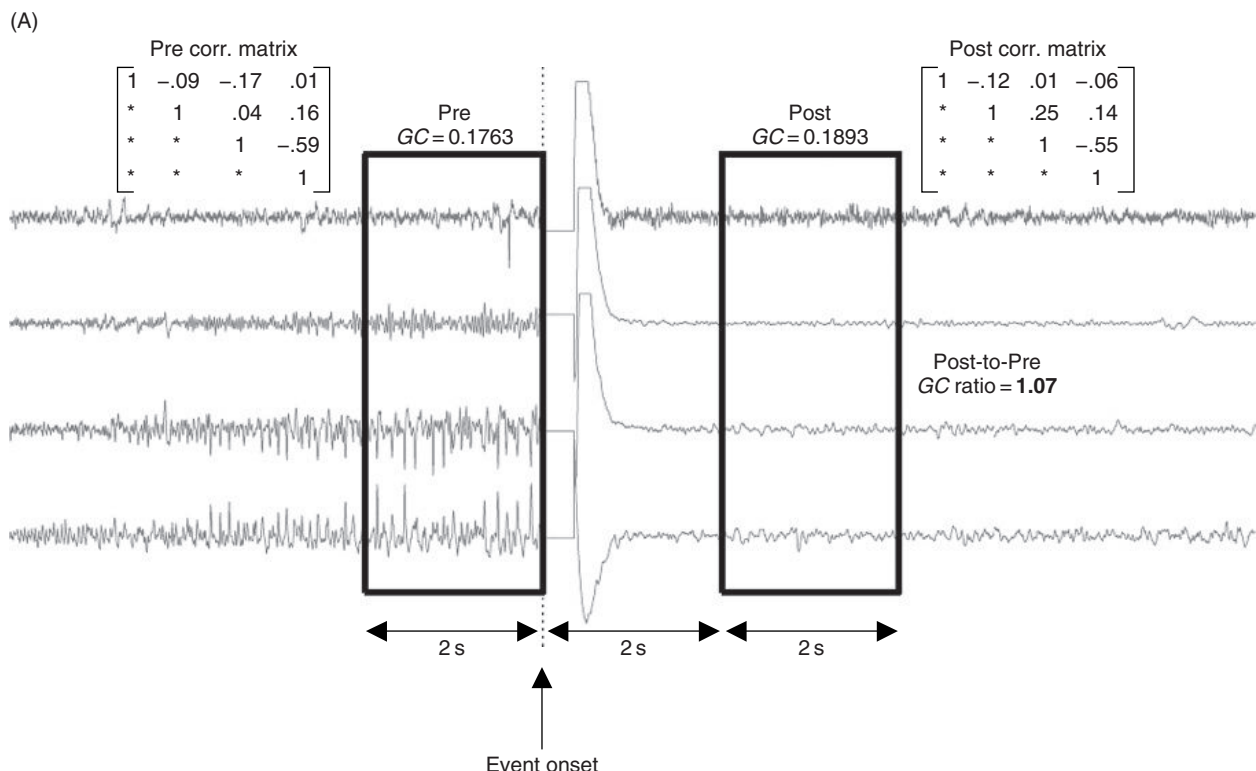


FIGURE 32.18 (A) Stimulated versus (B) non-stimulated event and definition of multivariate GC feature.

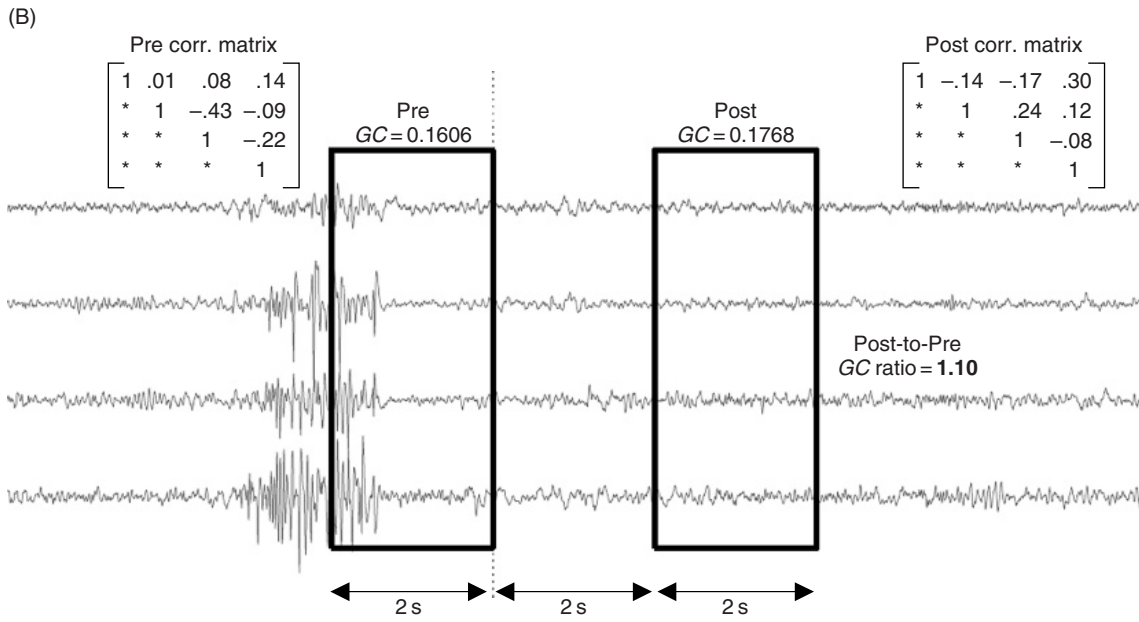


FIGURE 32.18 (Continued)

There were 3461 STIM leader events and 6275 NoSTIM events, all of which had to meet criteria of being 4 seconds or more apart from each other, STIM leaders being 30 seconds or more apart from each other (to eliminate any secondary stimulation disturbance on GC), having the 2-second pre- and post-ECoG segments exactly equal to that required length without missing data points, and ECoGs containing more than one channel (most contained 4 channels) since  $C_{xy}$  has meaning only for at least one pair of waveforms.

Two populations of post-to-pre GC ratios conditioned on event class were obtained for each patient. This grouping of the data provides for a global, channel-pair-independent analysis in which channel pair variation is simply viewed as spatial sampling of brain locations. The GC ratio distributions under STIM versus NoSTIM conditions (2 overlaid PDFs for each patient) were examined, and the mean GC ratio was recorded for each class of each patient. Only 20 out of the 70 mean GC ratios were smaller than 1, however, 14 out of the 20 fractional ratios belonged to the STIM class versus only 6 to the NoSTIM class. Almost 100 000 surrogate data simulations using 4 channels of white noise (random integers from 0 to 1023) of exactly the same lengths as in the analysis (500 time points pre- and post-epochs) revealed that spurious correlations account for a mean GC of 0.0357 and mean GC ratio of 1.11. Forty out of the 70 mean GC ratios were smaller than 1.11, which is not outside expectation, however, 27 of these 40 ratios belonged to the STIM class versus only 13 for the NoSTIM class.

Regardless of post-to-pre GC ratio absolute magnitudes, we investigated whether stimulation decorrelated channels more than non-stimulation. In the majority of cases (28 out of 35 patients), the STIM ratios were smaller than NoSTIM counterparts (that would be 3.5 standard deviations away from 17.5 in a coin flipping experiment). A rigorous permutation significance test was conducted for the difference in grand-mean (across patients) GC ratio under STIM versus NoSTIM. Assuming only exchangeability in the order of observations in a pooled  $k$ -sample problem, the permutation test ( $p$  calculation) is exact and unbiased and is often uniformly most powerful even for small samples, offering advantages over parametric tests including freedom from (often wrong) distributional assumptions (Good, 2000).

The grand-mean GC ratios were 1.0299 under STIM versus 1.1934 under NOSTIM. We ask how rare the experimentally observed difference ( $-0.1635$ ) would be if it happened merely due to chance when the null is true. Under the null hypothesis of no difference between STIM and NoSTIM, the distribution for the grand-mean difference statistic was obtained from 10 000 Monte Carlo repetitions of the calculation, where each time a random shuffling of the class labels is performed on the pooled sample of GC ratios. The critical value at 5% was  $-0.0891$ , so the observation far surpassed 5% significance. The probability of a difference being as negative as  $-0.1635$  or more negative was  $P = 0.0007$ . In conclusion, a significant reduction in global correlation across channels was found for stimulated events compared to non-stimulated ones.

## FUTURE WORK

In the sections above, we have represented a type of computational neuroscience different from traditional modeling, that focuses on practical clinical translation of basic research and solving straightforward clinical problems. While there is significant computational modeling implicit in this work, its core is extracting, classifying and making diagnostic and therapeutic decisions for patients based upon human electrophysiological recordings. Early phases of this work began years ago with an emphasis on detecting seizures from the routine clinical EEG. The focus of this work has changed over recent years and now spans broadband, high fidelity recordings, down to the level of individual cells. These recordings are similar to those that are interpreted by brain-computer interface devices meant to restore function to disabled individuals. Sensors and stimulation electrodes, as well as devices made to deliver other types of local therapy (e.g. infusion catheters, etc.) are already being guided by quantitative analysis and classification of EEG patterns to optimize therapy for individual patients. Focus on mapping the temporal and spatial characteristics of discrete waveforms associated with epileptic networks, such as fast ripples, chirps and high frequency epileptiform oscillations (HFOs) are replacing current focus on mapping interictal spikes and sharp waves on scalp recordings. Algorithms taken from the fields of machine learning and signal processing/communications, as well as hardware innovations from industry, are being focused on new therapeutic strategies to predict, pre-empt and arrest seizures.

Of course, at the core of all of this exciting technology is the patient and collaborating scientists from disparate disciplines, such as neurology, neurosurgery, engineering, mathematics, computer science, and statistics, all dedicated to improving that patient's quality of life through technological innovation. There is now a keen awareness that the focus of our work is to understand the mechanisms underlying epilepsy and seizures and to develop ways to eliminate them. Computational neuroscience, melded with bench and clinical research, has tremendous potential for clinical translation to help individuals with not only epilepsy, but a host of other neurological disorders. Unfortunately, many basic questions relevant to this work are not yet answered, such as the optimal temporal and spatial resolution of clinical recordings to detect and track seizures and the best stimulation strategies and parameters to eliminate them. Still, it is an extremely exciting time to be involved in this field and the potential of this area of research really to help people is very clear.

Future work in this field will likely center on broader band recordings, higher spatial resolution systems, coupled with much broader spatial sampling. There will be better crafted and newer methods of modulating network output, either with electrical stimulation, local application of drugs, cooling or other technologies. It is likely that, in addition to detailed structural atlases of brain anatomy, there will be more detailed functional maps of brain activity and connectivity, perhaps even some form of 'wiring diagrams' that will help target diagnostic and therapeutic investigations. As mechanisms underlying waveforms of interest, such as high frequency oscillations, 'microseizures' and unit ensemble activity in epilepsy are elucidated, it is our hope that this progress should directly translate into better patient care and clinical outcome.

## REFERENCES

- Berger, G., Britton, J., Cascino, G. et al. (2002). Implementation of an external responsive neurostimulator system (eRNS) in patients with intractable epilepsy undergoing intractable seizure monitoring. *Epilepsia* (AES abstract).
- Bragin, A. et al. (1999a). Hippocampal and entorhinal cortex high-frequency oscillations (100–500 Hz) in human epileptic brain and in kainic acid-treated rats with chronic seizures. *Epilepsia* 40(2):127–137.
- Bragin, A. et al. (1999b). High-frequency oscillations in human brain. *Hippocampus* 9(2):137–142.
- Bragin, A. et al. (2002a). Interictal high-frequency oscillations (80–500 Hz) in the human epileptic brain: entorhinal cortex. *Ann Neurol* 52(4):407–415.
- Bragin, A., Mody, I., Wilson, C.L. and Engel, J. Jr (2002b). Local generation of fast ripples in epileptic brain. *J Neurosci* 22(5):2012–2021.
- Bragin, A.W., Almajano, C., Mody, I. And Engel, J. Jr (2004). High frequency oscillations after status epilepticus: epileptogenesis and seizure genesis. *Epilepsia* 45(9):1017–1023.
- Cherkassky, V. and Mulier, F. (1998). Learning from data: concepts, theory, and methods. Wiley, New York.
- Coifman, R.R. and Wickerhauser, M.V. (1992). Entropy-based algorithms for best basis selection. *IEEE Trans Inf Theory* 38(2):713–718.
- Cristianini, N. and Shawe-Taylor, J. (2000). An introduction to support vector machines and other kernel-based learning methods. Cambridge University Press, New York.
- Croisier, A., Esteban, D. and Galand, C. (1976). Perfect channel splitting by use of interpolation/decimation/tree decomposition techniques. In: Proceedings of the International Conference on Information Science Systems, Patras, Greece, August 1976, pp. 443–446.
- Duda, R., Hart, P. and Stork, D. (2000). Pattern classification, 2nd edn. Wiley-Interscience, New York.
- Ebersole, J.S. and Milton, J. (2003). The electroencephalogram (EEG): a measure of neural synchrony. In: Epilepsy as a dynamic disease (J. Milton and P. Jung, eds). Springer Verlag, Berlin.
- Echauz, J., Esteller, R., Tcheng, T. et al. (2001). Long-term validation of detection algorithms suitable for an implantable device. *Epilepsia* 42(7):35–36 (abstract).

- Efron, B. and Tibshirani, R. (1993). An introduction to the bootstrap. CRC Press, Boca Raton.
- Esteller, R. (2000). Detection of seizure onset in epileptic patients from intracranial EEG signals. PhD dissertation, Georgia Institute of Technology.
- Esteller, R., Echauz, J., Tcheng, T., Litt, B. and Pless, B. (2001). Line length: an efficient feature for seizure onset detection. In: Proceedings of 23rd Annual International Conference of the IEEE Engineering in Medicine and Biology Society, Istanbul, Turkey, October. 25–28, 2001. IEEE Press 2:1707–1710.
- Firpi, H., Smart, O. and Vachtsevanos, G. (2007). High frequency oscillations detected in epileptic networks using swarmed neural-network features. Ann Biomed Engin (in press).
- Fisher, R., Ramsay, E., Laxer, K. and Gates, J. (1997). Assessment of vagus nerve stimulation for epilepsy: report of the Therapeutics and Technology Assessment Subcommittee of the American Academy of Neurology. *Neurology* 49(1).
- Gardner, A.B. (2004). A novelty detection approach to seizure analysis from intracranial EEG. PhD dissertation, Georgia Institute of Technology.
- Gardner, A., Krieger, A., Vachtsevanos, G. and Litt, B. (2006). One-class novelty detection for seizure analysis from intracranial EEG. *J Machine Learn Res* 7:1025–1044.
- Gardner, A.B., Worrell, G.A., Marsh, E., Dlugos, D. and Litt, B. (2007). Human and automated detection of high-frequency oscillations in clinical intracranial EEG recordings. *Clin Neurophysiol* 118(5):1134–1143.
- Glorioso, R.M. (1975). Engineering cybernetics. Prentice-Hall, Englewood Cliffs.
- Good, P. (2000). Permutation tests: a practical guide to resampling methods for testing hypotheses, 2nd edn. Springer, Berlin.
- Goodman, J.H., Berger, R.E. and Tcheng, T.K. (2005). Preemptive low-frequency stimulation decreases the incidence of amygdala-kindled seizures. *Epilepsia* 46(1):1–7.
- Guyon, I., Weston, J., Barnhill, S. and Vapnik, V. (2002). Gene selection for cancer classification using support vector machines. *Machine Learn* 46:389–422.
- Haken, H. (1983). Advanced synergetics. Springer, Berlin.
- Hastie, T., Tibshirani, R. and Friedman, J. (2003). The elements of statistical learning. Springer Verlag, New York.
- Hauptmann, C., Popovych, O. and Tass, P. (2005). Effectively desynchronizing deep brain stimulation based on a coordinated delayed feedback stimulation via several sites: a computational study. *Biol Cybernet* 93(6):463–470.
- Jefferys, J. (2003). Models and mechanisms of experimental epilepsies. *Epilepsia* 44(12):44–50.
- Jirsch, J.D., Urrestarazu, E., LeVan, P., Oliver, A., Dubeau, F. and Gotman, J. (2006). High-frequency oscillations during human focal seizure. *Brain* 129(6):1593–1608.
- Joachims, T., Nedellec, C. and Rouveiro, C. (1998). Text categorization with support vector machines: learning with many relevant features. In: Proceedings of Machine Learning: ECML-98 10th European Conference on Machine Learning, Chemnitz, Germany.
- Kay, S. (1998). Fundamentals of statistical signal processing, Vol. II: detection theory. Prentice-Hall, Englewood Cliffs.
- Kerrigan, J., Litt, B., Fisher, R. et al. (2004). Electrical stimulation of the anterior nucleus of the thalamus for the treatment of intractable epilepsy. *Epilepsia* 45(4):346–354.
- Khalilov, I., Le Van Quyen, M., Gozlan, H. and Ben-Ari, Y. (2005). Epileptogenic actions of GABA and fast oscillations in the developing hippocampus. *Neuron* 48:787–796.
- Kircher, J. and Raskin, D. (1988). Human versus computerized evaluations of polygraph data in a laboratory setting. *J Appl Psychol* 73:291–302.
- Kossoff, E.H., Ritzl, E.K., Politsky, J.M. et al. (2004). Effect of an external responsive neurostimulator on seizures and electrographic discharges during subdural electrode monitoring. *Epilepsia* 45(12):1560–1567.
- Larter, R., Worth, R. and Speelman, B. (2000). Nonlinear dynamics in biochemical and biophysical systems: from enzyme kinetics to epilepsy. In: Self-organized biological dynamics and nonlinear control: toward understanding complexity, chaos and emergent function in living systems (J. Waleczek, ed.) p. 51. Cambridge University Press, New York.
- Le Cun, Y., Denker, J.S. and Solla, S.A. (1990). Optimum brain damage. In: Advances in neural information processing systems 2 (D. Touretzky, ed.) pp. 598–605. Morgan Kaufmann.
- Lehnertz, K. and Litt, B. (2005). The first international collaborative workshop on seizure prediction: summary and data description. *Clin Neurophysiol* 116(3):493–505.
- Litt, B., Esteller, R., Echauz, J. et al. (2001). Seizure precursors may begin hours in advance of temporal lobe seizures: a report of five patients. *Neuron* 29 (4):51–64.
- Mallat, S. (1988). PhD dissertation, University of Pennsylvania.
- Mogul, D.J., Li, Y. and Colpan, M.E. (2005). Using electrical stimulation and control feedback to modulate seizure activity in rat hippocampus. *Epilepsia* 46(8):331 (abstract).
- Mormann, F., Andrzejak, R.G., Elger, C.E. and Lehnertz, K. (2007). Seizure prediction: the long and winding road. *Brain* 130(2):314–333.
- Murro, A.M., Park, Y.D., Bergey, G.K. et al. (2004). Multicenter study of acute responsive stimulation in patients with intractable epilepsy. *Epilepsia* (AES abstract).
- Olsen, D., Lesser, R., Harris, J., Webber, R. and Cristion, J. (1994). Automatic detection of seizures using electroencephalographic signals. US Patent 5,311,876.
- Osorio, I., Frei, M.G., Sunderam, S. et al. (2005). Automated seizure abatement in humans using electrical stimulation. *Ann Neurol* 57(2):258–268.
- Osorio, I., Frei, M.G. and Wilkinson, S.B. (1998). Real-time automated detection and quantitative analysis of seizures and short-term prediction of clinical onset. *Epilepsia* Jun 39(6): 615–627.
- Osuna, E., Freund, R. and Girosit, F. (1997). Training support vector machines: an application to face detection. In: Proceedings IEEE Computer Society Conference on Computer Vision and Pattern Recognition, San Juan.
- Ripley, R.D. (1996). Pattern recognition and neural networks. Cambridge University Press, Cambridge.
- Schiff, S.J., Colella, D., Jacyna, G.M. et al. (2000). Brain chirps: spectrographic signatures of epileptic seizures. *Clin Neurophysiol* 111(6):953–958.
- Shoeb, A., Edwards, H., Connolly, J., Bourgeois, B., Treves, S.T. and Guttag, J. (2004). Patient-specific seizure onset detection. *Epilepsy Behav* 5:483–498.

- Schölkopf, B., Platt, J., Shawe-Taylor, J., Smola, A. and Williamson, R. (1999). Estimating the support of a high-dimensional distribution. Microsoft Research, Redmond. MSR-TR-99-87.
- Smart, O.L., Worrell, G.A., Litt, B. and Vachtsevanos, G.J. (2005). Automatic detection of high frequency epileptiform oscillations from the intracranial eeg of patients with neocortical epilepsy. In: Proceedings of 2005 Technical, Professional and Student Development Workshop (TPS), Boulder.
- Smart, O., Firpi, H. and Vachtsevanos, G. (2007). Genetic programming of conventional features to detect seizure precursors. *Engin Appl Artific Intell* (in press).
- Suffczyński, P., Kalitzin, S. and Lopes da Silva, F.H. (2000). A lumped model of thalamic oscillations. In: Proceedings Computational Neuroscience Meeting. Brugge, Belgium.
- Suffczyński, P., Kalitzin, S. and Lopes da Silva, F.H. (2004). Dynamics of non-convulsive epileptic phenomena modeled by a bistable neuronal network. *Neuroscience* 126:467–484.
- Tass, P.A. (1999). Phase resetting in medicine and biology: stochastic modelling and data analysis. Springer-Verlag, Berlin.
- Tass, P.A. (2001). Desynchronizing double-pulse phase resetting and application to deep brain stimulation. *Biol Cybernet* 85:343–354.
- Tass, P.A. (2002). Effective desynchronization with bipolar double-pulse stimulation. *Phys Rev E* 66:036226.
- Tass, P.A. (2003). A model of desynchronizing deep brain stimulation with a demand-controlled coordinated reset of neural subpopulations. *Biol Cybernet* 89:81–88.
- Tass, P.A. and Majtanik, M. (2006). Long-term anti-kindling effects of desynchronizing brain stimulation: a theoretical study. *Biol Cybernet* 94(1):58–66.
- Vapnik, V.N. (1999). The nature of statistical learning theory. Springer Verlag, New York.
- Wendling, F., Bellanger, J.J., Bartolomei, F. and Chauvel, P. (2000). Relevance of nonlinear lumped-parameter models in the analysis of depth-EEG epileptic signals. *Biol Cybernet* 83(4):367–378.
- Wendling, F., Bartolomei, F., Bellanger, J.J. and Chauvel, P. (2002). Epileptic fast activities can be explained by a model of impaired GABAergic dendritic inhibition. *Eur J Neurosci* 15(9):1499–1508.
- Wilson, S.B. (2004). Algorithm architectures for patient dependent seizure detection. *Clin Neurophysiol* 117:1204–1216.
- Wong, S., Gardner, A., Krieger, A. and Litt, B. (2007). A stochastic framework for evaluating seizure prediction algorithms using hidden markov models. *J Neurophysiol* 97(3):2525–2532.
- Worrell, G.A. et al. (2004). High frequency oscillations and seizure generation in neocortical epilepsy. *Brain* 127:1–11.
- Worrell, G., Wharen, R., Goodman, R. et al. (2005). Safety and evidence for efficacy of an implantable responsive neurostimulator (RNS<sup>®</sup>) for the treatment of medically intractable partial onset epilepsy in adults. *Epilepsia* 46(8):226 (abstract).
- Yang, K., Yoon, H. and Shahabi, C. (2005). A supervised feature subset selection technique for multivariate time series. In: Proceedings of Workshop on Feature Selection for Data Mining: Interfacing Machine Learning and Statistics, Newport Beach, April 23, pp. 92–101.

# 33

## MICROELECTRODE-BASED EPILEPSY THERAPY: A HYBRID NEURAL PROSTHESIS INCORPORATING SEIZURE PREDICTION AND INTERVENTION WITH BIOMIMETIC MAINTENANCE OF NORMAL HIPPOCAMPAL FUNCTION

MICHELLE L. STEPHENS, DENNIS D. SPENCER, IDIL CAVUS, MIN-CHI HSIAO,  
DONG SONG, SAM A. DEADWYLER, ROBERT E. HAMPSON, DAVID PUTZ,  
JORGE E. QUINTERO, MERIEM K. BENSALEM-OWEN, KEVIN N. HASCUP,  
ERIN C. RUTHERFORD, B. KEITH DAY, JUSTIN R. NICKELL,  
FRANCOIS POMERLEAU, PETER HUETTL, JASON J. BURMEISTER,  
POOJA M. TALAULIKER, VASILIS Z. MARMARELIS, JOHN J. GRANACKI,  
THEODORE BERGER AND GREG A. GERHARDT

### ABSTRACT

Researchers and clinicians have become intrigued with coupling seizure prediction and local electrical stimulation or pharmacotherapy for treatment of the approximately one million individuals with persistent uncontrolled epilepsy in the USA. Critical for interventions aimed at halting seizure onset are (i) the ability to detect and characterize aberrant neuronal activity indicative of imminent seizure and (ii) the ability to maintain cognitive function normally supported by the brain tissue that must be treated to prevent seizures. A major goal of our research has been the development and refinement of an enzyme-based, mass-fabricated microelectrode array technology that can be implanted into the mammalian central nervous system and utilized for second-by-second assessment of localized glutamate neurotransmission. Based upon our experience, extracellular fluctuations in glutamate do not exhibit the spontaneity and complexity observed in the electrical characteristics of aberrantly firing neurons. We believe predictive modeling based upon chemical neuronal communication may present a very accurate seizure detection system with minimal false-positives and false-negatives currently complicating electroencephalography (EEG)-based seizure prediction. Though a prediction and local intervention therapeutic paradigm could offer a dramatic improvement in treatment of refractory seizures, we propose that achieving the ultimate goal of enhancing the daily functioning of these patients necessitates consideration of consequences experienced by the patient when hippocampal circuitry is ‘shut-down’ to thwart seizure onset. Therapeutic termination of seizure activity may produce memory-loss and other gross impairments of information processing in the brain; therefore, the second goal of our research stated above is the development of a hippocampal prosthesis to ‘patch’ therapeutically impaired hippocampal circuitry. Our prosthetic technology utilizes non-linear modeling to generate outputs characteristic of the normal functioning of the epileptic hippocampal circuit (i.e. when that circuit is not epileptiform) during the time when that circuit must be ‘shut down’ to suppress seizure. The outputs are computed from afferent neuronal input recorded from an indwelling microelectrode array ‘upstream’ from the impaired hippocampal tissue so as to bypass the malfunctioning portion of the hippocampus. The present chapter documents our current capabilities of measuring glutamate in rodents, primates

and humans with *in vivo* amperometry and our progress with a hippocampal prosthesis, as we work toward development of a ‘closed-loop’ system for seizure prediction and termination with maintenance of normal hippocampal function.

## INTRODUCTION

The hallmark of epilepsy is repeated unprovoked seizures characterized by abnormal synchronous discharge of cortical neurons (reviewed by Shin and McNamara, 1994). Epilepsy can develop from a variety of etiologies including traumatic, hypoxic, infectious and genetic origins, but demonstrates an affinity for certain brain regions, especially the hippocampus and neocortex (reviewed by Duncan et al., 2006). The spectrum of seizure symptomatology ranges from simple alterations in consciousness or sensation, to full loss of consciousness and posture (Shin and McNamara, 1994). This disorder affects approximately 3 million people in the USA (source: Epilepsy Foundation, [www.epilepsyfoundation.org](http://www.epilepsyfoundation.org)) and is considered to be the most prevalent neurological disease worldwide with an estimated 50 million individuals affected (source: World Health Organization, [www.who.int/en/](http://www.who.int/en/)). Though approximately two-thirds of all epilepsies are manageable with medication, one-third remain intractable and require alternative treatments (Leppik, 1992; Loscher, 1997). A fairly successful option for these patients is resection surgery if the seizure focus is localized and contained within a relatively expendable brain region. Seizures can originate from multiple brain regions, however, and from functionally critical areas, excluding the possibility of resection (reviewed by Nilsen and Cock, 2004).

Over the past 60 years, researchers and clinicians have become intrigued with the idea of local treatments as promising therapies for patients with uncontrolled epilepsy. Currently, seizure duration is being beneficially modified with local electrical stimulation or drug application in experimental settings (Stein et al., 2000; Richardson et al., 2003; Nilsen and Cock, 2004; Fountas et al., 2005; Morrell, 2006). As pointed out in a review by Litt and Lehnertz (2002), the notion of a pre-seizure state is catalyzing clinical and basic science researchers to pursue detection of an eminent seizure via computational prediction, and couple this recognition to local electrical or chemical intervention to halt seizure onset altogether. Litt and Lehnertz (2002) describe three pressing milestones necessary for clinical application of seizure prediction:

1. identification of seizure precursors and elucidation of underlying mechanisms
2. implementation of algorithms based upon the above information to govern implantable devices for seizure detection and abortion
3. demonstration of seizure prediction from prolonged human data sets.

Seizure prediction has become a classic multidisciplinary undertaking. Computational modeling of neuronal electrical activity has been utilized to explore the pathogenesis of ongoing seizure propagation, as well as to investigate the effects of different interventions on neuronal firing (Traub et al., 1987; Lopes da Silva et al., 1994; Lytton et al., 1997; Giannakopoulos et al., 2001; Wendling et al., 2002; Jefferys, 2003; among others). In 2005, Liley and Bojak put forth that the difficulty central to modeling epileptogenesis is not creation of computed output (cellular activity) characteristic of ongoing seizure, but rather production of this output in response to specific inputs, further complicated with the assumption these inputs actually represent ‘real’ and quantifiable physiological abnormalities indicative of impending seizure. Electroencephalography is the current gold standard method of seizure detection and focus localization. An electroencephalogram (EEG) measures neuronal electrical activity. Engineers in the 1950s through 1970s hypothesized that characteristic changes in the EEG could be used to recognize pre-ictal neuronal activity indicative of an impending seizure, but success has been slow coming and limited (Stein et al., 2000; Iasemidis et al., 2005; see Litt and Lehnertz for review, 2002). Contributing to the difficulties with EEG-based prediction are low spatial resolution and sensitivity to noise (e.g. patient movement). Therefore, development of sophisticated instrumentation and computational algorithms capable of accurately detecting abnormal activity and synchronization from background and noise artifacts (presumably unique for each patient) is necessary before EEG is utilized in a chronic seizure prediction and intervention therapeutic paradigm. Based upon microdialysis studies in patients with recurrent seizures that show increases in extracellular glutamate and other neurotransmitters during the several minutes preceding a seizure (During and Spencer, 1993; Cavus et al., 2005), we believe characteristic real-time changes in extracellular glutamate concentration compared to resting or normal levels may offer an alternative to neuronal firing for effective modeling of impending temporal lobe seizure, yielding more accurate prediction (though see Iatrou et al., 1999a, 1999b). We continue to improve upon the longevity of our glutamate-sensitive microelectrode arrays (currently two weeks) and are developing other necessary system components (human recoding system, power supply, etc.; see Sun et al., 2006; Sclabassi et al., 2006) to make this technology amenable to use in humans, as we move toward a chronic indwelling device for seizure prediction and intervention.

Studying the rapid chemical communication among neurons will offer a novel way to examine and model both the physiological changes preceding seizure, as well as mechanistically important ictal and post-ictal changes. Though more accurate prediction and subsequent local intervention could offer a dramatic improvement in treatment of previously uncontrolled seizures, we propose achieving the ultimate goal of improvement in the daily functioning of these patients necessitates expansion of the seizure prediction goals put forth by Litt and Lehnertz (2002).

Preliminary reports are showing that pharmacological or electrical ‘shut-down’ of the hippocampal circuitry can be effective for seizure prevention and termination when coupled to predictive methodology (Stein et al., 2000; Fountas et al., 2005; reviewed by Nilsen and Cock, 2004); however, this ‘down-time’ could leave a patient with information processing and memory dysfunction – still allowing temporal lobe epilepsy to compromise a patient’s day-to-day functionality. Herein we describe incorporation of a hippocampal prosthetic into developing prediction and intervention protocols, which will allow for maintenance of normal hippocampal communication through the trisynaptic circuit during therapeutic ‘down-time’. The hippocampal prosthetic will function to process information from afferent inputs to the inhibited neurons, compute output characteristic of the ‘downstream’ circuitry and route this output to efferent targets of the inhibited neurons. Though we plan to base our prediction models on chemical neuronal communication, electrical communication remains key for incorporation of a hippocampal prosthesis, our addition to the prevention and intervention prototype for continued improvement of overall patient outcome. Therapy comprised of prediction, intervention and prosthetic maintenance of normal hippocampal trisynaptic circuitry could greatly diminish the disruption of a patient’s life from treatment of intractable seizures (Figure 33.1).

A major goal of our research has been the development of technology for second-by-second measurements of neurotransmitter concentrations in the extracellular space of the brain. Our laboratory has worked to refine a mass-fabricated microelectrode array (MEA, Figure 33.2) technology that can be implanted into the mammalian central nervous system and utilized for electrochemical assessment of localized neurotransmission (Burmeister et al., 2000, 2002; Burmeister and Gerhardt, 2001; Pomerleau et al. 2003). Based on our experience, extracellular fluctuations in glutamate do not exhibit the spontaneity and complexity observed in the electrical characteristics of aberrantly firing neurons. This is supportive of the idea that computational modeling based upon chemical neuronal communication may present a very accurate seizure detection system with minimal false-positives and false-negatives currently complicating EEG-based seizure prediction. Another primary goal has been the development of a hippocampal prosthesis to ‘patch’ impaired trisynaptic circuitry,

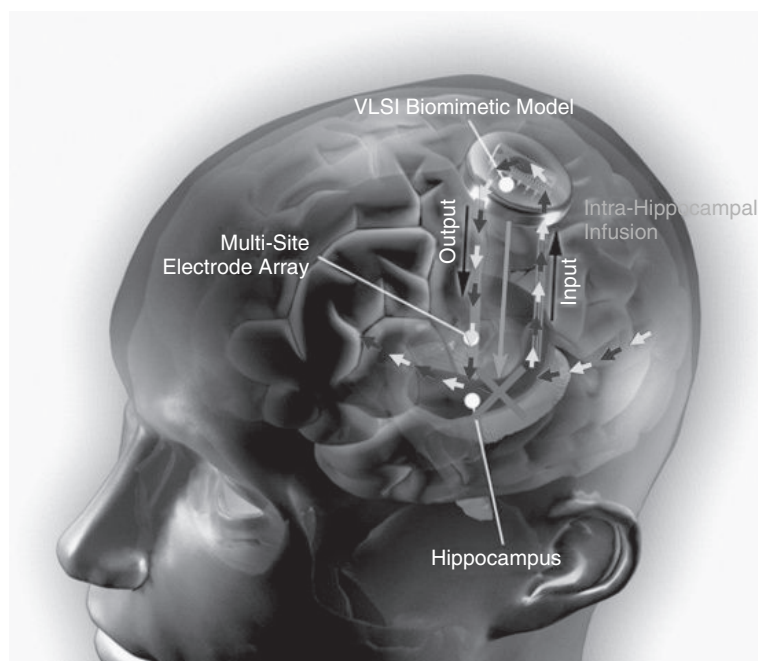


**FIGURE 33.1** Diagram illustrating proposed indwelling ‘closed-loop’ system for (i) detection of impending seizure with glutamate-sensitive microelectrode array, (ii) termination of seizure onset via local drug application to inhibit synaptic glutamate transmission, and (iii) maintenance of hippocampal mnemonic function through a biomimetic device that provides a means for ‘by-passing’ that portion of hippocampal circuitry (e.g. CA3) rendered inactive by the infusion of anti-epileptiform agents. (See Plate 26 in color plate section.)

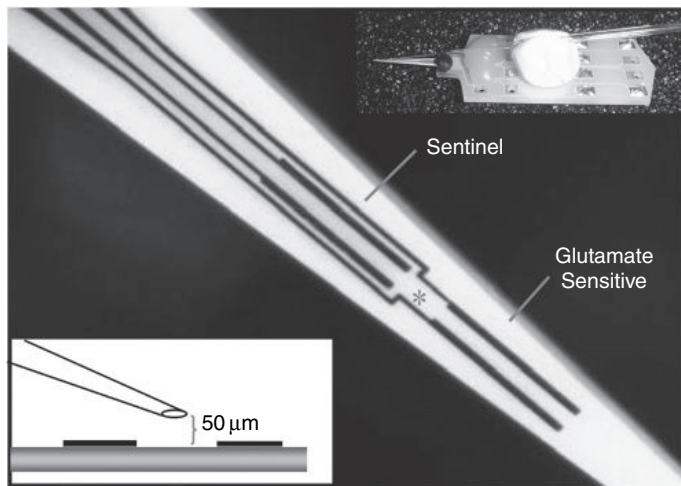


**FIGURE 33.2** S2 Glutamate-sensitive MEA. Glutamate-sensitive sites indicate Pt recording pair with glutamate oxidase enzyme coating for glutamate detection. Sentinel sites indicate Pt recording pair with inactive protein matrix. Pairs offer system redundancy for maximum utilization of each MEA. Lower left inset: diagram showing lateral view of ceramic MEA base with optimal pipette placement for local application of solutions. Upper right inset: ceramic MEA with affixed pipette for *in vivo* recordings in anesthetized animals or brain slices.

utilizing non-linear modeling to compute output characteristic of the impaired portion of the circuit from afferent input to the indwelling biomimetic microelectrode array. The present chapter documents our current capabilities of measuring glutamate in rodents, primates and humans with *in vivo* amperometry using enzyme-based ceramic MEAs and our progress with a hippocampal prosthesis as we work toward development of a ‘closed-loop’ system for seizure prediction and control to maintain normal hippocampal function.

#### PRINCIPLES OF *IN VIVO* ELECTROCHEMISTRY

The recording surface or ‘working-electrode’ of a microelectrode array (MEA) is usually an inert metal such as platinum (Pt), which can oxidize or reduce compounds of interest when a potential is applied to it versus a reference electrode (usually Ag/AgCl) in ionic contact with the MEA. Computer-controlled low noise ‘patch clamp-like’ potentiostats with custom multiple-input recording software allow us simultaneously to measure from several microelectrodes or several recording surfaces on a single MEA. Applying a constant fixed potential to the microelectrode, known as amperometry, is one of the most straightforward electrochemical techniques. If the potential is sufficient, a molecule at the working electrode may donate electrons (oxidize) or accept electrons (reduce), both Faradaic chemical reactions that generate current linear with respect to the concentration of electroactive molecules that touch the recording site. Our experimental protocol conveniently allows for *in vitro* calibration for *in vivo* recordings based upon this principle. Amperometry minimizes non-Faradaic background current measured by the microelectrode, offering highly sensitive measurements of electrochemically active molecules. This technique also allows for rapid sampling rates (ms to s), providing us a means to monitor fast neurochemistry of the extracellular space in real-time.

Several neurochemicals of interest in the extracellular space are electrochemically active at a Pt working electrode including dopamine, norepinephrine, serotonin, nitric oxide, uric acid and 3,4-dihydroxyphenylacetic acid (DOPAC). Most of these molecules can be easily shielded from the Pt site by applying selective coatings to the MEA recording surfaces. To expand the repertoire of measurable molecules, we also coat the recording sites with a variety of oxidase enzymes to convert electrochemically inactive molecules to ‘reporter’ hydrogen peroxide molecules. Applying a potential of +0.7 V versus an Ag/AgCl reference is sufficient to oxidize hydrogen peroxide at the Pt site. Current created by liberation of electrons during the oxidation of hydrogen peroxide is linear with respect to local concentration of the original enzymatic substrate (Figure 33.3). We have amassed a great deal of experience with the glutamate oxidase (GluOX)-coated MEAs developed by our laboratory and highlighted for review in this chapter (Burmeister et al., 2000, 2002; Burmeister and Gerhardt, 2001; Pomerleau et al., 2003; Day et al., 2006), but we have also had success with choline oxidase and acetylcholine oxidase (Bruno et al., 2006), L-lactate oxidase (Burmeister et al., 2005) and L-glucose oxidase (Burmeister and Gerhardt, 2001).

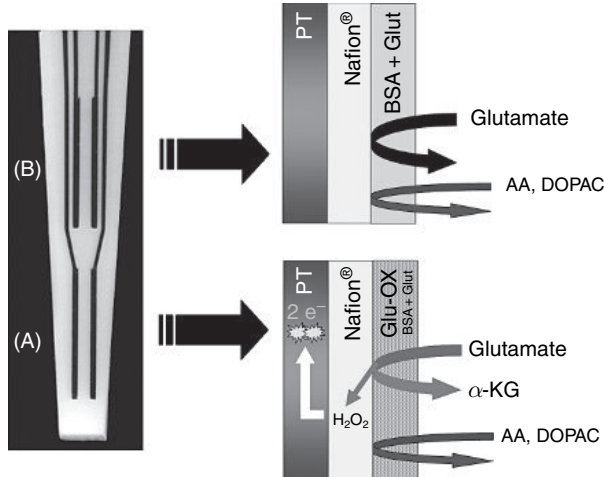


**FIGURE 33.3** S2 MEA image with illustrations showing Nafion® exclusion layer, bovine serum albumin-glutaraldehyde inactive protein matrix (BSA-Glut) and glutamate-oxidase (Glu-OX) active enzyme coatings. (A) Pt sites coated for glutamate detection. (B) Pt sites coated with inactive protein for self-referencing. Subtraction of signal collected with 'B' sites from signal obtained with 'A' sites yields glutamate measurement free of interferences. Amperometry performed at Pt electrodes using an applied potential of +0.7 V versus Ag/AgCl reference electrode, sufficient to oxidize hydrogen peroxide 'reporter molecule' and produce current, is linear with respect to local glutamate concentration. Potential applied and data collected with FAST-16 recording system (Quanteon L.L.C., Lexington, KY).

These enzymes provide us a mechanism to measure rapid kinetics of other neurotransmitters/neurochemicals identified to precede seizure (During and Spencer, 1993; Cavus et al., 2005).

#### ENZYME-BASED MULTISITE MICROELECTRODE ARRAYS

##### FABRICATION

Our MEAs are constructed in conjunction with Thin Films Technology, Inc. (Buellton, CA). The multisite MEAs are mass fabricated using photolithographic methods, as this technique routinely produces recording surfaces microns in size, greatly improving the spatial resolution as compared to microdialysis. Details of the fabrication process are outlined in Burmeister et al. (2001). Briefly, photolithography helps decrease overall production costs as multiple MEAs can be fabricated with minimal starting material waste. Cost is an ever-present concern for research instrumentation as well as clinical diagnostic and treatment technologies. We currently pattern our Pt recording arrays onto a ceramic substrate (Coors Superstrate 996 (alumina, Al<sub>2</sub>O<sub>3</sub>) Coors Ceramics, Golden, CO), which provides a strong, non-flexible base for precise stereotaxic placement, minimizes cross-talk noise between Pt recording sites, can be polished to achieve MEAs as thin as 37.5 μm and has demonstrated excellent biocompatibility in chronic implants, showing very little microglia activation or scarring as far out as six months (for histology and immunostaining see Hascup et al., 2007). Compared to a microdialysis probe, we believe our MEAs exhibit a superior ability better to maintain innate tissue integrity for more accurate sampling of the neuronal microenvironments. Extensive research and development of the MEA fabrication and cleaning processes have produced very deliberate protocols for the construction of durable and reusable MEAs, the details of which are beyond the scope of this chapter. For more information see Hascup et al. (2007).

The flexibility of Pt recording site arrangement allows for a variety of configurations, specifically manipulations of site layout for simultaneous localization in anatomically distinct brain subregions (i.e. conformal MEA). This has produced MEA configurations designed to access the CA1 and CA3 subregions of the rat hippocampus for simultaneous, locally self-referenced glutamate recordings (Figure 33.4).

Currently, our most utilized MEA design is the glutamate-sensitive S2, which has four Pt recording pads, each 15 × 333 μm (see Figure 33.2). The S2 sites are arranged in two pairs, stacked in a dorsal-ventral orientation with 100 μm spacing between pairs, and 30 μm spacing between sites within each pair. The intention of this design is selectively to configure one recording pair with glutamate oxidase for glutamate detection and the other pair with non-active protein for self-referenced comparison. As described above, enzymes provide novel means to convert a molecule like glutamate,

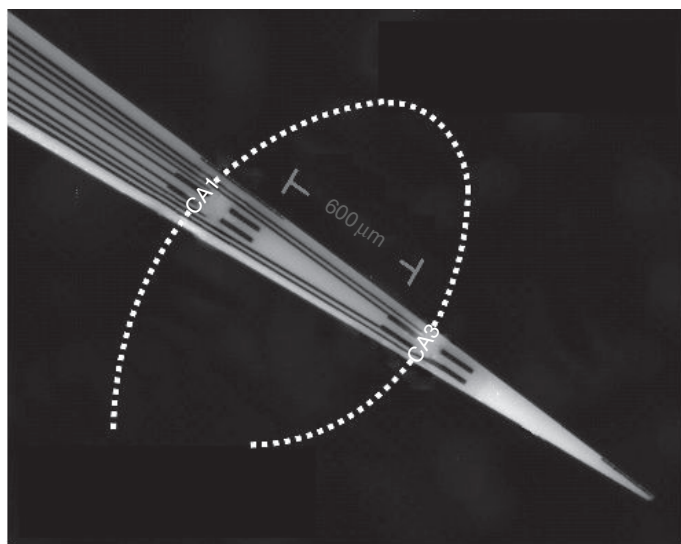


**FIGURE 33.4** Conformal MEA (W2) designed for simultaneous placement of Pt pairs for self-referenced glutamate measurements in CA1 and CA3 hippocampal subregions of the rat brain. Electrophysiology, electrochemistry, electrical stimulation or some combination thereof can be discretely performed at individual Pt sites. MEA placement in the left hippocampus of a rodent is shown.

not electroactive and therefore not measurable with voltammetry, into a reporter molecule such as peroxide that is active at the Pt recording surfaces of a microelectrode. The current measured from the oxidation of peroxide generated during the enzymatic metabolism of glutamate is directly proportional to the local concentration of glutamate which contacts the enzyme surface of the MEA. Currently, we use manual coating procedures for enzyme and non-active protein layer application, but automation will be a critical step in standardization of MEA construction for clinical utility.

We regularly utilize a layer of Nafion®, an anionic Teflon® derivative, to repel anions like ascorbic acid and DOPAC from Pt recording sites where they will be active (Gerhardt and Hoffman, 2001). If these molecules are not blocked, they cause high background signals from ascorbic acid (vitamin C) and metabolites of some neurotransmitters that interfere with reliable recordings of glutamate. Nafion® is the exclusion layer of choice for all chronic implants in freely-moving animals in our laboratory due to its biocompatibility and longevity. The breadth of experience with Nafion®, and its safety, make this exclusion layer the ideal choice for human MEA protocols as well.

As we enter into our next phase of MEA technology involving development of probes for human recordings, we continue investigating the structural integrity of the enzyme and inactive-protein coatings, as well as the robustness of enzyme activity following sterilization. Preliminary results with electron-beam sterilization are very promising. Longevity of MEA performance in chronic implants is a parameter we are currently working to characterize in mice, rats and non-human primates. Most promising about our human probe development is the continued use of the same ceramic MEA we have already amassed a great deal of experience with in rodents and non-human primates (Pomerleau et al., 2003; Nickell et al., 2005, 2006; Day et al., 2006; Quintero et al., 2007). Manipulation of the MEA construction for human use encompasses a design change only in the physical connections of the MEA to the final design of the indwelling electrode and our FAST-16 recording system (Quanteon, L.L.C., Lexington, KY). We have proven functionality and usefulness of our glutamate-sensitive MEA in investigations of the mammalian CNS and moving this technology into the human arena will expedite our progression to patient-based basic science investigation and ultimately clinical use.

#### POTENTIOSTAT/RECORDING SYSTEM

A headstage/potentiostat creates a difference in potential between the MEA and a reference electrode to produce chemical reactions at the Pt recording sites and measures the currents created by these reactions. For our electrochemical recordings, we use the Fast Analytical Sensing Technology (FAST-16/Mark II) system (Quanteon L.L.C., Nicholasville, KY) (see Hascup et al., 2007 for specifications of most current FAST system). Near real-time recording can be obtained from up to eight Pt recording sites simultaneously. FAST-16 files are exported to other Windows™ based applications, such as Excel™, for analysis. This analysis can also be performed directly with software included in the FAST-16 data acquisition

system. An intrinsic design element of our *in vivo* experimental setup is a requirement that the preparation not be grounded (i.e. ‘floating’). This has not hindered acquisition of data from either anesthetized or awake-behaving animal preparations, including non-human primates (our closest approximation to human recordings), but may force circuit reconfiguration for situations when patients must be grounded. Certain instrumentation important to seizure monitoring, like EEG, require grounding, in addition to unavoidable grounding that occurs through activities of daily living, important to chronic MEA therapeutic preparations.

## CALIBRATIONS

Due to subtle inconsistencies in Pt deposition during lithography and differences in thickness of each applied enzyme, inactive protein, or exclusion layer, individual Pt recording sites on microelectrodes can respond differently to peroxide. This necessitates selection and calibration of MEAs prior to experimentation to generate standard response curves for known concentrations of analyte (i.e. enzyme substrate). Calibrations are used to equate a change in current from the oxidation of peroxide with a proportional change in analyte concentration (Burmeister and Gerhardt, 2001). The linearity of the glutamate-sensitive MEA response with increasing concentrations of analyte allows for *in vitro* calibrations performed at 37°C for *in vivo* measurements. Known interferents, such as ascorbic acid, are added during the calibration to test selectivity of the recording sites for glutamate versus interferents (see Figure 33.5). When an experiment is being performed, the MEA calibration data (collected immediately prior to experimental use) are recalled and used to determine the local glutamate concentration from current measured *in vivo*. Parameters of MEA functionality automatically calculated by the FAST-16 include *slope* of the standard calibration curve, *limit of glutamate detection* (LOD,  $\mu\text{M}$ ), *selectivity ratio* and *linearity of the standard curve* ( $R^2$ ).

Slope, or sensitivity of the microelectrode site, refers to how well it can measure a change in glutamate, and is used to calculate the LOD or the minimum concentration of glutamate to which the site will respond. The LOD (signal-to-noise of 3) for our microelectrodes ranges from 0.2 to 1.0  $\mu\text{M}$ . This assures our ability to measure physiologically relevant concentrations of glutamate in the hippocampus, reported to range from 1.0  $\mu\text{M}$  in the extracellular space to 5.0 mM in the synapse (reviewed by Grewer and Rauen, 2005), as well as relevant fluctuations in glutamate concentration greater than 1.0  $\mu\text{M}$ . Selectivity refers to a ratio of the microelectrode sensitivity for glutamate over interferents and is calculated by dividing the slope of the standard MEA glutamate-response by the slope of the response to addition of interferents during calibration. Since the MEA fabrication procedure is highly reproducible, we have found that enzyme-coated sites respond linearly to changes in glutamate and consistently yield a linear regression curve fit (fit of the slope for the standard calibration curve to a straight line) with  $R^2 \cong 0.99$ . (For a more detailed description of the glutamate-sensitive MEA calibration, refer to Hascup et al., 2007 and Burmeister and Gerhardt, 2001.)

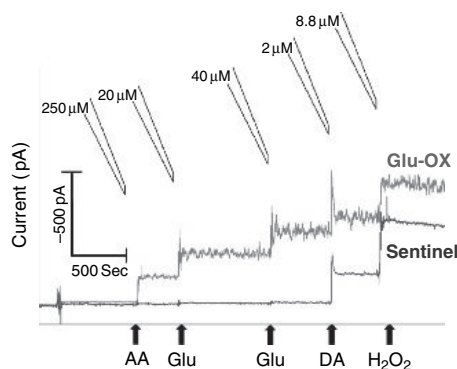


**FIGURE 33.5** Calibration of a Nafion[R] coated glutamate-sensitive, self-referencing microelectrode. Calibration solutions are added to determine the sensitivity to Glu, selectivity for Glu over AA, and responsiveness to other electroactive molecules (e.g. DA (interferent) and  $\text{H}_2\text{O}_2$  (positive control)) for each Pt recording site. Glu-OX sites (red trace) respond well to glutamate and some electroactive interferents. The enzyme-free sentinel sites (blue) do not respond to glutamate but show similar responses to the same electroactive interferents. Subtraction of sentinel site measurements from Glu-OX site measurements yields self-referenced local glutamate concentration free of interferents. Pipettes demonstrate sequence and time-course for addition of interferent and analyte aliquots. Final *in vitro* calibration concentrations following addition of various aliquots as shown: 250  $\mu\text{M}$  AA, 20 and 40  $\mu\text{M}$  Glu, 2  $\mu\text{M}$  DA, and 8.8  $\mu\text{M}$   $\text{H}_2\text{O}_2$ . (See Plate 27 in color plate section.)

## LOCAL APPLICATION OF SOLUTIONS AND DRUGS

After calibrations are completed, a glass micropipette or stainless steel cannula is often attached to the microelectrode so the tip lies among the Pt recording sites. These provide an access port through which solutions are ejected for local manipulation of neurotransmission or concentrations of the analyte. Glass pipettes are utilized for *in vitro* slice or anesthetized animal studies, however, all chronic awake-behaving preparations use a cannula to mimic methods already approved for delivery of solutions to the mammalian CNS (Grondin et al., 2002). For example, excess potassium chloride (isotonic solution) can be ejected locally and the subsequent increase in extracellular glutamate monitored second-by-second, as an indicator of local neuronal excitability. Local drug application has already been shown to decrease seizure duration (reviewed by Nilsen and Cock, 2004). Intervention to halt seizures altogether, triggered by EEG-based computational prediction, still needs much improvement (Stein et al. 2000; Iasemidis et al., 2005; for review, see Litt and Lehnertz, 2002). We believe seizure-prone tissue will display characteristic alterations in extracellular glutamate signaling which, when continuously monitored second-by-second, may provide indication of impending epileptiform activity. One of our primary goals is to minimize unnecessary drug administration or seizure breakthrough through adaptation of our glutamate-sensitive MEA for more sensitive and selective registration of physiological changes preceding seizure as compared to other technologies (EEG, etc.). We plan to improve prediction modeling by offering a chemical parameter, in contrast to traditionally used electrical parameters and, consequently, increase effectiveness of local intervention for termination of seizure onset.

## REFERENCE ELECTRODES

A functional reference electrode is absolutely necessary for electrochemical recordings. For small animal experiments, a small Ag/AgCl reference electrode must be made at the start of every experiment using Ag wire and an acidic supersaturated NaCl solution (Burmeister and Gerhardt, 2001). For *in vivo* recordings, the experimental subject must have ionic contact with the reference electrode. For our animal studies, both anesthetized and awake, the Ag/AgCl reference is embedded into brain parenchyma remote from the MEA recording locations. We are exploring the development of non-invasive ‘skin-patch’ reference electrodes for clinical applications.

## L-GLUTAMATE SIGNAL ANALYSIS

For all experimental glutamate recordings, current generated from the oxidation of ‘reporter’ hydrogen peroxide molecules is converted to concentration automatically by the FAST-16 software based upon Pt recording site sensitivity determined during each individual MEA calibration (see above). The real-time display can be viewed in either current or concentration. Because our MEA can be configured for self-referencing, we obtain resting glutamate measurements and remove possible interferences through subtraction of signal generated by non-active protein coated sites (sentinel) from signal generated by glutamate oxidase-coated sites (glutamate-sensitive) (see Figure 33.2). We hypothesize seizure-prone tissue will display altered glutamate neurotransmission when progressing toward epileptiform activity. By monitoring real-time fluctuations in resting glutamate levels preceding seizure, we predict that characteristic signatures of glutamate activity before and during an ictal event will provide information upon which to forge novel computational seizure models and prediction algorithms.

Alterations in resting glutamate can be the result of changes in clearance from the extracellular space, neuronal or glial release, or most likely some combination of the two. Our basic science investigations focus on normal variation of the glutamatergic system throughout various brain regions, as well as on variation due to aging or disease. We recognize, as often is the case in biological systems, compensatory mechanisms can develop over time, which mask underlying release and uptake dysregulation, leaving resting levels unchanged. We believe an ictal event is a classic example of glutamate dysregulation without the checks and balances of biological compensation, which will yield rapid and characteristic alterations in resting glutamate, which can be measured on a second-by-second basis with our MEA technology. We regularly monitor fluctuations in resting glutamate both in rodent and non-human primate brain of awake-behaving animals; however, to study release and uptake regulation of extracellular glutamate concentration effectively, we need to examine the features of rapid glutamate signals obtained when challenging the biological system. Novel therapeutic targets, or ability to distinguish diseased (seizure-prone) from non-diseased brain parenchyma may be revealed upon identification of alterations in glutamate neurotransmission specific to epileptic tissue.

To investigate glutamate release, we commonly pressure eject 70 mM KCl (isotonic solution – 70 mM KCl, 79 mM NaCl, 2.5 mM CaCl<sub>2</sub>, pH 7.4) to cause a depolarization event and subsequent release of neurotransmitters into the extracellular space. Maximum amplitude of signals obtained are compared across brain regions or treatment groups in relation to volume of KCl applied to achieve the signal as an indication of neuron excitability (Nickell et al., 2005; Day et al. 2006).

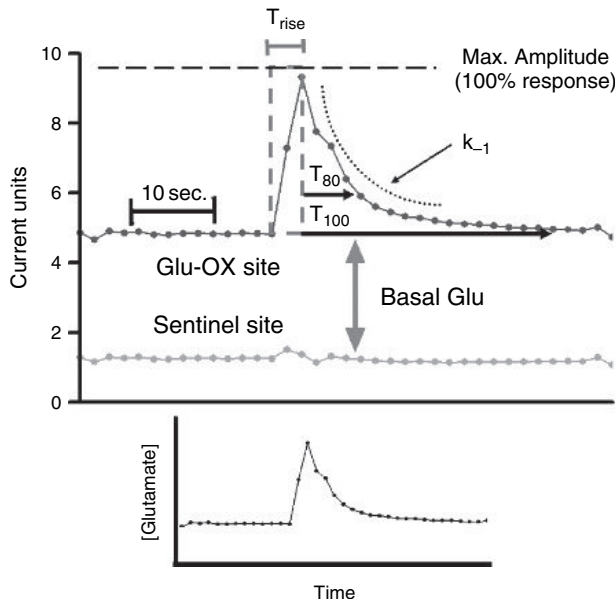


**FIGURE 33.6** Glutamate signal (collected at 2 Hz) illustrating signal parameters of interest (see text for details). When choosing peaks for analysis, a narrow range of maximum amplitudes is selected for comparison across brain regions or treatment groups. Glutamate transporters (responsible for majority of glutamate clearance from the extracellular space) exhibit Michaelis-Menton kinetics, therefore to expose and understand differences in glutamate neurotransmission, the biological systems in question must be compared when evoked or exogenously applied glutamate conditions in the extracellular space are similar. Upper panel shows raw current obtained from glutamate-oxidase coated and sentinel site. Lower panel shows self-referenced glutamate concentration with time, obtained following subtraction of sentinel signal from enzyme-coated signal.

To challenge the clearance capacity of a glutamatergic system, we locally apply, by pressure ejection, a known molar amount of exogenous glutamate (Nickell et al., 2006). Following this application, a signal is again produced. This signal will decay from maximum amplitude to baseline as a result of glutamate clearance from the extracellular space by rapid uptake via glial and neuronal transporters (for review, see Danbolt, 2001). The decay of the glutamate signal is fitted to the slope of the linear regression of the natural log transformation of the data over time, referred to as  $k^{-1}(s^{-1})$ . When  $k^{-1}$  is multiplied by the maximum amplitude of the signal, the *uptake rate*, or micromoles per liter of glutamate removed from the local extracellular space per second ( $\mu\text{M}/\text{s}$ ), is obtained. Finally, the decay of the signal can be examined at different percentages of the signal change from baseline. These include  $t_{50}$ ,  $t_{80}$  and  $t_{100}$ , all following the general format of  $t_D$  (s) where  $t$  refers to the time from maximum amplitude for the signal to decay by D percent (Figure 33.6).

Comparison of release and uptake parameters in our laboratory has allowed us to characterize glutamate regulation in normal and aged animals and also to explore the role of glutamate in Parkinson's disease, amyotrophic lateral sclerosis and attention-deficit/ hyperactivity disorder through animal models. As stated earlier, our glutamate-sensitive MEA can be utilized not only for real-time monitoring of resting glutamate levels, but also for investigation of complex release and/or uptake mechanisms. A better understanding of the glutamate neurotransmission dysregulation present in epilepsy may offer novel therapeutic targets and diagnostic techniques, in addition to more accurate seizure prediction. Glutamate regulation characteristics may also become important in rapidly distinguishing diseased from non-disease tissue. This could prove very helpful to neurosurgeons performing seizure focus resection surgery.

#### SECOND-BY-SECOND L-GLUTAMATE MEASUREMENTS IN THE MAMMALIAN CENTRAL NERVOUS SYSTEM

Glutamate is absolutely required for proper excitatory neurotransmission, but when not appropriately regulated, it can be harmful to the nervous system. When allowed to persist at excessive extracellular concentrations, glutamate initiates a cascade of events which can induce excitotoxicity (for review, see Choi, 1988; Danbolt, 2001). One approach for investigating glutamate regulation involves looking for fluctuation in resting levels. Due to the dynamic nature of glutamate

release and clearance, alterations in either aspect of neurotransmission without compensation can lead to altered resting concentrations. We believe glutamate neurotransmission is altered in the moments preceding an ictal event and continues through the time course of the actual seizure. To us, seizure is the classic neurological example of a possible consequence following breakdown of compensatory mechanisms. Coupling second-by-second monitoring of extracellular glutamate levels obtained via our glutamate-sensitive MEA with new prediction algorithms, we will likely be able to convert real-time fluctuations in resting glutamate (independent variable) into output commands (dependent variable) for computer-controlled therapeutic intervention targeted at seizure termination. A different type of merged MEA-computational modeling technology has utility as a biomimetic hippocampal prosthesis for maintenance of normal communication through the trisynaptic circuit during hippocampal dysfunction (see below). The same MEA with which we have successfully monitored extracellular glutamate in rodents and non-human primates will be used in human protocols. Our extensive characterization of the glutamate-sensitive MEA and previous experience lead us to believe we can accurately and safely measure glutamate in the human brain.

In tissue that is not actively seizing, alterations in release and uptake may not present with altered resting concentrations. We have completed several experiments exploring the underlying disruption of glutamate neurotransmission in circuitry, both with compensation and without, by challenging the glutamatergic system with potassium chloride stimulation and exogenous glutamate application to quantitate release and uptake parameters, respectively (Nickell et al., 2005, 2006; Day et al., 2006). Here, we present an overview of relevant rapid *in vivo* glutamate measurements obtained with our glutamate-sensitive MEA technology in discrete brains regions of the rat and non-human primate (NHP) as proof of concept that we will be able actively to record from seizure-prone brain parenchyma and characterize glutamate neurotransmission before, during and after epileptiform activity in humans. We are currently initiating studies in kainate treated rats to investigate glutamate neurotransmission in an animal model of temporal lobe epilepsy. We are also in the final stages of planning for the first second-by-second glutamate recordings in humans. Temporal lobe resection candidates populate this first cohort of human research subjects (see below).

#### L-GLUTAMATE KINETICS IN THE AGING RAT HIPPOCAMPUS

Histological examination of surgical resection specimens and autopsy studies of patients with chronic temporal lobe epilepsy most often reveal sclerosis of the hippocampus, characterized by marked loss of principal neurons with accompanying gliosis (Zentner et al., 1995). Glutamate uptake in the hippocampus is controlled predominantly by glial transporters, which function to terminate neurotransmission by shuttling glutamate against its concentration gradient from the extracellular space to the intracellular space (reviewed by Danbolt, 2001). We are currently investigating the affect of age-associated changes in hippocampal glial cell biology (i.e. glial cell proliferation and hypertrophy) (Miller and O'Callaghan, 2003), with the expectation of gaining some insight into glutamate regulation in the similarly gliotic epileptic hippocampus. Also of note, there is a positive correlation between increasing age and incidence of epilepsy (Leppik, 2006). An understanding of glutamate dysregulation predicted in the aging hippocampus might further our understanding of the mechanisms of excitotoxic disease. This may yield more specific and effective therapies to alter the onset and course of glutamate-induced neurotoxicity, like that associated with chronic seizure, when coupled with glutamate regulation data we are beginning to collect in a rodent seizure model.

Preliminary comparison of glutamate regulation in the discrete dorsal (CA1) and ventral (CA3) hippocampus showed no significant differences across age groups. A trend was seen in the length of time required for the glutamate peak to decay from maximum amplitude following application of exogenous glutamate to the CA1 and CA3 hippocampal subregions. Glutamate signals of similar maximum amplitude decayed approximately twice as fast in the aged hippocampus when compared to young and middle-aged rats (data to be published elsewhere). The more rapid clearance of glutamate from the extracellular space adjacent to the MEA in aged animals could be a consequence of increased numbers of glia in the aged hippocampus, though a study from our laboratory examining the aged striatum suggests glia may lose function with age (Nickell et al., 2006).

Ultimately, we believe our first hippocampal studies will characterize glutamate regulation in 'normal' aging. It is interesting to imagine how additional hippocampal glia from the aging process or in response to CNS injury, if not functional, could dramatically alter glutamate neurotransmission. This could occur from compromised ability adequately to clear glutamate from the extracellular space due to lack of functional transporters and/or anatomical crowding imposed by glial proliferation, both scenarios which would limit diffusion of glutamate away from the synapse. Disruption of glutamatergic neurotransmission, normally tightly controlled, may lead to excitotoxic environments from persistence of glutamate in the extracellular space and synapse. Seizure may be a consequence of such dysregulation.

### L-GLUTAMATE RECORDINGS IN THE NON-HUMAN PRIMATE BRAIN

In limited studies utilizing primates, microdialysis has been the technique of choice for measuring extracellular Glu levels. Microdialysis has been shown to damage the brain parenchyma sampled due to probe size and the technology and, furthermore, is limited in its usefulness for rapid glutamate measurements due to temporal resolution constraints. We adapted our MEA technology to allow recordings in the non-human primate CNS (Quintero et al., 2007). This established essential forward progress in the pursuit of human glutamate neurotransmission investigation. As emphasized throughout this chapter, the design of our glutamate-sensitive MEA allows for the same device, already well characterized for use in animals, to be incorporated into human recording protocols, with minor modification.

Our non-human primate studies have examined three components of the glutamatergic system: first, resting glutamate levels in cortical areas of young, middle-aged and aged rhesus monkeys; second, rapid kinetics of glutamate release after local KCl stimulation; and last, glutamate clearance following local delivery of exogenous glutamate (Quintero et al., 2007). Our ability to measure resting glutamate concentrations in the non-human primate neocortex is of particular interest, as resting level recordings will be the type of measurements first collected in humans. Our vision for MEA-based seizure prediction and intervention hinges on the ability continuously (second-by-second) to monitor fluctuations in resting glutamate and couple characteristic elevations of extracellular glutamate with computational modeling for accurate seizure prediction.

#### Cortical basal L-glutamate

Our laboratory successfully measured resting (basal) glutamate levels in the pre-motor and motor cortices of non-human primates using the S2 glutamate-sensitive MEAs (see Figure 33.1). This work was completed in a study of the effects of aging on glutamate neurotransmission in young ( $5.4 \pm 0.4$  years old, mean  $\pm$  SEM,  $n = 4$ ), middle-aged ( $16.8 \pm 0.5$  years old,  $n = 4$ ) and aged ( $25.5 \pm 0.3$  years old,  $n = 4$ ) female rhesus monkeys (*Macaca mulatta*). Briefly, we found a significant increase in average resting glutamate levels in the motor cortex of aged animals compared to young animals ( $P < 0.05$ ). The mean glutamate resting levels for middle-aged animals was in between the values recorded in the young and aged groups. Consistent with prior aging studies, variability from the mean increased with each age. Similar measurements in the prefrontal cortex, though not significant, established a trend of an age-associated increase in resting glutamate levels similar to that observed in the motor cortex. Our measurements agree with other reports of tonic glutamate concentrations in non-human primates (Kodama et al., 2002; Galvan et al., 2003) and humans (Cavus et al., 2005). The details of this study will be published elsewhere (Quintero et al., 2007).

We hypothesize that the elevated basal glutamate levels seen with aging result from underlying disruption of the glutamatergic system and contribute to the propensity of aging populations to develop neurodegenerative disease associated with excitotoxicity. The stability and consistency of resting measurements made within each brain region of the non-human primate support our beliefs that changes in resting glutamate (i.e. impending seizure) will be readily recorded with our glutamate-sensitive MEA and that diseased tissue with active glutamate-system pathology will be distinguishable from non-diseased tissue, important in seizure focus identification.

### MOVING INTO HUMANS

Patients undergoing epilepsy resection surgery provide basic scientists a very precious resource for investigation of the cellular processes occurring with seizure disorders. Of particular interest to researchers and clinicians alike, is the notion that distinct and redundant electrical and/or chemical patterns may be accessed to deduce ictal onset or method of neuronal recruitment and seizure propagation. Development of rational and effective therapies can be expedited by defining the fundamental mechanisms of seizure and epileptogenesis in humans. As pointed out by Engel (1998), experimentation in surgical patients can prove invaluable in the validation of current animal models, while also providing phenomena specific to the human epileptic brain for the development of new animal models. Building on our experience in non-human primates, we continue to work toward adaptation of the glutamate-sensitive MEA repeatedly utilized in investigations of the mammalian CNS for human recordings. Our initial human recordings will be aimed at continuously monitoring glutamate in the extracellular space of seizure-prone tissue within the hippocampi of intractable temporal lobe epilepsy (TLE) sufferers, for future prediction and intervention-based therapy development utilizing chronic MEA glutamate monitoring. We plan to eliminate the negative cognitive effects (e.g. memory loss) experienced with pharmacological suppression of hippocampal communication for seizure termination. For this, we have developed a biomimetic hippocampal prosthesis for preservation of normal hippocampal communication throughout the trisynaptic circuit when intrinsic hippocampal communication is compromised. Accurate prediction, based upon signature second-by-second changes in resting glutamate, pharmacological

intervention and maintenance of normal hippocampal function, is the ideal outcome of our research efforts targeted at therapy development for patients with intractable TLE.

### Prior work in the human hippocampus

The significance of intraoperative studies has been recognized since the development of epilepsy surgery (Engel, 1998). Several researchers have capitalized on the opportunity to conduct experimental electrophysiological and microdialysis recordings in humans during resection surgery. One of a variety of macroelectrodes can be used to perform electrophysiological recordings or to provide stimulation. Examples include stereotactically implanted depth electrodes (Williamson et al., 1995), electrocorticography (Oliveira et al., 2006) and subdural and strip electrodes (Cohen-Gadol and Spencer, 2003). Microdialysis has historically been considered the gold standard for measuring chemical constituents of the extracellular fluid and, with this technique, increases in the extracellular concentration of glutamate have been shown to precede seizure and persist during the ictal event (During and Spencer, 1993; Cavus et al., 2005). A recurrent theme of this chapter is our hypothesis that rapid signature alterations in extracellular glutamate will provide a parameter upon which to model novel seizure prediction algorithms, superior to electrophysiologically-based prediction of aberrant neuronal firing. In regards to studying the glutamatergic system, microdialysis provides a weak approximation of phasic glutamate neurotransmission, as the limited temporal resolution offers sampling rates on the order of several seconds. Glutamate release phenomena and transporter activation for clearance can be very rapid processes, taking less than a second to occur.

Our laboratory has worked to develop MEA technology for the detection and quantification of rapid (second-by-second) glutamate events with detection limits comparable to microdialysis (Burmeister et al., 2000, 2002; Burmeister and Gerhardt, 2001; Pomerleau et al., 2003). We can readily and accurately measure Glu concentrations equivalent to physiologically relevant levels, as indicated by the  $K_m$  of Glu receptors and  $K_d$  of glutamate transporters, reported to range from  $1.0 \mu\text{M}$  to  $5.0 \text{ mM}$  (for review, see Grewer and Rauen, 2005). Choice of the recording technique for monitoring extracellular glutamate should compromise the intact biological environment as little as possible so the value of *in vivo* recordings is not lost. The microdialysis probe can produce significant glial activation in the CNS and create a sizable area of cellular inflammation and damage around the insertion tract (Clapp-Lilly et al., 1999; Borland et al., 2005). The small size, smooth edges, tapered design and ceramic substrate material of our fabricated MEAs yield a very biocompatible device with minimal tissue disruption and cellular response out to six months (for histology and immunostaining see Hascup et al., 2007).

### Enzyme-based microelectrodes for deep brain structures

An adapted version of our enzyme-based multisite microelectrodes has been designed for recording from deep brain structures such as the hippocampus and temporal lobe in monkeys as well as humans. This new microelectrode, called the Spencer-Gerhardt electrode (SG-2, AD-TECH®, Figure 33.7) is a variant of the rodent and non-human primate MEA assembly and is capable of monitoring electrophysiological or electrochemical signals. The SG-2 has increased flexibility of the connections from MEA to recording system so it can be positioned and maintained with minimal concern of tissue damage as the brain moves. Major adaptation of the rodent/non-human primate glutamate-sensitive ceramic MEA for human use was not necessary, rather it was adapted to fit with-in the Spencer depth electrode. The universal design concept has been critical in our validation of human pursuits based upon experience and success in other mammals.

In addition to patient-based basic science investigation of seizure mechanisms and clinical prediction and intervention applications, monitoring resting glutamate fluctuations may help neurosurgeons distinguish a seizure focus and seizure-prone tissue for resection, from normal brain parenchyma. Though spectroscopy and functional imaging can often accurately identify seizure foci, these assessments are obtained from a brain confined within an intact skull. Following craniotomy, swelling can compromise image-based localization, warranting focus-detection techniques amenable to the operating room. Preparations for the first human recordings utilizing our MEA technology are in the final stages of planning and will proceed at Yale University under direction of Dennis Spencer, MD.

## THE ROLE OF MICROELECTRODES IN EPILEPSY THERAPY AND HIPPOCAMPAL REPAIR

In parallel with use of the enzyme-based MEA to monitor characteristic seizure-associated chemical neuronal communication, we also are currently exploring potential uses of combined MEA-computational modeling techniques for development of hippocampal prosthetics, incorporating unit recordings and electrical stimulation in specific conformal Pt site arrangements to assist information relay through an inhibited, or even damaged, trisynaptic circuit. Actual development of this

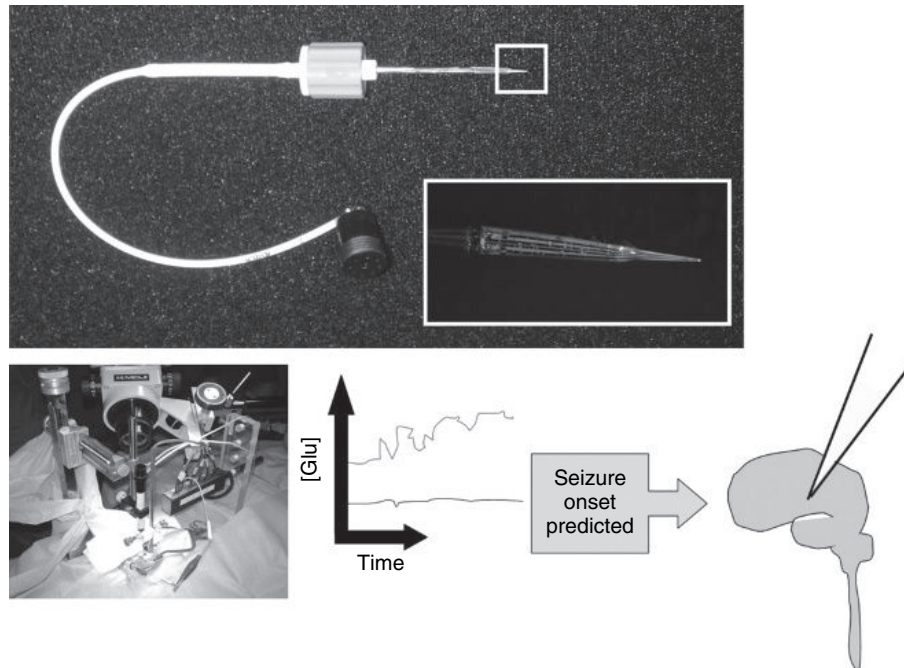


**FIGURE 33.7** Photograph of Spencer-Gerhardt electrode (SG-2), showing flexible shaft for chronic compatibility and optimal placement of MEA tip (magnified image) into human brain. Lower left panel: image taken during second-by-second glutamate recordings in anesthetized non-human primate. Studies conducted in operating room (OR) equipped for human surgeries to mimic closely stringent OR requirements as we prepare for human recordings. Lower right diagram: characteristic fluctuations in resting glutamate (top trace) recognized as signature of impending seizure, which triggers local application of drug to terminate seizure onset.

system will be preceded by the development of sterile electrodes with improved longevity for long-term recordings. The fundamental concept is a two-part system. The first, described above, monitors local glutamate concentration, senses abnormal pre-epileptiform activity and triggers local injection of pharmacological agents to suppress all hippocampal neuroelectric function. Such a procedure could provide a much wanted avoidance of an epileptiform episode. Unfortunately, with this approach normal hippocampal function is compromised and could leave a patient with cognitive deficits. We propose a second part of this therapeutic system, a hippocampal prosthetic, which will allow for closed-loop seizure prediction and intervention, with preservation of normal hippocampal function – the ideal patient outcome for once intractable temporal lobe epilepsy.

#### MICROELECTRODE-BASED EPILEPSY THERAPY COUPLED WITH NEURAL PROSTHESES FOR MAINTENANCE OF HIPPOCAMPAL FUNCTION

Outside basic science investigation, the clinical applications of our MEA technology are equally promising in their novelty and diversity. Based upon acute basal recordings during seizure focus resection surgery, discrete brain regions could conceivably be ‘mapped’ to isolate diseased from non-diseased tissue. With alternative modeling and prediction algorithm developments, chronic MEA technology could be coupled to local drug delivery, therefore circumventing adverse side-effects of systemic antiepileptic medication and offering a more tolerable and effective treatment option for intractable epilepsy patients unsuitable for surgery.

In this regard, we are currently exploring potential uses of combining MEA data with computational methodology for hippocampal prostheses, incorporating unit recordings and electrical stimulation in specific conformal Pt site arrangements to assist information relay through a damaged hippocampal trisynaptic circuit. The fundamental concept is a two-part system, the first of which is described above – a first system that senses local glutamate concentration and abnormal pre-epileptiform activity, triggering local injection of pharmacological agents to suppress all hippocampal neuroelectric function. Although such a procedure could provide a much-wanted prevention of epileptiform episode and seizure, it also

would have the unfortunate consequence of blocking memory function associated with hippocampal processing. Blocking hippocampal function would be the equivalent of ‘seizure-induced amnesia’, a severely debilitating phenomenon commonly reported among epilepsy patients (Gallazzi, 2006). Here, we propose the coupling of a pre-seizure detection and seizure prevention system with a second-part neural prosthesis that mimics and thus maintains hippocampal memory function during the time period of suppressing hippocampal activity to prevent epileptiform discharging. This neural prosthesis would take the form of a medical device interacting with the brain, which mimics the function of the hippocampal circuitry suppressed to avoid epileptiform activity and which, through bi-directional communication with the hippocampus, would bypass the non-functional hippocampal region. For example, assume an epileptic focus in hippocampal subregion CA3 and that glutamate-sensitive MEAs detected pre-seizure conditions, which in turn triggered an infusion of inhibitory substances (e.g. GABA agonists), thus rendering CA3 neurons inactive for some period of time. The major intrinsic circuitry of the hippocampus consists of an excitatory cascade of perforant path afferents exciting dentate granule cells, which in turn excite CA3 pyramidal cells, which subsequently excite the CA1 region (perforant path → dentate → CA3 → CA1) (Figure 33.8) (Andersen et al., 1971; Amaral and Witter, 1989). Inactivating neurons in the CA3 region would break the transmission of signals through the hippocampal intrinsic trisynaptic path and thus eliminate hippocampal memory function, at least for as long as the inhibitory agents infused into CA3 remain potent. The proposed prosthetic device would function in a biomimetic manner to replace information transmission between the dentate and CA1 subregions (Berger et al., 2001, 2005a,b). The inactivated CA3 region would be replaced with a biomimetic system comprised of silicon neurons (Figure 33.9; CA3 = B). The replacement silicon neurons would have functional properties specific to the collective network of neurons comprising CA3 (pyramidal cells, interneurons, recurrent collaterals, etc.). The CA3 neural prosthesis would receive as inputs neuroelectric signals (action potentials) from biological dentate granule cells

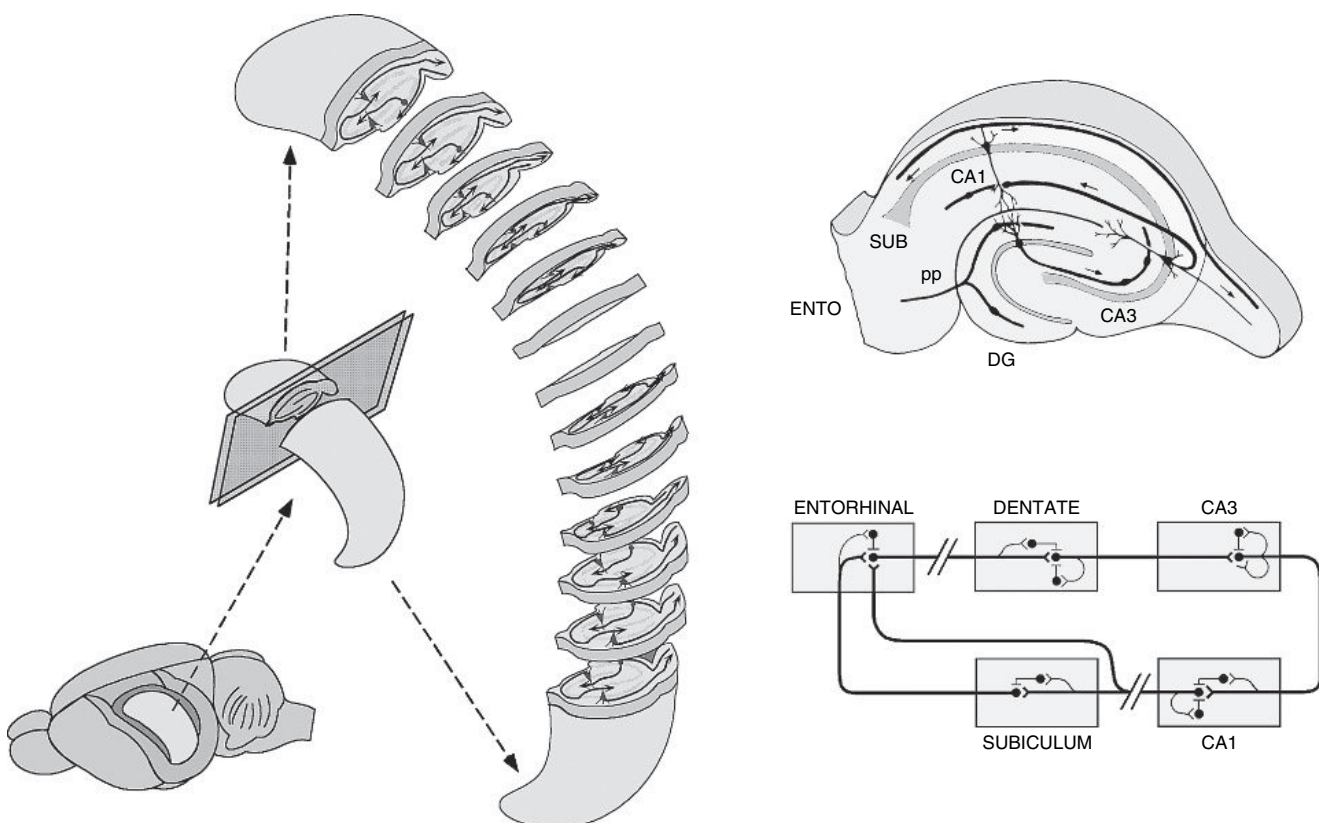


**FIGURE 33.8** Left panel: diagrammatic representation of the rat brain (lower left), showing the relative location of the hippocampal formation on the left side of the brain (shaded); diagrammatic representation of the left hippocampus after isolation from the brain (center) and slices of the hippocampus for sections transverse to the longitudinal axis. Right panel: diagrammatic representation of one transverse slice of hippocampus, illustrating its intrinsic organization: fibers from the entorhinal cortex (ENTO) project through perforant path (pp) to the dentate gyrus (DG); granule cells of the dentate gyrus project to the CA3 region, which in turn projects to the CA1 region; CA1 cells project to the subiculum (SUB), which in the intact brain then projects back to the entorhinal cortex.

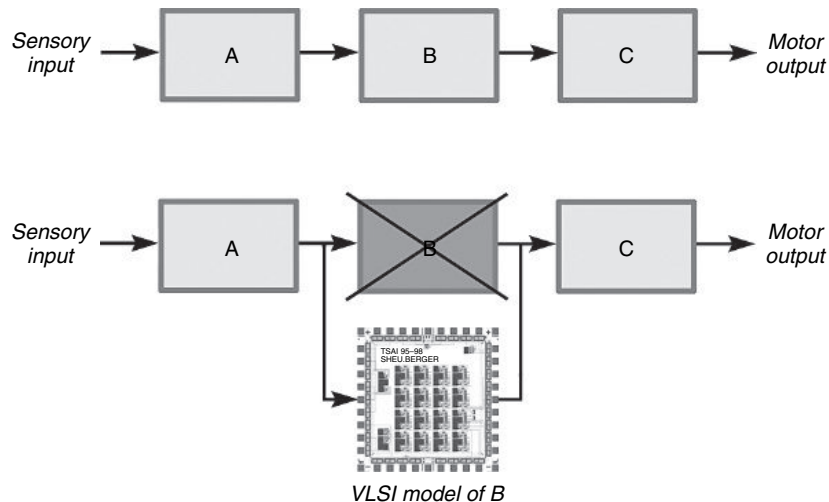


**FIGURE 33.9** Schematic diagram for the general case of substituting or replacing a damaged central brain region with a VLSI (very large scale integrated system) implementation of a biomimetic model, and connecting the inputs of the VLSI-based model to the afferents of the damaged region and the outputs of the VLSI-based model to the efferents of the damaged region. For the specific case of substituting for the function of area CA3 of the hippocampus considered here, A = dentate gyrus, B = CA3, and C = CA1.

(Figure 33.9; dentate = A) and send as outputs electrical impulses to activate afferents to the CA1 region (Figure 33.9; CA1 = C). Thus, the class of prosthesis being proposed is one that would replace the computational function of CA3 with a silicon-based model, establish dentate granule cell inputs to the biomimetic CA3 and transmit that computational result of the biomimetic device to CA1, thus restoring hippocampal trisynaptic circuit function.

#### A NEURAL PROSTHESIS FOR THE CA3 REGION OF HIPPOCAMPUS

We are in the process of developing such a cognitive prosthesis for the hippocampus and have constructed a multistage plan for ultimately achieving this goal in humans. The first stage will be described in this chapter, and involves a ‘proof-of-concept’ in which we develop a replacement biomimetic model of the CA3 subregion of hippocampal *in vitro* slice (Berger et al., 2005a). We have chosen to realize our first-generation prosthesis in the context of a hippocampal slice for several reasons. Among them is that the 400 µm thickness of the slice allows us essentially to reduce the problems of modeling the three-dimensional function of the hippocampus and of interfacing with its complex, three-dimensional structure, to a more tractable two-dimensions. This allows us to develop the initial stages of experimental strategies, modeling methodologies, hardware designs, and interfacing technologies within the context of a more simplified and controlled set of conditions.

As reviewed above, the major intrinsic circuitry of the hippocampus, consists of an excitatory cascade of the dentate, CA3 and CA1 subregions (dentate → CA3 → CA1; Figure 33.10A) and is maintained in a slice preparation. Our stage 1 prosthesis demonstration consists of:

1. surgically eliminating the CA3 subregion
2. replacing the biological CA3 with a very-large-scale-integrated (VLSI)-based model of the non-linear dynamics of CA3 (Figure 33.10B) and
3. through a specially designed multisite electrode array, transmitting dentate output to the VLSI model, and VLSI model output to the inputs of CA1 (Figure 33.10C).

The definition of a successful implementation of the prosthesis is the propagation of spatio-temporal patterns of activity from dentate → VLSI model → CA1 which reproduces that observed experimentally in the biological dentate → CA3 → CA1 circuit.

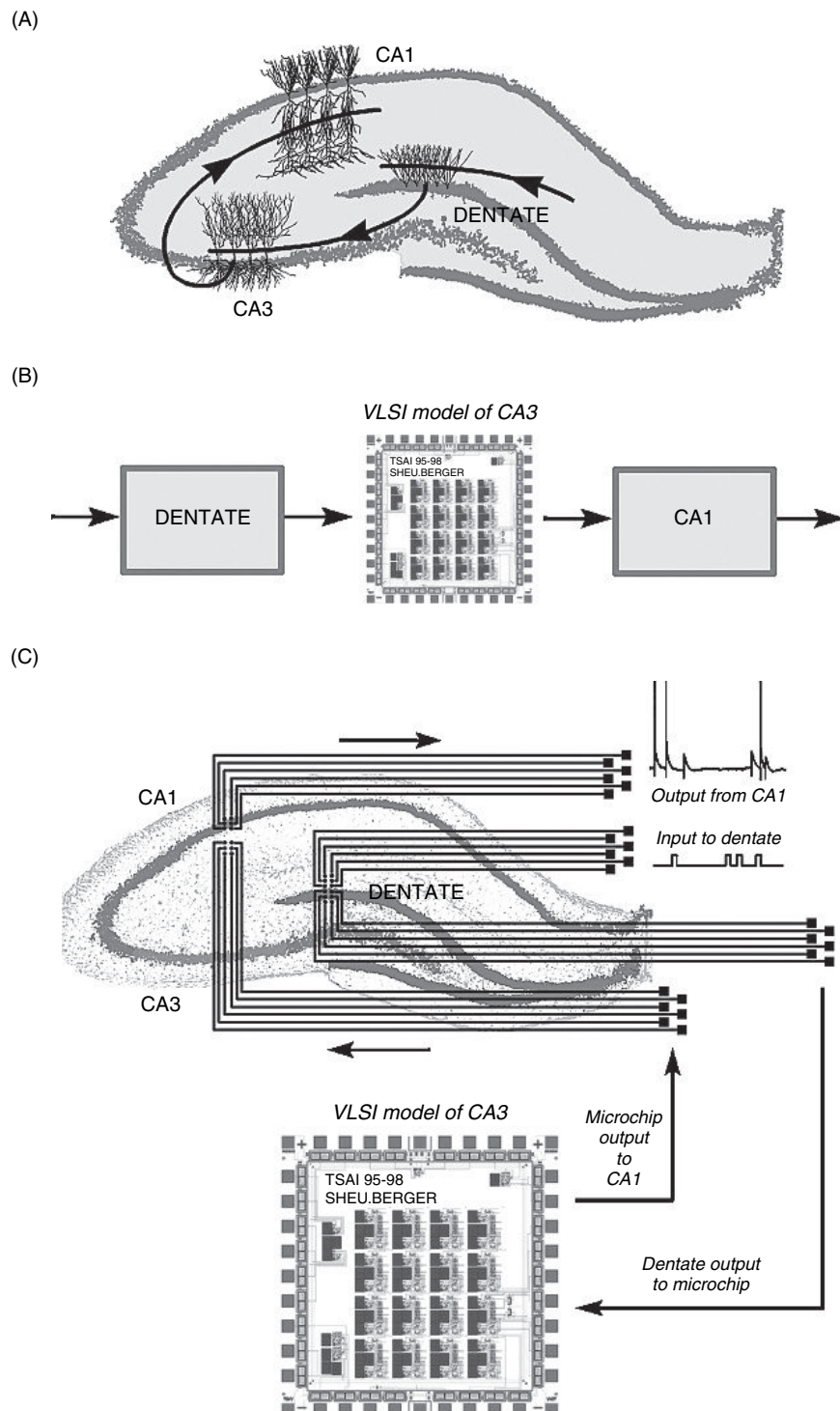


**FIGURE 33.10** Strategy for replacing the function of the CA3 region of hippocampus with a VLSI model of its non-linear dynamics and interfacing the VLSI biomimetic device with the remaining, active slice through a conformal, multisite electrode array, thus restoring whole-circuit dynamics. (A) Diagrammatic representation of the trisynaptic circuit of the hippocampus. (B) Conceptual representation of replacing the CA3 field with a VLSI-based model. (C) Hippocampal slice in which the CA3 field has been removed. Overlaid is an integrated system in which impulse stimulation from an external source is used to activate dentate granule cells and is delivered through one component of a multisite electrode array. A second component of the electrode array senses the responses of dentate granule cells and transmits the responses to the VLSI-based model. The VLSI device performs the same non-linear input/output transformations as biological CA3 neurons and transmits the output through the multisite electrode array to the dendrites of CA1 neurons, thus activating the last component of the trisynaptic pathway.

## EXPERIMENTAL CHARACTERIZATION AND MATHEMATICAL MODELING OF THE NON-LINEAR DYNAMIC PROPERTIES OF THE HIPPOCAMPAL CA3 REGION

Our strategy for achieving a hippocampal neural prosthesis is based on several system requirements for replacing any CNS region with a biomimetic device that interacts bi-directionally with the rest of the undamaged brain (i.e. sensing and communicating input to the biomimetic device from afferents of the damaged region; communicating and electrically stimulating outputs from the biomimetic device to efferents of the damaged region) (Berger et al., 2001). First and foremost is the nature of the biomimetic model that constitutes the core of the prosthetic system. Information in the hippocampus and all other parts of the brain is coded in terms of variation in the sequence of all-or-none point-process (spike) events, or temporal pattern (for multiple neurons, variation in the spatio-temporal pattern). The essential signal processing capability of a neuron is derived from its capacity to change an input sequence of inter-spike intervals into a different output sequence of inter-spike intervals (or amplitude-time course synaptic potentials). In all brain areas, the resulting input/output transformations are strongly non-linear, due to the non-linear dynamics inherent in the cellular/molecular mechanisms comprising neurons and their synaptic connections (Berger et al., 1992, 1994; Dalal et al., 1997; Gholmeh et al., 2005). As a consequence, the output of virtually all neurons in the brain is highly dependent on temporal properties of the input. Thus, identifying the non-linear input/output properties of hippocampal neurons and the composite input/output transformations of hippocampal circuitry is the fundamental functionality that must be captured by any mathematical model designed to replace damaged hippocampal tissue.

We are using a non-linear systems analytic approach to modeling hippocampal neurons (Volterra, 1930; Wiener, 1958; Sclabassi et al., 1988a; Marmarelis, 2004). In this approach, neurons and circuits or networks to be modeled are first characterized experimentally using a ‘broadband’ stimulus, e.g. a series of impulses (typically 1000–2000 total) in which the inter-impulse intervals vary according to a random (Poisson) process (Sclabassi et al., 1988b; Berger et al., 1988a, 1988b; Dalal et al., 1997; Dimoka et al., 2003; Gholmeh et al., 2005). Because the distribution of inter-impulse intervals is exponential, the mean frequency can remain relatively low (2 Hz) and thus be physiological, yet the range of intervals can be wide (10 ms–5000 ms). Such a stimulation protocol ensures that the majority, if not all, of synaptic and cellular mechanisms are activated and, as a consequence, contribute to neuron, circuit or network output which is measured (e.g. electrophysiologically). The modeling effort – identified as the Volterra-Poisson modeling approach – then becomes focused on estimating linear and non-linear components of the mapping of the known input to the experimentally measured output. The Volterra modeling approach is a mathematically rigorous, scalable method (Volterra, 1930; Wiener, 1958) that can be applied to biological systems (Marmarelis, 1993; Alataris et al., 2000). The non-linear dynamic input/output characteristics of the modeled system are quantitatively captured by the Volterra kernels. Volterra kernels are system descriptors that remain invariant with respect of the type or the power of the stimulus. Given accurate estimation methods (Marmarelis, 1993; Alataris et al., 2000; Gholmeh et al., 2003), the result is a model that is ‘compact’ (many fewer terms than a compartmental neuron network model), predictive for virtually any temporal pattern and that incorporates at least the majority of known and unknown biological mechanisms (thus, not requiring modification and optimization for each new discovery in the future).

Accordingly, our first step in developing a prosthesis for the hippocampus is to characterize experimentally the non-linear input/output properties both of field CA3 and of the entire trisynaptic pathway, i.e. the combined non-linearities due to propagation through the dentate → CA3 → CA1 subfields. The model of CA3 will be used to develop the biomimetic replacement device to substitute for CA3 dynamics after the biological CA3 has been removed from the slice. The input/output properties of the trisynaptic pathway will be used to evaluate the extent to which hippocampal circuit dynamics have been restored after substituting the biomimetic device for field CA3. Random impulse train stimulation is applied only to the perforant path afferents to dentate. Non-linearities of the dentate then determine the actual input to CA3; in turn, the non-linearities of CA3 determine the input to CA1. Field potentials are used as the measure of output from each of the three hippocampal regions: population spikes of dentate granule cells, population spikes of CA3 pyramidal cells and population EPSPs (excitatory postsynaptic potentials) of CA1 pyramidal cells (amplitudes of the negative-going waveforms shown in Figure 33.11). Thus, for both CA1 and CA3 fields, not only does the continuous input of the random train vary in terms of inter-impulse interval, but because of non-linearities ‘upstream’, the input also varies in terms of the number of active afferents, reflected as the amplitude of the population spike. This places a major constraint on modeling CA3 input/output properties, i.e. the model must be capable of predicting CA3 output as a function of both the temporal pattern and the amplitude of dentate input.

Experimental datasets of population spike sequences recorded at the granule cell layer (input) and the corresponding population spike sequences recorded at the pyramidal cell layer of CA3 (output) were used to estimate the Volterra-Poisson

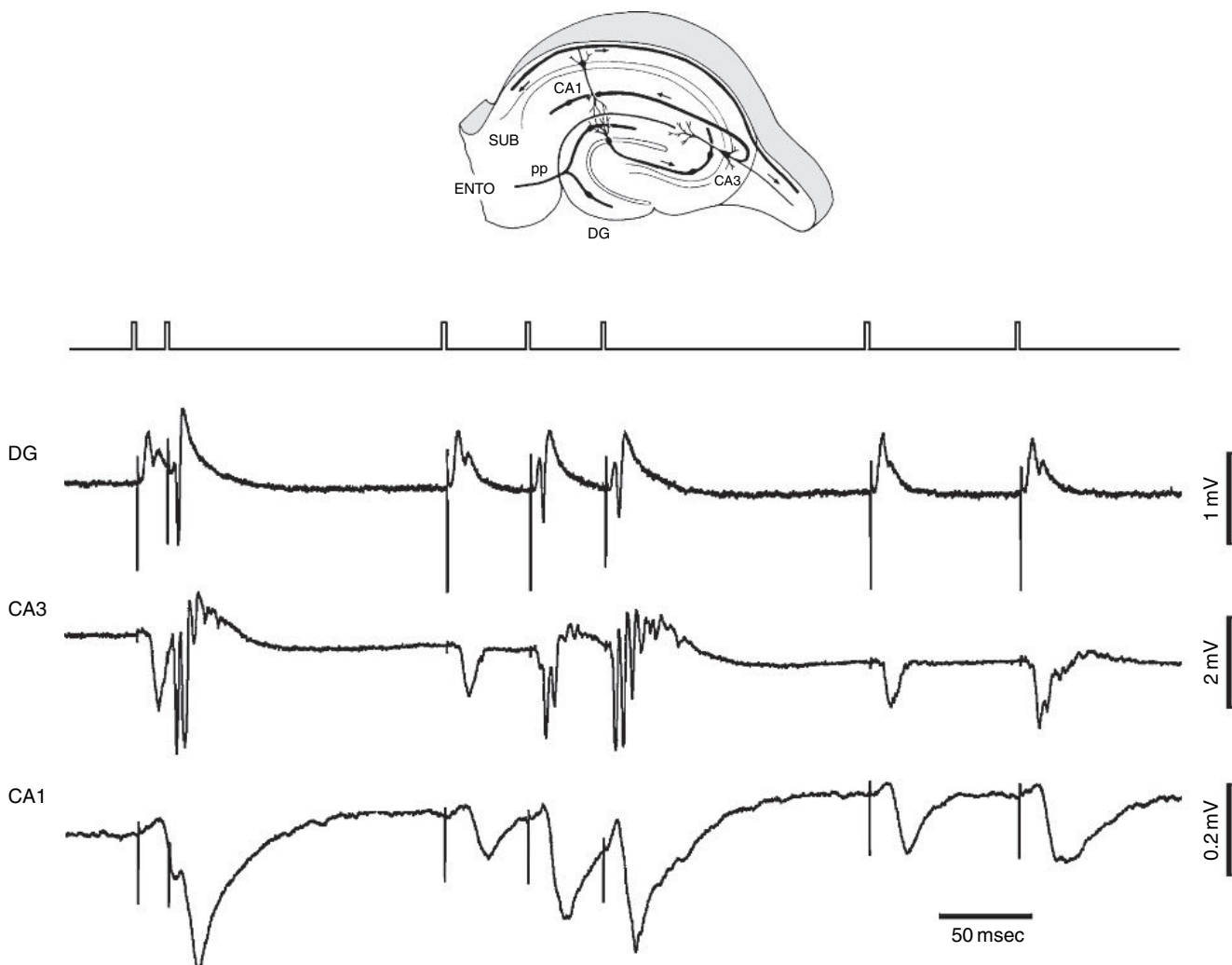


**FIGURE 33.11** Top: diagrammatic representation of a hippocampal slice (from Andersen). First trace: segment of a series of impulses with randomly varying inter-impulse intervals delivered in one *in vitro* hippocampal slice experiment to perforant path (pp) fibers originating from the entorhinal cortex (ENTO) and terminating in the dentate gyrus (DG). Second trace: field potential responses recorded from the DG. The narrow, biphasic deflections preceding the field potential responses are stimulation artifacts and thus, correspond to the occurrence of stimulation impulses in the first trace. The large negative-going deflection in each response is the ‘population spike’. Amplitude of the population spike correlates positively with the number of granule cells reaching threshold and generating an action potential. It is the amplitude of the population spike that is used as the measure of output from both DG and CA3. Third trace: field potential responses recorded from CA3. The stimulation artifacts are much smaller in amplitude. Note the occurrence of multiple population spikes, which is presumed to be due to excitatory, recurrent collaterals unique to the CA3 field. Bottom trace: field potential responses recorded from CA1. These responses are recorded from the dendritic region of CA1 and thus reflect population excitatory synaptic potential responses (EPSPs) of CA1 neurons rather than population action potentials (‘population spikes’). Note the progressively longer delay in the onset of response following the stimulation artifact for fields DG, CA3 and CA1, reflecting the propagation of activity through the hippocampal trisynaptic circuit.

model of CA3. The equation representing the single input/single output, third order Volterra-Poisson model employed to capture the CA3 nonlinear dynamic properties was adapted as follows:

$$y(n_i) = A_i k_1 + A_i \sum_{n_i - \mu < n_j < n_i} A_j k_2(n_i - n_j) + A_i \sum_{n_i - \mu < n_{j_1} < n_i} \sum_{n_i - \mu < n_{j_2} < n_i} A_{j_1} A_{j_2} k_3(n_i - n_{j_1}, n_i - n_{j_2})$$

where  $y(n_i)$  represents the amplitudes of the population spikes recorded at CA3 (output),  $A_i$ ,  $A_j$  represent the varying amplitudes of the population spikes recorded at the granule cell layer (input),  $k_1$ ,  $k_2$  and  $k_3$  are the first, second and third order kernels respectively,  $n_i$  is the time of occurrence of the current impulse in the input/output sequence and  $n_j$  is the

time of occurrence of the  $j^{\text{th}}$  impulse prior to the present impulse within the kernel's memory window  $\mu$ . Estimation of the kernels is facilitated by expanding them on the orthonormal basis of Laguerre polynomials, the coefficients of which were obtained via least squares as described previously (Marmarelis, 1993).

To understand what the kernels represent, consider the following. First, recall that even though each input event is of short duration (less than 1 ms at the level of perforant path input; less than 5 ms at the level of dentate input), each input event can generate neurobiological consequences extending for many 10s or even 100s of ms. Thus, the first order kernel represents the effect on CA3 output of the most recent dentate granule cell population spike, i.e. the probability of a CA3 population spike of a given amplitude in response to a dentate population spike of a given amplitude. The second order kernel represents the modulatory effect (facilitation or suppression) of any preceding dentate input on the CA3 response to the most current dentate input that cannot be predicted simply by assuming that the effects of the two inputs in question (the most current and any previous input) add linearly. Likewise, the third order kernel represents the modulatory effect (facilitation or suppression) of any *pair* of preceding dentate inputs on the CA3 response to the most current dentate input that cannot be predicted simply by assuming that the effects of the three inputs in question (the most current and any two previous inputs) add linearly. Etc. for higher order kernels; only third order kernels were computed in the studies reported here. Thus, the kernel functions provide a predictive model of how the CA3 pyramidal cells (as modulated by all feedforward and feedback interneurons, all recurrent collaterals, all field effects from ephaptic coupling – all mechanisms contained in the slice preparation – respond to essentially any temporal patterns comprised of up to three input events *and* for all levels of synchrony in the dentate granule cell population generating those events.

Data collected from hippocampal slices were analyzed and the associated Volterra-Poisson kernels were computed. A third order model (a model that considered the effects of the previous three impulses, i.e. the effects of all possible 'triplets' on the current output) was selected as it provided a consistent improvement in NMSE between 4% and 9% compared to a second order model. One of the most important properties of a Volterra-Poisson model is its predictive capability to arbitrary input patterns. It is a property that is necessary for the CA3 model to function as a CA3 replacement, since it is not bound to a specific input sequence and there is no reasonable way to predict what sensory inputs or short-term memories any patient will be experiencing at any given time. Each value predicted by the Volterra-Poisson model is the result of the non-linear functional terms of the corresponding Volterra-Poisson series. The  $n^{\text{th}}$ -term of the series contributes to the computation of the predicted output with the effect of  $n^{\text{th}}$ -order interactions among the input impulses weighed by the  $n^{\text{th}}$ -order kernel across its memory window. An example of model prediction using the Volterra-Poisson model developed for CA3 using the slice experimental data is shown in Figure 33.12. Although the figure shows only a small sample of the data from this one slice, it should be clear that our non-linear model predicts very well amplitudes of the CA3 population spikes in response to a wide range of dentate input.

#### HARDWARE IMPLEMENTATION OF THE NON-LINEAR MODEL OF HIPPOCAMPAL CA3

A biomimetic model of a hippocampal network of neurons must be reduced to a hardware implementation in microcircuitry (VLSI, or very large scale integrated system) for at least three reasons. First, for a neural prosthetic device used clinically, it will be necessary to simulate multiple neurons and neural circuits in parallel; hardware implementations provide the most efficient means for realizing parallel processing. Second, by definition, the device in question will be required to interact with the intact brain in real-time if it is to substitute for hippocampal function suppressed with anti-seizure agents, and at least partially reinstate normal levels of cognition and behavior. Again, the rapid operational rates of modern VLSI technology provide the best means for achieving the goal of real-time signal processing to support on-going interaction of a patient with the environment. Finally, there is the practical consideration of integration of the prosthetic system with the patient, i.e. it must be miniaturized sufficiently that it easily can be carried 'on board'.

The system-on-a-chip that we have developed for the hippocampal CA3 prosthesis, as depicted in Figure 33.14, accepts analog signals from the hippocampal dentate region (In: DG), buffers and amplifies the signals and then performs an analog-to-digital conversion (ADC) (Berger et al., 2003, 2005a). The sequence of processing is controlled by a finite state machine (FSM) and automatic gain control circuitry adjusts the amplitude of the input signal. Once the signals are in binary form, other circuitry identifies and calculates amplitude of the population spike (see Spike Detector in Figure 33.13) and transmits the result to the circuitry that performs the non-linear modeling function (see Polynomial Update and Response Generator in Figure 33.13). Each digital non-linear response prediction is delayed by a millisecond time period appropriate to dentate-to-CA3 propagation and then converted to a biphasic representation compatible with electrical stimulation of neuronal tissue ('Pulse-to-Biphasic'). The result is converted from digital to analog (digital-to-analog conversion, DAC) and is transmitted to the biological tissue through a conformal multi-site electrode array (described below).

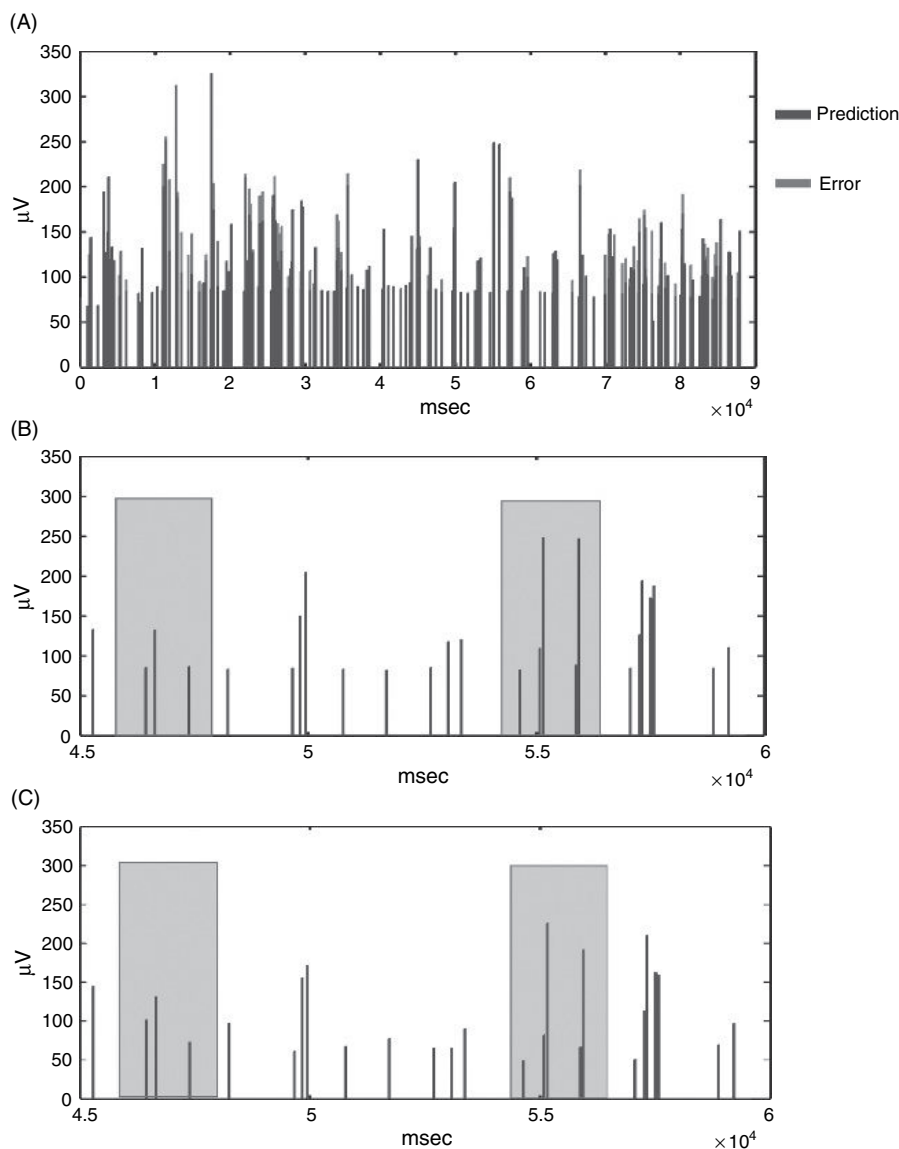


**FIGURE 33.12** An example of CA3 model prediction ( $NMSE = 8.21\%$ ). (A) Predicted population spike amplitudes (blue) and their differences from the corresponding measured population spike amplitudes (red). (B) Segment of the CA3 Model Prediction. (C) The corresponding segment of the measured CA3 population spike amplitudes. The shaded rectangles highlight two areas for comparison between model predicted values and recorded values. (See Plate 28 in color plate section.)

The real-time population spike amplitude identification and measurement is performed in the digital domain (Gholmeh et al., 2004; Srinivasan et al., 2004). Digital circuitry implemented on a field-programmable gate array (FPGA) is used to determine the population spike amplitude by a process of filtering, differentiation and intelligent integration. As described in the previous section, non-linearities of the hippocampal system are expressed as Volterra kernels. Each kernel is expressed as a summation of basis functions which are chosen to be generalized Laguerre functions. Laguerre functions can be evaluated indirectly using a recursive tableau. Recursion is desirable for hardware implementation for several reasons. First, only one time step of memory is required; we can over-write each memory location as ‘stale’ results that are no longer needed. Second, the operating speed of the circuit can be greatly increased: only values required for the current time step need be calculated. Finally, the calculation never changes: hardware required for direct computation is much less complicated than a full programmable processor. Figure 33.14A shows, for several inputs of a random impulse train applied to the perforant path, results of the FPGA-based CA3 model prediction compared to biological CA3 responses

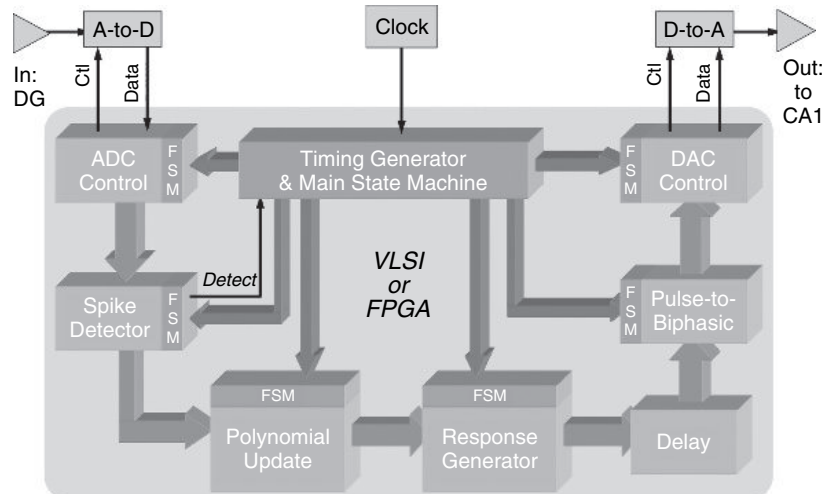


**FIGURE 33.13** A top-level system diagram showing the major functional blocks and the signal flow, including the relationship of the real time spike detection, the response generator and the output waveform generator which are all in the digital domain.

recorded from a hippocampal slice. It is evident that the correspondence between the hardware model and the biological system is high.

C programs for both population spike identification/measurement and non-linear input/output modeling were converted to VHDL code; the VHDL code then was used to program the FPGA. This is a common and convenient strategy to converge on a VLSI implementation, because the FPGA system provides a flexible, programmable environment for optimizing the desired functionalities in terms of a VHDL code, and the VHDL code is readily translated into VLSI design, minimizing the risk associated with developing a microchip device. Two generations of VLSI device have been designed, fabricated and tested. All functions necessary for implementing a CA3 model (for one hippocampal ‘slice’) are included on the small footprint of the chip (1.1 mm × 1.1 mm), except for the actual A/D and D/A converters (see Figure 33.14B).

#### ‘CONFORMAL’ MULTISITE ELECTRODE ARRAYS FOR INTERFACING THE BIOMIMETIC MODEL OF CA3 WITH HIPPOCAMPAL TISSUE

A biomimetic device for central brain regions must interact bi-directionally with the undamaged brain to support cognitive function and influence behavior. One of the indisputable characteristics of the mammalian brain is that anatomical connections between multiple neurons in one brain region and multiple neurons in a second brain region are not random – there is typically an identifiable topography in which neurons from one subregion of a given brain region project primarily to a localized subset of neurons in the target structure. Moreover, virtually all brain areas have region-specific cytoarchitectures, e.g. varying degrees of cellular and/or dendritic layering, geometries of curvature, etc., within which topographical connections are embedded. As a consequence of these considerations, bi-directional communication between a biomimetic device and the brain must be accomplished with one or more multisite electrode arrays, with the spatial distribution and density of recording/stimulating electrodes designed to match (be ‘conformal’ with) the cytoarchitecture and topography-density of the brain regions providing the inputs and outputs of the device.

Two specific types of conformal multielectrode arrays have been implemented (Berger et al., 2005a; Ghalmeh et al., 2006): (1) a multisite stimulation/recording multielectrode array capable of sampling the entire trisynaptic pathway, including the dentate gyrus, CA1 and CA3 regions of rat hippocampus (‘trisynaptic cMEAs’) and (2) a stimulation/recording multielectrode array capable of stimulating at the input to the dentate, recording the output from the dentate, interfacing with an external electronic or computer system that is capable of simulating the non-linear input/output characteristics of the CA3 hippocampal region, stimulating at the input to CA1, recording the output from CA1 and interfacing once again with an external electronic or computer system (‘CA3 replacement cMEAs’). CA3 replacement demonstration experiments to date have been based on both computer and field-programmable gate array (FPGA) interfaces, pointing toward full integration with an application-specific integrated circuit (ASIC) implemented in a silicon-based very-large-scale-integrated (VLSI) circuit.

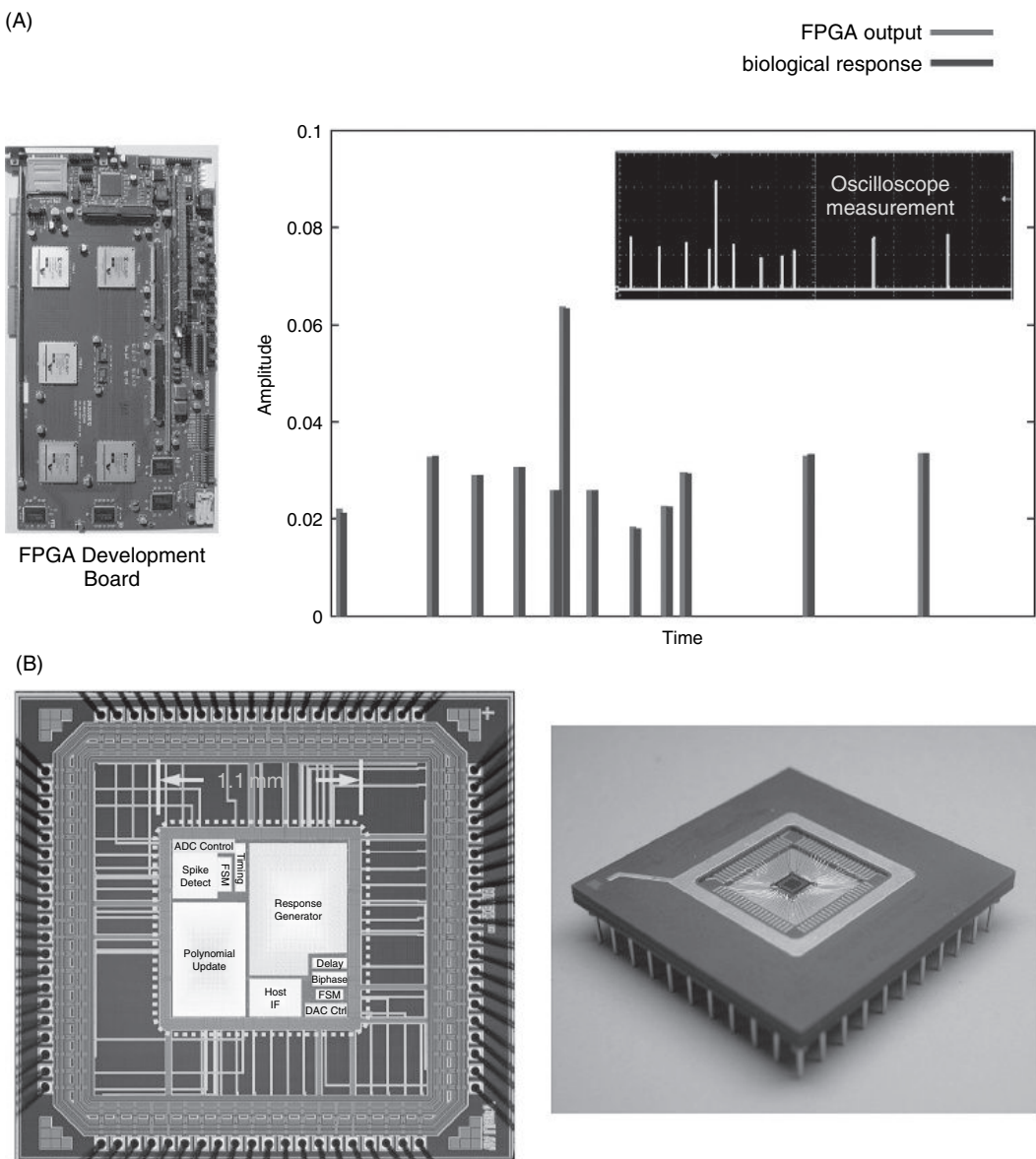


**FIGURE 33.14** (A) Comparison of FPGA-based non-linear model predictions of hippocampal CA3 output with biological CA3 output as a function of dentate population spike input for a segment of random impulse train stimulation of perforant path. Predicted (red bars) and electrophysiologically recorded CA3 population spike amplitudes (blue bars) are shown for a segment of random interval train stimulation. Recorded dentate population spike amplitudes for impulses within the random interval train were used as model input. (B) Left: schematic of the VLSI device to substitute for the CA3 region of one hippocampal slice. Right: photograph of the fabricated microchip. (See Plate 29 in color plate section.)

The trisynaptic cMEA design, as shown in Figure 33.15, includes nine sets of seven linearly-spaced 28  $\mu\text{m}$  diameter pads with a 50  $\mu\text{m}$  center-to-center spacing, each set spanning one of the key input/output regions of the DG, CA3 and CA1 regions of rat hippocampus, thereby allowing for a complete diagnostic assessment of the non-linear dynamics of the trisynaptic hippocampal circuitry. The CA3 replacement cMEA design, as shown in Figure 33.15, includes two different circular pad sizes: (i) 28  $\mu\text{m}$  diameter pads with a 50  $\mu\text{m}$  center-to-center spacing are grouped in series to form sets of stimulating pads in dentate gyrus (three at a time) and CA1 (two at a time), and (ii) 36  $\mu\text{m}$  diameter pads also with a 50  $\mu\text{m}$  center-to-center spacing are used for recording in DG, CA3 and CA1. By grouping sets of stimulating pads in series, we are able to achieve significantly larger pad surface areas and correspondingly larger total stimulating currents than are achievable with single pads, while still maintaining essential conformality to cytoarchitecturally relevant features. These

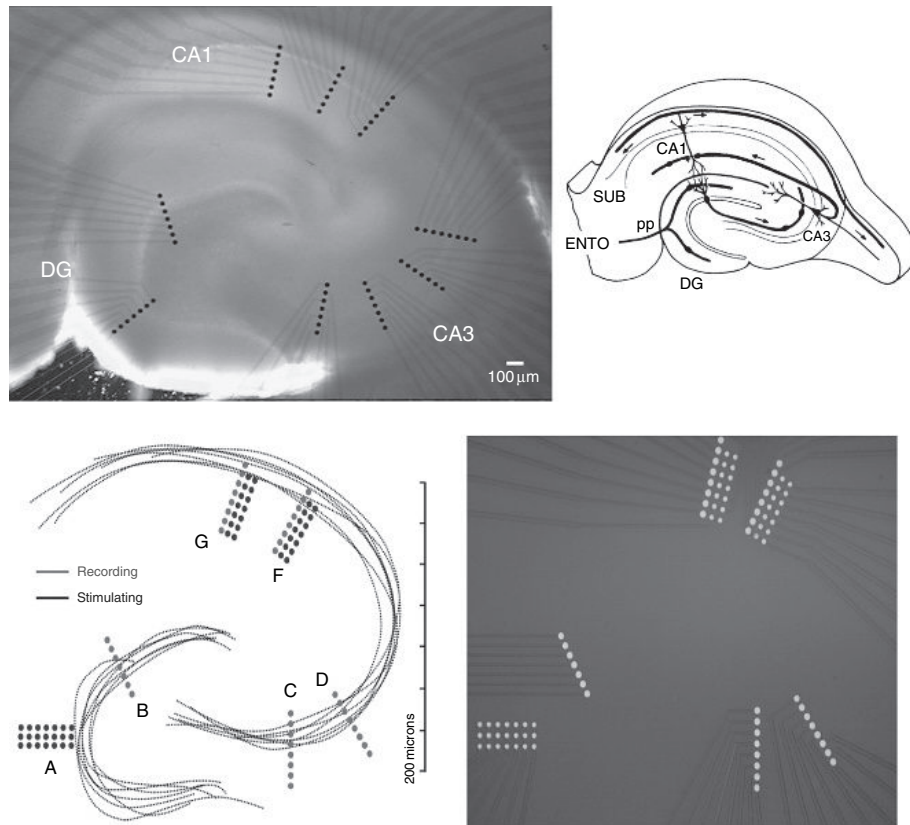


**FIGURE 33.15** Top panels: left, optical photomicrograph of a cMEA incorporating the trisynaptic electrode pad layout that is proximity-coupled to a rat hippocampal slice. The nine sets of seven linearly-spaced 28  $\mu\text{m}$  diameter pads conform to the DG, CA3 and CA1 regions. Right, diagram of hippocampal cell regions. Bottom panels: optical photomicrograph of the central region of a new conformal multielectrode array specifically designed for CA3 replacement demonstration. Stimulating and recording electrodes are arranged in both the DG and CA1 regions, while two sets of recording electrodes are provided in the CA3 region for pre-replacement characterization. (See Plate 30 in color plate section.)

stimulating pads have been placed only in DG and CA1 in order to interface with the FPGA/VLSI hardware that replaces the CA3 region entirely and, thereby, to support the envisioned CA3 replacement experiment protocol.

The general microfabrication procedure employed for these cMEAs is described below. A set of indium tin oxide (ITO) electrical leads is defined on an ITO-coated glass substrate of dimensions 49 mm  $\times$  49 mm  $\times$  1.1 mm by the first photomask exposure and subsequent acid-bath etching. A silicon nitride insulation layer is then deposited by means of plasma-enhanced chemical vapor deposition (PECVD). This layer electrically insulates individual ITO lines from each other and from the saline solution that the cMEA will be exposed to during acute slice testing. A second photomask is then used to define the vias that will form the *conformal* metal (Cr/Au) electrode tips. The Cr/Au metal layer is deposited by electron-beam evaporation. After deposition of a second insulating layer composed of SU-8 photoresist, a final photolithographic exposure is performed to pattern vias through the insulation layer to the previously deposited gold electrodes. The thick (1.5  $\mu\text{m}$ ) epoxy-based SU-8 photoresist provides for decreased shunt capacitance of the cMEA as a whole, thereby enabling higher amplitude neural recordings. The array pinout includes 60 signal channels and is designed to be compatible with the multichannel systems MEA-60 apparatus.

#### SYSTEM INTEGRATION: RESTORATION OF HIPPOCAMPAL CIRCUIT DYNAMICS WITH THE CA3 PROSTHESIS

Recall that the goal of this multidisciplinary effort is to achieve the stage 1 prosthetic system for the hippocampal slice by integrating the components described above. More specifically, we seek functionally to replace the biological CA3 subregion of the hippocampal slice with an FPGA/VLSI-based model of the non-linear dynamics of CA3, such that the

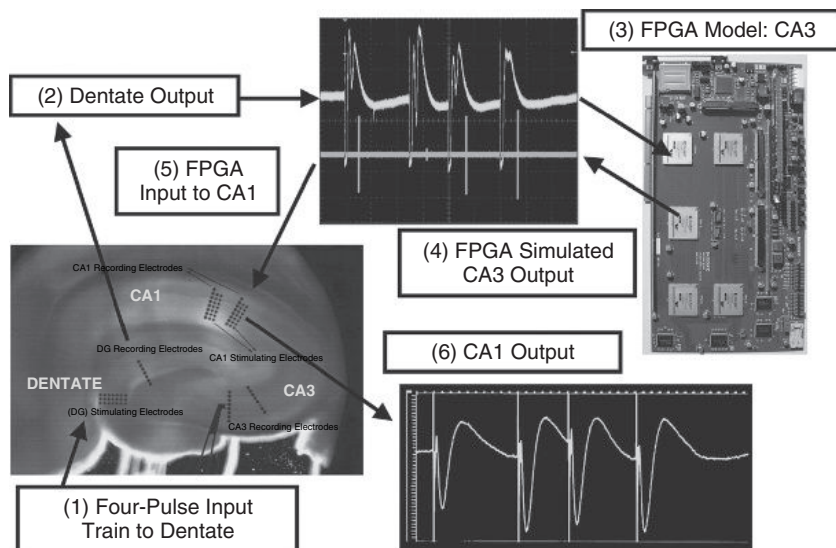


**FIGURE 33.16** System integration of an FPGA-based non-linear model of the CA3 hippocampal region with a hippocampal slice in which the output from the dentate gyrus (mossy fibers in the hilus) have been transected, thus eliminating the normal propagation of activity from dentate→CA3→CA1. The FPGA-based model bi-directionally communicates with the living slice through a conformal, planar, multisite electrode array. This system supports real-time, communication of stimulation-induced responses of dentate granule cells from the slice to the FPGA, generation of CA3-like outputs from the FPGA device, FPGA-triggered stimulation of CA1 and recording of electrophysiological output from CA1. (See Plate 31 in color plate section.)

propagation of temporal patterns of activity from dentate → VLSI model → CA1 reproduces that observed experimentally in the biological dentate → CA3 → CA1 circuit. We have successfully performed the first integration of an FPGA-based non-linear model of the CA3 hippocampal region with the hippocampal slice, by interconnecting the FPGA and the living slice through a conformal, planar, multisite electrode array. At the time of this review, we have succeeded in supporting real-time, communication of stimulation-induced responses of dentate granule cells from the slice to the FPGA, generation of CA3-like outputs from the FPGA device, FPGA-triggered stimulation of CA1 and recording of electrophysiological output from CA1.

The preparation we are using to test our stage 1 prosthetic system is a hippocampal slice with severed CA3 afferents (see Figure 33.16; hippocampal slice shown in lower left panel 1; the transection cannot be seen visually). Electrical stimulation of inputs to the dentate gyrus still evokes excitatory responses from dentate granule cells in this preparation, but excitation cannot propagate through the remainder of the trisynaptic pathway, i.e. to CA3 and from CA3 to CA1. To re-instate the function of CA3 and thus re-instate propagation through the trisynaptic circuit, we have interconnected our FPGA model of CA3 through the specially-designed, conformal multisite electrode array (black dots in the slice photomicrograph) described in the previous section, which allows recording electrical activity from, and stimulating electrical activity in, the slice.

A demonstration of the integration of all components of our hippocampal slice prosthesis is shown in Figure 33.16. In this example, we have used as inputs to a transected slice only a subset of possible stimulation patterns and, more specifically, four-impulse trains with variable inter-impulse intervals. Although limited in terms of number of impulses, the inter-impulse intervals were chosen to evoke large-magnitude non-linearities in the responses of dentate granule cells. Thus, stimulation of inputs to the dentate with a variable-interval four-impulse train (see Figure 33.16) generates variable-amplitude output from dentate granule cells (2). The output is recorded by the multisite array and transmitted to the FPGA model of CA3 (3). The FPGA model A/D converts the extracellular population waveform, identifies the population spike component of that waveform and calculates its amplitude. Based on the amplitude and history of inter-impulse intervals, the FPGA-based non-linear model of CA3 computes the appropriate CA3 output in terms of biphasic stimulation pulses (4) – the magnitude of which is equivalent to the population spike amplitude that would have been generated in the CA3 by that particular output. The biphasic output pulses generated by the FPGA are transmitted through the multisite array and used to stimulate electrically inputs to CA1 (5). The resulting variable-amplitude output (population excitatory postsynaptic potential, or population EPSP) is recorded from CA1 (6), demonstrating the functional re-instatement of the dentate →

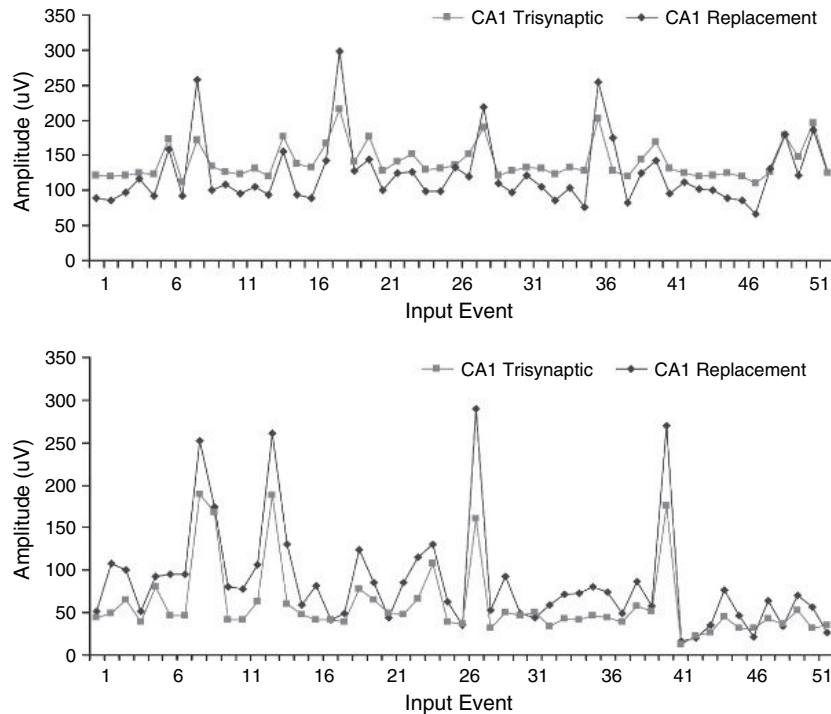


**FIGURE 33.17** A comparison of hippocampal CA1 output in response to the FPGA model of CA3 with the output of CA1 in response to the biological CA3. Examples of results from two random impulse train experiments are shown in the two panels, respectively: amplitudes of population EPSPs recorded from the CA1 region are shown as a function of 50 impulses chosen from among 2400 impulses of the random trains (1200 administered before transecting inputs to CA3; 1200 administered after transection). Time intervals between impulses are not represented in the figures; only ‘Input Event’ number (sequence of sample impulses) is shown to ‘collapse’ the x-axis. Data for the intact slice (CA1 Trisynaptic) are shown in pink boxes; data for the ‘hybrid’ slice with the substituted FPGA model of CA3 (CA1 replacement) are shown in blue diamonds. For what is a wide range of intervals captured in this 50-impulse sequence, and what is a 3–5-fold difference in population EPSP amplitude, note that CA1 output from the ‘hybrid’ slice matches extremely well the CA1 output from the intact slice. (See Plate 32 in color plate section.)

CA3 → CA1 circuit. These above results demonstrate that the various components we have proposed for our prosthesis can be developed and effectively integrated into a working system.

We are currently in the process of fully evaluating the output generated in the CA1 region by our CA3 prosthesis system, i.e. comparing CA1 output in response to the FPGA model of CA3 with the output of CA1 in response to the biological CA3 (Berger et al., 2005a). For these tests, we are using random impulse train stimulation of the perforant path (rather than four-impulse trains with variable inter-impulse intervals as described for Figure 33.16). Examples of results from two random impulse train experiments are shown in Figure 33.17. Each panel illustrates results from one experiment: amplitudes of population EPSPs recorded from the CA1 region are shown as a function of 50 impulses chosen from among 2400 impulses of the random trains (1200 administered before transecting inputs to CA3; 1200 administered after transection). Time intervals between impulses are not represented in the figures; only ‘Input Event’ number (sequence of sample impulses) is shown to ‘collapse’ the x-axis. Data for the intact slice (CA1 trisynaptic) are shown in pink boxes; data for the ‘hybrid’ slice with the substituted FPGA model of CA3 (CA1 replacement) are shown in dark blue diamonds. For what is a wide range of intervals captured in this 50-impulse sequence, and what is a 3–5-fold difference in population EPSP amplitude, CA1 output from the ‘hybrid’ slice matches extremely well the CA1 output from the intact slice. In particular, those intervals that generate large amplitude CA1 population EPSPs in the intact slice also are the only intervals that are associated with the large amplitude CA1 responses in the hybrid slice. The biomimetic device does not generate unexpected or ‘aberrant’ dysfunctional, large amplitude CA1 responses. Importantly, intervals that lead to smaller scale fluctuations in CA1 output of the CA1 slice also emerge in the hybrid system, i.e. subtle aspects of hippocampal trisynaptic circuit dynamics also are faithfully reproduced. We have begun the process of expanding the hippocampal ‘proof-of-principle’ prosthesis demonstrated for the hippocampal slice to an expanded multi-input, multi-output prosthesis for the behaving animal (Espana et. al., 2006; Granacki et al., 2006; Song et al., 2006).

## CONCLUSIONS

We have proposed here a novel combination of several cutting-edge technologies that, when fully integrated, would provide the basis for a closed-loop system that:

1. predicts the onset of hippocampal seizure using glutamate-sensitive microelectrodes
2. prevents the imminent epileptiform activity through intra-hippocampal infusion of inhibitory agents to suppress glutamatergic synaptic transmission and
3. maintains normal hippocampal mnemonic function through a biomimetic device that provides a means for ‘by-passing’ that portion of hippocampal circuitry (e.g. CA3) rendered inactive by the infusion of antiepileptiform agents.

We realize this is an ambitious goal and, frankly, it must be recognized as a futuristic goal. Accomplishing this end requires not only completing design and testing of each of the three systems just outlined above, but also effectively integrating all three of them into a global system working together. Despite the challenges, we are motivated to pursue this direction for several reasons. First, the benefit to epilepsy patients that would emerge from the success of such an endeavor would represent a remarkable advance in treatment. Second, as is hopefully apparent in this chapter, the global goal of a closed-loop system incorporating seizure prediction, prevention of epileptiform activity and maintenance of normal hippocampal activity, can in fact be reduced to a series of progressively smaller goals, each having their own measurable benefit upon completion. Third, and we feel importantly, the process of achieving such a goal would not only compel ‘beyond the envelope’ advances in fundamental neuroscience, engineering and clinical science, but also would hallmark the benefits of highly interdisciplinary, multitechnology research thrusts.

## REFERENCES

- Alataris, K., Berger, T.W. and Marmarelis, V.Z. (2000). A novel network for nonlinear modeling of neural systems with arbitrary point-process inputs. *Neural Netw* 13:255–266.
- Amaral, D.G. and Witter, M.P. (1989). The three dimensional organization of the hippocampal formation: a review of anatomical data. *Neuroscience* 31:571–591.
- Andersen, P., Bliss, T.V.P. and Skrede, K.K. (1971). Lamellar organization of hippocampal excitatory pathways. *Exp Brain Res* 13:222–238.
- Berger, T.W., Eriksson, J.L., Port, R., Robinson, G. and Sclabassi, R.J. (1988a). Nonlinear systems analysis of the hippocampal perforant path-dentate projection. II. Effects of random train stimulation. *J Neurophysiol* 60:1077–1094.
- Berger, T.W., Eriksson, J.L., Port, R., Robinson, G. and Sclabassi, R.J. (1988b). Nonlinear systems analysis of the hippocampal perforant path-dentate projection. III. Comparison of random train and paired impulse analyses. *J Neurophysiol* 60:1095–1109.
- Berger, T.W., Harty, T.P., Xie, X., Barrionuevo, G. and Sclabassi, R.J. (1992). Modeling of neuronal networks through experimental decomposition. *Proc IEEE 34th Mid Symp Cir Sys* 91–97.
- Berger, T.W., Chauvet, G. and Sclabassi, R.J. (1994). A biologically based model of functional properties of the hippocampus. *Neural Netw* 7:1031–1064.
- Berger, T.W., Baudry, M., Brinton, R.D. et al. (2001). Brain-implantable biomimetic electronics as the next era in neural prosthetics. *Proc IEEE* 89:993–1012.
- Berger, T.W., Granacki, J.J., Marmarelis, V.Z., Sheu, B.J. and Tanguay, A.R. Jr (2003). Brain-implantable biomimetic electronics as neural prosthetics. *Proc 1st Inter IEEE EMBS Conf on Neural Eng* 108–111.
- Berger, T.W., Ahuja, A., Courellis, S.H. et al. (2005a). Hippocampal-cortical neural prostheses to restore lost cognitive function. *IEEE EMBS Special Issue: Toward biomimetic microelectronics as neural prostheses* 24:30–44.
- Berger, T.W., Brinton, R.B., Marmarelis, V.Z., Sheu, B.J. and Tanguay, A.R. Jr (2005b). VLSI implementations of biologically realistic hippocampal neural network models. In: *Toward replacement parts for the brain: implantable biomimetic electronics as the next era in neural prosthetics* (T.W. Berger and D.L. Glanzman, eds) pp. 241–275. MIT Press, Cambridge.
- Borland, L.M., Shi, G., Yang, H. and Michael, A.C. (2005). Voltammetric study of extracellular dopamine near microdialysis probes acutely implanted in the striatum of the anesthetized rat. *J Neurosci Meth* 146(2):149–158.
- Bruno, J.P., Gash, C., Martin, B. et al. (2006). Second-by-second measurement of acetylcholine release in prefrontal cortex. *Eur J Neurosci* 24(10):2749–2457.
- Burmeister, J.J. and Gerhardt G.A. (2001). Self-referencing ceramic-based multisite microelectrodes for the detection and elimination of interferences from the measurement of L-glutamate and other analytes. *Anal Chem* 73(5):1037–1042.
- Burmeister, J.J., Moxon, K. and Gerhardt, G.A. (2000). Ceramic-based multisite microelectrodes for electrochemical recordings. *Anal Chem* 72(1):187–192.
- Burmeister, J.J., Pomerleau, F., Palmer, M., Day, B.K., Huettl, P. and Gerhardt, G.A. (2002). Improved ceramic-based multisite microelectrode for rapid measurements of L-glutamate in the CNS. *J Neurosci Meth* 119(2):163–171.
- Burmeister, J.J., Palmer, M. and Gerhardt, G.A. (2005). L-lactate measures in brain tissue with ceramic-based multisite microelectrodes. *Biosens Bioelectron* 20(9):1772–1779.

- Cavus, I., Kasoff, W.S., Cassaday, M.P. et al. (2005). Extracellular metabolites in the cortex and hippocampus of epileptic patients. *Ann Neurol* 57(2):226–235.
- Choi, D.W. (1988). Glutamate neurotoxicity and diseases of the nervous system. *Neuron* 1(8):623–634.
- Clapp-Lilly, K.L., Roberts, R.C., Duffy, L.K., Irons, K.P., Hu, Y. and Drew, K.L. (1999). An ultrastructural analysis of tissue surrounding a microdialysis probe. *J Neurosci Meth* 90(2):129–142.
- Cohen-Gadol, A.A. and Spencer, D.D. (2003). Use of an anteromedial subdural strip electrode in the evaluation of medial temporal lobe epilepsy. *J Neurosurg* 99(5):1–3.
- Dalal, S.S., Marmarelis, V.Z. and Berger, T.W. (1997). A nonlinear positive feedback model of glutamatergic synaptic transmission in dentate gyrus. *Proc 4th Joint Symp Neural Comput* 7:68–75.
- Danbolt, N.C. (2001). Glutamate uptake. *Prog Neurobiol* 65(1):1–105.
- Day, B.K., Pomerleau, F., Burmeister, J.J., Huettl, P. and Gerhardt, G.A. (2006). Microelectrode array studies of basal and potassium-evoked release of L-glutamate in the anesthetized rat brain. *J Neurochem* 96(6):1626–1635.
- Dimoka, A., Courellis, S.H., Song, D., Marmarelis, V.Z. and Berger, T.W. (2003). Identification of lateral and medial perforant path using single- and dual-input random impulse train stimulation. *Proc IEEE EMBS Conf* 1933–1936.
- Duncan J.S., Sander J.W., Sisodiya S.M. and Walker, M.C. (2006). Adult epilepsy. *Lancet* 1:1087–1100.
- During, M.J. and Spencer, D.D. (1993). Extracellular hippocampal glutamate and spontaneous seizure in the conscious human brain. *Lancet* 26:1607–1610.
- Engel, J. Jr (1998). Research on the human brain in an epilepsy surgery setting. *Epilepsy Res* 32(1-2):1–11.
- Espana, R.A., Shi, L., Collins, V. et al. (2006). A neural prosthesis for hippocampus: multichannel stimulation of rat hippocampal CA1 and CA3 layers with behaviorally relevant ensemble firing patterns. *Soc Neurosci Abstr* 31:65.7.
- Fountas, K.N., Smith, J.R., Murro, A.M., Politsky, J., Park, Y.D. and Jenkins, P.D. (2005). Implantation of a closed-loop stimulation in the management of medically refractory focal epilepsy: a technical note. *Stereotact Funct Neurosurg* 83(4):153–158.
- Gallassi, R. (2006). Epileptic amnesia syndrome: an update and further considerations. *Epilepsia*. 47 (Suppl 2):103–105.
- Galvan, A., Smith, Y. and Wichmann, T. (2003). Continuous monitoring of intracerebral glutamate levels in awake monkeys using microdialysis and enzyme fluorometric detection. *Neurosci Meth* 126(2):175–185.
- Gerhardt, G.A. and Hoffman, A.F. (2001). Effects of recording media composition on the responses of Nafion-coated carbon fiber microelectrodes measured using high-speed chronoamperometry. *J Neurosci Meth* 109(1):13–21.
- Gholmeh, G., Courellis, S.H., Song, D., Wang, Z., Marmarelis, V.Z. and Berger, T.W. (2003). Characterization of short-term plasticity of the dentate gyrus-CA3 system using nonlinear systems analysis. *Proc IEEE EMBS Conf* 1929–1932.
- Gholmeh, G., Courellis, S., Dimoka, A. et al. (2004). An algorithm for real-time extraction of population EPSP and population spike amplitudes from hippocampal field potential recordings. *J Neurosci Meth* 136:111–121.
- Gholmeh, G., Courellis, S., Marmarelis, V.Z. and Berger, T.W. (2005). Detecting CA1 short-term plasticity variations with changes in stimulus intensity and extracellular medium composition. *Neurocomputing* 63:465–481.
- Gholmeh, G., Soussou, W., Han, M. et al. (2006). Custom-designed, high-density conformal planar multielectrode arrays for brain slice electrophysiology. *J Neurosci Meth* 152:116–129.
- Giannakopoulos, F., Bihler, U., Hauptmann, C. and Luhmann, H.J. (2001). Epileptiform activity in a neocortical network: a mathematical model. *Biol Cybernet* 85(4):257–268.
- Granacki, J.J., Wills, J.D., LaCoss, J. et al. (2006). A neural prosthesis for hippocampus: mixed-signal system-on-chip. *Soc Neurosci Abstr* 31: 65.9.
- Grewer, C. and Rauen, T. (2005). Electrogenic glutamate transporters in the CNS: molecular mechanism, pre-steady-state kinetics, and their impact on synaptic signaling. *J Membr Biol* 203(1):1–20.
- Grondin, R., Zhang, Z., Yi, A. et al. (2002). Chronic, controlled GDNF infusion promotes structural and functional recovery in advanced parkinsonian monkeys. *Brain* 125:2191–2201.
- Hascup, K.N., Rutherford, E.C., Quientero, J.E. et al. (2007). Second-by-second measures of L-glutamate and other neurotransmitters using enzyme-based microelectrode arrays. In: *Electrochemical methods for neuroscience* (A.C. Michael and L.M. Borland, eds) pp. 407–451. CRC Press, Boca Raton.
- Iasemidis, L.D., Shiao, D.S., Pardalos, P.M., Chaovalltwongse, W., Narayanan, K., Prasad, A., Tsakalis, K., Carney, P.R. and Sackellares, J.C. (2005). Long-term prospective on-line real-time seizure prediction. *Clin Neurophysiol* Mar 116(3):532–544.
- Iatrou, M., Berger, T.W. and Marmarelis, V.Z. (1999a). Modeling of nonlinear nonstationary dynamic systems with a novel class of artificial neural networks. *IEEE Transact Neural Netw* 10:327–339.
- Iatrou, M., Berger, T.W. and Marmarelis, V.Z. (1999b). Application of a novel modeling method to the nonstationary properties of potentiation in the rabbit hippocampus. *Ann Biomed Eng* 27:581–591.
- Jefferys, J.G. (2003). Models and mechanisms of experimental epilepsies. *Epilepsia* 12:44–50.
- Kodama, T., Hikosaka, K. and Watanabe, M. (2002). Differential changes in glutamate concentration in the primate prefrontal cortex during spatial delayed alternation and sensory-guided tasks. *Exp Brain Res* 145(2):133–141.
- Leppik, I.E. (1992). Intractable epilepsy in adults. *Epilepsy Res Suppl* 5:7–11.
- Leppik, I.E. (2006). Epilepsy in the elderly. *Epilepsia* 47:65–70.
- Liley, D.T. and Bojak, I. (2005). Understanding the transition to seizure by modeling the epileptiform activity of general anesthetic agents. *J Clin Neurophysiol* 22(5):300–313.
- Litt, B. and Lehnertz, K. (2002). Seizure prediction and the preseizure period. *Curr Opin Neurol* 15(2):173–177.
- Lopes da Silva, F.H., Pijn, J.P. and Wadman, W.J. (1994). Dynamics of local neuronal networks: control parameters and state bifurcations in epileptogenesis. *Prog Brain Res* 102:359–370.
- Loscher, W. (1997). Animal models of intractable epilepsy. *Prog Neurobiol* 53(2):239–258.
- Lytton, W.W., Contreras, D., Destexhe, A. and Steriade, M. (1997). Dynamic interactions determine partial thalamic quiescence in a computer network model of spike-and-wave seizures. *J Neurophysiol* 77(4):1679–1696.
- Marmarelis, V.Z. (1993). Identification of nonlinear biological systems using Laguerre expansions of kernels. *Ann Biomed Eng* 21:573–589.
- Marmarelis, V.Z. (2004). Nonlinear dynamic modeling of physiological system. Wiley Interscience & IEEE Press, New York.

- Miller, D.B. and O'Callaghan, J.P. (2003). Effects of aging and stress on hippocampal structure and function. *Metabolism* 52:17–21.
- Morrell, M. (2006). Brain stimulation for epilepsy: can scheduled or responsive neurostimulation stop seizures? *Curr Opin Neurol* 19(2):164–168.
- Nickell, J., Pomerleau, F., Allen, J. and Gerhardt, G.A. (2005). Age-related changes in the dynamics of potassium-evoked L-glutamate release in the striatum of Fischer 344 rats. *J Neural Transm* 112(1):87–96.
- Nickell, J., Salvatore, M., Pomerleau, F., Apparsundaram, S. and Gerhardt, G.A. (2006). Reduced plasma membrane surface expression of GLAST mediates decreased glutamate regulation in the aged striatum. *Neurobiol Aging* (Epub ahead of print).
- Nilsen, K.E. and Cock, H.R. (2004). Focal treatment for refractory epilepsy: hope for the future? *Brain Res Brain Res Rev* 44(2-3):141–153.
- Oliveira, P.A., Garzon, E., Caboclo, L.O. et al. (2006). Can intraoperative electrocorticography patterns predict surgical outcome in patients with temporal lobe epilepsy secondary to unilateral mesial temporal sclerosis? *Seizure* 15(7):541–551.
- Pomerleau, F., Day, B.K., Huettl, P., Burmeister, J.J. and Gerhardt, G.A. (2003). Real time in vivo measures of L-glutamate in the rat central nervous system using ceramic-based multisite microelectrode arrays. *Ann NY Acad Sci* 1003: 454–457.
- Quintero, J.E., Day, B.K., Zhang, Z., Grondin, R., Stephens, M.L., Huettl, P., Pomerleau, F., Gash, D.M. and Gerhardt, G.A. Rapid amperometric measures of age-related changes in glutamate regulation in cortex of rhesus monkeys. *Experimental Neurology* (Article in Press).
- Richardson, K.A., Gluckman, B.J., Weinstein, S.L. et al. (2003). In vivo modulation of hippocampal epileptiform activity with radial electric fields. *Epilepsia* 44(6):768–777.
- Sclabassi, R.J., Krieger, D.N. and Berger, T.W. (1998a). A systems theoretic approach to the study of CNS function. *Ann Biomed Eng* 16:17–34.
- Sclabassi, R.J., Eriksson, J.L., Port, R., Robinson, G. and Berger, T.W. (1998b). Nonlinear systems analysis of the hippocampal perforant path-dentate projection. I. Theoretical and interpretational considerations. *J Neurophysiol* 60:1066–1076.
- Sclabassi, R.J., Liu, Q., Hackworth, S.A., Justin, G.A. and Sun, M. (2006). Platform technologies to support brain-computer interfaces. *Neurosurg Focus* 20(5):E5.
- Shin, C. and McNamara, J.O. (1994). Mechanism of epilepsy. *Annu Rev Med* 45:379–389.
- Song, D., Chan, H.M., Marmarelis, V.Z., Hampson, R., Deadwyler, S.A. and Berger, T.W. (2006). A neural prosthesis for hippocampus: physiological plausible stochastic nonlinear kernel models of CA3 spike train to CA1 spike train transformation. *Soc Neurosci Abstr* 31:65.3.
- Song, D., Chan, R.H.M., Marmarelis, V.M., Hampson, R.E., Deadwyler, S.A. and Berger, T.W. (2007). Nonlinear dynamic modeling of spike train transformations for hippocampal-cortical prostheses. *IEEE Transact Biomed Eng* (in press).
- Srinivasan, V., Will, J.D., LaCoss, J. et al. (2004). Real-time hardware neural spike amplitude extraction. *Proc IEEE Workshop Biol Cir Sys(BioCAS2004)*, Singapore.
- Stein, A.G., Eder, H.G., Blum, D.E., Drachev, A. and Fisher, R.S. (2000). An automated drug delivery system for focal epilepsy. *Epilepsy Res* 39(2):103–114.
- Sun, M., Justin, G.A., Roche, P.A. et al. (2006). Passing data and supplying power to neural implants. *IEEE Eng Med Biol Mag* 25(5):39–46.
- Traub, R.D., Knowles, W.D., Miles, R. and Wong, R.K. (1987). Models of the cellular mechanism underlying propagation of epileptiform activity in the CA2-CA3 region of the hippocampal slice. *Neuroscience* 21(2): 457–470.
- Volterra, V. (1930). Theory of functions and of integral and integro-differential equations. Dover Publications Inc., New York.
- Wendling, F., Bartolomei, F., Bellanger, J.J. and Chauvel, P. (2002). Epileptic fast activity can be explained by a model of impaired GABAergic dendritic inhibition. *Eur J Neurosci* 15(9):1499–1508.
- Wiener, N. (1958). Nonlinear problems in random theory. The Technology Press of MIT and Wiley, New York.
- Williamson, A., Spencer, S.S. and Spencer, D.D. (1995). Depth electrode studies and intracellular dentate granule cell recordings in temporal lobe epilepsy. *Ann Neurol* 38(5):778–787.
- Zentner, J., Hufnagel, A., Wolf, H.K. et al. (1995). Surgical treatment of temporal lobe epilepsy: clinical, radiological, and histopathological findings in 178 patients. *J Neurol Neurosurg Psychiatr* 58(6):666–673.

# INDEX

---

- Absence (petit mal) seizures, 19, 349, 375, 428  
GAERS model, 395, 402  
  fast spike-and-wave oscillations, 204  
hypersynchronized oscillations, 185–186  
interictal cortical output, 45  
mean-field models, 399, 400  
  scalp EEG data comparison, 395  
network model, 403–417  
prediction, 416–417  
spike and wave discharges *see* Spike and wave activity  
thalamic involvement, 186–188  
thalamocortical mechanisms, 197–203, 209–210  
thalamocortical network extended lumped model, 404–406, 414  
  anticonvulsant drug effects simulation, 415  
  bistability properties, 408–409, 414, 416  
  connectivity, 407  
  cortical/thalamic module time dependencies, 411–412  
  counter-stimulation, 412–413  
  inputs/outputs, 407, 412–413  
  mean membrane potential conversion to firing rate, 406  
  noise levels, 410–411, 416  
  paroxysmal discharges, 409, 414, 416, 421, 509  
  paroxysmal epoch duration, 409–411, 414  
  rat experimental observations comparison, 414, 415  
  spindle-like oscillatory behavior, 407, 409  
  synaptic transmission, 406  
  termination of paroxysmal activity, 410, 414, 416  
  wakefulness-sleep transition simulation, 415–416  
Wag-Rij rat genetic model, 208, 404, 410  
Action potential propagation speed, *neuroConstruct* network models, 58  
Activity spread (balanced activation), 132–139  
  current models, 132–133  
  inhibitory/excitatory nodes, 132  
  network topology, 133  
Activity-dependent neuronal regulation, 249–252, 255  
  computational models, 251  
  experimental evidence, 250  
gamma oscillations/synchronized bursts alternation, 347  
long-lasting excitability blockade effects, 261  
potassium ion extracellular concentration, 421  
  synaptic currents modulation, 435–437  
Afterhyperpolarization, 311  
  complex artificial cell models, 10  
data mining, 13  
seizure activity, 44  
Alpha rhythm, 359  
  mean-field corticothalamic model, 379, 380, 386  
  neuronal population models, 366–369, 372  
  thalamocortical network extended model, 404  
Alzheimer's disease, 256, 281  
AMBER, 519  
4-Aminopyridine seizure-like events, 291, 296–297, 305, 497–498  
  excitatory-inhibitory interplay, 503–504  
  with low magnesium concentration, 499–500  
  role of gap junctions, 507–508  
Amitriptyline, 525  
Ammon's horn  
  stratum lacunosum moleculare, 73, 76  
  stratum oriens, 73  
  stratum pyramidale, 73  
  stratum radiatum, 73, 76  
  volumetric analysis, 75  
AMPA receptors  
  blockade  
    neocortical seizure-like activity induction, 179–180  
    thalamic spindle oscillation effects, 187  
  computer-aided drug design, 525  
  gamma oscillation mechanisms, 344  
  network models  
    cortical spike-and-wave seizures, 196  
    dentate gyrus, 101, 102  
    neocortex, 179, 344  
    thalamocortical, 200  
  thalamocortical relay cell–thalamic reticular nucleus cell reciprocal circuit model, 186  
  cooperative GABA<sub>B</sub> response, 192  
AMPA synaptic activity  
  complex artificial cell models, 10  
  cortical homeostatic plasticity model, 266, 266–267  
  homeostatic processes following chronic activity blockade, 266  
  *neuroConstruct* granule cell 3D network model, 65  
  visual cortex modeling, 319  
Amperometry, 562  
Amygdala  
  graded persistent activity (spiking activity), 217  
  initial slow waves, 441, 446  
  medial temporal lobe epilepsy  
    interictal spikes, 361–363  
    transition to ictal activity, 360–361  
Amyotrophic lateral sclerosis, 567

- Anterior olfactory nucleus, 358–359  
 Anticonvulsants, 19  
   computer-aided design, 515–527  
   data mining applications, 15–16  
   effectiveness, 515  
   side effects, 515  
   simulation of effects in thalamocortical network extended lumped model, 414  
   timing of delivery, 524  
 Antiepileptic devices *see* Implantable devices  
 Artificial spiking cells, NEURON network modeling, 28–29  
 Associative learning, 281  
 Associative memory storage, 255  
 Attention-deficit/hyperactivity disorder, 567  
 Attractors  
   chaotic, 482, 484  
   graded persistent spiking activity modeling, 218–219  
   non-linear systems, 471, 472  
 Axo-axonic cells, 90, 113, 294  
   cell number estimation, 93  
   connectivity estimation, 94  
   inhibitory activity, 97  
 Basket cells, 89  
   cell number estimation, 93–94  
   connectivity estimation, 94–96  
   dentate gyrus sclerosis modeling, 97  
   feedforward/feedback inhibitory activity, 97  
   large network model  
    functional, 114  
    structural, 113  
   neocortex network model, 173–175  
   perforant path input, 102  
 Benzodiazepines, GABA<sub>A</sub> receptor effects, 67  
   experimental modulation in hippocampus CA3 area, 45  
 Beta rhythm  
   hippocampus neuronal population model, 376–377, 541  
   seizure initiation phase, 464–465  
 Beta2 oscillations, 349–351  
   conversion to very fast oscillations, 349, 351  
   epileptogenesis, 349  
   somatosensory cortex, 349  
 Bicuculline  
   GABA<sub>A</sub> antagonism  
    absence seizures, 193  
    spike and wave activity generation, 196  
    neocortical seizure-like activity, 180  
 Bifurcation analysis, 241  
   extracellular potassium ion concentration, slow bursting/tonic firing neural model behavior, 426–428  
   network model parameter values, 235–237  
 Biocytin histological method, 500  
 Bioinformatics, computer-aided drug design, 520  
 Biological accuracy, epilepsy models, 44  
 Blue Brain Project, 67  
*BrainSites*, 37, 38  
 Bursting mechanism  
   complex artificial cells, 10  
   single cell model transient oscillation triggered by potassium increase, 425–426  
   bifurcation analysis, 427–428  
   *see also* Epileptiform burst discharges  
 Cable properties, neuron modeling with NEURON, 21  
*Caenorhabditis elegans*, 48, 113  
 Calcium concentration/signaling  
   activity-dependent neuronal regulation, 249, 250, 255  
    network-level homeostasis, 255  
   graded persistent spiking activity, 217, 218, 221, 222, 224–225, 227  
   synaptic plasticity, 252  
    post-traumatic epileptogenesis, 261  
   thalamocortical relay cell/thalamic reticular nucleus cell reciprocal circuit model, 403  
    absence seizures, 410, 415  
 Calcium-activated cationic ion channels  
   graded persistent spiking activity, 215, 216, 221  
    calcium concentration influences, 217, 218, 220, 221–222, 225–226  
    computational modeling, 222  
    induction of new stable level, 220–221  
 Calretinin, 92  
 Cannabinoids, 50, 58  
 Carbamazepine, 16, 43, 525  
 Carbenoxolone, gap junction uncoupling, 297  
 Catacomb simulator, 25  
 Cationic ion channels, 217, 226  
   graded persistent spiking activity, 215, 217, 225, 227–229  
   hysteresis, 227  
 Cell models, *neuroConstruct* generation, 52  
 CellBuilder, 20, 21, 22, 23, 24  
 Cerebellar Purkinje neurons, 251  
   activity-independent regulation, 253  
 Chandelier cells, neocortex network model, 174, 175, 176  
 Channel Builder, 25  
 ChannelML, 59–60, 61, 63  
 Channelopathies, 19, 49  
 CHARMM, 519  
 Chemoinformatics, computer-aided drug design, 521  
 Chirps, instantaneous frequency estimation, 534–535, 537  
   from Hilbert transform, 537, 538  
   from line length, 537  
   from spectrogram peak, 537  
   from wavelet packets, 537  
 Chlorpromazine, 525  
 Cholecystokinin, 94  
 Cholinergic neurons  
   graded persistent activity, 216  
    hippocampal/entorhinal cortex theta rhythm, 282  
 Clinical data acquisition, 531–532  
 Clinical devices, 553–555  
   *see also* Implantable devices  
 Clonazepam, 186, 190, 415  
 Clonic discharges, 305  
 Cluster analysis, qualitative structure-activity relationships, 523  
 Clustering coefficient  
   cortical hierarchical cluster network model, 132  
   dentate gyrus large network model, 117, 125  
    topological assessment, 117  
    effects of progressive sclerosis, 118, 119  
 CoCoDat (Collation of Cortical Data) database, 34–42  
   access, 37  
    online browsing, 35, 37  
    adding content, 41  
   *BrainSites*, 37, 38  
   dataset extraction/visualization, 38–39  
   dataset inspection/export, 39–41  
   mapping concepts, 37

- structure, 35–36  
*SwitchBoard*, 35, 36, 37, 41
- Comparative molecular field analysis, computer-aided drug design, 524
- Compartmental models
- CoCoDat (Collation of Cortical Data) database, 35
  - dentate gyrus modeling, 89
  - large network simulations, 4, 5–7
    - supercomputing approaches, 7–9
    - time-step method, 6–7
  - neural function modeling, 173
  - neuronal gain modulation by background synaptic activity, 165
  - optimal parameter set determination for synchronous output, 234–237
  - simplification approaches, 5
  - simulation software, 49
  - simulation time, 4
  - single/multicompartment, 173
  - state variables, 9–10
- Complex artificial cells
- depolarization blockade, 10
  - epilepsy simulation, 11–12
    - latch-up (tonic) condition, 11, 16
  - large network simulations, 9–11
  - parameters, 9
  - post-spike afterhyperpolarization, 10, 11
  - refractory period, 10
  - state variables, 10
  - synaptic inputs, 10, 11
- Computer modeling goals, 3–4
- Computer-aided drug design, 516–527
- antiepileptic agents, 515–516
    - future targets, 526–527
    - protein folding problem, 522
    - receptor structure prediction, 522
    - specific examples, 524
  - assigning energy value to shape of drug/receptor, 518–520
  - bioinformatics, 520
  - chemoinformatics, 521
  - docking simulation, 523
  - energy minimization methods, 517, 518, 519–520
    - multiple minima problem, 519
  - lead compound identification, 522–523
    - high throughput screening, 517, 521, 523
    - rational drug design, 516, 522–523
  - lead compound optimization, 521, 522, 524
  - mechanics methods, 516, 517–519, 520
    - molecular mechanics, 516, 517, 518–519, 524
    - quantum mechanics, 517–518, 524, 525
  - molecular baggage component, 523
  - overview, 516
  - pharmacophore, 521, 522–523
    - receptor points of contact, 522
  - potential energy hyperspace exploration, 519, 520
  - quantitative structure-activity relationship studies, 521, 523, 525
- Connectivity, 48
- CoCoDat (Collation of Cortical Data) database, 35, 37
  - cortical extracellular potassium ion dynamics network model, 429
  - cortical hierarchical cluster organization, 133
    - activation spreading model, 134, 136–138
  - cortical homeostatic plasticity model, 267–269
  - cortical spike-and-wave seizure network models, 195
  - dentate gyrus
    - connectivity matrix development, 90–93, 113, 115
    - estimation from literature, 94–96
  - large network model, 113, 115
  - gap junction-mediated electrical coupling, 295
  - hippocampus 3D digital model, 72, 73, 76
    - intrinsic potential patterns, 80
  - local recurrent cortical circuits, 155
  - neocortex network model, 176
  - neural network models, 50
  - neuroConstruct* network models, 52, 55–56, 62
    - morphology based connections, 55
    - volume based connections, 55–56
  - NeuroML specifications, 57
  - NEURON network modeling, 27–28
  - neuronal population (macroscopic) models, 366, 370–374
  - pyramidal cells with local interneurons, 313
  - thalamocortical network model, 199
    - extended lumped model of absence seizures, 404
- Connexin36, 341, 346
- Correlation dimension, 472–474, 492
- computation
    - amplitude normalization, 477
    - autocorrelation, 478
    - data filtering, 478
    - embedding, 478
    - method, 475–477
  - lack of predictive power for seizures, 478–480, 493
    - electrocorticogram database, 478
    - surrogate analysis, 480
- Cortex
- gain modulation *see* Gain, neuronal
  - L-glutamate second-by-second measurements, 568
  - neural networks
    - balanced activation, 132
    - hierarchical cluster organization, 133
  - partial deafferentation
    - paroxysmal activity promotion, 261–265
      - acute changes, 261–262
      - experimental procedure, 261
      - long-term effects, 265
  - Cortical dysplasia, 298, 337, 339
  - Cortical map formation, 255–256
  - Cortical network models
    - homeostatic plasticity, 266, 267–274
      - acute deafferentation effects, 267, 272–273
      - alternative active cortex models, 273–274
      - asynchronous network state, 267, 273
      - intrinsic/synaptic current effects, 270–272
      - long-term deafferentation effects, 269–270
      - model design, 266–267
      - network bursting with nearly complete deafferentation, 272–273
      - processes following chronic activity blockade, 267–269
      - spontaneously active cells, 270–271
    - potassium ion concentration effects *see* Potassium ions, extracellular concentration, network model
  - Corticothalamic feedback, 49, 184–210, 305
    - absence seizures, 204–206
    - mean-field model *see* Mean-field models
    - see also* Thalamocortical cell–thalamic reticular nucleus cell models; Thalamocortical mechanisms
  - Creutzfeldt-Jakob disease, 336
  - Cryostat sections, digital imaging/data acquisition, 73
  - CVODES integrator, 6–7, 241
  - 6-Cyano-7-nitroquinoxaline-2,3-dione (CNQX), network seizure-like activity induction, 179–180

- Cytoplasmic resistivity  
*neuroConstruct* cell models, 52  
 NEURON modeling, 21, 22, 23
- Data mining  
 high-frequency oscillations mapping, 551–553  
 large network simulations/electrophysiology, 12–15  
 pharmacotherapeutic applications, 15–16
- Data windowing, 533–535
- Deafferentation triggers  
 homeostatic plasticity mechanisms, 273  
*see also* Cortex, partial deafferentation
- Degrees of freedom of model, 44
- Delta oscillations, mean-field corticothalamic model, 390
- Dendritic arborizations  
 hippocampus 3D digital reconstruction from thin cryostat sections, 77, 78  
 spatial occupancy estimation, 78–79
- Dendritic input  
 compartmental models, 4  
 complex artificial cell models, 11
- Dentate gyrus, 44, 48, 49, 235, 281  
 axo-axonic cells, 90, 94, 95, 97, 113  
 basket cells, 90, 93–94, 95, 97, 113, 114  
 cell types, 90  
   axonal distribution, 113  
   epilepsy-related loss, 120  
   excitatory/inhibitory, 93, 96, 97, 114, 120  
   multicompartmental single cell models, 98–101  
 granular layer (stratum granulosum), 73, 77, 91  
 granule cells, 90, 93, 94, 96, 107, 113, 114, 120  
 hilar cell loss, 81, 89, 92, 99, 114, 121, 123, 129  
   simulation, 105–106, 107, 118  
 hilar cells with axonal projections to commissural-associational pathway (HICAP cells), 90, 94, 96, 97, 113  
 hilar cells with axonal projections to perforant path (HIPP cells), 90, 94, 95, 97, 113, 114  
 hilus, 73, 93  
 interneuron-specific cells, 90, 94, 96, 97, 113  
 molecular layer cells with axonal projections to perforant path (MOPP cells), 90, 94, 95, 96, 113  
 molecular layer (stratum moleculare), 73, 76  
 mossy cells, 90, 93, 94, 96, 98, 99, 101, 102, 107, 113, 114, 120, 121  
 mossy fiber sprouting, 49, 81, 89, 107, 119, 120–121  
   functional network activity, 124–125  
   seizure activity spread, 59, 81–82, 90, 104, 105  
   simulation, 103, 104, 107, 118  
 neuron density variations, 107  
 seizure termination slow waves, 444  
 seizure-related pH change, 448  
 volumetric analysis, 75  
   spatial occupancy estimation, 79–80
- Dentate gyrus large network models, 90–92, 112–113, 118–128  
 afferent (perforant path) input, 102  
 axonal distributions, 96  
 cell number estimates, 93–94, 97  
 cell types, 93, 96–97, 113  
 clustering coefficient, 119, 120, 121  
 connectivity  
   estimation, 94–96  
   matrix development, 90–91, 113, 115  
 construction of networks, 101–102, 113, 117  
 edge effects, 102
- evaluation, 102, 117–118  
 excitability evaluation, 106–107  
 functional model, 114, 116  
   bifunctional activity patterns with progressive sclerosis, 121–123  
   control simulations, 125, 126  
   network activity assessment, 118  
   sprouting-only networks, 124–125  
 hilar cell loss simulation, 105–106, 107, 116–117  
 limitations, 107–108, 125–126  
 mossy fiber sprouting, 116–117  
 network size, 97, 107, 117–118  
*neuroConstruct* model, 59  
 neurotransmitter receptors, 101  
 non-topographic/topographic network connections, 101  
 path length, 117, 118–119, 121  
 sclerosis, 119–120  
   biphasic transformation of network architecture, 120–121, 127  
   network excitability changes, 121  
   network reorganization, 96  
   topological alterations, 116–117  
 software, 90  
 structural model, 113  
   average clustering coefficient, 117  
   average path length, 117  
   control simulations, 118–119, 126  
   topological assessment, 117–118  
 synapses, 99
- Dentate gyrus non-linear dynamic modeling, 574
- Diffusion processes, neuronal network modeling, 50  
*neuroConstruct*, 56
- Direct current shift (steady potentials), 443, 444, 449  
 blood–brain barrier changes, 449  
 extracellular potassium concentration increase, 448, 449  
 mechanisms, 449  
 pH changes in intracellular/extracellular space, 449  
 prior to seizure onset, 532  
 role of glial cells, 449
- Discrete-time maps, 472
- Docking simulation, computer-aided drug design, 523
- Double-bouquet cells, 174
- Drug design approaches, 515–516  
 lead compound identification, 515, 516  
   high throughput screening, 516  
   rational drug design, 516  
 lead compound optimization, 515, 516  
*see also* Computer-aided drug design
- Edge effects, 102
- Electrical stimulation, 3–4, 19  
*neuroConstruct* network models, 52
- Electrochemistry, 562–563  
*see also* Microelectrode arrays
- Electrocorticogram, 530  
 correlation dimension analysis, 475–477  
 database, 478  
 lack of predictive power for seizures, 478–480  
 seizure prediction, 472, 492  
*see also* Electrophysiological data
- Electrodes, optimal configuration, 532
- Electroencephalogram, 359, 497, 530–531  
 frequency bands, 372, 462–463  
 Gabor atom density (GAD) evaluation, 465  
 high-frequency epileptiform oscillations, 550–553  
 intracranial data acquisition, 532

- matching pursuit analysis, 459–460  
 mean-field models, 388, 389, 390  
   absence seizures comparison, 393  
   tonic-clonic seizures comparison, 395–398  
 neuronal population (macroscopic) models, 360  
 partial seizure stages, 498  
 physiological artifacts, 532  
 seizure detection, 560  
   computerized analysis, 544–550  
 seizure prediction, 469, 492  
   *see also* Electrophysiological data
- Electrophysiological data**  
 automated classification, 538–540  
   expected prediction error over future input data, 539  
   feature fusion, 539–540  
   model complexity, 539, 540  
   performance criteria, 539  
 bandwidth, 532  
 clinical data acquisition, 531–532  
 computational analysis, 532–535, 556  
 data windowing, 533–534  
 epileptogenic zone investigations, 359–365  
   stereoelectroencephalography, 359, 360  
 feature extraction, 535–538  
   automated seizure detection, 544–547  
   classifiers, 547–548  
 instantaneous frequency estimation, 534–535  
   from Hilbert transform, 535, 537, 538  
   from line length, 536–537  
   from spectrogram peak, 535, 537, 539  
   from wavelet packets, 535–536, 537, 538  
 spatial resolution, 532
- Energy minimization methods, computer-aided drug design, 516–517, 519–520
- Entorhinal cortex**  
 depolarizing plateaus, 217  
 epileptiform activity, 217  
 feedforward circuits, 305  
 gamma rhythm, 281, 346  
 graded persistent spiking activity, 215–216, 217  
   computation model *see* Graded persistent spiking activity  
 initial slow waves, 446–448  
 medial temporal lobe epilepsy  
   interictal spikes, 362  
   transition to ictal activity, 363  
 pyramidal cell inward rectifying current, 284–285  
 sensory-motor integration, 229  
 spiny stellate cells (layer 2), 283  
   mutual excitation, 283–284  
 synchronized activity, 281–283  
   cellular properties, 283  
   external pacing, 282–283  
   network properties, 283  
   phase-response techniques, 283–284  
 theta rhythm, 281–282
- Epilepsy models**  
 complex artificial cell simulations, 11–12  
   latch-up (tonic) condition, 11, 16  
 data requirements, 34–35  
 validation, 43–46  
   interictal-ictal transitions, 45  
   spatial output constraints, 45  
   temporal constraints, 45
- Epileptiform burst discharges  
 chronically isolated neocortex, 266  
 cortical homeostatic plasticity model, 269  
 hippocampus, 290–292  
   spike timing, 292
- Epileptogenic zone**, 360  
 ictal direct current shifts, 449  
 presurgical evaluation, 457
- Ethosuximide, 415
- Etiology of epilepsy**, 43, 49, 428
- Evolutionary algorithms**  
 automated parameter search for single cell modeling, 98  
 high-frequency oscillations automated detection, 551
- Fast ripples, 550
- FAST-16 recording system, 564–565
- Fast-Fourier transform, electroencephalogram frequency analysis, 458
- Feature extraction**, 533–538  
 instantaneous frequency estimation, 534–536  
   from Hilbert transform, 535, 537, 538  
   from line length, 536–537  
   from spectrogram peak, 535, 537, 539  
   from wavelet packets, 535–536, 537, 538  
   nested composition, 534
- Feature vector**, 533
- Feedforward networks**, 304–312  
 construction using iterative procedure, 305, 306–307  
 epileptiform activity, 305  
*in vitro* reconstruction, 305  
 modeling, 308–309  
   Fokker-Planck formulation, 309–312  
   synchrony development, 307–308
- Firing properties, CoCoDat (Collation of Cortical Data) database, 35, 37
- Fit error, 44
- Fixed time-step method, 6
- Focal cortical dysplasia, 298
- Focal tissue, *in vitro* studies, 169
- Focal-onset neocortical epilepsy, 45
- Fokker-Planck equations, feedforward networks, 309–311
- Force fields, drug design, 518
- FORTRAN, dentate gyrus modeling, 90
- Frequency analysis, 458
- Frequent itemset mining *see* Data mining
- Frontal lobe epilepsy, 363
- G protein, GABA<sub>B</sub> receptor-mediated potassium channel activation, 188–190
- GABAergic interneurons, 288, 289–290  
 cell number estimation, 93–94  
 cortical circuits, 288–289  
 dentate gyrus, 93  
 epileptiform discharge mechanisms, 289, 382  
 gap junction-mediated electrical coupling, 296–297  
   computational modeling, 299  
 hippocampus, 297–299  
   CA1 neuronal population model, 377, 382, 383  
   stratum lacunosum-moleculare, 296–297
- Inhibitory effect on CA3 pyramidal cells, 75–76, 80–81, 292  
 computational modeling, 293–294  
 experimental study, 292
- neocortex network model, 174
- network organization, 289
- oscillatory output generation, 232
- spike timing, 289–290, 291

- GABAergic interneurons (*Continued*)  
 subtype heterogeneity, 289  
 visual cortex modeling, 318
- GABA<sub>A</sub>** receptor-mediated currents  
 complex artificial cell models, 10  
   epilepsy simulation, 12  
 gamma rhythms in hippocampal pyramidal cells, 375  
 gap junction-mediated electrical coupling in stratum lacunosum-moleculare, 297–298  
 thalamocortical network model of absence seizures, 403, 404, 405  
 thalamocortical relay cell/thalamic reticular nucleus cell reciprocal circuit model, 403
- GABA<sub>A</sub>** receptors  
 blockade  
   4-aminopyridine seizure-like events, 497  
   neocortical seizure-like activity, 180, 420  
   spontaneous depolarizing after hyperpolarization, 315  
   thalamic spindle oscillation effects, 186  
 comparative homology modeling, 525  
 computer-aided drug design, 525  
 gene mutations, generalized epilepsy with febrile seizures plus, 143
- GABA<sub>A</sub>** synapses  
 cortical homeostatic plasticity model, 267  
 cortical network modeling, 195, 344  
 dentate gyrus network model, 101  
 gamma oscillation mechanisms, 344  
 hippocampus CA3 area modeling, 45  
 long-lasting homeostatic regulation, 261  
*neuroConstruct* granule cell 3D network model, 61  
 seizure mechanisms, 184, 490  
   spike and wave, 186, 195  
 thalamic reticular nucleus, 186  
 thalamocortical network model, 199  
   cooperative GABA<sub>B</sub> response modeling, 191  
   fast spike-and-wave oscillations, 203
- GABA<sub>B</sub>** receptor-mediated currents  
 absence seizures, 206, 403  
 complex artificial cell models, 10  
 corticothalamic feedback, 205, 206, 404  
 seizure mechanisms, 184, 186, 497  
 spike and wave seizures, 186, 193, 209  
   computational models, 194  
   cortical network models, 195–197  
 thalamocortical network model, 199  
   extended lumped model, 405  
   fast spike-and-wave oscillations, 203  
 thalamocortical relay cell–thalamic reticular nucleus cell reciprocal circuit model, 187, 188, 403–404
- GABA<sub>B</sub>** receptors  
 activation properties, 189  
 blockade, thalamic spindle oscillation effects, 186  
 clonazepam mode of action, 190  
 cooperative activity, 206  
   thalamic circuit oscillations, 185–186, 188, 192, 197–198  
   thalamocortical cell–thalamic reticular nucleus cell reciprocal circuit model, 191  
 transduction mechanism, 188, 190
- Gabor atom density (GAD) evaluation, 457, 465  
 organized rhythmic activity, 462  
 propagation maps, 465–466, 467  
 seizure detection algorithms, 546  
 seizure dynamic stereotypy, 461  
 seizure initiation phase, 461
- Gabor function, 459  
**GABRD**, 143
- GAERS** (generalized absence epilepsy rat from Strasbourg), 203, 206, 407, 414  
 calcium conductance in thalamic reticular nucleus, 415  
 GABA-mediated inhibition impairment, 415
- Gain, neuronal, 155–158  
 divisive inhibition, 156, 158, 160  
 excitatory postsynaptic current sensitivity, 162–163  
 membrane conductance increase effects, 160–161, 162  
 modulation, 158  
   response time-varying inputs, 162–166  
 multiplicative modulation, 158  
   with background synaptic input, 159–160  
   integrate-and-fire model, 159–160  
   mechanism, 158–162  
 noisy background synaptic activity, 158, 159, 162  
   inhibitory effects on neuron responses, 160, 161  
   stability/instability of network response, 156, 158, 165  
   subtractive inhibition, 156, 158, 161
- GAMESS**, 518
- Gamma oscillations, 282, 344, 345, 382  
 gap junctions, 346  
 hippocampus neuronal population model, 377, 379  
 network models, 346  
 seizure initiation phase, 458  
 synaptic plasticity, 346
- Gap junctions, 19  
 4-aminopyridine seizure-like events, 497  
 axonal electrical coupling, 341–345  
   beta2 oscillations, 351  
   experimental epileptogenesis, 343
- GABAergic networks  
 electrical coupling, 294  
 hippocampus, 293  
 propagation of postsynaptic activity, 295–296  
 gamma oscillations, 345–346  
   network model, 346
- interneuron computational models, 292
- neocortex network models, 345
- NEURON network modeling, 27  
 parallel processing, 30  
 ultrastructure, 341  
 very fast oscillations, 336, 339, 340  
   network model simulation, 344–345
- GAUSSIAN**, 518
- Gaussian filters, 81
- GBRG2**, 143
- Generalization error, 44
- Generalized absence epilepsy rat from Strasbourg *see* GAERS
- Generalized epilepsy with febrile seizures plus, 143–147  
 genetics, 147
- SCN1A** mutations, 143, 144  
 A1685V, 140  
 computer simulations, 147–152  
 D118V, 140  
 D1866Y, 144, 146, 150, 151–152  
 functional analysis, 143–144  
 I1656M, 146  
 modeling, 146–147  
 R859C, 146  
 R1648H, 144, 146, 150  
 R1657C, 146

- T875M, 144, 145, 148, 150  
 V1353L, 146  
 W1204R, 144, 146, 147, 150  
**GENESIS**, 49, 52, 54, 58  
 automated parameter search tools, 98  
 dentate gyrus model, 90  
 graphical user interface, 50  
 neocortex network model, 176  
*neuroConstruct* model implementations, 51, 52, 60, 61  
**GENESIS3/MOOSE**, 58, 67  
 Genetic algorithms, automated parameter search for single cell modeling, 98  
 Genetic factors, 43, 49  
 Gliosis, 116  
 Glutamate receptors  
 blockade, 45  
 long-lasting homeostatic alterations of excitability, 265  
 Glutamate release  
 granule cell, 93  
 hippocampus CA3 area synchronous events, 45  
 initial slow waves, 446–448  
 mossy cell, 93  
 post-traumatic epileptogenesis, 263–264  
 seizure activity, 43  
 prediction from extracellular concentration, 560, 561  
 Glutamate-sensitive microelectrode arrays, 560, 561  
 calibration, 565  
 construction, 563–564  
 FAST-16 recording system, 564, 565  
 L-glutamate second-by-second measurements, 567–568  
 aging rat hippocampus, 569  
 epilepsy surgery patients, 569–570  
 non-human primates, 569  
 L-glutamate signal analysis, 566–567  
 limit of glutamate detection, 565  
 linearity of standard curve, 565  
 local drug/solution application, 566  
 potentiostat, 564–565  
 reference electrodes, 566  
 selectivity ratio, 565, 566  
 slope, 565  
 therapeutic applications, 571–573  
**GNU Octave**, 55  
**Goldman equation**, 171  
**Golgi cells**, 63, 65  
 Graded persistent spiking activity, 215–229  
 balancing of conductances, 228  
 calcium concentration-dependence, 217, 218, 225–226  
 cellular mechanisms, 216–217  
 channel hysteresis, 227  
 computation model (entorhinal cortex layer V principal cells), 221–222  
 change to new stable level, 224–225  
 continuum of graded levels, 225  
 intracellular signaling pathway, 221–222  
 results, 222–225  
 semi-stable model, 225  
 stable activity, 224, 225  
 computational modeling approach, 217  
 conceptual model, 218–219  
 implementation, 220–221  
 induction of new stable level, 219–220, 221  
 line attractors, 218, 220, 228–229  
 point attractors, 217, 219, 228  
 stable firing, 218, 220  
 thresholds, 219, 220  
 diffusion models, 228  
 information storage, 227  
 network models, 216  
 voltage dependence, 217  
**Grand mal** *see* Tonic-clonic seizures  
**Granule cell layer**, 74, 91, 92  
 hippocampus 3D digital reconstruction from thin cryostat sections  
 dendritic tree spread, 79  
 spatial occupancy, 79, 81  
 volumetric analysis, 72, 74  
 mossy fiber collaterals, 96  
*neuroConstruct* model, 60–61  
 population spike sequence non-linear dynamic modeling, 575–577  
**Granule cells**, 57, 90, 93, 120  
 cell number estimation, 93  
 connectivity estimation, 94, 95, 96  
 density variation, 107  
 dentate gyrus sclerosis modeling, 96  
 large network model  
 functional, 114  
 structural, 113  
 mossy fiber sprouting simulation, 104  
 multicompartmental single cell models, 98  
 network excitability evaluation, 104  
 perforant path input, 106  
**Head injury, epilepsy/recurrent seizures**, 269  
 traumatic deafferentation, 260  
**Hebbian learning**, 252, 253, 255  
**Herpes simplex encephalitis**, 336  
**Heterogeneity in excitability, post-traumatic epileptogenesis**, 261  
**Heterogeneous neuronal morphologies**, *neuroConstruct* modeling, 67  
**Hierarchical network organization**  
 cortical neural networks, 132, 133  
 hierarchical cluster model, 134  
 activity spreading, 135  
 delay until large-scale activation, 136  
 influence of number/localization of initially activated nodes, 136  
 spreading simulation outcomes, 135–137  
 network topology contribution, 134, 138  
**High-frequency oscillations**, 550  
 automated detection/mapping, 551–553  
 data mining, 551–552  
 feature extraction, 551  
*see also* Very fast oscillations  
**High-throughput screening**, 515  
 computer-aided drug design, 516  
 antiepileptic agents, 522  
 chemoinformatics, 521  
**Hilar cell loss**, 103–104, 112  
 large network models, 116–117  
 small world topology effects, 119–120, 121, 127–128  
 simulation, 105–106, 107  
**Hilar cells with axonal projections to commissural-associational pathway (HICAP cells)**, 90, 113  
 cell number estimation, 93  
 connectivity estimation, 94, 95, 96  
 inhibitory activity, 97

- Hilar cells with axonal projections to perforant path (HIPP cells), 90
- cell number estimation, 93
- connectivity estimation, 94, 95, 96
- dentate gyrus sclerosis modeling, 97
- feedback inhibitory activity, 97
- large network model
- functional, 114
  - structural, 113
- Hilbert transform, 535
- quadratic chirp signal, 537
- Hilus, 73, 93
- mossy fibers, 94
- Hippocampal prosthesis, 561, 571–574
- bi-directional communication with brain, 579–581
  - CA3 region, 579–584
  - hardware implementation, 577–579
  - system integration, 581–583
- Hippocampal sclerosis, 112–128
- dentate gyrus large network model
  - biphasic transformation of topology, 120–121
  - implementation, 116–117
  - small world topology effects, 119–120, 127–128
- Hippocampus
- activity-dependent neuronal regulation, 251
  - circuitry ‘shut-down’ for seizure prevention, 561
  - computational neuroanatomy, 73–82
  - 3D digital reconstruction from thin cryostat sections, 74
    - applications to epilepsy, 81–82
    - cellular embedding/spatial occupancy, 78–80
    - image/data acquisition, 74
    - intrinsic potential connectivity patterns, 80
    - surface representation, 73–74
    - triangulation algorithm, 73–74
    - volumetric analysis, 74–76  - epileptiform bursting, 290, 292, 293
  - feedforward circuits, 307
  - GABAergic networks, 290, 297–298
  - L-glutamate second-by-second measurements, 567–568
  - initial slow waves, 441, 446–448
  - interneurons, 281, 327
  - intraoperative electrophysiological recordings, 570
  - medial temporal lobe epilepsy
    - interictal spikes, 361
    - transition to ictal activity, 363  - memory-related functions, 72, 281
  - network-level homeostatic regulation, 254
    - computational models, 255–256  - oscillatory output, 232–233
    - gamma oscillations, 344, 374–375  - seizure dynamics, 496
    - neuronal population models, 369–374  - structure–activity relationships, 72
  - synchronous population activity, 282–283, 294
    - cellular properties, 283
    - external pacing, 282–283
    - network properties, 283
    - phase-response techniques, 283–284
- Hippocampus CA1 region, 235, 281
- excitatory-inhibitory interplay, 80–81, 496
  - neuronal population models, 375
  - non-linear dynamic modeling, 575
  - potassium ion elevation-related seizure-like activity, 419
- seizure termination slow waves, 44, 446
- seizure-related pH change, 448
- Hippocampus CA3 region, 44, 95, 235, 281
- computational modeling of synchronized bursting, 290–294
  - network modeling, 45, 290
  - non-linear dynamic modeling, 575–577
  - potassium ion elevation-related epileptiform activity, 419
  - seizure termination slow waves, 444
- hoc code, 19, 20, 21–22, 23, 25, 29
- Hodgkin-Huxley parallel-conductance models, 4
- Homeostatic plasticity *see* Cortical network models
- Hydantoins, qualitative structure-activity relationships, 526
- Ictal phase discharges, 168, 305
- IGOR Pro, 52, 56
- Implantable devices, 531, 544
- refractory epilepsy treatment, 553
  - seizure detection algorithms, 531
- Import3D, 22
- Individual neuron models *see* Single cell models
- ING, 327
- Inhibitory network models, 233
- Initial slow waves, 441
- mechanisms of generation, 440
- Initiation phase, partial seizures, 457
- Instrumentation artifacts, 26
- Integrate-and-fire models, 18
- feedforward networks, 290, 305, 308
  - hierarchical cluster networks, 134
  - large network simulations, 4
  - complex artificial cells, 9–11
  - neuronal gain modulation, 155–156
  - with background synaptic input, 159, 160, 161–162
  - excitatory postsynaptic current sensitivity, 162, 172
  - membrane conductance increase effects, 158–159
  - state variables, 9
- Interictal activity, 168, 290, 305, 344
- excitatory-inhibitory interplay, 499
  - stereoelectroencephalography in temporal lobe epilepsy patients, 357
- Interictal–ictal transition
- epilepsy model validation, 45
  - mean-field models, 387
  - partial seizures, 460
  - temporal lobe epilepsy stereoelectroencephalography, 360
  - limbic structures, 357
  - neocortical structures, 363
  - neuronal population models, 357–358
- Intermittent bursting activity, 463
- Interneuron-specific cells
- connectivity estimation, 90
  - dentate gyrus, 89
  - cell number estimation, 93
  - inhibitory activity, 93
- Interneurons, 57
- activity-dependent regulation, 336
  - anticonvulsant agent targeting, 382
  - classification, 318
  - computational models of electrical coupling, 289
  - cortical homeostatic plasticity model, 259
  - cortical network model, potassium ion concentration effects, 419
  - gamma oscillations model, 336

- hippocampus, 71, 329  
 CA1 region, 375, 382  
 excitatory-inhibitory interplay, 499  
 spike timing, 282  
 neocortex, 168  
 neuronal population models, 357–358, 366, 374  
 oscillatory output generation, 241  
 seizure dynamics, 496  
 single compartment neuronal model, 233–235  
 thalamocortical feedback, 349  
 visual cortex, 317  
 voltage-dependent sodium channel mutations, 43  
 Intracellular communication, NEURON network modeling, 27–28  
 Intractable childhood epilepsy with generalized tonic-clonic seizures,  
*SCN1A* mutations, 143, 144  
 Ion channels  
   compartmental models, 4  
   conductance  
     CoCoDat (Collation of Cortical Data) database, 35, 37  
     *neuroConstruct* cell models, 52  
   hysteresis, graded persistent spiking activity, 227  
   neural function modeling, 170  
     equivalent electrical circuit, 170–171  
     leak channels, 171–172  
     resting membrane potential, 171  
     synaptic channels, 172–173  
     voltage-gated channels, 171–172  
 NeuroML specifications, 58  
 NEURON cell modeling, 24, 25  
 structure prediction for antiepileptic agent lead compound identification, 515  
 Ion currents  
   activity-dependent neuronal regulation, 247, 249  
     post-traumatic epileptogenesis, 259  
   activity-independent neuronal regulation, 260–261  
     cortical homeostatic plasticity, 261  
 Irritative zone, 360  
 Juxtafocal tissue, *in vitro* studies, 169  
 Kaplan-Yorke formula, 471, 472  
 KCNQ2/3 potassium channels, beta2 oscillations, 340, 341  
 L-Neuron, 67  
 Lamotrigine, 16, 215, 226  
 Large network simulations, 3–16  
   compartment cell techniques, 4, 5–7  
     supercomputing approaches, 7–9  
     time-step method, 6–7  
   complex artificial cells, 9–11  
     epilepsy simulation, 11–12  
   data-mining, 12–15  
   dentate gyrus *see* Dentate gyrus large network models  
   detailed versus simplifying approaches, 4–5  
   event-driven/continuous dynamical simulation combination, 5, 9  
   mean-field *see* Mean-field models  
   *neuroConstruct*, 63–64  
   parameters, 10  
   prediction of dynamics from two-cell network parameter values, 233–235  
   state variables, 10  
 Lateral geniculate nucleus, activity-dependent potassium ion regulation, 421  
 Lead compound identification, 515, 516  
 antiepileptic agents, 515  
   molecular shapes designed to fit known receptors, 522  
   receptor structure prediction, 522  
   high throughput screening, 517, 521  
   rational drug design, 516, 521  
 Lead compound optimization, 515  
   antiepileptic agents, 521  
 Leak channels, neural function modeling, 171  
 Lennox-Gastaut syndrome, 419, 437  
   neocortical seizures, 420  
 Lesional zone, 360  
 Lie detection systems, 537  
 Ligand-gated ion channels, structure prediction for antiepileptic agent lead compound identification, 524  
 Line attractors, graded persistent spiking activity modeling, 217, 218  
 Line length, 536–537  
   quadratic chirp signal, 537  
 Linear Circuit Builder, 26–27  
 Long-term depression, 252, 260, 266, 267  
 Long-term potentiation, 72, 225, 251, 252, 315  
 Lorenz chaotic system, 472  
 Low-dimensional non-linear dynamical systems, 492  
   seizure prediction ineffectiveness, 492  
 Low-voltage fast onset, 541  
 Lyapunov exponents, 472, 474–475, 481–482, 484  
   computation from time series, 474–475, 481–482  
   control model based on continuous-time flows, 488  
     lack of predictive power for local bifurcation, 489–490  
     control model using discrete-time maps, 482–483  
       moving window size, 483  
   fractal dimension relation (Kaplan-Yorke formula), 475, 492  
   noise sensitivity, 472, 475, 481, 483, 485  
   predictive power, 482, 485  
     autocorrelation comparison, 488  
     seizure prediction ineffectiveness, 472, 481, 482  
     statistical fluctuations, 482  
 Macroelectrodes, 383  
 Macroscopic models *see* Neuronal population models  
 Magnetic field brain stimulation, 19  
 Marching Cube, 73  
 Matching pursuit, electroencephalogram analysis, 459–460  
   partial seizures, 458, 460, 461  
 MATLAB, 73, 410  
   *neuroConstruct* data analysis, 52, 54–55  
   spectral analysis routines, 321  
 Mean-field models, 4  
   absence seizures, 393–395, 398, 399  
     scalp EEG data comparison, 388  
   bifurcations, 388  
     generalized seizures, 398  
   corticothalamic model, 388–389  
     general, 388–389, 396  
     global (spatially invariant), 389–391  
     linear instability, 393  
     physiological parameters, 391, 398  
     steady states, 391  
   EEG spectra interpretation, 387, 399  
   primary generalized seizures, 387  
   stability properties, 388, 412  
   tonic-clonic seizures, 395, 397, 399  
     scalp EEG data comparison, 372

- Mechanics methods, computer-aided drug design, 528, 531, 539, 540  
 molecular mechanics, 531  
 quantum mechanics, 517–516
- Medial temporal lobe epilepsy, 361  
 ictal evolution periods, 457, 461  
 organized rhythmic activity, 462  
 interictal spikes, 361  
 macroscopic models, 357  
 neuronal population model parameter validation, 377  
 transition to ictal activity, 377–379
- Medial temporal lobe epilepsy syndrome, 361
- Membrane conductance  
 NeuroML specifications, 58  
 neuron modeling with NEURON, 21, 22, 23
- Membrane, neural function modeling  
 equivalent electrical circuit, 170  
 membrane channels, 171
- Membrane potential  
 compartmental models, 9, 10  
 complex artificial cell models, 10  
 integrate-and-fire models, 9  
 neural function modeling, 173  
 NEURON modeling, 22  
 synaptic parameters estimation, 237
- Membrane time constant, 9
- Memory, 67, 255, 497  
 hippocampal theta/gamma rhythms, 283
- Metabotropic glutamate receptors  
 dentate gyrus network modeling, 96  
 graded persistent activity (spiking activity), 217, 227
- Microcircuits, 34–35
- Microelectrode arrays, 563  
 amperometry, 564  
 calibration, 565  
 construction, 563–564  
 exclusion layer, 563  
 glutamate-sensing *see* Glutamate-sensitive microelectrode arrays  
 hippocampal prosthesis bi-directional communication with brain, 569  
 measurable molecules, 562  
 recordings from deep brain structures, 564–565  
 sterilization, 564  
 therapeutic applications, 571
- Microelectrodes, 532, 570–573
- Mitral cell model, 249
- Model error, 44
- Model selection, 44
- Model View, 30
- ModelDB, 22, 98, 113
- Molecular connectivity, computer-aided drug design, 523
- Molecular dynamic calculations, 519, 520
- Molecular layer cells with axonal projections to perforant path  
 (MOPP cells), 90, 115  
 cell numbers estimation, 93  
 connectivity estimation, 93, 94  
 inhibitory activity, 510
- Molecular mechanics, computer-aided drug design, 518–519  
 docking simulation, 523  
 molecular shape designs to fit known receptors, 522
- Molecular orbital calculations, 518
- Monte Carlo methods  
 computer-aided drug design, 516, 517  
 neurostimulation device evaluation, 553
- MorphML, 54, 57, 58
- Morphology  
 CoCoDat (Collation of Cortical Data) database, 35, 37  
*neuroConstruct* network model generation, 51–52  
 NeuroML specifications, 57
- Mossy cells, 90, 93, 121  
 cell number estimation, 93  
 connectivity estimation, 94, 95, 97  
 density variation, 107  
 dentate gyrus sclerosis modeling, 90–91  
 effects of progressive sclerosis, 123  
 large network models, 104  
 loss, 89–107  
 simulation, 105–106  
 multicompartmental single cell models, 98  
 perforant path input, 102
- Mossy fiber sprouting, 90, 96, 97, 103, 116  
 dentate gyrus models, 49, 81  
 following head trauma, 274  
 functional network activity, 118  
 simulation, 103–103, 105, 118  
 small world topology effects in large network model, 119, 127  
 spread of hyperexcitability, 61, 90, 105, 107
- Mossy fibers, 94  
 boutons, 94  
*neuroConstruct* 3D network model, 61
- Muscarinic receptors, 216
- Myoclonic epilepsy in infancy, 49
- Neocortex  
 epileptogenesis, 349  
 initial slow waves, 441  
 oscillatory output, 234  
 gamma oscillations, 344, 345  
 network model, 346
- Neocortex network model, 168–181  
 basket cells, 174, 175, 176  
 cell types, 173–174  
 compartments, 175  
 excitatory, 174, 176–177  
 inhibitory, 174, 175, 176–177  
 cellular behavior, 176  
 chandelier cells, 174, 175, 176  
 connectivity, 176  
 double-bouquet cells, 174  
 experimental support, 179–180  
 gap junction-mediated very fast oscillations, 340–341  
 intrinsically bursting neurons, 176  
 model construction, 173–175  
 model implementation, 176  
 network behavior, 176–178  
 desynchronized, 177  
 inactive, 177  
 irregular bursting, 177, 178, 180  
 oscillatory, 177, 178, 179  
 regular bursting, 177, 178, 180
- pyramidal cells, 173–174, 176  
 deep, 174, 175, 176  
 network bursting behavior, 178  
 superficial, 173, 176
- regular spiking neurons, 180
- seizure activity, 177, 178, 180  
 axonal gap junction-mediated electrical coupling, 342  
 structural aspects, 173–174

- synaptic coupling-related activity, 176–178  
synchrony, 178, 180–181
- Neocortical seizures, 420  
dynamics, 496  
etiologies, 420  
ictal direct current shifts, 444  
ictal evolution periods, 46  
initial slow waves, 441  
physiology, 420  
spike-wave discharges, 420  
transition to ictal activity in medial temporal lobe epilepsy, 463, 364, 365
- Nernst equation, 171
- NetCon, 101
- Network Builder, 30
- Network models, 43, 49, 50, 170, 232–242, 358  
biologically-relevant mechanisms, 232–242  
cortical potassium ion concentration effects *see* Potassium ions, extracellular concentration, network model  
cortical spike-and-wave seizures, 195–197
- 3D connectivity, 50
- data requirements, 34–35
- dentate gyrus *see* Dentate gyrus large network models
- neuroConstruct* *see* *neuroConstruct*
- NEURON *see* NEURON
- rhythmic output, 232
- signaling events, 50
- simulator accessibility/format problems, 50
- synaptic parameters estimation, 237–239  
stochastic synapses, 239, 241–242
- thalamocortical mechanisms for absence seizures, 199–203
- two-cell inhibitory, 239–240, 240–241  
large network dynamics prediction from parameter values, 235–237, 239  
optimal parameter sets for synchronous output, 234–235, 239
- NetworkML, 59
- NeuGen, 67
- Neural function modeling, 170–173  
compartments, 173  
equivalent electrical circuit, 170–171  
extracellular current, 173  
membrane channels, 171–172  
resting membrane potential, 171  
*see also* Single cell models
- Neural networks, 48–49  
activity spread (balanced activation), 132  
homeostatic mechanisms, 253–256  
computational models, 255–256  
epilepsy models, 256  
experimental evidence, 253  
solution spaces, 253
- Neural Open Markup Language *see* NeuroML
- neuroConstruct*, 48–64  
action potential propagation substitution, 56  
advanced features, 54–55  
application practicalities, 51  
automatic validity checks, 53  
3D diffusion mechanisms, 56  
3D network analysis, 56  
3D positioning/connectivity algorithms, 55–56  
3D spatial information, 51, 63
- functionality, 51  
cell models, 52  
customization, 54, 62  
importation/validation of morphologies, 51–52  
network analysis, 52  
network generation, 52, 62  
simulation management, 52  
tutorials/examples, 54
- graphical user interface, 51, 53, 61, 62
- model implementations  
granule cell 3D network model, 60–61  
layer 5 pyramidal cells, 60  
neurological disorder, 59
- modularity, 53
- NeuroML applications, 58–59, 61
- region specific stimulation, 56
- scaling up of network models, 62–63
- scope of application, 51, 61–62  
future development, 62–63
- simulation configurations, 54
- simulation management/browsing, 54
- simulator-independent standards, 53, 61
- visualization of models, 52–53
- NeuroMatic, 55
- NeuroML, 56–59, 62  
levels in standards, 57  
*neuroConstruct* applications, 58–59, 61
- NeuroMorpho.org database, 22, 73, 75
- NEURON, 5–7, 11, 18–30, 49, 52, 54, 58, 75–76, 141  
complex artificial cells, 9–11  
cortical homeostatic plasticity model, 266–275  
CVODES integrator, 6–7  
3-D specification, 22  
dentate gyrus modeling, 89  
epilepsy research applications, 18–19
- GABAergic interneurons  
CA3 pyramidal cell inhibition, 290  
gap junction-mediated electrical coupling, 294–295
- graphical user interface, 19–20, 50
- CellBuilder, 20, 21, 22, 23, 24  
Channel Builder, 25  
Import3D, 22  
Linear Circuit Builder, 26–27  
Model View, 30  
Network Builder, 30
- individual neuron modeling, 5–6, 18, 19, 20–25  
adding new mechanisms, 25  
anatomically detailed cells, 22  
basic anatomical/biophysical properties, 21–22  
localized signal sources (point processes), 25  
sections, 21  
spatial discretization, 22–24  
spatially inhomogeneous properties, 24
- interpreter, 19
- model specification/management, 20
- models including electronic instrumentation, 26–27
- network modeling, 19–20, 27–30  
artificial spiking cells, 28–29  
connections between cells, 27–28  
construction steps, 29–30  
generating reusable code, 30
- NetCon, 28, 29, 95

- NEURON (Continued)**
- object-oriented programming, 29–30
  - on parallel computers, 30
  - neuroConstruct* model implementations, 51, 52, 59, 60, 61
  - Neuronal population (macroscopic) models, 356–357
  - absence seizures *see* Absence (petit mal) seizures, thalamocortical network extended lumped model
  - excitatory/inhibitory cells, 357, 358
  - generic model for electroencephalogram signal interpretation, 366–368
  - degree of coupling effects, 372–374
  - epileptic signal simulations, 370–374
  - excitation/inhibition balance analysis, 370, 372
  - extension to multiple coupled populations, 369
  - parameters, 370, 371
  - recurrent coupling effects, 374
  - transition to seizure activity, 372
  - hippocampus activity model, 374–377
  - activity maps, 379
  - EEG signal interpretation during transition to seizures, 377–379
  - excitatory/inhibitory synaptic interactions, 377, 379, 381
  - fast oscillations generation, 381
  - parameters, 377
  - historical background, 358–359
  - neural mass (neuron population), 359
  - seizure simulations, 540–544
  - desynchronization with stochastic phase resetting, 541–542
  - epileptic states, 399, 541–542
  - spontaneous seizure-like activity, 540, 541
- Neurons**
- activity-dependent regulation, 249–250
  - computational models, 251
  - experimental evidence, 250
  - activity-independent regulation, 251–252
  - homeostatic mechanisms, 247–250
  - solution spaces, 248–249
- Neuroscience Database Gateway*, 37
- Neurospaces**, 67
- Neurostimulation devices, 553–555
- Nitric oxide, diffusion modeling, 50, 56
- Nitric oxide synthase, 92
- NMDA receptors
- activity-related regulation, 261
  - computer-aided drug design, 524
  - dentate gyrus network modeling, 101
  - neocortex network model, 344
  - neuroConstruct* granule cell 3D network model, 65
  - thalamocortical network model, 199
- NMDA synaptic activity
- complex artificial cell models, 10
  - epilepsy simulation, 11
  - cortical homeostatic plasticity model, 267, 268, 272
- NMODL, 19, 25, 59
- NNET, 241
- Non-linear dynamics, 281, 458, 473
- electroencephalogram frequency analysis, 457
  - hippocampus CA3 region modeling, 575–577
  - hardware implementation, 577–578
  - seizure prediction ineffectiveness, 462, 469
- Non-linear synchrony, 502
- Numerical continuations, 241
- network model parameter values, 235, 236
- Olfactory bulb, 358, 359
- model, 254, 540
- Olfactory system model, 358
- Oscillatory output, 241
- absence seizures, 184
  - hippocampus, 71
  - inhibitory synapse influence on pyramidal cell firing, 81
  - isolated neocortex slices, 259
  - population modeling approach, 357–358
  - potassium ion extracellular dynamics in cortical network model, 419
  - synaptic excitation/inhibition balance, 431
  - preceding/initiating epileptic discharges, 335–353
- see also* High-frequency oscillations; Very fast oscillations
- Oxcarbazepine, 525
- Pannexins, 341, 344
- Parallel fibers, 57
- neuroConstruct* granule cell 3D network model, 63
- Parallel processing
- neuroCOnstruct* models, 63
  - NEURON network modeling, 30
  - see also* Supercomputing approaches
- Parkinsonian tremor, 541
- Parkinson's disease, 567
- Paroxysmal bursting
- cortical network models, 266
  - cortical origin, 420
  - neocortical seizures, 420, 421
- Paroxysmal depolarization shifts
- initial slow wave generation, 441
  - seizure activity, 43–44
- Parsimonious models, 45
- Partial seizures
- dynamics
  - clinical relevance of quantification, 468–469
  - correlation, 460
  - propagation analysis, 457–458, 460, 462
  - stereotyped patterns, 461, 464, 465
  - time-frequency approach, 464–468
  - electroencephalogram analysis methods, 457–458
  - evolution/propagation, 457–469
  - ictal evolution periods, 461
  - initiation phase, 461–462, 498
  - intermittent bursting activity, 463, 464
  - organized rhythmic activity, 462, 463
  - transition rhythmic activity, 462, 463, 464
  - phases, 460–461
  - secondary generalization, 458, 460, 498
  - seizure events (ictal activity), 168, 169
  - termination, 449
- Parvalbumin, dentate gyrus histochemistry, 93–94, 114
- Path length
- cortical hierarchical cluster network model, 132
  - dentate gyrus
  - large network model, 117, 124
  - network model topological assessment, 114
  - effects of progressive sclerosis, 117–118, 119
- Pattern recognition analysis
- computer-aided drug design, 515
  - feature extraction, 533
- Pattern-generating circuits self-assembly, 253
- Penicillin, GABA<sub>A</sub> antagonism, 186
- Percolation model, 341

- Periodic lateralized epileptiform discharges, 336
- Perirhinal cortex, 216
- Persistent active states, 497
- Petit-mal *see* Absence seizures
- pGENESIS, 67
- Phase-response techniques, 281, 283–285
- entorhinal cortex
    - pyramidal cell synchronized activity, 274–275
    - stellate cell synchronization via mutual excitation, 283–284
- Phenobarbital, 515
- Phenytoin, 16, 43, 217, 226
- Picrotoxin, GABA<sub>A</sub> antagonism, 45
- PING, 327
- Plateau potentials, 217, 218
- Point attractors, graded persistent spiking activity modeling, 219
- Post-ictal silence, 444
- Post-spike synaptic depression, 10
- Post-traumatic epileptogenesis, 19, 259–275, 419
- axonal sprouting, 274
  - excitation/inhibition balance shift, 260
  - homeostatic synaptic plasticity modeling, 266–270
  - long-lasting homeostatic alterations of excitability, 261
  - neuronal circuitry rearrangements, 274–275
- Potassium accumulation epilepsy model, 281, 282, 414–415
- Potassium channels
- computer-aided drug-design, 506
  - GABA<sub>B</sub> receptor-mediated activation, 197, 198
- Potassium ions, extracellular concentration, 448
- activity-dependent regulation, 419
  - direct current shift (steady potentials), 443, 444
  - dynamics, 419–437
  - epileptogenesis, 419, 421–422, 437, 524
- network model, 419, 429
- activity-dependent synaptic current modulation, 435–436
  - clinical seizures comparison, 433
  - intracellular chloride accumulation, 436–437
  - paroxysmal activity termination, 433–434
  - paroxysmal oscillations, 420–421
  - role of potassium buffering, 424
  - role of potassium pump, 424
  - slow state transitions, 429–433
  - synaptic excitation/inhibition balance, 431–432, 435–437
  - synaptic plasticity, 435–436
  - tonic firing/slow bursting bistability, 426, 428
- single cell model, 423
- bifurcation analysis, 419, 425–426
  - burst generation mechanism, 426–428
  - potassium dynamics, 419, 424
  - slow bursting/tonic firing bistability, 426
  - synaptic dynamics, 423
  - tonic spiking mechanism, 428–429
  - transient oscillation triggered by potassium increase, 425–426
  - spreading depression during seizure termination period, 440, 444
- Pre-emptive neurostimulation, 553–555
- Pre-ictal state, 489, 548
- Prediction error, 44
- Prepyriform cortex, 358
- Presynaptic terminal transmitter release, NEURON network modeling, 27, 28
- Primary generalized seizures, 387–400
- mean-field models, 387
- Protein structure, prediction for antiepileptic agent lead compound identification, 522
- Purkinje cells, 55
- Pyloric dilator neuron, 251, 256
- Pyloric pacemaker, 248
- Pyloric pattern-generating network, 253
- Pyramidal CA1 cells
- activity-dependent regulation, 249
  - axonal gap junction-mediated electrical coupling, 341
  - influence of inhibitory synapse position on firing, 75–76
  - neuronal population models, 366
- Pyramidal CA3 cells
- axonal gap junction-mediated electrical coupling, 341
  - epileptogenesis model, 335
  - interictal spike generation, 290
  - multicompartmental model, 293
  - non-linear dynamic modeling, 575
  - spike timing, 282, 283
- Pyramidal cells, 55, 56
- activity-dependent regulation, 255, 346
  - 4-aminopyridine seizure-like events, 497–498
  - with low magnesium, 499
  - beta2 oscillations, 344, 349
  - entorhinal cortex
    - graded persistent spiking activity, 215–216
    - inward rectifying current in synchronization, 284–285
- feedforward networks construction *see* Feedforward networks
- gamma oscillations, 345
- hippocampus
- excitatory-inhibitory interplay, 499
  - volumetric analysis, 74
  - see also* Pyramidal CA1 cells; Pyramidal CA3 cells
  - homeostatic plasticity model, 259
  - local interneuron connection probability, 313
  - neocortex network model, 168, 181, 336
  - deep, 174, 175, 176
  - network bursting behavior, 178
  - superficial, 173, 175
  - neuroConstruct* model of spike initiation, 64
  - neuronal population (macroscopic) model, 366–369
  - electroencephalogram signal interpretation, 363, 366
  - multiple coupled populations, 369
  - potassium ion concentration effects, 421, 422, 424–425
  - seizure termination-related depolarization, 444
  - spike timing, 285
  - spike-and-wave seizures, 209
  - network models, 195, 200
  - thalamocortical network model, 200, 400
- Quadratic-integrate-and-fire models, 313
- Qualitative structure-activity relationship
- computer-aided drug design, 516, 517
  - antiepileptic agents, 515, 521
  - 2-dimensional, 523
  - 3-dimensional, 523
- Quantum mechanics, computer-aided drug design, 517–518, 522, 523
- docking simulation, 523
  - molecular shape designs to fit known receptors, 522
- Rational drug design, 516
- antiepileptic agents, 515–516
  - molecular shapes designed to fit known receptors, 522
  - receptor structure prediction, 522
- large network simulations, 15–16

- Receiver-operating-characteristic (ROC) analysis  
 automated electrophysiological data classification, 538  
 integrate-and-fire models, 158, 159, 160
- Receptors, computer-aided drug design, 522–523  
 bioactive zone functional groups, 522  
 structure prediction, 522
- Reconstruct*, 73
- Refractory period, complex artificial cell models, 10
- Repetitive spikes, data mining of simulations, 14
- Responsive neurostimulation, 553–555
- Resting membrane potential, neural function modeling, 171
- Ripples, 532
- SCN1A*  
 mutations, 143  
 causing generalized epilepsy with febrile seizures plus, 143, 144
- voltage-gated sodium channel alpha subunit gene product, 144
- SCN1B*, 143
- SCN2A*, 143
- Seizure detection, 532  
 algorithms, 532, 545, 547, 566  
 implantable stimulation device coupling, 554  
 computerized electroencephalogram analysis, 550–553  
 classifiers, 545–547  
 patient-specific/patient-independent, 547  
 singleton/multiple features, 544–547  
 support vector machines, 547–550
- data observation window, 533
- electroencephalography, 560
- Seizure dynamics, 168–170, 304, 457, 496–510  
 cross-correlation evaluation, 498–501  
 autocorrelation, 502  
 use of Bartlett estimator, 502
- excitatory neuron interactions, 497–498
- excitatory-inhibitory interplay, 499–503, 508  
 during epileptiform bursts, 503  
 during seizures, 503  
 synchrony detection, 497
- role of gap junctions, 507
- role of inhibition, 497
- see also* Partial seizures
- Seizure focus  
*in vitro* tissue studies, 169  
 localization, 560
- Seizure initiation, 82, 169, 526  
 chirps, instantaneous frequency estimation, 534–535  
 clinical data acquisition, 531–532  
 disinhibition through deafferentation, 260  
 epilepsy model validation, 45  
 extracellular milieu changes, 419  
 potassium accumulation hypothesis, 421–422
- Seizure prediction, 3, 471–493  
 correlation dimension ineffectiveness, 471–474, 485, 486  
 data observation window, 533  
 glutamate, extracellular concentration, 560, 561  
 Lyapunov exponents ineffectiveness, 474–484, 485, 486  
 microelectrode arrays, 571  
 quantitative methods, 527
- Seizure prevention, 3, 4
- Seizure spread, 82, 169  
 epilepsy model validation, 45
- Seizure termination, 423, 437  
 partial seizures, 460  
 potassium accumulation hypothesis, 421  
 dynamics network model, 435–437  
 slow waves, 443–444, 449  
 mechanisms, 448  
 spreading depression, 444, 449
- Seizure-induced amnesia, 572
- Seizure-like discharge  
 cortical partial deafferentation, 263–264  
 neocortex network model, 177, 178  
 experimental support, 179–180
- Seizures  
 dynamical systems approach, 241  
 epilepsy model output, 43, 44  
 etiology, 524  
 mechanisms, 357  
 neuronal population models, 531  
 preceding/initiating fast oscillations, 336–340  
 recurrent excitatory connections, 317  
 synchronous neuron firing, 305, 307, 309, 313, 315  
 feedforward circuits, 305
- Sequence learning, 282
- Serotonin, 50
- Severe myoclonic epilepsy of infancy, *SCN1A*  
 mutations, 143  
*shal*, 251
- Signaling events, neural network modeling, 50  
*neuroConstruct* applications, 66
- Simulated annealing, automated parameter search, 98
- Single cell models, 4, 5, 423  
 automated parameter search, 92  
 cortical extracellular potassium ion dynamics, 420–421  
 data requirements, 34–35  
 dentate gyrus  
   functional model network, 114  
   multicompartmental models, 98–100  
 model fitting approaches, 98
- NEURON simulation environment *see* NEURON  
*see also* Neural function modeling
- Sleep, 380  
 absence seizure development, 416  
 electroencephalogram frequency analysis, 400  
 seizure initiation through disinhibition, 260  
 slow oscillations, 349  
 spindle waves, 403  
 wakefulness transition, 415–416
- Slow waves, 440–450  
 at seizure termination, 444–445  
 during seizure development, 443–444  
 initial (at seizure onset), 441  
 mechanisms of generation, 440  
*see also* Direct current shift (steady potentials)
- Small world networks, 66, 127  
 activity spreading evaluation, 135  
 dentate gyrus large network model, 121, 127  
 effects of progressive sclerosis, 123  
 topological assessment, 116
- neuroConstruct* network models, 61
- Social networks, 134
- Solution spaces, neuronal networks, 248–249
- Somatosensory cortex, 349
- Somatostatin, 114

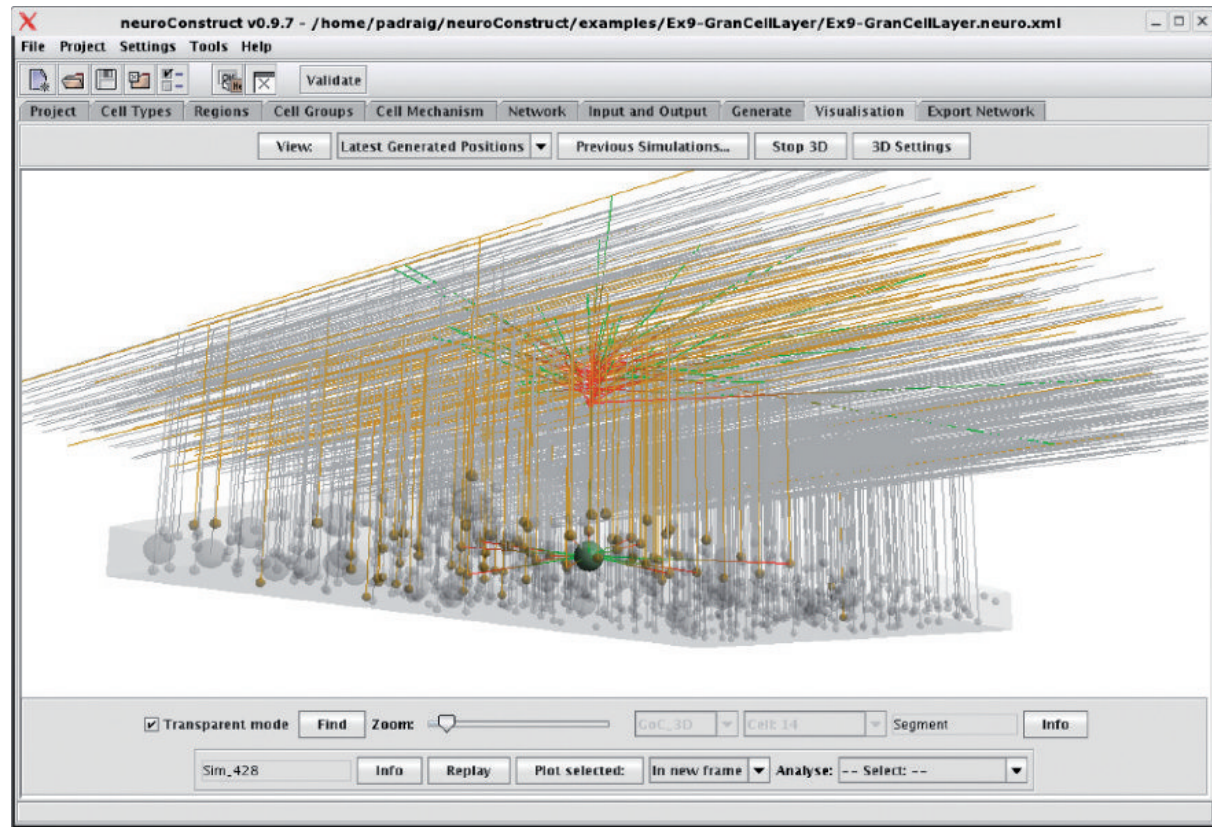
- Spatial occupancy  
  edge factors, 77  
  hippocampus 3D digital reconstruction from thin cryostat sections, 76–81
- Spatial organization  
  epilepsy model validation, 45–46  
  hippocampus, 76–77  
  neural networks, 48–49  
  *neuroConstruct* network models, 55, 61, 63  
  NeuroML specifications, 58
- Spatial working memory, 255
- Spectrogram peak, 535  
  quadratic chirp signal, 537
- Spencer-Gerhardt electrode, 570
- Spike and wave activity, 19  
  absence seizures, 184, 185, 188, 192, 197, 393, 394, 416  
  neocortical origins, 420, 421  
  cortical mechanisms, 197–203  
    computational models, 188–191  
    experimental studies, 209  
  corticothalamic model, 204–206  
  local field potentials model, 193  
  T-type calcium current, 185, 194  
  vigabatrin effects, 206
- Spreading depression, 19, 444  
  seizure termination period, 444, 446
- Stages of seizure, 446–447  
  dynamics, 496–482  
  excitatory-inhibitory interplay, 499–503
- Status epilepticus, 256  
  stages, 498
- Steady potentials *see* Direct current shift
- Stellate cells, 174, 283  
  neocortex network model, 336  
  synchronization via mutual excitation, 283–284
- Stereoelectroencephalography, 359, 360  
  data acquisition, 357  
  electrode positioning procedure, 360  
  interictal activity, 361–363  
  neuronal population models for signal interpretation, 357–366  
  simulation results, 366  
  transition to ictal activity, 356–359  
    limbic structures, 363  
    neocortical structures, 363
- Stimulation-induced epileptiform activity, 499
- Stomatogastric ganglion neurons  
  activity-dependent regulation, 249, 251  
  activity-independent regulation, 251  
  network-level homeostasis, 253  
  pacemaker behavior modeling, 248, 254, 283
- Stratum granulosum *see* Granule cell layer
- Stratum lacunosum-moleculare, 69, 71–72  
  GABAergic interneurons, 288–289  
  seizure dynamics, 498
- Stratum moleculare, 69, 74, 87, 88  
  GABAergic interneuron numbers estimation, 88
- Stratum oriens, 69  
  gap junction-mediated electrical coupling, 336, 496  
  interneurons, 281  
    seizure dynamics, 496, 498
- Stratum pyramidale, 69  
  Stratum radiatum, 69, 72
- Supercomputing approaches  
  CPU cache size, 7–8  
  large network simulations, 7–9  
    load balancing, 8–9  
    minimum delay, 7  
  NEURON simulation environment, 18  
    *see also* Parallel processing
- Supervised learning problem, automated seizure detection, 545
- Support vector machines, 547–550  
  novelty detection, 547
- Surface rendering, 69, 71
- Surface representation, hippocampus 3D digital reconstruction from thin cryostat sections, 69–71
- Switch-like components, graded information storage, 227
- Synapses, 19, 75  
  compartmental models, 4  
  complex artificial cell models, 10  
  GABAergic network electrical coupling, 295  
  neocortex network models, 176  
  neural function modeling, 166–167  
  *neuroConstruct*  
    cell models, 52  
    network models, 55, 56  
  NeuroML specifications, 57  
  neuron modeling with NEURON, 25  
  temperature-dependent conductance, 95
- Synaptic activity  
  following chronic activity blockade, 261, 267, 269  
  hippocampus CA3 area synchronous events, 45  
  use-dependent depression, 45
- Synaptic noise, feedforward networks construction, 307  
  synchrony elimination strategies, 312
- Synaptic parameters  
  CoCoDat (Collation of Cortical Data) database, 35, 37  
  data mining, 13  
  estimation from network models, 235–237, 240  
  integrate-and-fire models, 9
- Synaptic plasticity, 49, 252  
  dentate gyrus network modeling, 95  
  epileptogenesis modeling, 266–275  
  gamma oscillations, 344  
  induction by traumatic deafferentation, 260  
  network instability, 252, 285  
  postsynaptic spike timing, 285  
  potassium ion extracellular dynamics network model, 429–430  
  spike timing-dependent, 252  
  very fast oscillations, 336
- Synaptic scaling, 252–253, 255  
  long-lasting excitability blockade, 261  
  neuronal network models, 247, 252
- Synaptic transmission  
  cortical extracellular potassium ion dynamics, 419  
  NEURON network modeling, 27  
    parallel processing, 30  
    spike-triggered, 28  
  post-traumatic epileptogenesis, 259
- Synchronous activity, 6, 19  
  absence seizures, 184, 185  
  control of spread, 313–314  
  dentate gyrus large network model, 116  
  elimination strategies, 312–313

- Synchronous activity (*Continued*)  
 feedforward networks, 304–307  
   development, 298–299  
 gamma epoch alternations, 347  
 hippocampus, 45, 274, 281  
   response to potassium elevation, 290  
 human seizure studies, 498  
 hybrid neuronal networks, 281–285  
 initial slow waves, 441  
 interneuron modulation in visual cortex, 317, 318  
 neocortex network model behavior, 173, 174  
   experimental support, 179–180  
 network bursting, 342, 344  
 normal functioning brain, 304–305  
   input rate information, 304–305  
 pathological (global), 314, 329  
 phase-response techniques, 283, 285–286  
 recurrent excitation, 346  
 seizure mechanisms, 43, 176, 178, 179, 305, 356, 457, 458, 490, 507  
 two-cell inhibitory network model, 227–229, 239
- Temporal lobe epilepsy, 81, 89, 107, 281  
 dentate gyrus pathological changes, 83–84  
 electrophysiological data, 359–360  
   neuronal population models, 366–367  
 epileptogenic zone, 360  
 ictal direct current shifts, 443  
 initial slow waves, 441  
 irritative zone, 360  
 lateral subtype, 356, 361  
 lesional zone, 360  
 macroscopic models, 356–379  
 medial subtype *see* Medial temporal lobe epilepsy  
 potassium channel impairment, 419  
 presurgical evaluation, 360, 361  
 stereoelectroencephalography, 359, 360  
   ictal activity, 356, 357, 360  
   interictal activity, 361–363  
   transition to ictal activity, 356–359
- Temporal properties  
 epilepsy model validation, 45  
 neural networks, 49
- Thalamic anterior nucleus stimulation device, 553
- Thalamic reticular nucleus cells, 186  
 corticothalamic feedback, 204, 208  
 GABA<sub>A</sub>-mediated synaptic interactions, 188
- Thalamocortical cell–thalamic reticular nucleus cell models, 197–198  
 calcium-dependent currents, 188  
 clonazepam effects, 190  
 cooperative GABA<sub>B</sub> response, 190–191, 404  
 corticothalamic feedback, 204–206  
 spindle wave generation, 403  
 thalamocortical network model with cortical pyramidal cells, 199–203  
 voltage-dependent currents, 194
- Thalamocortical mechanisms, 49  
 absence seizures, 197–203, 208–209  
 neuronal population model, 357  
   *see also* Absence seizures, thalamocortical network extended lumped model  
 oscillations, 414  
   corticothalamic feedback, 197–198, 204–206, 208  
   fast spike-and-wave, 203  
   GABA<sub>B</sub> receptor cooperative activity, 197–199  
 modeling limitations, 215  
 network model, 195–197
- Thalamocortical relay cells, 186, 359  
 corticothalamic feedback, 198, 204, 205  
 thalamic reticulate nucleus cell interactions *see* Thalamocortical cell–thalamic reticular nucleus cell models
- Thalamus  
 absence seizures participation, 185–186  
 clonazepam effects, 190  
 mechanisms for hypersynchronized oscillations, 185–186  
   cooperative GABA<sub>B</sub> response models, 188–189  
   early computational models, 186–187  
   spindle oscillations, 186, 392  
   GABA<sub>A</sub> receptor blockade effects, 180  
   GABA<sub>B</sub> receptor blockade effects, 197  
   thalamocortical relay cell–thalamic reticular nucleus cell reciprocal circuit model, 188  
   transition to hypersynchronized oscillations, 184–185, 186  
 T-type calcium current, 185
- Theta activity, 281  
 cellular properties, 283  
 external pacing, 282  
 hippocampus neuronal population model, 36  
 mean-field models  
   absence seizures, 393–395  
   corticothalamic, 388, 391  
   network properties, 283  
   neuronal population models, 366  
   seizure initiation phase, 461
- Thresholds  
 data mining, 13  
 depolarization blockade, 10  
 integrate-and-fire models, 4, 9  
 NEURON synaptic transmission modeling, 28
- Tonic discharges, 296
- Tonic-clonic (grand mal) seizures, 395  
 mean-field models, 387–388, 399, 400  
   scalp EEG data comparison, 396–398  
   phases, 460
- Training data, 44  
 qualitative structure-activity relationships, 521
- Transient receptor potential (TRP) ion channels, graded persistent spiking activity, 216, 226
- Vagus nerve stimulation device, 553
- Validation of epilepsy models, 43–46
- Valproic acid, 515
- Very fast oscillations  
 gamma oscillations alternation, 345, 346  
 gap junctionally connected networks, 335–336, 341  
   network model simulation, 339–340  
 neocortex network model, 336–337  
 percolation model, 341  
 percolation plus refractoriness model, 341–342  
 preceding seizures, 335, 337, 342, 348, 351  
   experimental/clinical observations, 329  
 seizure causation, 337  
 synaptic plasticity, 348  
   *see also* High-frequency oscillations
- Very large scale integrated systems, 573, 577
- Vestibular nucleus neurons, activity-dependent regulation, 249–250
- Vigabatrin, 206, 409, 414
- Virtual Reality Modeling Language (VRML)

- hippocampus 3D digital reconstruction from thin cryostat sections, 69, 73  
*vrmlyview* viewer, 76
- Visual cortex  
activity-dependent neuronal regulation, 249  
attention modulation of response, 317  
experimental observations, 329–330  
interneurons, 317  
anatomical studies, 318  
complex, 317, 324, 330  
modeling, 321  
simple, 306, 317, 328  
network-level homeostatic regulation, 253  
orientation-selective neurons, 317, 318, 329  
firing rate responses, 329
- Visual cortex models, 317–331  
firing rate, 320, 327  
lateral geniculate nucleus spike trains calculation, 320–321  
neuron and synapse models, 321  
ring model, 317, 318–320  
attention effects on contrast response function, 322–323, 324  
coherence between excitatory/inhibitory populations, 325–326  
with complex inhibitory cells, 321–323  
complex version, 318, 319  
heterogeneity associated with stimulus onset, 327  
lateral geniculate nucleus input, 318, 319, 320  
orientation selective response, 322, 325, 330  
synaptic connections, 313  
synchrony modulation, 317, 327, 328  
spectral analysis, 321
- spike time histograms, 321, 325  
stimulus generation, 321
- Visual evoked potentials, 359, 540  
neuronal population model, 357, 359
- Voltage-gated ion channels  
compartmental models, 4, 10  
complex artificial cell models, 10  
computer-aided drug design, 516  
structure prediction for lead compound identification, 515  
graded persistent spiking activity, 215, 216  
neural function modeling, 173–175  
neuron modeling with NEURON, 21
- Voltage-gated sodium channels, 16, 43, 143  
α subunit, 143, 145  
modeling, 146–147  
mutation effects on function, 144–146  
β subunits, 144  
computer-aided drug-design, 515  
gene mutations, 49  
generalized epilepsy with febrile seizures plus, 143, 144
- Volumetric analysis, hippocampus 3D digital reconstruction from thin cryostat sections, 71–72
- Voxel-based volume representation, 73–74, 71
- WAG/Rij rat model, 409, 414  
GABA-mediated inhibition impairment, 415  
vigabatrin response, 410, 414
- Wavefunctions, drug design, 517–518
- Wavelet packets, 535–536  
quadratic chirp signal, 537
- West syndrome, 441

This page intentionally left blank

(A)



(B)

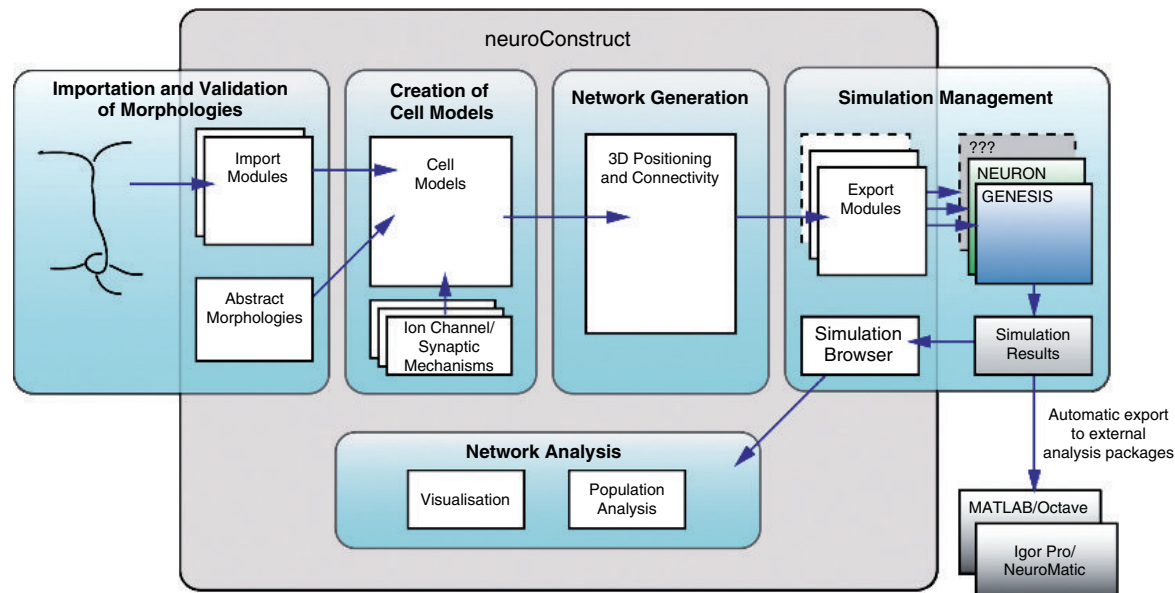


**PLATE 1** Application interface and main functionality. (A) The main interface to *neuroConstruct*, showing a visualization of a network model of the cerebellar granule cell layer in 3D, with a single Golgi cell highlighted to display its pre- and postsynaptic targets. (B) The main functional areas of the application. Modified from Gleeson et al., 2007, with permission. (For black and white version, see page 52 in the volume.)

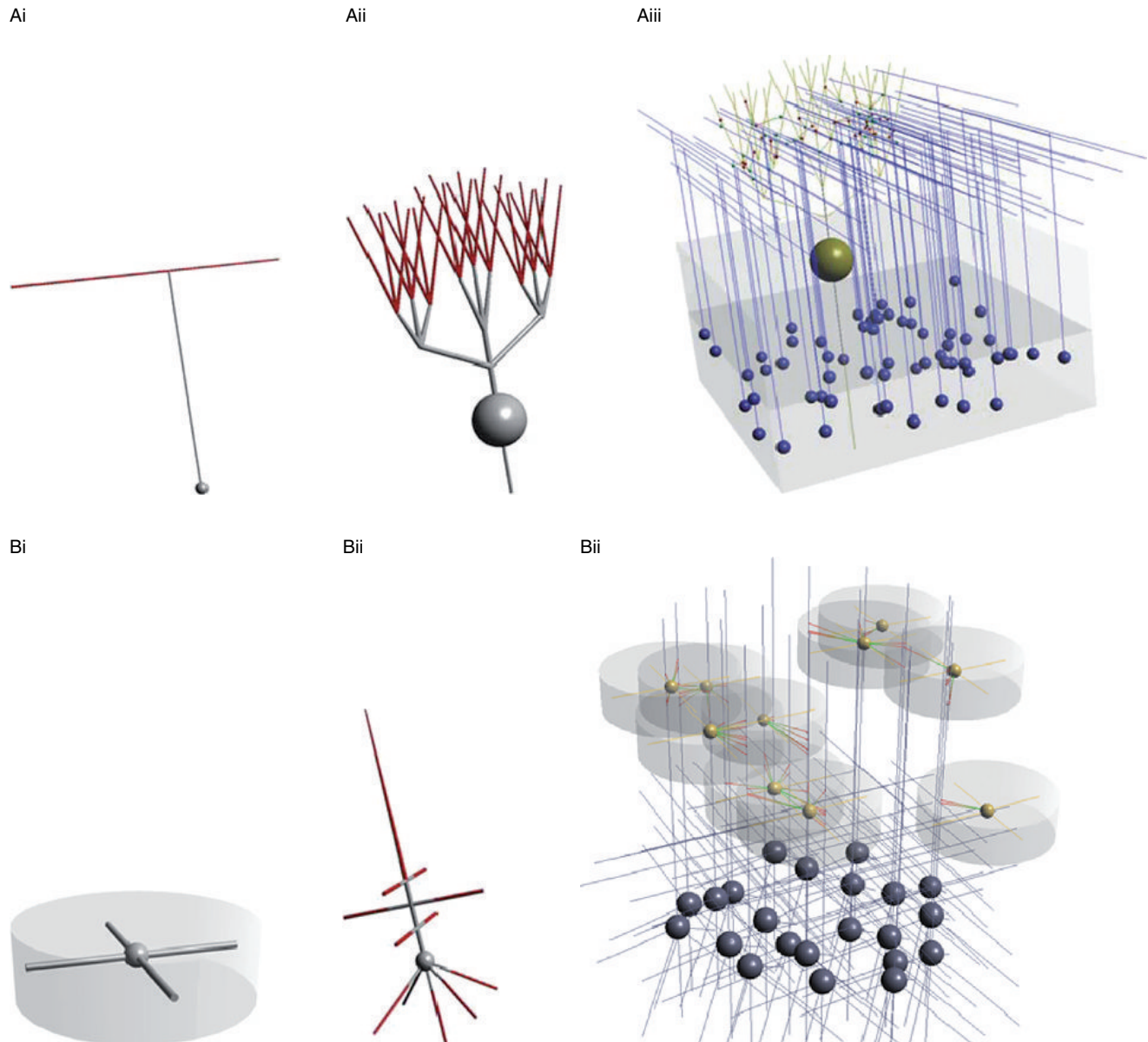
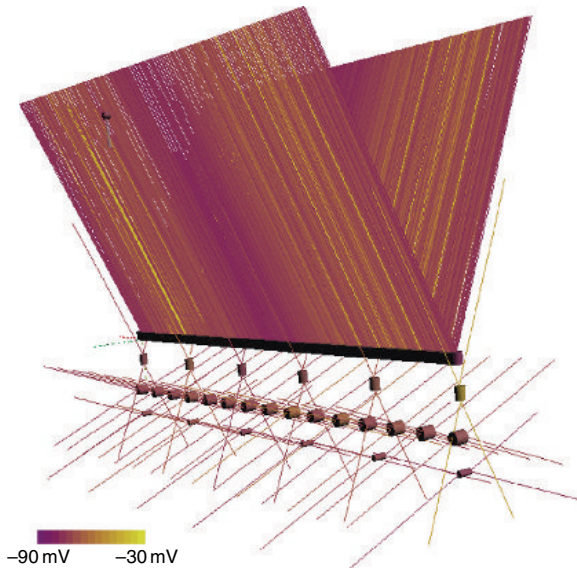
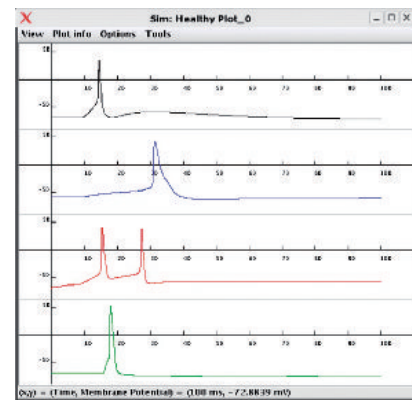


**PLATE 2** Connectivity schemes possible in *neuroConstruct*. (A) Morphology based connection. Connections can be made between specified subregions on the presynaptic granule cell (i) and postsynaptic Purkinje cells (ii). Various other parameters can be set including maximum/minimum length of connections and number of pre-/postsynaptic connections allowed per cell. The connections are shown as green (presynaptic) and red (postsynaptic) spheres connected by lines. (iii) (B) Volume based connection. A region can be specified around presynaptic cells where axonal connections can potentially be made (i). Postsynaptic cells have regions specified associated with this type of connection (ii). Intersections between the 3D axonal regions and permitted dendritic sections can lead to connections, in line with the other rules on numbers of connections per cell (iii). Reproduced from Gleeson et al., 2007, with permission. (For black and white version, see page 53 in the volume.)

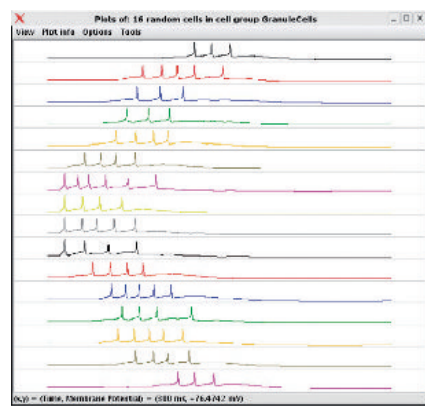
(A)



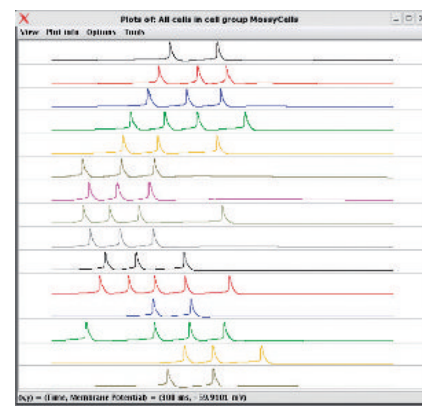
(B)



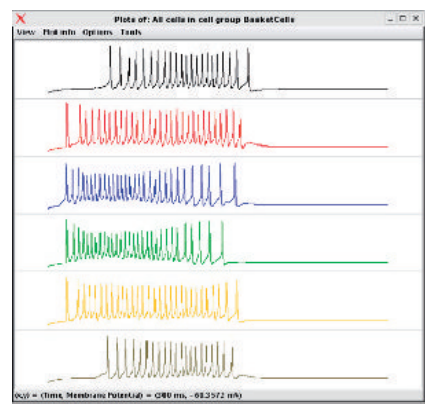
Ci



Cii



Ciii



Civ

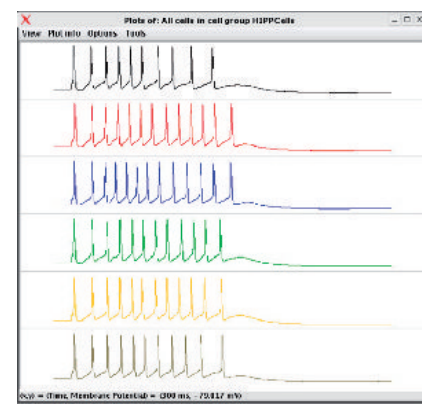


**PLATE 3** Dentate gyrus model in *neuroConstruct*. (A) The cell groups were all aligned in 1D, with a vertical separation added for clarity. The network consisted of (from the top down) 500 granule cells (GrCs), 6 basket cells, 16 mossy cells and 6 hilar perforant path associated (HIPP) cells. Synaptic connections have been removed for clarity (note: conditions on maximum/minimum connection lengths were applied along axis of cell bodies alone (z axis, see Figure 5.3)). The central 100 GrCs receive a pulse of stimulation at 5 ms. The coloring reflects the membrane potential of the cells at 110 ms after the stimulation and in this network, which includes the sprouted connections, the activity can be seen to have traveled to granule cells distant from those receiving the initial input. (B) The behavior of examples of each of the cell types in the normally connected network: a GrC which receives direct stimulation (black trace); a mossy fiber (blue); a basket cell (red) and a HIPP cell (green). All traces are 100 ms long. (C) The behavior of each cell group in the network with 10% mossy fiber sprouting. (i) Membrane potential versus time traces of 16 individual GrCs. These were chosen at random from the 500 GrCs, with cell number increasing from top to bottom of the traces. They illustrate the spread of excitation from the cells at the center which receive the initial input. (ii) Traces for all 15 mossy fibers. (iii) All 6 basket cells. (iv) All 6 HIPP cells. All traces are 300 ms long. Modified from Gleeson et al., 2007, with permission. (For black and white version, see page 62 in the volume.)

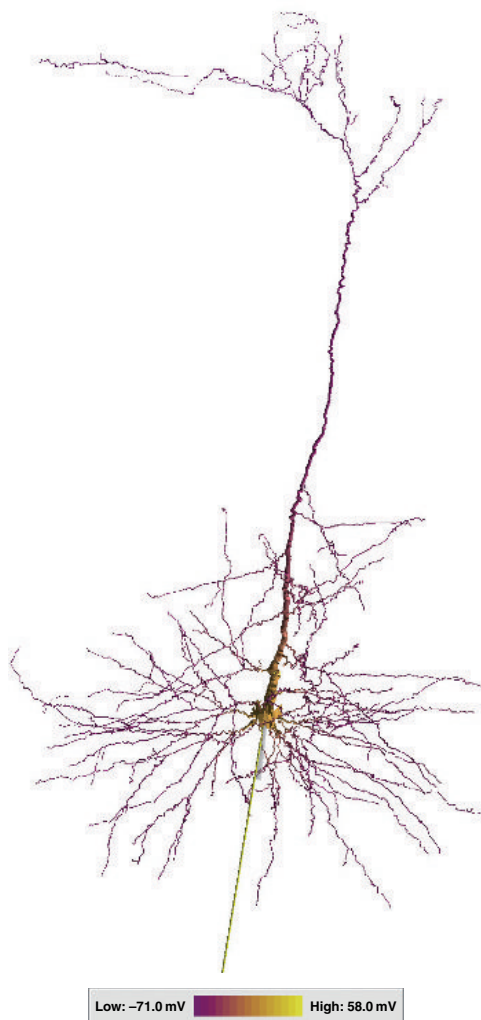
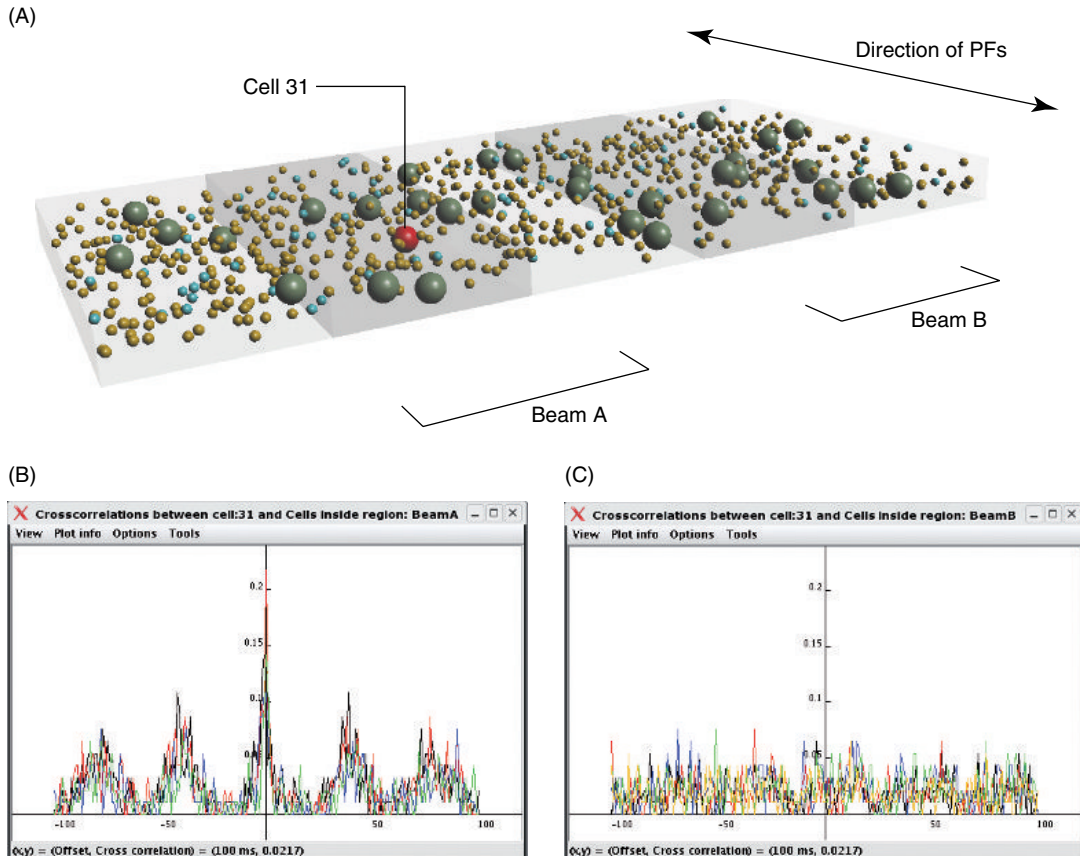
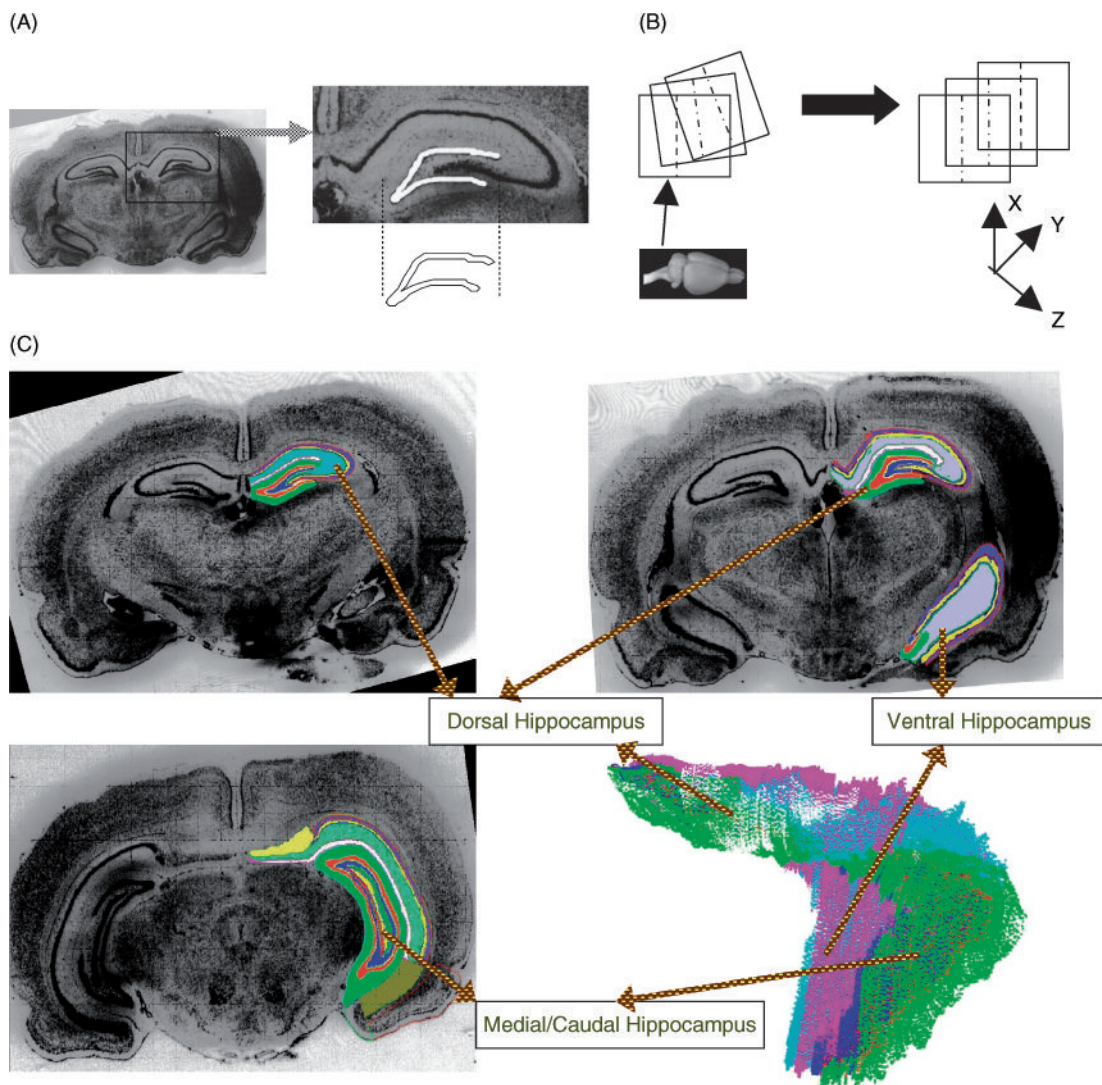


PLATE 4 Pyramidal cell. Screenshot of a layer 5 pyramidal cell model (Mainen et al., 1995) recreated in *neuroConstruct*, showing coloring based on membrane potential shortly after spike initiation in the initial segment of the axon. (For black and white version, see page 64 in the volume.)



**PLATE 5** Granule cell layer model. (A) Granule cell layer model with 600 granule cells (GrCs, orange), 32 Golgi cells (GoCs, dark green), and 96 mossy fiber terminals. Axons, dendrites and synaptic connections are hidden for clarity (see Plate 1). Two beams are identified within the cell body region, which run the direction of the parallel fibers. (B) Cross-correlation between cell 31 in A and the other 4 GoCs in beam A. Each trace of a different color represents a different cell. The y axis shows the probability of finding a spike in the other cell in a time window of 1 ms with the specified offset. (C) Cross-correlation between cell 31 and the 6 GoCs in beam B. Modified from Gleeson et al., 2007, with permission. (For black and white version, see page 65 in the volume.)



**PLATE 6** Image and data acquisition. (A) Representative Nissl stained section of the rat brain. Inset shows the dorsal hippocampus at a magnified resolution with granule cell layer segmented (shaded in white). The clearly distinguishable cyto-architectonic layers allow a reliable segmentation of the hippocampus. (B) Preliminary mid-line guided registration. (C) Manual segmentation of the internal and external boundaries of the hippocampus. Three different coronal sections depict the dorsal, ventral and medial/caudal hippocampus. A surface view of the hippocampus in the medio-lateral view is also shown. (For black and white version, see page 74 in the volume.)

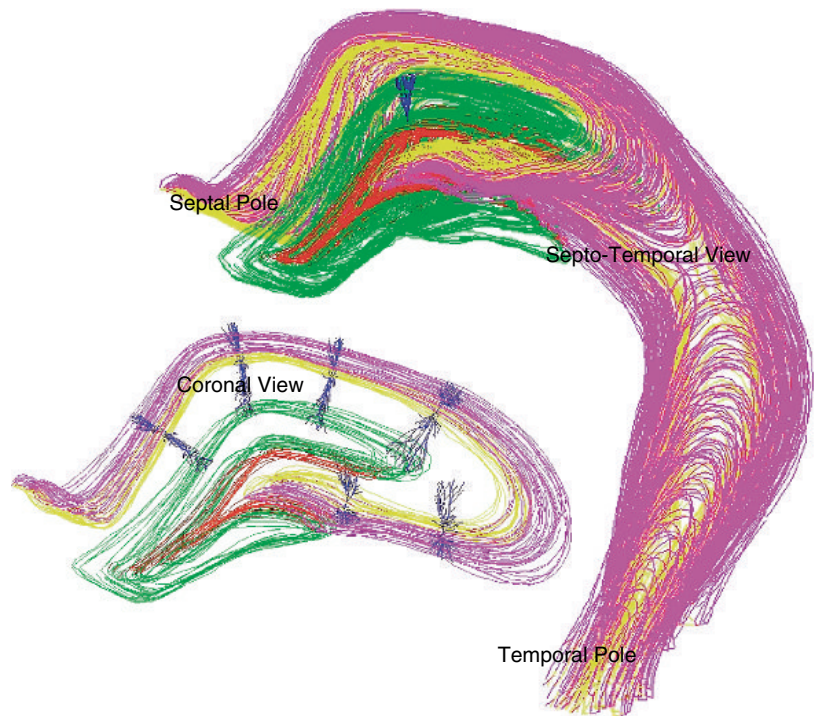


**PLATE 7** Separate views of a granule cell in the appropriate location and orientation of the whole hippocampal reconstruction, and of six pyramidal cells embedded in the (algorithmically identified) CA3c, CA3b, CA2, CA1a, CA1b and CA1c subregions (only a subset of the coronal sections are displayed for clarity). Dendritic trees are in blue, while the boundaries of the oriens, pyramidal, molecular and granule layers are in pink, yellow, green, and red, respectively. (For black and white version, see page 78 in the volume.)

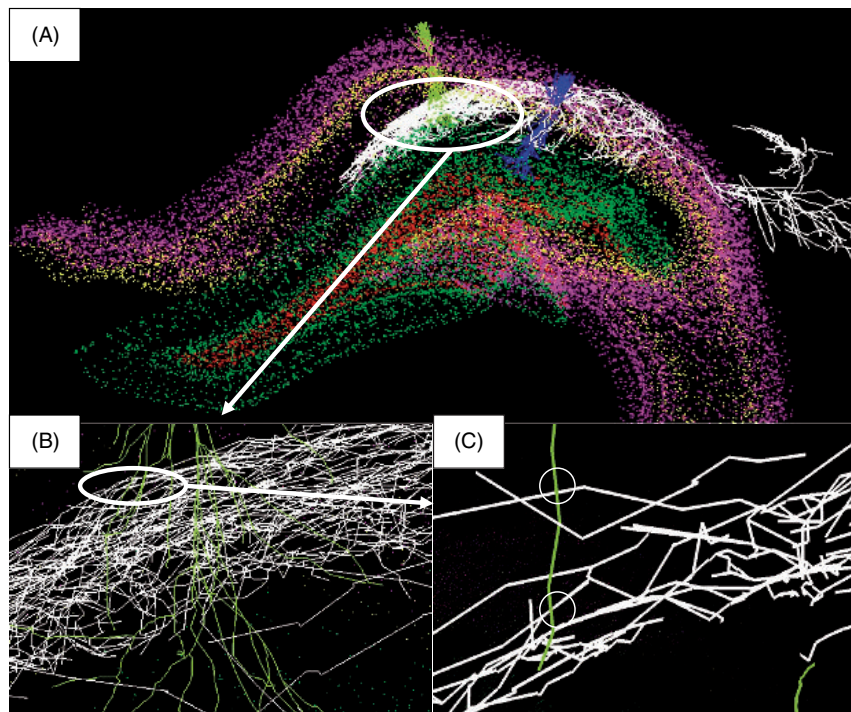


**PLATE 8** Estimating potential connectivity: (A) the axonal arborization (white) of a CA2 pyramidal cell (blue dendritic tree) invades a large portion of the CA radiatum region, and could establish synaptic contacts with a CA1 pyramidal cell (light green dendrites). (B) Spread of the axonal collaterals and possible overlaps with the CA1 dendritic tree. (C) Further magnification highlighting potential synapses (circles). (For black and white version, see page 80 in the volume.)

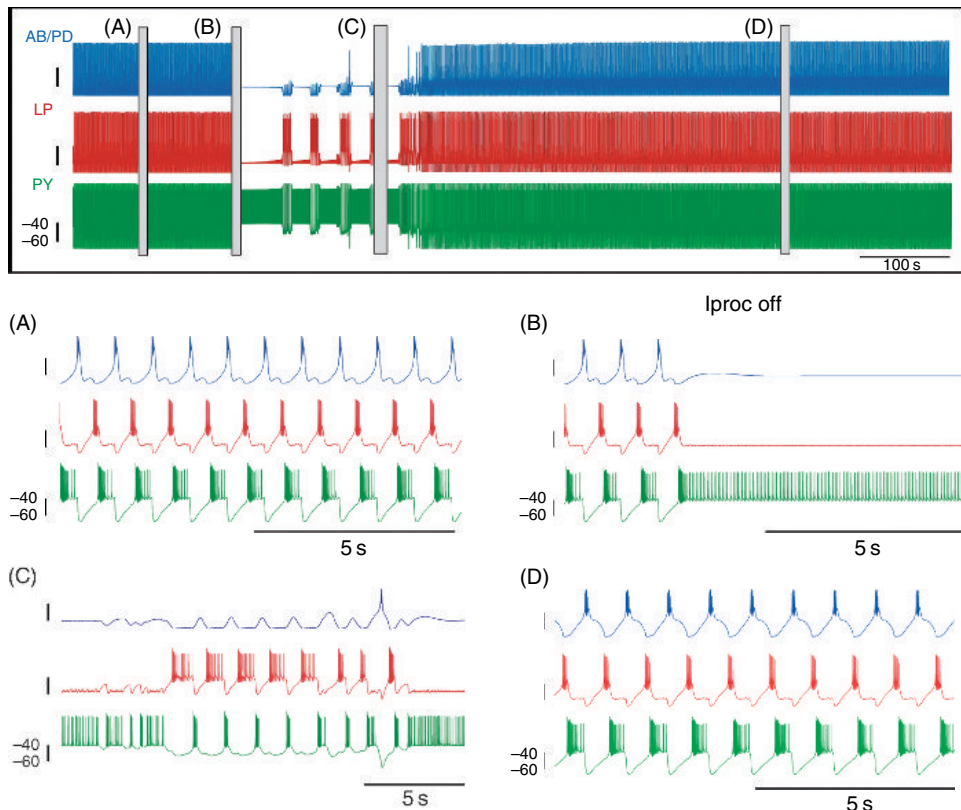


**PLATE 9** Homeostasis in a pyloric network model based on constrained regulation of cellular properties. Top: Voltage traces from the three neurons (AB: anterior burster, LP: lateral pyloric neuron, PY: pyloric neuron) in a pyloric circuit model before and after simulated deafferentation at time B. A–D: Network activity before (A), and immediately after (B) deafferentation simulated by switching off the neuromodulatory current  $I_{\text{proc}}$ , during bouting activity (C), and after recovery of rhythmic activity (D) in the continued absence of the neuromodulatory current. The initially rhythmic network loses rhythmicity upon deafferentation, goes through bouts of activity, and eventually recovers by reconfiguring its cellular properties. LeDoux and Marder, unpublished data. (For black and white version, see page 254 in the volume.)

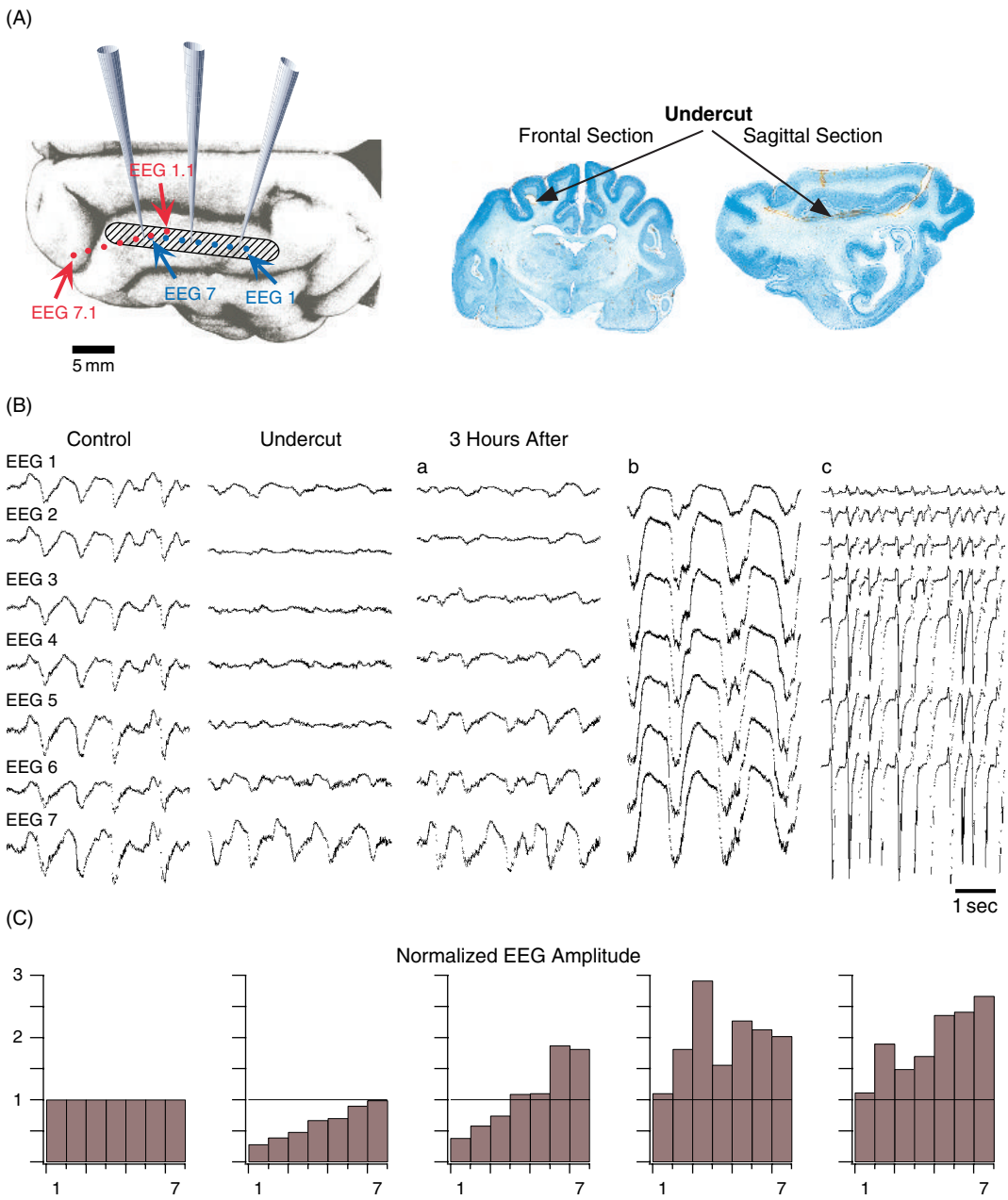
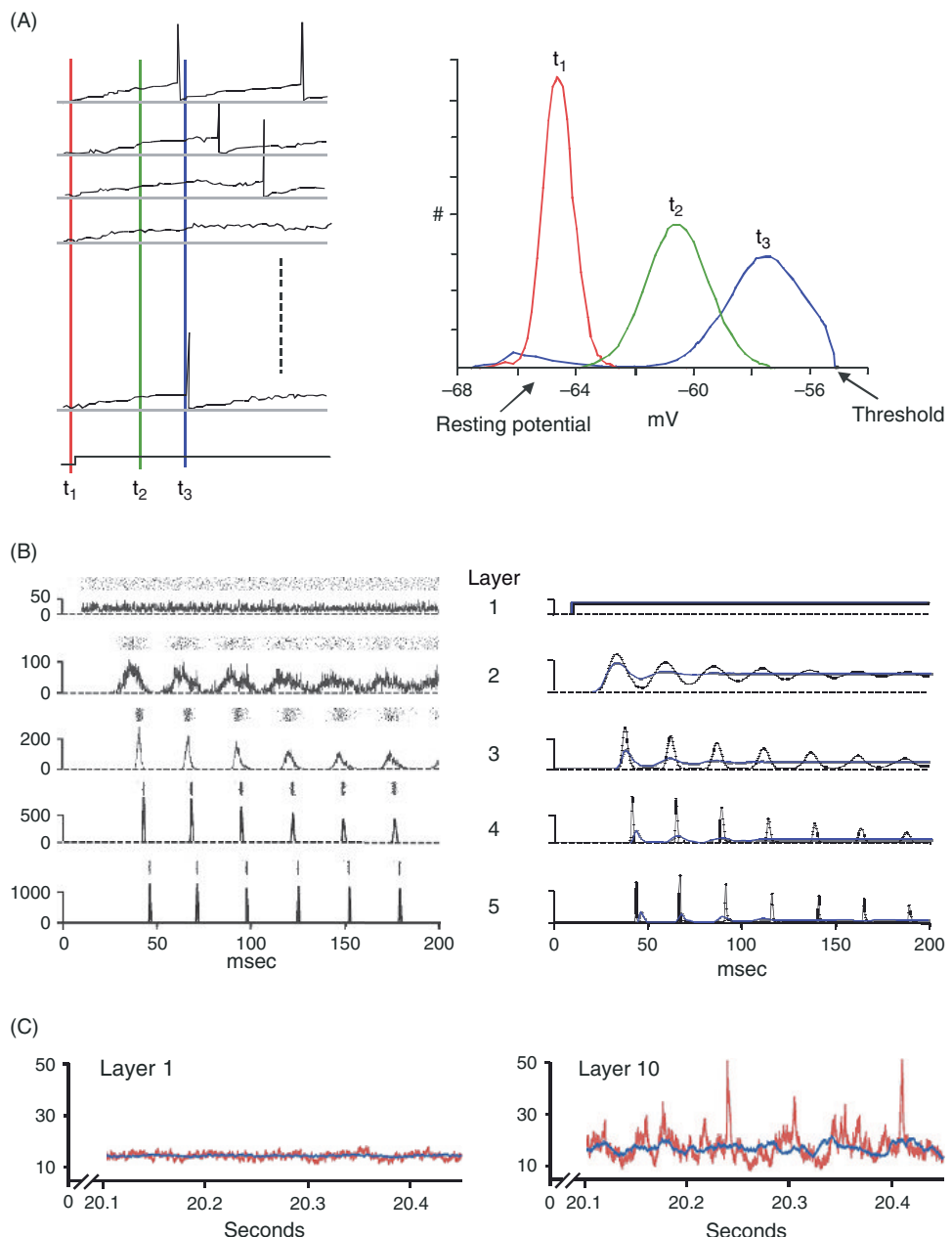
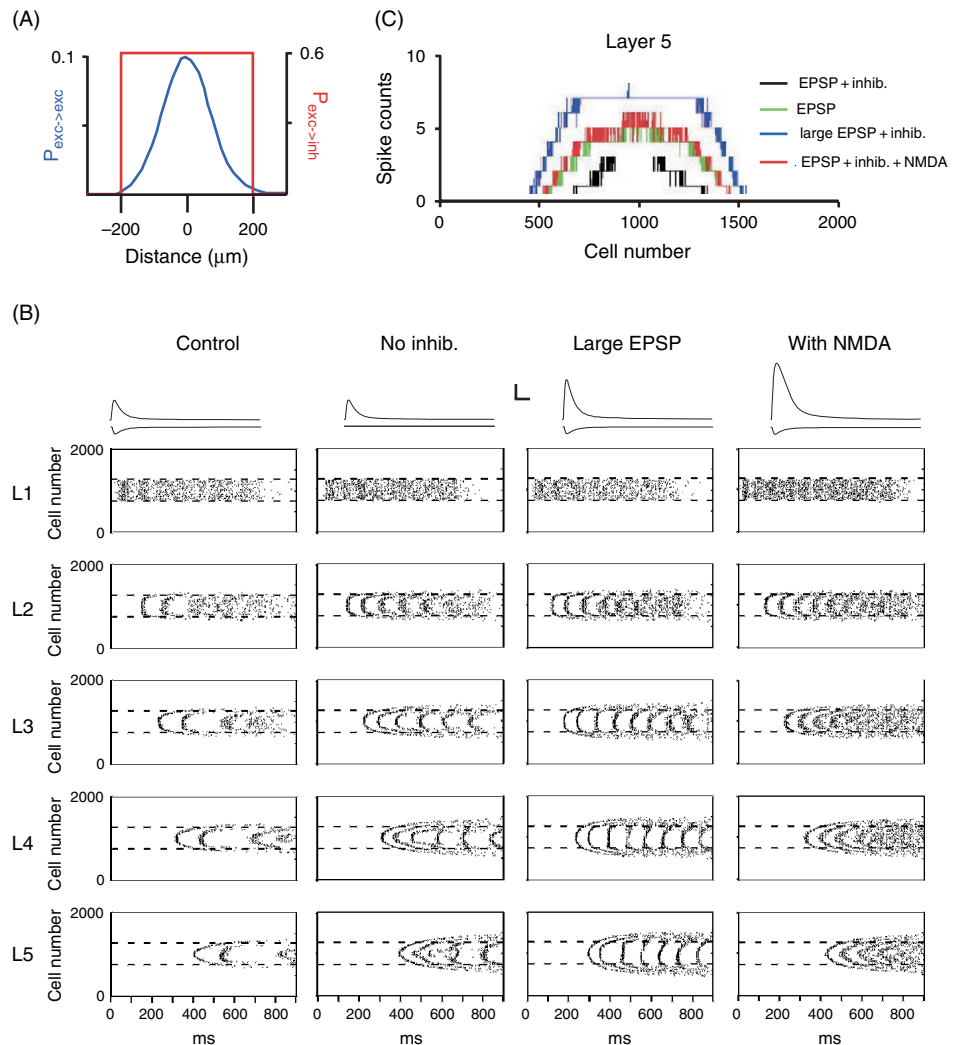


PLATE 1O Slow oscillation in intact suprasylvian gyrus is modified by cortical undercut. (A) Position of EEG arrays of electrodes and of intracellular pipettes and histology of the undercut suprasylvian gyrus. Upper panel: dorsal view of the left hemisphere. The zone of undercut is tentatively indicated by shaded area. Blue points show the generally used position of EEG electrodes (EEG1–EEG7) along the suprasylvian gyrus. Red points show the second position of EEG electrodes (EEG1.1–EEG7.1) in the postcruciate gyrus and anterior part of suprasylvian gyrus. Position of pipettes is schematically indicated. Bottom panel shows frontal and parasagittal section of the left hemisphere from two different cats showing the extent of the undercut (indicated by arrows). (B) Field potential recordings (EEG) from the intact cortex (left panel – Control), undercut suprasylvian gyrus, immediately after the undercut (middle panel – Undercut) and 3 hours later (three right panels; a, b and c, three different animals). Position of EEG electrodes was indicated in (A) by blue points. (C) depicts normalized EEG amplitude (vertical axis) of the corresponding EEG from different sites (horizontal axis). Mean EEG amplitude for each electrode in control was taken as 1. EEG1 – field potential recording from the posterior part of the suprasylvian gyrus, EEG7 – recording from the anterior part of this gyrus. Note the decreased EEG amplitude immediately after the undercut and partial recovery or increase in the amplitude 3 hours later, especially during the paroxysmal activity. From Topolnik et al., 2003a, with permission. (For black and white version, see page 262 in the volume.)



**PLATE 11** Fokker-Planck analysis of feedforward networks. (A, left) Firing of a population of leaky integrate-and-fire neurons in response to a current step with Gaussian white noise. Right, distributions of membrane potentials taken through 3 time points (vertical lines on left). (B) Poststimulus time histograms obtained with a feedforward network of leaky integrate and fire neurons. Right, prediction generated with a Fokker-Planck equation assuming that the neurons were Poisson processes (blue). Note that unlike the simulations and experiments, the predicted histogram flattens out by 100 ms, indicating asynchronous firing. Fit to the simulations was improved by relaxing the Poisson assumption (black). From Cateau and Reyes, 2006. (C) Poststimulus time histograms obtained when finite size effect perturbations are taken into account. Synchronous firing persisted when few, larger inputs were used (red). In contrast, asynchrony developed when there were many, small inputs (blue). From Doiron et al., 2006. (For black and white version, see page 310 in the volume.)



**PLATE 12** Spread of synchrony. (A) Probability distributions for connections between pyramidal cells (blue) and between pyramidal cells and inhibitory cells (red) as a function of distance. (B) Dot rasters for 5 layered feedforward networks of quadratic-integrate-and-fire neurons (columns) under 4 configurations (rows). First column: control condition was with excitatory and inhibitory neurons with the connection schemes in (A) (see text). Second column: network with only excitatory neurons. Third column: similar to control network except the amplitude of the excitatory input was doubled. Fourth column: similar to control except an NMDA component was added to the excitatory input. The horizontal dashed lines demarcate the boundary of the activated neurons in layer 1. Scale bars for synaptic potentials: 0.5 mV, 20 ms. (C) Total number of action potentials (ordinate) fired by cells (abscissa) in layer 5 under the 4 conditions. Note that the spread of activity in the non-control conditions was substantially greater than in the control network. (For black and white version, see page 314 in the volume.)

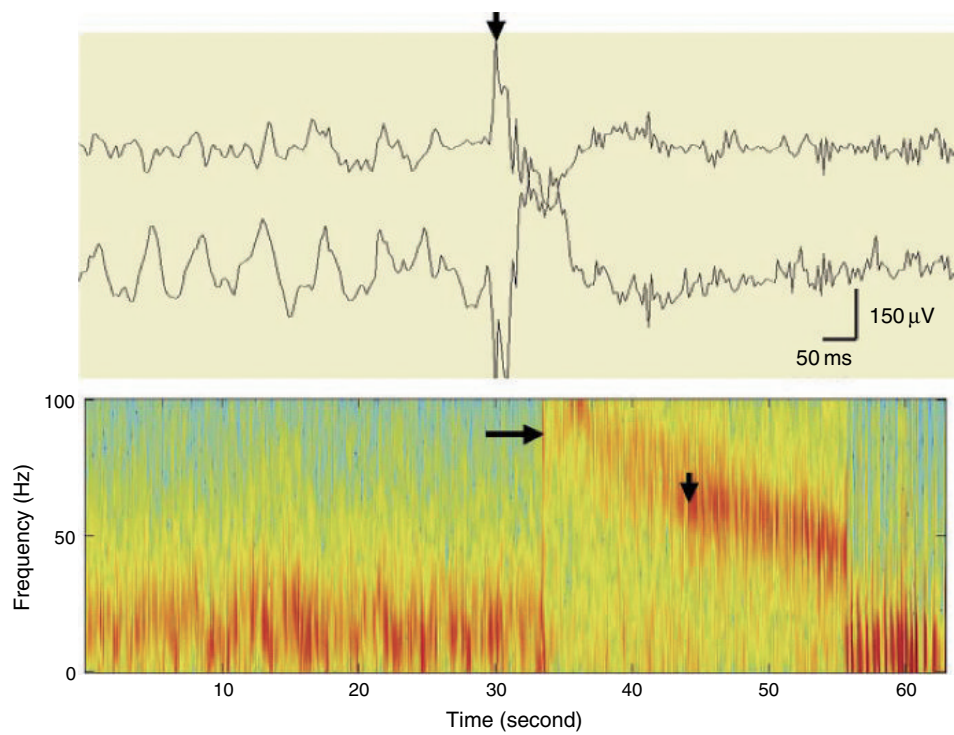


**PLATE 13** Demonstration of ~10 seconds of intracranial fast EEG oscillation prior to first motor evidence of ictal motor activity. This patient had seizures of frontal lobe onset. The upper traces show VFO in association with an EEG spike: compare Figure 22.1C and Figure 22.2. The color-coded time frequency plot below shows fast activity, beginning at ~90 Hz (horizontal arrow), that lasts about 15 seconds up to the first evident motor activity (vertical arrow). From Worrell et al. (2004), with permission. (For black and white version, see page 339 in the volume.)

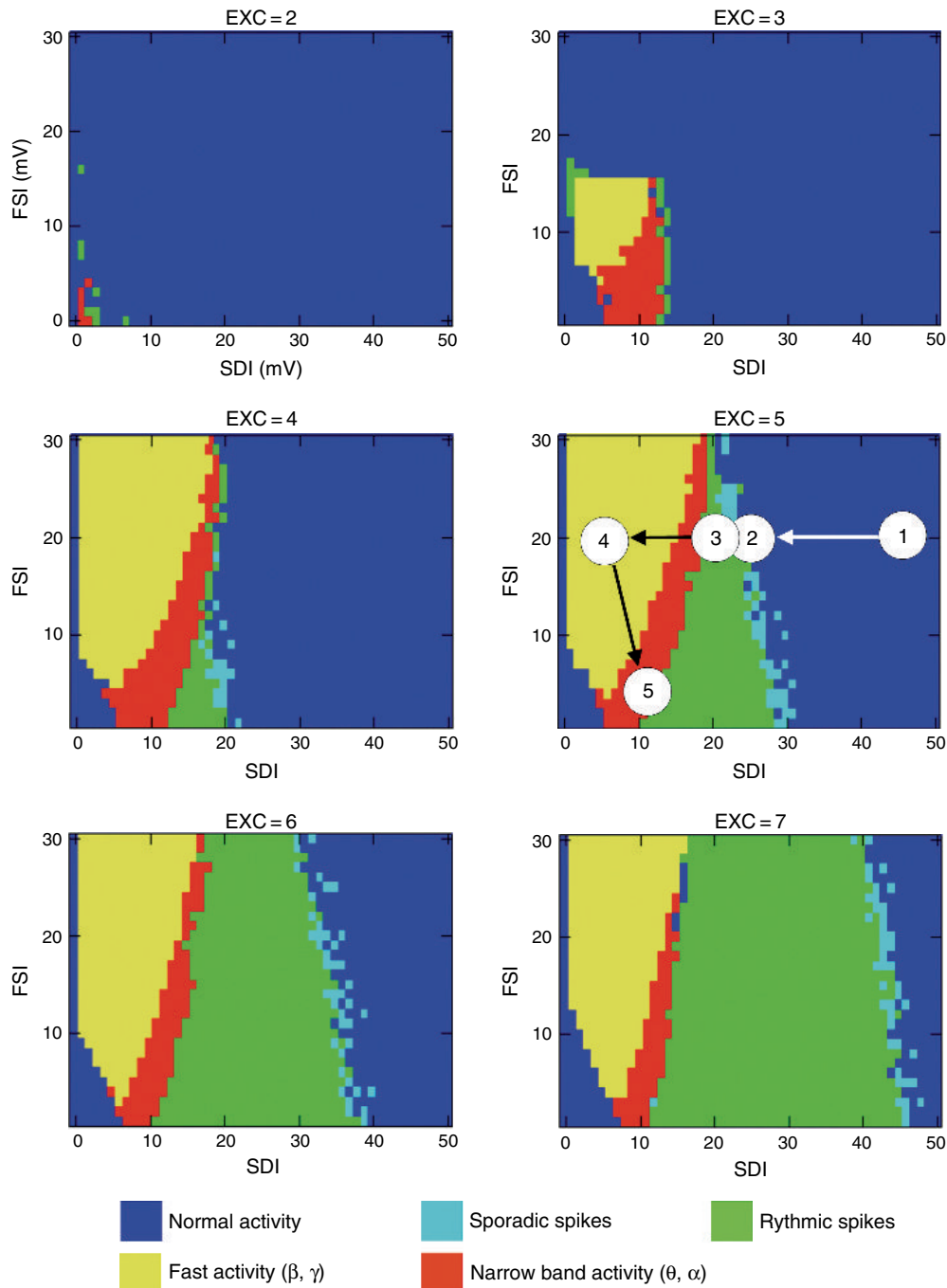


**PLATE 14** Activity maps describing the behavior of the hippocampus model as a function of variations of parameters EXC, SDI and FSI. On the fourth map, a candidate path is reported, consistent with the typical sequence of activities reflected in real SEEG signals during the transition to seizure: normal background activity (1), sporadic spikes (2), rhythmic spikes (3), fast activity (4) and ictal activity (5). This path provides a way to identify parameter variations for which dynamics and transitions observed in real signals are reproduced by the model. See text for interpretation of identified parameters. See also Figure 23.16. (For black and white version, see page 380 in the volume.)

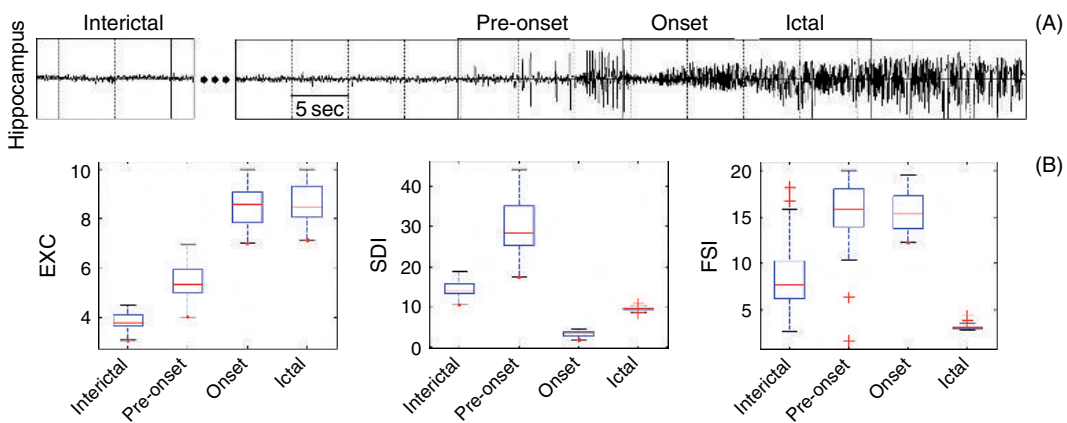


**PLATE 15** Parameter identification results using a procedure based on evolutionary algorithms (see Wendling et al., 2005 for details). (A) Visually selected segments of EEG signals during transition to seizure recorded from hippocampus in a patient with medial TLE. (B) Boxplots are calculated from 30 independent realizations of the identification process for each segment of real activity. Results show the stability of the identified solutions and depict a global tendency in the evolution (as a function of time) of the main model parameters (EXC, SDI and FSI). (For black and white version, see page 381 in the volume.)

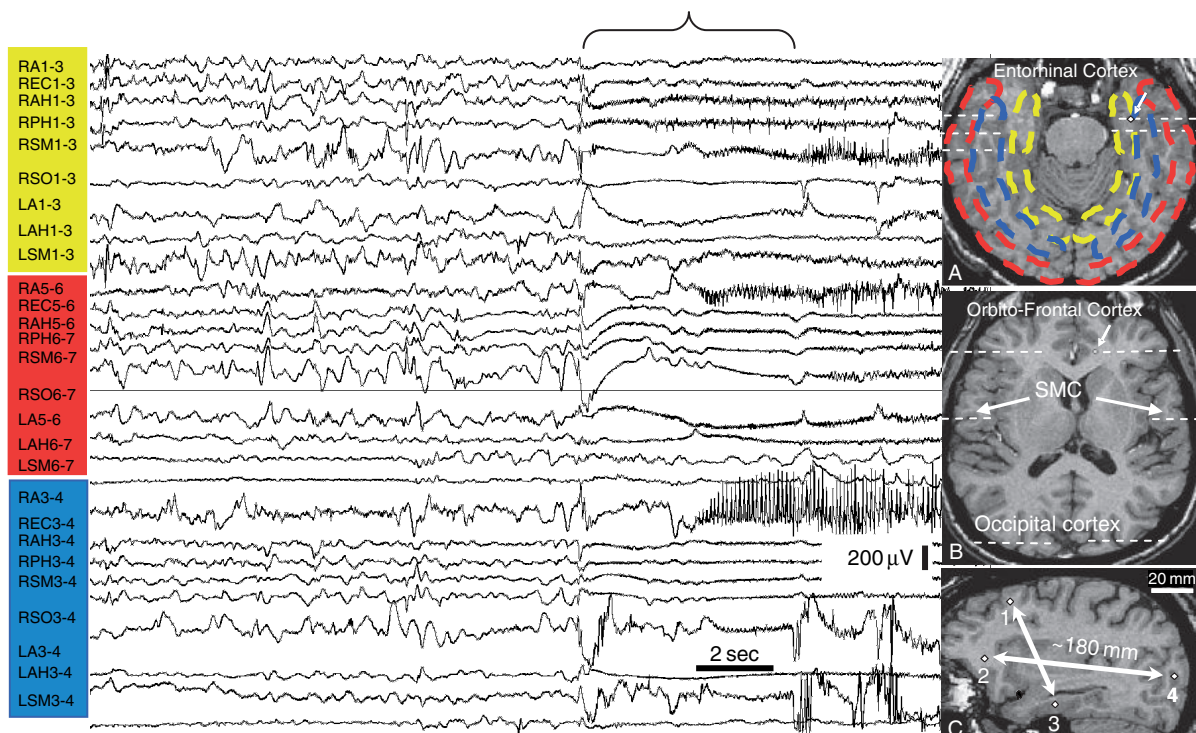


**PLATE 16** Example of a seizure recorded in bipolar montage with initial slow wave at the onset, indicated by the bracket at the top. Yellow, red and blue colors indicate correspondingly mesial, medial and lateral locations of the recorded sites, illustrated on part (A) of MRI image. (B,C) Examples of MR images indicating the location of the recorded sites. (For black and white version, see page 441 in the volume.)

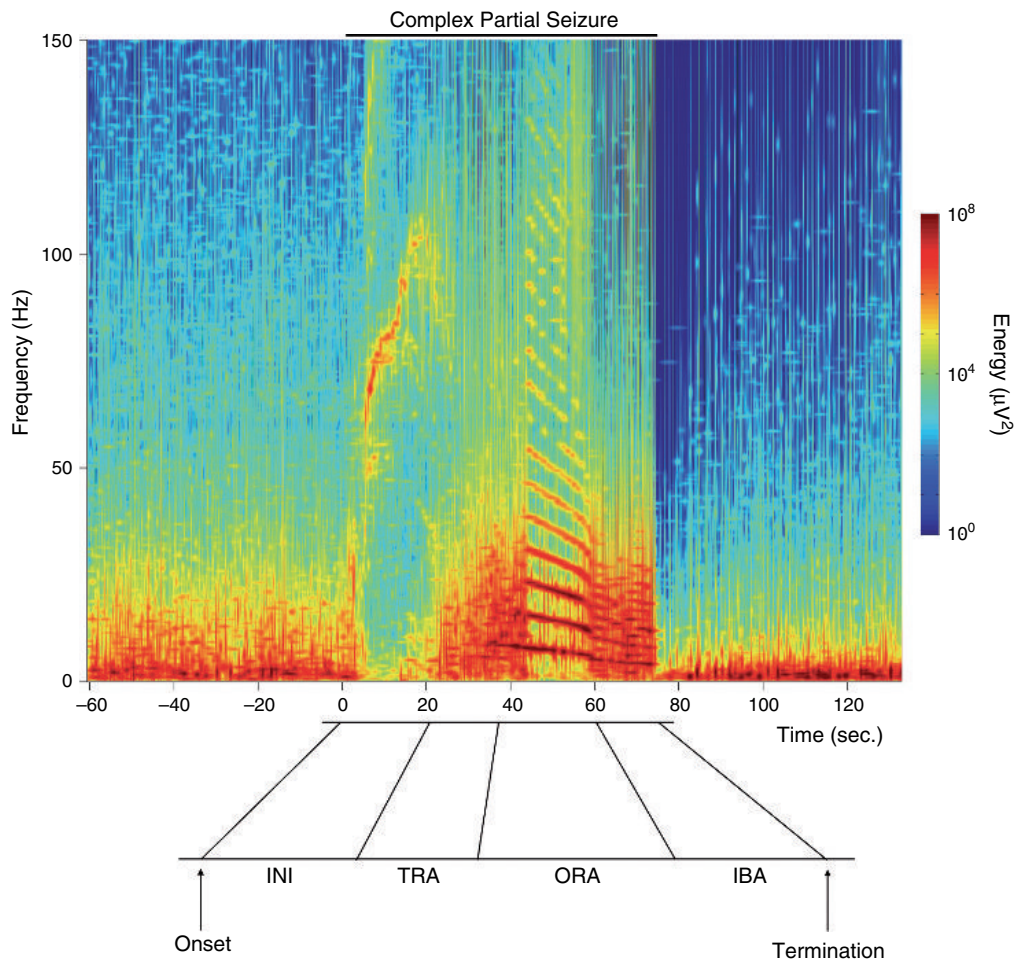


PLATE 17 The four phases of a partial seizure as seen on the time-frequency reconstruction of the energy of the ICEEG signal. Horizontal axis is time. Left axis is frequency. Color bar on the right is representing the scale of the energy representation. (For black and white version, see page 463 in the volume.)

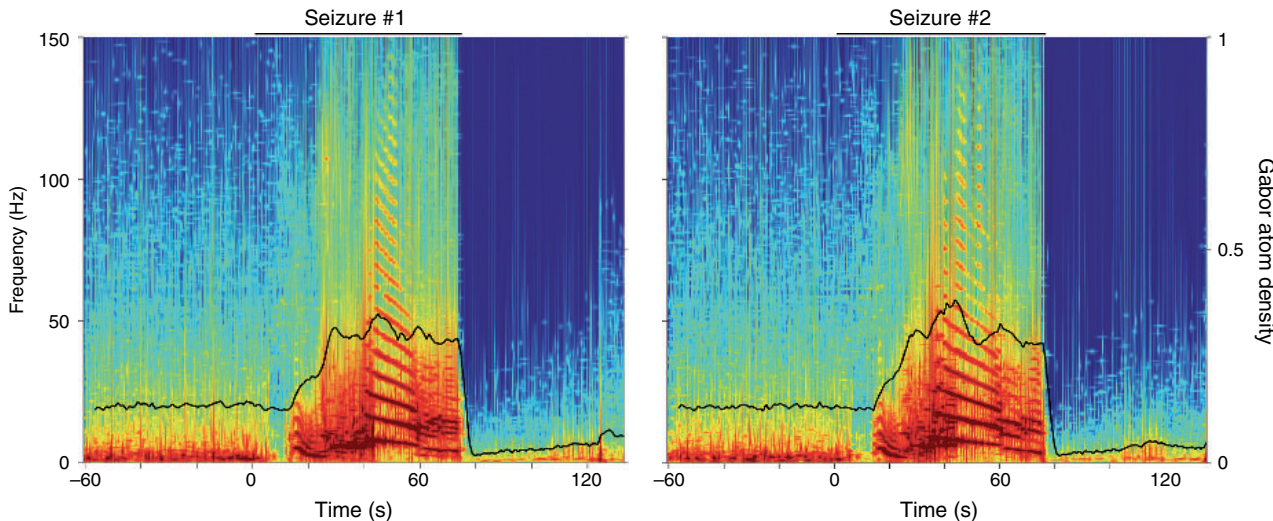
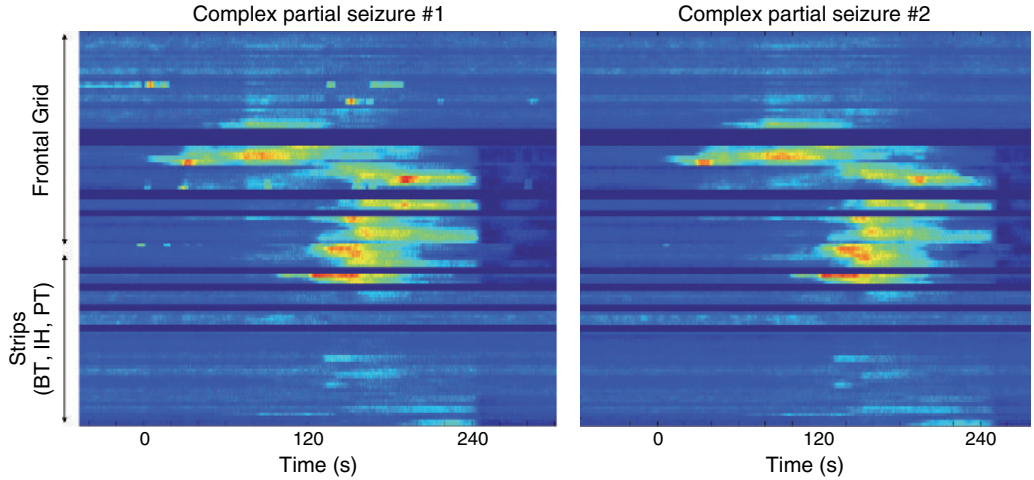
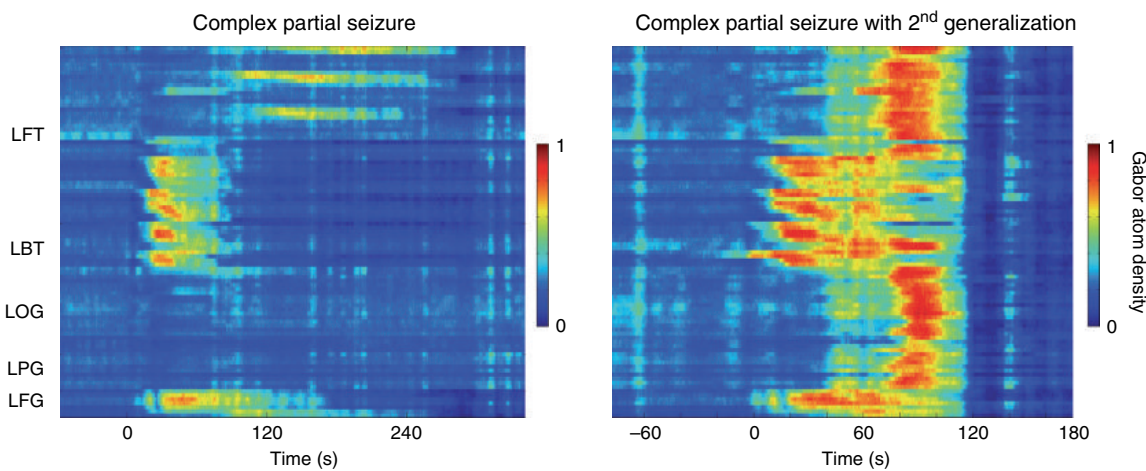


PLATE 18 Comparison of two time-frequency reconstructions for two different complex partial seizures from the same patient. The similarity of seizure evolution between two seizures translates into similar content in the time-frequency domain. Both seizures have identical spectral features and seizure phases: INI with low amplitude onset with rhythmic theta/delta, TRA, ORA, IBA and post-ictal depression. (For black and white version, see page 465 in the volume.)



**PLATE 19** Propagation maps for two complex partial seizures from the same patient. Time zero is the onset of the seizure. Blue represents low GAD value and red represents high GAD values. Two separate events recorded hours apart still exhibit highly similar dynamics. Onset location, timing of propagation pattern, seizure duration and pattern of termination are very similar. (For black and white version, see page 466 in the volume.)



**PLATE 20** Propagation maps for a complex partial seizure (left) and a complex partial seizure with secondary generalization (right). Time zero is the onset of the seizure. Blue represents low GAD value and red represents high GAD values. Both events appear to have similar dynamic and propagation during the early period of the seizure. (For black and white version, see page 467 in the volume.)

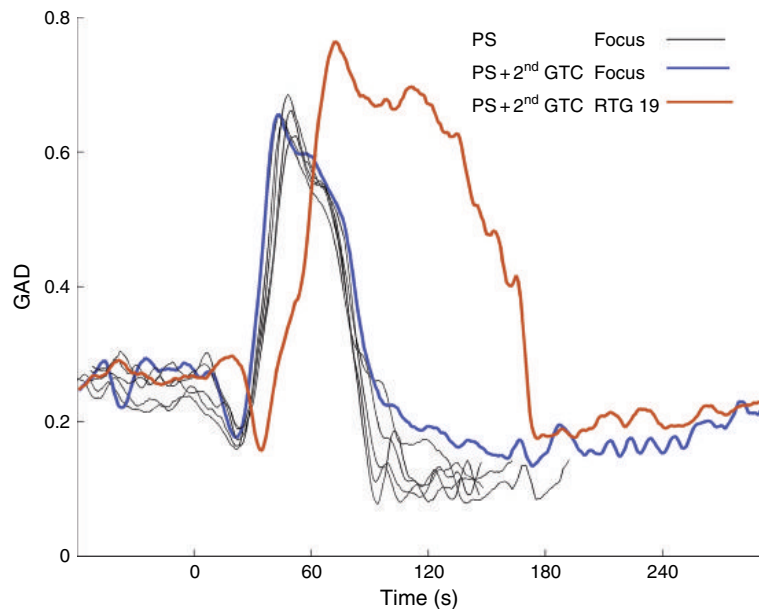


PLATE 21 GAD for five complex partial seizures (CPS) and one complex partial seizure with secondary generalization (CPS+2<sup>nd</sup> GTC) for the same patient. Black traces represent GAD for the focus during the CPS. Blue trace represents GAD for the focus during the GTCS. Orange trace represents GAD for a remote electrode (RTG19) during the GTCS. (For black and white version, see page 468 in the volume.)

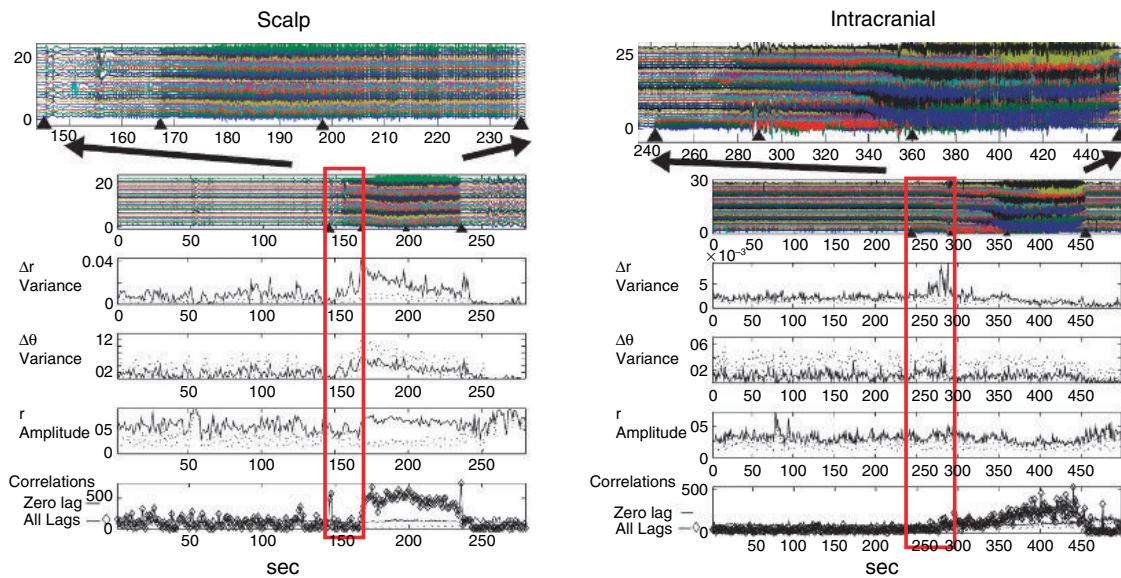
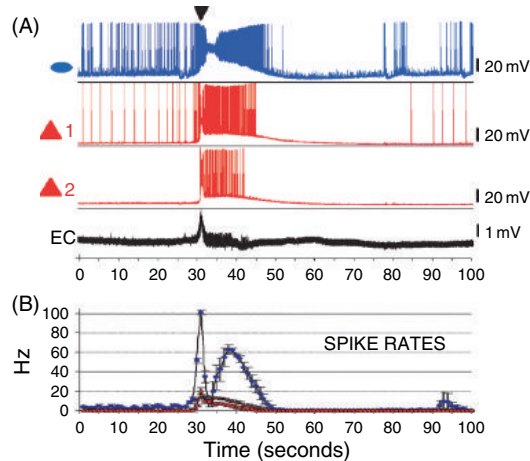
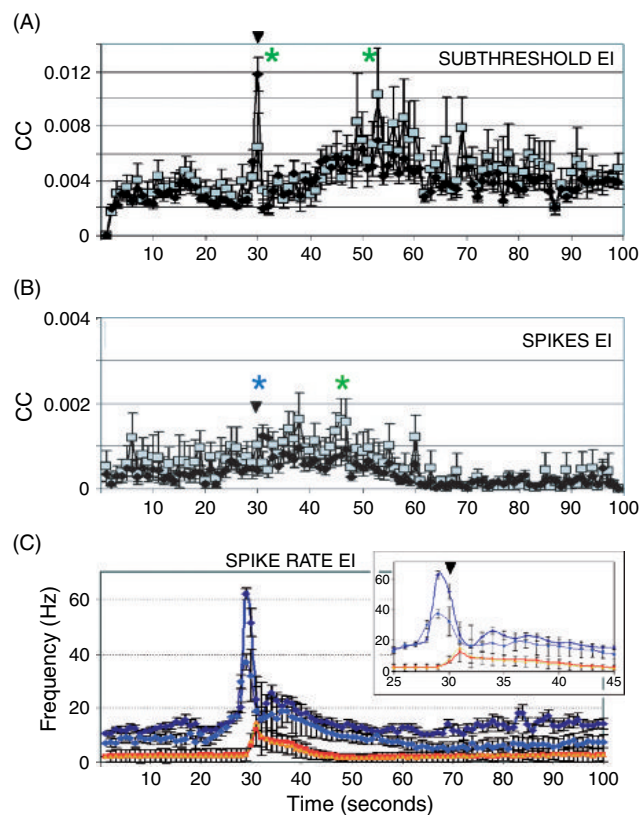


PLATE 22 Dynamical evolution of human seizures. On the left is shown an example of a human seizure recorded from scalp, and on the right, from intracranial electrodes. The dynamics were partitioned using an adaptation of multivariate linear discrimination (Schiff et al., 2005). Five separate measures inferring synchronization are shown: from a phase analysis, amplitude ( $r$ ) and angle ( $\theta$ ) magnitude and variance (dispersion), as well as cross-correlations shown for zero lag and at arbitrary lag. The initial stage of these seizures (red rectangles) shows no evidence of increased synchronization by any measure, whereas a consistent feature of both intracranial and extracranial seizure recordings is the statistically significant increase in correlations seen during the middle stage of these events. After Schiff et al., 2005 (reproduced with permission). (For black and white version, see page 499 in the volume.)



**PLATE 23** EI spike interplay during SLEs. (A) Traces from simultaneous whole cell measurements from one interneuron (blue, ellipse) and two pyramidal cells (red, triangles) and an extracellular DC mode recording (EC). Inverted black triangle denotes the FPES. (B) Average spike rates of the three cells (interneuron, blue circles, pyramidal 1, red diamonds, pyramidal 2, red triangles). Note that the plot in (B) is an average ( $n = 8$  SLEs in the experiment) and hence is not precisely time locked to the single SLE example shown in (A). (For black and white version, see page 506 in the volume.)



**PLATE 24** EI correlations during SLEs. (A) EI cross-correlation (CC) averages. The means of EI subthreshold cross-correlation values were significantly different (ANOVA:  $df = 10199$ ,  $F = 4.27$ ,  $P < 0.0001$ ) at distinct SLE stages (Tukey multicomparison, green asterisks). Unweighted pooled subthreshold EI cross-correlation values (represented as black diamonds) peaked at the onset of SLEs, followed by a decrease and then a gradual increase towards the end of the SLEs (Tukey multiple comparison test,  $P < 0.001$ ). With weighted resampled averages (gray squares) the peak at the onset of SLEs was less prominent, but the significance of the increase in subthreshold EI correlations was retained ( $P < 0.05$ ). Inverted black triangles denote the FPES in (A, B, inset in C). (B) A significant increase in EI spike correlations was observed at the beginning (unweighted, blue asterisk) and following the DB in interneurons (weighted averages, green asterisk). (ANOVA,  $df = 10199$ ,  $F = 3.27$ ,  $P < 0.0001$ ; Tukey multiple comparison test,  $P < 0.001$  for unweighted (black diamonds) and  $P < 0.005$  for weighted resampled (gray squares) averages). (C) Cumulative average spike rates ( $n = 15$  oriens interneurons and  $n = 40$  pyramidal cells from pairs and single whole cell recordings). Note the peak of inhibitory spiking preceding the FPES (dark blue, I unweighted pooled; light blue, I weighted resampled). Excitatory firing rates increase as interneurons enter into the DB and decreased as interneurons exit the DB (red, unweighted pooled; orange, unweighted pooled). Inset shows average spike rates at expanded time scale. After Ziburkus et al. (2006) (reproduced with permission). (For black and white version, see page 507 in the volume.)

(A)



(B)

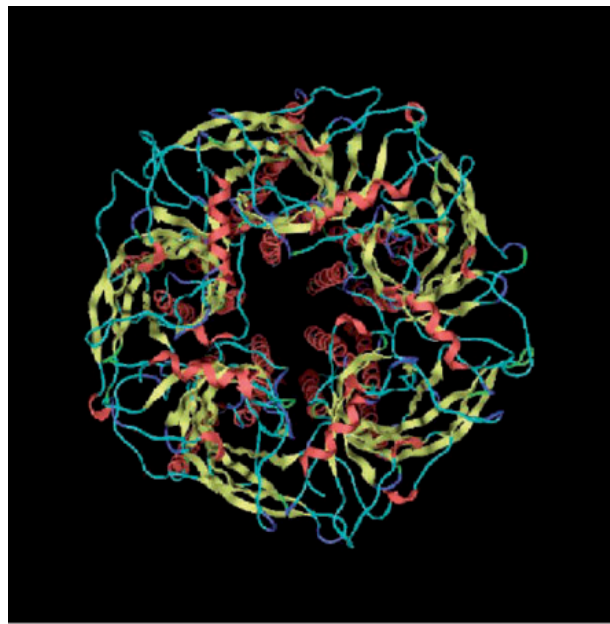


**PLATE 25** Computer model of the GABA-A receptor protein. A computer model of the GABA-A receptor protein achieved using homology modeling in conjunction with molecular mechanics energy minimizations. The side-view (A) and top-view (B) of the protein are shown. Such theoretical models of protein structure have not yet reached the level of accuracy to permit rational drug design. (For black and white version, see page 525 in the volume.)

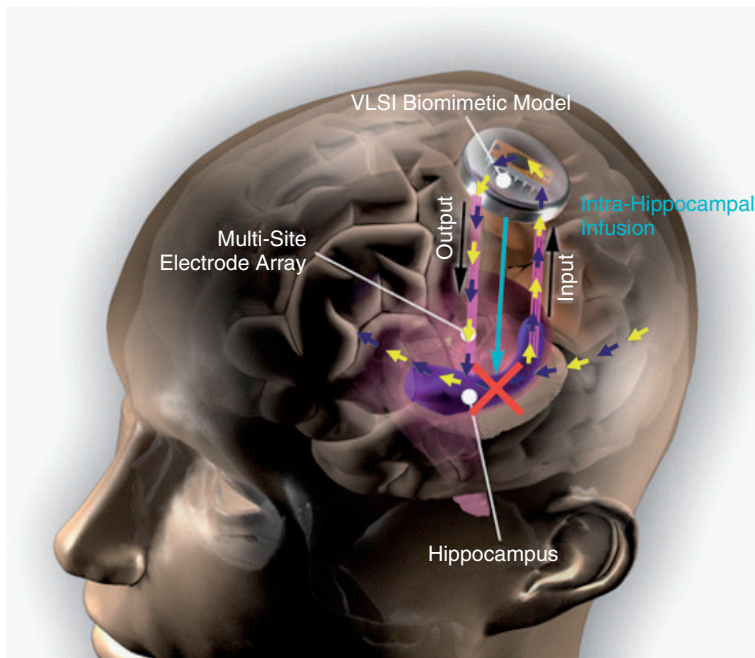


**PLATE 26** Diagram illustrating proposed indwelling ‘closed-loop’ system for (i) detection of impending seizure with glutamate-sensitive microelectrode array, (ii) termination of seizure onset via local drug application to inhibit synaptic glutamate transmission, and (iii) maintenance of hippocampal mnemonic function through a biomimetic device that provides a means for ‘by-passing’ that portion of hippocampal circuitry (e.g. CA3) rendered inactive by the infusion of anti-epileptiform agents. (For black and white version, see page 561 in the volume.)

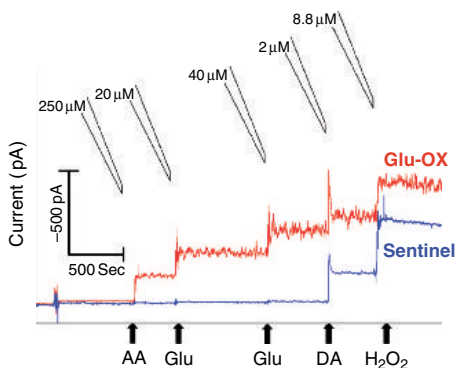


**PLATE 27** Calibration of a Nafion[R] coated glutamate-sensitive, self-referencing microelectrode. Calibration solutions are added to determine the sensitivity to Glu, selectivity for Glu over AA, and responsiveness to other electroactive molecules (e.g. DA (interferent) and H<sub>2</sub>O<sub>2</sub>(positive control)) for each Pt recording site. Glu-OX sites (red trace) respond well to glutamate and some electroactive interferents. The enzyme-free sentinel sites (blue) do not respond to glutamate but show similar responses to the same electroactive interferents. Subtraction of sentinel site measurements from Glu-OX site measurements yields self-referenced local glutamate concentration free of interferents. Pipettes demonstrate sequence and time-course for addition of interferent and analyte aliquots. Final *in vitro* calibration concentrations following addition of various aliquots as shown: 250  $\mu$ M AA, 20 and 40  $\mu$ M Glu, 2  $\mu$ M DA, and 8.8  $\mu$ M H<sub>2</sub>O<sub>2</sub>. (For black and white version, see page 565 in the volume.)

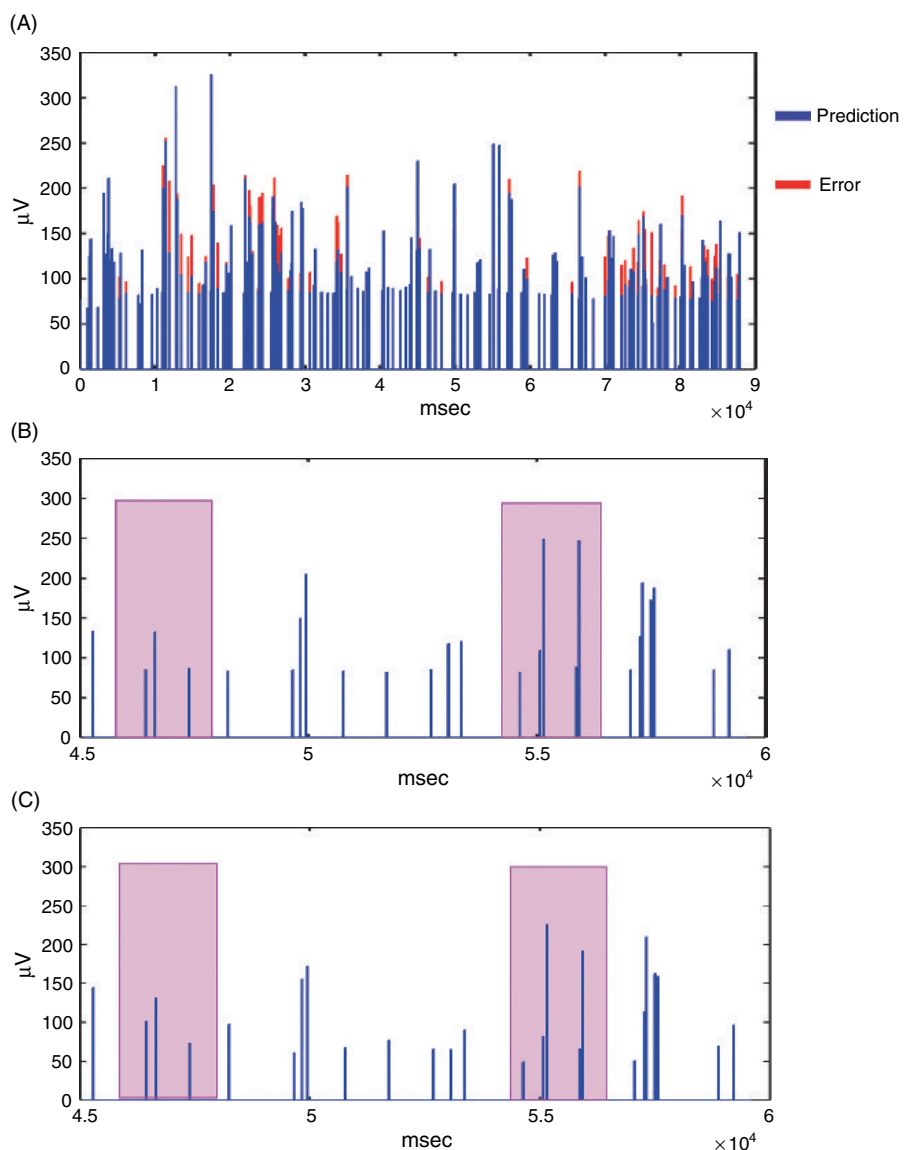
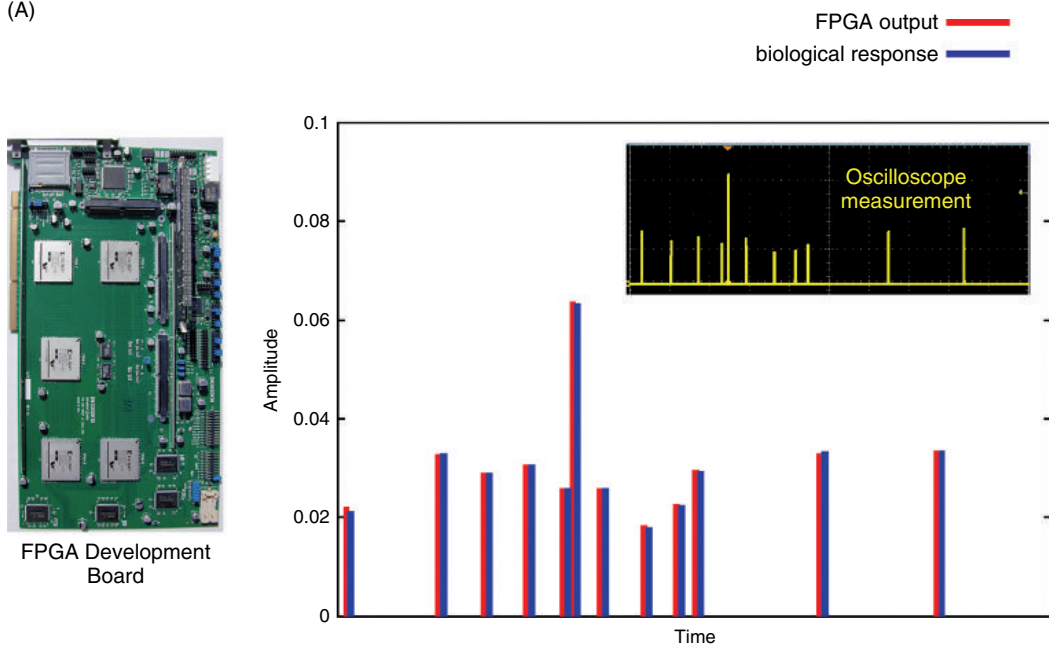


**PLATE 28** An example of CA3 model prediction (NMSE = 8.21%). (A) Predicted population spike amplitudes (blue) and their differences from the corresponding measured population spike amplitudes (red). (B) Segment of the CA3 Model Prediction. (C) The corresponding segment of the measured CA3 population spike amplitudes. The shaded rectangles highlight two areas for comparison between model predicted values and recorded values. (For black and white version, see page 578 in the volume.)

(A)



(B)

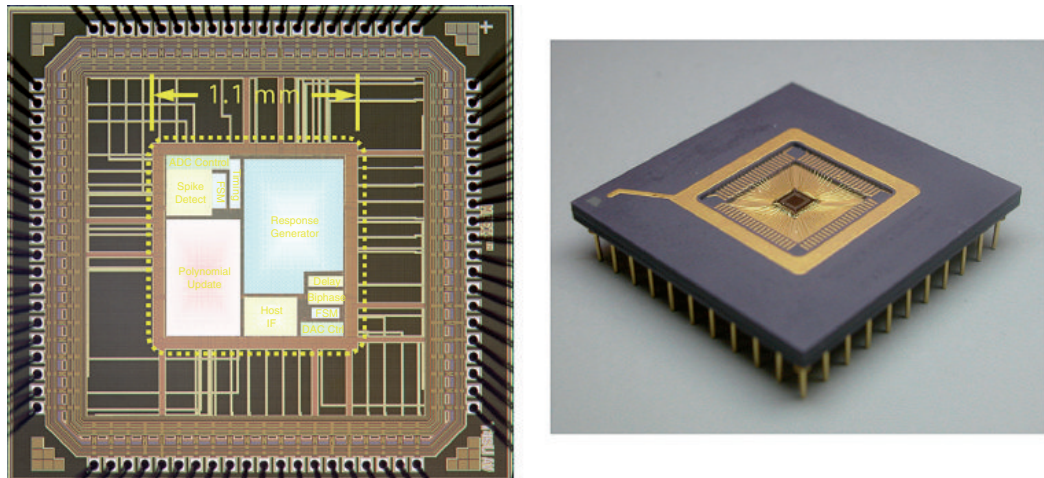
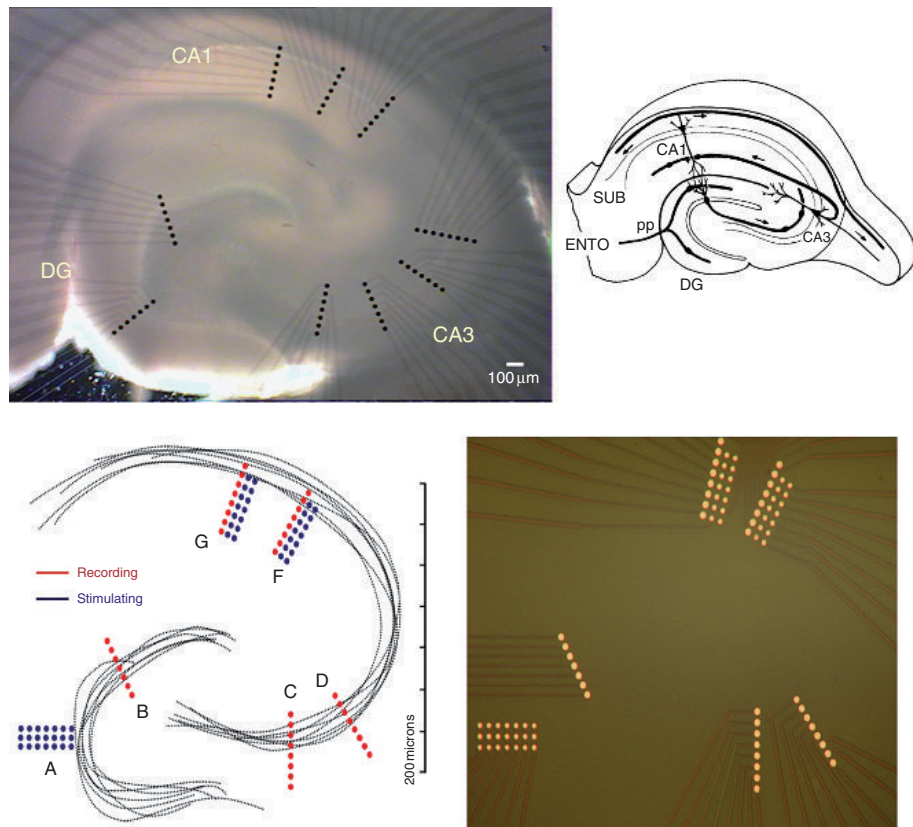
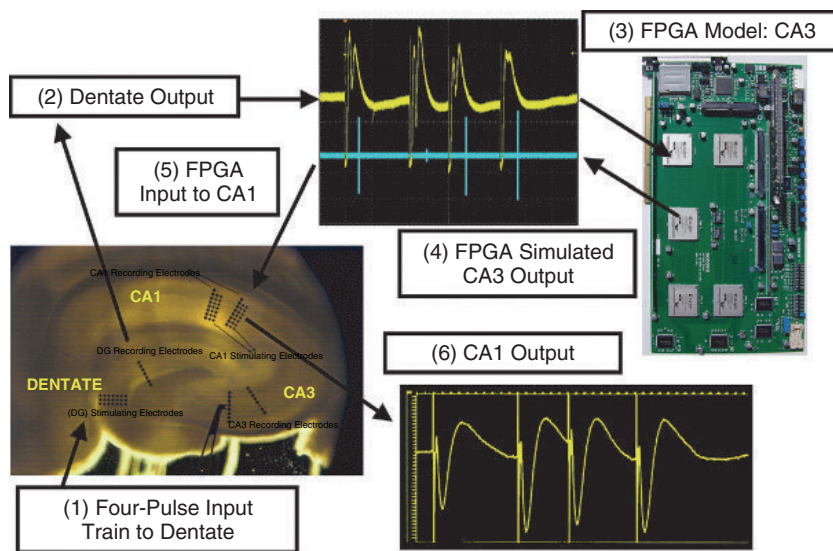


PLATE 29 (A) Comparison of FPGA-based non-linear model predictions of hippocampal CA3 output with biological CA3 output as a function of dentate population spike input for a segment of random impulse train stimulation of perforant path. Predicted (red bars) and electrophysiologically recorded CA3 population spike amplitudes (blue bars) are shown for a segment of random interval train stimulation. Recorded dentate population spike amplitudes for impulses within the random interval train were used as model input. (B) Left: schematic of the VLSI device to substitute for the CA3 region of one hippocampal slice. Right: photograph of the fabricated microchip. (For black and white version, see page 580 in the volume.)



**PLATE 30** Top panels: left, optical photomicrograph of a cMEA incorporating the trisynaptic electrode pad layout that is proximity-coupled to a rat hippocampal slice. The nine sets of seven linearly-spaced 28  $\mu\text{m}$  diameter pads conform to the DG, CA3 and CA1 regions. Right, diagram of hippocampal cell regions. Bottom panels: optical photomicrograph of the central region of a new conformal multielectrode array specifically designed for CA3 replacement demonstration. Stimulating and recording electrodes are arranged in both the DG and CA1 regions, while two sets of recording electrodes are provided in the CA3 region for pre-replacement characterization. (For black and white version, see page 581 in the volume.)



**PLATE 31** System integration of an FPGA-based non-linear model of the CA3 hippocampal region with a hippocampal slice in which the output from the dentate gyrus (mossy fibers in the hilus) have been transected, thus eliminating the normal propagation of activity from dentate $\rightarrow$ CA3 $\rightarrow$ CA1. The FPGA-based model bi-directionally communicates with the living slice through a conformal, planar, multisite electrode array. This system supports real-time, communication of stimulation-induced responses of dentate granule cells from the slice to the FPGA, generation of CA3-like outputs from the FPGA device, FPGA-triggered stimulation of CA1 and recording of electrophysiological output from CA1. (For black and white version, see page 582 in the volume.)

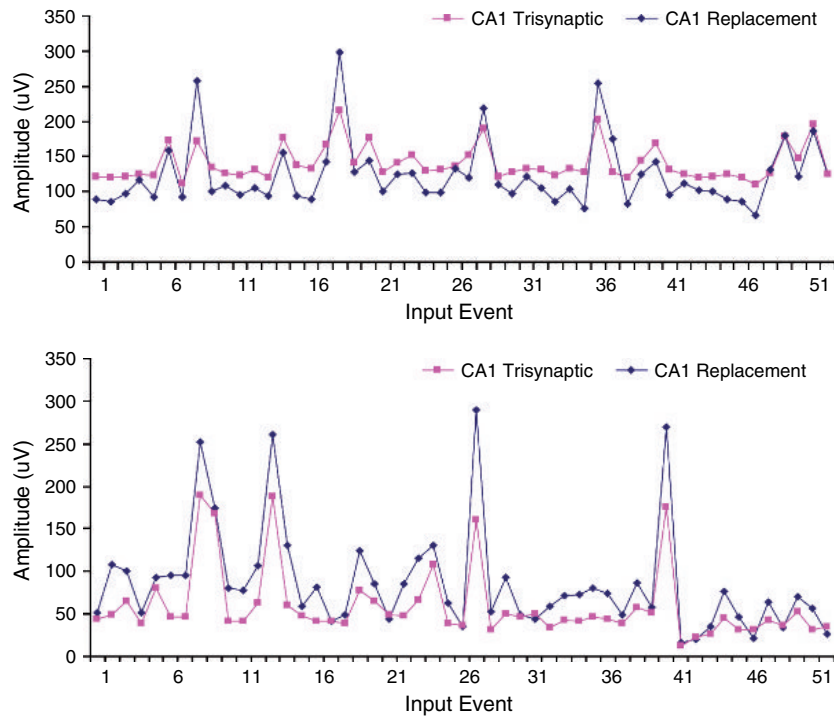


**PLATE 32** A comparison of hippocampal CA1 output in response to the FPGA model of CA3 with the output of CA1 in response to the biological CA3. Examples of results from two random impulse train experiments are shown in the two panels, respectively: amplitudes of population EPSPs recorded from the CA1 region are shown as a function of 50 impulses chosen from among 2400 impulses of the random trains (1200 administered before transecting inputs to CA3; 1200 administered after transection). Time intervals between impulses are not represented in the figures; only ‘Input Event’ number (sequence of sample impulses) is shown to ‘collapse’ the x-axis. Data for the intact slice (CA1 Trisynaptic) are shown in pink boxes; data for the ‘hybrid’ slice with the substituted FPGA model of CA3 (CA1 replacement) are shown in blue diamonds. For what is a wide range of intervals captured in this 50-impulse sequence, and what is a 3–5-fold difference in population EPSP amplitude, note that CA1 output from the ‘hybrid’ slice matches extremely well the CA1 output from the intact slice. (For black and white version, see page 583 in the volume.)

This page intentionally left blank